Revisiting Cu(II) Bound Amyloid-β40 and Amyloid-β42 Peptides: Varying Coordination Chemistries

Orkid Coskuner-Weber* ✉ iD

National Institute of Standards and Technology, Biochemical Reference Data Division, 100 Bureau Drive, Gaithersburg, Maryland 20899 USA, Turkish-German University, Molecular Biotechnology, Şahinkaya Caddesi No. 86, Beykoz, Istanbul 34820 Turkey, The University of Texas at San Antonio, Department of Chemistry, One UTSA Drive, San Antonio, Texas

Abstract: Metal ions and intrinsically disordered peptides amyloid-β40 and amyloid-β42 are at the center of Alzheimer´s disease pathology. Divalent copper ion binds to amyloid-β40 and amyloid-β42 peptides with varying coordination chemistries. Experiments face challenges in the measurements of divalent copper ion bound monomeric amyloid-β40 and amyloid-β42 in an aqueous solution medium because of fast conformational changes, rapid aggregation processes and solvent effects. Theoretical studies complement experiments and provide insights at the atomic and molecular levels with dynamics. However, until recently, potential functions for simulating divalent copper ion bound amyloid-β40 and amyloid-β42 peptides with varying coordination chemistries were lacking. Using new potential functions that were developed for divalent copper centers, Cu(II), including three histidine residues and an oxygen-ligated amino acid residue, the structures and thermodynamic properties of Cu(II)-bound amyloid-β40 and amyloid-β42 peptides in an aqueous solution medium were studied. For these purposes, extensive first principles calculations and replica exchange molecular dynamics simulations were conducted. In this study, the secondary and tertiary structural properties, conformational Gibbs free energy values, potential of mean force surfaces, salt bridges and aggregation propensities of aqueous Cu(II)-bound amyloid-β40 and amyloid-β42 peptides are presented. Different than previous findings in the literature, results clearly show that the coordination chemistry variations impact the structural and thermodynamic properties of divalent Cu(II) bound amyloid-β alloforms in water. Specificities about these differences are revealed in this study at the atomic level with dynamics. Results presented herein are the first to offer a comparison of the monomeric Cu(II)-bound amyloid-β40 and amyloid-β42 peptides with varying coordination chemistries using bonded model potential functions.

INTRODUCTION

Divalent copper ion impact on the aggregation rate of amyloid-β alloforms Aβ40 and Aβ42 is debated in the literature (1). Based on the solution pH, Cu(II) concentration, and the type of fibrillar or amorphous state monitored, both an increase and a decrease of Aβ aggregation have been shown (1-4). A few investigations reported that Cu(II) does not promote aggregation of Aβ (3, 5). On the other hand, several studies show that Cu(II) binding increases non-fibrillar, or amorphous, aggregation of Aβ, especially at low pH (6.6) and physiologically relevant concentrations of Cu(II) (2, 4, 6-16). Additionally, some research studies reported an

increase in oligomer formation while others presented the vice versa (6, 17). Nevertheless, Karr *et al.* reported the formation of fibrillar aggregates for Cu(II)-bound Aβ (18, 19). Moreover, some research groups presented that fibrillar aggregation of Aβ is promoted by Cu(II) at sub-equimolar Cu(II) concentrations, however, amorphous aggregation and spherical oligomer formation of Aβ is enhanced at supra-equimolar concentrations of Cu(II) (11, 20-22). The toxicity of Cu(II)-bound Aβ [Cu(II):Aβ] is also debated in the literature. Both protective and toxic effects have been reported for Cu(II):Aβ (1, 10, 23-27). Many studies report that Cu(II)-binding enhances the neurotoxicity of Aβ (8, 28). However, there are studies that report decreased neurotoxicity of Cu:Aβ in comparison to free Aβ (10, 29). Interestingly, a few studies have presented that Cu:Aβ exhibits significant neurotoxicity at sub-equimolar concentrations that is lost at super-equimolar concentrations (11, 30). Understanding the impact of Cu(II) binding on Aβ structures could aid in deciphering the role of divalent transition metal ions towards aggregation and toxicity in Alzheimer´s disease (AD) pathology. Cu(II) binding impact on the monomeric structures of Aβ including variations between the Aβ40 and Aβ42 alloforms has not yet reached a consensus.

Cu(II) and Aβ coordination chemistry is greatly debated in the literature (18, 19, 31-52). In general, the coordination chemistry of Cu(II) with Aβ is reported to exist as two separate species transition between each other depending on the pH. Species I occurs at low pH values while species II exists at high pH values with the transition between these two species occurring at pH 8 ± 1 (18, 33, 36, 42, 47, 49). The species I structure is proposed to be dominant at physiologically relevant pH. 3N1O coordination mode that is generally agreed upon was presented using extended X-ray absorption fine structure (EXAFS) and electron paramagnetic resonance (EPR) spectroscopies (1). Two main hypotheses regarding the identity of the nitrogen ligands are found in the literature: either three His amino acid residues (His6, His13 and His14) or two His amino acid residues and the N-terminus. Strong evidence for the three His residues coordination mode has been provided by EXAFS, CD and NMR measurements while the two His and N-terminus coordination mode is supported prominently by EPR measurements (1, 9, 33, 36, 41, 42, 45, 54). However, it is important to note that it is possible for both coordination mechanisms to occur due to the intrinsically disordered nature of Aβ (1). Several different candidates for a possible oxygen ligand in the Cu:Aβ metal-ligand sphere have also been proposed (1). Specifically, Glu3, Glu11, the carboxylate group of Asp1, a backbone carbonyl oxygen atom or the phenolate group of Tyr10 have each been presented as a potential Cu(II) coordination ligand in Aβ (1). Out of these potential coordination ligands, Asp1 and Tyr10

have been the most heavily implicated (18, 33, 36, 41). The Asp1 ligand is implicated from EPR measurements of D1N mutant-type and wild-type Aβ that present a modified EPR spectrum upon mutation (18). Despite, Tyr10 is supported by Raman and UV-visible spectroscopies, EXAFS measurements, and EPR studies of Y10A mutant-type Aβ42 with Cu(II) (33, 46-48, 55). Furthermore, Glu3 and water were eliminated as potential ligands based on an EPR study of E3Q Aβ16 and 17O-labelled H_2O (18, 33, 41). We should mention here that several studies including our own have shown that the mutation of a single residue of Aβ significantly alters the conformational ensemble of Aβ, which in turn might affect potential coordination sites differently than wild-type Aβ (56, 57).

Quantum mechanical (QM) techniques can provide valuable information but full-length structure of the transition metal ion-bound proteins cannot be studied using QM (50, 59-72). Therefore, active site truncated models are widely utilized. QM and molecular mechanics (MM) techniques (QM/MM) have also been utilized for investigating metalloproteins (73-83). Resulting simulation accuracies can be influenced by the time scale difference between the QM and MM regions, the treatment and location QM and MM regions boundary, and conformational sampling limitations without using special sampling techniques for enhancing the conformational sampling. Advancement of QM/MM to overcome these disadvantages is currently ongoing in various research groups. MM is the most commonly used technique for investigating the chemical and physical properties of full-length metalloproteins. However, many required force field parameters for the metalloproteins do not exist in the scientific literature. In a previous investigation, first principles calculations to optimize different divalent Cu coordination complexes that contain full-length residues were used: three His residues and a different fourth binding ligand (aspartic acid, tyrosine, or glutamic acid); Cu:His₃Asp, Cu(II):His₃Tyr, and Cu:His₃Glu (84). We developed the missing potential functions for Cu:His₃Asp, Cu:His₃Glu, and Cu:His₃Tyr (84). Using the potential functions for Cu:His₃Glu, the structures and thermodynamic properties of Cu:His₃Glu bound Cu(II):Aβ40 and Cu(II):Aβ42 in an aqueous solution environment using a continuum model for water were studied (85). Recent studies using an explicit model for water show that the confined aqueous volume has a significant impact on the structural and thermodynamic properties of the full-length Aβ peptide (86). In addition, there are studies that report the physical, biological and chemical characteristics of Cu(II):Aβ utilizing smaller fragments instead of using full-length metalloproteins (87). Such investigations are questionable in computing the properties of full-length disordered metalloproteins. Specifically, the fragment size affects the determined Aβ structures in water (88). In addition, Zn(II) force

field parameters were utilized in a few Cu:Aβ investigations because parameters for Cu(II) lacked before we developed those (see, for example, 89). Zn(II) and Cu(II) have varying number of electrons and coordination chemistry specificities; Jahn-Teller effects cannot be ignored. Strodel and co-workers developed a nonbonded model Cu(II) model that includes Jahn-Teller effects (56). However, recent investigations showed that the charge transfer effects and electrostatic charges and between the transition metal ion and biospecies dominate the determined biometallic structures (90-93). Development of force field parameters occurs using nonbonded or bonded models. Full ionic charge without charge transfer is used in nonbonded models. Previous MM studies used Zn(II) potential functions for Cu(II) simulations utilizing a bonded model. We develop the bonded model for potential functions in our studies (84). Kodali *et al.* showed that β-sheet conformation plays a key role in Aβ fibril formation mechanisms (94). NMR measurements presented parallel β-sheet structure within protofilaments (95). The vicinity of Ile41 and Ala42 provides a difference between the primary strutures of Aβ40 and Aβ42. Central hydrophobic core (Leu17-Ala21), turn region (Val24-Asp27) and second hydrophobic region (Gly29-Met35) play central roles in Aβ aggregation (56, 85, 96). Metal:Aβ structures have been investigated heavily using NMR, Fourier transform infrared spectroscopy and X-ray absorption spectroscopy (97-101). Hane *et al.* illustrated that the reactivity of the Aβ peptide increases upon Cu(II) coordination (102). Higher dimerization tendencies upon Cu(II) coordination, which presented that Cu:Aβ becomes more reactive toward Aβ were shown. Additionally, Nair *et al.* showed larger binding affinity values for Cu(II):Aβ than for Zn(II):Aβ, indicating stabilized Aβ aggregation processes with Cu(II) coordination (103). Moreover, Liao et al. studied the conformational transitions of the amyloid-β42 peptide upon Cu(II) binding and pH changes using Hamiltonian-REMD simulations and via utilizing the binding of Cu(II) to Asp and His

residues. They reported that Cu(II) binding and a low pH-mimicking acidosis, linked to inflammatory processes in vivo, accelerate the formation of β-strands in Aβ42 and lead to the stabilization of salt bridges that was previously shown to promote Aβ aggregation. Their results illustrated that Cu(II) binding and mild acidic conditions can shift the conformational equilibrium towards aggregation-prone conformers for the monomeric Aβ42 (57). In an additional study, Strodel and co-workers reported the conformational changes of the Aβ42 dimer upon Cu(II) coordination using the Asp and His coordination nodes via conducting H-REMD simulations (58). They showed that Cu(II) binding, oxidation and a decrease in pH are relevant to the oligomerization of Aβ42. An increased β-sheet content was reported upon Cu(II) binding.

Experiments face challenges in the measurements of Cu:Aβ monomers and oligomers due to rapid aggregation processes, fast conformational changes and solvent effects. Theoretical studies complement experiments and give detailed knowledge that are otherwise challenging to obtain utilizing conventional techniques. Here, we investigated the chemical and physical characteristics of Cu(II):Aβ40 and Cu(II):Aβ42 utilizing the Cu(II):His$_3$Asp and Cu(II):His$_3$Tyr coordination spheres and our new potential functions for these organometallic centers. We simulate and compare the structural and thermodynamic properties of Cu(II):Aβ alloforms utilizing the Cu(II):His$_3$Asp and Cu(II):His$_3$Tyr coordination spheres to those of Aβ and Cu(II):Aβ along with the Cu(II):His$_3$Glu coordination sphere. For these purposes, the structural and thermodynamic properties were investigated dynamically at the atomic level. To the best of our knowledge, this study represents the first investigation of Cu(II)-bound Aβ40 and Cu(II)-bound Aβ42 alloforms´conformational changes with varying coordination chemistries using a bonded model for the Cu(II) ion.

Aβ40/Aβ42: DAEFRHRSGYEVHHQKLVFFAEDVGSNKGAIIGLMVGGVV(I)(A)
Scheme 1. Primary structure of Aβ40 and Aβ42.

MATERIALS AND METHODS

Ab Initio Quantum Chemical Studies: First principles calculations were performed using the Becke, 3-parameter, Lee-Yang-6 Parr (B3LYP) hybrid functional utilizing the 6-31G*, 6-31G**, cc-pVDZ, ahlrichs-vdz, ahlrichs-vtz, def2-svpd, def2-tzvp and lanl2dz-ecp basis sets in extensive separate sets of calculations (104). In order to determine the structural properties and binding affinities as well as the impact of the chosen basis set on the Cu(II):His$_3$(H$_2$O), Cu(II):His$_3$Tyr, Cu(II):His$_3$Asp and Cu(II):His$_3$Glu organometallic complexes, we performed

separate sets of first principles calculations. We optimized the structures of Cu(II):His$_3$(H$_2$O), Cu(II):His$_3$Tyr, Cu(II):His$_3$Asp, Cu(II):His$_3$Glu, H$_2$O, Asp, Tyr, Glu and Cu(II):His$_3$ to estimate the binding affinities of H$_2$O, Asp, Glu and Tyr with the same receptor; Cu(II):His$_3$ using different basis sets for gaining insights into the impact of the chosen basis set on the predicted structures and energetics.

Replica Exchange Molecular Dynamics Simulations: To simulate the Cu(II):Aβ40 and Cu(II):Aβ42 alloforms using varying coordination chemistries; Cu(II):His$_3$Asp and

Cu(II):His$_3$Tyr coordination chemistries through a bonded model for the metal-ligand moiety, which embraces electrostatic interactions, the potential functions for the distorted square planar Cu(II):His$_3$Asp and Cu(II):His$_3$Tyr moieties utilizing full-size metal-ligand complexes and extensive first principles calculations were developed (84). These first principles calculations were validated by experiments and initial structures were generated using first principles calculations (84). Initial Cu(II):His$_3$Asp and Cu(II):His$_3$Tyr structures from first principles to the full-length Aβ40 and Aβ42 peptides´ residues were connected. REMD simulations were conducted utilizing these potential functions for the metal-ligand moities along with the Amber ff99SB parameters for the protein with which the potential functions are compatible with (84, 105-107). Furthermore, same parameters for the wild-type Aβ40, Aβ42, Zn(II):Aβ40, Zn(II):Aβ42, Cu(II):Aβ40 and Cu(II):Aβ42 with the Cu(II):His$_3$Glu coordination sphere were used before and the usage of the same sets of parameters is required for more accurate comparison reasons with these species (85, 88, 107). Additional simulations using the Amber ff14SB parameters and the TIP5P model for water were conducted (Supplementary information section; Fig. S1A and Fig. S1B). The correlations between Cα and Hα chemical shift values for the Aβ42 peptide in aqueous solution utilizing the structures from our simulations and experimental chemical shift values provided by Dr. Michael Zagorski (CWRU) are presented in Fig. S2A and Fig. S2B (supplementary information). Following previous investigations for comparison reasons, the Onufriev-Bashford-Case generalized Born implicit solvent model was used along with the particle mesh Ewald summation method with a cut-off value of 25 Å (105-108 and references therein). Langevin dynamics with a collision factor of 2 ps^{-1} was used to control the temperature (107). Structures were first equilibrated for 500 ps for each replica and trajectories were saved for every 500 steps. The integration time step for each replica was 2 fs. Exchange attempt time interval between different replicas was set to 5 ps and 16 replicas were used with exponentially distributed temperatures between 280 K and 408 K (56, 88, 96, 104, 108, 109). The production total time was 51.2 μs. To test the convergence, time-dependent secondary structure component abundances were used (see the supplementary information section; Fig. S3A and Fig. S3B). Results presented that the systems require 60 ns of the simulation time to converge, which is in agreement with previous studies (56, 85, 88, 96, 108-110). Physiological temperature results are reported.

We should mention here that simulations using an implicit model for water for overcoming the confined aqueous density effects do not embrace intermolecular hydrogen bonding interactions between the metallopeptides and the solvent molecules. Specific heat value for pure liquid water does not remain constant in parallel tempering replica exchange molecular dynamics simulations (111). Most recently, we showed that the secondary and tertiary structures as well as the thermodynamic properties of Aβ40 and Aβ42 are affected by the confined aqueous volume effects using an explicit model for water (86). Nevertheless, we also investigated the influences of intermolecular interactions between solute and solvent using our own explicit model for water (modified TIP5P) (109). These studies showed that the structural properties are affected by the usage of implicit/explicit water models. Thermodynamic trends are not affected by the usage of implicit or explicit water models. Following recent studies, the thermodynamic properties were investigated using the molecular mechanics/Poisson-Boltzmann surface area method and potential of mean force surfaces (83, 85, 86, 88, 96, 108-112). For the potential of mean force (PMF) surfaces, the coordinates of the end-to-end distances were used along with the radius of gyration values (56, 83, 85, 96, 108, 109). The software DSSP was used for predicting the secondary structure components and their abundances (56, 83, 85, 96, 108, 109, 113). Intra-molecular interactions exist when the two centers of mass of two residues are within a distance of 9.0 Å. Furthermore, a hydrogen bond exists when the same distance between the donor hydrogen atom and acceptor atom is less than or equals to 2.5 Å along with a criteria for the hydrogen bond angle (≥ 113°) (56, 83, 85, 96, 108, 109). A salt bridge exists between hydrogen bonded atoms with opposite electrostatic charges. The method developed by Pawar et al. for calculating the intrinsic aggregation propensities of individual amino acids was utilized (114).

RESULTS AND DISCUSSION
Figure 1 shows the optimized structures of the Cu(II):His$_3$(H$_2$O), Cu(II):His$_3$Tyr, Cu(II):His$_3$Asp and Cu(II):His$_3$Glu complexes at the DFT level.
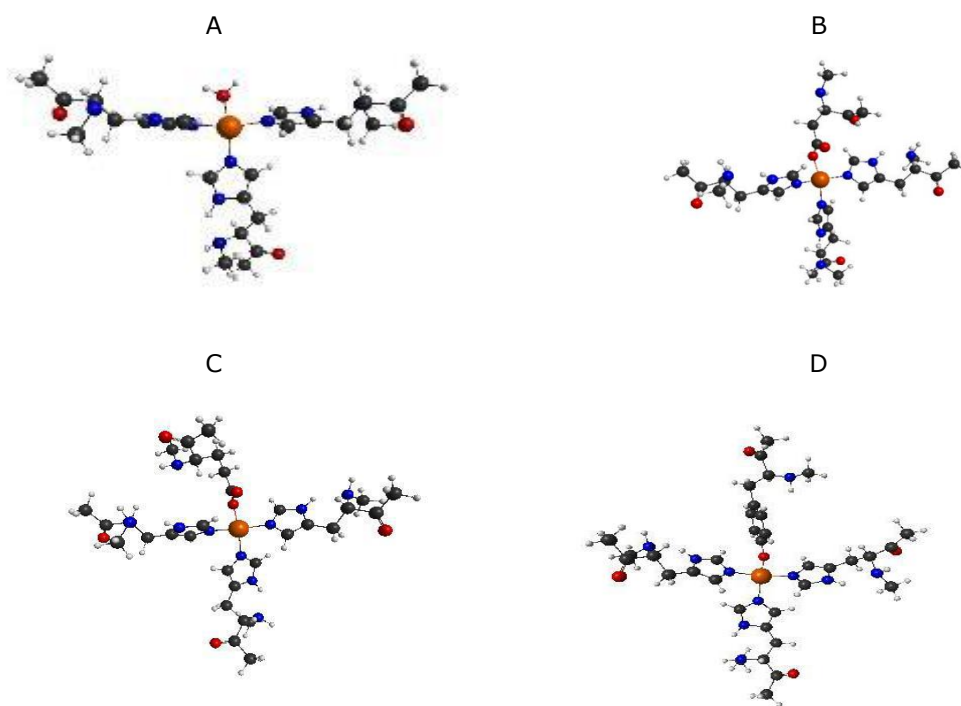
Figure 1. Optimized structures of (A) Cu(II):His$_3$(H2O), (B) Cu(II):His$_3$Asp, (C) Cu(II):His$_3$Glu and (D) Cu(II):His$_3$Tyr using the B3LYP functional along with the def2-tzvp basis set.

Figures S4 and S5 in the supplementary information section present the calculated bond distances - using varying basis sets - between Cu(II) and coordinating N and O atoms. Figure S6 in the supplementary information section depicts the optimized bond angles between coordinating residue atoms and Cu(II). Tables 1-4 present the total energies and binding energies for Cu(II):His$_3$(H$_2$O), Cu(II):His$_3$Tyr, Cu(II):His$_3$Asp and Cu(II):His$_3$Glu using all basis sets at the B3LYP level of theory. As expected, the smallest energy is obtained utilizing the def2-tzvp basis set for Cu(II):His$_3$(H$_2$O), Cu(II):His$_3$Tyr, Cu(II):His$_3$Asp and Cu(II):His$_3$Glu. Cu(II):His$_3$Tyr is energetically the most stable structure (-3930.6288 H) while Cu(II):His$_3$(H$_2$O) possesses the largest energy with a value of -3373.7600 H utilizing the def2-tzvp basis set. The order in stability follows: Cu(II):His$_3$Tyr > Cu(II):His$_3$Glu > Cu(II):His$_3$Asp > Cu(II):His$_3$(H$_2$O). Overall, the calculated binding energies of the Asp, Glu, Tyr and H$_2$O show that these bindings to the Cu(II):His$_3$ complex is preferred. The order of binding energies from the largest negative to the smallest negative value is (Tables 1-4): Asp > Glu > Tyr > H$_2$O. The same trend was obtained by Mantri *et al.* for Asp, Glu and Tyr residues (139). Cu(II):His$_3$(H$_2$O) has 14 heteroatoms, Cu(II):His$_3$Tyr possesses 17 heteroatoms while Cu(II):His$_3$Glu and Cu(II):His$_3$Asp each have 16 heteroatoms.

Quantum chemical energetics is not related to the number of heteroatoms and yields usually large amount of total energies as expected. For instance, Xu *et al.* calculated the binding energy using the B3LYP/6-31G(d) level of theory between Cu(II) and of different conformations of a smaller fragment Aβ16 and reported binding energies that vary between -911.73 kcal/mol and -415.78 kcal/mol (87). MacKerell and co-workers reported about 10 kcal/mol energy difference just for the anti and syn conformations of deoxyribonucleosides (138). Moreover, Rickard et al. calculated the binding affinities for model biologically available potential Cu(II) ligands relevant to Alzheimer´s disease using smaller models and the B3LYP/6-31G(d) level of theory utilizing the COSMO model for water and their energetics shows that the addition of one water molecule to a much smaller model compound namely Cu(II):(H$_2$O)$_3$ has an enthalpy change of 170.8 kJ/mol (68). Furthermore, Mantri *et al*. reported binding Gibbs free energies that vary between -45.34 kcal/mol and -95.06 kcal/mol for small model comlexes representing Asp, Glu, Ser and Tyr binding to Cu(II):His$_3$ (139) using the B3LYP/6-31G** level of theory. However, we should note that these calculations were conducted in the gas phase or using a continuum model for water at the electronic level and these results might change with the inclusion of explicit water molecules.

Table 1. The total energies calculated for Cu(II):His$_3$(H2O), Cu(II):His$_3$ and H$_2$O using the optimized structures with each basis set and through performing single point energy calculations on Cu(II):His$_3$ and on water. The binding energy of water was calculated as well.

Basis Set	Cu(II):His$_3$(H$_2$O) Total Energy (Hartree)	Cu(II):His$_3$ Total Energy (Hartree)	H$_2$O Total Energy (Hartree)	Binding Energy (kcal mol^{-1})
6-31G*	-3372,8092	-3296,3527	-76,4086	-30,04
6-31G**	-3372,8886	-3296,4214	-76,4194	-29,98
cc-pVDZ	-3373,2398	-3296,7751	-76,4215	-27,13
Ahlrichs-VDZ	-3370,9786	-3294,6068	-76,3202	-32,41
Ahlrichs-VTZ	-3373,0694	-3296,5641	-76,4303	-47,07
Def2-SVPD	-3371,7909	-3295,3767	-76,3817	-20,43
Def2-TZVP	-3373,7600	-3297,2626	-76,4635	-21,32
LANL2DZ-ECP	-1928,3955	-1851,9338	-76,4141	-29,84

Table 2. The total energies calculated for Cu(II):His$_3$Asp, Cu(II):His$_3$ and Asp using the optimized structures with each basis set and through performing single point energy calculations on Cu(II):His$_3$ and Asp. The binding energy of Asp was calculated as well.

Basis Set	Cu(II):His$_3$Asp Total Energy (Hartree)	Cu(II):His$_3$ Total Energy (Hartree)	Asp Total Energy (Hartree)	Binding Energy (kcal mol^{-1})
6-31G*	-3811,7815	-3296,3404	-515,1076	-209,26
6-31G**	-3811,8657	-3296,4086	-515,1234	-209,47
cc-pVDZ	-3812,2382	-3296,7658	-515,1468	-204,31
Ahlrichs-VDZ	-3809,4736	-3294,5954	-514,5541	-203,43
Ahlrichs-VTZ	-3812,0431	-3296,5843	-515,1528	-192,02
Def2-SVPD	-3810,4886	-3295,3678	-514,8192	-189,27
Def2-TZVP	-3812,9076	-3297,2553	-515,3487	-190,48
LANL2DZ-ECP	-2367,2858	-1851,9257	-515,0489	-195,26

Table 3. The total energies calculated for Cu(II):His$_3$Glu, Cu(II):His$_3$ and Glu using the optimized structures with each basis set and through performing single point energy calculations on Cu(II):His$_3$ and Glu. The binding energy of Glu was calculated as well.

Basis Set	Cu(II):His$_3$Glu Total Energy (Hartree)	Cu(II):His$_3$ Total Energy (Hartree)	Glu Total Energy (Hartree)	Binding Energy (kcal mol^{-1})
6-31G*	-3851,0868	-3296,3408	-554,4208	-204,08
6-31G**	-3851,1741	-3296,4082	-554,4399	-204,53
cc-pVDZ	-3851,5482	-3296,7661	-554,4644	-199,41
Ahlrichs-VDZ	-3852,2307	-3294,5966	-553,8326	-193,93
Ahlrichs-VTZ	-3851,3476	-3296,5842	-554,4694	-184,51
Def2-SVPD	-3849,7721	-3295,3690	-554,1103	-183,75
Def2-TZVP	-3852,2284	-3297,2556	-554,6771	-185,58
LANL2DZ-ECP	-2406,5832	-1851,9249	-554,3595	-187,49

Table 4. The total energies calculated for Cu(II):His$_3$Tyr, Cu(II):His$_3$ and Tyr using the optimized structures with each basis set and through performing single point energy calculations on Cu(II):His$_3$ and Tyr. The binding energy of Tyr was calculated as well.

Basis Set	Cu(II):His$_3$Tyr Total Energy (Hartree)	Cu(II):His$_3$ Total Energy (Hartree)	Tyr Total Energy (Hartree)	Binding Energy (kcal mol^{-1})
6-31G*	-3929,4664	-3296,3397	-632,8107	-198,28
6-31G**	-3929,5567	-3296,4081	-632,8326	-198,28
cc-pVDZ	-3929,9291	-3296,7584	-632,8617	-193,90
Ahlrichs-VDZ	-3927,0554	-3294,5935	-632,1596	-189,65
Ahlrichs-VTZ	-3929,7332	-3296,5793	-632,8595	-184,76
Def2-SVPD	-3928,1050	-3295,3656	-632,4493	-182,00
Def2-TZVP	-3930,6288	-3297,2536	-633,085	-181,79
LANL2DZ-ECP	-2484,9517	-1851,9234	-632,7333	-185,12

These findings are in accord with the calorimetric measurements conducted by Farkas and co-workers (115). Specifically, they presented more stable Cu(II):Asp and Cu(II):AspGly complexes as to the Cu(II):Glu and Cu(II):GluGly species, respectively. Moreover, Gassmann and co-workers showed that Asp is more firmly coordinated to Cu(II)-L-His than Glu (116) using electrophoresis. Same migration time tendency was also shown for Cu(II)-aspartame (117). These experimental results support our theoretical findings. Zare and co-authors showed a quicker migration time for Tyr as to Glu and Asp through capillary electrophoresis measurements (116, 117). However, this result could be caused by the utilization of di-dansyl-tyrosine in their measurements that yields a complex with different charge as to Cu(II) complexes with Asp or Glu, which decreases the migration time instead of tighter coordination. In excellent agreement with our theoretical results, the fluorescence measurement data indicate that Asp is more firmly coordinated to Cu(II)-L-His than Tyr. In addition, Rickard and co-authors conducted first principles calculations on Cu(II) species with either CH_3S^-, NH_3, 4-CH_3-imidazole, CH_3NH_2, $C_6H_5O^-$, or $CH_3CO_2^-$ to study possible coordinating amino acid moieties and the other three coordinating moeities represented by NH_3 or H_2O (68). Specifically, they presented that $CH_3CO_2^-$ binding is preferred over $C_6H_5O^-$ binding when the other ligands are nitrogen atoms and thus Asp and Glu binding is more favorable than Tyr binding, which is in excellent accord with our investigations using full-length amino acid ligands.

In this study, we have performed a detailed investigation of the structural and thermodynamic properties along with aggregation propensities of Cu(II)-bound Aβ40 and Aβ42 in aqueous solution using the new potential functions (84). Furthermore, we investigate the differential impact of different proposed coordination mechanisms of the species I coordination complex including three histidine residues. To the best of our knowledge, this is the first study to present the structural and thermodynamic differences upon Cu(II) binding via either the His$_3$Asp1 or His$_3$Tyr10 residues to the Aβ40 and Aβ42 peptides using the new potential functions. Results are compared to those obtained for Cu(II):Aβ40 and Cu(II):Aβ42 with Cu(II) binding via the His$_3$Glu11 residues and to those of apo Aβ (85, 88). Furthermore, results reveal that varying coordination chemistries and alloforms impact the calculated structural and thermodynamic properties.

The calculated average thermodynamic properties; enthalpy (*H*), entropy (*S*) and Gibbs free energy (*G*) for the apo and Cu(II)-bound Aβ alloforms including all three simulated binding sites are listed in Table 5. The conformational free energy values (*G*) indicate that the free Aβ40 and Aβ42 structures are more favorable than their Cu(II)-bound counterparts regardless of the chosen Cu(II) coordination chemistry. Specifically, the Cu(II)-bound Aβ40 and Aβ42 structures are less preferred than the free Aβ40 and Aβ42 structures by at least 500 kJ mol^{-1}. This result illustrates that Aβ40 and Aβ42 aggregation is increased upon Cu(II) binding since the reactivity of Cu(II):Aβ is increased due to less stability as to apo Aβ . Therefore, our results are in accord with experiments that report an increase in Cu(II)-bound Aβ peptide aggregation (2, 6, 8, 15, 17, 118, 119). We do observe that there is a difference in the thermodynamic preference of the Cu:Aβ structures that depends on the coordination chemistry. Cu(II)-bound Aβ40 peptide structures are less preferred than the

free-Aβ40 peptides by 930.1 kJ mol^{-1}, 589.0 kJ mol^{-1}, and 794.8 kJ mol^{-1} for the Cu:His$_3$Asp1, Cu:His$_3$Glu11 and Cu:His$_3$Tyr10 binding sites, respectively. For the Aβ42 peptides, the Cu(II)-bound peptides are less preferred than the free Aβ42 peptide by 886.8 kJ mol^{-1}, 536.2 kJ mol^{-1}, and 735 kJ mol^{-1} for the Cu:His$_3$Asp1, Cu:His$_3$Glu11 and Cu:His$_3$Tyr10 binding sites, respectively. This result suggests that the coordination chemistry involving the Glu11 residue results in the most preferred Cu(II)-bound Aβ conformations while the coordination chemistry involving the Asp1 residue results in the least preferred Cu(II)-bound Aβ conformations, regardless of the chosen alloform. Xu *et al.* reported binding Gibbs free energy values for different Cu(II) and Aβ16 conformations (not full-size Aβ40/Aβ42) that vary between -1288 kJ/mol and 303 kJ/mol (87). Furthermore, they reported that Cu(II)-bound Aβ16 species are by 232.7-420.9 kJ/mol less stable than the free Aβ16 peptide. However, we should note here that their force field parameters were not developed using full-length amino acid residues but model small size imidazole, acetic acid, and formamide structures. Moreover, Mantri *et al.* reported a less favorable potential energy by up to 477 kJ/mol for Cu(II)-bound Aβ42 in comparison to free Aβ42 (139). These trends

are in agreement with our findings. Due to the assumption that the least thermodynamically preferred metallopeptide structures are more likely to aggregate (56, 83, 85, 88, 96, 108, 109), our results also indicate that the coordination chemistry can influence the aggregation rate as well. Therefore, the aggregation rate of the Cu(II)-Aβ alloforms depending on the coordination chemistry would be on the order of Cu:His$_3$Glu < Cu:His$_3$Tyr < Cu:His$_3$Asp for both Aβ alloforms. In addition to the binding site differences, we also note that the Cu(II)-bound Aβ40 structures are more preferred than Cu(II)-bound Aβ42 structures by between 56.2 and 72.7 kJ mol^{-1}, which is the same trend observed for the free Aβ40 and Aβ42 alloforms with a difference of 116.0 kJ mol^{-1} (56, 85, 88, 96). Therefore, we predict that the Cu(II)-bound Aβ42 alloforms will aggregate more readily than the Cu(II)-bound Aβ40 alloforms regardless of the Cu(II) ion coordination chemistry. The same trend is also observed for the apo-Aβ40 and Aβ42 alloforms ($\Delta G_{A\beta40-A\beta42}$ = -116.0 kJ mol^{-1}), which agrees with experimentally reported increased aggregation rates of the Aβ42 peptide in comparison to the Aβ40 peptide in aqueous solution (2, 6, 8, 15, 17, 118, 119).

Table 5. The calculated enthalpy (*H*), entropy (-*TS*), and Gibbs free energy (*G*) of the simulated Cu(II)-bound Aβ40 and Aβ42 alloforms with varying coordination chemistries in aqueous solution.

	<*H*> (kJ mol^{-1})	**-*T*<*S*> (kJ mol^{-1})**	**<*G*> (kJ mol^{-1})**
apo-Aβ40	-2788.2 (±55.6)	-2114.4 (±9.9)	-4902.5 (±45.9)
Cu:His$_3$Asp1-Aβ40	-1884.7 (±43.0)	-2087.7 (±9.4)	-3972.4 (±33.8)
Cu:His$_3$Glu11-Aβ40	-2232.4 (±11.1)	-2081.0 (±0.8)	-4313.5 (±10.7)
Cu:His$_3$Tyr10-Aβ40	-1998.8 (±46.1)	-2109.0 (±12.8)	-4107.7 (±33.8)
apo-Aβ42	-2579.9 (±24.2)	-2206.6 (±4.1)	-4786.5 (±20.3)
Cu:His$_3$Asp1-Aβ42	-1719.1 (±13.4)	-2180.6 (±7.4)	-3899.7 (±7.2)
Cu:His$_3$Glu11-Aβ42	-2072.7 (±19.4)	-2177.6 (±3.2)	-4250.3 (±16.6)
Cu:His$_3$Tyr10-Aβ42	-1854.2 (±27.6)	-2197.4 (±6.4)	-4051.5 (±21.3)

Aβ accumulation inhibition in transgenetic mice utizilizing Cu chelators was reported by Bush and co-workers (2, 23). Additionally, the same group presented a high affinity for Cu coordination with Aβ42 in the presence of trace divalent copper ion contamination (2, 23, 119). However, they also presented that Cu(II) coordination with Aβ40 has lower affinity and thus they expected less self-aggregation for Aβ40. The less favorable coordination of Cu(II) with Aβ40 and Aβ42 in comparison to our earlier studies regarding Zn(II):Aβ40 and Zn(II):Aβ42 is also noted in our investigations. We anticipate though an increased propensity toward species that play a role in oligomerization and fibrillization because of larger conformational Gibbs free energy values (see Table 5 and Ref. 85 and

96). Furthermore, the coordination of these transition metals with Aβ40 via fluorescence spectroscopy was investigated by Palumaa *et al.* (39). They found that Cu(II) and Aβ40 bind to one another and that Cu:Aβ40 is active toward other species in the solution. Thermodynamic results (Table 5) including those that we presented for Zn(II):Aβ40 and Zn(II):Aβ42 (96) as well as Cu(II):Aβ with a Cu:His$_3$Glu coordination site (85) present that Cu(II):Aβ40 is expected to be active toward ligands because of its larger Gibbs free energy and associated reduced conformational stability in comparison to Zn(II):Aβ40. Additionally, Atwood and co-workers showed that Cu:Aβ is reactive toward other ligands and reported dityrosine croos-linking for Cu:Aβ (28, 120, 121). NMR measurements by

Zagorski and co-workers showed that Cu(II) coordination with Aβ yields nonfibrillar amorphous conformations and fast aggregation (9). Even though Cu(II):Aβ interacted with other compounds and disturbed high-quality K_D measurements of Cu(II) with Aβ, Faller reported the dissociation constants for Cu(II) and Zn(II) in an aqueous solution medium at neural pH as 10 to 200 pM and 1 to 20 µM, respectively (122). The binding of Cu(II) to NTA (chelator) influenced the accuracy of these measurements because Cu:NTA has a similar K_D value to Cu:Aβ (122). Smaller dissociation constants for Cu(II):Aβ in comparison to Zn(II):Aβ may be due to the different thermodynamic stabilities that we report here and in our previous studies. Experiments presented also similar binding affinities for Zn:Aβ40 and Zn:Aβ42 and our conformational Gibbs free energies that we reported recently for Zn:Aβ40 and Zn:Aβ42 are similar (124, 125).

Experiments presented that the aggregation building blocks are monomeric Cu(II):Aβ and Zn(II):Aβ in 1:1 ratio utilizing NMR spectroscopy and chromatography measurements (121-124). Cu(II) and Aβ40 were shown to form stable but soluble 1:1 species, however, K_D meauserements were influenced by buffer complexes that bound to Cu(II) as ligands (39). An active Cu(II):Aβ complex toward buffer species is expected because of our greater Gibbs free energy values for Cu(II):Aβ40 and Cu(II):Aβ42 that are presented in Table 5 in comparison to our values that we recently showed for Zn(II):Aβ40 and Zn(II):Aβ42 (96). Extensive studies were performed for gaining insights into the reversible formation of Cu(II) and Zn(II) complexes with Aβ (see Ref. 39). The binding affinity values fluctuate enormously, for instance, values varying between 10 nmol/L to 300 µmol/L were reported for Zn(II):Aβ (96). Values fluctuating between 0.1 nmol/L – 10 µmol/L were reported for Cu:Aβ (124-127). Thermodynamic studies provide insights onto these debates since experiments yield uncertainties in the vicinity of buffers. Moreover, our investigations support those of Hane *et al.* They presented greater dimerization tendencies for Aβ upon Cu(II) coordination (15). These findings present a less stable but more reactive monomeric Cu:Aβ toward Aβ. Amorphous structures were reported for Zn:Aβ while more ring-like and extended conformations were shown for Cu:Aβ, which in turn results in Cu:Aβ adopting varying oligomerization and fibrillization processes (see below tertiary structural properties subsection) (125-127).

In addition to the conformational Gibbs free energies, we evaluated the conformational favorabilities of the free and Cu(II)-bound Aβ40 and Aβ42 peptides via potential of mean force (PMF) calculations along in conjunction with end-to-end distance (R_{E-E}) and radius of gyration (R_g) (Figures 2A and 2B). In our previous works, we have shown that this method reveals differences in the conformational ensembles resulting from alloform length, mutation and zinc coordination (56, 85, 88, 96, 108, 109). Figure 2A displays the PMF surfaces for the free Aβ40 and Cu(II):Aβ40 peptides including different Cu(II) binding sites. Favorable PMF basins located at R_g values from 10.75 Å to 11.75 Å for basin IA and from 9.1 Å to 13.2 Å for basin IB and at R_{E-E} values varying from 10 Å to 17 Å for basin IA and from 17.6 Å to 34.8 Å for basin IB are detected. Paramounting energy barriers larger than 1 k_BT is required for structural transformation between basins IA and IB. Upon Cu(II) coordination via the His$_3$Asp1 binding site, the basin IA R_{E-E} values shift to 2.5 Å to 5 Å (Cu(II):His$_3$Asp1-Aβ40, basin IA) and basin IB shifts to R_g values between 9.5 Å to 10.5 Å along with R_{E-E} values 7.5 Å to 17.5 Å. The energy barrier for transitions between these two preferred basins is increased to greater than 2 k_BT. On the other hand, for the Cu(II)-bound structures utilizing the His$_3$Glu11 binding site, only one preferred basin is present at R_g values of 9.5 Å – 11 Å along with R_{E-E} values of 7.5 Å – 35 Å. Transitions between the structures located in this basin do not desire overriding large energy barriers. For the Cu:His$_3$Tyr10-Aβ40 peptide, basin IA is similarly located in comparison to the apo-Aβ40 peptide with R_g values of 10.25 Å – 11.3 Å and R_{E-E} values of 10.5 Å – 16.5 Å. However, the basin IB structures have a smaller range of R_g values (9.75 Å – 10.75 Å) and R_{E-E} values in comparison to the apo-Aβ40 structures even though transition between the two basins still require overriding energy barriers with a height of greater than 1 k_BT.

The PMF surfaces along R_g and R_{E-E} for the wild-type and free and Cu(II):Aβ42 peptides are presented in Figure 2B. Aβ42 shows two preferred basins located at R_g values of 10.5 Å – 11.6 Å and 10.1 Å – 10.9 Å and R_{E-E} values of 10 Å – 17 Å and 24 Å – 32 Å. Overriding of these two preferred basins via transitions needs energies of greater than 1 k_BT. Upon Cu(II) binding via the His$_3$Asp1 amino acid residues, the basin IA R_{E-E} values shift to between 2.5 Å to 5 Å, which is similar to the affect of Cu(II) binding via the His$_3$Asp1 coordination chemistry to the Aβ40 peptide. However, basin IB R_g and R_{E-E} values are expanded to 9.6 Å – 11.4 Å and 6 Å – 25.5 Å, respectively. This increase of R_g and R_{E-E} in the basin IB structures is the vice versa trend of that observed for Cu(II) binding via the same

coordination chemistry of the Aβ40 alloform. In addition, basin transitions require paramounting energy barriers of greater than 1 k_BT and not greater than 2 k_BT as observed for the Aβ40 alloform. Interestingly, the Cu:His$_3$Asp1-Aβ42 peptide also exhibits a third preferred PMF basin (basin IC) at R_g values of 13.7 Å – 14.2 Å and R_{E-E} values of 15.5 Å – 17.5 Å. Transitions between the basin IC structures and the basin IA or basin IB structures involve overriding energy barriers of greater than 2 k_BT. For the Aβ42 structures that bind Cu(II) via the His$_3$Glu11 binding site, two preferred basins are detected. These have R_g values of 9.8 Å – 11 Å for basin IA structures and 10.1 Å – 10.8 Å for basin IB structures along with R_{E-E} values of 5.5 Å – 16 Å and 20 Å – 27.5 Å, respectively. Larger than 1 k_BT barriers exist between these preferred basins. This effect of the Cu(II):Aβ42 with the

Cu:His$_3$Glu11 binding site shows different trends than for Cu(II):Aβ40, which possesses a single preferred basin (see above). Regarding the Cu:His$_3$Tyr10-Aβ42 peptide, we observe a single most preferred PMF basin at R_g values of 10.1 Å – 11.5 Å along with R_{E-E} values of 9.5 Å – 22.5 Å, which is a different conformational ensemble than the two favorable PMF basins presented for the Cu(II):His$_3$Tyr10-Aβ42 peptide. Overall, these data present that the Cu(II) binding to the Aβ40 and Aβ42 alloforms impacts the conformational ensemble of these two peptides and that the effect on the conformational ensemble depends on the chosen coordination site. Furthermore, the impact of Cu(II) coordination - depending on the coordination chemistry of the Cu(II) ion - varies between the two different Aβ alloforms.
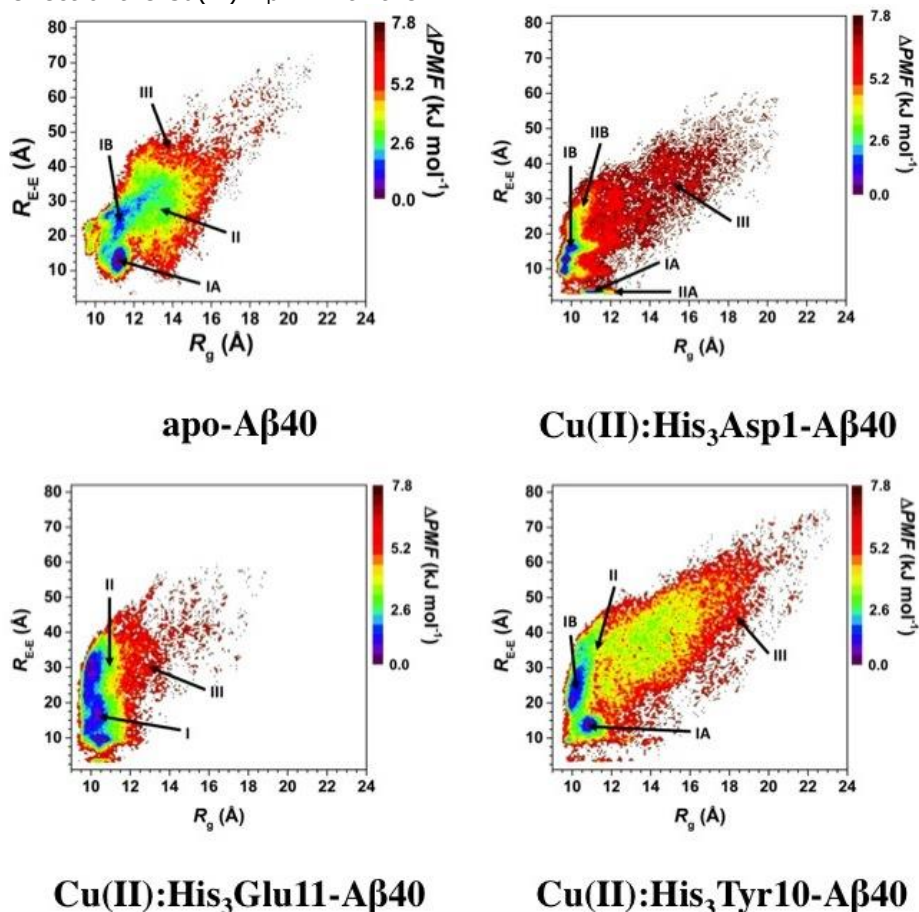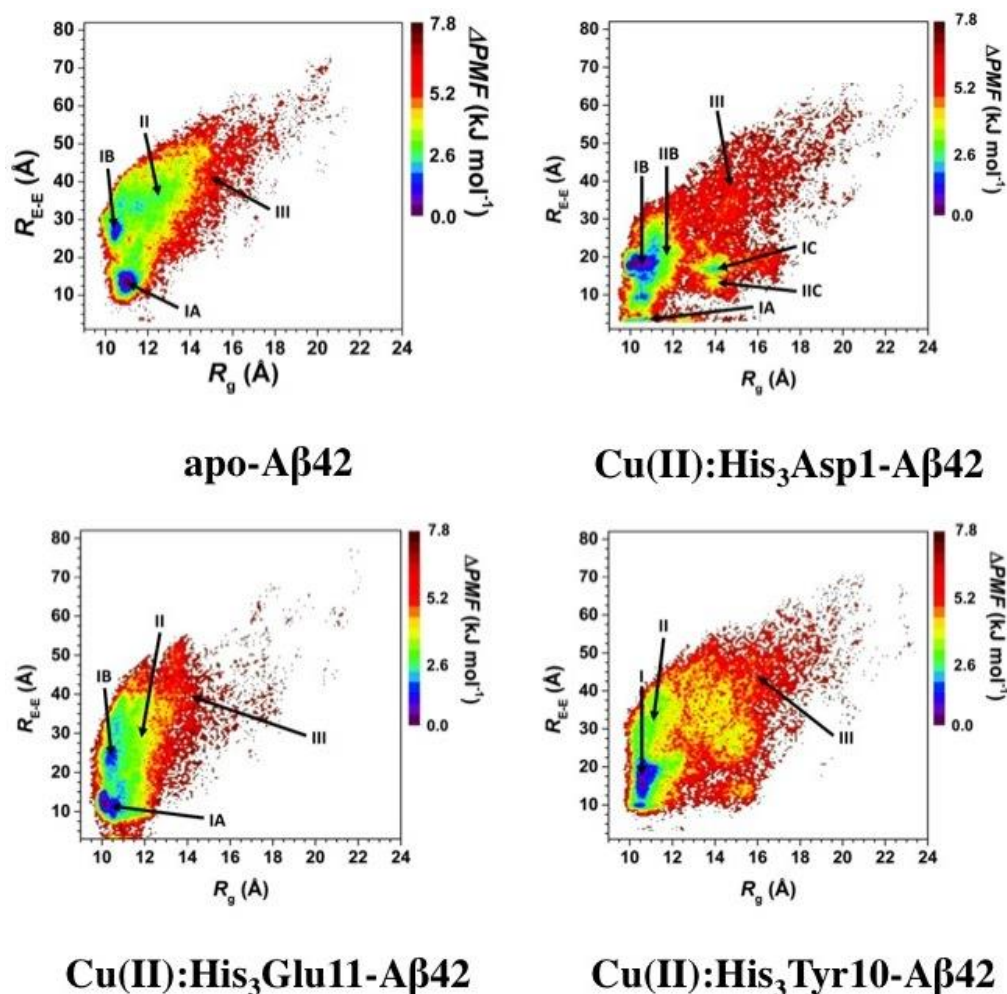

Figure 2A. Potential of Mean Force Surfaces of the apo and Cu(II)-bound Aβ40 Peptides. Potential of mean force (ΔPMF) of the Aβ40, Cu(II):His$_3$Asp1-Aβ40, Cu(II):His$_3$Glu11-Aβ40, and Cu(II):His$_3$Tyr10-Aβ40 structures along the coordinates of the radius of gyration (Rg) and end-to-end distance (R_{E-E}).

Figure 2B. Potential of Mean Force Surfaces of the apo and Cu(II)-bound Aβ42 Peptides. Potential of mean force (ΔPMF) of the Aβ42, Cu(II):His$_3$Asp1-Aβ42, Cu(II):His$_3$Glu11-Aβ42, and Cu(II):His$_3$Tyr10-Aβ42 structures along the coordinates of the radius of gyration (Rg) and end-to-end distance (R_{E-E}).

Our R_g values for aqueous Cu(II):Aβ40 and Cu(II):Aβ42 with varying coordination chemistries are illustrated in Figure S7 (supporting information section). Upon Cu(II) coordination, Aβ40 and Aβ42 become more compact. In comparison to our recent studies, Zn(II):Aβ40 is more compact than Cu(II):Aβ40 (85). The same trend is also obtained for Cu(II):Aβ42 and Zn(II):Aβ42 (85). Less compact and less stable disordered metalloprotein conformations are more active toward other species in the solution. Therefore, we expect Cu(II):Aβ to be more active than Zn(II):Aβ, which is in accord with experimental observations (see above). Calculated R_g values support our thermodynamic findings, which were presented and discussed above. IMS-MS experiments were conducted by Sietkiewicz *et al*. They measured the compactness changes of Aβ upon Zn(II) and Cu(II) coordination (126). In agreement with earlier investigations, they noted that the Asp23-Lys28 salt bridge stabilizes the conformations and provides compactness into the structures while Gly25 is active in extended oligomeric structure formations. Based on their results, the compact forms of Aβ dominate upon Zn(II) or Cu(II) addition. This finding is in accord with our data. With the inclusion of our previous studies, we find that transition metal ion coordination increase the compactness of monomeric Aβ in an aqueous solution medium. Moreover, the Asp23-Lys28 salt bridge is reduced in its abundance upon Cu(II) binding and disappears upon Zn(II) coordination with Aβ (details are provided below). A similar trend is observed in Aβ40 structures for the Glu22 and Lys28 salt bridge upon Zn(II) and Cu(II) ion coordination. In addition, intramolecular interations between the N- or C-terminal and CHC regions are reduced in probability upon Cu(II) binding (results are illustrated below). Our R_g values agree with light scaterring experiments and previous theoretical studies (127-133).

Secondary structure abundances of the apo and Cu(II)-bound Aβ40 peptides with different coordination chemistries are presented in Figure 3. Within the N-terminal region (Asp1-Lys16), a serious decrease (between 5% to 40%) in the abundance of the helical (α- and 3_{10}-helix), β-sheet and turn secondary structural elements occurs upon transition metal ion coordination to the Aβ40 peptide independent of the coordination chemistry. This decrease of ordered secondary structure component formation is expected due to this region participating in the Cu(II) coordination for all binding sites. An exception is the 15% - 52% increase in 3_{10}-helical content for residues Val12-Gln15 in the Cu:His₃Glu11-Aβ40 structures in comparison to the apo-Aβ40 structures. Furthermore, only residues Ala2, His13 and His14 in the N-terminal region present a larger turn content of greater than 10% for the Cu:His₃Asp1-Aβ40 peptide. We also note that the α-helix and β-sheet content is decreased by between 5% and 35% in the central hydrophobic core (Leu17-Ala21; CHC) region upon Cu(II) binding independent of the coordination chemistry except for the β-sheet composition at Leu17 and Val18 upon Cu(II) binding via the His₃Asp1 binding site. However, the 3_{10}-helical prominence at Leu17-Phe19 is more significant (by ≥ 5%) upon copper ion binding either to the His₃Asp1 or His₃Glu11 coordination sites. Additionally, the turn content at residues Phe19 and Phe20 in the Cu:His₃Asp1-Aβ40 peptide, Val18-Ala21 in the Cu:His₃Glu11-Aβ40 peptide, and Val18 in the Cu:His₃Tyr10-Aβ40 increases by at least 10% in comparison to apo Aβ40 in aqueous solution. The mid-domain (Glu22-Ala30) and C-terminal (Ile31-Val40) also presents a few residues with significant differences in the formed secondary structure content upon Cu(II) coordination. Specifically, the α-helix abundance at Glu22 and Asp23, the β-sheet content at Ser26-Ile32 and the turn content at Val24-Ser26 decrease by ≤ 25% upon copper ion coordination to Aβ40 independent of the coordination chemistry variations. Contrastingly, the 3_{10}-helix content at residues Ile32-Val36 is more significant (by ≥ 10%) upon Cu(II) binding to Aβ40 for all coordination sites. However, we also note a differential impact on secondary structure formations of the Aβ40 peptide upon Cu(II) binding depending on the coordination chemistry. Specifically, the α-helix and the 3_{10}-helix abundance at Val24-Lys28 and the β-sheet probability at Val39 increase in the Cu:His₃Glu11-Aβ40 peptide as to apo Aβ40. Furthermore, β-sheet at Leu34 in Cu:His₃Asp-Aβ40 and at Val36 and Val39 in the Cu:His₃Tyr10-Aβ40 peptide is higher by at least 5% than in the apo-Aβ40 peptide.
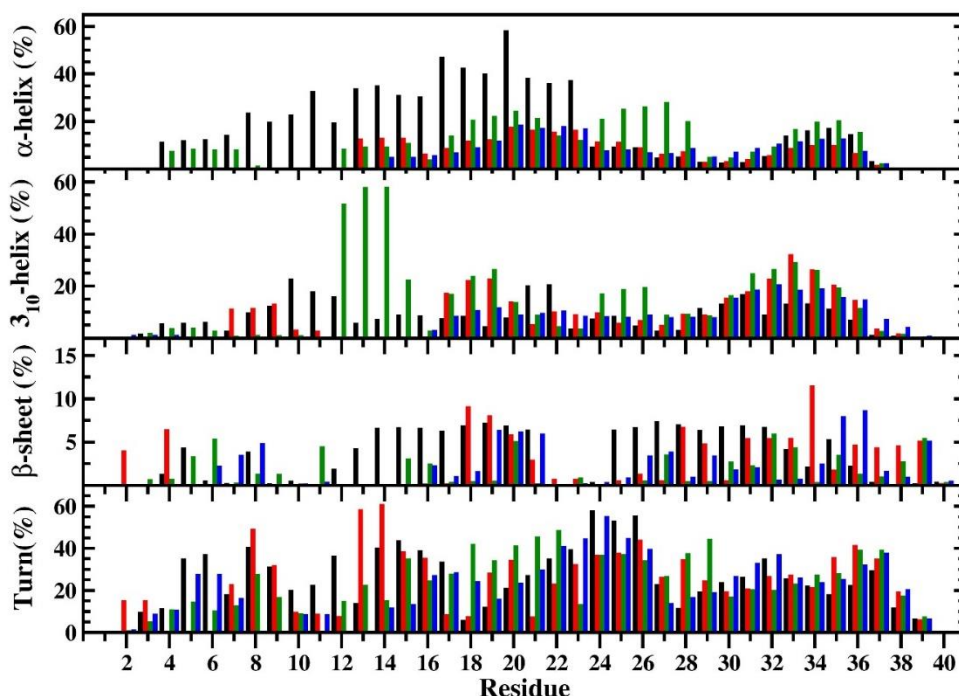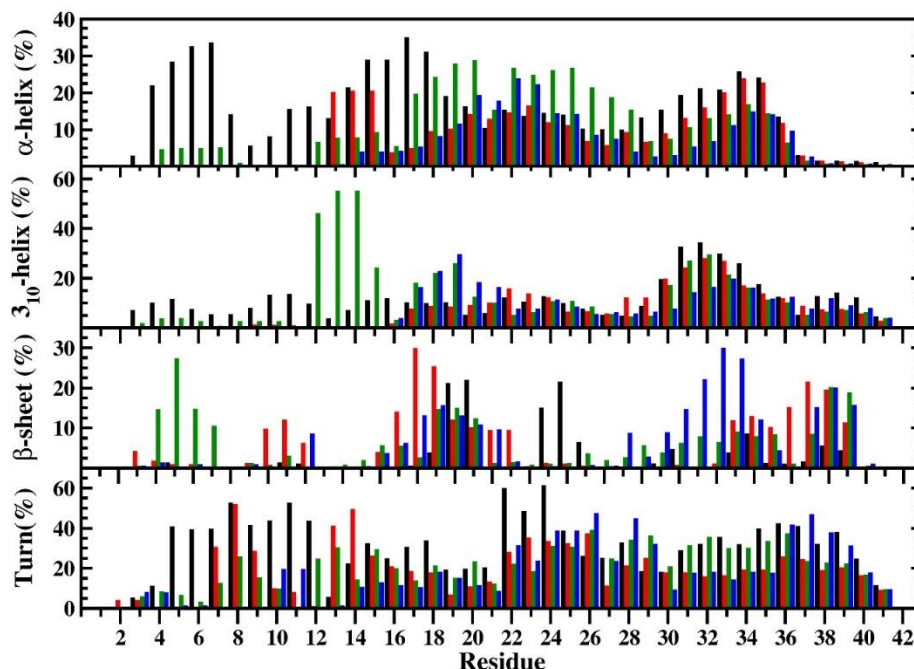

Figure 3: Residual Secondary Structure Abundances of the apo and Cu(II)-bound Aβ40 Peptides. Secondary structure abundances per residue of the Aβ40 (black), Cu(II):His₃Asp1-Aβ40 (red), Cu(II):His₃Glu11-Aβ40 (blue), and Cu(II):His₃Tyr10-Aβ40 (green) structures in an aqueous solution. The π-helix and coil structures are not displayed.

Figure 4 presents the secondary structure probabiities of apo- and copper ion-bound Aβ42. α- and 3_{10}-helix as well as turn content of the N-terminal region of the Aβ42 peptide decreases significantly upon Cu(II) binding regardless of the binding site except for residue His13 in the Cu:His$_3$Asp1-Aβ42 peptide and residues Val12-Gln15 in the Cu:His$_3$Glu11-Aβ42 peptide, which display vice versa trends. Interestingly, the increase in 3_{10}-helical content with the Cu:His$_3$Glu11 binding site was also detected for Aβ40. Unlike what we observed with the Aβ40 peptide, residues Tyr10-Val12 of Cu:His$_3$Asp1-Aβ42, Phe4-Asp7 of Cu:His$_3$Glu11-Aβ42, and Val12 of Cu:His$_3$Tyr10-Aβ42 present a larger abundant (> 5%) β-sheet content as to the apo-Aβ42 peptide. The 3_{10}-helical content in the CHC region of Aβ42 is not significantly impacted by Cu(II) binding to the His$_3$Asp1 but we do note a signifance reduction in α-helical abundance for residues Leu17-Phe19. Instead, a considerable reduction in β-sheet probability for residues Leu17-Phe19 is displayed in the Cu:His$_3$Asp1-Aβ42 structures as to the apo-Aβ42 peptide while the opposite trend is presented for residues Phe20 and Ala21. When Cu(II) is bound to the His$_3$Glu11 residues, we observe a boost in α-helical probability for Phe19-Ala21 and in 3_{10}-helix content for Leu17-Ala21 as to the apo-Aβ42 peptide. However, residues Leu17 and Val18 present α-helix abundance reduction (> 10%) upon Cu(II) coordination to the three His residues and the Glu11 residue. Furthermore, Leu17 and Phe19 adopt a larger β-sheet probability (≥ 5%) in the structures of Cu:His$_3$Glu11-Aβ42 as to apo-Aβ42 while the opposite trend was detected for Phe20 and Ala21. Cu:His$_3$Tyr10-Aβ42 peptide´s CHC region also presents significant differences from the apo-Aβ42 peptide. Namely, the α-helix abundance of residues Leu17 and Val18 as well as the β-sheet abundance of Phe20 and Ala21 decreases by at least 10% and 5% respectively when Cu(II) binds to the His$_3$Tyr10 residues. On the other side, we observe a significant increase in 3_{10}-helix content for residues Val18-Ala21 and in β-sheet probability of residues Leu17-Phe19 for the Cu:His$_3$Tyr10-Aβ42 structures as to the apo-Aβ42 peptide. We note that residues Glu22-Val42 and Gly25-Asn27 present significant decreases in turn and β-sheet contents for all three Cu(II)-bound Aβ42 peptides as to apo-Aβ42. Furthermore, we also note a boost in α-helical probability of residues Glu22 and Asp23 of the Cu:His$_3$Asp1-Aβ42 structures and residues Glu22-Lys28 of the Cu:His$_3$Glu11-Aβ42 structures as to apo-Aβ42. However, we do observe helical probability reduction of Gly29-Met35 for all three Cu(II)-bound Aβ42 peptides in comparison to the apo-Aβ42. The C-terminal

β-sheet content increases upon Cu(II) binding for all three coordination sites except at residues Ile31-Leu24 and Ala42 of the Cu:His3Asp1-Aβ42 peptide, Val36 and Gly38 of the Cu:His3Glu11-Aβ42 peptide, and Gly38 and Ala42 of the Cu-His3Tyr10-Aβ42 peptide.

In addition to the differences observed for each alloform upon Cu(II) binding, we also observe specific differences between the Cu(II)-bound Aβ40 and Aβ42 alloforms for each binding site (Figures 3 and 4). In the case of the Cu:His$_3$Asp1-Aβ alloforms, we note an increase in α-helical content of at least 10% for residues His13-Gln15 and Gly29-Val36. However, 3_{10}-helical content is significantly decreased (> 10%) for residues Asp7-Gly9 and Leu17-Phe19. Additionally, the β-sheet content of residues Tyr10-Val12, Lys16-Ala21, and Met35-Ala41 is increased in the Aβ42 rather than Aβ40 alloform when Cu(II) is bound to the His$_3$Asp1 residues. However, an opposite trend is observed at Lys28, Gly29, and Ile31-Leu34. Furthermore, the turn content of residues His13-Lys16, Phe19, Phe20, Asn27, Lys28 and Met35-Gly37 is decreased in the Aβ42 alloform in comparison to the Aβ40 alloform for the Cu:His$_3$Asp1 binding site.

For the Cu:His$_3$Glu11-Aβ alloforms, α-helical probability increase in the Aβ42 alloform as to the Aβ40 alloform is observed for residues Glu22 and Asp23. Ser26-Lys28 display an opposite trend. The 3_{10}-helical probability at Val24-Ser26 and Gly33-Met35 reduces from the Cu:His$_3$Glu11-Aβ40 to the Cu:His$_3$Glu11-Aβ42 alloform. The β-sheet abundances present that the β-sheet content of the Cu:His$_3$Glu11-Aβ42 peptide is boosted at residues Phe4-Asp7, Lys16-Ala21, Leu34-Gly37, Ile41 and Ala42 as to the Cu:His$_3$Glu11-Aβ40 peptide. Residues Leu17-Glu22 display a reduced turn probability in the Cu:His$_3$Glu11-Aβ42 structures rather than the Cu:His$_3$Glu11-Aβ40 peptide while a vice versa trend is observed for the both Ile residues (Ile31/Ile32).

Corresponding analysis of the Cu:His$_3$Tyr10-Aβ40 and Cu:His$_3$Tyr10-Aβ42 peptides reveals alloform differences between these two Cu(II)-bound peptides as well. Namely, the α-helical abundance of residues Glu22-Gly25 is increased in the Cu:His3Tyr10-Aβ(1-42) alloform as to Cu:His3Tyr10-Aβ(1-40). Furthermore, 3_{10}-helix probability is increased for residues Leu17-Ala21 and Gly38-Ile41 in the Aβ42 alloform rather than Aβ40 alloform upon Cu(II) coordination to His3Tyr10. Contrastingly, the opposite trend is observed for the overall helical content of residues Lys28-Ile32. Additionally, the abundance of

turn structure for residues Lys16-Val24 and Ala30-Met35 is increased in the Cu:His$_3$Tyr10-Aβ40 rather than the Cu:His$_3$Tyr10-Aβ42 alloform. Despite, the turn content of residues Asn27-Gly29 display the vice-versa trend. Similar to the other two Cu(II) binding sites, the β-sheet content in the Cu:His$_3$Tyr10-Aβ42

alloform is significantly increased in comparison to the Cu:His$_3$Tyr-Aβ40 alloform. Specifically, residues Val12, Leu17-Glu22, Gly29, Ile31-Met35 and Val39-Ile41 have a significant (> 5%) abundance of β-sheet component in Cu:His$_3$Tyr10-Aβ42 rather than the Cu:His$_3$Tyr10-Aβ40 alloform.

Figure 4: Residual Secondary Structure Abundances of the apo and Cu(II)-bound Aβ42 Peptides. Secondary structure abundances per residue of the Aβ42 (black), Cu(II):His$_3$Asp1-Aβ42 (red), Cu(II):His$_3$Glu11-Aβ42 (blue), and Cu(II):His$_3$Tyr10-Aβ42 (green) structures in an aqueous solution. The π-helix and coil structures are not displayed.

β-sheet structure formations, especially in the CHC and C-terminal regions, is a central event in aggregation processes of the Aβ peptides (56, 83, 85-87, 96, 108, 109 and references therein). The results presented predict β-sheet formation variations in the Aβ alloforms upon Cu(II) binding with varying coordination chemistries using our new potential functions. From these results, we note a similar or reduced β-sheet formation in the CHC region of Aβ40, depending on the Cu(II) ion coordination chemistry. However,the C-terminal region at Val36-Ile31 represents an increased or similar β-sheet probability upon Cu(II)-binding. Aβ42 presents β-sheet probability boost in the CHC region (Leu17-Phe19) and the C-terminal region (Ala30-Ile41) upon Cu(II) binding for all three binding sites. Results illustrate that divalent copper ion binding enhances Aβ42 aggregation moreso than Aβ40 aggregation. Furthermore, Cu(II)-bound Aβ42 β-sheet probability is significantly higher than the Cu(II)-bound Aβ40 alloforms regardless of the coordination chemistry in both regions (CHC/C-terminal regions). Therefore, reported enhaned β-sheet content

of the C-terminal region of the apo-Aβ42 as to the apo-Aβ40 peptide is not affected and is even enhanced for some residues. This finding indicates that the previously reported boosted aggregation rate of apo-Aβ42 as to the apo-Aβ40 peptide is not affected and may even be enhanced by Cu(II) coordination.

Boopathi and Kolandaivel investigated the secondary structures of Zn(II):Aβ40 and Cu(II):Aβ40 using MD simulations for only 50 ns without special sampling methods to gain insights into the secondary structure properties of these disordered metalloproteins without mentioning thermodynamic properties and without considering coordination chemistry variations (132). The results presented herein partially agree with their findings. For instance, we also detect turn component formation with high probability at Ala21-Ala30 of Aβ40 that is associated with Asp23-Lys28 less stable salt bridge occurance in comparison to the stability of Glu22-Lys28 (Table 6). Unlike the studies by Boopathi and Kolandaivel, our findings present β-sheet occurrence with high probability in the C-terminal region of Aβ40. Furthermore, the

same group presented prominent turn structure formation in the Asp23 to Asp27 region in Cu(II):Aβ40 conformations without investigating different coordination chemistry effects (132). Using the same coordination chemistry, turn structure abundance is decreased at Gly25 and Ser26 upon copper ion coordination with Aβ40. Furthermore, several research groups illustrated the structural properties of Cu(II):Aβ without investigating the coordination chemistry influences and they utilized either a potential function possessing a nonbonded model or they used the Zn(II) force field parameters for studying Cu(II):Aβ. As mentioned before (see above), the number of electrons and coordination chemistries differ for these metalloproteins and Jahn-Teller effects should not be disregarded. Therefore, simulation results for Cu(II):Aβ using the force field parameters for the zinc ion instead of those for the copper ion might be misleading. Dong and co-workers successfully investigated the intermolecular interactions between Aβ40 and Cu(II):Aβ40 with three modified clioquinol drugs (133). They performed extensive classical molecular dynamics simulations without special sampling methods. They could not detect β-sheet occurence in Aβ or in Cu(II):Aβ. Despite, Dong and co-workers expressed the self-assembly domains (CHC and C-terminal regions), highlighting β-sheet occurence in the CHC and C-terminal regions. Furthermore, our findings for apo Aβ42 are in accord with results presented by Velez-Vega and Escobedo but they used the OPLS-AA force field parameters for the disordered peptide (134). Specifically, their results present less probable α-helix occurence in Aβ42. Additionally, MD simulations without increasing the conformational sampling with specific methods utilizing the GROMOS9643A1 force field parameters showed that some residues of Aβ42 adopt helical structures (135). Our results are in partial accord with these data. Our findings also further are in accord with this study since the C-terminal region of Aβ42 forms β-sheet component. Various clustering algorithms were utilized by Garcia *et al.* They found that some residues in the N- and C-terminal regions form β-sheet element while Ser8-Val12 adopts α-helix structure (136). Our results show support to these findings (see above). Our results for apo Aβ42 are in accord with the REMD studies by Yang and Teplow (135). The structuring of the C-terminal region of apo Aβ42 including β-sheet structure adaptation with high probability have been investigated by few additional research groups (130-137). These results agree with our findings. However, these groups did not investigate the effect of coordination chemistry differences of Cu(II) on the

monomeric conformations of Aβ alloforms (Aβ40/Aβ42).

The intra-molecular interactions of the apo- and Cu(II)-coordinated Aβ40 peptides with different coordination sites are displayed in Figure 5. For the apo-Aβ40 peptide, we note abundant intra-molecular interactions within the N- and C-terminal regions, CHC and mid-domain regions as well as between the N-terminal and CHC, mid-domain and C-terminal regions. Specifically, Phe4-Arg5 interact with Leu17-Phe19, Arg5 interacts with Asp23, Val12-His13 interacts with Gly33, Leu34, Val36 and Gly37, and Gln15-Lys16 interact with Ile31, Gly33, and Met35-Val40 with abundances up to 40%. CHC and mid-domain regions interact with the C-terminal region as well; Val18-Phe19 with Val39-Val40 and Phe19-Gly25 with Gly29-Gly33 (up to 60%). Furthermore, the C-terminal region interacts with itself with abundances up to 50% between residues Ala30-Met35 and Val39-Val40.

We note – upon copper ion coordination - that these abundant intra-molecular interactions in the apo-Aβ40 peptide are significantly decreased or completely disappear depending on the coordination chemistry differences; abundant intra-molecular interactions in the C-terminal region with the C-terminus between Ala30-Met35 with Val39-Val40 are not present in any of the three Cu(II)-bound Aβ40 peptides. The interactions of the N-terminal residues Val12-His13 and Gln15-Lys16 with the C-terminal residues Ile31, Gly33, Leu34, and Met35-Val40 are significantly decreased for the Cu:His$_3$Asp1-Aβ40 and Cu:His$_3$Glu11-Aβ40 peptides and completely disappear for the Cu:His$_3$Tyr10-Aβ40 peptides. However, we do note the appearance of interactions between Arg5-His6 in the N-terminal with residues Val36-Val40 in the C-terminal region in the Cu:His$_3$Asp1-Aβ40 and Cu:His$_3$Glu11-Aβ40 peptides. Additionally, interactions of the CHC region with N-terminal region are shifted from residues Phe4-Arg5 to residues His13-His14 for the Cu:His$_3$Glu11-Aβ40 peptides and residues Asp1 and His13-His14 for the Cu:His$_3$Asp1-Aβ40 peptide but remain for the Cu:His$_3$Tyr10-Aβ40 peptide. CHC region and the C-terminal interactions through Val39 and Val40 disappear upon Cu(II) binding for all three binding sites yet interactions including residues Ala29-Met35 remain. Furthermore, mid-domain (Asp23-Ser26) and C-terminal (Ile31-Leu34) regions interactions increase when Cu(II) binds to the His$_3$Glu binding site in Aβ40. Finally, we observe that N-terminal and mid-domain region interactions are increased for Cu:His$_3$Asp1-Aβ40 and Cu:His$_3$Glu11-Aβ40 as to apo-Aβ40. Cu:His$_3$Asp1-Aβ40 peptide

presents interactions of residues Asp1, Ala2, and Phe4-Arg5 with residues Asp23, Val24, Ser26, Asn27 and Gly29 whereas the

Cu:His$_3$Glu11-Aβ40 peptide presents interactions of residues Glu3 and Arg5-His6 with Asp23-Gly25 and Lys28-Gly33.
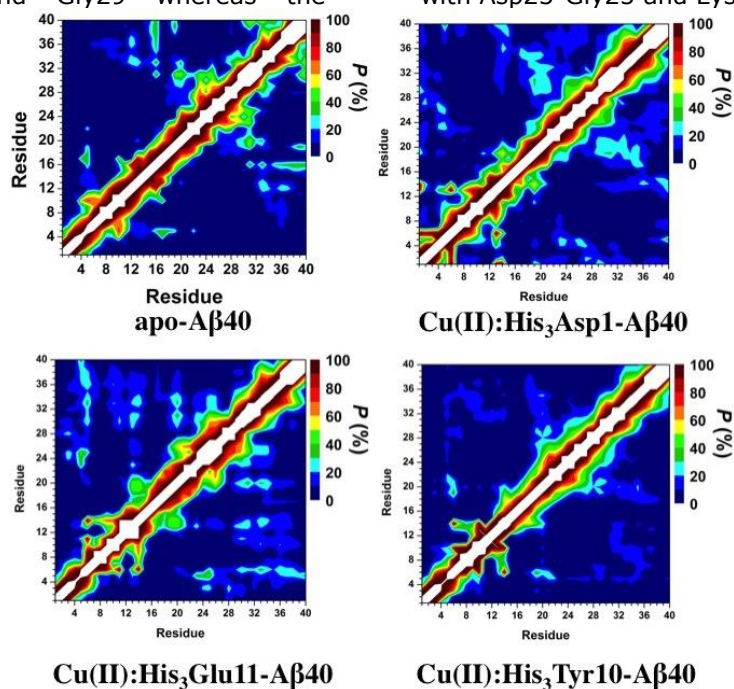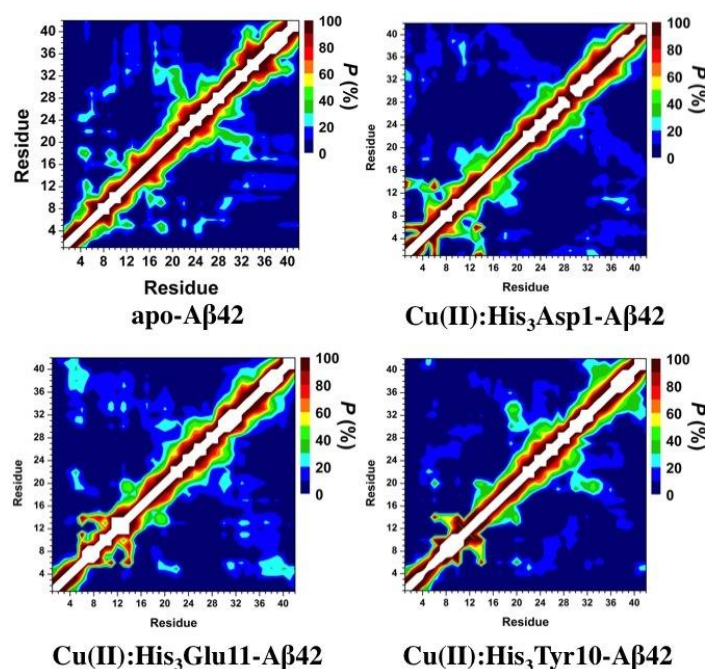

Figure 5: Intra-molecular Interaction of the apo and Cu(II)-bound Aβ40 Peptides. Calculated intra-molecular interactions for the structures of the Aβ40, Cu(II):His$_3$Asp1-Aβ40, Cu(II):His$_3$Glu11-Aβ40, and Cu(II):His$_3$Tyr10-Aβ40 peptides in an aqueous solution. The color scale corresponds to the computed probability (*P*) for these interactions.

Intra-molecular interactions of apo- and Cu(II)-coordinated Aβ42 with varying coordination chemistries - using our force field parameters - in aqueous solution medium are presented in Figure 6. For the N-terminal region, we note that residues Phe4-Arg5 interact with Glu11-His13. For the C-terminal region, Ile32-Leu34 interact with Val39-Val40. Interactions occur between the N-terminal and CHC regions; Phe4-Arg5 with Leu17-Phe19 and residues Gly9-Tyr10 with Leu17-Phe19. Interactions between the N-terminal and mid-domain regions exists through Phe4-His6 with Asp23-Gly29 and Gly9 with Asp23, Gly29 and Ala30. Moreover, Arg5 interacts with Ala42 and Val12 interacts with Gly33 demonstrating N-terminal and C-terminal interactions. We further note that the CHC region interacts with the mid-domain and C-terminal regions through Leu17-Ala21 with Lys28-Gly33 and Val36-Gly38.

Varying Cu(II) coordination chemistries impact significantly these interactions of apo-Aβ42. For example, N-terminal and mid-domain region interactions are less probable upon Cu(II)-coordination with only the Cu:His$_3$Glu11-Aβ42 and Cu:His$_3$Tyr10-Aβ42 peptides illustrating reduced interactions between these regions (Arg5 with Glu22). Moreover, N-terminal and CHC region interactions that we observed in apo-Aβ42 are

less probable upon copper ion coordination for all three coordination sites. Abundant intra-molecular interactions occur between the residues Glu11-Gln15 (N-terminal) and the residues Val18-Ala21 (CHC regşon) of Cu:His$_3$Glu11-Aβ42. Residues Glu3-His6, Tyr10 and Val12 interact with Ile31, Gly33, Leu34 and Gly37-Ala42 in Cu:His$_3$Glu11-Aβ42 (demonstrating N- and C-terminal interactions) and for residues Asp1-Ala2 with Gly29 and Ile32-Gly33, Phe4 with Ile32, Gly9 with Val39, Glu11 with Met35-Gly38 and Arg5 with Ala42 for Cu:His$_3$Asp1-Aβ42. Cu:His$_3$Tyr10-Aβ42 exhibits N- and C-terminal interactions through residues Arg5 and Ala42. Cu:His$_3$Glu11-Aβ42 and Cu:His$_3$Tyr10-Aβ42 display CHC and C-terminal regions interactions for residues Val18-Ala21 and Ala30-Leu34. Finally, only the Cu:His$_3$Tyr10-Aβ42 retains an interaction between the CHC and mid-domain regions between Phe19 and Asn27.

In addition to varying Cu(II) coordination affects on the Aβ40 and Aβ42 alloforms, we also note significant alloform specific differences between the Cu(II)-bound Aβ40 and Aβ42 peptides. Cu:His$_3$Asp1-Aβ40 and Cu:His$_3$Glu11-Aβ40 show CHC and C-terminal regions as well as N-terminal and mid-domain region interactions that are not present in Cu:His$_3$Asp1-Aβ42 and Cu:His$_3$Glu11-Aβ42.

Furthermore, the number of residues interacting between the N-terminal and CHC regions is increased for Cu:His$_3$Asp1-Aβ42 rather than Cu:His$_3$Asp1-Aβ40 even though the abundance displays the vice versa trend. We also note that Cu:His$_3$Glu11-Aβ42 N-terminal region interacts with a higher probability with the CHC region than in Cu:His$_3$Glu11-Aβ40. In the case of the Cu:His$_3$Tyr10 binding site, we notice that intra-molecular interactions of the CHC region are more abundant with the C-terminal region for the Aβ42 alloforms but with the N-terminal region for the Aβ40 alloforms. An increase in

the N-terminal interactions with the C-terminus is also observed for the Cu:His$_3$Tyr10-Aβ42 alloform rather than the Cu:His$_3$Tyr10-Aβ40 alloform. Results by Boopathi and Kolandaivel show strong N- or C-terminal and CHC regions interactions in Cu(II):Aβ42. They did not study the impact of coordination chemistry on these interactions. We detect similar interactions in Cu(II):His$_3$Glu-Aβ42. However, based on our findings, these interactions are more pronounced in apo Aβ42.

Figure 6. Intra-molecular Interaction of the apo and Cu(II)-bound Aβ42 Peptides. Calculated intra-molecular interactions for the structures of the Aβ42, Cu(II):His3Asp1-Aβ42, Cu(II):His3Glu11-Aβ42, and Cu(II):His3Tyr10-Aβ42 peptides in an aqueous solution. The color scale corresponds to the computed probability (P) for these interactions.

The formed salt bridges of apo- and Cu(II)-coordinated Aβ40 also reveal variations in the tertiary structure formations of Aβ40 upon Cu(II) binding with different coordination chemistries (Table 6). These probabilities of salt bridge formation reveal that the salt bridges between Lys16 and the C-terminus and between Arg5 and Glu22 are both significantly decreased upon Cu(II) binding for all three coordination sites. Furthermore, the salt bridge formation between Arg5 and Asp1 is significantly decreased for both the Cu:His$_3$Glu11-Aβ40 and Cu:His$_3$Tyr10-Aβ40 peptides in comparison to the apo-Aβ40. We also observe further coordination site dependent differences in the salt bridge

formations. For example, the salt bridge between Arg5 and Glu3 is significantly decreased in only the Cu:His$_3$Asp1-Aβ40 peptide. The Cu:His$_3$Tyr10-Aβ40 peptide displays more abundant salt bridge formations between Arg5 and Glu11 as well as between Asp23 and Lys28 that is not observed in the other two Cu(II)-bound Aβ40 peptides. The Cu:His$_3$Asp1-Aβ40 and Cu:His$_3$Glu11-Aβ40 peptides present more abundant salt bridge formations between Arg5 and the C-terminus as well as Asp23. Lastly, the salt bridge between the N-terminus and the Glu22 residues is more abundant in the Cu:His$_3$Asp1-Aβ40 peptide than the apo-Aβ40 and other two Cu(II)-bound Aβ40 peptides.

Table 6. Formed Salt Briges of the apo and Cu(II)-bound Aβ40 Peptides. The probabilities of salt bridges formations in the structures of Aβ40, Cu(II):His$_3$Asp1-Aβ40, Cu(II):His$_3$Glu11-Aβ40, and Cu(II):His$_3$Tyr10-Aβ40 with a probability of greater than 10%. R(Cγ-Nζ) is the distance between the carboxylate carbon atom and the side-chain or N-terminal nitrogen atom.

Donor	Acceptor	Apo-Aβ40	Cu(II):His$_3$Asp1-Aβ40 R(Cγ-Nζ)	Cu(II):His$_3$Glu11-Aβ40 R(Cγ-Nζ)	Cu(II):His$_3$Tyr10-Aβ40 R(Cγ-Nζ)
Arg5	Glu3	67.83	0.08	66.92	73.04
Lys16	Val40(-COO$^-$)	36.84	0.53	3.54	1.73
Arg5	Glu22	35.27	9.39	5.97	19.95
Arg5	Asp1	26.75	-	16.3	16.51
Arg5	Glu11	25.28	22.71	-	11.08
Lys16	Glu11	17.25	10.33	-	0
Arg5	Val40(-COO$^-$)	15.21	41.63	29.74	11.69
Lys28	Glu22	11.36	3.82	3.47	4.17
Lys28	Asp23	3.98	3.57	1.32	13.47
Arg5	Asp23	0	22.92	30.99	0.06
Asp1(-NH3$^+$)	Glu22	0	13.28	0.28	0.06

The formed salt bridges of the apo- and Cu(II)-bound Aβ42 peptides also present the impact of Cu(II) coordination on the tertiary structure formations of Aβ42 with varying coordination chemistries (Table 7). These probabilities of salt bridge formation reveal that the salt bridge between between Arg5 and Glu22 is both significantly increased upon Cu(II) binding for all three coordination sites. Furthermore, the salt bridge formation between Arg5 and Asp1 increases for both Cu:His$_3$Glu11-Aβ42 and Cu:His$_3$Tyr10-Aβ42 as to apo-Aβ42. Cu:His$_3$Tyr10-Aβ42 displays less abundant Arg5 and Glu11 salt bridge formations than the other two Cu(II)-bound Aβ42 peptides and the apo-Aβ42 peptide. However, salt bridge formation between Arg5 and the C-terminus is increased for Cu:His$_3$Tyr10-Aβ42 as to apo-Aβ42 and other two Cu(II)-bound Aβ42. These findings are the vice versa trend of that reported for the apo- and Cu(II)-coordinated Aβ40 peptides (see above). However, we also observe specific trends that depend on the coordination chemistry that are similar to the of the apo and Cu(II)-bound Aβ peptides. For example, the salt bridges between Arg5 and Glu3 in only the Cu:His$_3$Asp1-Aβ42 peptide and between Arg5 and Glu11 in only the Cu:His$_3$Glu11-Aβ42 peptide are significantly decreased. Last, we note that Lys28 and Glu22 salt bridge probability in the Cu:His$_3$Tyr10-Aβ42 peptide and between Arg5 and Asp7 in the Cu:His$_3$Asp1-Aβ42 peptide is increased in comparison to the other three peptides.

Due to the proposed importance of aggregation to the pathogenic mechanism of AD, it is of great importance to be able to assess the affect of varying of copper ion coordination chemistries on the aggregation propensity Aβ. Pawar et al. developed a method to assess the residual aggregation propensity of IDPs (see Methods section) and applied it to Aβ peptides and other IDPs in order to assess where in the protein mutations affect the aggregation propensity (114). Using this method, we have calculated the residual intrinsic aggregation propensities (Z_{agg}) of the free and Cu(II)-coordinated Aβ alloforms utilizing the residual α-helix and β-sheet propensities obtained from our REMD simulations (Figures 7A and 7B). Pawar et al. presented that a Z_{agg} score of one or more indicates a high propensity to aggregate (114). Residues Phe4, Tyr10, Val12, Leu17, Phe19, Phe20, Val24, Ala30-Ile32, Leu34-Val36, and Val39-Val40 show the highest propensity to aggregate for the apo-Aβ40 peptide. Upon Cu(II), we note that the aggregation propensity of residues Leu17-Phe20 in the CHC region presents a notable increase in intrinsic aggregation propensity. Thus, this result indicates that the CHC region of the Cu(II)-bound Aβ40 peptides might be a key in their aggregation mechanism. Furthermore, intrinsic aggregation propensity for the CHC region residues is slightly higher for Cu:His$_3$Asp1-Aβ40 and Cu:His$_3$Glu11-Aβ40 as to Cu:His$_3$Tyr10-Aβ40. For apo-Aβ42, residues Phe4, Tyr10, Val12, Leu17, Phe19-Ala21, Val24, Ile31, Ile32, Leu34, Val36, and Val39-Ile41 display an intrinsic aggregation

propensity greater than one. Similar to the Aβ40 alloform, residues Leu17-Phe20 present an increase in intrinsic aggregation propensity upon Cu(II) binding regardless of the coordination chemistry, with the Cu:His$_3$Tyr10-Aβ42 peptide showing a lower increase than the Cu:His$_3$Asp1-Aβ42 and Cu:His$_3$Glu11-Aβ42 peptides. Additionally, we observe an increase in intrinsic aggregation propensity for residues Ile31-Met35 for the Cu:His$_3$Glu11-Aβ42 and Cu:His$_3$Tyr10-Aβ42

peptides in comparison to the apo-Aβ42 peptide. These findings indicate that the CHC and C-terminal regions are also involved in the aggregation mechanism of Cu(II)-coordinated Aβ42 but the level of aggregation propensity may vary based on the differences in the coordination chemistry of the Cu(II) ion. See also, Tables S1 and S2 in the supporting information section.

Table 7. Formed Salt Briges of the apo and Cu(II)-bound Aβ42 Peptides. The probabilities of salt bridges formations in the structures of Aβ42, Cu(II):His$_3$Asp1-Aβ42, Cu(II):His$_3$Glu11-Aβ42, and Cu(II):His$_3$Tyr10-Aβ42 with a probability of greater than 10%. R(Cγ-Nζ) is the distance between the carboxylate carbon atom and the side-chain or N-terminal nitrogen atom.

Donor	Acceptor	Apo-Aβ42	Cu(II):His$_3$Asp1-Aβ42 R(Cγ-Nζ)	Cu(II):His$_3$Glu11-Aβ42 R(Cγ-Nζ)	Cu(II):His$_3$Tyr10-Aβ42 R(Cγ-Nζ)
Arg5	Glu3	61.9	1.1	65.6	41.9
Arg5	Glu11	37.5	39.0	-	2.7
Arg5	Ala42(-COO⁻)	18.0	16.8	14.2	30.7
Arg5	Asp1	17.8	-	27.1	23.3
Arg5	Asp23	14.9	7.5	7.1	9.9
Arg5	Glu22	5.6	20.9	24.5	19.2
Lys28	Glu22	3.1	3.3	2.5	13.0
Arg5	Asp7	0.1	33.3	0.3	12.1

Figure 7A. Residual intrinsic aggregation scores (Zagg) of the apo and Cu(II)-bound Aβ40 Peptides. Calculated Zagg values for each residue of the Aβ40, Cu(II):His$_3$Asp1-Aβ40, Cu(II):His$_3$Glu11-Aβ40, and Cu(II):His$_3$Tyr10-Aβ40 peptides in an aqueous solution.
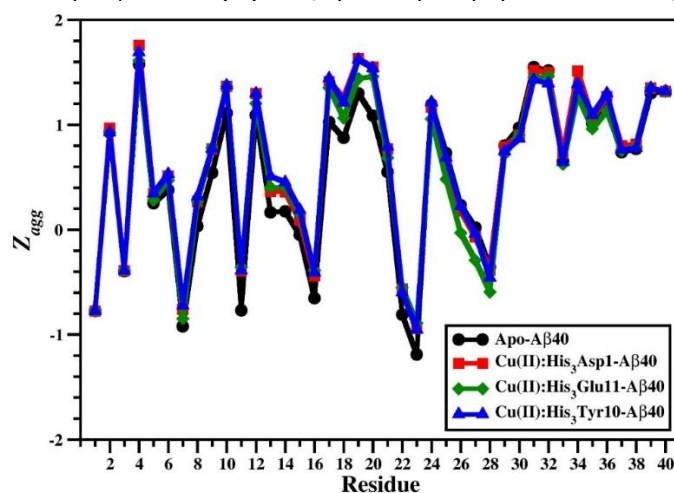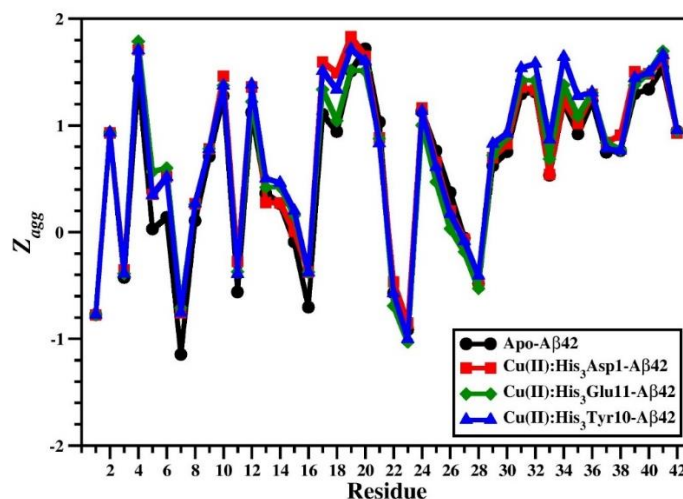
Figure 7B. Residual intrinsic aggregation scores (Z_{agg}) of the apo and Cu(II)-bound Aβ42 Peptides. Calculated Z_{agg} values for each residue of the Aβ42, Cu(II):His₃Asp1-Aβ42, Cu(II):His₃Glu11-Aβ42, and Cu(II):His₃Tyr10-Aβ42 peptides in an aqueous solution.

CONCLUSIONS

Overall, results show the specific structural and thermodynamic properties of aqueous Cu(II)-bound Aβ40 and Aβ42 peptides with different Cu(II) coordination chemistries. Furthermore, the affect of Cu(II) coordination on Aβ40 and Aβ42 peptides and the alloform specific differences in Cu(II)-bound Aβ including coordination specific differences is presented. The results presented herein are the first to offer a comparison of the monomeric Cu(II)-coordinated Aβ40 and Aβ42 peptides for these three different proposed species I binding sites including three histidine residues utilizing the new potential functions. Furthermore, this study presents the usefulness of our developed force field parameters for type II copper centers in proteins including three His residues (84).

In summary, the thermodynamic properties of apo- and Cu(II)-bound Aβ40 and Aβ42 present that the Cu(II)-bound structures are less preferred than apo-Aβ40 and apo-Aβ42 in aqueous solution. In addition, both Aβ alloforms display a difference in the favorability of the structures based on the coordination chemistry. Specifically, thermodynamic preference for the coordination sites is Cu:His₃Glu11 < Cu:His₃Tyr10 < Cu:His₃Asp1 for both Aβ alloforms. The PMF surfaces of the free and Cu(II)-bound Aβ peptides also reveal that the conformational ensemble of the Aβ peptides is altered by Cu(II) coordination and that the change in the conformational ensemble differs based on the chosen binding site.

In general, the helical content of the Cu(II)-bound alloforms decreases in the N-terminal and CHC regions for all three coordination chemistries except for the 3₁₀-helical content for Val12-Gln15 in the Cu:His₃Glu11-Aβ40 and Cu:His₃Glu11-Aβ42 peptides. The β-sheet content is decreased for the Aβ40 peptide upon Cu(II) binding except within residues Leu34-Val40 residing in the C-terminal region. Conversely, the Aβ42 peptide shows a boost in β-sheet content in the CHC and C-terminal regions for all three binding sites and an increase in the N-terminal region for the Cu:His₃Glu11 binding site. Furthermore, the increased structuring in the C-terminal region of the free Aβ42 in comparison to the free Aβ40 is still observed when Cu(II) binds to the peptide. Additionally, increased structuring in the CHC region due to β-sheet formation for the Cu(II)-bound Aβ42 peptides as to the Cu(II)-bound Aβ40 peptides is also observed. Altogether, these β-sheet content variations indicate that the Cu(II)-coordinated Aβ peptides have an increased aggregation rate in comparison to the free Aβ peptides and that the Cu(II)-bound Aβ42 peptides will aggregate more rapidly than the Cu(II)-bound Aβ40 peptides. The calculated tertiary structures also reveal differences due to Cu(II)-binding including the impact of the chosen coordination chemistry and alloform specific differences of the Cu(II)-bound Aβ peptides. Namely, intra-molecular interactions within the C-terminal region decrease when Cu(II) binds to the Aβ40 peptide. In addition, N- and C-terminal regions as well as CHC and N-terminal regions interactions are shifted upon Cu(II) binding to Aβ40 and Aβ42. Furthermore, alloform specific changes are also observed, indicating that the change in the conformational ensemble of the Aβ peptides depends on the coordination chemistry. Therefore, these different structural effects resulting from the different binding sites might help to elucidate the

coordination chemistry of the Aβ peptide under different solution conditions.

Intrinsic aggregation propensity calculation reveal that the CHC and C-terminal regions are most likely to be involved in the aggregation of the free and Cu(II)-bound Aβ40 and Aβ42 peptides in aqueous solution. Furthermore, the Cu(II) binding enhances the intrinsic aggregation of the CHC region for the Aβ40 peptide and of the CHC and C-terminal regions for the Aβ42 peptide. However, we should note that the α parameters for the intrinsic aggregation propensity equation were optimized based on aggregation information of the free and mutant-type Aβ peptides. Therefore, further optimization might be required to account for changes in the aggregation rate due to transition metal ion binding. In addition, the values typically used for this equation are based on general hydrophobicity, α-helix and β-sheet content information for individual amino acid residues. Therefore, further optimization may be required to include information from molecular dynamics simulations, such as the non-polar solvent accessible surface area. Finally, the results presented herein can provide potential targets for the development of aggregation inhibitors of Cu(II)-bound Aβ peptides as well as structural information that can be used to aid in differentiating the Cu(II) coordination chemistry for the Aβ peptides under different solution conditions once detailed structural information can be obtained from experimental measurements of the Cu(II)-bound Aβ peptides in aqueous solution.

ACKNOWLEDGMENTS

REFERENCES

1. Faller P, Hureau C. Bioinorganic chemistry of copper and zinc ions coordinated to amyloid-beta peptide. Dalton Trans. 2009 Feb;21:1080-1094.

2. Atwood C. S, Moir R. D, Huang X. D, Scarpa R. C, Bacarra N. M, Romano D. M, Hartshorn M. K, Tanzi R. E, Bush A. I. Dramatic aggregation of Alzheimer Aβ by Cu(II) is induced by conditions representing physiological acidosis. J. Biol. Chem. 1998 May;273:12817-12826.

3. Zou J, Kajita K, Sugimoto N. Cu2+ inhibits the aggregation of amyloid beta-peptide(1-42) in vitro. Angew. Chem. Int. Ed. 2001 Jun; 40:2274-2277.

4. Raman B, Ban T, Yamagucchi K, Sakai M. Kawai T, Naiki H, Goto Y. Metal ion-dependent effects of clioquinol on the fibril growth of an amyloid beta peptide. J. Biol. Chem. 2005 Apr; 280:16157-16162.

5. House E, Collingwood J, Khan A, Korchazkina O, Berthon G, Exley C. Aluminium, iron, zinc and copper influence the in vitro formation of amyloid fibrils of A beta(42) in a manner which may have consequences for metal chelation therapy in Alzheimer's disease. J. Alz. Dis. 2004 Jun;6:291-301.

6. Yang X-H, Huang H-C, Chen L, Xu W, Jiang Z-F. Coordinating to Three Histidine Residues: Cu (II) Promotes Oligomeric and Fibrillar Amyloid-β Peptide to Precipitate in a Non-β Aggregation Manner. J. Alz. Dis. 2009 Nov;18:799-810.

7. Yu H, Ren J, Qu X. Different Hydration Changes Accompanying Copper and Zinc Binding to Amyloid β-Peptide: Water Contribution to Metal Binding. ChemBioChem. 2008 Feb;9:879-882.

8. Dai X, Sun Y, Gao Z, Jiang Z. Copper enhances amyloid-β peptide neurotoxicity and non β-aggregation: a series of experiments conducted upon copper-bound and copper-free amyloid-β peptide. J. Mol. Neurosci. 2010 May;41:66-73.

9. Hou L, Zagorski M G. NMR reveals anomalous copper(II) binding to the amyloid A beta peptide of Alzheimer's disease. J. Am. Chem. Soc. 2006 Jun;128:9260-9261.

10. Yoshiike Y, Tanemura K, Murayama O, Akagi T, Murayama M, Sato S, Sun X Y, Tanaka N, Takashima A. New insights on how metals disrupt amyloid beta-aggregation and their effects on amyloid-beta cytotoxicity. J. Biol. Chem. 2001 Aug; 276:32293-32299.

11. Smith D. P, Ciccotosto G. D, Tew D. J, Fodero-Tavoletti M. T, Johanssen T, Masters C. L, Barnham K. J, Cappai R. Concentration dependent Cu2+ induced aggregation and dityrosine formation of the Alzheimer's disease Amyloid-β peptide Biochem. 2007 Mar;46:2881-2891.

12. Jun S, Saxena S. The aggregated state of amyloid-beta peptide in vitro depends on Cu2+ ion concentration. Angew. Chem. Int. Edit. 2007 May;46:3959-3961.

13. Bolognin S, Messori L, Drago D, Gabbiani C, Cendron L, Zatta P. Aluminum, copper, iron and zinc differentially alter amyloid-Aβ< sub>

1–42</sub> aggregation and toxicity. Int. J Biochem. & Cell Biol. 2011 Jun;43:877-885.

14. Mold M, Ouro-Gnao L, Wieckowski B. M, Exley C. Copper prevents amyloid-[bgr] 1-42 from forming amyloid fibrils under near-physiological conditions in vitro. Scientific Reports. 2013 Feb;3:1256.

15. Hane F, Tran G, Attwood S. J, Leonenko Z. Cu2+ affects amyloid-β (1–42) aggregation by increasing peptide-peptide binding forces. PloS one. 2013 Mar;8:e59005.

16. Attanasio F, De Bona P, Cataldo S, Sciacca M. F. M, Milardi D, Pignataro B, Pappalardo G. Copper(II) and zinc(II) dependent effects on A beta 42 aggregation: a CD, Th-T and SFM study. New J. Chem. 2013 37(4):1206-1215.

17. Huang X. D, Atwood C. S, Moir R. D, Hartshorn M. A, Tanzi R. E, Bush A. I. Trace metal contamination initiates the apparent auto-aggregation, amyloidosis, and oligomerization of Alzheimer's A beta peptides. J. Biol. Inorg. Chem. 2004 Dec;9:954-960.

18. Karr J. W, Szalai V. A. Role of aspartate-1 in Cu(II) binding to the amyloid-β peptide of Alzheimer's disease. J. Am. Chem. Soc. 2007 Mar;129:3796-3797.

19. Karr J. W, Kaupp L. J, Szalai V. A. Amyloid-beta binds Cu2+ in a mononuclear metal ion binding site. J. Am. Chem. Soc. 2004 Oct;126:13534-13538.

20. Sarell C. J, Wilkinson S. R, Viles J. H. Substoichiometric Levels of Cu2+ Ions Accelerate the Kinetics of Fiber Formation and Promote Cell Toxicity of Amyloid-beta from Alzheimer Disease. J. Biol. Chem. 2010 Dec;285:41533-41540.

21. Jun S, Gillespie J. R, Shin B.-k, Saxena S. The Second Cu(II)-Binding Site in a Proton-Rich Environment Interferes with the Aggregation of Amylold-beta(1-40) into Amyloid Fibrils. Biochem. 2009 Oct;48:10724-10732.

22. Lv Z, Condron M. M, Teplow D. B, Lyubchenko Y. L. Nanoprobing of the Effect of Cu 2D Cations on Misfolding, Interaction and Aggregation of Amyloid Beta Peptide. Biophys. J. 2013 Jan;104:513A-514A.

23. Bush A. I. The metallobiology of Alzheimer's disease. Trends in Neurosciences. 2003 Apr;26:207-214.

24. Opazo C, Huang X. D, Cherny R. A, Moir R. D, Roher A. E, White A. R, Cappai R, Masters C. L, Tanzi R. E, Inestrosa N. C, Bush A. I. Metalloenzyme-like activity of Alzheimer's disease beta-amyloid - Cu-dependent catalytic conversion of dopamine, cholesterol, and biological reducing agents to neurotoxic H2O2. J. Biol. Chem. 2002 Oct;277:40302-40308.

25. Cuajungco M. P, Faget K. Y. Zinc takes the center stage: its paradoxical role in Alzheimer's disease. Brain Res. Rev. 2003 Jan;41:44-56.

26. Huang X. D, Atwood C. S, Hartshorn M. A, Multhaup G, Goldstein L. E, Scarpa R. C, Cuajungco M. P, Gray D. N, Lim, J, Moir R. D, Tanzi R. E, Bush A. I. The A beta peptide of Alzheimer's disease directly produces hydrogen peroxide through metal ion reduction. Biochem. 1999 May;38:7609-7616.

27. Sharma A. K, Pavlova S. T, Kim J, Kim J, Mirica L. M. The effect of Cu2+ and Zn2+ on the A beta(42) peptide aggregation and cellular toxicity. Metallomics. 2013 Nov;5:1529-1536.

28. Huang X. D, Cuajungco M. P, Atwood C. S, Hartshorn M. A, Tyndall J. D. A, Hanson G. R, Stokes K. C, Leopold M, Multhaup G, Goldstein L. E, Scarpa R. C, Saunders A. J, Lim J, Moir R. D, Glabe C, Bowden E. F, Masters C. L, Fairlie D. P, Tanzi R. E, Bush A. I. Cu(II) potentiation of Alzheimer A beta neurotoxicity - Correlation with cell-free hydrogen peroxide production and metal reduction. J. Biol. Chem. 1999 Dec;274:37111-37116.

29. Nadal R. C, Rigby S. E. J, Viles J. H. Amyloid beta-Cu2+ Complexes in both Monomeric and Fibrillar Forms Do Not Generate H2O2 Catalytically but Quench Hydroxyl Radicals. Biochem. 2008 Nov;47:11653-11664.

30. Fang C.-L, Wu W.-H, Liu Q, Sun X. Ma Y, Zhao Y.-F, Li Y.-M. Dual functions of beta-amyloid oligomer and fibril in Cu(II)-induced H2O2 production. Regulatory Peptides. 2010 May;163:1-6.

31. Garzon-Rodriguez W, Yatsimirsky A. K, Glabe C. G. Binding of Zn(II), Cu(II), and Fe(II) ions to Alzheimer's A beta peptide studied by fluorescence. Bioorganic & Medicinal Chemistry Letters. 1999 Aug;9:2243-2248.

32. Atwood C. S, Scarpa R. C, Huang X. D, Moir R. D, Jones W. D, Fairlie D. P, Tanzi R. E, Bush A. I. Characterization of copper interactions with Alzheimer amyloid beta peptides: Identification of an attomolar-affinity copper binding site on amyloid beta 1-42. J. Neurochem. 2008 Sep;75:1219-1233.

33. Guilloreau L, Damian L, Coppel Y, Mazarguil H, Winterhalter M, Faller P. Structural and thermodynamical properties of CuII amyloid-β 16/28 complexes associated with Alzheimer's disease. J. Biol. Inorg. Chem. 2006 Aug;11:1024-1038.

34. Jiang D, Men L, Wang J, Zhang Y, Chickenyen S, Wang Y, Zhou F. Redox reactions of copper complexes formed with different beta-amyloid peptides and their neuropathalogical relevance. Biochem. 2007 Jul;46:9270-9282.

35. Karr J. W, Szalai V. A. Cu(II) binding to monomeric, oligomeric, and fibrillar forms of the Alzheimer's disease amyloid-beta peptide. Biochem. 2008 Apr;47:5006-5016.

36. Syme C. D, Nadal R. C, Rigby S. E. J, Viles J. H. Copper binding to the amyloid-beta (A beta) peptide associated with Alzheimer's disease - Folding, coordination geometry, pH dependence, stoichiometry, and affinity of A beta-(1-28): Insights from a range of complementary spectroscopic techniques. J. Biol. Chem. 2004 Apr;279:18169-18177.

37. Danielsson J, Pierattelli R, Banci L, Graslund A. High-resolution NMR studies of the zinc-binding site of the Alzheimer's amyloid beta-peptide. Febs J. 2007 Nov;274:46-59.

38. Bush A. I, Pettingell W. H, Multhaup G, Paradis M. D, Vonsattel J. P, Gusella J. F, Beyreuther K, Masters C. L, Tanzi R. E. Rapid Induction of Alzheimer a-Beta Amyloid Formation by Zinc. Science. 1994 Sep;265:1464-1467.

39. Tougu V, Karafin A, Palumaa P. Binding of zinc(II) and copper(II) to the full-length Alzheimer's amyloid-beta peptide. J. Neurochem. 2008 Mar;104:1249-1259.

40. Hatcher L. Q, Hong L, Bush W. D, Carducci T, Simon J. D. Quantification of the binding constant of copper(II) to the amyloid-beta peptide. J. Phys. Chem. B. 2008 Jul;112:8160-8164.

41. Karr J. W, Akintoye H, Kaupp L. J, Szalai V. A. N-terminal deletions modify the Cu2+ binding site in amyloid-beta. Biochem. 2005 Mar;44:5478-5487.

42. Kowalik-Jankowska T, Ruta M, Wisniewska K, Lankiewicz L. Coordination abilities of the 1-16 and 1-28 fragments of beta-amyloid peptide towards copper(II) ions: a combined potentiometric and spectroscopic study. J. Inorg. Biochem. 2003 Jul;95:270-282.

43. Ma Q.-F, Hu J, Wu W.-H, Liu H.-D, Du J.-T, Fu Y, Wu Y.-W, Lei P, Zhao Y.-F, Li Y.-M. Characterization of copper binding to the peptide amyloid-beta(1-16) associated with Alzheimer's disease. Biopolymers. 2006 Apr;83:20-31.

44. Hong L, Bush W. D, Hatcher L. Q, Simon J. Determining thermodynamic parameters from isothermal calorimetric isotherms of the binding of macromolecules to metal cations originally chelated by a weak ligand. J. Phys. Chem. B. 2008 Nov;112:604-611.

45. Curtain C. C, Ali F, Volitakis I, Cherny R. A, Norton R. S, Beyreuther K, Barrow C. J, Masters C. L, Bush A. I, Barnham K. J. Alzheimer's disease amyloid-beta binds copper and zinc to generate an allosterically ordered membrane-penetrating structure containing superoxide dismutase-like subunits. J. Biol. Chem. 2001 Jun;276:20466-20473.

46. Minicozzi V, Stellato F, Comai M, Dalla Serra M, Potrich C, Meyer-Klaucke W, Morante S. Identifying the minimal copper- and zinc-binding site sequence in amyloid-beta peptides. J. Biol. Chem. 2008 Apr;283:10784-10792.

47. Miura T, Suzuki K, Kohata N, Takeuchi H. Metal binding modes of Alzheimer's amyloid beta-peptide in insoluble aggregates and soluble complexes. Biochem. 2000 May;39:7024-7031.

48. Stellato F, Menestrina G, Dalla Serra M, Potrich C, Tomazzolli R, Meyer-Klaucke W, Morante S. Metal binding in amyloid β-peptides shows intra- and inter-peptide coordination modes. Eur. Biophys. J. 2006 Jan;35:340-351.

49. Ma Q. F, Hu J, Wu W. H, Liu H. D, Du J. T, Fu Y, Wu Y. W, Lei P, Zhao Y. F, Li Y. M. Characterization of copper binding to the peptide amyloid-beta(1-16) associated with Alzheimer's disease. Biopoly. 2006 Apr;83:20-31.

50. Streltsov V. A, Titmuss S. J, Epa V. C, Barnham K. J, Masters C. L, Varghese J. N. The structure of the amyloid-beta peptide high-affinity copper II binding site in Alzheimer disease. Biophys. J. 2008 Oct;95:3447-3456.

51. Drew S. C, Noble C. J, Masters C. L, Hanson G. R, Barnham K. J. Pleomorphic Copper Coordination by Alzheimer's Disease Amyloid-beta Peptide. J. Am. Chem. Soc. 2009 Jan;131:1195-1207.

52. Kowalik-Jankowska T, Ruta-Dolejsz M, Wisniewska K, Lankiewicz L. Cu(II) interaction with N-terminal fragments of human and mouse beta-amyloid peptide. J. Inorg. Biochem. 2001 Sep;86:535-545.

53. Curtain C. C, Ali F. E, Smith D. G, Bush A. I, Masters C. L, Barnham K. J. Metal ions, pH, and cholesterol regulate the interactions of Alzheimer's disease amyloid-beta peptide with membrane lipid. J. Biol. Chem. 2003 Jan;278:2977-2982.

54. Shin B.-k, Saxena S. Direct evidence that all three histidine residues coordinate to Cu(II) in amyloid-beta(1-16). Biochem. 2008 Sep;47:9117-9123.

55. Barnham K. J, Haeffner F, Ciccotosto G. D, Curtain C. C, Tew D, Mavros C, Beyreuther K, Carrington D, Masters C. L, Cherny R. A, Cappai R, Bush A. I. Tyrosine gated electron transfer is key to the toxic mechanism of Alzheimer's disease beta-amyloid. Faseb J. 2004 Jul;18:1427-1428.

56. Liao Q, Kammerlin S. C. L, Strodel B. Development and application of a nonbonded Cu(II) model that includes Jahn-Teller effect. Phys. Chem. Lett. 2015 Jun; 6:2657-2662.

57. Liao Q, Owen M. C., Olubiyi O. O, Bogdan B, Strodel B. Conformational Transitions of the Amyloid-β Peptide Upon Cu(II) Binding and pH Changes. Isr. J. Chem. 2017; 57:1-15.

58. Liao Q, Owen M. C, Bali S, Barz B, Strodel B. Aβ under stress: the effects of acidosis, Cu(II) binding, and oxidation on amyloid-β peptide dimers. Chem Commun. 2018 Jun; 54:7766-7769.

59. Ando K. The axial methionine ligand may control the redox reorganizations in the active site of blue copper proteins. J. Chem. Phys. 2010 Nov;133:0175101.

60. Bruschi M, Bertini L, Bonacic-Koutecky V, De Gioia L, Mitric R, Zampella G, Fantucci P. Speciation of Copper-Peptide Complexes in Water Solution Using DFTB and DFT Approaches: Case of the Cu(HGGG)(Py) Complex. J. Phys. Chem. B. 2012 Jun;116:6250-6260.

61. Hewitt N, Rauk A. Mechanism of Hydrogen Peroxide Production by Copper-Bound Amyloid Beta Peptide: A Theoretical Study. J. Phys. Chem. B. 2009 Jan;113:1202-1209.

62. Hodak M, Chisnell R, Lu W, Bernholc J. Functional implications of multistage copper binding to the prion protein. Proc. Nat. Acad.

Sci. USA 2009 Jul;106:11576-11581. DOI: 10.1073/pnas.0903807106.

63. Inoue T, Shiota Y, Yoshizawa K. Quantum Chemical Approach to the Mechanism for the Biological Conversion of Tyrosine to Dopaquinone. J. Am. Chem. Soc. 2008 Nov;130:16890-16897.

64. Kaila V. R. I, Johansson M. P, Sundholm D, Laakkonen L, Wikstrom M. The chemistry of the Cu-B site in cytochrome c oxidase and the importance of its unique His-Tyr bond. Biochim. Biophys. Acta-Bioenergetics. 2009 Apr;1787:221-233.

65. Konecny R, Li J, Fisher C. L, Dillet V, Bashford D, Noodleman L. CuZn superoxide dismutase geometry optimization, energetics, and redox potential calculations by density functional and electrostatic methods. Inorg. Chem. 1999 Feb;38:940-950.

66. Pavelka M, Simanek M, Sponer J, Burda J. V. Copper cation interactions with biologically essential types of ligands: A computational DFT study. J. Phys. Chem. A. 2006 Mar;110:4795-4809.

67. Prabhakar R, Siegbahn P. E. M. A theoretical study of the mechanism for the biogenesis of cofactor topaquinone in copper amine oxidases. J. Am. Chem. Soc. 2004 Mar;126:3996-4006.

68. Rickard G. A, Gomez-Balderas R, Brunelle P, Raffa D. F, Rauk A. Binding affinities for models of biologically available potential Cu(II) Ligands relevant to Alzheimer's disease: An ab initio study. J. Phys. Chem. A. 2005 Aug;109:8361-8370.

69. Rimola A, Rodriguez-Santiago, L, Sodupe M. Cation-pi interactions and oxidative effects on Cu+ and Cu2+ binding to Phe, Tyr, Trp, and his amino acids in the gas phase. Insights from first-principles calculations. J. Phys. Chem. B. 2006 Nov;110:24189-24199.

70. Rokhsana D, Dooley D. M, Szilagyi R. K. Structure of the oxidized active site of galactose oxidase from realistic in silico models. J. Am. Chem. Soc. 2006 Nov;128:15550-15551.

71. Rokhsana D, Howells A. E, Dooley D. M, Szilagyi R. K. Role of the Tyr-Cys Cross-link to the Active Site Properties of Galactose Oxidase. Inorg. Chem. 2012 Feb;51:3513-3524.

72. Sabolovic J, Tautermann C. S, Loerting T, Liedl K. R. Modeling anhydrous and aqua copper(II) amino acid complexes: A new

molecular mechanics force field parametrization based on quantum chemical studies and experimental crystal data. Inorg. Chem. 2003 Mar;42:2268-2279.

73. Blomberg M. R. A, Siegbahn P. E. M. Quantum chemistry applied to the mechanisms of transition metal containing enzymes - Cytochrome c oxidase, a particularly challenging case. J. Comp. Chem. 2006 Jun;27:1373-1384.

74. Hong G, Ivnitski D. M, Johnson G. R, Atanassov P, Pachter R. Design Parameters for Tuning the Type 1 Cu Multicopper Oxidase Redox Potential: Insight from a Combination of First Principles and Empirical Molecular Dynamics Simulations. J. Am. Chem. Soc. 2011 Apr;133(13):4802-4809.

75. Moon S, Patchkovskii S, Salahub D. R. QM/MM calculations of EPR hyperfine coupling constants in blue copper proteins. J. Mol. Struct.-Theochem. 2003 Aug;632:287-295.

76. Rodriguez-Granillo A, Crespo A, Wittung-Stafshede P. Conformational Dynamics of Metal-Binding Domains in Wilson Disease Protein: Molecular Insights into Selective Copper Transfer. Biochem. 2009 Jun;48:5849-5863.

77. Rose F, Hodak M, Bernholc J. Mechanism of copper(II)-induced misfolding of Parkinson's disease protein. Scientific Reports. 2011 Jun;1:11.

78. Sinnecker S, Neese F. QM/MM calculations with DFT for taking into account protein effects on the EPR and optical spectra of metalloproteins. Plastocyanin as a case study. J. Comput. Chem. 2006 Jun;27:1463-1475.

79. Brancato G, Rega N, Barone V. Microsolvation of the Zn(II) ion in aqueous solution: A hybrid QM/MM MD approach using non-periodic boundary conditions. Chem. Phys. Lett. 2008 Dec;451:53-57.

80. Hartsough D. S. Merz K. M. Dynamic Force Field Models – Molecular-Dynamics Simulations of Human Carbonic-Anhydrase-II Using a Quantum-Mechnaical Molecular Mechanical Coupled Potential. J Phys Chem. 1995 Jul;99:11266-11275.

81. Ryde, U. The coordination of the catalytic zinc ion in alcohol dehydrogenase studied by combined quantum-chemical and molecular mechanics calculations. J. Computer-Aided Molecular Design. 1996 Jan;10(2):153-164.

82. Ryde U. Combined quantum and molecular mechanics calculations on metalloproteins"

Current Opinion in Chemical Biology. 2003 Feb;7:136-142.

83. Mutter S. T, Deeth R. J, Turner M, Platts J. A. Benchmarking of copper(II) LFMM parameters for studying amyloid-β peptides. J. Biomol. Struct. Dyn. 2017 Apr;36:1145-1153.

84. Wise O, Coskuner O. New force field parameters for metalloproteins I: Divalent copper ion centers including three histidine residues and an oxygen-ligated amino acid residue. J. Comput. Chem. 2014 Apr;35:1278-1289.

85. Coskuner O. Divalent copper ion bound amyloid-β(40) and amyloid-β(42) alloforms are less preferred than divalent zinc ion bound amyloid-β(40) and amyloid-β(42) alloforms. J. Biol. Inorg. Chem. 2016 Sept;21:957.

86. Coskuner Weber O, Uversky V. N. How accurate are your simulations? Effects of confined aqueous volume and AMBER FF99SB and CHARMM22/CMAP force field parameters on structural ensembles of intrinsically disordered proteins: Amyloid-β42 in water. Intrinsically Disordered Proteins. 2017 Oct;5:1.

87. Xu L, Wang X, Shan S, Wang X. Characterization of the polymorphic states of copper(II)-bound Aβ(1–16) peptides by computational simulations. J. Comp. Chem. Aug;34:2524-2536.

88. Wise-Scira O, Xu L, Kitahara T, Perry G, Coskuner O. Amyloid-β peptide structure in aqueous solution varies with fragment size. J. Chem. Phys. 2011 Nov;135:205101.

89. Parthasarathy S, Long F, Miller Y, Xiao Y, McElheny D, Thurber K, Ma, Nussinov R, Ishii Y. Molecular-Level Examination of Cu2+ Binding Structure for Amyloid Fibrils of 40-Residue Alzheimer's β by Solid-State NMR Spectroscopy. J. Am. Chem. Soc. 2011 Feb;133:3390-3400.

90. Domingo A, Angeli C, de Graaf C, Robert V. Electronic reorganization triggered by electron transfer: The intervalence charge transfer of a Fe3+/Fe2+ bimetallic complex. J. Comp. Chem. 2015 Mar;36:861-869.

91. Bixon M, Jortner J. Electron Transfer – from Isolated Molecules to Biomolecules. 1999. John Wiley & Sons. ISBN: 9780471252924.

92. Coskuner O, Bergeron D. E, Rincon L, Hudgens J. W, Gonzalez C. A. Identification of

Active Sites of Biomolecules. 1. Methyl-α-mannopyranoside and FeIII. J. Phys. Chem. A 2008 Feb;112:2940-2947.

93. Coskuner O, Bergeron D. E, Rincon L, Hudgens J. W, Gonzalez C. A. Identification of active sites of biomolecules II: Saccharide and transition metal ion in aqueous solution. J. Phys. Chem. A 2009 Feb;113:2491-2499.

94. Kodali R, Williams A. D, Chemuru S, Wetzel R. Aβ(1–40) Forms Five Distinct Amyloid Structures whose β-Sheet Contents and Fibril Stabilities Are Correlated. J. Mol. Biol. 2010 Aug;401:503-517.

95. Tycko R, Wickner R. B. Molecular structures of amyloid and prion fibrils: consensus versus controversy. Acc. Chem. Res. 2013 Jul;46:1487-1496.

96. Wise-Scira O, Xu L, Perry G, Coskuner O. Structures and free energy landscapes of aqueous zinc(II)-bound amyloid-β(1–40) and zinc(II)-bound amyloid-β(1–42) with dynamics. J. Biol. Inorg. Chem. 2012 Jun;17:927-938.

97. Sharma A. K, Pavlova S. T, Kim J, Finkelstein D, Hawco N. J, Rath N. P, Kim J, Mirica L. M. Bifunctional compounds for controlling metal-mediated aggregation of the aβ42 peptide. J. Am. Chem. Soc. 2012 Apr;134:6625-6636.

98. Asandei A, Schiopu I, Iftemi S, Mereuta L, Luchian T. Investigation of Cu2+ binding to human and rat amyloid fragments Aβ (1-16) with a protein nanopore. Langmuir 2013 Dec;29:15634-15642.

99. Morante S. The Role of Metals in β - Amyloid Peptide Aggregation: X-Ray Spectroscopy and Numerical Simulations. Curr. Alz. Res. 2008 Dec;5:508-524.

100. Silva K. I, Michael B. C, Geib S. J, Saxena S. ESEEM Analysis of Multi-Histidine Cu(II)-Coordination in Model Complexes, Peptides, and Amyloid-β. J. Phys. Chem. B 2014 Jul;118:8935-8944.

101. El Khoury Y, Dorlet P, Faller P, Hellwig P. New Insights into the Coordination of Cu(II) by the Amyloid-B 16 Peptide from Fourier Transform IR Spectroscopy and Isotopic Labeling. J. Phys. Chem. B 2011 Oct;115:14812-14821.

102. Hane F, Tran G, Attwood S. J, Leonenko Z. Cu(2+) affects amyloid-β (1-42) aggregation by increasing peptide-peptide binding forces. PLoS One 2013 Mar;8:e59005.

103. Nair N. G, Perry G, Smith M. A, Reddy V. P. NMR studies of zinc, copper, and iron binding to histidine, the principal metal ion complexing site of amyloid-beta peptide. J. Alz. Dis. 2010 Mar;20:57-66.

104. Allison T. C, Coskuner O, Gonzalez C. A. Metallic Systems: A Quantum Chemist´s Perspective. Boca Raton CRC Press/Taylor & Francis; 2011432 p. ISBN: 978-4200-6986-7.

105. Hornak V, Abel R, Okur A, Strockbine B, Roitberg A, Simmerling C. Comparison of multiple Amber force fields and development of improved protein backbone parameters. Proteins. 2006 Nov;65:712-725.

106. Binder K, Horbach J, Kob W, Paul W, Varnik F. Molecular dynamics simulations. J. Phys.: Cond. Matter 2004 Jan;16:S429-S453.

107. Beeman D. Some multistep methods for use in molecular dynamics calculations. J. Comput. Phys. 1976 Feb;20:130-139.

108. Xu L, Wang X, Wang X. Characterization of the internal dynamics and conformational space of zinc-bound amyloid β peptides by replica-exchange molecular dynamics simulations. 2013 July;42:575-586.

109. Xu L, Wang X, Wang X. Effects of Zn2+ Binding on the Structural and Dynamic Properties of Amyloid B Peptide Associated with Alzheimer's Disease: Asp1 or Glu11? 2013 Aug;4:1458-1468.

110. Prakash M. K, Barducci A, Parrinello M. Replica Temperatures for Uniform Exchange and Efficient Roundtrip Times in Explicit Solvent Parallel Tempering Simulations. J. Chem. Theory Comput. 2011 Jun;7:2025-2027.

111. Lee M. R, Duan Y, Kollman P. A. Use of MM-PB/SA in estimating the free energies of proteins: application to native, intermediates, and unfolded villin headpiece. Proteins. 2000 Jun;39:309-316.

112. Kollman P. A, Massova I, Reyes C, Kuhn B, Huo S, Chong L, Lee M, Lee T, Duan Y, Wang W, Donini O, Cieplak P, Srinivasan J, Case D. A, Cheatham T. E. Calculating Structures and Free Energies of Complex Molecules: Combining Molecular Mechanics and Continuum Models. Acc. Chem. Res. 2000 Oct;33:889-897.

113. Kabsch W, Sander C. Dictionary of protein secondary structure: pattern recognition of hydrogen-bonded and geometrical features. Biopolymers. 1983 Dec;22:2577-2637.

114. Pawar A. P, DuBay K. F, Zurdo J, Chiti F, Vendruscolo M, Dobson C. M. Prediction of "aggregation-prone" and "aggregation-susceptible" regions in proteins associated with neurodegenerative diseases. J. Mol. Biol. 2005 Jul;350:379-392.

115. Nagypal I, Gergely A, Farkas E. Thermodynamic Study of Parent and Mixed Complexes of Aspartic-acid, Glutamic-acid and Glycine with Copper(II). Journal of Inorganic & Nuclear Chemistry. 1974 ;36:699-706.

116. Gassmann E, Kuo J. E, Zare R. N. Electrokinetic Separation of Chiral Compounds. Science. 1985 Nov;230:813-814.

117. Gozel P, Gassmann E, Michelsen H, Zare R. N. Electrokinetic Resolution of Amino-Acid Enantiomers with Copper(II) Aspartame Support Electrolyte. Analytical Chemistry. 1987 Jan;59:44-49.

118. Rickard G. A, Gomez-Balderas R, Brunelle P, Raffa D. F, Rauk A. Binding affinities for models of biologically available potential Cu(II) Ligands relevant to Alzheimer's disease: An ab initio study. J. Phys. Chem. A. 2005 Sep;109:8361-8370.

119. Smith D. P, Smith D. G, Curtain C. C, Boas J. F, Pilbrow J. R, Ciccotosto G. D, Lau T. L, Tew D. J, Perez K, Wade J. D, Bush A. I, Drew S. C, Separovic F, Masters C. L, Cappai R, Barnham K. J. Copper-mediated amyloid-beta toxicity is associated with an intermolecular histidine bridge. J. Biol. Chem. 2006 Jun;281:15145-15154.

120. Cherny R. A, Atwood C. S, Xilinas M. E, Gray D. N, Jones W. D, McLean C. A, Barnham K. J, Volitakis I, Fraser F. W, Kim Y, Huang X, Goldstein L. E, Moir R. D, Lim J. T, Beyreuther K, Zheng H, Tanzi R. E, Masters C. L, Bush A. I. Treatment with a copper-zinc chelator markedly and rapidly inhibits beta-amyloid accumulation in Alzheimer's disease transgenic mice. Neuron. 2001 Mar;30:665-676.

121. Cuajungco M. P, Goldstein L. E, Nunomura A, Smith M. A, Lim J. T, Atwood C. S, Huang X, Farrag Y. W, Perry G, Bush A. I. Evidence that the beta-amyloid plaques of Alzheimer's disease represent the redox-silencing and entombment of abeta by zinc. J. Biol. Chem. 2000 Jun;275:19439-19442.

122. Faller P. Copper and zinc binding to amyloid-beta: coordination, dynamics, aggregation, reactivity and metal-ion transfer. CHEMBIOCHEM. 2009 Dec;10:2837-2845.

123. Rajendran R, Minqin R, Ynsa M. D, Casadesus G, Smith M. A, Perry G, Halliwell B, Watt F. A novel approach to the identification and quantitative elemental analysis of amyloid deposits--insights into the pathology of Alzheimer's disease. Bichem. Biophys. Res. Commun. 2009 Apr;382:91-95.

124. Lovell M. A, Robertson J. D, Teesdale W. J, Campbell J. L, Markesbery W. R. Copper, iron and zinc in Alzheimer's disease senile plaques. J. Neurol. Sci. 1998 Jun;158:47-52.

125. Talmard C, Guilloreau L, Coppel Y, Mazarguil H, Faller P. Amyloid-beta peptide forms monomeric complexes with Cu(II) and Zn(II) prior to aggregation. CHEMBIOCHEM. 2007 Jan;8:163-165.

126. Sitkiewicz E, Kłoniecki M, Poznański J, Bal W, Dadlez M. Factors influencing compact-extended structure equilibrium in oligomers of aβ1-40 peptide--an ion mobility mass spectrometry study. J. Mol. Biol. 2014 Jul;426:2871-2885.

127. Noy D. Solomonov I, Sinkevich O, Arad T, Kjaer K, Sagi I. Zinc-Amyloid β Interactions on a Millisecond Time-Scale Stabilize Non-fibrillar Alzheimer-Related Species. J. Am. Chem. Soc. 2008 Jan;130:1376-1383.

128. Yang M, Teplow D. B. Amyloid beta-protein monomer folding: free-energy surfaces reveal alloform-specific differences. J. Mol. Biol. 2008 Dec;384:450-464.

129. Walsh D. M, Lomakin A, Benedek G. B, Condron M. M, Teplow D. B. Amyloid beta-protein fibrillogenesis. Detection of a protofibrillar intermediate. J. Biol. Chem. 1997 Aug;272:22364-22372.

130. Bitan G, Kirkitadze M. D, Lomakin A, Vollers S. S, Benedek G. B, Teplow D. B. Amyloid beta -protein (Abeta) assembly: Abeta 40 and Abeta 42 oligomerize through distinct pathways. Proc. Natl. Acad. Sci. USA 2003 Jan;100:330-335.

131. Raffa D. F, Rauk A. Molecular Dynamics Study of the Beta Amyloid Peptide of Alzheimer's Disease and Its Divalent Copper Complexes. J. Phys. Chem. B. 2007 Mar;111:3789-3799.

132. Boopathi S, Kolandaivel P. Role of zinc and copper metal ions in amyloid β-peptides Aβ1−40 and Aβ1−42 aggregation. RSC Adv. 2014 Aug;4:38951-38965.

133. Dong M, Li H, Hu D, Zhao W, Zhu W, Ai H. Molecular Dynamics Study on the Inhibition Mechanisms of Drugs CQ1−3 for Alzheimer

Amyloid-β40 Aggregation Induced by Cu2+. ACS Chem. Neurosci. 2016 Feb;7:599-614.

134. Velez-Vega C, Escobedo F. A. Characterizing the Structural Behavior of Selected Aβ-42 Monomers with Different Solubilities. J. Phys. Chem. B. 2011 Apr;115:4900-4910.

135. Yang C, Li J, Li Y, Zhu X. The effect of solvents on the conformations of Amyloid β-peptide (1–42) studied by molecular dynamics simulation. J. Mol. Struct. (THEOCHEM) Jan;895:1-8.

136. Sgourakis N. G, Yan Y, McCallum S. A, Wang C, Garcia A. E. The Alzheimer's peptides Abeta40 and 42 adopt distinct conformations in water: a combined MD / NMR study. J. Mol. Biol. 2007 May;368:1448-1457.

137. Yan Y, Wang C. Abeta42 is more rigid than Abeta40 at the C terminus: implications for Abeta aggregation and toxicity. J. Mol. Biol. 2006 Dec;364:853-862.

138. Foloppe N, Hartmann B, Nilson L, MacKerell A. D. Intrinsic conformational energetics associated with the glycosyl torsion in DNA: a quantum mechanical study. Biophys. J. 2002 Mar;82:1554-1569.

139. Mantri Y, Fioroni M, Baik M-H. Computational study of the binding of CuII to Alzheimer's amyloid-beta peptide: do Abeta42 and Abeta40 bind copper in identical fashion? J. Biol. Inorg. Chem. 2008 Nov;13:1197-1204.

Compounds derived from flavonoids for photovoltaic applications. Computational chemical investigations

Rachid Kacimi[1] ✉ **, Tayeb Abram[1]** ✉ **, Lahcen Bejjit[1]** ✉ **, Mohammed Bouachrine[1]*** ✉ iD

[1] MEM, EST Meknes, University Moulay Ismail, Morocco.

Abstract: In this paper, we present a quantum chemical analysis of geometries and optoelectronic properties of a series of flavonoids and derivatives with the aim to research new molecules for applications in the fields of chemical physics and materials science. The calculations are based on the functional density theory (DFT) level of the B3LYP with 6-31G (d, p). This method was used to calculate the energy of HOMO and LUMO level, the Egap (gap energy), the Voc open circuit voltage). The DFT (TD-B3LYP /6-31G (d, p)) was used to calculate (λ_{max} maximum of absorption) as well as other quantum parameters. The study of organic solar cells cannot be effective unless accompanied by a thorough understanding electronic distribution on the HOMO and LUMO energy levels of the components, so the researchers calculated and discussed the HOMO, LUMO, energy gap, and Voc of the test compounds. The result shows that these studied molecules are good candidates for application in the fields of optoelectronic devices such as OLED, conducting devices and organic solar cells.

INTRODUCTION

Flavonoids are derivatives of phenylobenzo-γ-pyrone and are frequently found in plants. They are natural pigments distributed throughout the plant kingdom where they function as UV filters and as a protective agent against pathogenic organisms (1). These compounds can be found in black tea and red wine, they are made in the body by the consumption of fruits, vegetables and cereals (2). Flavonoids are increasingly marketed for a variety of pharmaceutical, cosmetic and food products. The flavonoids have a common biosynthetic origin therefore have the same basic structural unit and fifteen carbon atoms consisting of two C6 rings (A and B) linked by a C3 chain (2-phenyl-1-benzopyran ring) (3). The effect of flavonoids in plants is partly due to their filter effect and their high absorption in the UV region of the spectrum (4). The flavonoids, according to their structure, have absorption maxima in the zone of 270 to 350 nm (5). Indeed, several patents and publications have claimed the analysis of flavonoids method microemulsion electrokinetic chromatography approach coupled with light-emitting-diode-induced fluorescence (LED-IF, 480 nm) detection. The results obtained by this method show that most flavonoids were completely separated within 5 min without derivatization (6).

We exhibit here a complete computational investigation using the method functional density theory (DFT) and employing the B3LYP (Becke three-parameter Lee–Yang–Parr) exchange correlation functional with 6-31G (d, p) in order to predict a qualitative description of the

interaction. Firstly, we start by optimizing the studied structures; then from the most stable optimized structure, we determine the energy HOMO, LUMO and gap energy (E_{gap}). This energy allows us to estimate and calculate the photovoltaic parameters. Extensive Time-Dependent Density Functional Theory (TD-DFT) calculations have been carried out in order to obtain the maximum absorption wavelength. The structures of the studied molecules are shown in Figure 1, we will perform quantitative calculations on of the studied compounds and we will determine their optoelectronic, absorption and photovoltaic properties, the results obtained show that these materials have been proposed as good candidates in the fields of optoelectronic devices such as OLED, conducting devices and organic solar cells.
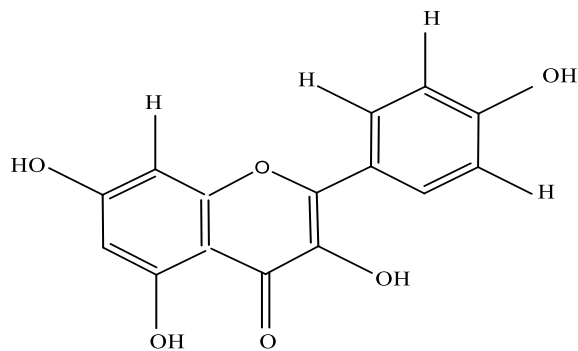
M1: Kaempferol
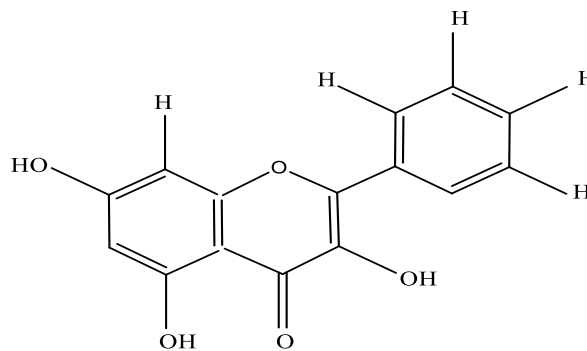
M2 :Galangin
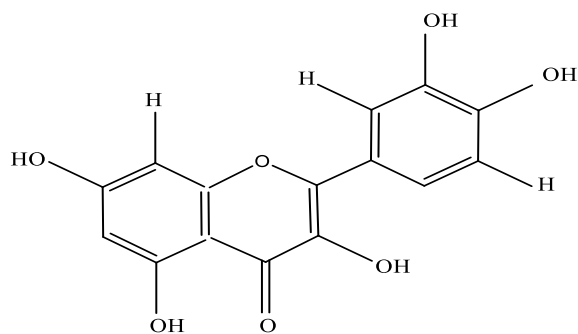
M3 :Quercetin
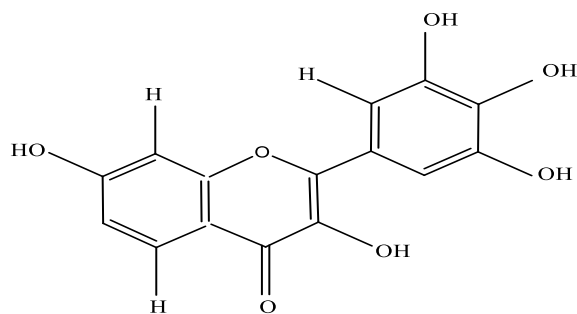
M4 : Robinetin
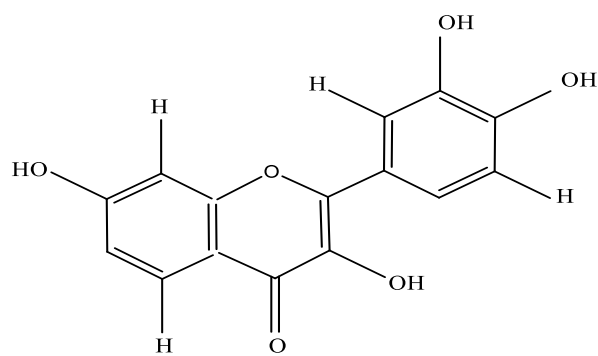
M5 : Fisetin
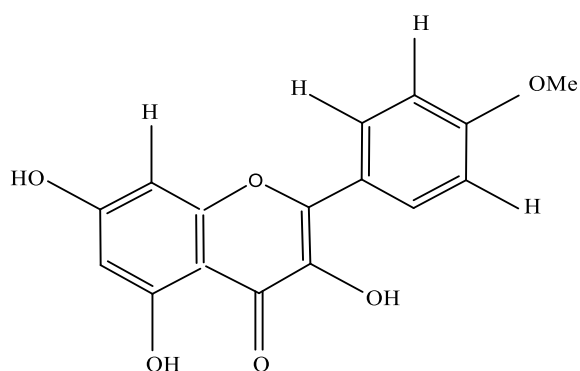
M6 : Kaempferide
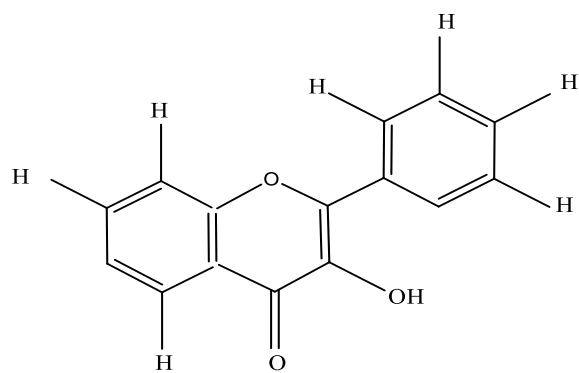
M7 : 3-Hydroxy- flavone
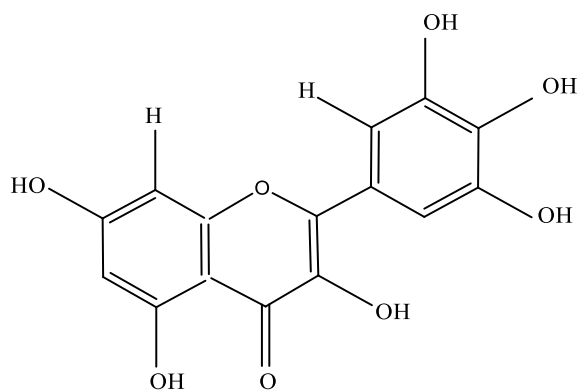
M8 : Myricetin
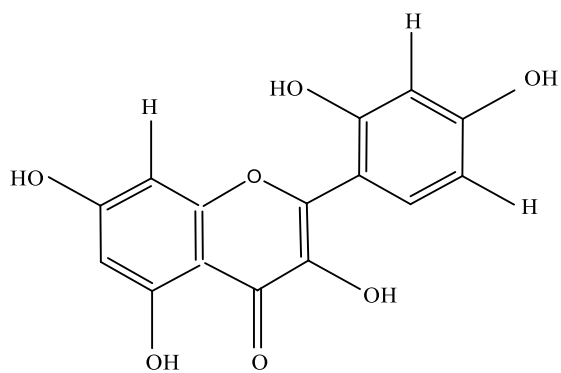
M9 : Morin
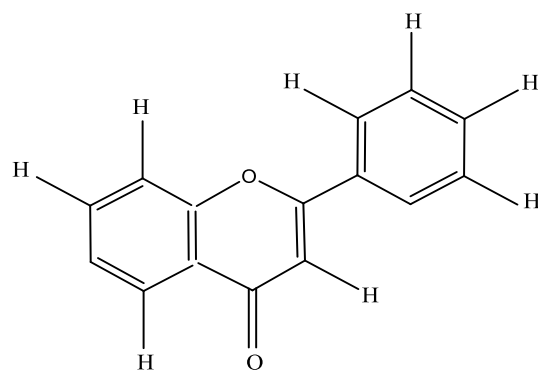
M10 : Flavone
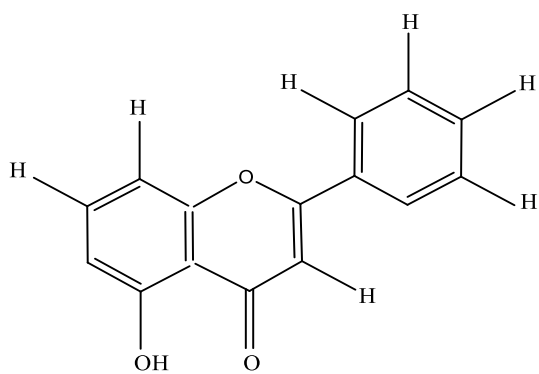
M11: 5-Hydroxy- flavone
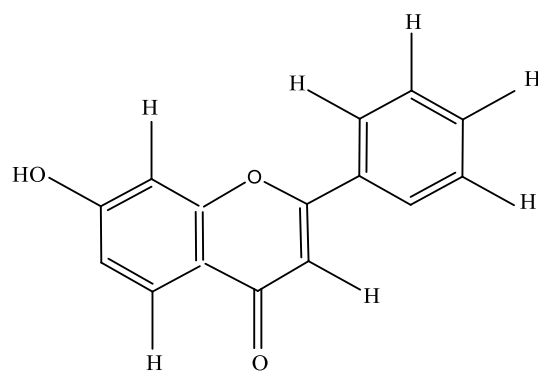
M12 :7-Hydroxy –flavone
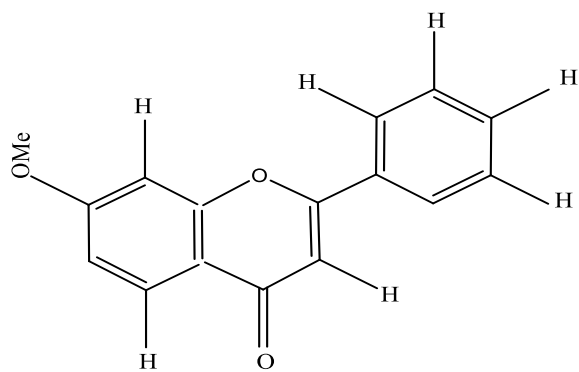
M13 : 8-Methoxy- flavone

Figure 1: The chemical structure of the studied compounds Mi.

MATERIALS AND METHODS

The ground-state geometries of the studied molecules were optimized using DFT (Density Functional Theory) and employing the B3LYP method with 6-31G(d, p) basis set for all molecules (7). In order to obtain the loaded structures, optimized structures of the neutral form are used. The calculations were carried out using the GAUSSIAN 9.0 program (8). The geometric structures of the neutral molecules have been optimized without constraint. We also reviewed the HOMO and LUMO levels; the E_{gap} energy is evaluated as the difference between the HOMO and the LUMO, energies oscillator forces were studied using TD/DFT calculations of these

optimized geometries. The energy of highest occupied molecular orbital (HOMO) and lowest unoccupied molecular orbital (LUMO) levels were examined and visualized using Gaussview 5 Program. In fact, these methods of calculation have been successfully applied to other conjugated polymers (9).

RESULTS AND DISCUSSION

The results of different optimizations to find the most stable structure for each studied molecule are presented in Figure 2. We found that the obtained structures have similar quasi-planar conformations.
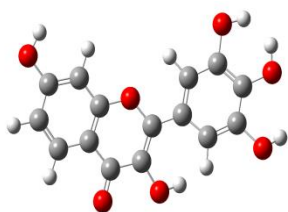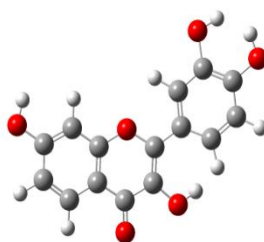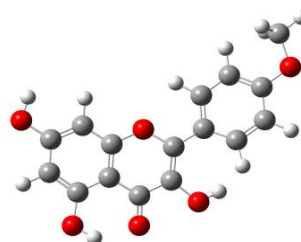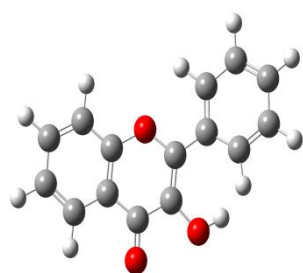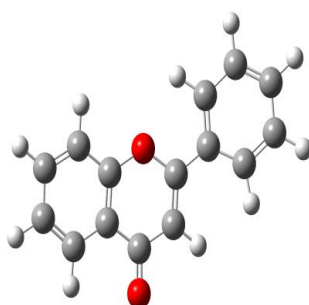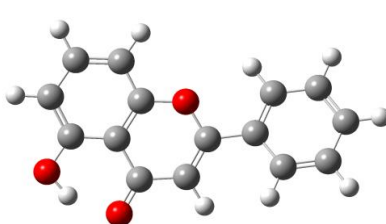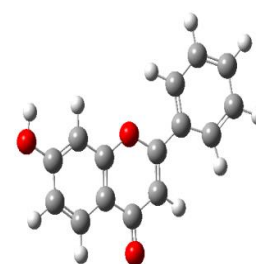

M1

M2

M3

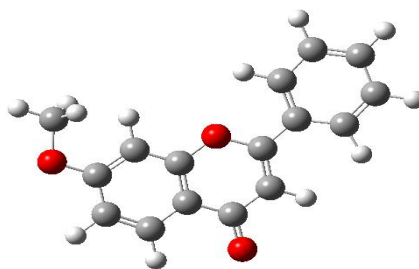M4

M5

M6

M7

M8

M9

M10
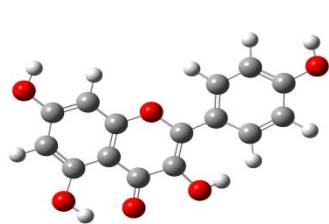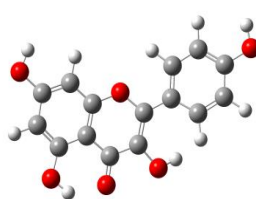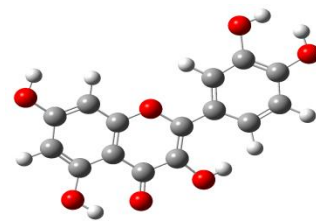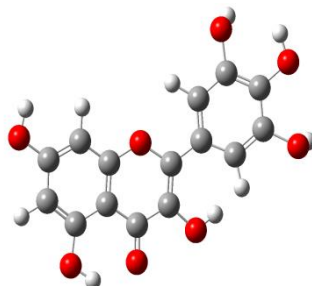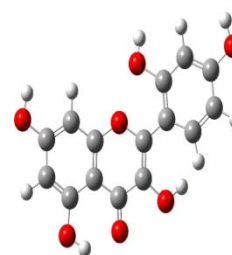
M11

M12

M13

Figure 2: Optimized geometries obtained by B3LYP / 6-31G (d,p) of the studied molecules.

From these optimized structures, we have determined the energies HOMO and LUMO in order to calculate the energy gap E_{gap} (E_{HOMO}-E_{LUMO}). The energies of the HOMO and the LUMO levels of these compounds have been compared to those of the PCBM C60 to estimate the effectiveness in a donor-acceptor organic solar cells structure where the donor is the studied molecules and the acceptor is the PCBMC$_{60}$ (10).

Efficiency of the studied compounds suggested for photovoltaic devices can be estimated by calculation of the power conversion efficiency (PCE) which measures the amount of energy produced by a solar cell in relation to the power available in incident solar radiation (P_{in}). Photovoltaic efficiency of the photovoltaic cell (power conversion efficiency) can be calculated using the following equation:

$$\eta = FF \; \frac{V_{oc} J_{sc}}{P_{inc}} \qquad (Eq\,1)$$

Where Jsc is the short-circuit current, and FF is the fill factor. For solar cells in the (BHJ), the

maximum open circuit voltage (V_{oc}) can be expressed according to Eq. 2 (11).

$$V_{oc} = \left| E_{HOMO} \,(Donor) \right| - \left| E_{LUMO} \,(Acceptor) \right| - 0.3 \qquad (Eq2)$$

We have also calculated for each couple (Donor / acceptor), the parameter alpha:

$$\alpha_i = E_{LUMO} \,(Donor) - E_{LUMO} \,(Acceptor) \qquad (Eq3)$$

The above analysis shows that the LUMO levels of the compounds Mi are higher than the conducting band of PCBM (-3.7 eV). In addition, to efficiently inject the electron in the CB PCBMC60; the value of LUMO donor must be greater than that of PCBMC60. These driving forces are large enough for an efficient injection of electrons, since in organic solar cells the open circuit voltage depends linearly on the HOMO level of the donor and the LUMO level of the acceptor. The maximum open circuit voltage V_{oc} of the solar cell BHJ is related to the difference between the HOMO of the donor and the LUMO of the electron acceptor.

We have presented, in the Table 1, the orbital energies of the studied flavonoids, E_{HOMO}, E_{LUMO}, E_{gap} and the voltage theoretical values in open circuit V_{oc} (eV) Equation (2). Another parameter noted as α_i is the difference between the energy levels of LUMO Mi compounds studied and the level of HOMO PCBMC60 energy equation (3).

As Table 1 shows, the HOMO and LUMO energies of the studied compounds are slightly different.

This shows that the nature of skeletons and substituents plays a key role in the electronic properties. In particular, the effect of the nature and position of the different substituents on the HOMO and LUMO energy level is clearly visible. The effect and the nature of the groups (OH and OMe) attached to the aromatic cycle of the studied molecule on the values of calculated energies is clearly visible.

Thus, the E_{gap} of the studied molecules differ slightly from 3.905 eV 4.314 eV according to this order:

M9 < M8 < M2 < M3 < M1 < M6 < M7 < M4 < M5 < M11 < M13 < M12 < M10

Let us remember that the E_{LUMO} of donor must be greater than that of CB of PCBM C60 (12) "the values of α must be positive". We have noted that the E_{LUMO} values of Mi are higher than that of PCBM. In fact, possibilities of electron transfer are possible. On the other hand, the heterojunction structure (BHJ stands for blend heterojunction) is a mixture of two organic semiconductors between two electrodes in which all the photogenerated

excitons will be able to diffuse without recombining to a donor / acceptor interface and dissociate whatever the of the exciton creation site. This structure therefore makes it possible to exceed the constraint of the limitation of the thicknesses by the diffusion length of the exciton (13, 14).

The values obtained of V_{oc} are in the range 1.510 eV - 2.205 eV (see Table 1). These results are sufficient to suggest these molecules for photovoltaic applications because the process of electron injection of the studied molecule to the PCBMC60 conduction band and the subsequent regeneration are feasible in an organic solar cell. Also, to effectively inject the electron into the PCBMC60 conduction band; the value of LUMO of the donor must be greater than that of PCBMC60, this is verified in Table 1 for the studied molecules.

Table 1: Energy values of E_{LUMO} (eV), E_{HOMO}(eV). E_{gap} (eV), the circuit voltage V_{oc} (eV) and α of the studied molecules.

Compounds	E_{HOMO}(eV)	E_{LUMO}(eV)	E_{gap} (eV)	Voc (eV)	α(eV)
M1	-5.678	-1.711	3.967	1.678	1.989
M2	-5.836	-1.901	3.935	1.836	1.799
M3	-5.717	-1.777	3.940	1.717	1.923
M4	-5.691	-1.717	3.974	1.691	1.983
M5	-5.662	-1.678	3.984	1.662	2.022
M6	-5.650	-1.683	3.967	1.650	2.017
M7	-5.833	-1.862	3.971	1.833	1.838
M8	-5.751	-1.817	3.933	1.751	1.883
M9	-5.510	-1.605	3.905	1.510	2.095
M10	-6.205	-1.891	4.314	2.205	1.809
M11	-6.036	-1.970	4.065	2.036	1.730
M12	-6.023	-1.818	4.204	2.023	1.882
M13	-5.978	-1.776	4.202	1.978	1.924
PCBM C60	-6.100	-3.700			
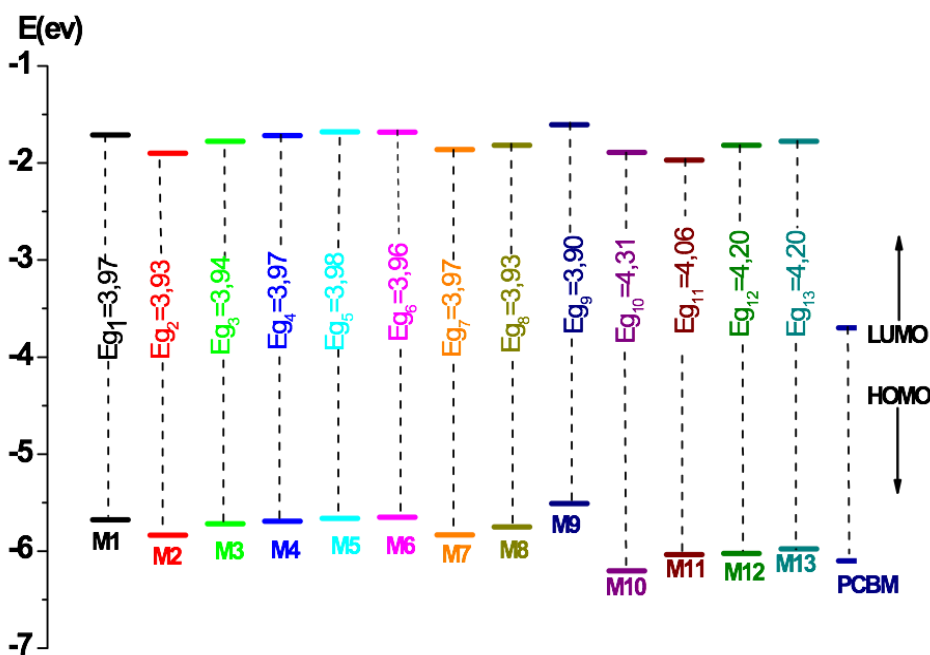
Figure 3: Sketch of the calculated energy of the HOMO. LUMO levels of studied molecules and PCBM.

In order to provide information regarding the excitation properties, one must examine the order and organization of the lobes in the HOMO and virtual LUMO occupied orbitals (12). So we 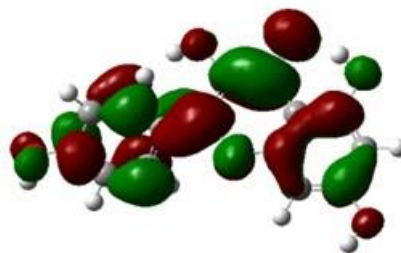have presented in Figure 4, the obtained lobes of the occupied orbital HOMO and the virtual LUMO from each optimized structure.
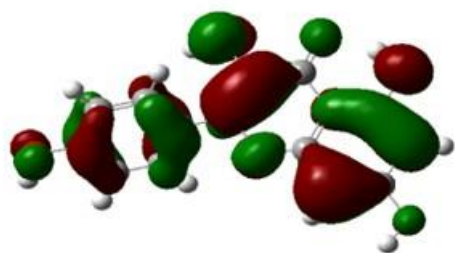
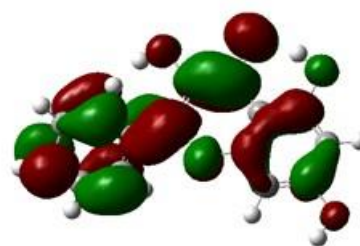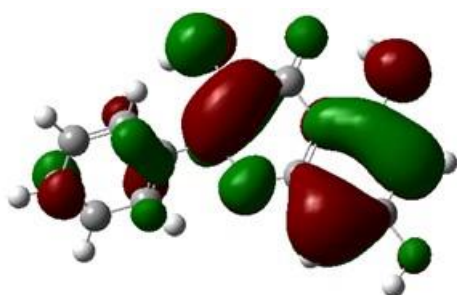The results of Figure 4 show that the HOMO has an anti-binding character while the LUMO of all

the compounds generally has a binding character
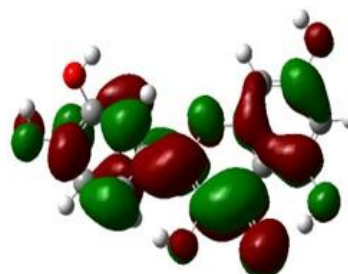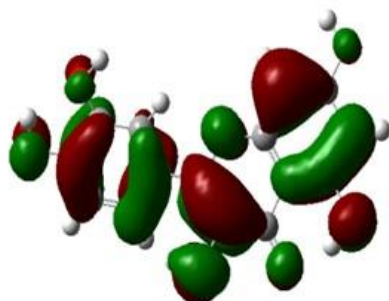between the subunits(13).

HOMO   **LUMO**

M1

M2

M3
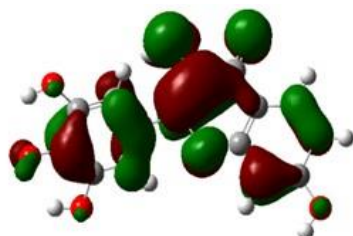

M4

M5

M6

M7

M8

M9

M10
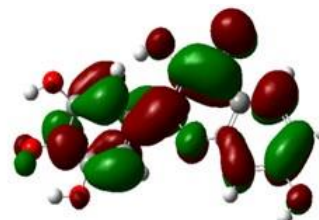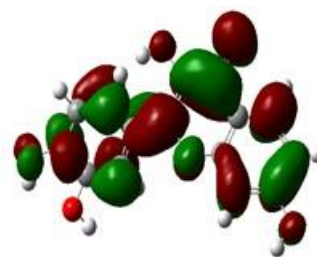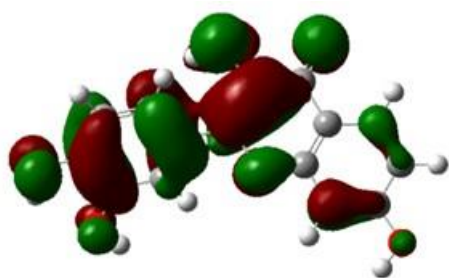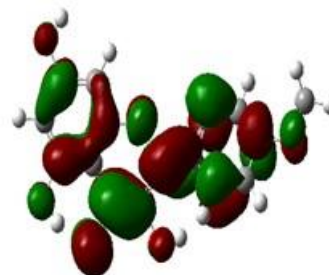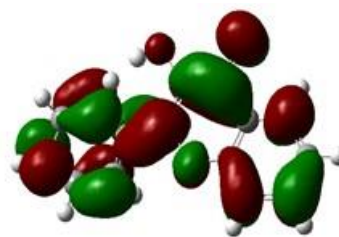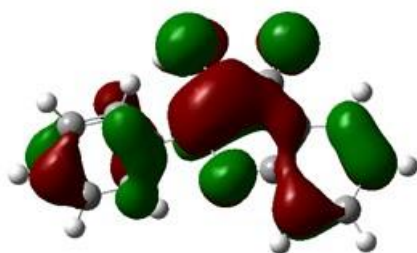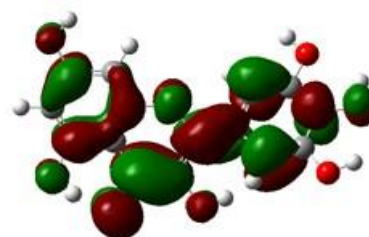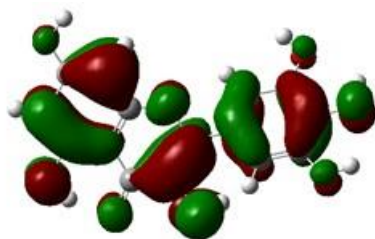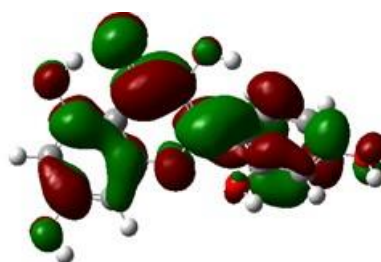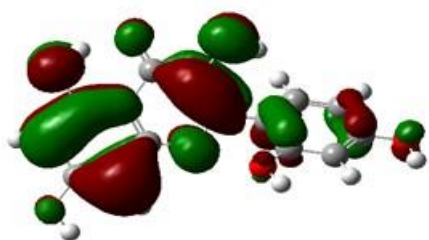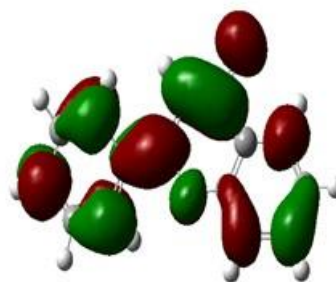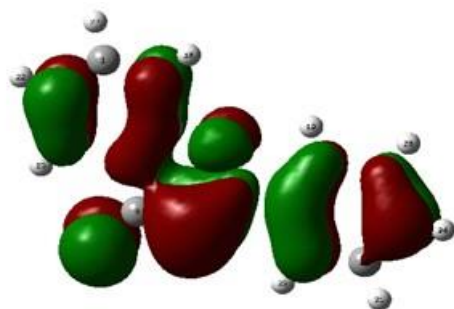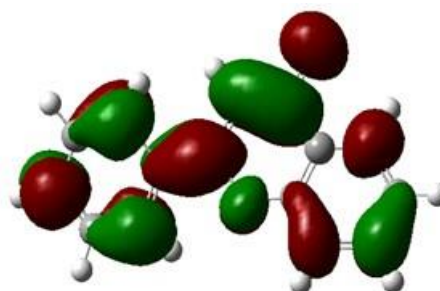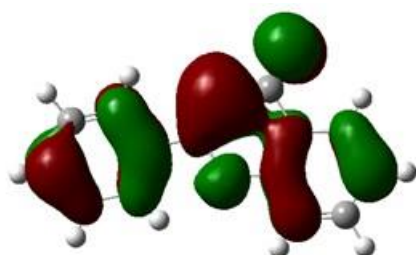
M11
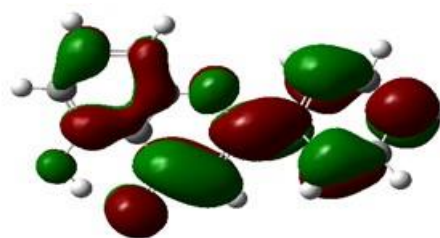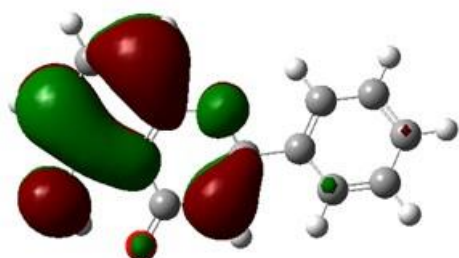
M12
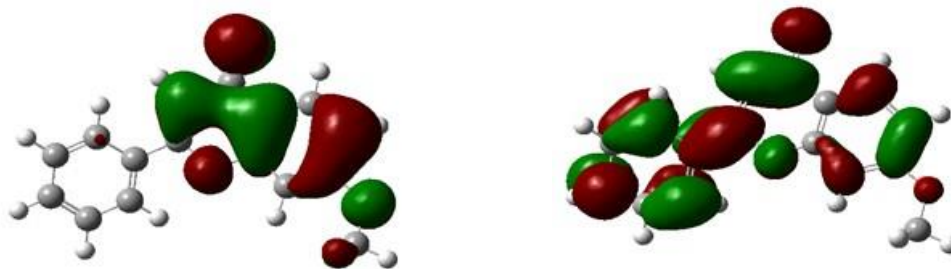
M13

Figure 4: The contour plots of HOMO and LUMO orbitals of the studied compounds obtained by B3LYP/6-31(d,p) level.

It is important to mention that a good photovoltaic material must have as wide spectrum of absorption as possible and absorb in the visible range of the electromagnetic spectrum(14). Because the absorption properties are a key factor for suggesting photovoltaic applications, the UV-visible spectra of the compounds (Mi) were determined by using TD-DFT method. So, we have presented in Table 2, the absorption maximum detailed calculation wavelength (λ_{max}), the oscillator strength (OS), the transition energy (E_{ex}) and the main molecular orbital (MO) involved in the transition are listed in Table 2. We found that all optical absorption corresponds to transitions from HOMO to LUMO +1. Moreover compared to M13, the maximum absorption peak shows a bathochromic shift of 398-522 nm.

Let us remember that the first excitation corresponds almost exclusively to the passage of an electron from the HOMO level to the LUMO level(15). The absorption wavelengths resulting from the electronic transition S0 → S1 increases progressively as the conjugated chain increases. This is reasonable since the transition HOMO → LUMO is predominant in the electronic transition S0 → S1; that the results are a decrease in LUMO and an increase in HOMO energy.

Table 2: Absorption spectra obtained by TD-DFT method for M (i = 1 to 13).

Compounds	λ_{max} (nm)	E_{ex} (eV)	O.S (eV)	MO/character (%)
M1	352.31	3.52	0.19	HOMO ⟶ LUMO+1 (83%)
M2	359.22	3.45	0.13	HOMO ⟶ LUMO+1 (87%)
M3	353.58	3.50	0.22	HOMO ⟶ LUMO+1 (81%)
M4	323.87	3.83	0.27	HOMO ⟶ LUMO+1 (70%)
M5	328.22	3.77	0.36	HOMO ⟶ LUMO+1 (83%)
M6	352.61	3.51	0.22	HOMO ⟶ LUMO+1 (83%)
M7	354.36	3.50	0.22	HOMO ⟶ LUMO+1 (87%)
M8	354.36	3.50	0.22	HOMO ⟶ LUMO+1 (81%)
M9	342.16	3.62	0.15	HOMO ⟶ LUMO+1 (86%)
M10	371.95	3.33	0.00	HOMO ⟶ LUMO+1 (89%)
M11	361.79	3.42	0.04	HOMO ⟶ LUMO+1 (93%)
M12	353.86	4.16	0.20	HOMO ⟶ LUMO+1 (66%)
M13	301.88	4.10	0.20	HOMO ⟶ LUMO+1 (58%)

Figure 5 shows the calculated optical absorption spectra. We note that the values of (λ_{max}) of thirteen studied compounds are in the order of M10 > M11> M2> M8 > M7 > M12 > M3 > M6 >

M1 > M9 > M5 > M4 > M13 (see Table 2).The strongest absorption in UV-visible (λ_{max} > 300 nm) corresponds to electronic transition HOMO-LUMO+1 of all compounds. The increase of a bathochromic shift of thirteen compounds is attributed to increase of the conjugated system of these compounds when going from M13-M1 which also can be seen respectively in M13 (301.88 nm), M4 (323.87 nm), M5 (328.22 nm), M9 (342.16 nm), M1 (352.31 nm), M6 (352.61 nm), M3 (353.58 nm), M12 (353.86 nm), M7 (354.36 nm) , M8 (354.36 nm), M2 (359.22 nm), M11 (361.79 nm) and M10 (371.95 nm). This effect comes from the fact that the studied compounds have different structures and different aromaticity, and the effects of the nature and the position of the substitution in the aromatic cycles. These interesting remarks are already confirmed by the study of the electronic properties in the previous paragraph.

Figure 5: Simulated UV–visible optical absorption spectra of studied compounds obtained by using TD-DFT/B3LYP/6-31G(d,p).

CONCLUSION

In this work, we have analyzed the quantum and electronic properties of various flavonoids and derivatives using the DFT / B3LYP6-31G (d,p) method. This allowed, first, the prediction of the geometric, electronic and absorption properties; then, the calculation of the photovoltaic properties by empirical formulas and finally, the possibility of proposing them for optoelectronic applications. The results show that:

The calculated E_{gap} vary from 3.905 to 4.314 (eV);

> The molecule M9 has a low band gap compared to other compounds;
> ✓ The calculated V_{oc} values vary from 2.205 eV to 1.510 eV;
>
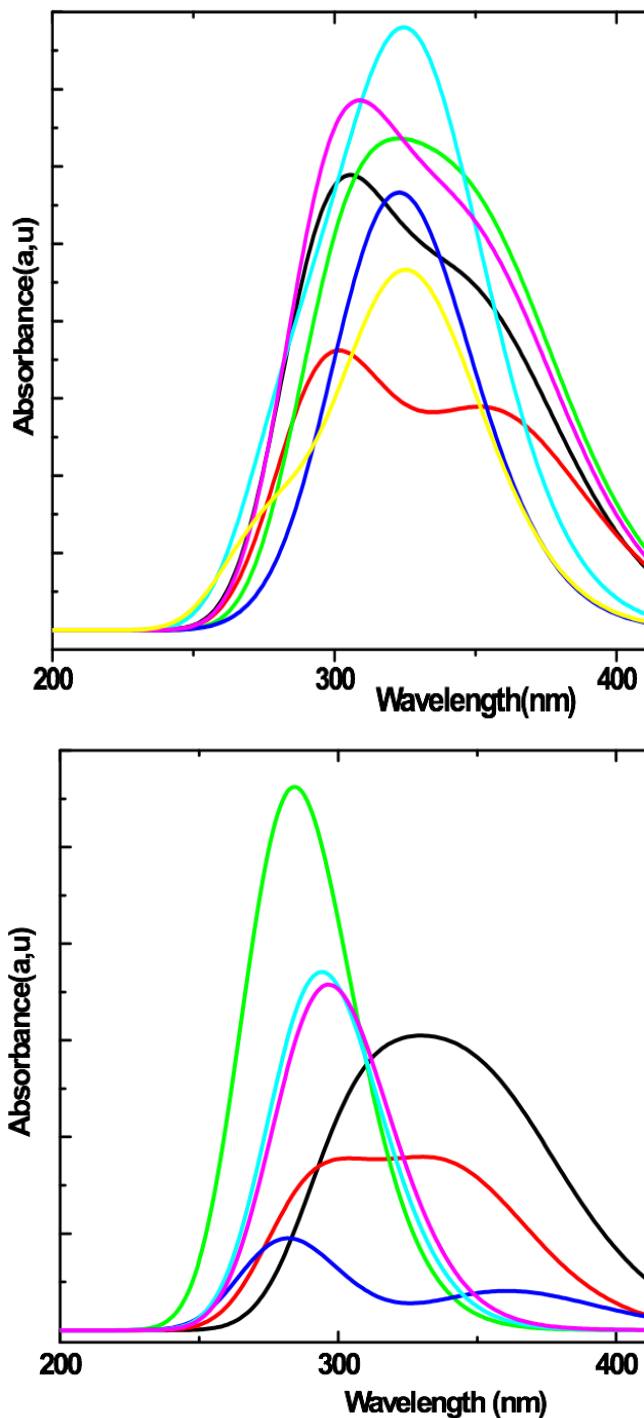> ✓ Absorption spectra were obtained at TD-B3LYP / 6-31G (d,p) levels, the absorption maxima obtained are in the range of 301.88-371.95 nm;

Finally, the results of the quantum chemical calculations used in this study show that all the studied flavonoids could be used as donor molecules with the PCBM receptor in BHJ type organic solar cells. Thanks to advanced computing tools such as GAUSSIAN 9.0, quantum chemistry can be used for the prediction of physicochemical properties, in particular electronic properties. This will guide the experimental chemists to design diversified structures precursors of new materials for optoelectronic applications.

REFERENCES

1.   Buer CS, Imin N, Djordjevic MA. Flavonoids: new roles for old molecules. Journal of integrative plant biology. 2010;52(1):98-111.

2.   Rice-Evans CA, Miller NJ, Paganga G. Structure-antioxidant activity relationships of flavonoids and phenolic acids. Free radical biology and medicine. 1996;20(7):933-56.

3.   Kong J-M, Chia L-S, Goh N-K, Chia T-F, Brouillard R. Analysis and biological activities of anthocyanins. Phytochemistry. 2003;64(5):923-33.

4.   Farkas O, Jakus J, Héberger K. Quantitative structure–antioxidant activity relationships of flavonoid compounds. Molecules. 2004;9(12):1079-88.

5.   Marcussi DG. Desenvolvimento e avaliação das atividades antioxidante e despigmentante in vitro de emulsões múltiplas a/o/a contendo dipalmitato kójico. 2012.

6.   Cao W, Hu S-S, Li X-Y, Pang X-Q, Cao J, Ye L-H, et al. Highly sensitive analysis of flavonoids by zwitterionic microemulsion electrokinetic chromatography coupled with light-emitting diode-induced fluorescence detection.

Journal of Chromatography A. 2014;1358:277-84.

7.   Li C, Ma C, Li D, Liu Y. Excited state intramolecular proton transfer (ESIPT) of 6-amino-2-(2'-hydroxyphenyl) benzoxazole in dichloromethane and methanol: a TD-DFT quantum chemical study. Journal of Luminescence. 2016;172:29-33.

8.   Kaya S, Guo L, Kaya C, Tüzün B, Obot I, Touir R, et al. Quantum chemical and molecular dynamic simulation studies for the prediction of inhibition efficiencies of some piperidine derivatives on the corrosion of iron. Journal of the Taiwan Institute of Chemical Engineers. 2016;65:522-9.

9.   Goswami S, Aich K, Das S, Pakhira B, Ghoshal K, Quah CK, et al. A Triphenyl Amine-Based Solvatofluorochromic Dye for the Selective and Ratiometric Sensing of OCl− in Human Blood Cells. Chemistry–An Asian Journal. 2015;10(3):694-700.

10.   Sabirov DS, Terentyev AO, Bulgakov RG. Counting the Isomers and Estimation of Anisotropy of Polarizability of the Selected C60 and C70 Bisadducts Promising for Organic Solar Cells. The Journal of Physical Chemistry A. 2015;119(43):10697-705.

11.   Bourass M, Benjelloun AT, Benzakour M, Mcharfi M, Hamidi M, Bouzzine SM, et al. DFT and TD-DFT calculation of new thienopyrazine-based small molecules for organic solar cells. Chemistry Central Journal. 2016;10(1):67.

12.   Wazzan N, El-Shishtawy RM, Irfan A. DFT and TD−DFT calculations of the electronic structures and photophysical properties of newly designed pyrene-core arylamine derivatives as hole-transporting materials for perovskite solar cells. Theoretical Chemistry Accounts. 2018;137(1):9.

13.   Jia C, Zhang J, Bai J, Zhang L, Wan Z, Yao X. Synthesis, physical properties and self-assembly of conjugated donor–acceptor system based on tetrathiafulvalene and functionalized with binding sites. Dyes and Pigments. 2012;94(3):403-9.

14.   Grinberg I, West DV, Torres M, Gou G, Stein DM, Wu L, et al. Perovskite oxides for visible-light-absorbing ferroelectric and photovoltaic materials. Nature. 2013;503(7477):509.

15.   Wojtkiewicz J, Iwan A, Pilch M, Boharewicz B, Wójcik K, Tazbir I, et al. Towards designing polymers for photovoltaic applications: A DFT and experimental study of polyazomethines with various chemical structures. Spectrochimica Acta Part A: Molecular and Biomolecular Spectroscopy. 2017;181:208-17.

RESEARCH ARTICLE

PREPARATION OF POLY(PYROMELLITIC DIANHYDRIDE-CO-THIONIN) MODIFIED VOLTAMMETRIC SENSOR FOR THE DETERMINATION OF EPICATECHIN

Serap TİTRETİR DURAN* ✉

*Department of Chemistry, Faculty of Arts and Sciences, İnönü University, 44280, Malatya-Turkey.

Abstract: In this study, the electrochemical oxidation of epicatechin and its voltammetric sensing is shown at a sensitive platinum electrode modified with poly(pyromellitic dianhydride-co-thionin). The electrochemical response of the sensor was improved in the presence of both electro-inactive (sucrose, fructose, lactose) and electroactive (gallic acid, cafeic acid, ascorbic acid) interferants and displayed an excellent analytical performance for the determination of epicatechin. A linear response was obtained over a range of epicatechin concentrations from 0.05 mM to 0.30 mM and was shown to be useful for quantifying low levels of epicatechin in phosphate buffer solution, PBS, pH 7.00. Regression coefficient (R2) was found to be to be 0.9969. Limit of detection (LOD) was calculated as 1.8×10^{-5} M by using 3s/m. Where m is the slope of the calibration curve and s is the standard deviation of the calibration graph calculated using the Excel Steyx function.

INTRODUCTION

Electrochemical sensors, providing a crucial analytical tool for rapid, sensitive and selective determination of various kinds of analytes, have been widely applied in many fields, such as detection of water quality, clinical chemistry and food quality control. Researchers are mainly working on the design and preparation of various polymeric materials to modify electrodes and the modified electrodes then be used for better electrochemical sensing (1). Polymer modified electrodes have received a great attention in recent years (2). Electrochemical detection of an analyte is a very elegant method in analytical chemistry. An interest in developing electrochemical sensing devices to be used in environmental monitoring, clinical assays or process control is growing rapidly.

Catechins are compounds regarded as important for human health. Epicatechin (EC) is a polyphenol with strong antioxidant properties found in vegetable sources, especially in green tea, cocoa, and grapes. Epicatechin and its derivatives have been shown to possess antibacterial, antiviral, anti-allergic, anti-inflammatory, anti-aging and anti-tumor properties, as well as inhibiting tumor growth, preventing wrinkling, eliminating heavy metal toxicity, reducing bacterial inflammation, improving immunity and exhibiting anti-rotavirus activity (3, 4). Additionally, epicatechin pretreatment has been reported to prevent mice exposed to gamma rays from causing more damage to the

liver (5) and testis (6). In other a study the radio protective property of such phytochemicals has been evaluated, epicatechin, belonging to the group of flavanols, is one of the most potent antioxidants present in the human diet predominantly in grapes, tea, apples and cocoa (7). Studies conducted by some researchers indicate that epicatechin may have a great influence on factors related to cancer metastasis (8).

It is very important to develop a simple, sensitive, accurate and sensitive method for the determination of epicatechins from food, medicine and cosmetic products. For this purpose, many methods such as nuclear magnetic resonance spectroscopy (NMR) (9), high performance liquid chromatography (HPLC) (10-13) thin layer chromatography (TLC) (14-17). Spectrophotometry (18, 19), GC-MS (20) and electrophoresis (4, 21) are used. However, these methods have some disadvantages such as the difficult sample preparation and measuring steps, time consuming and costly. However, in the determination of epicatechin, electrochemical methods have important advantages such as rapid response time, low detection limit, low cost, high reproducibility (22) and film thickness controllability (23). In recent years, polymer coating on electrodes namely electrode modification methods has shown considerable potential for application in the field of sensors (24). The electrochemical detection of epicatechin through adsorptive stripping voltammetry on poly(3,4-ethylenedioxythiophene)-modified Pt electrodes was investigated (25). The mechanism of electrochemical oxidation of epicatechin (EC) on a glassy carbon electrode was investigated over a wide range of conditions, using cyclic and square-wave voltammetry (26).

The aim of the present study was to develop an electrochemical method that will have important advantages such as rapid response time, low detection limit, low cost and high reproducibility for the determination of epicatechin. For this aim, polyimide membrane based voltammetric sensors were developed for epicatechin determination. As the polyimide membrane, poly(pyromellitic dianhydride-co-thionin) (PI), which has a very high film forming property was used to remove the interferants from the electrode surface in the analysis medium. In recent years, polyimide-based materials have attracted great interest, both in industry and in academia, because they exhibit unique properties not shared by conventional polymers (27). Polyimides have important advantages such as physical properties,

adhesive, thermal stability and mechanic strength (28, 29). For this reason, polyimides are widely used in the field of sensors as permselective membranes (27, 28).

EXPERIMENTAL

Reagents and Apparatus
Reagents were of analytical grade or of the highest commercially available purity. The polymer, poly(pyromellitic dianhydride-co-thionin), used for the modification was purchased from Sigma-Aldrich. Epicatechin solutions in 0.1 M phosphate buffer solution (PBS) at pH=7.00 were prepared just before running each experiment. Gallic acid, cumaric acid, ascorbic acid, and epicatechin from Sigma-Aldrich were used. Ultra-pure water was obtained from the Millipore brand Elix 20 model water system.

BAS (Bioanalytical System Inc.) 100BW electrochemical analyzer with C2 cell stand was used for voltammetric measurements. pH measurements were performed by using a HI 2211 model pH/ORP Meter. pH meter was frequently calibrated using standard pH buffers obtained from Merck. A KERN model ABJ-NM/ABS-N electronic balance was used for weighing. In a classical three electrode cell configuration working electrode was Platinum electrode (MF 2014). A platinum wire electrode (BASI MW-1032) was used as auxiliary together with an Ag/AgCl (3 M KCl) reference electrode (CHI111). Platinum electrode was mechanically cleaned using 15, 3 and 1 µm aqueous diamond pastes successively on diamond polishing pads and 0.05 µm alumina slurry on alumina polishing pads. After each polishing operation electrodes were rinsed with distilled water and ultra-sonicated 2-3 minutes in an ultrasonic bath (Branson model 3510).

All glassware including electrolysis cells were kept in 6 M HNO_3 overnight to remove impurities.

RESULT AND DISCUSSION

Preparation of poly(pyromellitic dianhydride-co-thionin) Electrodes
Before starting chemical modification of electrodes, the surface of working electrode was carefully cleaned and polished as described above. Firstly, about 0.1 g of poly(pyromellitic dianhydride-co-thionin) is dissolved in 1 mL of n-methylpyrrolidone (NMP). Then, different volumes (1, 2, 3, 4 and 5 µL) of the poly(pyromellitic dianhydride-co-thionin) solution were dropped on the surface of bare platinum working electrodes. Afterwards poly(pyromellitic dianhydride-co-

thionin) film was dried at room temperature for at least 72 h.

The oxidation steps of EC were located on benzene ring containing two hydroxyl groups on 3' and 4'-position, which represents a typical redox system with two electron oxidation process as showed in Figure 1.

(-)-Epicatechin (EC)   (-)-Epicatechin - quinone (oxEC)
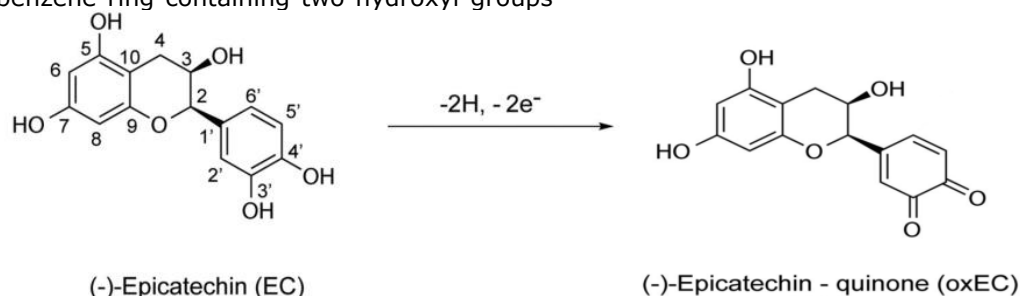
Figure 1. Oxidation mechanism of EC.

Effect of Polyimide (PI) Film Thickness
The most effective parameter that determines the permselectivity character of polymeric films is the thickness. At first, platinum electrodes were coated with by dropping different volumes (1, 2, 3, 4, and 5 µL) of poly(pyromellitic dianhydride-co-thionin) onto Pt electrode surfaces. Afterwards, DPV responses of the electrodes towards ascorbic acid (AA), gallic acid (GA), caffeic acid (CA) and epicatechin (EC) injections were separately measured for each film thickness in 0.1 M PBS solution (pH=7.0). Injected volumes of each analyte were carefully calculated so that final concentrations of the analytes were 2 mM. All of the solutions, regardless of what kind of analyte it contained and what the polymer film thickness was, also contained a mixture of lactose, sucrose and fructose, each at a concentration of 2 mM. Figure 2 shows the effect of PI film thickness upon DPV peak magnitudes of epicatechin and the electroactive interferants (AA, GA and CA) on electrodes coated at 5 different thicknesses. It is seen that at relatively thin film coatings electroactive interferants produced responses, although much smaller than that of EC, almost at the same potential as with EC. However, their responses at that potential diminished slowly with the increasing film thickness. At a film thickness of 4 µL PI it was evident that electroactive species did not interfere with the EC signal. It must be stated here that the same species are known to exhibit electroactivity with a bare Pt electrode. Furthermore, no interference effect was detected from nonelectroactive species of lactose, sucrose and fructose. As a result, optimal coating for electrochemical detection of epicatechin was that performed with 4 µL of PI.
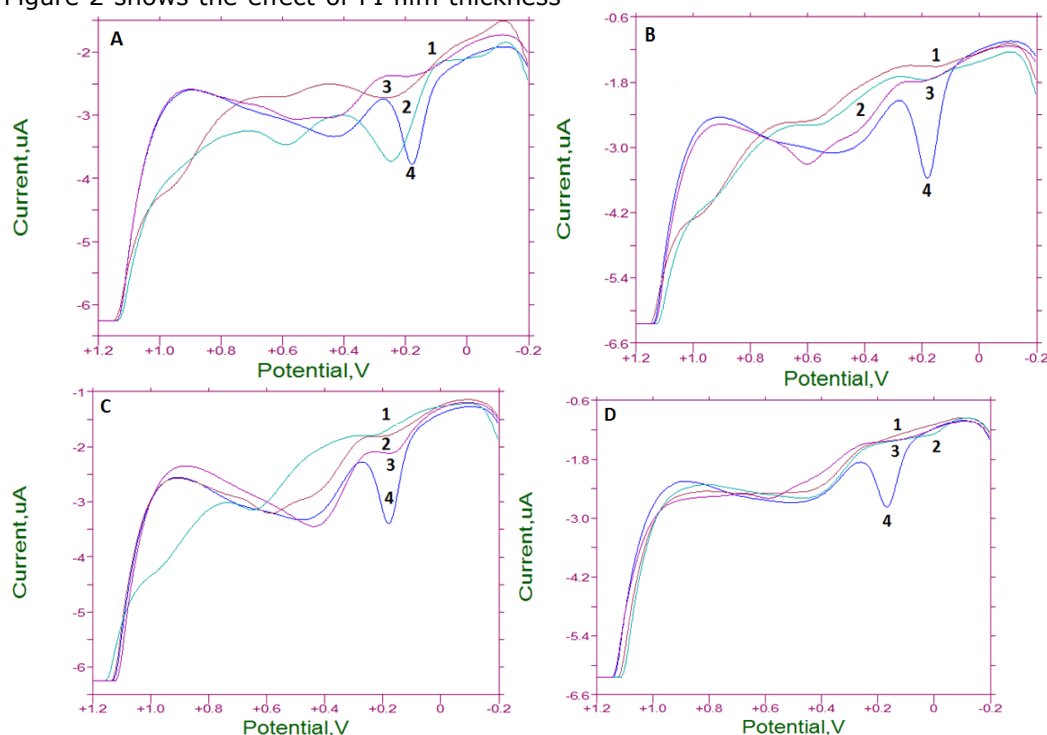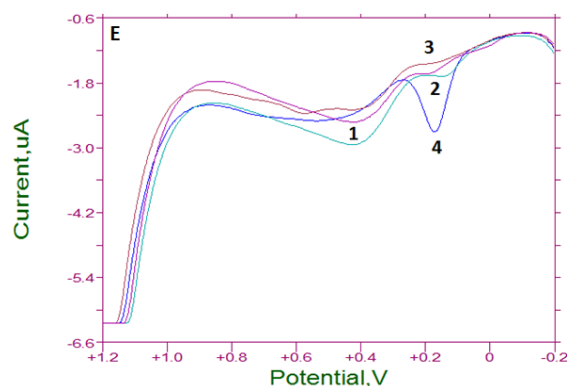
Figure 2. Effect of the **A:**1, **B:**2, **C:**3, **D:**4, **E:**5 µL PI film thickness on the DPV of 2 mM **1:** AA, **2:** GA, **3:** CA, **4:** EC in PBS pH=7.00 containing 2 mM lactose, sucrose and fructose.

Effect of Scan Rate

To see the effect of scanning rate on epicatechin signal, DPVs of 2 mM epicatechin at different scan rates were taken on PI electrode of optimal thickness in PBS pH 7.00.

The peak currents of epicatechins obtained under these conditions are shown in Table 1. As shown in Figure 3 that optimum scan rate is 20 mV/s. It is clear that the peak currents are smaller at higher and lower scan rates.
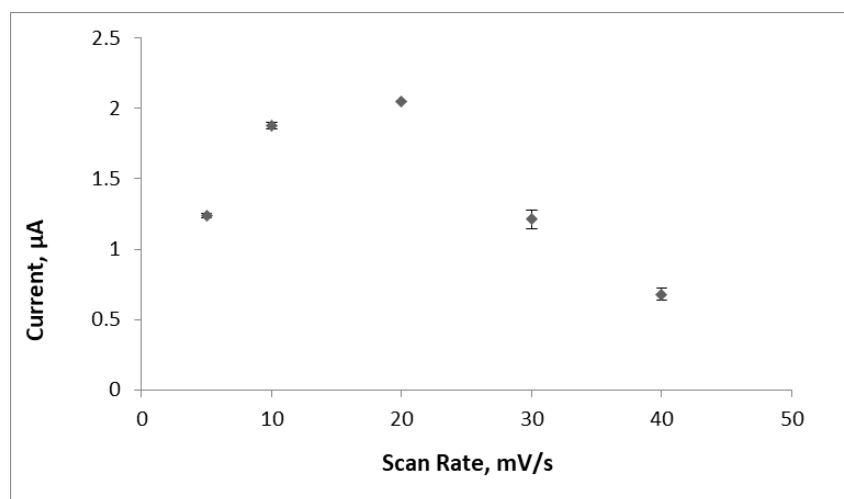
Figure 3. Effect of scan rate on epicatechin responses.

Repeatability and Stability

To test the repeatability of EC response and special stability of EC peaks on voltammograms obtained with the PI-based electrodes, fifteen scans were successively run using the same PI electrode in 0.1 M PBS (pH = 7.00). Results are shown for both high concentration (4 mM) and low concentration (0.02 mM) of epicatechin in Figure 4A and B, respectively. It can be deduced that repeatability of signal magnitude was quite high and stability with regard to EC peak shape and drift in voltammograms were extremely satisfactory.
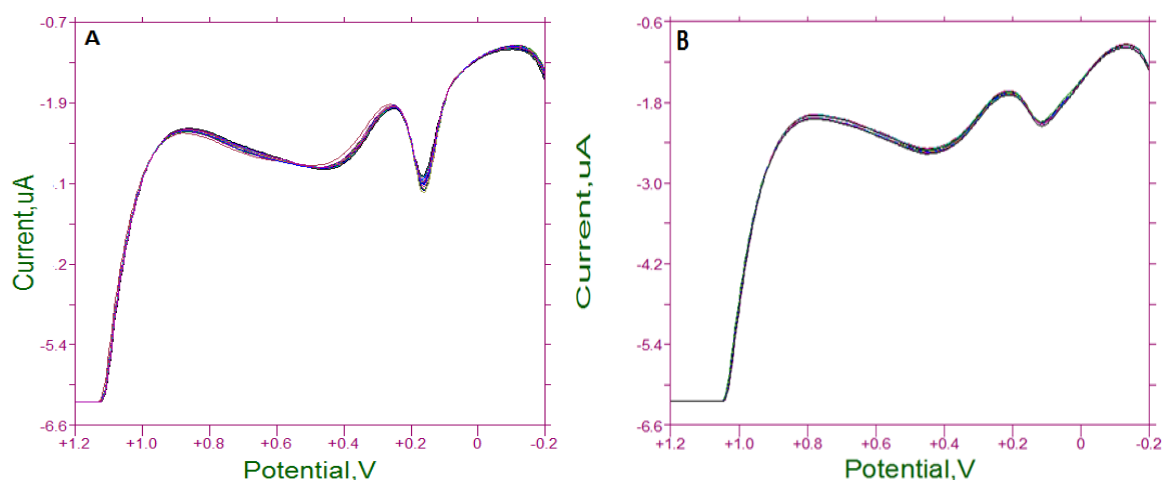
Figure 4. Stability on the same PI modified electrode in 0.1 M PBS with pH=7 at **A:** 4 mM, **B:** 0.02 mM epicatechin concentration (N=15).

Calibration curve for PI Electrodes

Calibration studies were performed employing PI modified electrodes coated with optimum PI film thicknesses. DPV signals for increasing epicatechin concentration measured in 0.1 M PBS (pH=7) are shown in Figure 5. As expected, epicatechin signal was shown to grow with increasing concentration.
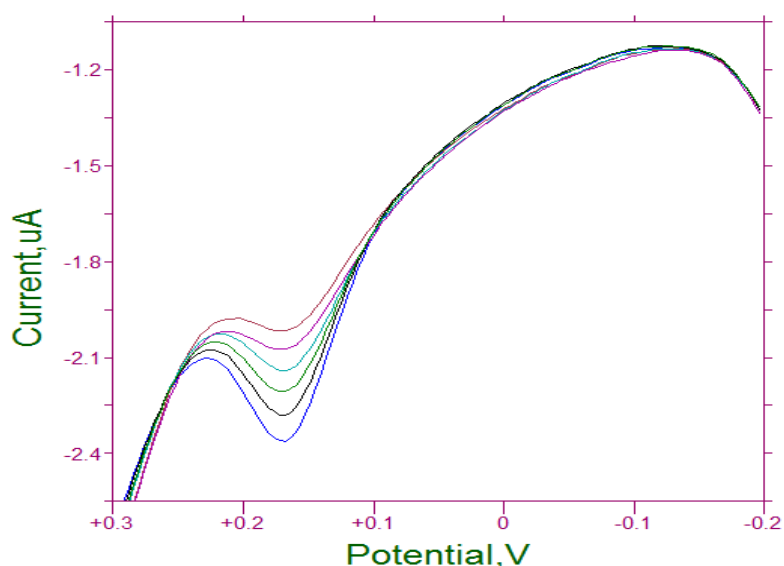
Figure 5: DPV of 0.05, 0.10, 0.15, 0.20, 0.25 and 0.30 mM epicatechin in PBS pH=7.00.

The measured peak currents are shown in Table 1 and the calibration graphs are shown in Figure 6 with R^2 0.9969.

Table 1. Calibration data.

C, mM	0.05	0.10	0.15	0.20	0.25	0.30
I, μA	2.010±0.003	2.066±0.026	2.150±0.006	2.221±0.007	2.277±0.022	2.362±0.021
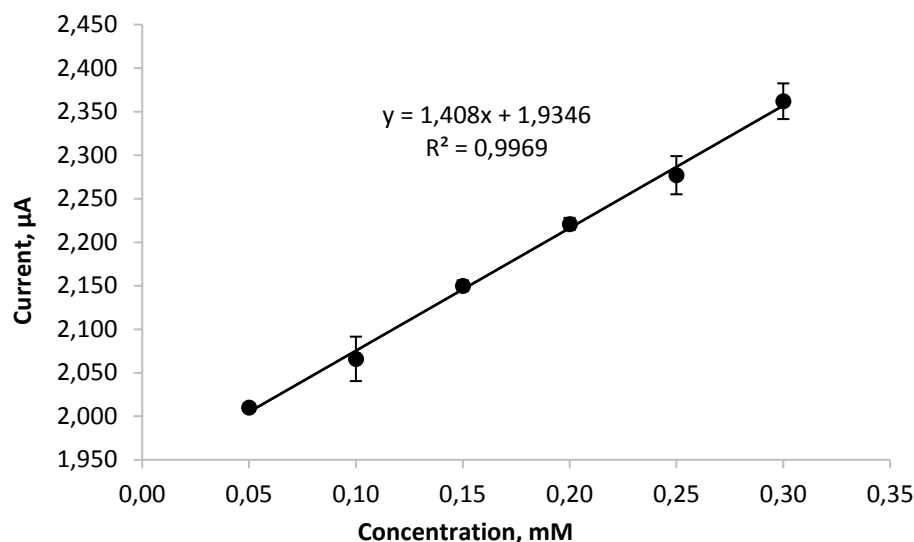
Figure 6. Calibration graph of epicatechin in PBS pH=7.00.

As the Fig 6 shows a linear response was obtained over a range of epicatechin concentrations from 0.05 mM to 0.30 mM in PBS with the indication that this electrode and method described in this work is a useful one for quantifying low levels of epicatechin in phosphate buffer solution, PBS, pH 7.00. Regression coefficient (R^2) was found to be 0.9969. Limit of detection (LOD) was calculated as 1.8×10^{-5} M.

The comparison of the properties of this sensor that was developed in this work with those mentioned in literature is shown in Table 2.

When Table 2 is examined, it can be stated that analytical parameters of the developed sensor, which involves no adsorption, deposition or incubation of the analyte on the electrode, is compatible with the data reported in literature.

CONCLUSION

A voltammetric electrode modified with polyimide membrane was prepared for the detection of epicatechin. In brief, our results demonstrate that poly(pyromellitic dianhydride-co-thionin) film can be easily coated on Pt electrode surfaces and that electrode with this polymeric film is extremely efficient in preventing the permeation of the mentioned electroactive or nonelectroactive interfering substances while allowing epicatechin passage through the film.

We believe that this polymeric film can be used as an inner / protective and a permselective membrane in epicatechin based sensor construction. This sensor has many important advantages such as rapid response time, low detection limit, low cost and high reproducibility for determination of epicatechin.

Table 2. The comparison of the properties of sensor with the literature.

Analyte	Electrode	Method	Polymer	Linear Range, M	R^2	LOD, M	pH	Reference
Epicatechin	Pt	AdSV	PEDOT	6.9×10^{-7} to 8.6×10^{-6}	0.980	-	7	(25)
Epigallocatechin gallat	MIP modified GC	DPV	MIP/GO/GC	3×10^{-8} to 1×10^{-5}	0.9989	8.78×10^{-9}	6	(23)
Epicatechin gallate	GC	SWV	-	1×10^{-8} to 1×10^{-5}	0.9997	3.26×10^{-7}	2	(26)
Epicatechin					0.9997	4.27×10^{-6}		
Epicatechin	CD	CE-ED	-	5×10^{-7} to 5×10^{-5}	0.9960	4×10^{-7}	7.6	(21)
Epicatechin	Pt	DPV	PI	5×10^{-5} to 3×10^{-4}	0.9969	1.8×10^{-5}	7	This work

(**AdSV:** Adsorptive stripping voltammetry, **CE-ED:** Capillary zone electrophoresis with electrochemical detection, **CD:** Carbon disc **GC:** Glassy carbon, MIP/GO/GC: Molecular imprinting polymer/graphene oxide/glassy carbon, **PEDOT:** poly(3,4-ethylenedioxythiophene),
PI: poly(pyromellitic dianhydride-co-thionin))

REFERENCES

1. Cui X, Fang X, Zhao H, Li Z, Ren H. An Electrochemical Sensor for Dopamine Based on Polydopamine Modified Reduced Graphene Oxide Anchored with Tin Dioxide and Gold Nanoparticles. Anal. Methods. 2017;9:5322-5332.

2. Jinn G.Y, Li H, Xu W.B. Sensitive Determination of Buformin Using Poly-Aminobenzoic Acid Modified Glassy Carbon Electrode. Journal of Pharmaceutical Analysis. 2012;26:458–461.

3. Gholivand M.B, Karimian N. Development of Piroxicam Sensor Based on Molecular Imprinted Polymer-Modified Carbon Paste Electrode. Materials Science and Engineering C. 2011;31:1844–1851.

4. Wang J, Wang H, Han S. Ultrasensitive Determination of Epicatechin, Rutin and Quercetin by Capillary Electrophoresis. Chemiluminescence Acta Chromatographica. 2012;24:679–688.

5. Sinha M, Das D.K, Manna K, Datta S, Ray T, Sil A.K, Dey S. Epicatechin ameliorates ionising radiation induced oxidative stress in mouse liver. Free Radical Research. 2012;467:842-849.

6. Das D.K, Sinha M, Khan A, Das K, Manna K, Dey S. Radiation Protection by Major Tea Polyphenol, Epicatechin. International Journal of Human Genetics. 2013;131:59-64.

7. Natsume M, Osakabe N, Oyama M, Sasaki M, Baba S, Nakamura Y. Structures of (-)

Epicatechin Glucuronide Identified From Plasma and Urine After Oral Ingestion of (-) Epicatechin: Differences Between Human and Rat. Free Radical Bio Med, 2003;34:840-849.

8. Abdulkhaleq L.A, Assi M.A, Noor M.H.M, Abdullah R, Saad M.Z, Taufiq-Yap Y.H. Therapeutic Uses of Epicatechin in Diabetes and Cancer. Veterinary World. 2017;106:2231-0916.

9. Berregi I, Santos J.I, Campo G, Miranda J.I. Quantitative Determination Of -) Epicatechin In Cider Apple Juices by ^{1}H NMR. Talanta. 2003; 61:139-145.

10. Philip M, Matthew J, Brian S, Catherine K.U, Dawn D. Method for the Determination of Catechin and Epicatechin Enantiomers in Cocoa-Based Ingredients and Products by High-Performance Liquid Chromatography: First Action 2013.04. 2014;972:506-509.

11. Song R, Cheng Y, Tian Y, Zhang Z.J. A Validated Solid-Phase Extraction HPLC Method for the Simultaneous Determination of Gallic Acid, Catechin and Epicatechin in Rhubarb Decoction. Chinese Journal of Natural Medicines. 2012;104:275-278.

12. Wang T.K, Yang Y.D, Du B, Yu S, Hou W.L. Simultaneous Determination of Gallic Acid, Protocatechuic Acid, Catechin, Epicatechin, Quercetin and Kaempferol in Chinese Chestnut Castanea mollissima Blume) Kernel by High-Performance Liquid Chromatography with Diode Array Detection. Acta Chromatographica. 2014;263:539–550.

13. Ricardo FN, Tamara A, Sandra MMS, Pérola O.M, Tais G, Marcílio SSC, Guilherme MG.

Versatile Chromatographic Method for Catechin Determination in Development of Topical Formulations Containing Natural Extracts. Biomedical Chromatography. 2018;32:4062-4069.

14. Fecka I, Cisowski W, Luczkiewicz M. Determination of Catechin and Epicatechin in An Extract From Uncaria Tomentosa Bark by TLC with Chemically Modified Stationary Phases. JPC-Journal of Planar Chromatography-Modern TLC. 2001;146:405-408.

15. Glavnik V, Simonovska B, Vovk I. Densitometric Determination of (+)-Catechin and (-)-Epicatechin by 4-Dimethylaminocinnamaldehyde Reagent. J Chromatogr A. 2009;121620:4485-4491.

16. Jaiswal Y, Tatke P, Gabhe S, Vaidya A. Rapid High Performance Thin Layer Chromatographic Method for Quantitation of Catechin from Extracts of Cashew Leaves – a Short Report. Pol. J. Food Nutr. Sci. 2013; 631:49-54.

17. Reich E, Schibli A, Widmer V, Jorns R, Wolfram E, DeBatt A.HPTLC Methods for Identification of Green Tea and Green Tea Extract. Journal of Liquid Chromatography & Related Technologies. 2006;29:2141–2151.

18. Solich P, Opletal L, Sovova M. Comparison of Different Methods for the Spectrophotometric Determination of -)-Epicatechin. Pharmazıe. 1996;5112:954-956.

19. Singh HP, Ravindranath SD, Singh C. Analysis of Tea Shoot Catechins: Spectrophotometric Quantitation and Selective Visualization on Two-Dimensional Paper Chromatograms Using Diazotized Sulfanilamide. *J. Agric. Food Chem.*,1999;473: 1041–1045.

20. Luthria, DL, Jones AD, Donovan JL, Waterhouse AL. GC-MS Determination of Catechin and Epicatechin Levels in Human Plasma.HRC Journal of High Resolution Chromatography. 1997;2011:621-623.

21. Cao YH, Zhang X, Ding XH, Fang YZ, Ye JN. Determination of Caffein, Epicatechin and Ascorbic Acid in Tea Samples by Capillary Zone Electrophoresis with Electrochemical Detection. Chinese Journal of Analytical Chemistry. 2001;299:1072-1075.

22. Wang XG, Li J, Fan YJ. Fast Detection of Catechin in Tea Beverage Using A Poly-Aspartic Acid Film Based Sensor. Microchim. Acta. 2010;169:173–179.

23. Liu Y, Zhu L, Hu Y, Peng X, Du J. A Novel Electrochemical Sensor Based on A Molecularly Imprinted Polymer for The Determination of Epigallocatechin Gallate. Food Chem. 2017;221:1128-1134.

24. Chatterjee TN, Das D, Roy RB, Tudu B, Sabhapondit S, Tamuly P, Pramanik P, Bandyopadhyay R. Molecular Imprinted Polymer Based Electrode for Sensing Catechin +C) in Green Tea. IEEE Sensors Journal. 2018;186:2236-2244.

25. Pigani L., Seeber R, Bedini A, Dalcanale E, Suman M. Adsorptive-Stripping Voltammetry at PEDOT-Modified Electrodes. Determination of Epicatechin. Food Anal. Methods. 2014;7:754–760.

26. Novak I, Šeruga M, Komorsky-Lovrić Š. Square-wave and cyclic voltammetry of epicatechin gallate on glassy carbon electrode. Journal of Electroanalytical Chemistry. 2009;631 :71–75.

27. Köytepe S., Paşahan A., Ekinci E., Seçkin T. Synthesis, characterization and H2O2-sensing properties of pyrimidine-based hyperbranched polyimides European polymer journal 2005;411: 121-127.

28. Paşahan A., Köytepe S., Ekinci E. Synthesis, characterization of naphthalene-based polyimides, and their use as immobilized enzyme membrane. Polymers for Advanced Technologies 2011;2212: 1940-1947.

29. Sheng W, Chen Q, Yang P, Chen C. Synthesis, Characterization, and Enhanced Properties of Novel Graphite-Like Carbon Nitride/Polyimide Composite Films. High Performance Polymers. 2015;27:950–960.

RESEARCH ARTICLE

Spectral, Thermal and In Vitro Antibacterial Studies on Cadmium(II)– bis(2,2$'$-methylidenephenol)diaminoethane

Nworie Felix Sunday ✉ 🆔

Department of Industrial Chemistry, Ebonyi State University, Abakaliki, Nigeria.

Abstract: The objective of this work is to prepare a new synthetic protocol of the cadmium(II) complex of bis(2,2'-methylylidenephenol)diaminoethane (H$_2$BMPDE) and study the antimicrobial bioefficacy. In this work, we report the extractive method for the synthesis of cadmium(II) complex of bis(2,2'-methylidenephenol)diaminoethane from salicylaldehyde, ethylenediamine, hydrochloric acid, and cadmium sulfate in a single, simple step. The ligand and the complex were characterized by FTIR, UV-Vis, ^{1}H and ^{13}C NMR, magnetic moment, GC-MS, thermal and elemental analysis. The chemical data indicated the formation of 1:1 (metal:ligand) mole ratio and distorted tetrahedral geometry was suggested as based on spectral data and magnetic moment. The results of preliminary antibacterial study revealed that Cd(II) H$_2$BMPDE complexes prepared from different acids (HCl, HNO$_3$, H$_2$SO$_4$) were effective against clinically important Gram-negative bacteria (*Escherichia coli, pseudomonas, Klebsiella*) and Gram-positive bacterium (*Staphylococcus aureus*).The result indicated a new synthetic protocol for the synthesis of H$_2$BMPDE complexes. On the application, H$_2$BMPDE and its complexes could be considered as a potential antibacterial agent with further investigative analysis.

INTRODUCTION

Cadmium, among various metals, transition and non-transition, requires special attention owing to its deleterious effects in nature. Anthropogenic activities such as mining and smelting have gradually increased its concentration in the environment (1). This thus calls for the development of suitable chelating agent for complexation and immobilization of cadmium(II) ion in matrices and even in organisms. Studies (1-3) have shown that certain group of compounds known as the phytochelatins naturally present in living cells effectively complex cadmium(II) ion in metabolically less active cellular part by acting as a chelating agent and protecting the cells from cadmium toxicity. There is inherent softness and lack of ligand field stabilization energy in cadmium as a consequence of its d^{10} electronic configuration leading to diverse co-ordination chemistry as it can toggle

between various oxidation states (4-7). This exceptional ability of cadmium resulting from its flexible co-ordination number in complexes has paved way for its wide applications in catalytic and exchange reactions, in the development of fluorescence materials when complexed with conjugated π substrates having phenyl rings and in biological studies (3,8-9).

The development of the area of bioinorganic chemistry has increased and many researchers have worked on Schiff bases with strong donor atoms such as oxygen and nitrogen due to their strong coordination abilities with transition metal ions. Similarly several authors have worked on H$_2$BMPDE, its derivatives and H$_2$BMPDE complexes of transition metals of the first series. Several studies of H$_2$BMPDE complexes has shown that it exhibits unique and excellent photoluminescence property, catalytic ability, antimicrobial activities, magnetic drugs and in

environmental cleaning (carbonic anhydrase cycle) (10-13).

Abou-Melha and Faruk (14) noted that the co-ordination of a ligand to metal ion synergistically increase the biological activity of the ligand and decrease the cytotoxic effect of ligand and metal ion as a consequence of chelation. In their study, Brown and co-workers (15) observed that a compound with long lipophilic chain would interact with cellular components and enhance transport of the compound to the active required site, thereby increasing the biological activity. The observation was explained on the basis of the greater lipophilic nature of the complexes than the ligand a consequence of chelation (15). H_2BMPDE and its complexes could be potentially

bacteriostatic due to the presence of azomethine group and the phenolic hydroxyl in the molecule. Biswas and co-workers (16) studied the in vitro antibacterial and antifungal effects of cadmium(II) complexes of hexamethyltetraazacyclotetradecadiene and isomers of its saturated analogue and noted the antibacterial potency of the macrocyclic ligand and complexes.

In this reasearch, we report the synthesis, spectral and thermal characterization as well as antibacterial bioefficacy of cadmium(II) complex derived from the condensation of Schiff base salicylaldehyde and ethylenediamine in 2:1 ratio (Scheme 1).
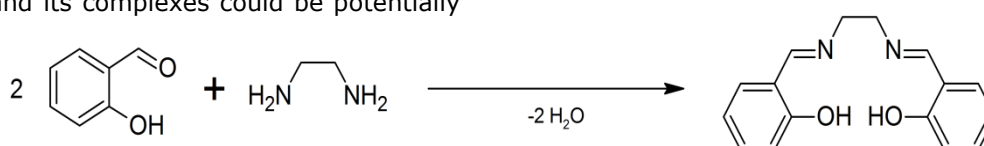
Scheme 1. Synthesis of bis(2,2' – methylidenephenol)diaminoethane (H_2BMPDE)

EXPERIMENTAL SECTION

Analytical grade of all the chemicals and solvents used for the syntheses were obtained from Merck Company and were not purified unless otherwise stated. The ligand (H_2BMPDE) was synthesized according to the modified Takeshima procedure (17) by condensation of salicylaldehyde and ethylenediamine in 2:1 mole ratio and used as 0.5% solution in absolute ethanol throughout the analysis. A stock solution of Cd(II) was prepared using $CdSO_4.8/3H_2O$. Stock solutions of mineral acids (HCl, HNO_3 and H_2SO_4) were prepared by diluting the concentrated acids and were standardized using appropriate standard bases. Solutions for antibacterial bioefficacy and sensitivity tests were prepared from nutrient broth powder and Mueller Hinton powder while aliquot of 0.5 Mac Farland standard was used as control (18).

Physical measurements
The electronic spectra of the ligand and complexes were recorded in dimethyl formamide on a Genesis 10S UV-Vis spectrophotometer. Infrared spectra of the ligand and the complexes were recorded on Perkin-Elmer FTIR-8400S Fourier transform infrared spectrometer (Shimadzu, Japan) in the range of 4000-400 cm^{-1} as KBr disks. Differential scanning calorimetry (DSC) analysis was determined using NETZSCH

DTA 404PC Differential scanning calorimeter. ^1H NMR and ^{13}C NMR and spectra were carried out on a Bruker AVANCE II 400 MHz NMR spectrometers using tetramethylsilane (TMS) as an internal reference. Elemental CHN analyses were performed using Vario-Elemental Microcube ELIII. Magnetic susceptibility was measured on a Johnson Matthey magnetic susceptibility balance Alfa product, Model No. MKI and diamagnetic corrections calculated using Pascal's constant. The conductivity measurements were carried out in DMF at room temperature using HQ4d conductivity meter. Microanalysis of the ligand and complexes were done at the Department of Chemistry, Rhodes University, South Africa.

Synthesis of the metal complex
An aliquot of a sample solution containing 100 µg of Cd(II) was transferred into a 50 mL calibrated extraction bottle and volume made up to 5 mL with an acidic solution at a concentration of 0.0001 M. Exactly 0.5 mL of the ligand solution in absolute ethanol was added and 5 minutes for color development allowed. The complex formed was extracted with 5 mL of chloroform. The organic extract was allowed to dry and product was recrystallized using carbon tetrachloride, dried, and the metal complex from HCl was characterized while others were kept for antimicrobial studies.
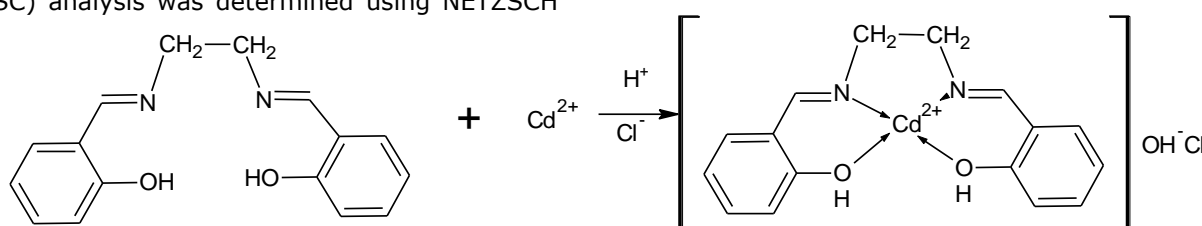
Scheme 2. Synthesis of cadmium(II)-bis(2,2' – methylidenephenol)diaminoethane complex.

Physical and analytical data

Ligand; M.p (127 °C ± 1). Appearance: yellow crystals; molecular formula: $C_{16}H_{16}N_2O_2$; formula weight: 268; percentage yield: 65%). Elemental analysis (ligand) calc. C, 71.64%; H, 5.97%; N, 10.44%; found: C, 70.89%; H, 6.05%; N, 10.41%. FTIR (Ligand): 3401 cm^{-1} v(O-H) aromatic, 3042 cm^{-1} v(C-H) aromatic, 2913 cm^{-1} v(C-H) aliphatic, 1615 cm^{-1} v(C=N) iminic, 1285 cm^{-1} v(C-O) phenolic; ^{1}H-NMR (ppm) (Ligand): 7.4 (1H, N=C(H) methine protons of azomethine); 7.11 (3H, the hydrogen of aromatic ring); 6.5 (1, N-H protons); 3.5 (4H, =NCH$_2$CH$_2$N= methine or methylene protons). ^{1}H-NMR (ppm) (Cd complex): 8.4 (1H, N=C(H) methine protons of azomethine); 7.0-7.3 (3H, hydrogen of aromatic ring); 6.9(1, N-H protons); 3.90(4H, =NCH$_2$CH$_2$N= methine or methylene protons). ^{13}C-NMR (ppm) (ligand): 221.44 (bonded to phenolic oxygen); 152.65 (aromatic carbons); 48.69 (methylene carbon); molar conductivity of complex: 32.00 µS; electronic spectrum of the ligand (DMF, nm, ε =mol^{-1} dm^3 cm^{-1}) 260 (ε =3.0 x10^2), 285 (ε =3.6 x 10^2), 335 (ε = 4.7 x 10^2).

Cd complex: M.p (Cd complex) >300 °C; appearance: yellow crystals; molecular formula: $C_{16}H_{16}N_2O_2$ Cl(OH)Cd; formula weight: 432.91; percentage yield: 40%). Elemental analysis (Cd complex): calc. C, 44.36%; H, 3.96%; N, 6.47%; found: C, 71%; H, 5.71%; N, 10.41%; FTIR (Cd complex): 3009 cm^{-1} v(C-H) aromatic, 2915 cm^{-1} v(C-H) aliphatic, 1624 cm^{-1} v(C=N) iminic, 1414 cm^{-1} v(C-O) phenolic, 556 cm^{-1} v(Cd-N), 655 cm^{-1} v(Cd-O). ^{13}C-NMR (ppm) (Cd complex): 165.28 (bonded to phenolic oxygen); 116.74, 118.63, 131.33, 132.21 (aromatic carbons); 160.91 (azomethine carbon); 59.60 (methylene carbon). Electronic spectrum of the Cd complex (DMF, nm, ε =mol^{-1} dm^{3}cm^{-1}) 230 (ε =9.20 x10^2), 310 (ε =4.36 x 10^3), 405 (ε =3.36 x 10^3). From magnetic measurement the complex was diamagnetic.

Thermal Analysis
The cadmium complex and reference pan were placed at separate furnaces maintained using separate heaters. The sample and reference were maintained at same temperature and the difference in thermal power required in maintaining them at the same temperature measured and plotted as a function of temperature. About 5.00 mg of sample was weighed into an alumina crucible and mass was indicated. The TA Blue DSC sample press was used to close the crucible. The enclosed sample was placed side by side with the empty alumina crucible as reference. The instrument was purged with ultra pure N$_2$ gas at regulated pressure between 100 and 140 Kpa gauge (15 and 20 Psig). The gas flow rate was set at 50 mL per minute and experiment was run from room temperature to 800 °C at scan rate of 10 °C min.

Gas Chromatography-Mass Spectrometry (GC–MS) Analysis

Mass spectra of the ligand and the complexes were performed by NARICT, Zaria using mass spectrometer (GCMS – QP2010 Plus Shimadzu, Japan) coupled with a gas chromatograph. The samples were dissolved in dimethyl formamide and filtered through a 1-mL syringe. A 1 µL aliquot of each sample was then injected into the GC-MS instrument. The carrier gas was nitrogen for desolvation, nebulization pressure of 108 kpa, injection temperature was 250 °C, oven temperature was 80 °C, solvent cut time was 2.50 minutes, start time was 3 minutes and ionization energy was 70 eV. The process involves electron ionization which accelerates electrons to 70 eV and pass them through a section which contains vaporized sample M which exited from GC to MS thereby generating radical cation [M]$^+$. The spectrum of the compound was generated since the ionization process was sufficiently energetic leading to fragmentation. The spectrum generated gave a characteristic fingerprint for the compound required and the mass to charge ratio (m/z) values of the prominent ions can be deconvulated from spectral libraries or using a fragmentation tree (19). The molecular formula determination also referred to as the elemental composition of the compound was generated by decomposing monoisotopic peaks by finding molecular formulas that are well very close to the measured peak mass (20). During GC-MS analysis, the mass spectrum was generated and represented as peaks. Two of the peaks are the most important namely base peak and molecular ion peak. The base peak otherwise regarded as parent peak was the largest analyzed peak and other peaks are regarded as relative abundance or percentage of the base peak. The analyzed molecule prior to fragmentation was shown by molecular ion peak always used as a reference point in fragment identification (21).

Antibacterial studies
Both gram negative bacteria (*Escherichia coli, pseudomonas, Klebsiella*) and gram-positive bacterium (*Staphylococcus aureus)* were used for *in vitro* screening of the antibacterial effect of the ligand and the complex. The bacterial strains were obtained from the department of Microbiology Ebonyi State University, Abakaliki. Antimicrobial test was performed on four bacteria (*Staph-aureus, Klebsiella, E-coli and Pseudomonas aeuroginosa*) as described (18). The media employed in the study was prepared by dissolving separately 2 g of the nutrient broth powder and 38 g of the Mueller Hinton agar powder in 250 mL and 1 L of distilled water respectively. The two media were sterilized in an autoclave at 121 °C for 15 minutes and thereafter left overnight in a refrigerator after cooling. Cultures of the micro-organisms were prepared in sterile nutrient broth and incubated for 24 hours at 37 °C. About 0.1 mL of the cultures left overnight in sterile tubes with caps was made up to 10 mL with sterile distilled water. Also, 10 mg/mL of the complex solutions prepared from different acids (HCl, HNO$_3$ and H$_2$SO$_4$) in ethanol

was used as solvent. The positive control was an aliquot of 0.5 MacFarland standard (10 μg of broad spectrum ampicillin) equivalent of test organism. The cultures of micro-organism was stretched on the surface of a dried Mueller Hinton agar plate and allowed for 20-25 minutes for pre-diffusion of the organism into the agar. Sterile No 4 cork borer was used to make 8 mm hole in the inoculated agar plate. The compounds were introduced into the four (4) different holes made on the innoculated agar plate whereas the control drug (ampicillin) was placed at the centre. The

where   A = zone of inhibition of test compound in diameter, B = zone of inhibition of standard in diameter.

RESULTS AND DISCUSSION

The UV-Vis spectrum of the free H₂BMPDE ligand (Figure 1) exhibits three absorption bands at 260, 285 and 335 nm. The absorption band at 260 and 285 nm could be assigned to $\pi - \pi^*$ transition of the benzene ring and azomethine or imine chromophore respectively (11, 22-23). The band at 335 nm was attributed to $n - \pi^*$ transition of the non-bonding electrons resident in the nitrogen of the azomethine group (C=N) in the ligand (intraligand charge transfer (CT) transition) (22-25).

The electronic spectrum of Cd(II) H₂BMPDE consists of three bands in the region of 42553, 32258 and 24691 cm⁻¹. The band at 24691 cm⁻¹ suggested a distorted tetrahedral structure (Figure 2) (26-27). The other band at 42553 and 32258 cm⁻¹ was due to charge transfer transition (26-28).

inoculated plates were incubated at 37 °C for 18-24 hours. The zones of inhibition of microbial growth that appeared around the walls of the compounds were examined, measured and recorded in millimeters (mm).

The evaluation of the antimicrobial activity followed after the incubation period by the measurement of the diameter of the inhibition zones. Activity index (%) (Calculated as percent activity index bacteria) is illustrated in Equation 1.

$$\frac{A}{B} \times 100 \qquad\qquad \text{(Eq. 1)}$$

The ligand exhibited the characteristic C=N stretching frequency at 1615 cm⁻¹. The shifting of ν(C=N) band to higher values by 9 cm⁻¹ (from 1615-1624 cm⁻¹) indicates the participation of the two azomethine nitrogen atoms in bonding (29). The corresponding phenolic C—O stretching frequency occurs at 1285 cm⁻¹ for the ligands and at 1414 cm⁻¹ for the complex. The shift in C—O stretching frequency confirms the participation of the phenolic O in C—O—M bond formation (30). The ν(-OH) stretching vibration frequency of 3401 cm⁻¹ observed in the ligand disappeared in the complex an indication that the hydroxyl group was not involved in complexation. The bands due to ν(Cd(II)—N) observed only in the complexes occurred at 556 cm⁻¹ while 655 cm⁻¹ was attributable to ν(Cd(II)—O) bond (31).

GC-MS result indicated the formation of M⁺ ion for the ligand and the complex at 264 and 433 respectively with various fragmentations as represented in Scheme 3.
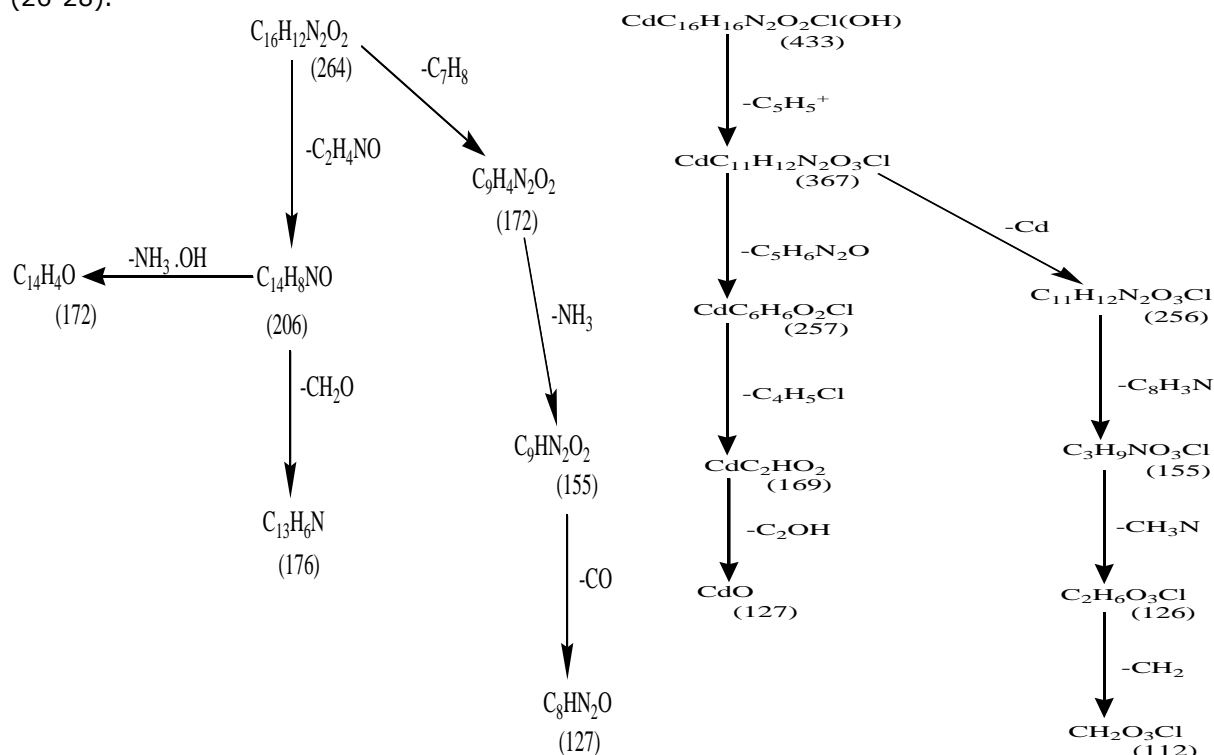
Scheme 3. Fragmentation pattern of H$_2$BMPDE and its complex.

The DSC curve of Cd(II) H$_2$BMPDE shows three peaks at 123.9 °C, 321.6 °C and 598.6 °C. The first weak endothermic peak at 123.9 °C corresponds to morphological transformation while the second sharp endothermic peak at 321.6 °C corresponds to the melting point of the complex and then broad exothermic peak at 598.6 °C corresponds to the decomposition of the complex. From DSC studies (Table 1), negative value of ΔS shown in the first step indicated the reaction was slower than expected thereby

establishing nonspontaneous nature. Similarly, positive value of ΔG in some steps supports the nonspontaneous nature of the degradation process (32). The positive value of enthalpy indicates the endothermic nature of the degradation process (33). The degree of denaturation entropy and denaturation enthalpy was high and indicated that the stability of these drugs is high. The values of ΔS_m^o was derived from the relation in Equation 2

$$\Delta S_m^o = \Delta H_m^o / \mathrm{T_m} ..$$ (Eq. 2)

$\Delta G^o(T)$ is calculated from the modified Gibb`s Helmholtz equation (34) as shown in Equation 3:

$$\Delta G^o(T) = \Delta H_m^o \left(1 - \frac{T}{T_m}\right) + \Delta Cp[(T - T_m) - T \, \mathrm{In}\left(\frac{T}{T_m}\right)]$$ (Eq. 3)

The denaturation entropies and enthalpies ΔS° (T) and ΔH° (T) respectively were derived from Kirchoff's laws (34) as shown in Equations 4 and 5.

$$\Delta H^o(T) = \Delta H_m^o + \Delta Cp(T - T_m)$$ (Eq. 4)

$$\Delta S^o(T) = \Delta S_m^o + \Delta Cp \, \mathrm{In}(\frac{T}{T_m})$$ (Eq. 5)

The stability of any given system is determined using the free energy ΔG° (T) which is the overall contribution of the enthalpic and entropic terms. These temperature-dependent parameters, enthalpic change, entropic change and heat capacity change are determined using the calorimetric method (DSC) or Van't Hoff method. Consequently, DSC studies the stability of biomolecules and helps in the proper understanding of biomolecular interactions and design of drugs.

The ^{1}H NMR spectra of H$_2$BMPDE and its metal complexes were recorded in CDCl$_3$ at room temperature using tetramethylsilane (TMS) as the internal reference standard.

^{1}H NMR analyses of ligand
The ^{1}H NMR spectrum of H$_2$BMPDE displayed the hydrogen of aromatic rings as complex multiplets at 7.11 ppm (3H) due to coupling of 4 hydrogen atoms in the ring whereas the methine proton of the ethylene bridge was observed as doublet at 3.5 ppm (4H) illustrating the symmetrical nature of the ligand. The appearance of triplet peak at 6.5 ppm (2H) was assigned to N-H proton. The azomethine proton was shown as quartet (1H) at 7.4 ppm (22,36).

^{1}H NMR analyses of complex
In Cd(II) H$_2$BMPDE, the singlet at 8.4 ppm (2H) was assigned proton of the azomethine group which was shifted downfield as a consequence of complexation between the metal and the ligand. The spectrum between 7.0-7.3 ppm was assigned to the hydrogen of aromatic ring. The triplet at 6.9 ppm integrated for 1 proton was assigned to the N-H group. The singlet at 3.90 ppm integrated for four protons was assigned to the proton of the ethylene bridge (37).

^{13}C NMR analyses of the ligand
The line pattern centered at 78 ppm was due to the solvent CDCl$_3$. H$_2$BMPDE is a symmetrical molecule and as such less than expected resonances appear in ^{13}C. The peaks at 221.44 ppm, 152.65 ppm, and 48.69 ppm are due to quaternary carbon atom bonded to oxygen of phenolic group (-C-O), imine bonded carbon (-N=C-H) due to SP^2 hybridization(37) and methylene carbon(-NCH$_2$CH$_2$N-) due to electronegative oxygen atom respectively (24, 35, 37).

^{13}C NMR analyses of the complex
In ^{13}C NMR spectrum of Cd(II) H$_2$BMPDE complex, peaks were observed at 165.28, 160.91, 132.21 131.33, 118.67, 118.63, 116.74 and 59.60 ppm. The peaks at 165.28, 160.91, 118.67 and 59.60 ppm were assigned to the quaternary carbon bonded to oxygen of the phenolic group, imine-bonded carbon atom, quaternary carbon bonded to imine and the methylene carbon (due to SP^3 hybridized carbon atom), respectively (37). The peaks at 132.21, 116.74, 118.63 and 131.33 ppm were assigned to methine carbon (C-H) of the aromatic ring. The upfield shift of 56.16 ppm between the ligand and the complex at the quaternary carbon bonded to oxygen of the phenolic group and downfield shift of 0.91 ppm between the ligand and the complex at the methylene carbon confirmed the involvement of C-O and NCH$_2$CH$_2$N group in bond formation. Generally, the less than expected signals in the ^{13}C NMR spectra were as the result of the symmetrical nature of the molecule (24).These observations are in line with the study of Pervaiz *et al* (37) on the synthesis and characterization of bimetallic post transition complexes for antimicrobial activity though little differences

observed could be because of the different synthetic protocols. This study is solution synthesis whereas the bimetallic study followed the constituent combination method hence the difference in the structure. The synthesis of the

complex of H$_2$BMPDE in a 1:1 ratio was observed in the study of Yang *et al.,*(11) on the synthesis of dye sensitized cells from zinc metal and H$_2$BMPDE.
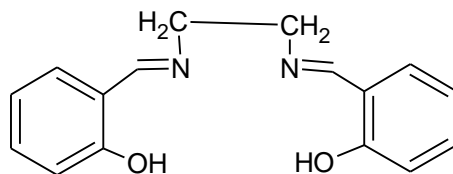
Figure 1: Structure of H$_2$BMPDE.
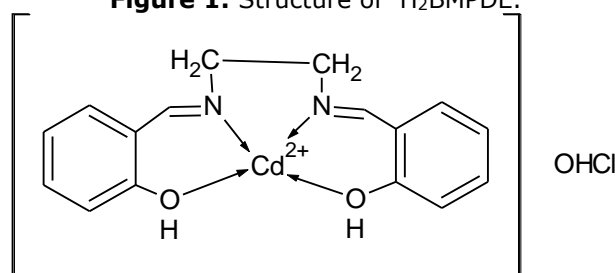
Figure 2: Proposed structure of Cadmium(II)H$_2$BMPDE

Table 1: Thermodynamic Data on the DSC Decomposition of H$_2$BMPDE Complexes.

	T	T$_m$	ΔH_m^o	ΔCp	ΔS_m^o	$\Delta G^o(T)$	$\Delta S^o(T)$	$\Delta H^o(T)$
Cd(II) H$_2$BMPDE	128.7	123.9	-124.3	12.2	-1.003	-0.028	-65.74	-0.539
	337	321.6	212.3	36	0.660	0.044	227.7	2.349
	598	598.6	28.57	8.5	0.048	-0.163	23.47	0.039

Legend:T(^{o}C)=Temperature,T$_m$(^{o}C) $= Transition\ midpoint\ temperature,\ \Delta H_m^o($ J/K$)\ = calorimetric\ enthalpy,$ $\Delta Cp($ ^{o}C)=change in heat capacity, ΔS_m^o(J/K) $= entropy\ change,\ \Delta G^o(T) = free\ energy\ change$, $\Delta S^o(T)$=denaturation entropy, $\Delta H^o(T)$= denaturation enthalpy.

Table 2: Antimicrobial activity of H$_2$BMPDE and its complexes.

H$_2$BMPDE /Metal complex	Micro-organism Zone of inhibition			
	P. aeruginosa	*K. pneumoniae*	*E. coli*	*S. aureus*
Cd(II) H$_2$BMPDE H$_2$SO$_4$	22	16	20	20
Cd(II) H$_2$BMPDE HCl	12	10	8	R
Cd(II) H$_2$BMPDE HNO$_3$	8	18	8	10
H$_2$BMPDE	R	08	06	06
Ampiclox (standard)	21$\pm$2	44$\pm$2	34$\pm$2	21$\pm$2

Table 3: Activity Index of H$_2$BMPDE and Complexes in Comparison to Standard Ampiclox.

H$_2$BMPDE /Metal complex	Activity Index (%)			
	P. aeruginosa	*K. pneumoniae*	*E. coli*	*S. aureus*
Cd(II) H$_2$BMPDE H$_2$SO$_4$	104.76	36.36	58.82	95.23
Cd(II) H$_2$BMPDE HCl	57.14	22.73	23.53	-
Cd(II) H$_2$BMPDE HNO$_3$	38.09	40.90	23.53	47.62
H$_2$BMPDE	-	18.18	17.65	28.57

The ligand and the complexes are shown to possess antimicrobial activities against the listed micro – organism possibly because of the presence of azomethine group (C=N). Studies have also shown (36) that ligands with hetero donor atoms (N and O) inhibiting enzyme activity and enzymes that need N or O groups for their activity are more susceptible to deactivation by

metal ions on complexation. As shown in Tables 2 and 3, complexes of cadmium prepared from H$_2$SO$_4$ had the highest inhibition property for *Pseudomonas.*

CONCLUSION

This study revealed that cadmium forms octahedral complex with H_2BMPDE and at acid concentration of 10^{-4} M there was no deprotonation of the phenolic hydroxyl groups thereby enhancing the antimicrobial bioefficacy. Therefore, H_2BMPDE and its complexes synthesized using extractive technique based on the results could be considered a potential antibacterial agent.

ACKNOWLEDGEMENT

REFERENCES

1. Zaky RR, Yousef TA, Ibrahim KM. Co(II), Cd(II),Hg(II) and U(VI)O2 complexes of o-hydroxyacetophenone[N-(3-hydroxy-2-naphthoyl)] hydrazone: physicochemical study,thermal studies and antimicrobial activity. Spectrochim. Acta Part A. 2012 Nov; 97: 683-94.

2. Zhang J A, Pan M, Zhang JY, Kang BS, Su CY. Syntheses, structures and bioactivities of cadmium(II) complexes with a tridentate heterocyclic N- and S-ligand. Inorg. Chim. Acta. 2009; 362: 3519-25.

3. Naz M, Aghatabay A, Neshat T, Karabiyik M, Somer D, Haciu B D. Synthesis, characterisation and antimicrobial activity of Fe(II), Zn(II), Cd(II) and Hg(II) complexes with 2,6-bis(benzimidazol-2-yl)pyridine. Euro. J. Med.Chem. 2007; 42:205-13.

4. Warad I, Ali Khan A, Azam M, Al-Resayes I, Haddad S F. Design and structural studies of diimine/CdX2 (X = Cl, I) complexes based on 2,2-dimethyl-1,3-diaminopropane ligand. J. Mol. Struct. 2014;1062: 167–73.

5. Shashidhar Reddy N, Shankara B S, Murali Krishana P, Basavaraj C, Mahesh B. Synthesis, characterisation, and antibacterial activity of Co(II), Ni(II), Cu(II), Zn(II), Cd(II), and Hg(II) complexes of Schiff's base type ligands containing benzofuran moiety. J. Inorg. Chem. Article ID 614628,2013: 1-10.

6. Montazerozohori M, Khani S, Tavakol H, Hojjati A, Kazemi M. Synthesis, spectroscopic and thermal studies of some IIB group complexes with a new N2-Schiff base ligand. Spectrochim. Acta Part A.2011; 81: 122-27.

7. Montazerozohori M, Joohari S, Musavi S A. Synthesis and spectroscopic studies of some cadmium(II) and mercury(II) complexes. Spectrochim. Acta Part A. 2009; 73: 231-37.

8. Mahmoudi G, Morsali A, Zeller M. Mercury(II) acetate/thiocyanate coordination polymers with n-donor ligands, spectroscopic, thermal and structural studies. Inorg. Chim. Acta. 2009;362: 217-25.n

9. Morteza M, Masoud N, Maryam H, Asghar N, Saeedeh S. Synthesis of some new antibacterial active cadmium and mercury complexes of 4-(3-(2-(4-(dimethyl aminophenyl allylidene aminopropyl-imino)prop-1-ethyl)-N,N-dimethylbenzene amine. Chemical Speciation and Bioavailability. 2014; 26(4): 240

10. Baleizao C, Garcia H. Chiral Salen Complexes: An Overview to Recoverable and Reusable Homogeneous and Heterogeneous Catalysts. Chem. Rev. 2006; 106: 3987-4043.

11. Yang S, Kon H, Wang H, Chang K, Wang J. Efficient Electrolyte of N, NI-bis(salicylidene) ethylenediamine zinc(II) Iodide in Dye-sensistized Solar Cells. New. J. Chem. 2010; 34: 313-17.

12. Bae HJ, Hwang KY, Lee M H, Do Y. Salen-Aluminium Complexes as Host Materials for Red Phosphorescent Organic Light Emitting Diodes. Bull. Korean. Chem. Soc. 2011;32(9): 3290-94.

13. Starkie C. Advances in Carbon Capture and Storage Research. John Matthey Technol. Rev. 2015; 59(3): 182-87.

14. Abou-Melha K S, Faruk H. Bimetallic Complexes of Schiff Base bis[4-hydroxy Coumarin-3-yl]–IN, 5-Nthiocarboxy drazone) as a Potentially Dibasic Pentadentate Ligand. Synthesis, Spectra and Antimicrobial Properties. J Iran. Chem Soc. 2008;5: 122-34

15. Brown R, Fischer R, Blunk J, Berlin KD, Ramalingam K, Durham N N. Biological Activity and Active Groups of Novel Pyrazoles, Thiosemicarbazones and Substituted Thiazoles. Proc. Okla. Acad. Sc. 1978; 56: 15 -17.

16. Biswas FB, Roy TG, Rahman MA, Mran TB .An in vitro antibacterial and antifungal effects of cadmium(II) complexes of hexamethyltetraazacyclotetradecadiene and isomers of its saturated analogue. Asian Pac J Trop Med.2014; 7S1:S534-39.

17. Nworie FS, Nwabue FI. Solvent Extraction Studies of Metal Complexes Derived from a Tetradentate Schiff Base Bis(salicylidene)ethylenediamine (H2SAL) in Acid Medium. International Journal of Innovative and Applied Research. 2014; 2 (6): 66-75.

18. Sreeramulu J, Jaffer Mohiddin G, Raffi MD, Mallikarjuna Rao M, Musthak Ahamad R. Synthesis, Spectral Analysis and Antimicrobial Activity of Novel Dithiocarbamate Schiff Base Metal Complexes. Archives of Applied Science Research. 2012; 4(2): 858-62.

19. Schaubert K, Hufsky F, Bocker S. Computational mass spectrometry for small molecules. Journal of cheminformatics.2013; 5:12-35

20. Robertson A I, Hamming M C. MASSFORM, a computer program for the assignment of elemental compositions to high resolutions mass spectra data. Biomed mass spectrum. 1977; 4(4): 203-08.

21. Wade L. Infrared Spectroscopy and Mass Spectrometry. Organic chemistry. 6th Edition. Pearson prentice Hull: New Jersey USA.2006: 508-58.

22. Emara AAA, Ali A M, El-Asmy AF, Ragab EM. Investigation of the Oxygen Affinity of Manganese(II), Cobalt (II) and Nickel(II) Complexes with Some Tetradentate Schiff Bases. Journal of Saudi Chemical Society.2011; 18 (6): 762-73.

23. Vedanayaki S, Jayaseedan P. Synthesis, Spectroscopic and Antimicrobial Studies of Binuclear Schiff Base Complexes with N2O2 Donor Groups. World Journal of Pharmacy and Pharmaceutical Sciences.2014; 3(9): 504-17.

24. Aranha P E, dos Santos M P, Romera S, Dockal ER. Synthesis, Characterization and Spectroscopic Studies ot Tetradentate Schiff Base Chromium(III) Complexes. Polyhedron.2006; 26:1373-82.

25. Ukoha PO, Oruma US. Synthesis and Antimicrobial Studies of N, N1-bis (4-methylaminobenzylidene) ethane-1,2-diamine (DAED) and its Nickel (II) and Platinium(IV) Complexes. J. Chem.Soc-Nigeria. 2014; 39(2): 102-07.

26. El-Gamel N EA, Zayed MA. Fluoroquinoline Antibiotic (Enrofloxacin) Metal Complexes. Synthesis, Spectroscopic and In vitro Antimicrobial Screening Properties.World Journal of pharmaceutical research. 2014;4(1):142-62.

27. El-Gamel NEA.Co-ordination Behavior and Biopotency of Metal N, N- Salen Complexes. RSC Advances. 2012;2: 5870-76.

28. Enedoh M C, Nwabueze JN. Complexes of Acetone-2-amino-4-4-thiazoleacetic acid hydrazone(ATASH) withsome M(II) sulphates and acetates(M= Ni, Cu, Co, Zn, Mn).Proceedings of the 37th Annual International Conference of Chemical Society of Nigeria.2014; 169-73.

29. Gluvchinsky P, Mocler G M. Nickel (II)

Complexes of Some Quadridentate Schiff Base Ligands –II. Infrared Spectra. Spectrochim. Acta A. 1977; 33: 1073-77.

30. Abd-Elzar MM. Spectroscopic Characterization of some Tetradentate Schiff Bases and their Complexes with Nickel, Copper and Zinc. J. Chin. Chem. Soc. 2011;148:53.

31. Percy GC, Thornton DA. N-Aryl Salicyladimine Complexes: Infrared and PMR Spectra of the Ligands and Vibrational Frequencies of their Metal(II) Chelates. Journal of Inorganic and Nuclear Chemistry.1972; 34(11):3357-67.

32. Borah D, Baruah MK. Kinetic and Thermodynamic Studies on Oxidation and Desulphurization of Organic Sulphur from India Coal at 50-150oC Fuel. Processing Technology.2001;72(2):83-101

33. Aghera VK, Parsania PH. Effect of Substituent's on Thermal Behaviour of some Symmetric Double Schiff Bases Containing a Cardo group. Journal of Scientific and Industrial Research.2008; 67: 1083-87.

34. Bruylant G, Wouters J, Michaux C. Differential Scanning Calorimetry in Life Science: Thermodynamics Stability, Molecular Recognition and Application in Drug Design. Current Medicinal Chemistry.2005; 12: 2011-20.

35. Amadi OK, Otuokere IE, Iroka CE. Co-ordination Behaviour of 4-[(7-chloroquinolin-4-yl)amino]-2-(diethyl amino)methyl]phenol ligandTowards Fe(II),Ni(II),Co(II) and Cu(II) Metal Ions.Proceedings of 37th Annual International Conference of Chemical Society of Nigeria. 2014; 6-11.

36. Wahab Z HA, Mashaly MM, Salman A, Elshetary B A, Faheim A A. Co(II), Ce (III) and UO2 (VI)bis salicylatothiosemicabazide Complexes: Binary and Ternary Complexes Thermal Studies and Antimicrobial Activity, Spectrochim. Acta. Part A.2004; 60: 2861-73.

37. Pervaiz M, Yousaf M, Sagir M, Mushtaq M, Naz M Y, Ullah S, Mushtaq R. Synthesis and Characterization of Bimetallic Post Transition Complexes for Antimicrobial Activity, Synthesis and Reactivity in Inorganic, Metal-Organic, and Nano-Metal Chemistry.2015; 45:546-552.

Synthesis and Structural Characterization of New Benzimidazole Compounds Derived from Electron-Rich Olefins Bearing 1,4-Bisbenzimidazole with CS₂, PhNCS, and Chalcogens

Ülkü Yılmaz[1]* ✉, Hasan Küçükbay[1] ✉

[1]Department of Chemistry, Faculty of Arts and Sciences, İnönü University, 44280 Malatya, Turkey

Abstract: In this work, 1,4-bis(3-isopropylbenzimidazolidine-2-ylidene-1-yl)butane (**1**) and 1,4-bis(3,5(6)-dimethylbenzimidazolidine-2-ylidene-1-yl)butane (**2**) were reacted with oxygen, sulfur, selenium, tellurium, phenyl isothiocyanate, and carbon disulfide. New zwitterionic compounds (**9-12**) and cyclic urea derivatives of benzimidazole as one (**3**), thione (**4,6**), selenone (**5,7**), tellurone (**8**) were prepared from enetetramines. The chemical structures of novel benzimidazole compounds were determined by FTIR, ¹H NMR, ¹³C NMR spectroscopic methods and elemental analysis.

Keywords: Bisbenzimidazole, electron-rich olefin, strong nucleophiles, urea derivatives, zwitterion.

INTRODUCTION

Benzimidazoles and their derivatives to possess antibacterial, antitumor, antineoplastic, antihistaminic, local analgesic, vasodilative, hypotensive, antifungal, antihelmintic, spasmolytic and antimicrobial pharmacological activities (1-6). In recent years, principally bis-benzimidazole derivatives have become of interest due to their possible use in cancer cure by immobilization of DNA binding (7,8). Benzimidazole derivatives, especially 2-substituted benzimidazoles (9), generally show physiological activity and even inhibitory effect on production of viruses in tissue cultures (10). Enetetramines, in other words, electron-rich olefins, have four electron donating substitutents and are strong nucleophiles and highly reactive (11-15). They act as vigorous reducing agents and are organic ligands to transition-metal carbene complex precursors as well as catalysts for acyloin type C-C pairing reactions (16-23). Moreover enetetramines react with proton-active compounds give insertion products of nucleophilic carbenes due to the separation of the main C=C double bond (24,25). Electron-rich olefins are reducing factors and its known that the oxidation product of electron rich olefins have been synthesized with oxygen in air, sulfur, selenium, and tellurium (26).

Here we present the synthesis of new electron rich olefins from 1,4-bisbenzimidazolium salts and the synthesis of new cyclic urea compounds incorporating oxygen, its group elements, and dipolar derivatives containing sulfur.

EXPERIMENTAL SECTION

The experiments were carried out under argon using dry solvents. NMR (¹H-NMR, 300 MHz; ¹³C-NMR, 75 MHz) spectra were defined using Bruker Avance 300 MHz Ultrashield FT NMR spectrometer. Infrared spectra were identified in the range 4000-650 cm⁻¹ on a Perkin-Elmer Spectrum One FT-IR spectrometer by ATR. Elemental analyses were identified with a LECO CHNS-932 elemental analyzer. Melting points were specified using an electrothermal-9200 melting point apparatus. Compounds **I** and **II** were synthesized according to the literature (27).

Synthesis of 1,4-bis(3-isopropylbenzimidazolidine-2-ylidene-1-yl)butane (1)

A blend of **I** (5.00 g, 7.94 mmol) and NaH (0.39 g, 16.25 mmol) in THF (40 mL) was stirred for 12 hours at room temperature. The solvent was removed from the medium and oily part was extracted with hot toluene (20 mL) and the extract was filtered when hot. The yellow filtrate was condensed (10 mL), n-hexane (10 mL) was put in and the solution was cooled to -20 °C to yield a yellow compound (**1**). Yield: 2.15 g (72 %). ^{1}H-NMR (300 MHz, C_6D_6, δ, ppm): 1.32 (8H, d, J = 6.9 Hz, CH(CH_3)$_2$), 1.58 (4H, m, NCH$_2$CH_2CH_2CH$_2$N), 3.29 (4H, m, NCH_2CH$_2$CH$_2$CH_2N), 4.15 (2H, sept, J = 6.9 Hz, CH(CH$_3$)$_2$), 6.29-6.32 (2H, m, Ar-H), 6.75-6.86 (6H, m, Ar-H). Compound **2** was synthesized with a similar process from related benzimidazolium salt (**I**).

1,4-Bis(3,5(6)-dimethylbenzimidazolidine-2-ylidene-1-yl)butane (2)

Yield: 2.16 g (75 %). ^{1}H-NMR (300 MHz, C_6D_6, δ, ppm): 1.46 (4H, m, NCH$_2$CH_2CH_2CH$_2$N), 2.29 (6H, s, Ar-CH_3), 2.90 (6H, s, N-CH$_3$), 3.31 (4H, m, NCH_2CH$_2$CH$_2$CH_2N), 6.24-6.53 (6H, m, Ar-H).

1,4-Bis(3-isopropylbenzimidazolidine-2-one-1-yl)butane (3)

The compound **1** (0.50 g, 1.34 mmol) was kept in air for 24 hours. Then it was observed that the color of the yellow-colored solid turned to white. The crude product was crystallized from toluene/n-hexane (2:1). Yield: 0.39 g (72 %). M.P.: 180-181 °C, FT-IR v (cm^{-1}): 3375, 2944, 1690 (C=O), 730. ^{1}H-NMR (300 MHz, CDCl$_3$, δ, ppm): 1.55 (12H, d, J = 6.9 Hz, CH(CH_3)$_2$), 1.85 (4H, m, NCH$_2$CH_2CH_2CH$_2$N), 3.95 (4H, m, NCH_2CH$_2$CH$_2$CH_2N), 4.76 (2H, sept, J = 6.9 Hz, CH(CH$_3$)$_2$),7.02-7.17 (8H, m, Ar-H). ^{13}C-NMR (75 MHz, CDCl$_3$): δ 20.3 (CH(CH_3)$_2$), 25.6 (NCH$_2$CH_2CH_2CH$_2$N), 40.4 (NCH_2CH$_2$CH$_2$CH_2N), 44.9 (CH(CH$_3$)$_2$), 107.8, 109.0, 120.7, 120.8, 128.2, 129.4 (Ar-C), 153.7 (C=O). Anal. Calcd. for $C_{24}H_{30}N_4O_2$: C, 70.91; H, 7.44; N, 13.79. Found: C, 70.29; H, 7.50; N, 13.43.

1,4-Bis(3-isopropylbenzimidazolidine-2-thione-1-yl)butane (4)

A blend of **1** (0.42 g, 1.12 mmol) and S$_8$ (0.08 g, 0.31 mmol) in toluene (5 mL) was boiled under reflux for 2 hours. Then the mixture was filtered to remove non-reacted sulfur and the solvent were removed *in vacuo*. The raw product was crystallized from ethanol /toluene (2:1). Yield: 0.35 g (71 %). M.P.: 177-178 °C, FT-IR v (cm^{-1}): 2975, 1481 (C=S), 1414, 730. ^{1}H-NMR (300 MHz, CDCl$_3$, δ, ppm): 1.56 (12H, d, J = 6.9Hz, CH(CH_3)$_2$), 1.97 (4H, m, NCH$_2$CH_2CH_2CH$_2$N), 4.39 (4H, m, NCH_2CH$_2$CH$_2$CH_2N), 5.70 (2H, sept, J = 6.9 Hz, CH(CH$_3$)$_2$), 7.14-7.41 (8H, m, Ar-H). ^{13}C-NMR (75 MHz, CDCl$_3$): δ 20.0 (CH(CH_3)$_2$), 25.2 (NCH$_2$CH_2CH_2CH$_2$N), 44.6 (NCH_2CH$_2$CH$_2$CH_2N), 49.1 (CH(CH$_3$)$_2$), 109.5, 110.8, 122.4, 122.6, 130.4, 132.4 (Ar-C), 168.6 (C=S). Anal. Calcd.

for $C_{24}H_{30}N_4S_2$: C, 65.72; H, 6.89; N, 12.77; S, 14.62. Found: C, 65.13; H, 6.21; N, 11.98; S, 14.92. The compounds **5**-**8** were synthesized in a similar pathway from **1** and **2** olefins and related chalcogens.

1,4-Bis(3-isopropylbenzimidazolidine-2-selenone-1-yl)butane (5)

Yield: 0.48 g (75 %). M.P.: 175-176 °C, FT-IR v (cm^{-1}): 3676, 2973, 1483 (C=Se), 747, 730. ^{1}H-NMR (300 MHz, CDCl$_3$, δ, ppm): 1.45 (12H, d, J = 6.9Hz, CH(CH_3)$_2$), 1.76 (4H, m, NCH$_2$CH_2CH_2CH$_2$N), 3.85 (4H, m, NCH_2CH$_2$CH$_2$CH_2N), 4.66 (2H, sept, J = 6.9 Hz, CH(CH$_3$)$_2$), 6.92-7.11 (8H, m, Ar-H). ^{13}C-NMR (75 MHz, CDCl$_3$): δ 19.8 (CH(CH_3)$_2$), 25.1 (NCH$_2$CH_2CH_2CH$_2$N), 39.9 (NCH_2CH$_2$CH$_2$CH_2N), 44.5 (CH(CH$_3$)$_2$), 107.3, 108.5, 120.2, 120.3, 127.7, 128.9 (Ar-C), 153.2 (C=Se). Anal. Calcd. for $C_{24}H_{30}N_4Se_2$: C, 54.14; H, 5.68; N, 10.52. Found: C, 54.02; H, 5.70; N, 10.47.

1,4-Bis(3,5(6)-dimethylbenzimidazole-2-thione-1-yl)butane (6)

Yield: 0.39 g (74 %). M.P.: 173-175 °C, FT-IR v (cm^{-1}): 2936, 1502 (C=S), 1439, 1389, 796. ^{1}H-NMR (300 MHz, CDCl$_3$, δ, ppm): 1.98 (4H, m, NCH$_2$CH_2CH_2CH$_2$N), 2.46 (6H, s, Ar-CH_3), 3.76 (6H, s, N-CH$_3$), 4.380 (4H, m, NCH_2CH$_2$CH$_2$CH_2N), 7.05-7.14 (6H, m, Ar-H). ^{13}C-NMR (75 MHz, CDCl$_3$): δ 21.3 (NCH$_2$CH_2CH_2CH$_2$N), 25.1 (Ar-CH_3), 32.5 (N-CH$_3$), 45.1 (NCH_2CH$_2$CH$_2$CH_2N), 109.1, 109.3, 109.6, 109.7, 124.2, 125.1, 128.2, 128.7, 130.5, 131.3, 132.6, 133.4 (Ar-C), 164.2 (C=S). Anal. Calcd. for $C_{22}H_{26}N_4S_2$: C, 64.36; H, 6.38; N, 13.65; S, 15.62. Found: C, 63.79; H, 6.02; N, 13.20; S, 15.75.

1,4-Bis(3,5(6)-dimethylbenzimidazole-2-selenone-1-yl)butane (7)

Yield: 0.59 g (78 %). M.P.: 166-167 °C, FT-IR v (cm^{-1}): 2934, 1498 (C=Se), 1439, 1384, 792, 739. ^{1}H-NMR (300 MHz, CDCl$_3$, δ, ppm): 2.05 (4H, m, NCH$_2$CH_2CH_2CH$_2$N), 2.48 (6H, s, Ar-CH_3), 3.88 (6H, s, N-CH$_3$), 4.51 (4H, m, NCH_2CH$_2$CH$_2$CH_2N), 7.07-7.30 (6H, m, Ar-H). ^{13}C-NMR (75 MHz, CDCl$_3$): δ 21.5 (NCH$_2$CH_2CH_2CH$_2$N), 25.2 (Ar-CH_3), 33.2 (N-CH$_3$), 46.2 (NCH_2CH$_2$CH$_2$CH_2N), 109.1, 109.4, 109.8, 110.0, 124.5, 125.3, 128.2, 129.0, 130.8, 131.6, 132.8, 133.7 (Ar-C), 165.5 (C=Se). Anal. Calcd. for $C_{22}H_{26}N_4Se_2$: C, 52.39; H, 5.20; N, 11.11. Found: C, 51.98; H, 5.19; N, 11.17.

1,4-Bis(3,5(6)-dimethylbenzimidazole-2-tellurone-1-yl)butane (8)

Yield: 0.68 g (65 %). M.P.: 168-169 °C, FT-IR v (cm^{-1}): 2928, 1432 (C=Te), 1313, 800, 788. ^{1}H-NMR (300 MHz, CDCl$_3$, δ, ppm): 2.09 (4H, m, NCH$_2$CH_2CH_2CH$_2$N), 2.50 (s, 6H, Ar-CH_3), 3.96 (6H, s, N-CH$_3$), 4.57 (4H, m, NCH_2CH$_2$CH$_2$CH_2N), 7.08-7.34 (6H, m, Ar-H). ^{13}C-NMR (75 MHz, CDCl$_3$): δ 21.5 (NCH$_2$CH_2CH_2CH$_2$N), 25.6 (Ar-CH_3), 36.9 (N-CH$_3$), 49.3 (NCH_2CH$_2$CH$_2$CH_2N), 109.9, 110.2, 110.4, 110.7, 125.0, 128.2, 129.0,

131.9, 132.8, 133.8, 134.1, 134.3 (Ar-C), 143.9 (C=Te). Anal. Calcd. for $C_{22}H_{26}N_4Te_2$: C, 43.92; H, 4.36; N, 9.31. Found: C, 43.82; H, 4.30; N, 9.30.

1.4-Bis(3-isopropyl-2-dithioatebenzimidazolium-1-yl)butane (**9**)

A blend of **1** (0.46 g, 1.23 mmol) in toluene (5 mL) was put in CS_2 (0.15 mL, 2.48 mmol). A red precipitate occuring was observed right away. The product was washed with diethyl ether and crystallized from DMF/ethanol (5:1). Yield: 0.63 g (97 %). M.P.: 239-240 °C, FT-IR v (cm^{-1}): 2975, 1671, 1469 (C=S), 1049, 748. ^{1}H-NMR (300 MHz, DMSO- d_6, δ, ppm): 1.66 (12H, d, J = 6.9Hz, CH(CH_3)$_2$), 1.92 (4H, m, NCH$_2$CH_2CH_2CH$_2$N), 4.27 (4H, m, NCH_2CH$_2$CH$_2$CH_2N), 4.85 (2H, sept, J = 6.9 Hz, CH(CH$_3$)$_2$), 7.50-7.58 (4H, m, Ar-H), 7.87-7.92 (2H, m, Ar-H), 8.09 (2H, m, Ar-H). ^{13}C-NMR (75 MHz, DMSO- d_6): δ 20.2 (CH(CH_3)$_2$), 26.1 (NCH$_2$CH_2CH_2CH$_2$N), 44.8 (NCH$_2$CH$_2$CH$_2$CH_2N), 51.4 (CH(CH$_3$)$_2$), 114.0, 115.4, 126.3, 126.4, 128.0, 130.8, 151.6 (Ar-C), 162.8 (NCN), 225.2 (SCS). Anal. Calcd. for $C_{26}H_{30}N_4S_4$: C, 59.28; H, 5.74; N, 10.64; S, 24.34. Found: C, 58.91; H, 5.55; N, 10.45; S, 23.92.

1.4-Bis(3,5(6)-dimethyl-2-dithioatebenzimidazolium-1-yl)butane (**10**)

Yield: 0.54 g (88 %). M.P.: 236-237 °C, FT-IR v (cm^{-1}): 2947, 1482 (C=S), 1048, 802. ^{1}H-NMR (300 MHz, DMSO- d_6, δ, ppm): 1.96 (4H, m, NCH$_2$CH_2CH_2CH$_2$N), 2.51 (6H, s, Ar-CH_3), 3.79 (6H, s, N-CH$_3$), 4.31 (4H, m, NCH_2CH$_2$CH$_2$CH_2N), 7.39-7.76 (6H, m, Ar-H). ^{13}C-NMR (75 MHz, DMSO- d_6): δ 21.7 (NCH$_2$CH$_2$CH$_2$CH$_2$N), 25.6 (Ar-CH_3), 31.5 (N-CH$_3$), 44.88 (NCH$_2$CH$_2$CH$_2$CH_2N), 113.1, 114.3, 127.7, 128.7, 129.8, 136.6, 151.9 (Ar-C), 167.9 (NCN), 224.9 (SCS). Anal. Calcd. for $C_{24}H_{26}N_4S_4$: C, 57.80; H, 5.25; N, 11.23; S, 25.71. Found: C, 57.13; H, 5.11; N, 10.95; S, 26.29.

1.4-Bis(3-isopropyl-2-mercapto-N-phenylformimidoylbenzimidazolium-1-yl)butane inner salt (**11**)

A blend of **1** (0.54 g, 1.45 mmol) in toluene (5 mL) was put in PhNCS (0.35 mL, 2.93 mmol). The blend was stirred at room temperature, and an exothermic reaction occured in seconds. All the liquid part were removed *in vacuo* and yellow raw product was obtained. The product was crystallized from ethanol. Yield: 0.76 g (82 %). M.P.: 214-216 °C, FT-IR v (cm^{-1}): 2976, 1497, 1470 (N=C), 747. ^{1}H-NMR (300 MHz, DMSO- d_6, δ, ppm): 1.46 (12H, d, J = 6.9Hz, CH(CH_3)$_2$), 2.03 (4H, m, NCH$_2$CH_2CH_2CH$_2$N), 4.44 (4H, m, NCH_2CH$_2$CH$_2$CH_2N), 5.08 (2H, sept, J = 6.9 Hz, CH(CH$_3$)$_2$), 6.86-6.91 (2H, m, Ar-H), 7.05-7.18 (8H, m, Ar-H), 7.46-7.50 (4H, m, Ar-H), 7.88-7.91 (2H, m, Ar-H), 8.01-8.04 (2H, m, Ar-H). ^{13}C-NMR (75 MHz, DMSO- d_6): δ 20.1 (CH(CH_3)$_2$), 25.9 (NCH$_2$CH_2CH_2CH$_2$N), 44.6 (NCH$_2$CH$_2$CH$_2$CH_2N), 51.2 (CH(CH$_3$)$_2$), 113.8, 115.6, 122.0, 122.4, 125.7, 125.8, 127.9, 128.0,

130.3, 148.8 (Ar-C), 150.8 (NCN), 166.3 (SCN). Anal. Calcd. for $C_{38}H_{40}N_6S_2$: C, 70.77; H, 6.25; N, 13.03; S, 9.94. Found: C, 69.88; H, 6.18; N, 12.95; S, 9.78.

1.4-Bis(3,5(6)-dimethyl-2-mercapto-N-phenylformimidoylbenzimidazolium-1-yl)butane inner salt (**12**)

Yield: 0.88 g (85 %). M.P.: 146-147 °C, FT-IR v (cm^{-1}): 3024, 1489 (N=C), 995, 770, 693. ^{1}H-NMR (300 MHz, CDCl$_3$ δ, ppm): δ 2.258 (4H, m, NCH$_2$CH_2CH_2CH$_2$N), 2.53 (6H, s, Ar-CH_3), 4.04 (6H, s, N-CH$_3$), 4.54 (4H, m, NCH_2CH$_2$CH$_2$CH_2N), 7.11-7.51 (16H, m, Ar-H). ^{13}C-NMR (75 MHz, CDCl$_3$): δ 21.8 (NCH$_2$CH$_2$CH$_2$CH$_2$N), 26.2 (Ar-CH_3), 31.7 (N-CH$_3$), 45.4 (NCH$_2$CH$_2$CH$_2$CH_2N), 111.7, 111.8, 112.4, 112.5, 122.3, 122.4, 124.2, 127.9, 128.1, 128.7, 128.9, 129.4, 130.4, 131.1, 137.1, 137.5, 149.3 (Ar-C), 150.1 (NCN), 167.3 (SCN). Anal. Calcd. for $C_{36}H_{36}N_6S_2$: C, 70.10; H, 5.88; N, 13.62; S, 10.39. Found: C, 69.70; H, 5.62; N, 13.29; S, 10.33.

RESULTS AND DISCUSSION

Enetetramines are strong reducing agents and react with sulfur, selenium, and tellurium to give cyclic thiourea, selenourea and tellurourea derivatives in high yield (28). N-heterocyclic carbenes as a source of electron-rich olefins to react isothiocyanates and carbon disulfide to form stable zwitterionic compounds (29).

In this study, reaction of 1,4-bis(3-isopropylbenzimidazolium-1-yl)butane diiodide and 1,4-bis(3,5-dimethylbenzimidazolium-1-yl)butane diiodide salts (**I** and **II**) with NaH in THF were prepared new electron-rich olefins (**1,2**). These strong nucleophilic compounds were reacted with oxygen, sulfur, selenium, and tellurium and novel cyclic urea benzimidazole derivatives (**3**-**8**) were synthesized in good yields. The reactions were performed in refluxing dry toluene for 2 h. The products were purified by crystallization from toluene/n-hexane and toluene/ethanol. The electron-rich olefins were reacted also with PhNCS and CS_2 at 20 °C for 5 min. Reactions were very fast and yielded compounds (**9**-**12**) were purified by crystallization from DMF and ethanol. The synthesis procedure of the novel benzimidazole derivatives (**1**-**12**) was given in Scheme 1.

The chemical structures of all novel compounds were elucidated with the ^{1}H and ^{13}C NMR data as well as from the IR data and elemental analysis. The peaks in the range of 6.24-8.09 ppm are caused by the aromatic protons and aromatic peaks of olefins (**1,2**) were observed at the lowest field compared with their derivatives (**3**-**12**). The electron-rich olefins are rapidly degrading because they are highly reactive carbene sources. Therefore, only ^{1}H-NMR analysis of synthesized olefins could be performed (**1,2**).

Benzimidazole contains a hydrogen atom bonded to nitrogen in the 1-position ready to tautomerize. Because of this tautomerism, two tautomer compounds are obtained in the reactions. So, 5-substituted benzimidazole is a tautomer of 6-substituted benzimidazole and both structures are expressed as 5(6)-substituted benzimidazole (30). For this reason, it was observed that 5-methyl substituted benzimidazole derivatives (**6,7,8,10,12**) have aromatic carbon peaks more than expected in the ^{13}C-NMR spectra.

The carbon peaks of C=A groups were observed at 153.7, 168.6, 153.2, 164.2, 165.5 and 143.9

ppm respectively, in the ^{13}C-NMR spectrums of related products (**3**-**8**). Also, SCS and SCN group peaks of dipolar compounds were observed at 225.2, 224.9, 166.3 and 167.3 ppm. The results are in line with the literature (3,26).

The FT-IR spectra of (**3**-**12**) were given in experimental section. The urea derivative compounds (**3**-**8**) showed stretching bands at 1690, 1481, 1483, 1502, 1498 and 1432 cm^{-1} respectively, corresponding to C=A groups. Also, absorbance bands belonging to the C=N and C=S groups of the dipolar compounds (**9**-**12**) were appeared at 1469, 1482, 1470 and 1489 cm^{-1} in agreement with the literature data (3).

I. Y: H, R: CH(CH$_3$)$_2$
II. Y: CH$_3$, R: CH$_3$

1. Y: H, R: CH(CH$_3$)$_2$
2. Y: CH$_3$, R: CH$_3$

3. Y: H, R: CH(CH$_3$)$_2$, A: O
4. Y: H, R: CH(CH$_3$)$_2$, A: S
5. Y: H, R: CH(CH$_3$)$_2$, A: Se
6. Y: CH$_3$, R: CH$_3$,   A: S
7. Y: CH$_3$, R: CH$_3$,   A: Se
8. Y: CH$_3$, R: CH$_3$,   A: Te

9. Y: H, R: CH(CH$_3$)$_2$
10. Y: CH$_3$, R: CH$_3$,

11. Y: H, R: CH(CH$_3$)$_2$
12. Y: CH$_3$, R: CH$_3$,
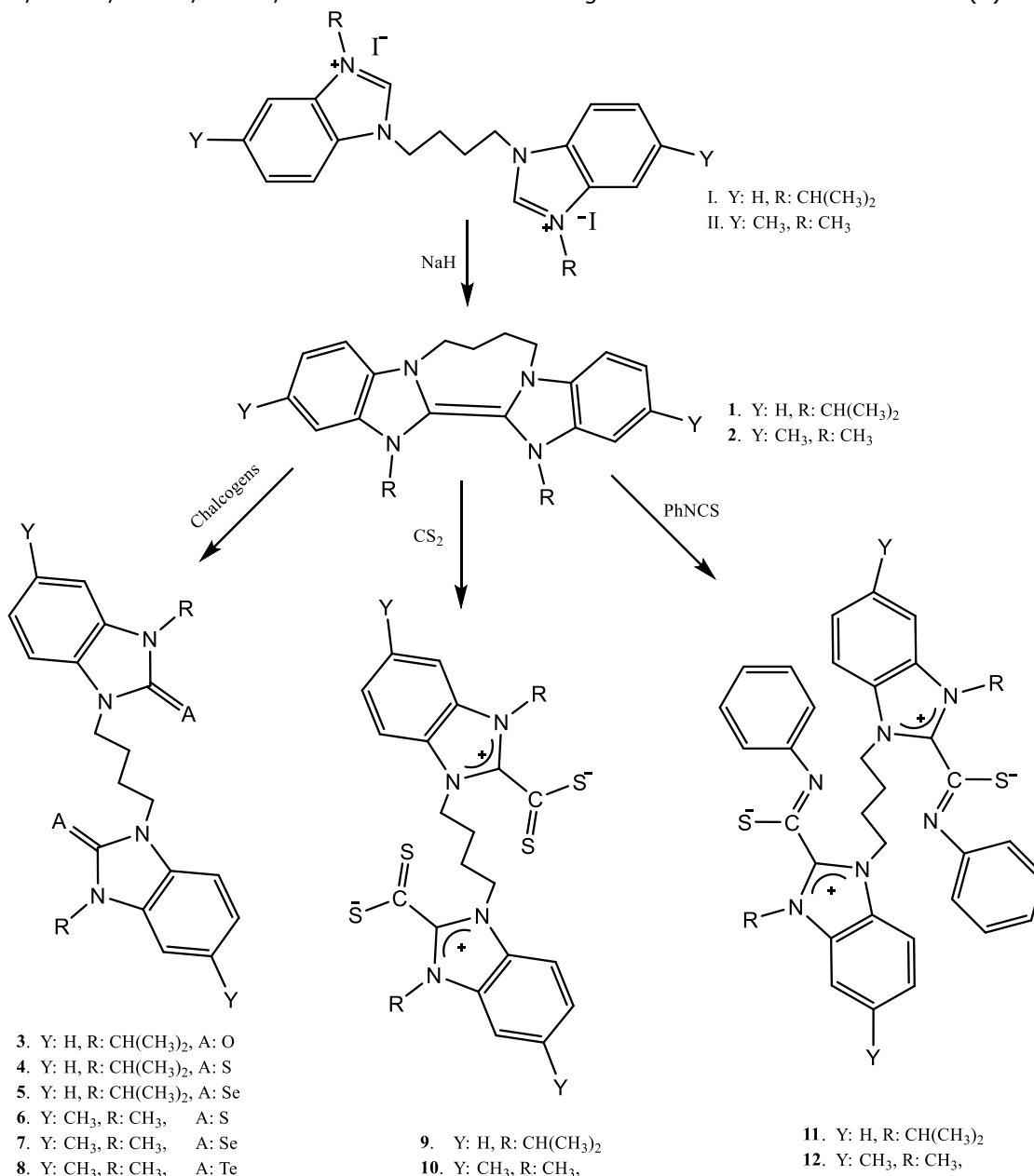
Scheme 1. Synthetic pathways of new benzimidazole derivatives.

CONCLUSIONS

In brief, we reported the synthesis and structural analysis of novel benzimidazole cyclic urea derivatives and zwitterionic compounds derived

from enetetramines as N-heterocyclic carbene sources. The novel benzimidazole derivatives (**1**-**12**) were synthesized in good yields.

REFERENCES

1. Easmon J, Puerstinger G, Roth T, Fiebig HH, Jenny M, Jaeger W, Heinisch G, Hoffmann J. 2-Benzoxazolyl and 2-benzimidazolyl hydrazones derived from 2-acetylpyridine: A novel class of antitumor agents. Int J Cancer. 2001;94:89-96.

2. Güneş HS and Cosar G. Synthesis of some hyroxamic acid-derivatives of benzimidazole and their antibacterial and antifungal activities. Arzneim-Forsch/Drug Res. 1992;42-2(8):1045-1048.

3. Küçükbay H, Durmaz R, Orhan E, Günal S. Synthesis, antibacterial and antifungal activities of electron-rich olefins derived benzimidazole compounds. Il Farmaco. 2003;58:431-437.

4. Yılmaz Ü, Küçükbay H, Şireci N, Akkurt M, Günal S, Durmaz R, Tahir MN. Synthesis, microwave-promoted catalytic activity in Suzuki-Miyaura cross-coupling reactions and antimicrobial properties of novel benzimidazole salts bearing trimethylsilyl group. Appl Organometal Chem. 2011;25(5):366-373.

5. Küçükbay H. Part I: Microvawe-assisted synthesis of benzimidazoles: An oveview (Until 2013). JOTCSA. 2017; 4(1):1-22.

6. Buğday N, Küçükbay FZ, Apohan E, Küçükbay H, Serindağ A, Yeşilada Ö. Synthesis and evaluation of novel benzimidazole conjugates incorporating amino acids and dipeptide moieties. Lett Org Chem. 2017; 14(3): 198-206.

7. Singh AK and Lown JW. Design, synthesis and antitumor citotoxicity of novel bis-benzimidazoles. Anti-Cancer Drug Des. 2000;15(4):265-275.

8. Soderlind KJ, Gorodetsky B, Singh AK. Bis-benzimidazole anticancer agents: targeting human tumour helicases. Anti-Cancer Drug Des. 1999;14(1):19-36.

9. Yılmaz Ü, Küçükbay H. Synthesis and characterization of novel phosphoramidates containing benzimidazole moiety. Phosphorus Sulfur Silicon Relat Elem. 2016;191(1):140-143.

10. Thompson RL. The effectof metabolites, metabolite antagonists, and enzyme inhibitorson the growth of vaccinia virus in Maitland type of tissue cultures. J Immunol. 1947;55:345-352.

11. Lappert MF. The coordination chemistry of electron-rich alkenes (enetetramines). J Organomet Chem. 1988;358(1-3):185-214.

12. Çetinkaya B, King GH, Krishnamuthy SS, Lappert MF, Pedley JB. Photoelectron spectra of electron-rich olefins and an isostructural boron compound; olefins of exceptionally low first ionisation potential J Chem Soc D. 1971;1370-1371.

13. Tudose A, Delaude L, Andre B, Demonceau A. Imidazol(in)ium carboxylates as N-heterocyclic carbene ligand precursors for Suzuki-Miyaura. Tetrahedron Lett. 2006;47(48):8529-8533.

14. Hahn FE, Paas M., Le Van D, Lugger T. Simple Access to unsymmetrically substituted, saturated N-heterocyclic carbenes. Angew Chem Int Edit. 2003;42(42):5243-5246.

15. Kamplain JW, Lynch VM, Bielawski CW. Synthesis and study of differantially substituted dibenzotetraazafulvalenes. Org Lett. 2007;9(26):5401-5404.

16. Küçükbay H, Çetinkaya B, Guesmi S, Dixneuf PH. New (Carbene)ruthenium-arene complexes: preparation and uses in catalytic synthesis of furans. Organometallics. 1996;15:2434-2439.

17. Vasam CS, and Lin IJB. Silver(I) N-heterocyclic carbenes. Com Inorg Chem. 2004;25(3-4):75-129.

18. Tudose A, Demonceau A, Delaude L. Imidazol(in)ium-2-carboxylates as N-heterocyclic carbene precursors in ruthenium-arene catalysts for olefin metathesis and cyclopropanation. J Organometal Chem. 2006;691(24-25):5356-5365.

19. Hahn FE, Paas M., Le Van D, Fröhlic R. Spirocyclic diaminocarbenes: Synthesis, coordination chemistry, and investigation of their dimerization behavior. Chem Eur J. 2005;11:5080-5085.

20. Khramov DM, Boydston AJ, Bielawski CW. Synthesis and study of janus bis(carbene)s and their transition-metal complexes. Angew Chem Int Edit. 2006;45:6186-6189.

21. Lappert MF. Contributions to the chemistry of carbenemetal chemistry. J Organometal Chem. 2005;690:5467-5473.

22. Çetinkaya E, and Küçükbay H. Effective acyloin condensations catalyzed by electron-rich olefins. Turk J Chem. 1995;19:24-30.

23. Lappert MF, Maskell RK. A new class of benzoin condensation catalyst, the bi-(1,3-dialkylimidazolidin-2-ylidenes). J Chem Soc Chem Commun. 1982;580-581.

24. Hocker J, and Metren R. Reactions of electron-rich olefins with proton-active compounds. Angew Chem Int Edit. 1972;11:964-973.

25. Küçükbay H, Çetinkaya E, Çetinkaya B, Lappert MF. Reactions of electron-rich olefins with proton-active compounds. Synth Commun. 1997;27(23):4059-4066.

26. Çetinkaya B, Çetinkaya E, Küçükbay H, Durmaz R. Synthesis and antimicrobial activity of electron rich olefin derived cyclic ureas. Arzneim-Forsch/Drug Res. 1996;46(12):1154-1158.

27. Küçükbay H, Durmaz R, Okuyucu N, Günal S, Kazaz C. Synthesis and antibacterial activities of new bis-benzimidazoles. Arzneim-Forsch/Drug Res. 2004;54(1):64-68.

28. Küçükbay H, Çetinkaya E, Durmaz R. Synthesis and antimicrobial activity of substituted benzimidazole, benzothiazole and imidazole derivatives. Arzneim-Forsch/Drug Res. 1995;45(12):1331-1334.

29. Li J-Q, Liao R-Z, Ding W-J, Cheng Y. Highly efficient and site-selective [3+2] cycloaddition of carbene-derived ambident dipoles with ketenes for a straightforward synthesis of spiro-pyrrolidons. J Org Chem. 2007;72:6266-6269.

30. Wright JB. The chemistry of the benzimidazoles. Chem Rev. 1951;48(3):397-541.

Biological Property of *Fritillaria imperialis* L. Extract

Ali Aydın*[1] 🆔 ✉, **Emine Dede [2]** ✉, **Mahfuz Elmastaş [2]** 🆔 ✉, **Şaban Tekin[1]** ✉

[1] *Faculty of Art and Science, Department of Molecular Biology and Genetics, Gaziosmanpaşa University, 60240, Tokat, Turkey*
[2] *Faculty of Art and Science, Department of Chemistry, Gaziosmanpaşa University, 60240, Tokat, Turkey*

Abstract: A preliminary in vitro screening revealed the therapeutic status of extracts of *Fritillaria imperialis* L. that belongs to the *Liliaceae* family. Its tendrilled bulbs are consumed fresh or prepared in a powdered form and used as a home remedy for cough and phlegm, high fever, hemorrhage, lack of milk, treatment of abscesses, asthma, rheumatism, and eye disease. Herein, we investigated the antiproliferative, cytotoxic effects and antibacterial activities of *Fritillaria imperialis* L. extracts on three cancer cell lines (HeLa, HT29, and C6), and a non-cancer cells (Vero). The potential antiproliferative and cytotoxic impact of *Fritillaria imperialis* L. extracts were investigated *in vitro* through MTT and LDH measurement techniques, and its antimicrobial effects were studied with MIC and disc-zone test. The extracts of *Fritillaria imperialis* L. have been shown to exhibit poor antiproliferative effects and antibacterial activities on some cancer cell lines and bacteria, respectively, at even high concentration. These data suggest that *Fritillaria imperialis* L. extracts are low cytotoxic to cancer cell lines and *Staphylococcus aureus* (ATCC 25923) and *Escherichia coli* (ATCC 25922). Our results indicate that clinic consideration of *Fritillaria imperialis* extracts for the treatment of malignant and bacterial disease needs to be re-evaluated due to its different extraction and isolation methods.

INTRODUCTION

Cancer, a common name for many diseases with poor prognosis is a persistent illness and constitutes a significant socioeconomic burden (1). Despite the dizzying advances in cancer studies, tumor treatments still remain far below the desired level with serious side effects together with persistent drug resistance. Therefore, we need to get more effective anticancer agents, natural products may be suitable anticancer drug candidates. From ancient times to present human beings have used plants as medicines for the treatment of different diseases, including cancer, or for the improvement of their health. Currently, human population preferring folk remedies reached approximately 70% of all populations (2, 3). Indeed, nowadays, natural products have received more research attention. This may be one reason that natural products examined so far have exhibited

potent antiproliferative effects adopting a mechanism-based approach. Also, based on their different kinetics, binding to organic molecules such as DNA, RNA or proteins and to be from natural source compared to synthetic drugs, natural products offer a great unexplored pharmacological area concerning the requirements of modern drug design. Today as in the past, the natural compounds and their by-products derived from remedies have gained importance in clinical use including cancer. Therefore, potential anticancer properties of medicinal plant extracts or isolated compounds can be monitored for anticancer drug development. As a result of these studies in the world, nearly 60% of drugs and 50% of all the currently used drugs in the clinic approved by FDA for cancer treatment are naturally occurring agents [4-6]. Several of them, such as taxol, vinblastine, vincristine, topotecan, irinotecan, and etoposide are in clinical use and some of them are about to enter the pipeline. Anatolian plants have marvelous diversity and are still untapped in current pharmacopeia, and they can be evaluated as an invaluable source of 'Hit to Lead' molecule (7, 8).

MATERIALS and METHODS

Preparation of extracts
The stem (MS), leaf (ML), and flower (MF) parts of the *Fritillaria imperialis* L. were dried in the shade for two months at room temperature (each part 50 g ±2.0 g). At the end of this stage, dried *Fritillaria imperi*alis L. parts were thoroughly powdered with the help of a blender. Then, powdered *Fritillaria imperialis* L. parts were placed in an Erlenmeyer flask for extraction. Distilled methanol (250 mL) was added to the samples and was kept for one day at room temperature. At the end of this period, the

Medical plants are often consumed by being put into various foods or decocted in herbal tea and they provide significant various products such as alkaloids that have healing activity of folkloric remedy. The topic of this study focused on assessment of the pharmacological activity of extracts from *Fritillaria imperialis* L using cell cytotoxicity assay and visualized morphological alteration. However, to the best of our knowledge, the antiproliferative and cytotoxic features of *Fritillaria imperialis* L. extracts on cancer cells and the mechanisms underlying it have not yet been revealed. The antiproliferative activity for all natural products is performed in compliance with the European Pharmacopoeia 8.0 protocol. According to this protocol, these natural products for *in vitro* antiproliferative activity against HeLa (Human Cervix Carcinoma), HT29 (Human Colorectal Adenocarcinoma), C6 (Rat Brain Tumor Cells), and Vero (African Green Monkey Kidney) cells were conducted using a cell proliferation assay, cytotoxicity assay (LDH), and phase-contrast microscopic image evaluation techniques. In our study, we tried to address the possible anticancer activity of *Fritillaria imperialis* L. extracts.

liquid fraction was filtered through a filter paper to exclude the rough particles. To obtain the methanolic extract, the solvent was removed using a rotary evaporator (45 °C water bath, 700 mmHg). The extracts were stored at +4 °C.

Preparation of cell culture
The anticancer potential of *Fritillaria imperialis* L. extracts was investigated on cancerous HT29 (ATCC® HTB-38™), HeLa (ATCC® CCL-2™), and C6 cells (ATCC® CCL-107™) and nontumorigenic Vero cells (ATCC® CCL-81™). The cell lines were cultured in a cell medium (Dulbecco's modified eagle's medium, DMEM)

enriched with 10% (v/v) fetal bovine serum and 2% (v/v) Penicillin-Streptomycin (10,000 U/mL). First, old medium was removed out of the flask while cells had reached approximately 80% confluence. Next, cells were taken from the flasks surface using 4 mL of 0.5% trypsin-EDTA solution and neutralized by the addition of 15 mL DMEM enriched with 10% (v/v) fetal bovine serum and then subjected to centrifugation. Following, the cell pellet was suspended with 4 mL of DMEM working solution and was counted to obtain a final concentration of 5×10^4 cells/mL, and inoculated into wells (100 µL cells/well).

Cell proliferation assay (MTT)

A cell suspension containing approximately 1×10^4 cells in 100 µL was seeded into the wells of 96-well culture plates. *Fritillaria imperialis* L. extracts and 5-fluorouracil (5FU) (control drug) were dissolved in sterile DMSO (Dimethyl sulfoxide) (max 0.5% of DMSO) at final concentrations of 25, 50, 100, 150, 200, 250, 375, and 500 µg/mL. The cells were treated with *Fritillaria imperialis* L. extracts and 5FU at 37 °C with 5% CO_2 for overnight. The final volume of the wells was set to 200 µL by medium. Cell proliferation assay was evaluated by MTT (3-(4,5-dimethylthiazolyl-

2)-2,5-diphenyltetrazolium bromide) method. Briefly, An MTT stock solution (5 mg of MTT/mL of distilled water) was filter sterilized and kept for at -20 °C until use. The cells were exposed to MTT reagent for 4 h to form MTT formazan dye followed by the dye dissolved in DMSO with Sorenson's buffer for 30 min at room temperature and then the plate was measured at 560 nm, with 690 nm as a reference interval, using a microplate reader. Each experiment was repeated at least three times for each cell line.

Calculation of IC$_{50}$ and % inhibition

IC_{50} value is a concentration that inhibits half of the cells in vitro. The half maximal inhibitory concentration (IC_{50}) (95% confidence intervals) of the *Fritillaria imperialis* L. *extracts* and control compounds was calculated using XLfit5 or excel spreadsheet. The proliferation assay results were expressed as the percent inhibition according to the following formula: where 'absorbance of treatments' provides information about the absorbance obtained from test compound treated cells and 'absorbance of DMSO' provide information about the absorbance obtained from DMSO treated control cells (maximum final concentration: 0.5 % DMSO).

$$Inhibition\ (\%) = 1 - \left(\frac{Absorbance\ of\ Treatments}{Absorbance\ of\ DMSO}\right) x 100 \qquad (Eq.1)$$

Cytotoxic activity assay

The cytotoxicity of the *Fritillaria imperialis* L. *extracts* and 5-fluorouracil on HeLa, C6, HT29, and Vero cells was determined through a Lactate Dehydrogenase Assay Kit according to the manufacturer's instructions (Roche, LDH Cytotoxicity Detection Kit). Approximately 5 x 10^3 cells in 100 µL were placed into 96-well plates as triplicates and treated with IC_{50} (µg/mL) concentrations of *Fritillaria imperialis*

L. extracts at 37 °C with 5% CO_2 for 24 h. LDH activity was obtained by determining absorbances at 492 and 630 nm using a microplate reader. The cytotoxicity assay results were noted as the percent cytotoxicity according to the following formula: where 'low control' provides information about the LDH activity released from the untreated cells, 'high control' is the maximum amount of releasable LDH enzyme activity which is

determined by lysing the cells with Triton X-100 (final concentration: 1% Triton X-100).

$$Cytotoxicity\ (\%) = \left[\frac{(Experimental\ Value - Low\ Control)}{High\ Control - Low\ Control} x100 \right]$$ (Eq. 2)

Cell imaging

Cells were seeded into 96-well plates at a density of 5.000 cells per well and allowed to 24 h. IC_{50} values of the *Fritillaria imperialis* L. extracts were administered and morphology alters of the cells were screened by phase contrast microscopy every 6 h for 24 h. Images of control and *Fritillaria imperialis* L. extracts treated cells were photographed at the end of the process using a digital camera attached to an inverted microscope.

Antimicrobial activity

We investigated the antimicrobial activity of the *Fritillaria imperialis* L. extracts against one gram-positive bacteria (*S. aureus* ATCC25923) and one gram-negative bacteria (*E. coli* ATCC25922) by using disc-diffusion method with reference to EUCAST.

RESULTS AND DISCUSSION

Antiproliferative effect of the *Fritillaria imperialis* L. extracts

Plants generally produce biologically active compounds to protect themselves against a variety of micro- and macro-organisms. For this reason, it is a very realistic approach that the majority of active molecules obtained from natural sources have anticancer and antimicrobial features. Important agents approved by US Food and Drug Administration (FDA) such as anti-cancer (Taxol), topoisomerase inhibitor (Camptothecin), antimicrobial (Erythromycin), antibiotic aminoglycoside (Kanamycin), and antibiotic β-lactam (Cephalosporin C) used in modern medicine are of herbal origin. In addition to the above mentioned medicines, herbal products, which have been known to be effective in the folk cure for many years, are used in various countries according to their pharmacopoeial monographs. The *Fritillaria imperialis* L., which is one of these, is an ornamental plant including various

pharmaceutically active components, which have been commonly used as a traditional remedy. Especially, in traditional Chinese medicine, *Fritillaria spp* bulbs are known to have some medicinal features such as treating bronchitis, becoming a diuretic, calming heart spasms (9 – 14). According to traditional descriptions, *Fritillaria spp* bulbs have been added into some special Chinese herbal formulas for cancer patients (9). Here, we aimed to understand the response of cells upon administering *Fritillaria imperialis* L. extract *in vitro*. The antitumor feature of the stem, leaves, and flower extracts of the *Fritillaria imperialis* L. on cancer cells were screened by MTT assay. In this assay, 5-fluorouracil (5-FU) was used as a positive control. As shown in Figure 1, *Fritillaria imperialis* L. extracts did not show any anticancer activity. In addition, none of the concentrations of the *Fritillaria imperialis* L. extracts reached the half maximal inhibitory concentration (IC50). It can be easily seen that stem, leave, and flower part of the

Fritillaria imperialis L. extracts have not shown therapeutic action against the cervix, colon, and brain cancer cells. It is likely that these parts of the plant do not contain a strong metabolite or the extraction method used may be insufficient. Actually, the bulb part of *Fritillaria spp* includes several interesting molecules such as steroidal alkaloids (imperialine and verticine), sesquiterpenes and glycosides as well as many other compounds such as saponins, terpenoids [9 - 14]. To date, stem, leave, and flower part of *Fritillaria spp* were not characterized for their chemical components with potential medicine utility. However, we may speculate that stem, leave, and flower part of *Fritillaria imperialis* L. extracts possibly can be used as an adjuvant agent in treatment along with conventional therapies.
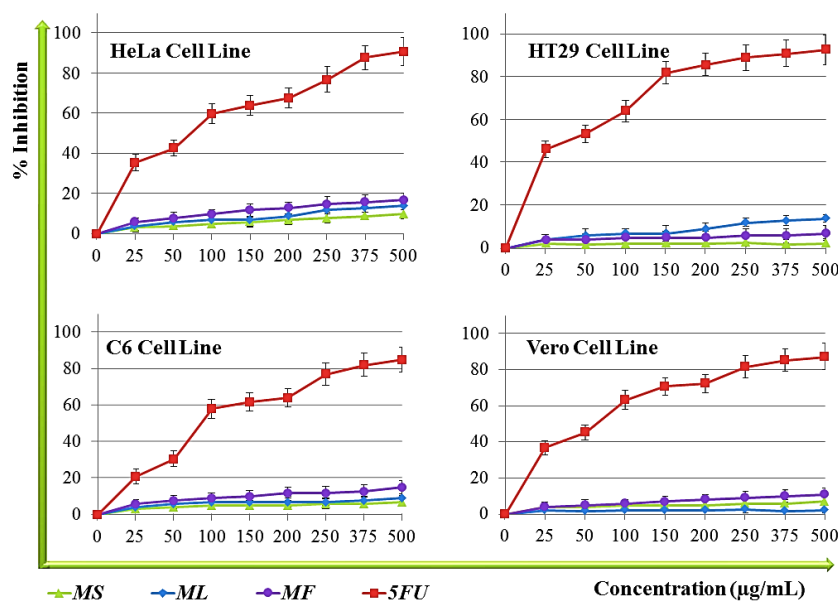

Figure 1. Antiproliferative effects of methanol (MS, ML, and MF) stem, leaves, and flower extracts, respectively, and positive control 5FU on HeLa, HT29, C6, and Vero cell lines. Cell proliferation measurement was carried out with MTT assay. Inhibition percentage was reported as ± SEM value of three independent measurements (P < 0.05). Each experiment was triplicated for each cell line.

Cytotoxic activity and morphological assessment of the *Fritillaria imperialis* L. extracts

One of the aims of the present study was to evaluate the effects of *Fritillaria imperialis* L. extracts on the membrane integrity and to determine the cytoprotective activities.

Cytotoxic activities of *Fritillaria imperialis* L. extracts on HeLa, HT29, C6, and Vero cell lines was assessed by the LDH cytotoxicity assay kit. HeLa, HT29, C6, and Vero cells were grown in the presence or absence of *Fritillaria imperialis* L. extracts (250 µg/mL) for a period of 24 h.
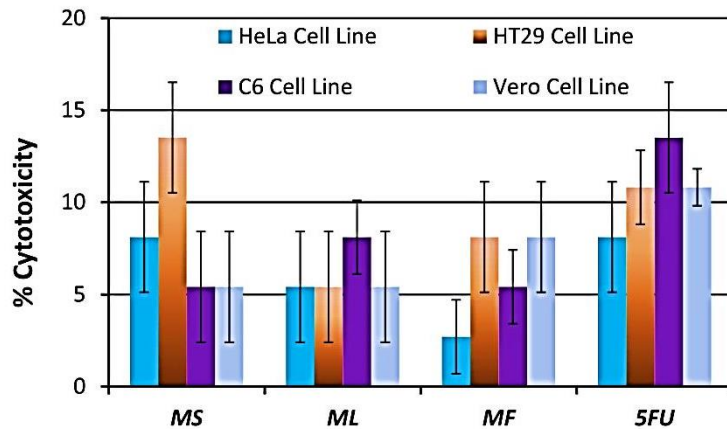
Figure 2. Cytotoxic effects of *Fritillaria imperialis* L. extracts on HeLa, HT29, C6, and Vero cell lines. Cell lines were incubated with extracts of 250 µg/mL for 24 hrs and cytotoxicity was determined using the LDH cytotoxicity kit. Inhibition percentage was reported as ± SEM value of three independent measurements (P < 0.05).
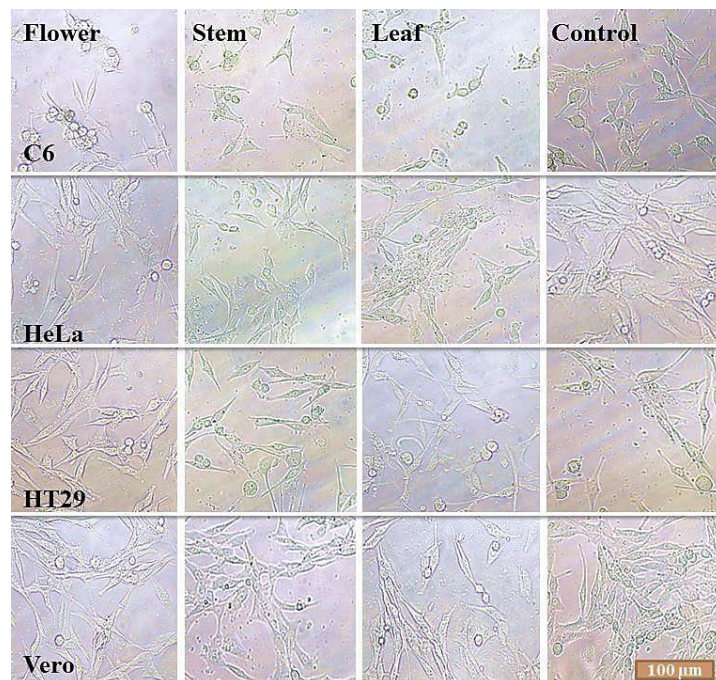
Figure 3. Effects of *Fritillaria imperialis* L. extracts on the morphologies of HeLa, HT29, C6, and Vero cell lines. Exponentially growing cells were incubated overnight with 250 µg/mL concentrations of the extracts at 37 °C. Control cells were treated with only DMSO.

Cytotoxicity results demonstrated that at concentrations 250 µg/mL, *Fritillaria imperialis* L. extracts did not affect LDH leakage from the cells (Figure 2). Therefore, *Fritillaria imperialis* L. extracts protected the cell membrane integrity. This probably means that *Fritillaria imperialis* L. extracts can be used as cytoprotective agents. In order to evaluate the effect of *Fritillaria imperialis* L. extracts on the cell morphology, phase contrast images were visualized by a digital camera attached inverted microscope (Leica IL10, Germany). The picture showed inverted microscope images of the morphology of treated cell lines with 250 µg/mL concentrations of *Fritillaria imperialis* L. extracts as compared to

respective controls. As shown in Figure 3, at 250 µg/mL concentration, treated cells continued to maintain their normal morphology when compared with control cells. Similar to the control cells, all treated cells were astrocyte-like or fibroblast-like appearance and displayed confluent situation in plate surface. Generally, *Fritillaria imperialis* L. extracts treated cells did not show any apoptotic indicator structures such as cell shrinkage, apoptotic bodies, and atypical forms. Thus, microscopic observations may indicate that *Fritillaria imperialis* L. extracts

CONCLUSION

Generally, chemotherapeutic cure resulted in the debilitating effect on cells, and this situation is the most important obstacle for the treatment of cancer. *Fritillaria* spp. bulbs have been long used in traditional medicine for primary health care to possess medicinal features. Today, we know that *Fritillaria* spp. bulbs extracts are found in formulations for treating cancer, Alzheimer's or respiratory system symptoms. However, to the best of our knowledge, the stem, leaf, and flower extracts of *Fritillaria imperialis* L. have not been studied yet. *Fritillaria* spp. bulbs contain various pharmaceutically active constituents that possess anticancer and cytotoxic features by using the cellular stress or immunomodulating mechanisms (17-20). On the other hand, *Fritillaria imperialis* L. extracts (stem, leaf, and flower) may activate survival pathways. The dual effect of *Fritillaria imperialis* L. bulb and the other parts on cells could provide a powerful strategy in cancer cure. Overall, our findings would seem to suggest that further study using both *Fritillaria imperialis* L. bulb extracts and stem, leaf, and flower extracts

may be associated with cell survival mechanism.

Antimicrobial effect
The screening results revealed that *Fritillaria imperialis* L. extracts showed no antimicrobial activity against *S. aureus* (ATCC 25923) and *E. coli* (ATCC 25922). In a similar study, it was noted that *Fritillaria imperialis* L. exhibited antifungal activity but not antimicrobial activity (15). However, another study displayed that some *Fritillaria* spp. accomplish strong antimicrobial activity due to different solvents (16).

can be promoted as an efficient way to open desirable treatment options.

AUTHOR CONTRIBUTIONS

Conceived and designed the experiments: AA ED ME. Performed the experiments: AA ED. Analyzed the data: AA ED ME ŞT. Contributed reagents/materials/analysis tools: AA ED ME.

REFERENCES

1. World Cancer Report 2014. http://www.iarc.fr/en/publications/books/wcr/wcr-order.php (accessed 15.09.16).

2. Elgorashi E. Screening of medicinal plants used in South African traditional medicine for genotoxic effects. Toxicol. Lett. 2003; 143, 195–207.

3. Fennell CW, Lindsey KL, McGaw LJ, Sparg SG, Stafford GI, Elgorashi EE, Grace OM, van Staden J. Assessing African medicinal plants for efficacy and safety: pharmacological screening and toxicology. J. Ethnopharmacol. 2004; 94: 205–17.

4. Sithranga Boopathy N, Kathiresan K. Anticancer Drugs from Marine Flora: An Overview. J. Oncol. 2010; 214186: 1–18.

5. Weerapreeyakul N, Nonpunya A, Barusrux S, Thitimetharoch T, Sripanidkulchai B. Evaluation of the anticancer potential of six herbs against a hepatoma cell line Chin. Med. 2012; 7: 15.

6. Lee CC, Houghton P. Cytotoxicity of plants from Malaysia and Thailand used traditionally to treat cancer. J. Ethnopharmacol. 2005; 100: 237–43.

7. Berrington D, Lall N. Anticancer Activity of Certain Herbs and Spices on the Cervical Epithelial Carcinoma (HeLa) Cell Line. Evidence-Based Complement. Altern. Med. 2012; 564927: 1–11.

8. Itharat A, Houghton PJ, Eno-Amooquaye E, Burke P, Sampson JH, Raman A. In vitro cytotoxic activity of Thai medicinal plants used traditionally to treat cancer. J. Ethnopharmacol. 2004; 90: 33–38.

9. Chinese Pharmacopoeia Commission. http://www.chp.org.cn/cms/home/ (accessed 15.09.16).

10. Shun-Wan C, Ping L, Yiu-Wa K, Ge L. In vitro Tracheobronchial Relaxation of Fritillaria Alkaloids. Chinese Journal of Natural Medicines. 2011; 9(5): 0345−53.

11. Kiani M, Sefidkon F, Babaei A, Naghavi MR. Phytochemical profiling of medicinal isosteroidal alkaloids of Iranian Fritillaria spp. (Liliaceae). Ind. Crops Prod. 2015; 70: 451–8.

12. Atta-Ur-RahmaN, Akhtar MN, Choudhary

MI, Tsuda Y, Sener B, Khalid A, Parvez M. New steroidal alkaloids from Fritillaria imperialis and their cholinesterase inhibiting activities. Chem. Pharm. Bull. 2002; 50: 1013–6.

13. HAO D-C, GU X-J, XIAO P-G, PENG Y. Phytochemical and biological research of Fritillaria Medicine Resources. Chin. J. Nat. Med. 2013; 11: 330–44.

14. Türktaş M, Aslay M, Kaya E, Ertuğrul F. Molecular characterization of phylogeneticrelationships in *Fritillaria* species inferred from chloroplast trnL-trnF sequences. Turk J Biol. 2012; 36: 552-60.

15. Maharjan BL, Devkota HK, Baral B. In-vitro Antimicrobial Activity and Phytochemical Screening of Fritillaria delavayi. Nepal J. Sci. Technol. 2012; 12: 85-90.

16. Erbil N, Alan Y, Digrak M. Antimicrobial Activity of Different Vegetative Parts of *Tulipa sintenisii* (Mus Lalesi) *and Fritillaria imperialis* (Aglayan Gelin). International Journal of Scientific and Technological Research. 2015; 1(2): 120-7.

17. Gilani AH, Shaheen F, Christopoulos A, Mitchelson F. Interaction of ebeinone, an alkaloid from Fritillaria imperialis, at two muscarinic acetylcholine receptor subtypes. Life Sci. 1997; 60(8): 535–44.

18. Akhtar MN, Atta-ur-Rahman, Choudhary MI, Sener B, Erdogan I, Y. Tsuda Y. New class of steroidal alkaloids from Fritillaria imperialis. Phytochemistry 2003; 63(1): 115–22.

19. Aydın A, Erenler R, Yılmaz B, Tekin Ş. Antiproliferative effect of Cherry laurel. JOTCSA, 2016; 3(3): 217-28.

20. Güler DA, Aydın A, Koyuncu M, Parmaksız İ. Anticancer Activity of Papaver somniferum L. JOTCSA, 2016; 3(3): 349-66.

RESEARCH ARTICLE

Preparation and investigation of aggregation, fluorescence and singlet oxygen generation properties of gallium and metal-free phthalocyanines

Emre Güzel* ✉ iD

Sakarya University, Department of Chemistry, TR54050, Sakarya, Turkey.

Abstract: The synthesis, characterization, aggregation, optical, fluorescence and singlet oxygen generation properties of 2-furylmethoxy substituted gallium and metal-free phthalocyanines (**2** and **3**, respectively) are reported for the first time. Characterization of the novel synthesized compounds was performed with elemental analysis, ultraviolet-visible spectrophotometry, fourier transform infrared spectrometry, ^{1}H-NMR spectroscopy and mass spectrometry. When the concentration behavior of the synthesized complexes is examined in a certain concentration range in THF, it has been shown that the phthalocyanines predominantly consist of monomeric species. Furyl-containing new phthalocyanines are quite soluble in common organic solvents and this makes them possible to be used in several important applications. Fluorescence behavior of these phthalocyanines were investigated. In this study, the metal ion's effect on the UV-Vis and photophysical features of the MPcs is also cited. These results show that the metal in the core of the phthalocyanine is an important factor in the fluorescence behavior and quantum yield (Φ_F) of the complexes. In singlet oxygen generation studies showed that the phthalocyanines containing the 2-furylmethoxy group indicated a high level of photosensitization and singlet oxygen generation capacity. Consequently, these gallium and metal-free complexes are promising photosensitizer for photodynamic therapy applications.

INTRODUCTION

Furan groups and their derivatives, which have important properties such as low viscosity, high reactivity and excellent solvent properties, are used as chemical building blocks for drug synthesis, as well as polymer-based resin construction as an intermediate for the synthesis of natural products and their analogues (1,2).

Phthalocyanines (Pcs) which are an important family of macrocyclic compounds class, have many uses such as gas sensors (3), catalysts (4), solar cells (5), electrochromic devices (6),

Langmuir Blodgett films (7), liquid crystals (8) and photosensitizers (9,10) in photodynamic cancer therapy (PDT). Photodynamic therapy (PDT) is a treatment modality that is widely used today against some types of cancer without surgical intervention (11). Therapy involves three components: light, molecular oxygen and a photosensitizer that absorbs light in the wavelength range of 600-800 nm. With these three important components, molecular oxygen ($^3O_2$) converts to singlet oxygen ($^1O_2$). Tetrapyrrolic macrocyclics include porphyrins, and especially phthalocyanines are among the most studied photosensitizers (10). To have an

effective photodynamic therapeutic effect, a phthalocyanine must absorb light in the 600-800 nm region, thereby providing penetration into human tissues. Up to this time, many photosensitizer have been tested *in vitro* and *in vivo* in PDT experiments, but very few of them have shown ideal properties. This has led to a focus on the development of new photosensitizer and the enhancement of their effectiveness in studies conducted. The features that a photosensitizer should have for a successful PDT operation; chemical purity, being selective for cancer cells, accumulating in the tissue shortly after application, rapid cleaning from the body. In the treatment of PDT, ensuring that sufficient quantities of light reach the entire tumor tissue is one of the most important steps in the success of treatment. To understand this, it is necessary to examine the passage of light from tissues, absorption and scattering. In addition, distribution, absorption, or scattering of light in tumorous tissue depends both on the type of tissue applied and on the wavelength of the light (12).

By introduction of different substituents, the photophysical and photochemical characteristics of Pcs can be fine-tuned. It is also accepted that the metal atom coordinating to the phthalocyanine ring can significantly change the physical, chemical and biological properties of the complex (13–21). Phthalocyanines' solubility in common organic solvents and water is low, which is a major disadvantage. These low solubilities of the phthalocyanines limit the number of applications in which soluble derivatives are used. This problem can be solved by increasing the solubility of the bulky groups or long alkyl, alkoxy groups in the nonpolar solvent by attaching to the peripheral/non-peripheral positions of the phthalocyanines (17).

Chemical derivatives containing furan group, which is substituted at the peripheral and non-peripheral positions of the phthalocyanines ring to eliminate the solubility problems of the phthalocyanines, can also play an important role in altering the solubility and absorption properties of the complexes. Therefore, in this study, peripherally tetrakis(2-furylmethoxy)-substituted gallium and metal free phthalocyanines have been prepared for the first time. The synthesized phthalocyanines were characterized in a spectroscopic manner. The optical, fluorescence and singlet oxygen generation properties of these Pcs were determined and compared.

EXPERIMENTAL SECTION

Materials and methods

All solvents and reagents were obtained from commercial suppliers. The solvents were stored over molecular sieves. The purity of the products was tested in each step by TLC. 4-(2-furylmethoxy)phthalonitrile (**1**) was prepared

according to the reported procedure (22). FT-IR spectra were recorded on a Perkin Elmer Spectrum One FT-IR (ATR sampling accessory) spectrometer. All absorption and fluorescence excitation, emission spectra were measured by using Shimadzu UV-2600 UV–Vis spectrophotometer and Hitachi F-7000 Fluorescence spectrophotometer, respectively. ^{1}H-NMR spectra were recorded on Agilent VNMRS 300 MHz. Mass spectra were performed on a Bruker Autoflex III MALDI-TOF spectrometer. Elemental analyses were performed in TÜBİTAK Marmara Research Center. The singlet oxygen generation study carried out under light irradiance of 100 mW cm^{-2} (AM1.5) from a 150 W solar simulator (Newport, 96000) with 650 nm cut-on filter.

Preparation

Synthesis of gallium phthalocyanine: A mixture of 4-(2-furylmethoxy)-phthalonitrile (0.100 g, 0.446 mmol), anhydrous GaCl$_3$ (0.026 g, 0.15 mmol) and DBU (0.2 mmol) as a strong base, in 2 mL of quinoline was refluxed at 160 ºC in a sealed glass tube for 12 hours. After cooling to room temperature, the green mixture was precipitated by adding n-hexane and it was filtered. The crude product was washed with methanol in order to remove impurities. The desired product was purified by basic silica gel column chromatography using a gradient of chloroform/ethanol (10/1) as eluents. Finally, it was dried *in vacuo*. Solubility: Highly soluble in THF, CH$_2$Cl$_2$, DMF and DMSO. Yield: 0.036 g, (33 %). FT-IR (u$_{max}$/cm^{-1}): 3010 (Ar-C-H), 2949-2865 (Aliph. -C-H), 1611 (Ar-C=C), 1482, 1288 (Ar-O-R), 1124 (-C-O-C Furan), 996, 932, 748, 595. UV-Vis λ$_{max}$ (nm) THF: 702, 633, 358. ^{1}H-NMR (300 MHz, DMSO-d$_6$): δ, ppm 7.68-7.72 (16H, m, 4H, Furan-H and 12H, Pc-Ar-H) 6.80-6.84 (4H, m, Furan-H), 6.64-6.68 (4H, m, Furan-H), 5.20-5.26 (8H, m, methylene -CH$_2$). Anal. Calc. for C$_{52}$H$_{32}$ClGaN$_8$O$_8$ %: C, 62.33; H, 3.22; Cl, 3.54; Ga, 6.96; N, 11.18; O, 12.77 Found: C, 62.24; H, 3.18; N, 11.36. MS (MALDI-TOF): m/z 1002.48 [M]$^+$.

Synthesis of metal-free phthalocyanine: Compound **3** was prepared and purified following the procedure described for complex **2**, starting from 0.100 g of compound **1** (0.33 mmol), 2 mL n-hexanol without metal salt. Solubility: Highly soluble in THF, CH$_2$Cl$_2$, DMF and DMSO. Yield: 0.026 g, (26%). FT-IR (u$_{max}$/cm^{-1}): 3266 (N–H), 3024 (Ar-C-H), 2946-2858 (Aliph.-C-H), 1660 (Ar-C=C), 1466, 1230 (Ar-O-R), 1142 (-C-O-C Furan), 1074 (N–H), 982, 928, 734, 556. UV-vis λ$_{max}$ (nm) THF: 701, 665, 607, 339. ^{1}H-NMR (300 MHz, DMSO-d$_6$): δ, ppm 7.15-7.95 (16H, m, 4H, Furan-H and 12H, Pc-Ar-H), 6.50-6.62 (4H, m, Furan-H), 6.35-6.45 (4H, m, Furan-H), 5.02-5.30 (8H, m, methylene -CH$_2$). Anal. Calc. for C$_{52}$H$_{34}$N$_8$O$_8$: C, 69.48; H, 3.81; N, 12.47; O, 14.24; found C, 69.52; H, 3.72; N, 12.36. MS (MALDI-TOF): *m/z* 899.90 [M+H]$^+$.

Fluorescence and singlet oxygen generation studies

$$\Phi F = \Phi F(\text{Std}) \frac{F \cdot A\text{Std} \cdot n^2}{F\text{Std} \cdot A \cdot n_{\text{Std}}^2} \qquad \textbf{(Eq.1)}$$

The fluorescence quantum yields (Φ_F) are determined in THF as compared to Equation 1 (23).

where **F** and **F$_{\text{Std}}$** are the areas under the fluorescence emission curves of the samples (**2** and **3**) and the standard, respectively. **A** and **A$_{\text{Std}}$** show the absorbance values of the excitation wave lengths of the samples and standards. n^2 and n_{Std}^2 represent the values of the refractive indices of the solvents used for the sample and the standard, respectively. Unsubstituted ZnPc ($\Phi_F = 0.23$) (24) was employed as the standard in THF.

The singlet oxygen generation study carried out under light irradiance of 100 mW cm^{-2} (AM1.5)

from a 150 W solar simulator (Newport, 96000) with 650 nm cut-on filter. The irradiation intensity was adjusted using a standard Si detector (Newport, 918D-SL-OD3).

RESULTS AND DISCUSSION

Synthesis and spectroscopic characterization

In Scheme 1, the synthetic pathway of tetrakis(2-furylmethoxy)phthalocyanines (M = Ga, **2**; 2H, **3**) at peripheral positions is depicted. Firstly, targeted peripherally substituted gallium (**2**) and metal-free (**3**) compounds were prepared using compound **1**. 2, 9(10), 16(17), 23(24)-tetrakis(2-furylmethoxy)phthalocyaninatogallium (GaPc, **2**) was synthesized by refluxing the precursor ligand and GaCl$_3$ in quinoline in the presence of DBU, when the color turned to dark green, the reaction was stopped. The crude product was washed with water / methanol series including different ratios of water and methanol to yield a precipitate.
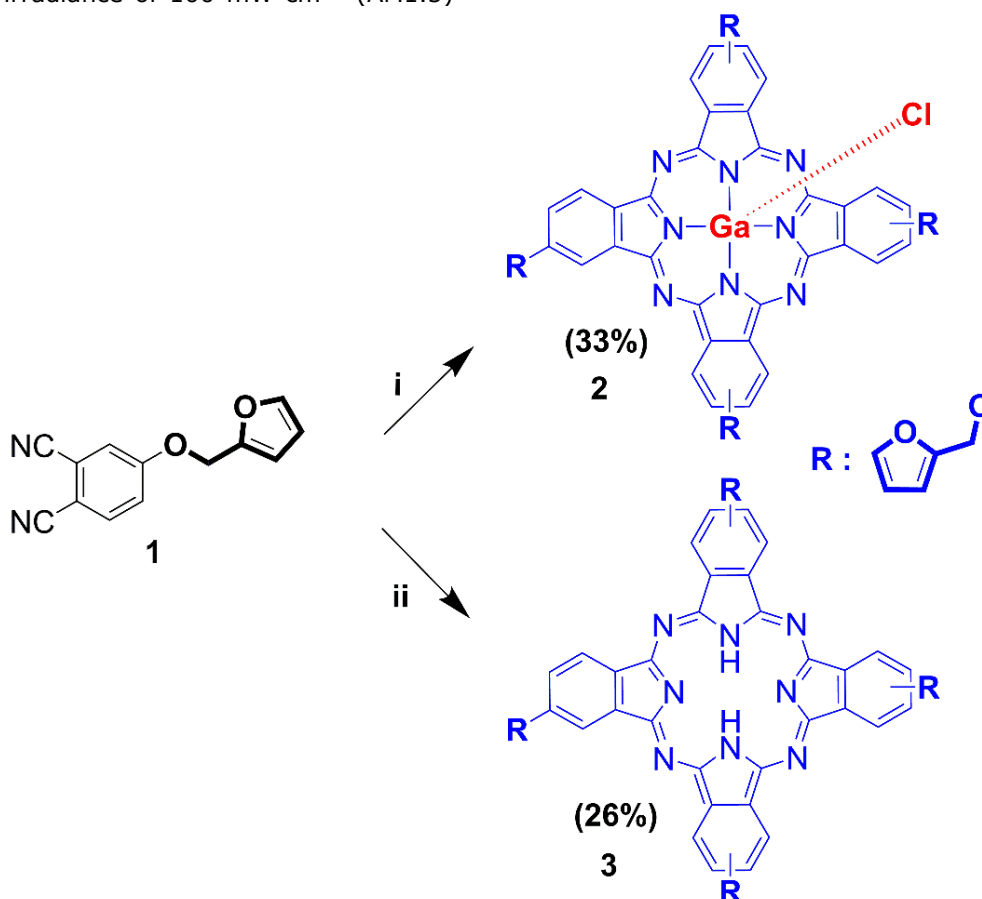
Scheme 1. The synthesis of gallium and metal-free phthalocyanines (**2** and **3**) (**i**) DBU, Quinoline, GaCl$_3$, 180 °C. (**ii**) DBU, n-hexanol, 160 °C.

Metal-free phthalocyanine compound (H$_2$Pc, **3**) was obtained by refluxing compound **1** for 8 hours in n-hexanol without using any metal salt. Secondly, 2-furylmethoxy-substituted phthalocyanines were readily purified by column chromatography. The yields of the gallium and metal-free phthalocyanines obtained were 33%

and 26%, respectively. UV-Vis, FT-IR, ^{1}H-NMR and MS methods were used to characterize compounds **2** and **3**. The structures are in harmony with the spectral data. Unlike unsubstituted phthalocyanines, the synthesized gallium and metal-free phthalocyanine complexes are quite soluble in many organic solvents.

The UV-Vis absorption spectra of deeply green colored peripherally substituted gallium and metal-free compounds in THF show two main peaks, the characteristic ligand-centered π-π* transitions of a monomeric metal-free or metallophthalocyanine derivatives **2** and **3** with

the Soret or B-band and Q-band maxima at 702, 358 nm (log ε = 4.72 and 4.55) and 701, 665 and 339 (log ε = 4.79, 4.76 and 4.72), respectively (Figure 1) (25). The Q band splits in metal-free phthalocyanine (**2**) owing to the D_2h symmetry.

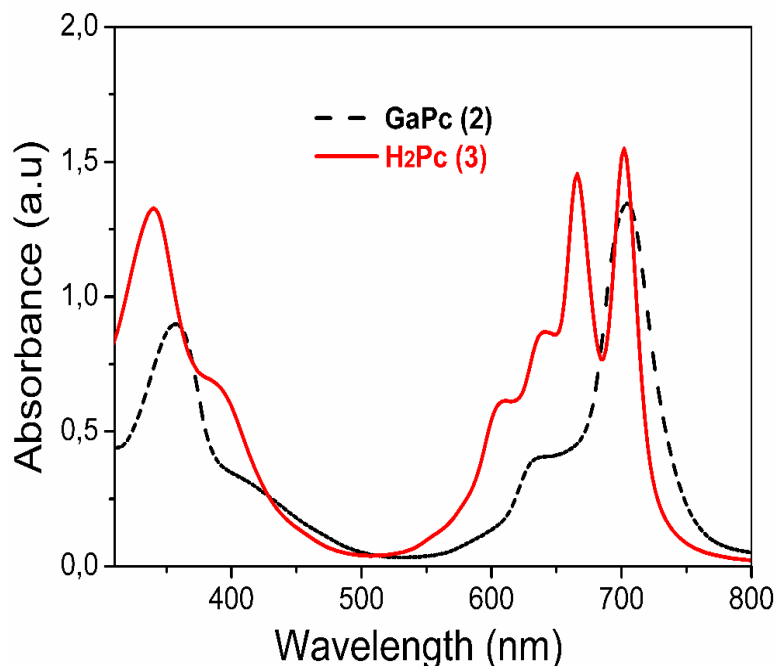**Figure 1.** Absorption spectra of **2** (GaPc) and **3** (H₂Pc) in THF (~ 2.5 x 10^{-5} mol dm^{-3}).

Gallium and metal-free phthalocyanine compounds were confirmed by FT-IR analysis. The formation of phthalocyanine complexes by cyclotetramerization of dinitrile **1** was approved by the absence of sharp (-C≡N) vibration at 2227 cm^{-1}. This sharp peak disappeared and the color changed after conversion, indicative of phthalocyanines' formation. FT-IR spectroscopy yielded that the compounds possessed stretching for etheric groups (-C-O-C, at 1274-1244 cm^{-1}), furyl groups (-C-O, at 1142-1124 cm^{-1}), aromatic groups (-C-O, at 1077-1087 cm^{-1}), and aliphatic groups (-CH, at 2965-2946 cm^{-1}). These stretching modes are all visible in the spectra and contributed to the elucidation of the structures. In addition, for metal free complex, the presence of the inner cavity –NH stretches at 1074 and 3266 cm^{-1} supported the structure of metal free phthalocyanine (**3**).

¹H-NMR investigation of the gallium and metal-free phthalocyanines provided the expected chemical shifts for the structure. In the ¹H-NMR spectrum of the phthalocyanine complexes displayed one multiplet for methylene protons at about 5.02-5.30 ppm integrating 8 protons for each complex. The signals for each 8 furan protons observed as two multiplets between 6.45-6.86 ppm for these complexes. Also signals observed for 16 protons of furan and phthalocyanines benzene as multiplets between 7.66-7.75 ppm and 7.25-8.02 ppm for complexes

2 and **3**, respectively. The ¹H-NMR spectra of gallium and metal-free phthalocyanines showed complex patterns since it is a mixture of constitutional isomers. In the ¹H-NMR spectra of **2** and **3**, broader chemical shifts were observed compared to dinitrile derivative **1**. ¹H-NMR spectra of phthalocyanines are of broad nature, because of the presence of four positional isomers which tend to show similar chemical shifts. The second reason for broad signals is that phthalocyanines show an equilibrium of aggregation and disaggregation.

The mass spectra of the complexes, which were obtained by MALDI-TOF technique, confirmed the proposed structures. Highly resolved signals of each species were successfully obtained in MALDI-TOF mass spectra using reflectron mode of the instrument to compare experimental and theoretical monoisotopic *m/z* values of metal complexes in detail. After evaluation of MALDI-TOF mass spectra, it was concluded that desired complex compounds could be successfully synthesized and purified using the experimental route explained in this study. Additionally, it was found that synthesized metal complexes were sufficiently stable under MALDI-MS conditions to determine their intact structures without significant fragmentation. The molecular ion peaks were observed at *m/z*: 1002.48 [M]⁺ for **2** (Figure 2), *m/z*: 899.89 [M+H]⁺ for **3**.
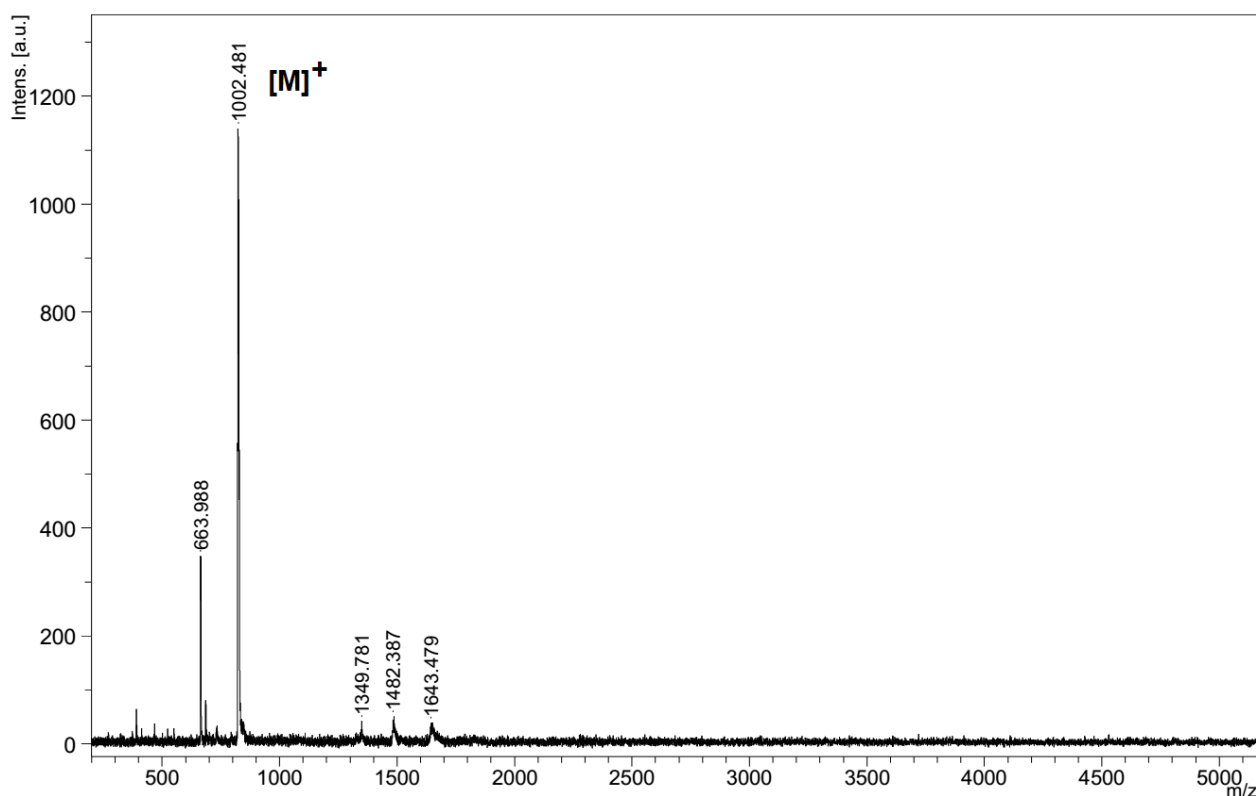
Figure 2: MALDI-TOF mass spectrum of complex **2**.

Aggregation studies

Aggregation can often be explained as the incorporation of monomers, dimers, and rings into higher-order complexes within the solvent. There are a number of parameters for aggregation in phthalocyanines; namely concentration, the nature of the solvent, substituents present at the periphery or non-periphery, the metal ion at the macrocyclic core, and the operation temperature. So as to better evaluate the solubility and aggregation properties of gallium (**2**) and metal-free (**3**) compounds, dilution studies were recorded in THF solvent. As an illustrative example, gallium complex (**2**) was studied using concentrations ranging from 2.5 µM to 40 µM (Figure 3). To demonstrate compliance with the Lambert-Beer law, a linear regression analysis was performed between the density of the Q-band and the concentration of **2**. The peripherally substituted gallium phthalocyanine are essentially free from aggregation in THF at the studied micromolar concentration. Increasing the temperature did not yield new bands on the higher energy side, which would mean the absence of aggregated species, and the absorption intensity obeys Lambert-Beer's law (see the inset of **Figure 3**) (20). Similar behavior has been observed in metal-free phthalocyanine complex.

Solvents may interact with absorbing species in the solution, which changes the absorption wavelength. This interaction depends on the polarity of the solvent, the refractive index, the coordination power, and the chemical structure of the solute. In general, the Q band wavelength of the phthalocyanine in the solvent shows red-shifting by increasing the refractive index of the solvent. This can best be explained by the Franck-Condon principle. According to this principle, the refraction index and the polarity of the solvent suggest that the species in the solvent can change the absorption wavelength. Thus, it is estimated that the Q band wavelength in a specific solvent is only related to the refractive index of the solvent, unless the solvent reacts with the species in the solution or induces any reaction (26). Non-coordinating solvents (chloroform and dichloromethane) and coordinating solvents (dimethyl sulfoxide and tetrahydrofuran) were investigated in the graph of the Q band plot versus the function $(n^2-1) / (2n^2+1)$, in which n is the refractive index of the given solvent, and the results are plotted in Figure 4.
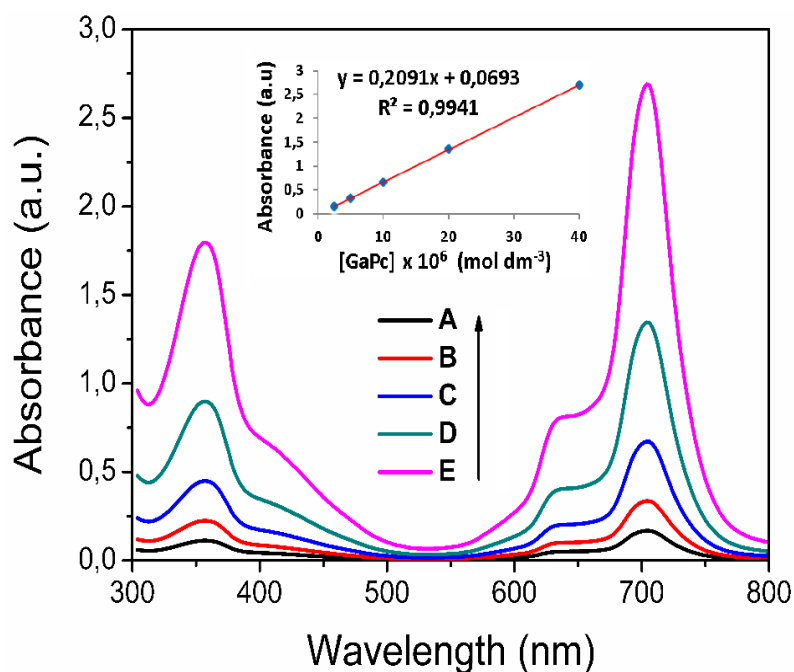
Figure 3. UV-Vis dilution studies of **2** in THF at different concentrations: (E) 40 X 10^{-6}, (D) 20 X 10^{-6}, (C) 10 X 10^{-6}, (B) 5 X 10^{-6}, (A) 2.5 X 10^{-6} mol dm^{-3}. The inset refers to the calibration values for the Q band maximum value.

It can be seen that Q-band frequencies are linearly related to this function, which explains that Q-band wavelengths are directly changed by interactions with the solution. However, oxygen-containing solvents (DMSO and THF) exhibit a similar tendency, which clearly indicates a coordination between complex **2** and these solvents.

Fluorescence studies
The first property that must be investigated in order for a photosensitizer be used in

photodynamic therapy is fluorescence behavior and fluorescence quantum yields. The fluorescence quantum yield (Φ_F) shows the efficiency of the fluorescence process. In this manner, the fluorescence emission and excitation spectra of novel peripherally tetra-substituted gallium phthalocyanine (**2**) and metal-free phthalocyanine (**3**) investigated and these complexes showed similar fluorescence behavior in THF (Figures 5 and 6).

Figure 4. Electronic absorption spectra of **2** in various solvents (15 × 10^{-6} mol dm^{-3}).

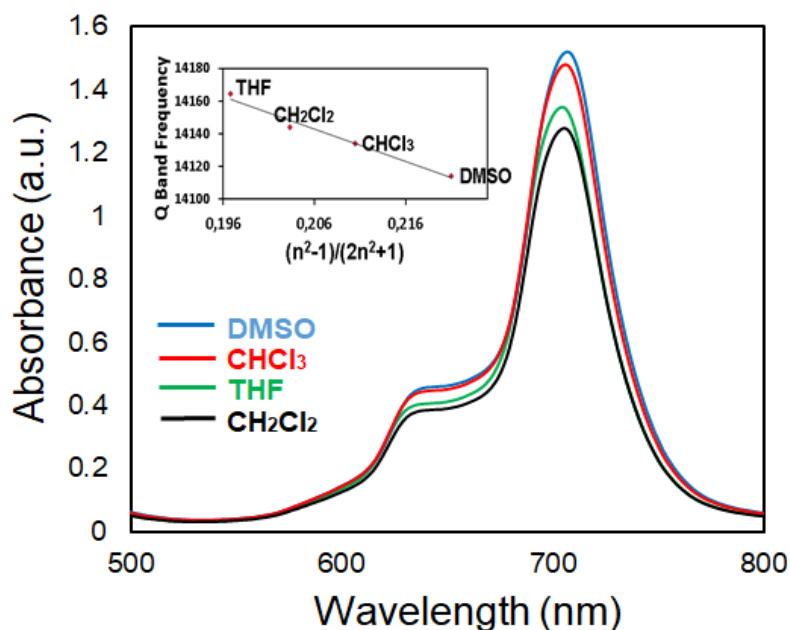**Figure 5.** Electronic absorption, fluorescence emission and excitation spectra of **2** (GaPc) in THF. (Excitation wavelength = 630 nm)

The UV-Vis absorption, emission, excitation and fluorescence quantum yield (Φ_F) of the complexes **2** and **3** are summarized in Table 1. Fluorescence emission maxima were observed at 711 nm for complex **2**, at 713 nm for compound **3** in THF. The Stokes shifts of the compounds were observed within the same region as the typical phthalocyanines. The Stokes shifts observed indicate that the structural change between the ground and excited states in phthalocyanines is very small.

Table 1. Optical and fluorescence properties of the phthalocyanine complexes in THF.

Phthalocyanine	λ_{max} (nm)[a]	(log ε)	Excitation λ_{Ex} (nm)	Emission λ_{Em} (nm)	Stokes Shift Δ_{Stokes} (nm)	Fluorescence quantum yield(Φ_F)
2(GaPc)	702	4.72	706	714	12	0.04
3(H_2Pc)	701,665	4.79,4.76	670,706	714	13	0.15
ZnPc[b]	666	5.19	666	673	7	0.23

[a] Absorption maximum wavelength (λ_{max}) in THF solution.
[b] Using unsubstituted ZnPc in THF as the reference (24).

Both photosensitizers show similar Q band absorption and Q band maxima of the excitation spectra. This suggests that the ground and excited states' nuclear configurations show a similarity and excitation in THF did not affect them.
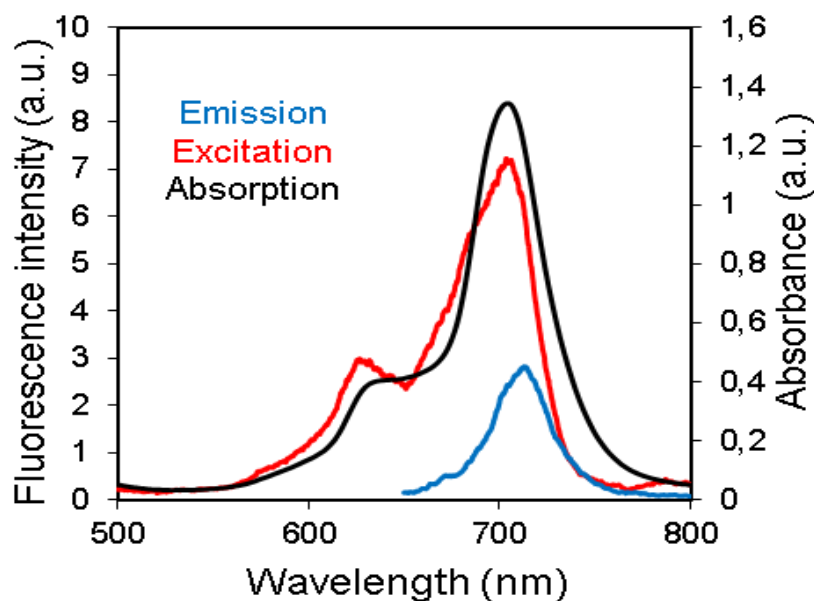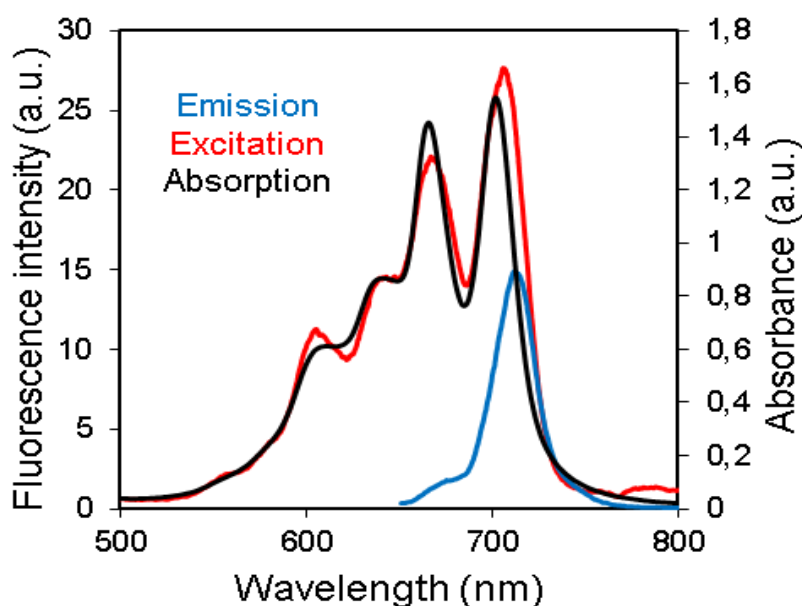
Figure 6. Electronic absorption, fluorescence emission and excitation spectra of **3** (H$_2$Pc) in THF. (Excitation wavelength = 640 nm)

Fluorescence quantum yield was determined using the comparative method. ZnPc in THF (Φ_F = 0.23) was used as the standard (24). The measured fluorescence quantum yields for **2** and **3** were lower than that for standard ZnPc. This means that the presence of peripheral 2-furylmethoxy substituents induced fluorescence quenching of the parent **2** and **3**. Fluorescence measurements showed that phthalocyanines having the same substituent; the metal-free complex showed a higher fluorescence quantum yield than gallium complex due to heavy atom effect of the gallium atom which enhances the number of triplet state species and induces quenching of fluorescence (27).

Singlet oxygen generation studies

It is presumed that by triggering the chemiluminescence reaction, the excited states of the species transferred their energy to a photosensitizer compound in the medium. The changes that occur during the quenching of the resulting excited state species can easily be monitored by spectroscopic methods. Diphenylisobenzofuran (DPBF) is known to be a singlet oxygen quencher with chemical addition reaction by forming endoperoxide species with singlet oxygen in the solution medium.
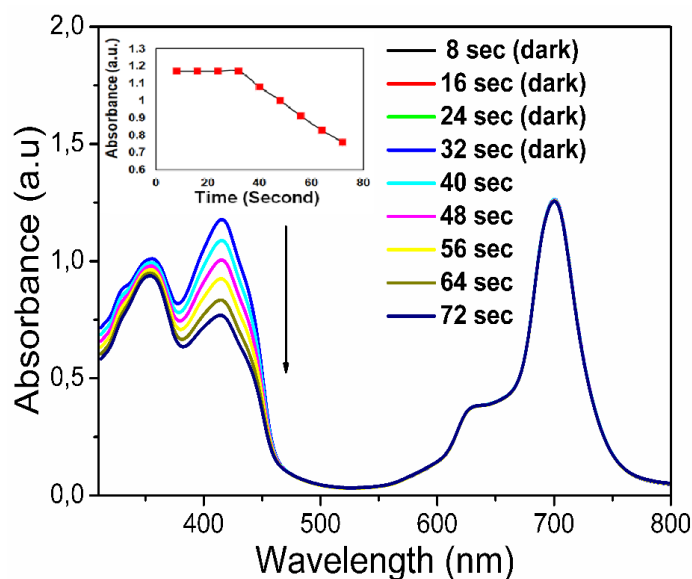

Figure 7. Reaction of singlet oxygen formed by gallium phthalocyanine complex (**2**) dissolved in DMSO with 1,3-diphenylisobenzofuran (DPBF). For the first 32 sec, the solution was kept in the dark; thereafter, it was irradiated with a light source (650 nm cut on filter) for 40 sec. The total volume of the solution was set to 3 mL. The absorption spectra were recorded every 8 seconds.

In order to demonstrate that the peripherally substituted gallium and metal-free phthalocyanines are satisfactory as effective photosensitizers, the phthalocyanine solutions were prepared in DMSO containing DPBF. Experiments have been performed by removing other potential sources of media that may affect the absorption decline. It was observed that there was no significant changing in the absorption spectrum when kept in the dark for 32 seconds (Figure 7). On irradiation with a red light (with 650 nm glass cut on filter, flow rate 16 mW/cm^2), however, the absorption peak owing to the trapping compound DPBF swiftly disappeared within 40 seconds.

CONCLUSION

In summary, synthesis, characterization, and investigation of the optical, fluorescence and singlet oxygen generation properties of furan-2-ylmethoxy-substituted gallium and metal-free phthalocyanine complexes have been reported. Not only the gallium phthalocyanine but also the metal-free phthalocyanine are essentially free from aggregation in THF at the studied micromolar concentration which makes important for PDT (photodynamic therapy) applications. The fluorescence quantum yields (Φ_F) of the phthalocyanine photosensitizers investigated for photophysical properties were determined and compared with an unsubstituted ZnPc. In THF, the fluorescence quantum yields (Φ_F) for photosensitizers (**2** and **3**) were found to be lower than unsubstituted ZnPc. This suggests that the existence of peripheral 2-furylmethoxy substituents induced some fluorescence quenching of the parent (**2** and **3**). Singlet oxygen generation studies showed that the phthalocyanine complexes containing the furan-2-ylmethoxy group indicated a high level of photosensitization and singlet oxygen generation capacity. As a consequence, these gallium and metal-free phthalocyanines are favorable photosensitizers for photodynamic cancer therapy applications.

REFERENCES

1. Barr JB, Wallon SB. The chemistry of furfuryl alcohol resins. J Appl Polym Sci. 1971 May;15(5):1079–90.

2. Ulbrich K, Kreitmeier P, Reiser O. Microwave- or microreactor-assisted conversion of furfuryl alcohols into 4-hydroxy-2-cyclopentenones. Synlett. 2010 Aug 28;2010(13):2037–40.

3. Çimen Y, Ermiş E, Dumludağ F, Özkaya AR, Salih B, Bekaroğlu Ö. Synthesis, characterization, electrochemistry and VOC sensing properties of novel ball-type dinuclear metallophthalocyanines. Sensors Actuators, B Chem. 2014;202:1137–47.

4. Jiang Y, Lu Y, Lv X, Han D, Zhang Q, Niu L, et al. Enhanced Catalytic Performance of Pt-Free Iron Phthalocyanine by Graphene Support for Efficient Oxygen Reduction Reaction. ACS Catal. 2013 Jun;3(6):1263–71.

5. Karaca H, Şişman İ, Güzel E, Sezer S, Selimoğlu F, Ergezen B, et al. Thiochalcone substituted phthalocyanines for dye-sensitized solar cells: Relation of optical and electrochemical properties for cell performance. Journal of Coordination Chemistry [Internet]. 2018; Available from: 10.1080/00958972.2018.1468027

6. Arıcan D, Erdoğmuş A, Koca A. Electrochromism of the Langmuir-Blodgett films based on monophthalocyanines carrying redox active metal centers. Thin Solid Films. 2014 Jan;550:669–76.

7. Shilpa Harish T, Viswanath P. Annealing assisted structural and surface morphological changes in Langmuir-Blodgett films of nickel octabutoxy phthalocyanine. Thin Solid Films. 2016 Jan;598:170–6.

8. Basova T V., Parkhomenko RG, Polyakov M, Gürek AG, Atilla D, Yuksel F, et al. Effect of dispersion of gold nanoparticles on the properties and alignment of liquid crystalline copper phthalocyanine films. Dye Pigment. 2016;125:266–73.

9. Güzel E, Yaşa Atmaca G, Erdoğmuş A, Koçak MB. Novel sulfonated hydrophilic indium(III) and gallium(III) phthalocyanine photosensitizers: preparation and investigation of photophysicochemical properties. J Coord Chem. 2017 Aug 3;70(15):2659–70.

10. Güzel E, Atsay A, Nalbantoglu S, Şaki N, Dogan AL, Gül A, et al. Synthesis, characterization and photodynamic activity of a new amphiphilic zinc phthalocyanine. Dye Pigment. 2013;97(1):238–43.

11. Detty MR, Gibson SL, Wagner SJ. Current clinical and preclinical photosensitizers for use in photodynamic therapy. J Med Chem. 2004 Jul;47(16):3897–915.

12. Robertson CA, Evans DH, Abrahamse H. Photodynamic therapy (PDT): A short review on cellular mechanisms and cancer research applications for PDT. J Photochem Photobiol B Biol. 2009 Jul 17;96(1):1–8.

13. Özçeşmeci I, Burat AK, Bayir ZA. Synthesis and photophysical properties of novel unsymmetrical metal-free and metallophthalocyanines. J Organomet Chem. 2014;750:125–31.

14. Sevim AM, Arıkan S, Özçeşmeci İ, Gül A. Photophysical properties of anthracenylmethyloxycarbonylmethylsulfanyl-phthalocyanines. Synth Met. 2013;183:1–7.

15. Yilmaz I, Gürek A, Ahsen V. Synthesis, electrochemical, and spectroelectrochemical properties of tetrakis(13,17-dioxa nonacosane-15-sulphanyl) phthalocyaninato zinc(II). Polyhedron. 2005;24(7):791–8.

16. Güzel E, Çetin Ş, Günsel A, Bilgiçli AT, Şişman İ, Yarasir MN. Comparative studies of photophysical and electrochemical properties of sulfur-containing substituted metal-free and metallophthalocyanines. Res Chem Intermed. 2018;44(2):971–89.

17. Akkurt B, Hamuryudan E. Enhancement of solubility via esterification: Synthesis and characterization of octakis (ester)-substituted phthalocyanines. Dye Pigment. 2008 Nov;79(2):153–8.

18. Özçeşmeci İ, Özçeşmeci M, Gül A, Hamuryudan E. Synthesis and spectroscopic investigation of boronic esters of metal-free fluorinated and non-fluorinated phthalocyanines. Synth Met. 2016 Dec 1;222:344–50.

19. Yaşa G, Erdoğmuş A, Uğur AL, Şener MK, Avcıata U, Nyokong T. Photophysical and photochemical properties of novel phthalocyanines bearing non-peripherally substituted mercaptoquinoline moiety. J Porphyr Phthalocyanines. 2012 Jul;16(07n08):845–54.

20. Güzel E, Koca A, Koçak MB. Anionic water-soluble sulfonated phthalocyanines: microwave-assisted synthesis, aggregation behaviours, electrochemical and in-situ spectroelectrochemical characterisation. Supramol Chem. 2017 Jul 3;29(7):536–46.

21. Güzel E, Güney S, Kandaz M. One pot reaction and three type products; 1(4),8(11)-15(18),22(25) adjacent azine attached as macrocyclically mono, bunk-type (dimer) and polymeric metallo phthalocyanines; Synthesis, spectroscopy, and electrochemistry. Dye Pigment. 2015;113:416–25.

22. Tuncer H, Görgülü AO, Hökelek T. 4-(Furan-2-ylmethoxy)benzene-1,2-dicarbonitrile. Acta Crystallogr Sect E Struct Reports Online. 2012;68(1):o153–o153.

23. Maree MD, Nyokong T, Suhling K, Phillips D. Effects of axial ligands on the photophysical properties of silicon octaphenoxyphthalocyanine. J Porphyr Phthalocyanines. 2002 Jun 9;06(06):373–6.

24. Saka ET, Durmuş M, Kantekin H. Solvent and central metal effects on the photophysical and photochemical properties of 4-benzyloxybenzoxy substituted phthalocyanines. J Organomet Chem. 2011;696(4):913–24.

25. Güzel E, Koca A, Gül A, Koçak MB. Microwave-assisted synthesis, electrochemistry and spectroelectrochemistry of amphiphilic phthalocyanines. Synth Met. 2015;199:372–80.

26. Bayliss NS. The Effect of the Electrostatic Polarization of the Solvent on Electronic Absorption Spectra in Solution. J Chem Phys. 1950;18(3):292.

27. Gürel E, Pişkin M, Altun S, Odabaş Z, Durmuş M. Synthesis, characterization and investigation of the photophysical and photochemical properties of highly soluble novel metal-free, zinc (ii), and indium (iii) phthalocyanines substituted with 2,3,6-trimethylphenoxy moieties. Dalt Trans. 2015 Mar 17;44(13):6202–11.

RESEARCH ARTICLE

A Novel One-Pot Green Synthesis and Characterization of 5-Substituted Bis-Iminothiazolidinones

Fatma Tülay Tuğcu[1]* ✉ iD

[1] Yildiz Technical University, Faculty of Arts and Sciences, Department of Chemistry, (34220), İstanbul, Turkey.

Abstract: In this study, some new 5-substituted bis-iminothiazolidinone derivatives have been synthesized via one-pot green synthesis. The study comprises two steps. In the first step, bis-thioureas were prepared by the reaction of aryl isothiocyanates with substituted amines. In the second step, substituted bis-thioureas prepared beforehand and chloroacetic acid were condensed with substituted thiophene-2-carboxaldehydes and new 5-substituted bis-iminothiazolidinone compounds were obtained. The structures of all these synthesized compounds were determined and characterized by infrared, nuclear magnetic resonance and mass spectral data.

INTRODUCTION

One-pot method without catalyst and solvent saves both time and energy since many intermediate products and final products do not need to be purified (1-2). Also, due to the growing concern for the influence of organic solvents on the environment as well as on the human body, development of solvent-free organic reactions have attracted the attention of synthetic organic chemists. These types of reactions are simple to handle, reduce pollution and comparatively cheaper to operate. For these reasons, solventless reaction complies with the fifth principle of green chemistry. It is believed that solvent-free synthesis is industrially useful and largely green. Green chemistry, also called sustainable chemistry, are processes that reduce or eliminate the use and generation of hazardous substances. From this point of view, one-pot solvent-free reactions are regarded as an ideal method of green synthesis (3).

Iminothiazolidinones have attracted much interest over the years since they are important and versatile scaffolds having engaged a pronounced position in medicinal chemistry. They are well-known to possess an extensive spectrum of biological activities (4-10). There are many existing methods for the synthesis of 5-substituted iminothiazolidinones, but they are generally synthesized in two steps (11-15). In the first step, iminothiazolidinones are formed by the reaction of thioureas or N-substituted thioureas with α-chloroacetic acid or their acid esters or amides. In the second step, these compounds are reacted with aromatic aldehydes in basic medium to give 5-substituted iminothiazolidinone compounds. For example, Ottana et al. (12) synthesized the 2-imino-4-thiazolidinone compound as a result of the reaction of N-propyl-N'-phenylthiourea compound prepared from phenylisothiocyanate and propylamine with chloroacetyl chloride in triethylamine medium; this compound was then condensed with aromatic aldehydes in piperidine-containing medium to give 5-arylidene-2-imino-4-thiazolidinones.

There are few articles in the literature for bis-iminotiyazolidinone (16) despite the many publications on the synthesis of 5-substituted iminotiazolidinone compounds. Therefore, in this article, reports the synthesis of new 5-substituted bis-iminothiazolidinone derivatives by the one-

pot solvent free green reaction from the corresponding substituted thiophene-2-carbaldehyde with bis-thiourea and chloroacetic acid at 70 °C. This article is consistent with the green chemistry approach because it describes a reaction which take place at low temperature and does not use solvents and catalysts, making it environmentally friendly, efficient and economic.

MATERIALS AND METHODS

Reagents purchased from Merck were as follows: dichloromethane, chloroform, ethyl acetate, n-hexane, chloroacetic acid, thiophene-2-carboxaldehyde, 3-methylthiophene-2-carboxaldehyde, phenyl isothiocyanate, p-tolyl isothiocyanate, 1,4-phenylenediamine, 4,4'-methylenedianiline, silica gel 60 (0.063-0.200 mm), and sea sand. All reagents were used as purchased from the manufacturer. Dichloromethane, chloroform, and n-hexane were used after purification for column chromatography. TLC was carried out on aluminum sheets pre-coated with silica gel 60 F254 purchased from Merck, and the spots were

visualized with UV light (254/366 nm) using a Camag UV lamp.

NMR (^{1}H and ^{13}C) spectra were saved on a Bruker 500 MHz NMR spectrometer at Yildiz Technical University and Erzurum Atatürk University, Department of Chemistry. CDCl$_3$ was used as a solvent. FTIR spectra were recorded on a Philips PU 9714 ATR spectrometer using a Perkin-Elmer Spectrum One program at Yildiz Technical University, Instrumental Analysis Laboratory. Melting points were obtained with a Gallenkamp Melting Point Apparatus in open capillaries with no correction.

Preparation of Bis-thiourea Derivatives (1a-d)
A mixture of the appropriate diamine (1 mmol) and substituted phenyl isothiocyanate (2.4 mmol) was stirred in CH$_2$Cl$_2$ at room temperature for 24 hours. The crude product was concentrated under vacuum and recrystallized from ethanol. General synthesis of bis-thioureas is summarized in Figure 1.
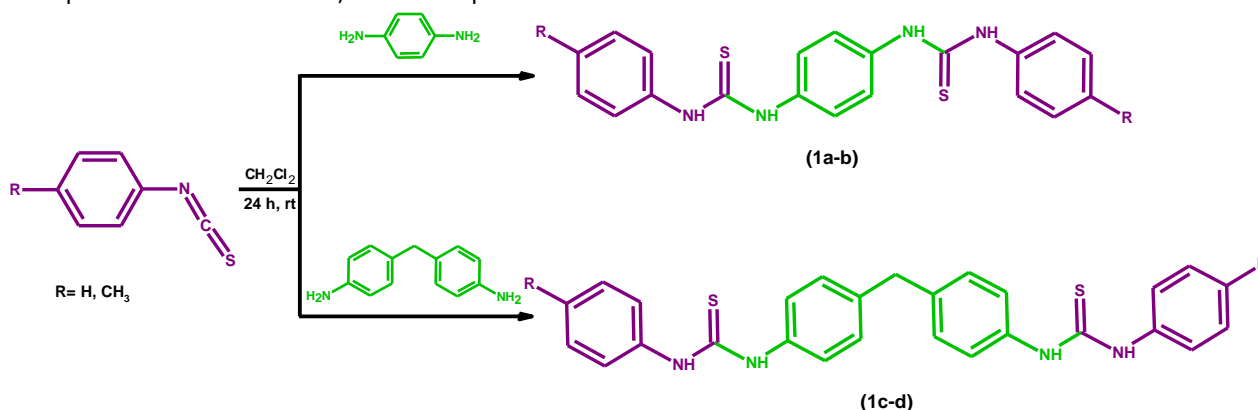
Figure 1. Synthesis of bis-thiourea derivatives.

Preparation of 5-Substituted Bis-Iminothiazolidinone Derivatives (2a-h)
To synthesize 5-substituted bis-iminothiazolidinone compounds, the appropriate bis-thiourea (1 mmol), chloroacetic acid (2.4 mmol) and substituted thiophene-2-carbaldehyde

(2 mmol) were stirred at room temperature for 4 hours and then heated at 70 ^{0}C for 6 hours. The product was purified by column chromatography. General synthesis of these compounds is summarized in Figure 2.

Figure 2. Synthesis of 5-substituted bis-iminothiazolidinone derivatives.

RESULTS AND DISCUSSION

The synthesis of bis-thiourea (**1a-d**) was done using diamine and substituted phenyl isothiocyanate in CH_2Cl_2 at room temperature.

They were recrystallized from hot ethanol and were characterized by recording their spectral data (Table 1). A mechanism for the reaction of bis-thiourea is shown in Figure 3 (17).

Figure 3. Proposed mechanism for the formation of bis-thiourea derivatives.

When the FTIR spectrum of bis-thioureas (**1a-d**) were analyzed, the conjugated C=C and C-N vibrations were observed in the ranges of 1600-1550 and 1540-1490 cm^{-1}, respectively. On the other hand, the N-H vibrations (3467-3438 and 3315-3360 cm^{-1}) of diamine used as reagents and the N=C=S stretching bands (2200-2000 cm^{-1}) of substituted isothiocyanate disappeared, which indicates that condensation had taken place.
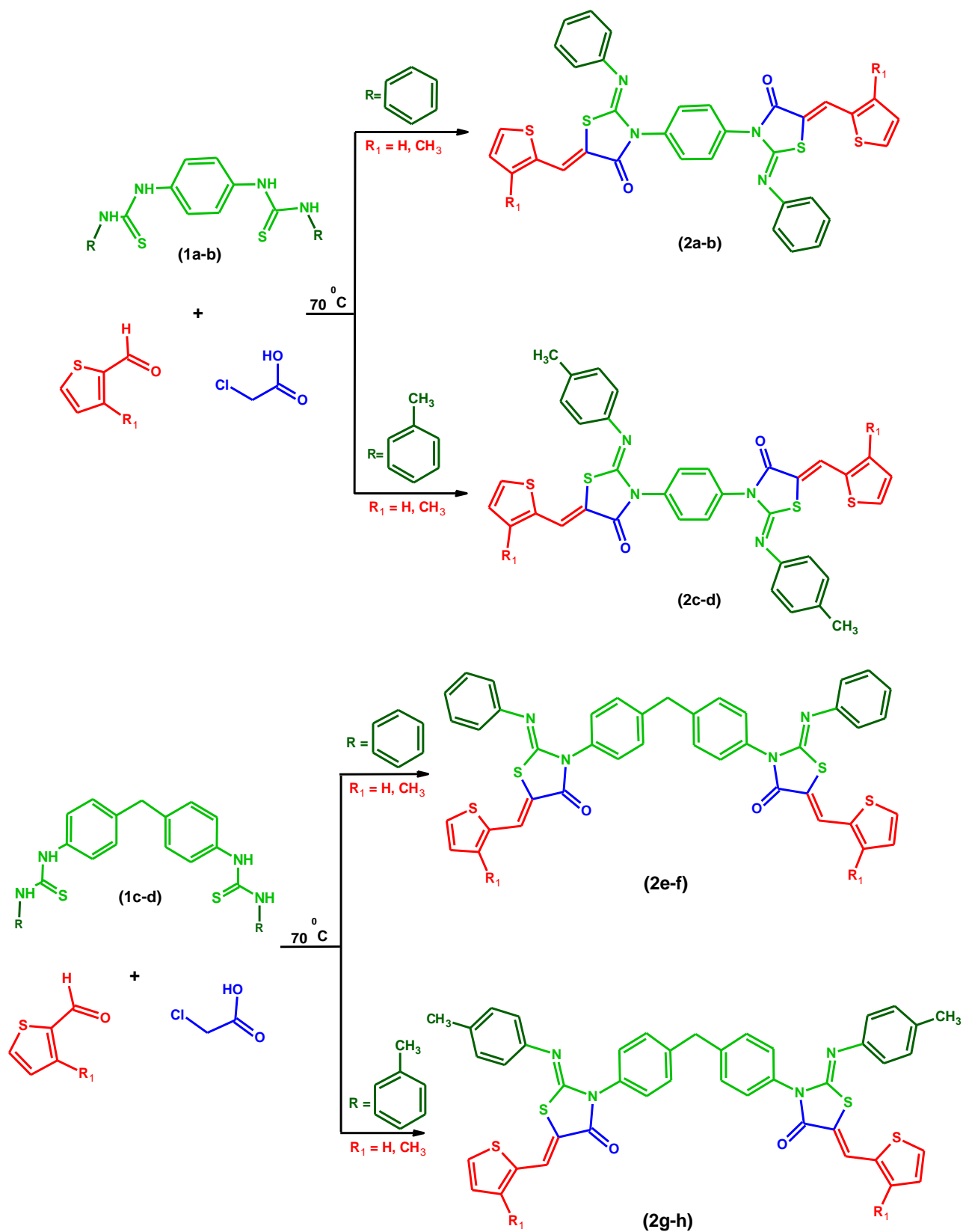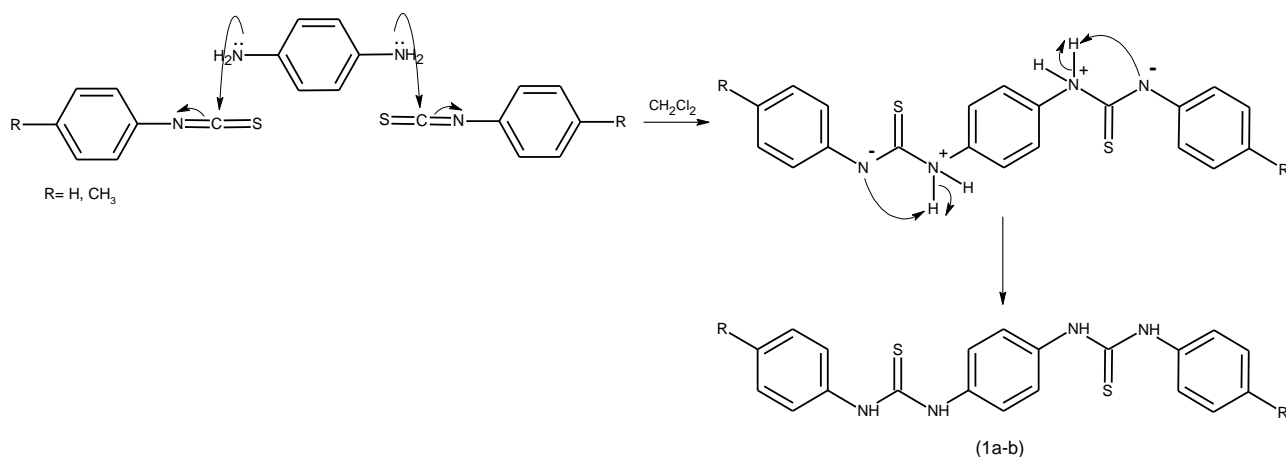
Eight new 5-substituted bis-iminothiazolidinone derivatives (**2a–h**) were obtained from the second step of the present study. The synthesized crude products were obtained in varying yield depending on the structure and were purified by column chromatography. For the one-pot condensation method between bis-thiourea, thiophene-2-carboxaldehyde and chloroacetic acid, an estimated mechanism for the formation of 5-substituted bis-iminothiazolidinone was proposed by referring to the literature in Figure 4 (18-19). The structures of all synthesized compounds (**2a–h**) were explained based on the analysis of their spectroscopic data (Table 1).

When the infrared spectra of 5-substituted bis-iminothiazolidinones were analyzed, the conjugated C=C and C=N stretching vibrations that were distinctive for nitrogen having heterocyclic compounds are observed in the ranges of 1600-1500 and 1670-1600 cm^{-1},

respectively. Moreover, the N-H vibrations (3295-3190 cm^{-1}) of bis-thiourea, the C=O stretching ($\sim$1674 cm^{-1}) of heteroaromatic aldehyde and the -OH vibration bands (3400-2800 cm^{-1}) of chloroacetic acid disappeared, which indicates that cyclization and condensation reactions occurred. The characteristic absorption bands of C=O groups were observed at 1680-1722 cm^{-1} in the FTIR spectrum of the 5-substituted bis-iminothiazolidinone derivatives.

In the second step of clarifying the structures, when the ^{1}H NMR spectra of the initial substances and those of the products were compared, the singlet pertaining to the –CHO group observed at around 11.0 ppm in the spectra of substituted thiophene-2-carboxaldehydes and the singlet at around 9.8 and 9.3 ppm belonging to the –NHgroup in bis-thiourea were not encountered in ^{1}H NMR of the 5-substituted bis-iminothiazolidinone **(2a-h)**, which is an evidence of the suggested structures. The multiple peaks seen between 6.8-7.7 ppm in the lower area of the spectra show the proton resonances of aromatic and the hetero aromatic bond. The H-atoms of –CH$_2$ and –CH$_3$ which belong to the compounds were observed in the ranges 4.03 ppm and 2.41-2.35 ppm respectively.
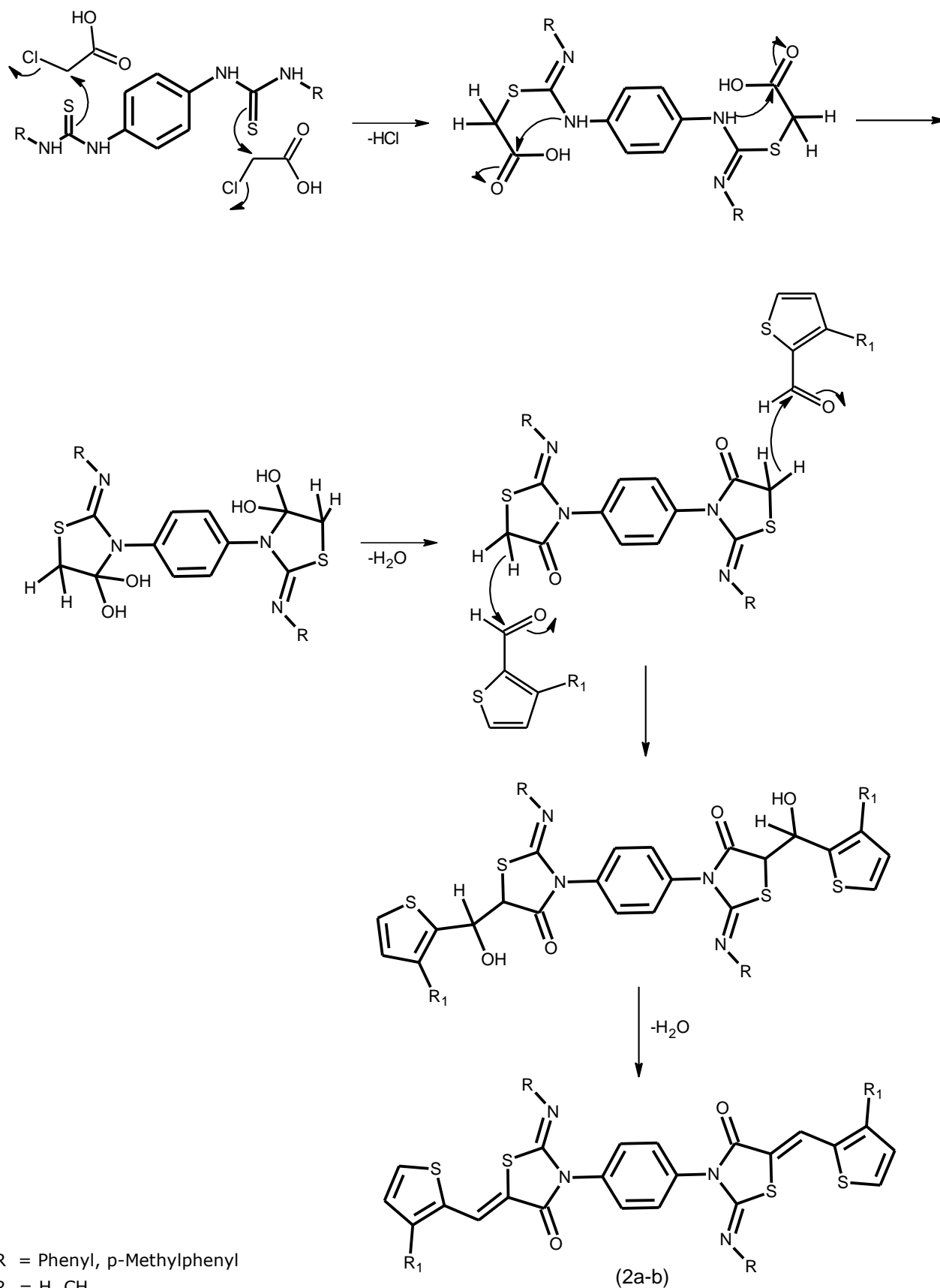
R = Phenyl, p-Methylphenyl

R_1 = H, CH_3

Figure 4. Proposed mechanism for the synthesis of 5-substituted bis-iminothiazolidinones.

Mass spectra of the products were obtained in order to give certainty to the determined structure. When the mass spectra of compounds (**2a-h**) were examined, the observed molecular ion peaks confirmed the molecular weights of the products (Table 1).

1

Table 1. Physical, chemical, and spectral properties of all synthesized compounds.

Compound	Crystal structure	M.p (^{0}C)	FTIR (ATR) ($\gamma_{max/cm}^{-1}$)	^{1}H NMR (500MHz, d-DMSO) ((δ ppm)	MS (m/z)
1,1'-(1,4-Phenylene)bis(3-phenylthiourea) **(1a)** (20)	White bar	205-6	3221 (N-H), 2922 (C-H), 1506 (N-H), 1072 (C-S), 746 (N-H)	7.13 (1H, t), 7.34 (2H, t), 7.44 (2H, s), 7.49 (2H, d), 9.80 (2H, s)	
1,1'-(1,4-Phenylene)bis(3-p-tolylthiourea) **(1b)** (21)	White powder	230-2	3295 (N-H), 2939 (C-H), 1509 (N-H), 1141 (C-S), 810 (N-H)	2.26 (6H, s), 6.52 (2H, d), 6.99 (2H, d), 7.10 (2H, d), 7.30 (2H, d), 9.31 (2H, s)	
1,1'-[4,4'-Methylenebis(1,4-phenylene)]bis(3-phenylthiourea) **(1c)** (22)	White bar	320-2	3190 (N-H), 2939 (C-H), 1509 (N-H), 1233 (C-S), 877 (N-H)	3.89 (2H, s), 7.12 (1H, t), 7.21 (2H, d), 7.32 (2H, t), 7.38 (2H, d), 7.47 (2H, d), 9.31 (2H, s)	
1,1'-[4,4'-Methylenebis(1,4-phenylene)]bis(3-p-tolylthiourea) **(1d)**	White powder	230-1	3195 (N-H), 2920 (C-H), 1586 (N-H), 1141 (C-S), 820 (N-H)	2.51(6H, s), 3.89 (2H, s), 7.21 (4H, t), 7.47 (4H, d), 9.31 (2H, s)	
3,3'-(1,4-Phenylene)bis[2-(phenylimino)-5-(thiophen-2-ylmethylene) thiazolidin-4-one] **(2a)**	Light yellow powder	161-2	3015 (=C-H), 1706 (C=O), 1626 (C=N), 1590 (C=C), 1352 (C-N), 827 (C-S)	6.57 (2H, d, J=7.0 Hz, Ar-H), 6.70 (2H, d, J=7.4 Hz, Ar-H), 7.10 (2H, d, J=7.0 Hz, Ar-H), 7.18 (1H, t, J=7.4 Hz, Ar-H), 7.28 (1H, t, J=4.9 Hz, Ar-H), 7.40 (2H, t, J=8.1 Hz, Ar-H), 7.65 (1H, d, J=3.7 Hz, Ar-H), 7.90 (1H, d, J=5.1 Hz, Ar H), 8.05 (1H, s, vinyl H)	647 (M+1), 646 (M$^+$), 645 (M-1), 563, 479, 443, 361, 329

3,3'-(1,4-Phenylene)bis{5-[(3-methylthiophen-2-yl)methylene]-2-(phenylimino)thiazolidin-4-one} **(2b)**	Light yellow layer	181-2	3082 (=C-H), 2917 (CH$_3$), 1704 (C=O), 1624 (C=N), 1595 (C=C), 1352 (C-N), 823 (C-S)	2.37 (3H, s, CH$_3$), 6.81 (2H, d, J=8.1 Hz, Ar-H), 7.20 (2H, d, J=8.1 Hz, Ar-H), 7.29 (1H, t, J=5.0 Hz, Ar-H), 7.38 (2H, d, J=8.4 Hz, Ar-H), 7.41 (2H, d, J=8.3 Hz, Ar-H), 7.64 (1H, d, J=3.5 Hz, Ar-H), 7.92 (1H, d, J=5.1 Hz, Ar-H), 8.05 (1H, s, vinyl H)	675 (M+1), 674 (M$^+$), 673 (M-1), 592, 508, 361, 329.
3,3'-(1,4-Phenylene)bis[5-(thiophen-2-ylmethylene)-2-(p-tolylimino)thiazolidin-4-one] **(2c)**	Light yellow bar	173-4	3082 (=C-H), 2917 (CH$_3$), 1704 (C=O), 1622 (C=N), 1585 (C=C), 1361 (C-N), 827 (C-S)	2.38 (3H, s, CH$_3$), 6.60 (2H, d, J=7.0 Hz, Ar-H), 6.95 (2H, bd, J=7.2 Hz, Ar-H), 7.09 (2H, d, J=7.0 Hz, Ar-H), 7.12 (1H, d, J=5.1 Hz, Ar-H), 7.18 (1H, t, J=7.4 Hz, Ar-H), 7.39 (2H, t, J=8.2 Hz, Ar-H), 7.82 (1H, d, J=5.1 Hz, Ar-H), 7.88 (1H, s, vinyl H)	675 (M+1), 674 (M$^+$), 673 (M-1), 576, 480, 361, 329
3,3'-(1,4-Phenylene)bis{5-[(3-methylthiophen-2-yl)methylene]-2-(p-tolylimino)thiazolidin-4-one} **(2d)**	Light yellow bar	186-7	3140 (=C-H), 2926 (C-H), 1722 (C=O), 1601 (C=N), 1502 (C=C), 1359 (C-N), 823 (C-S)	2.40 (3H, s, CH$_3$), 2.49 (3H, s, CH$_3$), 6.90 (2H, d, J=8.2 Hz, Ar-H), 7.13 (1H, d, J=4.9 Hz, Ar-H), 7.20 (2H, d, J=8.2 Hz, Ar-H), 7.35 (2H, d, J=8.6 Hz, Ar-H), 7.42 (2H, d, J=8.6 Hz, Ar-H), 7.86 (1H, d, J=4.9 Hz, Ar-H), 7.93 (1H, s, vinyl H)	704 (M+1), 703 (M$^+$), 702 (M-1), 605, 508, 402, 361, 329
3,3'-[4,4'-Methylene bis(4,1-phenylene)]bis[2-(phenylimino)-5-(thiophen-2-ylmethylene)thiazolidin-4-one] **(2e)**	Light yellow powder	205-6	3140 (=C-H), 2926 (C-H), 1682 (C=O), 1636 (C=N), 1591 (C=C), 1270 (C-N), 717 (C-S)	4.03 (2H, s, CH$_2$), 6.94 (2H, d, J=8.2 Hz, Ar-H), 6.99-7.17 (3H, m, Ar-H), 7.21 (2H, t, J=8.2 Hz, Ar-H), 7.29 (2H, m, Ar-H), 7.37-7.58 (3H, m, Ar-H), 8.00 (1H, s, vinyl H)	738 (M+1), 737 (M$^+$), 736 (M-1), 643, 569, 375, 314, 242

3,3'-[4,4'-Methylenebis(4,1-phenylene)]bis{5-[(3-methylthiophen-2-yl)methylene]-2-(phenylimino)thiazolidin-4-one} **(2f)**	Yellow powder	198-9	3060 (=C-H), 2924 (C-H), 1687 (C=O), 1670 (C=N), 1592 (C=C), 1362 (C-N), 840 (C-S)	2.43 (3H, s, CH₃), 3.97 (2H, s, CH₂), 6.92 (2H, d, *J*=8.2 Hz, Ar-H), 6.99 (1H, d, *J*=5.0 Hz, Ar-H), 7.13 (2H, d, *J*=8.2 Hz, Ar-H), 7.46 (2H, dd, *J*=8.6;1,7 Hz, Ar-H), 7.50 (1H, d, *J*=5.0 Hz, Ar-H), 7.54(3H, t, *J*=7.9;7.4 Hz, Ar-H), 8.06 (1H, s, vinyl H)	766 (M+1), 765 (M⁺), 764 (M-1), 569, 389, 314, 242
3,3'-[4,4'-Methylenebis(4,1-phenylene)]bis[5-(thiophen-2-ylmethylene)-2-(p-tolylimino)thiazolidin-4-one] **(2g)**	Light yellow powder	214-5	3024 (=C-H), 2910 C-H), 1712 (C=O), 1630 (C=N), 1596 (C=C), 1352 (C-N), 819 (C-S)	2.41 (3H, s, CH₃), 4.04 (1H, s, CH₂), 6.88 (2H, brd, *J*=8.2 Hz, Ar-H), 6.93 (1H, dd, *J*=4.9;4.7 Hz, Ar-H), 7.14 (1H, d, *J*=4.9 Hz, Ar-H), 7.18 (2H, brd, *J*=8.4, Ar-H), 7.21 (2H, brd, *J*=8.2, Ar-H), 7.40 (2H, brd, *J*=8.4, Ar-H), 7.53 (1H, d, *J*=4.5, Ar-H), 8.00 (1H, s, vinyl H)	766 (M+1), 765 (M⁺), 764 (M-1), 569, 389, 314, 242
3,3'-[4,4'-Methylenebis(4,1-phenylene)]bis{5-[(3-methylthiophen-2-yl)methylene]-2-(p-tolylimino)thiazolidin-4-one} **(2h)**	Yellow powder	207-8	3027 (=C-H), 2918 (C-H), 1712 (C=O), 1630 (C=N), 1596 (C=C), 1352 (C-N), 819 (C-S)	2.35 (3H, s, CH₃), 2.41 (3H, s, CH₃), 4.03 (1H, s, CH₂), 6.88 (2H, brd, *J*=8.2 Hz, Ar-H), 6.94 (1H, dd, *J*=8.5 Hz, Ar-H), 7.13 (1H, d, *J*=5.0 Hz, Ar-H), 7.19 (2H, brd, *J*=8.2, Ar-H), 7.39 (2H, brd, *J*=8.4, Ar-H), 7.46 (1H, d, *J*=4.5, Ar-H), 8.01 (1H, s, vinyl H)	794 (M+1), 793 (M⁺), 792 (M-1), 597, 389, 314, 242

1

CONCLUSION

In conclusion, this study reports an appropriate and reliable synthesis of 5-substituted bis-iminothiazolidinones **(2a-h)** starting from previously prepared bis-thioureas **(1a-d)**, chloroacetic acid and substituted thiophene-2-carbaldehyde via one-pot green synthesis.

ACKNOWLEDGEMENTS

REFERENCES

1. Marvaniya HM, Modi KN, Sen DJ. Greener reactıons under solvent free condıtıons. International Journal of Drug Development and Research. 2011;3(2):34–44.

2. Sarkar A, Santra S, Kundu SK, Hajra A, Zyryanov GV, Chupakhin ON, Charushin VN, Majee A. A decade update on solvent and catalyst-free neat organic reactions: A step forward towards sustainability. Green Chemistry. 2016;18:4475–4525.

3. Wender PA, Handy ST, Wright DL. Towards the ideal synthesis. Chemistry and Industry. 1997;19:765–768.

4. Verma A, Saraf SK. 4-Thiazolidinone – A biologically active scaffold. European Journal of Medicinal Chemistry. 2008;43(5):897–905.

5　Edwards PJ. Thiazolidinone derivatives targeting drug - resistant lung cancer cells. Drug Discovery Today. 2008;13(23/24):1107–1108.

6. Gududuru V, Hurh E, Dalton JT, Miller DD. Synthesis and antiproliferative activity of 2-aryl-4-oxo-thiazolidin-3-yl-amides for prostate cancer. Bioorganic and Medicinal Chemistry Letter. 2004;14: 5289-5293.

7. Liu HL, Li Z, Anthonsen T. Synthesis and fungicidal activity of 2-imino-3-(4-arylthiazol-2-yl)-thiazolidin-4-ones and their 5-arylidene derivatives. Molecules. 2000;5(9):1055–1061.

8. Romine J, Martin S, Snyder L, Serrano-Wu M, Deshpande M, Whitehouse D, et al. iminothiazolidinones as inhibitors of hcv replication. Princeton, New Jersey; US 2005/0096364A. p. 57.

9. Hu J, Wang Y, Wei X, Wu X, Chen G, Cao G, Shen X, Zhang X, Tang Q, Liang G, Li X. Synthesis and biological evaluation of novel thiazolidinone derivatives as potential anti-inflammatory agents. European Journal of Medicinal Chemistry. 2013;64:292–301.

10. Kücükgüzel SG, Oruç EE, Rollas S, Şahin F, Özbek A. Synthesis, characterisation and biological activity of novel 4-thiazolidinones, 1,3,4-oxadiazoles and some related compounds. European Journal of Medicinal Chemistry. 2002;37(3):197–206.

11. Metwally MA, Farahat AA, Abdel-Wahab BF. 2-Amino-4-thiazolidinones: synthesis and reactions. Journal of Sulfur Chemistry. 2010;31(4):315-349.

12. Ottana R, Maccari R, Barreca ML, Bruno G, Rotondo A, Rossi A, Chiricosta G, Di Paola R, Sautebin L, Cuzzocread S, Vigoritaa MG. 5-Arylidene-2-imino-4-thiazolidinones: Design and synthesis of novel anti-inflammatory agents. Bioorganic and Medicinal Chemistry. 2005;13:4243–4252.

13. Chavan AA, Pai NR. Synthesis and antimicrobial screening of 5-arylidene-2-imino-4-thiazolidinones. Arkıvoc. 2007;xvi:148-155.

14. Zhou JF, Sun XJ, Zhu FX, Li YL, Gong GX. A Facile Synthesis of 5-Arylidene-2-imino-4-thiazolidinones under microwave irradiation. Synthetic Communications. 2008;38:4182–4187.

15. Khazaei A, Veisi H, Safaei M, Ahmadian H. Green synthesis of 5-arylidene-2,4-thiazolidinedione, 5-benzylidene rhodanine and dihydrothiophene derivatives catalyzed by hydrated ionic liquid tetrabutylammonium hydroxide in aqueous medium. Journal of Sulfur Chemistr. 2014;35(3):270–278.

16. Abbas N, Zaib S, Bakht SM, Ibrar A, Khan I, Batool S, Saeed A, Iqbal J. Symmetrical aryl linked bis-iminothiazolidinones as new chemical entities for the inhibition of monoamine oxidases: Synthesis, in vitro biological evaluation and molecular modelling analysis. Bioorganic Chemistry. 2017;70:17–26.

17. Fakhar I, Yamin BM, Hasbullah SA. Synthesis and characterization of bis-thiourea having amino acid derivatives. American Institute of Physics Conference Proceedings, 2016;1784, 030012.

18. Masaki M, Kitahara T, Kurita H, Ohta M. A New Method for the Removal of Chloroacetyl Groups. Journal of the American Chemical Society. 1968;90:4508-4509.

19. Yella R, Ghosh H, Patel BK. It is "2-imino-4-thiazolidinones" and not thiohydantoins as the reaction product of 1,3-disubstituted thioureas and chloroacetylchloride. Green Chemistry. 2008;10:1307–1312.

20. Bhattacharjee SK, Mukherjee R, Hazarika D, Chakraborty A, Acharjee SR. Synthesis of bioactive organosulfur compounds from phenyl isothiocyanate (PITC). Acta Ciencia Indica Chemistry. 2007;33(3):295–302.

21. Zhang LP, Shang XB, Wu QF, Zhang Y, Li JP. Highly efficient method for the synthesis of 1,4-phenylenedithioureas under solvent- and catalyst-free conditions promoted by microwave irradiation. Synthetic Communications. 2012;42(7),1045–1052.

22. Pandya D, Nair KB. Bridged bis(4-thiazolidinones) and related compounds with antibacterial activity. Pharmazie. 1993;48(6):414–17.

RESEARCH ARTICLE

A New Approach To The Treatment of Leishmaniasis: Quercetin-Loaded Polycaprolactone Nanoparticles

Emrah Sefik Abamor [1] ✉ iD

[1] Yildiz Technical University, Chemical and Metallurgical Engineering Faculty, Bioengineering Department, Istanbul, Turkey

Abstract: Antileishmanial drugs used in the treatment of leishmaniasis are toxic and expensive. Moreover, parasites have recently developed resistance against them. Hence there is an increasing need for developing new antileishmanial medicines. Quercetin, found in the roots, leaves and fruits of many plants, is a natural polyphenolic flavonoid. Quercetin has antibacterial, antiviral, anti-carcinogenic, and antioxidant properties. On the other hand, because of its weak solubility in water, quercetin has had limited use on humans. To increase its bio-availability and maximize its therapeutic effects, quercetin has recently been encapsulated with nanoparticulate carrier systems. The aim of this study is to encapsulate quercetin in bio-degradable, bio-compatible poly-ε-caprolactone (PCL) nanoparticles, to characterize the synthesized nanoparticles and to analyze their *in vitro* antileishmanial efficacy on *L.infantum* parasites. Quercetin-loaded PCL nanoparticles (QPNPs) were synthesized using oil-in-water single emulsion solvent evaporation method. Their characterization was done using scanning electron microscopy (SEM) and dynamic light scattering (DLS) equipments. Encapsulation effectiveness and release profiles of QPNPs are calculated with UV-Vis spectrophotometry. The antileishmanial effectiveness of the synthesized nanoparticles was analyzed in *L.infantum* promastigote culture and amastigote-macrophage culture. The results indicated that QPNPs had an average size of 380 nm, a zeta potential of -6.56 mV, and a PDI value of 0.21. The measurements showed the quercetin-loaded nanoparticles to have an encapsulation effectiveness of 64% and a reaction efficiency of 55%. After an incubation of 192 hours, nanoparticles were seen to release 58% of their quercetin content. The synthesized QPNPs had IC50 values on *L.infantum* promastigotes and amastigotes of 86 and 144 µg/mL respectively. This means that QPNPs have reduced the vitality of promastigotes about 20 times and of amastigotes about 5 times as compared to the control group. These results demonstrate the strong antileishmanial potentials of QPNPs. It is believed that if these positive findings are supported by further *in vivo* studies, QPNPs may be used in the treatment of leishmaniasis.

INTRODUCTION

Leishmaniasis disease, caused by the Leishmania parasites, which are among the obligate intracellular protozoans, is one of the most important health concerns of our country and the world (1). The disease has three different clinical forms, cutaneous, visceral, and mucocutaneous. Its most common form, Cutaneous Leishmaniasis (CL), is a severe disease that causes the occurrence of single or multiple large lesions that can usually remain unhealed at the open areas of the body such as hands, face, arms, and legs. Another form of the disease, Visceral Leishmaniasis, causes hepatosplenomegaly in patients' visceral organs such as liver and spleen, and can have severe clinical manifestations that can lead to death if left untreated. Mucocutaneous Leishmaniasis is another form of the disease that mostly involves mucosal membranes and causes severe damage to organs such as mouth and nose, and sometimes leads to loss of the organ

(2, 3). Currently, leishmaniasis is an endemic disease seen in 98 countries of the world, including Turkey. It is estimated that a total of 12 million people worldwide are infected with Leishmania parasites and about 300 million people at risk of developing the disease. According to the report published by the World Health Organization, it is estimated that a total of 1.5 million people develop CL, while 500.000 people develop VL annually worldwide. According to the same report, it is estimated that each year, 60.000 people die due to the complications mediated by VL (4-7). Due to the fact that global warming and climate change increased their influence around the world, there is a concern that there would be an increase in the number of cases and mortality rate (8,9). No vaccines with protective effect have been developed against the disease. Therefore, the only alternative in fighting against this disease is therapeutic practices. On the other hand, toxicity and the high cost of the drugs used in the treatment of leishmaniasis and the decrease in their effect with time, are the disadvantages of these drugs (10, 11). Moreover, in recent years, the parasites have developed resistance to anti-leishmania drugs (12). These conditions restrict the use of the existing anti-leishmania drugs in the treatment of the disease. Due to all these reasons, there is a significant need for the development of novel drug formulations to be used in the treatment of leishmaniasis.

In recent years, the use of herbal compounds in therapeutic practices is increasing rapidly (13). Quercetin is an important flavonoid that can be isolated from nearly 20 different plant species. Due to its antioxidant, anti-inflammatory, antibacterial, antiviral, antimutagenic, and anticarcinogenic properties, quercetin has been attracting the attention of especially pharmaceutical and food industries (14-16). Quercetin is considered as one of the best antioxidant flavonoids due to a large number of hydroxyl groups in its chemical structure (17). In contrast, due to its poor water solubility, inability to maintain its stability within the biological systems, and short half-life, the use of quercetin in clinical practices has been limited. Therefore, in order to increase the bioavailability of quercetin, use of the appropriate carrier systems is required (18,19). Polycaprolactone (PCL), is a biodegradable polyester synthesized by the ring opening polymerization of ε-caprolactone. PCL is degraded by the hydrolysis of its ester linkages under physiological conditions. Due to this property, PCL has been used in drug carrier systems as a biomaterial that allows long-term release. At the same time, as PCL is non-toxic, biocompatible and FDA-approved, the interest in the use of this polymer in clinical studies has increased. In most of the previous studies, it has been reported that the therapeutic efficiency of the molecules with low stability and solubility has increased upon their encapsulation by the PCL nanoparticles, and more efficient drug formulations are developed (20, 21). In one of these studies, Zheng et al. have encapsulated the drug named docetaxel, which is used in cancer treatment, in PCL-Tween80 copolymers, and characterized the resulting nanoparticles, and then investigated their anticarcinogenic efficiency in vitro on C6 glioma cancer cells. Based on the results, it was found that the nanoparticles, which were about 200 nm in diameter, were encapsulated by approximately 10%, and made approximately 34% release within a 28-day period. Results from in vitro experiments have shown that the nanoparticles loaded with the drug had a much higher anticarcinogenic effect than the application of the drug alone (22).

Until now, there have been studies showing the encapsulation of the quercetin molecule by many polymeric nanoparticle carrier systems, primarily PLGA. However, there are no studies in the literature on the encapsulation of quercetin by PCL nanoparticles and its antileishmanial activity. Considering the potential of quercetin to show a high antileishmanial activity despite its low stability and hydrophobic character, while the PCL is biodegradable, biocompatible and allows long-term drug release, we estimate that encapsulation of quercetin in PCL nanoparticles will eliminate the stability- and solubility-related disadvantages and have a strong antileishmanial activity on Leishmania parasites. Thus, the aim of this study is to investigate the synthesis and characterization of quercetin-loaded PCL nanoparticles (QPNPs) and to identify the in vitro antileishmanial activity on Leishmania promastigotes and amastigotes.

EXPERIMENTAL SECTION

Materials
PCL (MW:14.000), polyvinyl alcohol (PVA) (average MW: 30.000–70.000), Methylthiazolyltetrazolium (MTT) were purchased from Sigma-Aldrich (St. Louis, MO). Dichloromethane (DCM), sodium nitrite, sulfanylamide, naphthylethylenediamide dihydrochloride were obtained from Merck (Darmstadt, Germany). Roswell Park Memorial Institute medium (RPMI 1640) was purchased from GIBCO (Life Technologies, USA). Nigella sativa essential oil (Zade Vital) was commercially obtained from a national pharmacy. A mouse J774 macrophage cell line was obtained from the Histology and Embryology Department, Istanbul University, Istanbul, Turkey. Ultra-pure water was obtained from a Millipore MilliQ Gradient system.

Preparation of Quercetin-Loaded PCL Nanoparticles
Quercetin-loaded PCL nanoparticles (QPNPs) were prepared by an o/w single solvent evaporation method. Briefly, 100 mg of ε-caprolactone was dissolved in 5 mL of DCM. Then 10 mg of quercetin was added into the organic phase. The organic phase was dropwise added

into 25 mL of an aqueous phase including PVA (2 % w/w) as a stabilizer. The mixture was emulsified for 5 minutes with a probe sonicator (Bandelin Sonopuls, Germany) at 80% amplitude in an ice bath. Evaporation of DCM from the emulsion was carried out by stirring at 750 rpm for 4 h. Nanoparticle suspensions were centrifuged at 14,000 rpm for 30 minutes. The pellet was rinsed twice with deionized distilled water. The obtained pellet was lyophilized for 48 h and stored at -40 °C until use.

Characterization of nanoparticles
Particle size, polydispersity index and zeta potential
Particle size, polydispersity index and zeta potential were identified by photon correlation spectroscopy (PCS) by using a Zetasizer Nano ZS (Malvern Instruments, Malvern, UK). Size measurements were performed in triplicate following preparation of nanoparticle suspensions by diluting in distilled water at a ratio of 1/100 (v/v) at 25 °C. The polydispersity index range was evaluated at between 0 and 1. The zeta potential analysis for synthetized nanoparticles was performed by using the same instrument at 25 °C.

Scanning electron microscopy

Lyophilized nanoparticles were fixed on metallic studs like a thin film using adhesive tape and then coated with gold under vacuum. The particles were monitored by using an Evo LS10 (Zeiss, Welwyn Garden City, UK) scanning electron microscope (SEM) at enhanced voltage of 10–20 kV.

Encapsulation efficiency measurements
The encapsulated amount of quercetin was determined by measuring the amount of quercetin remained in supernatant following to centrifugation process by using UV-Vis spectrophotometry at 374 nm. The quantification was done in triplicate.

In order to determine non-encapsulated quercetin concentrations in the supernatant, a standard calibration curve of quercetin that was prepared at various concentrations was used. The concentration of encapsulated quercetin was ascertained by calculating the differences between initial concentrations of quercetin (10 mg) and the concentration of free quercetin remained in the supernatant. The reaction yield (RY) and encapsulation efficiency (EE) of quercetin was calculated by using the following formulas:

$$\text{Encapsulation efficiency \%} = \frac{\text{Amount of encapsulated quercetin}}{\text{Initial amount of quercetin}} \times 100$$

$$\textit{Reaction Yield \%} = \frac{\text{Amount of weighed (quercetin) PCL Nps}}{\text{Amount of initial quercetin and PCL}} \times 100$$

In vitro drug release studies
In order to provide release of quercetin, 5 mg of quercetin encapsulated in PCL nanoparticles were suspended in 3 mL PBS at pH 7.4. Then suspension was incubated in a shaker incubator at 37 °C. At appropriate intervals, nanoparticles were centrifuged at 12,000 rpm for 20 min and the supernatant was collected for the analysis. The amount of released quercetin within the supernatant was evaluated by UV spectrophotometer as described previously.

Leishmania infantum Promastigote Culture
Leishmania infantum (L. infantum) promastigotes were cultivated in RPMI-1640 medium supplemented with 10% fetal bovine serum (FBS) at 27 °C. Metacyclic promastigotes were harvested at late log phase following to 120 h incubation.

J774 Macrophage Cell Culture
J774 macrophage cells were grown in RPMI 1640 medium supplemented with 100 U/mL penicillin-streptomycin and 10% FBS. Afterwards, macrophages were incubated at 37 °C incubator with 5% CO_2.

Cell Viability Assay
Cytotoxicity analysis of QPNPs and free nanoparticles were performed on J774 macrophage cells. At first, 1 x 10^4 macrophage

cells were seeded into each wells of 96-well plates and incubated for 24 h to allow cellular attachment. Then macrophages were exposed to free PCL nanoparticles and QPNPs at various concentrations ranging between 50 and 1000 µg/mL for 144 h. Cells that were not treated with neither free or loaded nanoparticles were identified as positive control. MTT test was used in order to detect cellular viabilities of macrophages after their exposure to different concentrations of formulations. For that purpose, 10 µL of MTT reactant (Thiazolyl Blue Tetrazolium Bromide) (10 mg/mL) was included into each well and cells were then incubated for 4 h. Following to incubation, DMSO was put into each wells in order to dissolve the formazan crystals. Absorbance values was measured at 570 nm using a microplate reader (Thermo Scientific, Multiskan FC).

Anti-promastigote Assay
Antileishmanial activities of quercetin-loaded PCL nanoparticles and free nanoparticles were performed on *L. infantum* promastigotes and amastigotes, *in vitro*. For anti-promastigote assay, 5 x10^5 *L. infantum* promastigotes were transfered into a 6-well plate and cells were incubated at 27 °C for 24 h. Afterwards, various concentrations of quercetin-encapsulated PCL nanoparticles and free nanoparticles varying between 50 and 1000 µg/mL was added into

wells. Treated promastigotes were incubated at 27 °C for 192 h. The number of viable promastigotes for each groups were counted with hemocytometer at the end of 96 and 192 h incubation period. For that purpose, a 50-µL *L. infantum* promastigote culture that was taken from each well was fixed with 2% formalin at a ratio of 1:10. Afterwards, suspensions were transferred into a hemocytometer, and the slide was investigated in an inverted microscope (Olympos CKX41). IC50 values of loaded and empty nanoparticles were determined by evaluating the concentration that inhibited half of *L. infantum* promastigotes.

Determination of Anti-amastigote Efficacies
Studies on determination of anti-amastigote effects of quercetin loaded and free nanoparticles were performed on amastigote-macrophage culture. For that purpose, 2.5×10^4 J774 macrophage cells were seeded into 6-well plates and incubated at 37 °C. Following to 24 h incubation, 2.5×10^5 *L. infantum* promastigotes were added into each well in order to provide infection of macrophage cells by parasites. After 4 h incubation at 37 °C, non-phagocytized promastigotes were removed by washing the plates triplicate with PBS. Thus, amastigote-macrophage culture was established. After that, various concentrations of quercetin loaded PCL nanoparticles and free nanoparticles ranging between 50 and 1000 µg/mL were included into 6-well plates in order to find efficacies of nanoparticles on *L. infantum* amastigotes.

Treated amastigote-macrophage culture was incubated at 37 °C for 192 h. Following to incubation, all wells were rinsed three times with sterile PBS and then fixed with methanol for 10 min. Afterwards, each well was stained with giemsa for 3 min and was washed with PBS following incubation. Then, slides that were inserted into each well were removed and investigated on inverted microscope at 100X dimensions. The infection index of all samples were evaluated by multiplying % infectivity values with amastigote number per macrophages. % infectivity was assessed by dividing the number of infected macrophages with the number of all macrophages in the zone.

RESULTS

Characterization of synthetized nanoparticles
Characterization of the QPNPs and empty PCL nanoparticles was performed using scanning electron microscope and Zetasizer equipment. At the same time, the reaction yields and encapsulation practices of the quercetin-loaded nanoparticles were calculated and nanoparticles were characterized. In Figure 1, a view of the SEM analysis of QPNPs is provided. As it can be seen from the image, the nanoparticles that are synthesized are round, uniform, and smooth. At the same time, the nanoparticles are close to each other in size. Their sizes vary between 200-400 nm.
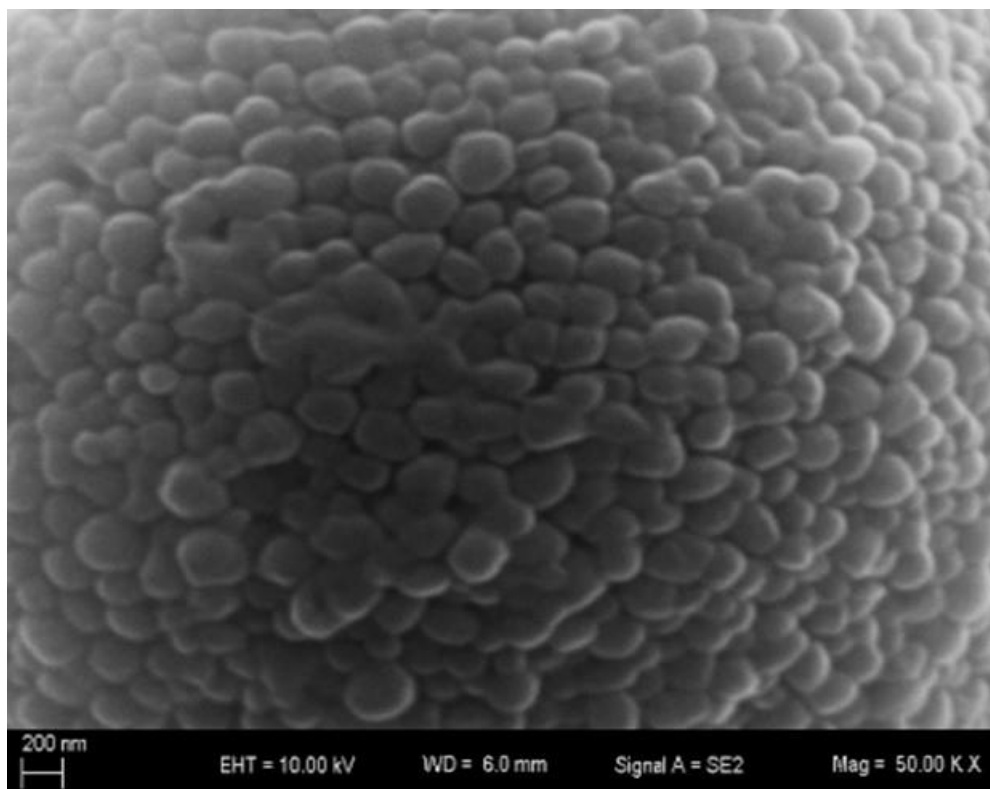

Figure 1. SEM image of quercetin encapsulated PCL nanoparticles.

The result of the size analysis performed by Zetasizer has shown that the empty nanoparticles have an average size of 220 nm, while QPNPs have an average size of 350 nm (Table 1). The

distribution of QPNPS due to their sizes as a result of Dynamic Light Scattering (DLS) analysis was also shown in Figure 2. It is estimated that the difference in size between the empty and loaded nanoparticles can be due to the encapsulation of quercetin by the PCL nanoparticles. On the other hand, polydispersity index (PDI) values, zeta potentials, encapsulation efficiencies and reaction yield of the empty and loaded nanoparticles are given in Table 1. As can be seen from the table, the zeta potentials of the empty nanoparticles and QPNPs are -4.92 and -6.56, respectively.

Negative values of the zeta potentials are due to the carboxyl end groups of the PCL polymers.

When PDI values of the empty and quercetin-loaded nanoparticles are analyzed, it was found that this value varied between 0.11 and 0.21 for the empty nanoparticle. These results show that the synthesized nanoparticles are close to each other in terms of size and are distributed homogeneously. In Table 1, it was shown that for the quercetin-loaded nanoparticles, the encapsulation efficiency is 64% and the reaction yield is 55%.

Table 1. Demonstration of mean size, PDI values, zeta potential measurements, encapsulation efficiency and reaction yield percentages of free nanoparticles and quercetin-loaded PCL nanoparticles.

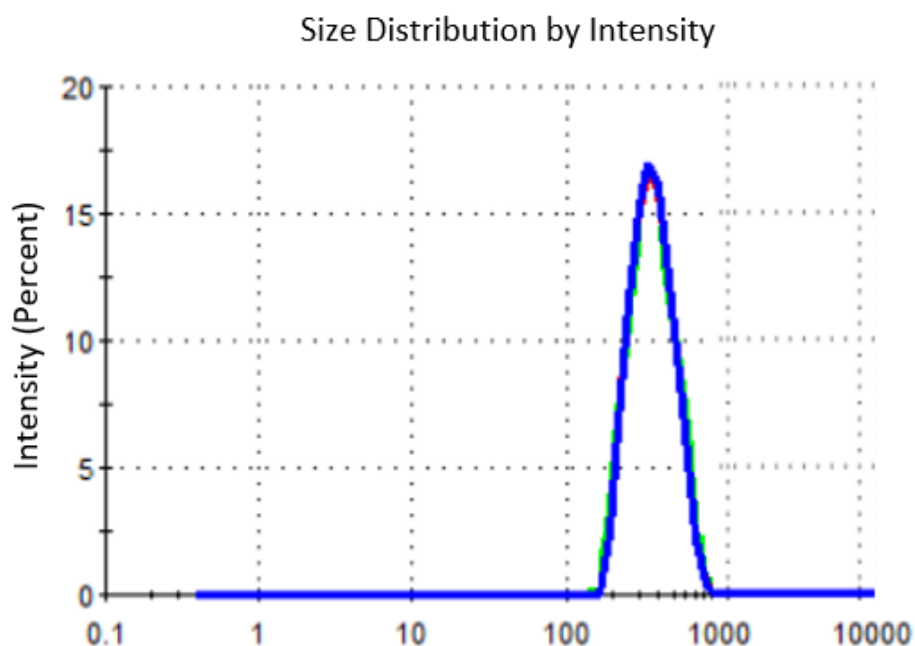| Formulations	Size (nm)	PDI	Zeta Potential (mV)	Encapsulation Efficiency (%)	Reaction Yield (%)
Free NPs	220	0,12	-4,92 ± 0,63	-	-
QPNPs	350	0,21	-6.56 ± 0,45	64	55

Figure 2. Size distribution analysis of quercetin loaded PCL nanoparticles by DLS.

In vitro Release Study

In order to determine the *in vitro* release of quercetin from the nanoparticle formulations, a dissolution method performed at pH 7.4 was used. 240 h cumulative release profiles of the quercetin-loaded nanoparticles are shown in Figure 3. As it can be seen from the graph, within the first 4 h, drug-loaded nanoparticles had a 9% initial burst effect. The amount of quercetin released from the nanoparticles until the 144th hour of the incubation increased every day. At the end of the 144th hour, the total amount of quercetin released from the PCL nanoparticles was 2.2 mg. This shows that the nanoparticles release approximately 32% of their quercetin load at the end of the 144-hour-long incubation. The release study was continued for 240 hours. At the end of 240 hours, it was found that the nanoparticles released approximately 58% quercetin. The cumulative amount of quercetin released from the beginning until the 240th h was calculated as 3.6 mg.
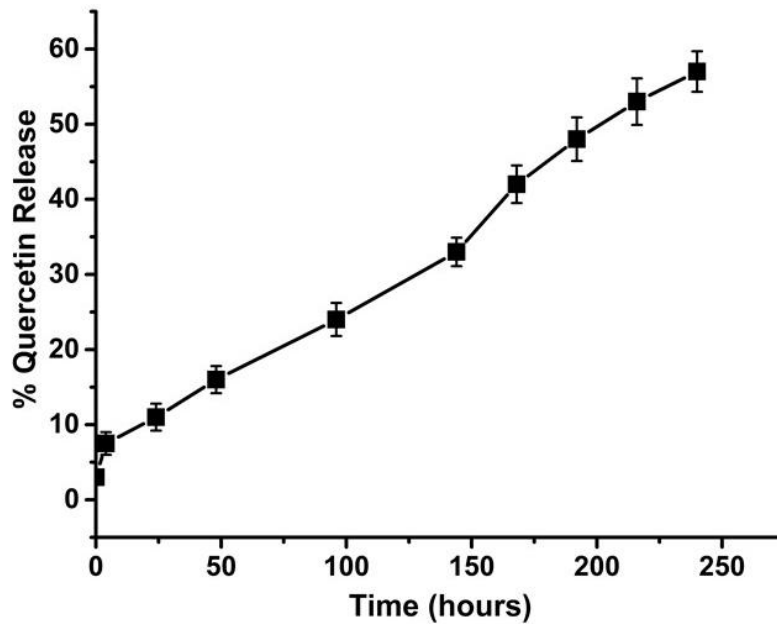
Figure 3. *In vitro* release profile of quercetin-encapsulated PCL nanoparticles after 240 hours of incubation.

Cytotoxicity Analysis

Cytotoxicity analysis for different concentrations of quercetin, quercetin-loaded PCL nanoparticles, and empty nanoparticles was performed using J774 cells. As it can be seen in Figure 4, the toxic effects of empty nanoparticles and quercetin-loaded nanoparticles on J774 cells are quite low. In particular, it was found that the vitality of these cells exposed to these nanoparticles at low concentrations is nearly the same with the control. The vitality rates of the cells exposed to the highest concentration (1000 μg/mL) of empty nanoparticles and QPNPs were found to be %90 and %84, respectively. On the other hand, cytotoxic effects of quercetin on cells was found to be higher compared to the other groups. It was found that the cells exposed to 1000 μg/mL quercetin had their vitality reduced to 66%.
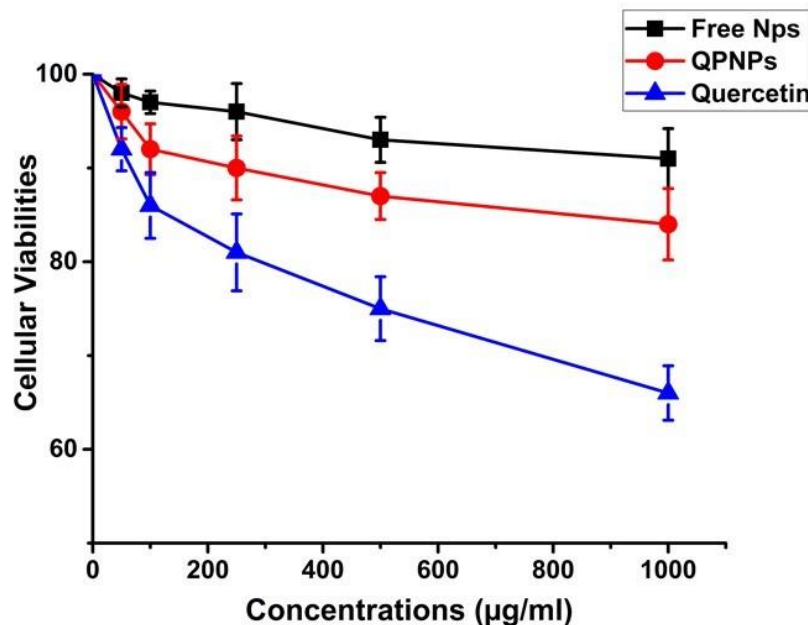
Figure 4. Cellular viability ratios of macrophage cells that were exposed to different concentrations of free NPs, QPNPs and quercetin, respectively.

Identification of the Anti-Promastigotic Activity

In the study, the activities of quercetin alone, quercetin-loaded PCL nanoparticles, and empty PCL nanoparticles on *L. infantum* promastigotes were studied using the measurements taken at the 192nd hour of the incubation. As can be seen from Figure 5, it was found that quercetin alone and QPNPs show high levels of antileishmanial activity on *L. infantum* promastigotes. However, empty nanoparticles have very low antileishmanial activity on *L. infantum* parasites. The activities of quercetin and QPNPs increase depending on the concentration. It was found that

while the vitality rate of *L. infantum* parasites exposed to quercetin at a 50 µg/mL concentration was 77%, the vitality of those exposed to 1000 µg/mL decreased to 20% (Figure 5). On the other hand, it was found that QPNPs have a higher antileishmanial activity compared to the quercetin alone. While the vitality rate of *L. infantum* parasites exposed to 50 µg/mL QPNPs was 69%, this ratio decreased gradually depending on the increase in the concentration and the vitality finally decreased to 8% for the L. infantum promastigotes exposed to 1000 µg/mL quercetin. On the other hand, it was found that

the vitality rate was around 80% for the group exposed to the empty nanoparticles at the highest concentration. Upon analyzing the IC50 values of the formulations, it was found that these values were 86 µg/mL, 149 µg/mL, and >1000 µg/mL for quercetin-loaded PCL nanoparticles, quercetin, and empty nanoparticles, respectively. As can be seen, among the formulations, QPNPs had the highest activity. The activity of quercetin on parasites increased after being encapsulated in the PCL nanoparticles. On the other hand, it was found that the empty nanoparticles did not have a significant effect on parasites.
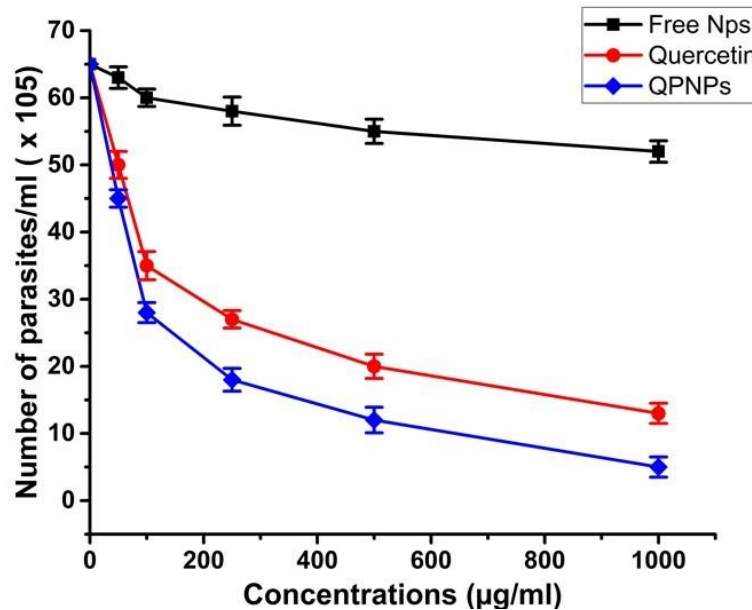
Figure 5. The decrease on the numbers of *L.infantum* promastigotes following to exposure to different concentrations of free NPs, QPNPs and quercetin for 192 h.

Identification of the Anti-Amastigotic Activity

In order to investigate the activities of quercetin alone, empty, and QPNPs on *L. infantum* amastigotes, infection indices of the infected macrophages on which the formulations were applied were calculated. Compared to the control group on which no formulations were applied, the change in the infection indices of the macrophages in the experimental groups revealed whether the formulations had a concentration-dependent effect on amastigotes. Infection index of the macrophages in the control group was 205. In the experimental group on which empty nanoparticles were applied, it was found that the infection index varied between 192 and 169 depending on the concentration (Figure 6). As can be seen, empty nanoparticles did not have a significant effect on *L. infantum* amastigotes. In contrast, the anti-amastigotic activity of quercetin alone and QPNPs were higher than the control and empty nanoparticle groups.

Infection indices of the macrophages exposed to quercetin alone varied between 164 and 69. Infection indices of the macrophages exposed to 50 µg/mL quercetin were 164, whereas that of the macrophages exposed to 1000 µg/mL quercetin was 69. IC50 value of quercetin on *L. infantum* amastigotes was 300 µg/mL. It was found that QPNPs have a higher anti-amastigotic activity compared to the application of quercetin alone. While the infection index of the macrophages exposed to 50 µg/mL QPNPs was 146, that of the macrophages exposed to 1000 µg/mL was 45. As can be seen, compared to the control group, QPNPs decreased Leishmania amastigotes by 5 fold when used at the highest concentration. The IC50 value of the QPNPs on *L. infantum* amastigotes was calculated as 144 µg/mL. These results suggest that quercetin-loaded nanoparticles have a 2-fold higher anti-amasigotic activity compared to the quercetin alone.
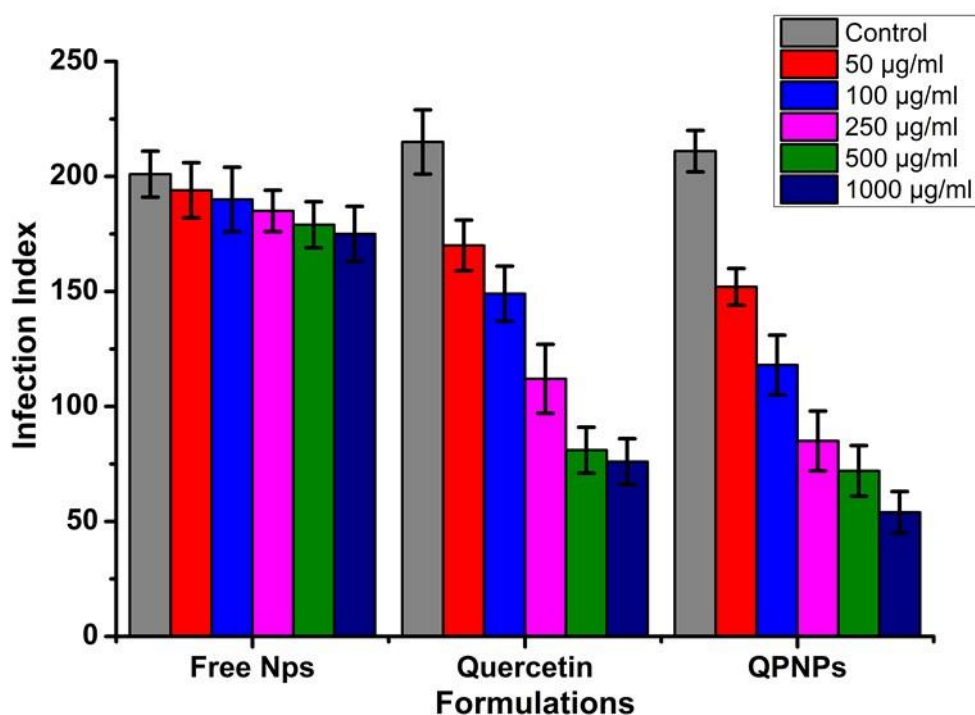
Figure 6. Infection index values of infected macrophages that were exposed to different concentrations of free NPs, QPNPs and quercetin for 192 h.

DISCUSSION

Currently used anti-leishmanial drugs have various disadvantages such as toxicity, resistance, and high cost. Thus, there have been studies toward the development of new generation antileishmanial compounds in the recent years (23). Quercetin molecule, which is obtained from various plants, is one of the strongest known flavonoids. Anti-microbial, anti-oxidant, anti-carcinogenic and anti-inflammatory effects of quercetin have been proven in the previous studies (24-26). However, low water solubility of this molecule reduces its applicability in clinical practices. Therefore, encapsulation of quercetin by carrier systems in order to increase its solubility, bio-availability and therapeutic efficiency has been considered as an appropriate method. In this study, we encapsulated quercetin molecule in PCL nanoparticles and investigated the antileishmanial activities of the formulations on L. infantum promastigotes and amastigotes *in vitro*.

Encapsulation of quercetin by PCL nanoparticles was performed using oil-in-water single emulsion solvent evaporation technique. In the study by Arasoglu *et al.,* this technique was shown to be more successful than nano-precipitation and salting out techniques used in the encapsulation of quercetin by PLGA nanoparticles. In the same study, it was found that the nanoparticles synthesized using single emulsion solvent evaporation have higher reaction yield and have a more significant antibacterial activity compared to the nanoparticles synthesized by other techniques (27). Size analysis and other characterization tests of the nanoparticles we

prepared using oil-in-water single emulsion solvent evaporation technique were performed using SEM and zetasizer devices. According to the zetasizer analysis, the average size of empty nanoparticles was approximately 220 nm, and the average size of quercetin-loaded nanoparticles was approximately 350 nm. The larger size of the quercetin-loaded nanoparticles compared to the empty nanoparticles can be considered as an indicator of the efficient and effective encapsulation of quercetin by the PCL nanoparticles. In the previous studies, it was stated that the drug-loaded nanoparticles can be larger in size compared to the empty nanoparticles (28, 29). It was found that, particularly in cancer research, carrier systems smaller than 500 nm are more successful in delivering the drugs to the target tissues, therefore enabling active transport (30). On the other hand, it is known that nanoparticles larger than 200 nm are more effective in targeting macrophages that are used as host cells by the parasites, and that the nanoparticles of this size are phagocytosed by the macrophages (31). Thus, due to their size, it is estimated that the nanoparticles obtained in our study can directly target the parasites living inside the macrophages. Negative zeta potentials of the synthesized nanoparticles can be completely correlated with the negatively charged carboxyl groups of the used PCL polymer. Low PDI values is an indicator that the synthesized nanoparticles are close to each other in size. Based on the uptake analysis, it was found that following 240 hours of incubation, PCL nanoparticles release approximately 58% of the quercetin they contain into the environment. As known, PCL nanoparticles decompose more slowly than the

other polymeric nanoparticles used in the drug carrier systems, especially PLGA. The reasons behind this are that PCL has a higher molecular weight and is more hydrophobic (32). In a study similar to the one we performed, Pathak *et al.* encapsulated the antibiotics doxycycline and metronidazole in PCL nanoparticles and investigated the activity of the synthesized nanoparticles in the treatment of intravaginal inflammatory diseases. In the release analysis performed within the context of the said study, it was found that the synthesized nanoparticles release approximately 60-70% of the drug molecules they contain at the end of the incubation period of 14 days. These results corroborate the results we obtained in our study (33).

Following the synthesis and characterization, we investigated the *in vitro* antileishmanial activities of the QPNPs we synthesized on *L. infantum* promastigotes and amastigotes. Antileishmanial activity of quercetin, one of the strongest known flavonoids, has been shown in previous studies. In a study by Belkhelfa-Slimani *et al.* in 2016, the apoptotic effects and cytotoxic activities of caffeic acid and quercetin on Leishmania major promastigotes were studied. In that study, it was found that caffeic acid and quercetin at a concentration of 400 µmol/L decrease the vitality of *L. major* parasites by 68.90% and 59.22%, respectively. In the same study, it was shown that quercetin leads to caspase-independent apoptosis in parasites and cause cell death (34). The antileishmanial activity of quercetin is thought to be related to the production of reactive oxygen species (ROS), of which parasites are highly sensitive, causing damage to the mitochondria and cell membranes of parasites and inhibiting the nucleic acid synthesis. Due to these properties, quercetin and quercetin-containing extracts are known as strong antiparasitic agents (35, 36). However, as discussed earlier, low water solubility of quercetin is one of the most significant obstacles to the development of quercetin-based drug molecules. In recent years, studies have been performed toward the production of quercetin-loaded polymeric carrier systems to eliminate this obstacle and increase the therapeutic activity of quercetin. In these studies, PLGA nanoparticles are frequently used. Arasoglu *et al.* have investigated the antibacterial activities of the quercetin-loaded PLGA nanoparticles prepared using various synthesis methods on foodborne pathogens such as *Listeria monocytogenes*, *Salmonella typhimurium*, *Escherichia coli*, and *Staphylococcus aureus*. While quercetin and quercetin-loaded PLGA nanoparticles showed nearly similar levels of antibacterial activity on *Salmonella typhimurium*, *Escherichia coli*, and *Staphylococcus aureus*, quercetin-loaded PLGA nanoparticles showed higher level of antibacterial activity on *Listeria monocytogenes*. The MIC value of quercetin-loaded PLGA nanoparticles on these bacteria was 100 µg/mL whereas the MIC

value of quercetin alone was 200 µg/mL (27). In a similar study from 2016, Sun *et al*. investigated the *in vitro* and *in vivo* antibacterial effects of quercetin-loaded PLGA nanoparticles on *E. coli* and *Micrococcus tetragenus* bacteria. Unlike the other study, quercetin-loaded nanoparticles had a higher level of antibacterial activity compared to the quercetin alone. Based on the results, the vitality of the *E. coli* exposed to 70 µL quercetin-loaded PLGA nanoparticle decreased by 92% whereas this rate was 66% in the *E. coli* exposed to quercetin alone. Similarly, the vitality of the *M. tetragenus* exposed to the nanoparticles loaded with the same dose was calculated as 26% and the vitality of the bacteria exposed to quercetin was calculated as 49%. Based on these results, it can be said that quercetin and quercetin-loaded PLGA nanoparticles have a higher antimicrobial effect on *E. coli* than on *M. tetragenus*. Moreover, it was found that the therapeutic activity of quercetin increases upon its encapsulation by the PLGA nanoparticles (37). On the other hand, so far no studies have been performed on the encapsulation of the quercetin by the biocompatible, biodegradable, FDA-approved polymer PCL and its antileishmanial activities. In the present study, *in vitro* antileishmanial activities of the QPNPs on *L. infantum* promastigotes and amastigotes are investigated for the first time. Based on the results, the IC50 values of the QPNPs on *L. infantum* promastigotes and amastigotes were calculated as 86 and 144 µg/mL, respectively. On the other hand, the IC50 values of quercetin on *L. infantum* promastigotes and amastigotes were calculated as 149 and 300 µg/mL. These results indicate that the antileishmanial activity of the quercetin encapsulated in the PCL nanoparticles increases significantly. At the same time, it was found that QPNPs are more effective on *L. infantum* promastigotes than on amastigotes. Since the nanoparticles should be penetrated inside the macrophages in order to contact with the amastigotes, their efficiency on amastigotes can be lower. It has also been emphasized in previous studies that in order for the drug-loaded nanoparticles to penetrate in the macrophages more efficiently and inhibit amastigotes, they should be applied at higher concentrations than the concentrations required for the promastigotes. On the other hand, it was found that QPNPs inhibited 78% of the amastigotes when used at the highest concentration after 192 hours of incubation. Considering that nanoparticles only allow 50% quercetin release within that period, it is estimated that after longer incubation periods, more of the quercetin can be released, and thus, nearly all of the amastigotes can be inhibited.

In conclusion, within the context of this study, encapsulation of the quercetin in PCL nanoparticles has been performed with success for the first time, and the significant antileishmanial activity of the QPNPs on *L. infantum* promastigotes and amastigotes has

been observed. These promising data suggest that QPNPs can be successful in the eradication of leishmaniasis. In case of obtaining positive results in the in vivo studies, QPNPs can be used in the treatment of leishmaniasis.

REFERENCES

1. Vannier-Santos MA, Martiny A, de Souza W. Cell biology of Leishmania spp.: invading and evading. Curr Pharm Des. 2002;8(4):297-318.

2. de Vries HJ, Reedijk SH, Schallig HD. Cutaneous leishmaniasis: recent developments in diagnosis and management. Am J Clin Dermatol. 2015;16(2):99-109.

3. Bailey MS, Lockwood DN. Cutaneous leishmaniasis. Clin Dermatol. 2007;25(2):203-11.

4. Torres-Guerrero E, Quintanilla-Cedillo MR, Ruiz-Esmenjaud J, Arenas R. Leishmaniasis: a review. F1000Res. 2017;6:750.

5. Reithinger R, Dujardin JC, Louzir H, Pirmez C, Alexander B, Brooker S.Cutaneous leishmaniasis. Lancet Infect Dis. 2007;7(9):581-96.

6. Bravo F, Sanchez MR. New and re-emerging cutaneous infectious diseases in Latin America and other geographic areas. Dermatol Clin. 2003;21(4):655-68

7. Gurunath U, Joshi R, Agrawal A, Shah V. An overview of visceral leishmaniasis elimination program in India: a picture imperfect. Expert Rev Anti Infect Ther.2014;12(8):929-35.

8. González C, Wang O, Strutz SE, González-Salazar C, Sánchez-Cordero V, Sarkar S. Climate change and risk of leishmaniasis in north america: predictions from ecological niche models of vector and reservoir species. PLoS Negl Trop Dis. 2010;4(1):e585.

9. Stamm LV. Human Migration and Leishmaniasis-On the Move. JAMA Dermatol. 2016;152(4):373-4.

10. Singh OP, Singh B, Chakravarty J, Sundar S. Current challenges in treatment options for visceral leishmaniasis in India: a public health perspective. Infect Dis Poverty. 2016;5:19.

11. Moore EM, Lockwood DN. Treatment of visceral leishmaniasis. J Glob Infect Dis. 2010;2(2):151-8.

12. Chakravarty J, Sundar S. Drug resistance in leishmaniasis. J Glob Infect Dis. 2010;2(2):167-76.

13. Ekor M. The growing use of herbal medicines: issues relating to adverse reactions and challenges in monitoring safety. Front Pharmacol. 2014;4:177.

14. Anand David AV, Arulmoli R, Parasuraman S. Overviews of Biological Importance of Quercetin: A Bioactive Flavonoid. Pharmacogn Rev. 2016;10(20):84-89.

15. Salvamani S, Gunasekaran B, Shaharuddin NA, Ahmad SA, Shukor MY. Antiartherosclerotic effects of plant flavonoids. Biomed Res Int. 2014;2014:480258.

16. Sultana B, Anwar F. Flavonols (kaempeferol, quercetin, myricetin) contents of selected fruits, vegetables and medicinal plants. Food Chem. 2008;108(3):879-84.

17. Moalin M, Strijdonck GP, Beckers M, Hagemen G, Borm P, Bast A, Haenen GR. A planar conformation and the hydroxyl groups in the B and C rings play a pivotal role in the antioxidant capacity of quercetin and quercetin derivatives. Molecules. 2011;16(11):9636-50.

18. Kumari A, Yadav SK, Pakade YB, Singh B, Yadav SC. Development of biodegradable nanoparticles for delivery of quercetin. Colloids Surf B Biointerfaces. 2010;80(2):184-92.

19. Natarajan V, Krithica N, Madhan B, Sehgal PK. Formulation and evaluation of quercetin polycaprolactone microspheres for the treatment of rheumatoid arthritis. J Pharm Sci. 2011 Jan;100(1):195-205.

20. McNeil SE, Griffiths HR, Perrie Y. Polycaprolactone fibres as a potential delivery system for collagen to support bone regeneration. Curr Drug Deliv. 2011;8(4):448-55.

21. Madhaiyan K, Sridhar R, Sundarrajan S, Venugopal JR, Ramakrishna S. Vitamin B12 loaded polycaprolactone nanofibers: a novel transdermal route for the water soluble energy supplement delivery. Int J Pharm. 2013 Feb 28;444(1-2):70-6.

22. Ma Y, Zheng Y, Zeng X, Jiang L, Chen H, Liu R, Huang L, Mei L. Novel docetaxel-loaded nanoparticles based on PCL-Tween 80 copolymer for cancer treatment. Int J Nanomedicine. 2011;6:2679-88.

23. de Menezes JP, Guedes CE, Petersen AL, Fraga DB, Veras PS. Advances in Development of New Treatment for Leishmaniasis. Biomed Res Int. 2015;2015:815023.

24. Nam JS, Sharma AR, Nguyen LT, Chakraborty C, Sharma G, Lee SS. Application of Bioactive Quercetin in Oncotherapy: From Nutrition to Nanomedicine. Molecules. 2016;21(1):E108.

25. Johari J, Kianmehr A, Mustafa MR, Abubakar S, Zandi K. Antiviral activity of baicalein and quercetin against the Japanese encephalitis virus. Int J Mol Sci.2012;13(12):16785-95.

26. Ramos FA, Takaishi Y, Shirotori M, Kawaguchi Y, Tsuchiya K, Shibata H, Higuti T, Tadokoro T, Takeuchi M. Antibacterial and antioxidant activities of quercetin oxidation products from yellow onion (Allium cepa) skin. J Agric Food Chem. 2006;54(10):3551-7.

27. Arasoglu T, Derman S, Mansuroglu B, Uzunoglu D, Kocyigit B, Gumus B, Acar T, Tuncer B. Preparation, characterization, and enhanced antimicrobial activity: quercetin-loaded PLGA nanoparticles against foodborne pathogens. Turk J Biol. 2017;41:p127-140.

28. Zheng D, Li X, Xu H, Lu X, Hu Y, Fan W. Study on docetaxel-loaded nanoparticles with high antitumor efficacy against malignant melanoma. Acta Biochim Biophys Sin (Shanghai). 2009 Jul;41(7):578-587

29. Rachmawati H, Yanda YL, Rahma A, Mase N. Curcumin-Loaded PLA Nanoparticles: Formulation and Physical Evaluation. Sci Pharm. 2016 Feb 14;84(1):191-202.

30. Li B, Li Q, Mo J, Dai H. Drug-Loaded Polymeric Nanoparticles for Cancer Stem Cell Targeting. Front Pharmacol. 2017 Feb 14;8:51.

31. Kalluru R, Fenaroli F, Westmoreland D, Ulanova L, Maleki A, Roos N, Paulsen Madsen M, Koster G, Egge-Jacobsen W, Wilson S, Roberg-Larsen H, Khuller GK, Singh A, Nyström B, Griffiths G. Poly(lactide-co-glycolide)-rifampicin nanoparticles efficiently clear Mycobacterium bovis BCG infection in macrophages and remain membrane-bound in phago-lysosomes. J Cell Sci. 2013;126(14):3043-54.

32. Danafar H, Schumacher U. MPEG–PCL copolymeric nanoparticles in drug delivery systems. Cogent Medicine. 2016;3:1

33. Pathak M, Coombes AGA, Ryu B, Cabot PJ, Turner MS, Palmer C, Wang D, Steadman KJ. Sustained Simultaneous Delivery of Metronidazole and Doxycycline From Polycaprolactone Matrices Designed for Intravaginal Treatment of Pelvic Inflammatory Disease. J Pharm Sci. 2018;107(3):863-869.

34. Belkhelfa-Slimani R, Djerdjouri B. Caffeic acid and quercetin exert caspases-independent apoptotic effects on Leishmania major promastigotes, and reactivate the death of infected phagocytes derived from BALB/c mice. Asian Pacific Journal of Tropical Biomedicine. 2017;7(4):321-331

35. Fonseca-Silva F, Inacio JD, Canto-Cavalheiro MM, Almeida-Amaral EE. Reactive oxygen species production and mitochondrial dysfunction contribute to quercetin induced death in Leishmania amazonensis. PLoS One. 2011;6(2):e14666.

36. Kheirandish F, Delfan B, Mahmoudvand H, Moradi N, Ezatpour B, Ebrahimzadeh F, Rashidipour M. Antileishmanial, antioxidant, and cytotoxic activities of Quercus infectoria Olivier extract. Biomed Pharmacother. 2016;82:208-15.

37. Sun D, Li N, Zhang W, Yang E, Mou Z, Zhao Z, Liu H, Wang W. Quercetin-loaded PLGA nanoparticles: a highly effective antibacterial agent in vitro and anti-infection application in vivo. J Nanopart Res. 2016;18:1-21.

A New Highly Thermally Stable Co(II)-coordination polymer with Semi-flexible Bis(Imidazole) Directed Secondary Building Unit: Solvothermal Synthesis and Structure

Fatih SEMERCİ* ✉ iD

Department of Energy Systems Engineering, Technology Faculty, Kırklareli University, Kırklareli, Turkey

Abstract: A new thermally highly stable 2D coordination polymer, formulated as [Co(μ6-abtc)$_{0.5}$(μ-obix)]$_n$ (abtc = dioxygenated form of 3,3',5,5'-azobenzenetetracarboxylate) obtained employing the semi-flexible 1,2-bis(imidazole-1-ylmethyl)benzene (obix) linker in hydro(solvo)thermal method. The complex was characterized by various techniques such as IR spectroscopy, elemental analysis, single crystal and powder crystal analysis. Crystallographic study of complex **1** reveal that two metal(II) ions are linked by O atoms of carboxylate groups of abtc ligand to build paddle-wheel SBU (secondary building unit). These SBUs are stabilized by the connection of obix ligand. The Co(II) ions are μ$_6$-bridged by hexadentate abtc ligand to generate 2D polymer layers with 3,4-connected binodal net (point symbol {4.6^2}$_2${4^2.6^2.8^2}) and topological type is 3,4L13. Thermal analysis shows that complex **1** thermally stable up to 401 °C.

INTRODUCTION

The quickly expanding area of coordination polymers has attracted interest for the fascinating architectures and their potential applications (1-5). Many efforts have been given for constructing new structures, new topologies, as well as new functionalities (6-8). These materials can be synthesized relying on the mixture of metal salts, carboxylate-based ligand and N-donor bridging ligands (9-12). The coordination polymers can be synthesis by using highly symmetrical multifunctional organic ligands owing to their various coordination behavior and special topologies. Furthermore, secondary building units (SBUs) that can predict the structures of

coordination polymers are largely utilized to construct them (13-15).

Properties of flexible coordination polymers can be synthesis practically at will by a preference of flexible ligands (16). The employment of flexible ligands often gives rise to increased disorder, which hampers the arrangement of self-assembly of coordination polymers. Nonetheless, flexible ligands can appropriate the coordinative demands of metal ions and form architecture in another way unavailable with rigid ligands (17).

Azobenzenecarboxylic acid compounds such as azobenzenedicarboxylic (18), azobenzene-tricarboxylic, (19) and

azobenzenetetracarboxylic acids (20-30) were employed to synthesis functional materials. The rigid 3,3′,5,5′-azobenzenetetracarboxylate ($abtc^{4-}$) ligand has four carboxylate functional group, and they can be deprotonated and can be oxidized to generate an azoxy structure in the reaction media to build various architectures. In these architectures, highly strong metal-oxygen bonds can improve stability of the framework. Additionally, an important and useful strategy for synthesis coordination polymers with interesting structures is to employ semi-flexible imidazole-based ligands (31-33). The semi-flexible N-donor ligand, obix is a wise choice for the synthesis of coordination polymers (11, 34).

Taking all these into account, $abtcH_4$ and semi-flexible bis(imidazole) derivative ligands, namely obix, were prepared and their Co(II) coordination polymer, $[Co(\mu_6\text{-}abtc)_{0.5}(\mu\text{-}obix)]_n$ was synthesized. The synthesized complex was structurally characterized by various techniques such as elemental analysis, IR spectroscopy, and X-ray diffraction. Moreover, thermal and topological analysis were studied.

MATERIAL AND METHODS

All starting materials were commercially available and AR grade. Obix and $abtcH_4$ ligands were synthesized according to previous studies (34, 35). PerkinElmer 2400C Elemental Analyzer was used to elemental analyses (C, H and N). The IR spectrum was taken in the range of 4000–400 cm^{-1} with a Bruker Tensor 27 spectrometer. TG, DTG and DTA curves are recorded in the static air atmosphere in the range of 30–700 °C with platinum crucibles.

Suitable crystals of **1** were selected for data collections, which were performed on a Bruker

D8-QUEST diffractometer equipped with graphite-monochromatic Mo-Kα radiation. The structure of complex **1** was obtained by direct methods using OLEX2 (36) and SHELXS-97 (37) software. All non-hydrogen atoms were refined anisotropically by full-matrix least squares methods in SHELXL-97 (37). The figures were drawn by using MERCURY (38). Topological analysis was performed using ToposPro software (39).

Synthesis of $[Co(\mu_6\text{-}abtc)_{0.5}(\mu\text{-}obix)]_n$ (1): A mixture of $abtcH_4$ (0.25 g, 0,69 mmol), obix (0,16 g; 0.69 mmol, $Co(NO_3)_2\cdot6H_2O$ (0.40 g; 1,38 mmol), DMF (10 mL) and two drops of conc. HNO_3 was mixed at 30 °C for half an hour. The obtained solution was sealed in a glass vial and heated at 120 °C for 3 days. Red-colored crystals of **1** were obtained (yield: 0.16 g, 12.17% based on $Co(NO_3)_2\cdot6H_2O$. Anal. Calcd. for $C_{22}H_{19}N_5O_4Co$: C, 55.47; H, 4.02; N, 14.70; Found: C, 56.03; H, 4.38; N, 13.84. IR data (KBr, cm^{-1}): 3142w, 3122w, 2955w, 2854w, 1622s, 1573sh, 1527sh, 1443m, 1408m, 1368s, 1233w, 1111w, 1090w, 937w, 829w, 780m, 707s, 654m, 615w, 566w, 490w, 471sh.

RESULTS AND DISCUSSION

Synthesis and Spectral Characterization: Obix and $abtcH_4$ ligands were synthesized, and its Co(II)-complex was obtained in acidic medium in DMF. Elemental analysis results agreed with single crystal X-ray results. FT-IR spectra of complex 1 is given in **Figure 1**. In the FT-IR spectrum of 1, the bands observed between 3142 and 2854 cm^{-1} are assigned to aromatic and aliphatic $\nu(C-H)$ stretching vibrations, respectively. The stretching vibrations of carboxylate groups of $abtc^{4-}$ ligand are seen at 1622 and 1443 cm^{-1}, respectively.
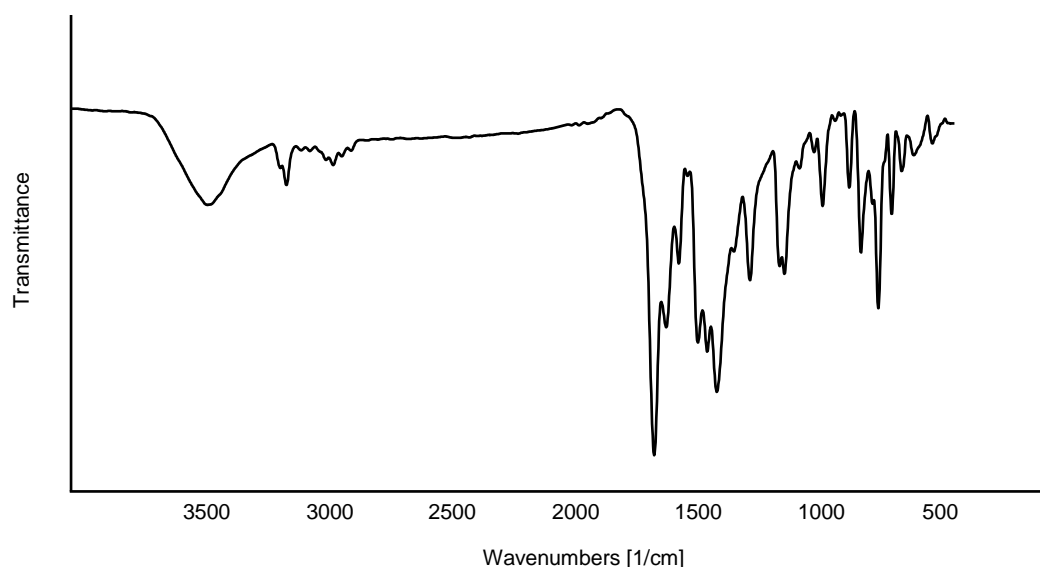
Figure 1. FT-IR spectrum of **1**.

Crystal Structure Description of [Co(μ$_6$-abtc)$_{0.5}$(μ-obix)]$_n$ (1): The X-ray crystal structural analysis shows that complex **1** is a two-dimensional (2D) coordination polymer. Complex **1** has monoclinic system and it has space group of $P2_1/n$. The asymmetric unit of **1** includes Co(II) ion, half abtc anionic ligand and one obix ligand (**Figure 2**). Each Co(II) ion in **1** shows a distorted trigonal bipyramidal environment composed of three carboxylic O atoms from different abtc^{4-} anions [Co1−O1 = 1.980 (3); Co1−O2^i = 2.009 (3) and Co1−O3^{ii} = 1.958 (3) Å ((i) −x+1, −y+1, −z; (ii) x+1, y, z)] and two nitrogen atoms from two different obix ligands [Co1−N1 = 2.106 (3) and Co1−N4^i = 2.101 (3) Å]. Secondary building units (SBU) in complex **1** were formed by two Co(II) ions that are bridged by carboxylate groups of abtc ligands. In SBU units obix ligands exhibit chair-conformation and these SBUs are stabilized by the coordination of obix ligand (34). The Co···Co distance in SBU is 3.917 (4) Å. The SBU units are bridged by oxygen atoms of anionic ligands to generate 1D structures of **1** (Figure 3). Adjacent 1D structures are bridged by other carboxylate atoms of abtc ligands to achieve layered 2D unit (Figure 4). The neighboring 2D units are further connected via van der Waals interaction, thus generating the 3D supramolecular structure (Figure 5). Topologically, complex **1** is 3,4-connected binodal net with point symbol {4.6^2}$_2${4^2.6^2.8^2} (Figure 6).
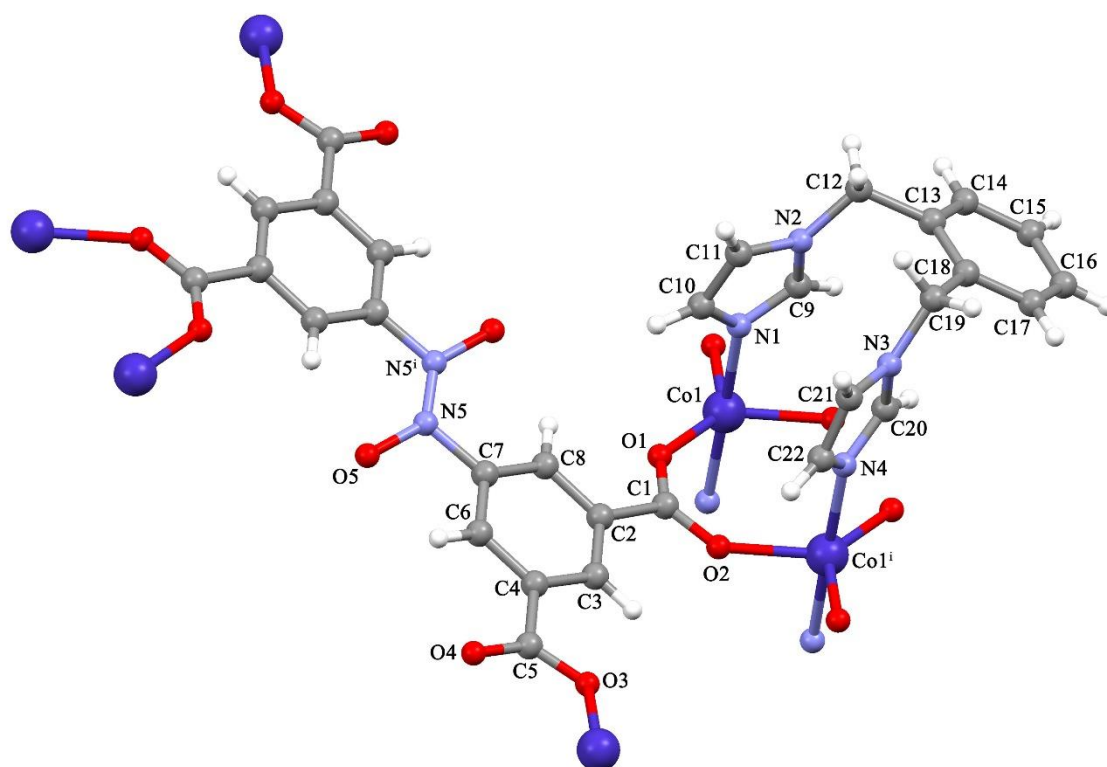
Figure 2. The molecular structure of **1**.
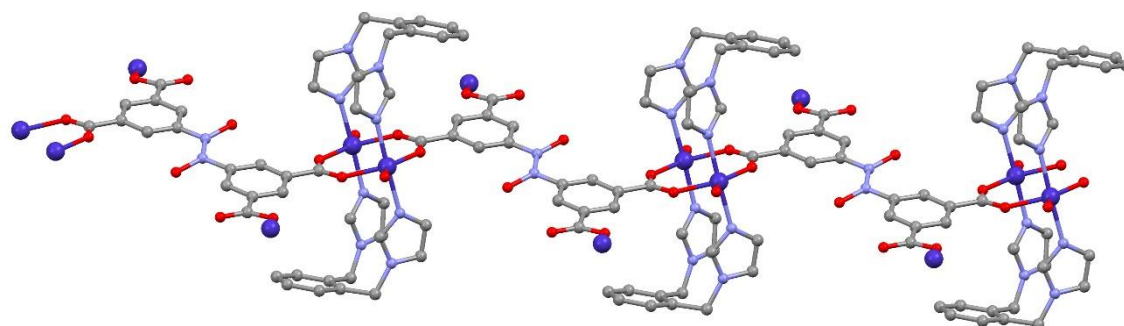
Figure 3. 1D structure of complex **1**.
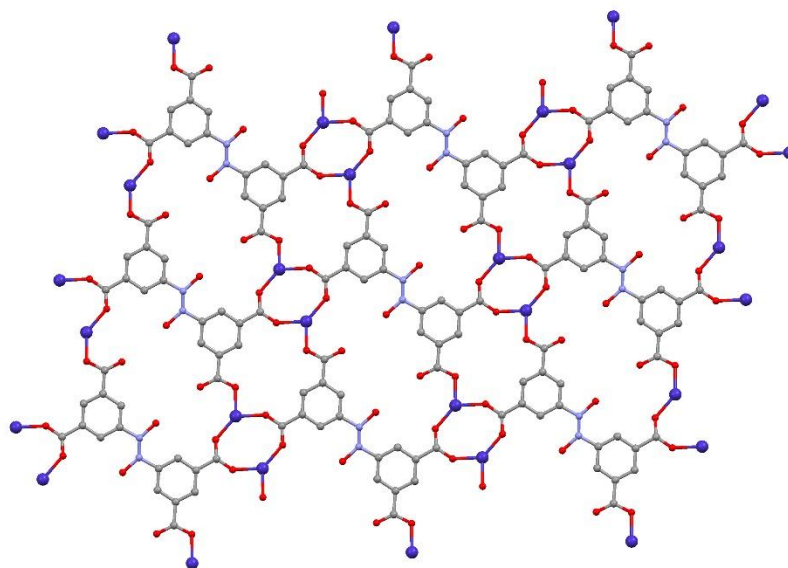
Figure 4. 2D structure of complex **1**.
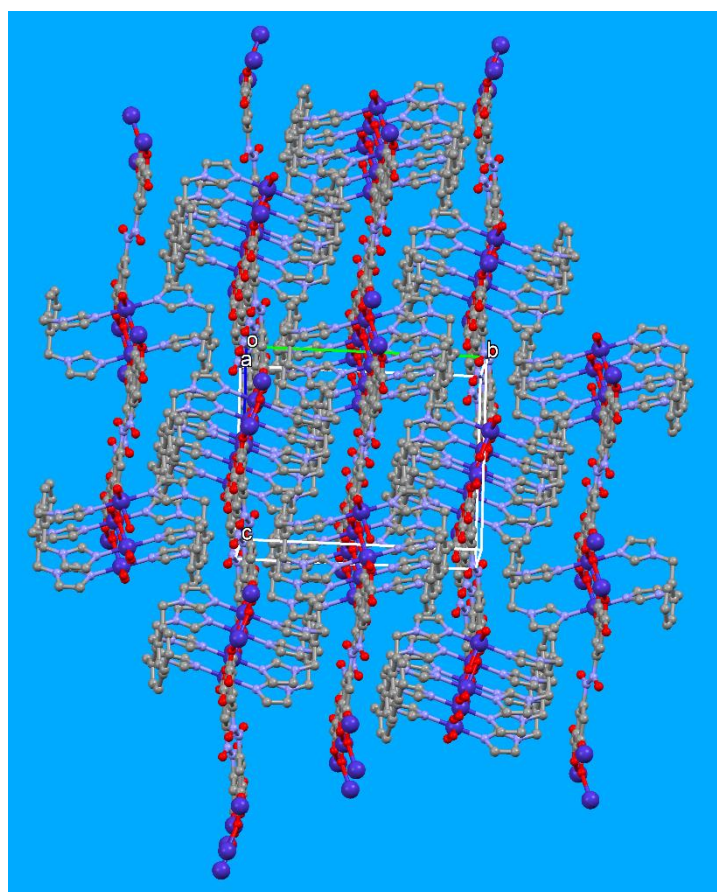
Figure 5. 3D structure of complex **1** with unit cell.

(**a**)
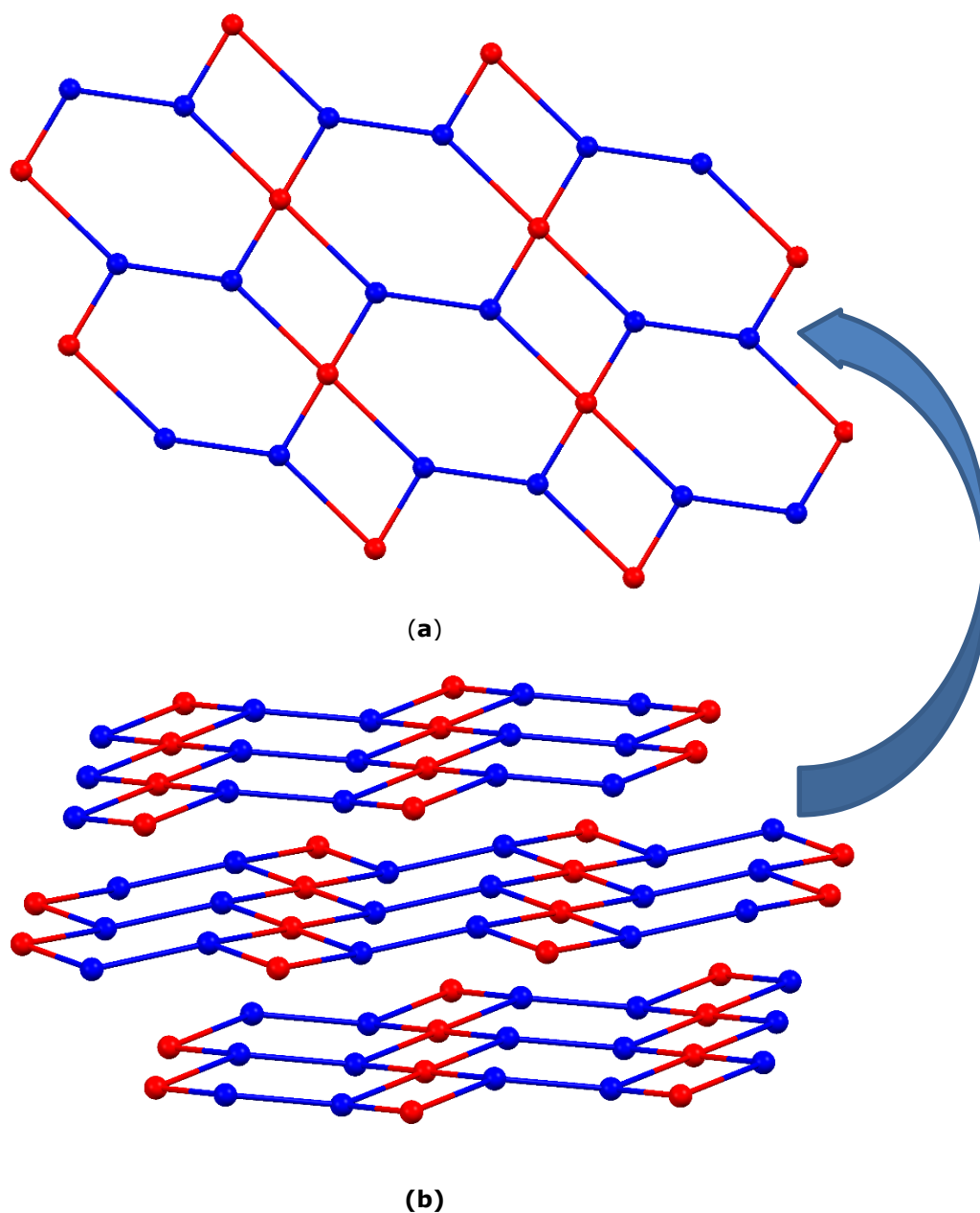
(**b**)
Figure 6. Topological presentation of complex **1.**

Table 1. Crystal data and structure refinement parameters for complex **1**.

Item	Value
Crystal data	**1**
Empirical formula	$C_{22}H_{17}CoN_5O_5$
Formula weight	490.34
Crystal system	Monoclinic
Space group	$P2_1/n$
a (Å)	9.9166 (2)
b (Å)	15.6800 (4)
c (Å)	14.0749 (3)
α (º)	90
β (º)	109.3028(11)
γ (º)	90
V (Å³)	2065.51 (8)
Z	4
D_c (g cm⁻³)	1.577
μ (mm⁻¹)	0.88
θ range (º)	2.5–27.5
Measured refls.	34803
Independent refls.	4727
R_{int}	0.034
S	1.06
R1/wR2	0.056/0.159
$\Delta\rho_{max}/\Delta\rho_{min}$ (eÅ⁻³)	2.05 /−1.24

Table 2. Selected bond distances (Å) and angles (°) for **1.**

Bond Lengths (Å)			
Co1—O1	1.980 (3)	Co1—N1	2.106 (3)
Co1—O2^i	2.009 (3)	Co1—N4^i	2.101 (3)
Co1—O3^{ii}	1.958 (3)		
Angles (°)			
N4^i—Co1—N1	176.37(11)	O2^i—Co1—N4^i	91.87 (11)
O3^{ii}—Co1—O1	136.8 (3)	O2i—Co1—N1	89.45 (11)
O3^{ii}—Co1—N1	93.24 (14)	O1—Co1—N4^i	89.75 (11)
O3^{ii}—Co1—O2^i	93.9 (3)	O1—Co1—O2^i	129.26 (18)
O3^{ii}—Co1—N4^i	90.05 (15)	O1—Co1—N1	86.79 (11)

Symmetry codes: (i) −x+1, −y+1, −z; (ii) x+1, y, z; (iii) −x+1, −y+1, −z+1; (iv) x−1, y, z.

Thermal Analysis and X-ray Powder Diffraction: The thermal behaviors and thermal stability of complex **1** were investigated by TG/DTA techniques in a dry air atmosphere with a heating rate of 10 °C/min in the temperature range 30-700 °C (Figure 7(a)). Complex **1** is thermally stable up to 401 °C, respectively. For complex **1**, on further heating, the complex is exothermically decomposed. The final residual product of complex **1** is possible CoO (obsd.: 15.21%, calcd.: 15.73%).

The crystalline product of **1** was characterized by powder X-ray diffraction (PXRD) (**Figure 7(b)**). The experimental XRD pattern is comparable with the results simulated from the single crystal data. This is show that the purity of the synthesized samples.

(**a**)
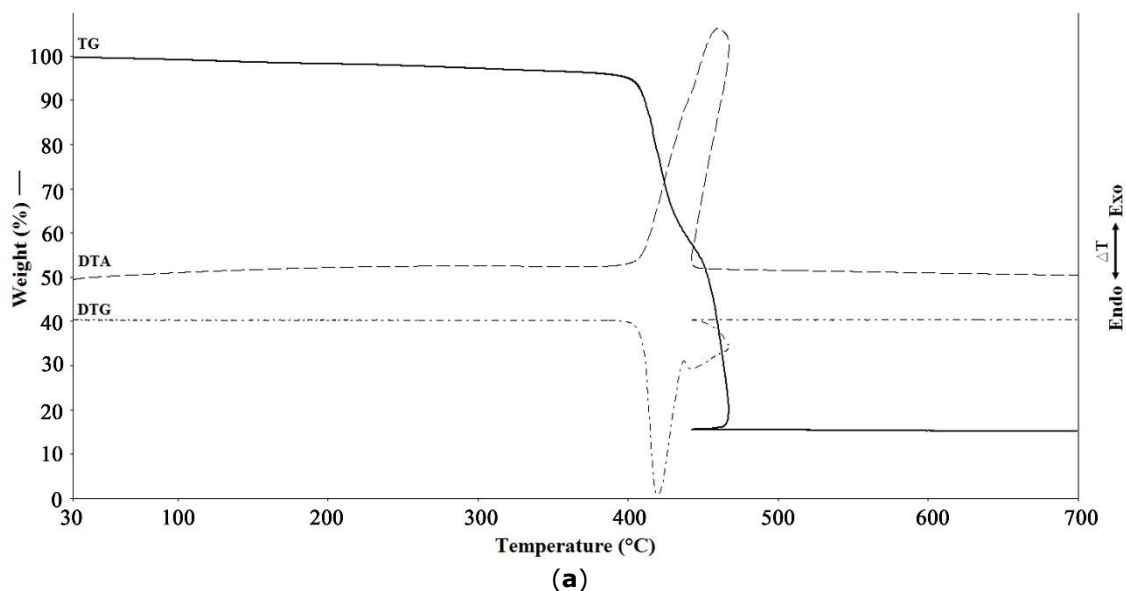
(**b**)
Figure 7. (**a**) Thermal analysis (TG, DTG and DTA) curves (**b**) XRPD pattern of complex **1.**
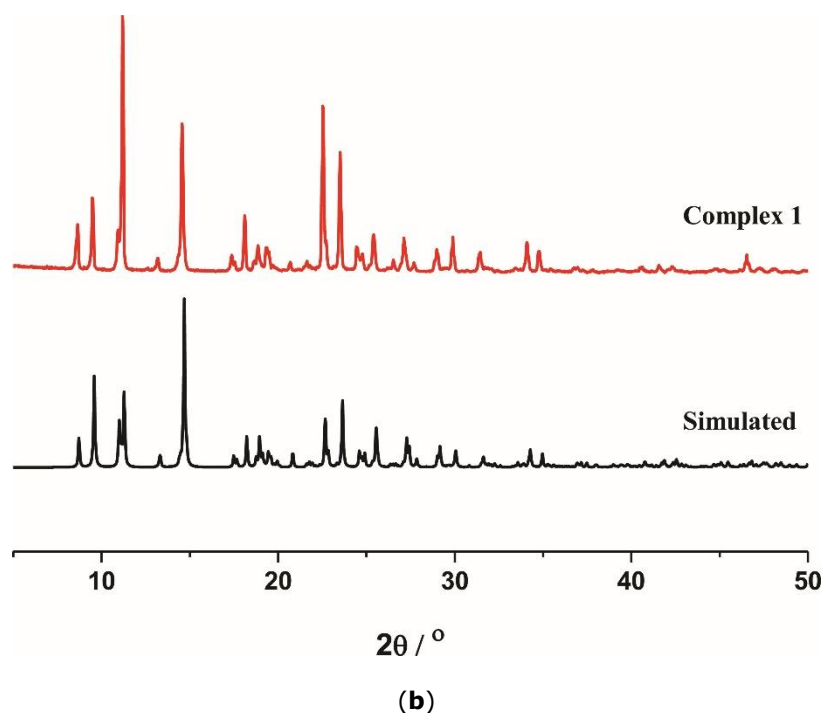
CONCLUSION

A new 2D Co(II)-coordination polymer with 3,3′,5,5′-azobenzenetetracarboxylate and semi-flexible obix was synthesized and structurally characterized. μ_6-bridged by hexadentate abtc ligands are coordinated by Co(II) ions to generate 2D polymer chains with 3,4-connected binodal net (point symbol $\{4.6^2\}_2\{4^2.6^2.8^2\}$) and topological type is 3,4L13.

REFERENCES

1.   Lu JY. Crystal engineering of Cu-containing metal–organic coordination polymers under hydrothermal conditions. Coordination Chemistry Reviews. 2003;246(1):327-47.

2.   Janiak C. Engineering coordination polymers towards applications. Dalton Transactions. 2003(14):2781-804.

3.   Thapa KB, Chen J-D. Crystal engineering of coordination polymers containing flexible bis-pyridyl-bis-amide ligands. CrystEngComm. 2015;17(25):4611-26.

4.   Biradha K, Sarkar M, Rajput L. Crystal engineering of coordination polymers using 4,4[prime or minute]-bipyridine as a bond between transition metal atoms. Chemical Communications. 2006(40):4169-79.

5.   Semerci F, Yesilel OZ, Keskin S, Darcan C, Tas M, Dal H. Construction of homo- and heterometallic-pyridine-2,3-dicarboxylate metallosupramolecular networks with structural diversity: 1D T5(2) water tape and unexpected coordination mode of pyridine-2,3-dicarboxylate. CrystEngComm. 2013;15(6):1244-56.

6.   Li X-L, Liu G-Z, Xin L-Y, Wang L-Y. Binuclear and tetranuclear Mn(II) clusters in coordination polymers derived from semirigid tetracarboxylate and N-donor ligands: syntheses, new topology structures and magnetism. Journal of Solid State Chemistry. 2017;246:252-7.

7.   Ma J, Tran LD, Matzger AJ. Toward Topology Prediction in Zr-Based Microporous Coordination Polymers: The Role of Linker Geometry and Flexibility. Crystal Growth & Design. 2016;16(7):4148-53.

8.   Zhu X-D, Li Y, Gao J-G, Wang F-H, Li Q-H, Yang H-X, et al. Two new coordination polymers with flexible alicyclic carboxylate and bipyridyl co-ligands bearing trinuclear [Ni3(COO)6] SBUs: Synthesis, crystal structures, and magnetic properties. Journal of Molecular Structure. 2017;1130:89-95.

9.   Semerci F. Syntheses and photoluminescence properties of new Zn (II) and Cd (II) coordination polymers prepared from 5-sulfoisophthalate ligand. Turkish Journal of Chemistry. 2017;41(2):243-55.

10.   Yang Y, Yang J, Du P, Liu Y-Y, Ma J-F. A series of metal-organic frameworks based on a semi-rigid bifunctional ligand 5-[(1H-1,2,4-triazol-1-yl)methoxy] isophthalic acid and flexible N-donor bridging ligands. CrystEngComm. 2014;16(28):6380-90.

11.   Semerci F, Yeşilel OZ, Yüksel F. Self-assembly of three new metal organic coordination networks based on 1,2-bis(imidazol-1yl-methyl)benzene. Polyhedron. 2015;102:1-7.

12.   Semerci F, Yeşilel OZ, Yüksel F, Şahin O. One-pot synthesis of two new metal–organic networks: hydrogen bonded mononuclear Cu(II) complex and mixed-valence Cu(I,II) coordination polymer with encapsulated 14-membered unique water cluster. Inorganic Chemistry Communications. 2015;62:29-33.

13.   Schoedel A, Li M, Li D, O'Keeffe M, Yaghi OM. Structures of Metal–Organic Frameworks with Rod Secondary Building Units. Chemical Reviews. 2016;116(19):12466-535.

14.   Ren G-J, Chang Z, Xu J, Hu Z, Liu Y-Q, Xu Y-L, et al. Construction of a polyhedron decorated MOF with a unique network through the combination of two classic secondary building units. Chemical Communications. 2016;52(10):2079-82.

15.   Eddaoudi M, Moler DB, Li H, Chen B, Reineke TM, O'Keeffe M, et al. Modular Chemistry: Secondary Building Units as a Basis for the Design of Highly Porous and Robust Metal−Organic Carboxylate Frameworks. Accounts of Chemical Research. 2001;34(4):319-30.

16.   Liu T-F, Lu J, Cao R. Coordination polymers based on flexible ditopic carboxylate or nitrogen-donor ligands. CrystEngComm. 2010;12(3):660-70.

17.   Heim D, Écija D, Seufert K, Auwärter W, Aurisicchio C, Fabbro C, et al. Self-Assembly of Flexible One-Dimensional Coordination Polymers on Metal Surfaces. Journal of the American Chemical Society. 2010;132(19):6783-90.

18.   Reineke TM, Eddaoudi M, Moler D, O'Keeffe M, Yaghi OM. Large Free Volume in Maximally Interpenetrating Networks: The Role of Secondary Building Units Exemplified by Tb2(ADB)3[(CH3)2SO]4·16[(CH3)2SO]1.

Journal of the American Chemical Society. 2000;122(19):4843-4.

19.   Meng M, Zhong D-C, Lu T-B. Three porous metal-organic frameworks based on an azobenzenetricarboxylate ligand: synthesis, structures, and magnetic properties. CrystEngComm. 2011;13(22):6794-800.

20.   Lee Y-G, Moon HR, Cheon YE, Suh MP. A Comparison of the H2 Sorption Capacities of Isostructural Metal–Organic Frameworks With and Without Accessible Metal Sites: [{Zn2(abtc)(dmf)2}3] and [{Cu2(abtc)(dmf)2}3] versus [{Cu2(abtc)}3]. Angewandte Chemie International Edition. 2008;47(40):7741-5.

21.   Zhang S, Ma J, Zhang X, Duan E, Cheng P. Assembly of Metal–Organic Frameworks Based on 3,3',5,5'-Azobenzene-tetracarboxylic Acid: Photoluminescences, Magnetic Properties, and Gas Separations. Inorganic Chemistry. 2015;54(2):586-95.

22.   Xu Y-C, Chen Y, Qiu H-J, Zeng X-S, Xu H-L, Li J, et al. Metal nuclearity affects network connectivity: a series of highly connected metal-organic frameworks based on polynuclear metal clusters as secondary building units. CrystEngComm. 2016;18(42):8182-93.

23.   Li Y-P, Zhang L-J, Ji W-J. Synthesis, characterization, crystal structure of magnesium compound based 3, 3', 5, 5'-azobenzentetracarboxylic acid and application as high-performance heterogeneous catalyst for cyanosilylation. Journal of Molecular Structure. 2017;1133:607-14.

24.   Fan L, Fan W, Li B, Liu X, Zhao X, Zhang X. Structural diversities and related properties of four coordination polymers synthesized from original ligand of 3,3[prime or minute],5,5[prime or minute]-azobenzenetetracarboxylic acid. Dalton Transactions. 2015;44(5):2380-9.

25.   Liu W, Ye L, Liu X, Yuan L, Jiang J, Yan C. Hydrothermal syntheses, structures and luminescent properties of d10 metal-organic frameworks based on rigid 3,3[prime or minute],5,5[prime or minute]-azobenzenetetracarboxylic acid. CrystEngComm. 2008;10(10):1395-403.

26.   Miller SR, Alvarez E, Fradcourt L, Devic T, Wuttke S, Wheatley PS, et al. A rare example of a porous Ca-MOF for the controlled release of biologically active NO. Chemical Communications. 2013;49(71):7773-5.

27.   Arıcı M, Yeşilel OZ, Taş M. Coordination Polymers Assembled From 3,3',5,5'-Azobenzenetetracarboxylic Acid and Different Bis(imidazole) Ligands with Varying Flexibility. Crystal Growth & Design. 2015;15(6):3024-31.

28.   Arıcı M, Yeşilel OZ, Taş M, Demiral H. Effect of Solvent Molecule in Pore for Flexible Porous Coordination Polymer upon Gas Adsorption and Iodine Encapsulation. Inorganic Chemistry. 2015;54(23):11283-91.

29.   Arıcı M, Yeşilel OZ, Taş M, Demiral H, Erer H. Construction, Structural Diversity, and Properties of Seven Zn(II)-Coordination Polymers Based on 3,3',5,5'-Azobenzenetetracarboxylic Acid and Flexible Substitute Bis(imidazole) Linkers. Crystal Growth & Design. 2016;16(9):5448-59.

30.   Arıcı M, Yeşilel OZ, Taş M. Cd(II)-coordination polymers based on tetracarboxylic acid and diverse bis(imidazole) ligands: Synthesis, structural diversity and photoluminescence properties. Journal of Solid State Chemistry. 2017;245:146-51.

31.   Erer H, Yeşilel OZ, Arıcı M. A Series of Zinc(II) 3D → 3D Interpenetrated Coordination Polymers Based On Thiophene-2,5-dicarboxylate and Bis(Imidazole) Derivative Linkers. Crystal Growth & Design. 2015;15(7):3201-11.

32.   Erer H, Karaçam S, Arıcı M, Yeşilel OZ, Çelik Ö. Hydrothermal synthesis and characterization of Zn(II), Cd(II) and Ag(I)-saccharinate complexes containing bis(imidazol) derivatives. Polyhedron. 2015;98:180-9.

33.   Wang XX, Liu YG, Van Hecke K, Goltsev A, Cui GH. Three Silver(I) Coordination Polymers Constructed from Flexible Bis(benzimidazole) and Carboxylates Ligands. Zeitschrift für anorganische und allgemeine Chemie. 2015;641(5):903-10.

34.   Tan H-Y, Zhang H-X, Ou H-D, Kang B-S. Chair-form [Ag2(1,2-bimb)2]2+ in silver(I) complexes containing the ditopic ligand 1,2-bis(1-imidazolylmethyl)benzene (1,2-bimb). Inorganica Chimica Acta. 2004;357(3):869-74.

35.   Wang X-S, Ma S, Rauch K, Simmons JM, Yuan D, Wang X, et al. Metal−Organic Frameworks Based on Double-Bond-Coupled Di-Isophthalate Linkers with High Hydrogen and Methane Uptakes. Chemistry of Materials. 2008;20(9):3145-52.

36.   Dolomanov OV, Bourhis LJ, Gildea RJ, Howard JAK, Puschmann H. OLEX2: a complete structure solution, refinement and analysis program. Journal of Applied Crystallography. 2009;42(2):339-41.

37.   Sheldrick G. A short history of SHELX. Acta Crystallogr A. 2008;64(1):112-22.

38.   Macrae CF, Edgington PR, McCabe P, Pidcock E, Shields GP, Taylor R, et al. Mercury: visualization and analysis of crystal structures. Journal of Applied Crystallography. 2006;39(3):453-7.

39.   Blatov VA, Shevchenko AP, Proserpio DM. Applied Topological Analysis of Crystal Structures with the Program Package ToposPro. Cryst Growth Des. 2014;14(7):3576-86.

Synthesis and characterization of Ti-/Zr-diphenylpropanedione complexes and their application in the ring opening polymerization of ε-caprolactone

Yağmur Gökalp ✉ **, Asgar Kayan*** ✉ (iD)

Department of Chemistry, Kocaeli University, Kocaeli, 41380, Turkey.

Abstract: The purpose has been to achieve a controlled ring-opening polymerization of ε-caprolactone, resulting in polymers with desirable properties such as high molecular weight, low polydispersity index, and highly regio-/stereo regular forms. Therefore, it is important to synthesize single site or reduced number of active site metal alkoxide compounds as catalysts. Ti(IV)/Zr(IV) diphenylpropanedione complexes were synthesized by reactions of titanium or zirconium alkoxides with diphenylpropanedione (dion) ligand. The obtained complexes were characterized by nuclear magnetic resonance (^{1}H-, ^{13}C-NMR), high resolution mass (HRMS), Fourier transform infrared (FTIR) spectroscopies and elemental analysis. These compounds were tested as catalysts for the ring opening polymerization of ε-caprolactone. The structure of poly-caprolactone (PCL) was analyzed by some spectroscopic techniques (NMR, FTIR) and gel permeation chromatography (GPC). In this work, all Ti-/Zr-complexes were effective over polymerization of ε-caprolactone in solventless environment. Consequently, ε-caprolactone polymers were obtained different average molecular weights between 7000-34000 Da with the PDI values of 1.14-1.60.

INTRODUCTION

The reactions between tetraalkoxy titanium or zirconium precursors and β-diketones and β-diketoesters have been known for over 30 years. Structures of titanium and zirconium β-diketonate complexes for the ethoxide, *n*-propoxide and other derivatives were prepared by different research groups (1-4). The allylacetoacetate and other derivatives were later prepared by Hoebbel, Schubert and co-workers (5-7). However, it is still unclear whether the complexes are monomeric, dimeric or oligomeric. For example, [Ti(acac)(OMe)$_3$]$_2$ compound is binuclear, centrosymmetric structures with asymmetric alkoxide bridges (8). In the reactions of titanium or zirconium alkoxides with β-diketonates, β-diketoesters and carboxylates the third or fourth alkoxy groups are not replaced with these organic chelate ligands because of a preferred coordination number of six or higher for metals (9,10).

It is important to stabilize the titanium or zirconium center with β-diketone ligand and also important to reduce the number of active alkoxy groups to prepare single-site or double-site titanium or zirconium complexes for catalytic activity. There are many examples of the use of metal-alkoxides based catalytic systems in polymerization reactions for manufacturing polymeric substances such as polyether, polylactone, and poly-lactides (11-

14). Due to their biocompatibility and biodegradability, these polymers have a lot of potential usage in medical, agricultural, and packaging areas (12-15).

Catalysts including single-site or reduced number of alkoxide groups stabilized with β-diketone have had a breakthrough impact in polymer synthesis. With the aim of these catalysts' molecular weights, molecular weight distributions and stereochemistry of polymers and copolymers can be controlled (15). The general formula of these catalysts are LnMOR or LnM(OR)2 (M:Metal, Ln: β-diketone) where the OR is an alkoxy group that initiates the polymerization (16,17).

In this study, our main objective is to prepare single site or double sites active catalysts by using different mole ratio of metal alkoxides and diphenylpropanedione and to characterize their structure by a combination of FTIR, ^{1}H-NMR, ^{13}C-NMR, HRMS spectroscopies and elemental analysis technique. The second objective is to see their catalytic efficiency on the ring opening polymerization of Ɛ-caprolactone. Finally, it is also important to characterize poly-ε-caprolactone by gel permeation chromatography (GPC), ^{1}H-NMR and ^{13}C-NMR, and FTIR spectroscopies.

EXPERIMENTAL

Materials and Instrumentation

Zirconium(IV) butoxide ($C_{16}H_{36}O_4Zr$, %80, Aldrich), zirconium(IV) propoxide ($C_{12}H_{28}O_4Zr$, %70, Aldrich), titanium(IV) butoxide ($C_{16}H_{36}O_4Ti$, %97), titanium(IV) isopropoxide ($C_{12}H_{28}O_4Ti$, %97, Aldrich), 3-diphenyl-1,3-propanedione ($C_{15}H_{12}O_2$, %98, Aldrich), and Ɛ –caprolactone ($C_6H_{10}O_2$, Alfa Aesar) were used as received. Solvents such as n-butanol (C_4H_9OH, 99%, Aldrich), isopropanol (C_3H_7OH, Aldrich), and others were dried over activated 4 Å molecular sieves before use. Polymerization reactions were carried out under nitrogen atmosphere.

The infrared spectra of synthesized compounds and PCL were recorded on a Bruker Tensor 27 FTIR spectrometer using single reflection ATR universal plate of diamond crystal. The Ti-/Zr-compounds, and PCL were scanned from 400 to 4000 cm^{-1} with a resolution of 4 cm^{-1}. ^{1}H and ^{13}C[^{1}H]NMR measurements were carried out with a Bruker 400 MHz spectrometers. The elemental analyses were carried out on a LECO CHNS-932 elemental analyzer.

Mass spectrometry (SCIEX 4000 QTRAP LC–MS/MS, HRMS) were used for measuring the molecular masses of complexes with electrospray ionization (ESI ±) method. GPC analysis was performed at 30 °C on a Shimadzu prominence GPC system equipped with a RID-10A refractive index detector, a LC-20AD solvent delivery unit, a CTO10AS column oven and a set of two columns, PSS SDV 5 µL 1000 Å and PSS SDV 5 µL 50 Å. THF (HPLC grade) was used as the mobile phase at 1.0 mL/min. The sample concentration was 10 mg/5mL and the injection volume was 50 µL. The calibration curve was made with polystyrene standards covering the molecular weight range from 162 to 34,300 Da.

Reaction of titanium(IV) butoxide with 1,3-diphenyl-1,3-propanedione in 1:1 mole ratio (1)

The reaction of 1,3-diphenyl-1,3-propanedione (2.0×10^{-3} mol, 0.46 g) with titanium n-butoxide (2.0×10^{-3} mol, 0.70 g) in 20 mL of n-butanol was carried out similarly to the preceding reaction. ^{1}H-NMR(CDCl$_3$, ppm): δ 1.03 (t, CH$_3$, OBu), 1.53 (m, CH$_3$-C$\underline{H}_2$, OBu), 1.78 (pentet, C$\underline{H}_2$-CH$_2$O, OBu), 3.73 (t, J=6.40 Hz, CH$_2$O, OBu, *cis* to dion), 4.74 (t, J= 6.56 Hz, CH$_2$O, OBu, *trans* dion), 7.07 (1H, OC-C$\underline{H}$=, dion), 7.38 (2H, C$_6$H$_5$, dion), 7.46 (1H, C$_6$H$_5$, dion), 7.62 (3H, C$_6$H$_5$, dion), 7.94 (2H, C$_6$H$_5$, dion), 8.30 (2H, C$_6$H$_5$, dion). ^{13}C- NMR (CDCl$_3$, ppm): δ 14.10 (CH$_3$, OBu), 19.39 (CH$_3$-C$\underline{H}_2$, OBu), 35.30 (C$\underline{H}_2$-CH$_2$O , OBu) , 73.17 (CH$_2$O, OBu, *cis* to dion), 76.82 (CH$_2$O, OBu, *trans* to dion), 94.93 (OC-CH$_2$-CO, dion, keto-form, the ratio of keto to enol form is ~1/5), 96.13 (dyad, OC-$\underline{C}$H=, dion), 127.81-138.64 (C=C, C$_6$H$_5$, dion), 182.29 (CH=$\underline{C}$-O, dion, enol form), 184.84 (C=O, dion). FTIR (cm^{-1}): 3056, 2954, 2927, 2869, 2838, 1594, 1546, 1518, 1476, 1363, 1222, 1071, 745, 682, 617, 430. Mass spectrum: 529.184 Da for molecular ion [Ti(OBu^n)$_3$(dion) +K]$^+$ (=TiC$_{27}$H$_{38}$O$_5$+K$^+$) or [Ti(OBu^n)$_3$(dion) +H]$^+$ (=TiC$_{27}$H$_{38}$O$_5$+H$^+$).

Reaction of titanium(IV) butoxide with 1,3-diphenyl-1,3-propanedione in 1:2 mole ratio (2)

The reaction of 1,3-diphenyl-1,3-propanedione (4.0×10^{-3} mol, 1.0 g) with titanium n-butoxide (2.0×10^{-3} mol, 0.70 g) in 20 mL of n-butanol was carried out similarly to the preceding reaction. ^{1}H-NMR(CDCl$_3$, ppm): δ 0.95 (t, CH$_3$, J=7.4 Hz, OBu), 1.54 (CH$_3$-C$\underline{H}_2$, OBu), 1.79 (pentet, C$\underline{H}_2$-CH$_2$O, OBu), 4.74 (t, CH$_2$O, J=6.58 Hz, OBu), 7.07 (2H, OC-C$\underline{H}$=, dion), 7.40 (4H, C$_6$H$_5$, dion), 7.49 (2H, C$_6$H$_5$, dion), 7.64 (6H, C$_6$H$_5$, dion), 7.95 (4H, C$_6$H$_5$, dion), 8.30 (4H, C$_6$H$_5$, dion). ^{13}C- NMR (CDCl$_3$, ppm): δ 14.14 (CH$_3$, OBu), 19.37 (CH$_3$-C$\underline{H}_2$, OBu), 35.31 (C$\underline{H}_2$-CH$_2$O, OBu) , 78, 60, 76.84 (CH$_2$O, OBu), 96.12 (dyad, OC-$\underline{C}$H=, dion), 127.83-137.97 (C=C, C$_6$H$_5$, dion), 182.28 (CH=$\underline{C}$-O, dion, enol form), 184.82 (C=O, dion). FTIR (cm^{-1}): 3055, 2954, 2926, 2885,

2837, 1592, 1542, 1517, 1470, 1451, 1366, 1313, 1299, 1226, 1071, 1022, 749, 714, 685, 550. Elemental analysis, $C_{38}H_{40}O_6Ti$ (640.59 g/mol): Calc. C 71.25, H 6.29% ; found: C 69.20, H 6.70%. Mass spectrum: 641.2386 Da for molecular ion $[Ti(OBu^n)_2(dion)_2 +H]^+$ $(=TiC_{38}H_{40}O_6+H^+)$.

Reaction of titanium(IV) isopropoxide with 1,3-diphenyl-1,3-propanedione in 1:1 mole ratio (3)

The reaction of 1,3-diphenyl-1,3-propanedione (2.0×10^{-3} mol, 0.46 g) with titanium iso-propoxide (2.0×10^{-3} mol, 0.59 g) in 20 mL of isopropanol was carried out similarly to the preceding reaction. ^{1}H-NMR(CDCl$_3$, ppm): δ 1.29 (d, J=6.12 Hz, CH$_3$, OPr^i), 5.05 (septet, J=6.15 Hz, OCH, OPr^i), 7.02 (H, OC-C$\underline{H}$=, dion), 7.38 (m, 2H, C$_6$H$_5$, dion), 7.46 (t, 1H, J= 6.92 Hz, C$_6$H$_5$, dion), 7.60 (m, 3H, C$_6$H$_5$, dion), 7.92 (d, 2H, J= 7.5 Hz, C$_6$H$_5$, dion), 8.25 (d, 2H, J= 7.0 Hz, C$_6$H$_5$, dion). FTIR (cm^{-1}): 3060, 2980, 2930, 2870, 1592, 1548, 1520, 1465, 1360, 1330, 1120, 1005, 940, 860, 618, 460. Elemental analysis, $C_{24}H_{32}O_5Ti$ (448.37 g/mol): Calc. C 64.29, H 7.19% ; found: C 62.90, H 6.65%.

Reaction of titanium(IV) isopropoxide with 1,3-diphenyl-1,3-propanedione in 1:2 mole ratio (4)

The reaction of 1,3-diphenyl-1,3-propanedione (4.0×10^{-3} mol, 1.0 g) with titanium isopropoxide (2.0×10^{-3} mol, 0.59 g) in 20 mL of isopropanol was carried out similarly to the preceding reaction. ^{1}H-NMR (CDCl$_3$, ppm): δ 0.94 (CH$_3$, OPr^i), 3.57 (CHO, OPr^i), 7.62 (OC-CH=, dion), 7.30-7.89 (CH=, C$_6$H$_5$,dion). Elemental analysis, $C_{36}H_{36}O_6Ti$ (612.53 g/mol): Calc. C 70.59, H 5.92% ; found: C: 69.08, H: 6.37%.

Reaction of zirconium(IV) butoxide with 1,3-diphenyl-1,3-propanedione in 1:1 mole ratio (5)

1,3-diphenyl-1,3-propanedione (2.0×10^{-3} mol, 0.46 g) was added to a solution of zirconium(IV) butoxide (2.0×10^{-3} mol, 0.96 g) in 20 mL of n-butanol. The reaction mixture was stirred for three hours at 35 °C over an oil bath. Then, the solvent was removed by rotary evaporator at 50 °C under vacuum. ^{1}H-NMR (DMSO, ppm): δ 0.709 (CH$_3$, OBu) , 1.14 (CH$_3$-C$\underline{H}_2$- , OBu), 1.25 (C$\underline{H}_2$-CH$_2$O , OBu), 4.1 (CH$_2$O, OBu), 7.3-7.7 (C$_6$H$_5$, dion) 7.9 (OC-CH=, dion). ^{13}C- NMR (DMSO, ppm): δ 13.8 (CH$_3$, OBu), 18.6 (CH$_3$-C$\underline{H}_2$, OBu), 34.6 (C$\underline{H}_2$-CH$_2$O, OBu), 70.7 (CH$_2$O, OBu), 95.05 (CO-C$\underline{H}$=, dion), 127-137 (C$_6$H$_5$, dion), 182.9 (C$_6$H$_5$-C$\underline{O}$, dion). FTIR (cm^{-1}): 3060 (CH=C, asym str), 3027 (CH=, Ph), 2953 (sp^3-CH, asym str), 2868 (sp^3-CH, asym str), 1594 (C=C, Ph), 1546 (C=O, asym), 1518 (C=C,

Ph), 1476, 1363 (C-O, sym), 1222, 1071 (C-O, C-C), 745, 682, 617, 430.

Reaction of zirconium(IV) butoxide with 1,3-diphenyl-1,3-propanedione in 1:2 mole ratio (6)

The reaction of 1,3-diphenyl-1,3-propanedione (4.0×10^{-3} mol, 1.0 g) with zirconium n-butoxide (2.0×10^{-3} mol, 0.96 g) in 20 mL of n-butanol was carried out similarly to the preceding reaction. ^{1}H-NMR (CDCl$_3$, ppm): δ 1.0 (brd, CH$_3$, OBu), 1.46 (sextet, J= 7.55 Hz, CH$_3$-C$\underline{H}_2$, OBu), 1.62 (pentet, J=7.87 Hz, C$\underline{H}_2$-CH$_2$O, OBu), 3.69 (brd, CH$_2$O, OBu), 7.08 (2H, OC-C$\underline{H}$=, dion), 7.37 (brd, 2H, C$_6$H$_5$, dion), 7.44 (brd, 6H, C$_6$H$_5$, dion), 7.50 (d, J=6.8 Hz, 4H, C$_6$H$_5$, dion), 8.11 (d, J=6.3 Hz, 4H, C$_6$H$_5$, dion), 8.16 (d, J=6.3 Hz, 4H, C$_6$H$_5$, dion). ^{13}C- NMR (CDCl$_3$, ppm): δ 13.93 (CH$_3$, OBu), 19.01 (CH$_3$-C$\underline{H}_2$, OBu), 34.93 (C$\underline{H}_2$-CH$_2$O, OBu), 77.43 (CH$_2$O, OBu), 95.81 (OC-C$\underline{H}$=, dion), 128.04-138.73 (C=C, C$_6$H$_5$, dion), 182.88 (CH=C$\underline{C}$-O, dion, enol form), 183.65 (C=O, dion). FTIR (cm^{-1}): 3059, 2953, 2868, 1593, 1519, 1476, 2365, 1319, 1220, 1068, 1024, 944, 719, 684, 617, 534, 454. Mass spectrum: 759.135 Da for $[Zr(OBu^n)_2(dion)_2$ .C$_4$H$_9$OH+H]$^+$, 683.195 Da for molecular ion $[Zr(OBu^n)_2(dion)_2+H]^+$.

Reaction of zirconium(IV) propoxide with 1,3-diphenyl-1,3-propanedione in 1:1 mole ratio (7)

The reaction of 1,3-diphenyl-1,3-propanedione (2.0×10^{-3} mol, 0.46 g) with zirconium n-propoxide (2.0×10^{-3} mol, 0.94 g) in 20 mL of n-propoxide was carried out similarly to the preceding reaction. ^{1}H-NMR(CDCl$_3$, ppm): δ 0.80 (t, J=6.69 Hz, CH$_3$, OPr), 1.46 (m, CH$_3$-C$\underline{H}_2$, OPr), 3.48, 3.90 (brd, CH$_2$O, OPr), 7.13 (H, OC-C$\underline{H}$=, dion), 7.28 (t, J=7.53 Hz, 3H, C$_6$H$_5$, dion), 7.35 (d, J=7.33 Hz, 1H, C$_6$H$_5$, dion), 7.79 (d, J=7.22 Hz, 2H, C$_6$H$_5$, dion), 7.88 (t, J=7.56 Hz, 2H, C$_6$H$_5$, dion), 7.96 (d, J=7.22 Hz, 2H, C$_6$H$_5$, dion).

Reaction of zirconium(IV) propoxide with 1,3-diphenyl-1,3-propanedione in 1:2 mole ratio (8)

The reaction of 1,3-diphenyl-1,3-propanedione (4.0×10^{-3} mol, 1.0 g) with zirconium n-propoxide (2.0×10^{-3} mol, 0.94 g) in 20 mL of n-propoxide was carried out similarly to the preceding reaction. ^{1}H-NMR(CDCl$_3$, ppm): δ 0.94 (t, J=7.46 Hz, CH$_3$, OPr), 1.59 (sextet, J=7.18 Hz, CH$_3$-C$\underline{H}_2$, OPr), 3.57, 3.60 (brd, CH$_2$O, OPr), 7.03 (2H, OC-C$\underline{H}$=, dion), 7.33 (brd, H, C$_6$H$_5$, dion), 7.38 (brd, 3H, C$_6$H$_5$, dion), 7.44 (brd, 2H, C$_6$H$_5$, dion), 8.06 (brd, 2H, C$_6$H$_5$, dion), 8.10 (brd, 2H, C$_6$H$_5$, dion). FTIR (cm^{-1}): 2969, 2872, 2319,1738, 1593, 1538, 1518, 1476, 1454, 1376-1300, 1224, 1182, 1145, 1073, 1008, 969, 944, 785, 751, 618. Elemental analysis,

$C_{36}H_{36}O_6Zr$ (655.89 g/mol): Calc. H: 5.53% ; found: H 5.40%.

Polymerization of ε-caprolactone with Ti/Zr-dion complexes (9)

Ti/Zr-dion complexes (20 mg) were mixed with ε-caprolactone (1.5 mL) in a vial under nitrogen atmosphere. The mixture was stirred without solvent at 80°C for different times as indicated in Table 1. ^1H NMR (CDCl$_3$, ppm): δ 4.08 (t, J = 7.0 Hz, $^eCH_2$-O), 2.30 (t, J = 7.0 Hz, $^aCH_2$-C = O), 1.67 (m, J = 7.0 Hz, $^{b,d}CH_2$), 1.39 (m, J = 7.0 Hz, $^gCH_2$). ^{13}C NMR (CDCl$_3$, ppm): δ 173.80 (C = O), 64.4 ($^eCH_2O$), 34.3 ($^aCH_2$), 28.6 ($^dCH_2$), 25.7 ($^bCH_2$), 24.8 ($^gCH_2$). [O = C-$^aCH_2$$^bCH_2$$^gCH_2$$^dCH_2$$^eCH_2$O-]. FTIR (cm^{-1}): 2940 (CH$_2$, asym str), 2864 (CH$_2$, sym str), 1720 (C=O), 1470 (CH$_2$, bending), 1365 (CH$_2$, bending), 1292 (C–C), 1240 (C–O–C, asym), 1165 (C–O–C, sym), 1046, 961,730.

RESULTS AND DISCUSSION

Stoichiometric reactions of 1,3-diphenyl-1,3-propanedione with zirconium or titanium alkoxides in 1:1 or 2:1 molar ratio in corresponding alcohols at 35 °C produced compounds (1-8). The formulation of compounds was based on combinations of ^1H, ^{13}C-NMR, FTIR, and mass spectroscopies, and elemental analysis. The structure of compounds can be drawn as seen in Scheme 1 for 1:1 mole ratio of 1,3-diphenyl-1,3-propanedione to M(OR)$_4$ and 2:1 mole ratio of 3-diphenyl-1,3-propanedione to M(OR)$_4$, [M-OR: Ti-OBu^n, Ti-OPr^i, Zr-OBu^n, Zr-OPr^n)], respectively.

C$_6$H$_5$=Ph

n=1, A　　　　　　　　n=2, B
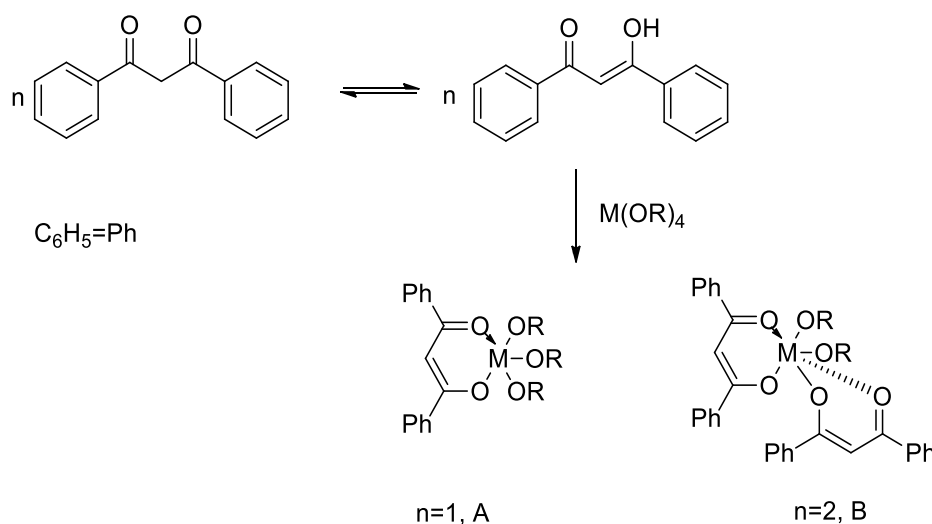
Scheme 1. Structures of [M(OR)$_3$(dion)] and [M(OR)$_2$(dion)$_2$], (M=Ti, Zr; OR=OBu^n, OPr^n, OPr^i).

High resolution mass spectrometry (ESI-TOF-MS) was used to determine the masses of complexes. The samples were measured under positive and negative soft ionization conditions (ES+/ES-). The evaluation of the mass spectra which is based on isotopic patterns clearly showed metal-containing ions.

For example, the mass spectrum of the product resulted from reaction between 1,3-diphenyl-1,3-propanedione and Ti(OBu^n)$_4$ in 1:1 molar ratio gave peaks at 529.184 Da for molecular ion [C$_{27}$H$_{38}$O$_5$Ti + K]$^+$ and at 491.228 Da for [C$_{27}$H$_{38}$O$_5$Ti]$^+$ (Figure 1).
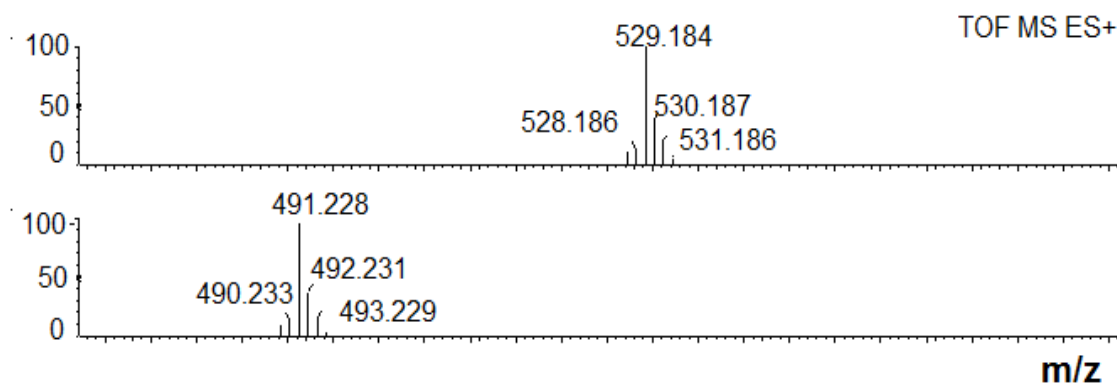

Figure 1. Mass spectrum of [Ti(OBu^n)$_3$(dion)] compound.

The suggested formula of monomeric compound was consistent with elemental analysis and ^1H, ^{13}C-NMR and FTIR results. The FTIR spectra of the metal alkoxides $Zr(OBu^n)_4$, $Ti(OBu^n)_4$ and others are similar and show no absorption bands in the region of 1500–1800 cm^{-1}. The FTIR spectrum of $[Ti(OBu^n)_3(dion)]$ shows no free dion groups and but the two stretching vibrations (C=C and C=O) of the enolic form of the β-diketone at ~1615 and 1546 cm^{-1} show that all of dion is bonded to the Ti-butoxide. There was no stretching vibrations of $\upsilon(C=O)$ of the keto form of free β-diketone was at about 1740 cm^{-1}. These results were consistent with literature studies [5, 18]. ^1H and ^{13}C NMR spectra of compound supported the mass and FTIR spectra. For instance, The ^1H NMR spectrum of $[Ti(OBu^n)_3(dion)]$ complex showed the expected peaks and peak multiplicities. For example, ^1H NMR spectrum of $[Ti(OBu^n)_3(dion)]$ showed triplets at 0.95 ppm with J = 7.4 Hz for CH_3 protons, multiplet at 1.54 ppm with J = 7.4 Hz for CH_2 protons, triplets at 3.73 ppm with J = 6.4 Hz for OCH_2 protons of butoxide groups *cis* to dion and triplets at 4.74 ppm with J = 6.6 Hz for OCH_2 protons of butoxide groups *trans* to dion in titanium complex (Figure 2). The presence of very small CH_2 keto-form protons signal at around 2.35 ppm indicates that dion is predominantly coordinated to the titanium atom in the enolate form. The signal for the CH= proton of enol-form was at 7.64 ppm in the ^1H NMR spectrum. The integration of ^1H NMR spectrum indicated that very small amounts of the alkoxide groups underwent hydrolysis and condensation reactions. The deviation less than 2% in elemental analysis for carbon atoms also supported the presence of small amounts of hydrolysis and condensation reactions.
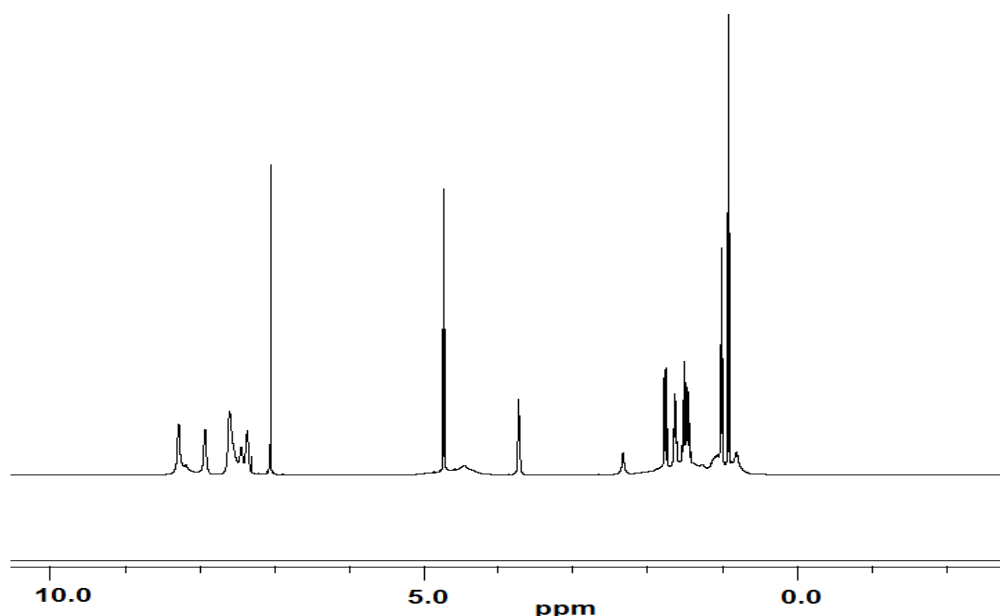

Figure 2. ^1HNMR spectrum of $[Ti(OBu^n)_3(dion)]$.

^{13}C NMR spectrum of $[Ti(OBu^n)_3(dion)]$ compound (Figure 3) gave the expected characteristic peak for enol-form of dion bonded to titanium at 96.13 ppm for OC-$\underline{C}$H=. As seen in the ^{13}C NMR spectrum, there was no peak for carbonyl carbon atom of free keto-form of 1,3-diphenyl-1,3-propanedione at ~ 190 ppm regions. The peaks at 182.28 and 184.82 ppm belongs to CH=$\underline{C}$-O (dion, enol form) and 184.82 (C=O, dion, enol form), respectively.

Reactions 1,3-diphenyl-1,3-propanedione with $M(OR)_4$ in 2:1 mole ratio resulted in the formation of $[M(OR)_2(dion)_2]$. All spectroscopic measurements given in the experimental parts support the suggested formulations. The studies of dion/$Ti(OBu^n)_4$ in 2:1 mole ratio showed that diones are completely coordinated to titanium atom just in enolate form as drawn in Scheme 1. The mass spectrum of $[Ti(OBu^n)_2(dion)_2]$ showed the molecular ion having a mass of 641.2386 Da (Figure 4). The molecular weight of 641.2386 Da confirmed the suggested formula for the compound prepared from $Ti(OBu^n)_4$ and 1,3-diphenyl-1,3-propanedione in 1:2 mole ratio.
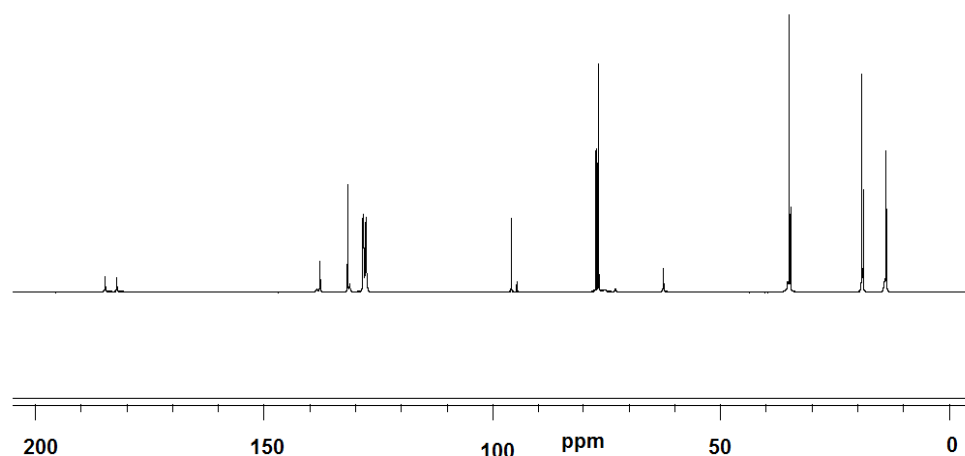
Figure 3. ^{13}C NMR spectrum of [Ti(OBu^n)$_3$(dion)].
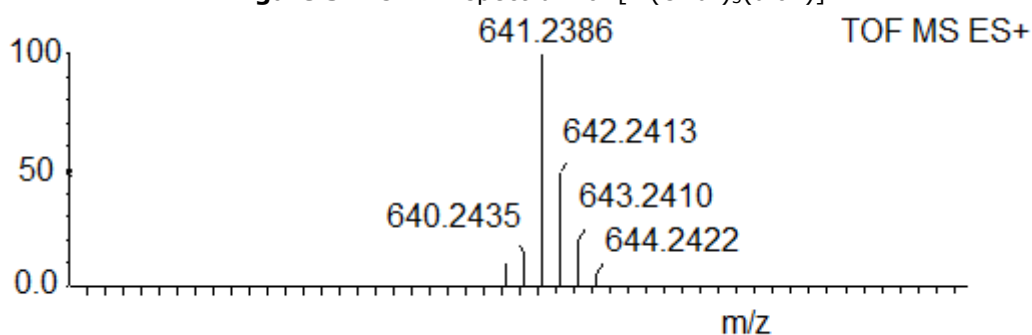
Figure 4. Mass spectrum of [Ti(OBu^n)$_2$(dion)$_2$].

As in titanium-dion compounds, the reaction between 1,3-diphenyl-1,3-propanedione and Zr(OBu^n)$_4$ in 2:1 mole ratio resulted in the formation of [Zr(OBu^n)$_2$(dion)$_2$]. The mass spectrum of [Zr(OBu^n)$_2$(dion)$_2$] showed the molecular ion having a mass of 683.1950 Da for (=ZrC$_{38}$H$_{40}$O$_6$+H$^+$) (Figure 5). The molecular weight of 683.1950 Da confirmed the suggested formula with the presence of one mole of n-butanol.

In contrast to β-diketone metal alkoxide compounds, the imine, amine, and carboxylate metal alkoxide compounds were resulted in oligomeric structures like tetramer or hexamer structures (19-21). The degree of oligomerization is affected by the acidity or basicity of ligands, stirring times and

temperatures of reactions, the freshness of metal alkoxides, solvent types, *etc*.

The development of "single-site" or "reduced number of active sites" catalysts has been a key goal for producing polymers with controllable molecular weights and low polydispersity index (22). The Ti/Zr-dion complexes were very effective in the polymerization reactions of ε-caprolactone when they were used as catalysts (Table 1). For example, ε-caprolactone polymers prepared with Zr(OBu^n)$_2$(dion)$_2$ by stirring at 80 °C for 18 hours, the main peak appeared at 21140 Da for weight average molecular weight (M*w*) with a conversion of 78%.
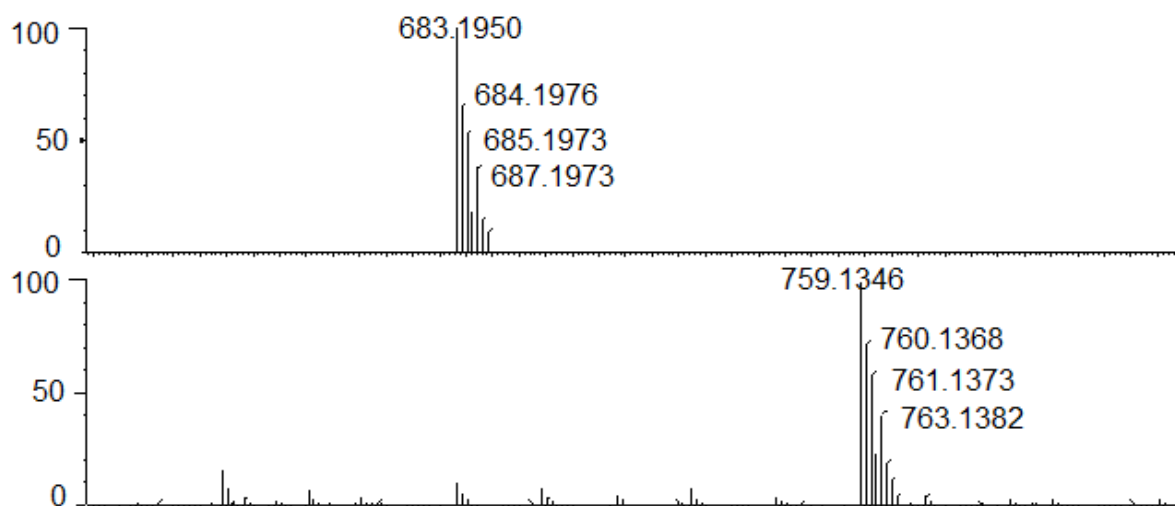
Figure 5. Mass spectrum of $[Zr(OBu^n)_2(dion)_2] \cdot C_4H_9OH$.

Metal alkoxide compounds proceed through a coordination-insertion mechanism for the ring opening polymerization (ROP) of ε-caprolactone [23, 24]. In this mechanism (Scheme 2), the Ti/Zr-dion compounds first allow bonding of the ε-caprolactone to the metal center by oxygen atom of the carbonyl group. Then, the nucleophilic alkoxide group attacks the carbon atom of the activated carbonyl group, leading to ester cleavage. Subsequently, ε-caprolactone monomers incorporate to the metal center and insert into the metal-alkoxide bond. Consequently, polycaprolactone with an alkoxide end group is obtained.
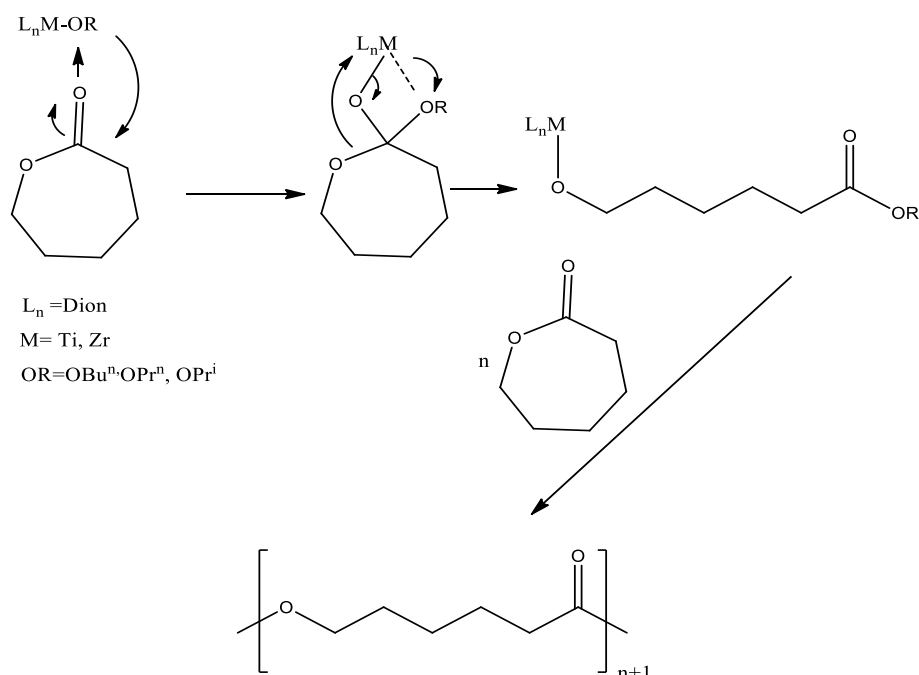
Scheme 2. Polymerization of ε-caprolactone with Ti/Zr-dion catalysts.

Each carbon atom of PCL appeared at only one region 173.80 (C = O), 64.4 ($^eCH_2O$), 34.3 ($^aCH_2$), 28.6 ($^dCH_2$), 25.7 ($^bCH_2$), 24.8 ($^gCH_2$) ppm in ^{13} C-NMR spectrum. These data are the evidence of regular polymerization of ε-CL and are consistent with the literature data (25).

The Mw, Mn, and PDI values for PCL prepared with metal(dion)alkoxide catalysts at 80 °C are summarized in Table 1.

Table 1. Data for PCL obtained from GPC measurements.

Catalysts	Time (h)	M_w (Da)	M_n (Da)	PDI(M_w/M_n)	Conversion (%)
Ti(OBu^n)$_3$(dion)	12	10640	9410	1.14	54
Ti(OBu^n)$_3$(dion)	24	12770	11000	1.16	92
Ti(OBu^n)$_2$(dion)$_2$	24	6990	5880	1.19	45
Ti(OBu^n)$_2$(dion)$_2$	36	8990	7300	1.21	90
Ti(OPr^i)$_3$(dion)	24	13720	11780	1.16	60
Ti(OPr^i)$_3$(dion)	36	15900	13475	1.18	92
Ti(OPr^i)$_2$(dion)$_2$	36	20260	16010	1.26	59
Zr(OBu^n)$_3$(dion)	4.0	30820	25710	1.20	44
Zr(OBu^n)$_3$(dion)	10	34000	27420	1.24	93
Zr(OBu^n)$_2$(dion)$_2$	18	21140	13290	1.59	78
Zr(OPr^n)$_3$(dion)	2	22420	17650	1.27	66
Zr(OPr^n)$_2$(dion)$_2$	10	17360	11970	1.45	60
Zr(OPr^n)$_2$(dion)$_2$	16	19800	13380	1.48	92

The PDI values for PCL produced using [M(OR)$_3$(dion)] catalysts are noticeably smaller than that for PCL produced using [M(OR)$_2$(dion)$_2$] catalysts. As seen from Table 1, the polymerization with [M(OR)$_2$(dion)$_2$] catalysts exhibited a slower kinetic of reaction and the polymer synthesized lower weight

average molecular weight than with [M(OR)$_3$(dion)] catalysts.

The GPC curve of polycaprolactone displayed unimodal behavior with narrow distribution index indicating regular polymerization of ε-caprolactone (Figure 6).
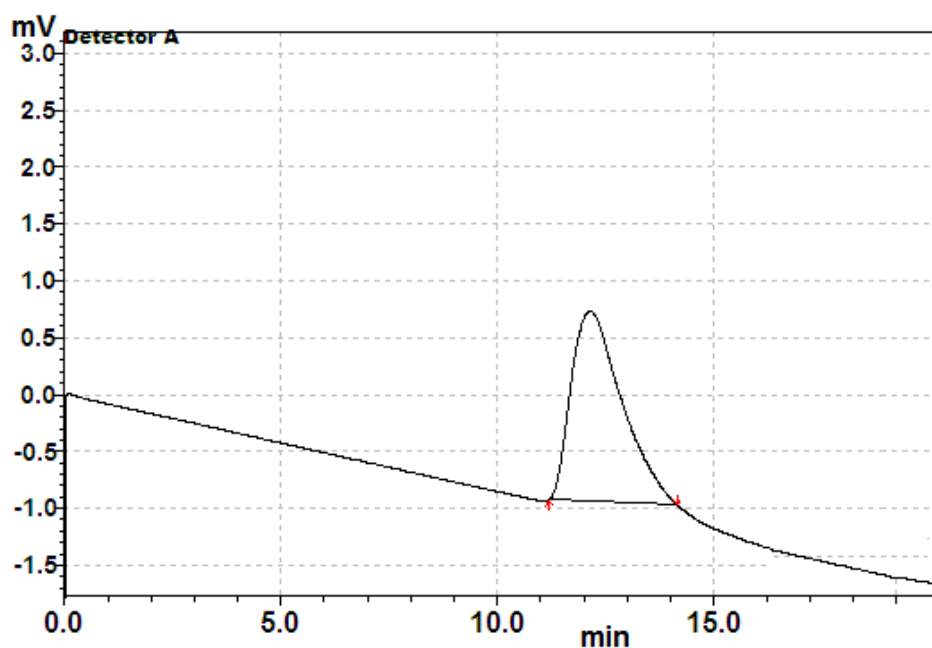
Figure 6. Gel permeation chromatogram of PCL prepared at 80 °C with the catalyst [Zr(OPr^n)$_3$(dion)].

CONCLUSIONS

In this study, Ti/Zr alkoxide precursors were stabilized by diphenylpropanedione (dion) ligand using sol-gel process. It is interesting to note that the alkoxide groups are significantly more reactive than the β-diketonate ligands. The β-diketonate ligands are bidentate ligands and form stronger bonds with the coordinating Ti/Zr atom than monodentate (alkoxide)

ligands. Therefore, the dion ligands displace the alkoxide groups bonded to Ti/Zr atoms. The synthesized Ti/Zr-dion compounds were characterized by elemental analysis and spectroscopic techniques such as ^{1}H-, ^{13}C-NMR, high resolution mass (HRMS), FTIR. These complexes were used as catalysts on the ring opening polymerization of ε-caprolactone. These results demonstrated that an alkoxide substituent on the

diphenylpropanedione-Ti/Zr compounds acted as the initiator on ε-caprolactone under solvent-free conditions. As expected, the changes in the number of alkoxide groups bonded to Ti/Zr atoms have a dramatic influence not only on the activity of the catalyst, but also on the degree of the polydispersity index and molecular weights of polymers. The aim of this work was to make a contribution to the research for catalyst systems on ROP of ε-caprolactone.

ACKNOWLEDGMENTS

REFERENCES

1. Mehrotra RC, Bohra R, Gaur DP, Metal β-Diketonates and Allied Derivatives, Academic Press, London (1978).

2. Fay RC, Lindmark AF. Nuclear magnetic resonance studies of inversion and diketonate R-group exchange in dialkoxybis (.beta.-diketonato) titanium (IV) complexes. Evidence for a twist mechanism. Journal of the American Chemical Society. 1983; 105(8): 2118-2127.

3. Schubert U, Huesing N, Lorenz A. Hybrid inorganic-organic materials by sol-gel processing of organofunctional metal alkoxides. Chemistry of materials. 1995; 7(11): 2010-2027.

4. Fleeting KA, O'Brien P, Otway DJ, White AJ, Williams DJ, Jones AC. Studies on Mixed β-Diketonate/Isopropoxide Compounds of Zirconium and Hafnium, the X-ray Single-Crystal Structures of $[M_2(OPr^i)_6 (tmhd)_2](M=$ Zr, Hf): Some Chemistry Important in the MOCVD of Oxides. Inorganic Chemistry. 1999; 38(7): 1432-1437.

5. Hoebbel D, Reinert T, Schmidt H, Arpac E. On the hydrolytic stability of organic Ligands in Al-, Ti-and Zr-alkoxide complexes. Journal of sol-gel science and technology. 1997;10 (2): 115-126.

6. Maurer C, Pittenauer E, Du VA, Allmaier G, Schubert U. Cyclic bis (β-diketonate)-and bis (β-ketoesterate)-bridged titanium and zirconium alkoxide derivatives. Dalton Transactions. 2012; 41(8): 2346-2353.

7. Kurajica S, Skoric I, Mandic V. Ethyl acetoacetate ligand distribution in the course of titanium n-butoxide chelation. Materials Chemistry and Physics. 2014: 147(3): 1058-1067.

8. Errington RJ, Ridland J, Clegg W, Coxall RA, Sherwood JM. β-Diketonate derivatives of titanium alkoxides: X-ray crystal structures and solution dynamics of the binuclear complexes $[\{Ti (OR)_3 (dik)\}_2]$. Polyhedron. 1998; 17(5): 659-674.

9. Kickelbick G, Schubert U. An unusual ring structure of an oligomeric oxotitanium alkoxide carboxylate. European journal of inorganic chemistry. 1998; 1998(2): 159-161.

10. Schubert U. Organically modified transition metal alkoxides: Chemical problems and structural issues on the way to materials syntheses. Accounts of chemical research. 2007; 40(9): 730-737.

11. Yalcin G, Yildiz U, Kayan A. Preparation of Al, Ti, Zr-perfluoroheptanoate compounds and their use in ring opening polymerization. Applied Catalysis A: General. 2012; 423: 205-210.

12. Mert, O., Kayan, A. Synthesis of silyliminophenolate zirconium compounds and their catalytic activity over lactide/epoxide. Applied Catalysis A: General. 2013; 464, 322-331.

13. Umare PS, Tembe GL, Rao KV, Satpathy US, Trivedi B. Catalytic ring-opening polymerization of L-lactide by titanium biphenoxy-alkoxide initiators. Journal of Molecular Catalysis. 2007; 268(1-2): 235-243.

14. Saridis E, Maroulas SD, Pitsikalis M. Ring-opening polymerization of L‐lactide using half‐titanocene complexes of the ATiCl$_2$Nu type: Synthesis, characterization, and thermal properties. Journal of Polymer Science Part A: Polymer Chemistry. 2013; 51(5): 1162-1174.

15. He JX, Duan YL, Kou X, Zhang YZ, Wang W, Yang Y, Huang Y. Dinuclear group 4 alkoxides: Excellent initiators for ring-opening polymerization of cyclic esters. Inorganic Chemistry Communications. 2015; 61: 144-148.

16. D'Auria I, Lamberti M, Mazzeo M, Milione S, Roviello G, Pellecchia C. Coordination chemistry and reactivity of zinc complexes supported by a phosphido pincer ligand. Chemistry-A European Journal. 2012; 18(8), 2349-2360.

17. Chisholm. MH, Gallucci JC, Zhen H, Huffman JC. Three-coordinate zinc amide and phenoxide complexes supported by a bulky

Schiff base ligand. Inorganic chemistry. 2001; 40(19): 5051-5054.

18. Hubert-Pfalzgraf, LG, Cauro-Gamet L, Brethon A, Daniele S, Richard P. (2007). Lanthanide molecular oxohydroxides: Synthesis and characterisation of [Y_4 (μ_4-O)(μ-OEt)$_2$ (μ, η^2-AAA)$_2$ (η^2-AAA)$_3$]$_2$ (μ_3-OH)$_4$ (μ_3-OEt)$_2$ (HAAA= allylacetatoacetate). Inorganic Chemistry Communications, 2007;10(2): 143-147.

19. Kayan A. Preparation and characterization of TAMP/TIMP-Ti and Zr compounds and their catalytic activity over propylene oxide and ε-caprolactone. Journal of the Turkish Chemical Society, Section A: Chemistry. 2017; 4(1): 59-80.

20. Schubert U. Silica-based and transition metal-based inorganic-organic hybrid materials-A comparison. Journal of sol-gel science and technology, 2003; 26(1-3): 47-55.

21. Faustini M, Nicole L, Ruiz-Hitzky E, Sanchez C. History of Organic–Inorganic Hybrid Materials: Prehistory, Art, Science, and Advanced Applications. Advanced Functional Materials. 2018.

22. Chisholm MH. Trispyrazolylborate ligands as ancillary ligands in the development of single-site metal alkoxide catalysts for ring-opening polymerization of cyclic esters. Inorganica Chimica Acta. 2009; 362(12): 4284-4290.

23. Mert O, Kayan A. Synthesis and characterization of substituted salicylate zirconium compounds and their catalytic activity over ε-caprolactone. Journal of Inclusion Phenomena and Macrocyclic Chemistry. 2014; 80(3-4): 409-416.

24. Chmura AJ, Davidson MG, Jones MD, Lunn MD, Mahon MF. Group 4 complexes of amine bis (phenolate) s and their application for the ring opening polymerisation of cyclic esters. Dalton Transactions. 2006; (7): 887-889.

25. Yildiz BC, Kayan A. Preparation of single-site tin (IV) compounds and their use in the polymerization of ε-caprolactone. Designed Monomers and Polymers. 2017; 20(1): 89-96.

RESEARCH ARTICLE

Synthesis of an (AB)₄-type Star Block Copolymer of L-lactide and Cyclohexene Oxide from a Tetra-Arm Telechelic Macrophotoinitiator

Zafer UYAR* ✉ iD **and Emel KAYA** ✉ iD

Harran University, Science Faculty, Department of Chemistry, 63290, Şanlıurfa, Turkey.

Abstract: A multi-step reaction process was applied for the synthesis of a novel and well-defined star-shaped telechelic macrophotoinitiator with four poly(L-lactide) (PLLA) arms connected to photoinitiating benzoin groups at the chain ends (PLLA-PI)₄. To achieve this, 2,2-bis(hydroxymethyl)-1,3-propanediol was used as the initiator which constitutes the core of the star-shaped polymeric scaffold. Benzoin photoreactive end groups of the telechelic (PLLA-PI)₄, capable of entering into further polymerization, allowed its use as a polymeric photoinitiator in photoinduced free radical promoted cationic polymerization of cyclohexene oxide (CHO) monomer at $\lambda=350$ nm to produce an (AB)₄-type star-shaped block copolymer composed of both esteric L-lactide and etheric cyclohexene oxide chains on each arm, (PLLA-PCHO)₄. Structural analysis and characterization of all intermediate and final compounds were done by a series of analytical and spectral methods. Molecular weights of the prepared polymers up to telechelic macrophotoinitiator (PLLA-PI)₄ were determined based on ^{1}H-NMR ($M_{n\ H-NMR}$), GPC ($M_{n\ exp}$) analyses and theoretical calculations ($M_{n\ theo}$) and were found to be in good agreement with each other. Thermal properties and degradations of the prepared polymers were examined by thermogravimetric and differential thermal analyses (TG/DTA). The melting temperature for (PLLA-PCHO)₄ was found higher compared to the other homo-type polymers in the literature. The thermogravimetric (TG) analyses showed that incorporation of the thermally stable PCHO block into the structure via photopolymerization improved its stability by increasing its decomposition temperature compared to the prepolymers.

INTRODUCTION

Telechelic polymers are defined as macromolecules comprising functional end-groups having utility in further polymerization or other reactions. In general, when a polymer chain is functionalized with the same group at both ends, the term of telechelic polymer is used. The idea of telechelics has recently been extended from classical linear polymers to many other types of polymers such as star, dendritic, and hyperbranched comprising functional end groups (1,2). The telechelic polymers can be synthesized by a wide variety of polymerization methods such as free radical (3), cationic (4), anionic (5), and step-growth (6) polymerization. Recent advances

in controlled/living polymerization techniques (ATRP, RAFT, NMP, and ROP) allow the synthesis of well-defined telechelic polymers (2, 6-8). If these controlled/living polymerization techniques are combined with a coupling, addition or conjugation method, telechelic polymers with low polydispersity and desired chain lengths can be obtained (9,10). Among the combining methods, ROP with click chemistry is often favored as it provides a well control of functionality, polydispersity, and molecular weight during the preparation of well-defined biodegradable linear or star telechelic polymers. For example, Yilmaz and coworkers have synthesized a star-shaped telechelic PCL with terminal azido groups and then clicked it with ethynylferrocene groups (11).

Yang and co-workers have synthesized a well-defined star-shaped telechelic hydrophobic PCL with alkyne terminal groups and then coupled it with an azido-terminated PEG via "click chemistry" to prepare well-defined novel amphiphilic PCL/PEG copolymer conetworks (12).

Synthesis of well-defined polymers having photoreactive end groups, often called macrophotoinitiators or polymeric photoinitiators, has recently received great interest in the field of polymer chemistry because they can be used as cross-linkers, chain extenders, and precursors to prepare block, graft, and star type polymers or polymer networks (13-15). They are also important due to their unique structure which accommodates properties of both macromolecular and small molecular photoinitiators in a single body. Compared to the small photoinitiator molecules, macrophotoinitiators have not only better reactivity but also lower migration rate and lower volatility (16-18). Practically, macrophotoinitiators are used as photoreactive agents in photopolymerization to synthesize copolymers such as block and graft (19-21). Recently, we have successfully applied the combination of ROP and click chemistry to prepare well-defined macrophotoinitiators whose core were connected to both photoreactive group(s) such as benzoin and polymer chain(s) such as PCL or PLLA (22-24). Next, these polymers were used as precursors in photopolymerization for the preparation of different types of block copolymers.

Depending on the telechelic definition as stated above, if a macrophotoinitiator contains the same photoactive groups at the chain-ends, it can be considered as telechelic macrophotoinitiator. Degirmenci group previously synthesized a well-defined telechelic macrophotoinitiator of polystyrene with two benzoin groups at the both ends of the polymer chain via the combination of ATRP and click chemistry (9), and then used this as a prepolymer in photopolymerization to synthesize a linear ABA type tri-block copolymer. Even though there exist various studies about the telechelic polymers in the literature as shown above, to the best of our knowledge, very few linear-type telechelic macrophotoinitiators and no star-type telechelic macrophotoinitiator have been reported so far. Thus, here we report synthesis, characterization, and thermal analyses of a novel well-defined star-shaped telechelic macrophotoinitiator of PLLA with benzoin photoreactive end groups $(PLLA-PI)_4$ and an $(AB)_4$-type star block copolymer $(PLLA-PCHO)_4$ which was prepared by the photoinitiated free radical promoted cationic polymerization of CHO monomer with the $(PLLA-PI)_4$. As far as we are concerned, the synthesis of such type of telechelic PLLA macrophotoinitiator $(PLLA-PI)_4$ and star block copolymer $(PLLA-PCHO)_4$ have not been reported yet.

MATERIALS AND METHODS

Materials and Instrumentation
Azido end-functional benzoin photoinitiator (PI-N_3), namely 2-oxo-1,2-diphenylethyl-2-azidopropanoate, was synthesized according to the reported method (22,25). Benzoin (Aldrich) was recrystallized from ethanol. Other reagents used in the synthesis of (PI-N_3) such as 2-bromopropanoyl bromide (Aldrich) and sodium azide (NaN_3) (Merck) were used as received from the commercial suppliers. Cyclohexene oxide (CHO) (Aldrich) was purified by distillation over calcium hyride (CaH_2) under reduced pressure and L-lactide (LLA) (Aldrich) was recrystallized from toluene. Pentaerythritol (Aldrich), the initiator for ROP, was used without further purification. 1-Ethoxy-2-methylpyridinium hexafluorophosphate ($EMP^+PF_6^-$) was synthesized by following the published process (26). Solvents, dichloromethane (CH_2Cl_2), toluene, dimethylformamide (DMF), and tetrahydrofuran (THF), were dried by distilling over the proper drying agents under N_2 before use. All other reagents and solvents were used as received from the commercial sources unless otherwise stated.

An Agilent 400 MHz NMR spectrometer was used to record NMR measurements at ambient temperature and the data were processed with MestReNova 12 software. Fourier transform infrared (FT-IR) analyses were carried out using a Perkin-Elmer Spectrum Two FT-IR spectrometer. The number and average molecular weights (M_n and M_w) and molecular weight distributions (M_w/M_n) of the polymers were determined by gel permeation chromatography with a Viscotek GPCmax VE 2001 Autosampler system having Viscotek VE 3580 refractive index (RI) detector. Three Viscotek GPC columns (T3000, LT4000L and LT5000L), (7.8 mm internal diameter, 300 mm length) and a Viscotek guard column (CLM3008, 4.6 mm internal diameter, 10 mm length) were used in series. The effective molecular weight ranges were 456–42800, 1050–107000, and 10200–2890000, respectively. THF was used as an eluent at flow rate of 1.0 mL/min at 35°C. Detector was calibrated with PS standards having narrow molecular weight distribution. Data were analyzed using Viscotek OmniSEC 4.7.0 software. Molecular weights were calculated with the aid of polystyrene standards. The experimental molecular weights ($M_{n\ exp}$) of $(PLLA-OH)_4$, $(PLLA-alkyne)_4$ and $(PLLA-PI)_4$ were calculated from GPC with the help of polystyrene calibration curve using a correction coefficient, $M_{n\ exp} = 0.58 \times M_{n\ GPC}$ (27). A Perkin-Elmer model Lambda 25 spectrophotometer and a Perkin–Elmer model LS 55 spectrometer were used to record UV-vis and Fluorescence spectra, respectively. An S II EXSTAR TG/DTA 7300 thermal analysis systems under N_2 flow with a heating rate of 10 °C min^{-1} was used to determine

the thermal stabilities and the glass transition temperatures of the polymers.

Preparation of tetra-arm star-shaped poly(L-lactide) by ring opening polymerization (PLLA-OH)$_4$

2,2-Bis(hydroxymethyl)-1,3-propanediol (188.8 mg, 1.39 mmol), L-lactide (10 g, 69.4 mmol), and Sn(Oct)$_2$ (95%) (5.26 mg, 12.3 x 10^{-3} mmol, 0.05% w/w$_{monomer}$) were placed in a Schlenk flask with a ratio of 1/50 (initiator/monomer). The flask was vacuumed for 30 min to dry the reaction mixture and then charged with N$_2$ gas. The reaction was stirred for 10 h at 130 °C under N$_2$ until the reaction bulk was viscous enough to stop stirring bar. The reaction mixture was solidified by immersing it in an ice-water bath. The glassy solid polymer was then dissolved in dichloromethane and the resulting solution was added drop wise to 250 mL of cold methanol. The title polymer (PLLA-OH)$_4$ was obtained as a white solid after the filtration of the mixture by a Gooch crucible. Yield: 9.5 g, 93%, $M_{n\ theo}$ = 6838, $M_{n\ H\ NMR}$ = 6626, $M_{n\ exp}$ = 6600, M_w/M_n = 1.06.

Preparation of alkyne end-functional tetra-arm star-shaped poly(L-lactide) (PLLA-alkyne)$_4$

To a two-necked round-bottom reaction flask were placed (PLLA-OH)$_4$ (2g, 0.30 mmol based on NMR calc), 4-pentynoic acid (98%) (237 mg, 2.37 mmol), DMAP (36.5 mg, 0.30 mmol), and DCC (610 mg, 3.00 mmol). The flask was vacuumed and then flushed with Ar atmosphere and then 45 mL of dry dichloromethane was added. The reaction was stirred for 3 days at rt under Ar. The reaction mixture was concentrated with a rotary evaporator and then the insoluble part was removed by filtration through No:1 Whatman filter paper. The title polymer was reprecipitated by the dropwise addition of the filtrate into 250 mL of cold methanol. The white polymer solid, (PLLA-alkyne)$_4$, was then filtered by a pore-4 Gooch crucible and dried under vacuum. Yield: 2.0 g, 96%, $M_{n\ theo}$ = 7158, $M_{n\ H\ NMR}$ = 7119, $M_{n\ exp}$ = 7000, M_w/M_n = 1.06.

Preparation of benzoin end-functional tetra-arm star-shaped telechelic poly(L-lactide) macrophotoinitiator by click chemistry (PLLA-PI)$_4$

To a Schlenk flask equipped with a stirring bar were added (PLLA-alkyne)$_4$ (514 mg, 0.1 mmol based on NMR calc), PI-N$_3$ (186 mg, 0.6 mmol), CuBr (172 mg, 1.2 mmol), and bipyridine (375 mg, 2.4 mmol) and 20 ml of dry THF under Ar. The dark-brown suspension was degassed by

three freeze-pump-thaw cycles. After 24 h stirring at room temperature, the reaction suspension looking like pale brown ash was diluted with THF and filtered through a short silica gel column to remove excess CuBr and other particulate matters. Dropwise addition of the filtrate to cold methanol resulted in solid precipitation which was filtered through a pore-4 Gooch crucible and dried under vacuum to give (PLLA-PI)$_4$ as a white polymer. Yield: 580 mg, 96%, $M_{n\ theo}$ = 8396, $M_{n\ H-NMR}$ = 8312, $M_{n\ exp}$ = 8200, M_w/M_n = 1.12.

Preparation of (AB)$_4$-type star block copolymer by photoinduced free radical promoted cationic polymerization (PLLA-PCHO)$_4$

The macrophotoinitiator (PLLA-PI)$_4$, onium salt (Ph$_2$I$^+$PF$_6^-$ or EMP$^+$PF$_6^-$) and 1 mL of cyclohexene oxide (CHO) were placed in a Pyrex tube and the mixture was degassed by bubbling N$_2$ for 6 min. The tube was tightly sealed and put in a merry-go-round type photoreactor with 15 lamps (Philips 8W/08) emitting light nominally at 350 nm at rt. The transparent clear bulk solution became quite viscous after subjected to irradiation for 45 min. The viscous solution was diluted with dichloromethane and added dropwise to cold methanol. The precipitation formed was filtered with a pore-4 Gooch crucible and dried under vacuum to give (AB)$_4$-type star block copolymer of (PLLA-PCHO)$_4$. Conversions were determined gravimetrically.

RESULTS AND DISCUSSION

Synthesis of (PLLA-OH)$_4$ and (PLLA-alkyne)$_4$

Ring opening polymerization (ROP) of lactides such as L-lactide (LLA) with stannous-2-ethylhexanoate, Sn(Oct)$_2$ catalyst, and an –OH functionalized initiator is a very convenient method for synthesizing polylactides with well-defined structures (24). Here, we have applied ROP to prepare a tetra-arm star-shaped poly(L-lactide) with controlled molecular weight and low molecular weight distribution. The ROP of LLA was accomplished using 2,2-bis(hydroxymethyl)-1,3-propanediol as the initiator and Sn(Oct)$_2$ as the catalyst by taking the molar ratios of [Initiator]/[LLA]: 1/50 under inert atmosphere at 130 °C (Scheme 1). The resulting (PLLA-OH)$_4$ was then reacted with 4-pentynoic acid via condensation reaction to obtain the first click couple compound (PLLA-alkyne)$_4$. The results and conditions of the synthesized (PLLA-OH)$_4$ and (PLLA-alkyne)$_4$ are summarized in Table 1.
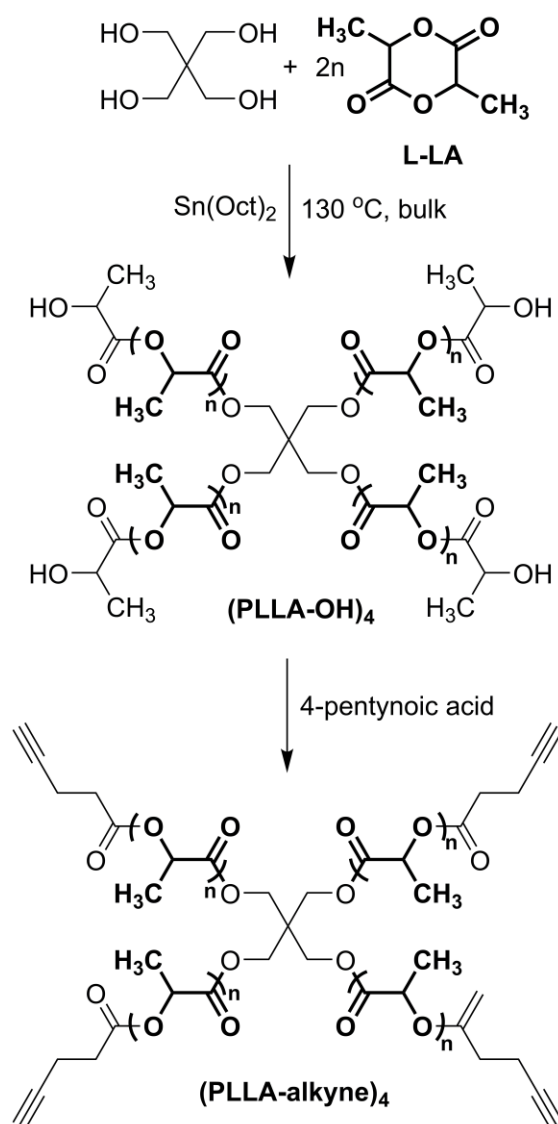
Scheme 1. Synthesis of (PLLA-OH)$_4$ and (PLLA-alkyne)$_4$.

Table 1: Results and conditions of the (PLLA-OH)$_4$[a], (PLLA-alkyne)$_4$[b], and (PLLA-PI)$_4$[c]

Run	Polymer	Temp (°C)	Conversion (%)	$M_{n\ theo}$ (g/mol)	$M_{n\ H\ NMR}$[d] (g/mol)	$M_{n.exp}$[e] (g/mol)	M_w/M_n[f]
1	(PLLA-OH)$_4$	130	93	6838	6626	6600	1.06
2	(PLLA -alkyne)$_4$	rt	96	7158	7119	7000	1.06
3	(PLLA -PI)$_4$	rt	96	8396	8312	8200	1.12

- [a]Prepared by ROP of LLA in bulk, [I]/[LLA] = 1/50
- [b]Prepared from the reaction between (PLLA-OH)$_4$ and 4-pentynoic acid
- [c]Prepared via "click" reaction between (PLLA-alkyne)$_4$ and PI-N$_3$
- [d]Determined by ^{1}H NMR measurements
- [e]Determined by GPC measurements. GPC values corrected with the polystyrene calibration curve using a correction coefficient, $M_{n\ exp}$ = 0.58 x $M_{n\ GPC}$ (27)
- [f]Determined by GPC analysis with polystyrene standards

As can be seen from Table 1, the molecular weight distribution of (PLLA-OH)$_4$ is low and the theoretical molecular weight determined according to the following equation is in good agreement with the measured values by GPC and ^{1}H-NMR analyses. A similar situation was also observed in the case of (PLLA-alkyne)$_4$.

$$M_{n\ theo} = [M_0]/[I_0] \times M_m \times \%\ Conv. + M_I \quad (Eq.\ 1)$$

where $[M_0]$ and $[I_0]$ are the initial molar concentrations of monomer (LLA) and initiator, and (M_m) and M_I are the molecular weights of the monomer and initiator, respectively. The theoretical molecular weight of (PLLA-alkyne)$_4$ was determined by adding 97 (the molecular weight of the residue of 4-pentynoic acid) to that of (PLLA-OH)$_4$.

The structure of (PLLA-OH)$_4$ and (PLLA-alkyne)$_4$ were confirmed by ^{1}H NMR, FT-IR, and GPC analyses. Figure 1 indicates the ^{1}H NMR spectra of (PLLA-OH)$_4$ and (PLLA-alkyne)$_4$ polymers. The typical PLLA proton signals at 5.25-5,12 ppm (protons b) and 1.60−1.48 ppm (protons a), and the protons of the initiator in the core were clearly observed for both polymers. ^{1}H-NMR spectrum of (PLL-OH)$_4$ (Figure 1a) showed that the signals of the methylene protons of the initiator residue (proton c) and the methine protons adjacent to the ω-chain-end hydroxyl groups (proton b') overlap at 4.34-4.20 ppm while the -CH$_3$ protons at the last L-lactide unit at the end of the chain (proton a') appear at 1.37 ppm. However, in the case of (PLLA-alkyne)$_4$ (Figure 1b), the ω methine proton (b') and -CH$_3$ protons (a') of the last L-lactide unit of (PLLA-alkyne)$_4$ shifted downfield to where the other b and a protons are, respectively. This is because introduction of the 4-pentynoic acid to the chain end of (PLLA-OH)$_4$ changed the chemical environment of the last unit and ω methine proton (b') and -CH$_3$ protons (a') are now adjacent to esteric groups rather than hydroxyl groups just like the other repeating units. This clearly shows successful conversion of hydroxyl groups to esteric groups by condensation reaction. The protons of the initiator residue (protons c) in the center of the polymer are not affected by the conversion taking place at the chain ends thus they resonate at the same chemical shift, 4.28 ppm, for both polymers. The successful conversion of the reaction was further supported by the presence of new signals belonging to 4-pentynoic acid protons which were absent in the ^{1}H-NMR spectrum of (PLLA-OH)$_4$. Neighboring CH$_2$ protons adjacent to -C≡C- group (protons e) and carbonyl group (protons d) showed triplet peaks at 2.47 and 2.60 ppm, respectively, while the terminal ≡CH proton displayed a singlet at 2.36 ppm. The complete end functionalization of each PLLA arm with alkyne group was also proved by the comparison of the integration values for methylene protons of the initiator (proton c) moiety to those of alkyne (proton d or e) moieties.

The total polymerization degree for 4-arm polymer was found as 46, approximately 12 for each arm, by comparing the integral value of repeating −CH_2− protons of the polymer units to those of terminal −CH-OH (proton b') or methylene protons of initiator residue (proton c). The ^{1}H NMR molecular weight of (PLLA-OH)$_4$ and (PLLA-alkyne)$_4$ were determined according to the equations 2-4 below, respectively;

$$M_{\text{n H NMR}} = 4 \times (DP_n \times M_m) + M_I \qquad \text{(Eq. 2)}$$
$$M_{\text{n H NMR}} = 4 \times (DP_n \times M_m + 80.1) + M_I \quad \text{(Eq. 3)}$$
$$DP_n = I_{\text{Poly}}/I_I \qquad \text{(Eq. 4)}$$

where, $M_{\text{n H-NMR}}$ is the molecular weight of each polymer designated by ^{1}H-NMR; DP_n is the polymerization degree of each polymer arm; M_m is the molecular weight of LLA monomer; M_I is the molecular weight of the initiator moiety in the core of polymers; 80.1 represents the molecular weight of pentynoic acid residue at the end of each PLLA arm after the condensation reaction; I_{Poly} represents the integral value of the signals of two identical −CH− protons in PLLA backbone (b protons); I_I represents the integral value of the signals of -CH_2- protons in the initiator unit at the core of PLLA arms (c protons).

The structure of (PLLA-OH)$_4$ and (PLLA-alkyne)$_4$ polymers were also evidenced by FT-IR measurements. The typical ester carbonyl group band of the PLLA backbones could clearly be seen at 1756 cm^{-1} from the FT-IR spectra as shown in Figure 2 (a) and (b). The spectrum of the (PLLA-alkyne)$_4$ (Figure 2 (b)) showed a new peak at 3285 cm^{-1} due to the ≡CH stretch revealing the presence of alkyne groups at the polymer chain-ends after the functionalization reaction.
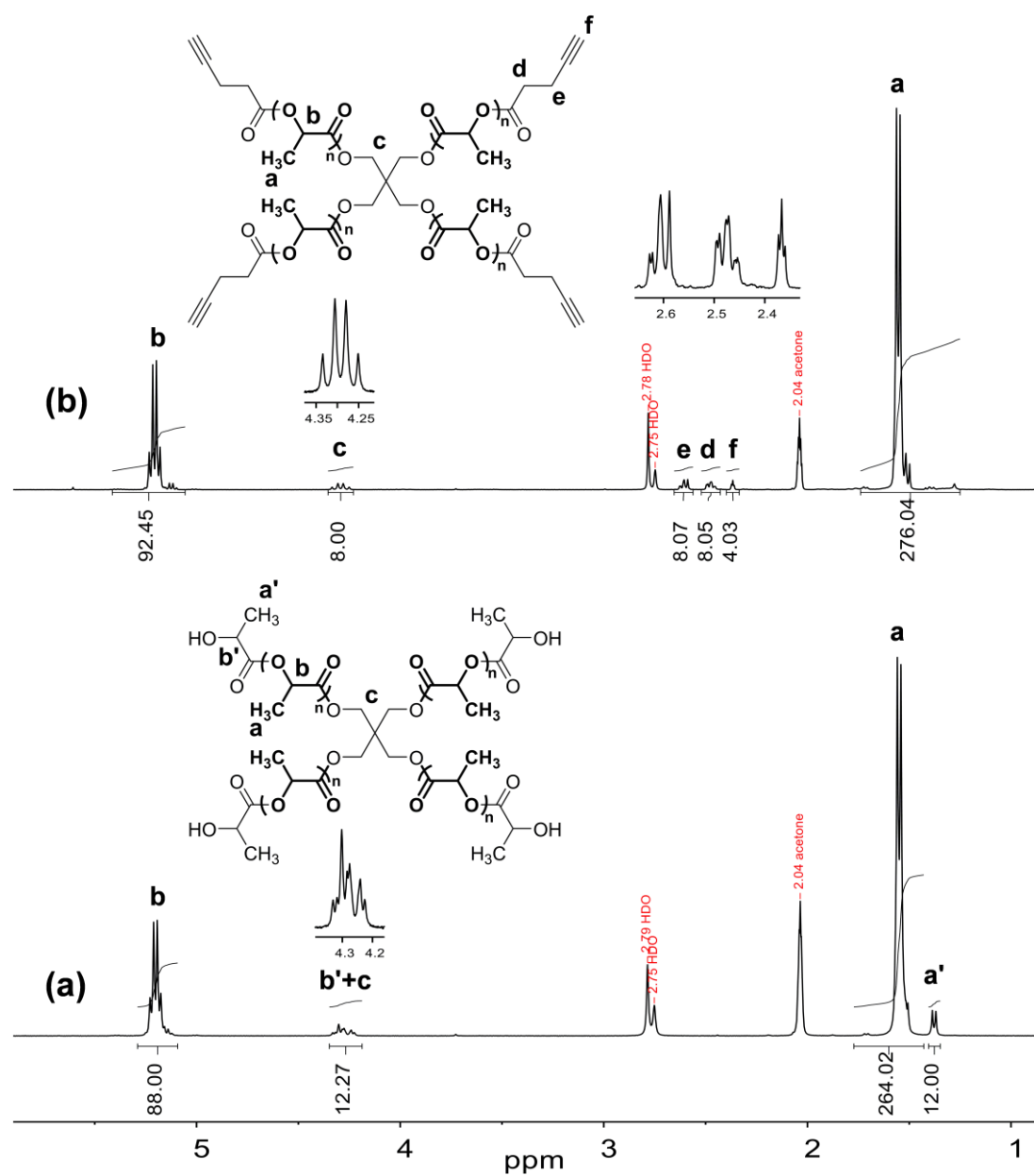
Figure 1. ^{1}H-NMR spectra of (PLLA-OH)$_4$ (a) and (PLLA-alkyne)$_4$ (b) in deuterated acetone.
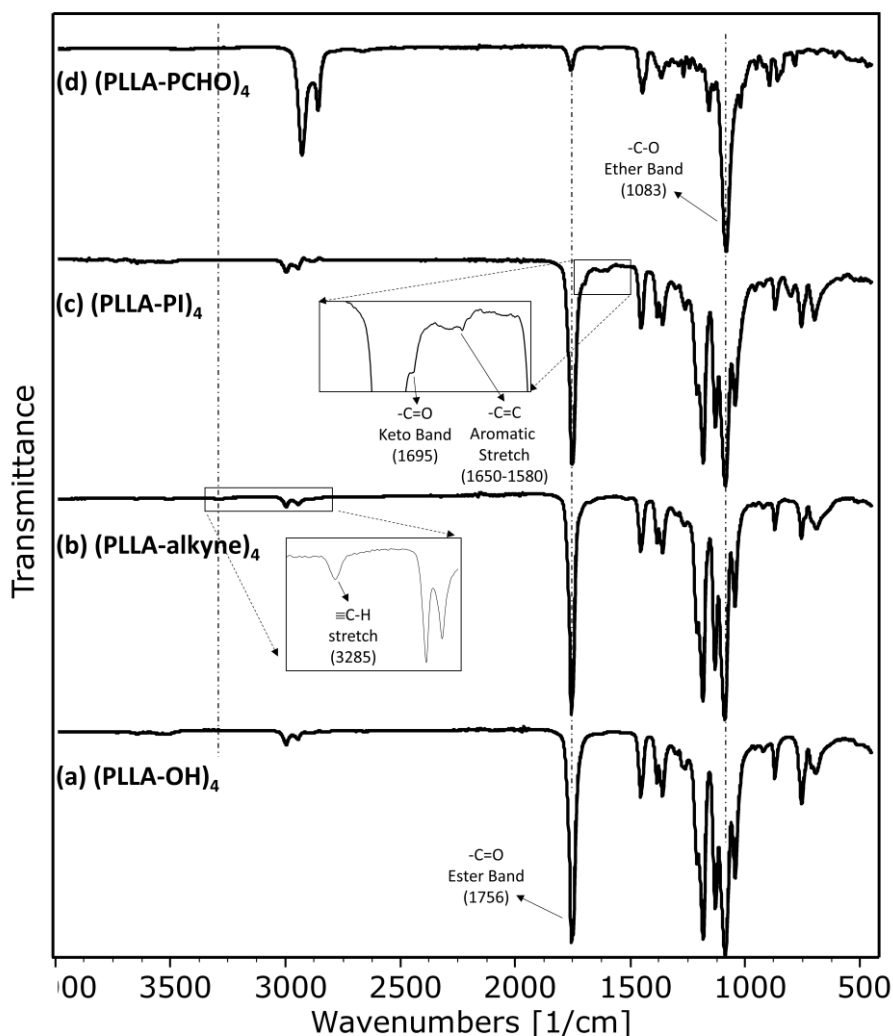
Figure 2. FT-IR spectra of (PLLA-OH)₄ (a), (PLLA-alkyne)₄ (b), (PLLA-PI)₄ (c), and (PLLA-PCHO)₄ (d).

Both (PLLA-OH)₄ and (PLLA-alkyne)₄ polymers showed unimodal and narrow GPC traces (Figure 3) indicating the controlled process of ROP of LLA and no occurrence of side reactions during the alkyne introduction.
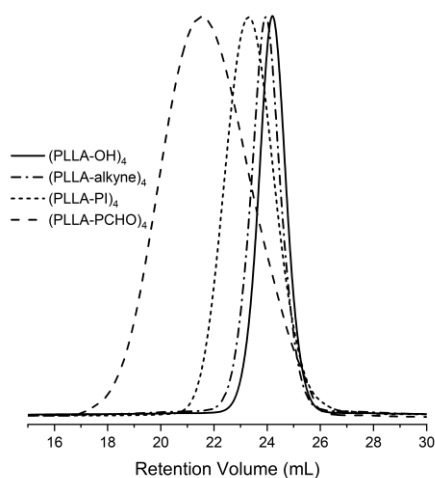
Figure 3. GPC traces (PLLA-OH)₄, (PLLA-alkyne)₄, (PLLA-PI)₄, and (PLLA-PCHO)₄.

Synthesis of the star-shaped telechelic macrophotoinitiator (PLLA-PI)₄
The "click chemistry", which is the Cu(I)-catalyzed dipolar cycloaddition reaction between an organic azide and a terminal alkyne, method was applied for the synthesis of the star-shaped telechelic macrophotoinitiator, (PLLA-PI)₄. For this aim, PI-N₃ and (PLLA-alkyne)₄ were used as the

click couple molecules. The click reaction of these compounds in the presence of CuBr/2,2′-bipyridine catalyst system produced a tetra-arm star-shaped telechelic PLLA macrophotoinitiator

with benzoin end-functional groups, (PLLA-PI)$_4$, (Scheme 2).

Scheme 2. Synthesis of the tetra-arm star-shaped telechelic poly(L-lactide) macrophotoinitiator with benzoin end-functional groups, (PLLA-PI)$_4$, by click reaction.

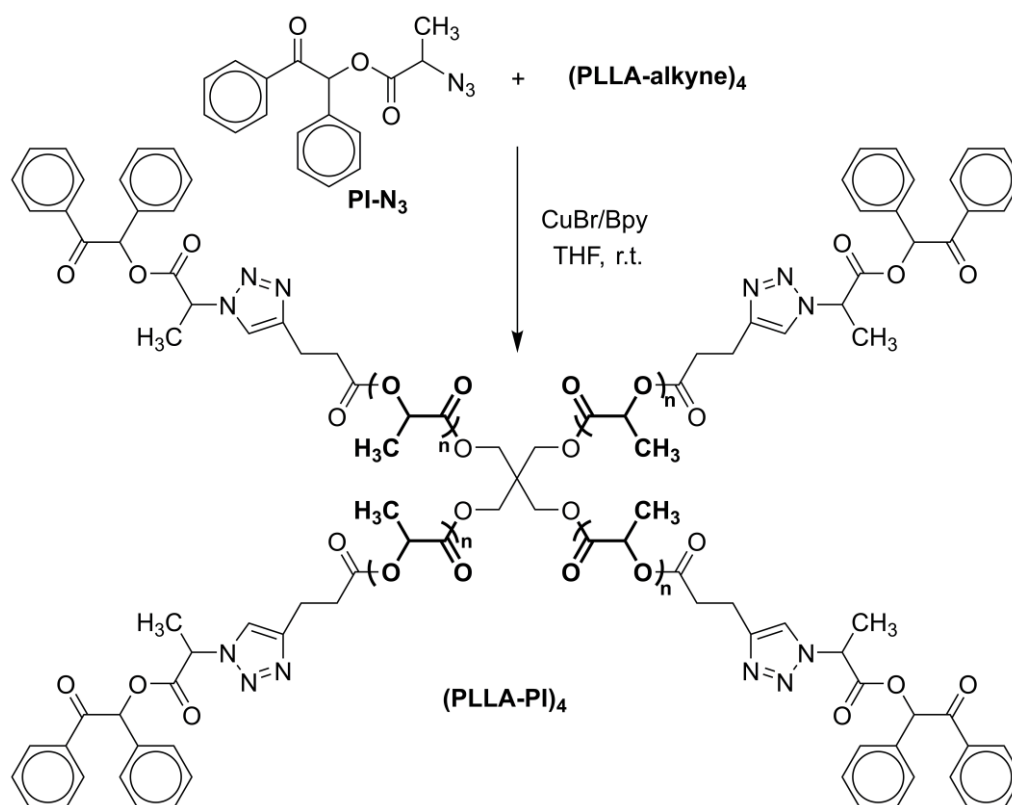FT-IR, ^{1}H NMR, GPC, UV-Vis and Fluorescence analyses were used to characterize the structure of (PLLA-PI)$_4$ macrophotoinitiator. The appearance of typical absorption of the aromatic C=C double bond at 1650-1580 cm^{-1} and the disappearance of the ≡C–H stretching band at 3285 cm^{-1} in the FT-IR spectrum of the macrophotoinitiator as shown in Figure 2(c) indicates the completion of the click reaction quantitatively. Also, a new peak at 1695 cm^{-1} due to the C=O keto groups of the photoinitiator moieties appeared on the main ester peak as a sharp shoulder. ^{1}H-NMR measurements also support the formation of (PLLA-PI)$_4$ macrophotoinitiator.

Figure 4(a) shows that the repeating PLLA proton peaks (protons a and b) resonate exactly at the same chemical shift as the previous polymers, (PLLA-OH)$_4$ and (PLLA-alkyne)$_4$. Aromatic region shows the absorptions that belong to both aromatic protons of benzoin moieties and the only proton of triazole ring (proton f) at 8.10-7.30 ppm. Non-aromatic methine proton of benzoin moiety (proton i) also resonates in this downfield at 7.08 ppm due to the de-shielding effect of the highly electronegative adjacent atoms. The ^{1}H NMR molecular weight ($M_{n\ H\ NMR}$) of (PLLA-PI)$_4$ was calculated as 8312 g/mol by using the following equation;

$$M_{n\ H\ NMR} = 4 \times (DP_n \times M_m + 389.4) + M_I \quad \text{(Eq. 5)}$$
$$DP_n = I_{Poly}/I_{CH} \quad \text{(Eq. 6)}$$

where, $M_{n\ H-NMR}$ is the ^{1}H NMR molecular weight of macrophotoinitiator; DP_n is the polymerization degree of each polymer arm; M_m is the molecular weight of LLA monomer; 389.4 represents the molecular weight of the end-group of each PLLA arm; M_I is the molecular weight of initiator unit at the central group; I_{Poly} represents the integral value of the signals of two identical –CH– protons in PLLA backbone (b protons); I_{CH} represents the integral value of –CH– protons in benzoin unit (i protons), respectively.

The GPC chromatogram of (PLLA-PI)$_4$ (Figure 3) still shows a symmetrical and narrow peak just like those of (PLLA-OH)$_4$ and (PLLA-alkyne)$_4$ suggesting that the click reaction progressed without association of any side reaction or byproducts. GPC analysis also exhibited that the macrophotoinitiator has a quite low polydispersity (M_w/M_n) just like the previous polymers meaning no change occurred in the well-defined structure of polymeric chains during the click reaction and the reaction took place on the end groups as expected. Another important data obtained from GPC analysis is the molecular weight of the polymer ($M_{n\ exp}$) and this value is in good

agreement with the molecular weights calculated by ^{1}H-NMR ($M_{n\,H\,NMR}$) and theoretically ($M_{n\,theo}$).

Since the star-shaped telechelic macrophotoinitiator bears photoreactive benzoin moieties at the end of each polymer chain, UV-Vis and Fluorescence measurements were also recorded to confirm the successful introduction of these chromophore groups to the chain ends. Figure 5 shows the comparison of UV-Vis absorption spectra of PI-N$_3$, and (PLLA-PI)$_4$. Both spectra are similar to each other with respect to displaying characteristic benzoyl chromophore absorptions between 300 and 400 nm. It should be noted that the previous polymers, (PLLA-OH)$_4$

or (PLLA-alkyne)$_4$, do not have absorptions in this region. As seen in Figure 6, a similar behavior was observed in comparison of fluorescence spectra of PI-N$_3$ and (PLLA-PI)$_4$. Both molecules showed emissions pertaining to the vibrational structure of the phenyl ketone chromophore. Judging from the data from various spectroscopic and analytical methods presented above, it is safe to claim that a successful and quantitative click reaction occurred yielding a tetra-arm star-shaped telechelic macrophotoinitiator with a photoreactive benzoin group at the end of each polymer arm, (PLLA-PI)$_4$.

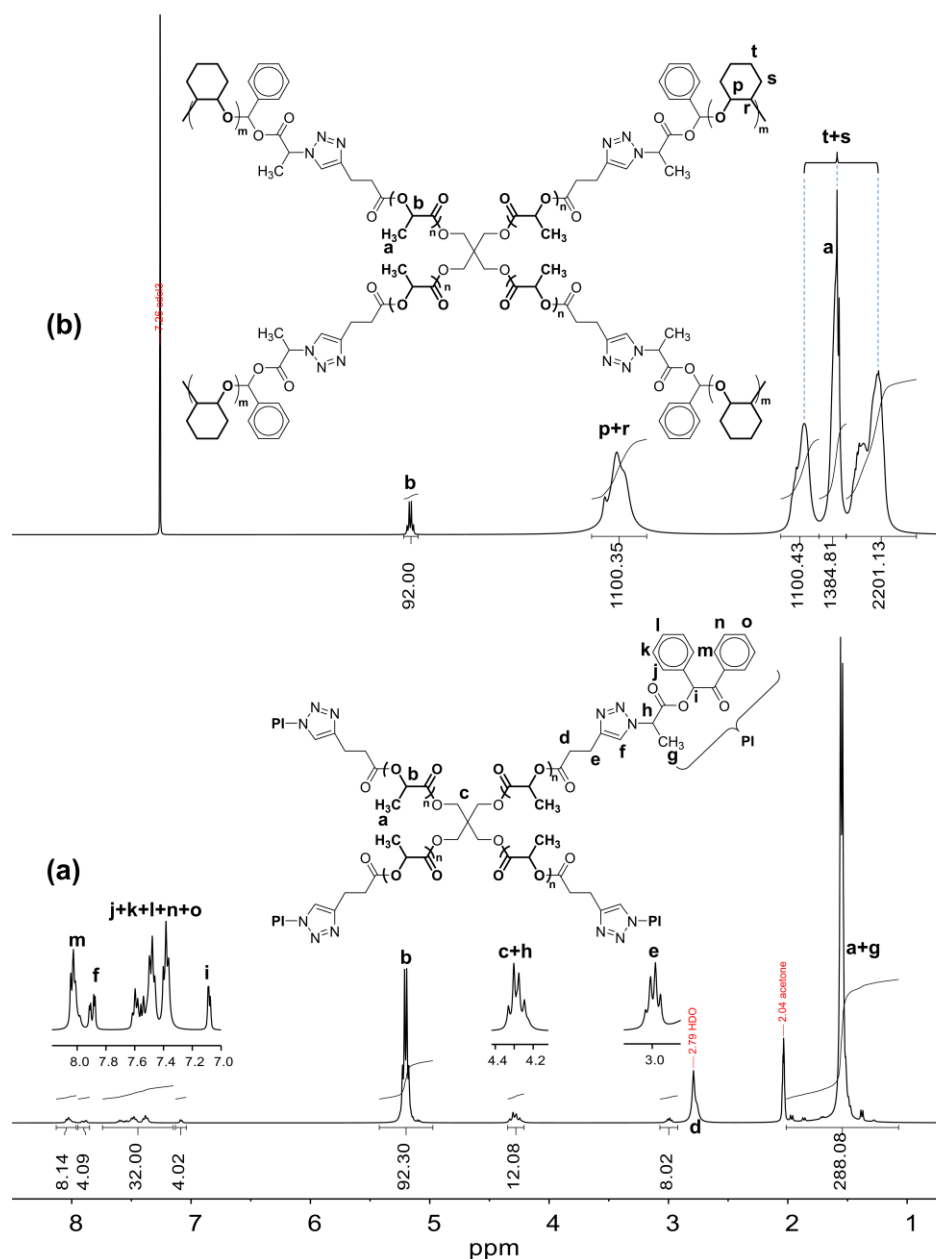**Figure 4.** ^{1}H-NMR spectra of (PLLA-PI)$_4$ (a) and (PLLA-PCHO)$_4$ (b).
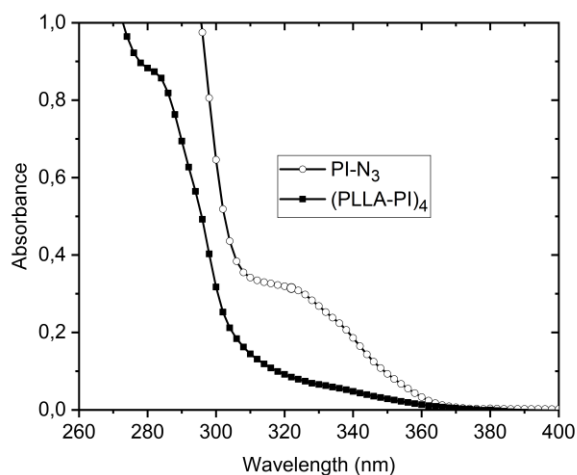
Figure 5. UV absorption spectra of PI-N$_3$ (1.12 x 10^{-3} mol L^{-1}), and (PLLA-PI)$_4$ (8.25 x 10^{-5} mol L^{-1}) in CH$_2$Cl$_2$.

Figure 6. Fluorescence spectra of PI-N$_3$ (7.12 x 10^{-5} mol L^{-1}), and (PLLA-PI)$_4$ (7.93 x 10^{-5} mol L^{-1}) in CH$_2$Cl$_2$, λ_{exc} = 340 nm.

Synthesis of (AB)$_4$-type star block copolymer (PLLA-PCHO)$_4$

The synthesis of (AB)$_4$-type star block copolymer, or (PLLA-PCHO)$_4$ in short, has been conducted using (PLLA-PI)$_4$ as the macrophotoinitiator, cyclohexene oxide (CHO) as the monomer, and Ph$_2$I$^+$PF$_6^-$ or EMP$^+$PF$_6^-$ as the oxidizing agent in photoinduced free radical promoted cationic polymerization. UV irradiation of (PLLA-PI)$_4$ caused *a*-cleavage in photoreactive benzoin moieties generating benzoyl and alkoxybenzyl radicals connected to polymer chains in the initial step as described in Scheme 3. While the strong electron donor PLLA-bonded alkoxybenzyl radicals are oxidized by the onium salt (Ph$_2$I$^+$ or EMP$^+$) to give the corresponding carbocations, electron withdrawing benzoyl radicals cannot be oxidized. Thus, polymer attached alkoxy carbocations are able to react with CHO monomer to produce an (AB)$_4$-type star block copolymer consisting of PLLA as the A blocks and PCHO as the B blocks, whereas benzoyl radicals do not interfere the polymerization and can be easily removed from the reaction mixture during the work-up process. The control experiment done with all reagents except for the macrophotoinitiator resulted in no polymer formation even after 4 h of irradiation. This is yet another proof that the starting material, (PLLA-PI)$_4$, was successfully prepared considering that the photoinduced free radical promoted cationic polymerization only progresses in the presence of

a proper photoinitiator group such as benzoin as the free radical source.

^{1}H NMR spectrum of the star block copolymer, (PLLA-PCHO)$_4$, is shown in Figure 4 (b). The typical signals of the −OC*H* group protons in the PCHO blocks (proton p and r) appeared at 3.70-3.15 ppm. The other repeating proton signals of PCHO blocks resonate at upfield region between 2.06 and 1.04 ppm and assigned properly in Figure 4 (b). There is not a significant chemical shift observed for the repeating units of PLLA block compared to the previous polymer as expected. The degree of polymerization (*DP*$_n$) for each PCHO blocks was found as 138, by comparing the integral ratio of –C*H*– protons (b) of PLLA backbone to those of –OC*H*C*H*O– protons (p+r) of PCHO backbone.

The successful photoinduced free radical promoted cationic polymerization processes and the formation of star block copolymer (PLLA-PCHO)$_4$ were also supported by FT-IR measurements (Figure 2(d)). A very intense band at 1083 cm^{-1}, which is even surpassing the intensity of the characteristic band of carbonyl peak of PLLA blocks at 1756 cm^{-1}, appeared due to the repeating etheric band of PCHO blocks. This is an expected phenomenon considering that PCHO segment has many more repeating units compared to PLLA segment based on the calculations from ^{1}H-NMR and GPC data.
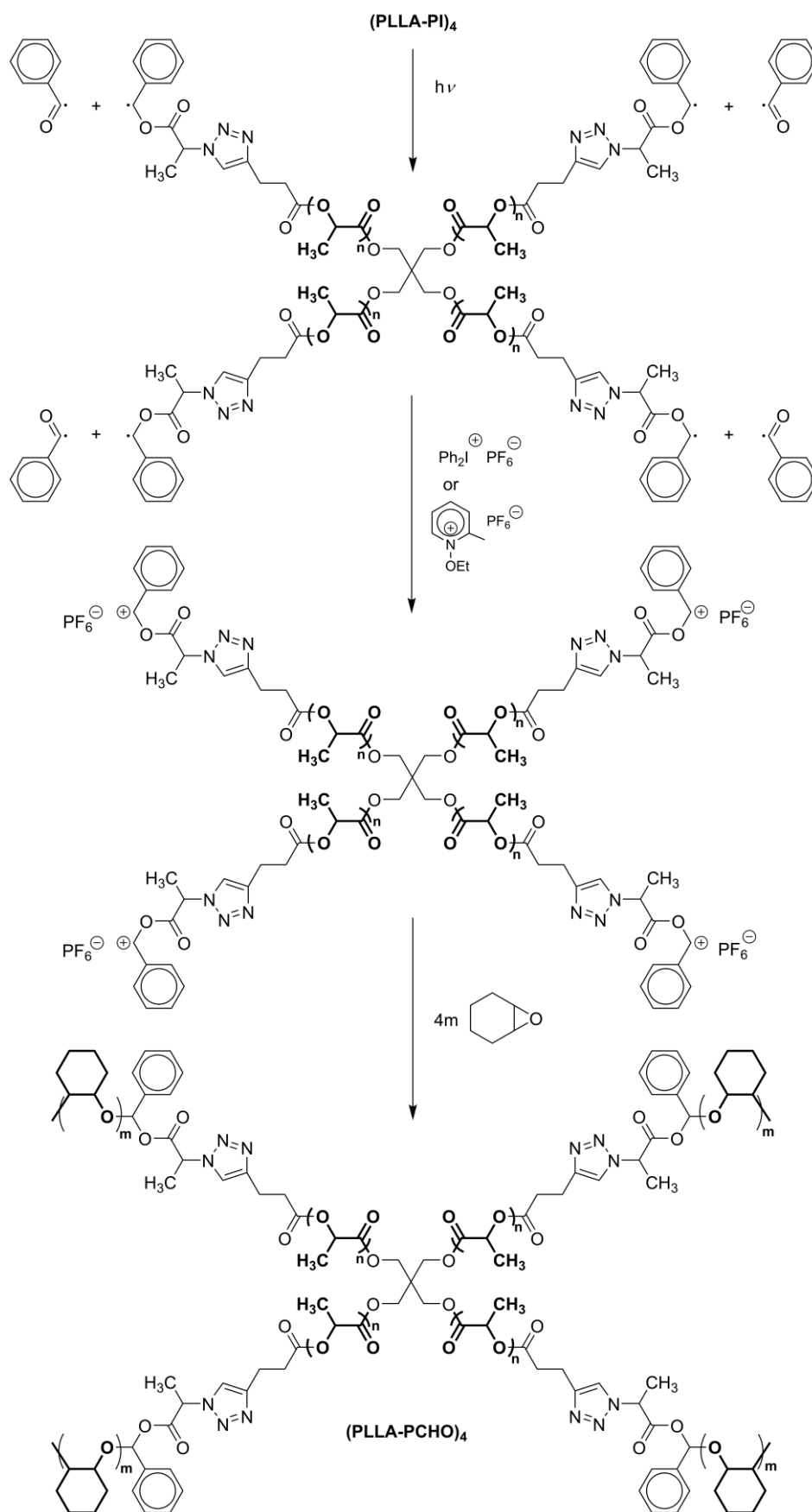
Scheme 3. Synthesis of the (AB)₄-type star block copolymer (PLLA-PCHO)₄ by photoinitiated free radical promoted cationic polymerization.

The unimodal and relatively broader GPC peak of (PLLA-PCHO)$_4$ compared to those of the well-defined pre-polymers is a typical result observed for the uncontrolled polymerizations. GPC curve of the (PLLA-PCHO)$_4$ shows no peak attributed to the starting macrophotoinitiator (Figure 3), indicating completely depletion of the macrophotoinitiator used during the photopolymerization process.

Thermal analyses of polymers

Thermogravimetric and differential thermal analyses (TG/DTA) of (PLLA-OH)$_4$, (PLLA-alkyne)$_4$, (PLLA-PI)$_4$, and (PLLA-PCHO)$_4$ were carried out under N$_2$ atmosphere. The DTA analyses of the polymers are shown in Figure 7.

While (PLLA-OH)$_4$, (PLLA-alkyne)$_4$, and (PLLA-PCHO)$_4$ have displayed two endothermic peaks, (PLLA-PI)$_4$ has shown three endothermic peaks. The glass transition temperatures (T_g) were observed as endothermic peaks at 62.45 °C for (PLLA-OH)$_4$, 68.17 °C for (PLLA-alkyne)$_4$, 62.55 and 84.54 °C for (PLLA-PI)$_4$, and 62.22 °C for (PLLA-PCHO)$_4$. The other main endothermic peaks at 128.87 °C, 127.44 °C, 113.43 °C, and 178.80 °C indicate the melting temperature (T_m) of (PLLA-OH)$_4$, (PLLA-alkyne)$_4$, (PLLA-PI)$_4$, and
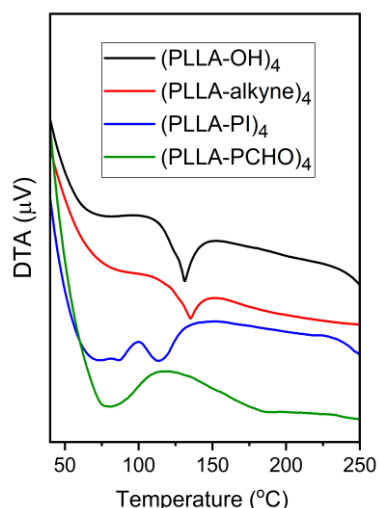
Figure 7. DTA traces of the synthesized polymers.

(PLLA-PCHO)$_4$, respectively. In addition, the exothermic peak observed at 99.25 °C represents the crystallization temperature (T_c) of the (PLLA-PI)$_4$ while ((PLLA-OH)$_4$, (PLLA-alkyne)$_4$, and (PLLA-PCHO)$_4$ displayed no crystallization temperatures most probably owing to the groups linked to the PLLA chains. The T_gs and T_ms found for the polymers synthesized in this study are the typical temperatures of PLLA based polymers and are consistent with the literature. The higher T_m observed for (PLLA-PCHO)$_4$ in comparison with the other homo type polymers is probably attributed to the conformation and construction of star block copolymer.
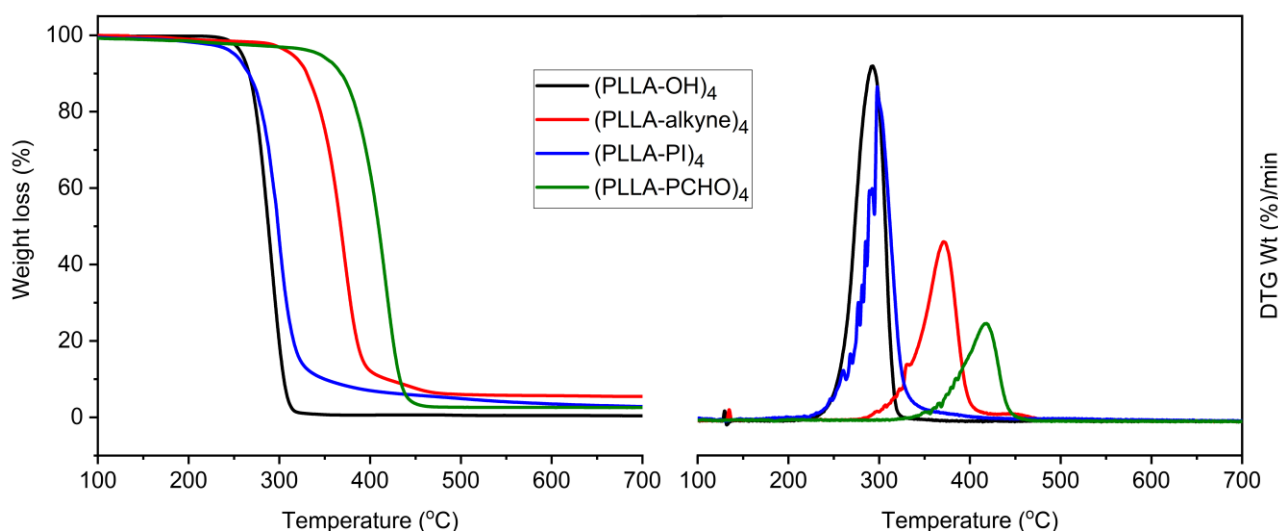
Figure 8. TG and DTG profiles of the synthesized polymers.

The thermogravimetric (TG) curves and derivative (DTG) curve of the polymers are shown in Figure 8. The onset decomposition temperatures of the (PLLA-OH)$_4$, (PLLA-alkyne)$_4$, (PLLA-PI)$_4$, and (PLLA-PCHO)$_4$ were found as 227 °C, 274 °C, 225 °C, and 377 °C, respectively. The onset decomposition temperatures and degradation rates of homo-

type PLLAs are lower than those of star-type block copolymer, indicating higher thermal stability of (PLLA-PCHO)$_4$ polymer. It is well- known that non-crystalline PCHO is a thermally stable polymer with a decomposition temperature over 400 °C. It seems introducing this durable block into the structure of the polymer has enhanced its thermal stability judging from its boosted

decomposition temperature in comparison with the prepolymers (24). Figure 8 shows that terminal alkyne groups also contribute to the thermal stability of the polymer positively compared to other homopolymers, (PLLA-OH)$_4$ and (PLLA-PI)$_4$. As seen from the figure, while (PLLA-OH)$_4$ has shown one maximum decomposition rate at 290 °C, (PLLA-alkyne)$_4$ and (PLLA-PI)$_4$ have shown three maximum decomposition rates at 324 °C, 362 °C, 436 °C and 258 °C, 290 °C, 300 °C, respectively. The obtained star block copolymer has displayed two maximum decomposition rates at 357 °C and 408 °C.

CONCLUSION

The combination of a controlled polymerization technique with click chemistry is a very versatile method to prepare custom-tailored copolymers with well-defined structures and desired functionalities. We have used this approach to synthesize a novel tetra-arm star-shaped telechelic macrophotoinitiator of poly(L-lactide) with photoreactive benzoin groups at the end of each polymer arm by combining ROP and click chemistry. These photofunctional benzoin groups at the end of each PLLA block served as a means to introduce a new polymer block of cyclohexene oxide to each arm to create an (AB)$_4$-type star block copolymer by photoinduced free radical promoted cationic polymerization. Structural elucidations of the intermediate and final polymers confirmed the all the compounds were successfully synthesized. Thermal behaviors of the polymers indicated that the star block copolymer, (PLLA-PCHO)$_4$, is more stable than the prepolymers. All data and results are in good agreement with each other. As a conclusion, this approach can be used to prepare star-type block copolymers with monomers having different nature and polymerizing with different mechanisms.

ACKNOWLEDGEMENTS

REFERENCES

1. Verso FL, Likos CN. End-functionalized polymers: Versatile building blocks for soft materials. Polymer. 2008;49(6):1425-34.

2. Tasdelen MA, Kahveci MU, Yagci Y. Telechelic polymers by living and controlled/living polymerization methods. Prog Polym Sci. 2011;36(4):455-567.

3. Yagci Y, Onen A, Schnabel W. Block copolymers by combination of radical and promoted cationic polymerization routes. Macromolecules. 1991;24(16):4620-3.

4. Kennedy JP, Iván B. Designed Polymers by Carbocationic Macromolecular Engineering: Theory and Practice. Munich - New York: Hanser-Gardner Publications; 1992. 167 p.

5. Fontanille M. 27 - Carbanionic Polymerization: Termination and Functionalization. In: Bevington JC, Allen G, editors. Comprehensive Polymer Science and Supplements. 3. Amsterdam: Pergamon; 1989. p. 425-32.

6. Yagci Y, Nuyken O, Graubner V-M. Telechelic Polymers. In: Kroschwitz JI, editor. Encyclopedia of Polymer Science and Technology. 12. 3rd ed. New York: John Wiley & Sons, Inc.; 2005. p. 57-130.

7. Mannion AM, Bates FS, Macosko CW. Synthesis and rheology of branched multiblock polymers based on polylactide. Macromolecules. 2016;49(12):4587-98.

8. Guillaume SM. Recent advances in ring-opening polymerization strategies toward α, ω-hydroxy telechelic polyesters and resulting copolymers. Eur Polym J. 2013;49(4):768-79.

9. Degirmenci M, Genli N. Synthesis of Well-Defined Telechelic Macrophotoinitiator of Polystyrene by Combination of ATRP and Click Chemistry. Macromol Chem Phys. 2009;210(19):1617-23.

10. Akeroyd N, Klumperman B. The combination of living radical polymerization and click chemistry for the synthesis of advanced macromolecular architectures. Eur Polym J. 2011;47(6):1207-31.

11. Sumerlin BS, Vogt AP. Macromolecular engineering through click chemistry and other efficient transformations. Macromolecules. 2009;43(1):1-13.

12. Wang CW, Liu C, Zhu XW, Yang ZY, Sun HF, Kong DL, et al. Synthesis of well-defined star-shaped poly (ε-caprolactone)/poly (ethylbene glycol) amphiphilic conetworks by combination of ring opening polymerization and "click" chemistry. J Polym Sci, Part A: Polym Chem. 2016;54(3):407-17.

13. Sivaram S, Chowdhury SR. Synthesis of Functional Polymers of Polar and Nonpolar Monomers by Living and/or Controlled Polymerization. Functional Polymers: Apple Academic Press; 2017. p. 29-82.

14. Yagci Y, Tasdelen MA. Mechanistic transformations involving living and controlled/living polymerization methods. Prog Polym Sci. 2006;31(12):1133-70.

15. Jakubowski W, Matyjaszewski K. New Segmented Copolymers by Combination of Atom Transfer Radical Polymerization and Ring Opening Polymerization. Macromol Symp. 2006;240:213-23.

16. Yagci Y, Jockusch S, Turro NJ. Photoinitiated polymerization: advances, challenges, and opportunities. Macromolecules. 2010;43(15):6245-60.

17. Wen Y, Jiang X, Liu R, Yin J. Amphipathic hyperbranched polymeric thioxanthone photoinitiators (AHPTXs): Synthesis, characterization and photoinitiated polymerization. Polymer. 2009;50(16):3917-23.

18. Corrales T, Catalina F, Peinado C, Allen N. Free radical macrophotoinitiators: an overview on recent advances. J Photochem Photobiol A: Chem. 2003;159(2):103-14.

19. Yagci Y, Mishra MK. Macroinitiators for Chain Polymerization. In: Mishra M, editor. Macromolecular Design : Concept and Practice. New York: Polymer Frontiers International Inc.; 1994. p. 229-64.

20. Durmaz YY, Tasdelen MA, Aydogan B, Kahveci MU, Yagci Y. Light induced processes for the synthesis of polymers with complex structures. New smart materials via metal mediated macromolecular engineering: Springer; 2009. p. 329-41.

21. Degirmenci M, Benek N, Durgun M. Synthesis of benzoin end-chain functional macrophotoinitiator of poly (D, L-lactide) homopolymer and poly (ε-caprolactone)-poly (D, L-lactide) diblock copolymer by ROP and their use in photoinduced free radical promoted cationic copolymerization. Polym Bull. 2017;74(1):167-81.

22. Degirmenci M, Besli PA, Genli N. Synthesis of a well-defined end-chain macrophotoinitiator of poly (ε−caprolactone) by combination of ring-opening polymerization and click chemistry. J Polym Res. 2014;21(9):540.

23. Uyar Z, Degirmenci M, Genli N, Yilmaz A. Synthesis of well-defined bisbenzoin end-functionalized poly (ε-caprolactone) macrophotoinitiator by combination of ROP and click chemistry and its use in the synthesis of star copolymers by photoinduced free radical promoted cationic polymerization. Designed Monomers and Polymers. 2017;20(1):42-53.

24. Uyar Z, Durgun M, Yavuz MS, Abaci MB, Arslan U, Degirmenci M. Two-arm PCL and PLLA macrophotoinitiators with benzoin end-functional groups by combination of ROP and click chemistry and their use in the synthesis of A_2B_2 type miktoarm star copolymers. Polymer. 2017;123:153-68.

25. Yagci Y, Degirmenci M. Photoinduced Free Radical Promoted Cationic Block Copolymerization by Using Macrophotoinitiators Prepared by ATRP and Ring-Opening Polymerization Methods. Advances in Controlled/Living Radical Polymerization. ACS Symposium Series. 854: American Chemical Society; 2003. p. 383-93.

26. Yağci Y, Kornowski A, Schnabel W. N-alkoxy-pyridinium and N-alkoxy-quinolinium salts as initiators for cationic photopolymerizations. J Polym Sci, Part A: Polym Chem. 1992;30(9):1987-91.

27. Save M, Schappacher M, Soum A. Controlled Ring-Opening Polymerization of Lactones and Lactides Initiated by Lanthanum Isopropoxide, 1. General Aspects and Kinetics. Macromol Chem Phys. 2002;203(5-6):889-99.

RESEARCH ARTICLE

Synthesis of an Antimicrobial Thio-anthraquinone Compound to Produce Biodegradable Electrospun Mats for Tissue Engineering Purposes

Yesim Muge Sahin* ✉ iD

¹Istanbul Arel University, ArelPOTKAM (Polymer Technologies and Composite Application and Research Center), 34537, Istanbul, Turkey

²Istanbul Arel University, Faculty of Engineering and Architecture, Department of Biomedical Engineering, 34537, Istanbul, Turkey

Abstract: In this work, a novel S-substituted bioactive anthraquinone compound is synthesized with a new, easy and less energetic reaction methodfrom 1-chloro-9,10-dihydrodiagnosisxy-anthraquinone and butyl-3-mercaptopropionate (Compound 3) for the first time in the literature. The synthesized structure is purified by column chromatography and then characterized with various spectroscopic methods (NMR, MS, FT-IR, UV). The investigation of the antimicrobial properties of the purified structure reveals remarkable biological properties. Compound 3 is not only effective against yeasts and fungi but also displays significant inhibitory effects on the growth of the tested Gram positive bacteria similiar to that of a positive control (Gentamicin). Subsequently, biodegradable electrospun mats are produced via electrospinning method for their usage as a biomaterial. Structural (FTIR), morphological (FEG-SEM) biological (antimicrobial and in-vitro tests) and mechanical (tensile testing) characterizations are conducted for these nanobiomaterials. Presenting an advantage of the novel antimicrobial compound, all produced electrospun nanobiocomposites exhibit remarkable cell viability% and mechanical properties as the amount of Compound 3 increases. Cell viability values are 95% or greater for all polymeric nanocomposites whereas, the best cell viability% and mechanical proprties are obtained for PCL-8% Compound3 composite. The obtained electrospun mats are good candiates for biomaterials for tissue engineering purposes and wound healing materials with a purposeful compound synthesis and a subsequent nanobiocomposite production.

INTRODUCTION

Natural products have great potential for medical applications. Recently, anthraquinone derivatives have gained special interest owing to their large potential applications as antifungal, antiviral, antibacterial agents for biological activities (2-6). Aloe-emodin, an anthraquinone derivative, is a potential antileukemic material (7). This molecule chemically stumilates the growth and proliferation of normal mouse splenocytes and shows dose-dependent cytoxicity against cancer cell lines. On the other hand, being effective to various cancer type and multiple sclerosis, Mitoxantrone, an anthraquinone analogue, is known as a synthetic anticancer analog of anthracycline antibiotics (8-12). Several studies have been conducted to understand the mechanism of mitoxantrone and it is revealed that the nuclear DNA is the primary target and the planar anthraquinone ring inserts between DNA base pairs. Consequently, negatively charged phosphate groups of DNA are found to bind to the nitrogen-containing side chains (13-15). Being an anticancer drug, Mitoxantrone is

a valuable inhibitor for the enzymes that are responsible for repairing a damaged DNA (16,17). Several anthraquinone analogues have been evaluated as potential materials in various applications.

Recently, many studies have been conducted with both isolated [18,19] and synthesized anthraquinone derivatives [20,21] since they present potential therapeutic uses such as antibacterial, antifungal agents, and in other biological activities. Furthermore, various functional groups have been substituted to anthraquinone molecules to improve biocompatibility, antimicrobial and anticancer properties for tissue engineering purposes. Among these molecules amino, hydroxy, metoxy, cyano, thiazoline, and thiophene etc. derivatives [22-25] have been synthesized. Although, for naphthaquinones, a family of quinones, thiol derivatives have been evaluated detailly for their antibacterial and antifungal activity [26] , very few studies have been conducted with thio-substituted anthraquinones to identify their biological properties [27]. Moreover, in the literature some isolated natural thioantraquinone derivatives were extensively used for their antimicrobial and anticancer properties [28]. These investigations have been the motivation of this work to focus on the synthesis of anthraquinone molecules and their subsequent nanocomposite production for tissue engineering materials.

Synthesis of some anthraquinone derivatives in the literature have been conducted with expensive and hardly obtained chemicals like cesium carbonate. Also organic solvents, which are hazardous and hardly purified, are used for such synthesis under nitrogen conditions (29,30). Thus sustainable production of an anthraquinone has become difficult. In our previous study, a novel practical, economical and one-step synthesis methodology has been established to simple synthesis of anthraquinone derivatives (1). Ethylene glycol is used as an organic solvent in the present study. Since reactions are conducted under heat, the usage of nonvolatile, readily available and inexpensive solvent such as ethylene glycol presents the novelty of our synthesis method. On the other hand, being biocompatible, biodegradable and presenting higher mechanical properties in comparison to its natural polymer analogues, Polycaprolactone (PCL) is preferred especially in tissue engineering applications. Moreover, the degradation products (succinic acid, butyric acid, valeric acid and caproic acid) of PCL don't present a toxic effect and inflammatory reactions. These effects make PCL preferable in the regeneration of bone, epidermis, nerve and retina in tissue engineering (31,32). The synthetic polymer PCL, among the few FDA (Food and Drug Administration) approved polymers and present antimicrobial effect can

be utilized as biomaterials for such purposes (33).

Electrospinning is an efficient technique that is used for the fabrication of polymer nanofibers. In recent years, various polymeric and composite solutions have been successfully converted into electrospun mats of ultrafine fibers (34,35). Presenting higher volume/surface area, these nanofiber mats result in superior properties especially in biological (antimicrobial and cell adhesion) and mechanical aspects (31, 36, 37). As a consequence of these, obtained electrospun mats can have potential applications as regenerative or wound healing biomaterials in tissue engineering (38,39).

In the present paper, a comprehensive study has been conducted starting from the synthesis of a noval, biologically active compound, and its production of to electrospun biocomposites. The obtained biomaterials can find applications as wound healing material or a biomaterial for regenerative tissue engineering purposes.

MATERIALS AND METHODS

Materials and Characterization
All chemicals are obtained from Sigma Aldrich and used as received. The obtained products are purified by column chromatography on Silica gel (Fluka Silicagel 60, particle size 63-200 µm). TLC plates coated with silica 60F254 (Merck, Darmstadt) are used under ultraviolet light (254 nm). To identify the melting points of the products, a Buchi B-540 melting point apparatus is used. Structure investigations for both Compound 3 and the nanocomposites are identified by Fourier transform infrared (FTIR) spectroscopy. The IR spectra were recorded on a JASCO (model 6600) FTIR spectroscopy in the region 400–4000 cm^{-1} at a resolution of 1 cm^{-1} and 8 scans are performed for each detection. ATR technique is used. UV spectrum is gauged by using Shimadzu UV-VIS Spectrophotometer 2600. ^{1}H and ^{13}C NMR spectra are conducted by Varian UNITY INOVA which are operated at 500 MHz. Mass analysis is done on a Thermo Advantage MAX LC/MS/MS spectrometer.

Synthesis and structural characterization of thio-substituted anthraquinone (Compound 3) (1)
1-Butylpropionylthio-9,10-dioxo-anthraquinone (3)
Cl substitution on anthraquinone ring can give a nucleophilic substitution reaction and different nucleophilic groups can chemically bond to the ring. Compound **3** is synthesized from the reaction of 1-chloro-9,10-dioxo-anthraquinone **1** (1 g, 4.12 mmol) with butyl-3-mercaptopropionate **2** (0.66 g, 4.06 mmol) in a mixture of ethylene glycol and aqueous KOH solution (1). Orange solid, mp: 153-154 °C. Yield: 1.18 g (78%)

Rf [(Petroliumether/Dichloromethane) (1:1)]: 0.51.

IR (cm⁻¹): υ = 3019, 2959 (C-H$_{arom}$), 1573 (C=C), 1676 (C=O). UV-vis (CHCl$_3$): λ$_{max}$ (logε) = 382 (3.91); 254 (5.03) nm.

^{1}H NMR (499.74 MHz, CDCl$_3$): δ = 0.89 (s, 3H, CH$_3$), 1.33-4.04 (m, 6H, CH$_2$), 2.59 (s, 2H, S-CH$_2$-<u>CH$_2$</u>), 3.17 (s, 2H, S-<u>CH$_2$</u>-CH$_2$) 7.37-8.28 (m, 7H, H$_{arom}$).

^{13}C NMR (125.66 MHz, CDCl$_3$): δ = 13.7 (CH$_3$), 19.1 (CH$_2$), 28.7 (S-CH$_2$-CH$_2$), 31.4 (CH$_3$CH$_2$CH$_2$), 31.5 (S-CH$_2$-CH$_2$), 64.7 (COOCH$_2$), 126.75, 129.96, 131.10, 132.05, 132.58, 133.84, 134.25, 138.21, 139.94 (C$_{arom}$ and CH$_{arom}$), 182.21, 184.25 (C=O). MS [+ESI]:m/z 369.65 [M+H]$^+$, C$_{20}$H$_{21}$N$_3$O$_2$, (M, 368.45 g/mol). Schematic representation of ester-substituted thio-anthraquinone compound (Figure 1.).
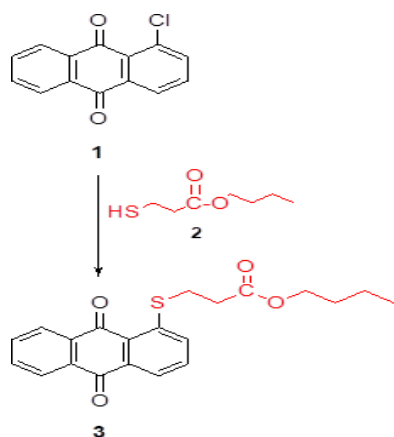

Figure 1. Schematic representation of ester-substituted thio-anthraquinone compound.

Biological characterization of ester substitued thio-anthraquinone compound

a) Antibacterial activity of thio-anthraquinone (Compound 3)

For antibacterial effect detection of the thio-anthraquinone compound, the agar dilution method according to clinical and laboratory standards institute (formerly CLSI) is performed quantitatively (40). The antimicrobial activities are assessed against Gram- positive (*Staphylococcus epidermidis* (ATCC 12228), *Staphylococcus aureus* (ATCC 29213), *Bacillus subtilis* (ATCC 6633), *Enterococcus faecalis* (ATCC 29212), and Gram- negative bacteria (*Klebsiella pneumoniae* (ATCC 4352), *Pseudomonas aeruginosa* (ATCC 27853), *Salmonella enteritidis* (KUEN 349), *Escherichia coli* (ATCC 25922). Mueller–Hinton Agar (Fluka 70191) is utilized for identification of the qualitative antibacterial effect and to provide the strains. In order to specify the quantitative antibacterial effect, Mueller– Hinton broth (Fluka 90922) (CAMBH) with MgCl$_2$·2H$_2$O (10 mg Mg^{2+}/L) and CaCl$_2$·6H$_2$O (20 mg Ca^{2+}/L) are used as a

medium. Furthermore, gentamicin sulfate (Sigma G1272) is utilized as the reference antibiotic standard. 10 serial dilutions of the thio-anthraquinone compound between 0,01 mg/mL – 5,4 mg/mL with CAMBH are prepared in sterile tubes. 1 ml of each inoculum are poured to each petri dishes and 9 ml of Muller-Hinton agar which is brought to 50 °C and is added onto inoculum. Subsequently, it is mixed with a circular dial until cooling to room temperature. Bacterial suspensions with 10^7 cfu/ml final concentration are prepared and added into the microplate wells. The sterilized replicator with 3-mm pins which deliver 2 μL are placed into the microplate to soak the pins and transferred onto the agar plate. The agars are incubated at 37 °C for 24 hours. The minimum inhibitory concentration, MIC, value is determined beyond the level no inhibition of growth of test organisms are observed.

b) Antifungal activity of thio-anthraquinone (Compound 3)

The antifungal effect of the thio-anthraquinone compound against yeast and fungi is examined with minimum inhibitor concentration using (MIC) broth macro dilution method according to CLSI (32). The antifungal activities are evaluated against yeasts (*Candida albicans, Malassezia pachydermatis*) and fungi (*Microsporum canis* and Trichophyton mentagrophytes.

Suspension equal to 0.5 McFarland turbidity in physiological salty water among 48-hour *C. albicans* and *M. pachydermatis* strains and 5 days *M. canis* and *T. mentagrophytes* strains in Sabouraud Dextrose Agar (SDA) (Sigma S3181) are prepared in order to get the inoculum. The MIC of the compound is determined by two-fold micro-dilution method in RPMI 1640 Medium (Sigma R8758) according to CLSI. Amphotericin B (Sigma 1032007) is used as the positive control. The lowest concentration that completely inhibits the reproduction and can be determined with the naked eye, i recorded as the MIC value.

Preparation of electrospinning solutions
Polycaprolactone, average molecular weight (Mw) 80,000 g/mol, is obtained from Sigma-Aldrich and used without further treatment or purification. PCL is dissolved in chloroform/dimethylformamide (DMF) solution with a constant w/w 3:2 ratio. On the other hand, the synthesized ester-substituted thio-anthraquinone compound is also added to the obtained solution and both of them are stirred sufficiently at range of 30-40 °C. Different compositions are prepared as 6% PCL, 6% PCL-1% Compound 3, 6% PCL-5% Compound 3 and 6% PCL-8% Compound 3.

Properties of the electrospinning solution (viscosity, molecular weight of the polymer),

should be determined before the jet. High molecular weight PCL is chosen purposefully in the present study, in order to produce nanofibers not nanoparticles. If lower molecular weight ones are used, low viscous solutions are obtained and hence the presence of beads are observed. Whereas, with very high molecular weight polymer, fibers wider than nano scale are produced which is not preferred. The viscosity of polymeric solution has been adjusted as well, to maintain nanofibers and optimize their fiber sizes, hence their morphology. Too high a viscosity results in drying of the droplet when coming out at the tip of the needle. PCL solution density is adjusted as 6% PCL and so the viscosity. So as an optimum solution viscosity and Mw is chosen for continuous smooth fibers without any agglomeration and beads.

Production of Nanobiocomposite Mats via Electrospinning Method
In order to get nanofiber structures but not nanoparticles solution parameters should be determined and process parameters should be adjusted. **(a)** The prepared electrospinning solution **(b)** Nanocomposite mat production via electrospinning method (Figure 2.).
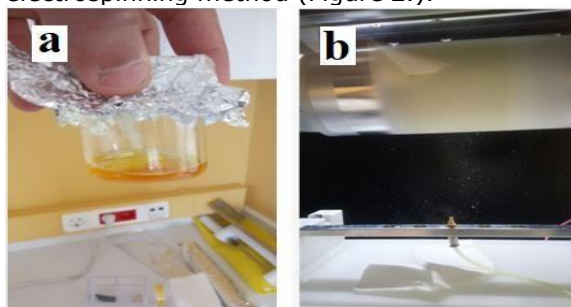

Figure 2. (a) The electrospinning solution **(b)** Nanocomposite mat production via electrospinning method.

One of the most important parameters among the controllable variables during electrospinning is the applied voltage. Taylor cone is an indication of the critical voltage for electrospinning to occur. The critical voltage depends on the distance between the collector and the tip, surface tension of the solution, the tip radius and length of the pipette. Once the critical voltage is reached, the electrical force become sufficient to overcome the surface tension resulting in a taylor cone for electrospinning. Higher voltage yields to better electrospun fibers in nanoscale. Size of the fibers can also be easily varied by altering the distance between the tip and the collector. When the distance between the tip and collector are too small, the fibers are deposited on the collector even before the solvent evaporates. Schematic representation of the electrospinning method (Figure 3.).

To obtain homogenous fiber structures, process parameters have been set. The applied voltage is in the range of 15-31.8 kV while a Taylor cone is observed at a voltage of 12.3 kV. Humidity of the internal process area is recorded as 44.6±5%. The flow rate of the digital syringe pump is 1 ml/h and the average distance between the tip of needle and collector is set to 12 cm. Solution parameters of the obtained biocomposite electrospun mats are given in Table 1.

In the present study, solution parameters are also determined. Table 1 summarizes the solution parameters that are worked with. Increasing the crystalline content by incorporating Compound 3, mixture temperature or the mixing time to maintain a clearly dissolved solution increased (42,43). This can be attributed to the rigid anthraquinone structure which increases the crystallinity (37,44).

Table 1. Solution parameters of the obtained biocomposite electrospun mats.

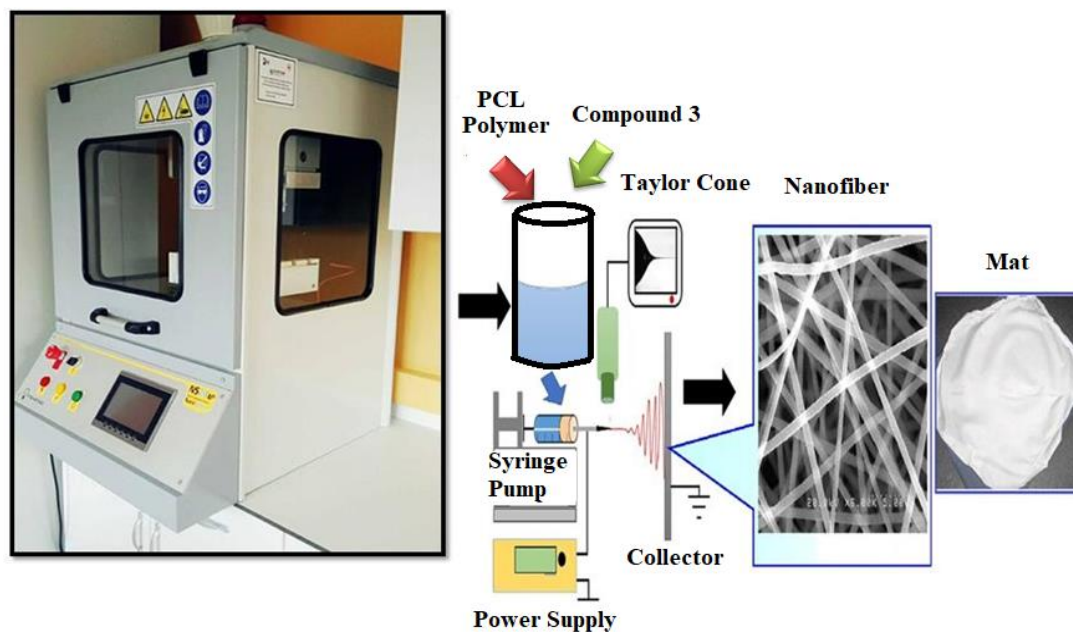| Polymer/ Compound 3	Solvent	Solvent ratio(w/v)	Mixture Temp.(˚C)	Mixing time (min)
PCL	Chloroform/ DMF	3:2	30	45
PCL–1% Compound 3	Chloroform/ DMF	3:2	30	45
PCL–5% Compound 3	Chloroform/ DMF	3:2	33	47
PCL–8% Compound 3	Chloroform/ DMF	3:2	36	48

Figure 3. Schematic representation of the electrospinning method.

Characterization of the Nanobiocomposite Mats

Morphological investigation of PCL and PCL composites having 1%, 5%, 8% Compound 3 by electrospinning method have been performed using FEI Quanta 450 FEG model scanning electron microscope (FEGSEM) under an applied voltage of 7.0 kV. Dimensional analysis and the topological investigation have also been conducted for the samples. Nanofibers' diameters are estimated using Image J software (National Institutes of Health, Bethesda, MD, USA) over 100 places in SEM images. Additionally, topologies of the samples are calculated similarly (45,46).

Tensile tests of the electrospun nanofiber mats (PCL and PCL composites having 1%/5%/ 8% content of Compound 3) are conducted according to ASTM E4 standards. Tensile strengths of the nanofiber mats are calculated with a rectangular specimen and a size of 1x5 cm, under 500 N load by an Instron Brand test machine. The nanofiber thicknesses measured before the mechanical test and are in the range of 0.01-0.18 mm. Tests have been carried out at a constant jerk of 5 mm / min at a jaw distance of 10 cm (32). Elongation values and UTS (ultimate tensile strength) points are measured by Instron 4411 tensile test machine with specific software (Bluehill 2, Elancourt, France). Each set of sample is tested 5 times and their averages are taken.

For antibacterial effect detection of the electrospun mats, the agar dilution method according to clinical and laboratory standards institute (formerly CLSI) is performed quantitatively (3,47). The antimicrobial activities are assessed against Gram-positive (*Staphylococcus aureus* (ATCC 29213)), and

Gram-negative (*Escherichia coli* (ATCC 25922) bacteria and yeast (*Candida albicans).*

In-vitro tests for the electrospun mats have been conducted as follows;

Sample Preparation:

The nanocomposite mat films are cut to 10 x 10 mm and the films are washed 3 times in 70% ethanol. In the third wash, the samples are left in the alcohol for 30 min. The samples are then washed 3 times with PBS for 5 minutes. One sample from each group is covered with culture media and kept in incubator at 37°C for 48 hours for degradation and contamination control.

Cell culture:

After control experiments, samples are cultured with immortalized human lung bronchial epithelial cell line (BEAS-2B) to detect any toxic effects of the molecule. $6x10^6$ cells are seeded on three samples from each group with 200 µl culture media (RPMI 1640 with 10% Fetal Bovine Serum and 1% Penisilin/Streptomisin). After 10 minutes, 1.8 ml of culture media is added to each well of culture plates. Three wells without polymers are used as controls. The samples are then incubated with the cells for 72 hours and observed on an inverted microscope after 24, 48 and 72 hours, they were observed on an inverted microscope. After 72 hours, the cells are microscopically examined for viability. The wells are collected, washed with PBS and fixed with 70% methanol for 20 minutes in a refrigerator. For the detection of dead cells, samples are stained and incubated with 100 ng/ml propidium iodide (PI) solution for 10 minutes. The cells are evaluated and photographed under a Zeiss AxioScope Z1 LED fluorescent microscope (48-51).

RESULTS AND DISCUSSION

Synthesis and characterization of ester-substituted thio-anthraquinone compound
The synthesized of thio-anthraquinone compound has been obtained by the reaction of 1-chloro-9,10-dihydroxy-anthraquinone (1) and butyl-3-mercaptopropionate in a mixture of ethylene glycol and aqueous solution of KOH (1). The obtained thio-anthraquinone compound is an orange solid and is stable. The resultant thio-anthraquinone compound has been synthesized for the first time in the literature and its applications as a biomaterial are discussed in the present study.

Structural characterization results of ester-substituted thio-anthraquinone compound
The characteristic –C=O band of anthraquinone skeleton for Compound 3 is detected at 1671 cm^{-1}, on the other hand, 3019 cm^{-1} and 1557 cm^{-1} can be attributed to the aromatic structure in the IR spectrum. In the ^{13}C NMR of compound 3**,** carbon atom of the ester carbonyl gave a peak at 184.25 ppm whereas, in ^{1}H NMR haracteristic sulfur-hydrogen peaks are detected at 2.59 and 3.17 ppm. Moreover, the molecular ion peak of S- substituted anthraquinone compound 3 is observed at m/z 369.65 [M+H]$^{+}$.

Antimicrobial Test Results of ester-substituted thio-anthraquinone compound
It is found that the thio-anthraquinone compound demonstrates effectiveness against *S.aureus, S.epidermidis* and *B. subtilis* (0,27 mg/mL). It is observed that the extract has no activity on *Enterococcus faecalis, Escherichia coli, Klebsiella pneumoniae*, *Pseudomonas aeruginosa,* and *Salmonella enteritidis*. Regarding the antibacterial activity, the results reveal that the compound displays significant inhibitory effects on the growth of the tested Gram positive bacteria similiar to that of a positive control (Gentamisin).
No antibacterial activity has been observed against all of the tested Gram negative bacteria. The result concerning the in vitro antibacterial activity of the thio-anthraquinone compound is presented in Table 2.

Table 2. The result concerning the in vitro antibacterial activity of the Thio-anthraquinone compound.

Bacteria	Thio-anthraquinone compound (3) (mg/mL)
S.aureus	0.27
S.epidermidis	0.27
B.subtilis	0.27
K.pneumoniae	(-)
E.faecalis	(-)
E.coli	(-)
P.aeruginosa	(-)
S.enteritidis	(-)

(-); MIC value is not detected in the test concentrations

Table 3. The result concerning the in vitro antifungal activity of the thio-anthraquinone compound.

	Thio-anthraquinone compound 3 (mg/mL)
Yeasts	
C.albicans	0,0675
M.pachydermatis	0,0843
Fungi	
M.canis	0.27
T.mentagrophytes	0.27

The effectiveness of the thio-anthraquinone compound is recorded effectiveness in different concentrations against yeasts and fungi. The compound showed a significant activity against *C. albicans* (0.0675 mg/mL) and *M. pachydermatis* (0.0843 mg/mL) and moderate inhibitory activity profile against *M. canis* and *T. mentagrophytes* (0.27 mg/mL). The results concerning the in vitro antifungal activity of the compound with MIC values are presented in Table 3. Regarding the antibacterial and antifungal activity, the results reveal that the thio-anthraquinone compound displays significant inhibitory effects on the growth of the tested Gram positive bacteria as *S. aureus, S. epidermidis, B. subtilis* and yeasts as *C. albicans, M. pachydermatis*. Additionally, antifungal activity against fungi is moderate and any antibacterial activity is not determined against all of the tested Gram negative bacteria.

Production and Characterization of Nanobiocomposites
PCL and ester-substituted thio-anthraquinone (Compound 3) solution was successfully converted into solid nanofibers through a single fluid-blending electrospinning. Calculated amounts of PCL and Compound 3 were used to obtain nanofiber mats. The nanofibers were produced with a single cone during electrospinning and exhibit homogenious morphology and without any agglomeration or discerned bead of Compound 3. For all nanfiber composites FEGSEM images with two different magnifications (3000x and 12000x) as well as their topology and fiber diameter histograms are illustrated in Figure 5. illustrated.
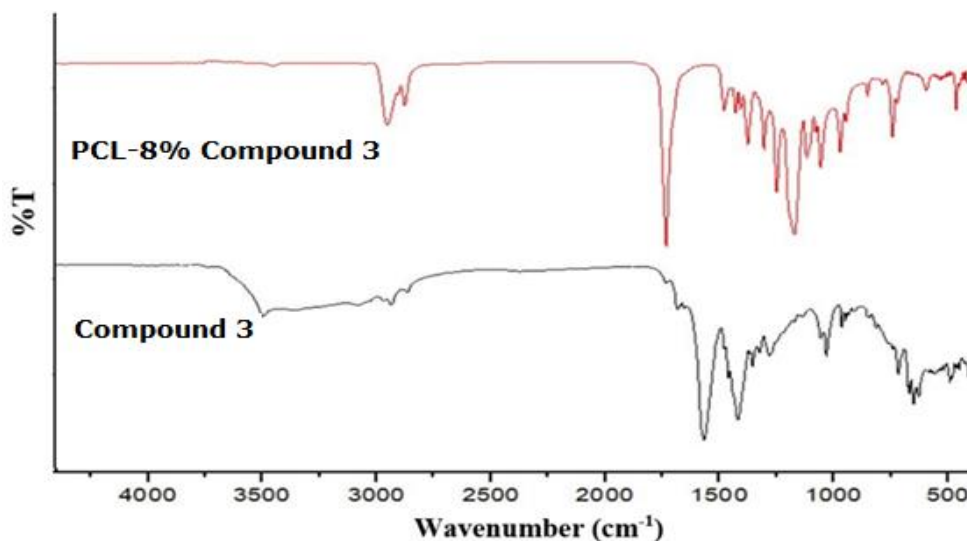
Structural Characterization Result

Figure 4. FTIR Spectra of thio-anthraquinone (Compound 3) and PCL- 8% Compound 3 Nanocomposite.

FTIR Spectra of thio-anthraquinone (Compound 3) and PCL-8% Compound 3 Nanocomposite are shown in Figure 4. For the nanocomposite, aliphatic -CH$_2$ stretching can be observed in between 2945-2866 cm^{-1}. The bands at 1164 cm^{-1}, 1239 cm^{-1} and 1294 cm^{-1} are due to the symmetric stretching of C-O-C groups in the polymer. The strong band at 1721 cm^{-1} belongs to the characteristic carbonyl (C=O) stretching for PCL (52) Moreover, aromatic bands at 3019 cm^{-1}, aliphatic stretching bands between 2800-2900 cm^{-1} and bands between 1200-1000 cm^{-1} comes from the synthesized thio-anthraquinone structure. The distinguishable bands for thio-anthraquinone Compound 3 on the other hand, carbonyl (C=O) and aromatic (C=C) peaks, are observed at 1676 cm^{-1} and 1573 cm^{-1} respectively (53).

FEGSEM images of nanocomposites at two different magnifications (3000x and 12000x), their histograms and topological views are shown in Figure 5. PCL and ester-substituted

thio-anthraquinone (Compound 3) solution is successfully converted into solid nanofibers through a single fluid-blending electrospinning. Calculated amounts of PCL (as indicated in materials and methods section) and Compound 3 were used to obtain nanofiber mats. The nanofibers were produced by a single cone electrospinning method and homogenious morphology, without any agglomeration or discerned bead of Compound 3, are obtained. For all nanofibers, FEGSEM images with two different magnifications (3000x and 12000x) as well as their topology and histogram of the fiber diameters were illustrated. In all the nanofiber mats, the size distribution is narrow and the histograms reveal that the size of the produced nanofibers are in the range of nanoscale. By incorporation of Compound 3, the solution conductivity is increased due to anthraquinone structure, hence thinner and finer fiber formation is achieved (42,54). As a result, when FEGSEM images and histograms of the biocomposite mats are examined, a noticeable decreament in mean fiber diameters is observed.

Morphological Characterization and EDS Test Results
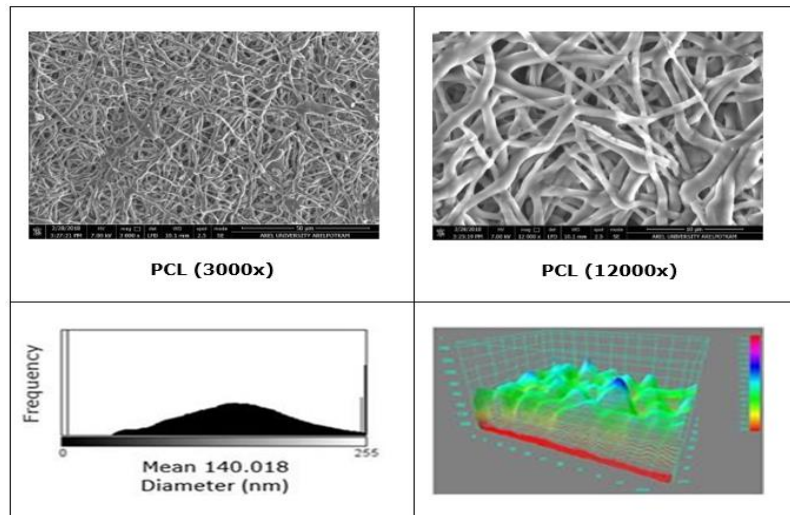
A. FEGSEM images for PCL nano mats at two different magnifications (3000x and 12000x), histogram and topology of PCL nano mats.

B. FEGSEM images for PCL-1% Compound 3 SEM nano mat at two different magnifications (3000x and 12000x), histogram and topology of PCL-1% Compound 3 nano mats
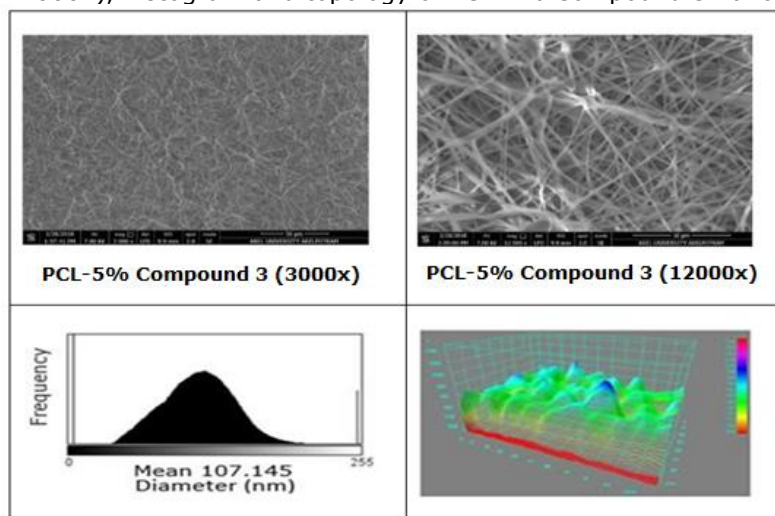
C. FEGSEM images for PCL-5% Compound 3 SEM nano mat at two different magnifications

(3000x and 12000x), histogram and topology of PCL-5% Compound 3 nano mats
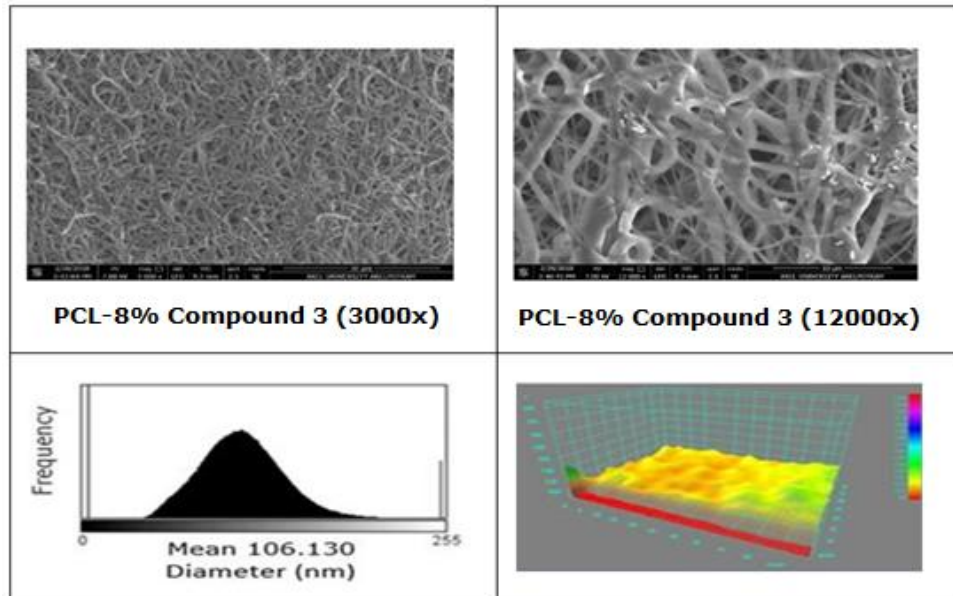
D.   FEGSEM images for PCL-8% Compound 3 SEM nano mat at two different magnifications (3000x and 12000x), histogram and topology of PCL-8% Compound 3 nano mats

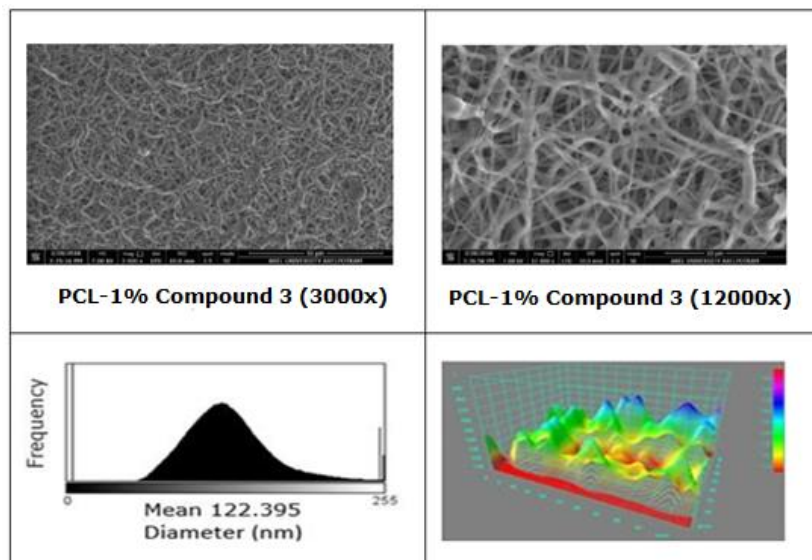**Figure 5.** FEGSEM images of nanocomposites at two different magnifications (3000x and 12000x), their histograms and topological views.

Additionally, topology investigations reveal that porosity of the nanofiber mats are decreased owing to thinner fibers, thus enabling more uniform coatings and diameters distribution of the fibers. The porosity is important in cell growth and regeneration. For such a porous biodegradable biomaterial cells can find (42, 55-57).

Antimicrobial Test Results
Figure 6 shows the antimicrobial test results of the nanocomposites. as it is seen in Figure 7, the best antimicrobial activity can be seen for PCL/5% Compound 3 samples. PCL/Compound

3 composite nanofibers have different antimicrobial effect against Gram (+) positive and Gram (-) negative bacteria and yeast. Considering the results, PCL/Compound 3 composite nanofibers are highly active against proliferation of the *Candida albicans* fungal colonies, moderately effective against Gram (+) positive *Staphylococcus aureus* strains and not very effective against *Escherchia coli* which is Gram (-) negative bacteria strain.

Antimicrobial Effects-24 hr
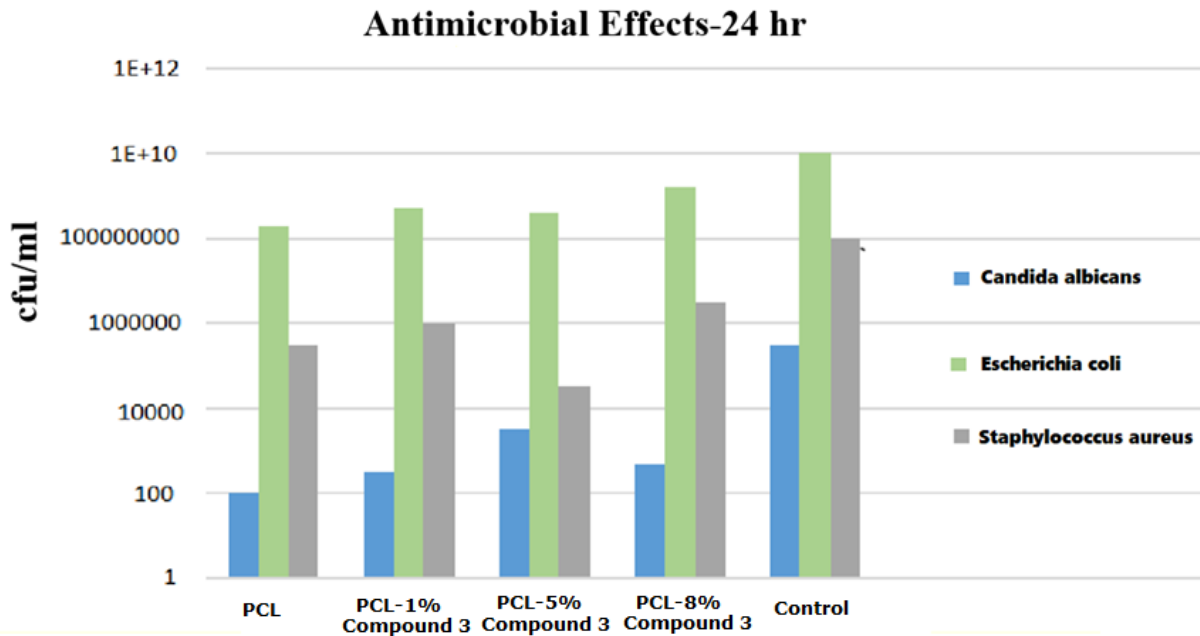
Figure 6. Antimicrobial results of the samples against three different kinds of microorganisms.

In comparison to PCL/5% Compound3 nanocomposite, PCL/8% Compound3 nanocomposite is less effective against all microorganisms. This can be attributed to the agglomeration of Compound 3 and bead accumulation on nanofibers as can be supported by SEM images of PCL/8% Compound3 composite system. Irregularities such as bead formation or agglomeration on nanofiber mat ensure the adhesion of bacteria to the surface of the material. These homogeneities in the structure adversely affect the antimicrobial properties of the material (42, 58, 59).

It was determined that there is no suitable environment for the adhesion and repletion of bacteria on flat surfaces. Such a flat surface hinders adhesion to the surface material (60,61). For this purpose, to increase the antimicrobial activity of this active compound, nanofiber production are planned and conducted during this study (62-64). In comparison to PCL the electrospun nanomat of PCL presents a slightly enhanced antimicrobial activity (65,66). As it can be seen from the FEGSEM images, nanobiocomposites are found to be homogeneous and thinner nanofibers are produced as stable anthraquinone as percentage increases. This result is due to the conductivity increase of the solution by incorporation of Compound 3 and enhanced antimicrobial effect of our novel thio-anthraquinone compound.

In vitro Test Results

Figure 7. Light microscope images of nanofiber mats.

Figure 8. Light microscope images of cell-cultured nanofiber mats.

Figure 9. % Viability of nanofiber mats with fluorescent dyeing.

1129

Figure 7-9, summarize the in vitro tests of the nanobiocomposites. The examinations are conducted with light microscope revealing that for all nanofibers, cells protect their viability in high order. For the nanocomposite fibers, cell attachments are also observed in all groups. During the examination of nanofibers, local repla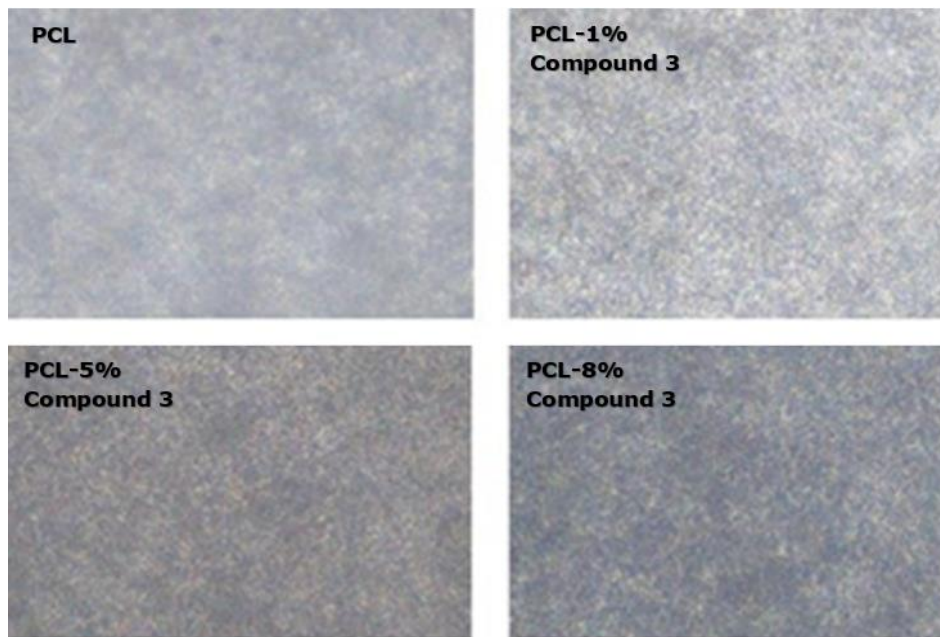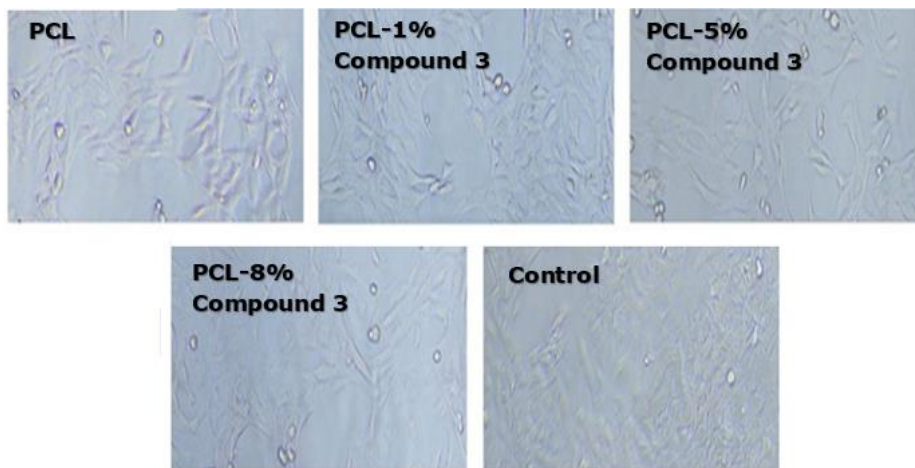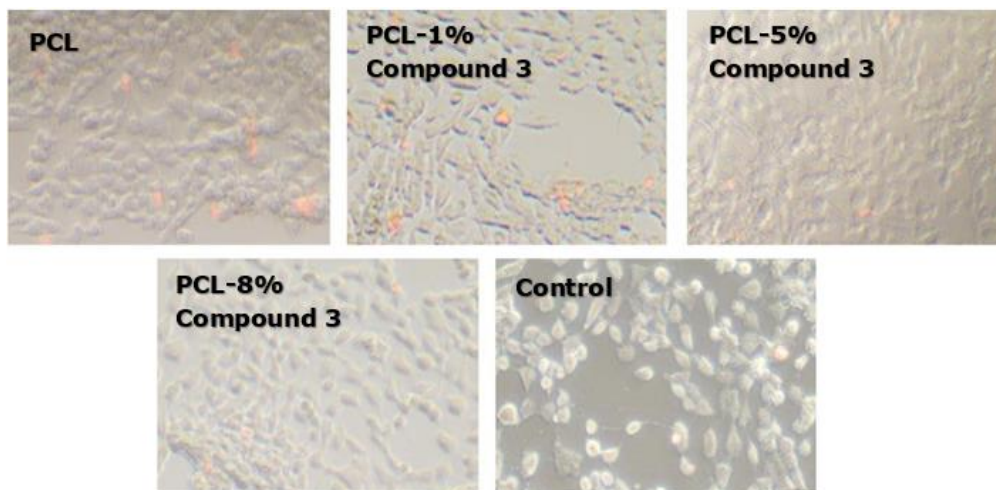cement of cells are observed due to the movement of nanofibers on cells. In the fluorescence microscopy studies, nanocomposite fibers are observed to emit low level visible light under UV illumination. Fluorescence microscopy studies, reveals that the percentage of cells stained with PI is over 94% and no significant difference is detected

in comparison to the control. For all nanocomposite mats, live cells, attached to the surface and stained with DAPI, were reported. Cell viability was 95% or greater for all polymer composites and the control.

Mechanical Tests
Tensile test results of pure PCL mat and the nanobiocomposites are shown in Figure 10. Mechanical properties of the electrospun nanofiber mats (PCL and PCL composites having 1%/ 5% /8% content of Compound 3) are identified according to ASTM E4 standards (33,67). Figure 11 summarizes the tensile test results of the biocomposites.
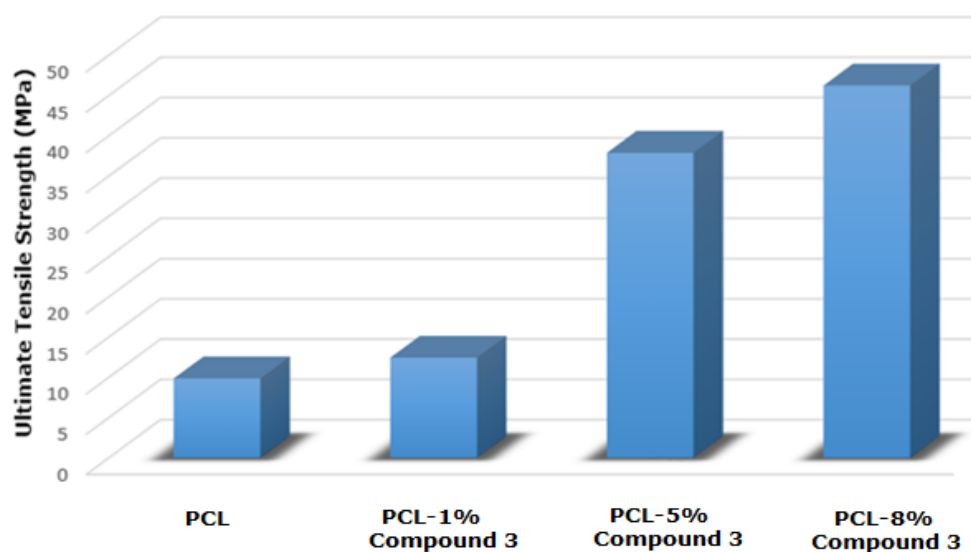
Figure 10. Tensile test results of pure PCL mat and the nanobiocomposites.

When the dimensions of the fibers are reduced to nano scale, owing to an increament in surface area/volume ratio, materials present better magnetic, optic, thermal, chemical, biological, and mechanical properties (68). Moreover, a rise in Compound 3 percent of the composite, enhances the mechanical strength of the material which can be attributed the rigid anthraquinone structure (69). In the light of morphological investigations, as can be understood from the FEGSEM images, the nanofibers are coated homogeniously with Compound 3 and no bead formation is observed which strenghtens the nanocomposites. Being consistent with morphological investigations, mechanical properties of the composites enhanced as Compound 3 content is increased. Several different PCL electrospun nanobiocomposites are present in the literature, however our mechanical results are one of the highest tensile strength among all (31, 70-72). This result is due to high surface area and homogeneity of the fibers, as well as a rigid anthraquinone structure incorporation to the composite mats.

CONCLUSIONS

A novel and simple synthesis method for biologically active ester-substituted anthraquinone derivative has been reported by our previous study. Having antimicrobial and bioactive properties, this stable thio-anthraquinone derivative can find applications in drug delivery systems or in biomedical studies for regenerative and healing purposes.

Using this biologically active ester-substituted anthraquinone derivative nanocomposite mats have been produced. Nanocomposite morphologies have such a porous structure that can permit cell migration and growth. For the produced nanofiber mats cell viability percentages are found over 95% and enhanced mechanical properties are obtained by Compound3 incoorporation. The results indicate that the purposefully produced electrospun nanofiber composites from this novel antimicrobial, biocompatible, ester-substituted anthraquinone compound hold potential for functional tissues, biomaterials such as stents and catheters or as wound healing materials.

REFERENCES

1. Ozkok F, Sahin Y M. Biyoaktif Antrakinon Analogları Ve Bunların Sentezine Yönelik Metot. TR. Patent No TR2016/19610.

2. Rath G Ndonzao M, Hostettmann K. Antifungal anthraquinones from Morinda lucida. International journal of pharmacognosy. 1995; 33(2): 107-114.

3. Cowan M M. Plant products as antimicrobial agents. Clinical microbiology reviews. 1999; 12(4): 564-582.

4. Nomura T, Fukai T. Phenolic constituents of licorice (Glycyrrhiza species). In: Fortschritte der Chemie organischer Naturstoffe/Progress in the Chemistry of Organic Natural Products. Springer Vienna, 1998; p 1-140.

5. Ali A M, Ismail N H, Mackeen M M, Yazan L S, Mohamed S M, Ho A S H, Lajis N H. Antiviral, cyototoxic and antimicrobial activities of anthraquinones isolated from the roots of Morinda elliptica. Pharmaceutical Biology. 2000; 38(4): 298-301.

6. Agarwal S K, Singh S S, Verma S, Kumar S. Antifungal activity of anthraquinone derivatives from Rheum emodi. Journal of ethnopharmacology. 2000; 72(1-2): 43-46.

7. Kupchan S M, Karim A. Tumor inhibitors. 114. Aloe emodin: antileukemic principle isolated from Rhamnus frangula L. Lloydia. 1976; 39(4): 223-224.

8. Velasquez W S, Lew D, Grogan TM, Spiridonidis C H, Balcerzak S P, Dakhil S R, Fisher R
I. Combination of fludarabine and mitoxantrone in untreated stages III and IV low-grade lymphoma: S9501. Journal of clinical oncology. 2003; 21(10): 1996-2003.

9. Thomas X, Archimbaud E. Mitoxantrone in the treatment of acute myelogenous leukemia: a review. Hematology and cell therapy. 1997; 39(4): 163-174.

10. Shenkenberg T D, Von Hoff D D.

11. Neuhaus O, Kieseier B C, Hartung H P. Therapeutic role of mitoxantrone in multiple sclerosis. Pharmacology & therapeutics. 2006; 109(1-2): 198-209.

12. Berger T. Current therapeutic recommendations in multiple sclerosis. Journal of the neurological sciences. 2009; 287: S37-S45.

13. Li N, Ma Y, Yang C, Guo L, Yang X. Interaction of anticancer drug mitoxantrone with DNA analyzed by electrochemical and spectroscopic methods. Biophysical chemistry. 2005; 116 (3): 199-205.

14. Lown J W, Morgan A R, Yen S F, Wang Y H, Wilson W D. Characteristics of the binding of the anticancer agents mitoxantrone and ametantrone and related structures to deoxyribonucleic acids. Biochemistry. 1985; 24(15): 4028-4035.

15. Agarwal S, Jangir D P, Mehrotra R. Spectroscopic studies of the effects of anticancer drug mitoxantrone interaction with calf-thymus DNA. Journal of Photochemistry and Photobiology B: Biology. 2013; 120: 177-182.

16. Pommier Y, Leo E, Zhang H, Marchand C. DNA topoisomerases and their poisoning by anticancer and antibacterial drugs. Chemistry & biology. 2010; 17(5): 421-433.

17. Hande K R. Topoisomerase II inhibitors. Update on Cancer Therapeutics. 2008; 3(1): 13-26.

18. Montoya, S. N., Comini, L. R., & Cabrera, J. L. (2011). Antimicrobial activity of natural photosensitizing anthraquinones.

19. Ali, A. M., Ismail, N. H., Mackeen, M. M., Yazan, L. S., Mohamed, S. M., Ho, A. S. H., & Lajis, N. H. (2000). Antiviral, cyototoxic and antimicrobial activities of anthraquinones isolated from the roots of Morinda elliptica. *Pharmaceutical Biology*, *38*(4), 298-301

20. Gouda, M. A., Berghot, M. A., Shoeib, A. I., & Khalil, A. M. (2010). Synthesis and antimicrobial of new anthraquinone derivatives incorporating pyrazole moiety. *European journal of medicinal chemistry*, *45*(5), 1843-1848.

21. Nor, S. M. M., Sukari, M. A. H. M., Azziz, S. S. S. A., Fah, W. C., Alimon, H., & Juhan, S. F. (2013). Synthesis of new cytotoxic aminoanthraquinone derivatives via

nucleophilic substitution reactions. *Molecules*, *18*(7), 8046-8062.

22.   Routier, S., Cotelle, N., Catteau, J. P., Bernier, J. L., Waring, M. J., Riou, J. F., & Bailly, C. (1996). Salen-anthraquinone conjugates. Synthesis, DNA-binding and cleaving properties, effects on topoisomerases and cytotoxicity. *Bioorganic & medicinal chemistry*, *4*(8), 1185-1196:

23.   Ishmael, D. R., & Adelsteinsson, O. (2014). 1, 4, 5, 8-Tetrakis-[(2-N, N-dimethylaminoethyl) amino] anthraquinone as a potential anticancer agent: its synthesis, characterization and anticancer properties.

24.   Teng, C. H., Won, S. J., & Lin, C. N. (2005). Design, synthesis and cytotoxic effect of hydroxy-and 3-alkylaminopropoxy-9, 10-anthraquinone derivatives. *Bioorganic & medicinal chemistry*, *13*(10), 3439-3445.

25.   Gouda, M. A., Berghot, M. A., Shoeib, A. I., & Khalil, A. M. (2010). Synthesis and antimicrobial of certain new thiazolidinone, thiazoline, and thiophene derivatives. *Phosphorus, Sulfur, and Silicon and the Related Elements*, *185*(7), 1455-1462.

26.   Ibis, C., Tuyun, A. F., Bahar, H., Ayla, S. S., Stasevych, M. V., Musyanovych, R. Y., ... & Novikov, V. (2013). Synthesis of novel 1, 4-naphthoquinone derivatives: antibacterial and antifungal agents. *Medicinal Chemistry Research*, *22*(6), 2879-2888.

27.   Huang, H. S. (2005). *U.S. Patent Application No. 10/615,695*.

28.   Huang, H. S., Chiou, J. F., Chiu, H. F., Hwang, J. M., Lin, P. Y., Tao, C. W., ... & Jeng, W. R. (2002). Synthesis of symmetrical 1, 5-bis-thio-substituted anthraquinones for cytotoxicity in cultured tumor cells and lipid peroxidation. *Chemical and pharmaceutical bulletin*, *50*(11), 1491-1494.

29.   Lord W M, Peters A T. Reactions in NN-dimethylformamide.   Part   II.   Halogen replacement   in   the   anthraquinone   series. Journal of the Chemical Society C: Organic. 1968; 783-785.

30.   Ruediger E H, Kaldas M L, Gandhi S S, Fedryna C, Gibson M S. Reactions of 1, 5-dichloroanthraquinone with nucleophiles. The Journal of Organic Chemistry. 1980; 45(10): 1974- 1978.

31.   Zhang Y, Ouyang H, Lim C T, Ramakrishna S, Huang Z M. Electrospinning of gelatin fibers and   gelatin/PCL composite fibrous scaffolds. Journal of Biomedical Materials Research Part B: Applied Biomaterials. 2005; 72(1): 156-165.

32.   Kehoe S, Zhang, X F, Boyd D. FDA approved guidance conduits and wraps for peripheral nerve injury: a review of materials and efficacy. Injury. 2012; 43(5): 553-572.

33.   Polat E. Polikaprolaktonun Elektrostatik Eğirmesi ve Rgd Yüzey Modifikasyonu ile Periferik Sinir İyileşme Kanalları Üretim ve Karakterizasyonu. Fen Bilimleri Enstitüsü, Yüksek Lisans Tezi, 2013 Ankara.

34.   Sahin Y M, Su S, Ozbek B, Yucel S, Pinar O, Kazan   D,   Gunduz   O.   Production   and characterization   of   electrospun   fish sarcoplasmic protein based nanofibers. Journal of Food Engineering. 2018; 222: 54-62.

35.   Aliakbarshirazi S, Talebian A. Electrospun gelatin nanofibrous scaffolds for cartilage tissue engineering.   Materials   Today: Proceedings. 2017; 4(7): 7059-7064.

36.   Erdem   R,   Sancak   E.   Elektroçekim yöntemiyle elde edilen poliamid 6/kitosan bazlı nanoliflerin   morfolojik   özelliklerinin incelenmesi. *İstanbul Ticaret Üniversitesi Fen Bilimleri Dergisi*. 2013; 12.24: 53.

37.   Burger C, Hsiao B S, Chu B. Nanofibrous materials and their applications. Annual Review of Materials Research. 2006; 36: 333-368.

38.   Buluş   E.   Doğal   izole   edilmiş biyoseramiklerden elektrospinning yöntemi ile polimerik biyokompozit malzeme eldesi, Fırat Üniversitesi, Fen Bilimleri Enstitüsü, Yüksek lisans tezi, 2017 Elazığ.

39.   Sill T J, Von Recum H A. Electrospinning: applications in drug delivery and tissue engineering. Biomaterials. 2008; 29(13): 1989-2006.

40.   Jones R N, Sader H S, Mendes R E, Flamm R K. Update on antimicrobial susceptibility trends among Streptococcus pneumoniae in the United States: report of ceftaroline activity from the SENTRY Antimicrobial Surveillance Program (1998–2011).   Diagnostic   microbiology   and infectious disease. 2013; 75(1): 107-109.

41.   Cuenca-Estrella   M,   Gomez-Lopez   A, Alastruey-Izquierdo   A,   Bernal-Martinez   L, Cuesta I, Buitrago M J, Rodriguez-Tudela J L. Comparison   of   the   Vitek   2   antifungal susceptibility system with the Clinical and Laboratory Standards Institute (CLSI) and European   Committee   on   Antimicrobial Susceptibility   Testing   (EUCAST)   broth microdilution reference methods and with the Sensititre YeastOne and Etest techniques for in vitro detection of antifungal resistance in yeast isolates. Journal of clinical microbiology. 2010; 48(5): 1782-1786.

42.   Zhu G, Li T. Properties of polyurethane–

polystyrene graft copolymer membranes used for separating water–ethanol mixtures. European polymer journal. 2005; 41(5): 1090-1096.

43. Jeevitha D, Amarnath K. Chitosan/PLA nanoparticles as a novel carrier for the delivery of anthraquinone: Synthesis, characterization and in vitro cytotoxicity evaluation. Colloids and Surfaces B: Biointerfaces. 2013; 101: 126-134.

44. Meng J G, Feng X T, Bai J. Aloe Fiber and Pure Yarn Research on Performance. In: Advanced Materials Research. Trans Tech Publications. 2012; p. 284-288.

45. Oflaz K. Manyetik nanofiber membranlar, Selçuk Üniversitesi, Fen Bilimleri Enstitüsü, Doktora Tezi, 2016 Konya.

46. Liu X, Shao W, Luo M, Bian J, Yu D G. Electrospun Blank Nanocoating for Improved Sustained Release Profiles from Medicated Gliadin Nanofibers. Nanomaterials. 2018; 8(4): 184.

47. Pfaller M A, Farrell D J, Sader H S, Jones R N. AWARE Ceftaroline Surveillance Program (2008– 2010): trends in resistance patterns among Streptococcus pneumoniae, Haemophilus influenzae, and Moraxella catarrhalis in the United States. Clinical infectious diseases. 2012; 55.suppl_3: S187-S193.

48. Imam S H, Cinelli P, Gordon S H, Chiellini E. Characterization of biodegradable composite films prepared from blends of poly (vinyl alcohol), cornstarch, and lignocellulosic fiber. Journal of Polymers and the Environment. 2005; 13(1): 47-55.

49. Pan H, Fan D, Cao W, Zhu C, Duan Z, Fu R, Ma X. Preparation and Characterization of Breathable Hemostatic Hydrogel Dressings and Determination of Their Effects on Full-Thickness Defects. Polymers. 2017; 9(12): 727.

50. Karp J M, Shoichet M S, Davies J E. Bone formation on two-dimensional poly (DL-lactide-co- glycolide)(PLGA) films and three-dimensional PLGA tissue engineering scaffolds in vitro. Journal of biomedical materials research. Part A 2003; 64(2): 388-396.

51. Çaydamlı Y. Elektrospinning yöntemi ile biyopolimer esaslı nanoyapıların hazırlanması ve karakterizasyonu, Dokuz Eylül Üniversitesi, Fen Bilimleri Enstitüsü, Doktora Tezi, 2012 İzmir.

52. Davila J L, Freitas M S, Inforçatti N P, Silveira Z C, Silva J V L, d'Ávila M A. Fabrication of PCL/β- TCP scaffolds by 3D mini-screw extrusion printing. Journal of Applied Polymer Science. 2016; 133(15).

53. Shakhes J, Zeinaly F, Marandi M A, Saghafi T. The effects of processing variables on the soda and soda-aq pulping of kenaf bast fiber. BioResources. 2011; 6(4): 4626-4639.

54. Kuhn H H. Anthraquinone-2-sulfonic acid doped conductive textiles. U.S. Patent No 5,108,829, 1992.

55. Üstündağ G C. Electrospinning Yöntemi ile Biyomedikal Kullanıma Yönelik Nanolif Yüzey Üretimi ve Uygulaması. Fen Bilimleri Enstitüsü, Yüksek Lisans Tezi, 2009 Bursa.

56. Zeytuncu B. Elektrospinning Tekniği Ve Uv Işımasının Eşzamanlı olarak Uygulanması İle nanofiber Membranların Hazırlanması Ve Kıymetli Metallerin Adsorpsiyonunda Uygulanması, İstanbul Teknik Üniversitesi, Fen Bilimleri Enstitüsü, Doktora Tezi, 2014 İstanbul.

57. Suzuki M. Antibacterial composite non-woven fabric. U.S. Patent No 5,652,049, 1997.

58. Anitha S, Brabu B, Thiruvadigal D J, Gopalakrishnan C, Natarajan T S. Optical, bactericidal and water repellent properties of electrospun nano-composite membranes of cellulose acetate and ZnO. Carbohydrate Polymers. 2012; 87(2): 1065-1072.

59. An Y H, Friedman R J. Concise review of mechanisms of bacterial adhesion to biomaterial surfaces. Journal of Biomedical Materials Research Part A. 1998; 43(3): 338-348.

60. Nilay C A N, Ersoy M S. Nanofiber Structured Polymeric Tissue Scaffolds. 2014; (Volume: 21), 2014, 95.

61. Erem A D. Nanokompozit Yapılı Tekstillerin Geliştirilmesi Ve Antimikrobiyal Özellik Kazandırılması, İstanbul Teknik Üniversitesi, Fen Bilimleri Enstitüsü, Doktora Tezi, 2012 İstanbul.

62. Schiffman J D, Schauer C L. Cross-linking chitosan nanofibers. Biomacromolecules. 2007; 8(2): 594-601.

63. Kayaci F, Um O. C, Tekinay T, Uyar T. Antibacterial electrospun poly (lactic acid)(PLA) nanofibrous webs incorporating triclosan/cyclodextrin inclusion complexes. Journal of agricultural and food chemistry. 2013; 61(16): 3901-3908.

64. Augustine R, Malik H N, Singhal D K, Mukherjee A, Malakar D, Kalarikkal N, Thomas S. Electrospun polycaprolactone/ZnO nanocomposite membranes as biomaterials with antibacterial and cell adhesion properties. Journal of Polymer Research. 2014; 21(3): 347.

65. Lowery J L, Datta N, Rutledge G C. Effect of fiber diameter, pore size and seeding method on growth of human dermal fibroblasts in electrospun poly (ε-caprolactone) fibrous mats. Biomaterials. 2010; 31(3): 491-504.

66. Cengiz Çallıoğlu F. The Effect of Glyoxal Cross-Linker and Nacl Salt Addition on The Roller Electrospinning of Poly (Vinyl Alcohol) Nanofibers. Journal of Textile & Apparel/Tekstil ve Konfeksiyon. 2014; 24(1).

67. Kumru A. Elektroüretimle Nanolif Eldesine Etki Eden Faktörlerin Ve Jelatin-pektin İçeren Nanoliflerin Model Gıdaların Reolojik Özelliklerine Etkilerinin İncelenmesi, İstanbul Teknik Üniversitesi, Fen Bilimleri Enstitüsü, Doktora Tezi, 2014 İstanbul.

68. Erdem R, Sancak E. İkili Besleme Ünitesi Sistemi ile Elektroçekimi Gerçekleştirilen PVA/Aloe barbadensis ve PEO/Kitosan Bazlı Nanolifli Yapıların Morfolojik ve Mekanik

Özelliklerinin İncelenmesi. Afyon Kocatepe Üniversitesi Fen Ve Mühendislik Bilimleri Dergisi. 2015; 14(1): 1-6.

69. Gaumer J, Prasad A, Lee D, Lannutti J. Structure–function relationships and source-to-ground distance in electrospun polycaprolactone. Acta Biomaterialia. 2009; 5(5): 1552-1561.

70. McClure M J, Sell S A, Simpson D G, Walpoth B H, Bowlin G L. A three-layered electrospun matrix to mimic native arterial architecture using polycaprolactone, elastin, and collagen: a preliminary study. Acta biomaterialia. 2010; 6(7): 2422-2433.

71. Ebersole G C, Buettmann E G, MacEwan M R, Tang M E, Frisella M M, Matthews B D, Deeken C
R. Development of novel electrospun absorbable polycaprolactone (PCL) scaffolds for hernia repair applications. Surgical endoscopy. 2012; 26(10): 2717-2728.

72. Lee S J, Oh S H, Liu J, Soker S, Atala A, Yoo J J. The use of thermal treatments to enhance the mechanical properties of electrospun poly (ε-caprolactone) scaffolds. Biomaterials. 2008; 29: 1422-1430.

Mineralization of Hydrochlorothiazide using Hydrogen Peroxide in Subcritical Water

Erdal Yabalak[1]*, Özkan Görmez[1], Yahya Nural[2]*

[1]University of Mersin, Faculty of Arts and Science, Department of Chemistry, TR-33343, Mersin, Turkey.
[2]University of Mersin, Faculty of Pharmacy, Department of Analytical Chemistry, TR-33169, Mersin, Turkey.

Abstract: In this paper, we investigated the mineralization of hydrochlorothiazide, a diuretic drug which is used for the treatment of hypertension, using H_2O_2 as the oxidizing agent in subcritical water as a medium. Response surface methodology was applied to optimize experimental parameters such as temperature, treatment time, and concentration of the oxidizing agent. The highest TOC removal was obtained as 85.22% in 147.3 minutes of treatment time at 403 K using 80 mM of hydrogen peroxide. The reliability of the performed method was evaluated by ANOVA and the theoretical equation of TOC removal of hydrochlorothiazide was proposed. *F* and *p* values of the model were determined as 62.88 and lower than 0.0001, respectively.

INTRODUCTION

Pharmaceuticals are released to the environment during the production, storage, and post-consumption phases. Their damage to the environment, hence their damage to living systems, may be restrained by considering their environmental fate. For this reason, a large number of studies have been carried out on identification of degradation product of the pharmaceuticals and how to release them to the environment in a harmless manner (1-5). In this context, it is known that many methods have been developed to convert pharmaceuticals into harmless or less harmful species, thus safely releasing them into the environment. One of these methods is degradation of the pharmaceuticals using various chemicals in a variety of media (2). Yabalak *et al*. (6-9) have used hydrogen peroxide in subcritical water medium for degradation of various drugs such as propham, ticarcillin, paracetamol and oxacillin. Turabik *et al.* (10), have performed oxidative degradation of imidacloprid by electrochemical

advanced oxidation. Hasan *et al* (11), have carried out degradation of sulfisoxazole on pure TiO_2 under visible light irradiation. Furthermore, Giahi (12) has carried out photodegradation of diclofenac sodium by addition of a small amount of $K_2S_2O_8$ in the medium and Ji *et al.* (13) have carried out degradation of sulfaquinoxaline by a ferrous ion-activated peroxymonosulfate oxidation process.

Hydrochlorothiazide (abbreviated as HCT, 6-chloro-3,4-dihydro-2*H*-1,2,4-benzothiadiazine-7-sulfonamide 1,1-dioxide, Figure 1) belongs to the class of thiazides and is mainly used as a diuretic as well as for the treatment of hypertension, and symptomatic edema (14, 15). However, it is reported that HCT is one the most ubiquitous contaminants in the sewage and river waters in some countries (16) such as Serbia (17) and Spain (4). There are various studies in the literature related to the degradation of HCT using different methods. Real *et al.* (18) have reported the degradation of HCT in different media via oxidation by means of UV radiation, Fenton's

reagent and ozone. Mahajan *et al.* (19) have performed the degradation of HCT under hydrolytic, oxidative, photolytic and thermal stress conditions, and have characterized its degradation products using high performance liquid chromatography. In another study, Márquez *et al.* (20) have carried out the degradation of HCT and some other drugs in ultrapure water and in water from a municipal wastewater treatment plant, by various oxidation methods such as conventional ozonation, photolytic ozonation, TiO_2 catalytic ozonation, *etc*. Contreras *et al.* (21) have reported the degradation of HCT via electrochemical oxidation. Moreover, there are several other studies in the literature for the degradation of HCT using similar degradation methods (22-25). However, to the best of our knowledge, there is not any study related to the degradation of HCT using hydrogen peroxide in subcritical water medium.
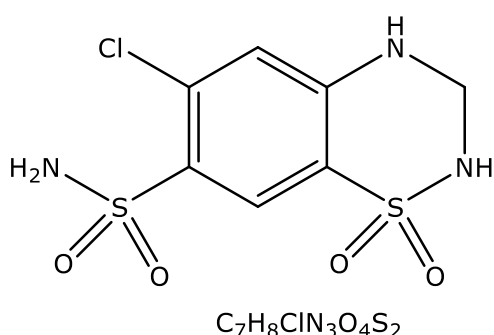

$$C_7H_8ClN_3O_4S_2$$

Figure 1: Chemical structure of HCT.

Subcritical water is defined as water which is heated to a temperature range of 373 K - 647 K and pressurized to keep it in the liquid state in this temperature range (26). It is known that subcritical water has been used in many processes such as oxidation, extraction (9, 26), solubility (27) and in organic synthesis (28), due to its important properties such as being a green solvent, good availability, cheapness, and having an easily adjustable polarity (29). Subcritical water has been widely used in oxidation processes, because during the subcritical water oxidation process hydroxyl radicals and active oxygen species originate at elevated temperatures and pressures without the addition of an oxidizing agent. Furthermore, if an oxidizing agent such as oxygen, permanganate, hydrogen peroxide, *etc.*, is added to the subcritical medium, this treatment can assist the process to efficiently oxidize various potential pollutants which are difficult to oxidize with conventional methods (8, 30, 31). Subcritical water medium favors the formation of free hydroxyl radicals in the presence of hydrogen peroxide. Hydroxyl radical is a reactive species and attacks to target molecule and provides its mineralization. This feature of subcritical water medium and hydrogen peroxide system indicates that it is a superior method comparing to the conventional methods (7).

Response surface methodology (RSM) is one of the most widely used and accepted chemometric methods. RSM is a useful statistical-based method which is used to optimize the process parameters with a limited number of experiments from many varieties. RSM can also be used to analyze the effects of several independent variables on the response, evaluating the individual and interaction effects of independent variables and to evaluate the performance of a system and the interactions between the experimental parameters in the multivariable chemical process (6, 32, 33).

In the present study, the degradation of HCT using hydrogen peroxide as oxidizing agent in subcritical water medium is reported. The optimal experimental parameters such as temperature, treatment time and concentration of oxidizing agent, and the theoretical maximum total organic carbon (TOC) removal rates were determined using RSM.

EXPERIMENTAL SECTION

Materials
HCT and H_2O_2 were supplied from Sigma-Aldrich (St. Louis, MO, USA). N_2 gas was obtained from Linde gas (Turkey). Ultra-pure water (18 MΩ.cm, 25 °C) was prepared by using Millipore Milli-Q Advantage A10 apparatus (Darmstadt, Germany). 1000 mg/L TOC standard solution was obtained from Merck (Darmstadt, Germany).

Degradation method
The experimental set-up (a home-made reactor, heater with a magnetic stirrer and digital thermometer), which is reported in a previous paper (7), was used to carry out the degradation experiments. Preliminary experiments were done to determine treatment conditions. Further, the central composite design (CCD) method, which is one of the design methods of the RSM, was used to design the experimental conditions. The treatment conditions were lying in the temperature range of 352.5 K - 453.5 K, concentration of oxidizing agent range of 12.7 mM - 147.3 mM, and treatment time range of 12.7 min - 147.3 min as demonstrated in Table 1. The degradation method, which is briefly summarized below, was performed according to Yabalak, 2018 (7). A specific amount of HCT was dissolved in ultra-pure water to prepare 50 ppm of stock aqueous solution of HCT. 150 mL of freshly prepared stock solution was placed in the reactor. In each experiment, a certain amount of H_2O_2, which is displayed in Table 2, was added into the reactor. The reactor was closed, screwed and pressurized to 30 bar by using N_2 gas. The reactor was heated to the target temperature according to the experimental design given in Table 2. After keeping a constant temperature during the treatment time, the reactor was cooled down to the room temperature, depressurized and opened. Finally, at the end of the treatment

time, 20 mL of the treated sample was collected and stored at 277 K for TOC analysis.

TOC method
TOC analysis is a common and practical application used to assess the quality of waters by determining its organic content (34). TOC values of the stock solution and treated samples were determined by using a TOC-L analyzer with an ASI-L autosampler (Shimadzu). TOC removal percentages were calculated according to the equation given in the previous work (7).

CCD modeling
RSM, which is a statistical tool that consists of mathematical techniques, enables the optimization of the process (6). CCD is one of the several RSM models and it provides the explanation of the correlation between the experimental variables and responses by designing experiments (7,35). It is based on full factorial or fractional factorial second-order designs and it consists of factorial, central, and axial points in the experimental region (9,36).

Design Expert 9.0.6.2 was used to design the three-factor experimental matrix. Table 1 demonstrates the design of the experimental factors along with their coded levels. Independent variables such as temperature, concentration of oxidizing agent, H_2O_2, and treatment time were coded as x_1, x_2, and x_3, respectively. 20 runs from the experimental region were performed and experimental and predicted results of TOC removal efficiency of all runs were displayed in Table 2. Furthermore, the correlation between response and independent variables was enlightened according to the obtained quadratic equation (Eq 1) of the model. In this equation, Y indicates the response (TOC removal percentage), where x_1, x_2, and x_3 depicts the coded independent variables, x_1^2, x_2^2, and x_3^2 represent the square effects. x_1x_2, x_1x_3, and x_2x_3 symbolize interaction effects. The coefficients of linear and quadratic terms indicate their magnitudes (7,9). ANOVA was done and 3D plots were constructed to identify the consistency of the model and to evaluate the interactions between experimental variables.

Table 1: CCD design of the experimental factors along with their coded levels.

Factors	Independent Variables	Coded Levels				
		-1.682	-1	0	1	1.682
x_1	Temperature (K)	352.5	373	403	433	453.5
x_2	Concentration of oxidizing agent (M)	12.7	40	80	120	147.3
x_3	Treatment time (min)	12.7	40	80	120	147.3

RESULTS AND DISCUSSION

The CCD method was employed to identify the effects of system variables on the TOC removal percentage and the relationship between them. Experimental and predicted results of TOC removal percentages are displayed in Table 2.

As clearly seen from Table 2, the highest experimental and predicted TOC removal percentage was obtained in run 20 and run 8 as 85.22% and 87.81%, respectively, while the lowest experimental and predicted TOC removal percentage was obtained in run 11 as 22.51% and 22.63 %, respectively.

Evaluation of the CCD modeling of mineralization of HCT

ANOVA results of the CCD model of the mineralization of HCT were tabulated in Table 3. Statistical analysis, which is based on the evaluation of the Fisher's 'F' tests, and p-values of the model, is crucial to prove the significance of the employed model (7). p and F values of the model were found to be below 0.0001 and 62.88, respectively. The P-value of any model term is desired to be less than 0.05 to claim its significance (37). In addition, possessing the highest F value indicates a term as the most favourable term of the model. Thus, considering the p and F values of the model, one can say that the employed model is significant and it can be used to designate the effects of the experimental factors on the response, which is the TOC removal percentage. Furthermore, x_1, x_2, x_3, x_1x_2, x_1x_3, x_1^2, and x_3^2 are significant terms of the employed model.

Table 2: Experimental and predicted results of the TOC removal efficiency.

Run	Temperature (K)	Concentration of oxidizing agent (M)	Treatment time (min)	TOC removal, % Exp.	CCD pre.	Residual	AD, %
1	403 (0)	80 (0)	80 (0)	82.89	82.49	0.399	0.48
2	403 (0)	80 (0)	80 (0)	80.94	82.49	1.551	1.92
3	373 (-1)	120 (+1)	120 (+1)	82.06	83.78	1.723	2.10
4	433 (+1)	40 (-1)	40 (-1)	84.01	80.34	3.675	4.37
5	403 (0)	80 (0)	80 (0)	82.36	82.49	0.131	0.16
6	373 (-1)	40 (-1)	120 (+1)	70.99	71.07	0.077	0.11
7	352.5 (-1.682)	80 (0)	80 (0)	38.42	39.33	0.909	2.37
8	403 (0)	147.3 (+1.682)	80 (0)	84.35	87.81	3.460	4.10
9	373 (-1)	120 (+1)	40 (-1)	44.03	39.00	5.028	11.42
10	433 (+1)	120 (+1)	40 (-1)	84.87	82.84	2.029	2.39
11	373 (-1)	40 (-1)	40 (-1)	22.51	22.63	0.116	0.52
12	433 (+1)	120 (+1)	120 (+1)	84.18	82.11	2.068	2.46
13	403 (0)	80 (0)	80 (0)	84.12	82.49	1.629	1.94
14	403 (0)	80 (0)	80 (0)	84.89	82.49	2.399	2.83
15	453.5 (+1.682)	80 (0)	80 (0)	84.60	86.45	1.851	2.19
16	403 (0)	80 (0)	80 (0)	80.22	82.49	2.271	2.83
17	433 (0)	40 (-1)	120 (+1)	80.19	83.27	3.076	3.84
18	403 (0)	80 (0)	12.7 (-1.682)	37.12	42.49	5.370	14.47
19	403 (0)	12.7 (-1.682)	80 (0)	75.71	75.01	0.700	0.92
20	403 (0)	80 (0)	147.3 (+1.682)	85.22	82.61	2.610	3.06

AD: Absolute difference between experimental and predicted values

Table 3: ANOVA results of the CCD model of the mineralization of HCT.

Source	TOC Removal Sum of Squares	df	Mean Square	F Value	p-value prob > F
Model	7252.12	9	805.79	62.88	< 0.0001
x_1	2680.36	1	2680.36	209.17	< 0.0001
x_2	197.77	1	197.77	15.43	0.0028
x_3	1942.95	1	1942.95	151.63	< 0.0001
$x_1 x_2$	96.19	1	96.19	7.51	0.0208
$x_1 x_3$	1035.58	1	1035.58	80.82	< 0.0001
$x_2 x_3$	6.70	1	6.70	0.52	0.4863
x_1^2	692.08	1	692.08	54.01	< 0.0001
x_2^2	2.10	1	2.10	0.16	0.6939
x_3^2	716.30	1	716.30	55.90	< 0.0001
Residual	128.14	10	12.81		
Lack of Fit	112.03	5	22.41	6.95	0.0264
Pure Error	16.11	5	3.22		

$Y = 14.01x_1 + 3.81x_2 + 11.93x_3 - 3.47x_1x_2 - 11.38x_1x_3 - 0.91x_2x_3 - 6.93x_1^2 - 0.38x_2^2 - 7.05x_3^2 + 82.49$ (Eq. 1).

The predicted TOC removal percentages of all runs were obtained by employing CCD. The second-order polynomial equation (Eq. 1) was used for this purpose. Also, using Eq. 1 is a practical way for predicting the response of the system for given levels of system factors. In addition, the coefficient of the coded factors of the equation shows the level of effectiveness of each factor on the TOC removal percentages. Thus, it is clearly seen that temperature is the most effective variable on the TOC removal rates followed by treatment time, while the quadratic effect of the H_2O_2 concentration remains negligible.

Table 4: Regression coefficients of the CCD model.

Regression coefficients			
Standard Deviation	3.58	R^2	0.9826
Mean	72.68	Adjusted R^2	0.9670
C.V. %	4.92	Predicted R^2	0.8768
PRESS	909.56	Adequate Precision	25.752

The regression coefficients of a model show its reliability. Table 4 demonstrates the regression coefficients of the employed CCD model. The obtained predicted residual sum of squares (PRESS) value of 909.56 shows that the model adapts each point in the design. The adequate precision value of 25.752 verifies that the model can be applied to navigate the design space (7). Also, the conformity of the model was provided based on the R^2 value of 0.9826. The adjusted R^2 value of 0.9670 represents the amount of variation around the mean. The reasonable agreement of the R^2 value with adjusted R^2 indicate a high correlation level between experimental and predicted values. Further, Figure 2, which depicts the correlation between actual (experimental) and predicted TOC removal values, supports this accordance. Closeness of colored points to the linear line demonstrates the conformity of experimental and predicted values. Thus, Figure 2 shows that both actual and predicted points of the applied method match each other.
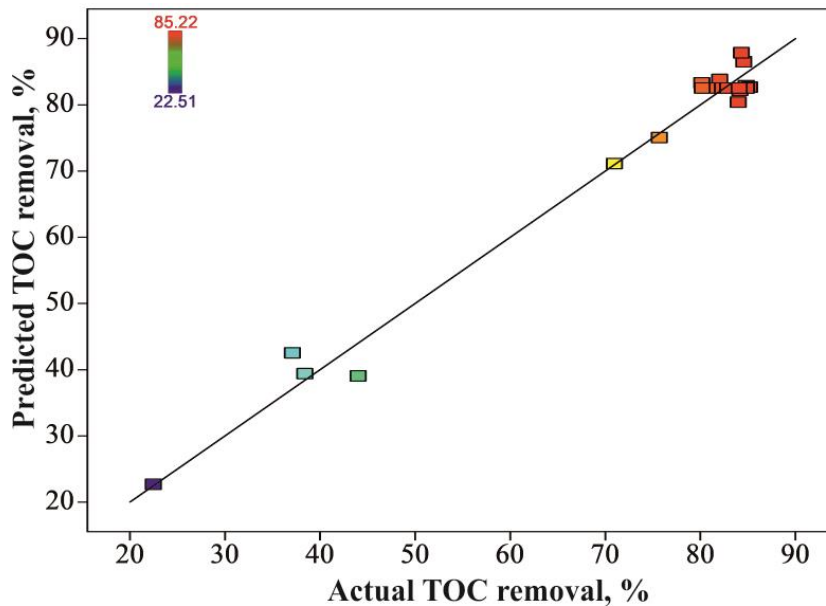
Figure 2: Correlation between actual and predicted values of the TOC removal rates.

Figure 3 shows the cube plot of CCD model of the TOC removal. It is feasible to predict the response in any case that consists of three experimental factors in the working range by using Figure 3. In addition, the evaluation of the further experiments and estimation of the experimental conditions can be performed by the aid of Figure 3. It can be seen from this figure that 83.78 % of TOC removal percentage can be obtained at the highest level of treatment time and H_2O_2 concentration but at the lowest level of temperature. Moreover, almost the same value of TOC removal percentage can be obtained (83.26 %) by increasing the temperature and treatment time to their highest value and decreasing the concentration of H_2O_2 to its lowest value.

TOC Removal, %

(a)

Figure 3: Cube plot of the model.

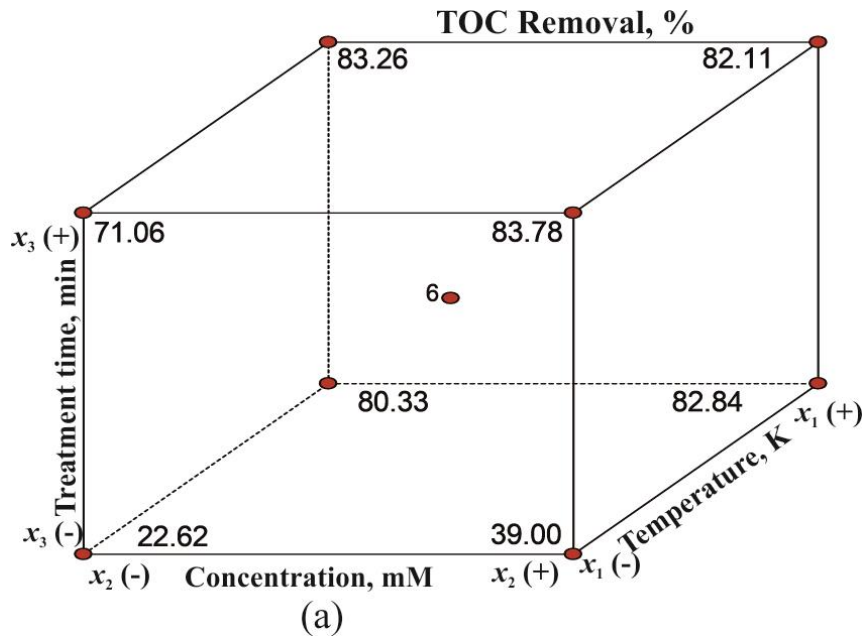Binary effects of experimental variables on the response can be demonstrated by using three-dimensional surface plots. Figure 4 shows the binary effects of H_2O_2 concentration and temperature on the TOC removal at the fixed treatment time of 50 min. It is clearly seen that the combined effect of temperature and H_2O_2 concentration increases TOC removal percentages, especially above 413 K, at the fixed treatment time of 50 min. Moreover, 50 min and above treatment times are quite sufficient for formation of hydroxyl and other radicals at above medium levels of temperature and H_2O_2 concentration. Thus, when the reaction medium contains an appropriate amount of H_2O_2, temperature plays the major role in providing these radicals and elevating the mineralization percentage of HCT. The role of H_2O_2 concentration remains minor considering the role of temperature in the above-mentioned conditions. While the effect of temperature increases in its high levels, the effect of H_2O_2 concentration gains importance in the lower level of temperature in the fixed 50 min of treatment time. For example, 69.58% of TOC removal increases to 85.19% by elevating the temperature from 403 K to 433 K at the fixed treatment time of 50 min and H_2O_2 concentration of 80 mM. However, only about 2 % increase is seen in the 83.78% of TOC removal value by increasing H_2O_2 concentration from 40 mM to 120 mM at the fixed treatment time of 50 min and 433 K of temperature. Moreover, when the same enhancement was applied at the same treatment time, about 9% and 16% of enhancement are observed at 403 K and 373 K, respectively.
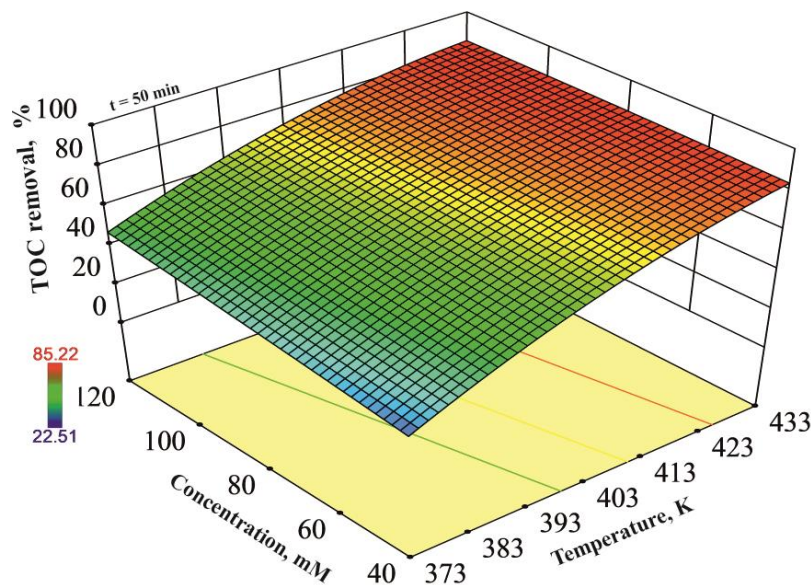

Figure 4: Binary effects of H_2O_2 concentration and temperature on the TOC removal at fixed treatment time of 50 min.

The combined effect of treatment time and temperature on the TOC removal at the fixed H_2O_2 concentration of 40 mM is shown in Figure 5. This effect is quite noteworthy, especially at above the medium level of both temperature and treatment time at the fixed H_2O_2 concentration of 40 mM.
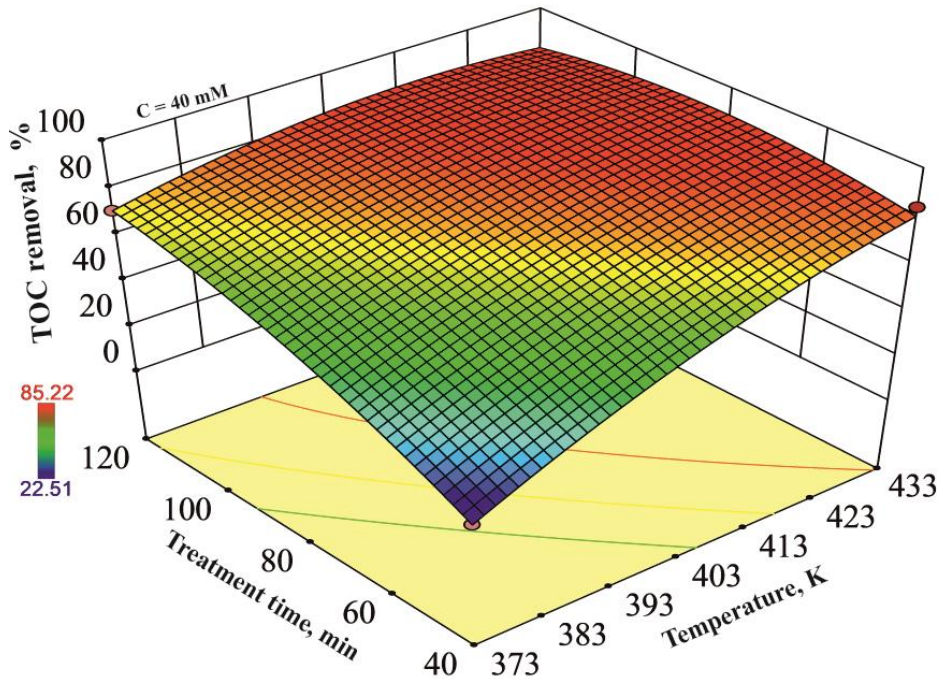
Figure 5: Binary effects of treatment time and temperature on the TOC removal at fixed H_2O_2 concentration of 40 mM.

Alternatively, short treatment time-high temperature and long treatment time-low temperature conditions provide elevated TOC removal rates at the fixed H_2O_2 concentration of 40 mM, according to Figure 5. Based on these results, one can say that adequate free radicals might be formed by keeping treatment time or temperature at specific values. For instance, to obtain 80.34 % of TOC removal, 433 K of temperature and 40 min of treatment time is required at the fixed H_2O_2 concentration of 40 mM. The same efficiency can be obtained at 390.5 K of temperature and 120 min of treatment time at the same H_2O_2 concentration.

Figure 6: Binary effects of treatment time and H_2O_2 concentration on the TOC removal at the fixed temperature of 390 K.

Binary effects of treatment time and H_2O_2 concentration on the TOC removal at the fixed temperature of 390 K are demonstrated in Figure 6. This figure shows that, while moderate TOC removal percentages can be obtained at low levels of H_2O_2 concentration and treatment time at the fixed temperature of 390 K, the treatment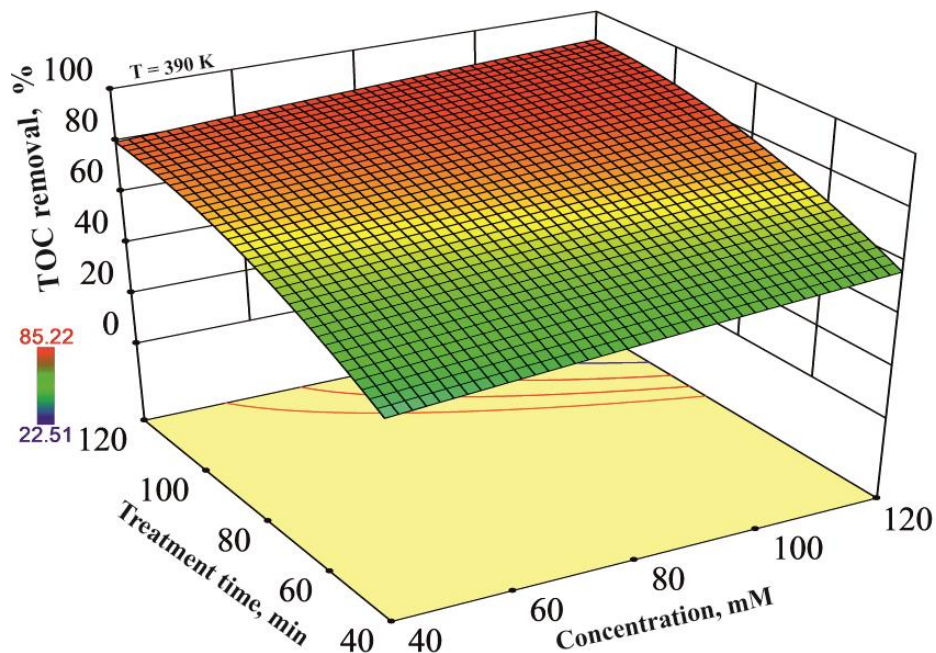 time must be increased to obtain high TOC removal percentages. Further, increasing the H_2O_2 concentration at moderate and upper levels of treatment time at the fixed temperature of 390 K only has little influence on the TOC removal percentages. It may be attributed to the fact that, while the role of H_2O_2 concentration is crucial in the mineralization of HCT, increasing the H_2O_2 concentration above a specific level does not directly elevate degradation rates due to possible self-quenching of free radicals present in the reaction medium (7). According to Figure 6, this method should be regarded as superior to the conventional methods in terms of achieving the same efficiency with different application conditions. Thus, the possibility of achieving high efficiency of TOC removal of HCT at long treatment time and low temperature or at short treatment time and high temperature provides important advantages in reducing the operating costs on the industrial scale (large scale applications).

CONCLUSIONS

Mineralization of HCT was effectively achieved by using subcritical water oxidation as an applicable, efficient and environmentally friendly method, and by using H_2O_2 as a green oxidizing agent. Subcritical water favoured the formation of free radicals, and in the presence of H_2O_2, at an adequate treatment time. Thus, it can be said that on the basis of the obtained results, subcritical water and H_2O_2 have synergetic effects on the TOC removal of HCT. High TOC removal rate (85.22%) proved the reliability of this method as well as its applicability in the mineralization process of similar contaminants. Moreover, the CCD method was performed and the interaction of experimental variables as well as their effects on the response was evaluated. Temperature, followed by treatment time, were found to be effective experimental factors on the efficiency of the method. Also, the obtained high TOC removal rates in the short treatment time show that the applied method is a time-saving method.

REFERENCES

1. Ahmed MB, Kumer A, Islam M, Islam TSA. The Photochemical Degradation (PCD) of Nitrobenzene (NB) using UV Light and Fenton Reagent Under Various Conditions. Journal of the Turkish Chemical Society, Section A: Chemistry. 2018;5(2):803-818.

2. Lima DRS, Tonucci MC, Libânio M, Aquino SFD. Pharmaceuticals and etrndocrine disrupting compounds in Brazilian waters: occurrence and removal techniques. Engenharia Sanitaria E Ambiental. 2017 Nov-Dec;22(6):1043–1054.

3. Li Z, Sobek A, Radke M. Fate of pharmaceuticals and their transformation products in four small European rivers receiving treated wastewater. Environmental Science & Technology. 2016 Jun;50(11):5614–5621.

4. López-Serna R, Jurado A, Vázquez-Suñé E, Carrera J, Petrović M, Barceló, D. Occurrence of 95 pharmaceuticals and transformation products in urban groundwaters underlying the metropolis of Barcelona, Spain. Environmental Pollution. 2013 Mar;174:305–315.

5. Benotti MJ, Trenholm RA, Vanderford BJ, Holady JC, Stanford BD, Snyder SA. Pharmaceuticals and endocrine disrupting compounds in US drinking water. Environmental Science & Technology. 2009 Feb;43(3):597–603.

6. Yabalak E, Görmez Ö, Gizir AM. Subcritical water oxidation of propham by H_2O_2 using response surface methodology (RSM). Journal of Environmental Science and Health, Part B. 2018;53(5):334–339.

7. Yabalak, E. Degradation of ticarcillin by subcritial water oxidation method: Application of response surface methodology and artificial neural network modeling. Journal of Environmental Science and Health, Part A. 2018. https://doi.org/10.1080/10934529.2018.147102 3.

8. Emire Z, Yabalak E, Görmez Ö, Gizir AM. Solubility and degradation of paracetamol in subcritical water. Journal of the Serbian Chemical Society. 2017;82(1):99–106.

9. Yabalak E, Adiguzel SK, Adiguzel AO, Ergene RS, Tuncer M, Gizir AM. Application of response surface methodology for the optimization of oxacillin degradation by subcritical water oxidation using H_2O_2: genotoxicity and antimicrobial activity analysis of treated samples. Desalination and Water Water Treatment. 2017 Jun;81:186–198.

10. Turabik M, Oturan N, Gözmen B, Oturan MA. Efficient removal of insecticide "imidacloprid" from water by electrochemical advanced oxidation processes. Environmental Science and Pollution Research. 2014 Jul;21(14):8387–8397.

11. Hasan N, Moon GH, Park J, Park J, Kim J. Visible light-induced degradation of sulfa drugs on pure TiO_2 through ligand-to-metal charge transfer. Separation and Purification Technology. 2018 Sep;203:242–250.

12. Giahi M. Photocatalytic degradation of diclofenac sodium in aqueous solution using N, S,

and C-doped ZnO. Russian Journal of Applied Chemistry. 2015 Dec;88(12):2044–2049.

13. Ji Y, Wang L, Jiang M, Yang Y, Yang P, Lu J, Ferronato C, Chovelon, J-M. Ferrous-activated peroxymonosulfate oxidation of antimicrobial agent sulfaquinoxaline and structurally related compounds in aqueous solution: kinetics, products, and transformation pathways. Environmental Science and Pollution Research. 2017 Aug;24(24):19535–19545.

14. Altamimi MA, Elzayat EM, Alhowyan AA, Alshehri S, Shakeel F. Effect of β-cyclodextrin and different surfactants on solubility, stability, and permeability of hydrochlorothiazide. Journal of Molecular Liquids. 2018 Jan;250:323–328.

15. Phechkrajang CM, Quynh PTN, Suntornsuk L. Forced Degradation Studies of Candesartan Cilexetil and Hydrochlorothiazide Using a Validated Stability-Indicating HPLC-UV Method. Pharmaceutical Chemistry Journal. 2017 Aug;51(5):416–424.

16. Armaković SJ, Armaković S, Četojević-Simin DD, Šibul F, Abramović BF. Photocatalytic degradation of 4-amino-6-chlorobenzene-1,3-disulfonamide stable hydrolysis product of hydrochlorothiazide: Detection of intermediates and their toxicity. Environmental Pollution. 2018 Feb;233:916–924.

17. Petrović M, Škrbić B, Živančev J, Ferrando-Climent L, Barcelo D. Determination of 81 pharmaceutical drugs by high performance liquid chromatography coupled to mass spectrometry with hybrid triple quadrupole–linear ion trap in different types of water in Serbia. Science of the Total Environment. 2014 Jan;468:415–428.

18. Real FJ, Acero JL, Benitez FJ, Roldán G, Fernández LC. Oxidation of hydrochlorothiazide by UV radiation, hydroxyl radicals and ozone: Kinetics and elimination from water systems. Chemical Engineering Journal. 2010 May;160(1):72–78.

19. Mahajan AA, Thaker AK, Mohanraj K. LC, LC-MS/MS studies for the identification and characterization of degradation products of hydrochlorothiazide and establishment of mechanistic approach towards degradation. Journal of the Brazilian Chemical Society. 2012 Mar;23(3):445–452.

20. Márquez G, Rodríguez EM, Beltrán FJ, Álvarez PM. Solar photocatalytic ozonation of a mixture of pharmaceutical compounds in water. Chemosphere. 2014 Oct:113;71–78.

21. Contreras N, Vidal J, Berríos C, Villegas L, Salazar R. Degradation of antihypertensive hydrochlorothiazide in water from pharmaceutical formulations by electro-oxidation using a BDD anode. International Journal of Electrochemical Science. 2015 Sep;10(11):9269–9285.

22. Paiva VAB, Paniagua CES, Ricardo IA, Gonçalves BR, Martins SP, Daniel D, Machado AEH, Trovó AG. Simultaneous degradation of pharmaceuticals by classic and modified photo-Fenton process. Journal of Environmental Chemical Engineering. 2018 Feb;6(1):1086–1092.

23. Armaković SJ, Armaković S, Četojević-Simin DD, Šibul F, Abramović BF. Photocatalytic degradation of 4-amino-6-chlorobenzene-1, 3-disulfonamide stable hydrolysis product of hydrochlorothiazide: Detection of intermediates and their toxicity. Environmental Pollution. 2018 Feb;233:916–924.

24. Phechkrajang CM, Quynh PTN, Suntornsuk L. Forced Degradation Studies of Candesartan Cilexetil and Hydrochlorothiazide Using a Validated Stability-Indicating HPLC-UV Method. Pharmaceutical Chemistry Journal. 2017 Aug;51(5):416–424.

25. Borowska E, Bourgin M, Hollender J, Kienle C, McArdell CS, Von Gunten U. Oxidation of cetirizine, fexofenadine and hydrochlorothiazide during ozonation: Kinetics and formation of transformation products. Water Research. 2016 May;94:350–362.

26. Yabalak E, Gizir MA. Subcritical and supercritical fluid extraction of heavy metals from sand and sewage sludge. Journal of the Serbian Chemical Society. 2013;78(7):1013–1022.

27. Yabalak E, Görmez Ö, Gözmen B, Gizir AM. The solubility of sebacic acid in subcritical water using the response surface methodology. International Journal of Industrial Chemistry. 2015 Mar;6(1):23–29.

28. Nural Y, Gemili M, Yabalak E, De Coen L, Ulger M. Green synthesis of highly functionalized octahydropyrrolo[3,4-c]pyrrole derivatives using subcritical water, and their anti(myco)bacterial and antifungal activity. Arkivoc. 2018;2018(5):51–64.

29. Demirkol O, Akbaşlar D, Giray ES. Clean and efficient synthesis of flavanone in sub-critical water. The Journal of Supercritical Fluids. 2013 Sep;81:217–220.

30. Ribeiro RS, Silva AM, Figueiredo JL, Faria JL, Gomes HT. Catalytic wet peroxide oxidation: a route towards the application of hybrid magnetic carbon nanocomposites for the degradation of organic pollutants. A review. Applied Catalysis B: Environmental. 2016 Jun;187:428–460.

31. Fu J, Kyzas GZ. Wet air oxidation for the decolorization of dye wastewater: An overview of

the last two decades. Chinese Journal of Catalysis. 2014 Jan;35(1):1–7.

32. Singh KP, Gupta S, Singh AK, Sinha S. Optimizing adsorption of crystal violet dye from water by magnetic nanocomposite using response surface modeling approach. Journal of Hazardous Materials. 2011 Feb;186(2-3):1462–1473.

33. Abdullah AZ, Salamatinia B, Kamaruddin AH. Application of response surface methodology for the optimization of NaOH treatment on oil palm frond towards improvement in the sorption of heavy metals. Desalination. 2009 Aug;244(1–3):227–238.

34. Llop A, Pocurull E, Borrull F. Evaluation of the removal of pollutants from petrochemical wastewater using a membrane bioreactor treatment plant. Water, Air, and Soil Pollution. 2009 Feb;197(1–4):349–359.

35. Krowiak AW, Chojnacka K, Podstawczyk D, Dawiec A, Pokomeda K. Application of response surface methodology and artificial neural network methods in modelling and optimization of biosorption process. Bioresource Technology. 2014 May;160:150–160.

36. Pilkington JL, Preston C, Gomes RL. Comparison of response surface methodology (RSM) and artificial neural networks (ANN) towards efficient extraction of artemisinin from Artemisia annua. Industrial Crops and Products. 2014 Jul;58:15–24.

37. Yabalak E, Görmez Ö, Sönmez Gözmen B. Degradation, dephenolisation and dearomatisation of olive mill wastewater by subcritical water oxidation method using hydrogen peroxide: Application of multi-response central composite design. Journal of the Serbian Chemical Society. 2018;83:489–502.

DNA Base Bioisosteres, Bis-benzoxazoles, Exert Anti-proliferative Effect on Human Prostate and Breast Cancer Cells

Furkan Ayaz[1*], Rusmeenee Kheeree[1], Qadar Ahmed Isse[1], Ronak Haj Ersan[2], Oztekin Algul[2*]

[1]Mersin University, Biotechnology Department, (33110), (Mersin), (Turkey)
[2]Mersin University, Faculty of Pharmacy, Department of Pharmaceutical Chemistry, (33169), (Mersin), (Turkey)

Abstract: A series of symmetric bis-benzoxazole derivatives were synthesized using one-pot cyclization between 4-chloro substituted 2-aminophenol and suitable dicarboxylic acids. Synthesized compounds' anticancer activities were tested by using MTT assay on human prostate (DU145) and breast (MCF7) cancer cells. Screening results revealed that all compounds possessed a high level anti-cancer potential by significantly decreasing the cell proliferation in prostate and breast cancer cell lines. Our compounds exerted their anti-proliferative effects in a dose and time dependent manner. Our results suggest that they can be highly potent since they were biologically active even at low concentrations. Our study presents a series of new bis-benzoxazole based compounds with potential therapeutic effects against tumor cells. Therefore, characterization of new generation bis-benzoxazole derivatives will have a significant contribution on the development of new era anti-cancer drug candidates.

INTRODUCTION

Cancer is one of the leading causes of death globally (1). Under normal conditions there is a cell renewal and replacement homeostasis in the tissues (2-5). After losing some of the cells, tissue would make up its loss by stimulating cell division and growth (2-6). In case of tumor cells, they circumvent the checkpoints of cell division which is enabled by multiple genetic alterations (7-15). This situation leads to uncontrolled cell growth and outnumbering of non-tumorous tissue-resident cells which eventually causes the loss of function in these affected tissues (7-18).

As a treatment option, chemotherapy is widely used in the cancer patients (19-20).

Chemotherapeutics pause or slow down the pace of the abnormal cell division or cause the death of the rapidly dividing tumor cells (21, 22). These drugs have side effects that can exert its effect on healthy cells (23, 24). Severity of their side effects depends on the type and location of the cancer as well as the dosage used and patient's overall health condition (23-25). The most crucial side effect of chemotherapeutics is on the fast dividing blood cells of the patient (23-25). These drugs decrease the blood cell counts of the patients taking the treatment (23-25). This decrease of the blood cells compromises the immune system of the patients and makes them prone to infections (23-25). In order to avoid the common side effects such as fatigue, pain, diarrhea, hair loss, vomiting and nausea, new

Ayaz F et al. JOTCSA. 2018; 5(3): 1145-1152.

RESEARCH ARTICLE

candidates of chemotherapeutics should be developed as alternatives (26, 27).

Newly developed benzoxazole compounds are important fragments in medicinal chemistry because of their wide range of biological activities, including anticancer activities (28-30). They serve as topoisomerase-I inhibitors (31) and have antibacterial (32), antifungal (33), antimicrobial (34), and antiviral activities (35).

One of the main examples to benzoxazole based compounds is UK-1 (Bis-benzoxazole) (Figure 1) which has cytotoxic activity against a variety of tumorous cell types. In the quest of synthesizing more potent anticancer drugs, we designed and produced new bis-benzoxazole derivatives with high yields. In our study, we are presenting screening results for their anticancer activity against human breast cancer cell line (MCF-7) and prostate cancer cell line (DU145).
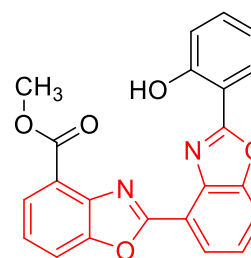

Figure 1. Molecular Structure of UK-1.

MATERIALS AND METHODS

Chemistry

General: Each reaction was followed by thin layer chromatography (TLC). UV (ultraviolet) light (254 nm) was used in the determination of stains on ready-made TLC plates (Kieselgel 60 F254, ready-to-use aluminum plate coated with 0.2 mm thickness). Flash column chromatography was performed with silica gel 60 (Merck, 63–200 μm particle size, 60–230 mesh). (Solvent of the flash column chromatography: n-hexane/ethyl acetate 80:20)

^{1}H NMR and ^{13}C NMR spectra (*Bruker 400* spectrometer) and Fourier transform infrared (FT-IR) spectra (*Perkin Elmer Spectrum One* FT-IR spectrometer) were used to elucidate the structures of the products.

Materials: All reagents and solvents for synthesis and analysis were of analytical and/or spectroscopic A grade (Sigma-Aldrich and ACROS) and used without further purification.

Synthesis: General Procedure for Synthesis of Bis-benzoxazole derivatives (Fig.2). Five mmol of the 4-chloro-2-aminophenol (**1**) and 2.5 mmol of the corresponding dicarboxylic acid derivatives (**2, and 3**) are refluxed under a reflux condenser with a magnetic stirrer for a period of 13-15 hours after being dissolved in polyphosphoric acid (PPA) and heated in an oil-bath at 180 °C. The reactions were followed by TLC. After cooling, the reaction mixture was poured onto ice water and neutralized by mixing with 5N NaOH until being of slightly basic pH (8–9) to get the precipitate. The resulting precipitate was filtered off and washed with cold water. Then compounds purified by flash column chromatography finally crystallized with a suitable solvent. The resulting crystalline compounds were filtered and the vacuumed product was dried.
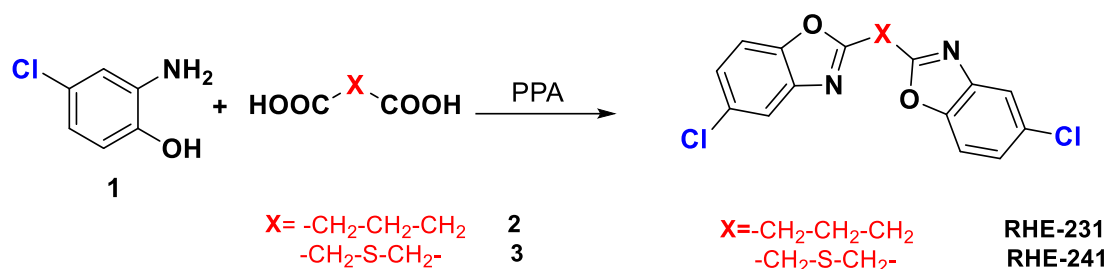
Figure 2. General synthesis method of the compounds.

1,3-bis(5-chlorobenzo[d]oxazol-2-yl)propane RHE-231: The above procedure was followed with **1** and **2** to yield RHE-231 as a white crystalline solid (47% yield). The crystallization solvent was ethanol-water (with the ratio of 1/1). R_f (n-hexane:ethyl acetate 1:1)= 0,48; mp= 200 °C; IR (KBr, cm^{-1}) V_{max} 3065, 1567, 1447, 800, 753, 701. ; ^{1}H NMR (400 MHz, CDCl$_3$) δ =7.52 (d, J=1.99 Hz, 2H, Ar-H), 7.32-7.29 (m, 1H, Ar-H), 7.20 (dd, J=1.99 Hz, J=8.25 Hz, 3H, Ar-H), 3.05 (t, J=7.28 Hz, 4H, -CH$_2$), 2.43 (p, J=2.48 Hz, 2H, -CH$_2$). ^{13}C NMR (100 MHz, CDCl$_3$) δ=167.3, 149.4, 142.4, 129.8, 125.0, 119.7, 111.0, 27.8, 23.4.

1,3-bis((5-chlorobenzo[d]oxazol-2-yl)methyl)sulfane RHE-241: The above procedure was followed with **1** and **3** to yield RHE-241 as a beige crystalline solid (45% yield). The crystallization solvent was ethanol-water (with the ratio of 1/1). R_f (n-hexane:ethyl acetate 1:1)= 0,64 ; mp= 197 °C; FT-IR (cm^{-1}) V_{max} 2979, 2923, 1560, 1447,1332, 812, 703. ; ^{1}H NMR (400 MHz, CDCl$_3$) δ = 7.30-7.26 (m, 2H, Ar-H), 7.21 (dd, J=2.58 Hz, J=8.69 Hz, 2H, Ar-H), 6.98 (td, J=2.58 Hz, J=8.69 Hz, 2H, Ar-H), 4.03 (s, 4H, -CH$_2$). ^{13}C NMR (100 MHz, CDCl$_3$) δ=164.6, 161.2, 158.8, 147.4, 142.0, 141.9, 113.1, 112.8, 110.9, 110.8, 106.6, 106.4, 28.5.

Biological studies
In this study, breast cancer cell line MCF-7, prostate cancer cell line DU-145 and fibroblast cell line L929 were purchased from ATCC. The chemicals used in the study were bis-benzoxazole based RHE 231 and 241 coded compounds.

Reagents and Chemicals: RHE231 and RHE241; 2 mg of RHE231 and RHE241 were dissolved in 1000 µL (1mL) of sterile dimethyl sulfoxide (DMSO).

Cell Culture: In this study the following cell lines were used: Fibroblast cell line; L929 from ATCC, breast cancer cell line; MCF7 from ATCC, and prostate cancer cell line; DU145 from ATCC. Cells were cultured in tissue culture plates with Roswell Park Memorial Institute media (RPMI 1640) media with %10

fetal bovine serum, %1 antibiotics (100 µg/mL penicillin and 100 µg/mL streptomycin), and sodium pyruvate. Cultures were incubated at 37 °C in an atmosphere of 95% air and 5% CO$_2$.

Cell Plating: Adherent cells from confluent cultures were detached, after they grew completely to reach the number of 10×10^6 cells/plate in 10 mL of RPMI-based complete culture medium as specified above. Cell counting was done by using Trypan Blue dye which stains the dead cells with dark blue color. The dye cannot penerate through living cells therefore we could differentiate between living and dead cells and have a reliable living cell number for the plating.

100 µL of 10×10^6 cells/mL were seeded in individual wells of 96 well tissue culture treated plates and allowed to adhere to the surface by overnight incubation at 37 °C and 5% CO$_2$ before adding the reagents. 50 µg/mL, 75 µg/mL, and 100 µg/mL of reagent were added into appropriate wells. Afterwards the samples were incubated at 37 °C and 5% CO$_2$ humidified incubator for different three time-points; 24h, 48h, and 72h.

Cytotoxicity Evaluations: MTT assay: Cell viability was evaluated by using MTT assay. This assay is based on the ability of viable cells to metabolize yellow tetrazolium salt MTT to purple formazan crystals by mitochondrial dehydrogenases and spectrophotometric measurement of the product at 570 nm.

Briefly, cells were seeded at a density of 1×10^5 per well in 96-well plates; subsequently, after overnight incubation, they were treated with various concentrations (50 µg/mL, 75 µg/mL, 100 µg/mL) of RHE 231 & RHE 241. Cells were put back to 37 °C 5% CO$_2$ incubator for 24 hours, 48 hours, and 72 hours of incubation. The untreated or DMSO treated well was considered as a negative control, and all samples were prepared in triplicates.

After 24 h, 48 h, and 72 h of incubation, 10 µL of MTT reagent was added into each well and samples were further incubated for 4 h at 37

°C, 5% CO_2. As a last step, 100 μL of detergent reagent was added into each well. Cytotoxic effects were monitored by measuring the absorbance values of each well at 570 nm.

Statistical Analysis: In order to determine the % cell viability average absorbance value of the reference blank sample was subtracted from each sample's average absorbance. The equation used for the calculations is given below and further plotting as well as statistical analysis were performed by GraphPad Prism Software version 5. For each condition there were nine independent data points and

unpaired two tail t-test was done to draw the statistical significance.

$$\% \text{ Viability} = \frac{Sample\ absorbance - Reference\ absorbance}{Reference\ absorbance} \times 100$$

RESULTS AND DISCUSSION

Cell viability analysis indicated that both of the compounds, RHE231 and RHE241, were effective as anti-proliferative agents on DU145 prostate cancer cells, MCF7 breast cancer cells, and L929 fibroblast cells.
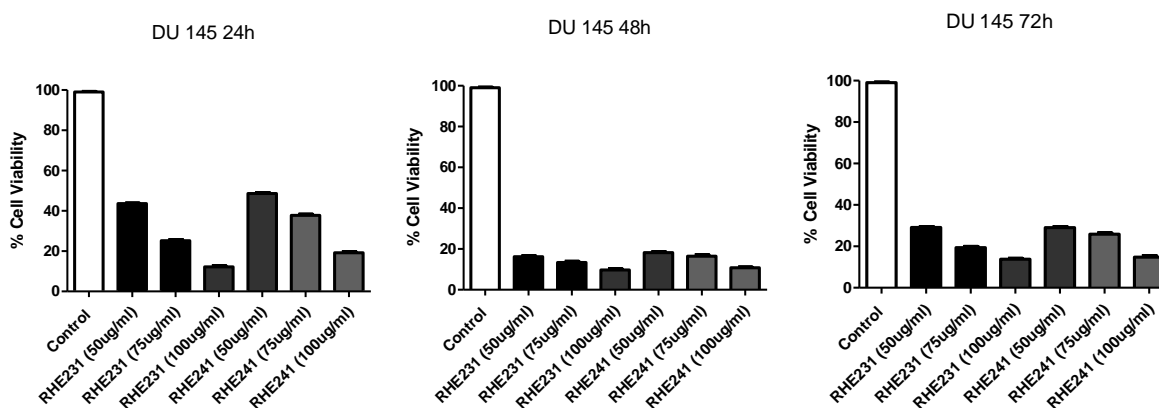
Figure 3: Dose-dependent effect of RHE231 and RHE241 on DU145 cell lines for 24h, 48h, and 72h incubation, respectively.

MTT assay was done to asses cell viability. The t test was applied for statistical analysis, $p<0.0001$ N=9.

The proliferation rate of prostate cancer cells (DU145) was negatively affected by RHE231 and RHE241, at all time points and at all concentrations compared to the untreated control wells which had 100% cell viability. There was a substantial decrease in RHE 231

and 241 treated prostate cancer cells' percent viability compared to the untreated control wells. This difference was statistically significant. Dose dependent anti-proliferative effect of our reagents was more obvious at 24 hour time point but at later time points even the lowest dose (50 µg/mL) of both of the reagents was almost as effective as the highest one (100 µg/mL) (Figure 3).
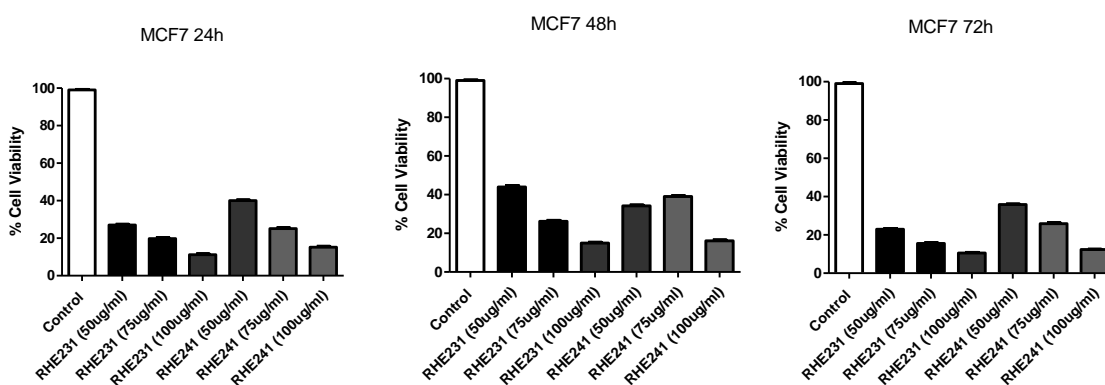

Figure 4: Dose-dependent effect of chemicals, including RHE 231 and RHE 241 on MFC7 cell lines for 24h, 48h, and 72h incubation, respectively.

MTT assay was performed to assess cell viability. The t test was applied for statistical analysis, $p<0.0001$ N=9.

We obtained similar results when we tested the effect of RHE 231 and RHE 241 on the

breast cancer cells (MCF7) as those of the prostate cancer cells (DU145). When we took the untreated cells as reference point there was a substantial and significant decrease in the level of cell proliferation in RHE 231 and RHE 241 treated cells. We observed a dose dependent effect since at higher concentrations of used chemicals there was more substantial decrease in the percent cell viability compared to the wells treated with the

lower concentrations of the chemicals (Figure 4). RHE 231 and 241 exerted their effect in a time dependent fashion on DU145 cells whereas on MCF7 cells, the anti-proliferative effect was fully shown even at the 24 hour time point since at 48 and 72 hour time points the observed anti-proliferative effect was similar to that of 24 hour time point (Figures 3 and 4).
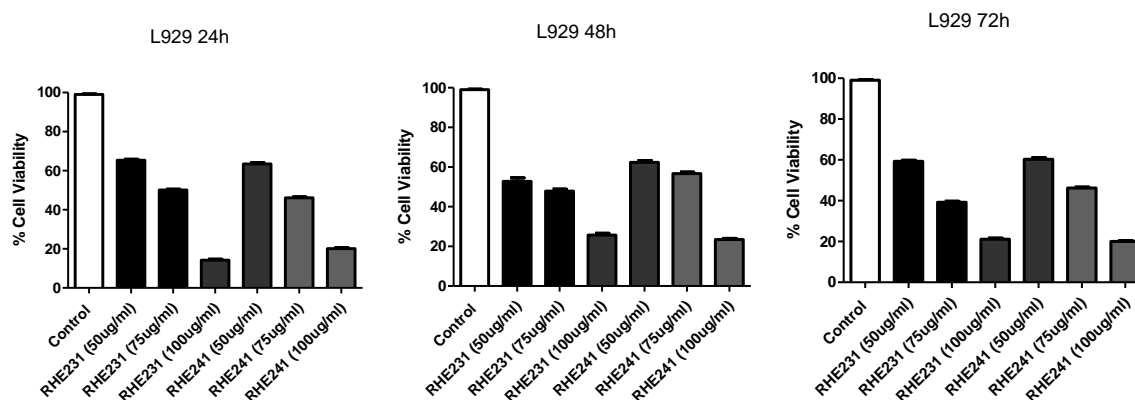

Figure 5: Dose-dependent effect of chemicals, including RHE 231 and RHE 241 on L929 cell lines for 24 h, 48 h, and 72 h incubation, respectively.

MTT assay was performed to assess cell viability. The t test was applied for statistical analysis, p<0.0001 N=9.

In order to test the possible cytotoxic side effects of our compounds we tested their anti-proliferative effect on the mouse fibroblast cells L929. Our chemicals exerted anti-proliferative activity on fibroblast cells in a time and dose dependent manner as well (Figure 5). There was a significant decrease in the cell viability of treated fibroblasts compared to the untreated control wells. When we compared the results to those of breast cancer (MCF7) and prostate cancer (DU145) cells, fibroblasts (L929) had higher cell viability at all time points especially at lower dosages (Figure 5). This implies that our reagents would show less cytotoxic effect on normal cell types compared to the breast and prostate cancer cells. Especially, lower doses of RHE 231 and 241 can be effectively used against breast and prostate cancer since event at 50 µg/mL concentration our reagents had highly potent anti-proliferative activity on these cancer cells whereas they did not cause as substantial of a decrease in the viability of the fibroblasts (Figures 3-5). In the presence of our chemicals, fibroblasts had higher cell viability, compared to those of prostate and breast cancer cells.

DISCUSSION

Chemotherapy stands as the most viable option in the current medicinal approaches

against the cancer (19-22). These drugs target the fast-dividing cells in the body (21, 22). Tumor cells fall into this category due to their higher proliferation rate compared to the normal cells (7-15, 19-22). One major problem with this treatment is the side effects associated with it (23, 24). Normal cell types with high proliferation and cell division rates such as endothelial cells of the intestines, hair and blood cells are severely affected by the treatment (23-25). The severity of the side effects depends on the patient's genetic background as well as the type of the cancer and chemotherapeutics used (23-25).

In order to circumvent these side effects, there is an urgent need of design and synthesis of new drug candidates and of their testing on the cancer cells (26, 27). In our study, we focused on two cancer types that have one of the highest incidence rates among men (prostate cancer) and women (breast cancer). Anti-proliferative activity of some other bis-benzoxazole derivatives have been shown by previous studies (36, 37). In our study we designed two new bis-benzoxazole derivatives and further examined their effect on the prostate (DU145) and breast (MCF7) cancer cells.

Our study supports that RHE231 and RHE241 have anti-proliferative effect on breast cancer and prostate cancer cells in a time and dose dependent fashion. Both of the reagents caused a significant decrease in cell viability compared to the untreated control wells. MCF7 cells were affected more by the treatment

Ayaz F et al. JOTCSA. 2018; 5(3): 1145-1152.

RESEARCH ARTICLE

compared to the DU 145 cells. But at later time points 48 and 72 hours, our reagents showed their strong anti-proliferative effect on the prostate cancer cells as well.

In order to test the cytotoxic activity of our reagents on normal cells we used fibroblast cells (L929). Our compounds caused a significant decrease in the cell viability of fibroblasts compared to the untreated cells, but this decrease was not as substantial as those of treated breast and prostate cancer cells at all time points. Especially the lowest concentrations of the chemicals would be effective chemotherapeutics since while they would have high potency against breast and prostate cancer cells during the treatment; they would not affect the normal cell types like fibroblasts of the tissues as substantially. This would enable an efficient anti-proliferative effect on the tumor cells while sparing majority of the normal cells in the tissue so that those cells can heal the tissue aftermath of the treatment.

CONCLUSION

Our results support anti-proliferative, therefore anti-cancer, activities of bis-benzoxazole derivatives RHE 231 and RHE 241. In our future studies we will be focusing more on the molecular mechanism of our compounds action on the cancer cells as well as normal cell types. Possible hit points include oncogenes such as p53, Ras and Notch pathways.

ACKNOWLEDGMENTS

REFERENCES

1. Fitzmaurice C, Dicker D, Pain A, Hamavid H, Moradi-Lakeh M, MacIntyre M, et al. Global Burden of Disease Cancer Collaboration The Global Burden of Cancer 2013. JAMA Oncol. 2015;2015(1):505–27.

2. Biteau B, Hochmuth CE, Jasper H. Maintaining Tissue Homeostasis: Dynamic Control of Somatic Stem Cell Activity. Cell Stem Cell. 2011 Nov;9(5):402–11.

3. Alvarado C, Fider NA, Wearing HJ, Komarova NL. Optimizing homeostatic cell renewal in hierarchical tissues. Traulsen A, editor. PLOS Computational Biology. 2018 Feb 15;14(2):e1005967.

4. Pellettieri J, Alvarado AS. Cell Turnover and Adult Tissue Homeostasis: From Humans to Planarians. Annual Review of Genetics. 2007 Dec;41(1):83–105.

5. Antonello ZA, Reiff T, Dominguez M. Mesenchymal to epithelial transition during tissue homeostasis and regeneration: Patching up the Drosophila midgut epithelium. Fly. 2015 Jul 3;9(3):132–7.

6. Hunt T, Nasmyth K, Novak B. The cell cycle. Philosophical Transactions of the Royal Society B: Biological Sciences. 2011 Dec 27;366(1584):3494–7.

7. Williams GH, Stoeber K. Cell cycle markers in clinical oncology. Current Opinion in Cell Biology. 2007 Dec;19(6):672–9.

8. Bower JJ, Karaca GF, Zhou Y, Simpson DA, Cordeiro-Stone M, Kaufmann WK. Topoisomerase IIα maintains genomic stability through decatenation G2 checkpoint signaling. Oncogene. 2010 Aug;29(34):4787–99.

9. Hartwell L, Kastan M. Cell cycle control and cancer. Science. 1994 Dec 16;266(5192):1821–8.

10. Classon M, Harlow E. The retinoblastoma tumour suppressor in development and cancer. Nature Reviews Cancer. 2002 Dec;2(12):910–7.

11. Xu B, Kim S -t., Kastan MB. Involvement of Brca1 in S-Phase and G2-Phase Checkpoints after Ionizing Irradiation. Molecular and Cellular Biology. 2001 May 15;21(10):3445–50.

12. Wang R-H, Yu H, Deng C-X. A requirement for breast-cancer-associated gene 1 (BRCA1) in the spindle checkpoint. Proceedings of the National Academy of Sciences. 2004 Dec 7;101(49):17108–13.

13. Santarpia L, Iwamoto T, Di Leo A, Hayashi N, Bottai G, Stampfer M, et al. DNA Repair Gene Patterns as Prognostic and Predictive Factors in Molecular Breast Cancer Subtypes. The Oncologist. 2013 Oct 1;18(10):1063–73.

14. Sorlie T, Perou CM, Tibshirani R, Aas T, Geisler S, Johnsen H, et al. Gene expression patterns of breast carcinomas distinguish tumor subclasses with clinical implications. Proceedings of the National Academy of Sciences. 2001 Sep 11;98(19):10869–74.

15. Nakagawa T, Hayashita Y, Maeno K, Masuda A, Sugito N, Osada H, et al. Identification of Decatenation G 2 Checkpoint Impairment Independently of DNA Damage G 2 Checkpoint in Human Lung Cancer Cell Lines. Cancer Research. 2004 Jul 15;64(14):4826–32.

16. Hinck L, Näthke I. Changes in cell and tissue organization in cancer of the breast and colon. Current Opinion in Cell Biology. 2014 Feb;26:87–95.

17. Cho EH, Wendel M, Luttgen M, Yoshioka C, Marrinucci D, Lazar D, et al. Characterization of circulating tumor cell aggregates identified in patients with epithelial tumors. Physical Biology. 2012 Feb 1;9(1):016001.

18. De Smedt L, Palmans S, Sagaert X. Tumour budding in colorectal cancer: what do we know and what can we do? Virchows Archiv. 2016 Apr;468(4):397–408.

19. Gustavsson B, Carlsson G, Machover D, Petrelli N, Roth A, Schmoll H-J, et al. A Review of the Evolution of Systemic Chemotherapy in the Management of Colorectal Cancer. Clinical Colorectal Cancer. 2015 Mar;14(1):1–10.

20. Huang C-Y, Ju D-T, Chang C-F, Muralidhar Reddy P, Velmurugan BK. A review on the effects of current chemotherapy drugs and natural agents in treating non–small cell lung cancer. BioMedicine. 2017 Dec;7(4):23.

21. Harrison's principles of internal medicine [Internet]. NCBI; [cited 2018 Jun 1]. Available from: https://www.ncbi.nlm.nih.gov/nlmcatalog/10 1643730

22. Andreae S, editor. Lexikon der Krankheiten und Untersuchungen. 2., überarbeitete und erw. Aufl. Stuttgart ; New York: G. Thieme; 2008. 1468 p.

23. Pearce A, Haas M, Viney R, Pearson S-A, Haywood P, Brown C, et al. Incidence and severity of self-reported chemotherapy side effects in routine care: A prospective cohort study. Ganti AK, editor. PLOS ONE. 2017 Oct 10;12(10):e0184360.

24. Ihbe-Heffinger A, Ehlken B, Bernard R, Berger K, Peschel C, Eichler H-G, et al. The impact of delayed chemotherapy-induced nausea and vomiting on patients, health resource utilization and costs in German

cancer centers. Annals of Oncology. 2004 Mar;15(3):526–36.

25. Khoshbin AR, Mohamadabadi F, Vafaeian F, Babania A, Akbarian S, Khandozi R, et al. The effect of radiotherapy and chemotherapy on osmotic fragility of red blood cells and plasma levels of malondialdehyde in patients with breast cancer. Reports of Practical Oncology & Radiotherapy. 2015 Jul;20(4):305–8.

26. Hu Q, Sun W, Wang C, Gu Z. Recent advances of cocktail chemotherapy by combination drug delivery systems. Advanced Drug Delivery Reviews. 2016 Mar;98:19–34.

27. Hoelder S, Clarke PA, Workman P. Discovery of small molecule cancer drugs: Successes, challenges and opportunities. Molecular Oncology. 2012 Apr;6(2):155–76.

28. Ueki M, Ueno K, Miyadoh S, Abe K, Shibata K, Taniguchi M, et al. UK-1, a novel cytotoxic metabolite from Streptomyces sp. 517-02. I. Taxonomy, fermentation, isolation, physico-chemical and biological properties. The Journal of Antibiotics. 1993;46(7):1089–94.

29. Cheng CC, Dong Q, Liu DF, Luo YL, Liu LF, Chen AY, et al. Design of antineoplastic agents on the basis of the 2-phenylnaphthalene-type structural pattern. 2. Synthesis and biological activity studies of benzo[b]naphtho[2,3-d]furan-6,11-dione derivatives. Journal of Medicinal Chemistry. 1993 Dec;36(25):4108–12.

30. Kamal A, Srinivasa Reddy T, Polepalli S, Paidakula S, Srinivasulu V, Ganga Reddy V, et al. Synthesis and biological evaluation of 4-aza-2,3-dihydropyridophenanthrolines as tubulin polymerization inhibitors. Bioorganic & Medicinal Chemistry Letters. 2014 Aug;24(15):3356–60.

31. Kim JS, Sun Q, Gatto B, Yu C, Liu A, Liu LF, et al. Structure-activity relationships of benzimidazoles and related heterocycles as topoisomerase I poisons. Bioorganic & Medicinal Chemistry. 1996 Apr;4(4):621–30.

32. Sun L-Q, Chen J, Bruce M, Deskus JA, Epperson JR, Takaki K, et al. Synthesis and structure–activity relationship of novel benzoxazole derivatives as melatonin receptor agonists. Bioorganic & Medicinal Chemistry Letters. 2004 Jul;14(14):3799–802.

33. Ertan T, Yildiz I, Tekiner-Gulbas B, Bolelli K, Temiz-Arpaci O, Ozkan S, et al. Synthesis, biological evaluation and 2D-QSAR analysis of

benzoxazoles as antimicrobial agents. European Journal of Medicinal Chemistry. 2009 Feb;44(2):501–10.

34. Alper-Hayta S, Arisoy M, Temiz-Arpaci Ö, Yildiz I, Aki E, Özkan S, et al. Synthesis, antimicrobial activity, pharmacophore analysis of some new 2-(substitutedphenyl/benzyl)-5-[(2-benzofuryl)carboxamido]benzoxazoles. European Journal of Medicinal Chemistry. 2008 Nov;43(11):2568–78.

35. Sun A, Prussia A, Zhan W, Murray EE, Doyle J, Cheng L-T, et al. Nonpeptide

Inhibitors of Measles Virus Entry. Journal of Medicinal Chemistry. 2006 Aug;49(17):5080–92.

36. Padmavathi V, Venkatesh BC, Muralikrishna A, Padmaja A. Synthesis and Antioxidant Activity of a New Class of Bis and Tris Heterocycles. Archiv der Pharmazie. 2012 Sep;345(9):745–52.

37. Ravez S, Castillo-Aguilera O, Depreux P, Goossens L. Quinazoline derivatives as anticancer drugs: a patent review (2011 – present). Expert Opinion on Therapeutic Patents. 2015 Jul 3;25(7):789–804.

RESEARCH ARTICLE

Transition Metal Doped Solid Oxide Fuel Cell Cathodes

Ayşenur Eslem Kısa[1], Oktay Demircan[1], *

[1] Department of Chemistry, Faculty of Arts and Science, Boğaziçi University, İstanbul, Turkey.

Abstract: Fuel cells have developed of excessive interest as a probable economical, efficient, and clean candidate for alternative and environmental friendly power generation services. Solid Oxide Fuel Cell (SOFC) is an elevated temperature fuel cell, dealing with power generation as well as heat. Up to now many studies have been made to replace platinum, Pt, with a new cathode catalyst for intermediate temperature-solid oxide fuel cells (IT-SOFC) (500 °C<T) range but research has become inadequate. Since Pt sources are limited and very expensive, they could not meet the supply for the commercial fuel cells, the scientists started for searching new materials. There are two important aspects about SOFC cathodes, different cathode materials effect on the electrode electrochemical performance and the oxygen reduction reaction (ORR) kinetics. Understanding in these concepts would lead to improvements of SOFC systems. The production of novel and supreme cathode electrodes used in IT-SOFC is aimed to employ cheaper metals (Fe, Co, Cr, Mn, Gd, and V) by using superior properties of perovskite structure. The reduction of oxygen on metal oxide surface is achieved within the complicated mechanism. The completion of these steps depends on the nature of oxide ion carrier in cathode, atomic formation in crystal structure, and microstructure of cathode materials. The analysis of the impedances required the use of three to four (RQ) circuits in series in the equivalent circuit model. Of the four cathodes synthesized, the vanadium doped cathode on YSZ showed the highest area specific resistance.

INTRODUCTION

Contemporary attention on building on hydrogen energy and diminishing the ecological pollution has propelled the research on fuel cell innovation, especially, in the area of solid oxide fuel cells (SOFCs) (1). SOFCs, as an electrochemical energy production device, have noteworthy benefits over the ordinary power generation technologies. They are electrochemical systems that transform chemical energy into useful electrical energy with better efficiency because their effectiveness is independent from Carnot cycle of a heat engine (2). Additional efficiency can be achieved when the generated energy is utilized with joint heat and power, or gas turbines (3).

Among the several types of fuel cells, SOFCs own several attractive features, such as better energy conversion efficiency, multiple fuel flexibility, solid-state parts, low greenhouse gas emissions, high power density, environmental friendliness, and lower system noise (4). Similar to other fuel cells, SOFC systems comprises of an electrolyte and the electrodes (anode and cathode). The anode side of the cell is fed with the fuel, *e.g.* hydrogen and an oxidant such as air is flowed over the cathode side, whereas the electrolyte transfers the oxide ions from cathode to anode or vice versa.

Baur and Preis in 1937 developed the very first SOFC that operated at 1000 °C (5). Although several decades have passed since their introduction, commonly used SOFCs still work at higher temperatures (~ 900 °C) (6, 7). This

causes to material deterioration and consequences in higher costs, hence delaying their economic feasibility. Thus, lowering their operation temperature to intermediate range (<800 °C) can diminish the cost and expand life time (8).

Furthermore, high working temperatures limits the choice of materials used in the SOFCs, since deterioration during process will limit the life span of SOFC (9). An obvious site of degradation is air electrode where reduction of oxygen (ORR) occurs, which is generally the key rate limiting step for the functioning of the entire SOFC structure (10). Hence, one of the most important goals in the area of SOFCs is development of new cathode materials that offer a desired electrochemical performance at intermediate temperature range (600-800 °C) (11). Required attributes for such cathode materials are high electronic and ionic conductivity, thermal expansion coefficient values similar to other SOFC compartments, large triple phase boundary (TPB) area, high performance of the catalyst for the dissociation of oxygen, and low cathode resistance (12). Most of these requirements are met by mixed ionic and electronic conductors (MIEC) and their composites. These materials provide synchronized transport of both electrons and ions, hence enhancing the potential reaction sites at the triple phase boundaries, at which the active side of the electrode, the electrolyte and the gases meet. Mixed ionic and electronic conductors generally derive their distinctive properties form their special crystal structure, often referred to as the perovskite structure. The perfect oxide perovskite structure ABO_3 contains a cubic array of corner sharing BO_6 octahedral with the A cation at the body center location. However, imperfect matching between A and B ionic radii create alterations in the cubic lattice (often rhombohedral or orthorhombic),(13) and these intrinsic alterations leads to vacancies at lattice crystal that exhibit ionic conductivity (14).

Perovskite materials such as $La_{1-x}Sr_xMnO_{3-\delta}$ (LSM) with x between 0.15 and 0.50 are the most commonly used and studied cathode material for standard SOFC (15). These Sr-doped lanthanum perovskites stay stable both in excess-oxidizing and deficient-reducing of oxygen (16). Oxygen deficiency leads to oxygen deficiencies while oxygen-excess results in metal deficient sites, which improves electrode properties. However, the ionic conductivity of LSM is extremely low due to low concentration of oxide ion vacancies (17). This causes useful limitations and restraints to the function of LSM particularly at intermediate temperatures (<800 °C). As the working temperature of SOFC system lowers below 800 °C, the oxide ion conductivity for the traditional cathode materials like LSM, in that case distresses the oxygen reduction reaction performance (18). Therefore, incorporation of a material or doping with another metal with comparable higher oxide ion conductivity may ripen the cathode performance.

The study concerned a comparison is made between four different cathode materials under identical conditions. The cathodes investigated LV05SC ($La_{0.595}V_{0.005}Sr_{0.4}CoO_{3-\delta}$) LV3SF ($La_{0.57}V_{0.03}Sr_{0.4}FeO_{3-\delta}$), and LV05SM ($La_{0.595}V_{0.005}Sr_{0.4}MnO_{3-\delta}$) were successfully synthesized by sol-gel process and are characterized with XRD (X-Ray Diffraction) and XPS (X-Ray Photoelectron Spectroscopy). For electrical conductivity measurements, four-probe conductivity method was performed. Also, for the electrochemical characterization of the electrodes impedance measurements were completed. Of the four cathodes, the LV05SC on YSZ showed the highest area specific resistance. The results for other cathode materials were in good agreement with literature.

EXPERIMENTAL SECTION

Synthesis and characterizations of cathode materials
The cathode materials were synthesized by employing a sol–gel method. Figure 1 displays the flow sheet for the synthesis of $La_{0.6-x}V_xSr_{0.4}MnO_{3-\delta}$ (LV_xSM, x = 0.005–0.1) as an example of cathode material by sol–gel process. La, Sr and Mn nitrates and V acetate (purity>99.9%, Aldrich Chemicals, USA) were employed as reagents.
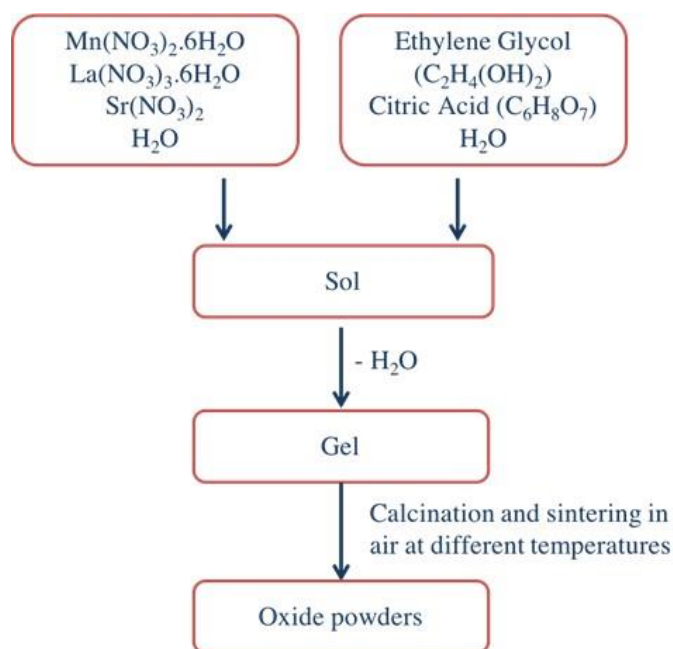
Figure. 1. The preparation of $La_{0.595}V_{0.005}Sr_{0.4}MnO_{3-\delta}$ cathode powders by sol–gel process.

All of the reagents, in requisite stoichiometric ratio, were dissolved in the distilled deionized water in a separate manner. Thereafter, all the solutions were mixed together and stirred to obtain a homogeneous solution. After their complete dissolution, a certain amount of citric acid and ethylene glycol were introduced as polymerization and complexation agents, correspondingly.

The molar ratio of citric acid/total metal ions was kept as 1:2:1. The solution was evaporated on a hot plate using a magnetic stirrer until a chocolate-colored gel was formed. When the heating was continued further, the gel completely burns to yield a light and fragile ash. After this mild heating induced gelation, the resulting gel was held in a drying oven at 400 °C for 2 h to remove organics and sintered at 900 and 1100 °C for 3 h to obtain the perovskite compounds with sufficient crystallinity, as confirmed by X-ray diffraction analysis. The X-ray powder diffraction data (crystal structure and phase composition of the synthesized powders) were collected on a Rigaku D/MAX-Ultima+/PC Diffractometer using Cu-Kα radiation (λ = 1.54056 Å). The data obtained was compared with reference data for identification of the crystal structure. The morphology of the surface and cross-section of the sintered symmetric cells were examined by scanning electron microscope (ESEM-FEG, Philips XL 30) at a potential of 10 kV.

The XPS experiments were performed using a Thermo Scientific K-Alpha Surface Analysis instrument at room temperature. An Al K Alpha X-Ray source was used with a spot size of 400 μm and the spectra of powdered samples were recorded with the constant pass energy values at 150 eV. The energy step size was set as 0.100 eV and the charge effect was calibrated using the BE of C1s (284.5eV).

Symmetric cell preparation for EIS analysis
Symmetrical electrochemical cells for impedance studies were prepared using various cathode materials and yttria-stabilized zirconia (YSZ) electrolyte. The electrolyte pellets were prepared by pressing commercial powders in a cylindrical stainless-steel mold (5 mm in diameter and a thickness of about 0.5 mm) with a uniaxial dry press at a pressure of 400 MPa. After that, the prepared electrolyte disks were initially calcined at 400 °C for 2 h and followed by sintering at 1300 °C for 2 h. For symmetrical cells, cathode samples were mixed thoroughly with organic binder (Polyvinylbutyral (PVB)) to make the cathodic slurry. The paste obtained was painted on both sides of the pellets with dimensions of 2 × 2 mm by using masking tape. The symmetrical cell was then dried at 150 °C for 1 h and sintered at 1300 °C for 1 h in air to form porous electrodes well adhered to the electrolytes. The final active area of each cathode was about 0.04 cm². Finally, the cathodes were connected with Au paint and wire as current collectors. The symmetrical cells were assembled into a lab-designed setup that allows performing the experiments in different atmospheres. To determine the resistance of the various cathode processes, the manufactured symmetric cells were characterized by EIS measurements in ambient air from 400 to 700 °C with an increment of 50 °C. O_2 concentrations (% O_2) around the cell during the measurements were maintained using electronic mass flow controllers and nitrogen was used as the carrier gas. Impedance spectra were measured in the frequency range of 0.1 Hz to 1 MHz with 10 mV amplitude of the AC signal. The spectra were analyzed using GAMRY Interface 1000 Potentiostat/ Galvanostat, which was interfaced with a computer-controlled program for data acquisition.

Electrical conductivity measurements
Electrical conductivity of materials was measured as a function of temperature by the standard DC four-terminal method. The conductivity measurements were performed in air on sintered rectangular bars of approximate dimensions 20 × 5 × 2 mm. Electrical contacts using Au wires (0.25 mm in diameter, Alfa Aesar) and Au conductor paste (Heraeus) were placed onto the edges of the sample ensuring a homogeneous current flow. Voltage contacts were prepared as small as possible to prevent any disturbance of the contacts on the current flow. Measurements were performed from 400 to 800 °C with an interval of 50 °C. The conductivity (σ) was determined from a set of V−I values by taking $\sigma=1/\rho=L/A\times dI/dV$, where L is the distance between voltage contacts and A is the sample cross-section.

RESULTS and DISCUSSION

X-Ray Diffraction (XRD) Results
Through the primary phase of SOFC progress, platinum and other noble metals were employed as cathodic supplies. Nonetheless, the observations suggest that by enlarging effective area at which chemical steps happen as well as extending the electrochemical boundary including the complete electrode/electrolyte contact area (not only TPB) could elaborate the transport mechanism of electro-active species from the top to the majority of the electrode material. Some of the metal oxides, other than being better O_2 catalysts and conductors, demonstrate vital ionic conduction while remaining comparatively stable at running conditions. The bulk appears to play a significant role in determining the electrode kinetics for these mixed conductors (materials conducting both oxide ions and electrons). Hence, these materials deliver another useful key factor to consider when inferring to more multifaceted materials such as *perovskites*. The very first perovskite materials considered was $La_{1-x}Sr_xCoO_{3-\delta}$ (LSC) which is now one of the well-known mixed conductors and it was trailed quickly afterwards by a number of other materials with perovskite crystal structure, including $La_{1-x}Sr_xMnO_{3-\delta}$ (LSM), which has developed the favored material for SOFC cathodes.

Ideal perovskite crystallizes in cubic close-packed lattice structure. The structure and purity of the crystal samples were determined by XRD. As previously stated LV_xSC ($La_{0.6-x}V_xSr_{0.4}CoO_{3-\delta}$) (x = 0.005, 0.01, 0.02, 0.03, 0.04, 0.05, 0.10) examples were synthesized by a sol-gel method after calcination at 1100 °C with open air for 2h. Figure 2 displays the XRD configurations of the resulting LV05SC ($La_{0.595}V_{0.005}Sr_{0.4}CoO_{3-\delta}$) crystals measured at room temperature.
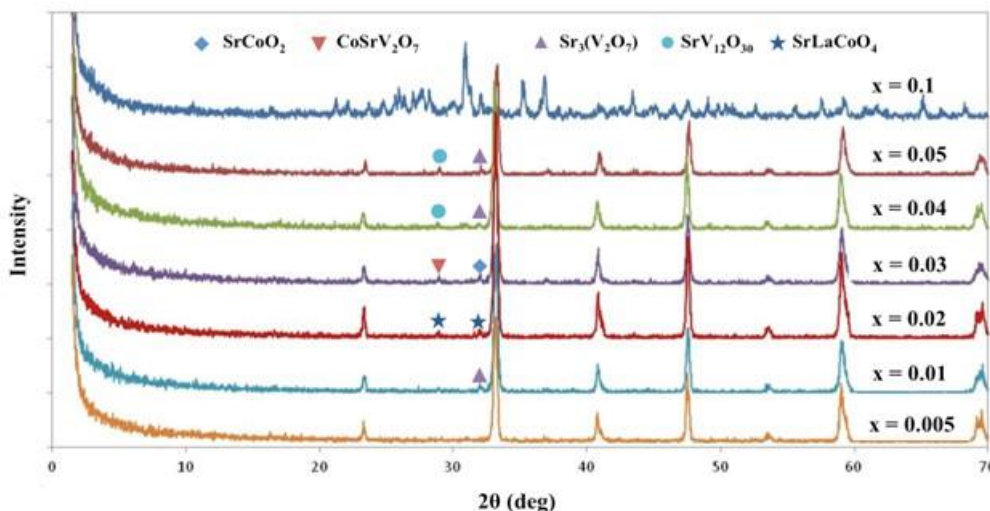

Figure 2. XRD patterns of LV05SC ($La_{0.6-x}V_xSr_{0.4}CoO_{3-\delta}$) (x= 0.005 – 0.1) material sintered at 1100 °C in air for 2h.

It is deduced that the crystals with vanadium portions of x ≤ 0.005 exhibit an evidently defined perovskite structure with a single-phase. Nevertheless, when the doping ratio of vanadium was additional increased (x ≥ 0.01) other phases like different kinds of oxides could be observed in the LV05SC ($La_{0.595}V_{0.005}Sr_{0.4}CoO_{3-\delta}$) samples. For example, as seen in the above figure for LV10SC sample, two impurities were identified as $Sr_3V_2O_8$ and $SrVO_3$. This implies that the edge of V doping in these sequences of LVxSC materials would not be more than 0.5 mol %. With rising V content, the diffraction patterns of LVxSC moved slightly to higher angle direction, as can be deduced clearly from Figure 2, representing the reduction of crystal parameters. A cubic perovskite series of LVxSC materials were prepared and the effect of V content on the lattice structure was considered in relation to their possible employment as cathode materials for SOFC. The solid content limit of V in LV05SC ($La_{0.595}V_{0.005}Sr_{0.4}CoO_{3-\delta}$) is almost x=0.005 at 1100 °C. As the cubic structure crystallinity of LV05SC ($La_{0.595}V_{0.005}Sr_{0.4}CoO_{3-\delta}$) materials decreases with V-doping level, LV05SC ($La_{0.595}V_{0.005}Sr_{0.4}CoO_{3-\delta}$)

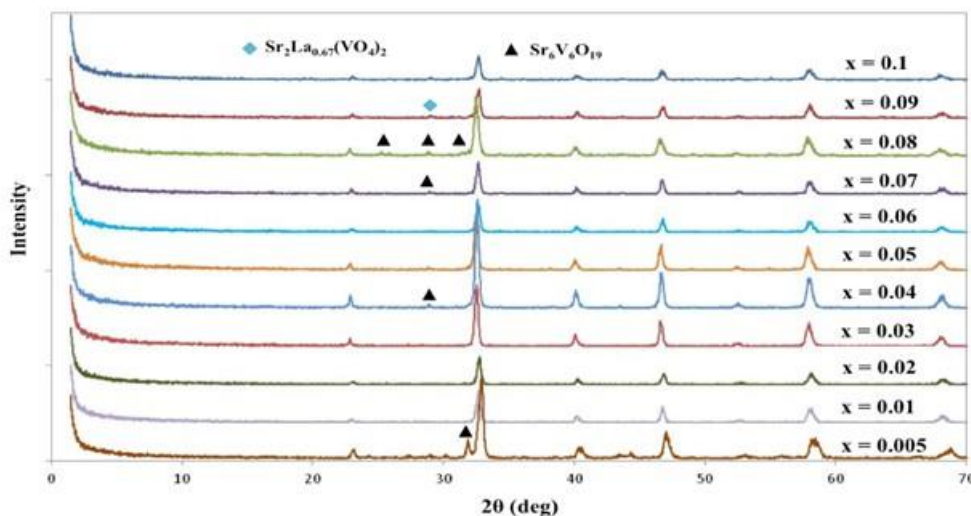was selected as the candidate cathode material on emphasis.

Figure 3. XRD patterns of the as-synthesized LVxSF ($La_{0.6-x}V_xSr_{0.4}FeO_{3-\delta}$), (x = 0.005 – 0.1) material sintered at 1100 °C in air for 2h.

Figure 3 shows the XRD patterns of the as-synthesized LVxSF ($La_{0.6-x}V_xSr_{0.4}FeO_{3-\delta}$), (x = 0.005 – 0.1), abbreviated as LVxSF correlated with the vanadium content hereafter. All compositions exhibit a perovskite structure, which is either orthorhombic or rhombohedral, and no extra phase appears. This implies that fractional exchange of V for La has no effect on the growth of layered perovskite phase. The slightly diverse structure change in this case is because of ionic radii and the introduction of V^{3+} ions. However, it can be seen that all samples were nearly phase pure, but for the nominal LV3SF (which is $La_{0.57}V_{0.03}Sr_{0.4}FeO_{3-\delta}$ for x = 0.03) sample, a second phase marked with ▲ was observed. As indicated in Figure 3, the second phase can be indexed to Strontium Vanadium Oxide, $Sr_6V_6O_{19}$. This result emphasizes the solid solution limit of V in $La_{0.57}V_{0.03}Sr_{0.4}FeO_{3-\delta}$ is greater than 0.5%. As the LV4SF samples showed

a second phase as evidenced by additional peaks at 2θ value of 29.8°, even though the phase was not unambiguously identified but closely matched that of $Sr_6V_6O_{19}$, LV3SF ($La_{0.57}V_{0.03}Sr_{0.4}FeO_{3-\delta}$) was selected as the candidate cathode material on consideration due to its single-phase crystallinity and relatively high peak intensity among others.

Phase homogeneity of $La_{0.6-x}V_xSr_{0.4}MnO_{3-\delta}$ (x= 0.005 – 0.1) was compared as in Figure 4 by XRD analysis. $La_{0.6-x}V_xSr_{0.4}MnO_{3-\delta}$ like all the $La_{1-x}Sr_xMnO_3$ materials develops in a rhombohedral structure. The rhombohedral development of the perfect perovskite octahedron is described by the split of the major reflection, in which performs as two peaks in between 32° and 33°.
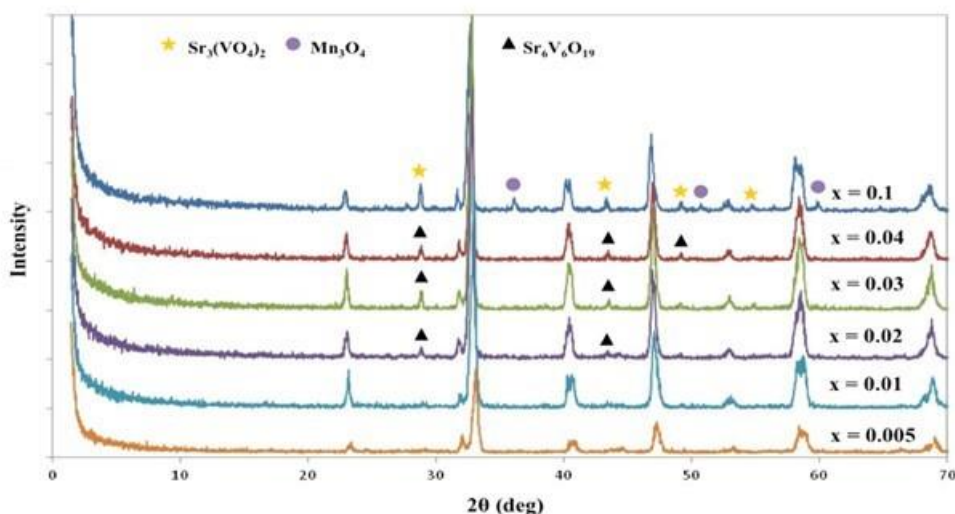

Figure 4. XRD patterns of the as-synthesized $La_{0.6-x}V_xSr_{0.4}MnO_{3-\delta}$ (x= 0.005–0.1) material sintered at 1100 °C in air for 2h.

Figure 4 presents typical XRD patterns of $La_{0.6-x}V_xSr_{0.4}MnO_{3-\delta}$ (x= 0.005–0.1) fired exactly at 1100 °C. The patterns suggest that the LVxSM samples have the only phase of perovskite structure with no extra impurities till x = 0.01 and $Sr_6V_6O_{19}$ secondary phase at 29.6° observed with V ratio above x = 0.01. This shows that LVxSM can crystallize with a perovskite structure under the V percent of x ≤ 0.01. No extra phases, either $La_2Zr_2O_7$ or $SrZrO_3$, are observed by XRD for the LV10SM cathode material. A well-defined perovskite phase can be perceived from Figure 4. Nevertheless, there can be seen some impurity patterns as small peaks in XRD. It is found that these belong to $Sr_3(VO_4)_2$ by XRD phase analysis software. This impurity as $Sr_3(VO_4)_2$ is the perovskite type of structure associated with mixed ionic-electronic conductor, and this phase is not recognized as detrimental to the SOFC cathode. However, it is obvious that the perovskite crystallinity distorted as seen. It recommends that the limit of V content in $La_{0.6-x}V_xSr_{0.4}MnO_{3-\delta}$ (x= 0.005 – 0.1) systems would not be exceeding of 10 mol%. The diffraction pattern confirms the pure rhombohedral phases of LV05SM ($La_{0.595}V_{0.005}Sr_{0.4}MnO_{3-\delta}$, x = 0.005) and replacement of V at a range of 0.5 mol % would not change the crystallinity of the structure, thus LV05SM had possible claim as a cathode material.

X-Ray Photoelectron Spectroscopy (XPS) Results

The main function of the cathode material in SOFC can be described as contributing reaction spots for oxygen reduction reaction (ORR). Hence, in order to address the reaction mechanisms and processes in ORR, the description of the activity on the site of materials for ORR is vital. The properties of electrocatalysts and ion transport of the cathode samples mostly depend on the oxygen diffusion and adsorption. The degree of the reaction, which oxygen is first land on from the atmospheric environment, relies greatly on the composition and structure of the outmost oxides' surface. The structure and the composition of oxide surface can vary from the bulk of the material. Improved characterization of the surface properties of cathode materials is so fundamental. Early studies on cathode samples are mainly centered upon the electrochemical properties (63) and there are few studies done for the view of surface of the sample. In this respect, XPS is an extremely beneficial technique for characterization of these important restrictions as the oxidation state of metals employed, their comparative content and the surface metals' proportion.

XPS survey spectrum of LV05SC ($La_{0.6-x}V_xSr_{0.4}CoO_{3-\delta}$, x = 0.005) in Figure 5 shows that the oxidation states of metals in the control and this content of the as-synthesized LV05SC cathode material and the fitted curves about elements within the powder proved that no extra impurity of metals other than La, Co, Sr and V except C1s are displayed on whole spectrum.
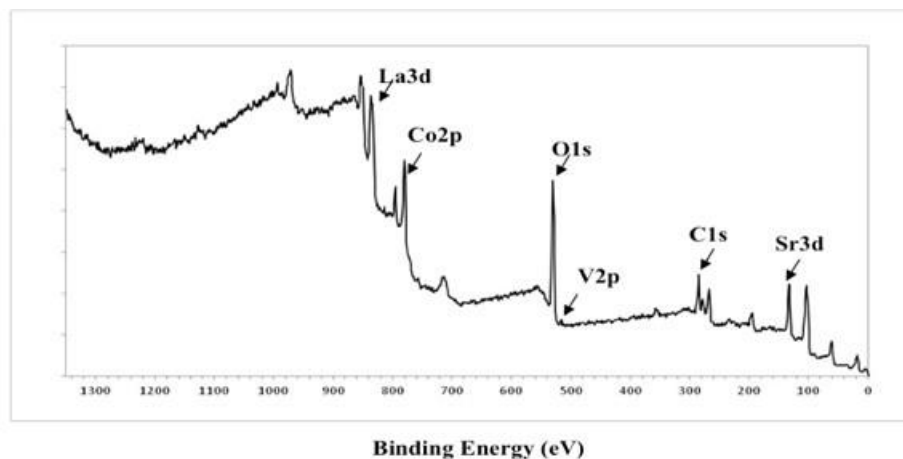

Figure 5. XPS survey spectrum of the LV05SC material.

The reason for the splitting in the La3d peaks in the XPS is not only because of a spin–orbit type interaction seen as two lines $3d_{5/2}$ and $3d_{3/2}$, furthermore, each line is divided because of a relocation of an electron from oxygen atom to La4f, which is originally empty. As can be seen from the Figure 5, the V2p signal is split into two peaks of $V2p_{3/2}$ and $V2p_{1/2}$ seen at binding energies of 515.68 and 517.48 eV, ascribed to V^{5+} and V^{4+}, correspondingly. Therefore, the V2p core-level spectra further approves that the as-synthesized LV05SC sample contains both V^{5+} and V^{4+}. The Sr3d region in XPS as shown in

Figure 5, contains a doublet, on which the binding energies are 132.8 and 130.98 eV appointed to $Sr3d_{3/2}$ and $Sr3d_{5/2}$ peaks, correspondingly. These values are very similar to compounds considered as the Sr^{2+} ions in LV05SC. The Co2p XPS region Figure 5 for LV05SC. The peak at 779.58eV arose from $Co2p_{3/2}$, and the one with peak at 795eV was because of $Co2p_{1/2}$. For the Co2p spectrum, a key peak at around 779.58eV supplemented by a smaller shoulder at around 789.5eV is existing and this smaller shake-up line displays the existence of Co^{3+}. For the systems containing cobalt, a weak shoulder offering on the

higher binding energy range of the Co2p3/2 spectrum at roughly 788eV can be recognized as Co^{4+}.

XPS survey spectrum of LV05SM (La$_{0.6-x}$V$_x$Sr$_{0.4}$MnO$_{3-\delta}$, x = 0.005) illustrates the chemical nature of La, V, Sr, and Mn ions estimated by fitting of La3d, V2p, Sr3d and V2p spectrum, as

shown in Figure 6. No extra metals except La, Mn, Sr and V except C1s are detected on the whole spectra. The La3d states of LV05SM can be seen in Figure 6. The La3d$_{3/2}$ line is split into two peaks seen at 853.38 and 850.68eV binding energy values, and the corresponding of La3d5/2 is 837.3 and 833.5eV.
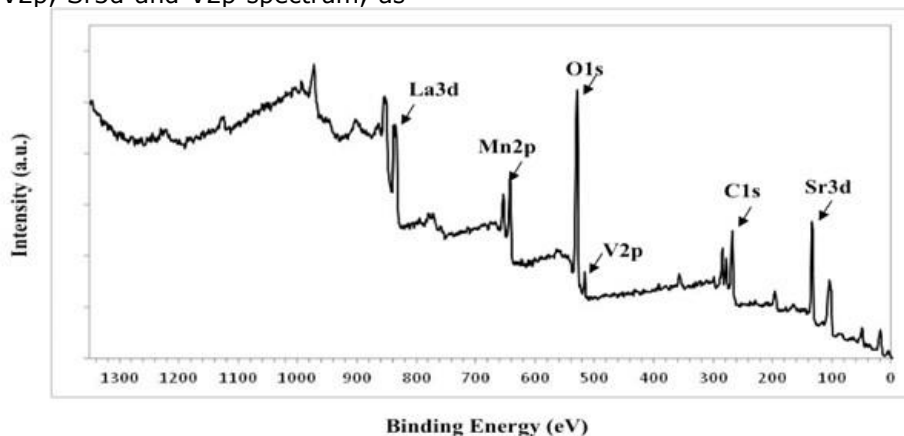

Figure 6. XPS survey spectrum for LV05SM material.

Binding variance in energy level of the 3d3/2 and 3d5/2 is almost 17 eV. These binding energies and the shape of splitting agrees well with published results for La^{3+} materials in Figure 6. The V2p peaks in binding energy levels are 515.88 and 516.6 eV for V2p$_{3/2}$ and V2p$_{1/2}$, correspondingly. Peaks are considered as the states of V^{5+} and V^{3+} in XPS analysis. The Sr 3d spectrum analysis of the LV05SM comprises two peaks as seen in Figure 6, on which peaks at 132.2 and 133.08 eV are assigned as Sr3d$_{5/2}$ and Sr3d$_{3/2}$ lines, correspondingly, indicating that these Sr ions are placed in two different chemical natures. As concerning the XPS analysis of Sr3d$_{5/2}$ line, the component at 132.1-132.7 eV originates from Sr ions united into the structure as perovskite. This peak observed for Sr3d$_{3/2}$ may be appointed to Sr^{2+}. From the XP spectra, it is

decided that these binding energy values are similar for compounds attributed to the Sr^{2+} ions in LV05SM. Also, the Mn2p XP spectra of LV05SM in Figure 6 exhibits a wide-ranging emission with a maximum close to 641.2 eV for Mn2p3/2 and 653.08 eV for Mn2p$_{1/2}$ emissions. With respect to the binding energy values of Mn2p$_{3/2}$, the oxidation degrees of Mn ions are +3 and +4.

XPS survey spectrum of LV3SF (La$_{0.6-x}$V$_x$Sr$_{0.4}$FeO$_{3-\delta}$, x = 0.03) displays the composition of the surface and the valance states of elements in the as-synthesized LV3SF sample as shown in Figure 7 and further investigated by the fitted curves about elements within the powder. Just La, Sr, Mn, C and O elements are detected on the material surface. No extra peaks related to the impurities were observed in XPS analysis.
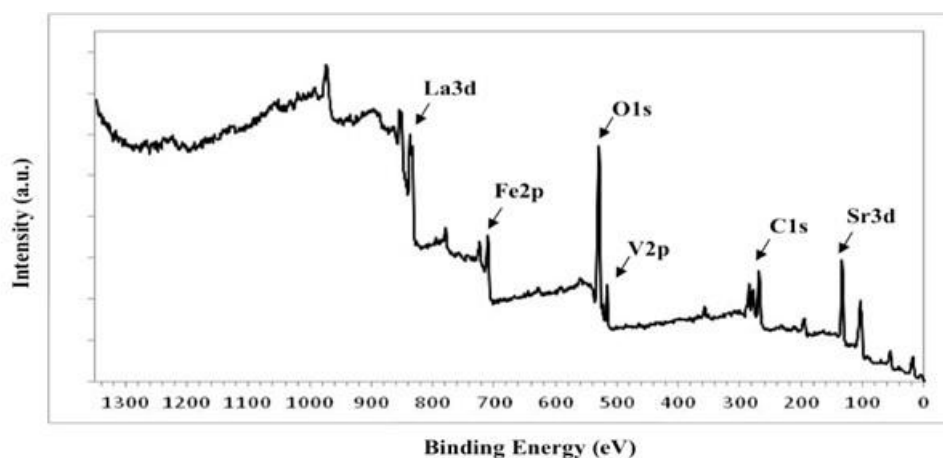
Figure 7. XPS survey spectrum of the LV3SF material.

In Figure 7, the La3d states of LV3SF are shown. In the binding energy region for La, there are two lines, first at 833 eV corresponding to La^{3+} in perovskite phase and, another at 836 eV,

corresponding to La^{3+} in La$_2$O$_3$. From XPS spectra, it can be judged that only La^{3+} ions exist in LV3SF sample. The V2p XPS, as shown in Figure 7, contains a broad peak, for which binding energy

values are 515.98 and 517 eV assigned as $V2p_{3/2}$ and $V2p_{1/2}$ lines, correspondingly. These are presumed to be V as V^{5+} and V^{3+} states. From the spectra, it can be concluded that vanadium exists in a mixed oxidation state. The chemical state of the Sr element was revealed by XPS (Figure 7). The binding energy for the $Sr3d_{3/2}$ and $Sr3d_{5/2}$ peak of as-prepared LV3SF cathode is 132.8 eV and 131.68 eV, respectively, corresponding to Sr^{2+} in LV3SF and few SrO, because this binding energy value is near to the similar compounds. Figure 7 also displays the asymmetric Fe 2p spectrum of the LV3SF material and two oxidation states, Fe^{3+} and Fe^{4+}. Two peaks with energy values at 719.5 and 723.3eV may be ascribed to the Fe^{3+} $2p_{3/2}$ and $2p_{1/2}$ spectrum, correspondingly. Remarkably, a small shoulder peak at 718.8 eV emerges between the doublet peaks, agreeing to the Fe^{4+} $2p_{3/2}$.

Electrical Conductivity - Four Probe Measurement Results

The electrical conductivity of as-synthesized materials was characterized by the four-probe direct current (DC) technique on the calcined rectangular bars. These measurements were completed while ramping the temperature between 400 and 800 °C in open air, and with a temperature ramping rate of 1 °C/min. Four gold (Au) connection wires were placed, which were smeared with gold conductor paste. Two current wires were attached at the bar edges, and two voltage wires in between at a certain distance l. The bar was then sintered at 500 °C for 1 h to achieve comprehensive connection of the probes and reduction of the connection resistance. The bar was then located horizontally in a tube oven. An electric current in this method is delivered through a bar of the material and a voltage decline is measured across a distance in the middle of the bar. The bar was held at each temperature till measurement completed. The electrical conductivity σ was analyzed by the following equation: $R = \rho. \, l \, /A$, where R is the polarization resistance, A is the bar cross-sectional area, l is the distance between the inner electrodes (either current or voltage), and ρ is the specific resistance. Electrical conductivity (σ) parameters were acquired through the converse of the specific resistance. The as-synthesized LV05SC, LV05SM and LV3SF cathode materials were prepared for four-probe DC method and the conductivity value acquired is controlled with reference data for each material.
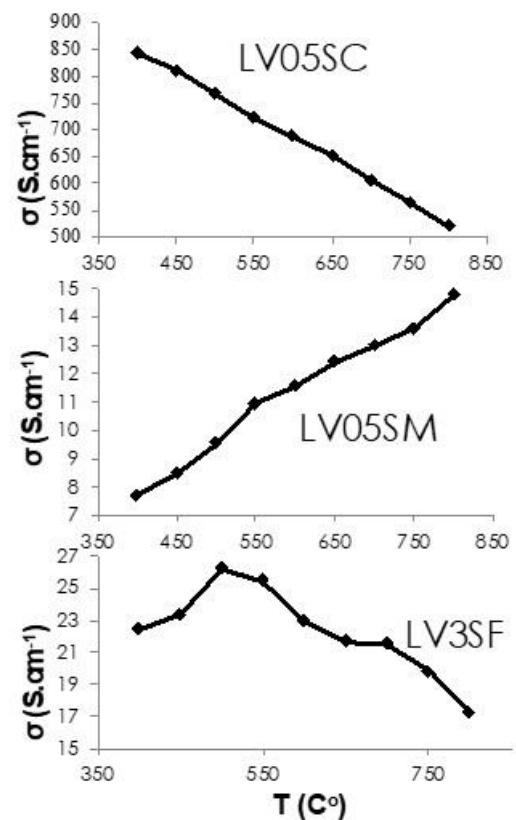
Figure 8. Temperature dependence of the electrical conductivity of LV05SC, LV05SM, and LV3SF sample sintered at 1100 °C.

Electrical conductivity of LV05SC, LV05SM, and LV3SF and its dependence on temperature have been reported for cathode materials shown in Figure 8. A clarification of these ideas is intricate in particular to two main aspects contributed to the electrical conductivity of cathode materials. The distinct parameter of the crystal structure is the first factor due to interatomic distances and angles, on the other hand, as the second factor the charge carrier content is the concentration of electron vacancies. In these kind of metal oxides, oxide ion transport happens through the oxygen deficiencies hopping in the perovskite structure, at which the transfer of the electrons is alongside the way $B^{n+}-O-B^{n+1}$ as second metal bond owing to overlying between the B-metal 3d orbitals and oxygen 2p orbitals.

The highest conductivity for LV05SC achieved to its maximum with 843 S/cm around 400 °C and reduced to 521.50 S/cm at 800 °C in Figure 8. It reveals the anticipated metal conductivity behavior and it signifies to the reduction in the electron-hole content with rising temperature. The metal conductivity behavior is detected in $La_{1-x}Sr_xCoO_3$ cubic phase, whereas the semiconductor performance is scrutinized in the rhombohedral part. When the electrical conductivity decreases with increasing temperature this means metallic behavior, on the hand, as the electrical conductivity increases with temperature, this means semiconducting behavior.

Four probe electrical conductivity measurements of LV05SM in Figure 8 show that the conductivity of LV05SM material under air was measured using a four-probe DC method. LSM has been acknowledged as a p-type semiconductor with electronic holes as charge carriers and essentially this hole motion in the d-orbitals energy levels of manganese is the reason for the electrical conductivity. This is elucidated by the minor polaron hopping of electron holes between Mn^{4+} and Mn^{3+} on octahedral corners. The mechanism of electrical conduction was accomplished by the hopping of electrons between multivalent metal ions at B-site and oxide ion resulting the way along B–O–B bonds. The equilibrium between Mn^{4+} and Mn^{3+} ions are controlled by a thermally activated disproportionation of Mn^{3+} in crystalline solids. Mn^{2+} ion is formed due to disproportionation but the conduction process occurs just via the carriers hopping amongst Mn^{4+} and Mn^{3+} sites. As a result of charge transfer from Mn^{3+} site to neighboring Mn^{4+} site, the conduction process is assumed to develop, such as jumps of p-type carriers over available sites. Since the electronic conductivity is typically 100-1000 times higher than the ionic conductivity for these kinds of oxides, the measured values reported herein are attributed to the electronic conductivity only. Generally, the electrical conductivity gradually rises with increasing temperature. However, there is a variation in conductivity at around 550 °C, which can be attributed to the loss of the lattice oxygen resulting to more oxygen vacancies because of the thermally stimulated lattice oxygen losses. However, the lattice oxygen loss in p-type semiconductors at higher temperatures could be the reason for the decline of electrical conductivity, because of the decrease of charge carrier content (electron holes). There is only electrical conductivity variation at around 550 °C and no stable fall of conductivity is detected in the temperature between 400 °C and 800 °C. This means that there is a slight lattice oxygen decrease and hence comparatively well structural stability of LV05SM.

Electrical conductivity analysis of LV3SF seen in Figure 8 pointed that the sample must acquire the higher electrical conductivity at the desired working temperatures meanwhile the lower electrical conductivity can consequence in a reduced current-collecting effectiveness and the higher ohmic resistance of cathode material. Values of complete mixed conductivity parameter include both electronic and ionic conductivity values because of the existence of charge carriers and oxygen vacancies, correspondingly. Nevertheless, ionic conductivity in perovskite structure is recognized to be slight in judgement with the complete conductivity. Hence, the experimentally calculated values of the electrical conductivity are expected to be contributor to the electronic conductivity only. The conductivity ascents gradually with rising temperature, achieves the maximum value of 26.23 S/cm at almost 500 °C and then falls with additional temperature increase. It may be elucidated as the electrical conductivity in Sr-doped $LaFeO_3$ is commonly considered to appear by the lattice oxygen loss, implying a semiconductor behavior, related with the tetravalent state of the Fe cations. The decrease in the conductivity at high temperatures is essentially because of the oxygen vacancies formation, complemented by reduction of Fe^{4+} to Fe^{3+} that consequences in a decrease of the charge carrier content.
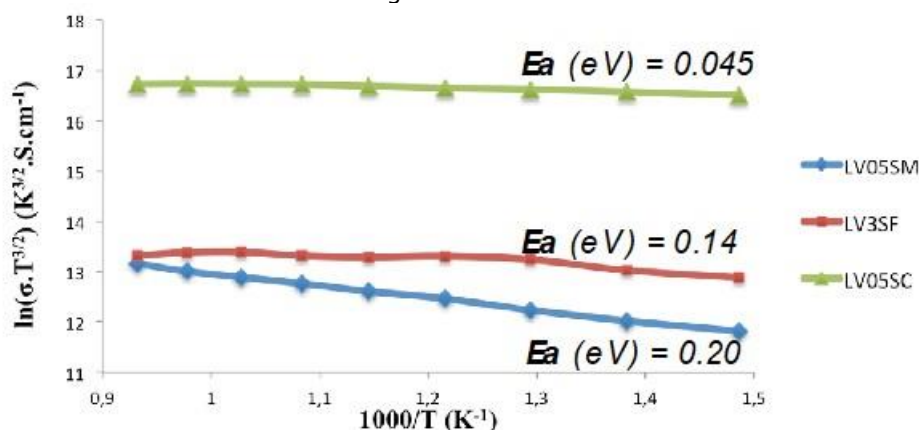
Figure 9. Activation energy (E_a) of LV05SC, LV05SM, and LV3SF measured over 400-800 °C.

The logarithm of electrical conductivity of LV05SC, LV05SM, and LV3SF measured while increasing temperature from 400 to 800 °C in open air and the electrical conductivity of sample are calculated as a temperature function in Figure 9. The temperature dependence of electrical conductivity is shown in Figure 9 summarizes the E_a values for LV05SC, LV05SM, and LV3SF. It was calculated as 0.045 eV for LV05SC, 0.20 eV for LV05SM, and 0.14 eV for LV3SF.

The dependency of electrical conductivity on temperature is generally given as:

$$\sigma = \left(\frac{A}{kT^s}\right) \exp\left(-\frac{E_a}{kT}\right)$$

in which *k* is the Boltzmann constant, E_a is the activation energy for electrical conductivity, *T* is the absolute temperature and *A* is the pre-exponential parameter that covers a number of constants such as the number of charge carriers and the standard distance between the B- site ions. The part of s is accepted as either 1 or 3/2 for an adiabatic or non-adiabatic hopping manner, correspondingly. The graph of ln $\sigma.T^S$ vs. 1000/T would provide a straight line. The plot of synthesized sample direct fit was achieved for s = 3/2, signifying a non-adiabatic hopping manner, seen in Figure 9.

Electrochemical Impedance Spectroscopy Results
The results from Four Probe Method measurements show that the conductivity values are lower than expected. However, there are more important expectations than the electrical conductivity like the ionic one, which is one of the main features of the cathode performance for SOFC. The most complex and least understood

process in the overall SOFC-cathode mechanism is for the oxygen reduction reaction. This process is often referred to as the surface exchange of oxygen, perhaps because it is still not known which of the many elementary reactions are rate limiting the overall reaction and in which order they occur. The surface exchange reaction is generally believed to consist of the following sub reactions (not elementary): O_2 adsorption, O_2 dissociation, and integration of oxide ion species into the lattice and the reduction of either diatomic or mono-atomic oxygen species. The reduction reaction is generally considered to proceed simultaneously with the other reactions to form arbitrarily charged surface species depending on which reaction is the rate-limiting step and there is much recognition in literature. To understand the ORR mechanism, the complex impedance measurements were completed on a selected number of compositions, versus the value of oxygen partial pressure, PO_2, at different temperatures.

Figure 10. Complex impedance plots for LV05SC/YSZ/LV05SC symmetric cell at between 400-800 °C for different oxygen partial pressures.

Figure 10 displays the selected impedance results for the solid crystal LV05SC electrode on the YSZ electrolyte that is measured under various oxygen partial pressure values and collected in each 50 °C increments in the range of temperature between 400 and 800 °C.

EIS diagrams are comprised of arcs found in high frequency and low frequency regions, correspondingly. This indicates that as a minimum of two singular steps engaged in the ORR on the cathode. It is clearly seen that below the 500 °C, two clear arcs are perceived in the high frequency part of the Nyquist graphs. While

rising working temperature, the size of high-frequency semi-circle reduced remarkably, and the semi-circle was completely vanished at 500 °C. Both the electrodes and electrolyte shape the impedance spectrum of a symmetric cell. The electrolyte typically exhibits behavior as an ideal resistor, which signifies the intercept resistance in the impedance graph at higher frequency region with the real impedance axis. With the decline in working temperature, an arc related to the oxide ion diffusion near the electrolyte grain boundary appeared in the higher frequency region.

Figure 11. Complex impedance plots for LV05SM/YSZ/LV05SM symmetric cell at between 400-800 °C for different oxygen partial pressures.

Figure 11 shows the impedance responses for the solid crystalline LV05SM cathode on the YSZ electrolyte that is measured in various oxygen partial pressure values and collected in each 50 °C increments in the temperature region of 400-800 °C.

It is clearly grasped in Figure 11 that the higher frequency region of the two obvious arcs of impedance parts has a clear form in the Nyquist plots below the 500 °C. With rising working temperature, the higher frequency arc size is reduced noticeably, and this arc is entirely extinct at 500 °C. An extra arc at the lower frequency region emerged when the working temperature

was elevated to 700 °C. The symmetric cell impedances can result from both the cathodes and electrolyte. The electrolyte classically executes as a perfect resistor and exhibits only a spot in the Nyquist graphs at higher temperature

range in the inspected frequency region of 10^6-10^{-1} Hz. Though, an arc correlated with the oxide ion diffusion near the electrolyte grain boundary also emerged in the higher frequency region with decline in working temperature.

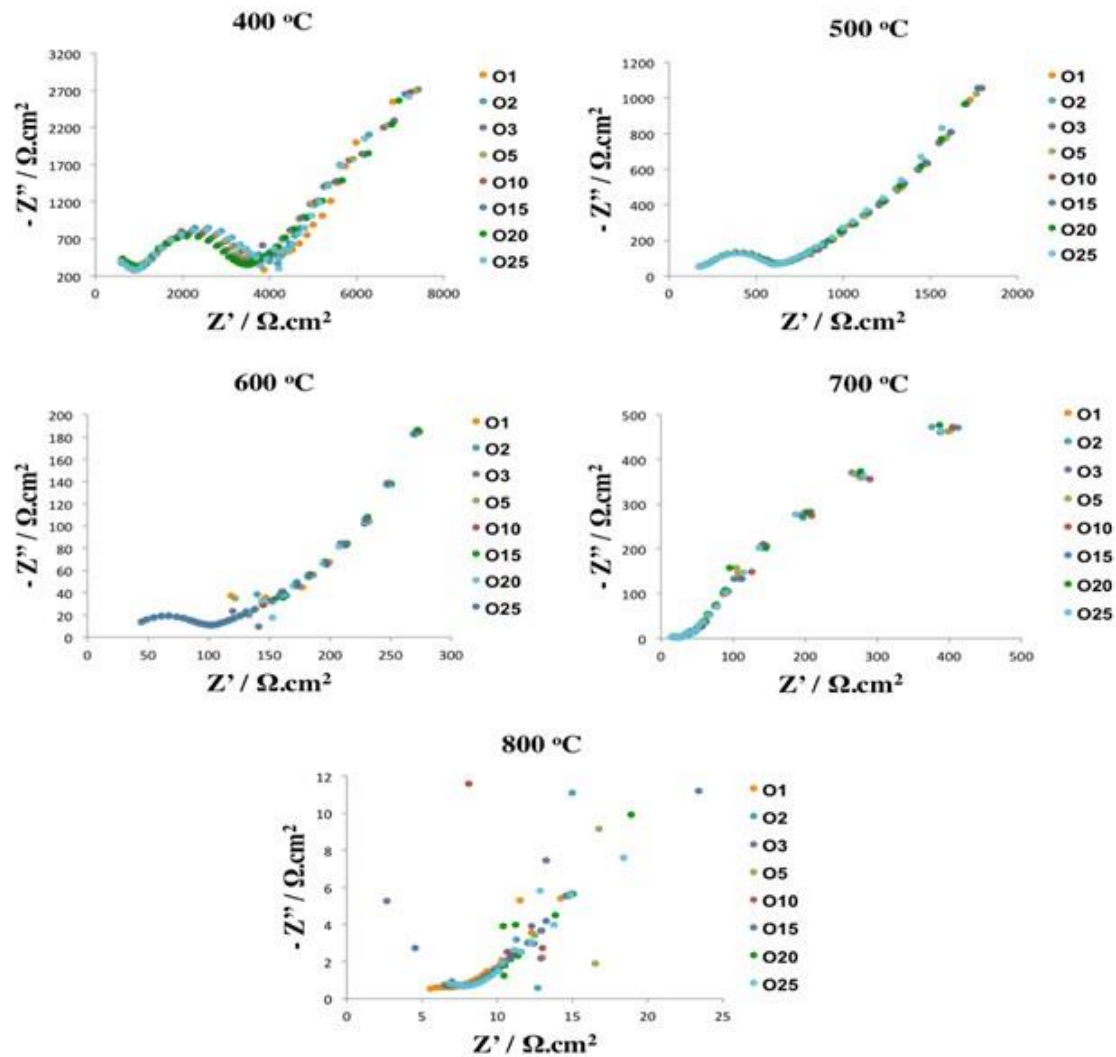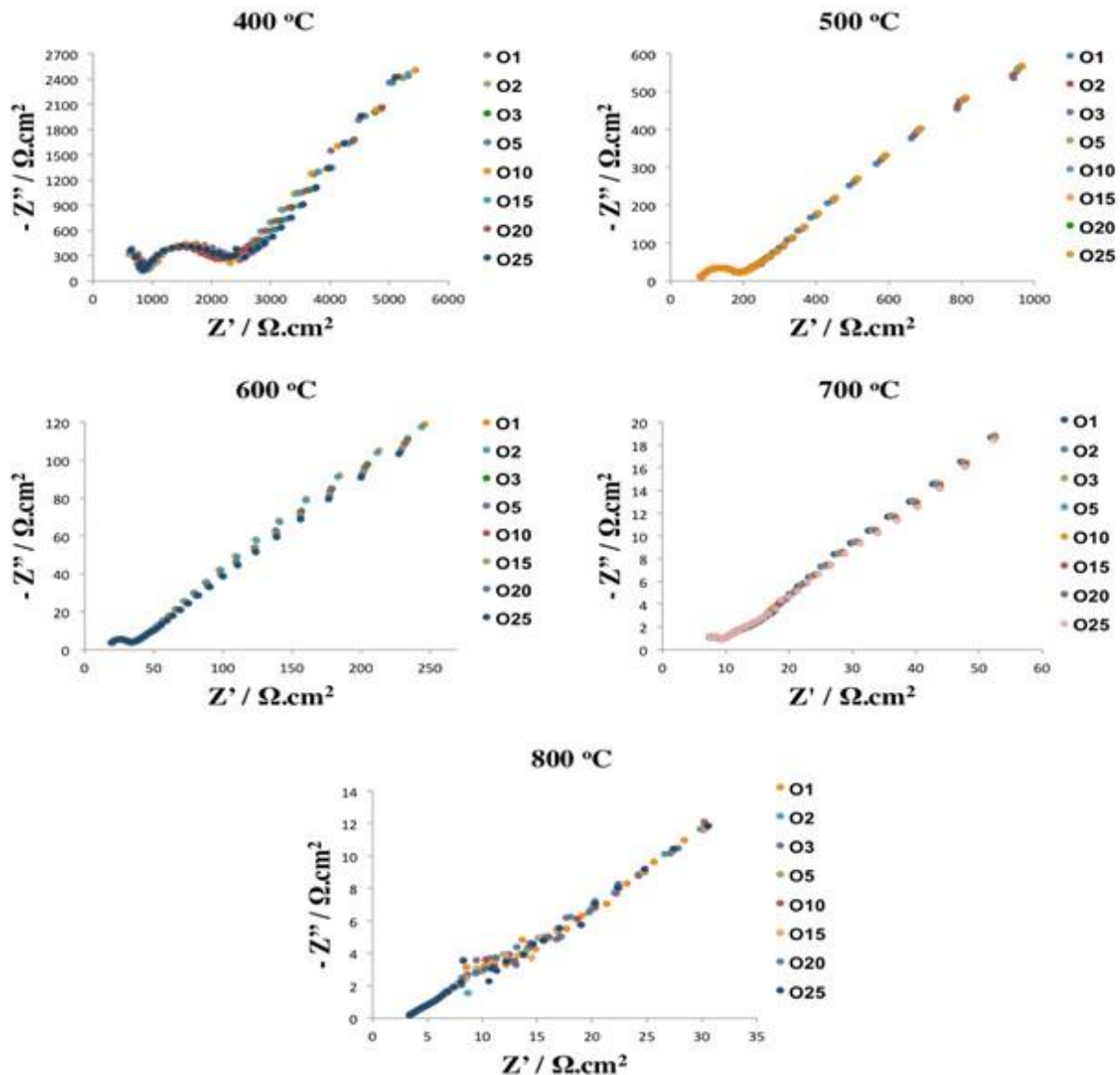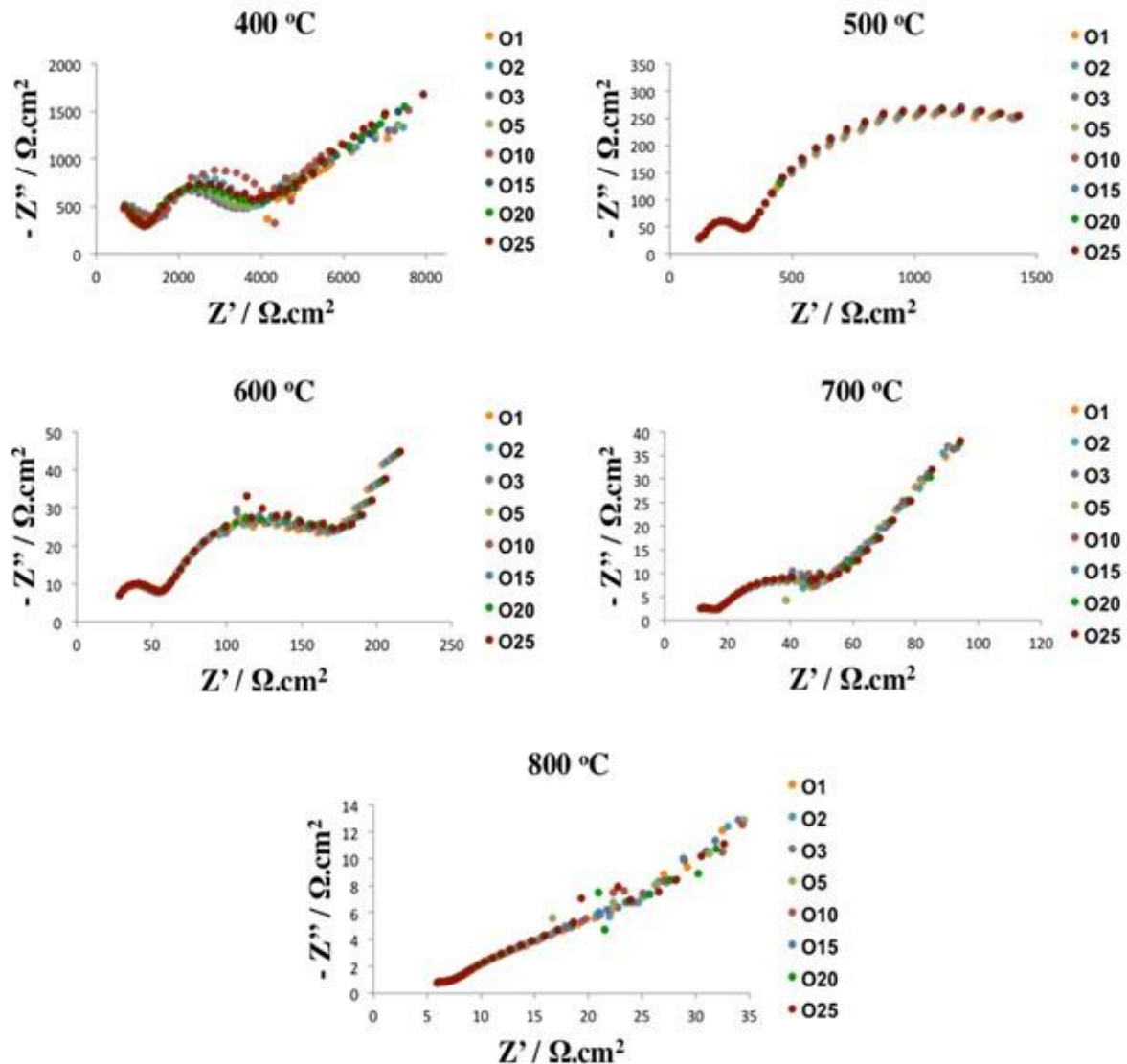**Figure 12.** Complex impedance plots for LV3SF/YSZ/LV3SF symmetric cell at between 400-800 °C for different oxygen partial pressures.

Figure 12 shows some impedance responses for the solid crystalline LV3SF electrode on the YSZ electrolyte that is measured with various oxygen partial pressure values and collected in each 50 °C increments in temperature between 400 to 800 °C. From the Figure 12, it is clearly seen that below the 500 °C, two impedance contributions have an apparent shape in the high frequency part of the Nyquist graphs. With rising working temperature, the size of higher frequency arc is reduced importantly, and the arc was fully vanished at 500 °C. An extra arc at the range of lower frequency emerged when the working temperature was raised to 600 °C. The symmetric cell impedances can be resulted from both the cathodes and electrolyte. The electrolyte typically performs as a perfect resistor, which denotes the

intercept point in the impedance graph at higher frequency region with the real axis. Yet, with the reduction in working temperature, an arc related to oxide ion transfer on the surface near the electrolyte grain boundary also performed in the high frequency region.

The merely ohmic part of the electrode resistance is called polarization resistance (Rp). This may be calculated as the sum of the resistances of all separate processes ($Rp = R_1 + R_2 + R_3 ... + Rn$). The experimental polarization resistance for the symmetrical cell reveals the addition of the polarization resistance of the two different cathodes explored. Consequently, all the cell impedances were standardized by the electrode area (0.04 cm^2), so the R parameter attained in

fitting for each parameter were divided by two to deliberate the influence of the two electrodes, therefore, R parameter called area specific resistance (ASR).

This is well identified that various courses for ORR on mixed ionic and electronic conducting electrodes with different relationships are affected by oxygen partial pressure. The most frequently employed factor to define the rate-limiting step in ORR is n, which specifies the relationship between the cathode resistance and oxygen partial pressure displayed in Figure 13. The n value presents evidence concerning the species elaborated in the electrode reaction. The overall ORR may be summarized as O_2 converted into $2O^{2-}$ ions by accepting four electrons. This is an intricate multi-phase reaction, in which practically contains the gas diffusion, surface adsorption/dissociation and charge transfer steps. Generally, on behalf of metal oxides having solid electrolytes, $n = 1$ can be credited to gas diffusions and adsorptions of oxygen as a restrictive step; $n = 1/2$ linked to the oxygen adsorption-desorption step, linking oxygen diffusion at the border of gas/cathode and surface diffusion of connected to intermediate oxide species as a limiting stage; and $n = 3/8$ deduced a process coordinated by the atomic oxygen diffusion step (beside the two stages electrode/electrolyte contact) continued by a charge transfer as a limiting step; $n = 1/4$ associated to the charge transfer step on the electrode, happening at the boundaries of current collector/electrode and the electrode/electrolyte as a limiting step; and $n = 1/8$ stated to the production of oxide ions as the intermediate species as a restrictive process; and $n = 1/10$ or $n = 0$ can be recognized to the oxide ion diffusion from the triple phase boundary (TPB) to solid electrolyte, correspondingly.

The ASR estimates for oxygen reduction reaction are calculated via the addition of separate resistances related with every single step. Like anticipated, the ASR for LV05SC/YSZ boundary declines particularly with rising temperature and marginally with the oxygen partial pressure as revealed in Figure 13. The feature of ASR displays rather weak PO_2 reliance ($n = 0.3022 – 0.5212$), which would be associated to oxygen adsorption-desorption steps or a step coordinated by the atomic oxygen diffusion (beside the two phases electrode/electrolyte contact) trailed by a charge transfer. Consequently, these two steps are the main rate-limiting processes for LV05SC cathode. As projected, the ASR for LV05SM/YSZ interface drops remarkably with rising temperature and marginally with the oxygen partial pressure as illustrated in Figure 13. The property of ASR confirms very weak PO_2 dependence ($n = 0.0042 – 0.0607$), which would be correlated to the oxide ion transfer within the electrode bulk and/or from electrode to YSZ electrolyte through the TPB. Therefore, this process can be considered as the main rate-limiting step for LV05SM. Like

accepted, the ASR for LV3SF/YSZ boundary reduces outstandingly with rising temperature and faintly with the oxygen partial pressure as seen in Figure 13. The representation of ASR indicates also very weak PO_2 dependence ($n = 0.0053 – 0.0426$), which would be linked to the oxide ion transfer within the bulk electrode and/or from electrode to electrolyte through the TPB. Consequently, this step can be deliberated as the main rate- limiting step for LV3SF material.
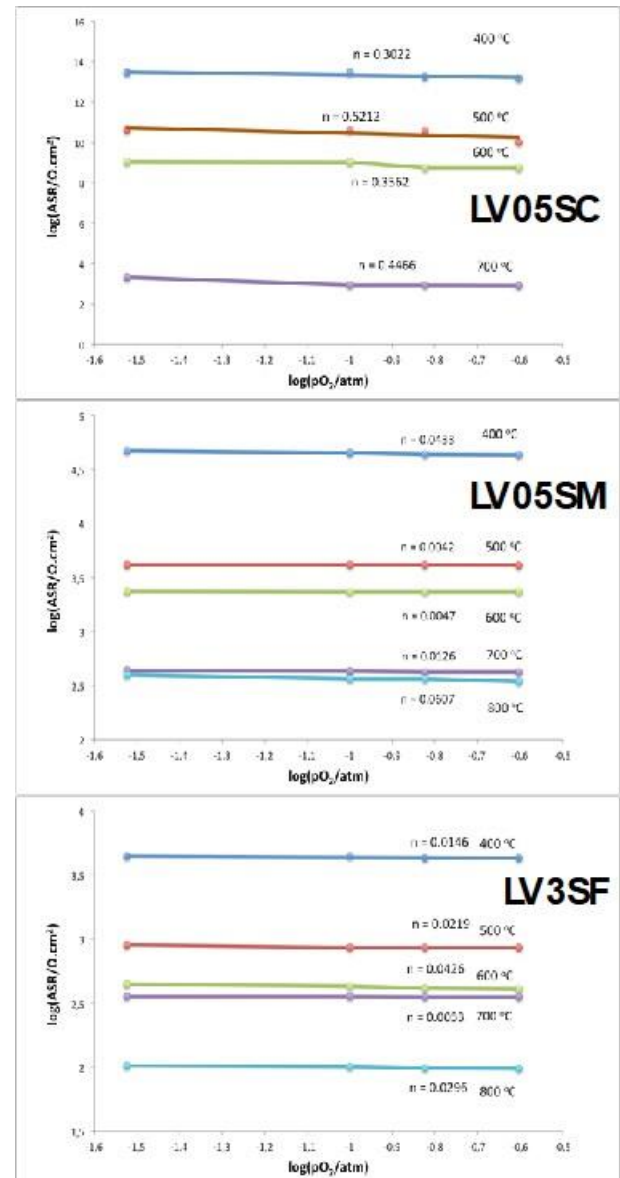
Figure 13. The dependence of the area specific resistance of the LV05SC/YSZ, LV05SM/YSZ, and LV3SF/YSZ interfaces as a function of oxygen partial pressure at different temperatures.

CONCLUSION

This study deals with fundamental experimental analysis on mixed electronic and ionic conducting model perovskite cathode electrodes, in particular for the application as catalytically active cathode in SOFC systems. As an SOFC cathode candidate, the stability of the developed cathode materials

with regard to the application was first studied on materials synthesized from the metal nitrates by the sol-gel process. XRD results reveals a crystalline perovskite structure for all materials with a rhombohedral unit cell. All peaks in the XRD pattern of the cathode samples are relatively visible, demonstrating well-incorporated into crystal lattice of the metal oxides employed in the preparation. XPS analyses show that the oxidation states of metals in the composition of the surface of the samples were confirmed. According to advance conductivity studies, the materials exhibit high conductivities and all compositions except LV05SC showed metal-like temperature dependences *i.e.* decrease in conductivity with temperature. While in the studied temperature region, the electrical conductivity is augmented with rising temperature for LV05SM, typical of semiconductor behavior. In the case of LV3SF sample, with rising temperature the conductivity grows and extents to maximum value at about 500 °C. The low value of activation energy emphasizes the high catalytic activity of the electrode material. Vanadium doped LSM sample (LV05SM) has the lowest conductivity value of 14.8 S/cm with activation energy of 0.20 eV and it continues with LV3SF material with a value of 26.23 S/cm and Ea of 0.14 eV.

The electrolyte classically acts as a perfect electrical resistor and the oxide ion diffusion through the electrolyte material could be observed as an arc in the higher frequency range inside the impedance spectrum and it is independent of PO_2. However, at lower temperatures the electrolyte becomes the limiting factor for SOFC applications. With diminishing in the partial pressure of oxygen, the impedance values rise considerably, particularly at lower frequency regions. For most of the impedance arcs, two steps could be deduced at higher and lower frequencies. It signifies that at least two electrochemical steps control the whole electrochemical reaction. The analysis of the effect of both the partial pressure of oxygen and the temperature in the electrode impedance was achieved and the data were fitted to the equivalent circuits in order to have more information to interpret properly steps included in the cathode/electrolyte interface. From the fitting parameters, it can be said that the resistances related to the kinetics of electrode steps decline with rising temperature.

The area specific resistance (ASR) analysis shows that oxide ion relocation within the cathode bulk is the main rate-limiting step for the LV05SM, and LV3SF cathode materials. The polarization resistance value for LV05SC material was associated to the oxygen adsorption-desorption steps or a step ordered by the atomic oxygen diffusion. Therefore, these two steps are the main rate-limiting processes for LV05SC cathode. The comparison of the polarization and impedance behavior of pronounced cathode materials under identical experimental conditions showed that the much higher electrode performance of LV3SF, and LV05SM compared to that of LV05SC is clearly due to their better ionic conductivity values. As a result of this study, it is concluded that these cathode materials would be candidates as IT-SOFC cathode materials.

ACKNOWLEDGMENT

REFERENCES

1.   Lashtabeg A, Skinner SJ. Solid oxide fuel cells - a challenge for materials chemists? Journal of Materials Chemistry. 2006;16(31):3161-70.

2.   Winter M, Brodd RJ. What are batteries, fuel cells, and supercapacitors? Chemical Reviews. 2004;104(10):4245-69.

3.   Ormerod RM. Solid oxide fuel cells. Chemical Society Reviews. 2003;32(1):17-28.

4.   Choudhury A, Chandra H, Arora A. Application of solid oxide fuel cell technology for power generation-A review. Renewable & Sustainable Energy Reviews. 2013;20:430-42.

5.   Baur E, Preis H. Über Brennstoff-Ketten mit Festleitern. Zeitschrift fur electrochemie. 1937;43(9):727.

6.   Yamamoto O, Takeda Y, Kanno R, Noda M. Perovskite-Type Oxides As Oxygen Electrodes For High-Temperature Oxide Fuel-Cells. Solid State Ionics. 1987;22(2-3):241-6.

7.   Yamamoto O. Solid oxide fuel cells: fundamental aspects and prospects. Electrochimica Acta. 2000;45(15-16):2423-35.

8.   Wachsman ED, Lee KT. Lowering the Temperature of Solid Oxide Fuel Cells. Science. 2011;334(6058):935-9.

9.   Brett DJL, Atkinson A, Brandon NP, Skinner SJ. Intermediate temperature solid oxide fuel cells. Chemical Society Reviews. 2008;37(8):1568-78.

10.   Istomin SY, Antipov EV. Cathode materials based on perovskite-like transition metal oxides for intermediate temperature solid oxide fuel cells. Russian Chemical Reviews. 2013;82(7):686-700.

11.   Tsipis EV, Kharton VV. Electrode materials and reaction mechanisms in solid oxide fuel cells: a brief review. Journal of Solid State Electrochemistry. 2008;12(9):1039-60.

12. Sun CW, Hui R, Roller J. Cathode materials for solid oxide fuel cells: a review. Journal of Solid State Electrochemistry. 2010;14(7):1125-44.

13. Tezuka K, Hinatsu Y, Nakamura A, Inami T, Shimojo Y, Morii Y. Magnetic and neutron diffraction study on perovskites La1-xSrxCrO3. Journal of Solid State Chemistry. 1998;141(2):404-10.

14. Sengodan S, Choi S, Jun A, Shin TH, Ju YW, Jeong HY, et al. Layered oxygen-deficient double perovskite as an effcient and stable anode for direct hydrocarbon solid oxide fuel cells. Nature Materials. 2015;14(2):205-9.

15. Carpanese MP, Clematis D, Bertei A, Giuliano A, Sanson A, Mercadelli E, et al. Understanding the electrochemical behaviour of LSM-based SOFC cathodes. Part I - Experimental and electrochemical. Solid State Ionics. 2017;301:106-15.

16. Mizusaki J, Mori N, Takai H, Yonemura Y, Minamiue H, Tagawa H, et al. Oxygen nonstoichiometry and defect equilibrium in the perovskite-type oxides La1-xSrxMnO3+d. Solid State Ionics. 2000;129(1-4):163-77.

17. De Souza RA, Kilner JA, Walker JF. A SIMS study of oxygen tracer diffusion and surface exchange in La0.8Sr0.2MnO3+delta. Materials Letters. 2000;43(1-2):43-52.

18. Chen YB, Shen J, Yang GM, Zhou W, Shao ZP. A single-/double-perovskite composite with an overwhelming single-perovskite phase for the oxygen reduction reaction at intermediate temperatures. Journal of Materials Chemistry A. 2017;5(47):24842-9.

Polyoxotungstate/Oxy-Graphene Nanocomposite Multilayer Films For Electrocatalytic Hydrogen Evolution

Yasemin Torlak[1]* ✉ iD

[1] Pamukkale University, 20700, Denizli, Turkey.

Abstract: In this study, nanocomposites were formed together with Keggin-type $K_{7-x}Na_xPW_{11}O_{39} \cdot 14H_2O$ polyoxotungstates (POTs) clusters and oxygenated-graphene (Oxy-G). It was produced as a multilayer via layer-by-layer self-assembly method using protonated poly (ethylenimine) (PEI). The produced $(PEI/POTs/Oxy-G)_n$ multilayer films were controlled by XRD, cyclic voltammetry, and UV-Visible spectrophotometry. $(PEI/POTs/Oxy-G)_n$ multilayers are modified on a glassy carbon electrode. The hydrogen evolution reaction takes place by taking advantage of the electrocatalytic activity of this nanocomposite. They have been shown to exhibit a potentially good electrocatalytic activity at -0.4 V. A notable electrocatalytic hydrogen evolution reaction could be identified on the $(PEI/POTs/Oxy-G)_n$ multilayer. We demonstrate that expanded the application of POTs/G nanocomposites to the electrocatalysis of oxygen reduction reaction and hydrogen evolution reaction. This excellent approach will offer new insights into different electrode structure and the development of novel electroactive catalysts.

INTRODUCTION

Recently, global energy crisis externalized in the consuming of fossil fuels and the enlarging menace of environmental contamination, has induced a unique endeavor for the improve of novel renewable conversion technologies and energy storage, operating maintainable different chemical methods (1). Hydrogen can be an alternative for renewable and environmentally friendly fossil fuels of the next generation (1–2). Hydrogen production by the electrocatalytic reduction method provides a simple and effective solution for future energy demands. Graphene has recently been the focus of research because of unique surface area, electrical conductivity, and mechanical strength (1). The properties possessed of this advantage for graphene is the most remarkable materials for methods of immobilizing it into functional molecules (2). At the same time, these functional molecules can be adsorbed onto the graphene surface. Currently, metals (3), polymers (4), noble metals (5),

semiconductors (6), inorganic nanoparticles (7) enzymes (8) have been used to build graphene containing hybrid composites, and generally used in different fields such as supercapacitors and biosensors (9), photocatalysts or electrocatalysts (10) and lithium-ion batteries (11). Polyoxotungstates (POTs) are another vast class of well-defined, early transition metal-oxo clusters with different properties, sizes, nuclearities, and shapes. They are widely used as an electrocatalyst in the field of photocatalysis and electrocatalysis (11-13).

POTs/graphene (POTs/G) nanocomposites have significant improvements in different applications with the catalytic properties of POTs. Essentially, such an idea firstly derived from graphene oxide/POMs (Polyoxometalates) (14-15). The first studies on POTs/G nanocomposites and the experimental results were evaluated by Zhou in 2010 (16-20). First, phosphomolybdic acid was synthesized and then graphene composites were formed by hydrazine hydrate with POM

compound. Guo formed the graphene-modified electrode in a solution prepared with the Ru-POT compound dissolved in water and formed the Ru-POT / G composite structure for use as an electrocatalyst (18). Both Li (19) and Wang (20) studied different electrochemical methods to produce POT/G composites with electron-rich POTs. These studies with regard to the properties of POTs/G composites investigated as the microelectrodes used for generally in areas like photodetector devices, sensors to detect H_2O_2, catalysts for water oxidation, (18) and methanol oxidation (21). For oxygen reduction reaction (ORR) and hydrogen evolution reaction (HER) (22), there is not much research on the development of POTs/G electrocatalysts. A powerful and non-expensive electrocatalyst for ORR is important component for speeding the extensive trading of proton exchange membrane fuel cells.

In this study, synthesis of POT material acting as an electrocatalyst was made and then composite material was formed with graphene. Nanocomposite based on the Keggin-type POT clusters and oxidized graphite flakes was formed and we showed that these are structures exhibiting electrocatalytic activity for HER. In addition to the formation of POT-Oxy-G nanocomposite, there is not much work on electrocatalytic application for HER. POT clusters were immobilized via a one-step electroreduction synthesis on reduced oxidized graphite flakes. We contribute the high performance of our POT/Oxy-G hybrid catalyst in the HER to strong chemical and electronic coupling between the Oxy-G and POT. Chemical coupling/interactions afforded the selective growth of extremely dispersed POT nanoparticles on Oxy-G free of aggregation. The small size and high dispersion of Oxy-G and POT afforded an plenty of penetrable edges that could operate as active catalytic sites for the HER. Electrical coupling to the underlying Oxy-G in an interconnected conducting network afforded rapid electron transport from the less-conducting POT nanoparticles to the electrodes. Thus, the approach of materials composite on graphene has led to an advanced POTs electrocatalyst with highly competitive performance relative to various HER electrocatalytic materials.

MATERIALS AND METHODS

Materials and Instrumentation
Quartz slides, graphite flakes and silicon wafer and all chemicals were purchased from Aldrich. All the chemicals were used directly without any purification.

Instruments
UV-Vis spectral calculations were evaluated on a Hitachi-U4100 UV-Vis-NIR model spectrophotometer and IR spectra with a Nicolet 6700 FTIR model spectrometer. X-ray diffraction (XRD) patterns results were performed under a Bruker D8 Advance X-ray difractometer using Cu

Kα radiation λ = 1.5406 Å. AFM images were recorded on an (NT-MDT,Ntegra Solaris) model in tapping mode. The electrochemical behavior of nanocomposite was investigated by cyclic voltammetry with CH instruments 660B electrochemical workstation model in acetonitrile at a glassy carbon electrode, by using tetrabutylammonium tetrafluoroborate (NBu_4BF_4) as the supporting electrolyte. Platinum wire was used as the counter electrode and Ag/AgCl (KCl saturated) as reference electrode and a glassy carbon electrode as working electrode. The electrochemical behavior of nanocomposite was investigated by cyclic voltammetry with CH instruments 660B electrochemical workstation model in acetonitrile at a glassy carbon electrode, by using NBu_4BF_4 as the supporting electrolyte. All electrochemical measurements throughout the experiment were carried out at room temperature under nitrogen atmosphere. All cyclic voltammetric and amperometric measurements were carried out by this system.

Preparation of $K_{7-x}Na_xPW_{11}O_{39}\cdot14H_2O$ (POTs)
$Na_2WO_4.2H_2O$ (181.5 g, 0.550 mol) is dissolved in 300 mL of water and 50 mL of 1M H_3PO_4 is added followed by 88 mL of CH_3COOH. The solution is refluxed for 1 hour then potassium chloride (60 g, 0.805 mol) is added. The resulting white residue was filtered and washed with water and then dried to give POT (Yield: 104.4 g, 58%) (24).

Preparation of Oxygenated Graphene (Oxy-G)
GO was synthesized following Hummer's method. H_2SO_4, $NaNO_3$, and $KMnO_4$ were mixed together and reacted with natural graphite powder. Upon completion of the reaction, H_2O_2 was added onto this mixture. The resulting Oxy-G was separated by centrifugation and washed three times with 1 M hydrochloric acid solution, then washed with distilled water ten times to rinse. The product was dried in vacuum to afford brown sheets. Oxy-G dispersion was prepared by ultrasonically dissolving a required amount of Oxy-G solid into deionized water (10-11).

Preparation of POTs/Oxy-Graphene
Oxy-G dispersion was prepared for use in the reduction process. The synthesized POT compound and Oxy-G dispersion were mixed together to provide a homogeneous mixture. Then, pH =1.0 H_2SO_4 was added. In a three-electrode conventional glass cell, POT and Oxy-G mixture by means of cyclic voltammetry were measured in the acetonitrile solvent in the electrolyte solution. The POTs completely reduced on working electrode. Thanks to the multiple electrons found in the structure of the POT compound with the help of electrochemical and chemical processes, its redox state changes quickly. After completion of the electrochemical reduction process, POT/Oxy-G adsorbs on the glassy carbon electrode. This nanocomposite

formed was subjected to a vacuum oven at 80°C for 24 h.

Multilayer Assembly
Substrates were fabricated multilayer films via studies in the literature (23). The fabrication of POT/Oxy-G nanocomposite is shown schematically in Figure 1. The surface was immersed in PEI (polyethylenimine) solution (2 mg/mL, pH:7) solution for 20 minutes to load the surface with positive charges. The distillate was then washed with water and dried with nitrogen gas. Substrates coated with PEI were after immersed in a solution of POT (1 mg/mL) and Oxy-G (0.5 mg/mL) in pH 6.2 for 20 minutes.

Figure 1. Schematic representation of the fabrication of POT/Oxy-G nanocomposite.

A nanocomposite was formed by the electrostatic interaction between the positively charged PEI and negatively charged POT/Oxy-G layer. And, then the distillate was then washed with water and dried with nitrogen gas. This procedure is repeated when multiple layers are formed. This is called a multilayer (PEI/POT/Oxy-G)$_n$ (n:number of multilayers)

RESULTS AND DISCUSSION

Growth of Multilayers
With the help of cyclic voltammetric (CV) methods and for UV-Visible spectroscopy, the growth of PEI/POT/Oxy-G)$_n$ multilayer film was controlled. On a quartz slide as shown in Figure 3 was evaluated the UV−Visible spectra of (PEI/POT/Oxy-G)$_n$ multilayers with a number ranging from one to eleven deposited. As shown in the inset of Figure 3, when UV-Visible absorption spectrum are evaluated, electrons are transferred from the oxygen atom to the tungsten atom and the values 215 and 270 nm are calculated.

These spectra show the presence of multiple layers and show that the POT compound is well incorporated into the Oxy-G structure. Characteristic bands and comparisons with each other can be seen in the UV-Vis spectral results. POT and Oxy-G structures overlap with each other, which is shown in Figure 3, but it is not clear based on this metamorphism that multiple layers are formed. Due to these reasons (PEI/POT/Oxy-G), other methods are used to show that multiple layers are formed. Figure 2 demonstrated that the cyclic voltammograms of the multilayer structures (PEI/POT/Oxy-G) with one to ten layer counts were taken on a glassy carbon electrode surface with 5×10^{-3} mol/L of TBABF in acetonitrile solutions.

The electrochemical window was set between 0 and -1.5 V outside which, towards more negative values. In Figure 2a, compared to the voltammograms, there were three redox peaks in the cyclic voltommogram of the POT compound, as shown in Figure 2b, but this peak was turned into five peaks when the composite was formed. They exhibit several reversible redox waves and this property can be exploited for construction of electrocatalytic hydrogen evolution.
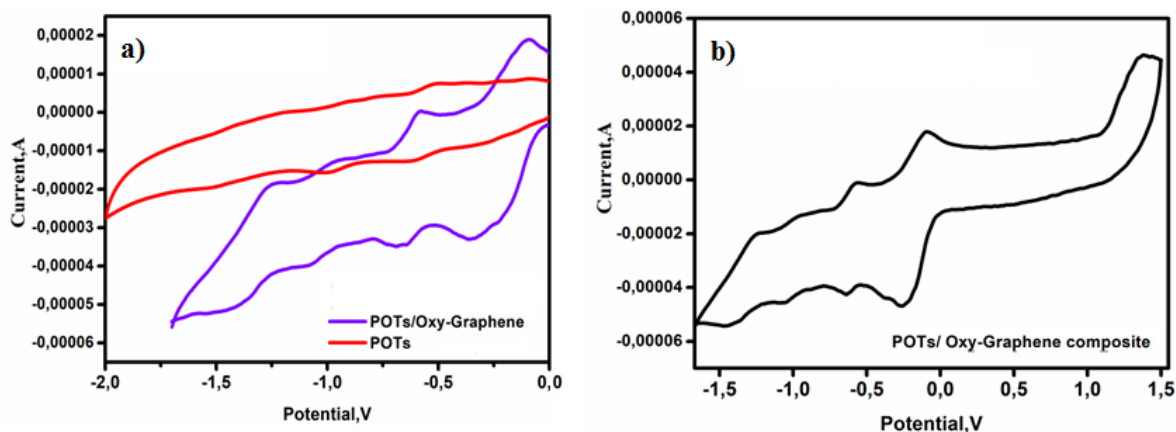
Figure 2. Cyclic voltammograms of a) POTs and POTs/Oxy-G b) (PEI/POT/Oxy-G)$_{10}$ multilayers deposited on GCE in 5×10^{-3} mol/L acetonitrile solution at 100 mV/s scan rates.

Due to the presence of many electrons in the POT structure and the presence of reversible redox peaks (-0.215, -0.317, -0.392, -0.446, and -0.598 V) potential changes are clearly visible in the nanocomposite structure. More than these redox peaks are because of the fact that the POT compound has undergone two successive electron transfer processes and the transition metal nature of this compound. As the number of layers increased, the current in the redox peaks increased. Although the Oxy-G structure is not very good in terms of electrical conductivity, there is no negative change in the electrochemical property of the POT compound while forming a multiple layer. And there is no change in the redox peaks in the cyclic voltammogram during

magnification of the (PEI/POT/Oxy-GO)$_n$ multilayers. At the same time the (PEI/POT/Oxy-GO)$_n$ multilayers showed a smooth growth without any peak potential change in the CV.

Spectral Characterization of (PEI/POT/Oxy-G)$_n$ Multilayers

(PEI/POT/Oxy-G)$_{10}$ multilayer was observed to change color when exposed to UV light. As shown in Figure 3, this multilayer and only the UV-Visible absorption spectra of the POT compound are comparable. This can be interpreted as an increase of the absorbance of the multilayers from 250 to 700 nm compared to the POT compound.
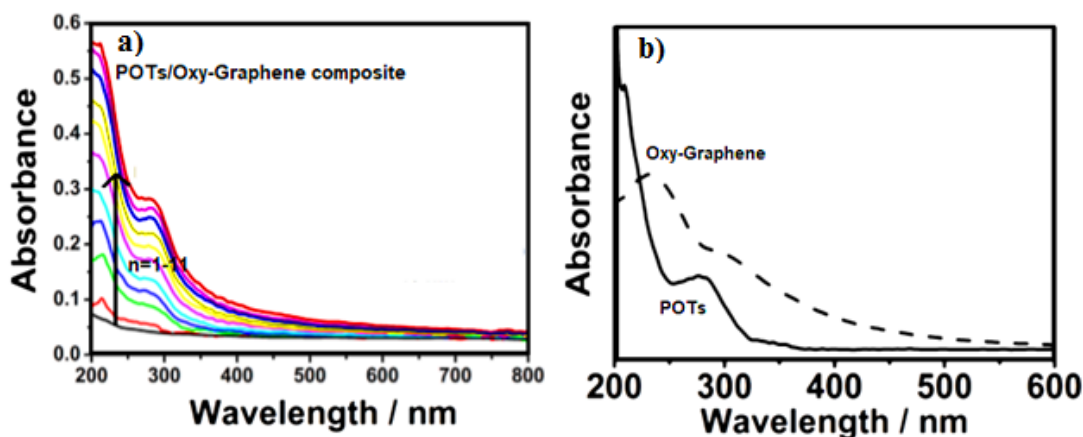
Figure 3. Absorption spectra of (PEI/POT/Oxy-G)$_{10}$ multilayers before a) and after b) exposure to UV light.

Figure 4 shows the XRD patterns of POT and POT/Oxy-G. As shown in Figure 4b, the sharp peak centered at $2\theta = 28.5°$ corresponds to the (002) interplanar spacing of 0.35 nm in Oxy-G. After the composite is formed, diffraction angle of

POT appears to be shifting to higher. The presence of oxygen-bearing groups such as epoxides, hydroxyls, and carboxyls increased the basal spacing of Oxy-G after the process.
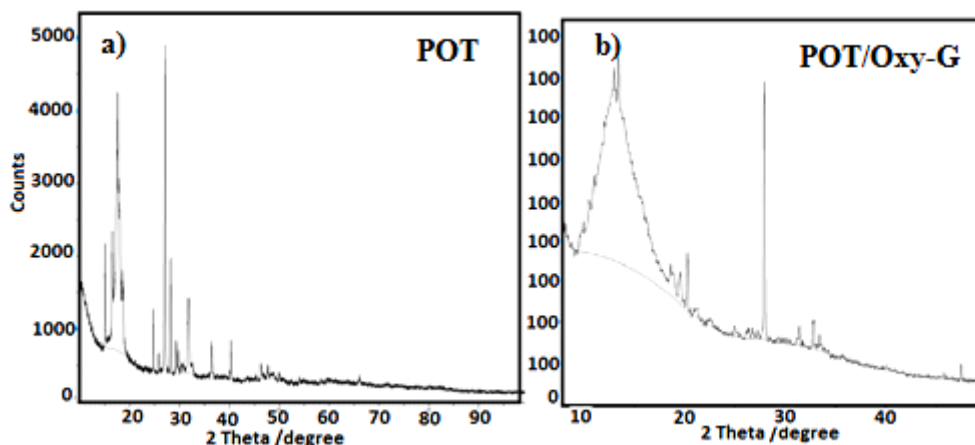
Figure 4. X-ray diffraction patterns of a) POT and b) POT/Oxy-G.

AFM (Atomic Force Microscopy) images of (PEI/POT/Oxy-G)₃ multilayers coated on silicon wafer are obtained for the morphological characteristic. In Figure 5a, it is clearly seen that some of the lamellar films were dimly visible with the appearance of aggregated nanoparticles underneath. As shown in Figure 5b, granular texture showed the morphology of the multilayers was composed of POTs and Oxy-G. Two types of negatively charged species, POT and Oxy-G were demonstrated to be distributed in the multilayers.
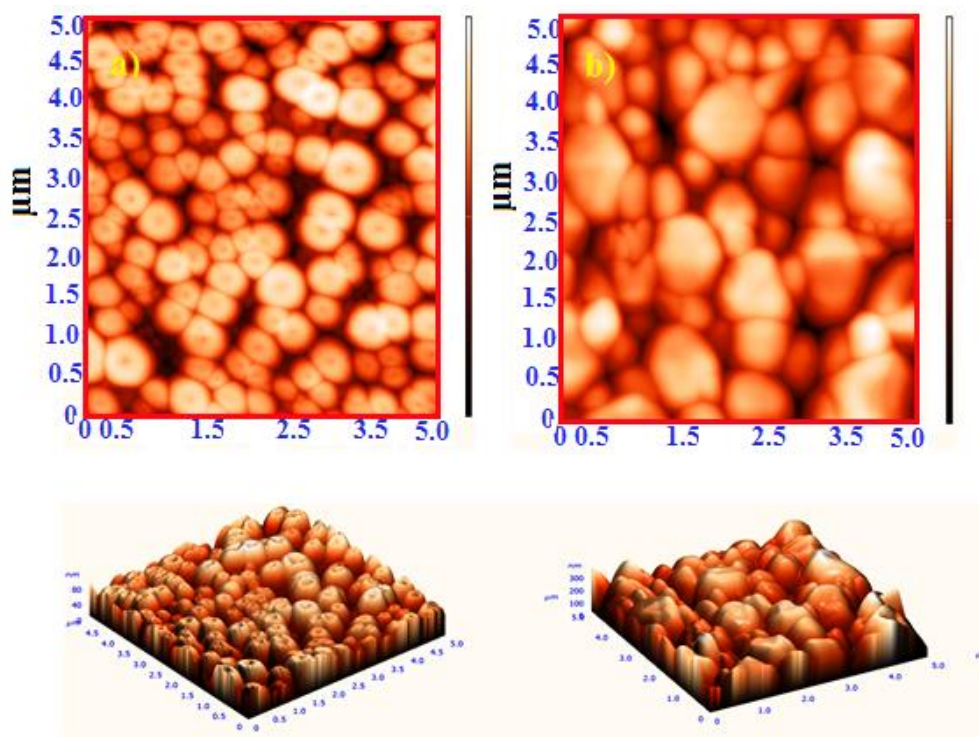
Figure 5. AFM images of a) POT and b) (POT/Oxy-G)₃ multilayers on silicon wafer at different scales.

It is foreseen that these changes will be due to the conjugated aromatic structure when electrons are transferred to the Oxy-G structure (17).

Figure 6a-b displays scanning electron microscopy (SEM) images of POT and POT/Oxy-G composites. Surface analysis with SEM is essential concerning the interaction of Oxy-G with POT surface and the observation of the morphological changes occurring on the surface of POT. As for this purpose, SEM images were recorded to verify the interaction of the synthesized POT with Oxy-G surface (Figure 6b). The Oxy-G exhibits porous architecture composed of ultrathin nanosheets conformed to electrically conductive framework beneficial for electron transfer and ion transport while maintaining electrical conductivity with substantial accessible specific surface area for ion sorption. As shown in Fig.6b., POTs appears to be distributed relatively uniformly over or within the Oxy-G nanosheets as aggregated molecular clusters with average size

graphene sheet edges and regions where the sheets are either folded or crumpled.

Electrocatalytic Behavior of POTs/Oxy-G Multilayers toward Hydrogen Evolution Reaction

The electrocatalytic activity of POTs/Oxy-G multilayers immobilized on glassy carbon electrode (GCE) toward HER was investigated. As shown in Figure 7, HER did not occur on the bare GCE before the potential of -0.8 V in 5×10^{-2} mol/L H_2SO_4 aqueous solution. When (POTs/Oxy-G)$_{10}$ multilayers were immobilized on GCE, the (POTs/Oxy-G)$_{10}$ multilayers exhibited good electrocatalytic activity for HER with a rapid increase in the cathodic peak current. This result indicates that the POTs/Oxy-G multilayer played a crucial role in electrocatalyzing HER.
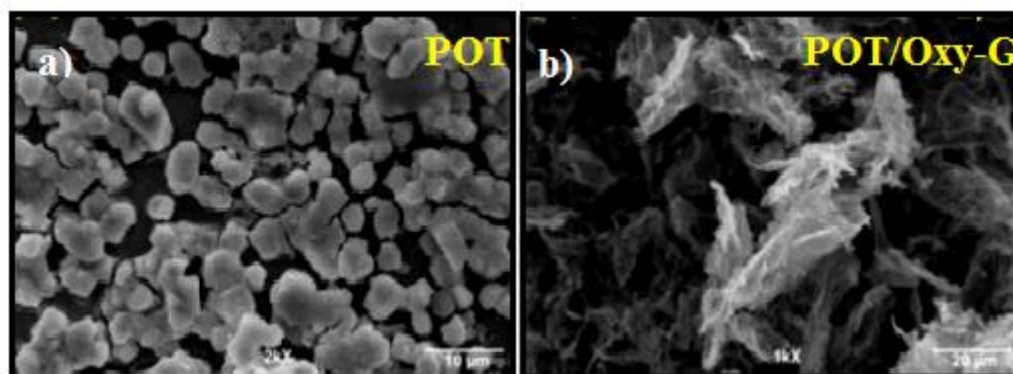
Figure 6. SEM images of a) POT (10 μm) and b) (POT/Oxy-G)$_3$(20 μm) multilayers on silicon wafer at different scales.
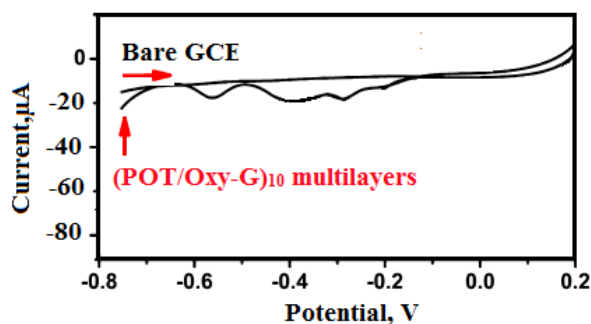
Figure 7. Linear sweep voltammograms of bare GCE and (POTs/Oxy-G)$_{10}$ multilayers in a 5×10^{-2} mol/L H_2SO_4 at a scan rate of 50 mV/s.

CONCLUSIONS

POTs/Oxy-G multilayer nanocomposite was formed with Keggin type polyoxotungstates (POT) and oxygenated-graphene (Oxy-G) together by postphotoreduction method and LbL self-assembly technique. The POT compound and Oxy-G together were deposited on different substrates utilizing the synergistic and electrostatic interaction between these two compounds. These two compounds are covered every step of the way and this number may vary depending on the desired operation. The transfer of electrons between PEI and Oxy-G can be successfully achieved by the successful transfer of charge transfer between POT and PEI. The photoreduction process is carried out under UV light and the POT compound acts as both a photocatalyst and an electron-transfer mediator to reduce the Oxy-G structure and provides a structural advantage in the formation of multiple layers. The (PEI/POT/Oxy-G)$_n$ multilayer formation provides a different structure for use in electrocatalytic field. The electrocatalytic activity for the ORR application is the desired level, since the POT compound is unique in electrochemical aspects. In addition, these multilayers are clearly audible due to the presence of the Oxy-G signal. A synthetic approach in this way offers the opportunity as an alternative method of applying POTs/Oxy-G multilayer nanocomposites ORR and HER electrocatalysis. With the advantage of electronic interaction between POT and Oxy-G in addition to the accessible and reversible redox behavior of POTs, they could have different applications as a design of functional molecular materials or future generation of hybrid molecular devices.

REFERENCES

1. Geim AK, Novoselov KS. The rise of graphene. Nature Materials.2007 Mar; 6(3): 183−191.

2. Xie GC; Zhang K, Guo BD, Liu Q, Fang L, Gong JR. Graphene-based materials for hydrogen

generation from light-driven water splitting. Adv. Mater. 2013 Jul; 25(1): 3820−3839.

3. Kim YK, Han SW, Min DH. Graphene oxide sheath on Ag nanoparticle/Graphene hybrid films as an antioxidative coating and enhancer of surface-enhanced Raman scattering. ACS Appl. Mater. Interfaces. 2012 Sep; 4: 6545−6551.

4. Seger B, Kamat PV. Electrocatalytically active Graphene-Platinum nanocomposites. Role of 2-D carbon support in pem fuel cells. J. Phys. Chem. C. 2009; 113: 7990−7995.

5. Zhang K, Zhang LL, Zhao XS, Wu J. Graphene/Polyaniline nanofiber composites as supercapacitor electrodes. Chem. Mater. 2010; 22: 1392−1401.

6. Williams G, Seger B, Kamat PV. TiO_2-Graphene nanocomposites. UV-Assisted photocatalytic reduction of Graphene oxide. ACS Nano. 2008; 2: 1487−1491.

7. Wang QH, Jiao LF, Du HM, Wang YJ, Yuan HT. Fe_3O_4 nanoparticles grown on Graphene as advanced electrode materials for supercapacitors. J. Power Sources. 2014; 245: 101−106.

8. Zeng G, Xing Y, Gao J, Wang Z, Zhang X. Unconventional Layer-by-Layer assembly of Graphene multilayer films for enzyme-based glucose and maltose biosensing. Langmuir. 2010; 26: 15022−15026.

9. Liu R, Li S, Yu X, Zhang G, Zhang S, Yao J, Keita B, Nadjo L, Zhi L. Facile synthesis of Au-nanoparticle/Polyoxometalate/Graphene tricomponent nanohybrids: An enzyme-free electrochemical biosensor for hydrogen peroxide. Small. 2012 May;8(9):1398-406.

10. Zhang QL, Xu TQ, Wei J, Chen JR, Wang AJ, Feng JJ. Facile synthesis of uniform Pt nanoparticles on polydopamine-reduced Graphene oxide and their electrochemical sensing. Electrochim. Acta. 2013; 112: 127−132.

11. Xu CH, Xu BH, Gu Y, Xiong ZG, Sun J, Zhao XS. Graphene-based electrodes for electrochemical energy storage. Energy Environ. Sci. 2013; 6: 1388−1414.

12. Stracke JJ, Finke RG. Electrocatalytic water oxidation beginning with the Cobalt Polyoxometalate $Co_4(H_2O)_2(PW_9O_{34})_{2}10^-$:Identification of heterogeneous CoO_x as the dominant catalyst. J. Am. Chem. Soc. 2011; 133: 14872−14875.

13. Coquelard CC, Sébastien Sorgues S, Ruhlmann L. Photocatalysis with polyoxometalates associated to porphyrins under visible light: An application of charge transfer in electrostatic complexes. J. Phys. Chem. A. 2010; 114: 6394−6400.

14. Kovtyukhova NI, Ollivier PJ, Martin BR, Mallouk TE, Chizhik SA, Buzaneva EV, Gorchinskiy AD. Layer-by-Layer assembly of ultrathin composite films from micron-sized graphite Oxide sheets and polycations. Chem. Mater. 1999; 11: 771−778.

15. Petit C, Bandosz TJ. Graphite Oxide/Polyoxometalate nanocomposites as adsorbents of ammonia. J. Phys. Chem. C. 2009; 113: 3800−3809.

16. Zhou D, Han BH. Graphene-based nanoporous materials assembled by mediation of polyoxometalate nanoparticles. Adv. Funct. Mater. 2010; 20: 2717−2722.

17. Li HL, Pang SP, Wu S, Feng XL, Müllen K, Bubeck C. Layer-by-Layer assembly and UV photoreduction of Graphene-Polyoxometalate composite films for electronics. J. Am. Chem. Soc. 2011; 133: 9423−9429.

18. Guo SX, Liu YP, Lee CY, Bond AM, Zhang J, Geletii YV, Hill CL. Graphene-supported $\{Ru_4O_4(OH)_2(H_2O)_4\}^-$(Gamma-$SiW_{10}O_{36})_{21}^{0−}$ for highly efficient electrocatalytic water oxidation. Energy Environ. Sci. 2013; 6: 2654−2663.

19. Li SW, Liu RJ, Ngo Biboum R, Lepoittevin B, Zhang G, Dolbecq A, Mialane P, Keita B. First Examples of Hybrids Based on Graphene and a Ring-Shaped Macrocyclic Polyoxometalate: Synthesis, Characterization, and Properties. Eur. J. Inorg. Chem. 2013: 1882−1889.

20. Wang S, Li HL, Li S, Liu F, Wu DQ, Feng XL, Wu LX. Electrochemical-reduction-assisted assembly of a Polyoxometalate/Graphene nanocomposite and its enhanced lithium-storage performance. Chem. Eur. J. 2013; 19: 10895−10902.

21. Liu RJ, Li SW, Yu XL, Zhang GJ, Zhang SJ, Yao JN, Zhi LJA. General green strategy for fabricating metal nanoparticles/Polyoxometalate/Graphene tri-component nanohybrids: enhanced electrocatalytic properties. J. Mater. Chem. 2012; 22: 3319−3322.

22. Nohra B, El Moll H, Albelo LMR, Mialane P, Marrot J, Mellot-Draznieks C, O'Keeffe M, Biboum RN, Lemaire J, Keita B. Polyoxometalate-based metal organic frameworks (Pomofs): structural trends, energetics, and high electrocatalytic efficiency for hydrogen evolution reaction. J. Am. Chem. Soc. 2011; 133: 13363−13374.

23. Zhang HY, Miao AJ, Jiang M. Fabrication, characterization and electrochemistry of organic-inorganic multilayer films containing polyoxometalate and polyviologen via Layer-by-Layer self- assembly. Mater. Chem. Phys. 2013; 141: 482−487.

24. Contant R. Relation entre les tungstophophates apparentés à l'anion $PW_{12}O_{40}^{3-}$. Synthèse et propriétés d'un nouveau polyoxotungstophosphate lacunaire $K_{10}P_2W_{20}O_{70}\cdot24H_2O$, Can. J. Chem. 1987; *65*: 568-573.

RESEARCH ARTICLE

Thermally Stable Rice Husk Microcrystalline Cellulose as Adsorbent in PTLC Plates

Arowona MT*[1] ✉, Olatunji GA[2] ✉, Saliu OD[2] ✉, Adeniyi OR[1] ✉, Atolani O[1] ✉, Adisa MJ[3] ✉

[1]Department of Chemistry, University of Ilorin, Ilorin, P.M.B. 1515, Nigeria.
[2]Department of Industrial Chemistry, University of Ilorin, Ilorin, P.M.B. 1515, Nigeria.
[3]Department of Chemistry, Ibrahim Badamasi Babangida University, P.M.B. 11, Lapai, Niger State.

Abstract: Microcrystalline cellulose (MCC) was prepared from rice husk by subjecting it to alkaline pretreatment, delignification, bleaching, and hydrolytic operations. MCC was also prepared from cotton wool and used as a reference because of its high cellulose content to estimate a relative yield and quality of the MCC produced from rice husk. The characteristic morphological feature was established by scanning electron micrograph (SEM) and the crystallinity of the Rice husk Microcystalline cellulose was further confirmed using the X-RD technique; the functional group was confirmed by the Fourier transform infrared (FTIR) spectroscopic method with characteristic absorption bands of ;−OH stretching at 3416 cm^{-1}; C-H stretching at 2918 cm^{-1}; -OH bending at1377 cm^{-1};, 1159 cm^{-1}; and C-O-C pyranose ring skeletal vibrations at 1026-1033 cm^{-1}, and the thermal stability was determined from thermogravimetric analysis (TGA). The characterized MCC of rice husk was applied as a stationary phase in Preparative Thin Layer Chromatography gave good separation (PTLC).

INTRODUCTION

Rice which is one of the most generally consumed cereal crop in the world has its husk usually discarded as raw biomass material. This raw biomass material which forms waste can be well harnessed, processed or manipulated into other forms of research materials and industrial raw materials that can be further employed in the fabrication of products with high market, economical, industrial and usage values. This rice husk can undergo combustion to produce ash which is rich in silica which can be applied singly or as composite for adsorption, water treatment, degradation of persistent contaminants and pollutants, *etc*. Another way to use rice bran involves the exploitation of its cellulose content which therefore makes the use of rice husk as a primary source for producing cellulose fibres and microcrystals promising.

Recently, lignocellulosic biomass like the rice husk has become the most widely used organic biomaterial in the world, with a worldwide consumption that is even higher than steel, coal or sugar (1). Pretreatment is a crucial process step for the biochemical conversion of lignocellulosic biomass and it is important to remove lignin, hemicelluloses, holocelluloses, increase cellulose quality and improve the porosity of the materials (2). The preparation of microcrystalline cellulose from readily available agricultural residues such as

rice husk will therefore, have good impact on the economy through the conversion of waste to wealth and consequently reduce the cost of the purchase of commercially produced modified microcrystalline cellulose.

Microcrystalline cellulose is a purified partially depolymerized non-fibrous form of cellulose that occurs as a white, odorless, tasteless, crystalline powder composed of porous particles. Microcrystaline cellulose (MCC) produced from a naturally occurring substance (cellulose) has proven to be stable, safe and physiologically inert and has revolutionized tableting. Microcrystalline cellulose is one of the few materials used in tableting due to its potential to produce hard tablet that also disintegrate readily in bodies due to swelling of the MCC particles and collapse of the intermolecular bonding forces holding the molecules together (3). Currently, MCC is used in various fields such as pharmacy, cosmetics, food industries, and plastics industries. In the powder form, it is used as a filler and binder in medical tablets and food tablets for dietary purposes. In the gel form, MCC is used as viscosity regulator, a suspending agent, emulsifier in different pastes, creams, *etc*. (4).

Success of the separation of a complex mixture by TLC and PTLC greatly depends on the choice of stationary phase. Adsorbents generally used include silica gel, alumina, cellulose, polyamide, polymeric ion exchange, impregnated silica gel and chiral phases. While all these adsorbent are in current use, silica gel is by far the most widely used adsorbent followed by alumina. For effective separations, most stationary phases were impregnated with other materials such as ion exchangers, metal ions, chiral selectors, cellulose, *etc* in ranging proportions. The aim of this work is to obtain microcrystalline cellulose that can be thermally stable and suitable for use as an alternative adsorbent in preparative thin layer chromatography.

MATERIALS AND METHOD

Materials
Dried rice bran was collected from local rice mill at Ipata market, Ilorin, Kwara State,North Central region of Nigeria. Cotton wool was purchased commercially. All reagents and solvents used which include sodium chlorite, acetic acid, potassium hydroxide, sodium hypochlorite, sulfuric acid, silica gel, and ethanol were obtained from Sigma Aldrich, USA.

Preparation of crude cellulose
The cellulose was prepared using the procedure described by Liu *et al.* (5) with slight modifications. 100 g of the sample was weighed and transferred into a 1000 mL beaker containing a solution of 100 g sodium chlorite adjusted to a pH 4.0 using 10% acetic acid at 75 °C for 1 h for delignification. Then, 100 g of sodium chlorite was added while stirring continuously for another 1 h at same temperature to further delignify the biomass material. The residue was washed with distilled water and ethanol until its pH became neutral, the resulting solution was filtered, the residue was thereafter washed and dried in an oven at 60 °C for 5 h. Afterwards, the dried residue was treated with 10% potassium hydroxide for 6 h to complete the delignification process. The cellulose gotten was washed with distilled water and ethanol and dried for 3 h at 60 °C. Thereafter, it was treated with sodium hypochlorite, washed with distilled water and ethanol and dried in an oven at 60 °C for 3 h. The cellulose was blended to obtain a smooth powdery texture, weighed, stored in sample bottles and kept in a cool dry place until further analysis.

Preparation of Microcrystalline Cellulose
The delignified pre-weighed cellulose was transferred into a quick fit flask and 500 mL of 2 M H_2SO_4 was added and then refluxed at 60 °C for 3 h. The microcrystalline cellulose obtained was then washed with distilled water and ethanol, dried in the oven, blended, weighed and then stored. Also, MCC from cotton wool was prepared using the same procedure.

Characterization
Surface morphology of the cellulose fibers and metal oxides composites was investigated using Phenom ProX Scanning Electron Microscopy, USA. Before the analysis, the composites were sputtered with thin gold layer to avoid electrostatic charging during examination. The micrographs with a magnification of 50,000 times were obtained by back scattered electron detector (BSE) in order to register both topography and compositional contrast. X-ray diffraction pattern of the sample was investigated using X-ray diffraction (D8 Advance, Bruker, Germany) equipped with Cu Kα radiation in the 2θ range 5°–60° with step size of 0.03° was used under the operational conditions of 40 kV and 40 mA. All of the assays were performed with a scan rate of 12 °/min and wavelength of 1.540562. TGA measurements were performed using (STA449 F3, Netzsch, Germany) under a nitrogen atmosphere (40 mL/min), and the samples were heated at 10 °C/min from 50 °C to 850 °C. The weight loss (%) was evaluated by measuring the residual weight at 8500 °C. TGA and derivative thermo-gravimetric analysis (DTG) data were obtained.

The functional groups in the crude and microcrystalline cellulose prepared were analyzed by using the Agilent Cary 630 FTIR

spectrophotometer, USA, in the range of 400-4000 cm^{-1} in transmittance mode.

Application of Microcrystalline Cellulose as Adsorbent on Chromatographic Plates

Five grams of MCC prepared from rice bran were weighed and mixed with 50 g of silica gel (ratio 1:10) and 100 mL water was used to coat on a plate 20 x 20 cm. The ethanolic extract of the leaves of *Momordica charantia* was spotted on the plate and developed in n-hexane and dichloromethane in the ratio 2:1. The separation of the crude extract into different components was observed.

RESULTS AND DISCUSSION

Isolation and preparation of microcrystalline cellulose:

The microcrystalline cellulose (MCC) obtained from both rice husk and cotton wool, as well as the crude cellulose obtained from rice husk was all white and powdery. The crude cellulose obtained from rice husk was white while the MCC obtained from both the rice husk and cotton wool was white and powdery (**Figure 1 a, b, c, d, e**). The percentage yield (Table 1) of MCC obtained indicated that the rice husk crude cellulose produced more MCC than the cotton wool cellulose.

Figure 1(a): Ground rice husk
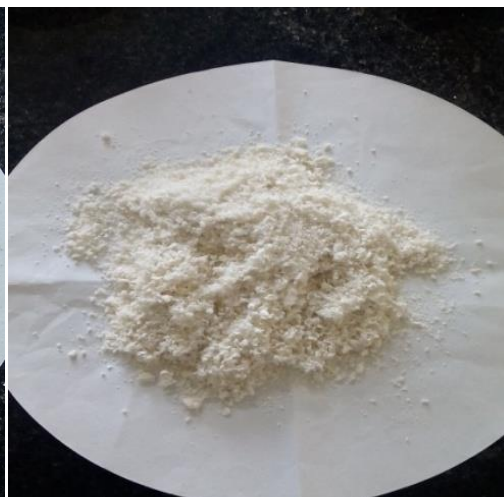
Figure 1(b): Crude cellulose from rice husk
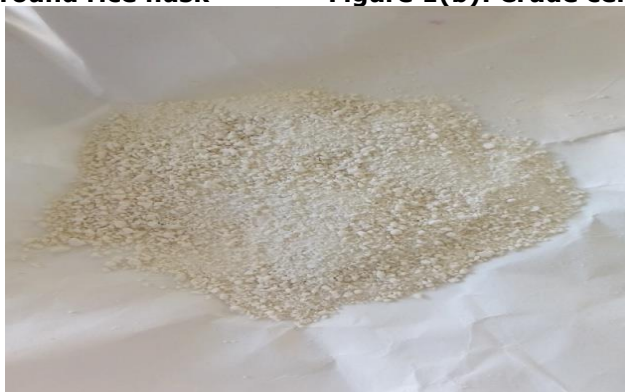
Figure 1(c):Microcrystalline cellulose from rice husk
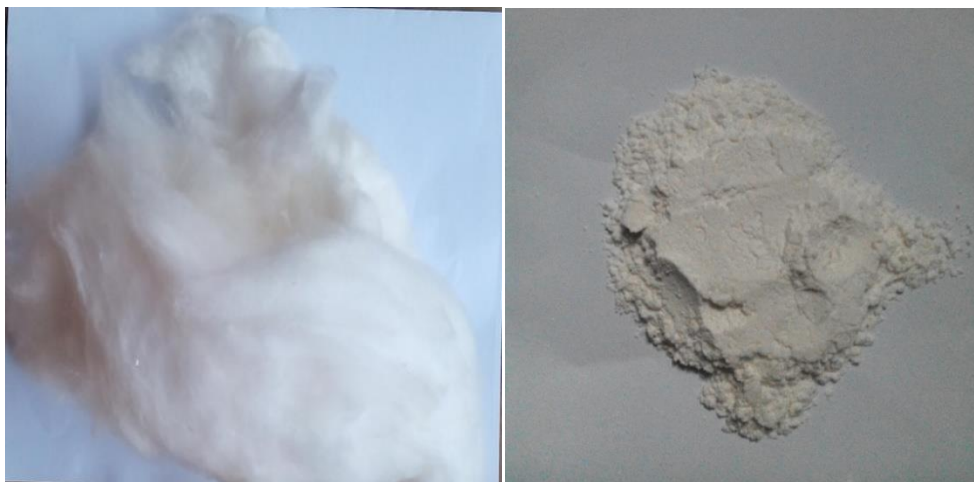
Figure 1(d): Cotton wool   **Figure 1(e) : Microcrystalline cellulose from cotton wool**

Table 1: Percentage Yield of Microcrystalline Cellulose from Rice Husks and Cotton Wool.

Masses and % Yield	Rice Husk	Cotton Wool
Initial Mass (g)	20.84	30.00
Final Mass (g)	20.33	26.10
% Yield	97.55%	87.00%

FOURIER TRANSFORM INFRARED (FT-IR) Analysis
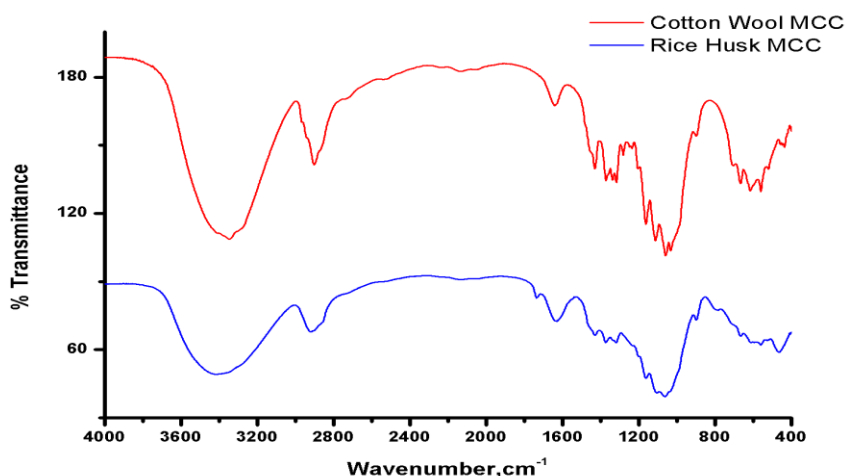
Figure 2: FT-IR Spectrum of Cotton and Rice Husk MCC.

The FTIR spectra in red and blue colors revealed the important absorption bands for the cotton wool and rice husk MCC respectively. This showed similarity with the important peaks on crude cellulose from other source (sugarcane bagasse) reported in literature by Liu *et al.*, (5). The absorption bands and their assignments are: 3416 cm^{-1}; –OH characteristic absorptions, 2918 cm^{-1}; C-H stretching, 1629 cm^{-1}; bending mode of absorbed water, 1377 cm^{-1}; -OH bending, 1159 cm^{-1}; -C-O stretching in acetyl group, 1026-1033 cm^{-1}; C-O-C pyranose ring skeletal vibrations, (6). Oxidation and sulfonation signals were seen at 1736 and 2131 cm^{-1} as a result of the sulfuric acid treatment for microcrystalline cellulose generation. Cotton wool is 99% pure cellulose, therefore similarity in absorption for both spectra revealed the successful isolation and purification of cellulose from rice husk.

Morphological Investigation of the Microcrystalline Cellulose

Scanning electron micrography (SEM): The Scanning Electron Micrographs (SEM) for the MCC of rice husks and cotton wool are as shown in **Figure 3** (a and b). This was used to analyze the morphology of the microcrystalline celluloses from rice husk and MCC from cotton wool.
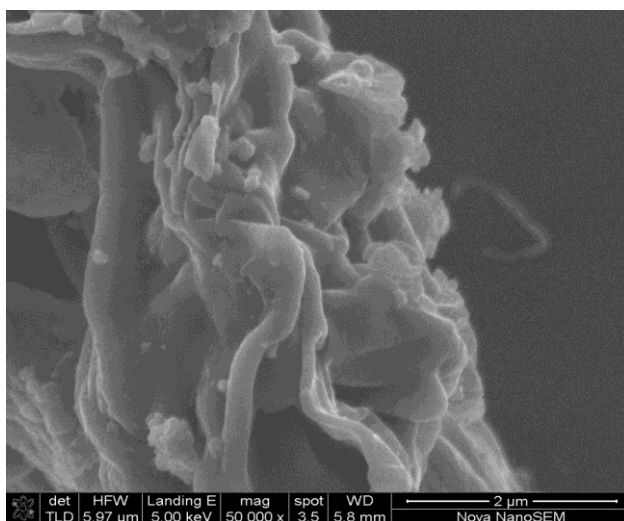
Figure 3 (a): SEM of Microcrystalline Cellulose from rice husk

Figure 3 (b): SEM of Microcrystalline Cellulose from cotton wool

Comparatively, the SEM of the microcrystalline cellulose from both samples (cotton and rice husk) show non- uniformly dense microcrystalline particles thereby forming microcrystals from the overall view. The MCC are irregularly packed and sponge-like. The high level of aggregation and agglomeration was evident due to a large number of fiber bundles. Since the rice husk MCC also displayed some level of aggregation like the cotton wool MCC, it is assumed to possess similar morphological properties which resemble that of cotton wool.

X-RAY DIFFRACTION PATTERN (XRD)
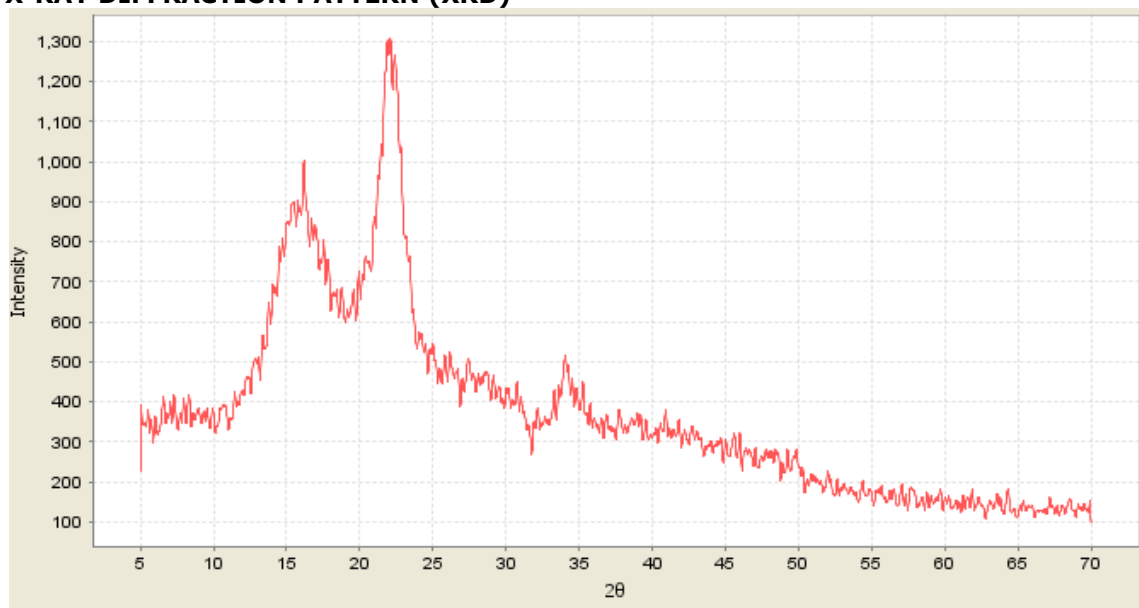
Figure 4: Diffractogram of Rice Husk MCC.

X-ray diffraction (XRD) was carried out to study the crystallinity of the MCC of rice husk. In the X-ray patterns, three main reflections at $2\theta=14.70°$, $22.09°$ and $34.24°$ were observed for the sample, indicating that the rice husk microcrystalline cellulose and were cellulose I type (7). Furthermore, the similar patterns of X-ray diffraction of standard microcrystalline cellulose reported in literature by (8) demonstrated that hydrolysis did not change the cellulose structure of the rice husk MCC, which was in accordance with the results of FT-IR. The crystallinity index was 67%.

The presence of noise in the X-ray micrograph might be due to the presence of some residual amorphous cellulose in the sample.
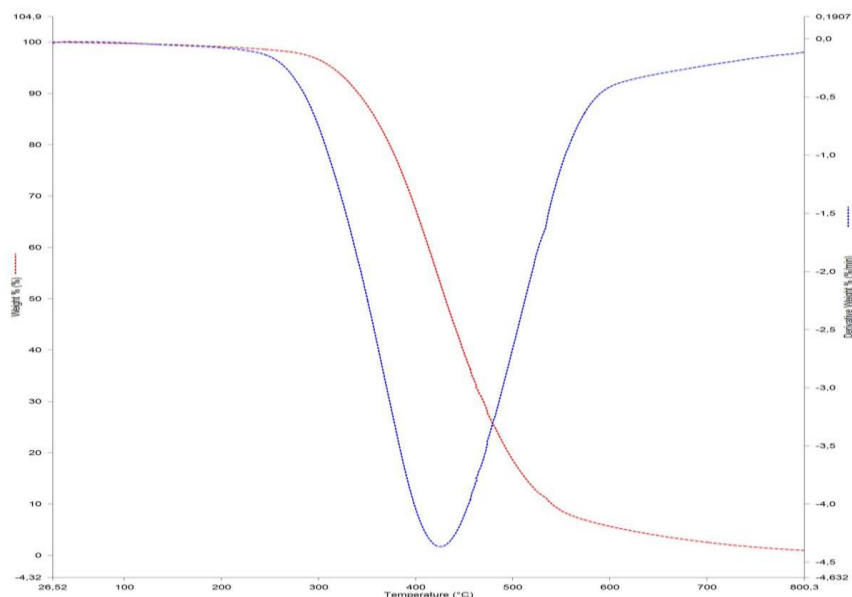
Figure 5: TGA analysis of the sample.

The thermogravimetric analysis (TGA) curve revealed a single step thermal degradation of the microcrystalline cellulose from 360 to 460 °C with 87% weight loss. This single step thermal degradation profile displayed by this microcrystalline cellulose confirmed the absence of impurities, hemicelluloses, lignin, and any form of attached water within its internal pores. The microcrystalline cellulose is a thermally stable one; and this is further established by the result of the differential thermogravimetric analysis (DTGA) which revealed that the T_{max} (the temperature at which maximum weight loss occurs) which occurred at 410 °C is high and make the MCC a suitable material as adsorbent even in preparative thin layer chromatographic applications.

Use of microcrystalline cellulose as adsorbent

The absence of pores in the MCC after hydrolysis at a concentration less than 50% (2 M H_2SO_4) of the acid shows that the MCC of rice husk is a suitable stationary phase that will permit easy flow of sample mixture and will not in any way affect the movement of the solute by adsorbing the sample and reacting with it thereby interfering with the elution process on the PTLC plate**.** The crude extract applied on the PTLC plates were clearly separated into different components after development in appropriate solvents. This result showed that the MCC cellulose obtained from rice husk which was meant to be a waste product from the local rice mill could be converted into useful laboratory material and therefore, serves as an alternative adsorbent.

CONCLUSIONS

Purification of cellulose was performed using chemical pretreatments involving alkali and bleaching treatments. The MCC were successfully extracted from the purification of rice husk and cotton wool cellulose using an acid hydrolysis treatment. The morphology of the MCC confirmed its suitability for use as stationary phase in PTLC. The percentage yield of the rice husk and cotton wool MCC was determined and gotten to be 97.55% and 87% respectively. From the results, it is visible that high percentages of MCC can be gotten from rice husk which is an agricultural residue of little significance in our society today. Instead of disposal of these residues, more MCC can be prepared from them thereby harnessing the potentials embedded in such residues. Since it is suitable as stationary phase in chromatography, it reduces the cost of purchasing commercial stationary phases such as silica gel or alumina. Consequently, the economy of our society in general is enhanced.

REFERENCES

1. Sanchez OJ, Cardona CA. Trends in biotechnological production of fuel ethanol from different feedstocks. Bioresource technology. 2008;99(13):5270–5295.

2. Sun Y, Cheng J. Hydrolysis of lignocellulosic materials for ethanol production: a review. Bioresource technology. 2002;83(1):1–11.

3. Ejikeme PM. Investigation of the physicochemical properties of microcrystalline

cellulose from agricultural wastes I: Orange mesocarp. Cellulose. 2008;15(1):141–147.

4. Laka M, Chernyavskaya S. Obtaining of microcrystalline cellulose from softwood and hardwood pulp. BioResources. 2007;2(4):583–589.

5. Liu C-F, Sun R-C, Zhang A-P, Qin M-H, Ren J-L, Wang X-A. Preparation and characterization of phthalated cellulose derivatives in room-temperature ionic liquid without catalysts. Journal of agricultural and food chemistry. 2007;55(6):2399–2406.

6. Liu C, Sun R, Zhang A, Ren J. Preparation of

sugarcane bagasse cellulosic phthalate using an ionic liquid as reaction medium. Carbohydrate Polymers. 2007;68(1):17–25.

7. Zhao T, Chen Z, Lin X, Ren Z, Li B, Zhang Y. Preparation and characterization of microcrystalline cellulose (MCC) from tea waste. Carbohydrate polymers. 2018;184:164–170.

8. Kharismi RRAY, Sutriyo HS. Preparation and Characterization of Microcrystalline Cellulose Produced from Betung Bamboo (Dendrocalamus asper) through Acid Hydrolysis. Journal of Young Pharmacists. 2018;10(2):S79.

Preparation and Determination of *In Vivo* and *In Vitro* Performance of Doxycycline-Imprinted Contact Lenses for Corneal Neovascularization Treatment

Sibel Erkal Ilhan[1] ✉, **Özge Kürkçüoğlu[2]** ✉, **Tuğçe Inan[2]** ✉, **Özde Zeynep Güner[2]** ✉, **Dilek Dalgakıran[3]*** ✉, **Begüm Okutan[4]** ✉, **Gamze Torun Köse[4]** ✉, **Ayça Kırmızı[5]** ✉, **Aylin Okçu Heper[5]** ✉, **Özlem Gürses[6]** ✉, **F. Seniha Güner[2]**** ✉ 🆔

[1]Ankara University, Faculty of Health Sciences, Midwifery Department, 06080 Altındağ Ankara, Turkey
[2]Istanbul Technical University, Department of Chemical Engineering, Maslak 34469 Istanbul, Turkey
[3]Istanbul Technical University, Polymer Science and Technology, Maslak 34469 Istanbul, Turkey
[4]Yeditepe University, Faculty of Engineering, Department Genetics and Bioengineering, Ataşehir 34755 Istanbul, Turkey
[5]Ankara University, School of Medicine, Department of Medical Pathology, 06100 Sıhhıye Ankara, Turkey
[6]New York Medical College, Department of Microbiology and Immunology, Valhalla, New York, USA
*Dilek Dalgakıran's present address is Department of Polymer Engineering, Yalova University, Yalova 77200, Turkey

Abstract: The aim of this study is to develop doxycycline imprinted contact lenses that will be used in the treatment of corneal neovascularization, which can eventually cause blindness. For this purpose, doxycycline imprinted contact lenses were first prepared in two different diameters, 5.7 and 5.8 mm, then they were loaded with doxycycline and their in vitro and in vivo performances were determined. In the synthesis of the contact lenses, 2-hydroxyethyl methacrylate was used as a backbone monomer. The functional monomer was selected as itaconic acid using molecular simulations. Doxycycline release profile of the lenses was determined in NaCl solution at 37 °C. Their doxycycline release was reached about 3 µg/mg contact lenses in 6 hours. Higuchi model was fitted better than the others as a kinetic model. Swelling degrees of the contact lenses were determined as 38.8 %. Cytotoxic response of the lenses was investigated on retinal pigment epithelium cells. According to the results the lenses were not cytotoxic to RPE cell line. In vivo experiments in rat models were performed to study the treatment patterns. The rats were sacrificed fifteen days after treatment, and clinical examination under optical microscope was performed to evaluate neovascularization, infiltration of inflammatory cells, and corneal epithelial changes. In conclusion; doxycycline imprinted contact lenses promise as an effective treatment method for corneal neovascularization.

INTRODUCTION

Approximately 90% of ocular diseases are treated with eye drops and ointments, and the remaining with various oral medications. Both concentration and residence time of the drug in the eye are critical for the effective treatment of ophthalmological diseases in general. However,

only 1 to 7% of eye drops is absorbed effectively after the application (1). The remaining of the drug joins the bloodstream leading to low drug bioavailability. In order to assure an effective drug concentration, eye drop should be applied to the patient frequently while watching the toxic concentration limit. When the drug is taken orally, it can cause toxic effect on the gastrointestinal

system and again the bioavailability can be very low.

Corneal neovascularization (NV) is one of the most common eye diseases, which is characterized by the growth of new blood vessels into the cornea (2). Similar problems mentioned above can be encountered in treatments of corneal NV. Bevacizumab (3), ranibizumab (4) and doxycycline *etc.* are some topical vascular endothelial growth factor (VEGF) inhibitors used in the treatment of corneal NV (5). Diffusion of the eye drop into deeper levels of the corneal tissue may remain inadequate. On the other hand, treatment with high levels of drug concentration can lead to a toxic effect on the surface of the corneal epithelium in the long term. The necessity of satisfying the indispensable needs in the treatment of corneal NV due to mentioned disadvantages, establishes the basis of this study.

In recent years, scientific researches on contact lenses have been focused on the treatment of ophthalmological diseases (6, 7). Hydrogels have been extensively used in the production of contact lenses, due to their high water absorption capacity and high gas permeability. Various methods for drug delivery from hydrogels have recently become available. Controlled drug delivery has been tried to be obtained by practices such as drug absorption in hydrogel lenses from a solution and interjecting colloidal particles into the lenses. Lately, molecularly imprinted hydrogel lenses have been used for improved controlled drug delivery properties (8-12). In this technique, a complex is formed between a drug and a functional monomer. For obtaining a 3D structure, a cross-linking agent should be used in the synthesis. Drug molecules are removed from the polymer after the completion of polymerization. Thus, some special cavities having complementary in shape, size and chemical functionality to the drug molecule are formed (7, 13).

Recently, a series of doxycycline imprinted hydrogels have been prepared from acrylic acid as a functional monomer and ethylene glycol dimethylacrylate as a cross-linker (14). We investigated the reaction kinetics for photo- and thermal polymerization via real-time FTIR spectroscopy and differential photocalorimetry. We found that doxycycline was excited during photopolymerization; thus, the conversion and the overall reaction rate decreased when the template concentration increased in the reaction mixture. After evaluating all results, we chose thermal polymerization method for preparation of doxycycline imprinted hydrogels.

In this study, hydrogel contact lenses were synthesized using molecular imprinting method as in our previous study (14). The active ingredient of the drug chosen for the treatment is doxycycline. The study was realized under three steps; the selection of the functional monomers by a computational method for the synthesis of contact lenses, synthesis and characterization of the contact lenses, and investigation of the biocompatibility of developed contact lenses and their performances during the treatment.

MATERIALS AND METHODS

Molecular simulations
Possible functional monomers for the contact lens synthesis were determined as acrylic acid (AA), methacrylic acid (MAA) and itaconic acid (IA). Simulated annealing technique was employed to select a functional monomer for effective imprinting of the drug. 1 ns long simulations were carried in Materials Studio, using the COMPASS force field. Simulation box under periodic boundary conditions contained drug, functional monomer, backbone monomer 2-hydroxyethyl methacrylate (HEMA) and cross-linker ethylene glycol dimethacrylate (EGDMA) molecules. 25 cycles of annealing were performed between 498 K and 298 K to obtain the lowest energy configurations of functional monomers and drugs. The monomer, which had the highest number of hydrogen-bonding interactions from different regions of the drug was selected for synthesis.

EXPERIMENTAL STUDY

Chemicals
HEMA was used as a backbone monomer and IA was used as a functional monomer, as was suggested by molecular simulations. Triethylene glycol dimethacrylate (TEGDMA) and 2,2'-Azobis(2,4-dimethylvaleronitrile) (Vazo®52) were used as a crosslinking agent and a thermal initiator, respectively. Doxycycline hyclate used as a template molecule was gifted by Deva (Istanbul, Turkey).

Synthesis of Contact Lens
Molecular imprinted contact lenses were synthesized via free radical polymerization (14). Doxycycline (0.205% mole) was dissolved in HEMA (92% mole) during 30 min in ultrasonic bath below 40 °C. IA (3% mole), TEGDMA (5% mole) and Vazo®52 (0.12 by weight %) were added to the reaction mixture. In order to dissolve the initiator, the reaction mixture was put into ultrasonic bath for 15 min. Because Vazo®52 is a low temperature initiator, the temperature of ultrasonic bath was protected under 20 °C. The oxygen in the solution was removed by bubbling nitrogen for 30 min. Then, the reaction mixture was injected into a hydrophobic polymer coated lens mold. The mold was placed into an oven at 45 °C for 24 h. After synthesis, the contact lenses were removed from the mold and they were immersed in boiling water for 15 minutes to remove unreacted monomers. After that, they were washed in three steps; in 0.01 M oxalic acid:methanol:acetonitrile solution

(65:15:20), in methanol and in water. Finally, the lenses were dried at 37 °C for 72 hours in a vacuum oven. Swelling degree of the contact lenses was determined by using equation 1 after they were gently rinsed with distilled water at 37 °C for 48 h.

$$\text{Swelling degree (\%)} = \frac{(W_2 - W_1)}{W_1} \, x \, 100 \qquad (1)$$

where W_1 is the weight of the polymer before swelling and W_2 is the weight of the polymer after swelling.

In Vitro Drug Loading and Release
For determination of loading capacity of the contact lenses, dried samples were immersed in 75 µM DOXH aqueous solutions (10 mL) and kept at 4 °C for 24 h, shaken with orbital shaker and protected from light. The initial and final concentrations of the solution were determined by Perkin Elmer Lambda 25 UV/VIS spectrophotometer.

In order to observe release kinetics, the doxycycline imprinted contact lenses were firstly placed into 1 mM doxycycline solution for 48 h at 4 °C. After loading, samples were washed with distilled water to remove doxycycline hyclate that was absorbed on the surface and then surfaces of the lenses were dried gently by a paper to remove excess water. Each lens was immersed into 10 ml 0.9% NaCl solution at 37°C with gentle shaking at 100 rpm in amber bottles. Releasing solution (0.8 mL) was withdrawn at regular intervals and the concentration was detected by the UV/Vis spectrophotometer at 274 nm.

Doxycycline concentration of the loading and release solutions were not same due to limitations of measurements with UV spectrophotometer.

Cytotoxic Response
Samples were sterilized before adding them to the cell culture. Retinal pigment epithelium cell (RPE cell) line was used for this study. RPE cells (2.5 10^3 cells/well) were seeded in 24 well culture plate. After 6 hours of incubation for the cell attachment, 1 mL of fresh medium and a piece of contact lens were added into each well, and every week 500 µL of fresh medium containing 10% heat-inactivated fetal bovine serum and 100 units/mL streptomycin were added. Cells were incubated at 37 °C in 5% CO_2 incubator throughout 21 days. There were 4 groups in this study: blank (including medium only), only RPE cells (control), only contact lens, and contact lens with RPE cells. At the end of each time period, XTT (2,3-bis-(2-methoxy-4-nitro-5-sulfophenyl)-2H-tetrazolium-5-carboxanilide, Cell Signaling Technology) was used according to kit protocol. First, the electron coupling (PMS) and XTT labeling reagents were thawed and immediately combined in a 1 µL : 50 µL ratio. Then the XTT solution (500 µL) was added to the cell culture

wells. The absorbance at 450 nm was determined after 1, 7, 14 and 21 days of cultivation by using Elisa spectrophotometry (Bio-Tek ELx800 Absorbance microplate reader, USA).

In Vivo Study and Histopathological Examination
Alkaline burn injury model was used in the rat cornea (3). For this purpose, twenty-seven Wistar albino rat corneas injured with 1 N NaOH solution were divided into three groups: untreated, eye drop-treated and contact lens-treated groups. The lens treatment was applied during 5 hours per day. Eye drops of doxycycline solution (2 mg/mL) were administered two times daily. The rats were sacrificed fifteen days after treatment.

Corneal specimens were fixed in 10 % buffered formalin for 24 hours. Fixed tissue samples were processed routinely by paraffin embedding technique. Sections of 4 µm were obtained and stained with hematoxylin-eosin. The preparations were evaluated under the light microscope by two pathologists who were blinded to the knowledge of groups. Vascularization, infiltration of inflammatory cells, and corneal epithelial changes were examined.

The sections were overviewed for the highest vascular area and the number of blood vessels per square millimeter were counted on the (10×) objective of the microscope. The vascularity was recorded as "superficial" if the vascular structures were seen just below the epithelium, superficial stromal, "deep" if the vascular structures were seen deep stromal, above the Descemet's membrane. Inflammatory cells were scored as 0: no inflammation, 1: perivascular and scattered few inflammatory cells (mainly neutrophils, few lymphocytes) 2: Mild-moderate inflammation 3: moderate inflammation 4: severe inflammation (many diffusely distributed inflammatory cells).

Statistical Analysis
Statistical analysis was performed with frequency, percentage, standard deviation, Mann Whitney U, and Kruskal Wallis tests.

RESULTS AND DISCUSSION

Functional Monomer Selection
Molecular interactions between the drug and functional monomers were revealed by the radial distribution function g(r). This statistical measure represents the probability of finding a specific particle in a shell dr at a distance r from another particle. A high peak at r = 2 Å indicates hydrogen-bonding between a hydrogen atom and an electronegative atom such as N, O or F. In Figure 1, g(r) values of peaks at 2 Å show that doxycycline molecule made hydrogen-bonding with functional monomers from six different positions. Among the functional monomers, IA made the most stable interactions with the drug from all six positions. In terms of number of

interactions with the drug, IA was followed by AA then MAA. Therefore, IA acid was used in the contact lens synthesis.
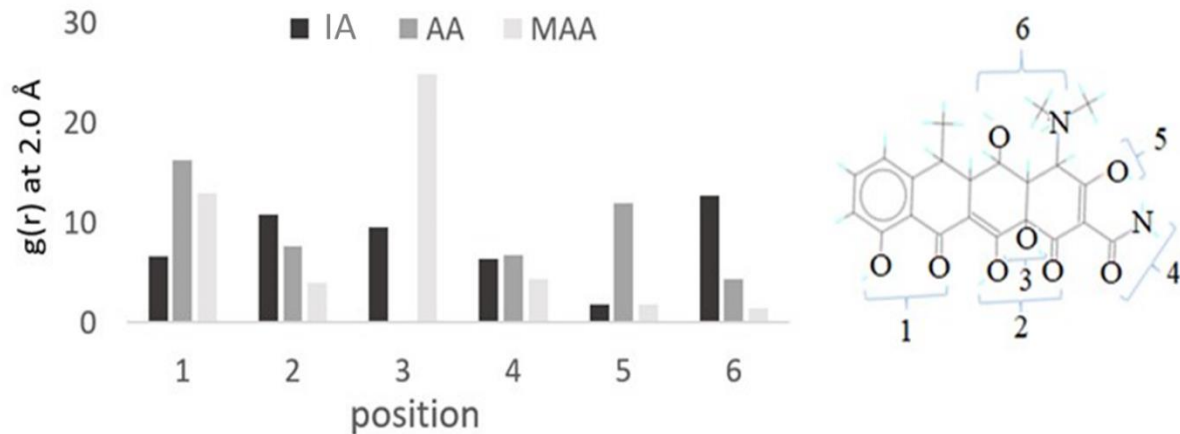
Figure 1. Radial distribution function g(r) results at r = 2 Å for itaconic acid (■), acrylic acid (■) and methacrylic acid (■)

Synthesis of Contact Lenses

There were two alternative methods for synthesis of contact lens; photo- and thermal polymerization. We chose thermal polymerization, since doxycycline molecule is sensitive to UV light (14). Teflon mold built for rat's eyes was used in contact lens synthesis, and the contact lenses were prepared in two different diameters (Figure 2). Swelling degrees of the contact lenses were determined as 38.8 % ± 2.0.
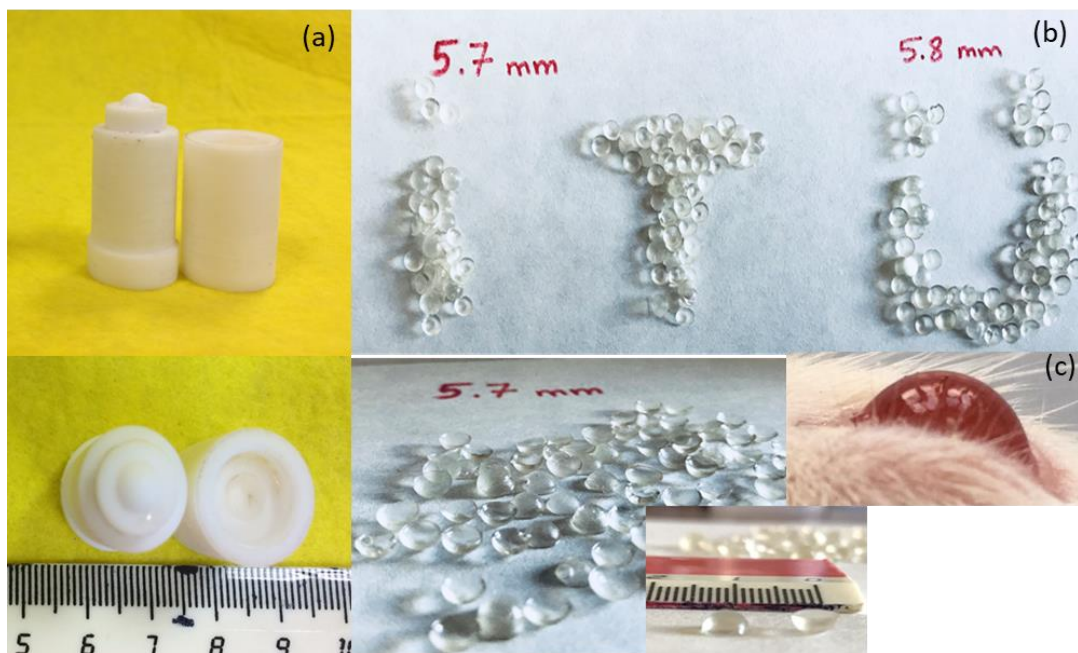
Figure 2. Mold (a), contact lenses synthesized (b) and rat's eye (c)

In Vitro Drug Loading and Release

Doxycycline loading capacity of the contact lenses was found as 0.1805 ± 0.0100 µM (0.9258 ± 0.0500 µg) drug/mg contact lens. As explained in the experimental part, loading capacity was investigated in 75 µM loading solution. On the other hand, 1 mM doxycycline solution was used for release kinetics. So, the loading and release results cannot be compared.

In order to determine release behavior of the contact lenses, they were loaded with doxycycline in 1 mM doxycycline solution, then their release kinetics were observed in human body conditions which were in 0.9% NaCl solution at 37 °C. Obtained results are given in Figure 3. As can be seen, doxycycline release was reached about 3 µg/mg contact lenses in 6 hours in our study. The mass of a contact lens was measured to be 13.7 ± 0.7 mg. So, according to our results, doxycycline release was about 41 µg (3 µg/mg x 13.7 mg) from each contact lens. In literature, doxycycline concentration for treatment of corneal NV was reported as 37.5 µg/day (15). In

conclusion, in our study doxycycline imprinted contact lenses could be prepared in the recommended dose for treatment of NV.
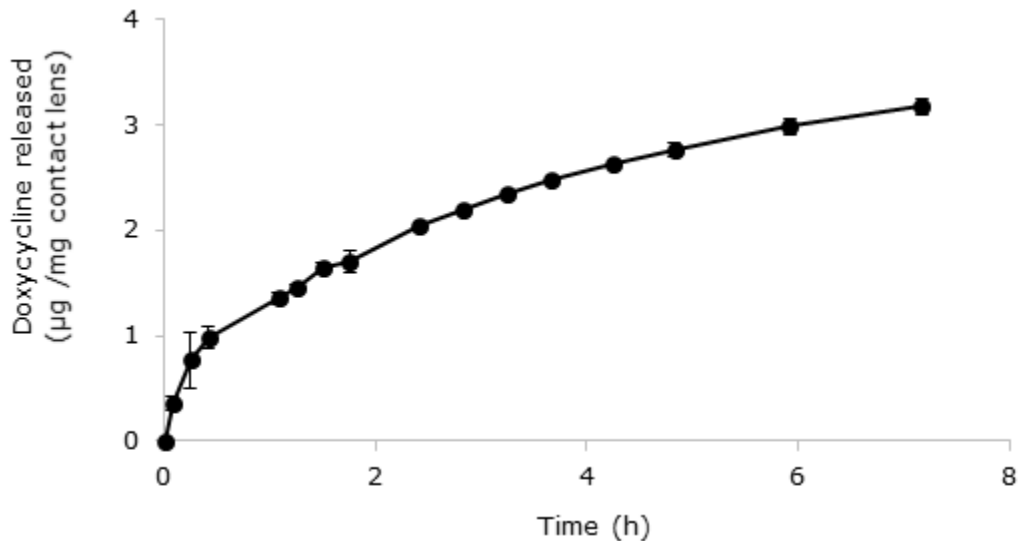
Figure 3. Release profile of doxycycline from contact lens in NaCl solution at 37°C.

Cytotoxic Response

Cell proliferation was observed during 21 days. According to results, the cell viability increased starting from the first day of the cultivation till the end of 7th day in all samples (Figure 4). After 7 days of incubation, cell viability decreased in all samples including only cell (OC). This might be related with the excessive cell proliferation, which led to cell detachment. Therefore, it can be said that this decline was not due to the toxic effect of the contact lens since we can observe the same decrease in all cell containing groups. After 14 and 21 days of incubation, the cell viability increased in all samples again. To conclude, as it can be seen from the results that these lenses were not cytotoxic to RPE cell line.

In this study, zero-order, first-order, Higuchi and Korsmeyer-Peppas models were used to analyze the release of doxycycline from the lenses (Figure 5). Higuchi model was fitted better than the others. This model demonstrates cross-linker effect on imprinted contact lens and it explains drug release based on Fick's law (16). According to the Higuchi model, initial concentration of the drug in the matrix is much higher than drug solubility, drug diffuses only in one dimension, particle size of the drug molecules is much smaller than matrix thickness, and drug diffusivity is constant.

Results of *In Vivo* Study and Histopathological Examination

The selected rat's eyes before and after alkaline injury are shown in Figure 6. Our experimental series showed that contact lens treatment had a beneficial effect on the vascular calibers of NV.

Neovascularization, infiltration of inflammatory cells, and corneal epithelial changes were examined in histopathological examination. The obtained results are given in Table 1 for the contact lens-treated, drop-treated and control groups. Histopathological examination was done for all damaged and undamaged eyes. Since the vascular structures were seen just below the epithelium, superficial stromal, all corneas were reported to be superficial. Additionally, no change or epithelial slaughter or necrosis was recorded. According to the results, treatment with doxycycline imprinted contact lenses was effective but not as much as drop treatment.

Our observation during the study was that rats were uncomfortable related to the lens treatment and they were in tendency to remove their lenses. Therefore, we hypothesized that therapeutic effect of the doxycycline imprinted contact lenses was less than expected. We recommended that *in vivo* study should be repeated and the lens molds should be redesigned for rabbit's eyes.
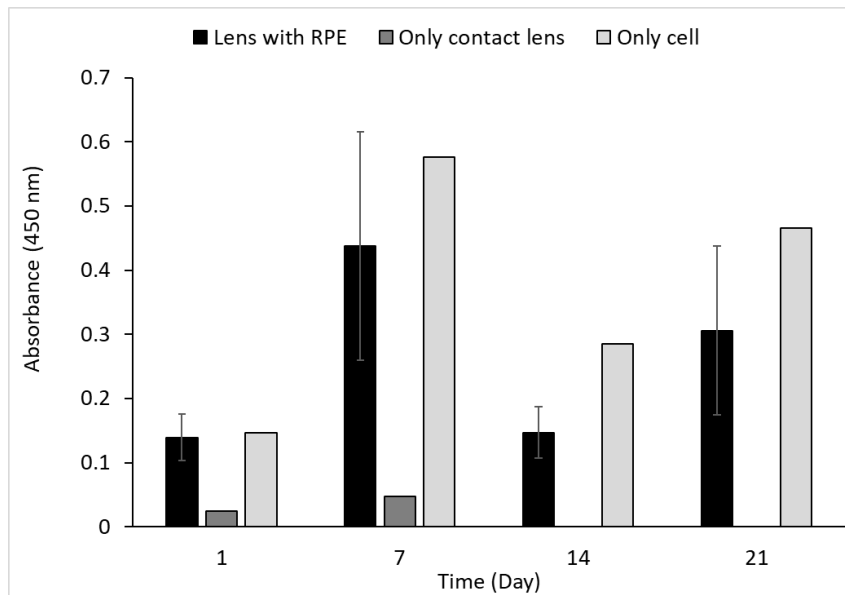
Figure 4. Cytotoxicity of contact lenses (Initial cell seeding density was 2.5 103 cells/well. RPE cell proliferation was determined by XTT assay)

Table 1. Vascularization and infiltration of inflammatory cells.

Sample code[*]	Vascularization	Infiltration of inflammatory cells
CLT-damaged	14.3 ± 4.1	1.5 ± 1.1
CLT-undamaged	2.3 ± 0.7	1.4 ± 1.1
DT-damaged	3.3 ± 2.5	0.8 ± 0.5
DT-undamaged	2.0 ± 0.0	0.3 ± 0.5
C-damaged	18.3 ± 18.2	1.6 ± 1.1
C-undamaged	2.0 ± 0.0	1.0 ± 0.0

[*]Abbreviations: CLT-Contact lens treatment, DT-Drop treatment, C-Control
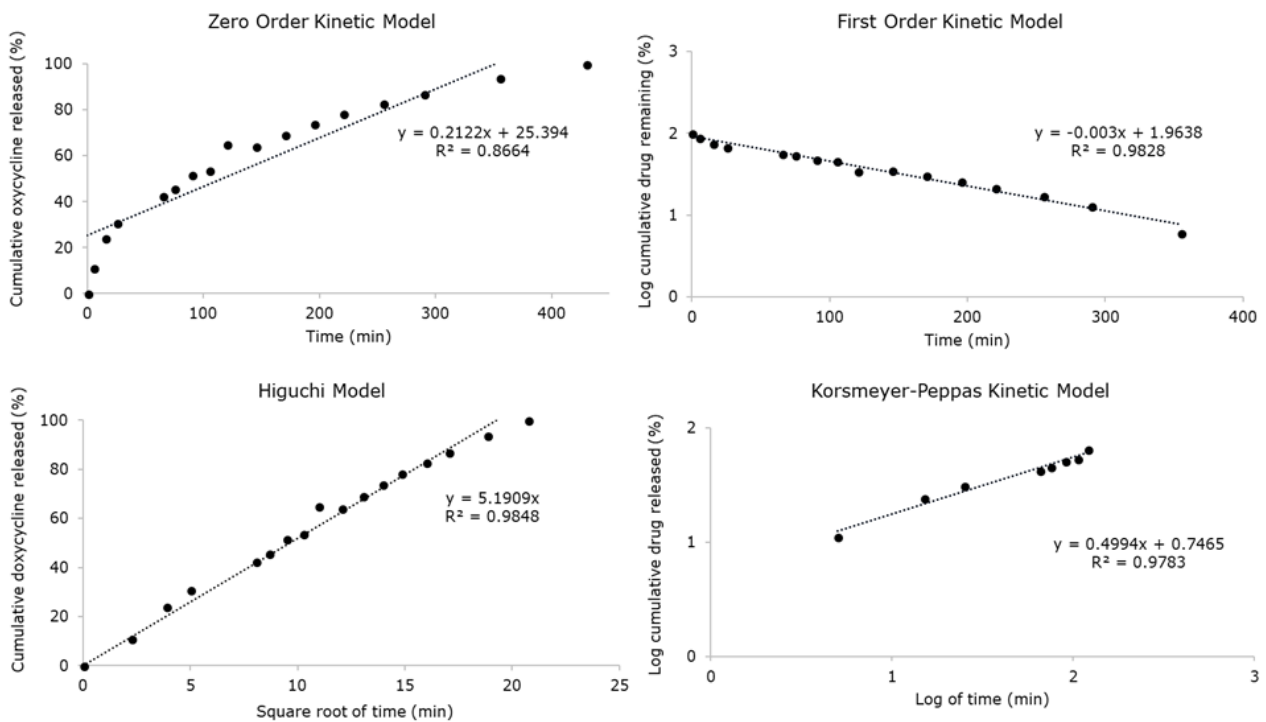
Figure 5. Zero-order, first-order, Higuchi and Korsmeyer-Peppas models for the *in vitro* release data of doxycycline in NaCl solution
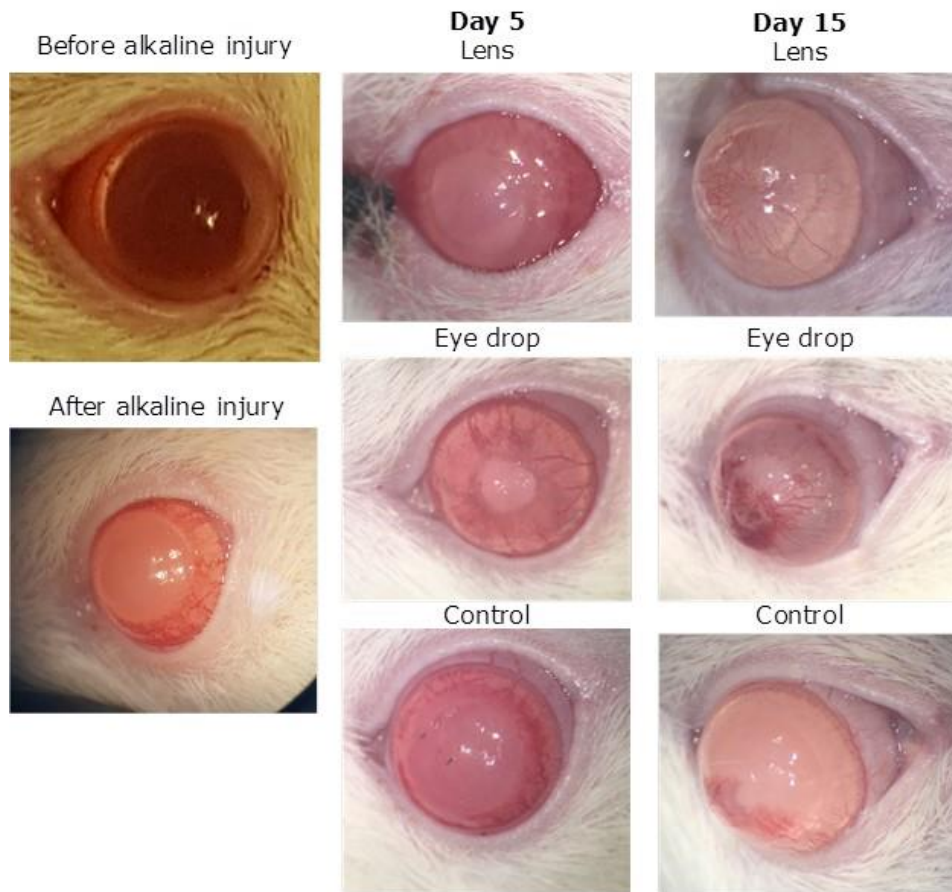
Figure 6. Rat's eyes before and after alkaline injury

Statistical Analysis

The Kruskal Wallis test was used because there was no homogeneous distribution between groups and the number of groups was less than 30. Corneal vessel count was found to be statistically significant according to Kruskal Wallis test result (p <0.05). Mann-Whitney U test was used to compare the two groups in order to determine the significance between the groups. According to this test, statistically significant results were obtained between the drop group and the control group (p = 0.038), and the number of corneal vessels in the drop-treated group was found to be less. The statistical comparison between the lens-treated group and the drop-treated group was found to be significant (p<0.001), and the number of vessels in the drop-treated group was found to be lower. When the lens-treated group and the control group were statistically compared, no significant results were found (p> 0.05). When the arithmetic average and standard deviation values between these two groups were examined, this result was evaluated as clinically significant when the lens-treated group average was lower and the standard deviation was within the narrow limits.

CONCLUSIONS

In this study, a new method was described for treatment of corneal neovascularization. First of all, the formulation of doxycycline imprinted contact lens was determined by using computational and experimental methods. All lenses were synthesized with a special mold designed for rat's eye. Their release performances were investigated with four different mathematical models, and Higuchi model fitted data better than the others.

Contact lenses were not cytotoxic to RPE cell line. According to our *in vivo* results, treatment with contact lens had a beneficial effect on the vascular calibers of neovascularization. The data were reported for the first time in literature.

REFERENCES

1. Aquil M, Gupta H. Contact lenses in ocular therapeutics. Drug Discovery Today. 2012;17(9-10):522-7.

2. Forbes JM, Cooper ME. Mechanisms of diabetic complications. Physiological Reviews. 2013;93:137-88.

3. Yoeruek E, Ziemssen F, Henke-Fahle S, Tatar O, Tura A, Grisanti S, Bartz-Schmidt KU, Szurman P. Safety, penetration and efficacy of topically applied bevacizumab: evaluation of eyedrops in corneal neovascularization after chemical burn. Acta Ophthalmologica, 2008;86:322-8.

4. Giulio F, Dastjerdi MH, Okanobo A, Cheng SF, Amparo F, Nallasamy N, Dana R. Topical ranibizumab as a treatment of corneal neovascularization. Cornea. 2013;32(7):992-7.

5. Feizi S, Azari AA, Safapour S. Therapeutic approaches for corneal neovascularization. Eye and Vision. 2017;4:28-38.

6. Byrne ME, Salian V. Molecular imprinting within hydrogels II: Progress and analysis of the field. International Journal of Pharmaceutics. 2008;364:188-212.

7. Cheong WJ, Yang SH, Ali F. Molecular imprinted polymers for separation science: A review of reviews. Journal of Separation Science. 2013;36(3):60928.

8. Magdy Elnashar, editor. Biopolymers. IntechOpen; 2010. Open access peer-reviewed chapter 28. Molecularly Imprinted Polymers (PIMs) in Biomedical Applications by Puoci F, Cirillo G, Curcio M, Iemma F, Parisi OI, Spizzirri UG, Picci N. ISBN: 978-953-307-109-1.

9. Hu X, Hao, L, Wang, H, Yang X, Zhang G, Wang G, Zhang X. Hydrogel contact lens for extended delivery of ophthalmic drugs. International Journal of Polymer Science. 2011; Article ID 814163.

10. Alverez-Lorenzo C, Yanez F, Barreiro-Iglesias R, Concheiro A. Imprinted soft contact lenses as norfloxacin delivery systems. Journal of Controlled Release. 2006;113(3)236–44.

11. Garcia DM, Escobar J., Noa Y, Bada N, Hernaez E, Katime I. Timolol maleate release from pH-sensible poly(2-hydroxyethyl methacrylate-co-methacrylic acid) Hydrogels. European Polymer Journal. 2004;40(8):1683-90.

12. Tieppo A, White CJ, Paine AC, Voyles ML, McBride MK, Byrne ME. Sustained in vivo release from imprinted therapeutic contact lenses. Journal of Controlled Release. 2012;157(3):391-7.

13. Vasapollo G, Sole RD, Mergola L, Lazzoi MR, Scardino A, Scorrano S, Mele G. Molecularly Imprinted Polymers: Present and Future Prospective. International Journal of Molecular Science. 2011; 12:5908-45.

14. Dalgakiran D, Inan T, Güner FS. Investigation of photoinduced polymerization of doxycycline-imprinted hydrogels: effect of template on initiator reactivity, conversion, and reaction rate. Turkish Journal of Chemistry. 2017;41: 862-73.

15. Gordon MK, DeSantis A, Deshmukh M, Lacey CJ, Hahn RA, Beloni J, Anumolu SS, Schlager JJ, Gallo MA, Gerecke DR, Heindel ND, Svoboda KKH, Babin MC, Sinko PJ. Doxycycline Hydrogels as a Potential Therapy for Ocular Vesicant Injury. Journal of Ocular Pharmacology and Therapeutics. 2010;26(5):407-19.

16. Lobo MS, Costa P. Modeling and Comparison of Dissolution Profiles. European Journal of Pharmaceutical Sciences. 2001;13:123-33.

Structural, Spectroscopic and Activity Calculations on Methanesulfonylhydrazone Derivative Chromium Pentacarbonyl Complexes

Sultan ERKANa* ✉ iD **, Koray SAYIN**b ✉ **, Duran KARAKAŞ**b ✉ iD

*a Chemistry and Chemical Processing Technologies, Cumhuriyet University Yildizeli Vocational School, 58140 Sivas, Turkey
b Inorganic Chemistry, Faculty of Science, Cumhuriyet University, 58140 Sivas, Turkey

Abstract: The thiophene-2-carboxyaldehyde methanesulfonylhydrazone (msh1), 2-acetylthiophene methanesulfonylhydrazone (msh2) and 2-acetyl-5-methylthiophene methanesulfonylhydrazone (msh3) ligands, a heteroatomic methanesulfonylhydrazone derivative, was optimized by using HF and DFT (B3LYP) method with 6-31G(d,p) basis set. The calculated IR spectra for msh1, msh2 and msh3 were compared with experimental data and the suitability of the calculation methods was discussed. LANL2DZ and GEN basis sets were used for calculations of chromium pentacarbonyl complexes containing msh1, msh2 and msh3 ligands. According to the experimental IR spectra the most appropriate method and basis set was determined. Structural parameters of ligands and complexes were predicted. To investigate the biological activities of ligands and complexes, some activity descriptors were obtained from optimized structures. Molecular electrostatic potential (MEP) maps of the mentioned ligands and complexes were examined and active sites were determined. The molecular docking study of ligands and complexes with *Bacillus cereus* (PDB ID=5V8E), *Staphylococcus aureus* (PDB ID=1BQB), and *Candida albicans* (PDB ID=1AI9) were performed.

INTRODUCTION

The pharmacological and chemical interest of the compounds containing the sulfonyl hydrazone moiety is increasing day by day (1). Sulfonamide drugs are used as chemotherapeutic agents because they have a broad spectrum of activity (2). Most compounds containing carboxylic acid hydrazones exhibit cytostatic activity. Sulfonamides ($-SO_2NH-$) are widely used as antimicrobial agents due to their lower cost, lower toxicity and most of their activity against bacterial diseases (3). Methane sulfonamide derivatives have DNA binding ability and show cytostatic effects that are used in cancer chemotherapy.

Hydrazonic compounds have interesting biological properties such as antibacterial (4), antidepressant (5), antiinflammatory, analgesic (6,7) and antipyretic activity (8). Hydrazones are important compounds for drug design with the synthesis of metal complexes, organocatalysis and heteroaromatic compounds (9). Sulfones containing heteroaromatic moieties have been discovered to exhibit interesting antibacterial and antifungal bioactivity. For this reason, the synthesis of sulfones has attracted great interest in pesticides and medical formulations (10). Sulfonylhydrazones derived from sulfonamides have pharmacological properties such as

antibacterial, anticancer, antiviral, antinociceptive activity, and particularly enzyme inhibition to carbonic anhydrase species (11-14). Most physiologically active hydrazones have applications in the treatment of diseases such as tuberculosis, leprosy and mental damage.

Theoretical studies based on quantum mechanics are used to obtain information on some physical and chemical properties of chemical compounds (15,16). For example, vibration spectroscopy is versatile and an easily available tool to interpret and predict the properties of chemically and biologically active molecules. These theoretical studies have been used in both chemical kinetic and chemical analysis studies (17,18). However, in addition to the labeling of vibration modes, the relationship between the observed spectroscopic properties and the molecular structure may be difficult to understand (19). In recent years, DFT and HF methods have been used to determine the molecular structure and vibration spectra of molecules with low computational cost (20-25). These calculation methods can give systematic errors due to limited basis sets, harmonic approaches and neglect in electron correlations (26).

The thiophene-2-carboxyaldehyde methanesulfonylhydrazone (msh1), 2-acetylthiophene methanesulfonylhydrazone (msh2) and 2-acetyl-5-methylthiophene methanesulfonylhydrazone (msh3) which are the heteroatomic methanesulfonylhydrazone derivatives and chromium pentacarbonyl complexes of these ligands were synthesized by G. Orhan et al. in 2014. The synthesized ligands and complexes were examined only in terms of spectroscopy. In this work, msh1, msh2 and msh3 were optimized with HF/6-31G(d,p) and B3LYP/6-31G(d,p) level. The experimental data were compared with the calculated IR spectra of msh1, msh2 and msh3. The suitability of the calculation methods according to the correlation coefficients were discussed. The HF and DFT (B3LYP) methods LANL2DZ and GEN (LANL2DZ for metal and 6-31G(d,p) for other atoms) basis sets were used for the calculations of chromium pentacarbonyl complexes are given in Figure 1. The suitability of the levels used for the mentioned complexes was discussed according to the experimental stretching frequencies. Structural parameters of the studied ligands and complexes were predicted.

There were antimicrobial studies for sulfonylhydrazone derivatives in the literature. For example, Gunduzalp *et al.* examined the antimicrobial activities of aromatic/heteroaromatic sulfonylhydrazone derivatives in 2014 (27). For this reason, some quantum chemical identifiers such as the highest occupied molecular orbital (E_{HOMO}), energy of the lowest unoccupied molecular orbital (E_{LUMO}), energy gap between LUMO and HOMO (E_{GAP}), absolute hardness (η), absolute softness (σ),

absolute electronegativity (χ), chemical potential (μ), electrophilicity index (ω), nucleophilicity index (ε) and global softness (S) were studied to investigate the structure-activity relationship. Molecular electrostatic potential (MEP) maps were examined to determine the active areas of the molecules. Finally, molecular docking studies were done theoretically for some types of bacterial and fungal activities. The lack of experimental biological activity for the ligands and complexes mentioned was theoretically illuminated.
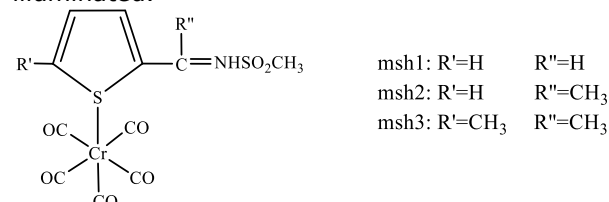
Figure 1. Schematic diagram of studied chromium complexes.

Calculation method

The input files of msh1, msh2 and msh3 ligands and their chromium pentacarbonyl complexes were prepared with GaussView 5.0.8 (28). All calculations were done using Gaussian 09 AML64L-Revision-C.01 (29). The HF (30) and B3LYP (31) methods and 6-31G(d,p) level for optimization of the mentioned ligands and HF and B3LYP methods and LANL2DZ and GEN levels for optimization of the mentioned complexes were performed in gaseous phase.

B3LYP/6-31G(d,p) for ligands and B3LYP/GEN for complexes were determined to be the optimal level. DFT methods are taken in account of electron exchange and correlation. Basis sets are often used to create molecular orbitals. 6-31G(d, p) is a polarized basis set. It states that p-functions are added to the hydrogen atom other d-functions are attached to heavy atoms (32,33). The LANL2DZ is a basis set that uses the effective core potential to model metal atoms (34). So this basis set neglects the inner shell electrons in the bond formation. The GEN keyword is determined by the user. The atomic orbitals of the central atom and the groups bound to the central atom are calculated using separate basis set (35). The molecular identifiers required to predict biological activity are obtained by quantum chemical calculations. Some quantum chemical parameters which are energy of the highest occupied molecular orbital (E_{HOMO}), energy of the lowest unoccupied molecular orbital (E_{LUMO}), energy gap between LUMO and HOMO (E_{GAP}), absolute hardness (η), absolute softness (σ), absolute electronegativity (χ), chemical potential (μ), electrophilicity index (ω), nucleophilicity index (ε) and global softness (S), were calculated by using following equation.

According to the Koopmans' theorem, the ionization energies and the electron affinities of the chemical species are related to the energies

of their frontier orbitals and are calculated using Equations 1 and 2 (36).

$$I = -E_{HOMO} \qquad (1)$$
$$A = -E_{LUMO} \qquad (2)$$

The difference between the energies of HOMO and LUMO is calculated according to Equation (3).

$$\Delta E = E_{LUMO} - E_{HOMO} \quad (3)$$

The absolute hardness, softness, absolute electronegativity and chemical potential of the molecules are calculated by Equation (4) - (7) according to R. G. Pearson (37).

$$\chi = \frac{I + A}{2} \qquad (4)$$
$$\mu = -\chi \qquad (5)$$
$$\eta = \frac{I - A}{2} \qquad (6)$$
$$\sigma = \frac{1}{\eta} \qquad (7)$$

R. G. Parr *et al.* proposed an identifier called electrophilicity index (ω). The electrophilicity index is calculated using the following equation (38). The nucleophilicity index (ε) is the inverse of the electrophilicity index (39). The global softness is a function of absolute hardness, as seen in Equation 10 (40,41).

$$\omega = \frac{\mu^2}{2\eta} \qquad (8)$$
$$\varepsilon = \frac{1}{\omega} \qquad (9)$$
$$S = \frac{1}{2\eta} \qquad (10)$$

RESULTS AND DISCUSSION

Optimized structures of ligand and complexes

Optimized structures of the ligands msh1, msh2 and msh3 and the $Cr(CO)_5msh1$, $Cr(CO)_5msh2$ and $Cr(CO)_5msh3$ complexes are given in Figures 2 and 3. The optimized structures in the figures were obtained at the B3LYP/GEN level for complexes and at the B3LYP/6-31G(d,p) for ligands in gaseous phase.

Figure 2. The optimized structures of complexes obtained at B3LYP/GEN level. Hydrogen atoms have been removed for aperture.
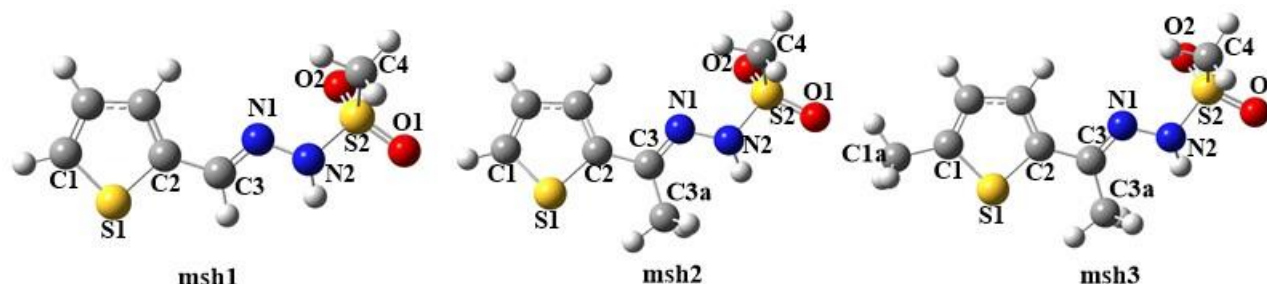
Figure 3. The optimized structures of ligands obtained at B3LYP/6-31G(d,p) level.

Vibrational Frequencies and Benchmark analysis

Vibrational spectrum is the most important component of molecular structure illumination. Nowadays, the methods computational chemistry provide very useful information in assignment the vibrational spectrum of molecules. However, many methods and basis sets in computational chemistry studies required accurate optimization to be achieved with correct calculation.

In this case, the most accurate results, or as mentioned, the most accurate optimization should be that the correlation between the experimental data and the calculated data by using the different methods and the basis set should be investigated. For this reason, Benchmark analysis is an important section of computational studies. The experimental frequencies values of the mentioned ligands and complexes are compared with those of the calculated harmonic frequencies in each level. The distribution graph is plotted by using experimental and computational frequencies for each level and correlation coefficient (r) is calculated from this graph. The experimental vibration spectra and the calculated frequencies with the HF/6-31G(d,p) and DFT/B3LYP/6-31G(d,p) level and assignments of frequencies for

msh1, msh2 and msh3 ligands are given in Table 1.

Table 1. The experimental and calculated IR spectra (v/cm^{-1}) and their assignment for msh1, msh2 and msh3.

Msh1			Msh2			Msh3			
HF	**B3LYP**	**EXP.**	**HF**	**B3LYP**	**EXP.**	**HF**	**B3LYP**	**EXP.**	**ASSIGN.**
3745.77	3420.14	3180	3766.77	3449.36	3226	3766.19	3448.22	3233	νNH
3427.79	3223.67	3090	3384.53	3222.91	3093	3375.23	3211.86	3024	νCHring
1920.61	1678.96	1607	1911.73	1658.68	1593	1910.35	1656.96	1598	νCN
1470.06	1337.5	1332	1470.32	1342.28	1331	1469.22	1341.3	1331	ν(SO$_2$)asym
1258.62	1135.1	1158	1260.79	1137.27	1166	1259.85	1136.56	1169	ν(SO$_2$)sym
1047.92	916.64	844	1046.56	859.51	845	1030.28	964.44	923	νCSCring
891.92	817.46	770	922.34	619.44	771	724.41	745.36	703	νCSsym
815.45	747.46	664	-	-	-	804.46	684.05	583	νCSasym
0.9951*	0.9975*		0.9937*	0.9976*		0.9944*	0.9976*		
sym: symmetric, asym: asymmetric, * the calculated correlation coefficients (r)									

Table 1 gives the experimental, calculated frequencies for ligands and their labelling. The most appropriate method and basis set were determined according to the correlation coefficients between the calculated and the experimental vibration frequencies. B3LYP/6-31G(d,p) was determined as the most appropriate method and basis set because the calculated correlation coefficients (r) were closer to 1 for the three ligands. In addition, for the msh3 ligand, it was experimentally found that

symmetric and asymmetric CS stretching bands at 703 and 583 cm^{-1}, respectively, were the opposite in animation.

The carbonyl complexes are optimized with HF and B3LYP methods LANL2DZ and GEN basis sets in gaseous phase. The frequencies obtained from the optimized structures, the experimental stretching frequencies and their labelling are given in Tables 2-4.

Table 2. The harmonic vibration frequencies calculated at HF and B3LYP methods with LANL2DZ and GEN basis sets in gas phase for Cr(CO)$_5$msh1

HF/LANL2DZ	**HF/GEN**	**B3LYP/LANL2DZ**	**B3LYP/GEN**	**EXP.**	**ASSIGN.**
2152.5	2317.89	2031.15	2065.7	2060	νCO
2147.34	2303.82	1931.45	2055.46	1921	νCO
2118.72	2291.25	1913.58	2046.81	1894	νCO
860.42	1043.06	863.62	909.66	858	νCSCring
830.77	883.79	805.48	847.46	805	νCSCring
654.85	650.94	732.52	804.22	650	νCSsym
752.17	622.32	681.31	722.5	603	νCSasym
0.9896*	0.9927*	0.9976*	0.9918*		
sym: symmetric, asym: asymmetric, *the calculated correlation coefficients (r)					

Table 3. The harmonic vibration frequencies calculated at HF and B3LYP methods with LANL2DZ and GEN basis sets in gas phase for Cr(CO)5msh2

HF/LANL2DZ	**HF/GEN**	**B3LYP/LANL2DZ**	**B3LYP/GEN**	**EXP.**	**ASSIGN.**
2146.7	2317.89	2029.61	2180.42	2060	νCO
2132.31	2310.66	1947.21	2053.08	1935	νCO
2126.36	2291.25	1916.91	2049.42	1859	νCO
1426.37	1650.35	941.31	896.74	852	νCSCring
893.91	1043.06	840.87	845.42	798	νCSCring
755.3	883.79	769	724.99	655	νCSsym
670.63	792.53	680.64	674.76	591	νCSasym
0.9314*	0.9115*	0.9978*	0.9979*		
sym: symmetric, asym: asymmetric, * the calculated correlation coefficients (r)					

Table 4. The harmonic vibration frequencies calculated at HF and B3LYP methods with LANL2DZ and GEN basis sets in gas phase for Cr(CO)5msh3

HF/LANL2DZ	HF/GEN	B3LYP/LANL2DZ	B3LYP/GEN	EXP.	ASSIGN.
2255.05	2311.66	2028.45	2151.58	2070	νCO
2145.76	2305.26	1945	2056.76	1940	νCO
2126.79	2298.52	1918.64	2051.53	1889	νCO
1020.89	1045.12	1169.34	1038.87	955	νCSCring
785.02	792.65	1042.42	960.81	870	νCSCring
679.41	713.89	932.95	724.08	618	νCSsym
597.29	624.62	709.13	671	577	νCSasym
0.9934*	0.9863*	0.9886*	0.9985*		
sym: symmetric, asym: asymmetric, *the calculated correlation coefficients (r)					

According to Tables 2-4, B3LYP/GEN level was chosen as the most appropriate method and basis set according to the correlation coefficients of the experimental and calculated vibration frequencies in the charts. When the Tables 2-4 are examined, the experimentally determined carbonyl vibrational frequencies for the Cr(CO)$_5$msh1 complex were determined to be 2060, 1935 and 1859 cm^{-1}, these frequencies were calculated as 2065.7, 2055.46 and 2046.81 cm^{-1}, respectively. For other complexes the carbonyl stretching frequencies were also similar. The experimental values were 655 and 591 cm^{-1} and were labeled

as symmetrical and asymmetric CS bond vibrational in the Cr(CO)$_5$msh2 complex. But when examined with the animation, it is observed that symmetrical bond tension is asymmetric bond tension and asymmetric bond stretching is symmetrical.

Structural Parameters
The bond lengths and ligand angles, which are geometric structure parameters calculated at the gas phase at the B3LYP/6-31G(d,p) level of the three mentioned ligands, are given in Table 5.

Table 5. Calculated bond lengths (Å) and bond angles (°) at the gas phase for B3LYP/6-31G(d, p) for the msh1, msh2 and msh3.

Bonds	msh1	msh2	msh3
S1-C1	1.730	1.730	1.745
S1-C2	1.751	1.754	1.757
C2-C3	1.452	1.466	1.465
C3-N1	1.285	1.292	1.292
N1-N2	1.374	1.377	1.378
N2-S2	1.722	1.723	1.722
S2-O1	1.464	1.465	1.465
S2-O2	1.462	1.462	1.462
S2-C4	1.796	1.796	1.796
Angles			
C1-S1-C2	91.59	91.80	92.30
C2-C3-N1	121.27	116.09	116.18
C3-N1-N2	117.36	118.06	117.98
N1-N2-S2	114.93	114.12	114.04
O1-S2-O2	121.16	121.02	120.95

When the bond lengths and bond angles of the ligands are examined, it can be seen that the bond lengths of the S1-C1, C2-C3, C3-N1, N1-N2, N2-S2 and S-O bonds are very close to each ligand. It is seen that C1-S1-C2 angle is 90° and C2-C3-N1 angle is about 120° in the msh1 and about 115° in the msh2 and msh3. A decrease in the angle due to the presence of methyl groups in msh2 and msh3 is expected.

The calculated geometric structure parameters in gas phase with the B3LYP/GEN level of Cr(CO)$_5$msh1, Cr(CO)$_5$msh2 and Cr(CO)$_5$msh3

complexes are given in Table 6. In the literature, the terminal C-O bond lengths is about 1.15 Å. This value was calculated at the B3LYP/GEN level for C-O bonds. The fact that the Cr-S bond length is numerically larger than the Cr-C bond length is due to the large diameter of the sulfide. The angle between chromium and the surrounding carbonyl and methylsulfonylhydrazone ligands is about 90°, indicating that the chromium complex has octahedral geometry. It is also evident that the angle between the C1-S1-C2 atoms of the methylsulfonylhydrazone ligand has not changed.

Table 6. The bond lengths (Å) and bond angles (°) calculated in gas phase with B3LYP/GEN level for Cr(CO)5msh1, Cr(CO)5msh2 and Cr(CO)5msh3

Bonds	Cr(CO)$_5$msh1	Cr(CO)$_5$msh2	Cr(CO)$_5$msh3
Cr-C1	1.855	1.854	1.856
Cr-C2	1.904	1.909	1.907
Cr-C3	1.914	1.906	1.909
Cr-C4	1.911	1.909	1.908
Cr-C5	1.910	1.915	1.912
Cr-S1	2.564	2.570	2.574
S1-C1	1.746	1.747	1.767
S1-C2	1.767	1.769	1.772
C1-O1	1.156	1.156	1.156
C2-O2	1.154	1.152	1.153
C3-O3	1.151	1.156	1.153
C4-O4	1.151	1.153	1.152
C5-O5	1.153	1.151	1.152
Angles			
C1-Cr-C2	89.1	90.4	90.2
C1-Cr-C3	90.7	89.2	89.2
C1-Cr-C4	90.4	89.3	89.1
C1-Cr-C5	89.2	90.7	90.4
C1-Cr-S	179.1	177.4	178.1
C2-Cr-C3	90.4	90.0	90.1
C2-Cr-C4	89.6	90.3	89.5
C2-Cr-C5	178.3	178.7	179.3
C2-Cr-S	91.4	88.7	89.1
C3-Cr-C4	178. 8	178.5	178.3
C3-Cr-C5	90.0	89.5	89.7
C3-Cr-S	89.9	93.2	92.5
C4-Cr-C5	89.9	89.5	90.7
C4-Cr-S	88.9	90.1	89.1
C5-Cr-S	90.2	90.1	90.3
C1-S-C2	91.6	91.7	92.3

The Activity Studies with Quantum Chemical Descriptor

Some quantum chemical parameters obtained from optimized molecular structures are useful for predicting biological activity. In many recent studies, there is a unique relationship between calculated quantum chemical parameters and experimental inhibition activities. Since HOMO is the highest energy orbital containing electrons, it acts as an electron donor orbital. If E_{HOMO} increases, the inhibitor electron emission is facilitated and the inhibition activity is increased. Similarly, if the E_{LUMO} energy is low, the ability of the inhibitor to interact increases and this means an increase in inhibitory activity. Absolute electronegativity (χ) is a chemical identifier that is considered in the comparison of inhibitory activities of chemical species. Inhibitors with low electronegativity values have easy electron donating ability and thus show high inhibition activity. The chemical potential (μ) is exactly the opposite of electronegativity. For this reason, the inhibition activity is increased by the increase of the chemical potential. The electrophilicity index (ω) is a numerical representation of a molecule's global electrophilic force. The electrophilicity index represents chemical reactivity and is a measure of the ability to receive electrons. These indexes were presented in the calculation method section. According to them, biological reactivity increases with increasing of nucleophilicity index (ϵ) and decreasing of electrophilicity index. The increasing of the value of global softness implies that biological activity of the compound is the increasing. In this light, these parameters examined for the mentioned molecules are given in Table 7.

Table 7. The calculated quantum chemical descriptors of the studied molecules.

	msh1	msh2	msh3	Cr(CO)$_5$(msh1)	Cr(CO)$_5$(msh2)	Cr(CO)$_5$(msh3)
E_{HOMO}*	-1.6504	-1.4664	-1.3883	-6.4032	-6.3602	-6.2589
E_{LUMO}*	-6.0769	-5.9602	-5.7672	-2.4469	-2.2983	-2.2289
ΔE*	-4.4265	-4.4937	-4.3789	3.9563	4.0619	4.0300
η*	-2.2133	-2.2469	-2.1894	1.9781	2.0309	2.0150
σ**	-0.4518	-0.4451	-0.4567	0.5055	0.4924	0.4963
χ*	3.8636	3.7133	3.5778	4.4250	4.3292	4.2439
μ*	-3.8636	-3.7133	-3.5778	-4.4250	-4.3292	-4.2439
ω*	-3.3723	-3.0684	-2.9232	4.9493	4.6142	4.4692
ε**	-0.2965	-0.3259	-0.3421	0.2021	0.2167	0.2238
S**	-0.2259	-0.2225	-0.2284	0.2528	0.2462	0.2481
*In eV, **In eV−1.						

According to Table 7, the order of activity of the investigated compounds according to the respective parameters is as follows:

According to **E_{HOMO}, χ, μ, ω and ε**: msh3 > msh2 > msh1

   Cr(CO)$_5$(msh3) > Cr(CO)$_5$(msh2) > Cr(CO)$_5$(msh1)
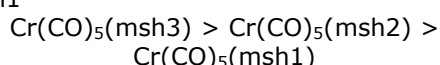
According to **E_{LUMO}**: msh1 > msh2 > msh3

   Cr(CO)$_5$(msh1) > Cr(CO)$_5$(msh2) > Cr(CO)$_5$(msh3)
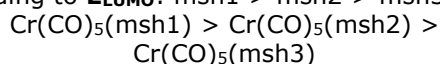
According to **ΔE, η, σ and S**: msh2 > msh1 > msh3

   Cr(CO)$_5$(msh1) > Cr(CO)$_5$(msh3) > Cr(CO)$_5$(msh2)
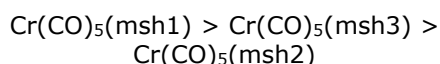
Molecular electrostatic potential (MEP) maps

Molecular electrostatic potential (MEP) maps show electrostatic regions within the molecule. MEP maps define the region of high electron density in red and low electron density in blue color. This is important in determining the electrostatic attack on the red zone and the nucleophilic attack on the blue zone. MEP maps obtained with computational chemistry methods provide useful information even in drug design. For example, it is important to know where to bind the species to be inhibited by the molecule synthesized as the drug (42-45). The MEP maps calculated for the investigated ligands and complexes were shown in Figures 4 and 5, respectively.
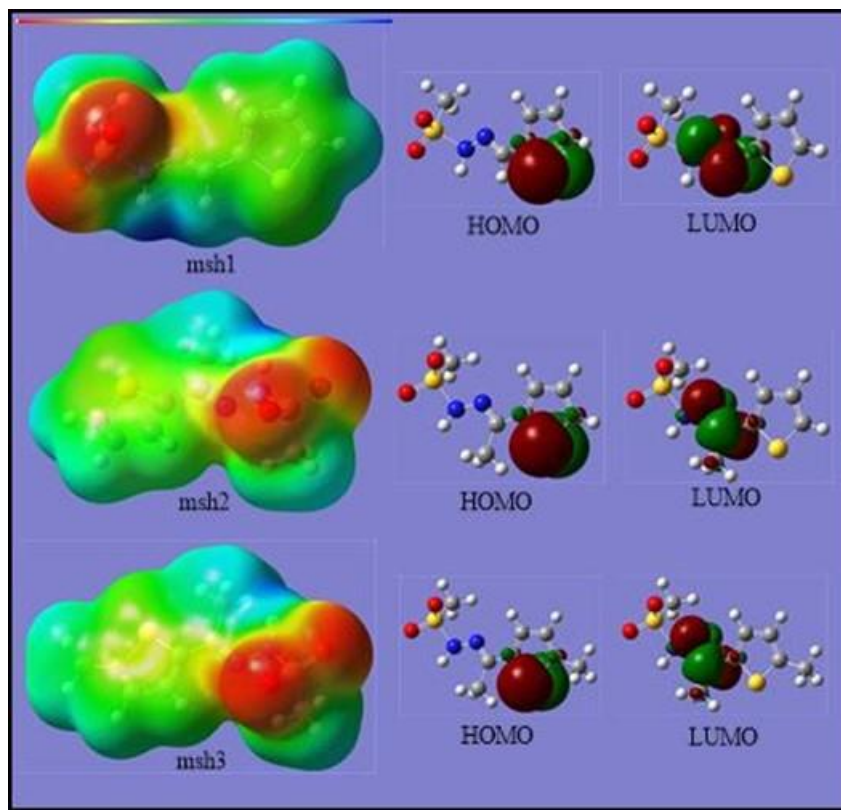
Figure 4. MEP maps and contour diagrams of mentioned ligands.
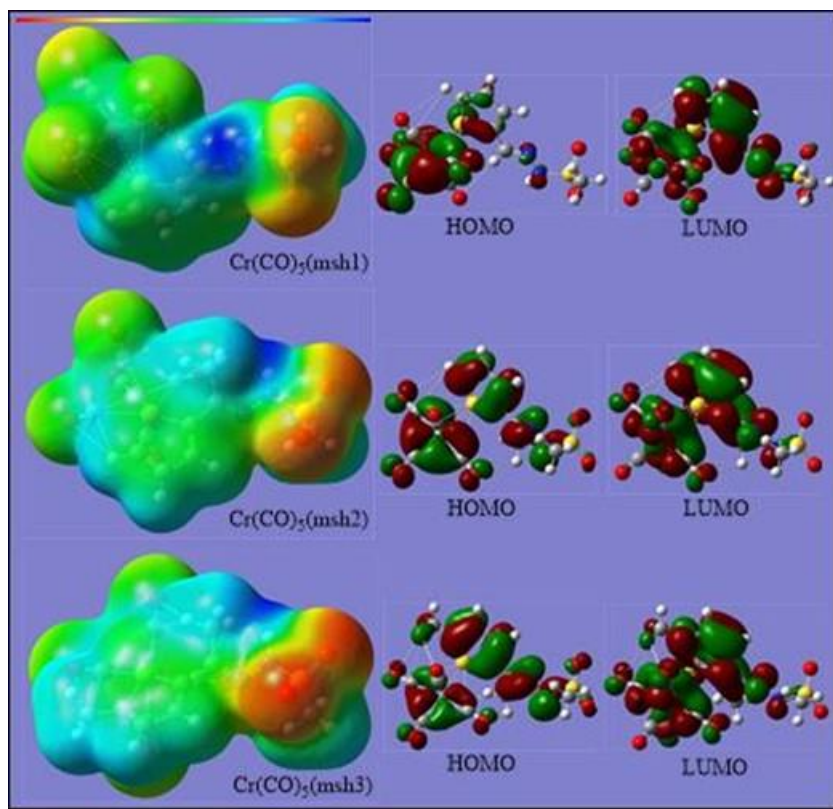
Figure 5. MEP maps and contour diagrams of mentioned complexes.

When MEP maps are examined, active sites in the ligands and complexes are usually regions where oxygen atoms are present. It can be considered as electrophilic sites in regions where oxygen atoms are present. The frontier molecular orbitals, the highest occupied molecular orbital (HOMO) and the lowest unoccupied molecular orbital (LUMO) are associated with spectral properties and activities of the compounds.

Molecular Docking
As is known, molecular docking studies support experimental antimicrobial studies. The antimicrobial effects of many sulfonylhydrazone derivatives have been experimentally investigated. Antimicrobial efficiency is not included in the literature for the mentioned ligands and complexes. For this reason, molecular docking studies for ligands and complexes against some bacterial and fungal cells that were studied experimentally were performed with the HEX8 program. The binding energies between *Bacillus cereus* (PDB ID:5V8E) (46), *Staphylococcus aureus* (PDB ID:1BQB) (47) and *Candida albicans* (PDB ID:1AI9) (48) and the studied ligands and complexes were investigated and these binding energies are listed in Table 8. Forms of active binding with target proteins for the studied ligands and complexes were given in Figures 6 and 7, respectively.

Table 8. The binding energies (kJ/mol) between the msh1-3 and $Cr(CO)_5(msh1)$-$Cr(CO)_5(msh3)$ with the target proteins.

	5V8E	**1BQB**	**1AI9**
Msh1	-198.60	-201.70	-194.55
Msh2	-193.22	-196.42	-192.82
Msh3	-202.88	-214.96	-204.51
$Cr(CO)_5(msh1)$	-511.18	-494.93	-318.60
$Cr(CO)_5(msh2)$	-409.79	-473.45	-321.82
$Cr(CO)_5(msh3)$	-487.06	-465.73	-325.02
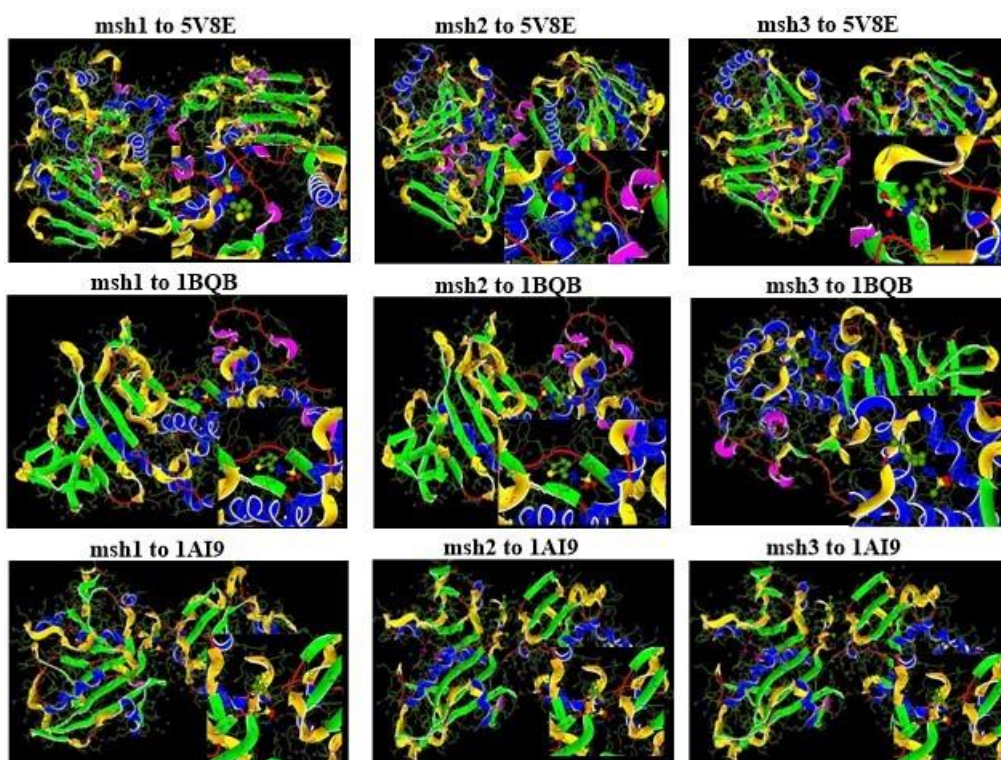
Figure 6. The binding region between the mentioned ligands with the target proteins.
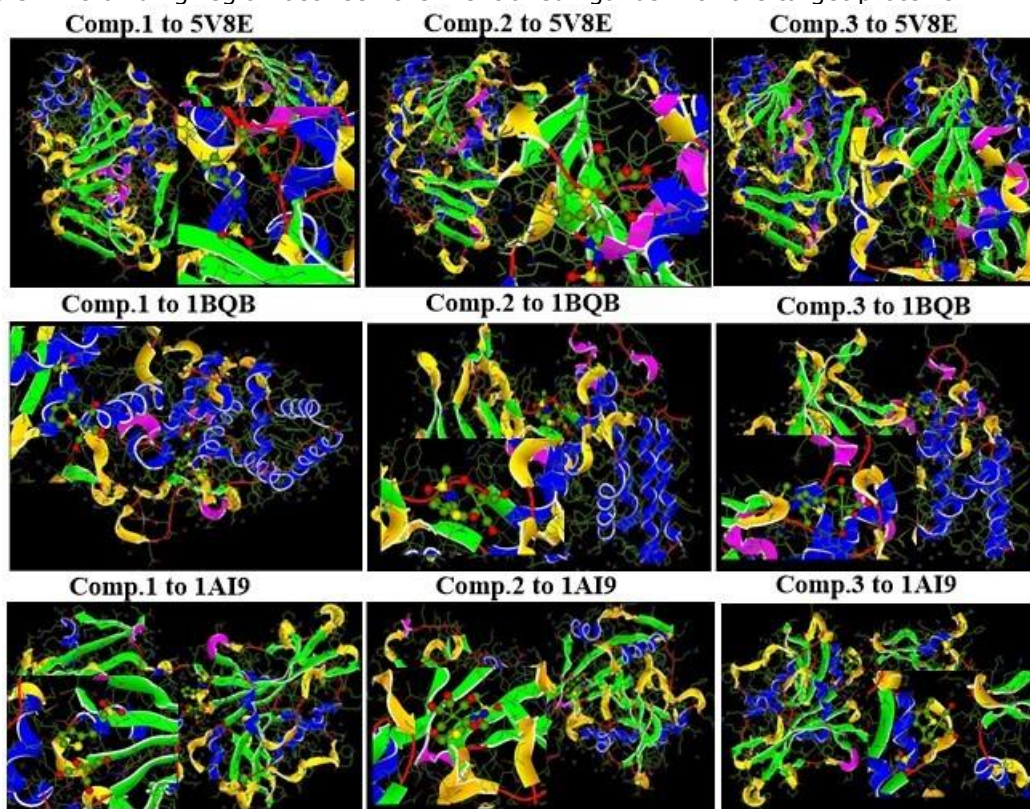
Figure 7. The binding region between the mentioned complexes with the target proteins.

When the binding energies are examined, it is that seen the cobalt carbonyl complexes of methylsulfonylhydrazone derivatives are more advantageous in terms of antimicrobial effectiveness. According to the binding energies of the ligands with the target proteins, msh3 has the highest antimicrobial activity. However, in complexes, $Co(CO)_5msh1$ has the highest binding energy value with all target proteins.

CONCLUSIONS

IR spectra calculated with HF and DFT (B3LYP) methods were labeled for msh1, msh2 and msh3 ligands and $Co(CO)_5msh1$, $Co(CO)_5msh2$ and

Co(CO)$_5$msh3 complexes according to experimental frequencies. According to the correlation coefficients, the most appropriate method is DFT(B3LYP) method. The most appropriate results were obtained at the B3LYP/6-31G(d, p) level for ligands, at the B3LYP/GEN level for the complexes. Structural parameters of these ligands and complexes were studied and were predicted about geometrical structures. The biological activity sequences of ligands and complexes were predicted with some quantum chemical identifiers. As a result, the biological activity order of the ligands and complexes according to ΔE, η, σ and S values is msh2 > msh1 > msh3 and Cr(CO)$_5$(msh1) > Cr(CO)$_5$(msh3) > Cr(CO)$_5$(msh2), respectively. In the MEP maps, the electrophilic sites of the ligands and complexes were appointed as the region of oxygen atoms. Finally, molecular docking calculations are performed between mentioned ligands complexes and proteins. Msh3 in ligands and Cr(CO)$_5$(msh1) in complexes is generally found the best complex in protection from cancer. The binding energies for msh3 with 5V8E, 1BQB and 1AI9 are -202.88, -214.96 and -204.51 kJ/mol, respectively. The binding energies for Cr(CO)$_5$(msh1) with 5V8E, 1BQB and 1AI9 are -511.18, -494.93 and -318.60 kJ/mol, respectively.

REFERENCES

1. Albert A, Selective Toxicity, first ed., Chapman and Hall, London, 1985; 24.

2. Shyam K, Penketh PG, Divo AA, Loomis RH, Patton CL, Sartorelli AC. Synthesis and Evaluation of l,2,2-Tris(sulfonyl)hydrazines as Antineoplastic and Trypanocidal Agents. J. Med. Chem. 1990; 33: 2259.

3. Özçelik S, Dinçer M, Şekerci M, Balaban A, Özdemir U. NPhenyl-N-(2-thienylmethylene)hydrazine. Acta Crystallogr Sect. E 2004; 60: 1552–3.

4. Özdemir ÖU, Güvenc P, Sahin E, Hamurcu F. Synthesis, characterization and antibacterial activity of new sulfonamide derivatives and their nickel(II), cobalt(II) complexes. Inorg.Chim. Acta 2009; 362: 2613-8.

5. Kalluraya B, Isloor AM, Frank PV, Jagadeesha RL. Synthesis and pharmacological activity of some-4-(substituted)-2-4-arylhydrazono-3-methyl-5- oxo-2-pyrazolin-1-yl] thiazoles. Ind. J. Het. Chem. 2004; 13: 245-8.

6. Oliveira KN, Costa P, Santin JR, Mazzambani L, Bürger C, Mora C, Nunes RJ. Synthesis and antidepressant-like activity evaluation of sulphonamides and sulphonyl-hydrazones. Bioorg. Med. Chem. 2011; 19: 4295-306.

7. Sondhi SM, Dinodia M, Kumar A. Synthesis, anti-inflammatory and hydrazine derivatives, Bioorg. Med. Chem. 2006; 14: 4657-63.

8. Raynaud FI, Parker P, Workman P, Waterfield MD. Synthesis and biological evaluation of sulfonylhydrazone-substituted imidazo[1,2-a]pyridines as novel PI3 kinase p110alpha inhibitors. Bioorg. Med. Chem. 2007; 15: 5837-44.

9. Hamurcu F, Mamas S¸ Ozdemir UO, Gündüzalp AB, Senturk OS. New series of aromatic/ five-membered heteroaromatic butanesulfonyl hydrazones as potent biological agents: Synthesis, physicochemical and electronic properties. Journal of Molecular Structure 2016; 1118: 18-27.

10. Mahajan NS, Jadhav RL, Pimpodkar NV, Dias RJ, Manikrao AM. Green Solid Oxidation of Sulfides to Sulfones Using Oxone and Biological Evaluation, Asian J. Chem. 2009; 21: 5415-20.

11. Ozdemir UO, Olgun G, Synthesis, characterization and antibacterial activity of new sulfonyl hydrazone derivatives and their nickel(II) complexes. Spectrochim. Acta Part A 2008; 70: 641-5.

12. Ozdemir UO, Akkaya N, Ozbek N. New nickel(II), palladium(II), platinum(II) complexes with aromatic methanesulfonylhydrazone based ligands, Synthesis, spectroscopic characterization and in vitro antibacterial evaluation. Inorg. Chim. Acta 2013; 400: 13-9.

13. Ozdemir UO, Arslan F, Hamurcu F. Synthesis, characterization, antibacterial activities and carbonic anhydrase enzyme inhibitor effects of new arylsulfonylhydrazone and their Ni(II), Co(II) complexes. Spectrochim. Acta Part A 2010; 75: 121-6.

14. Ozdemir UO, Altuntas A ¸ Gündüzalp AB, Arslan F, Hamurcu F. New aromatic/heteroaromatic propanesulfonylhydrazone compounds: Synthesis, physical properties and inhibition studies against carbonic anhydrase II(CAII) enzyme. Spectrochim. Acta Part A 2014; 128: 452-60.

15. Chermette H. Density functional theory: A powerful tool for theoretical studies in coordination chemistry. Coord. Chem. Rev. 1998;178–180: 699–721.

16. Corminboeuf C, Tran F, Weber J. The role of density functional theory in chemistry: Some historical landmarks and applications to zeolites. J. Mol. Struct: THEOCHEM 2006; 672: 1–7.

17. Kart SÖ, Tanbog AE, Soyleyici HC, Ak M, Kart HH. Theoretical study of the structure–properties relationship in new class of 2,5-di(2-

thienyl)pyrrole compounds. Spectrochimica Acta Part A: Molecular and Biomolecular Spectroscopy 2015; 137: 1174–83.

18. Krishnakumar V, Xavier RJ, Chithambarathanu T. Ab initio/DFT calculations of butyl ammonium salt of O, O'-dibornyl dithiophosphate. Spectrochimica Acta Part A: Molecular and Biomolecular Spectroscopy 2014; 129: 421-8.

19. Karabacak M, Sahin E, Cinar M, Erol I, Kurt M. X-ray, FT-Raman, FT-IR spectra and ab initio HF, DFT calculations of 2-[(5-methylisoxazol-3-yl)amino]-2-oxo-ethyl methacrylate. J. Mol. Struct. 2008; 886: 148–57.

20. Sayin K, Karakaş D, Erkan SK, Sayin TA. Computational study of some fluoroquinolones: Structural, spectral and docking investigations. Journal of Molecular Structure, 2018; 1156: 172-81.

21. Erkan SK, Sayin K, Karakaş D. Theoretical study on the antitumor properties of Ru (II) complexes containing 2-pyridyl, 2-pyridine-4-carboxylic acid ligands. Journal of Molecular Structure, 2017; 1149: 473-86.

22. Erkan SK. Spectroscopic and Quantum Chemical Studies on Some β-Lactam Inhibitors. Turkish Computational and Theoretical Chemistry, 2017; 1.2: 13-26.

23. Sarigul M, Erkan S K, Deveci P, Atabey H, Karakas D, Kurtoglu M. Multi-properties of a new azo-Schiff base and its binuclear copper (II) chelate: Preparation, spectral characterization, electrochemical, potentiometric and modeling studies. Journal of Molecular Structure 2017; 1149: 520-9.

24. Gungor SA, Sahin I, Gungor O, Erkan SK, Tumer F, Kose M. Pamoic acid esters and their xanthene derivatives: Flourimetric detection of nitroaromatic compounds and non-linear optical properties. Sensors and Actuators B: Chemical 2018; 255: 3344-54.

25. Karakaş D, Erkan SK. Theoretical investigation on the vibrational and electronic spectra of three isomeric forms of dicobalt octacarbonyl. Journal of Molecular Structure 2014; 1062: 77-81.

26. Katsyuba S, Vandyukova E. Scaled quantum mechanical computations of vibrational spectra of organoelement molecules, containing the atoms P, S, and Cl. Chem. Phys. Lett. 2003; 377: 658–62.

27. Dennington II RD, Keith TA, Millam JM. GaussView 5.0, Wallingford, CT, 2009.

28. Balaban Gunduzalp A, Ozdemir Ozmen U, Cevrimli BS, Mamas S, Cete S. Synthesis, characterization, electrochemical behavior, and antimicrobial activities of aromatic/heteroaromatic sulfonylhydrazone derivatives. Med Chem Res 2014; 23: 3255–68.

29. Frisch MJ, Trucks GW, Schlegel HB, Scuseria GE, Robb MA, Cheeseman JR, Scalmani G, Barone V, Mennucci B, Petersson GA, Nakatsuji H, Caricato M, Li X, Hratchian HP, Izmaylov AF, Bloino J, Zheng G, Sonnenberg JL, Hada M, Ehara M, Toyota K, Fukuda R, Hasegawa J, Ishida M, Nakajima T, Honda Y, Kitao O, Nakai H, Vreven T, Montgomery Jr JA, Peralta JE, Ogliaro F, Bearpark M, Heyd JJ, Brothers E, Kudin KN, Staroverov VN, Kobayashi R, Normand J, Raghavachari K, Rendell A, Burant JC, Iyengar SS, Tomasi J, Cossi M, Rega N, Millam JM, Klene M, Knox JE, Cross JB, Bakken V, Adamo C, Jaramillo J, Gomperts R, Stratmann RE, Yazyev O, Austin AJ, Cammi R, Pomelli C, Ochterski JW, Martin RL, Morokuma K, Zakrzewski VG, Voth GA, Salvador P, Dannenberg JJ, Dapprich S, Daniels AD, Farkas O, Foresman JB, Ortiz JV, Cioslowski J, Fox DJ, Gaussian, Inc., Wallingford CT, 2009.

30. Pople JA, Raghavachari K, Schlegel HB, Binkley JS, Derivative Studies in Hartree-Fock and Møller-Plesset Theories, Int. J. Quantum Chem., Quant. Chem. Symp., 1979; S13: 225-41.

31. Frisch MJ, Trucks GW, Schlegel HB, Gill PMW, Johnson BG, Wong MW, Foresman JB, Robb MA, Head-Gordon M, Replogle ES, Gomperts R, Andres JL, Raghavachari K, Binkley JS, Gonzalez C, Martin RL, Fox DJ, Defrees DJ, Baker J, Stewart JJP, Pople JA, Gaussian 92/DFT(Gaussian, Inc., Pittsburgh, PA, 1993.

32. Frisch MJ, Pople JA, Binkley JS, Self-Consistent Molecular Orbital Methods 25: Supplementary Functions for Gaussian Basis Sets, J. Chem. Phys. 1984; 80: 3265-9.

33. Foresman JB, Frisch E, Exploring Chemistry with Electronic Structure Methods, Gaussian. 2010

34. Dunning TH, Hay Jr, Hay PJ, in Modern Theoretical Chemistry, Ed. H. F. Schaefer, III, Plenum: New York, 1976, 1-28.

35. http://www.uam.es/departamentos/ciencias/qui mica/estruct/Manuales/Gaussian98/00000439.ht m

36. Pearson, Ralph G. Recent advances in the concept of hard and soft acids and bases. Journal of Chemical Education, 1987, 64.7: 561.

37. Pearson RG, Inorg. Chem., 1988; 27: 734-40

38. Parr RG, Yang W, Density-functional Theory of Atoms and Molecules Oxford Univ. Press, New-York, 1989.

39. Domıngo LR, Pérez P, The nucleophilicity N index in organic chemistry. Organic & biomolecular chemistry, 2011; 9.20: 7168-75.

40. Vela A, Gazquez JL, A relationship between the static dipole polarizability, the global softness, and the fukui function. Journal of the American Chemical Society, 1990; 112.4: 1490-2.

41. De Proft F, Amira F, Choho S, Geerlings P, Quantum-chemical study of the acidity of substituted acetic acids with density functional theory based descriptors. The Journal of Physical Chemistry, 1994; 98.20: 5227-33.

42. Tüzün B, Theoretical Evaluation of Six Indazole Derivatives as Corrosion Inhibitors Based on DFT, Turkish Comp Theo Chem (TC&TC), 2018; 2(1): 12 – 22.

43. Üngördü A, Tezer N. The solvent (water) and metal effects on HOMO-LUMO gaps ofguanine base pair: a computational study, J. Mol. Graph. Model. 2017; 74: 265-72.

44. Üngördü A, Tezer N. DFT study on metal-mediated uracil base pair complexes, J. Saudi Chem. Soc. 2017; 21.7: 837-44.

45. Erkan SK, Sayın K, Karakaş D. Theoretical Studies on Eight Oxovanadium(IV) Complexes with Salicylaldehyde and Aniline Ligands. Hacettepe J. Biol. & Chem. 2014; 42 (3): 337–42.

46. Sychantha D, Jones CS, Little DJ, Moynihan PJ, Robinson H, Galley NF, Clarke AJ. In vitro characterization of the antivirulence target of Gram-positive pathogens, peptidoglycan O-acetyltransferase A (OatA). PLoS pathogens. 2017; 13(10):e1006667.

47. Aldape MJ, Tao A, Heeney DD, McIndoo ER, French JM, Xu D. Experimental identification and computational characterization of a novel extracellular metalloproteinase produced by Clostridium sordellii. RSC advances. 2017; 7(23): 13928-38.

48. Elavarasan T, Bhakiaraj DP, Gopalakrishnan M. Synthesis, spectral analysis, in vitro microbiological evaluation, and molecular docking studies of some novel 1-(1-aryl-1H-tetrazol-5-yl)-2-(piperidin-1-yl) ethanone derivatives. ISRN organic chemistry, 2014.

RESEARCH ARTICLE

A Sensitive Quantification of Agmatine Using a Hybrid Electrode Based on Zinc Oxide Nanoparticles

Hilal İNCEBAY[1]

[1]University of Nevsehir Hacı Bektas Veli, 50300, Nevsehir, Turkey.

Abstract: An electrochemical sensor was prepared by modifiying a hybrid of multi-walled carbon nanotubes (MWCNTs) and zinc oxide nanoparticles (ZnONPs) to a glassy carbon (GC) electrode surface to accurately determine agmatine. The ZnONPs+MWCNTs/GC electrode surface was characterized using scanning electron microscopy (SEM) and energy dispersive X-ray (XRD). Agmatine did not exhibit any peak on the GC electrode surface, but exhibited a large oxidation peak at 637.9 mV on the MWCNTs/GC electrode surface. Furthermore, it was observed that the electrochemical behavior of agmatine was greatly improved on the MWCNT+ZnONPs/GC electrode surface and that this surface exhibited a well-defined higher current peak at 581.9 mV. The electrochemical responses of agmatine on the MWCNT+ZnONPs/GC electrode surface were performed using square-wave voltammetry (SWV). A linear plot was obtained for the current responses of agmatine against concentrations in the range of 0.1 μM–5.2 μM yielding a detection limit of 4.13×10^{-8} M (based on $3S_b/m$). The accurate quantification of agmatine makes the ZnONPs+MWCNTs/GC electrode system of great interest for the treatment of schizophrenia.

INTRODUCTION

Agmatine is a cationic polyamine produced naturally by the decarboxylation of L-arginine by arginine decarboxylase enzyme. It is produced in the mammalian brain and is also preserved in nature (1, 2). Agmatine has the properties of a neurotransmitter synthesized in the brain, stored in the vesicles and released from the brain (3-5). Current studies demonstrate that agmatine meets all the necessary criteria for the definition of a neurotransmitter and has been accepted as a new neurotransmitter (6-8). In addition, many studies have shown that agmatine degradation products such as spermidine and spermine are found at high rates in the brains, cerebrospinal fluid, and blood of patients with schizophrenia. The high levels of these metabolites in patients

with schizophrenia have led to the idea that agmatine may be present at high concentrations (9). As a matter of fact, a study published by Uzbay *et al.* found that the levels of agmatine in patients with schizophrenia who did not take any medication for at least 6 months were significantly higher than those of healthy controls (10). There are studies that suggest that there may be a relationship between schizophrenia and increased agmatine concentrations due to excessive release of agmatine and agmatine derivatives in the brain and cerebrospinal fluid (2, 11, 12). For this reason, it is important to determine agmatine levels correctly and quickly. High-performance liquid chromatography methods are generally used for agmatine measurements. However, due to problems such as selectivity and time-consuming steps

for derivatization, these techniques can create problems in conducting correctly analysis of samples. Nevertheless, voltammetric techniques with modified electrodes provide advantages such as high selectivity, speed, and simplicity. Furthermore, voltammetric methods have attracted attention in the analysis of many samples since they have the properties of speed, selectivity, and reproducibility (13, 14). The preparation of electrode surfaces in the nanostructure has also attracted focus, particularly regarding the

design of electrochemical sensing electrodes (15-17). Of these nanostructures, carbon nanotubes (CNTs), which have excellent electrocatalytic activity and sensitivity, are applied to obtain electrochemical sensors and biosensors. In addition, electrodes modified with hybrids of nanoparticles of CNTs and metal oxides offer good performance benefits, such as increased sensitivity, reduced overvoltage, mass transport, catalysis, and a high effective surface area and detection limit (18-19).
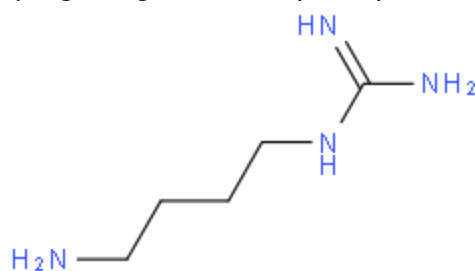

Figure 1. Chemical structure of agmatine.

In this study, a GC electrode surface was modified with a hybrid of MWCNTs and ZnO nanoparticles for agmatine quantification. The modification of the GC electrode surface with this hybrid provided excellent electrocatalytic efficiency, good selectivity and high sensitivity.

EXPERIMENTAL

Chemical reagents
Agmatine, multi-walled carbon nanotubes (MWCNTs), zinc oxide nanoparticles (ZnONPs), sodium hydroxide (NaOH) and disodium phosphate dibasic (Na_2HPO_4) were purchased from Sigma (Missouri, USA). Acetonitrile and chloroform were obtained from VWR International (Radnor, USA). Potassium dihydrogen phosphate (KH_2PO_4) was purchased from Merck (Darmstadt, Germany). The solutions were prepared with ultrapure water.

Instrumentation
A Gamry Interface 1000B Potentiostat/Galvanostat/ZRA was used to apply electrochemical measurements with cyclic voltammetry (CV) and square-wave voltammetry (SWV) techniques. Electrochemical measurements were performed in a three-electrode cell. A glassy carbon (GC) electrode was used as working electrode (MF–2012 BASi, USA), Ag/AgCl/(KCl$_{sat.}$) was used as the reference electrode (MF–2052 BASi, USA), and Pt wire was used as the counter electrode. All experimental data was plotted with the Origin

8.0 program so that a comparison between the data was made.

Preparation of modified electrodes
GC electrodes were first polished with 0.05 μm and 0.30 μm alumina slurry on a velvet cleaning pad and then the electrodes were sonicated for 5 minutes in pure water and acetonitrile. Then commercial MWCNTs were sonicated in concentrated $HClO_4+HNO_3$ (3:7, v:v) for 5 hours to functionalize the MWCNTs surfaces (20). The functionalized MWCNTs were washed with ultrapure water and dried. MWCNTs, ZnONPs, and ZnONPs+MWCNTs suspensions were then prepared by sonicating 1.0 mg of functionalized MWCNTs, 0.1 mg of ZnONPs and 0.1 mg of ZnONPs plus 1.0 mg of functionalized MWCNTs in 5 mL of chloroform for 50 min. MWCNTs/GC, ZnONPs/GC and ZnONPs+MWCNTs/GC electrode surfaces were prepared by dropping 5 μL of each of the prepared suspensions onto cleaned GC electrode surfaces. Afterward, the surfaces of these electrodes were extensively washed with ultra-pure water.

Optimization of Modified Electrode
The experimental results showed that the best results were obtained by sonicating MWCNTs and ZnONPs mixture in 5 mL chloroform at a 10:1 ratio for 50 minutes. On the other hand, the composite layer on GC electrode surface showed a clear peak formation for agmatine when the amount of ZnONPs/MWCNTs suspension was 5 μL. Besides, a considerable decrease in sensitivity and reproducibility was observed when higher amounts of this

suspension were added to the GC electrode surface.

Voltammetric analysis of agmatine
The prepared ZnONPs+MWCNTs/GC electrode was immersed in a cell containing agmatine with a concentration of 1.0×10^{-7} M dissolved in 50 mM phosphate buffer solution (PBS) (pH 7.0) and the voltammogram was recorded with CV. Under the same conditions, voltammograms of agmatine were taken at the bare/GC and MWCNTs/GC electrode surfaces and compared with the ZnONPs+MWCNTs/GC electrode. Then, voltammograms were taken at different scan rates for the ZnONPs+MWCNTs/GC electrode surface at the maximum voltammetric response to accurately conceptualize the electrochemical process of agmatine. Voltammograms of agmatine at the ZnONPs+MWCNTs/GC electrode surface were then taken at various pH values to determine the pH level at which the best voltammetric response was observed for agmatine

oxidation. Furthermore, square-wave voltammetry was applied to detect the sensitivity to different concentrations of agmatine at the ZnONPs+MWCNTs/GC electrode surface.

RESULTS AND DISCUSSION

Characterization of MWCNTs/GC and ZnONPs+MWCNTs/GC electrode surfaces
The modified electrode surfaces were examined using SEM. The image of the MWCNTs/GC electrode surface in Figure 2A shows that the MWCNTs are homogeneously distributed on the electrode surface and that there is no significant agglutination. In addition, Figure 2B shows the distribution of ZnONPs on the MWCNTs and Figure 2C shows the EDX data for the ZnONPs+MWCNTs/GC electrode surface. C, O, N and Zn were observed in the EDX analysis in Figure 2C.

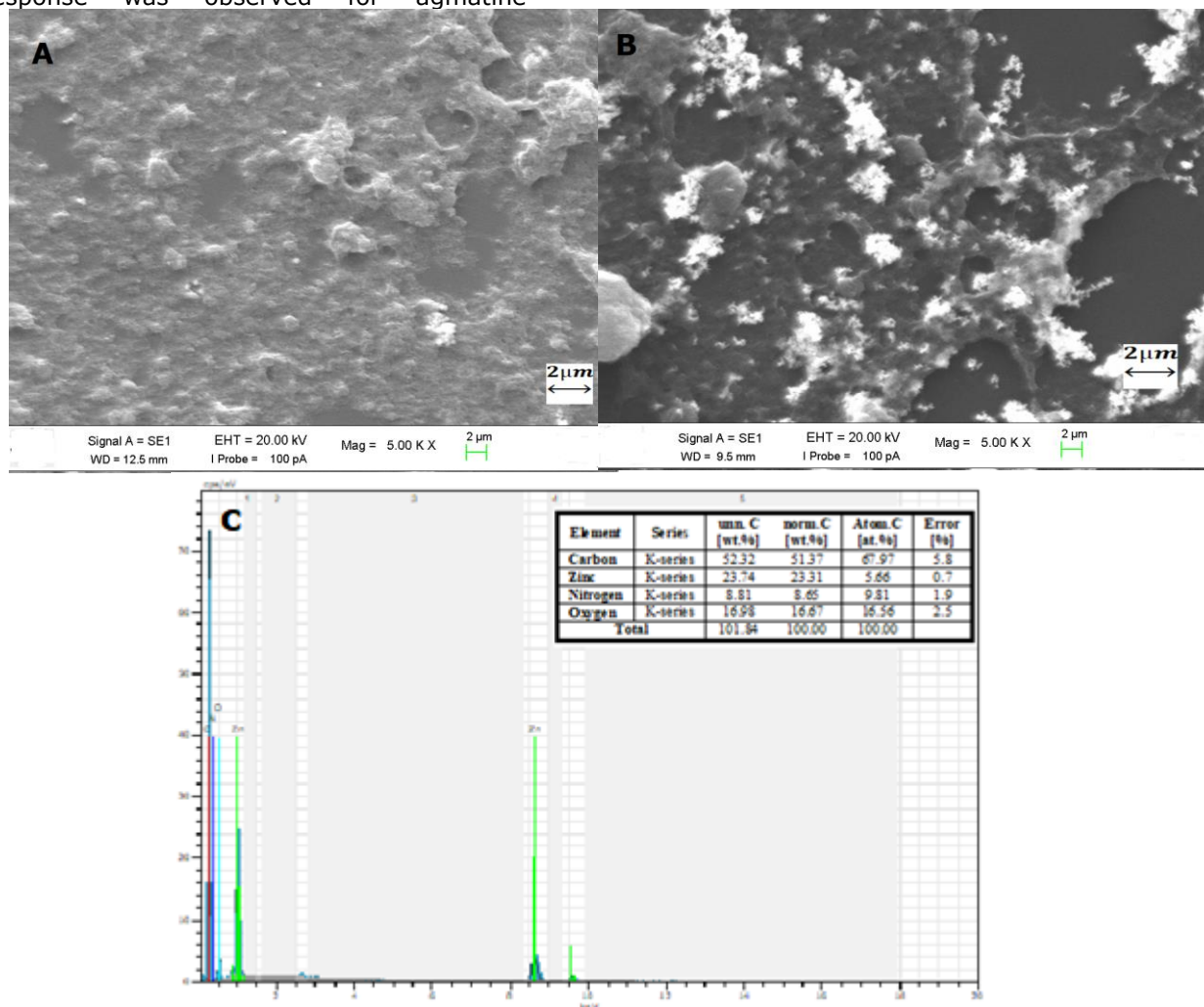| Element	Series	unn. C [wt.%]	norm.C [wt.%]	Atom.C [at.%]	Error [%]
Carbon	K-series	52.32	51.37	67.97	5.8
Zinc	K-series	23.74	23.31	5.66	0.7
Nitrogen	K-series	8.81	8.65	9.81	1.9
Oxygen	K-series	16.98	16.67	16.56	2.5
Total		101.84	100.00	100.00	

Figure 2. SEM images of **A)** MWCNTs/GC electrode surface, **B)** ZnONPs+MWCNTs/GC electrode surface, **C)** EDX analysis of ZnONPs+MWCNTs/GC electrode surface.

Electrochemical behavior of agmatine at the ZnONPs+MWCNTs/GC electrode surface

Figure 3 shows the cyclic voltammograms of the agmatine molecule on the surface of a) bare/GC, b) MWCNTs/GC, c) ZnONPs/GC and d) ZnONPs+MWCNTs/GC electrodes in PBS with 50 mM at pH 7.0. No peak was observed because no electrochemical response was detected for the agmatine molecule on the surface of the bare GC electrode (a). However, a broad and poor oxidation peak for the agmatine molecule was observed at Epa=+637.9 mV on the surface of the GC electrode modified with MWCNTs (b), while a weak and clearly undefined oxidation peak for the agmatine molecule was observed at Epa=+668.2 mV on the surface of the GC electrode modified with ZnONPs (c). Additionally, a well-defined peak with a higher current of the agmatine molecule was observed at Epa=+581.0 mV on the surface of the GC electrode modified by the hybrid

formation of MWCNTs and ZnONPs (d). Compared to the bare/GC, MWCNTs/GC and ZnONPs/GC electrode surfaces, the voltammetric behavior of agmatine was found to be greatly enhanced on the ZnONPs+MWCNTs/GC electrode surface with a large enhancement in the voltammetric current response. The observation of a higher current response for the agmatine molecule at the ZnONPs+MWCNTs/GC electrode surface is mainly due to the catalytic effect of the ZnO nanoparticles and an increase in the electron transfer rate by providing an active layer on the electrode surface (21-23). There are also studies that claim that the peak potential observed for nanoparticles of metal oxides can be attributed to the oxygen vacancies on the nanoparticles (24, 25). In addition, the voltammetric data indicates that agmatine oxidation is irreversible at the MWCNTs/GC and ZnONPs+MWCNTs/GC electrode surfaces due to the absence of any peak in the cathodic region.
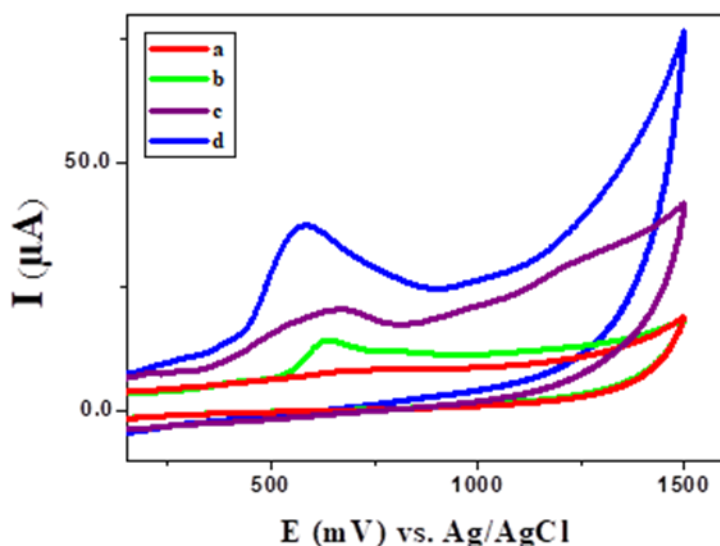
Figure 3. Cyclic voltammograms of 1.0×10^{-7} M agmatine in 50 mM PBS at pH 7.0. at a) bare/GC, b) MWCNTs/GC, c) ZnONPs/GC, d) ZnONPs+MWCNTs/GC electrode surfaces (Scan rate: 50 mV/s).

Figure 4A shows the voltammograms at different scan rates of the agmatine solution at 1.0×10^{-7} M concentration prepared in pH 7.0 PBS buffer, in order to examine the effect of the scan rate on agmatine oxidation at the ZnONPs+MWCNTs/GC electrode surface. A linear curve is obtained by plotting the peak current values against the square root of the scanning speed, indicating that the reaction is diffusion-controlled. The slope of graphic obtained by plotting the logarithm of the peak current

against the logarithm of the scanning rate is close to 0.5, suggesting that electron transfer is diffusion-controlled, while a slope closer to 1.0 indicates adsorption control (26). It was determined that the graph obtained from the plot of the peak currents against the square root of the scan rate is linear ($R^2=0.9988$) in Figure 4B, and therefore, it is thought that a diffusion-controlled reaction occurs at the electrode surface. In Figure 4C, the equation of the graph obtained from the logarithm of the

peak current versus the logarithm of the scanning rate is calculated as being y=0.4983x-3.538. The slope of the graph is 0.4983, indicating that the diffusion reaction is controlled. In addition, it has also been observed that agmatine peak potentials are shifted towards more anodic values (higher potentials) due to increased scanning speeds. When the agmatine peak potential shifts towards anodic values and the absence of any reduction peak are assessed together, it can be concluded that the oxidation of agmatine on the ZnONPs+MWCNTs/GC electrode surface is irreversible. Further, the behavior of the oxidation peak potential of the agmatine

molecule at various pH values is given in Figure 5. A shift in the negative direction of the peak potential of the agmatine molecule was observed due to the increase in pH of the solution. This indicates that the proton is transferred during the oxidation of the agmatine molecule. Also, the voltammetric signals at pH 6.0, 7.0 and 8.0 were observed at values close to each other, as shown in Figure 5. However, since the observed voltammetric signal at pH 7.0 has a relatively higher and smoother peak shape, this pH value was chosen for quantification of the agmatine molecule.
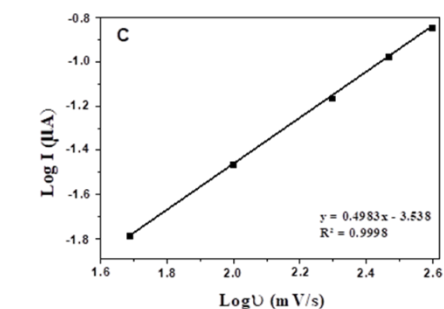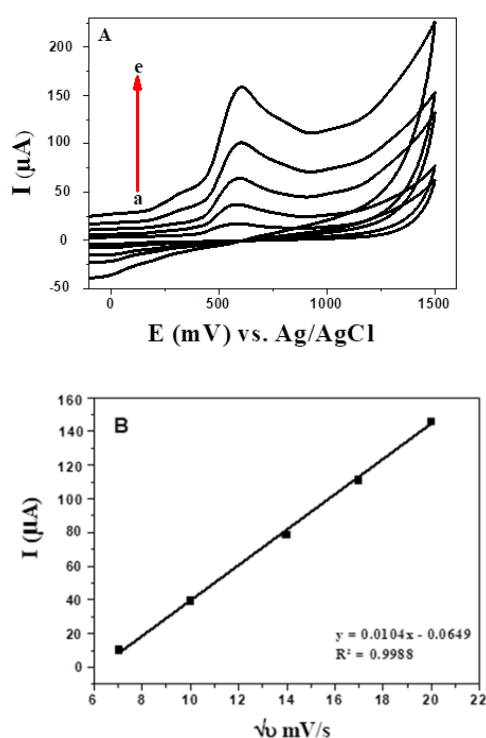
Figure 4. A) Cyclic voltammograms of 1.0×10^{-7} M agmatine at ZnONPs+MWCNTs/GC electrode in 50 mM PBS at pH 7.0. Scan rates: a) 50 mV/s; b) 100 mV/s; c) 200; d) 300 mV/s; e) 400 mV/s (Equilibrium time: 5 s); B) A plot of anodic peak current of agmatine versus the square root of scan rates at ZnONPs+MWCNTs/GC electrode surface; C) A plot of logarithm of anodic peak current of agmatine versus the logarithm of scan rates at ZnONPs+MWCNTs/GC electrode surface.
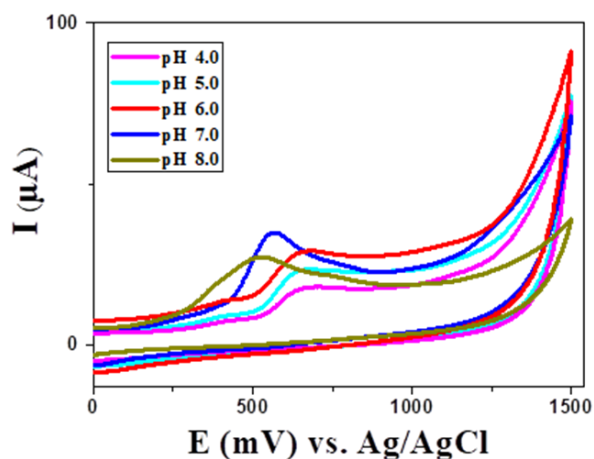
Figure 5. Cyclic voltammograms of 1.0×10^{-7} M agmatine at ZnONPs+MWCNTs/GC electrode in 50 mM PBS at pH=3.0; 4.0; 5.0; 6.0;7.0;8.0 values. (Scan rate: 50 mV/s, Equilibrium time: 5 s).

Quantification of agmatine

The quantification of agmatine was performed using the SWV technique at the ZnONPs+MWCNTs/GC electrode surface. Figure 6A exhibits square-wave voltammograms for different concentrations of agmatine at the ZnONPs+MWCNTs/GC electrode surface in 50 mM PBS at pH 7.0. A linear plot was obtained with measured peak currents versus agmatine concentrations ranging from 0.1 µM to 5.2 µM. (Figure 6B). The regression equation was calculated as Ipa(µA)=0.002C(µM)+0.0013 with a correlation coefficient of 0.9990. In addition, the detection limit (LOD) of the agmatine molecule was calculated as 4.13×10^{-8} M by using $Cm=3S_b/m$ (S_b is the standard deviation of the blank signal and m is the slope of the regression equation).
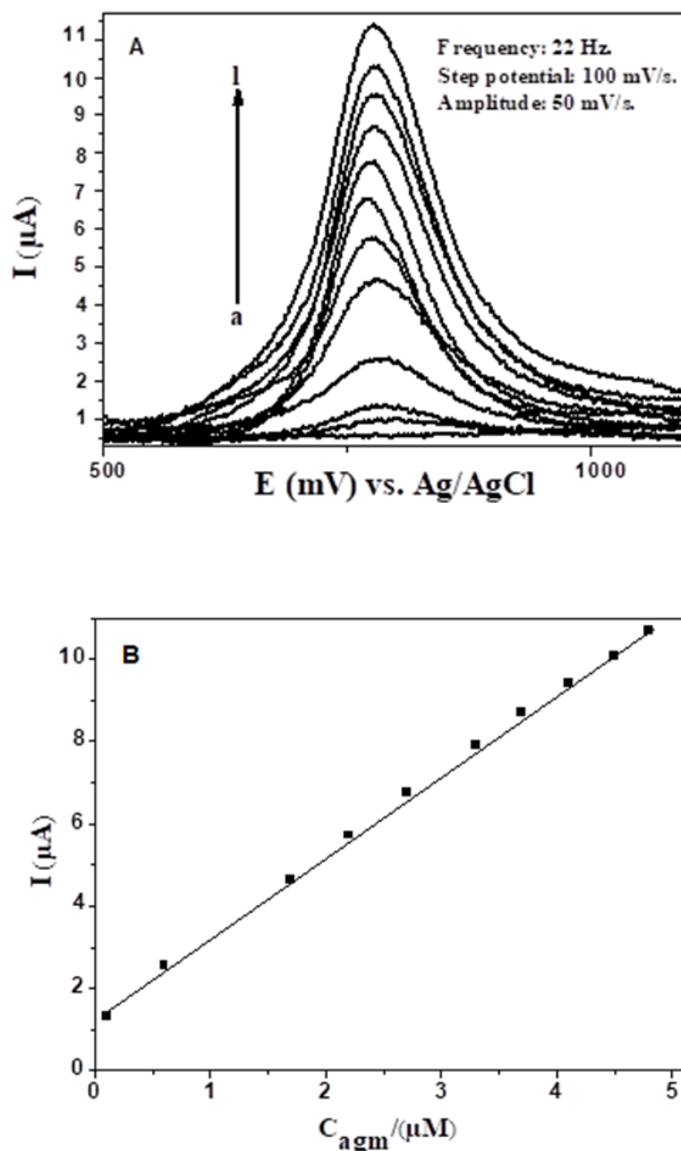
Figure 6. A) Square-wave voltammograms of various agmatine concentrations at ZnONPs+MWCNTs/GC electrode in 50 mM PBS at pH 7.0. Agmatine concentrations: a)0.0 µM b) 0.1 µM; c) 0.6 µM; d) 1.7 µM; e) 2.2 µM; f) 2.7 µM; g) 3.3 µM; h) 3.7 µM; i) 4.1 µM; j) 4.5 µM; k) 4.8 µM; l) 5.2 µM. **B)** A plot of peak currents against the concentrations of agmatine.

Stability and reproducibility of the ZnONPs+MWCNTs/GC electrode

The reproducibility of the ZnONPs+MWCNTs/GC electrode was determined by calculating the relative

standard deviation of eight consecutive runs with the electrodes prepared in two different ways. In the first method, the electrode was redeveloped every time and voltammograms were recorded. In the second, eight different electrodes were prepared in the same way and voltammograms were recorded. The RDS of both reproducibilities for 0.2 µm agmatin was calculated to be 1.8% and 1.6%, respectively. This showed that the ZnONPs+MWCNTs/GC electrode had excellent reproducibility. The stability of the ZnONPs+MWCNTs/GC electrode was also examined by incubation in PBS for 40 days. Then, the voltammograms of the incubated modified electrode were recorded in 50 mM PBS at pH 7.0 by CV and compared with the voltammograms taken before incubation. Compared to those obtained before immersing the recorded voltammograms, the change in the peak current was observed to be less than 5%. This slight reduction in current indicated that the ZnONPs+MWCNTs/GC electrode system had good stability.

Interference study

In order to verify the selectivity of the proposed electrode, the effects of some molecules that could make possible interference on the agmatine were also investigated by CV. For this purpose, voltammograms of the mixture containing 30 µM ascorbic acid (AA), 45 µM seratonin (SE) and 60 µM dopamine (DA) in the presence of 0.3 µM agmatine were taken on bare GC and ZnONPs+MWCNTs/GC electrodes. In Figure 7A, no peak currents of these molecules were observed on the bare GC electrode, whereas a broad and overlapping voltammetric peak current of DA and SE, a small and relatively distinct peak current of AA, and a clearly defined peak current of agmatine molecule were observed on the ZnONPs+MWCNTs/GC electrode. This showed that ZnO nanoparticles did not have a successful effect on the catalysis of AA, SE and DA molecules. Since AA, SE and DA have similar oxidation potentials and overlapping signals, it is already known that the detection of these species separately is a major problem on most solid electrodes (27). However, it was observed that these molecules did not have any interference effect in determining the agmatine molecule. In addition, voltamograms of increased concentrations of agmatine were also taken in the presence of AA, SE and DA. The voltamograms showed that the increased concentration of agmatine exhibited a linear increase in anodic peak currents in Figure 7B. But there was no change in AA, SE and DA peak currents. The results showed that 100-fold AA, 150-fold SE and 200-fold of DA molecules had no effect on the selective determination of the agmatine molecule in the proposed electrode.
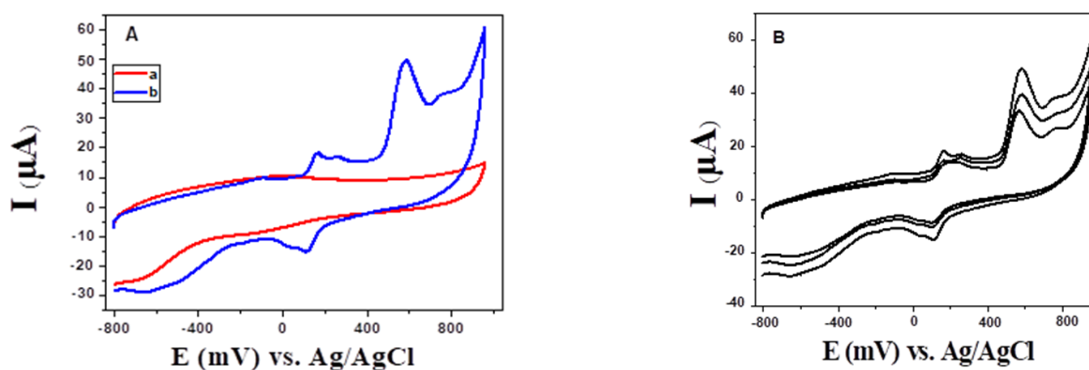
Figure 7. A) Cyclic voltammograms of 30 µM AA, 45 µM SE, 60 µM DA 0.3 µM agmatine in 50 mM PBS at pH 7.0. at a) bare/GC, b) ZnONPs+MWCNTs/GC electrode surfaces (Scan rate: 50 mV/s). **B)** Cyclic voltammograms of increasing concentrations of agmatine in the presence of 30 µM AA, 45 µM SE, 60 µM DA at ZnONPs+MWCNTs/GC in in 50 mM PBS at pH 7.0. (Agmatine concentrations: 0.1 µM, 0.2 µM, 0.3 µM)

CONCLUSIONS

An electrode surface system prepared with a multi-walled carbon nanotubes (MWCNTs) hybrid decorated with ZnOPs was designed to quantify agmatine molecules quickly, economically, and reliably. The ZnONPs+MWCNTs/GC electrode system was performed to quantifying agmatine using SWV. A linear plot of the current-concentration calibration graph in the range of 0.1 µM to 5.2 µM was obtained with a detection limit of $4.13×10^{-8}$ M. In accordance with the direction of this data, the rapid and reliable determination of the agmatine molecule,

which causes schizophrenia and is secreted in the brain, makes this electrode system of great interest for drug development studies and clinical use.

ACKNOWLEDGMENT

REFERENCES

1. Singh T, Bagga N, Kaur A, Kaur N, Gawande DY, Goel RK. Agmatine for combined treatment of epilepsy, depression and cognitive impairment in chronic epileptic animals. Biomedicine & Pharmacotherapy. 2017;92:720-5.

2. Freitas AE, Neis VB, Rodrigues ALS. Agmatine, a potential novel therapeutic strategy for depression. European Neuropsychopharmacology. 2016;26(12):1885-99.

3. Gilad GM, Salame K, Rabey JM, Gilad VH. Agmatine treatment is neuroprotective in rodent brain injury models. Life sciences. 1995;58(2):PL41-PL6.

4. Feng Y, LeBlanc MH, Regunathan S. Agmatine reduces extracellular glutamate during pentylenetetrazole-induced seizures in rat brain: a potential mechanism for the anticonvulsive effects. Neuroscience letters. 2005;390(3):129-33.

5. Reis DJ, Regunathan S. Is agmatine a novel neurotransmitter in brain? Trends in pharmacological sciences. 2000;21(5):187-93.

6. Benítez J, García D, Romero N, González A, Martínez-Oyanedel J, Figueroa M, et al. Metabolic strategies for the degradation of the neuromodulator agmatine in mammals. Metabolism-Clinical and Experimental. 2018;81:35-44.

7. Bahremand T, Payandemehr P, Riazi K, Noorian AR, Payandemehr B, Sharifzadeh M, et al. Modulation of the anticonvulsant effect of swim stress by agmatine. Epilepsy & Behavior. 2018;78:142-8.

8. Gawali NB, Bulani VD, Chowdhury AA, Deshpande PS, Nagmoti DM, Juvekar AR. Agmatine ameliorates lipopolysaccharide induced depressive-like behaviour in mice by targeting the underlying inflammatory and oxido-nitrosative mediators. Pharmacology Biochemistry and Behavior. 2016;149:1-8.

9. Uzbay TI. The pharmacological importance of agmatine in the brain. Neuroscience & Biobehavioral Reviews. 2012;36(1):502-19.

10. Uzbay T, Goktalay G, Kayir H, Eker SS, Sarandol A, Oral S, et al. Increased plasma agmatine levels in patients with schizophrenia. Journal of psychiatric research. 2013;47(8):1054-60.

11. Kotagale NR, Taksande BG, Wadhwani PJ, Palhade MW, Mendhi SM, Gawande DY, et al. Psychopharmacological study of agmatine in behavioral tests of schizophrenia in rodents. Pharmacology Biochemistry and Behavior. 2012;100(3):398-403.

12. Uzbay IT, Kayir H, Göktalay G, Yildirim M. P. 3. b. 004 Agmatine induces schizophrenia-like symptom in Wistar rats. European Neuropsychopharmacology. 2008;18:S399.

13. Zhang M, Wang S, Li T, Chen J, Zhu H, Du M. Nitrogen and gold nanoparticles co-doped carbon nanofiber hierarchical structures for efficient hydrogen evolution reactions. Electrochimica Acta. 2016;208:1-9.

14. Baytak AK, Duzmen S, Teker T, Aslanoglu M. Voltammetric determination of methylparaben and its DNA interaction using a novel platform based on carbon nanofibers and cobalt-nickel-palladium nanoparticles. Sensors and Actuators B: Chemical. 2017;239:330-7.

15. Wang L, Pumera M. Electrochemical catalysis at low dimensional carbons: Graphene, carbon nanotubes and beyond–A review. Applied Materials Today. 2016;5:134-41.

16. Rahman MM, Ahmed J. Cd-doped Sb_2O_4 nanostructures modified glassy carbon electrode for efficient detection of melamine by electrochemical approach. Biosensors and Bioelectronics. 2018;102:631-6.

17. Ramamoorthy C, Rajendran V. Synthesis and characterization of CuS nanostructures: Structural, optical, electrochemical and photocatalytic activity by the hydro/solvothermal process. International Journal of Hydrogen Energy. 2017;42(42):26454-63.

18. Baytak AK, Teker T, Duzmen S, Aslanoglu M. A composite material based on nanoparticles of yttrium (III) oxide for the selective and sensitive electrochemical

determination of acetaminophen. Materials Science and Engineering: C. 2016;66:278-84.

19. Baghayeri M, Zare EN, Lakouraj MM. A simple hydrogen peroxide biosensor based on a novel electro-magnetic poly (p-phenylenediamine)@ Fe3O4 nanocomposite. Biosensors and bioelectronics. 2014;55:259-65.

20. Baytak AK, Teker T, Duzmen S, Aslanoglu M. A sensitive determination of terbutaline in pharmaceuticals and urine samples using a composite electrode based on zirconium oxide nanoparticles. Materials Science and Engineering: C. 2016;67:125-31.

21. Xu C-X, Huang K-J, Fan Y, Wu Z-W, Li J, Gan T. Simultaneous electrochemical determination of dopamine and tryptophan using a TiO2-graphene/poly (4-aminobenzenesulfonic acid) composite film based platform. Materials Science and Engineering: C. 2012;32(4):969-74.

22. Baytak AK, Aslanoglu M. Voltammetric quantification of tryptophan using a MWCNT modified GCE decorated with electrochemically produced nanoparticles of nickel. Sensors and Actuators B: Chemical. 2015;220:1161-8.

23. Ye D, Luo L, Ding Y, Liu B, Liu X. Fabrication of Co 3 O 4 nanoparticles-decorated graphene composite for determination of L-tryptophan. Analyst. 2012;137(12):2840-5.

24. Wei M-Y, Huang R, Guo L-H. High catalytic activity of indium tin oxide nanoparticle modified electrode towards electro-oxidation of ascorbic acid. Journal of Electroanalytical Chemistry. 2012;664:156-60.

25. Yang J, Lin C, Wang Z, Lin J. In (OH) 3 and In2O3 nanorod bundles and spheres: microemulsion-mediated hydrothermal synthesis and luminescence properties. Inorganic chemistry. 2006;45(22):8973-9.

26. Sanguansak Y, Srimuk P, Krittayavathananon A, Luanwuthi S, Chinvipas N, Chiochan P, et al. Permselective properties of graphene oxide and reduced graphene oxide electrodes. Carbon. 2014;68:662-9.

27. Fayemi OE, Adekunle AS, Ebenso EE. Electrochemical determination of serotonin in urine samples based on metal oxide nanoparticles/MWCNT on modified glassy carbon electrode. Sensing and Bio-Sensing Research,2017;13: 17-27.

Supercritical Carbondioxide Extraction of *Lavandula Officinalis* (Lavender) and *Hypericum Perforatum* (Centaury) Plants Grown in Mersin Region: Investigation of Antioxidant and Antibacterial Activities of Extracts and Usage as Cosmetic Preservatives in Creams

Göktürk AVŞAR[1] ✉ iD **, Derya YÜKSEL[1] , Fatih Mehmet EMEN[2]** ✉ **, Ruken Esra DEMiRDÖĞEN[3]** ✉ **, Tuncay YEŞİLKAYNAK[4]** ✉ **, Levent KAHRIMAN[5]** ✉

[1]Mersin University, Faculty of Science and Letters, Department of Chemistry, Mersin, TURKEY
[2]Mehmet Akif Ersoy University, Faculty of Arts and Sciences, Department of Chemistry, Burdur, TURKEY
[3]Çankırı Karatekin University, Faculty of Science, Department of Chemistry, Çankırı, TURKEY
[4]Department of Chemistry Technology, Afsin Vocational School, Sütcü Imam University, Kahramanmaras, TURKEY
[5]Laber Organic Cosmetics R & D Production, Marketing, Industry Trade Co., İzmir, TURKEY

Abstract: The extraction of *Lavandula Officinalis* (lavender) and *Hypericum Perforatum* (centaury) plants grown in Mersin region were extracted by supercritical carbon dioxide extraction system (P=100 bar, T=40 °C). The chemical compositions of the lavender and centaury extracts were analyzed by Gas Chromatography–Mass Spectrometry (GC-MS). For antioxidant activity experiments, 1,1-diphenyl-2-picrylhidrazine (DPPH) radical was used in radical effect tests. For antimicrobial activity studies, *Bacillus subtilis, Klebsiella pneumoniae, Escherichia coli, Staphylococcus aureus, Pseudomonas aeruginosa* and *Streptococcus pneumoniae* with Nutrient Agar Broth (NA) and Eosin Methylene-blue lactose sucrose agar (EMB) broth were used. For determining antimicrobial effect of plant extracts, diffusion method was used. Antibacterial and antioxidant properties of the obtained extracts were examined and have been determined that the resulting extracts have significant antioxidant and antimicrobial effects. The extracts were also used in cosmetic cream formulas as protectives. Effective results have also been determined in antibacterial activity studies of creams after 6 months.

INTRODUCTION

Plants are one of the most essential fundamental resources of life ever since the beginning of human kind because of their useful bioactive compounds such as lipids, phytochemicals, pharmaceutics, flavors, fragrances, and pigments. Oils and extracts of plants are still being used in many applications such as food preservation, cosmetics, pharmaceuticals, alternative medicine and natural therapies. Plant oils and extracts can be used to prevent the formation of microorganisms that cause many diseases and they also provide protection against pathogenic bacteria that pose a threat to human health due to their antioxidant and antibacterial properties. Previous studies have shown that there is a correlation between antioxidant from plants and oxidative stress and age-dependent diseases (1-5).

Turkey is one of the leading countries in plant trade with its geographical place, climate and plant variety, agricultural potential, and wide surface area. Especially, Mersin region is a commercially important location due to the plant variety. In addition, Mersin has a significant share in plant trading with about 60% of plants in Turkey. *Lavandula officinalis* (Lavender) and *Hypericum perforatum* (Centaury) plants have an important place in the flora of Turkey after *Rosa damascena* Mill (rose).

Hypericum perforatum   Lavandula officinalis

Plant extracts are being produced by mainly conventional techniques such as hydro and steam distillation and solvent extraction methods which have several disadvantages. In these methods, heat-sensitive compounds can easily be destroyed while performing the extraction and the quality of oil extracts is extremely impaired (6,7).

In recent years, supercritical carbon dioxide (scCO$_2$) extraction has been started to be used as an alternative technique for the extraction of essential oil and extracts of plants since it has several advantages such as non-toxic, non-explosive and readily available, and solvent-free production (7).

In this study, extracts of lavender and centaury plants grown in Mersin region were extracted by scCO$_2$ extraction method which is eco-friendly. Antibacterial and antioxidant properties of the obtained extracts were examined.

MATERIAL AND METHODS

Plant material
Lavender and centaury plants grown in Mersin region from Turkey were dried in the air without exposure to sunlight and stored at room temperature.

Supercritical CO$_2$ Extraction
10 grams of milled flowers of lavender and centaury plants were loaded into a 100 mL stainless steel extraction vessel, which was then pressurized via a CO$_2$ pump (ISCO Model 260D Syringe pump). Plants were extracted by scCO$_2$ extraction system as seen in Scheme 1. (P=145 bar, T=45 $^\circ$C for lavender and P=150 bar, T=40 $^\circ$C for centaury).
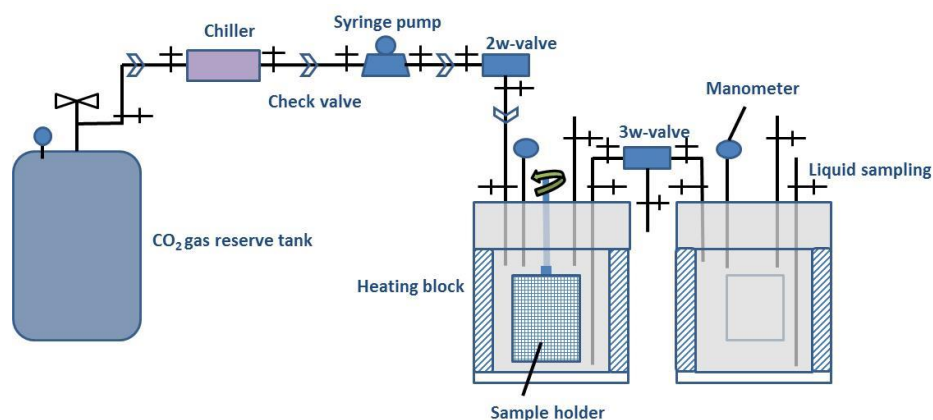
Scheme 1. Supercritical CO$_2$ extraction system.

Chemical Analysis
The chemical composition of the lavender and centaury extracts were analyzed by Gas Chromatography–Mass Spectrometry (GC-MS) and GC. The GC-MS analyses were performed on a Agilent Technologies 7890 A GC system with a HP-5MS capillary column (30.0 m x 0.25 mm; film thickness 0.25 µm) coupled with an Agilent Technologies 5975 mass selective detector. Injector and detector temperatures were set to 220 $^\circ$C and 260 $^\circ$C, respectively for operating GC analysis. The helium flow rate was 1.0 mL/min for GC.

Antioxidant Activity Assay

Six different concentrations (3-9 mg/mL) of the lavender and centaury extracts were prepared for antioxidant activity measurement. 1,1-Diphenyl-2-picrylhydrazine (DPPH) radical was used to determine the radical scavenging effect. Different concentrations of plant extracts were prepared with equal volumes of ethanolic solution of DPPH (100 µL) and incubated in the dark for 1/2 hour. The experiments were carried out at three different time intervals. Butylhydroxytoluene (BHT) was used as standard controls. The absorbance was then measured by a UV-visible spectrophotometer at a wavelength of 515 nm. DPPH solution was used as control (A$_0$). The radical scavenging effect was calculated as inhibition percentage from the following formula:

DPPH scavenging effect (%) = [(A$_0$-A$_1$) / A$_0$] x100   (Eq. 1)

A$_0$ = absorbance of control (DPPH solution), A$_1$ = Absorbance measured in the presence of sample.

Antibacterial Activity Assay
For antimicrobial activity experiments, bacteria were obtained from the Microbiology Laboratory of the Biology Department of the Faculty of Science and Letters of Mersin University. Three strains of gram-positive bacteria *Bacillus subtilis*, *Staphylococcus aureus* and *Streptococcus pneumoniae* were used for Nutrient Agar (NA) media. Three strains of gram negative bacteria *Escherichia coli*, *Klebsiella pneumoniae*, *Pseudomonas aeruginosa* were used for Eosin Methylene-blue lactose sucrose agar (EMB) media. The diffusion method was used to determine the antimicrobial effect of plant extracts. Mueller-Hinton Agar (MHA) was used as a nutrient in this method, which is based on the inhibition of the development of microorganisms in the field where the substance to be tested diffused in the agar. MHA nutrient was prepared by dissolving 2 g of meat infusion, 17.5 g of casein hydrolyzate, 1.5 g of starch and 17 g of agar in 1000 mL distilled water (pH 7.2).

Prior to the test, the colonies in cultures incubated for 18-24 hours in Nutrient Agar were solubilized using physiological saline in equal turbidity to 0.5 McFarland standard solution. Then, the prepared solution was diluted to contain about 1-5 X 10^6 bacteria and used as inoculum. 100 µL of the prepared inoculum was transferred to the MHA surface and spread and immediately afterwards 10 mm holes were drilled in the medium. After transferring 200 µL per well of plant extracts (50 mg/mL), the petrel was incubated at 37 °C for 24-48 hours. At the end of the incubation, formation of open zone (area where microorganism could not grow) was observed around the holes where plant extracts were transferred. The resulting zone diameters are measured in mm. All tests were performed in 3 repetitions and the standard deviation of the zone diameters was calculated (Figure 1). After adding the extracts in cream formulation as preservatives, antibacterial activity measurements were performed at the first month (t$_0$), third month (t$_1$) and 6th month (t$_2$) (Figures 2 and 3).
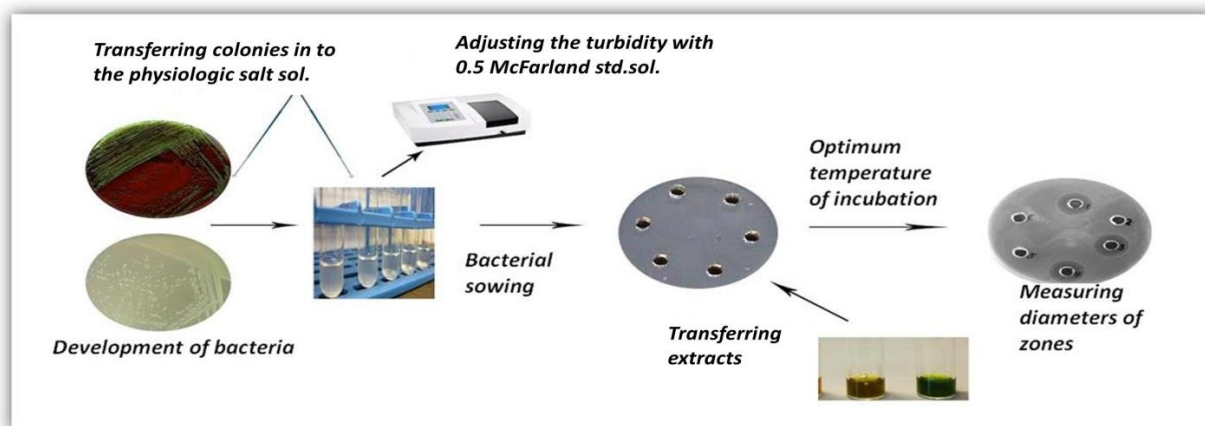
Figure 1. Antibacterial activity determination method

RESULTS AND DISCUSSION

Extraction Yield
Lavender and centaury plants were extracted by scCO$_2$ extraction system. The extraction yields for lavender and centaury were 4.68% and 3.83%, respectively.

Chemical Composition
Main chemical compositions of centaury and lavender extracts are given in Tables 1 and 2, respectively.

Table 1. Main composition of the supercritical CO_2 extract of centaury.

Compound	Content (%)
Menthone	0.44
(+)-Isomenthone	0.21
L-Menthol	2.42
Caryophyllene oxide	1.38
Cyclotetradecane	1.82
3-Tetradecene	3.80
2-Pentadecanone	1.29
7-Hexadecene	2.86
1,2-Benzenedicarboxylic acid	13.43
Phytol	7.12
n-Tricosane	1.27
n-Octacosane	1.47
n-Dotriacontane	1.36
n-Tetratriacontane	22.61
Hexacosanal	4.19

Table 2. Main composition of the supercritical CO_2 extract of lavender.

Compound	Content (%)
1-Octen-3-ol	0.28
1,8-Cineole	1.15
α-Terpinene	0.17
Linalool	36.20
Camphor	8.03
Borneol	6.65
Lavandulol	0.49
Terpinen-4-ol	2.13
α-Terpineol	0.70
Linalyl acetate	19.37
Lavandulyl acetate	1.32
β-Farnesene	3.53
Germacrene D	0.88
α-Bisabolol	1.06

Antioxidant Activity

The free radical scavenging activities of centaury and lavender extracts are given in Tables 3 and 4, respectively. The inhibition rates of the plant extracts were examined. It was observed that as the inhibition times and concentration increased, the radical scavenger activity increased**.**

Table 3. DPPH scavenging effects of centaury *(inhibition %).*

Concentration/ time	3 mg/mL	4 mg/mL	5 mg/mL	6 mg/mL	7 mg/mL	8 mg/mL	9 mg/mL
0 min.	80.7	81.7	83.7	87.8	89.6	91.3	93.3
15 min.	85.0	82.6	84.8	87.9	90.7	92.1	94.2
30 min.	86.7	87.1	88.2	89.0	91.4	96.2	97.1

Table 4. DPPH scavenging effects of lavender *(inhibition %).*

Concentration/ Time	3 mg/mL	4 mg/mL	5 mg/mL	6 mg/mL	7 mg/mL	8 mg/mL	9 mg/mL
0 min.	0	7.9	8.7	14.9	12.2	21.8	23.8
15 min.	4.3	14.4	11.6	21.6	24.0	32.3	35.6
30 min.	7.3	17.9	13.8	26.2	28.5	37.8	40.9

Antibacterial Activity

Antibacterial activity of plants extracts was determined with the zone diameters by the agar disc diffusion method, given in Table 5. Gram-negative bacteria *Escherichia coli, Klebsiella pneumoniae*, and *Pseudomonas aeruginosa* are pathogenic bacteria that cause diseases. Gram-positive bacteria *Bacillus subtilis*, *Staphylococcus aureus* and *Streptococcus pneumoniae* are known as non-noxious bacteria. According to the results, the plant extracts inhibit the formation of gram-positive and gram-negative bacteria. Antibacterial effect of lavender extract was higher than that of the centaury *extract.*

Table 5. Antibacterial activity test results of plant extracts.

BACTERIA	Gram	Lavender (mm)	Centaury (mm)
Streptococcus pneumoniae	+	32.7 ± 2.5	12.0 ± 1.0
Escherichia coli	-	24.7 ± 0.6	10.7 ± 0.6
Staphylococcus aureus	+	37.0 ± 1.7	11.7 ± 0.6
Klebsiella pneumoniae	-	25.7 ± 1.5	10.3 ± 0.6
Pseudomonas aeruginosa	-	18.7 ± 1.2	10.0 ± 1.0
Bacillus subtilis	+	31.3 ± 1.2	14.3 ± 1.5

The Use of Plant Extracts in Cosmetic Creams

The extracts of lavender and centaury plants were added to standard cream formulations as preservatives with a ratio of 2%, 3% and 4% and their antibacterial properties were examined. Phenoxyethanol was used as a preservatives for the same purpose of preserving the same amount of creams for comparison. Finally the non-protective cream is prepared. Samples were taken from the prepared creams at the first month (t_0), third month (t_1) and 6th month (t_2) for measurements of the number of the bacteria (Table 6).

Table 6. Bacterial formation values of different time and concentrations in creams with and without preservatives.

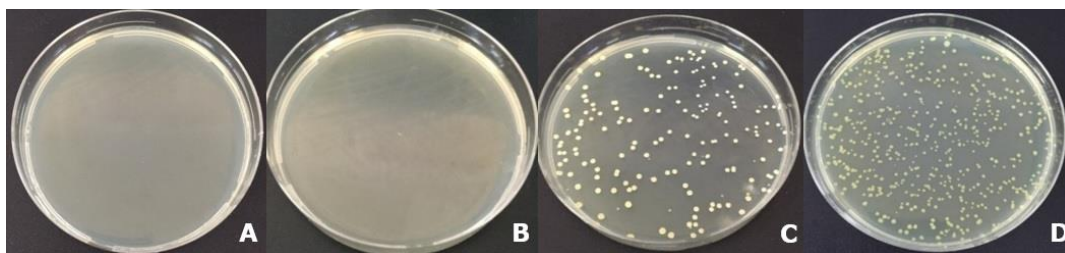|			Cream with Lavender Extract			Cream with Centaury Extract			Cream with preservatives			Cream without preservatives
			Concentration			Concentration			Concentration			
			2%	3%	4%	2%	3%	4%	2%	3%	4%	
Nutrient Agar (NA)	TIME	t_0	10	6	1	7	3	0	0	0	0	0
		t_1	0	0	0	0	0	0	0	0	1	4
		t_2	0	0	0	0	0	0	1	0	185	944
EMB Agar		t_0	0	0	0	0	0	0	0	0	0	0
		t_1	0	0	0	0	0	0	0	0	0	10
		t_2	0	0	0	0	0	0	0	0	0	896

Figure 2. Bacterial growth on Nutrient Agar (NA) medium at the end of the 6th month (t_2) of cream samples added to 4% plant extract, **A;** cream with lavender extract, **B;** cream with centaury extract, **C;** cream with preservative, **D;** cream without preservative.
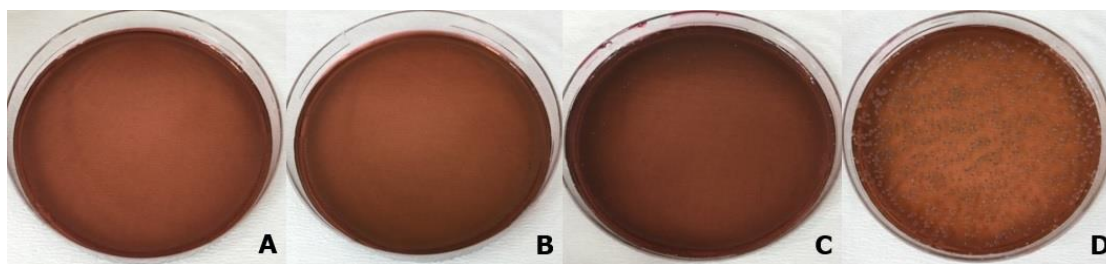
Figure 3. Bacterial growth on Eosin Methylene-Blue. Lactose Sucrose Agar (EMB) medium at the end of the 6th month (t_2) of cream samples added to 4% plant extract, **A;** cream with lavender extract, **B;** cream with centaury extract, **C;** cream with preservative, **D;** cream without preservative.

CONCLUSIONS

Creams are the cosmetic products used frequently in our daily life. In addition, properties such as preservatives, moisturizers and nutrients, these products must be suitable for long-term and daily use in terms of microbiology. Due to the substances present in the composition of cosmetic products, microorganisms that occur during or after production cause contamination. Metabolites resulting from contamination are known for their damages to the skin. In recent years, plant extracts have started to be used instead of chemical preservatives used to prevent contamination. While the upper limit of the number of non-pathogenic microorganisms that cosmetic products may contain is 10^3, it is known that it should not contain pathogenic microorganisms that poses a danger to human health (8-10).

In this study, the extracts of lavender and centaury plants were also used in cosmetic cream formulas as protectives. It has been determined that the resulting extracts have significant effects even after 6 months passed as seen in Figures 2 and 3.

According to the results, $scCO_2$ extraction is useful technique for extraction of essential oils from lavender and centaury. Moreover, these extracts can be used in cosmetics as preservatives in creams. Due to their antioxidant and antibacterial effects, the extracts may also be used in pharmaceutical and food industries.

ACKNOWLEDGEMENTS

REFERENCES

1. Hammer KA, Carson CF, Riley TV. Antimicrobial activity of essential oils and other plant exracts. Jourmal of Applied Microbiology. 1999; (86): 985-90.

2. Prabuseenivasan S, Jayakumar M, Ignacimuthu S. In vitro antibacterial activity of some plant essential oils. BMC Complementary and Alternative Medicine. 2006; (6):39.

3. Wang L, Weller CL. Recent advances in extraction of nutraceuticals from plants. Trends in Food Science & Technology. 2006; (17): 300–12.

4. Zou Y, Lu Y, Wei D. Antioxidant Activity of a Flavonoid-Rich Extract of Hypericum perforatum L. In Vitro. J. Agric. Food Chem. 2004; (52): 5032-9.

5. Robu S, Aprotosoaie AC, Miron A, Cioanca O, Stanescu U, Hancianu M. In Vitro Antioxidant Activity of Ethanolic Extracts from Some Lavandula Species Culti Ated in Romania. Farmacia. 2012; (60): 3.

6. Danh TL, Han LN, Triet NDA, Zhao J, Mammucari R, Foster N. Comparison of Chemical Composition, Antioxidant an Antimicrobial Activity of Lavender (Lavandula angustifolia L.) Essential Oils Extracted by Supercritical CO_2, Hexane and Hydrodistillation. Food Bioprocess Technol. 2003; (6): 3481-9.

7. Pourmortazavi SM, Hajimirsadeghi SS. Supercritical fluid extraction in plant essential and volatile oil analysis. J. Chromatogr. A. 2007; (1163): 2–24.

8. Çelik GY and Çelik E, Antimicrobial Properties of Plant Essential Oils. Orlab On-Line Journal of Microbiology. 2007; 5(2): 1-6.

9. Underwood E et al. Ecology of Microorganisms as It Affects the Pharmaceutical Industry. Pharmaceutical Microbiology. 6th ed. Oxford: Blackwell Science. 1998, 339-54.

10. Smart R and Spooner DF. Microbiological Spoilage in Pharmaceuticals and Cosmetics. J. Soc. Cosmet. Chem. 1972; (23): 721-37.

RESEARCH ARTICLE

Synthesis of Dihydrobenzofuranone Derivatives with Biotechnological Methods

Zerrin ZERENLER ÇALIŞKAN* ✉ **, Ebru Nur AY** ✉

[1]Yildiz Technical University, Faculty of Science and Arts, Department of Molecular Biology and Genetics, Davutpasa Campus, Davutpasa St. No: 127, Esenler 34210, Istanbul-TURKEY

Abstract: Benzofuranone derivatives have important skeletons which are widely present in various biologically active molecules, thus, synthesis of optically pure compounds presents great interest for medicinal chemistry. In our study, the enantioselective synthesis of 4-oxo-6-phenyl-4,5,6,7-tetrahydrobenzofuran-5-yl acetate **(3)** and 4-oxo-6-phenyl-4,5,6,7-tetrahydrobenzofuran-5-ol derivative **(4)** was achieved for the first time. Several lipases were used for the kinetic resolution of different pH values and different solvent systems of racemic 4-oxo-6-phenyl-4,5,6,7-tetrahydrobenzofuran-5-yl acetate (*rac*-**3**) in which the lipases from HPL, PPL, RNL and PCL displayed high enantioselectivity towards 4-oxo-6-phenyl-4,5,6,7-tetrahydrobenzofuran-5-ol derivative **(4)** at pH=7.

INTRODUCTION

The compounds bearing a benzofuranone skeleton are found to have potential for large scale implementation as pharmacological agents because of their biological activity (1).

The benzofuranone derivatives with important biological activity are present in a large range of natural products and also therapeutic substances. Therefore, benzofuranone derivatives are encouraged in the design and synthesis of thousands of benzofuranone-containing pharmaceuticals (2). Some benzofuranone-containing drugs are capable lead compounds that could possibly be useful as potent anti-tumor agents against several human cancer cell lines (3-10).

It is known that benzofuranones are significant intermediates used in the synthesis of natural products. For example, the use of benzofuranone is reported as a most important intermediate for the main and total synthesis of taxol (7).

There is demand for the development of synthetic methodologies leading to the structure of chiral benzofuranone-type compounds, considering the attractive pharmaceutical effects and different biological properties of the afore-mentioned

natural products, drugs and other related products.

The synthesis of drugs discovered through efficient stereoselective synthetic methods is one of the most current industrial research subjects. There are significant variations in the pharmacological activities of the enantiomers. There are chiral receptor domains in the human body, which interact only with drug molecules with an acceptable absolute configuration. For this reason, the relationship between molecular chirality and pharmacological activity is very important in pharmacology (11).

Nowadays, with the discovery of modern medicines, the prominence of enzymatic kinetic solution reactions has emerged (12,13). From the broad range of enzymatic classes, lipases have improved and have attracted attention owing to their stereoselective-wide substrate, ease of use, non-requirement of added cofactors and low cost (14, 15). These kinds of enzymes are also used in the enantioselective hydrolysis of acetoxy enones which are widely used in enantioselective esterification reactions of optically active alcohols, carboxylic acids and esters in organic solvents (16).

In the literature, there are not many examples of enzymatic resolution of 4-oxo-tetrahydro benzofuranone derivatives which have multifunctional structural benefits. For this reason, it is important to develop new methods for preparing benzofuranone derivatives, which are significant compounds in pharmacy in enantiomerically pure form. In the synthetic procedure, new benzofuranone derivatives with optically pure form were obtained under the guidance of our previous work (17, 18). As a part of our ongoing research, we examined the reaction of compound **2** via Mn(OAc)$_3$ and 4-oxo-6-phenyl-4,5,6,7-tetrahydrobenzofuran-5-yl acetate (*rac***-3)** was obtained . Afterwards, these

compounds can be used as important intermediates in medicinal chemistry. Kinetic resolution was performed in the presence of various lipase enzymes of different pH values and different solvent systems. Therefore, optically active α-hydroxy derivative was achieved as a high enantiomerically pure compound.

EXPERIMENTAL

Materials and methods
NMR spectra were obtained on a Bruker Avance III spectrometer at 500 MHz. Chemical shifts δ are reported in ppm relative to CDCl$_3$ (^{1}H: δ=7.27), CDCl$_3$ (^{13}C: δ=77.0) and CCl$_4$ (^{13}C: δ=96.4) as internal standards. Column chromatography was performed on silica gel 60 (40-63 μm). TLC was implemented on silica gel 60F$_{254}$ (Merck), and the spots were observed with UV light (λ=254 nm). IR spectra were recorded on a Perkin Elmer Spectrum 100 FT-IR Spectrometer. Enantiomeric excesses were defined by HPLC analyses using an Agilent 1100 Series supplied with a suitable chiral phase column. Lipases WGL (Wheat Germ Lipase) BioChemika (62306), CAL B (*Candida Antarctica* Lipase B) BioChemika (62288), CCL (*Candida Cyclindracea* Lipase) BioChemika (62316), HPL (Hog Pancreas Lipase) BioChemika (62300), MJL (*Mucor Javanicus* Lipase) BioChemika (62304), PLL (*Pseudomonas Lipoprotein* Lipase) BioChemika (62335), PCL (*Penicillum Camemberti* Lipase) BioChemika (96888), PRL (*Penicillum Roqueforti* Lipase) BioChemika (62323), and CRL (*Candida Rugosa* Lipase) BioChemika (74793) were taken from a Fluka lipase basic kit (62327). Only Amano Lipase PS from *Burkholderia Cepacia* (*Pseudomonas Cepacia*) was obtained from Aldrich (534641). Optical rotations were determined with Bellingham Stanley ADP-410 electronic-automation Sucromat digital automatic saccharimeter. Mass spectra were measured with

an Agilent G6530B instrument quadrupole time of flight LC/MS instrument.

General Procedure for the synthesis of 4-oxo-4,5,6,7-tetrahydrobenzofuran (19)

Chloroacetaldehyde (C_2H_3ClO, 40% solution, 20 mL) and $NaHCO_3$ (10 g) were added into water (80 mL) at 0-5 °C. To this mixture, an aqueous solution of 5-phenyl-1,3-cyclohexanedione **(1)** (1880 mg/9 mL) was added drop wise (0.4 mL/min) with stirring. After the addition, the reaction mixture was further stirred overnight at room temperature. Throughout the reaction, the acidity of the solution was within pH=6-9. To the mixture, ethyl acetate (*ca*. 100 mL) was added, and the resulting solution was acidified (pH=1) and stirred for 1 hour. The organic layer was separated, washed with aqueous K_2CO_3 solution, dried over $MgSO_4$, and concentrated. The crude product was purified by column chromatography (1:1:6 EtOAc: n-hexane: $CHCl_3$) to yield 6,7-dihydro-6-phenylbenzofuran-4 (5H) -one **(2).**

General procedure for Mn(OAc)₃ oxidation

7.5 mmol $Mn(OAc)_3$ in 100 mL benzene–acetic acid (10:1) was refluxed. To this solution, 1.8 mmol of benzofuranone was added and reflux was continued for 42 h. After all the starting material was consumed, the reaction mixture was extracted with diethyl ether and the organic layer was washed with brine. The resulting organic phase was dried over $MgSO_4$ and concentrated under vacuum. The crude product was purified by column chromatography (1.5:10:0.5 EtOAc: *n*-hexane: $CHCl_3$) to yield acetoxy-benzofuranone.

General procedure for the lipase-catalyzed kinetic resolution

Lipase (200-300 mg) was dissolved in phosphate buffer (pH 7, 300 μL) and added to a solution of the pure substrate (0.5 mmol) in the solvent (3 mL) and the reaction mixture was left to shake at 37 °C. Conversion was monitored by TLC and HPLC up to 50%. Then, the filtrate was extracted

with chloroform, dried over $MgSO_4$, concentrated and purified by column chromatography (1:7:1 EtOAc: Hexane: $CHCl_3$).

6,7-Dihydro-6-phenylbenzofuran-4 (5H)-one (2)

Yield: 127.2 mg, 60%. IR ($CHCl_3$) ν = 1673.14 cm⁻¹. ¹H NMR (500 MHz, $CDCl_3$) δ (ppm): 2.79 (m, 2H), 3.14 (m, 2H), 3.57 (m, 1H), 6.74 (d, J = 1.6 Hz, 1H), 7.31 (m, 5H). ¹³C NMR (500 MHz, $CDCl_3$) δ (ppm): 31.20, 41.37, 45.02, 106.54, 121.04, 126.75, 127.29, 128.92, 142.46, 143.46, 166.34, 193.07.

4,5,6,7-tetrahydro-6-phenyl-4-oxo-benzofuran-5-yl acetate (3)

Yield: 865 mg, 60%, white crystals, (mp: 115,3 °C). IR ($CHCl_3$) ν = 1679.25, 1219.38 cm⁻¹. ¹H-NMR (500 MHz, $CDCl_3$) δ (ppm): 1.98 (s, 3H), 3.27 (m, 2H), 3.29 (d, 1H), 3.73 (m, H), 5.84 (d, J =12.5 Hz, 1H), 6.74 (d, J= 2.0 Hz, 1H), 7.35 (m,5H). ¹³C-NMR (500 MHz, $CDCl_3$) δ (ppm): 20.44, 31.40, 46.56, 76.70, 107.01, 120.17, 127.46, 127.74, 128.86, 139.08, 144.01, 164.42, 170.15, 187.32. LCMS (ES-QTOF) m/z: Anal. Calcd for $C_{16}H_{14}O_4$ 270,08921; Found: 271,0946 [M+H]⁺.

(+)-4,5,6,7-tetrahydro-6-phenyl-4-oxo-benzofuran-5-yl acetate (+)-3

Yield: 20.20 mg, 15%. [α]D²⁰: -0,03 (c 0.01, $CHCl_3$); HPLC: Chiralcell OD-H column, UV detection at 254 nm, eluent: *n*-hexane/2-propanol = 9:1, flow 1.0 mL min⁻¹ 20 °C, retention time: 14.5 min.

(+)-4,5,6,7-tetrahydro-6-phenyl-4-oxo-benzofuran-5-ol (+)-4

Yield: 53.50 mg, 47%. (mp: 105,5 °C). IR ($CHCl_3$) ν = 3462.36 cm⁻¹, 2922.17 cm⁻¹. ¹H-NMR (500 MHz, $CDCl_3$): δ (ppm)= 3.15 (m, 2H), 3.35 (m, 1H), 3.73 (s, 1H), 4.51 (d, J = 11.9 Hz, 1H), 6.68 (d, J = 2.0 Hz, 1H), 7.3 (m, 5H). ¹³C-NMR (500 MHz, $CDCl_3$): δ (ppm)= 31.44, 49.44, 76.64,

106.80, 118.74, 127.67, 128.96, 140.09, 144.13, 166.34, 193.86. LCMS (ES-QTOF) m/z: Anal. Calcd for $C_{14}H_{12}O_3$ 228,07864; Found: 229,0845 $[M+H]^+$.

$[\alpha]D^{20}$ = +18.18 (c 0.01, CHCl$_3$); HPLC: Chiralcell OD-H column, UV detection at 254 nm, eluent: *n*-hexane/2-propanol = 9:1, flow 1.0 mL min^{-1} 20 °C, retention time: 24 min.

RESULTS AND DISCUSSIONS

The use of enzyme-mediated processes for enantioselective transformations is of great interest for a large range of enzymatic species, such as lipases which have gained much interest in recent years because of their easy handling, low expense, and broad substrate region. It is known that in the enantioselective reactions of the hydrolysis of esters and acylation of alcohols, lipase-type enzymes are generally used. In this work, chiral hydroxy benzofuranone derivatives with high potential for biological activity were synthesized. Enzymatic biotransformation of the synthesized chiral hydroxybenzofuranone compounds was performed to determine the enantiomeric excess (e.e.) values.

Scheme 1. (a) Chloroacetaldehyde (C$_2$H$_3$ClO), (b) Mn(OAc)$_3$, benzene/AcOH, reflux; (c) enzyme; solvent, pH = 7, 35 °C.

Initially, the synthesis of 6,7-dihydro-6-phenylbenzofuran-4(5*H*)-one **(2)** was performed from commercially available 5-phenyl-1,3-cyclohexadione **(1)** using the method of Matsumoto and Watanabe (19) even though an alternative reaction of 1,3-cycloadditions to olefins was available (20, 21). Nevertheless, in our study the Matsumoto and Watanabe method was used for obtaining the compound **(2)** due to its general ease of reaction condition, one-step reaction and the convenient commercial availability of the starting materials. Then, selective oxidations of 6,7-dehydro-6-phenylbenzofuran-4(5H)-one **(2)** were performed in the presence of manganese(III) acetate. As is known, many scientists have published different studies with Mn(III) acetate, which is known as a regioselective acetylation reagent (22). Therefore, (*rac*-**3**) compound was to be synthesized by the reaction of **(2)** and

Mn(III) acetate as the oxidizing agent in benzene as the solvent, in the light of these publications (23, 24). Then the enzyme-mediated hydrolysis reaction of α-acetoxyenone was performed to ensure production of compound **(3)** and compound **(4)** with high enantiomeric excess and great yields (Scheme 1).

To obtain the ideal conditions for the enzymatic hydrolysis of *rac*-**3**, we applied analytical screening. To do that, the reactions were made in analytical scale. The lipases were used for enantioselective hydrolysis of α-acetoxy enones. Because of the low solubility of the substrate in aqueous medium, a few milliliters of organic solvent was also necessary. DMSO, toluene or THF was used for this purpose. About 0.5 mmol of acetoxy enone was dissolved in a minimum amount of organic solvent. All reactions were carried out in phosphate buffer (pH=7 or pH=6 or pH=8) at room temperature. For 0.5 mmol of acetoxy enone, 300-μL phosphate buffer was added. Subsequently, the enzyme was added to the mixture and the mixture was stirred at 37 C. The reaction was observed by TLC. At the point where approximately 50% conversion was observed, chloroform was added to terminate the reaction.

In our ongoing work, we have previously provided information related to biocatalyst-mediated reactions (17, 18, 25). Here, we performed enzymatic hydrolysis of *rac***-3** by using a variety of lipase enzymes which were used for analytical screening (Table 1).

Twelve different enzymes were used to find the enzyme that gave the best results: WGL (Wheat Germ Lipase), Amano Lipase, CAL B (*Candida Antarctica* Lipase B), CCL (*Candida Cyclindracea* Lipase), MJL (*Mucor Javanicus* Lipase), HPL (*Hog Pancreas Lipase*), PCL (*Penicillum Camemberti Lipase*), PLL (*Pseudomonas Lipoprotein Lipase*), PRL (*Penicillum Roqueforti Lipase*), RAL (*Rhizopus*

Arrhizus Lipase), RNL (*Rhizopus Niveus* Lipase), and CRL (Candida Rugosa Lipase) were realized, as summarized in Table 1. In the kinetic resolution step, three different organic solvents (DMSO, Toluene, and THF) were tested. They were also tested in phosphate buffer at pH=6, pH=7, and pH=8 for the enzymatic hydrolysis step in DMSO. HPLC with chiral cell OD-H column was used to determine the enantiomeric excess of acetate and alcohol.

To specify the conversion, the reaction was monitored with TLC and HPLC as references by using a chiral column using *rac*-**3** (synthesized from *rac*-**3** with K_2CO_3/MeOH). The reaction was followed at regular intervals by TLC and terminated when 50% conversion was reached. The pure product was obtained after flash column chromatography.

Because of the worldwide use of lipases, there is a need to understand the mechanisms of lipase-catalyzed reactions in organic solvents. Since most lipases easily become denatured in organic solvents and therefore lose their catalytic activities, it becomes important to find lipases that are stable in non-aqueous systems. Lipases act in organic solvents and are connected with their capacity in both synthetic and hydrolytic reactions.

It has also been found that the various lipases behave differently in different organic solvents with different reaction systems. However, so far, none of them has enabled validation of any serious predictive analysis about catalysis in organic solvents (26). In this study, the effect of solvents was investigated and it was observed that esterification in hydrophobic solvents such as toluene and DMSO generally provided relatively high enantiomeric excess for alcohol (+)-**(4).** However, the hydrophilic solvents such as THF gave low yields, and very low enantiomeric excess values (Table 1).

All results are summarized in Table 1. The best results for the hydroxy enones with PPL for the high enantioselectivity 81% ee, 24% conversion and E value: 11 were obtained for the reaction at pH=7 in DMSO (entry 19). According to the preparative scale, the PPL (Pseudomonas Lipoprotein Lipase) enzyme was used for the synthesis of (+)-**4** (Table 1, entry 19), which gives the best result with the highest enantiomeric excesses (81% ee, 47% yield) in the presence of DMSO.

Changing the enzyme as well as the solvent affected the enantioselectivity of the reaction. As the results show, 81% enantiomeric excess was found in HPL (in toluene) (entry 14), PPL (in toluene) (entry 20) and 80% RNL (in DMSO) (entry 31) for the hydroxy benzofuranone **(+)-4**. As shown in Table 1, the lipase Amano achieved 32% enantiomeric excess in toluene (entry 5), PPL with 25 % enantiomeric excess in DMSO (entry 19), and PPL with 21% enantiomeric excess in toluene (entry 20), (-)-**3** showing reverse selectivity.

In this study, the acetoxy enantiomer was not resolved in the high enantiomeric excess. The probable cause for this may be the presence of large groups such as the acetate groups in addition to the phenyl group on the ring.

In this paper, we examined the effects of pH as well as the solvent effect. Optimal pH determined the most effective enzyme activity point. Pepsin enzyme is very effective at pH 1.5-1.6 and urease enzyme shows maximum activity at pH 7, which is a good example of the fact that enzymes can usually function in a narrow pH range (27). The structure and ionization state of the enzymes and reactants may be changed by monitoring the reaction of the pH. Additionally, most of the enzymes possibly lose their influence either at higher or lower pH values. In order to find good ee values, the solvent and pH values were changed while keeping the enzyme the same. For an increase of enantiomeric excess value, DMSO with three different pH values was also tested.

The best results were in the MJL catalyzed resolution: at pH=6, the determined ee values are 83% (entry 16), at pH= 8 the determined ee values are 59% (entry 18), in PPL catalyzed resolution at pH=7 the determined ee values are 81% (entry 20) and at pH=6 the determined ee values are 59% (entry 19), as can be seen in Table 2 for compound (+)-**4**.

Moreover, some enzyme and solvent combinations and phosphate buffer increased the E value of the reaction (PPL with 81% ee and E value: 11; (entry 20 in Table 1) for DMSO at pH=7, PPL with 81% ee and E value: 10; (entry 20 in Table 1) for toluene at pH=7, PCL with 79% ee and E value: 10; (entry 22 in Table 1) for DMSO at pH=7 as indicated in (-)-**(4)**. Additionally, high conversion values were achieved. The efficient conversion of the esterification in the RAL catalyzed solution was 61% with DMSO at pH= 7 which showed 23% ee for (-)-(4-oxo-6-phenyl-4,5,6,7-tetrahydrobenzofuran-5-yl acetate) (**3**) selectivity and 15% (+)-(4-oxo-6-phenyl-4,5,6,7-tetrahydrobenzofuran-5-ol) (**4**) selectivity (Table 1, entry 28).

Table 1. Enzymatic hydrolysis of *(rac-***3**).

Entry	Enzyme	Solvent	Time(d)	Alcohol ee[a](%) Yield[b]	Acetate ee[a](%)	Conversion C(%)	E[c]
1	WGL	DMSO	7	23	6	21	2
2		Toluene	4	45	9	19	2
3		THF	>26	-	1	-	-
4	Amano Lipase	DMSO	>26	**-**	16	-	-
5		Toluene	8	**-**	32*	-	-
6		THF	>26	**-**	3	-	-
7	CAL B	DMSO	>26	-	16	-	-
8		Toluene	>26	-	2	-	-
9		THF	>26	-	0.3	-	-
10	CCL	DMSO	>26	8	0.1	1	1
11		Toluene	>26	9	2	20	1
12		THF	>26	13	0.3	2	1
13	HPL	DMSO	>26	9	1	10	1
14		Toluene	>26	81	5	6	9
15		THF	>26	-	0.07	-	-
16	MJL	DMSO	>26	-	7	-	-
17		Toluene	>26	-	2	-	-
18		THF	>26	50	4	7	3
19	PLL	DMSO	>36	81 yield: 47	25*	24	11
20		Toluene	>36	81	21*	21	10
21		THF	>36	66	1	2	3
22	PCL	DMSO	>36	79	9	10	10
23		Toluene	>36	47	4	8	3
24		THF	>36	-	1	-	-
25	PRL	DMSO	>36	38	7	16	2
26		Toluene	>36	77	4	5	8
27		THF	>36	-	0.5	-	-
28	RAL	DMSO	>36	15	23*	61	2
29		Toluene	>36	-	7	-	-
30		THF	>36	-	0.5	-	-
31	RNL	DMSO	>36	80	5	6	1
32		Toluene	>36	1	10	91	1
33		THF	>36	38	4	10	2
34	CRL	DMSO	>36	2	3	60	1
35		Toluene	>36	8	0.2	2	1
36		THF	>36	-	0.5	-	-

[a]Determined Chiralcell OD-H column, eluent: n-hexane/2 propanol = 9:1, flow 1.0 mL min^{-1} 20 °C, UV detection at 254 nm, [b] Yield value was obtained using flash column chromatography.

[c]See Ref. (28).

Table 2. Enzymatic hydrolysis of (*rac*-**3**) with different lipase enzymes at pH 6, pH 7, pH 8 and DMSO medium.

Entry	Enzyme	Solvent (DMSO)	Time (d)	Alcohol ee[a](%) (yield[b])	Acetate ee[a](%)	Conversion C(%)	E[c]
1	WG	pH 6	7	22	8	27	2
2		pH 7	7	23	6	21	2
3		pH 8	7	10	7	41	1
4	Amano Lipase	pH 6	>26	13	3	19	1
5		pH 7	>26	-	16	-	-
6		pH 8	>26	-	20*	-	-
7	CAL B	pH 6	>26	5	3	38	1
8		pH 7	>26	-	16	-	-
9		pH 8	>26	7	3	30	1
10	CCL	pH 6	>26	6	1	14	1
11		pH 7	>26	8	0.1	1	1
12		pH 8	>26	7	0.3	4	1
13	HPL	pH 6	>26	-	0.6	-	-
14		pH 7	>26	9	1	10	1
15		pH 8	>26	2	0.3	13	1
16	MJL	pH 6	>26	83	5	6	1
17		pH 7	>26	-	7	-	5
18		pH 8	>26	59	5	8	4
19	PLL	pH 6	>36	59	14*	19	5
20		pH 7	>36	81 (47)	25*	24	11
21		pH 8	>36	24	5	17	2

[a]Determined with Chiralcell OD-H column, eluent: n-hexane/2 propanol = 9:1, flow 1.0 mL min^{-1} 20 °C, UV detection at 254 nm, [b] Yield value was obtained using flash column chromatography.
[c]See Ref. (28).

Evaluations of different pH values of the acetoxy enantiomer (+/-)-**3**, which were not completely successful in producing enantiomeric excesses of esterification reactions, are summarized in Table 2. The lipases, Amano with 20% enantiomeric excess at pH=8 (entry 6), PPL with 25 % enantiomeric excess at pH=7 (entry 20), and PPL with 14% enantiomeric excess at pH=6 (entry 19), show reverse selectivity and (-)-**3** is found.

In our previous study, we observed that the enzymatic kinetic resolution reactions gave related alcohol and acetate product in high yields with more than 99% enantiomeric excess. However, in this study we got a maximum value of 88% enantiomeric excess from esterification reactions. This clearly demonstrates that the identity of the phenyl group in the benzofuranone structure is very important and it may reduce the kinetic resolution process as seen from the enantiomeric excess values of the steric mass of the group. In our studies, we will continue to increase the enantiomeric excess and use different types of lipase enzymes as well as various microorganisms, and all cell systems will

be used with different solvents at different pH values.

In this paper, the enantioselective syntheses of **(3)** and **(4)** were undertaken by using hydrolysis reactions in the presence of a lipase enzyme with moderately high enantiomeric excess for the first time in the literature.

As seen in Scheme 1, easy and efficient methods of benzofuranone formation (19) have been used for the synthesis of 6,7-dehydro-6-phenylbenzofuran-4(5H)-one **(2)** with a good yield (60%). It is known that $Mn(OAc)_3$ which is used as an oxidizing agent, is important to functionalize the α- positions of the enones with high regioselectivity. For this reason, we used an effective oxidation procedure with 6,7-dihydro-6-phenylbenzofuran-4 (5H)-one **(2)** and $Mn(OAc)_3$. Thus, the desired product α-acetoxy-4-oxo-tetrahydrobenzofuranone **(rac-3)** derivative was successfully achieved.

It has been seen that enzyme-mediated hydrolysis of acetoxy enone (*rac*-**3**) gave only a single enantiomer of (+)-(**4**) when using three different phosphate buffers and various enzyme and solvent combinations. However, the acetoxy enantiomer is not resolved with good enantiomeric excess. The (+)-**3** and (-)-**3** enantiomers are shown in Table 1 and Table 2.

CONCLUSION

Enzymatic biotransformation can be utilized as a tool for the drug industry. Herein, we focused on the chemoenzymatic synthesis of optically active benzofuranone derivatives which are very important in medicinal chemistry.

We anticipate that this work will provide a new viewpoint to chemists and will increase the interest in biocatalysts and active substance synthesis. In the present work, enantioselective synthesis of **(3)** and **(4),** which is a significant objective in pharmacology, through enzymatic kinetic resolution, was performed for the first time. Enzyme-catalyzed enantioselective hydrolysis of **((-)-3)** was achieved with a 32 % enantiomeric excess. The lipase-catalyzed esterification reactions of **((+)-4)** had high enantiomeric excesses of 83%. This method is an effective way for studies of the synthesis of compound **(3)** and compound **(4)** which could be used to develop optically pure drugs which are important for human health.

Such important research as this plays a significant role in simplifying the synthesis of desired products and relevant analogues for medicinal chemistry evaluation. This type of study lends itself to the improvement of new therapeutic agents.

REFERENCES

1. Keay BA, Hopkins JM, Dibble PW. Furans and their benzo derivatives: Applications. Comprehensive Heterocyclic Chemistry III. 2008:571-623.

2. Mishra RC. Second Generation Benzofuranone Ring Substituted Noscapine Analogs: Synthesis and Biological Evaluation. Biochemical Pharmacology. 2011; 82:110-21.

3. Tan YX, Wang HQ, Chen RY. Anti-inflammatory and cytotoxic 2-arylbenzofurans from *Morus wittiorum.* Fitoterapia. 2012; 83:750-3.

4. Tan YX, Yang Y, Zhang T, Chen RY, Yu DQ. Bioactive 2-arylbenzofuran derivatives from *Morus wittiorum*. Fitoterapia. 2010; 81:742-6.

5. Kim YJ, Sohn MJ, Kim WG. Chalcomoracin and moracin C, new inhibitors of *Staphylococcus aureus* enoyl-acyl carrier protein reductase from *Morus alba*. Biol Pharm Bull. 2012; 35: 791-5.

6. Romagnoli R, Baraldi PG, Sarkar T, et al. Synthesis and biological evaluation of 2-aroyl-4-phenyl-5-hydroxybenzofurans as a new class of antitubulin agents. Med Chem. 2008; 4:558-64.

7. Flynn BL, Gill GS, Grobelny DW, et al. Discovery of 7-hydroxy-6-methoxy-2-methyl-3-(3,4,5-trimethoxybenzoyl)benzofuran (BNC105), a tubulin polymerization inhibitor with potent antiproliferative and tumor vascular disrupting properties. J Med Chem. 2011; 54:6014-27.

8. Shi W, Lowary TL. Structure-activity relationships in glycosylated 2-phenyl-indoles, 2-phenyl-benzo[b]thiophenes and 2-phenylbenzo[b]furans as DNA binding and potential antitumor agents. Bioorg. Med. Chem. 2011; 19:1779-89.

9. Kossakowski J, Ostrowska K, Hejchman E, Wolska I. Synthesis and structural characterization of derivatives of 2- and 3-benzo[b]furan carboxylic acids with potential cytotoxic activity. II Farmaco. 2005; 60:519-27.

10. George JH, Baldwin JE, Adlington RM. Enantiospecific, biosynthetically inspired formal total synthesis of (+)-liphagal. Org Lett. 2010; 12:2394-7.

11. Caner H, Groner E, Levy L, Agranat I. Trends in the development of chiral drugs. Drug Discovery Today. 2004; 9(3):105-10.

12. Carey JS, Laffan D, Thomson C, Williams MT. Analysis of the reactions used for the preparation of drug candidate molecules. Org. Biomol. Chem. 2006; 4:2337–47.

13. Gotor V, Alfonso I, García-Urdiales E. Asymmetric Organic Synthesis with Enzymes. Weinheim, Germany: Wiley-VCH; 2008.

14. Patel RN. Synthesis of chiral pharmaceutical intermediates by biocatalysis. Coord. Chem. Rev. 2008; 252:659–701.

15. Hudlicky T, Reed JW. Applications of biotransformations and biocatalysis to complexity generation in organic synthesis. Chem. Soc. Rev. 2009; 38(11):3117–32.

16. Schnell B, Faber K, Kroutil W. Enzymatic Racemisation and its Application to Synthetic Biotransformations. Adv. Synth. Catal. 2003; 345: 653-66.

17. Demir AS, Caliskan Z, Sahin E. Enantioselective synthesis of 4,5,6,7-tetrahydro-4-oxo-benzofuran-5-yl acetate and 1-benzyl-4,5,6,7-tetrahydro-4-oxo-1(H)-indol-5-yl acetate using chemoenzymatic methods. Journal of Molecular Catalysis B: Enzymatic. 2007; 44:87-92.

18. Caliskan ZZ, Ersez MS. Stereoselective synthesis of optically active1-benzyl-4,5,6,7-tetrahydro-6,6-dimethyl-4-oxo-1H-indol-7-ylacetate and 1-benzyl-6,7-dihydro-7-hydroxy-6,6-dimethyl-1H-indol-4(5H)-onethrough lipase-catalyzed esterification and transesterificationprocesses. J. Mol. Catal. B: Enzym. 2015; 111:64-70.

19. Matsumoto M, Watanabe N. A facile synthesis of 4-oxo-4,5,6,7-tetrahydroindoles. Heterocycles. 1984; 22:2313-6.

20. Xia L, Lee YR, Kim SH, Lyoo WS. AgBF4/[Bmim]BF4-catalyzed [3+2] cycloaddition of cyclic diazodicarbonyl compounds. Efficient synthesis of 2,3-dihydrofurans and conversion to 3-acylfurans. Bulletin of the Korean Chemical Society. 2011; 32(5): 1554-8.

21. Mueller P, Allenbach YF, Bernardinelli G. On the Enantioselectivity of Transition Metal-

Catalyzed 1,3-Cycloadditions of 2-Diazocyclohexane-1,3-diones. Helvetica Chimica Acta. 2003; 86(9): 3164-78.

22.(a) Heiba EI, Dessau RM, Koehl WJJr. Oxidation by metal salts. IV. A new method for the preparation of γ-lactones by the reaction of manganic acetate with olefins. J. Am. Chem. Soc. 1968; 90(21):5905-6. (b) Bush JB Jr, Finkbeiner H. Oxidation reactions of manganese(III) acetate. II. Formation of γ-lactones from olefins and acetic acid. J. Am. Chem. Soc. 1968; 90(21):5903-5. (c) Heiba EI, Dessau RM. Oxidation by metal salts. XI. Formation of dihydrofurans. J. Org. Chem. 1974; 39:3456-7.

23. Williams GJ, Hunter NR. Situselective α'-acetoxylation of some α, β-enones by manganic acetate oxidation. Can. J. Chem. 1976; 54(24):3830–2.

24. Tanyeli C, Caliskan ZZ. A Facile Synthesis of Various Butenolides. Synth. Commun. 2000; 30(16):2855–62.

25. Demir AS, Caliskan Z, Aydın AE, Bicer I. A new and efficient chemoenzymatic route to both enantiomers of α'-acetoxy and α'-hydroxy-α-methoxy cyclic enones. Tetrahedron: Asymmetry. 2006; 17:786-91.

26. Ashok K, Kartik D, Shamsher SK, Pankaj KA. Lipase catalysis in organic solvents: advantages and applications. Biol Proced Online. 2016; 18/2: 1-11.

27. [URL]

28. Shih-Hsiung Wu, Su-Yuan Lai, Shu-Ling Lin, Fei-Ya Chu, Kung-Tsung Wang. Enantiomeric separation of 2-(phenoxy)propionate derivatives by chiral high-performance liquid chromatography. Chirality. 1991; 3(6):476–9.

REVIEW ARTICLE

Artificial Intelligence Algorithms Inspired By Life Sciences

Hüseyin TURGUT*

Mehmet Akif Ersoy University, Vocational School of Technical Sciences, 15100, Burdur, Turkey

Abstract*: Nature and life include many mysterious events, behaviors and format within themselves. There is harmony between the environmental conditions, behavior and forms of all living organism. Computer science, especially data and information science, is based on the structure or behavior of living things in the creation of many artificial intelligence algorithms by examining this attitude of life. The rapid progress of the developing artificial intelligence and information technology has increased the data and hidden data in our lives many times and has tried to solve (1). Artificial intelligence has examined many areas or environments and has developed approaches based on it. Expert systems, artificial neural networks, genetic algorithms, inductive learning, explanation-based learning, similarity-based learning, common sense information processing, model based reasoning, model based reasoning, rational protection mechanism, distributed artificial intelligence, natural language processing, chaos theory, logic programming are the artificial intelligence algorithms used for these approaches (2). Among artificial intelligence algorithms; The ant colony algorithm imitates the behavior and direction of ants, and artificial neural networks imitates the behavior and functions of neurons in the nervous system and genetic algorithms imitates the theoretical form of genetic science (3, 4). Many algorithms such as these algorithms are based on the vital form and behavior of living things. The purpose of this review is the relations between the mentioned algorithms and the living science are examined.

INTRODUCTION

The process of making meaningful meaning, meaning meaningless imagery, is made possible by the command sequences called algorithms in computer science (5). This system, which runs the rules in order, is just an application. Learning involves stages such as understanding, perception and thinking. In general, machine learning is defined as the ability of computers to learn information and experiences about an event, to be able to decide on future events or to solve problems.

Machine learning is nowadays known as artificial intelligence. Artificial intelligence aims to develop computer processes that understand human thinking and bring out similarities; computer systems equipped with human intelligence-specific capacities such as

information acquisition, perception, vision, thinking and decision-making.

Artificial intelligence is being developed by imitating human or natural intelligence. These imitations are inspired by the structural flow of many living or inanimate systems. This system, which is formed by working with many sciences, creates the greatest contribution in the identification and imitation process (6). Natural sciences are needed to improve the artificial intelligence and improve its performance. The nervous system, the genetic structure, the lives of animals and plants have created popular algorithms for artificial intelligence.

ARTIFICIAL INTELLIGENCE ALGORITHM

Ant Colony Algorithm
Natural Ants
The ants have the ability to find the shortest way to the source of food from their nest. They are making this move without hinting. They can get rid of obstacles and produce a new way (7). This function is shown in Figure 1.

The system used by the ants for the route finder is pheromone. Pheromone is a kind of chemical secretion that some animals use to influence other animals in their genus. The ants have some pheromones in motion. During the road finding process, the pheromone is preferred to the path with the least path. In this respect, the other ants who will come after themselves also help with the pheromones they leave. If an obstacle is encountered or can not be maintained, the ant will select a path with equal probability and create a new path. This ventricle is called the leading ant. If

it reaches food, it will return to the house using the same way. This route will be the proper route because the route it follows will take more pheromones. The new shortest path will take place thanks to the fact that later ants choose this new path (7).

Ant Colony Algorithm - Virtual Ants
Researchers produce a new algorithm for solving problems by examining the behaviors of ants. The generated algorithm imitates the progress of these ants in the nature leaving traces. The structure formed by this method is called "virtual ant". Computer Science shows that most problems simulated by creating "virtual tinkering" can be solved more easily (8). The most popular problem solved using this algorithm is the traveler seller problem. The first study was conducted in 1991 by Dorigo *et al* (7).

Since it is inspired by the ant colony, the system is called the "ant system"; The algorithm is called the "ant colonies algorithm".
The algorithm is like this:
1. Initial pheromone values are determined.
2. The ants are placed randomly at each knot.
3. Each ant completes the round by selecting the next address based on the local search probability given in the equation.
4. The distance traveled by each ant is calculated and the local pheromone is updated.
5. The best solution is calculated and used in global pheromone renewal.
6. Go to Step 2 until the maximum number of iterations or qualification criteria is met.
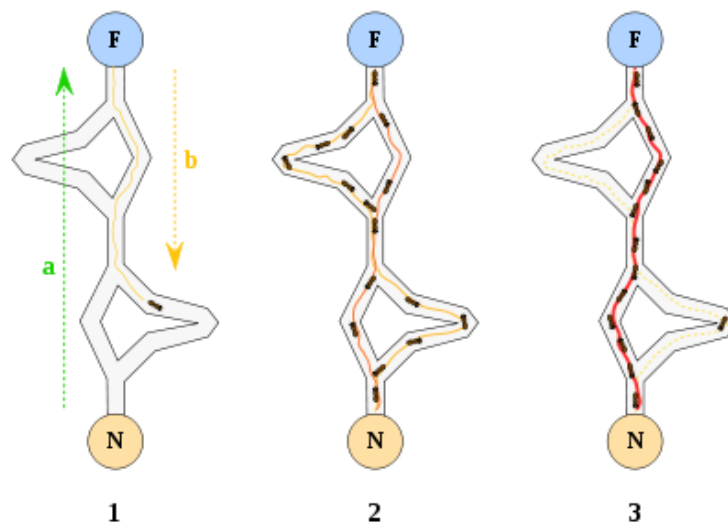

Figure 1: Simulation of ant colony algorithms (9)

ANN algorithms are often used to produce the nearest formula in problem solving. It can be

used to determine the route of distribution of a cargo company or to reach the closest results of search engines (9).

Genetic Algorithms

Genetic algorithms are a search and optimization method that works in a manner similar to the evolutionary process observed in nature. In the complex multi-dimensional search space, the best solution is holistic according to the principle of survival of the best.

The basic principles of genetic algorithms were first proposed by John Holland at the University of Michigan. Holland, in 1975, assembled his work in his book "Adaptation in Natural and Artificial Systems". First, Holland used evolutionary laws for optimization problems in genetic algorithms (10,11). Genetic algorithms generate a set of solutions consisting of different solutions rather than producing a single solution to the problems. The solutions in the solution set are completely independent of each other. Each is a vector on multidimensional space. Genetic algorithms simulate the evolutionary process in computer environment for solving problems. This cluster, representing many possible solutions to the problem, is called "population" in the genetic algorithm terminology. A population consists of a number sequence called a vector, chromosome, or individual. Each element within an individual is called a "gene". The most important factor in deciding the success of genetic algorithms in solving the problem is the representation of the individuals representing the solution of the problem. There is a "conformity function" that decides whether each individual in the population will be a solution to the problem. According to the return value from the fitness function, individuals with high values are given the opportunity to multiply with other influential individuals. These individuals produce new individuals called "children" at the end of the crossing process. The child carries the characteristics of parents (mother, father) who bring themselves to the festival. Since individuals with low fitness values will be chosen less, these individuals are excluded from the population after a while. The new population is formed by the gathering of high-fit individuals in the previous population. Thus, through many generations, good traits are propagated in the population and are combined with other good traits through genetic processes. The greater the number of individuals with higher fitness values come together to create new individuals, the better the working space is obtained within the search space (10,11).
For the best solution;

- The representation of the individual must be done correctly,
- The conformity function must be established effectively,
- The right genetic operators should be chosen.

Genetic algorithms are effective and useful only in areas where search space is large and complicated, resolution is difficult in the search space limited by the available information, where the problem can not be expressed by a specific mathematical model, and where the desired result is not obtained from conventional optimization methods.

Difference from other methods

1-Genetic algorithms search for solutions of problems by their codes, not by the values of parameters. The solution can be produced as long as the parameters can be coded. For this reason, genetic algorithms do not know what they are doing, they know how to do it.
2-Genetic algorithms begin with a set of points, not a single point of search. For this reason, they are often not trapped in the local best solution.
3-Genetic algorithms use the value of the fitness function instead of the derivative. Use of this value also does not require the use of auxiliary information.
4-Genetic algorithms use probabilistic rules, not necessity rules

Genetic algorithms are used in studies with function optimization. This artificial intelligence algorithm is more effective in terms of difficulty, continuity and noise from traditional optimization techniques (12).

Artificial Neural Networks

A biological nerve cell consists of four parts in total. These are the trunk, axon, numerous dendrites and synapses. Dendrites transmit the incoming signals to the nucleus. The nuclei collect the signals from the dendrites and transmit them to the axon. These collected signals are processed by axon and sent to synapses. Synapses also transmit newly produced signals to other nerve cells.

Artificial Neural Cell

Artificial Neural Networks (ANN) are computer systems developed with the intention of automatically generating the ability to derive new information, learn new information, and discover new ones through learning from the characteristics of the human brain without any help. It is difficult or impossible to realize these capabilities with traditional programming methods. For this reason, artificial neural networks can be described as a computer science dealing with adaptive information processing developed for very difficult or impossible events (6).

Entrances from the outside or other cells are connected to the cell by means of weights. The net input is calculated together with the summation function. The net output is calculated by passing the pure input through the activation function. This process is also equal to the exit of the cell (13).

Elements of Artificial Neural Cell
• Inputs: Information from the outside world or from another cell to the artificial neural networks.
• Weights: Represents the numerical value of the connections between cells. It shows the value of information coming to a cell and its effect on the cell.
• Aggregation Function: Calculates the net input of that cell by multiplying the input from the cell by weights.
• Activation Function: It processes the net entry into the cell and allows the cell to determine whether it will produce a response to this input.

• Outputs: Output values determined by the activation functions. The output produced can either be sent to the outside world, to another cell or to itself as input.

ANN Structure
Input Layer: The layer from which the entrances come from the outside world. In this layer, there are as many cells as there are inputs, and the inputs are transmitted to the hidden layer without any processing.
Hidden Layers: Transfers the information from the entry layer to the next layer. The number of hidden layers and the number of cells in the hidden layer may vary in each network. Cell numbers in hidden layers are independent of input and output numbers.
Output Layer: Processes data from hidden layer. The output generated according to the input to the entrance layer transfers to the outside world. The number of cells in the output layer can be more than one. Each output cell has one output. Each cell is dependent on all the cells in the previous layer.
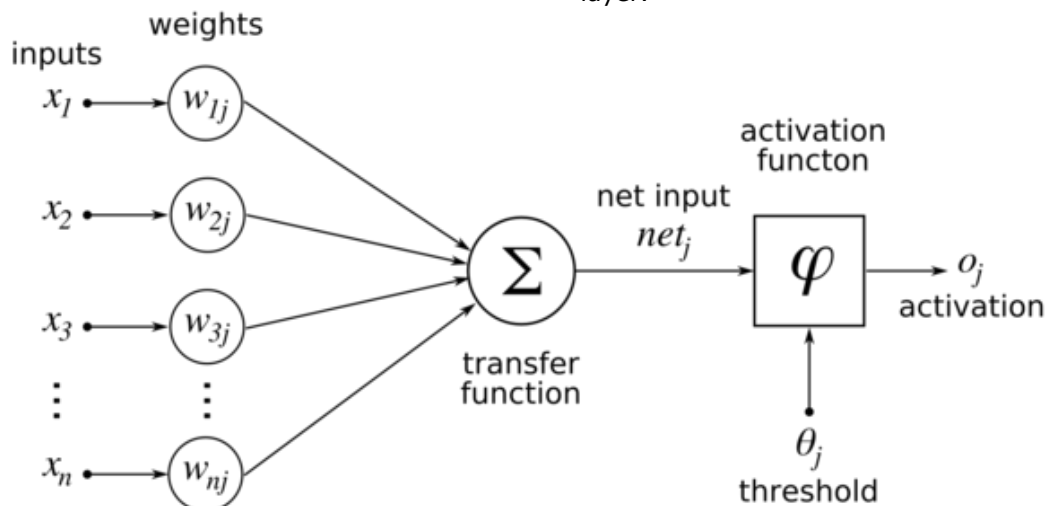

Figure 2. Structure of ANN algorithm (6)

Properties of ANN
• They have the ability to self-organize and learn.
• They can work with missing data.
• Has fault tolerance.
• They can process indefinite and incomplete information.
• ANN does not exhibit sudden deterioration.
• They can only work with numerical information.
• ANN is designed to solve problems that are difficult to solve by known solutions.

Advantages of ANN
• ANN is successful in situations where there is no definite mathematical model or algorithm to solve the problem.

• Successful results are found in situations with a large number of exceptional and abnormal data.
• Has the ability to adapt.
• Information is stored entirely on the network.
• Produce information about previously unseen samples.

Disadvantages of ANN
• 'Black Box' can not explain the final result.
• There is no specific rule for determining proper network structure.
• There is no specific rule for setting network parameter values.
• There is no general rule in selecting training samples.
• Displaying the problem to the network is an important problem.

• There is no specific method of when network training should be finished.

DISCUSSION & CONCLUSIONS

Computer science has created algorithms called programming, primarily to speed up people's work and save on labor power. These algorithms mimic only the work done. For example, paper work done by an officer in daily life is now made faster and more economically thanks to the computer. However, artificial intelligence, in addition to imitating the work of human beings, allows people to make decisions in their work and reach the results without doing business.

Computer technologies not only accelerate work but also offer solutions. Social life and scientific processes are accelerated by using Computer Programming. However, artificial intelligence technology can imitate the solutions of nature. Life and biology have been imitated in the creation of many artificial intelligence algorithms. The ants, neurons, genetic structure are examples of these.

REFERENCES

1. Fayyad U, Stolorz P. Data mining and KDD: Promise and challenges. Future generation computer systems. 1997;13(2-3):99–115.

2. Baykal N, Beyan T. Bulanık mantık: uzman sistemler ve denetleyiciler. Bıçaklar Kitabevi; 2004.

3. Rosenblatt F. The perceptron: a probabilistic model for information storage and organization in the brain. Psychological review. 1958;65(6):386.

4. Holland JH. Genetic algorithms. Scientific american. 1992;267(1):66–73.

5. Moschovakis YN. What is an algorithm? Içinde: Mathematics unlimited—2001 and beyond. Springer; 2001. s. 919–936.

6. Turgut H. Veri madenciliği süreci kullanılarak alzheimer hastalığı teşhisine yönelik bir uygulama [Master Thesis]. Süleyman Demirel Üniversitesi Fen Bilimleri Enstitüsü; 2012

7. Dorigo M, Maniezzo V, Colorni A. Dipartimento Di Elettronica-Politecnico Di Milano. 1991;

8. Parpinelli RS, Lopes HS, Freitas AA. An ant colony algorithm for classification rule discovery. Içinde: Data mining: A heuristic approach. IGI Global; 2002. s. 191–208.

9. Maniezzo V, Gambardella L, Luigi FD. New Optimization Techniques in Engineering. Içinde: An ANTS Heuristic for the Long-Term Car Pooling Problem. Springer Berlin, Heidelberg; 2004. s. 411–430.

10. Gen M, Cheng R, Oren SS. Network design techniques using adapted genetic algorithms. Içinde: Evolutionary Design and Manufacture. Springer; 2000. s. 107–120.

11. Beasley D, Bull DR, Martin RR. An overview of genetic algorithms: Part 1, fundamentals. University computing. 1993;15(2):56–69.

12. Beasley D, Bull DR, Martin RR. A sequential niche technique for multimodal function optimization. Evolutionary computation. 1993;1(2):101–125.

13. Wang S-C. Interdisciplinary computing in Java programming. C. 743. Springer Science & Business Media; 2012.

Syntheses and Spectroscopic Characterization on New [O–3-phenyl-1-propyl-(4-methoxyphenyl)dithiophosphonato] Ni(II), Cd(II) and Hg(II) Complexes

Ertuğrul Gazi Sağlam✉ 🆔 **and Ahmet Ebinç**✉

Department of Chemistry, Bozok University, 66900, Yozgat, Turkey

Abstract : Four new [(R)(OR')dithiophosphonato] metal complexes (Metal= Ni(II), Cd(II) and Hg(II)) were synthesized (R= 4-methoxyphenyl-, R'= O–3-phenyl-1-propyl-). The complexes were of the general structure $[Ni((R)(OR'))_2]$, $[Cd\{\mu-(R)(OR')\}_2\{(R)(OR')\}_2]$ and $[Hg\{\mu-(R)(OR')\}_2\{(R)(OR')\}_2]$. $[Ni((R)(OR'))_2]$ was capable of coordinating two moles of pyridine per mole as many four-coordinated nickel(II) complex do leading to the six-coordinated complex, $[Ni((R)(OR'))_2(Py)_2]$. The structures of the complexes were investigated by elemental analysis along with mass spectra; FTIR and Raman spectroscopies. Further evidence for the structures of $[Ni((R)(OR'))2]$, $[Cd\{\mu-(R)(OR')\}2\{(R)(OR')\}2]$ and $[Hg\{\mu-(R)(OR')\}2\{(R)(OR')\}2]$ were also obtained through 1H-, 13C- and 31P-NMR studies. The magnetic susceptibility of the pyridine nickel complex was measured to verify the hybridization patterns and the geometry.

INTRODUCTION

2,4-bis-organo-1,3-dithia-2,4-diphosphetane 2,4-disulfides (DTDPA) react with nucleophilic reagents to produce organo-dithiophosphorus compounds. [2,4-bis (4-methoxyphenyl)-1,3,2,4-dithiadiphosphetane-2,4-disulfide] which is called Lawesson's reagent, (LR), a good example for DTDPAs, reacts with amines and bring about such as a dithiohosphonamido acid (1,2). LR also reacts with carbo anion such as Grignard compounds to produce dithiophosphinic acid (3). Moreover, the reaction of LR with aliphatic or aromatic alcohols ends up with the formation of dithiophosphonic acids (DTPOA) (4). DTPOA-type compounds are the best known organo-dithiophosphorus compounds (5). They are of several industrial applications; for example, some of them are used in the industry to serve as metal chelating agents (6), and antioxidants (in lubricating oils) (7, 8). They also have agricultural applications as herbicides (9) and insecticides (10). Some medicinal and pharmacological applications are of prospect (11-15).

The DTPOAs are also known to act as soft bases to react with metal cations, some of them being neutral, molecular species. Specifically Group 10 metal cations tend to form mononuclear molecules with square planar coordination environments (16). On the other hand, the cations Zn(II), Cd(II) and Hg(II) tend to form dinuclear DTPOA

complexes that have tetrahedral cores (17-20). Square planar Ni(II)-DTPOA complexes can react with two moles of amine such as pyridine to produce a six-coordinated DTPOA complex (21). In these complexes, the sulfur atoms of -PS$_2$- group may serve as a singly bonded ligand or as a bridge-head (22-24).

EXPERIMENTAL

Materials and Instruments
The LR, 3-phenyl-1-propanol were purchased from Merck and used without any purification. CHCl$_3$, C$_2$H$_5$OH, C5H$_5$N, NiCl$_2$.6H$_2$O, CdCl$_2$ and HgCl$_2$ were purchased from Sigma-Aldrich.

The LC/MS system was composed of a Waters Alliance HPLC with a C-18 column and a Waters Micromass ZQ combined to an ESI ionizer. ^{1}H-, ^{13}C-(proton decoupled) and ^{31}P-(proton decoupled) NMR spectra were recorded with a Varian Mercury (Agilent) 400 MHz FT instrument in CDCl$_3$. SiMe$_4$ (^{1}H, ^{13}C) and 85% H$_3$PO$_4$ (^{31}P) were used as standards. IR spectra were done on a Perkin Elmer Spectrum 400 FTIR spectrometer (200–4000 cm^{-1}) and are reported in cm^{-1} units. Raman spectra were recorded in the range of 4000–100 cm^{-1}, at room temperature, using a Renishaw in-Via Raman microscope, equipped with a Peltier-cooled CCD detectors (−70°C). For Raman microscopy, a 50X objective was usually used and all the spectra were excited by the 785 line of a diode laser. Microanalyses were measured using a LECO CHNS-932 C elemental analyzer. Melting points were measured with a Gallenkamp apparatus using a capillary tube. Magnetic susceptibilities were performed measured on a Sherwood Scientific magnetic susceptibility balance (Model MK1) at room temperature (25°C).

Preparation of the compounds

Preparation of ammonium O−3-phenyl-1-propyl-(4-methoxyphenyl) dithiophosphonate, ([NH$_4$][(R)(OR')])
This ligand was synthesized according to the literature (25).

Preparation of [Ni((R)(OR'))$_2$]
A solution of the NiCl$_2$.6H$_2$O, (0.17 g, 0.70 mmol) in ethanol (10 mL) was added to the solution of ammonium O−3-phenyl-1-propyl-(4-methoxyphenyl)dithiophosphonate (0.5g, 1.41 mmol) in ethanol (25 mL). After stirring for an hour, the mixture was left aside. The nickel(II) complex was violet. The crystalline solids were filtered off, and recrystallized from ethanol.

Preparation of [Cd{μ-(R)(OR')}$_2${(R)(OR')}$_2$]
A solution of the CdCl$_2$ (0.13 g, 0.70 mmol) in ethanol (10 mL) was added to the solution of ammonium O−3-phenyl-1-propyl-(4-methoxyphenyl)dithiophosphonate (0.5g, 1.41 mmol) in ethanol (25 mL). After stirring for an hour, the mixture was left aside. Cd(II) complex was white-colorless and recrystallized from a mixture of chloroform/ethanol (2/1; v/v).

Preparation of [Hg{μ-(R)(OR')}$_2${(R)(OR')}$_2$]
The same procedure as in [Cd{μ-(R)(OR')}$_2${(R)(OR')}$_2$] was applied for the [Hg{μ-(R)(OR')}$_2${(R)(OR')}$_2$] (HgCl$_2$, 0.13 g, 0.70 mmol in 10 mL ethanol for the of ammonium O−3-phenyl-1-propyl-(4-methoxyphenyl)dithiophosphonate, 0.5g, 1.41 mmol in 25 mL ethanol). Hg(II) complex was white-colorless and recrystallized from a mixture of chloroform/ethanol (2/1; v/v).

Preparation of [Ni((R)(OR'))$_2$(Py)$_2$]
To a chloroform solution of [Ni((R)(OR'))$_2$] (0.5 g, 0.73 mmol) complex in a beaker (50 mL) was added excess amount of pyridine. The color of the solution turned to from violet to light brown color. Green crystals formed were recrystallized from chloroform/ethanol (0.5/1 v/v). This powder is stable in the vacuum desiccator; but unstable at open atmosphere and returns to the violet colored complex.

[Ni((R)(OR'))$_2$] : Yield: 0.47 g (92%). Violet. M.P. 85-86 °C. LC/MS MS: m/z 733.15 ([Ni((R)(OR'))$_2$]$^+$, 5%), 395.08 ([Ni((R)(OR'))]$^+$, 100%), 339.20 ([(R)(OR')+H]$^+$, 6%). Anal. Calcd. for C$_{32}$H$_{36}$NiO$_4$P$_2$S$_4$ (733.53 g.mol^{-1}): C, 52.40; H, 4.95; S, 17.49; found: C, 52.37; H, 4.89; S, 17.53 %.

[Ni((R)(OR'))$_2$(Py)$_2$] : Yield: 0.59 g (97%). Green. M.P. Decomposition upon heating. μ$_{eff}$ = 2.99 B.M. LC/MS: MS m/z 916.1 [(Ni((R)(OR'))$_2$Py$_2$+Na]$^+$, 1%), 812.2 [(Ni((R)(OR'))$_2$Py$_2$-Py]$^+$, 2%), 553.2 [(Ni((R)(OR'))$_2$Py$_2$-(R)(OR')]$^+$, 12%), 395.1 [(Ni((R)(OR'))]$^+$, 3%), 444.3 [(Ni((R)(OR'))Py-(OCH$_3$)]$^+$, 100%). Anal. Calcd. for C$_{42}$H$_{46}$N$_2$Ni$_2$O$_2$P$_2$S$_4$ (891.73 g.mol^{-1}): C, 56.57; H, 5.20; N, 3.14; S, 14.38; found: C, 56.53; H, 5.24; N, 3.08; S, 14.45 %.

[Cd{μ-(R)(OR')}$_2${(R)(OR')}$_2$] : Yield: 0.44 g (80%). White-colorless. M.P. 120°C. LC/MS: MS m/z 1240.2 [(Cd$_2$((R)(OR'))$_3$]$^+$, 1%), 806.7 [(Cd((R)(OR'))$_2$]$^+$, 15%), 451.0

[(Cd((R)(OR'))+H]$^+$, 15%), 413.3 [(O-C$_6$H$_4$-PS$_2$)$_2$O+Na]$^+$, 100%) 391,4 [(O-C$_6$H$_4$-PS$_2$)$_2$O+H]$^+$, 77%). Anal. Calcd. for C$_{64}$H$_{72}$Cd$_2$O$_8$P$_4$S$_8$ (1574.49 g.mol^{-1}): C, 48.82; H, 4.61; S, 16.29; found: C, 48.76; H, 4.58; S, 16.23 %.

[Hg{μ-(R)(OR')}$_2${(R)(OR')}$_2$] : Yield: 0.52 g (85%). White-colorless. M.P. 94-95°C. LC/MS MS: m/z 1412.4 [(Hg$_2$((R)(OR'))$_3$]$^+$, 3%), 877.2 [(Hg$_2$((R)(OR'))$_2$+H]$^+$, 4%), 391.4 [(O-C$_6$H$_4$-PS$_2$)$_2$O]$^+$, 64%), 189.3 [(S$_2$P-C$_6$H$_4$-O)+H]$^+$, 100%). Anal. Calcd. for C$_{64}$H$_{72}$Hg$_2$O$_8$P$_4$S$_8$ (1750.85 g.mol^{-1}): C, 43.90;

H, 4.14; S, 14.65; found: C, 43.86; H, 4.11; S, 14.59 %.

RESULT AND DISCUSSION

LR and O−3−phenylpropanol were reacted to yield a crude dithiophosphonic acid. The DTPOA obtained is a viscous liquid with a disagreeable odor. To get rid of the impurities and the bad odor, it was converted to the corresponding ammonium derivative, that is, the ammonium dithiophosphonate (Scheme 1).
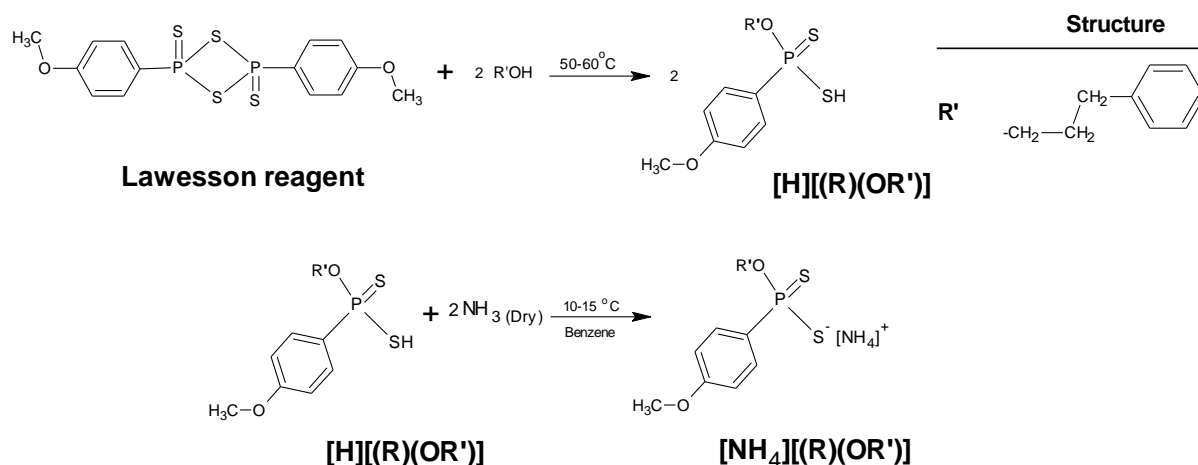
Scheme 1. Synthesis reaction for the ligand.

[NH$_4$][(R)(OR')] was reacted with nickel(II), cadmium(II) and mercury(II) to give the corresponding complexes. The complex [Ni((R)(OR'))$_2$] was further treated with pyridine to convert it to [Ni((R)(OR'))$_2$(Py)$_2$], a six-coordinated structure (Scheme 2).
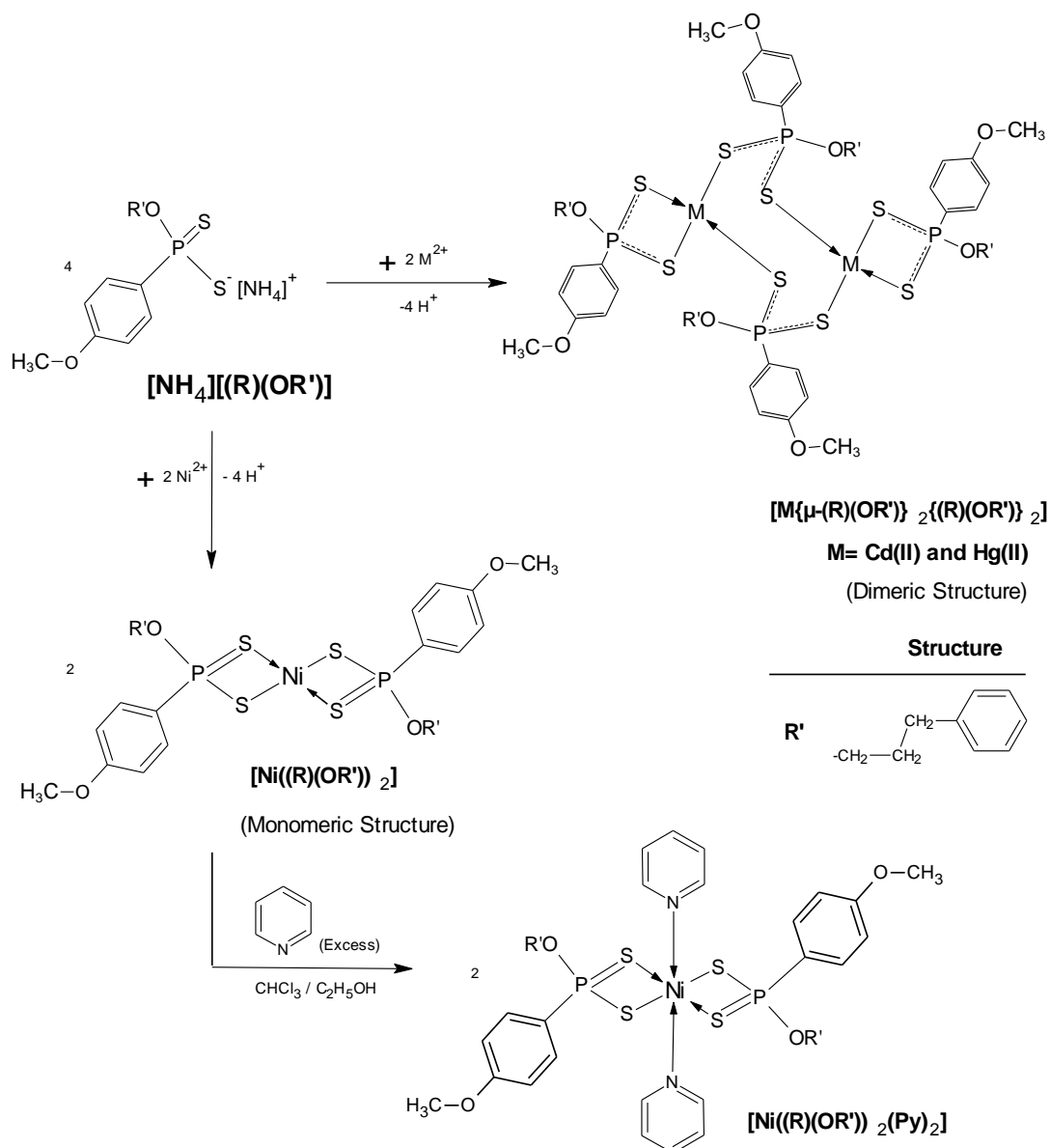
Scheme 2. Syntheses of the complexes.

The magnetic susceptibility measured for the octahedrally coordinated complex [Ni((R)(OR'))$_2$(Py)$_2$] indicates a two-electron paramagnetism which agrees with the literature findings for similar structures (26).

Spectroscopic Studies
Mass spectra
The m/z values of the mass signals agree well with the theoretical isotopic abundance of the elements, nickel, cadmium, mercury as well as sulfur. The molecular ion and some fragments display m/z values that are 23 units higher than that of the calculated counterparts. Na$^+$ ions known to be presented in the buffer solution of the LC/ES system, are assumed to be responsible for this observation. Similar observations were reported in the literature (27).

The compounds [Cd{μ-(R)(OR')}$_2${(R)(OR')}$_2$] and [Hg{μ-(R)(OR')}$_2${(R)(OR')}$_2$] appear to display no molecular ions but [Ni((R)(OR'))$_2$] does display one. The masses of the fragments observed in the mass spectra of [Cd{μ-(R)(OR')}$_2${(R)(OR')}$_2$] and [Hg{μ-(R)(OR')}$_2${(R)(OR')}$_2$] agree well with the structures suggested. The MS spectra of the octahedral compounds [Ni((R)(OR'))$_2$(Py)$_2$] displays [M+Na]$^+$ peaks of measurable intensity. In the mass spectrum of [Ni((R)(OR'))$_2$], the m/z value of the molecular ion peak matches perfectly with the theoretically calculated figure for the complex itself. The mass spectra of [Cd{μ-(R)(OR')}$_2${(R)(OR')}$_2$] and [Hg{μ-(R)(OR')}$_2${(R)(OR')}$_2$] complexes display

peaks corresponding to a species formed by the removal of a ligand from the whole molecule, that is, $[M_2\{(R)(OR')\}_3]^+$. In the mass spectra of the dimeric complexes of Cd(II) and Hg(II), ion peaks attributable to the moieties $[Cd\{\mu-(R)(OR')\}_2\{(R)(OR')\}_2]$ and $[Hg\{\mu-(R)(OR')\}_2\{(R)(OR')\}_2]$ are obvious, respectively. Experimental m/z data for the mass spectral peaks of the complexes are listed in the Experimental section relating to the individual complexes. The patterns of disintegration given in the literature for similar structures (28-30) are compatible with the ones we obtained here.

IR and Raman Spectra

The specific ν_{N-H} vibration band is visible at 3198 cm^{-1} in the ligand disappears in the complexes (25).

IR spectral symmetric and asymmetric PS stretching bands (ν(PS) $_{sym}$ and ν(PS) $_{asym}$) of the compounds are located at 547–552 cm^{-1} and 646–664 cm^{-1}, respectively. In the vibrational spectra of the Raman, similar bands are located at 541–555 cm^{-1} and 634–668 cm^{-1}, respectively.

M-S stretching vibrations appear at 306–308 cm^{-1} on IR and 280–306 cm^{-1} on Raman spectra. In the complex $[Ni((R)(OR'))_2(Py)_2]$, the metal-nitrogen stretching signals appear at the expected frequency region of the IR and Raman spectra (31). All the IR and Raman data are in good agreement with the previous observations (5,21,32–34). The significant peaks are given in Table 1.

Table 1: The selected vibrational spectral data ((FTIR and Raman, R, cm^{-1}) assignments of the important bands

Compound	ν(M-N)		ν(M-S)		ν(PS)$_{sym}$		ν(PS)$_{asym}$		ν(P-O-C)	
	IR	R	IR	R	IR	R	IR	R	IR	R
[Ni((R)(OR'))₂]	-	-	306	307	548	555	664	668	1011	1003
[Ni((R)(OR'))₂(Py)₂]	232	236	304	305	547	547	655	659	1004	1012
[Cd{μ-(R)(OR')}₂{(R)(OR')}₂]	-	-	279	280	550-538	541-555	650	659	999	1005
[Cd{μ-(R)(OR')}₂{(R)(OR')}₂]	-	-	308	306	552-533	552-537	646	634	999	1004
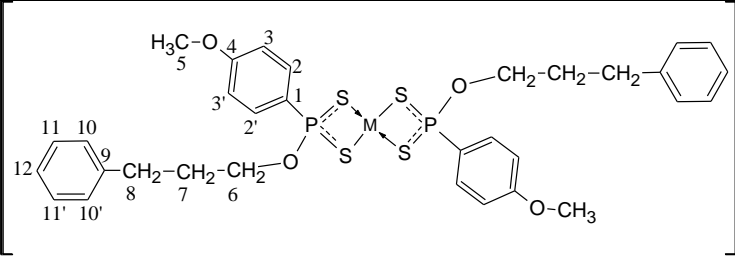
NMR Spectra
The complex $[Ni((R)(OR'))_2(Py)_2]$ is paramagnetic and its ambient temperature NMR spectra is nearly unidentified to comment on.

^{1}H–NMR Spectra
^{1}H-NMR spectral data of the three complexes are presented in Table 2. The chemical shifts of the signals in the ^{1}H-NMR spectrum of the ligand (25) are somewhat higher than those of the corresponding signals for the complexes. The phenyl ring protons in the anisole moiety that are *ortho*- to the phosphorus are split in the frequency range of 14.0–14.5 Hz. This is explained on account of the phosphorus ($^3J_{PH}$) and a further

splitting of 8.9 Hz due to the geminal protons. The *meta* protons (in relation to phosphorus) do interact with the phosphorus by 3.3–3.4 Hz ($^4J_{PH}$).

In the spectra of all the complexes, the $C_{10,10''}$-**H** and C_{12}**H** protons on the O–3-phenylpropyl- accidentally superimpose. The integral curve of the multiplet corresponds to six (for the $[Ni((R)(OR'))_2]$) and twelve (for $[Cd\{\mu-(R)(OR')\}_2\{(R)(OR')\}_2]$ and $[Hg\{\mu-(R)(OR')\}_2\{(R)(OR')\}_2]$) protons; which supports the idea of superimposition. All the ^{1}H-NMR chemical data are in agreement with the literature (35,36).

Table 2: ^{1}H NMR spectral data for [Ni((R)(OR'))$_2$], [Cd{μ-(R)(OR')}$_2${(R)(OR')}$_2$] and [Hg{μ-(R)(OR')}$_2${(R)(OR')}$_2$].

	n=1, M=Ni(II)	**n=2, M=Cd(II)**	**n=2, M=Hg(II)**
Ar-**H**$_{ortho}$	δ= 8.02 (dd, 4H) $^3J_{PH}$= 14.03; $^3J_{HH}$ = 8.8	δ= 8.02 (dd, 8H) $^3J_{PH}$= 14.52; $^3J_{HH}$ = 8.9	δ= 8.01 (dd, 8H) $^3J_{PH}$= 14.44; $^3J_{HH}$ = 8.8
C11-**H**	δ= 7.32 (t, 4H) $^3J_{HH}$ = 7.5	δ= 7.27 (t, 8H) $^3J_{HH}$ = 7.5	δ= 7.31 (t, 8H) $^3J_{HH}$ = 7.4
C12-**H** C10-**H**	δ= 7.20-7.26 (m, 6H) C-10 and C-12 superimposed	δ= 7.18-7.20 (m, 12H) C-10 and C-12 superimposed	δ= 7.25-7.21 (m, 12H) C-10 and C-12 superimposed
Ar-**H**$_{meta}$	δ= 7.04 (dd, 4H) $^4J_{PH}$= 3.13; $^3J_{HH}$ = 8.9	δ= 6.95 (dd, 8H) $^4J_{PH}$= 3.25; $^3J_{HH}$ = 8.9	δ= 7.00 (dd, 8H) $^4J_{PH}$= 3.4; $^3J_{HH}$ = 8.9
C6-**H**	δ= 4.42(m, 4H) $^4J_{PH}$= 12.62; $^3J_{HH}$ = 9.0	δ= 4.25 (m, 8H) $^4J_{PH}$= 12.6; $^3J_{HH}$ = 9.1	δ= 4.42(m, 8H) $^4J_{PH}$= 12.6; $^3J_{HH}$ = 9.0
OC**H**$_3$	δ= 3.91 (s, 6H)	δ= 3.85 (s, 12H)	δ= 3.89 (s, 12H)
C8-**H**	δ= 2.79 (t, 4H) $^3J_{HH}$ = 7.7	δ= 2.73 (t, 8H) $^3J_{HH}$ = 7.8	δ= 2.80 (t, 8H) $^3J_{HH}$ = 7.7
C7-**H**	δ= 2.140 (m, 4H) $^3J_{HH}$ = 7.0	δ= 2.05 (m, 8H) $^3J_{HH}$ = 7.0	δ= 2.15 (m, 8H) $^3J_{HH}$ = 7.0

(Chemical shifts (δ) are reported in ppm. *J* values are reported in Hz. s: singlet; d:doublet; t:triplet dd:doublet of doublets; m:multiplet. The atom responsible for the signal is boldfaced.)

^{13}C-NMR Spectra

The ^{13}C-NMR data for the complexes are summarized in Table 3. The two-bond coupling, $^2J_{P-C}$, for the phenyl carbon atoms in the anisole group (*ortho*- to the phosphorus) are situated within the frequency range 14.2–14.7 Hz. The anisole group *meta*-phenyl carbon atoms (with reference to phosphorus) display a three-bond [31]P-^{13}C coupling of 16.2 Hz.

[31]P–[13]C couplings (single bond) of the *ipso*-carbon for all the complexes are found to be in the range, 116.5–124.3 Hz. The $^2J_{P-C}$ coupling for C6 is 5.7 Hz in [Ni((R)(OR'))$_2$] while the $^2J_{P-C}$ coupling for C6 is 7.4 and 7.2 Hz in [Cd{μ-(R)(OR')}$_2${(R)(OR')}$_2$] and [Hg{μ-(R)(OR')}$_2${(R)(OR')}$_2$], respectively. The $^3J_{P-C}$ for C7 atom is 7.3 Hz, although the $^3J_{P-C}$ coupling for C7 is 7.4 and 7.2 Hz in [Cd{μ-(R)(OR')}$_2${(R)(OR')}$_2$] and [Hg{μ-(R)(OR')}$_2${(R)(OR')}$_2$], respectively. All the ^{13}C-NMR chemical shift data compare well with those given in the literature (3, 37, 38).

Table 3: ^{13}C-NMR spectral data for [Ni((R)(OR'))$_2$], [Cd{μ-(R)(OR')}$_2${(R)(OR')}$_2$] and [Hg{μ-(R)(OR')}$_2${(R)(OR')}$_2$]

	M=Ni(II)	M=Cd(II)	M=Hg(II)
C4	δ= 162.98 (s)	δ= 162.62 (d) $^4J_{P-C}$ = 3.1	δ= 162.75 (d) $^4J_{P-C}$ = 3.3
C9	δ= 141.10 (s)	δ= 141.36 (s)	δ= 141.23 (s)
C1	δ= 129.03 and 128.11 (d) $^3J_{P-C}$ = 116.5	δ=129.10 and 128.14 (d) $^3J_{P-C}$ =121.2	δ= 129.27 and 128.28 (d) $^3J_{P-C}$ = 124.3
Ar-**C$_{ortho}$**	δ= 131.64 (d) $^3J_{P-C}$ = 14.7	δ= 132.39 (d) $^3J_{P-C}$ =14.4	δ= 132.16 (d) $^2J_{P-C}$ = 14.2
C10	δ= 128.52 (s)	δ= 128.53 (s)	δ= 128. 56 (s)
C11	δ= 128.49 (s)	δ= 128.38 (s)	δ= 128. 45 (s)
C12	δ= 126.05 (s)	δ= 125.89 (s)	δ= 126 (s)
Ar-**C$_{meta}$**	δ=114.00 (d) $^3J_{P-C}$ = 16.2	δ=113.72 (d) $^3J_{P-C}$ = 16.2	δ=113.87 (d) $^3J_{P-C}$ = 16.2
C6	δ= 65.74 (d) $^2J_{P-C}$ = 5.7	δ= 65.9 (d) $^2J_{P-C}$ = 7.4	δ= 65.77 (d) $^2J_{P-C}$ = 7.2
C5	δ= 55.52 (s)	δ= 55.44 (s)	δ= 55.48 (s)
C8	δ= 32.02 (s)	δ= 32.06 (s)	δ= 32.07 (s)
C7	δ= 31.83 (d) $^3J_{P-C}$= 7.3	δ= 31.81 (d) $^2J_{P-C}$ = 8.6	δ= 31.79 (d) $^3J_{P-C}$ = 8.6

(Chemical shifts (δ) are reported in ppm. *J* values are reported in Hz. s: singlet; d: doublet.)

^{31}P–NMR Spectra

^{31}P–NMR spectra of all the complexes is composed of a single ^{31}P peak except for the paramagnetic [Ni((R)(OR'))$_2$(Py)$_2$]. This finding indicates that all the phosphorus atoms in one compound are of the same environment. The ^{31}P chemical shifts for [Ni((R)(OR'))$_2$], [Cd{μ-(R)(OR')}$_2${(R)(OR')}$_2$] and [Hg{μ-(R)(OR')}$_2${(R)(OR')}$_2$] are 101,3, 105,7 and 103,5 ppm, respectively. These findings agree well with the literature (3,37,38).

CONCLUSIONS

A dithiophosphonato ligand (([NH$_4$][(R)(OR')]) and four complexes thereof, namely, [Ni((R)(OR'))$_2$], [Cd{μ-(R)(OR')}$_2${(R)(OR')}$_2$] and [Hg{μ-(R)(OR')}$_2${(R)(OR')}$_2$] were prepared. All the complexes are stable and soluble in organic solvents. The octahedral pyridino complex is relatively unstable and tends to reversibly lose pyridine at high temperatures (and even at room temperature in the long run). The singlet peak in the ^{31}P-NMR spectrum confirms that the phosphorus atoms are of identical environments in the complex. The structural details of the compounds were elucidated by elemental

analysis, MS, FTIR and Raman spectroscopies, ^{1}H-, ^{13}C- and ^{31}P-NMR.

ACKNOWLEDGEMENT

REFERENCES

1. Fluck E, Binder H. Reaktionen der Perthiophosphonsäureanhydride mit Aminen und Ammoniak. Z. Anorg. Allg. Chem. 1970;377(3):298-304.

2. Aragoni M C, M Arca, Demartin, F, Devillanova, F A, Graiff C, Isaia F, Lippolis V, Tiripicchio A, Verani G. Ring-Opening of Lawesson's Reagent: New Syntheses of Phosphono- and Amidophosphono-Dithioato Complexes–Structural and CP-MAS ^{31}P-NMR Characterization of [p-CH$_3$OPh(X)PS$_2$]$_2$M (X = MeO, *i*PrNH; M = Ni^{II}, Pd^{II}, and Pt^{II}). Eur. J. Inorg. Chem. 2000;2000(10):2239-44.

3. Sağlam E G, Çelik Ö, Yılmaz H., İde S. Synthesis, spectroscopic characterization and X-ray single crystal structures of trans-bis(4-methoxyphenyl　　　(3-methylbutyl)

dithiophosphinate] nickel(II) and bis [4-methoxyphenyl (3-methyl butyl) dithiophosphate]cobalt(II) complexes. Transition Met. Chem. 2010;35(4):399-405.

4. Karakus M, Kara I, Çelik Ö, Orujalipoor I, İde S, Yılmaz H. Synthesis, characterization, single crystal structure and theoretical studies of trans-Ni(II)-complex with dithiophosphonate ligand. J. Mol. Struct. 2018;1163:128–36.

5. Karakus M, Yılmaz H, Bulak E. Synthesis and Characterization of Zn(II) and Cd(II) Complexes with Bisdithiophosphonates. Russian J. Coord. Chem. 2005;31(5):316–21.

6. Dimitrov K, Rollet V, Saboni A, Alexandrova S. Separation of Cobalt and Nickel by Pertraction in a Rotating Film Contactor Using Cyanex 302 as a Carrier. Sep. Sci. Technol. 2005;40(10):2111–23.

7. Colclough T. Role of additives and transition metals in lubricating oil oxidation. 1987; Ind. Eng. Chem. Res. 1987;26(9):1888-95.

8. Ziyatdinova G K, Budnikov G K, Samigullin A I, Gabdullina G T, Sofronov A V, Al'metkina L A, Nizamov I S, Cherkasov R A. Electrochemical determination of synthetic antioxidants of bisdithiophosphonic acids. J. Anal. Chem. 2010;65(12):1273–9.

9. Kishore G M, Shah D M. Amino Acid Biosynthesis Inhibitors as Herbicides. Annu. Rev. Biochem. 1988;57:627-30.

10. Kabra V, Mitharwal S, Singh S. Synthesis and Insecticidal Activity of Novel Dithiophosphonates. Phosphorus, Sulfur Silicon Relat. Elem. 2009;184(9):2431–42.

11. Cherkasov R A, Nizamov I S, Gabdullina G T, Almetkin, L A, Shamilov R R, Sofronov A V. Dithiophosphoric and Dithiophosphonic Acids and Their Derivatives on the Basis of Thymol: Synthesis and Antimicrobial Activity. Phosphorus, Sulfur Silicon Relat. Elem. 2013;188(1-3):33–5.

12. Mckenna C E, Li Z-M, Ju J-Y, Pham P-T T, Kilkuskie R, Loo T L, Straw J. Simple and Conjugate Bifunctional Thiophosphonates: Synthesis and Potential as Anti-Viral Agents. Phosphorus, Sulfur Silicon Relat. Elem. 1993;74(1-4):469-70.

13. Karakuş M, Ikiz Y, Kaya HI, Şimşek O. Synthesis, characterization, electrospinning and antibacterial studies on triphenylphosphinedithiphosphonates Copper(I) and Silver(I) complexes. Chem. Cent. J. 2014;8(18):18.

14. Cherkasov R A, Nizamov I S, Martianov Y M, Almetkina L A, Nikitin Y N, Shamilov R R. Thiophosphorylation of Pharmacophoric Phenols, Diols, and Triols. Phosphorus, Sulfur Silicon Relat. Elem. 2013;188(1-3):24-6.

15. Bara A, Socaciu C, Silvestru C, Haiduc I. Antitumor Organometallics. I. Activity of some diphenyltin(IV) and diphenylantimony(III) derivatives on in vitro and in vivo ehrlich ascites tumor. Anticancer Res. 1991;11:1651–6.

16. Van Zyl W E, Woollins J D. The coordination chemistry of dithiophosphonates: An emerging and versatile ligand class. Coord. Chem. Rev. 2013;257(3-4):718– 31.

17. Liu H–L, Mao H-Y, Xu C, Zhang H-Y, Hou H-W, Wu Q-A, Zhu Y, Ye B-X, Yuan L-J. Four novel sulfur-rich complexes: syntheses, crystal structures of three nickel(II) and one cobalt(II) complex with derivatives of Lawesson's Reagent. Polyhedron. 2004;23(10): 1799–804.

18.Karakuş M, Lönnecke P, Hey-Hawkins E. Zwitterionic ferrocenyldithiophosphonates: the molecular structure of [FcP(S)S(OCH$_2$CH$_2$NH$_2$Me)] [Fc = Fe(η^5-C$_5$H$_4$)(η^5-C$_5$H$_5$)]. Polyhedron. 2004;23(14):2281–4.

19. Arca M, Cornia A, Devillanova F A, Fabretti A C, Isaia F, Lippolis V, Verani G. New perspectives in phosphonodithioate coordination chemistry. Synthesis and X-ray crystal structure of trans-bis-[O-ethyl-(4-methoxyphenyl)phosphonodithioato] nickel(II). Inorg. Chim. Acta. 1997;262(1):81–4.

20. Blaurock S, Edelmann F T, Haiduc I, Mezei G, Poremba P. Dimeric thiophosphorus complexes of sodium and zinc: Structural characterization of [(THF)$_2$NaO(S)PPh$_2$]$_2$ and [Zn{S$_2$P(OMe)C$_6$H$_4$OEt-p}$_2$]$_2$. Inorg. Chim. Acta 2008;361(1): 407–10.

21. Aragoni M C, Arca M, Demartin F, Devillanova F A, Graiff C, Isaia F, Lippolis V, Tiripicchio A, Verani G. Reactivity of phosphonodithioato NiII complexes: solution equilibria, solid state studies and theoretical calculations on the adduct formation with some pyridine derivatives. J. Chem. Soc., Dalton Trans. 2001;18:2671–7.

22.Sewpersad S, Van Zyl W E. Bis[µ-O-isopropyl(4-ethoxyphenyl)-dithiophosphonato - κ 2S : S'] bis { (O-isopropyl(4-ethoxyphenyl) dithiophosphonato- κ2S:S'] mercury(II)}. Acta Cryst. 2012;E68:m1488–9.

23. Karakus M, Yilmaz H. Synthesis and Characterization of Ni(II), Zn(II), and Cd(II) Complexes with Dithiophosphonate Derivatives. Russian J. Coord. Chem. 2006;32(6):437–43.

24. Van Zyl W E, Facler J P: A General and Convenient Route to Dithiophosphonate Salt Derivatives. Phosphorus, Sulfur Silicon Relat. Elem. 2000;167(1):117-32.

25. Sağlam E G, Erden S, Tutsak Ö, Eskiköy Bayraktepe D, Durmuş Z, Dal H, Ebinç A. Syntheses, characterization of and studies on the electrochemical behaviour of ferrocenyl dithiophosphonates and 4-methoxyphenyl dithiophosphonates. Phosphorus, Sulfur Silicon Relat. Elem. 2017;192(3):322-9.

26. Sağlam E G, Çelik Ö, İde S, Yılmaz H. Synthesis and Determination of Crystal and Molecular Structure of {Bispyridine-bis(4-methoxyphenyl(3-methylbutyl)dithiophosphinato]}nickel(II). Japan Soc. Anal. Chem. X-ray Struct. Anal. Online 2011;27:23-4.

27. Chakravarty M, Pailloux S, Ouizem S, Smith K A, Duesler E N, Paine R T, Williams N J, Hancock R D. Synthesis and metal coordination chemistry of (phenyl)(pyridin-2-ylmethyl)phosphinodithioic acid, (2-C$_5$H$_4$N]CH$_2$P(S)(SH)(Ph). Polyhedron. 2012;33(1):327-35.

28. Keck H, Kuchen W. Massenspektrometrische Untersuchungen An Organophosphorverbindungen IV. Über den massenspektrometrischen Zerfall von Dithiophosphinsären, Phosphorus, Sulfur Silicon Relat. Elem. 1983;14(2): 225-8.

29. Heinz S, Keck H, Kuchen W. Mass spectrometric studies of dithiophosphinato metal complexes. Org. Mass Spoctrom.1984;19:82-6.

30. Mohan P N, Keck H, Kuchen W, Haegele G. Metal complexes of phosphinic acids—XII: Praseodymium(III), neodymium(III) and europium(III) complexes of dimethyldithiophosphinic acid. J. Inorg. & Nuclear Chem. 1977;39(5):833-5.

31.Sundee S, Hanlan L, Bernstein J. Resonance Raman Spectra of Metal Complexes of Substituted Dithiophosphinic acids. Inorg. Chem. 1975;14:2012-3.

32. Casas J S, García-Tasende M S, Sánchez A, Sordo J, Castellano E E, Zukerman-Schpector J. Synthesis, crystal structure and spectroscopik properties of bis (diphenylditihiophosphinato)cadmium(II). Inorg. Chim. Acta. 1994;219(1-2):115-9.

33.Noji M, Kidani Y, Koike H. Studies Bivalent Metal Chelates of 2-Aminomethylpyridine. Bull. Chem. Soc. Japan. 1975;48:245-9.

34. Czernuszewicz R, Maslowsky E, Jr Nakamoto K, Infrared and Raman Spectra of Bis(imidotetraphenyldithiodiphosphino-S,S') Complexes with Cu(II), Co(II) and Fe(II), Inorg. Chim. Acta. 1980;40: 199-202.

35. Karakuş M, Yılmaz H, Bulak E, Lonnecke, P. Bis{µ-(O-cyclopentyl(4-methoxyphenyl) dithiophosphonato]1κ: S,2κ: S-[O-cyclopentyl (4- methoxyphenyl) dithiophosphonato] 1κ2S,S } dizinc (II). Appl. Organometal. Chem. 2005;19(3):396-7.

36. Sağlam E G, Acar N. JOTCSA. Syntheses and characterization of new dithiophosphinato zinc complexes. 2018;5(2):931-40.

37. Ernst L. ^{13}C-N.m.r. Spectroscopy of Diethyl Alkyl- and Benzyl-phosphonates. A Study of Phosphorus-Carbon Spin-Spin Coupling Constants over One to Seven Bonds. Org. Magn. Reson. 1977;9(1):35-43.

38. Karakuş M, Solak S, Hökelek T, Dal H, Bayrakdal A, Özdemir Kart S, Karabacak M, Kart H H: Synthesis, crystal structure and ab initio/DFT calculations of a derivative of dithiophosphonates. Spectrochim. Acta. Part A. 2014;122:582–90.

RESEARCH ARTICLE

Green Preparation of Multiwalled Carbon Nanotubes-Supported Pd and Cu Nanoparticles with Novel *Vic*-dioxime Metal Complexes

Fatma Ulusal* iD ✉, **Bilgehan Güzel** ✉

Chemistry Department, Art and Science Faculty, University of Çukurova, 01330, Adana, Turkey.

Abstract: The preparation of multi-walled carbon nanotubes (MW-CNTs) supported Cu and Pd nanoparticles utilizing a supercritical carbon dioxide ($scCO_2$) deposition method were investigated. Novel *vic*-dioxime complexes of Cu(II) and Pd(II) were used as metallic precursors. The ligand used in these precursors was 4-(trifluoromethyl)aniline-*vic*-dioxide. Ligand and metal complexes were synthesized and identified with various analysis methods including ^1H and ^{19}F NMR, FT-IR, UV-Vis, elemental analysis and magnetic susceptibility. MW-CNTs supported Pd and Cu nanoparticles were characterized by high-resolution transmission electron microscopy (HR-TEM), X-ray diffraction (XRD) and scanning electron microscopy with EDX (SEM-EDX). SEM-EDX and HR-TEM micrographs showed a homogenous distribution of reasonably well-dispersed Cu and Pd nanoparticles on the support. The nature and crystallinity of the nano metal particles were confirmed using XRD. Crystallite sizes ranged from 7-20 nm for palladium and 20-30 nm for copper. This study demonstrated that these oxime complexes are suitable precursors for the preparation of supported nanoparticles using a supercritical carbon dioxide deposition method.

INTRODUCTION

Preparation of transition metal nanoparticles such as Pd, Pt, Rh, Ru, Ni and Cu on a solid support surface gain importance due to the increasingly widespread application of nanocatalysts (1-3). In order to deposit these metals, various organic and inorganic supporting materials such as silica aerogel, carbon black, active carbon, CNT, and alumina are used. Especially carbon-containing materials are preferred due to their unique applications. Nano metal particles deposited on high surface area carbon materials are prominently used as catalysts for many reactions in a wide range. There are many methods for preparing these nanoparticles, such as microemulsion, chemical vapor deposition, modified polyol reduction, impregnation, sonochemical preparation, and deposition-precipitation has been reported (1,4-7).

Supercritical fluids (SCF) has been used in various application areas such as extraction, cosmetics,

sterilization, energy, pharmaceutics, chemistry, organic synthesis, formulation, impregnation, cleaning, food, materials, waste treatment and deposition of metals on the solid materials (1,8). The deposition in supercritical fluids has recently been receiving a growing interest for its use in preparing deposited catalysts. This method includes the dissolving of a precursor (is usually a metalorganic compound) in an SCF and the subsequent exposure of the support material to this supercritical precursor solution. There are currently very few precursors used that are known to have the necessary characteristics for successful deposition in SCF. These include acetylacetonate, hexamethyl triethylene, hexamethylene glycol dimethyl ether, tetramethyl heptanedionate, cyclooctadiene and their derivatives (1, 9-12). We have proved that bipyridyl, phenanthroline, and oximes can also be used in a supercritical deposition with our previous studies (1,13).

In our previous studies, we have contributed to the literature by using new precursors that can be used in the scCO$_2$ deposition technique. Pd(II) complexes of *vic*-dioxime ligands were prepared and used for Pd deposition on alumina in the scCO$_2$ medium for application in Suzuki-Miyaura reaction (1). In another study, the Pd(II) complex of the bipyridyl ligand was used to prepare Pd/MW-CNT in the scCO$_2$ medium. The prepared catalyst was then used for hydrogen storage (13). In this paper, novel fluorous *vic*-dioxime ligand and its Cu(II) and Pd(II) complexes soluble in supercritical carbon dioxide were synthesized. MW-CNTs supported Pd and Cu metallic nanoparticles were prepared with scCO$_2$ deposition technique by hydrogen-assisted chemical reduction method. We investigated the properties of Pd and Cu loaded MW-CNTs by HR-TEM, SEM-EDX, and XRD.

MATERIALS AND METHODS

All chemicals were supplied from Sigma Aldrich and used as obtained without further purification. Multiwall carbon nanotubes were used had the following average dimensions: O.D. xL (6-9 nm x5 μm), diameter (mode, 5.5 nm; median, 6.6 nm). The complexes and ligands have been characterized by the spectroscopic techniques listed below and have been compared with the reported characterizations of analogous compounds. FT-IR spectra of compounds were recorded on a Thermo FT-IR spectrometer; Smart ITR diamond attenuated total reflection (ATR). Elemental analyses (C, N, H) were recorded on a Thermo Scientific Flash 2000, CHNS elemental analyses apparatus. ^{1}H and ^{19}F NMR spectra were recorded on a Bruker AVANCE-500 (in CHCl$_3$ and DMSO). Electronic spectra were obtained on a Perkin Elmer Lambda 25 UV spectrophotometer. Magnetic susceptibilities of metal complexes were determined on a Sherwood Scientific Magnetic Susceptibility balance (Model MK1) using CuSO$_4$.5H$_2$O as a calibration standard at room temperature; diamagnetic corrections were calculated from Pascal's constants. The separation and washing of the MW-CNTs by

precipitation were performed with a Serico 80-2 centrifuge machine. HR-TEM spectra were recorded on Jeol 2100F HR-TEM, 200kv (high-resolution transmission electron microscopy). XRD spectra were recorded on Rigaku Miniflex CuKα, λ=0.154 nm. Scanning Electron Microscopy (SEM) images were recorded on Zeiss Supra 55. The resolution of this microscope is a working distance of 10 mm at an accelerating voltage of 10 kV. The metal/MW-CNTs nanoparticles were mounted on platinum pins with double-sided carbon tape and their corresponding SEM images were recorded. Elemental analysis was obtained from the EDAX Genesis EDS system.

Preparation of ligands and complexes
Synthesis of 4-(trifluoromethyl) aniline-*vic*-dioxime [4TFVD]: As shown in Figure 2, a solution of antimonochloroglyoxime (1.8 g, 3.5 mmol) in 40 mL of absolute ethanol at -10 °C was put in a solution of 4-(trifluoromethyl)-aniline (0.45 g, 3.5 mmol) in 20 mL of ethanol at -10 °C (14). Then the mixture was stirred for 4 hours keeping its temperature under -10 °C. When it became yellow, the pH was brought to 6 by adding 0.1 M NaOH drop-wise. Subsequently, its color turned yellowish-orange. The solvent (ethanol) was allowed to evaporate at room temperature, producing crystals, which were filtered and dried in a vacuum desiccator. The high-resolution microscope image of 4-(trifluoromethyl)aniline-vic-dioxime crystal was shown in Figure 1. Yield: 63%, m.p.: 85°C. Elemental Analysis [C$_{16}$H$_8$F$_{17}$N$_3$O$_2$]; Found 135 C, 43.48; H, 3.12; N,16.41%; calculated C, 43.73; H, 3.26; N, 17.00%; IR (ATR, mmax/cm^{-1}); 3382 (N-H), 3150 (O-H), 1627 (C=N), 1526 (C=C), 1321 (N-O), 1109(C-F), 1066(N-O); ^{1}H NMR (CDCl$_3$), δppm: 11.5(d, 2H, -OH), 8.4(s, 1H, -NH), 7.7-7.4(m, 4H, Ph), 2.1(s, 1H,=CH), ^{19}F NMR (CDCl$_3$), δ ppm: -63.6(Ph-CF$_3$). The yellow ligand proved insoluble in chloroform, DMSO, water and n-hexane and soluble in solvents such as THF, ethanol, and acetone. (FT-IR, ^{1}H and ^{19}F NMR spectra are given in Supporting data; S1, S2 and S3).

Figure 1. The high-resolution microscopic image of 4-(trifluoromethyl)aniline-vic-dioxime crystal.

Synthesis of bis(4-(trifluoromethyl)aniline-*vic*-dioxime) copper(II) [Cu(4TFVD)₂]: As shown in Figure 2, a solution of 4TFVD (2 mmol) in 15 mL of ethanol was dripped on a solution of copper(II) acetate monohydrate (1 mmol) in 10 mL of ethanol. Then, the solution was refluxed at 65 °C for 5 hours. It was allowed to cool to room temperature. Then, the precipitate was filtered, washed with ethanol and dried in a desiccator under vacuum to furnish the pure Cu oxime complex. Yield: 68.0%, m.p.:197 °C. Elemental Analysis [$C_{12}H_{20}O_4N_4Cu$]; Found C, 37.94; H, 2.05; N, 14.41%; calculated, C, 38.89; H, 2.54; N, 15.12%; IR(ATR, mmax/cm^{-1}); 3384(N-H), 3063 (C-H, Ph), 1656 (O···H–O, w), 1610 (C=N), 1513-1320 (N-O) 1106-1064 (C-F), 1012(N-O). The green complex was insoluble in chloroform, DMSO, water and n-hexane and soluble in solvents such as THF, ethanol, and acetone. (FT-IR spectrum is given in Supporting data; S4).

Synthesis of bis(4-(trifluoromethyl)aniline-*vic*-dioxime) palladium(II) [Pd(4TFVD)₂]: As shown in Figure 2, a solution of 4TFVD (2 mmol) in 20 mL of ethanol was dripped on a solution of palladium(II) chloride (1 mmol) in 10 mL of ethanol. For the palladium complexes, sodium acetate (0.5 g) was added to the solution. Then the mixture was refluxed at 75 °C for 4.5 hours. It was allowed to cool to room temperature. The solution was filtered, washed with ethanol and dried in a desiccator by vacuum to furnish the pure Pd-oxime complex. Yield: 98%, m.p.:225 °C. Elemental Analysis [$C_{12}H_{20}O_4N_4Pd$]; Found C, 35.90; H, 2.47; N, 13.58%; calculated, C, 36.11; H, 2.36; N,14.04%; FT-IR(ATR, mmax/cm^{-1}); 3380(N-H), 3058(C-H, Ph), 1690 (O···H–O, w), 1612(C=N), 1542(C=C), 1328 (N-O), 1165-1068 (C-F), 1015 (N-O). The yellow complex was insoluble in chloroform, DMSO, water and n-hexane and soluble in solvents such as THF, ethanol, and acetone. (FT-IR spectrum is given in Supporting data; S5).
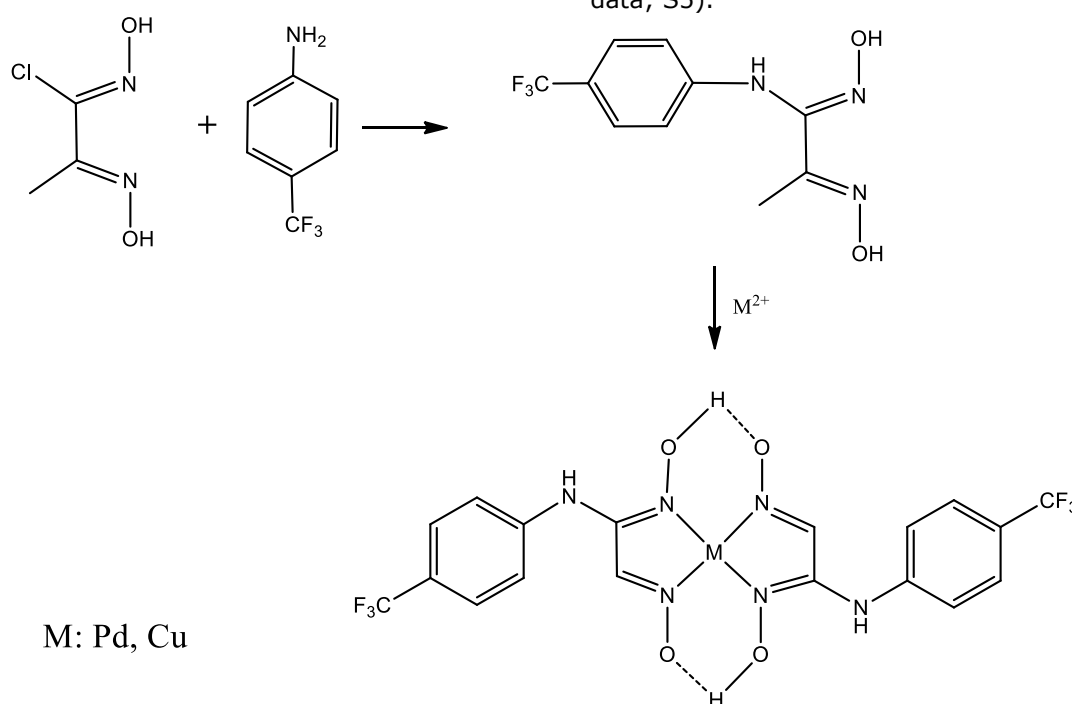
Figure 2. Synthesis reaction of 4TFVD and its metal complexes.

Determination of Solubility in Supercritical Carbon Dioxide: The solubility of the metal complexes was investigated at 276 bar and 363 K in a stainless steel reactor (an inner volume of 54 mL). The reactor was first cleaned with ethanol and CO₂. A known amount (45-50 mg) of the complex was weighed and placed inside the reactor. After the saturated supercritical solution was obtained, the solution was taken out of the vessel to a receptacle of known volume from a side vent. The gas solution was slipped through 5 mL of ethanol. The receptacle was washed with ethanol and added to the initial solution. The amount of complex solving in scCO₂ was measured with UV-Vis spectrophotometer.

Deposition of metals on MW-CNT
The process of preparation of the metals supported on the MW-CNTs by the scCO₂ deposition technique was generally carried out in 3 steps.
   a. Dissolution of the precursor in scCO₂
   b. Absorption of the precursor on MW-CNTs
   c. Finally, the chemical reduction of the metal with hydrogen in scCO₂
A 100 mL inner volume stainless steel reactor (Amar brand) was used for the adsorption of the precursors onto an MW-CNTs and their reduction to metal particles. In a typical experiment held in scCO₂, the reactor was first purged by CO₂. 200 mg MW-CNT and desired amount of precursor was used to obtain 7.5% of M/MW-CNTs. After the addition of the materials to the reactor, the

system was gradually heated to 363 K by a circulating cooler/ heater. The reactor was filled with 276 bar CO_2 gas with a syringe pump (Isco 260D brand) and allowed to stand under these conditions for 1 h. Then the pressure of the vessel was reduced to 138 bar. A CO_2 (10.3 bar) and the H_2 gas mixture were prepared in a high-pressure vessel with 10 mL volume at 276 bar capacity. After stirring for 5 hours, the reactor was allowed to cool to room temperature. The gas was released very slowly and carefully. The solid that had formed was placed on a filter paper and washed with THF until it became clear. Prepared MW-CNTs supported metals nanoparticles were dried in a drying oven. The quantitative analysis of metals was done by ICP-OES. The surface properties of nanoparticles were analyzed with XRD, SEM-EDX, and HR-TEM.

RESULTS AND DISCUSSION

Synthesis of Ligands and Complexes
The oxime ligand was synthesized from fluorinated aniline and *anti* monochloroglioxime. The Cu(II) and Pd(II) complexes of *vic*-dioximes were synthesized using 4-(trifluoromethyl)aniline-*vic*-dioxime, copper(II) acetate monohydrate and palladium(II) chloride. The ligand and metal complexes were characterized by ^{1}H and ^{19}F NMR, FT-IR, elemental analysis, UV-Vis spectrophotometry and magnetic susceptibility.

The elemental analyses of the [4TFVD] were in agreement with the calculated values, confirming that the ligands were indeed synthesized. In the IR spectra of the ligands, the characteristic peaks appeared at 3382 cm^{-1} (N-H), 3150-3000 cm^{-1} (O-H), and 1627 cm^{-1} (C=N). The other peaks observed in the [4TFVD] spectra appeared between 1608-1520 cm^{-1} (C=C), 1320-1299 cm^{-1} (N-O), 1196-1100 cm^{-1} (C-F) and 1066-953 cm^{-1} (N-O). New bands in the IR spectra of the synthesized [4TFVD], which were not present in the starting material, belonging to the C-F bond, appeared between 1100-1200 cm^{-1}. The presence of these peaks, as well as the O-H, C=N and N-O bond, confirmed that the desired ligand was obtained. The ^{1}H NMR spectra of the ligands showed two overlapping singlet peaks at 11.5 ppm for [4TFVD]. This is the result of there being two different =N-OH groups present in the ligand. The other peaks that were observed in the ^{1}H NMR and ^{19}F NMR spectra are consistent with what is expected for these structures. The ^{19}F NMR spectrum contained the expected number of peaks. These results combine to show that the desired ligand was indeed synthesized.

The elemental analyses of the Cu(II) and Pd(II) oxime complexes are also in agreement with the calculated values (14). The physical and analytical results show a metal: ligand ratio of 1:2 for both Pd(II), and Cu(II). The reactions of the oxime ligands with Pd(II) and Cu(II) salts were yielded complexes with the overall formulas

[Cu(4TFVD)$_2$] and [Pd(4TFVD)$_2$]. In the IR spectra of the Cu(II) and Pd(II) complexes, the peaks assigned to the ν(C=N) frequency was shifted to lower frequencies than in the free ligand due to C=N--M metal coordination. For the [4TFVD] ligand, the N=C peak observed at 1627 cm^{-1} shifted to 1610 cm^{-1} for [(Cu(4TFVD)$_2$] and 1612 cm^{-1} for [Pd(4TFVD)$_2$]. The bands corresponding to the γ(O-H) frequency observed in the free ligand was lost after complexation. Weak bands appearing around 1800–1700 cm^{-1} in the FT-IR spectra of the Cu(II) complex corresponded to intramolecular hydrogen bridges (O···H–O) which are in agreement with accepted values as these peaks generally appear between 2000-1700 cm^{-1} (14). As expected, this peak is lacking for the ligand. The magnetic susceptibility of [(Cu(4TFVD)$_2$] was found as 1.81 µB while [(Pd(4TFVD)$_2$] was found as 0 µB. The results showed that the geometry of these complexes is square planar.

Solubility of the Precursors
In order to understand the suitability of these complexes for using as a precursor in scCO$_2$ deposition method, a solubility test of complexes was performed. Fluorous groups are CO$_2$-phile and these groups increase solubility depending on elongation and increasing number of the tail. The solubility of synthesized *vic*-dioxime precursors was in agreement with commonly known precursors reported in the literature (15-17). The solubility of Pd(4TFVD)$_2$ is 7.19x10^{-5} g/mL CO$_2$ while Cu(4TFVD)$_2$ is 3.95x10^{-5} g/mL CO$_2$. The distance between the ligand and the center atom is the bigger in palladium complexes because of palladium diameter is bigger than that of copper. The distance between the ligand and the center atom is inversely proportional to the shielding of the center palladium atom by the ligands. These two effects reduce the solubility of the precursor. So the solubility of Pd precursors was almost 2 times higher than Cu precursors in scCO$_2$.

Deposition of Nanoparticle Metals
Metallic Cu and Pd were been deposited onto MW-CNTs via a supercritical fluid deposition method and H$_2$ assisted reduction. We also analyzed the reduction residual by FT-IR and characteristic -NH$_2$ peaks appear at 3300-3400 cm^{-1}. The peaks of OH (3100-3000 cm^{-1}) and C=N (1600-1650 cm^{-1}) which were present in the precursors, did not appear in this frequency.

The *vic*-dioxime-metal complexes of Pd and Cu used to deposit the metals were bis(4-(trifluoromethyl)aniline-*vic*-dioxime) palladium(II) and bis(4-(trifluoromethyl)aniline-*vic*-dioxime) copper(II). The XRD patterns of the metal support show that the metals were polycrystalline on the MW-CNT. The XRD patterns of Pd deposited on MW-CNT from [Pd(4TFVD)$_2$] is shown in Figure 3. The main diffraction peaks of metallic Pd nanoparticles on the MW-CNTs observed were as expected. In the XRD pattern of Pd deposited on MW-CNT from [Pd(4TFVD)$_2$],

three very sharp peaks were seen: 38.8, Pd(111); 44.8, Pd(200); and 67.3, Pd(220). These three sharp peaks referred to reflections of the face-centred cubic palladium lattice system, with the space group referred to Fm−3m (1,18). The main

peak, Pd(111), was used for calculation of the average particle size of Pd nanoparticles according to the Scherrer equation. The calculated average metal particle size of Pd/MW-CNT was 7.3 nm.
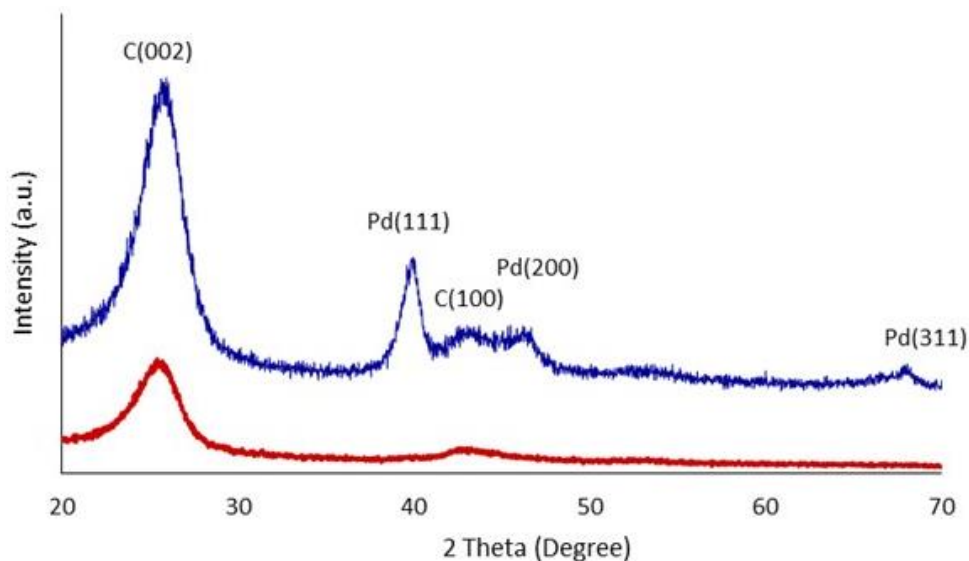
Figure 3. XRD result of (a) MW-CNTs (in red), (b) MW-CNTs supported Pd nanoparticles (in blue).

The XRD patterns of the metal/MW-CNTs show that the metals were polycrystalline on the MW-CNT for Cu as well. The XRD patterns of Cu supported on MW-CNT for [Cu(4TFVD)$_2$] is shown in Figure 4. Four very sharp diffraction peaks were observed in the XRD pattern of Cu supported on C(002): 17.0, Cu$_2$O(111); 36.4, Cu(111); 42.3, Cu$_2$O(111); 61.5, and Cu(220);

73.7 (7,19,20). It can be said that some of the Cu nanoparticles were oxidized from the obtained peaks. All peaks indicate that the Cu has a cubic crystallite structure. The main peak, Cu$_2$O (111), was used for calculation of the average particle size of Cu nanoparticles and average metal particle size was 27.5 nm.
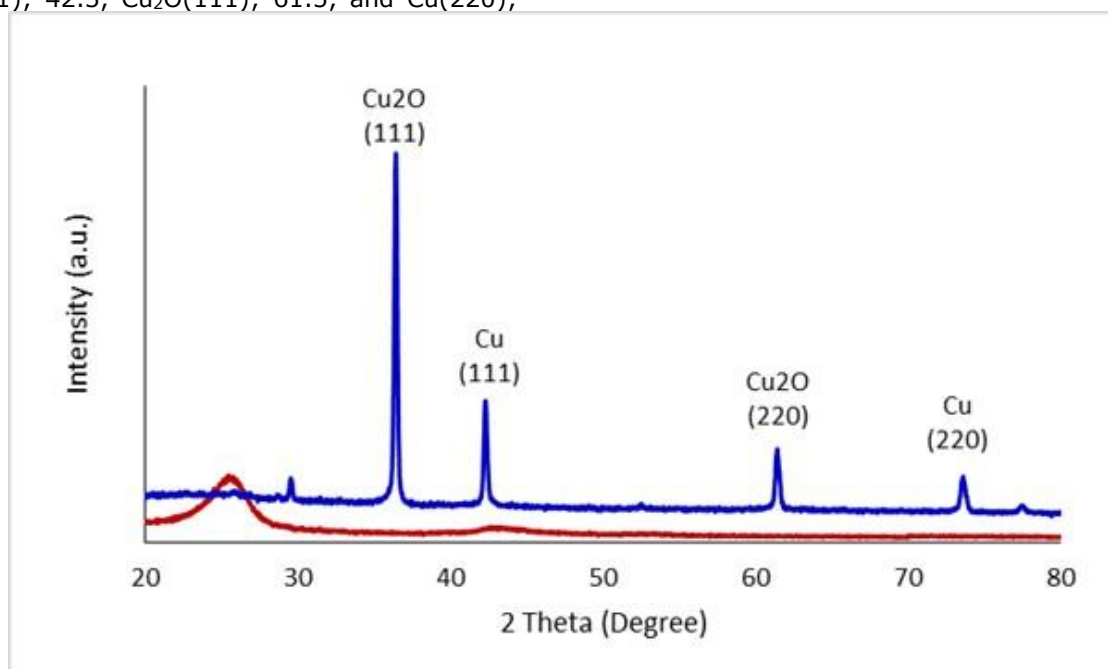
Figure 4. XRD result of (a) MW-CNTs (in red), (b) MW-CNTs supported Cu nanoparticles (in blue).

Figure 5a; it shows the HR-TEM image of the Pd/MW-CNTs obtained from the deposition of Pd on MW-CNTs by using [Pd(4TFVD)$_2$] precursor. The grey background corresponds to MW-CNTs and the black dots on this grey area are Pd

nanoparticles. MW-CNTs channels are shown which are parallel to each other from TEM images. The Pd particles were distributed homogeneously on the MW-CNTs. Pd had an average particle size of 7-10 nm. We also were able to decorate MW-

CNTs with Cu nanoparticles using the same technique. HR-TEM images of Cu/MW-CNTs obtained from [Cu(4TFVD)$_2$] are shown in Figure 5b. Cu had an average particle size of 2-10 nm.
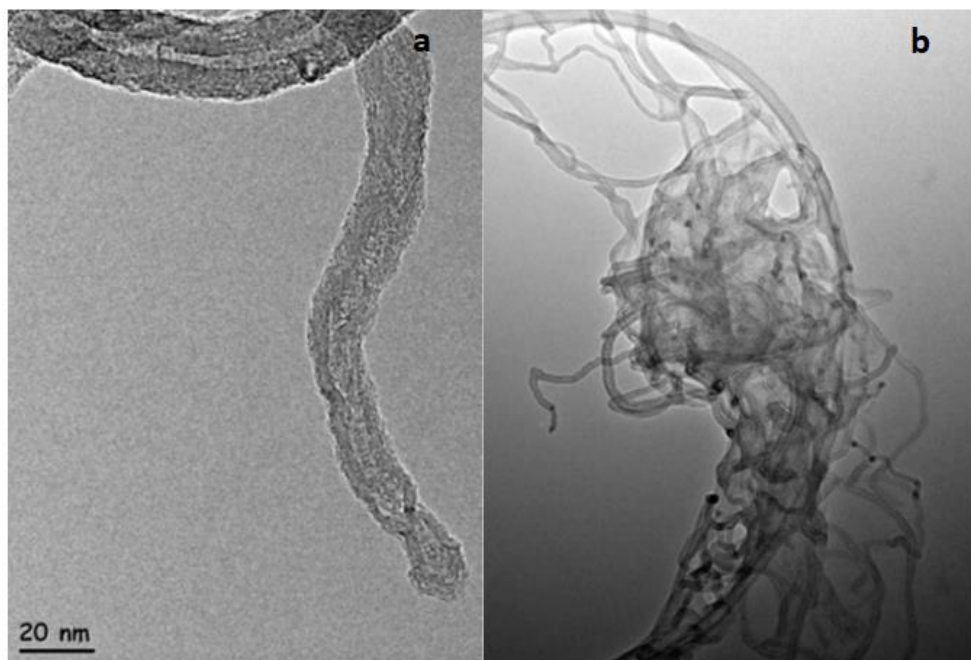
Figure 5. HR-TEM images of (a) Pd/MW-CNTs and (b) Cu/MW-CNTs.

Cu/MW-CNTs and Pd/MW-CNTs samples were analyzed through SEM with EDX. Typical SEM micrographs taken of copper and palladium deposited MW-CNTs composites created by scCO$_2$ deposition method are shown in Figure 6. The identity of the metals was determined by XRD and HR-TEM and confirmed by EDX. The metal nanoparticles were clearly visible on the surface of the MW-CNTs in the EDX spectrum, which also showed that Cu, Pd, and carbon are the major elements in the composite. While carbon peaks of high intensity were observed, the copper and palladium peaks were of low intensity. The percentage of the metal present was calculated and shown in these figures. A wide particle size distribution is observed. The experiments resulted in 6 wt.% Cu loading which accounted for 74.6% of the total Cu in the [Cu(4TFVD)$_2$] system according to ICP-OES and EDX.
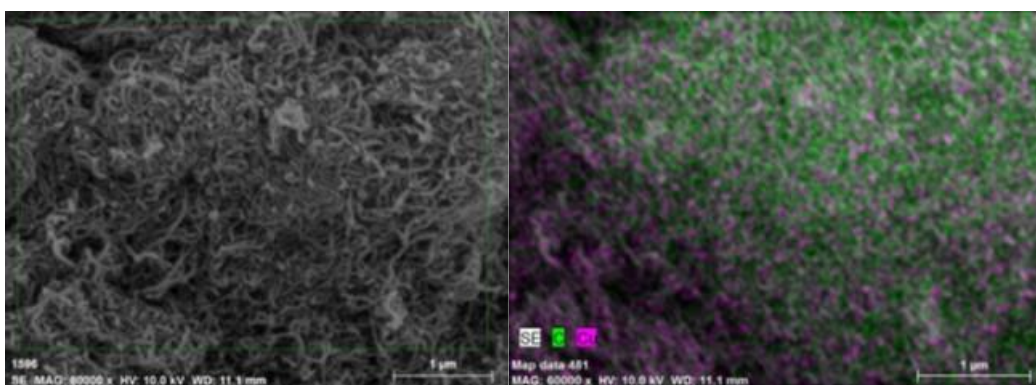
Figure 6. SEM-EDX images of Cu/MW-CNT obtained from [Cu(4TFVD)$_2$].

The SEM micrograph of Cu/MW-CNT composites shown in Figure 7, revealed not only the homogenous distribution of copper in the MW-CNTs matrix but also Cu nanoparticles were small, devoid of large particles on the MW-CNT's surface. Homogenous distribution of the palladium MW-CNT in the matrix was also observed. Pd/MW-CNT obtained from [Pd(4TFVD)$_2$] experiments resulted in 4 wt.% Pd loading which accounted for 49.4% of the total Pd in the system according to ICP-OES and EDX. The SEM micrograph of Pd/MW-CNT composites, shown in Figure 7, revealed not only the homogenous distribution of palladium in the MW-CNTs matrix but also Pd nanoparticles were small. However, large particles on the MW-CNT surface were also observed.

Figure 7. SEM-EDX images of Pd/MW-CNT obtained from [Pd(4TFVD)$_2$].

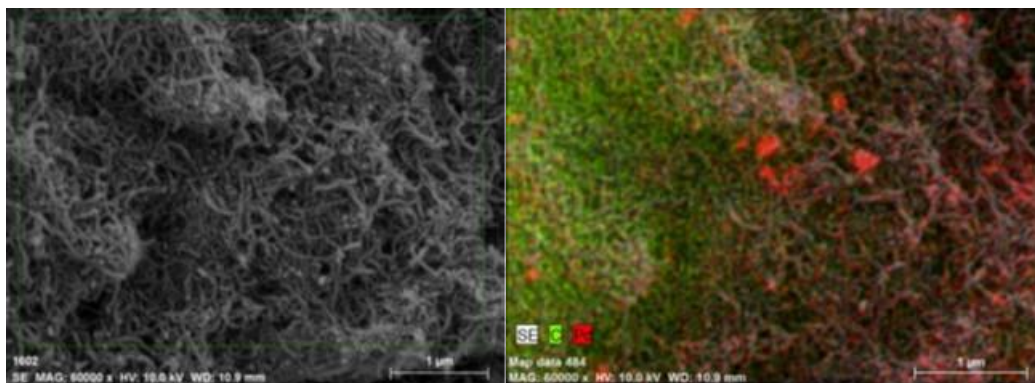This study has shown that metal *vic*-dioxime complexes used as precursors can result in the successful deposition of palladium and copper nanoparticles on MW-CNTs using a scCO$_2$ medium and chemical reduction process. The results of this study regarding the suitability of these precursors will help in defining the mechanisms by which the deposition occurs. This, in turn, will allow for better future research in this area and allow for the advancement of nanocatalyst technology.

CONCLUSION

Fluorinated *vic*-dioxime metal complexes were dissolved in scCO$_2$ and deposited on MW-CNTs. The resulting materials were analyzed by HR-TEM, SEM-EDX, and XRD. These results showed that the metal particles formed were dispersed homogeneously with particles as small as 7 nm. These results show that these novel fluorous *vic*-dioxime metal precursors are a viable alternative for use in a supercritical deposition. Further research on the different isomers of *vic*-dioximes, such as the syn form, could also provide insightful information. In continuation of this research, the deposition of other various oxime derivatives on various supports and further testing on the effects of different temperature and pressures in the deposition process will be studied. The effect of different precursors on the distribution and particle size will be explained by having enough data in continuation of this research.

REFERENCES

1.   Ulusal F, Darendeli B, Erünal E, Eğitmen A, Güzel B. Supercritical carbon dioxide deposition of γ-Alumina supported Pd nanocatalysts with new precursors and using on Suzuki-Miyaura coupling reactions. The Journal of Supercritical Fluids. 2017;127:111–120.

2.   Cangul B, Zhang LC, Aindow M, Erkey C. Preparation of carbon black supported Pd, Pt and Pd–Pt nanoparticles using supercritical CO2 deposition. The Journal of Supercritical Fluids. 2009; 50: 82–90.

3.   Zhang Y, Erkey C. Preparation of supported metallic nanoparticles using supercritical fluids: A review. The Journal of Supercritical Fluids. 2006;38:252–267.

4.   Daoush WM, Lim BK, Mo CB, Nam DH, Hong SH. Electrical and mechanical properties of carbon nanotube reinforced copper nanocomposites fabricated by electroless deposition process. Materials Science and Engineering: A. 2009;513–514:247–253.

5.   Park PW, Ledford JS. The influence of surface structure on the catalytic activity of alumina supported copper oxide catalysts. Oxidation of carbon monoxide and methane. Applied Catalysis B: Environmental. 1998;15:221–231.

6.   Rather S, Zacharia R, Hwang SW, Naik M, Nahm KS. Hydrogen uptake of palladium-embedded MW-CNTs produced by impregnation and condensed phase reduction method. Chemical Physics Letters. 2007;441:261–267.

7.   Lam F, Hu X. A new system design for the preparation of copper/activated carbon catalyst by metal-organic chemical vapor deposition method. Chemical Engineering Science. 2003;58:687 – 695.

8.   Ulusal H, Fındıkkıran G, Demirkol O, Akbaşlar D, Giray ES. Supercritical diethylether: A novel solvent for the synthesis of aryl-3,4,5,6,7,9-hexahydroxanthene-1,8-diones. The Journal of Supercritical Fluids. 2015;105:146–150.

9.   Zhang Y, Erkey C. Preparation of supported metallic nanoparticles using supercritical fluids: A review. The Journal of Supercritical Fluids. 2006;38:252–267.

10.   Dobrovolna Z, Kacer P, Cerveny L. Competitive hydrogenation in alkene–alkyne–

diene systems with palladium and platinum catalysts. Journal of Molecular Catalysis A: Chemical. 1998;130:279-284.

11.   Ye XR, Lin Y, Whang C, Engelhard MH, Wang Y, Wai CM. Supercritical fluid synthesis and characterization of catalytic metal nanoparticles on carbon nanotubes. Journal of Materials Chemistry. 2004;14:908-913.

12.   Kim J, Kelly MJ, Lamb HH, Roberts GW, Kiserow D. Characterization of palladium (Pd) on alumina catalysts prepared using liquid carbon dioxide. The Journal of Physical Chemistry C. 2008; 112: 10446–10452.

13.   Erünal E, Ulusal F, Aslan MY, Güzel B, Üner D. Enhancement of hydrogen storage capacity of multi-walled carbon nanotubes with palladium doping prepared through supercritical CO2 deposition method. International Journal of Hydrogen Energy. 2018; 43: 10755-1076

14.   Yildirim B, Özcan E, Deveci P. New glyoxime derivatives and their transition metal complexes. Russian Journal of Coordination Chemistry. 2007;33:417–421.

15.   Teoh WH, Mammucari R, Foster NR. Solubility of organometallic complexes in supercritical carbon dioxide: A review. Journal of

Organometallic Chemistry. 2013;724:102-116.

16.   Aschenbrenner O, Kemper S, Dahmena N, Schaber K, Dinjus E. Solubility of β-diketonates, cyclopentadienyls, and cyclooctadiene complexes with various metals in supercritical carbon dioxide. Journal of Supercritical Fluids. 2007; 41: 179–186.

17.   Guzel B, Avşar G, Çınkır H. Supercritical carbon dioxide-soluble fluorus vic-dioxime ligands and their Ni(II) complexes: synthesis, characterization and solubility properties. Synthesis and Reactivity in Inorganic, Metal-Organic, and Nano-Metal Chemistry. 2007;37:801-804.

18. Ulusal F, Güzel B. Deposition of palladium by the hydrogen assisted on SBA-15 with a new precursor using supercritical carbon dioxide. The Journal of Supercritical Fluids. 2018; 133: 233–238.

19. Cabanas A, Blackburn J, Watkins J. Deposition of Cu films from supercritical fluids using Cu(I) β-diketonate precursors. Microelectronic Engineering. 2002;64:53-61.

20.   Ulusal F. Güzel B. Synthesis and Characterization of Novel Pd and Cu vic-dioxime Precursors for Their Supercritical Deposition on Multiwalled Carbon Nanotubes. Journal of the Turkish Chemical Society, Section A: Chemistry. 2018; 5(2): 635-52.

RESEARCH ARTICLE

Activated Plantain Peel Biochar As Adsorbent For Sorption of Zinc(II) Ions: Equilibrium and Kinetics Studies.

*Nworie F. S[1] ✉ iD , Nwabue F[1] ✉. Ik, Ikelle I. I[1] ✉., Ogah A.O[1] ✉., Elom N[1] ✉; Illochi, N.O[2] ✉, Itumoh E.J[1] ✉. and Oroke C.E[1] ✉

[1]Department of Industrial Chemistry, Ebonyi State University, Abakaliki, Nigeria.
[2]Department of Pure Chemistry Evangel University, Akaeze, Ebonyi State, Nigeria.

Abstract: Plantain peel biomass was carbonized, activated, and characterized using BET surface area and XRD. The XRD diffraction indicated crystalline structure with crystallite size of 14.56 nm evaluated through Debye-Scherrer equation. The pore size (cc/g) and pore surface area (m^2/g) of the biochar was 8.79 and 16.69 respectively from BET surface area. Various parametric properties such as effect of initial metal ion concentration, pH, and contact time were studied in a batch reaction process. Adsorption of zinc from aqueous solution decreased with an increase of pH and initial concentration. Equilibrium modeling studies suggested that the data fitted mainly to the Langmuir isotherm. Adsorption kinetic data tested using various kinetic models fitted the Bangham's pore diffusion model implicating pore diffusion as the main rate limiting step. The sorption studies indicated the potential of plantain peel biochar as an effective, efficient and low cost adsorbent for remediating zinc (II) ions contaminated environment.

INTRODUCTION

Biomass from decaying plant or other agricultural remnants can be converted to biochar which is important in carbon sequestration, and averting global climate change. Consequently in recent years, the use of agricultural biomass to create biochar has given promising results in carbon dioxide reduction (1). Biochar as an important soil amender is a carbon-rich charcoal that is produced by the thermal decomposition of agricultural biomass. Biochar obtained from the pyrolysis of readily accessible biomasses such as organic, industrial and agricultural wastes has been proved to be an effective and efficient means of carbon sequestration and immobilization of organic

contaminants in soil adsorbent (1,2). Specifically, plantain peels have been noted to exert effects on clinically important agents and are important as good adsorbent (1,3-5).

The wastes from plantain constitute serious environmental hazard as they are most of times carelessly disposed leading to clogging of waterways and converting the town centers to foul smelling scenes. Peels of plantain are wastes and are shown to be a very good source of phyto-chemicals and dietary fibers which are beneficial to human body (6).

Trace metals occur in aqueous solutions from two main sources which could be pedogenetic involving

weathering of parent materials in which case it is less than 1000 mg/kg and less or rarely toxic and from anthropogenic sources such as smelting, electroplating, mining energy and fuel production, agricultural activities and other industrial and commercial activities (7). The last sources and especially the mining and land filling sites are the major contributor of trace metals to aqueous media. Trace metal ions always regarded as those metals with relatively high density and are deleterious even at low concentrations is major environmental contaminants and poses threat to human life and animal wellbeing (8).

Some studies (9,10) have noted that trace metals are non-degradable and continuous accumulation leads to increase in contamination of coastal waters and estuaries. Similarly, these heavy metals bioaccumulate in tissues and organs of biotas adversely affect the distribution of marine organisms. Zinc is a heavy metal highly essential for both plants and animals (8) but becomes deleterious at excess concentration. Zinc from anthropogenic sources such as sludge application, industrial activities and mining, wastewater sources can easily contaminate the environment and present itself as serious threat to man, animals and soil (11). Zinc toxicity is mainly in the form of free zinc(II) ions and the bioavailability and toxicity of the zinc(II) ions can be reduced by immobilization process using biomaterials without adverse effect to the ecosystem.

The removal of soluble metal ions from aqueous solution by the use of biochar has been currently advocated for as it is gradually replacing the expensive materials such as complexing agents and activated carbon (10). Source of biomass and variation of conditions of biochar production are factors that influence biochar characteristics (12). Previous studies on the use of biochar from variety of biomasses for sorption of zinc(II) ions are limited as well as expansive equilibrium and kinetic studies. In other to explore the sorption mechanism of zinc(II) ions and influence of sorption conditions of time of contact, pH, initial metal ions concentration and provide useful data for biochar usability, this study was conducted. The main focus was on the synthesis of the plantain peel biochar, its characterization, metal sorption studies at different conditions of pH, time of contact and initial zinc(II) ions concentration, mechanism of adsorption and the equilibrium and kinetics of the adsorption of zinc onto activated plantain peel biochar.

MATERIALS AND METHODS

Materials
Analytical grade reagents H_2SO_4, HNO_3, NaOH, Na_2CO_3, Eriochrome black-T, EDTA, NaCl, $ZnSO_4$

were all obtained from Sigma Aldrich® and used without further purification unless indicated. Double distilled water was used for all experiments.

Characterization of the activated plantain peel biochar
The BET surface area was measured using Micromeritics ASAP 2020 system. X-ray diffraction pattern was obtained on a Bruker® D8 Discover diffractometer, equipped with a Lynx Eye detector, under Cu-Ka radiation (I ¼ 1.5405 Å). With data collected in the range of 2θ =10 to 100 °, scanning rate at $0.010°min^{-1}$,192 s per step and samples placed on a zero background silicon wafer slide.

Sample Collection and Preparation
The unripe plantain peels *(Musa paradisiaca)* was collected from Abakaliki metropolis in Ebonyi state of Nigeria in plastic containers. The samples after collection were cleaned of soil and other impurities, sun dried to reduce moisture content for 7 days and then oven dried at 60 °C for 24 h. The modified method (13) was adopted for carbonization of the plantain peels. This was done at a temperature of 600 °C in nitrogen environment in a muffle furnace for 6 h. The resulting biochar was cooled at room temperature, ground to fine powder, and then subjected to activation. A portion of 10 g of the carbonized biochar was measured into a 500 mL beaker and 30 mL of concentrated HNO_3 added with stirring for 2 h continuously. The mixture was diluted with deionized water and decanted several times and then washed with double distilled water until the pH was tested to be 6.5. The activated biochar was then dried in an oven at a temperature of 110 °C.

EXPERIMENTAL

Adsorption of Zinc(II) Ions by batch process
Batch experiments were done to obtain adsorption data by varying different conditions of time of contact, pH and initial metal ion concentration. The adsorption of zinc(II) ions from aqueous solution was investigated by initially adding 0.1 g of the adsorbent to 10 mL 0.01 M Zn(II) ions aqueous solution in a 500 mL vessel at room temperature (30 ± 1 °C) for 120 min. The solution was equilibrated using mechanical shaker and resulting solution filtered. The isotherm and kinetics experiments helped to elucidate the characteristics and mechanism of zinc sorption onto the activated plantain peel biochar. For each experiment, 0.1 g of the activated biochar was mixed with 10 mL zinc solution in the vessel. The mixture was shaken at 100 rpm on a rotary mechanical shaker at room temperature. Consequently to measure the sorption kinetics, 0.01 M zinc solutions were used and time varied between 10-120 seconds. To get sorption isotherms, 0.1 g of the activated biochar was added to different concentrations of zinc

solution (0.1, 0.2, 0.3, 0.4 M)   and the mixture equilibrated for 120 seconds. Similar method was applied for pH varied between 2-10. The mixtures were separated by filtration using Whatman No1 filter paper at the end of each experiment. The

method (14) was used for the determination of zinc left in the solution after adsorption. To determine the concentration of zinc in the filtrate, Equation 1 was used.

$$Concentration\ of\ Zinc\ in\ solution = \frac{Molarity\ of\ EDTA \times Volume\ of\ EDTA}{Volume\ of\ zinc\ solution}$$ (Eq. 1)

The complexation of EDTA with zinc is represented in Equation 2 indicating 1: 1 number of moles of each reactant involved.

$$Zn^{2+} + EDTA^{4-} \rightarrow ZnEDTA^{2-}$$ (Eq. 2)

The amount of zinc adsorbed per unit mass of adsorbent at equilibrium, (qe) (mg/g) was evaluated using the relation in Equation 3.

$$qe = \frac{Co}{Ce} \times \frac{V}{M}$$ (Eq. 3)

where Co is initial concentration of zinc(II) ions in solution, Ce is the equilibrium concentration of zinc(II) ions, V is the volume of the solution and m the mass of the activated plantain peel adsorbent.

RESULTS AND DISCUSSION

XRD analysis of the solid sorbent
The diffraction pattern of activated plantain peel biochar (Figure 1) showed crystalline nature with significant intense peak observed at 2θ = 40.65 with observed decomposition of some compound after forming the biochar of plantain peels (15,16). The crystallite size (nm) was calculated from Debye-Scherrer equation(Equation 4):

$$d = \frac{K\lambda}{\beta Cos\theta}$$ (Eq. 4)

Where K is Debye-Scherer constant, β is the full width at half maximum, is the wavelength and θ is Bragg angle. The average crystal size of the particles as calculated from the width of the XRD peaks using Debye-Scherrer equation was 14.56 nm indicating that the biochar is nanosized (17).
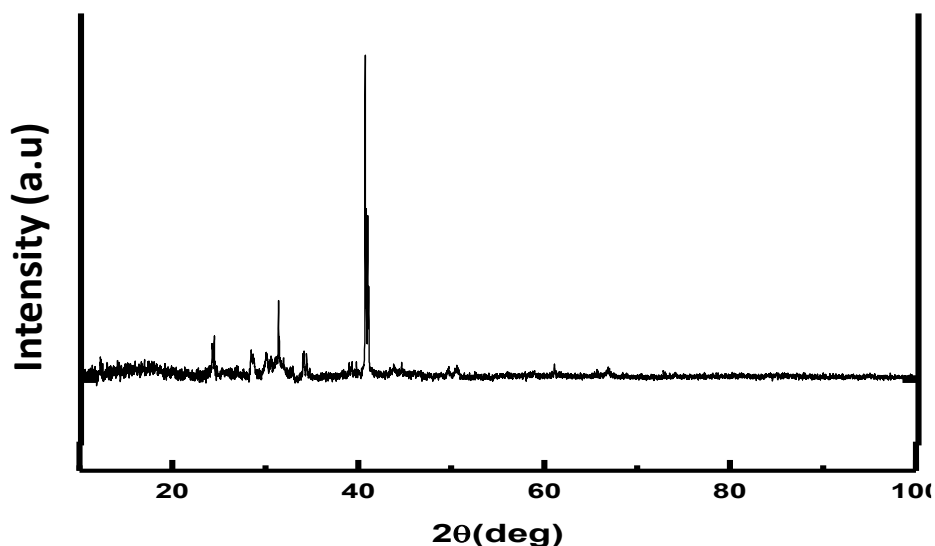
Figure 1: X-ray diffractogram of activated plantain peel biochar.

Brunauer, Emmett, Teller (BET) surface area characterization
BET surface area was applied to determine the surface area and pore size of the plantain peel biochar. The pore size (cc/g) and pore surface area (m^2/g) of the biochar was 8.79 and 16.69 respectively and represented in Figure 3. The large surface area per gram of a sample of the biochar

indicates that there is less erosion and more ability to capture metallic particulates present in a given media (18). BET surface area analysis and XRD analysis of the biochar showed nanosize forms of the biochar typical of a nanocrystalline material (12).
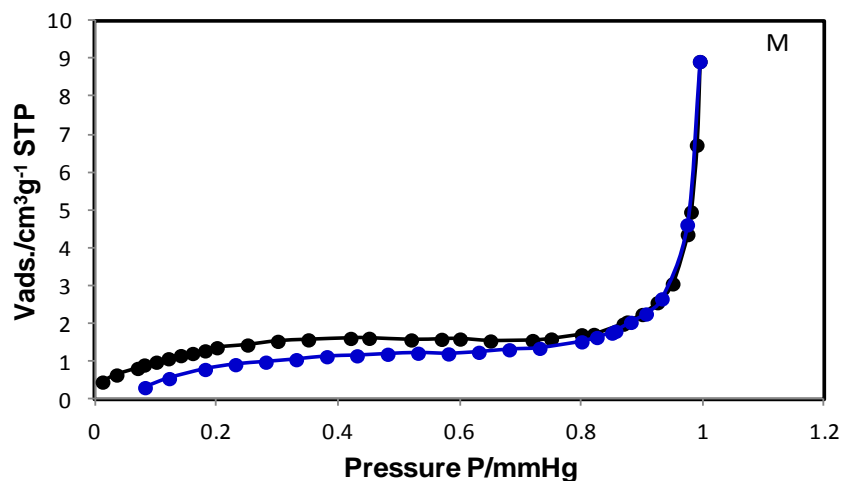
Figure 2: BET surface area plot of activated plantain peel biochar.

Batch Experiments
pH influence
Data obtained for the influence of pH on the sorption of zinc(II) ions on batch equilibration are plotted as shown in Figure 3. The adsorbent consumption of zinc(II) ions as shown in Figure 3 was highly influenced by the variation of the pH of the solution. As the pH of the solution was varied from 2 to 10, there was observed decrease of adsorbed zinc (II) ions from the equilibration mixture. At higher pH, the observed decrease in adsorption could be as the result of basic dissociation of active sites of the adsorbent forming positively charged species on the solid which interfered with the metal adsorption or due to the anionic surface of the biochar at lower pH promoting increased metal ion uptake (13).
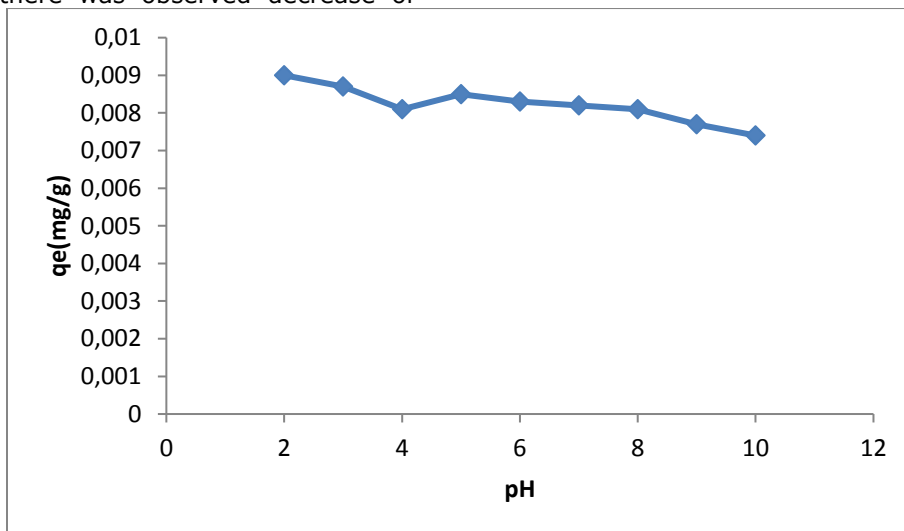
Figure 3: Effect of the initial pH of solution on equilibrium adsorption capacity of activated plantain peel biochar.

Effect of time of contact
Adsorption increased with increase in time of contact as shown in Figure 4. The plot of the variation of zinc(II) ions adsorbed against time of contact shown in Figure 4 indicated that the adsorption increased with time of contact until equilibrium was reached. This means that as adsorption starts, there are active sites available which got occupied and co-ordinatively consumed with increased time thereby clogging the sorption sites and a reduction or unavailability of free site. This observation is in line with the study (11) on the removal of prevalent heavy metals ions by sorption on scots pine and silver birch biochar.
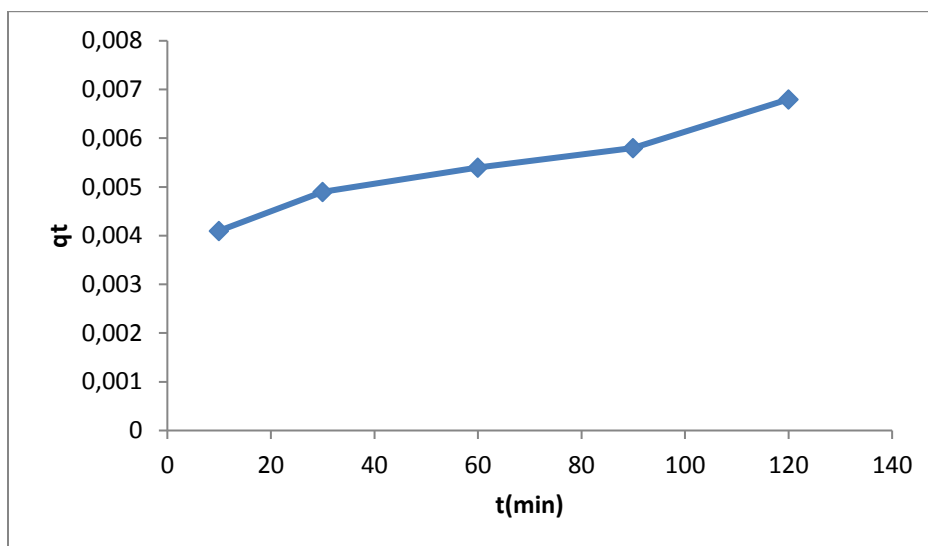
Figure 4: Effect of time of contact on the adsorption of zinc (II) ions on activated plantain peel biochar (pH = 6.5; initial metal ion concentration = 0.01 M).

Effect of initial metal ion concentration

The equilibrium stage sorption of the zinc(II) ions is plotted against the initial concentration of the sorptive solution as shown in Figure 5. There is enhanced sorption of zinc(II) ions at lower sorptive concentration which decreased linearly with increase in sorptive concentration. This observation could be that as concentration of zinc(II) ions increased, active adsorption sites get adsorptively saturated leading to decrease in adsorption efficiency. The observation could as well be as a result of increased active centres available at higher dilutions for relatively smaller amount of the sorbing ions (13,19,20). This is also in line with the study (14) which reported on the determination of zinc using EDTA complexometric studies. The sorption efficiency was high and the mechanism of the removal of zinc(II) ions from solution could be surface electrostatic interaction, cation exchange, precipitation or surface complexation (4,11,21).

Based on the equilibrium and kinetic result for the simulated data, sorption capacity increased as initial concentration increased. Thus, fractional adsorption of zinc (II) ions increased as initial concentration increased until at equilibrium and intraparticle mechanism primarily involving surface electrostatic interaction, cation exchange, precipitation or surface complexation could be in operation. Kinetic model explanation as given under Weber and Morris intraparticle diffusion and Bangham's pore diffusion model clearly explained that both mechanisms could be in operation based on the fitting of the simulated data. Similarly, increase in pH leads to decrease in negative charges on biochar due to decrease in negative sites. This led to decreased adsorption as electrostatic attraction was decreased and surface functional group dissociation could be responsible for alteration of adsorption.
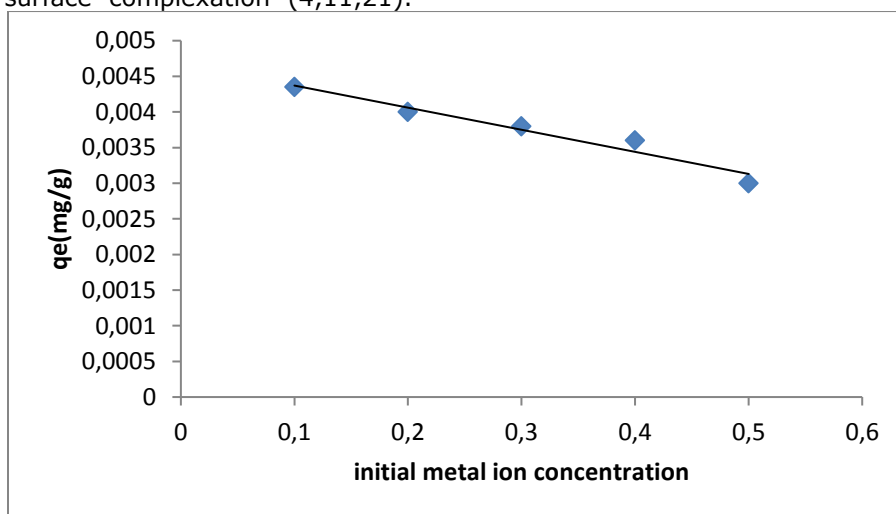

Figure 5: Effect of zinc (II) ions initial concentration on the adsorption onto activated plantain peel biochar(pH =6. 5; contact time = 120 min).

Equilibrium Adsorption Isotherms
(1)   Langmuir isotherm
The Langmuir adsorption isotherm considers adsorption to take place on homogenous site and ceases as sites become unavailable. The adsorption is thus monolayer without established interaction between the adsorbate (22,23). Langmuir model is expressed with Equation 4.

$$qe = Q_m \frac{bCe}{1} + bCe \qquad \text{(Eq. 4)}$$

Ce(mg/g) is the concentration of adsorbate at equilibrium, q_e (mg/g) the mass of adsorbate, Qm and b are constants regarded as Langmuir constants and stands for maximum adsorption capacity and adsorptive bonding energy respectively determined graphically by linearizing Langmuir isotherm as shown in Equation 5a.

$$\frac{Ce}{qe} = \frac{Ce}{Qm} + \frac{1}{bQm} \qquad \text{(Eq. 5a)}$$

Qm and b are constants from the graphical plot of $\frac{Ce}{qe}$ against Ce and represented as slope and intercept determined as 490 and -1,111 respectively. The

Langmuir constant Qm was very high indicating a very strong affinity for zinc. From Figure 6, the correlation coefficient (R^2) equals 1 indicating a perfect fit of the monolayer adsorption. This indicates that the adsorption sites are energetically identical and equivalent, structurally homogeneous and no observed interaction between the molecules adsorbed and close sites. Transfer of the adsorbate from the available sites to another is inhibited in the surface of the sites and the plantain peel biochar has finite adsorptive capacity for the zinc(II) ions. To evaluate the dimensionless separation factor a measure of the desirability and favourability of the model, the Langmuir parameter b regarded as Langmuir isotherm model constant was employed and values optimized from Hall equation (Equation 5b) (23).

$$RL = \frac{1}{1+bCo} \qquad \text{(Eq. 5b)}$$

Where Co is the initial concentration of zinc (II) ion and the values of b was found to be between 0 and I indicating the favorability of the adsorption process (23).

y = 10,006x - 0,0009
R² = 1

Figure 6: Langmuir adsorption isotherm for the adsorption of zinc(II) ions onto activated plantain peel biochar.

(2)   Freundlich Isotherm
Freundlich sorption isotherm model considers the adsorption to occur in a heterogeneous surface where there is no limited degree of adsorption with sites and energies exponentially distributed (22,23). As expressed in Equation 6, n is the adsorption intensity and K_f the adsorption capacity obtained as the intercept and slope respectively and shown as the linear plot of In qe against In Ce illustrated in Equation 7. The values of n and K_f are -3.544 and 9.65 respectively. This shows that the

Freundlich adsorption process is not favorable as the value of n is not within 1- 10 (23, 24.25, 26, 27, 28). The value of correlation coefficient was 0.8665 from Table 1 and Figure 7 indicating that the Langmuir isotherm simulated the data better (12).

$$qe = K_F Ce^{1/n} \qquad \text{(Eq. 6)}$$
$$Inq_e = InKf + \frac{1}{n}InCe \qquad \text{(Eq. 7)}$$
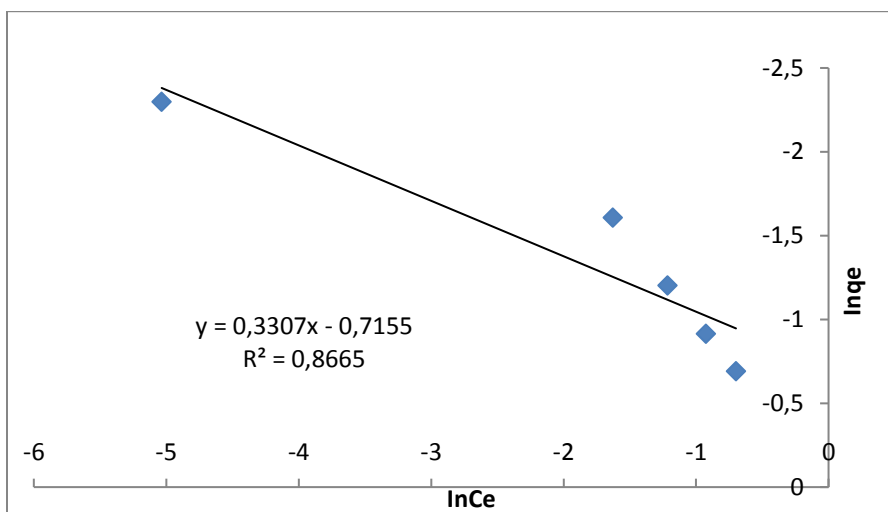
Figure 7: Freundlich adsorption isotherm for the adsorption of zinc(II) ions onto activated plantain peel biochar.

(3)　　Temkin isotherm

This considers the fall in the heat of sorption of molecules in the layer to decrease linearly with area of coverage owing to sorbent or sorbate interaction instead of logarithmic (22,23). The linear form of Temkin isotherm model is shown in Equation 8.

$$q_e = \beta \ln A_t + \beta \ln C_e$$

$\qquad\qquad\qquad\qquad\qquad$ (Eq. 8)

β is related to the heat of sorption and A is the binding constant at equilibrium state. The plot of q_e versus $\ln C_e$ gives the slope and intercept as A_t and β respectively. From Table 1 and Figure 8, the value of R^2 (0.6898) is less than Langmuir and Freundlich isotherms but greater than that of Elovich model. The values of A_t and β are 2161.47 and -68.87 respectively indicated weak affinity of the sorbate confirming that the model could not explain explicitly the sorption process.

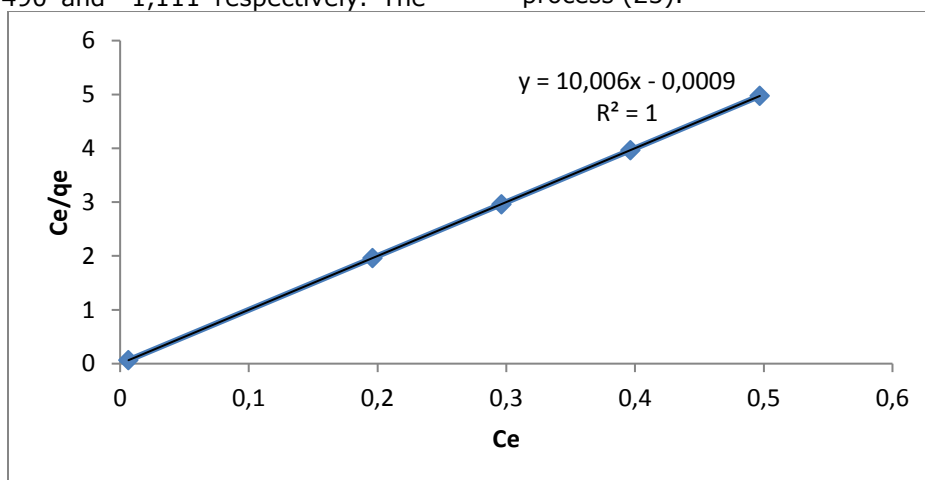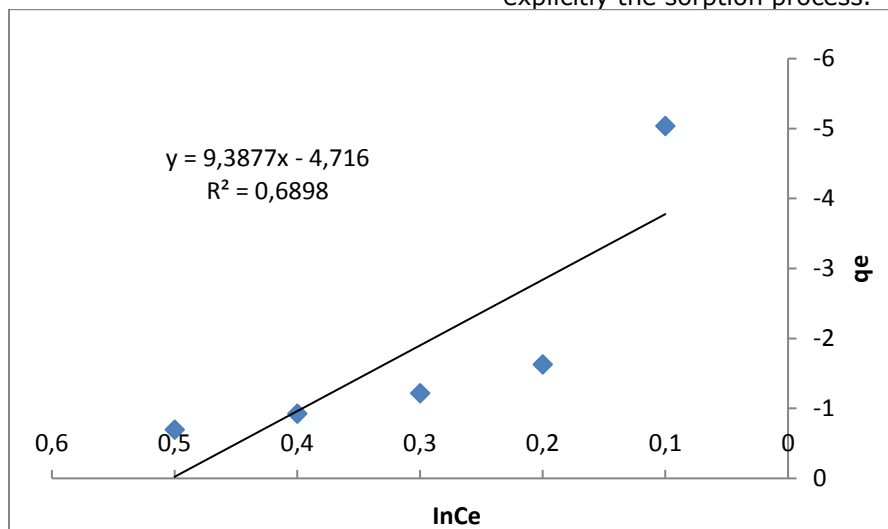**Figure 8:** Temkin adsorption isotherm for the adsorption of zinc(II) ions onto activated plantain peel biochar.

(4)　　Elovich isotherm

Elovic isotherm model describes a multilayer sorption process (23,24) that exponentially increase with adsorption site. The isotherm is represented in Equation 9:

$$\frac{q_e}{q_m} = K_E C_e e^{\frac{q_e}{q_m}}$$
$\qquad\qquad$ (Eq. 9)

Elovich maximum sorption capacity and sorption constant K_m and K_E respectively are evaluated from

the slope and intercept of the plot of $\ln(q_e/C_e)$ versus q_e to be 115.62 and 591.78. As shown in Table 1 and Figure 9, the value of R^2 is 0.5039 which is less than Langmuir, Freundlich and Temkin isotherms illustrating that the adsorption does not fit the Elovich isotherm model. The low value of the sorption capacity confirms the monolayer adsorptivity and defies the fact that the sorption is multilayer (23,24).
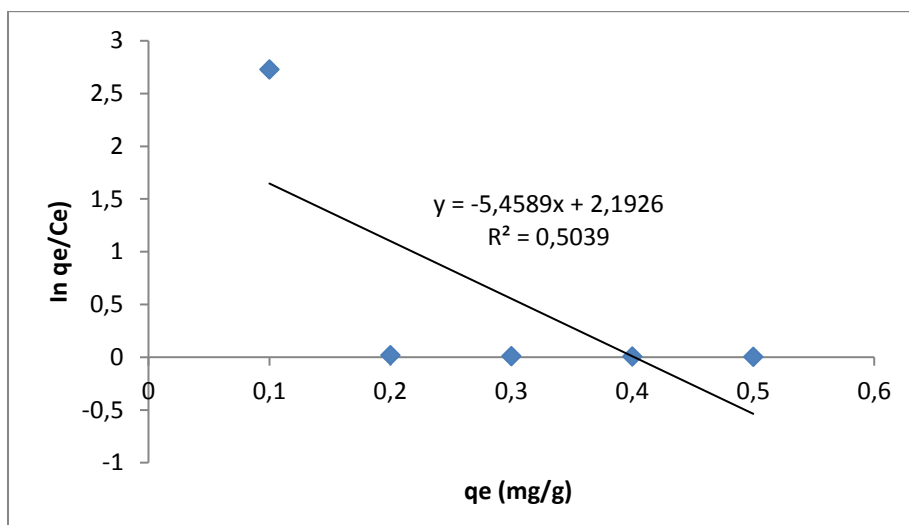
Figure 9: Elovich sorption isotherm for the adsorption of zinc(II) ions onto activated plantain peel biochar.

Adsorption Kinetics
Different parametric adsorption kinetics models were used to analyze the adsorption processes.

Pseudo-first- order model
The sorption of adsorbate from liquid phase is considered and this remains the most widely used Lagergren's rate equation (24).

Equation 10 shows the linearized pseudo-first order model with t as time of contact, qt is mass of zinc(II) ions, qe is equilibrium mass of zinc(II) ions adsorbed, K_1 pseudo first order constant. As shown in Table 1 and Figure 10, the data have low regression coefficient of 0.8143 and low value of K_I of -0.0376 showing that the sorption process does not agree with the model.

$$\text{In}(\text{qe} - \text{qt}) = \text{In}qe - k_I t \qquad (Eq. 10)$$
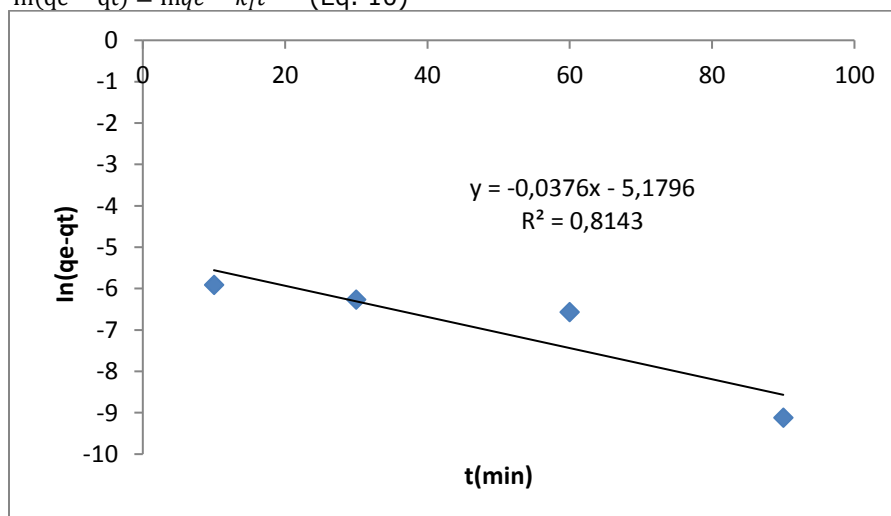
Figure 8: Pseudo-first –order kinetic plot for the adsorption of zinc(II) ions onto activated plantain peel biochar.

Pseudo-second-order kinetic model
Chemisorption defines the rate-controlling step in pseudo-second-order process as illustrated in Equation 11 (12).

$$t/qt = 1/K_2 \, qe^2 + t/qe \qquad (Eq. 11)$$

Where K_2 is pseudo second order constant. The obtained data of R^2 (0.9773)(Figure 9) indicates a good relationship between the parameters and shows that the adsorption kinetic model could be in control of the process. The value of K_2 was 71.42 high enough but lower than Bangham's pore diffusion model and indicated that chemisorption could be part of the rate-determining step.
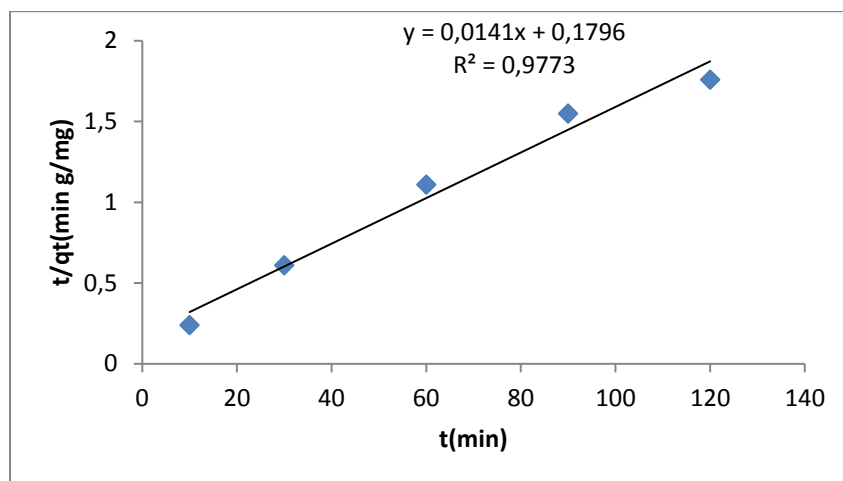
Figure 9: Pseudo -second –order kinetics plot for the adsorption of zinc(II) ions onto activated plantain peel biochar.

Elovich kinetic model

Elovich model describes the kinetics of chemisorption of gas and or solute onto solid sorbents and represented in Equation 12 (12,19).

$$q_t = \frac{1}{\beta}\ln(\alpha\beta) + \frac{1}{\beta}In(t) \qquad \text{(Eq. 12)}$$

The constants ą and β represents the initial adsorption rate (mg/gmin^{-1}) and the degree of surface coverage and activation energy for chemisorption (g/mg) respectively. These values were obtained from the slope and intercept of the linearized plot of q_t against In t (12,23) as 0.001 and 0.0017, respectively. From Table 1 and Figure 10, the regression coefficients of the data was high and good fitting (R^2 =0.903). The values obtained suggested that diffusion could be part of the rate determining step and accounted for the parameters in Elovich model a confirmation that chemisorption could be part of the rate-limiting step. Chakrapani *et al* (24) in his study made similar observation and maintained that the equation prevails at situations where the rate of desorption is negligible.
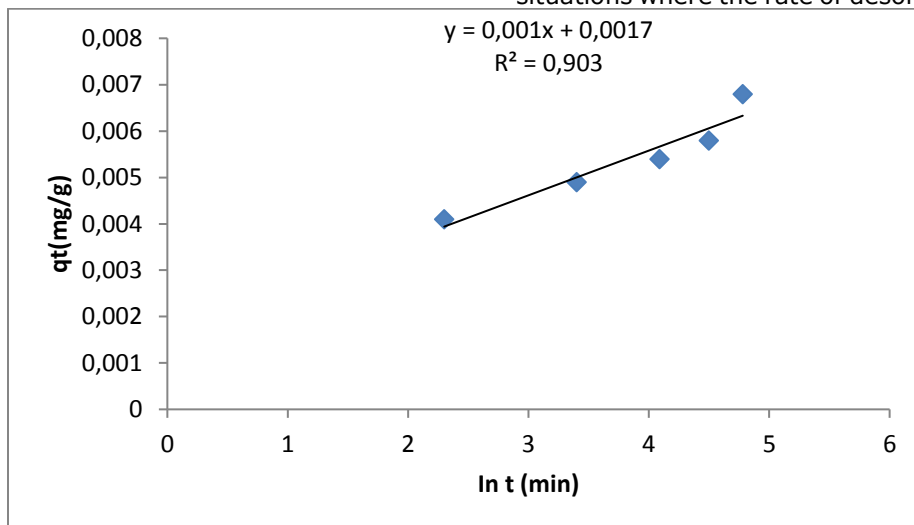
Figure 10: Elovich kinetics plot for the adsorption of zinc(II) ions onto activated plantain peel biochar.

Weber and Morris intraparticle diffusion model

The linear form of Weber and Morris intraparticle diffusion model is shown in Equation 13 (25,26).

$$qt = K_I t^{1/2} + C$$

$$\text{(Eq. 13)}$$

Where K_I (slope) is intraparticle diffusion rate constant (mg/g min$^{1/2}$) and C the intercept representing the sorption strength of the boundary layer calculated from the linear plot of qt against $t^{1/2}$ as 0.003 and 0.0031 respectively with high regression coefficient (R^2) of 0.9584. A high value of C indicates high sorption capacity (25) and justifies the extent of intraparticle diffusivity of the adsorbate through the adsorbent surface. From Figure 11, the plot is linear but never passed through the origin indicating that intra particle diffusion could be among the mechanistic steps but

not the only rate determining process. The failure of the intercept line to go through the origin could be as the result of the differences in mass movement of adsorbate in the beginning and ending processes of the sorption implicating boundary layer control in the adsorption (26).
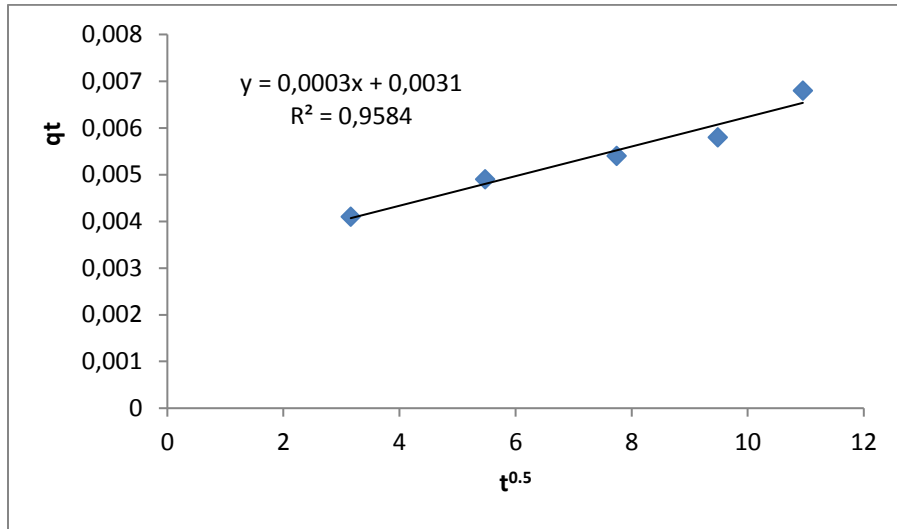
Figure 11: Weber and Morris intraparticle diffusion model for the adsorption of zinc(II) ions onto activated plantain peel biochar.

Liquid film diffusion kinetic model
Diffusion is controlled by liquid films in contact with the adsorbent and represented in Equation 14 (12).

$$In(1 - \frac{qt}{qe}) = -K_{lf}t \qquad \text{(Eq. 14)}$$

A plot of ln $(1 - \frac{qt}{qe})$ versus t gave the slope as K_{lf} representing the liquid diffusion constant regarded as the external mass transfer coefficient (1/min). Figure 13 gave the slope as 0.0002 with poor regression coefficient (R^2) of 0.7478. The result confirms that the sorption is not liquid film diffusion dependent and this was strongly in agreement with the study of Panida and Xianshe (26).

Figure 12: Liquid film diffusion model for the adsorption of zinc(II) ions onto activated plantain peel biochar.

Bangham's pore diffusion model
Linearized Bangham's pore diffusion model is represented in equation 15 (25).

$$\text{Log} \log \left\{ \frac{Co}{Co - mqt} \right\} = \text{Log} \left\{ \frac{mK_B}{2.303V} \right\} + \delta\beta logt$$

(Eq. 15)

Where Co is the initial zinc(II) ion concentration (mg/L), V is solution volume (mL), m the weight of adsorbent(g/L), đβ and K_B are constants representing the slope and intercept obtained from linearized plot of log log [Co/Co-mqt] versus log t. The plot as shown in Figure 13 is linear with high

regression coefficient (R^2) of 0.992 indicating that the kinetic model confirmed the Bangham equation and that pore diffusion processes are prevalently in control of the sorption of zinc(II) ions onto plantain peel biochar(24).
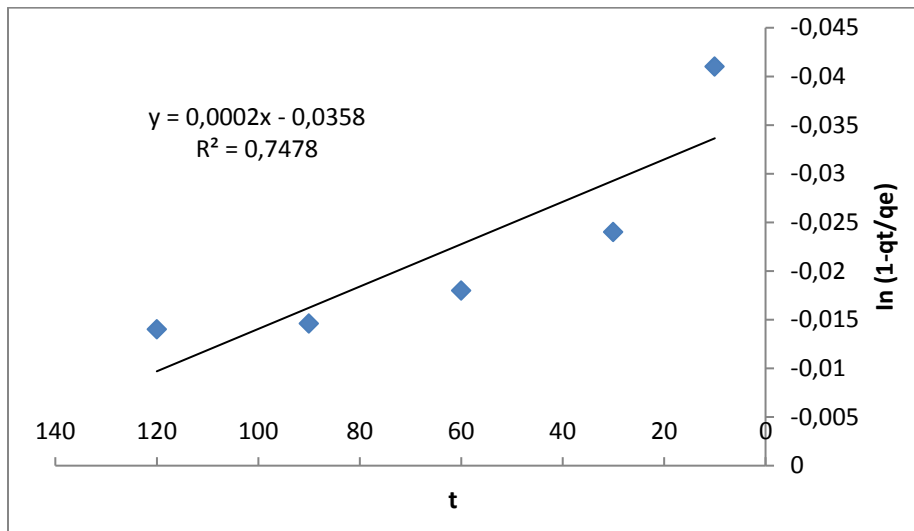

$$y = -2,2082x - 5,0993$$
$$R^2 = 0,992$$
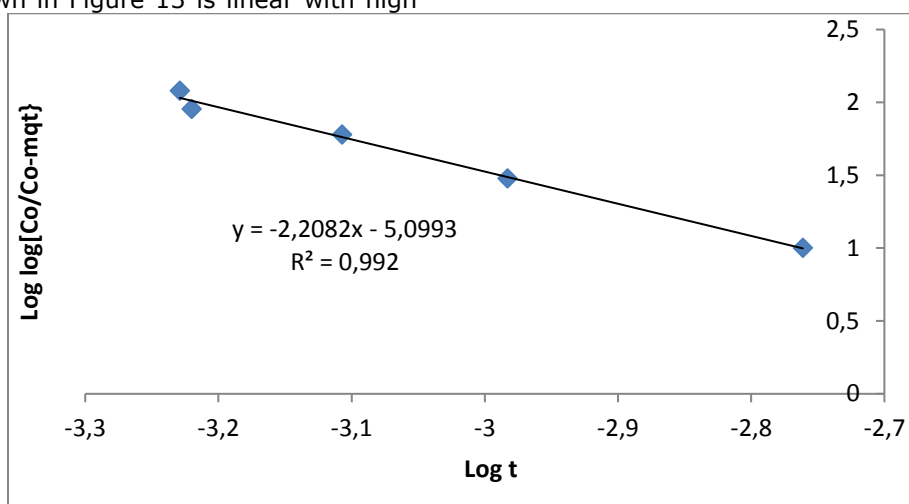
Figure 13: Bangham's pore diffusion model for the adsorption of zinc(II) ions onto activated plantain peel biochar.

Table 1: Equilibrium and kinetic model parameters for the adsorption of zinc(II) ions on activated plantain peel biochar.

S/N	Models	Parameter 1 K_f(mg/g)	Parameter 2 qe(mg/g),b(L/mg)	R^2
	Kinetic models			
1	Pseudo-First order	$K_1 = -0.0376$	$q_e = -5.1796$	0.8143
2	Pseudo-second order	$K_2 = 71.42$	$q_e = 0.1796$	0.9773
3	Elovich	$α = 0.001$	$β = 0.0017$	0.903
4	Weber and Morris intraparticle	$K_I = 0.003$	$C = 0.0031$	0.9584
5	Liquid film diffusion	$K_{lf} = 0.0002$	$qe = -0.0358$	0.7478
6	Bangham pore diffusion	$đβ = -2.208$	$K_B = -5.099$	0.992
	Equilibrium models			
7	Langmuir	$q_m = 490.00$	$b = -1,111$	1
8	Freundlich	$K_f = 9.65$	$n = -3.544$	0.8665
9	Temkin	$A_t = 2161.47$	$B = -68.87$	0.6898
10	Elovich equation	$Km = 115.62$	$K_E = 591.78$	0.5039

CONCLUSION

The presence of Zn(II) ion from aqueous media was removed by adsorption using an effective, efficient and low cost plantain peel biochar. XRD analysis of the biochar indicated that it is of nanosize form corroborating the BET surface analysis of pore size and pore surface area typical of a nanocrystalline material. Zinc(II) ions sorption increased with increase in time until equilibrium at 120 minutes but decreased with increase in pH and initial zinc(II) ion concentration. Sorption equilibrium and kinetic models were applied to test the effectiveness, efficiency and applicability of the processes. The adsorption isotherm obeyed Langmuir monolayer process whereas the kinetic mechanism showed mainly pore diffusion process

been prevalent. The study serves as a green approach to the removal of zinc(II) ions from contaminated media. The method is green because it sequestrates metal contaminants from the environment without contaminating the environment. A green or benign analytical approach is an environmentally friendly approach for which the adsorption process presents. The zinc metal can be eluted or desorbed from the activated plantain peel biochar for reuse or before discarding to the environment as a soil amender.

REFERENCES

1. Oberio HS, Vadlani P V, Saida L, Hughes J D. Ethanol production from plantain peels using statistically optimized simultaneous

saccharification and fermentation process. Waste Management. 2011; 31: 1576-85.

2. Onyebado CO, Iyagba ET, Offor OJ. Solid soap production using plantain peels ash as source of alkali. Journal of Applied Science and Environmental Management.2004; 6**:** 73-7.

3. Mitani N, Jian FM. Uptake system of silicon in different plant species. J. Exp. Bot. 2005; 56 (414): 1255–61.

4. Uchimiya M, Chang S, Klasson KT. Screening biochars for heavy metal retention in soil: Role of oxygen functional groups. J. Haz. Mat. 2011; 190 (1-3): 432-41.

5. Betiku E, Sheriff O A. Modeling and optimization of Thevetiaperuviana (yellow oleander) oil biodiesel synthetic via Musa paradisiacal (plantain) peels as heterogeneous base catalyst: A case of artificial neural network vs. response surface methodology. Ind. crop. prod. 2014; 53: 314-22.

6. Wolfe K, Wu K, Liu RH. Antioxidant activity of apple peels. J. Agric. Food Chem. 2003; 51:609-14.

7. Ismail S, Khan F, Zafar- Iqbal M. Phytoremediation: Assessing tolerance of tree species against trace metal (Pb and Cd) toxicity. Pakistan J Botany. 2013; 45: 2181-6.

8. Parizanganeh AH, Bijnavand V, Zamani AA, Hajabolfath A. Concentration, distribution and comparison of total and bioavailable trace metals in top soils of Bonab district in Zanjan province. Open J. Soil Sci. 2012; 2: 123-32.

9. Dada AO, Ojediran JO, Olalekan AP. Sorption of Pb^{2+} from aqueous solution unto modified rice husk: isotherm studies. Adv Chem Phys. 2013: 1–6 (id: 842425).

10. Babel S, Kurniawan TA. Low-cost adsorbents for heavy metals uptake from contaminated water: a review. J Hazard Mater. 2003; 97(1–3): 219–43.

11. Komkiene J, Baltrenaite E. Biochar as adsorbent for removal of heavy metal ions [Cadmium(II), Copper (II), Lead(II), Zinc(II) from aqueous phase. Int. J. Environ. Sci. Technol. 2016; 13: 471-82.

12. Inyang M, Cao B, Pullammannappallil P, Zimmerman A R. Enhanced lead sorption by biochar derived from anaerobically digested sugarcane bagasse. Sep. Sci. Technol. 2011; 46(12): 1950-6.

13. Tiwari LD, Lee S. Activated carbon and manganese coated activated carbon precursor to

dead biomass in the remediation of arsenic contaminated water. Environmental Engineering Research. 2012; 17:541-8**.**

14. Prasad AS. Zinc deficiency by global health organization. British Medical Journal. 2003; 326 (7386): 409-10.

15. Jindapon W, Jaiyen S, Ngamcharussrivichai C. Al_2O_3-supported Mixed Ca and Zn Compounds Prepared from Waste Seashells for Synthesis of Palm Fatty Acid Methyl Esters, Chemical Engineering Communications. 2015; 202: 1591–9.

16. Morin TJ, Chengeto SW, Makura V, Tatlock HM, Lindeman SV, Bennett B, Long GJ, Grandjean F, Gardinier JR. Pyrazolylmethyls prescribe the electronic properties of iron(II) tetra(pyrazolyl)lutidine chloride complexes, Dalton Trans. 2011; 40: 8024–34.

17. Zhou Y, Gao B, Zimmerman AR, Cao X. Biochar-supported zerovalent iron reclaims silver from aqueous solution to form antimicrobial nanocomposite. Chemosphere. 2014; 117: 801-5.

18. Demirbas A. Effects of temperature and particle size on biochar yield from pyrolysis of agricultural residues. Journal of Analytical and Applied Pyrolysis. 2003; 72: 243-8.

19. Thavamani SS, Rajkumar R. Removal of Cr(II), Pb(II) and Ni(II) from aqueous solution by adsorption on alumina. Res. J. Chem. Sci. 2013; 3(8): 44-8.

20. Okareh OT, Adeolu AT. Removal of Lead ion from industrial effluent using plantain wastes. Br. J. App. Sci. Technol. 2015; 8(3): 267-276.

21. Cao XD, Ma L, Gao B, Harris W. Dairy manure derived biochar effectively sorbs lead and atrazine. Environ. Sci. Technol. 2009; 43(9): 3285-91.

22. Mazhar IK, Saima QM, Sajida P, Muhammed YK. Citrus paradise: An effective bio-adsorbent for arsenic(V) remediation. Pak. J. Anal. Environ. Chem. 2014; 15(1): 35-41.

23. Farouq R, Yousef NS. Equilibrium and Kinetics Studies of Adsorption of Copper (II) Ions on Natural Biosorbent. Int. J. Chem. Eng. Appl. 2015; 6: 319-24.

24. Chakrapani CH, SureshBabu CH, Vani KNK, Somasekhara Rao K. Adsorption kinetics for the removal of fluoride from aqueous solution by activated carbon adsorbents derived from the peels of selected citrus fruits.. E- journal of chemistry. 2010; 7(SI): S419-27.

25. Antonija k, Natlija V, Dam H, Davor K. Lignocellulosic materials as dye adsorbents: Adsorption of methylene blue and congo red on brewers spent grain. Croat. Chim. Acta, 2018; 91: 53-64.

26. Panida S, Xianshe F. Kinetic models on

chromium(VI) adsorption onto carbonized oil palm kernel with potassium hydroxide activation. Intl J. Adv. Chem. Eng. Biol. Sci. 2016; 3(1): 68-75.

27. Erol K. The adsorption of calmoduline via nicotinamide immobilized poly(HEMA-GMA) cryogels. JOTCSA. 2017; 4(1): 133-48.

28. Yildiz A. Adsorption of Acid Red 114 onto Fe_3O_4 at Caffeic acid recyclable magnetic nanocomposite. JOTCSA. 2017; 4(1): 327-40.

RESEARCH ARTICLE

A Schiff Base Sensor Selective to Anions, Biological Activity, and Spectral Studies

Nuray Yıldırım[1] (iD) (✉), **Mustafa Yıldız[2]*** (iD) (✉)

[1]Health Services Vocational School, Çanakkale Onsekiz Mart University, TR-17100 Çanakkale, Turkey
[2]Department of Chemistry, Faculty of Arts and Sciences, Çanakkale Onsekiz Mart University, 17100 Çanakkale, Turkey

Abstract: In this study, synthesis, characterization, anion sensor properties, and DNA binding of a benzothiazole-based Schiff base 4-bromo-2-((6-methoxybenzo[d]thiazol-2-ylimino)methyl)phenol have been investigated. The structure of the Schiff base was revealed with elemental analysis and spectroscopic methods. The colorimetric and fluorescent anion sensor properties of the Schiff base in DMSO were investigated by adding an equivalent amount of anions. In this context, the solution containing Schiff base had a color change after the addition of F^-, CN^-, AcO^-, $H_2PO_4^-$ and OH^- anions, while the color change was not observed with the addition of Br^-, I^-, SCN^-, ClO_4^- and HSO_4^- anions. The anion-binding power of the compound was found to be $F^- > OH^- > AcO^- > CN^- > H_2PO_4^-$ using UV-Vis spectrophotometry, respectively. The antimicrobial activity of the compound was investigated against some microorganisms. The compound showed activity against bacteria and yeast. Schiff base showed a similar effect against both bacteria and yeast. Interactions between the compound and CT-DNA were studied with UV-Vis spectra. The UV-Vis experiment results confirm that the Schiff base binds to CT-DNA in an intercalative mode. The compound did not show any cleavage effect on SC DNA as hydrolytic and oxidative.

Keywords: Schiff base, Spectroscopy, Anion Sensors, DNA-Binding.

INTRODUCTION

Some characteristic properties of Schiff bases, such as antimicrobial, antioxidant, anticancer, anti-helmintic, anti-inflammatory, anticonvulsant, antitubercular and analgesic activities (1-5) as well as chemosensory and DNA binding properties (6-19) have been reported. The technique used in chemosensors is concerned with the quenching of the colorimetric chemosensor of fluorescence by interaction with various anions. Chemosensors are very useful because they provide fast and visible color changes in the presence of ions. In the last decade, many chemosensors have been developed and studied to recognize and select ions with precise selectivity and sensitivity (4-20).

2-Hydroxy imines exhibit interesting properties both in solution and solid state. Tautomerism occurs in ortho-hydroxy imines. It was studied in ortho-hydroxy imines using various methods (21,22). If the H proton in the O-H is taken by the imine nitrogen, the keto-amine form occurs. This form is always observed if the imine is formed by 2-hydroxy-1-naphthaldehyde and aromatic amine. It is not observed in solution and solid state in Schiff bases composed of 2-hydroxy benzaldehyde and aromatic amines. But it has been observed in compounds derived from substituted salicylaldehydes and aromatic amines. Many properties of Schiff bases, especially sensor properties, are associated with tautomerism. Depending on the tautomerism of

the ortho-hydroxy imines, hydrogen bonds such as O-H...N and N-H...O are formed (21,23).

Colorimetric sensors are used for ion detection because the signaling phenomenon is easily detected by the naked eye (22,24). A visible color change occurs after the formation of the hydrogen bond between the anion and the sensor. 2-Hydroxy Schiff bases can produce hydrogen bonds that can be used in chromogenic and fluorogenic sensors (11, 25). Benzothiazole-based Schiff bases are nitrogen and sulfur-heterocyclic bicyclic ring systems (26). Benzothiazoles have many applications. Anticancer, antimicrobial and antidiabetic, anticonvulsant, anti-inflammatory, antiviral, and antitubercular activities of benzothiazoles are known (27,28). Furthermore, biological activities of bicyclic Schiff bases have been investigated and reported as DNA repair agents (29).

In the present work, a receptor was prepared by the reaction of 2-amino-6-methoxybenzothiazole with 5-bromosalicylaldehyde with the ability to detect some anions by colorimetry and spectrophotometry (UV-Vis) in dimethyl sulfoxide (DMSO). In addition, the antimicrobial activity of the synthesized compound and its interaction with DNA was investigated.

MATERIALS AND METHODS

Reagents and techniques
The ^{1}H- and ^{13}C-NMR spectra were recorded on a JOEL NMR- 400 spectrometer operating at 400 and 101,6 MHz, respectively. Infrared absorption spectra were obtained from a Perkin Elmer BX II spectrometer in KBr discs and were reported in cm^{-1} units. The UV-Vis spectra were measured using PG Instruments T+80 UV/Vis spectrophotometer. Elemental analyses were performed on a Vario EL III CHNS elemental analyzer. Melting points were measured with an Electro Thermal IA 9100 apparatus using a

capillary tube. 2-Amino-6-methoxybenzothiazole, 5-bromosalicylaldehyde, EtOH, DMSO, Ethidium bromide (EB), calf thymus DNA (CT-DNA), (Bu)$_4$NF, (Bu)$_4$NBr, (Bu)$_4$NI, (Bu)$_4$NCN, (Bu)$_4$NSCN, (Bu)$_4$NClO$_4$, (Bu)$_4$NHSO$_4$, (Bu)$_4$NCH$_3$COO, (Bu)$_4$NH$_2$PO$_4$, (Bu)$_4$NN$_3$, (Bu)$_4$NOH and DMSO were purchased from Aldrich. The Tris–HCl buffer solution was prepared with triple-distilled water. CT-DNA stock solution was prepared by diluting DNA to Tris–HCl/NaCl buffer (5 mM Tris–HCl, 50 mM NaCl, pH 7.2), and kept at 4 °C for no longer than two days.

Synthesis of 4-bromo-2-((6-methoxybenzo[d]thiazol-2-ylimino)methyl)phenol
2-Amino-6-methoxybenzothiazole (1.00 g; 5.55 mmol), ethanol (100 mL) and 5-bromo-2-hydroxybenzaldehyde (1.115 g; 5.55 mmol) were added to a 250 mL round-bottomed flask. The mixture was stirred and refluxed for 2 h. The compound was obtained from the evaporation of ethanol and was crystallized from CHCl$_3$:n-hexane (3:1) as a yellow crystal, m.p. 213-215 °C, 1.79 g (89%) yield (Scheme 1). Experimental: C, 49.05; H, 3.05; N, 7.71. Calculated: C$_{15}$H$_{11}$BrN$_2$O$_2$S; C, 49.58; H, 3.04; N, 7.71. FT-IR (KBr, cm^{-1}) νO-H; 3291 m-br, νAr-H; 3077 w, νC-H; 2974-2925 w, νC=N; 1598 s, νC=C; 1558 s, νC-N; 1497 s, νC-O; 1346 s, νC-O-C; 1262-1220-1169-1050 s. ^{1}H-NMR (DMSO); δ ppm, 9.30 (s, 1H, Ar-O<u>H</u>); 8.06 (s, 1H, Ar-C<u>H</u>=N-); 7.85-6.98 (m, 6H, Ar-<u>H</u>). ^{13}C-NMR (DMSO); δ ppm, 168.10 (s, 1C, <u>C8</u>); 163.08 (s, 1C, <u>C7</u>); 159.85 (s, 1C, <u>C2</u>); 157.91 (s, 1C, <u>C13</u>); 145.86 (s, 1C, <u>C10</u>); 137.78 (s, 1C, <u>C9</u>); 135.93 (s, 1C, <u>C6</u>); 132.28 (s, 1C, <u>C11</u>); 123.90 (s, 1C, <u>C4</u>); 122.25 (s, 1C, <u>C1</u>); 119.82 (s, 1C, <u>C3</u>); 116.48 (s, 1C, <u>C12</u>); 111.23 (s, 1C, <u>C5</u>); 105.56 (s, 1C, <u>C14</u>); 56.19 (s, 1C, <u>C15</u>). The carbons were numbered according to the order of Scheme 1.
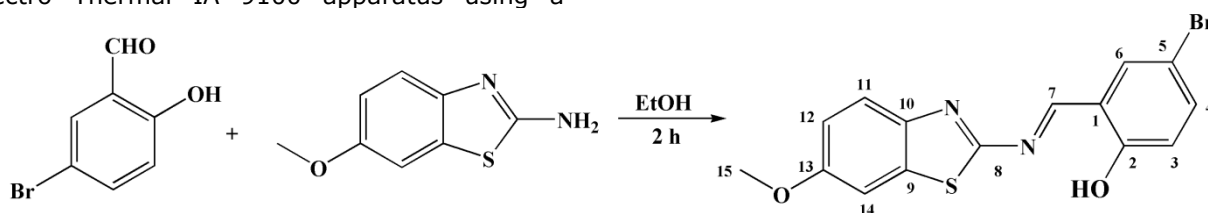
Scheme 1. Synthesis of the Schiff base.

Screening for antimicrobial activities
Staphylococcus aureus ATCC 25923, *Enterococcus faecalis* ATCC 29212, *Escherichia coli* ATCC 25922, *Pseudomonas aeruginosa* ATCC 254992, *Candida albicans* ATCC 60193, and *Candida tropicalis* ATCC 13803 were used as microorganisms. Ampicillin and fluconazole were used as controls in this study as they are well-known broad-spectrum antibiotics that have different mechanisms of activity, such as interruption of cell wall synthesis (ampicillin) (30). The compounds were dissolved in DMSO

(dimethyl sulfoxide) to a final concentration of 500 μg/mL. The concentration of the compounds on different plates was 500 μg/mL, 250 μg/mL, 125 μg/mL, 62.5 μg/mL, 31.25 μg/mL, 15.6 μg/mL, 8 μg/mL, 4 μg/mL, 2 μg/mL, and 1 μg/mL.

DNA-Binding experiments

The UV-Visible spectral titrations were carried out in Tris–HCl/NaCl buffer at room temperature to investigate the binding affinity between CT-DNA and the Schiff base. The UV-Vis absorbance at 260 and 280 nm of CT-DNA solution in Tris buffer gives a ratio of 1.8–1.9, indicating that the DNA was sufficiently free of the protein (31). Tris–HCl/NaCl buffer (1.8 mL) and the solutions of Schiff base (1.8 mL, 1×10^{-5} M) were respectively placed into two cuvettes. Then one aliquot (5.4 µL, 0.01 M) of buffered CT-DNA solution was added to each cuvette in order to eliminate the absorbance of DNA itself. Before the absorption spectra were recorded, the Schiff base-DNA solutions were incubated at room temperature for 5 min.

DNA Cleavage experiments

The DNA cleavage activity of the Schiff base was studied by agarose gel electrophoresis method. pBR322 DNA (0.1 µg µL^{-1}) in Tris-HCl buffer (10 µM, pH:7,2) treated with the compound at 37 °C for 3 h. To determine the mechanism of cleavage activity H_2O_2 was added to one of the group of mixture as an oxidizing agent. After incubation loading buffer was added and samples were subjected to electrophoresis for 1 hour at 60 V on 1% agarose gel in TBE (Tris-Boric acid-EDTA, pH:8.0) buffer. Then, the bands were visualized by UV light and photographed.

Anion Sensors Measurements

The Schiff base (0.05 µmol) was dissolved in DMSO (50 mL). Tetrabutylammonium salts(F^-, Br^-, I^-, CN^-, SCN^-, ClO_4^-, HSO_4^-, CH_3COO^-, $H_2PO_4^-$, OH^-) (0.05 µmol) were dissolved in DMSO (50 mL). Each solution of tetrabutylammonium salts was added to the Schiff base solution (1:1) in the tube. After mixing them, UV absorption spectra and the photos were taken at room temperature under daylight and UV light (λ= 365 nm).

RESULTS AND DISCUSSION

Spectroscopic Studies
FT-IR studies

The IR spectrum of the Schiff base is given in Figure 1. The vibration bands with the wavenumbers (ν, cm^{-1}) of 3291 (Ar-OH), 3077 (Ar-H), 2925 (aliph-H), 1598 (C=N + C=C), 1558 (C=C), 1497 (C-N), 1346 (C-O) and 1262-1220-1169-1050 cm^{-1} (Ar-O-CH$_3$) were observed in the spectrum. Also, the C=N and C=C peaks overlap at 1598 cm^{-1} in the spectrum (Figure 1). Due to the intramolecular hydrogen bond O-H...N, a peak at 2828 cm^{-1} was observed in the spectrum of the compound. The presence of a strong band at 1346 cm^{-1} in the Schiff base indicates that the compound is in phenol-imine form due to the stabilization of the phenolic C-O bond. Very strong etheric ArC-O-C vibrations were observed between 1262 cm^{-1} and 1050 cm^{-1} for the compound.
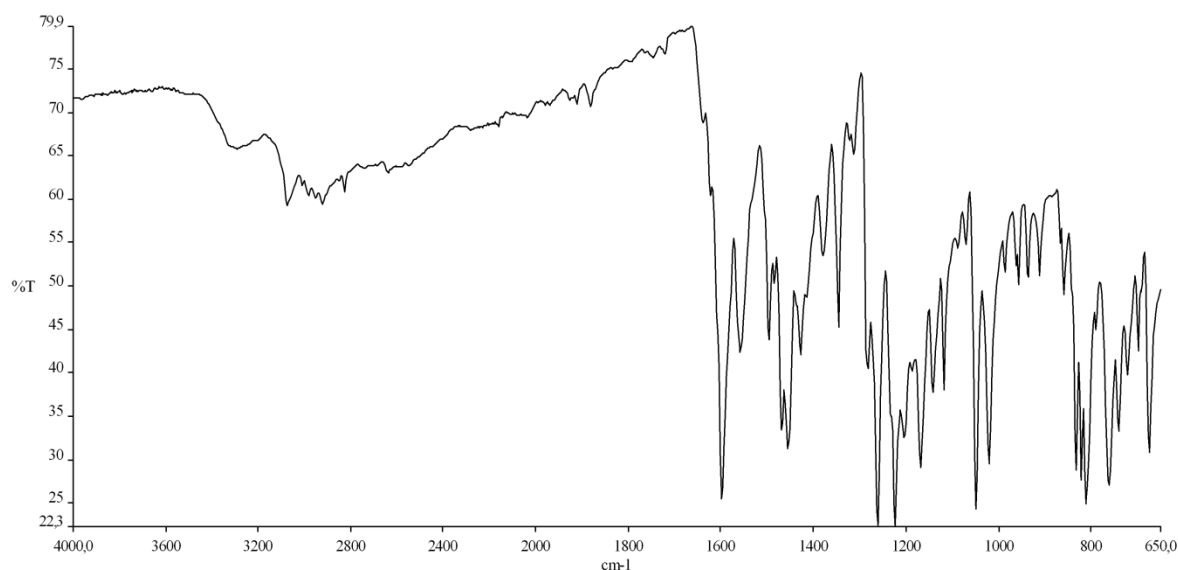
Figure 1. FTIR spectrum of the Schiff base.

^{1}H- and ^{13}-CNMR spectroscopy

The NMR spectrum of the compound is given in Figures 2 and 3. According to the ^{1}H NMR results, the Schiff base has phenol-imine form in DMSO solution (Fig. 2). In the NMR spectrum of the compound, a singlet for the OC$\underline{H}_3$ protons, and multiplets for the Ar-H protons are observed. In the compound, the O$\underline{H}$ and -C$\underline{H}$=N- protons are observed as a singlet. It can be said that the compound is in phenol-imine form in DMSO since

the imine (-C$\underline{H}$=N-) and hydroxyl (O$\underline{H}$) protons do not split. From the ^{13}C NMR spectrum, it appears that the compound has 15 signals (Figure 3). When the chemical shift values are ordered from highest to lowest, they are N-$\underline{C}$(S)-, -$\underline{C}$H=N, Ar$\underline{C}$-OH, Ar$\underline{C}$-OCH$_3$, Ar-$\underline{C}$, and O$\underline{C}$H$_3$, respectively, for the compound. According to the NMR results, the compound is in the phenol-imine form in DMSO solution.
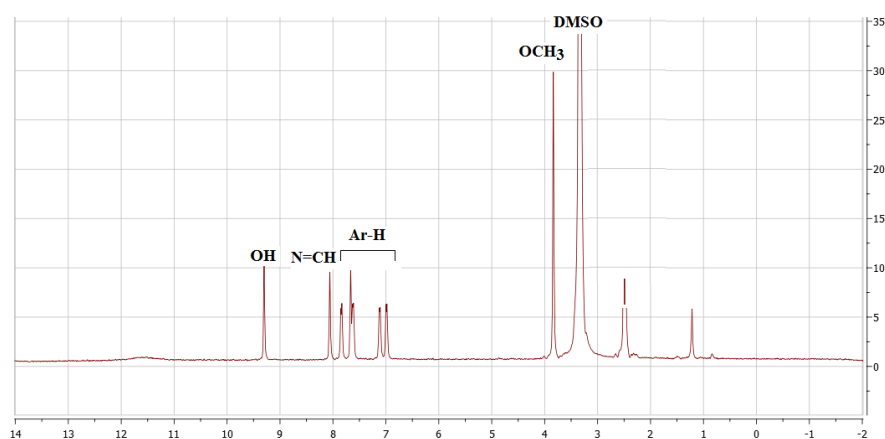
Figure 2. ^{1}H-NMR spectra of the Schiff base.
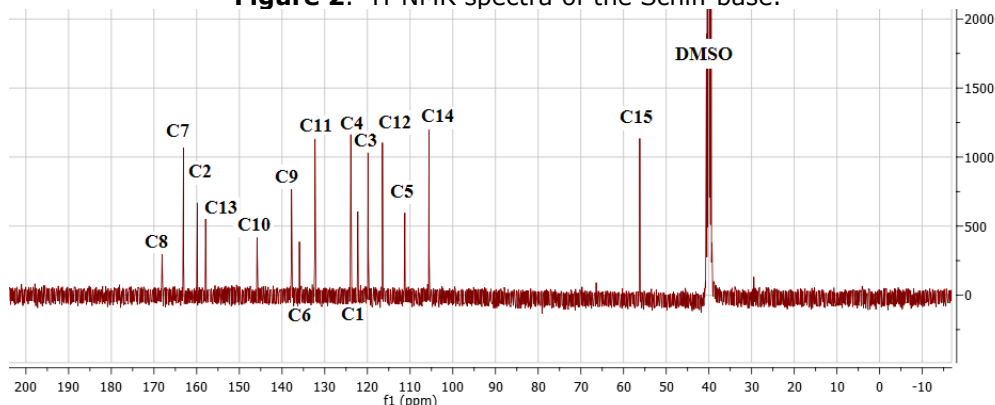
Figure 3. ^{13}C-NMR spectra of the Schiff base.

UV-Vis spectroscopy

In this study, the electronic spectrum of the compound was also investigated in dimethyl sulfoxide (Figure 4). Some imines give absorption bands in both polar and non-polar solvents greater than 400 nm. It was reported that the new band in 2-hydroxy imines belongs to the keto-amine form in polar and non-polar solvents in both acidic and basic solutions. A new peak was not observed after 400 nm in DMSO for the Schiff base. Hence, the compound has phenol-imine form in DMSO. According to the UV-Vis results of the compound, only a shoulder and a band appear at 276 nm and 399 nm, which are assigned to the π–π* and n–π* transition of the C=C and C=N.

As a result, the compound was in the phenol-imine form according to the FTIR, UV-Vis, ^{13}C-NMR and ^{1}H-NMR data.
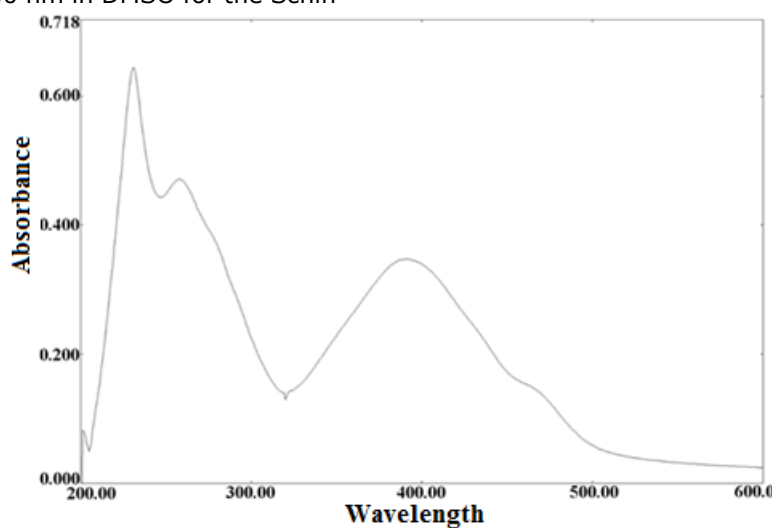
Figure 4. UV-Vis spectrum of the Schiff base.

Colorimetric anion sensing of the compound

For the colorimetric anion sensor properties of the Schiff base, the color of the solution formed by the addition of anions to the DMSO solution containing the Schiff base was photographed and is shown in Figure 5.

As shown in the photographs taken under two different lights, the color of the compound changes with the addition of F^-, CN^-, AcO^-, $H_2PO_4^-$ and OH^- anions to the sensor compound (Figures 5a; under day light, 5b and 5c; under UV lamp). In daylight, the observed color changes were from yellow to red for F^- and CN^-, dark orange for AcO^- and OH^-, and to light orange for $H_2PO_4^-$ (Fig. 5a). Significant fluorescence changes were observed under long-wave UV lamp for anions (Figure 5b). The color of the anion solutions is light-red for F^- and CN^-, and it is light-orange for AcO^-, $H_2PO_4^-$ and OH^-. There were more pronounced fluorescence changes under the shortwave UV lamp. In the solutions, turquoise

and light-red were observed for F^-, AcO^-, $H_2PO_4^-$ and OH^-, and CN^-, respectively. Intensive color change is formed by the addition of anions such as F^-, CN^-, AcO^-, $H_2PO_4^-$ and OH^-. This shows that there is strong binding between these selective ions and the Schiff base. For the above anions, the sensor compound gave a visible color change under both the short wave and the long wave UV lamp. There is no visible color or fluorescence change for all other less basic anions (Br^-, I^-, SCN^-, ClO_4^- and HSO_4^-) studied under both daylight and UV lamp. Accordingly, we can say that there is very weak binding or no binding between these anions and the Schiff base.
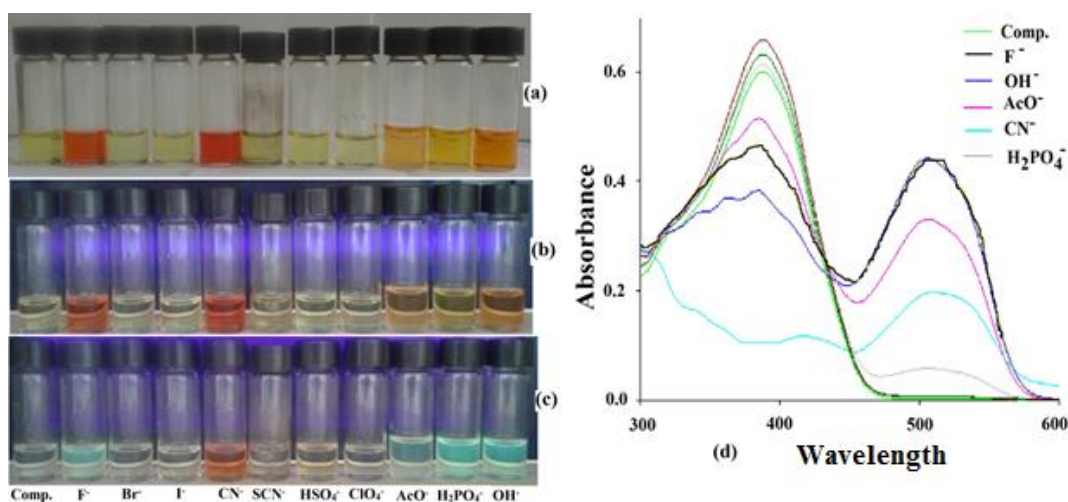
Figure 5. a) Color changes of compound (50 μM) under normal light, **b**) hand held UV lamp (λ=365 nm), **c**) hand held UV lamp (λ=254 nm), d) UV-Vis absorption spectra upon the addition of 1.0 equivalence of various anions in DMSO.

The ability of Schiff base (50 μM) to detect F^-, CN^-, AcO^-, $H_2PO_4^-$ and OH^- anions was studied using UV-Visible spectrophotometry in DMSO as shown in Figure 5c. A band at 385 nm in the UV-Vis spectrum for the Schiff base was observed before the addition of the selective anions. When the F^-, CN^-, AcO^-, $H_2PO_4^-$ and OH^- anions were gradually added, the intensity of the band decreased at 385 nm and a new band was formed at 505 nm. In 2-hydroxy Schiff bases, the absorption band at > 400 nm was reported to belong to the ketamine form (32). In this case, the keto-amine form occurs because the H atom from the O-H group is transferred to the N atom of the CH=N group. This resulted in a change of color from yellow to red and orange. This band was probably due to the intramolecular charge transfer of electrons, which are resultant phenol protons and the anion interactions (16-20). All the other anions (Br^-, HSO_4^-, Cl^- and ClO_4^-) did not exhibit any discernible changes (15-20). UV-Vis results show that the Schiff base exhibits excellent selectivity for F^-, CN^-, AcO^-, $H_2PO_4^-$ and OH^- anions in the presence of other anions and can be useful in practical applications. Furthermore, the anion-binding capacity of the compound was found to be $F^->OH^->AcO^->CN^->H_2PO_4^-$ using a UV-Visible spectrophotometer, respectively.

In our previous study, while the salicylaldehyde-based sensor did not show selectivity against phosphate anion (17), the 5-bromosalicylaldehyde-based sensor showed selectivity against phosphate in this study. In this study, addition of phosphate anion to the DMSO solution of the 5-bromosalicylaldehyde-based sensor resulted in a rapid color change from yellow to light orange with an accompanying new band appearing at 505 nm in the absorption profile. The title compound showed chromogenic and fluorogenic sensor properties against phosphate anion. In addition, for the same anions under both daylight and UV lamp, each sensor gave a different solution color. Consequently, it can be said that the substituted bromine in the title compound affects the anion selectivity.

These results demonstrate that the receptor title Schiff base exhibits good selectivity for F^-, OH^-, AcO^-, CN^- and $H_2PO_4^-$ anions in the presence of other anions and is useful in practical applications.

Minimum Inhibitory Concentration (MIC)
Minimum inhibition concentration (MIC) was determined with broth microdilution test. The average of three experimental results is given in Table 1. The antimicrobial activity spectrum of the

Schiff base showed great diversity. As can be seen from Table 1, it can be said that Schiff base antimicrobial activity results have a similar effect against bacteria and yeast. This compound showed activity against the tested microorganisms. Surprisingly, the compound exhibits similar activity, although Gram-positive, Gram-negative and yeast cell walls are very different.

Table 1. MIC (µg/mL) of the compound.

Microorganisms	Compound	Antibiotic	
		Ampicillin	Fluconazole
S. aureus ATCC 25923	256	5	-
E. faecalis ATCC 29212	128	8	-
E. coli ATCC 25922	128	-	-
P. aeruginosa ATCC 254992	256	5	-
C. albicans ATCC 60193	128	-	128
C. tropicalis ATCC 13803	128	-	64

Interaction of Schiff base and DNA

The effect of Schiff base on CT-DNA was investigated using electronic spectroscopy. With the increase in the concentration of CT-DNA, decreases of 18.89-56.26% and 13.50-20.00%, and higher wavelength of 1-37 nm and 1-3 nm are observed at 258 nm and 390 nm (Figure 6). Furthermore, the red shift of maximum absorption shows the energy decrease in energy between the HOMO and LUMO. This indicates that DNA interacts with the Schiff base (14-20). If the DNA interacts with the Schiff base, π-π* transition energy decreases, and the absorption shifts to red. The decrease, increase and shift long wave of absorption in the UV absorption spectra show that the Schiff base interacts with CT-DNA, presumably because of stacking of the interaction between an aromatic ring and the base pairs of DNA (14-20). According to the UV-Vis results, the compound binds to CT-DNA intercalatively.
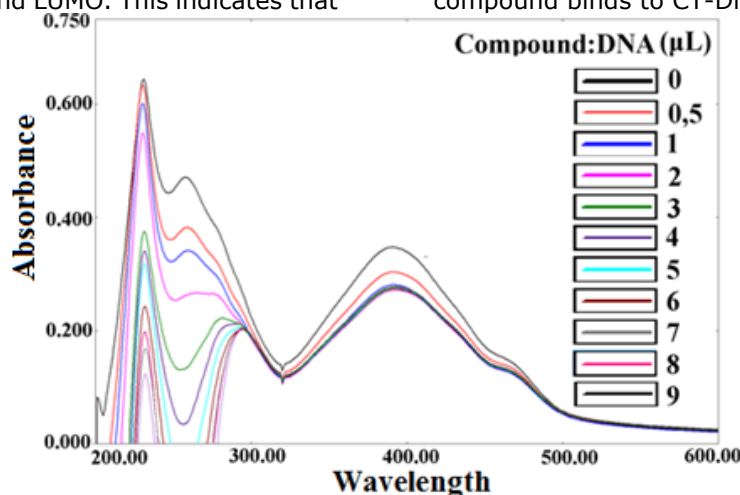
Figure 6. Absorption spectra of compound in the absence and presence of increasing amounts of CT-DNA at room temperature in Tris–HCl/NaCl buffer (pH 7.2).

DNA-Cleavage activity

The cleavage of DNA is determined with the agarose gel electrophoresis method. Supercoiled (SC) plasmid pBR322 DNA was used in the study. Cleavage experiments were performed by adding Schiff base at concentrations ranging from 5 µM to 400 µM in TAE buffer. If the DNA interacts with the Schiff base, SC DNA form is degraded to nicked circular (NC) form. According to the result of the cleavage assay, it is seen that the SC form of DNA is preserved (Fig.7). Consequently, the Schiff base which is both hydrolytic and oxidative does not show any cleavage of SC DNA (Figure 7 a: hydrolytic b: oxidative).
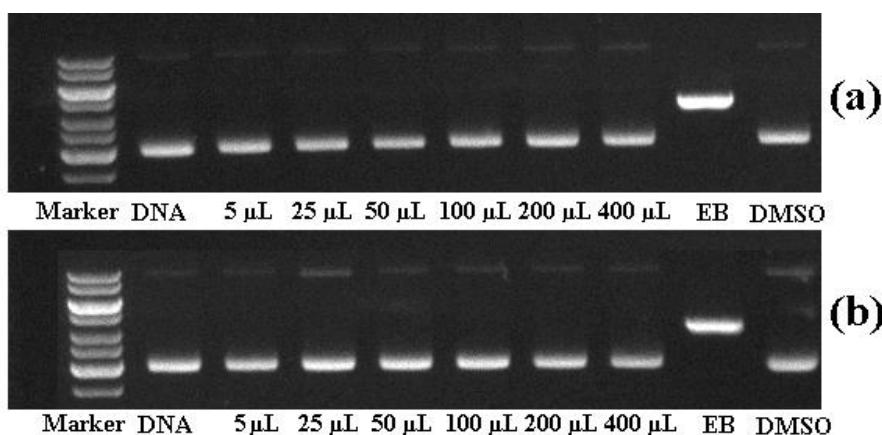
Figure 7. Agarose gel electrophoresis patterns for the hydrolytic cleavage of pBR322 DNA by Schiff base. DNA: Deoxyribonucleic acid; µL: Microliters; EB: Ethidium bromide; DMSO: Dimethyl sulfoxide.

CONCLUSIONS

In this work, a benzothiazole-based Schiff base was synthesized and its structure was elucidated. In addition, biological activity and chemical sensor applications were investigated. Minimum inhibitory concentration (MIC) against yeast and bacteria was determined. Interactions with DNA were studied. It was found that it binds interactively to DNA, but it does not cleave DNA. The sensor properties were tested against anions. The Schiff base was found to be selective for fluoride, cyanide, acetate, dihydrogen phosphate and hydroxyl anions in DMSO. A color change was observed for these anions, but not for the other anions. As a result of all these studies, it was found that it could be used as an agent for DNA and anions.

REFERENCES

1. Kajal A, Bala S, Kamboj S, Saini V. Schiff Bases: A versatile pharmacophore. J. Catal. 2013 August; 1-14.

2. Kumar S. Protease inhibiting and other biological activities of Schiff base derivatives. IJRT. 2016; 2(7):439-54.

3. Luo H, Xia Y-F, Sun B-F, Huang L-R, Wang X-H, Lou H-Y, Zhu X-H, Pan W-D, Zhang X-D. Synthesis and evaluation of in vitro antibacterial and antitumor activities of novel N,N-disubstituted Schiff bases. Biochem. Res. Int. 2017 Jun; 2017:6257240.

4. Guo Z, Xing R, Liu S, Zhong Z, Ji X, Wang L, Li P. Antifungal properties of Schiff bases of chitosan, N-substituted chitosan and quaternized chitosan. Carbohydr. Res. 2007; 342(10):1329–32.

5. Przybylski P, Huczynski A, Pyta K, Brzezinski B, Bartl F. Biological properties of Schiff bases and azo derivatives of phenols. Curr. Org. Chem. 2009; 13(2):124–48.

6. Li H-G, Yang Z-Y, Qin D.D. A new Schiff-base type selective fluorescent chemosensor for Cu2+. Inorg. Chem. Commun. 2009 June; 12 (6):494-7.

7. Zhu W, Yang L, Fang M, Wu Z, Zhang Q, Yin F, Huang Q, Li C. New carbazole-based Schiff base: Colorimetric chemosensor for Fe3+ and fluorescent turn-on chemosensor for Fe3+ and Cr3+. J. Lumin. 2015 February; 158:38-43.

8. Gupta V.K, Singh A.K, Kumawat L.K. Thiazole Schiff base turn-on fluorescent chemosensor for Al3+ ion. Sens. Actuat. B: Chem. 2014 May; 195:98-100.

9. Singh T.S, Paul P.C, Pramanik H.A. Fluorescent chemosensor based on sensitive Schiff base for selective detection of Zn2+. Spectrochim. Acta A Mol. Biomol. Spectrosc. 2014; 121:520-6.

10. Xu Y, Aderinto S.O, Wu H, Peng H, Zhang H, Zhang J, Fan X. A highly selective fluorescent chemosensor based on naphthalimide and Schiff base units for Cu2+ detection in aqueous medium. Z. Naturforsch. B. 2016; 72(1):35–41.

11. Hijji Y.M, Barare B, Kennedy A.P, Butcher R. Synthesis and photophysical characterization of a Schiff base as anion sensor. Sens. Actuators B: Chem. 2009 March; 136(2): 297-302.

12. Dalapati S, Jana S, Guchhait N. Anion recognition by simple chromogenic and chromo-fluorogenic salicylidene Schiff base or reduced-Schiff base receptors. Spectrochim. Acta A Mol. Biomol. Spectrosc. 2014 Aug; 129:499-508.

13. Mohammadi A, Jabbari J. Simple naked-eye colorimetric chemosensors based on Schiff-base for selective sensing of cyanide and fluoride ions. Can. J. Chem. 2016; 94(7): 631-6.

14. Yıldız M, Demir N, Ünver H, Sahiner N. Synthesis, characterization, and application of a novel water-soluble polyethyleneimine-based Schiff base colorimetric chemosensor formetal

cations and biological activity. Sens. Actuators B: Chem. 2017 May; 252: 55–61.

15. Zeyrek C.T, Boyacioğlu B, Yıldız M, Ünver H, Yolal D, Demir N, Elmali A, Tadesse S, Aslan K. Synthesis, characterization, and evaluation of (E)-methyl-2-((2-oxonaphthalen-1(2H)-ylidene)methylamino)acetate as a biological agent and an anion sensor. Bioorg. Med. Chem. 2016 Sept.; 24:5592–601.

16. Ünver H, Boyacioglu B, Zeyrek C.T, Yıldız M, Demir N, Yıldırım N, Karaosmanoğlu O.K, Sivas H, Elmalı A. Synthesis, spectral and quantum chemical studies and use of (E)-3-[(3,5-bis(trifluoromethyl)-phenylimino)methyl]benzene-1,2-diol and its Ni(II) and Cu(II) complexes as an anion sensor, DNA binding, DNA cleavage, anti-microbial, anti-mutagenic and anti-cancer agent. J. Mol. Struct. 2016 June; 1125:162-76.

17. Barare B, Yıldız M, Ünver H, Aslan K. Characterization and use of (E)-2-[(6-methoxybenzo[d]thiazol-2-ylimino)methyl]phenol as an anion sensor and a DNA-binding agent. Tetrahedron Lett. 2016; 57:537–42.

18. Yıldız M, Tan E, Demir N, Yıldırım N, Ünver H, Kiraz A, Mestav B. Synthesis and spectral, antimicrobial, anion sensing, and DNA binding properties of Schiff base podands and their metal Complexes1. Russ. J. Gen. Chem. 2015; 85(9):2149–62.

19. Barare B, Yıldız M, Alpaslan G, Dilek N, Ünver H, Tadesse S, Aslan K. Synthesis, characterization, theoretical calculations, DNA binding and colorimetric anion sensing applications of 1-[(E)-[(6-methoxy-1,3-benzothiazol-2-yl)imino]methyl]naphthalen-2-ol. Sens. Actuat. B: Chem., 2015 March; 215:52–61.

20. Yıldız M, Karpuz Ö, Zeyrek C.T, Boyacioğlu B, Dal H, Demir N, Yıldırım N, Ünver H. Synthesis, biological activity, DNA binding and anion sensors, molecular structure and quantum chemical studies of a novel bidentate Schiff base derived from 3,5-bis(triflouromethyl)aniline and salicylaldehyde. J. Mol. Struct. 2015 April; 1094:148–60.

21. Yeap G.-Y, Ha S.-T, Ishizawa N, Suda K, Boey P.-L, Mahmood W.A.K, Synthesis, crystal structure and spectroscopic study of

parasubstituted 2-hydroxy-3-methoxybenzalideneanilines. J. Mol. Struct. 2003; 658:87-99.

22. Martínez-Máñez R, Sancenón F. Fluorogenic and chromogenic chemosensors and reagents for anions. Chem. Rev. 2003; 103:4419-76.

23. Uysal UD, Berber H, Ercengiz D. Theoretical investigation on solvent dependent shift and electronic transition properties of certain Schiff bases. JOTCSA, 2018; (4-sp.is.1): 111-30.

24. Kang J, Song E.J, Kim H, Kim Y-H, Kim Y, Kim S-J, Kim C. Specific naked eye sensing of cyanide by chromogenic host: studies on the effect of solvents. Tetrahedron lett. 2013 february; 54:1015-19.

25. Piątek P, Jurczak J, A selective colorimetric anion sensor based on an amide group containing macrocycle. Chem. Commun. 2002; 20:2450-1.

26. Gan C, Zhou L, Zhao Z, Wang H. Benzothiazole Schiff-bases as potential imaging agents for β-amyloid plaques in Alzheimer's disease. Med. Chem. Res. 2013; 22(9): 4069-74.

27. Piscitelli F, Ballatore C, Smith A. Solid phase synthesis of 2-aminobenzothiazoles. Bioorg. Med. Chem. Lett. 2010; 20(2):644-8.

28. Ali R, Siddiqui N. Biological Aspects of Emerging Benzothiazoles: A Short Review. J. Chem. 2013; 1-12.

29. Vijayalakshmi R, Kanthimathi M, Parthasarathi R, Nair B.U, Interaction of chromium(III) complex of chiral binaphthyl tetradentate ligand with DNA. Bioorg. Med. Chem. 2006 May; 14:3300-6.

30. Li F, Feterl M, Mulyana Y,. Warner J.M, Collins J.G, Keene F.R. In vitro susceptibility and cellular uptake for a new class of antimicrobial agents: Dinuclear ruthenium(II) complexes. J. Antimicrob. Chemother. 2012; 67:2686-95.

31. Marmur J. A procedure for the isolation of deoxyribonucleic acid from micro-organisms. J. Mol. Biol. 1961 April; 3:208-18.

32. Nazır H, Yıldız M, Yılmaz H, Tahir M.N, Ülkü D. Intramolecular hydrogen bonding and tautomerism in Schiff bases. Structure of N-(2-pyridil)-2-oxo-1-naphthylidenemethylamine. J. Mol. Struct. 2000 June; 524:241-50.

RESEARCH ARTICLE

Pharmacophore-Based Virtual Screening of Novel GSTP1-1 Inhibitors

Kayhan Bolelli[1,2]* ✉ (iD), **Tugba Ertan-Bolelli[1]** ✉ (iD)

[1]Department of Pharmaceutical Chemistry, Faculty of Pharmacy, Ankara University TR-06560 Ankara Turkey
[2]LumiLabs, TR-06050 Ulus Ankara Turkey

Abstract: Glutathione transferase enzymes have significant role in the metabolism and detoxification of many xenobiotic, oxidative stress products, environmental carcinogens, and electrophilic drugs. Human GSTP1-1 enzyme participates in a particular role in resistance for anticancer agents in chemotherapy by overexpression. Because of these reasons this enzyme could be a promised target for new anticancer drugs. Herein, pharmacophore analysis was performed using bioactive conformation of the known inhibitor of GSTP1-1, ethacrynic acid (pdb ID:2GSS). Phase module which is available in Schrödinger software was used to generate pharmacophore hypothesis. Among the commercially available compounds in the ZINC database, with same pharmacophoric features were screened and Qikprop module was used for ligand filtration to obtain an efficient collection of hit molecules by employing Lipinski's "rule of five". As a result, some of the compounds obtained from this study, could be the promising inhibitors of hGSTP1-1 enzyme.

Keywords: ADME/Tox, drug resistance, GSTP1-1, pharmacophore analysis, virtual screening

*Corresponding author. E-mail: bolelli@ankara.edu.tr

INTRODUCTION

GSTs are soluble dimeric proteins which catalyze the conjugation of glutathione (GSH) to electrophiles resulting in the formation of the corresponding GSH conjugates. Each GST monomer contains an independent catalytic site composed of two components (H site and G site). Although H site which is a hydrophobic substrate binding site is formed structurally variable amino acid residues, G site formed from a conserved group of amino acid residues which is specific for GSH or an intimate related homolog (1-4). Glutathione transferase enzymes have significant role in the metabolism and detoxification of many xenobiotic, oxidative stress products, environmental carcinogens, and electrophilic drugs. Resistance of various human tumors to cancer chemotherapeutic agents has been directly correlated with conjugation capabilities of the GST enzymes to GSH and overexpression of these enzymes. Human GST P1-1 enzyme participates in a particular role in resistance for anticancer agents in chemotherapy (5-10).

Since decades, pharmacophore analyses studies has been established, and the pharmacophore modeling techniques has been used as a tool for computational drug discovery area (11–14). One of the pharmacophore models generating approaches is structure-based approach, based on the interaction of a molecule and its target are directly extracted as X-ray crystallographic structures from Protein Data Bank (PDB). Virtual screening approach is used for searching virtual libraries or large scale databases of chemical structures by using computational methods and for selecting a limited number of drug candidate compounds that are likely to be active against the target protein (15,16).

In this study, pharmacophore analysis (Phase module of Schrödinger software) were performed using bioactive conformation of the known inhibitor of GSTP1-1, ethacrynic acid (PDB ID:2GSS) in order to screening approximately ten thousand compounds taken from ZINC database. Ligand filtration step was also done to acquire an efficient collection of hit molecules by employing Lipinski's "rule of five" and predicted the ADME/Tox properties using Qikprop module (15-17).

MATERIAL AND METHODS

Ligand preparation
For virtual screening study, 10,241 commercially available compounds were obtained from ZINC database. All of these ligands were prepared by using Schrödinger, LigPrep module. The bond angles and orders were assigned after ligand minimization step. For the minimization OPLS 2005 force field was used. In order to keep the ligands in the right protonation state in biological conditions, epik option was used.

Pharmacophore-based Virtual Screening
The method of pharmacophore-based virtual screening focus on active ligands 3D (three-dimensional) information. Firstly, pharmacophore model generation studies were performed by using bioactive conformation of the known inhibitor of GSTP1-1, ethacrynic acid (PDB ID:2GSS). This initial pharmacophore modeling was carried out by using the Phase module in Schrödinger software (18). Then, we used pharmacophore based virtual screening method with commercially available 10,241 compounds in the ZINC database. Concurrently with the search process, for each ligand, the sites of the hypothesis were matched against a pre-computed set of conformers. Screened compounds were read to match a minimum of four sites of the six featured hypotheses. The database searches were performed flexibly, with conformations generated on-the-fly while keeping the initial conformations stored in the database. Conformations were generated during the search. The maximum number of conformers were limited as per structure 50. Hits were sorted by decreasing Phase Screen Scores. Conformer generation was skipped for structures with >15 rotatable bonds. Among

the commercially available compounds in the ZINC database, with same pharmacophoric features were screened and Qikprop module was used for ligand filtration to obtain an efficient collection of hit molecules by employing Lipinski's "rule of five".

ADME/Tox Analyses
According to the Phase Screen Scores, selected top 20 compounds (Table 1) were filtered by calculating the ADME/Tox properties using QikProp module of Schrödinger (19). Table 2 shows the overall ADME/Tox evaluation for the four compounds, investigated here: ZINC000083150112, ZINC000083150113, ZINC000083149157, ZINC000049536498. This analysis includes aqueous solubility (Plog S), brain/blood partition coefficient (QP log BB), total solvent accessible surface area (SASA), log Khsa for human serum albumin binding (QPlogKhsa), octanol/water partition coefficient (QP log Po/w), predicted apparent MDCK cell permeability (QPMDCK), human oral absorption, and Lipinski's "rule of five" violations. For all the hGSTP1-1 inhibitor candidates have no violations of Lipinski's "rule of five" (Table2).

RESULT AND DISCUSSION

In this study, pharmacophore analysis were performed using bioactive conformation of the known inhibitor of GSTP1-1, ethacrynic acid (pdb ID:2GSS) (20). Phase module of the Schrödinger suite was used to generate pharmacophore hypothesis. The six-feature pharmacophore model was generated which has two acceptor groups (A3, A4), three hydrophobic groups (H7, H8, H9) and a ring aromatic feature (R10). 10.241 compounds taken from ZINC database were screened using the generated pharmacophore model (AAHHHR) to search for potential hGSTP1-1 inhibitors. According to the Phase Screen Scores (Table 1) and ADME/Tox properties (Table 2) we selected four potent hGSTP1-1 inhibitor candidates (ZINC000083150112, ZINC000083150113, ZINC000083149157, ZINC000049536498) (Figure 1) which are all fitted five features of the pharmacophore model with permissible ADME/Tox properties. These compounds were taken for further analyses.

ZINC000083150112   **ZINC000083150113**

ZINC000083149157   **ZINC000049536498**
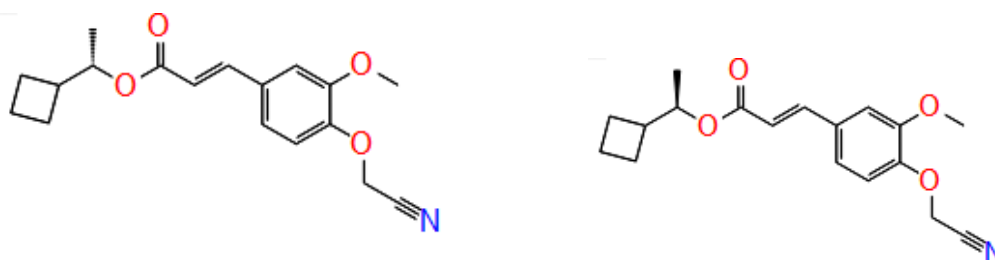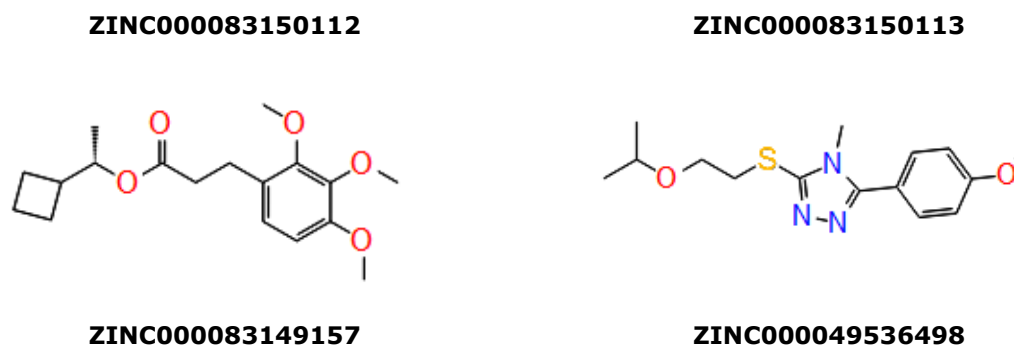
Figure 1. Structures of the hGSTP1-1 inhibitor candidate compounds.

Table 1. Matched Ligand sites and Phase Screen Scores of the best fitted compounds.

zinc_id	Matched Ligand Sites	PhaseScreenScore
ZINC000083150112		2.082
ZINC000083150113		2.050
ZINC000083149157		2.036
ZINC000015019926		2.018
ZINC000079860441		2.014
ZINC000083148985		2.014
ZINC000079860439		2.011
ZINC000079860920		2.011
ZINC000129414177		2.002
ZINC000049536498		2.000
ZINC000006648767		1.999
ZINC000083149044		1.998
ZINC000079860915		1.996
ZINC000006646321		1.994
ZINC000129416189		1.994
ZINC000083149043		1.990
ZINC000129413974		1.988
ZINC000091709630		1.985
ZINC000006648779		1.980
ZINC000083148986		1.972

According to the QikProp Properties Predictions, the human oral absorption percentage of selected four compounds were found 100%. The partition coefficient (QP log Po/w) was within the permissible range of 3.21-4.16. Log Khsa for human serum albumin binding (QPlogKhsa), SASA and brain/blood partition coefficient (QP log BB) were also found to be within satisfactory range. Violations of Lipinski's "rule of five" were also calculated (21). Because of no violations of the Lipinski's "rule of five", all selected compounds indicating their potential as a drug-like molecule. Additionally, compounds are in the acceptable range for predicted apparent MDCK cell permeability (QPMDCK) and predicted aqueous solubility (QPLog S). Table 2 showed some calculated pharmacokinetic properties for the selected compounds by Qikprop simulation.
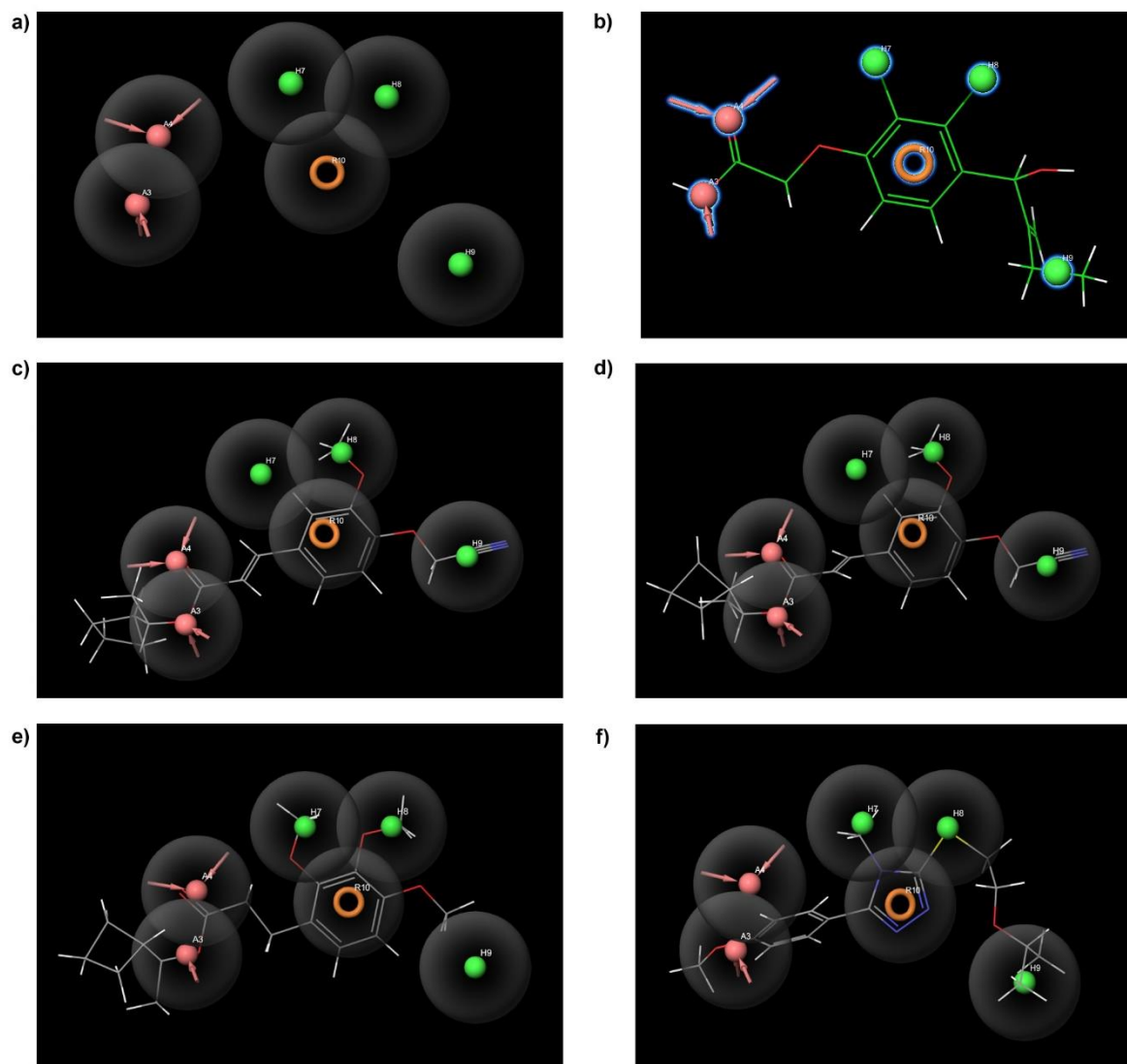
Figure 2 a) The six-feature pharmacophore model AAHHHR generated using PHASE illustrating acceptor group (A3, A4; pink), hydrophobic group (H7, H8, H9; green) and ring aromatic (R10; orange) **b)** Mapping of ethacrynic acid with pharmacophore model. **c)** Mapping of **ZINC000083150112** with pharmacophore model. **d)** Mapping of **ZINC000083150113** with hypothesis 2. **e)** Mapping of **ZINC000083149157** with hypothesis 2. **e)** Mapping of **ZINC000049536498** with pharmacophore model.

Table 2. QikProp Properties Predictions topo II inhibitor candidate compounds.

Code	Molecular Weight	Percent Human Oral absorption	SASA	QPlog BB	QPlog S	QPlog Po/w	QPPMDCK	QPlog Khsa	Rule of Five
ZINC000083150112	315.368	100	626.086	-1.048	-4.998	3.284	493.053	0.016	0
ZINC000083150113	315.368	100	630.746	-1.139	-5.087	3.211	419.214	0.006	0
ZINC000083149157	322.400	100	626.486	-0.262	-4.561	4.163	2626.108	0.293	0
ZINC000049536498	307.410	100	589.076	0.038	-4.235	3.905	5037.826	0.135	0
Ethacrynic Acid	305.157	79.127	516.962	-0.942	-3.393	2.843	177.378	-0.291	0

CONCLUSION

Virtual screening methods have been an important tool for new hit compound search. According to the Phase Screen Scores selected top 20 compounds (Table 1) were filtered by calculating the ADME/Tox properties. According to the pharmacophore screening results and ADME/Tox properties, it can be concluded that ZINC000083150112, ZINC000083150113, ZINC000083149157, ZINC000049536498 showed better fit score than all other tested compounds that are all fitted five features of the pharmacophore model. Besides, most of the pharmacokinetic properties conducted by Qikprop were within the permissible range. Approximately ten thousand compounds from ZINC database were screened and selected these 4 top chemical structures (Figure 1) for further studies and they could be promising inhibitors of hGSTP1-1 enzyme.

ACKNOWLEDGMENT

REFERENCES

1. Hayes JD, Flanagan JU, Jowsey IR. Glutathione transferases. Ann Rev Pharmacol Toxicol. 2005; 45:51–88.

2. Commandeur JNM, Stijntjes GJ, Vermeulen NPE. Enzymes and transport-systems involved in the formation and disposition of glutathione S-conjugates—Role in bioactivation and detoxication mechanisms of xenobiotics. Pharmacol Rev. 1995; 47:271–330.

3. Josephy PD, Mannervik B. Molecular toxicology. 2nd ed. New York (NY): Oxford University Press; 2006.

4. Kazemnejad S, Rasmi Y, Sharifi R, Allameh A. Class-Pi of glutathione S transferases. Iran J Biotechnol. 2006; 4(1):1–16.

5. Sau A, Tregno FP, Valentino F, Federici G, Caccuri AM. Glutathione transferases and development of new principles to overcome drug resistance. Arch Biochem Biophys 2010; 500(2):116-22.

6. Kong KH, Takasu K, Inoue H, Takahashi K. Tyrosine-7 in human class-Pi glutathione-S-transferase is important for lowering the pka of the thiol-group of glutathione in the enzyme-glutathione complex. Biochem Biophys Res Commun. 1992; 184:194–7.

7. Tew KD, Dutta S, Schultz M. Inhibitors of glutathione S-transferases as therapeutic agents. Adv Drug Deliv Rev. 1997; 26(2-3):91-104.

8. Mathew N, Kalyanasundaram M, Balaraman K. Glutathione S-transferase (GST) inhibitors. Expert Opin Ther Pat. 2006; 16:431–44.

9. DePierre J, Morgenstern R. Comparison of the distribution of microsomal and cytosolic glutathione S-transferase activities in different organs of the rat. Biochem Pharmacol. 1983; 32:721–3.

10. Van Bladeren PJ. Glutathione conjugation as a bioactivation reaction. Chem Biol Interact. 2000; 129:61–76.

11. Guner OF. Pharmacophore perception, development, and use in drug design. Int Univ Line. 2000.

12. Mason JS, Good AC, Martin EJ. 3-D pharmacophores in drug discovery. Curr Pharm Des. 2001; 7(7):567–97.

13. Leach AR, Gillet VJ, Lewis RA, Taylor R. Three-dimensional pharmacophore methods in drug discovery. J Med Chem. 2010; 53(2):539–58.

14. Langer T, Hoffmann RD. Pharmacophores and Pharmacophore Searches. Wiley-VCH, 2006.

15. Diniz EMLP, Poiani JGC, Taft CA, da Silva CHTP. Structure-Based Drug Design, Molecular Dynamics and ADME/Tox to Investigate Protein Kinase Anti-Cancer Agents. Curr Bioact Comp. 2017; 13(3):213–22.

16. Kaserer T, Beck KR, Akram M, Odermatt A, Schuster D. Pharmacophore Models and Pharmacophore-Based Virtual Screening: Concepts and Application Exemplified on Hydroxysteroid Dehydrogenases. Molecules. 2015; 20:22799–832.

17. Rohini K, Shanthi V. Discovery of Potent Neuraminidase Inhibitors Using a Combination of Pharmacophore-Based Virtual Screening and Molecular Simulation Approach. Appl Biochem Biotechnol. 2018; 184:1421–40.

18. Schrödinger Release 2018-2: Phase, Schrödinger, LLC, New York, NY, 2018.

19. Schrödinger Release 2018-2: QikProp, Schrödinger, LLC, New York, NY, 2018.

20. Oakley AJ, Rossjohn J, Lo Bello M, Caccuri AM, Federici G, Parker MW. The three-dimensional structure of the human Pi class glutathione transferase P1-1 in complex with the inhibitor ethacrynic acid and its glutathione conjugate. Biochemistry. 1997; 36:576-85.

21. Lipinski CA, Lombardo F, Dominy BW, Feeney PJ. Experimental and computational approaches to estimate solubility and permeability in drug discovery and development settings. Adv Drug Deliv Rev. 2012; 64(1-3):4-17.

Modeling of Anthocyanin Derivatives as Anti-UV Agents

Khusna Arif Rakhman*[1, 2] ✉ (iD) **, Khadijah[1]** ✉ (iD) **, Muhammad Ikhlas Abdjan[1]** ✉ (iD) **,**

Nurbaiti Kumendong[2] ✉ (iD) **, and Setyani Dian Puspitasari[2]** ✉ (iD)

1. Department of Chemistry Education, Khairun University, Ternate 97751, Indonesia
2. Environmental Laboratory, Khairun University, Ternate 97751, Indonesia

Abstract: The optimization of molecular geometry and the modeling of electronic transition to anti-UV activities on anthocyanin derivatives in computationally have been conducted using the Hyperchem 8.0.10 application. Semi-empirical PM3 method is applied and the parameter of data is measured *i.e.* charge and total energy. The objective of study is to get a potential model of anthocyanin derivatives as anti-UV agents. The results show that each anthocyanin derivative has optimal geometry in stable energy. Electronic transition modeling of anthocyanin derivatives has been done using semi-empirical ZINDO/s method with a limited change of gradient 0.01 kcal/(Å.mol). The results show that the transition type in 10 anthocyanin derivatives is n → π̃ and π → π̃ with anti UV activity in the UV-A and UV-C wavelength regions. Electron excitation for each anthocyanin derivative occurs in four molecule orbitals. The energy difference of HOMO-LUMO shows that malvidin compound has the smallest energy gap which around 5.61, whereas the luteolinidin compound has the biggest energy gap which around 5.94 eV.

INTRODUCTION

UV electromagnetic wave radiation is divided into three parts based on its wavelength range, namely UV-C (100-280 nm), UV-B (280-320 nm) and UV-A (320-400 nm) (1). Chemical compounds that have the ability to interact with UV electromagnetic waves are compounds that have chromophore and auxochrome groups because of their ability to absorb at certain wavelengths (2). The combination of several aromatic compounds such as cinnamic acid derivatives, benzophenone, aminobenzoate, and anthocyanins have the potential as UV absorbing agents because of the content of

chromophore and auxochrome groups in these compounds (3, 4).

The UV interactions with chemical compounds can be studied by computational modeling, instead of experimental measurements. Modeling of UV interaction with chemical compounds that lead to the potential of chemical compounds in counteracting UV (anti-UV activity) can be known through the relationship of intensity with absorbed wavelengths (5). Modeling of UV activity on the chemical compound can be determined by electronic transition modeling using semi-empirical methods (6, 7). The ZINDO/s method (Zerner's Intermediate Negative of Differential

Overlap/Spectroscopy) is one of the semi-empirical methods that is led to model electronic transitions in the form of discontinuous spectra (8, 9). Compounds that have the potential as anti-UV agents will show peaks with high-intensity values in ZINDO/s modeling (10).

Anthocyanin (Figure 1) is one of the secondary metabolites of the flavonoid family which is usually contained in fruits and vegetables that are red or purple such as *Aerva sanguinolenta*, and *Hylocereus undatus* (11). Research on anthocyanin used as natural dyes, antioxidants and anti-UV agents (12, 13, 14). Unlike other flavonoid derivatives, anthocyanin have attractive color characteristics to investigate their activity against UV radiation. This study aims to get a potential model of anthocyanin derivatives as anti-UV agents. The modeling object of this study was several derivatives of anthocyanins like Aurantinidin, Cyanidin, Delphinidin, Europinidin, Malvidin, Pelargonidin, Peonidin, Petunidin, and Rosinidin. The basic structure of anthocyanidin has seven functional groups which will be combined with substitution with -H, -OH and $-OCH_3$ substituents. This article reports the potential of anthocyanin as anti-UV agents in the form of electronic transition modeling. Electron transition characteristics that occur in anthocyanin derivatives will reflect the energy needed when subjected to light at certain wavelengths (15, 16). Then, the determination of the ease of derivation of anthocyanin that experience electron excitation from HOMO to LUMO is the easiest to see photosensitivity properties which will affect their potential as anti UV agents (17). The modeling results of anthocyanin derivative compounds can be used to conduct further research that leads to the development of dyes for food, medicine, and materials, especially for UV capture materials such as solar cells.

METHODOLOGY

Geometry Optimization of PM3 Anthocyanin

The modeling of molecule geometry optimization and molecule energy calculations are using semi-empirical PM3 method (18), in limited change of gradient around 0.01 kcal/(Å.mol) till reach nearly limited gradient based on the Polak-Ribiere method. The purpose of molecular geometry optimization is to obtain a stable molecule geometry (19).

Electronic Transition Modeling Analysis and Anthocyanin UV Spectra

The modeling on structure results in semi empirical PM3 geometry optimization is continued to measure the single point of configuration interaction (CI) by using semi empirical ZINDO/s methods. This method is used to get spectra electronic transition data. Modeling of orbital molecule on single excitation (CI) uses two levels on HOMO-LUMO energy.

RESULTS AND DISCUSSION

Geometry Optimization of Anthocyanin-Derived Compounds

Optimization of molecular geometry of anthocyanin-derived compounds using PM3 semi-empirical method shows data in the form of molecular structure and charge accompanied by energy, to be able to determine the stability of the molecular geometry. Table 1 shows the existence of 7 different functional groups in the 10 molecules of anthocyanin derivatives from the basic structure of the compounds which have 3 benzene rings with simple conjugated bonds. The functional group substitution produces 10 anthocyanin derivatives with a combination of substitute groups in the form of -H, -OH and $-OCH_3$.
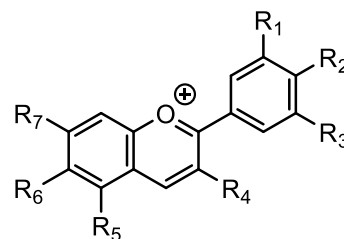

Figure 1. The molecular structure of anthocyanins.

Table 1: Derivatives of Anthocyanin

Derivatives of Anthocyanin	R_1	R_2	R_3	R_4	R_5	R_6	R_7
Aurantinidin	-H	-OH	-H	-OH	-OH	-OH	-OH
Cyanidin	-OH	-OH	-H	-OH	-OH	-H	-OH
Delphinidin	-OH	-OH	-OH	-OH	-OH	-H	-OH
Europinidin	$-OCH_3$	-OH	-OH	-OH	$-OCH_3$	-H	-OH
Luteolinidin	-OH	-OH	-H	-H	-OH	-H	-OH
Malvidin	$-OCH_3$	-OH	$-OCH_3$	-OH	-OH	-H	-OH
Pelargonidin	-H	-OH	-H	-OH	-OH	-H	-OH
Peonidin	$-OCH_3$	-OH	-H	-OH	-OH	-H	-OH
Petudinin	-OH	-OH	$-OCH_3$	-OH	-OH	-H	-OH
Rosinidin	$-OCH_3$	-OH	-H	-OH	-OH	-H	$-OCH_3$

Table 2: Geometry Optimization of Anthocyanin

Derivatives of Anthocyanin	Total Energy (kcal/mol)	Binding Energy (kcal/mol)	Heat Formation (kcal/mol)
Aurantinidin	-85338.1028542	-3510.6412492	-16.8152492
Cyanidin	-85339.2443358	-3511.7827308	-17.9567308
Delphinidin	-92116.2174990	-3616.2400320	-62.8550320
Europinidin	-98986.3988524	-4150.3655134	-46.7925134
Luteolinidin	-78572.3759095	-3417.4301665	16.8368335
Malvidin	-98986.0858247	-4150.0524857	-46.4794857
Pelargonidin	-78567.4389408	-3412.4931978	21.7738022
Peonidin	-88775.4466615	-3779.9571205	-11.0371205
Petudinin	-95552.6605097	-3884.6551067	-56.1761067
Rosinidin	-92212.3418400	-4048.8243630	-4.8103630

The results of molecular geometry optimization on 10 anthocyanin derivatives using semi-empirical method PM3 showed that pelargonidin are compounds that have the smallest total energy (Table 2). The bond energy and heat of formation are one part of the total energy of the molecule derived from anthocyanin. The lowest or near zero total energy and formation heat obtained from geometry optimization shows the stability of a molecule (20).

Electronic Transitions and UV Spectra of Anthocyanin Derivative Compounds
Electronic transition modeling was performed using semi-empirical ZINDO/s method with data parameters taken in the form of wavelength, intensity, MO level, and HOMO-LUMO energy to study anti-UV activity of anthocyanin derivatives. Wavelengths and intensity values read on each anthocyanin derivative compound contained 4 peaks with a range of values of wavelengths of 200-400 nm in the UV region (Table 3). Discontinuous spectrum modeling on these 10 compounds has an orbital molecular level which is useful for studying the ease of electron excitation through the energy gap approach in the valence band (24).

Determination of the transition type in 10 anthocyanin derivatives for each wavelength shows the transition types n to ñ* and π to ñ* at the 4 transition peaks. Transition n to ñ* occurs because there is a simple conjugated chromophore group in aromatic rings and the transition π to ñ* shows the substitution group (R1-R7) which is an auxochrome group which influences the wavelength shift. The intensity value read on the electronic transition causes a wavelength shift to occur. Transitions that occur at these wavelengths indicate the potential for anti-UV activity in the UV-A and UV-C regions for 10 anthocyanin derivatives.
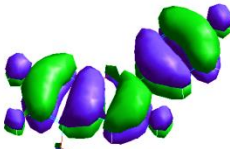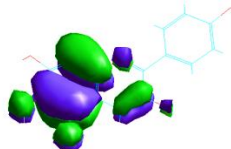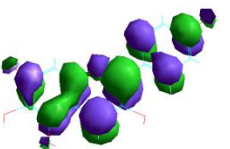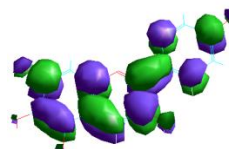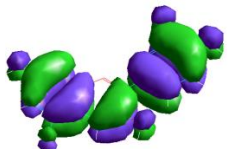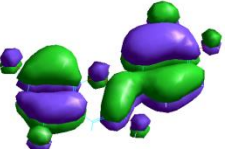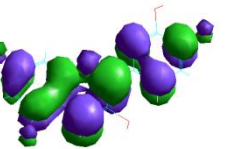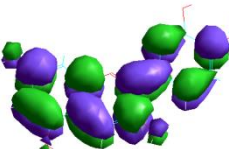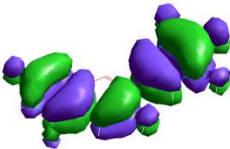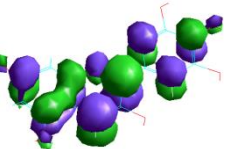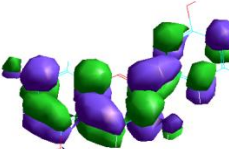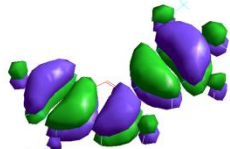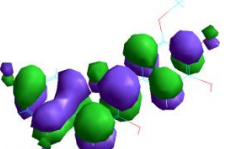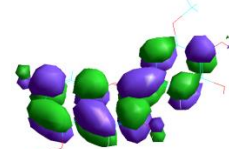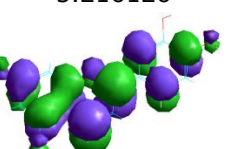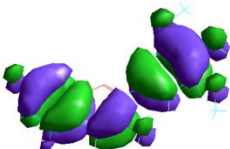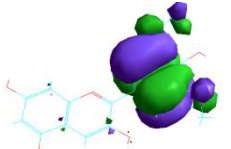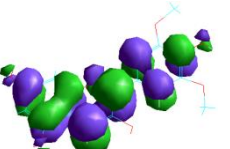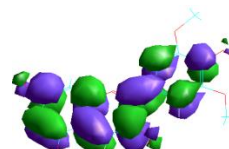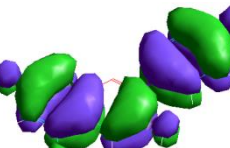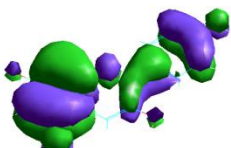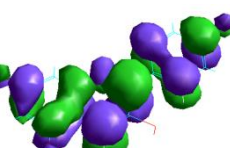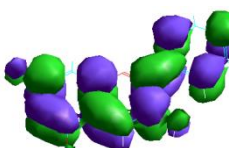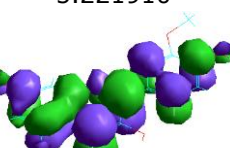
Table 3 : Electronic Transition and UV Activity of Derivative of Anthocyanin

Derivatives of Anthocyanin	λ(nm)	Osc	MO Level	Transition level	UV Activity
Aurantinidin	456.3	1.0958	53→54	$n \to \pi^*$	
	386.1	0.0741	52→54	$n \to \pi^*$	
	268.4	0.4613	53→55	$n \to \pi^*$	UV-A - UV-C
	249.5	0.4097	52→55	$\pi \to \pi^*$	
Cyanidin	459.0	1.1685	53→54	$n \to \pi^*$	
	360.1	0.0207	52→54	$n \to \pi^*$	
	267.0	0.3221	53→55	$n \to \pi^*$	UV-A - UV-C
	232.9	0.2948	52→55	$\pi \to \pi^*$	
Delphinidin	449.3	1.1335	56→57	$n \to \pi^*$	
	383.2	0.0492	55→57	$n \to \pi^*$	
	265.7	0.2854	56→58	$n \to \pi^*$	UV-A - UV-C
	232.6	0.1081	55→58	$\pi \to \pi^*$	
Europinidin	450.2	1.1245	62→63	$n \to \pi^*$	
	386.6	0.0465	61→63	$n \to \pi^*$	
	266.1	0.2908	62→64	$n \to \pi^*$	UV-A - UV-C
	234.5	0.1185	61→64	$\pi \to \pi^*$	
Luteolinidin	425.4	1.1514	50→51	$n \to \pi^*$	
	340.7	0.0152	49→51	$n \to \pi^*$	
	255.5	0.2273	50→52	$n \to \pi^*$	UV-A - UV-C
	227.2	0.3056	49→52	$\pi \to \pi^*$	
Malvidin	451.3	1.1402	62→63	$n \to \pi^*$	
	389.8	0.0452	61→63	$n \to \pi^*$	
	266.8	0.2773	62→64	$n \to \pi^*$	UV-A - UV-C
	234.2	0.1085	61→64	$\pi \to \pi^*$	
Pelargonidin	452.1	1.1973	50→51	$n \to \pi^*$	
	346.0	0.0220	49→51	$n \to \pi^*$	
	265.0	0.3706	50→52	$n \to \pi^*$	UV-A - UV-C
	238.6	0.4060	49→52	$\pi \to \pi^*$	
Peonidin	453.8	1.1663	56→57	$n \to \pi^*$	
	361.3	0.0143	55→57	$n \to \pi^*$	
	266.6	0.3174	56→58	$n \to \pi^*$	UV-A - UV-C
	230.0	0.2732	55→58	$\pi \to \pi^*$	
Petudinin	450.7	1.1407	59→60	$n \to \pi^*$	
	384.1	0.0481	58→60	$n \to \pi^*$	
	266.7	0.2772	59→61	$n \to \pi^*$	UV-A - UV-C
	232.5	0.0973	58→61	$\pi \to \pi^*$	
Rosinidin	454.1	1.1578	59→60	$n \to \pi^*$	
	359.6	0.0123	58→60	$n \to \pi^*$	
	266.6	0.3289	59→61	$n \to \pi^*$	UV-A - UV-C
	229.9	0.2772	58→61	$\pi \to \pi^*$	

One of the parameters measured in determining the UV activity of anthocyanin derivatives is HOMO (eV) and LUMO (eV) energy. The Highest Occupied Molecular Orbitals (HOMO) are the highest energy molecular orbitals filled with electrons and the Lowest Unoccupied Molecular Orbitals (LUMO) are the lowest energy molecular orbitals that are not filled with electrons (25). The energy gap between HOMO and LUMO is known as the energy gap (gEg), where the gap energy is the minimum energy needed to excite electrons from HOMO to LUMO (26). The energy gap (eV) between HOMO-LUMO will reflect the ease of an excited electron when subjected to an electromagnetic wave with a certain wavelength.

Table 4. HOMO-LUMO Energy Level of Anthocyanin Derivatives.

Derivatives of Anthocyanin	HOMO (eV)	HOMO-1 (eV)	LUMO (eV)	LUMO+1 (eV)
Aurantinidin	-11.035057	-11.698295	-5.318554	-3.559058
Cyanidin	-11.009844	-11.780312	-5.322355	-3.550417
Delphinidin	-10.965636	-11.606985	-5.318181	-3.557562
Europinidin	-10.854637	-11.451558	-5.216126	-3.461004
Luteolinidin	-11.125949	-11.870198	-5.185068	-3.507093
Malvidin	-10.847209	-11.461916	-5.235400	-3.476526
Pelargonidin	-11.000199	-11.996816	-5.221910	-3.473720
Peonidin	-10.916036	-11.651897	-5.217128	-3.463220

Petudinin				
	-10.903310	-11.565510	-5.278661	-3.519875
Rosinidin				
	-10.875191	-11.615891	-5.173106	-3.418870
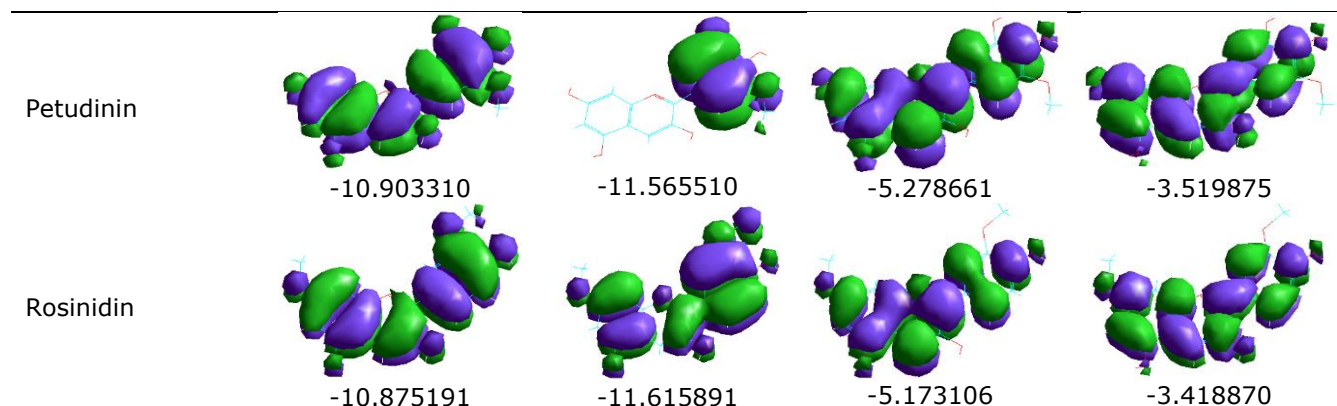
Table 5: HOMO-LUMO Energy Difference

Derivative of Anthocyanin	$E_{LUMO}-E_{HOMO}$ (eV)	$E_{LUMO}-E_{HOMO-1}$ (eV)	$E_{LUMO+1}-E_{HOMO}$ (eV)	$E_{LUMO+1}-E_{HOMO-1}$ (eV)
Aurantinidin	5.71	6.37	7.47	8.13
Cynidin	5.68	6.45	7.45	8.22
Delphinidin	5.64	6.24	7.39	8.04
Europinidin	5.63	6.23	7.39	8.00
Luteolinidin	5.94	6.68	7.61	8.36
Malvidin	5.61	6.22	7.37	7.98
Pelargonidin	5.77	6.77	7.52	8.52
Peonidin	5.70	6.43	7.45	8.18
Petudinin	5.62	6.28	7.38	8.04
Rosinidin	5.70	6.44	7.45	8.19

Modeling of HOMO energy and LUMO anthocyanin derivatives were carried out using the semi-empirical method of ZINDO/s. The modeling results of changes in energy resulting from UV interactions with compounds indicate that there are four molecular orbitals that experience electron transitions (Table 4), namely HOMO (0 and -1) and LUMO (0 and +1) for every 10 anthocyanin derivatives. The interaction between anthocyanin and UV wave compounds in this modeling is indicated by the electron transition from HOMO to LUMO for each molecular orbitals of anthocyanin compounds derived from HOMO to LUMO, HOMO-1 to LUMO, HOMO to LUMO + 1 and HOMO-1 to LUMO +1. The lowest HOMO-LUMO Energy Difference based on modeling using semi-empirical ZINDO/s method is found in malvidin compound with a value of 5.61 eV (Table 5).

CONCLUSION

The molecular geometry optimization of anthocyanin derivatives was carried out using the semi-empirical method of PM3 which showed a stable change in charge and energy with the lowest total energy value in the pelargonidin of -78567 (kcal/mol). Determination of electronic transitions on each anthocyanin derivative compound shows that there are four electron transition peaks with transition types, namely n to ñ* and π to ñ*. The potential of anthocyanin derivatives as anti UV agents shows activity in the UV-A and UV-C wavelength regions. Malvidin compounds have a better potential than some anthocyanin derivatives as anti UV based on a review of the HOMO-LUMO energy difference of 5.61 eV.

REFERENCES

1. Zam ZZ, Juniyanti D, Rakhman KA. Effectivity of ethanolic extracts from jambulang fruit (syzigium cumini. l) as Ultraviolet Anti-Radiation agent. Inter. J Adv Res. 2018; 6(4): 949-54.

2. Shah RS, Shah RR, Pawar RB, Gayakar PP. UV-Visible spectroscopy-A review. J Pharm Sci. 2015; 5(5): 491-505.

3. Moldovan B, David L. Influence of temperature and preserving agents on the stability of cornelian cherries anthocyanins. Molecules. 2014; 19: 8177-88.

4. Eren E, Gok EC, Seyhan BN, Maslakci NN, Oksuz AU. Evaluation of anthocyanin, a rose residue extract, for use in dye-sensitized solar cell. Asian J. Chem. 2015; 27(10): 3745-8.

5. Hadi AA. Quantum-chemical study for some coumarin compounds by using semi-empirical methods. J. ChemTech Res. 2016; 9(10): 139-48.

6. Marković Z, Manojlović N, Zlatanović S. Electronic absorption spectra of substituted anthraquinones and their simulation using ZINDO/S method. Int J Serb Soc Comput Mechan. 2008; 2(2): 73-9.

7. Zeroual S, Dridi S. Ab-initio and semi-empirical study of tree mechanisms for the indole synthesis. Der Pharm. Chem. 2015; 7(6): 175-90.

8. Young DC. Computational chemistry: A practical guide for applying techniques to real-world problem. New York: John Wiley & Sons Inc; 2001. p. 328.

9. Lewars E. Computational chemistry: introduction to the theory and applications of molecular and quantum mechanics. USA: Kluwer Academic Publishers; 2004. p. 373.

10. Pei K, Cui Z, Chen W. An Adduct of Cl-substituted benzotriazole and hydroxy benzophenone as a novel UVA/UVB absorber: Theory-guided design, synthesis, and calculations. J Mol Struct. 2013; 1032: 100–4.

11. Junqueira-Gonçalves MP, Yáñez L, Morales C, Navarro M, Contreras RA, Zúñiga GE. Isolation and characterization of phenolic compounds and anthocyanins from murta (ugni molinae turcz.) fruits. Assessment of antioxidant and antibacterial activity. Molecules. 2015; 20: 5698-713.

12. Huner D, Eksr A. Antioxidant capacity, monomeric anthocyanin and total phenolic concent of sour cherry nectar. Asian J. Chem. 2016; 28(5): 1103-7.

13. Gümrükçü G, Özgür MU, Gültekin C. Extraction of anthocyanin pigments from red onion (alliumcepa L.) and dyeing woolen fabrics. Asian J. Chem. 2008; 20(4): 2891-902.

14. Alcázar-Alay SC, Cardenas-Toro FP, Osorio-Tobón JF, Barbero GF, Meireles MAA. Obtaining anthocyanin-rich extracts from frozen açai (Euterpe oleracea Mart.) pulp using pressurized liquid extraction. Food Sci Technol. 2017; 37(1): 48-54.

15. Pavia DL, Lampman GM, Kriz GS, Vyvyan JR. Introduction of spectroscopy. USA: Cengage Learning; 2013. p. 578-579.

16. Kumar S. Organic chemistry: Spectroscopy of organic compounds. Amristar: Dept. of Chemistry Guru Nanak Dev University; 2006. p. 4-6.

17. Itte P, Amshumali MK, Pasha M. Molecular modeling, geometry optimization and characterization of bimetallic complexes derived from s-indacene. Univ J Chem. 2017; 5(3): 48-57.

18. Abdelmalek O, Belaidi S, Mellaoui M, Mazri R. Geometry and electronic structure of isoxazole and isothiozole derivatives by PM3 and density functional theory. Asian J Chem. 2011; 23(3): 1183-5.

19. Odunola OA, Semire B. Semi-empirical (PM3) study of conformational analysis and electronic properties of functionalized. Asian J Chem. 2008; 20(6): 4343-52.

20. Saraha AR, Rakhman KA, Sugrah N. Anti UV-activity and elektronic transition study of 1,3-diphentyl-2-propenone using semi-empirical method ZINDO/s. Asian J Chem. 2018; 30(5): 1057-60.

21. Hadanu R. A QSAR analysis of flavone derivatives of antimalarial compounds based on PM3 semi-empirical method. Asian J Chem. 2018; 30(1): 148-156.

22. Brown WH, Foote CS, Iverson BL, Anslyn EV, Novak BM. Organic chemistry. USA: Cengage Learning; 2012. p. 13-14.

23. Miller A, Solomon PH. Writing reaction mechanisms in organic chemistry. USA: Elsevier Science & Technology Books; 1999. p. 34.

24. Walree CAV, Lenthe JHV, Wiel BCVD. On the UV spectrum of cross-conjugated 2,3-diphenyl-1,3-butadiene. Chem Phys Lett. 2012; 528: 29-33.

25. Brown TL, LeMay HE, Bursten BE, Murphy CJ, Woodward PM, Stoltzfus MW. Chemistry the central science. USA: Pearson Education; 2012. p. 370.

26. Brown TL, LeMay HE, Bursten BE, Murphy CJ, Woodward PM, Stoltzfus MW. Chemistry the central science. USA: Pearson Education; 2015. p. 514-515.

RESEARCH ARTICLE

Pentafluoropropionic Anhydride Functionalized PAMAM Dendrimer as miRNA Delivery Reagent

Ali Oztuna[1]* ✉ iD **, Hasan Nazir[2]** ✉ iD

[1]Gulhane Training and Research Hospital, Department of Medical Genetics, 06010, Ankara, Turkey.
[2]University of Ankara, Faculty of Science, Department of Chemistry, 06100, Ankara, Turkey.

Abstract: Poly(amidoamine) (PAMAM) dendrimers are good candidates for nucleic acid delivery with their well-defined characteristics. MicroRNA mediated regulation of biological process is also active an area of investigation. Fibroblast cells, such as MRC-5, are one of the cell lines used in biological researches due to their hard to transfect nature. In this two-staged study, cystamine core generation 5 PAMAM dendrimers were synthesized and fluorinated with pentafluoropropionic anhydride and subsequently tested as miRNA delivery reagent on MRC-5 cells. Effect of fluorination against to naked generation 5 dendrimer on transfection efficiency was also investigated by molecular docking and quantitative structure-activity relationship calculations. Structural characterization of the synthesized dendrimers was verified by spectroscopic techniques. Gel retardation assay, particle size and transmission electron microscopy results demonstrated polyplex formation of fluorinated dendrimers with miRNA at nanoscale level. Zeta potential values indicated non-aggregation and increased stability of the polyplexes. Prepared polyplexes with fluorinated dendrimer showed over 90% cell viability and transfection efficiency. In silico calculations confirmed the stable complexation with miRNA and good penetration capability into the cell.

INTRODUCTION

PAMAM [poly(amidoamine)] dendrimers are well defined nano-sized architectural macromolecules and they are potential candidates for nanoscale nucleic acid delivery vehicles (1, 2). PAMAM dendrimers transform nucleic acid-dendrimer complex into nanoscale dendriplexes with its primary amine terminal groups at the periphery. Dimethyl- or bisacrylamide-cystamine as a core initiator provides bioreducibility of PAMAM dendrimers and selective intracellular release of nucleic acids (2-4). Since the cytotoxicity of naked dendrimers is increased with its higher generations, despite increase in their transfection efficiency, studies are being conducted in order to increase biocompatibility and transfection efficiency of PAMAM dendrimers. One of the strategies used in this context is fluorination and it increases dendrimer affinity to the lipid bilayer

and enables them to get across cell and endosome/lysosome membrane (5, 6).

MicroRNAs (miRNAs) are remarkable candidates for the RNA-interference based therapeutic approach if they are successfully delivered to the target (7, 8). However, the major drawbacks for direct miRNA administration in vitro or in vivo are low cellular internalization and enzymatic degradation (9). Researches to overcome these obstacles and to develop efficient nucleic acid delivery agents are being conducted.

In literature, pentafluoropropionic anhydride (PA) and heptafluorobutyric anhydride modified PAMAM dendrimers have been tested in HEK293, HeLa, NIH3T3, COS-7, CHO and primary mouse mesenchymal stem cells for DNA and siRNA delivery and promising results have been reported (5, 10, 11). In this study, cystamine

core generation 5 (G5) PAMAM dendrimers were synthesized and fluorinated with PA and subsequently cytotoxicity and transfection efficiency of the prepared polyplexes were examined on MRC-5 cells which are known with their hard-to-transfect nature. Also, the effect of fluorination on polyplex formation was evaluated by molecular docking and quantitative structure-activity relationship (QSAR) calculations.

EXPERIMENTAL

Preparation of G5 PAMAM dendrimer
Ethyl acrylate, cystamine dihydrochloride, ethylenediamine, pentafluoropropionic anhydride, trimethylamine, methanol, 2-mercaptoethanol and toluene were purchased from Sigma-Aldrich (Germany) and they were used as received. Cystamine core G5 PAMAM dendrimer was synthesized by using divergent method. Methanolic solutions of methylacrylate and ethylenediamine were added into cystamine according to iterative Michael addition and exhaustive amidation reactions until to get a G5. During the synthesis process azeotropic evaporations were made by using 10:1 (v/v) toluene:methanol mixture and product purification of the half generations were performed by column chromatography on silica gel [Kieselgel 60 (230-400 mesh ASTM); Merck, Germany] and Sephadex LH-20 (GE Healthcare, Sweden) (12, 13).

The products were characterized by $^{13}C\{H\}$-NMR (Varian Mercury 400 MHz NMR Spectrometer, Agilent) and FT-IR (IRAffinity-1 FT-IR Spectrometer, Shimadzu) at the end of each step. Also ^{1}H-NMR (Varian Mercury 400 MHz Spectrometer NMR, Agilent), ESI-MS (Micromass ZQ Mass Spectrometer with 2695 HPLC Separations Module, Waters) and MALDI-TOF-MS (MALDI Synapt G2-Si High Definition Mass Spectrometry, Waters) were used when required. PAMAM G5: FT-IR (ATR, 4000-450 cm^{-1}): 3338 (m), 3275 (m), 3190 (m), 3050 (w), 2924 (m), 2834 (m), 1650 (s), 1556 (s), 1460 (s), 1150 (m), 1030 (m); ^{13}C-NMR (D$_2$O, 400 MHz, δ ppm): 32.6, 37.8, 38.7, 41.8, 42.3, 47.9, 49.1, 51.5, 177.3.

Preparation of fluorinated dendrimers
Fluorinated dendrimers were prepared by adding methanolic solutions (1 mL) of PA (696 μL, 3.52 mmol) into a methanolic solution (1 mL) of G5 PAMAM dendrimer (100 mg, 3.46 μmol) and following the 48 h stirring at room temperature the mixture was dialyzed against distilled water. The products were lyophilized and examined by ^{19}F-NMR. ^{19}F-NMR (CD$_3$OD, 400 MHz, δ ppm): -84.577, 84.722, 84.898 (-CF$_3$), -122.010, 123.184, 124.468 (-CF$_2$-CO-). Fluorination ratios of the dendrimers were calculated by using integrals of the internal standard (2,2,2-trifluoroethanol; Sigma-Aldrich, Germany). About 25% of the -NH$_2$ groups on the surface of the G5 PAMAM dendrimers was fluorinated with PA.

Polyplexes' preparation and characterization
Different amount of G5-PA and 10 pmol (w/w) cel-miR-67 (Dharmacon, Germany) were mixed in nuclease-free water and incubated at room temperature for 60 min. The polyplexes were subjected to electrophoresis on 4.5-5% (w/v) agarose gels and run at 70 V for 60-75 min to find minimum required dendrimer amount. Polyplexes at 1× (determined from gel retardation results), 3× and 6× ratio of dendrimer/miRNA (w/w) were prepared for zeta-potential and size analyses. Size and zeta-potential of the polyplexes were measured by using Zetasizer Nano ZS-90 (Malvern, UK) at 25 °C in disposable polystyrene cuvettes and folded capillary zeta cell, respectively. Morphology and size of the polyplexes at 6× ratio were also examined by using Tecnai G2 220 kV transmission electron microscope (FEI, USA) at an acceleration voltage of 120 kV.

Cell culture and transfections
MRC-5 (human lung fibroblast cell line, ATCC® CCL-171™) cells were maintained in 0.1% gelatin-coated plates containing FibroGRO™ Complete Media Kit (EMD Millipore, Germany) and no antibiotics at 37 °C and 5% CO$_2$. TrypLE™ Express Enzyme solution (Gibco, USA) was used for passaging the cells. 10 pmol Dy547-labelled cel-miR-67 (Dharmacon, Germany) was used for transfection. 24 h prior to the transfection MRC-5 cells were cultured and polyplexes prepared at 1×, 3× and 6× ratios were dropped on to the cells. Subsequent to 8 h incubation the media were changed and cells were incubated for additional 48 h.

Cytotoxicity and transfection efficiency of fluorinated dendrimer/miRNA polyplexes
Cell Proliferation Kit, XTT based (Biological Industries, Israel) was used to examine the cytotoxicity of the G5-PA/miRNA polyplexes. Briefly, MRC-5 cells were seeded at a density of 6×10^3 cells/well on 96-well plates and incubated overnight. Transfections were made and following 48 h post-transfection period, the reaction solution containing XTT [2,3-bis(2-methoxy-4-nitro-5-sulfonyl)-2H-tetrazolium-5-carboxanilide inner salt] reagent and PMS (N-methyl dibenzopyrazine methyl sulfate) was added to the wells and incubated for further 8 h at 37 °C and 5% CO$_2$. Five repeats were conducted for each sample and untransfected cells were used as controls. Absorbance of the each well was measured at 450 nm by a microplate reader (Synergy H1, BioTek, USA). The data were given as mean (SD) and analyzed by One Way ANOVA Test (with Bonferroni Corrected).

Cells were transfected as described above and following 8 h post-transfection period cells were detached with TrypLE™ and centrifuged for 4-5 min at 200 g. Resuspended cells in PBS were analyzed by flow cytometer on a Beckman

Coulter's CytoFLEX in order to evaluate transfection efficiencies. To examine intracytoplasmic localization of the polyplexes confocal imaging was also performed (LSM 780 NLO Multi Photon and Confocal Microscope, Zeiss, Germany). Following to transfections and 48 h post-transfection, cells were fixed with 4% paraformaldehyde solution in PBS (Affymetrix, Germany) for 15 min at 37 °C and then stained with 5 µg/mL wheat germ agglutinin (WGA), Alexa Fluor® 647 conjugate solution (Thermo Fisher, USA) in PBS and 1:4000 Hoechst 33342 (Thermo Fisher, USA) dye.

Molecular docking and QSAR calculations
In order to discuss the effect of fluorination on polyplex formation, global energy (binding energy), atomic contact energy (ACE) and topological polar surface area (TPSA) values of the naked and PA modified G5 PAMAM dendrimers were calculated. Molecular mechanics calculations of the fluorinated dendrimers were performed by Polak-Ribiere algorithm (conjugated gradient) with root mean square (RMS) gradient of 0.010 kcal/(Å mol). Duplex miRNA was generated by the Nucleic Acid Builder (http://casegroup.rutgers.edu/). Docking analysis was carried out using PatchDock Beta 1.3 Version program and RMS deviation tolerance for each docking was set at 4.0 Å (14, 15). The refinement of the first 10 docked complexes determined by PatchDock was carried out using FireDock and global energy and ACE values were

obtained (16, 17). TPSA values were obtained by QSAR calculations (18).

RESULTS AND DISCUSSION

Synthesis and characterization of dendrimers
Due to the symmetric structure of the G5 PAMAM dendrimer, obtained by iterative addition reactions of methyl acrylate and ethylene diamine, FT-IR and ^{13}C-NMR spectra give specific peaks. When the FT-IR values given in the preparation of G5 PAMAM dendrimer section has examined, stretching bands at 3338 cm^{-1} and 3275 cm^{-1}, 3190 cm^{-1} are belong to the -NH and -NH$_2$, respectively. -CH- and -CH$_2$- stretching bands forming the skeletal structure of G5 are observed at 2924 cm^{-1} and 2854 cm^{-1}, respectively. Stretching bands of the -CO- group distributed throughout the structure and S-S bending vibrations of the cystamine constituting the dendrimer core appear at 1642 cm^{-1} and 815 cm^{-1}, respectively. -C=O- and -S-CH$_2$-CH$_2$-NH$_2$ specific peaks of the G5 are located at 177.3 ppm and 37.8 ppm in ^{13}C-NMR spectrum.

Fluorination reaction of G5 PAMAM dendrimer and ^{19}F-NMR spectra of the PA and G5-PA are given in Figure 1a and Figure 1b, respectively. When ^{19}F-NMR spectrum of the G5-PA at the Figure 1b is examined, two singlet peaks belonging to the -CF$_3$- and -CF$_2$- of the PA are seen at 84.58 ppm and 122.01 ppm with 1.5 ppm and 0.5 ppm shifts, respectively.

a)

b)
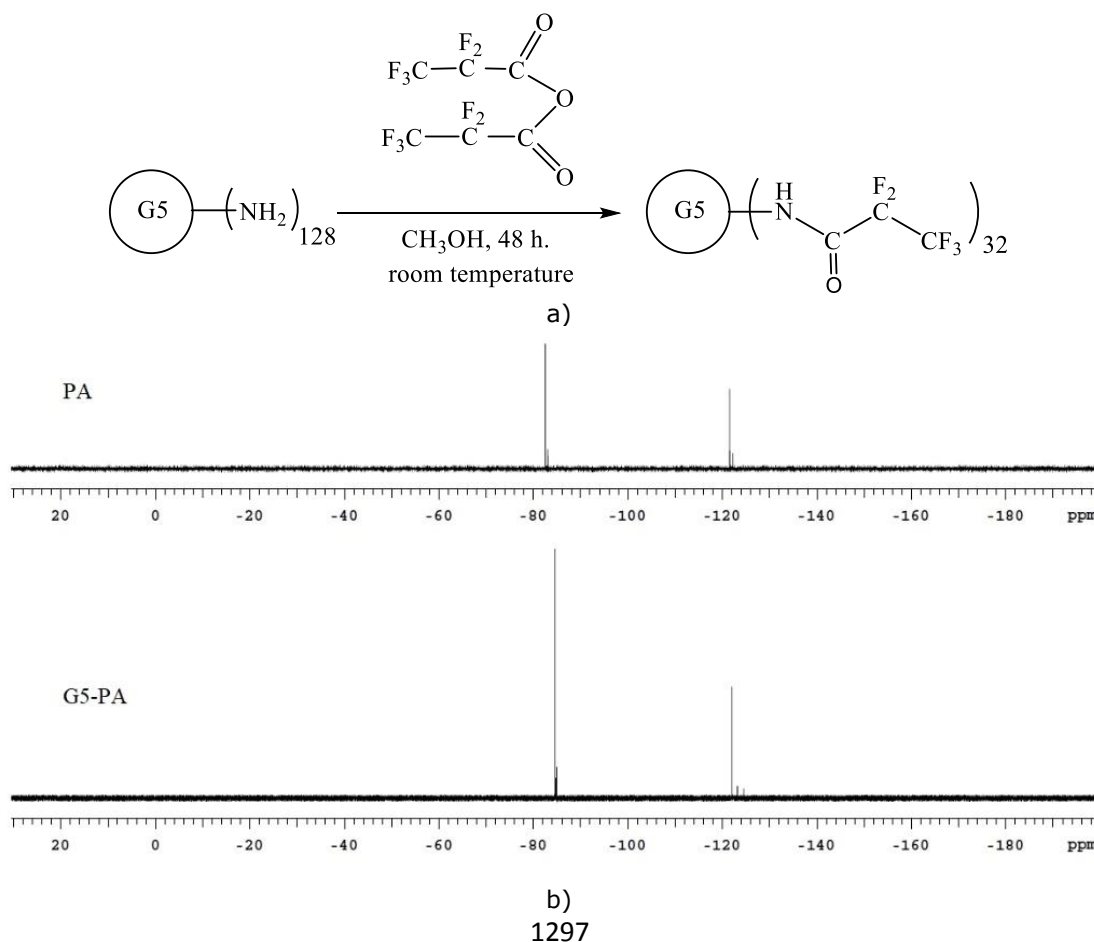
Figure 1. a) Fluorination reaction of G5 PAMAM, b) ^{19}F-NMR spectra of PA and G5-PA.

Characterization of polyplexes

Complete miRNA complexation ability was observed for G5-PA dendrimers by gel retardation assay (Figure 2). Size and zeta potentials for three different G5-PA/miRNA (w/w) ratios are given in Table 1. Zeta potential and particle size measurements showed the formation of positively charged and ~200 nm polyplexes. Size is one of the factors effecting polyplex transfection and studies suggest that the optimal size for the non-viral vectors are below 200 nm (19-21). Nanoparticles with zeta potentials of greater than +30 mV are considered strongly cationic and

exhibits increased stability. The positive charge of particles also facilitates their permeation from the membranes and increases their solubility in the aqueous environment (22, 23). Dynamic Light Scattering (DLS), is a popular technique and allows particle sizing down to 1 nm diameter but it detects light scattering rather than real particle size. Therefore, information about particle size and morphology of the polyplexes were also obtained by transmission electron microscopy. As seen in Figure 3, spherical polyplexes below 200 nm were formed with G5-PA.
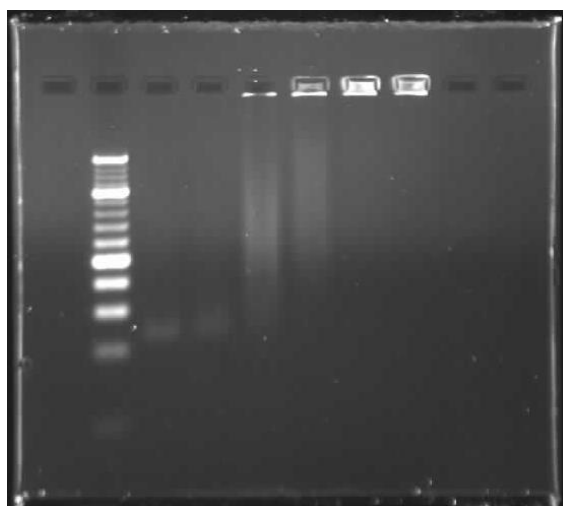
Figure 2. G5-PA/miRNA (w/w) gel retardation assay: Line 1- 10 bp DNA Ladder; 2- 0.7:1; 3- 1.4:1; 4- 3.5:1; 5- 7:1; 6- 14:1; 7- 21:1.

Table 1. Size and zeta potential of dendrimer/miRNA polyplexes.

Dendrimer	w/w	Z-Average, (d.nm)	Zeta potential, (mV ± SD)
G5	1×	223.0	18.91 ± 3.93
	3×	220.7	28.9 ± 5.89
	6×	190.1	56.1 ± 8.70
G5-PA	1×	237.4	55 ± 8.03
	3×	216.2	80.3 ± 11.2
	6×	207.7	74.6 ± 10.6
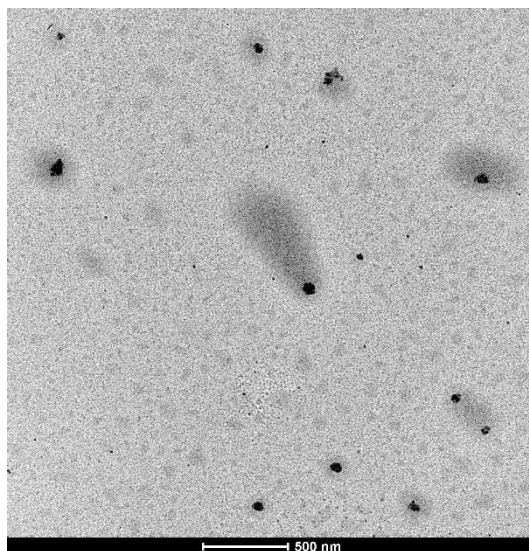
Figure 3: TEM image of G5-PA/miRNA polyplexes.

Cytotoxicity and transfection efficiency of polyplexes

XTT assay was used to evaluate the cytotoxicity of the polyplexes. Cell viability has increased with the fluorination of the dendrimers and G5-PA showed superior viability than the naked G5 (Figure 4). Dose-dependent cytotoxicity was observed with increasing dendrimer concentrations but G5-PA showed cell viability above 90% for all 3 ratios. The percentage of Dy547-labeled miRNA positive cells was used to determine the transfection efficiency of the prepared G5-PA dendrimers. Transfection efficiencies were 71.6% and 98.3% at a w/w ratio

of 6× for G5 and G5-PA, respectively (Figure 5). Confocal laser scanning microscopy images were also obtained after transfections in order to check the cellular distribution of the miRNAs. Bright green fluorescent signals of Dy547 were captured and confirmed the intracytoplasmic localization of the miRNAs (Figure 6). Major problem of the transfection reagents is the correlation between efficiency and toxicity and their efficiency and toxicity are cell type dependent. As seen in Figure 4 and 5, G5-PA provided both efficient transfection and above 90% cell viability after miRNA transfection.
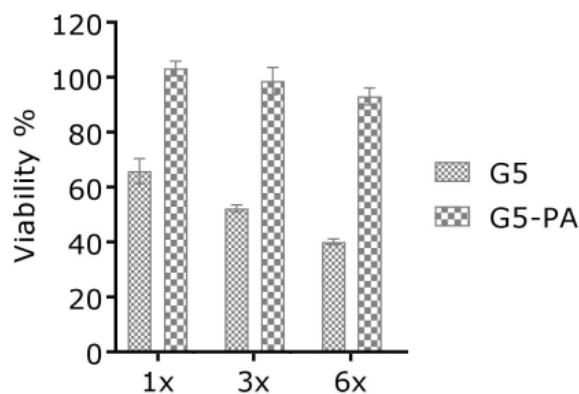
Figure 4: Cytotoxicity of the polyplexes.
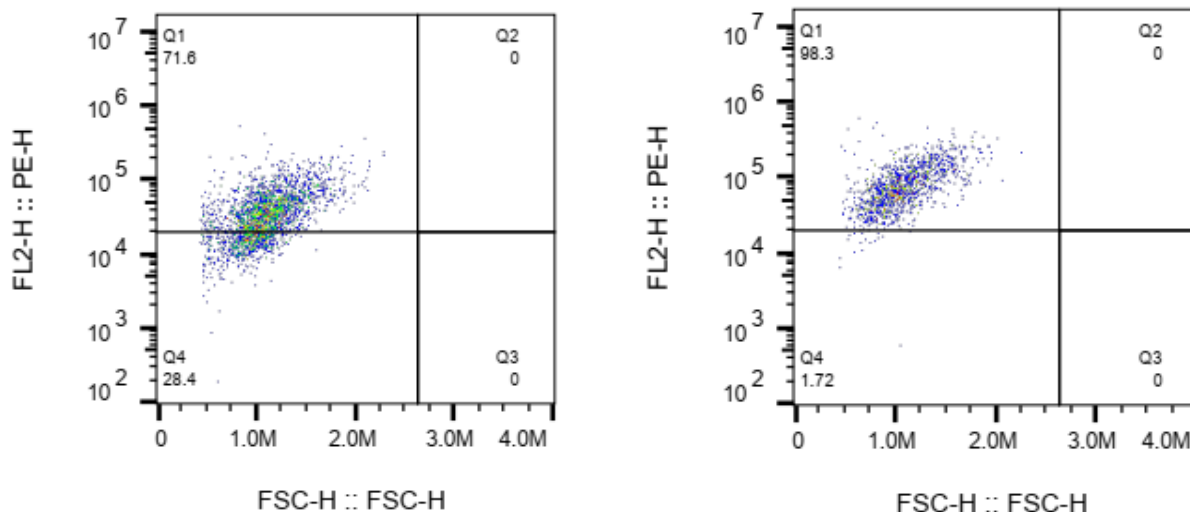
Figure 5: Flow cytometry results of the polyplexes: (Left) G5/miRNA, (Right) G5-PA/miRNA.
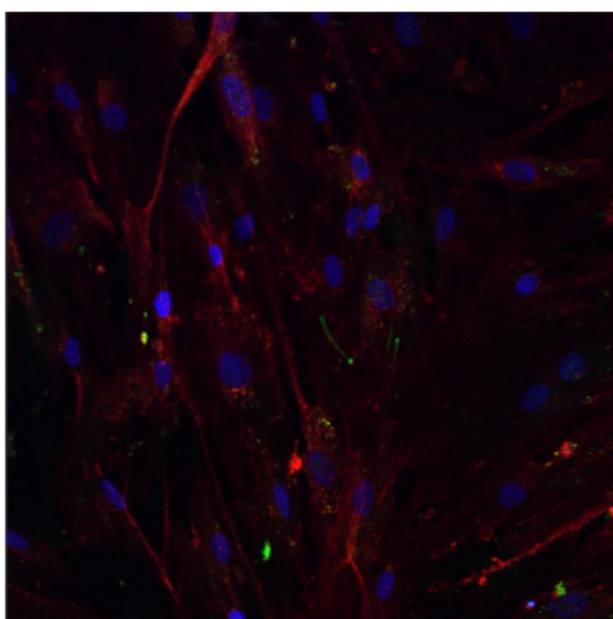
Figure 6: Confocal image of MRC-5 cells transfected with G5-PA/miRNA; Red: plasma membrane stain, WGA Alexa Fluor® 647 conjugate; Blue: nucleus stain, Hoechst 33342; Green: Dy547-labelled miRNA.

In silico calculations for effect of fluorination on transfection

Global energy, ACE, and TPSA values obtained from molecular docking and QSAR calculations are given in Table 2. As seen in Table 2, while G5-PA/miRNA polyplexes showing better ACE (-73.43 kcal/mol) and global binding energy (-198.82 kcal/mol), there was no significant difference between G5/miRNA and G5-PA/miRNA for TPSA values. Low ACE and global binding energy values point out strong and stable dendrimer/miRNA complexation and complex stability seems to arise from van der Walls interactions. TPSA values show that the sum of surfaces of polar atoms in a molecule and high values also indicate smooth penetration capability into the cell. All these directly shows the effect on transfection efficiency.

Table 2. Docking and QSAR results.

	Firedock				QSAR
Polyplex	Global Energy[a] kcal/mol	aVdW[b], kcal/mol	rVdW[b], kcal/mol	ACE$_2$[c] kcal/mol	TPSA[d], Å^2
G5/miRNA	-21.92	-9.74	1.29	-6.38	11072
G5-PA/miRNA	-198.82	-87.62	46.46	-73.43	10610

[a]Binding energy of the docked solution; [b]Contribution of the van der Waals forces to the global binding energy; [c]Contribution of the atomic contact energy to the global binding energy; [d]Topological polar surface area.

CONCLUSION

The chemical structure is one of the key parameters effecting polymer/nucleic acid complexation, polyplex properties and transfection efficiency. In this study, the effect of fluorination with pentafluoropropionic anhydride on transfection was investigated and G5-PA PAMAM dendrimer showed higher performance in terms of cell viability, miRNA complexation and transfection efficiency. These obtained results encourage the use of pentafluoropropionic anhydride for new dendrimer modifications and future tests on different cell lines. Also, consistency of the theoretical and experimental results show that design of the new transfection agent could be discussed with in silico analysis.

REFERENCES

1. Abbasi E, Aval SF, Akbarzadeh A, Milani M, Nasrabadi HT, Joo SW, Hanifehpour Y, Nejati-Koshki K, Pashaei-Asl R. Dendrimers: synthesis, applications, and properties. Nanoscale Res Lett. 2014;9(1):247.

2. Kaur D, Jain K, Mehra NK, Kesharwani P, Jain NK. A review on comparative study of PPI and PAMAM dendrimers. J Nanopart Res. 2016 Jun;18(6):146.

3. Kesharwani P, Banerjee S, Gupta U, Amin MCIM, Padhye S, Sarkar FH, Arun KI. PAMAM dendrimers as promising nanocarriers for RNAi therapeutics. Mater Today. 2015 Dec;18(10):565-72.

4. Oupický D, Li J. Bioreducible polycations in nucleic acid delivery: past, present, and future trends. Macromol Biosci. 2014 Jul;14(7):908-22.

5. Wang M, Liu H, Li L, Cheng Y. A fluorinated dendrimer achieves excellent gene transfection efficacy at extremely low nitrogen to phosphorus ratios. Nat Commun. 2014 Jan;5:3053.

6. Liu H, Wang Y, Wang M, Xiao J, Cheng Y. Fluorinated poly(propylenimine) dendrimers as gene vectors. Biomaterials. 2014 Jul;35(20):5407-13.

7. Bartel DP. MicroRNAs: genomics, biogenesis, mechanism, and function. Cell. 2004 Jan;116(2):281-97.

8. Christopher AF, Kaur RP, Kaur G, Kaur A, Gupta V, Bansal P. MicroRNA therapeutics: Discovering novel targets and developing specific therapy. Perspect Clin Res. 2016 Apr-Jun;7(2):68-74.

9. Gary D J, Puri N, Won YY. Polymer-based siRNA delivery: perspectives on the fundamental and phenomenological distinctions from polymer-based DNA delivery. J Control Release. 2007 Aug;121(1-2):64-73.

10. Wang M, Cheng Y. Structure-activity relationships of fluorinated dendrimers in DNA and siRNA delivery. Acta Biomater. 2016 Dec;46:204-10.

11. Liu H, Chang H, Lv J, Jiang C, Li Z, Wang F, Wang H, Wang M, Liu C, Wang X, et al. Screening of efficient siRNA carriers in a library of surface-engineered dendrimers. Sci Rep. 2016 Apr;28,6:25069.

12. Tomalia DA, Huang B, Swanson DR, Brothers II HM, Klimash JW. Structure control within poly(amidoamine) dendrimers: size, shape and regio-chemical mimicry of globular proteins. Tetrahedron. 2003 May;59(22):3799-813.

13. Oztuna A, Nazir H. In-vitro transfection potential of fluorinated G5 PAMAM dendrimers for miRNA delivery to MRC-5 cells. Eur Res J. 2018 Apr;4(2):92-100.

14. Duhovny D, Nussinov R, Wolfson HJ. Efficient Unbound Docking of Rigid Molecules. In: Guigó R, Gusfield D, editors. Algorithms in Bioinformatics.

WABI 2002, LNCS 2452, Springer-Verlag, Berlin, Heidelberg, p. 185-200. Available from: https://link.springer.com/chapter/10.1007/3-540-45784-4_14

15. Schneidman-Duhovny D, Inbar Y, Nussinov R, Wolfson HJ. PatchDock and SymmDock: servers for rigid and symmetric docking. Nucleic Acids Res. 2005 Jul;33(2):W363-7.

16. Andrusier N, Nussinov R, Wolfson HJ. FireDock: fast interaction refinement in molecular docking. Proteins. 2007 Oct;69(1):139-59.

17. Mashiach E, Schneidman-Duhovny D, Andrusier N, Nussinov R, Wolfson HJ. FireDock: a web server for fast interaction refinement in molecular docking. Nucleic Acids Res. 2008 Jul;36(2):W229-32.

18. Puzyn T, Leszczynska D, Leszczynski J. Toward the development of "Nano-QSARs": Advances and challenges. Small. 2009 Nov;5(22):2494-509.

19. Gao H, Shi W, Freund LB. Mechanics of receptor-mediated endocytosis. Proc Natl Acad Sci USA. 2005 Jul;102(27):9469-74.

20. Kim SH, Jeong JH, Lee SH, Kim SW, Park TG. PEG conjugated VEGF siRNA for anti-angiogenic gene therapy. J Control Release. 2006 Nov;116(2):123-29.

21. Li W, Szoka FC Jr. Lipid-based nanoparticles for nucleic acid delivery. Pharm Res. 2007 Mar;24(3):438-49.

22. Dobrovolskaia MA, Patri AK, Simak J, Hall JB, Semberova J, De Paoli Lacerda SH, McNeil SE. Nanoparticle size and surface charge determine effects of PAMAM dendrimers on human platelets in vitro. Mol Pharm. 2012 Mar;9(3):382-93.

23. Ferenc M, Pedziwiatr-Werbicka E, Nowak KE, Klajnert B, Majoral JP, Bryszewska M. Phosphorus dendrimers as carriers of siRNA-characterisation of dendriplexes. Molecules. 2013 Apr;18(4):4451-66.

Volatile compounds of the *Lavandula angustifolia* Mill. (Lamiaceae) Species Cultured in Turkey

Sevim Küçük[1]* ✉ iD, Esra Çetintaş[1] ✉, Mine Kürkçüoğlu[2] ✉ iD

[1]Department of Pharmaceutical Botany, Faculty of Pharmacy, Anadolu University, Eskişehir, Turkey
[2]Department of Pharmacognosy, Faculty of Pharmacy, Anadolu University, Eskişehir, Turkey

Abstract: Within this family there are many medical species such *as Lavandula* L*., Lavandula angustifolia* Mill. known as medical lavender, is conducting culture and research studies in many places in the world. It is also known as the "English lavender" or *L. officinalis*. Lavender is used in aromatherapy. Its sedative nature, on inhalation has been shown both in animals and man. Experimental studies in humans and animals have shown that the sedative effect comes from linalool and linalyl acetate. Tanins contained in flowers of lavender is shown antidiarrheal effect. Essential oil of lavender is used in various skin diseases and wound healing. Essential oil of lavender shortens the sleeping period, prolongs the sleeping period. In addition, it also shows antimicrobial, antiinflammatory, fungicidal, insecticidal and acaricidal effects (Zeybek and Haksel, 2010). In this study, we were made to create sources Lavandula agriculture in Turkey. We collected four different provinces in the *Lavandula (*5 samples and 1 commercial oil). The results of a total five local and commercial are given below. The flowers of Lavandula were water distilled for 3 h using a Clevenger type apparatus. The essential oils were analyzed by GC and GC-MS simultaneously. The main constituents were identified as linalool 31.9–50.0 % and linalyl acetate 15.4–42.0 %.

Keywords: *Lavandula,* Lamiaceae, Essential oils, Medicinal and aromatical plant, Cultivation, GC-MS.

INTRODUCTION

The Lamiaceae family spans all regions of the earth, especially the Mediterranean region. It is one of the largest families with approximately 224 genera and 5600 species in the world. (1) In Turkey, 45 genera, 565 species and with 735 taxa is one of the important families. (2). The genus *Lavandula* L. (Lamiaceae) is represented in Turkey by 3 taxa (*Lavandula angustifolia* Mill. subsp. *angustifolia*, *L. pedunculata* (Mill.) subsp. *cariensis* (Boiss.), *L. stoechas* L. subsp. *stoechas*). *L. angustifolia* is locally known as "lavanta", *L. pedunculata* subsp. *cariensis* is locally known as "karan", *L. stoechas* subsp. *stoechas*. is locally known as "karabaş" (3,4).

Within this family there are many medical species such *as Lavandula* L., *Lavandula angustifolia* Mill. known as medical lavender, is conducting culture

and research studies in many places in the world. Lavender grows very well at the arid field and then this plant is an economical. It is also known as the English lavender or *L. officinalis*. Lavender is used in aromatherapy. Its sedative nature, on inhalation has been shown both in animals and man. Experimental studies in humans and animals have shown that the sedative effect comes from linalool and linalyl acetate. Tanins contained in flowers of lavender is shown antidiarrheal effect. Essential oil of lavender is used in various skin diseases and wound healing. Essential oil of lavender shortens the sleeping period, prolongs the sleeping period. In addition, it also shows antimicrobial, antiinflammatory, fungicidal, insecticidal and acaricidal effects (5).

We collected four different Lavandula species (5 samples and 1 commercial oil). We aimed to identify and compare the compounds in essential

oils. Lavender adapts very well to the arid area, so it is an economical plant. In Turkey, the results of a total five local and commercial are given below.

MATERIAL AND METHODS

Plant material

L. angustifolia were collected in 26 June, 2017 in Edirne, 8 July 2017 in Burdur, 10 July 2017 in Yalova, Turkey. Collected plant samples were identified and prepared voucher specimens are kept at the Herbarium of Faculty of Pharmacy of Anadolu University, Turkey. ESSE No: A: Yalova-Greenhouse 15485, B: Yalova 15422, C: Edirne 15421, D: Burdur-Jubileuo 15486, E: Burdur-Sevtapolis 15487.

A: Yalova- Greenhouse   (yield of essential oil: 4.1%)
B: Yalova   (yield of essential oil: 5.0%)
C: Edirne   (yield of essential oil: 4.0%)
D: Burdur-Jubileuo   (yield of essential oil: 3.5%)
E: Burdur-Sevtapolis   (yield of essential oil: 6.0%)
F: Commercial oil

Isolation of essential oil

The flowers of Lavandula were water distilled for 3 h using a Clevenger type apparatus. The essential oils were analyzed by GC and GC-MS simultaneously. The essential oils were stored at 4°C in the dark until analyzed.

GC and GC-MS conditions

The oils were analyzed by Gas Chromatography (GC) and Gas Chromatography-Mass Spectrometry (GC-MS) using an Agilent GC-MSD system (Mass Selective Dedector-MSD).

GC-MS analysis

The GC-MS analysis was carried out with an Agilent 5975 GC-MSD system (Agilent, USA; SEM Ltd., Istanbul, Turkey). Innowax FSC column (60m x 0.25mm, 0.25μm film thickness) was used with helium as carrier gas (0.8 mL/min.). GC oven temperature was kept at 60 °C for 10 min and programmed to 220 °C at a rate of 4 °C/min, and kept constant at 220 °C for 10 min and then programmed to 240 °C at a rate of 1 °C/min. Split ratio was adjusted 40:1. The injector temperature was at 250 °C. The interphase temperature was at 280 °C. MS were taken at 70 eV. Mass range was from m/z 35 to 450.

GC analysis

The GC analysis was carried out using an Agilent 6890N GC system. In order to obtain the same elution order with GC/MS, simultaneous injection was performed by using the same column and appropriate operational conditions. The FID temperature was 300°C.

Identification of Compounds

The components of essential oils were identified by comparison of their mass spectra with those in the Baser Library of Essential Oil Constituents, Adams Library (6), MassFinder Library (7), Wiley GC/MS Library (8) and confirmed by comparison of their retention indices. These identifications were accomplished by comparison of retention times with authentic samples or by comparison of their relative retention index (RRI) to a series of n-alkanes. Alkanes were used as reference points in the calculation of relative retention indices (RRI) (9). Relative percentage amounts of the separated compounds were calculated from FID chromatograms. The results of analysis are shown in Table I.

Table I. The Composition of the Essential Oils of *Lavandula angustifolia* Mill.

RRI	Compounds	A	B	C	D	E	F	IM
1014	Tricyclene	tr	tr	-	tr	tr	-	MS
1032	α-Pinene	0.2	0.9	0.3	0.2	0.2	0.2	t_R, MS
1035	α -Thujene	tr	0.1	0.2	0.1	0.1	-	MS
1076	Camphene	0.2	0.4	0.1	0.1	0.2	0.2	t_R, MS
1118	β-Pinene	0.1	1.1	tr	tr	0.1	0.1	t_R, MS
1132	Sabinene	tr	0.4	tr	tr	0.1	0.1	t_R, MS
1159	δ-3-Carene	tr	0.2	tr	0.1	tr	tr	t_R
1174	Myrcene	1.7	0.9	1.1	1.1	1.0	0.6	t_R, MS
1176	α -Phellandrene	-	0.1	tr	0.1	0.1	-	t_R, MS
1188	α-Terpinene	tr	0.1	0.1	tr	tr	tr	t_R, MS
1203	Limonene	0.8	1.5	0.4	0.3	0.6	0.5	t_R, MS
1213	**1,8-Cineole**	1.4	**13.3**	0.7	0.7	1.9	3.0	t_R, MS
1230	n-Butyl n-butyrate	-	-	-	0.1	0.1	tr	MS
1246	**(Z)-β-Ocimene**	1.7	4.4	**8.0**	**6.1**	3.1	1.1	t_R, MS
1255	γ-Terpinene	tr	0.2	0.4	0.2	0.1	tr	t_R, MS
1266	(E)-β-Ocimene	2.8	1.7	2.4	3.1	2.3	1.2	t_R, MS
1267	3-Octanone	0.3	tr	0.6	0.7	1.3	0.4	t_R, MS
1280	*p*-Cymene	tr	0.1	0.2	0.1	0.1	tr	t_R, MS
1282	Hexyl acetate	0.5	0.2	0.4	0.5	0.8	0.4	t_R, MS

1290	Terpinolene	0.5	0.5	0.2	0.2	0.2	0.2	t_R, MS
1345	3-Octyl acetate	0.1	-	tr	0.1	0.2	0.1	t_R, MS
1350	Hexyl propionate	0.1	tr	tr	tr	tr	0.1	MS
1353	Hexyl isobutyrate	0.2	tr	0.1	0.1	0.1	0.1	MS
1360	Hexanol	0.1	0.3	-	-	tr	tr	t_R, MS
1382	*cis*-Alloocimene	tr	tr	tr	tr	tr	tr	MS
1386	Octenyl acetate	0.2	-	1.0	0.9	0.4	0.1	MS
1393	3-Octanol	tr	-	-	0.2	0.4	tr	MS
1424	Hexyl butyrate	1.1	0.6	0.4	0.4	0.6	0.8	MS
1438	Hexyl 2-methyl butyrate	0.1	0.2	-	-	tr	-	MS
1450	*trans*-Linalool oxide (*Furanoid*)	tr	tr	0.1	tr	tr	-	MS
1457	Hexyl isovalerate	0.1	-	-	-	-	-	MS
1459	1-Octen-3-ol	tr	0.5	0.2	0.1	tr	-	t_R, MS
1474	*trans*-Sabinene hydrate	-	0.2	0.2	0.2	0.1	-	t_R, MS
1479	*cis*-Linalool oxide (*Furanoid*)	0.1	tr	tr	tr	tr	-	MS
1483	1-Octyl acetate	0.1	**-**	**-**	**-**	**-**	**-**	t_R, MS
1532	**Camphor**	4.7	**6.9**	0.2	0.2	0.3	4.8	t_R, MS
1544	7-epi- Sesquithujene	-	-	-	tr	-	-	MS
1553	**Linalool**	**50.0**	**45.9**	**31.9**	**38.9**	**43.0**	**32.3**	t_R, MS
1556	*cis*-Sabinene hydrate	-	tr	0.3	0.2	0.2	-	t_R, MS
1562	Octanol	-	tr	-	-	-	-	t_R, MS
1565	**Linalyl acetate**	**6.0**	1.8	**17.5**	**16.3**	**15.4**	**42.0**	t_R, MS
1583	α-Santalene	-	-	0.2	0.3	0.2	-	MS
1590	Bornyl acetate	-	-	0.2	0.2	0.1	-	t_R, MS
1611	**Terpinen-4-ol**	0.2	4.2	**14.9**	**8.3**	3.0	tr	t_R, MS
1612	β-Caryophyllene	0.4	0.3	2.5	3.3	2.4	1.8	t_R, MS
1617	**Lavandulyl acetate**	2.0	0.7	2.2	3.0	**5.2**	1.8	t_R, MS
1618	Hexyl hexanoate	tr	0.1	-	tr	0.1	tr	MS
1631	Hexyl tiglate	0.3	tr	-	0.1	0.1	0.3	t_R, MS
1661	Sesquisabinene	-	-	-	tr	-	-	t_R, MS
1668	(Z)-β-Farnesene	0.1	1.3	1.8	2.7	3.2	1.1	MS
1684	(E)-Ocimenol	0.2	1.0	-	-	-	-	t_R
1686	Lavandulol			0.6	0.7	1.2	tr	t_R, MS
1687	α-Humulene	-	-	-	tr	tr	-	t_R, MS
1690	Cryptone	-	0.1	-	-	0.3	tr	MS
1706	**α-Terpineol**	**8.7**	1.5	3.6	3.6	3.3	1.1	t_R, MS
1719	**Borneol**	2.2	**5.7**	0.4	0.4	0.9	1.9	t_R, MS
1726	Germacrene D	0.1	0.2	0.1	0.2	0.3	0.5	MS
1733	Neryl acetate	1.8	0.1	1.0	1.0	1.0	0.4	t_R, MS
1765	Geranyl acetate	3.6	0.2	1.9	1.8	1.7	0.6	t_R, MS
1776	Cumin aldehyde	0.1	0.1	0.1	tr	0.2	0.1	t_R, MS
1808	Nerol	1.6	0.1	0.7	0.7	0.6	0.2	t_R, MS
1830	2,6-Dimethyl-3(E),5 (E),7-octatriene-2-ol	-	-	0.1	tr	-	-	t_R, MS
1856	Geraniol	4.6	0.3	2.0	2.0	1.8	0.5	t_R, MS
1864	*p*-Cymen-8-ol	0.1	tr	-	-	tr	0.1	t_R, MS
2008	Caryophyllene oxide	0.1	tr	0.7	0.4	0.8	0.1	t_R, MS
2191	T-Cadinol	0.1	-	tr	-	0.5	tr	MS
2232	α-Bisabolol	0.9	1.5	-	-	-	0.7	MS

RRI :Relative retention indices.

(Relative retention indices) calculated against n-alkanes, %: calculated from FID (Flame ionization detection) data; tr : Trace (< 0.1 %); IM, identification method: t_R, identification based on the retention times (t_R) of genuine compounds on the HP Innowax column; MS, identified on the basis of computer matching of the mass spectra with those of the Wiley and MassFinder libraries and comparison with literature data; A: Yalova-Greenhouse, B: Yalova, C: Edirne, D: Burdur-Jubileuo, E: Burdur-Sevtapolis, F: Commercial oil

RESULTS AND DISCUSSION

The flowers of Lavandula were water distilled using a Clevenger type apparatus. The essential oils were analyzed by GC and GC-MS. The oil yields obtained from flowers are between 3.5 and 6%. Forty eight – fifty nine compounds

constituting about 99.5-100.0 % of the essential oils of *Lavandula angustifolia* Mill. were characterized.

Oxygenated monoterpenes (44.0-79.2 %) were the main group of constituents of the oil of *L. angustifolia* followed by monoterpene hydrocarbons (4.2-13.4 %). The oils of *L. angustifolia* is contained linalool (31.9-50.0 %) and linalyl acetate (1.8-17.5%) as main constituents. Commercial oil is contained linalool (32.3 %) and linalyl acetate (42.0%) as main constituents.

The quality of *Lavandula* essential oils are regulated by ISO standards (The International Organization for Standardization). Also various international standarts such as European Pharmacopoeia (PhEur) contain monographs on various *Lavandula* sp. preparations securing pharmaceutical grade quality. (EP; linalool 20.0-45.0% and linalyl acetate 25.0-47.0%, limonen: max.% 1.0, 1,8-cineole: max. % 2.5, 3-octanone: % 0.1- 5.0, camphor: max % 1.2, terpinen-4-ol: % 0.1- 8.0, lavandulyl acetate: min % 0.2, lavandulol: min % 0.1, α-terpineol: max. % 2.0) (10,11)

The lavender essential oil composition determined by the International Organization for Standardization (ISO 3515:2002) (12) according to quality standards. Linalool, linalyl acetate, and camphor must be between 25.0-38.0 %, 25.0-45.0 % and 0-0.5 % resp. for Australian sample. (12-14). Only the linalyl acetate content (42.0%) of the F sample is within the limits (ISO 3515:2002, linalyl acetate 25.0–47.0%).
ISO for camphor content max. The limit is 1.5% (12).

Camphor content is 0.2–0.3% for samples C, D and E. However; sample A (4.7%), B (6.9%) and F (4.8%) contain camphor content higher than 1.5%.

For camphor, the company and Yalova samples (A, B and F) are not in the standard of oil quality, but it is suited to the quality standards of samples C, D, and E.

Lavender (*L. angustifolia*) attracts attention due to the active compounds in the essential oil composition.
Kivrak studied lavender and lavandin cultures samples (*L. angustifola* and *L.* x *intermedia*) cultivars in Turkey. These samples are compatible with the legislation of international standard. Lavender and lavandin samples have high antioxidant activity (14).

Low camphor plants tend also to have higher levels of terpenes. *L. angustifolia* is used in the perfumery and cosmetic industries while the high camphor plants are used as insect repellents and for other non-perfumery uses (16).

REFERENCES

1. Hickey, M and King, C. Common Families of Flowering Plants. Cambridge Univ, 1997, pp 119-27.

2. Guner, A., Ozhatay, N., Ekim, T and Baser, K.H.C. Flora of Turkey and East Aegean Islands. Supplement II. Edinburgh Univ, 2000, Vol. 11.

3. Mill, R.R. *Lavandula* L. In: Davis P.H. (Ed.) Flora of Turkey and the East Aegean Islands, vol. 7, Edinburgh University Press, 1982, 76-8.

4. Dirmenci, T. *Lavandula* L. In: Guner, A., Aslan, S., Ekim, T., Vural, M. and Babac M.T. (eds.). A Checklist of the Flora of Turkey -Vascular Plants (Türkiye Bitkileri Listesi -Damarlı Bitkiler), Nezahat Gokyigit Botanik Bahcesi ve Flora Araştırmaları Dernegi Yayını, Istanbul, 2012, 558.

5. Zeybek U. and Haksel M., Türkiye'de ve Dünyada Önemli Tıbbi Bitkiler ve Kullanım Alanları, İzmir, Zade Sağlık Yayınları, 2010, 131-2.

6. Adams, R.P. Identification of Essential Oil Components by Gas Chromatography/Mass Spectrometry. Allured Publ. Corp, Carol Stream, IL. 2007.

7. Hochmuth, D. H. MassFinder-4, Hochmuth Scientific Consulting, Hamburg, Germany. 2008.

8. McLafferty, F.W., Stauffer, D.B. The Wiley/NBS Registry of Mass Spectral Data, J.Wiley and Sons: New York. 1989.

9. Curvers, J., Rijks, J., Cramers, C., Knauss, K., Larson, P. Temperature pro-grammed retention indexes: calculation from isothermal data. Part 1: Theory.Journal of High Resolution Chromatography 8, 1985, 607–10.

10. Council of Europe European Pharmacopoeia (PhEur), vol. 8.0. Council of Europe, Strasbourg. 2014.

11. Kirimer, N., Mokhtarzadeh S., Demirci B., Goger F., Khawar K.M. and Demirci F. Phytochemical profiling of volatile components of *Lavandula angustifolia* Miller propagated under in vitro

conditions, Industrial Crops and Products 96, 2017, 120–5.

12. ISO 3515:, Oil of Lavender (*Lavandula angustifolia* Mill.) Standard. 1985. http://www.iso.org.

13. Kara, N., Baydar H. F. Determinaton of Lavender and Lavandin Cultivars (*Lavandula* sp.) Containing High Quality Essential Oil in Isparta, Turkey, Turkish Journal of Field Crops, 2013, 18(1), 58-65.

14. Kivrak, S. Essential oil composition and antioxidant activities of eight cultivars of Lavender and Lavandin from western Anatolia, Industrial Crops & Products, 2018, 117, 88–96.

15. Sharifi-Rad J., Sureda A., Tenore G.C., Daglia M., Sharifi-Rad M., Valussi M., Tundis R., Sharifi-Rad M., Loizzo M.R., Ademiluyi A.O., Sharifi-Rad R., Ayatollahi S.A. and Iriti M. Biological Activities of Essential Oils: From Plant Chemoecology to Traditional Healing Systems, Molecules, 2017, 22, 70; doi:10.3390/molecules22010070.

16. Cavanagh, H.M.A. and Wilkinson, J.M. Biological Activities of Lavender Essential Oil, Phytother. Res. 16. 2012, 301–8.

Evaluation and Advantages of Algae as an Energy Source

Fevzi Yaşar ✉ 🆔

Batman University, Vocational School, Chemistry and Chemical Process Technology Department,
72100 Batman, Turkey

Abstract: Primary energy consumption is increasing gradually together with population growth, urbanization and industrialization in the world. It is known that most of the energy used throughout the world is obtained from fossil fuels called primary energy sources such as coal, petroleum and natural gas. Within this context, the more the humanity continue to search for sustainable development and better living conditions, the more the renewable energy production will be a priority in whole world. As a result of all these, renewable energy sources used in the world today are classified as solar, wind, wave and geothermal, hydroelectric, biomass and hydrogen energies. Biomass energy, depending upon agriculture within the context of alternative energy politics, has found a wide range of application field in all over the world with its properties which target development and provide eco-friendly, sustainable energy production and environmental management. However, biofuel production that increases along with agricultural potential and technological levels of the countries brings about some crucial debates with itself. In this case, scientists express that algal biomasses, defined as third generation fuel, might be an alternative energy source; and that they have a lot of advantages. In recent years, algae have started to be seen as a promising energy source as a result of biomass energy researches accelerated due to increasing oil prices. The studies, in which biofuels such as biodiesel, renewable aviation fuel/biojet fuel, biogasoline/green gasoline, biobutanol, bioethanol, and methane are obtained from algal biomass, have enhanced widely. Algae are potentially best-yielding product that can be produced in large quantities of biofuels. This microscopic plant can be produced in dirty water, saltwater, deserts and in environments unsuitable for any other plant. Because they connect the carbon dioxide in the environment, it is produced especially around the power plants, thus reducing the damage caused by the carbon dioxide from the plants. One of the most important advantages of algae is that the amount of oil obtained is very high. Moreover, it is one of the other advantages that they are not affected by changing climate conditions and can be produced in high quantities in a short period of time.

*Corresponding author. E-mail: yasarf75@gmail.com.

INTRODUCTION

Most countries in the world meet great deal of their energy need from fuels of fossil origin. Climate change, caused by fossil fuels, and environmental problems it brings together and rural development policies applied by countries lead to the usage of renewable energy sources. For countries, such as Turkey, that export great majority of their energy of fossil origin, it is a very critical issue to obtain energy out of alternative energy sources, which can be produced from domestic sources. It is essential that alternative fuel sources be

sustainable for economic development and obtainable from domestic sources for a cleaner environment, and people oriented, renewable, applicable and easily attainable. The fact that biofuels, which are gradually gaining significance throughout the world among the alternative energy sources, and that they can be used as alternative to fossil origin fuels attracts all attentions to this point in energy issue (1).

Biofuels, becoming more and more common these days, provide contribution to the energy supply of the countries; and especially in rural areas, they provide alternative income and employment for producers who conduct biofuel raw material production. The decreasing amount of agricultural crop supply in relation with drought being lived across the world and the increasing food prices because agricultural crops are used in biofuel production have increased the debates on production and use of biomasses for food and energy. Because of the reasons mentioned above, a need to develop an alternative source against the usage of agricultural corps as biofuels has come into existence.

On the other hand, the usage of biofuels in energy technology by producing equivalent alternative solid, liquid and gas biofuel equal to present fuels is provided by means of direct burning or physical and chemical processes (2). Among biomass sources whose use is rising every passing day worldwide, especially algae, which are environmentally friendly energy sources, are studied comprehensively since we use these fuel sources without interfering in other available sources which may lead to increases in food prices; and without utilizing the agricultural areas. More than to come to the agenda as an alternative energy source, algae have been produced and evaluated as food additives in animal breeding for years (3). In recent years, as a result of biomass energy researches having accelerated

due to increasing oil prices, algae have started to be seen as promising energy sources. The idea to make use of algae as fuel is not a new issue. The studies were carried out at the beginning of 1950s after methane was produced out of them. Energy crisis in 1970s caused more researches not only on methane production from algae but also obtaining hydrogen from algae. The researches which were carried out in 1980s headed for oil production from algae; and today, in research and development of the oil produced from algae called biofuel, a significant progress has been made. Scientists are interested in algae biofuel seriously since they are edible, and they can be grown relatively easily in bio reactors, and they are likely to take place of fossil fuels (4). It is expected that algae will be the most important biofuel source in the near future (5). As an alternative and renewable energy source, algal biomass has been a promising source recently owing to its high lipid content. Today, algal oil production is basically intended for biofuel production (6). With their relatively high lipid, carbohydrate and food content and rapid growth potential, algal biomasses attract great attention in today's energy scenario. All these properties are thought to be excellent properties for biodiesel, bioethanol and biomethane (7).

Through the studies carried out today, it is seen that biofuels such as biodiesel, renewable aviation turbine fuel/biojet fuel, biogasoline/ green gasoline, biobutanol, bioethanol, and methane are obtained from algal biomass. Table 1 shows the lipid contents, lipid efficiencies; volumetric and spatial efficiencies of biomass of some types of algae used in production of bio fuel. The most widely used algal types in biodiesel production are Chlorella, Dunaliella, Isochrysis, Nannochloris, Nannochloropsis Oculata, Neochloris, Nitzschia, Phaeodactylum and Porphyridium sp. The oil content of these algal ranges from 20% wt to 50% wt.

Table 1. Lipid contents and efficiencies of some algal types used in biofuel production (8).

Type of Algae	Lipid content (Dry Weight %)	Lipid efficiency (mg/L/day)	Volumetric efficiency of biomass (mg/L/day)	Areal efficiency of bio mass (mg/m²/day)
Ankistrodesmus sp.	24-31	-	-	11.5-17.4
Chlorella emersonii	25-63	10.3-50	0.036-0.041	0.91-0.97
Chlorella vulgaris	5-58	11.2-40	0.02-0.20	0.57-0.95
Chlorella sp.	10-48	42.1	0.02-2.5	1.61-16.4
Chlorella pyrenoidosa	2	-	2.90-3.64	72.5-130
Chlorella	18-57	18.7	-	3.5-13.9

Type of Algae	Lipid content (Dry Weight %)	Lipid efficiency (mg/L/day)	Volumetric efficiency of biomass (mg/L/day)	Areal efficiency of bio mass (mg/m²/day)
Dunaliella salina	6-25	116	0.22-0.34	1.6-3.5/20-38
Dunaliella primolecta	23.1	-	0.09	14
Haematococcus pluvialis	25	-	0.05-0.06	10.2-36.4
Nannochloropsis sp.	12-53	37.6-90	0.17-1.43	1.9-5.3
Porphyridium cruentum	9-18.8	34.8	0.36-1.50	25
Scenedesmus sp.	19.6-21.1	40.8-53.9	0.03-0.26	2.43-13.52
Spirulina platensis	4-16.6	-	0.06-4.3	1.5-14.5/24-51
Spirulina maxima	4-9	-	0.21-0.25	25
Tetraselmis suecica	8.5-23	27-36.4	0.12-0.32	19

As can be seen from the table, it is observed that algal types such as *Chlorella emersonii*, *Chlorella vulgaris*, *Chlorella*, *Nannochloropsis sp*. have considerably high lipid contents, whereas they have low volumetric efficiencies (mg/L/day). In the initial studies, *Nannochloropsis sp.,* a cold sea algal type, which is tolerant to salty water and has an inclination to absorb CO_2, was used for biofuel production. *Nannochloropsis sp.* has also high triglyceride rate and a relatively high growth rate. Thus, it was established that *Nannochloropsis sp.* algae type was appropriate for biofuel production, yet with the studies going on, it was found out that there are more appropriate algal types (9). In the studies carried out, it was determined that *Schizochytrium* sp. (50–77% wt), *Botryococcus braunii* (25–75% wt), *Nitzschia* sp. (45–47% wt), *Cylindrotheca* sp. (16–37% wt) and *Chlorella* sp. (28–32% wt) are the algae which have the highest amount of oil content (10). The fact that agricultural fields are not used when algae are grown, and that they can rapidly proliferate even in small areas, and that there is no need for soil for their growth, and that they can adapt desert conditions, and they can be grown in nylon sacks and tanks around energy plants emitting carbon dioxide to the environment are the most important advantages of algae. Due to the fact that some algae types contain more oil compared to field crops, and that their growth process is easier, and that they are not affected from changing seasons and climatic conditions, and that they can be produced in large amounts in a short time, they are advantageous. In Figure 1, the processes of obtaining fuel gases, ethanol, gasoline, jet fuels, diesel, heavy oils, and some chemical raw material products by using different production methods from algae biomass are given.

In general, though it changes according to the species, algae may contain approximately between 15-77% oil. The fact that algae have high oil rate and growth efficiency compared to other plants grown for oil; this makes it attractive for production of biofuels. The fact that these fuels are produced from algae makes them possess a potential to meet increasing global energy crisis and to contribute to prevent global warming by, though partly, converting excessive carbon dioxide into efficient products via photosynthesis. One of the advantages of algae use as raw material for biofuels is that it is possible to produce different types of fuels. The properties of algae meet the need of biofuels such as biodiesel and biogas ethanol, bio jet fuel, bio gasoline or other fuels (12).

Biodiesel
Biodiesel is an alternative diesel fuel which is produced from plant oils or animal fats (liquid or solid oil/fat). Studies show that some algae types contain more than 80% oil than their total dry weight. Since most of the algae cells are grown with water, CO_2 and dissolved nutrient in aqueous suspension environment, they possess great scale biomass production capacities. The oil produced from algae can then be converted into biodiesel to be used in engines as fuel (13). Because of the cost of biodiesel production, especially the high forage cost of vegetable oils, they still set a significant obstacle for large scale of use in trade. Another important issue is that first and second generation biodiesel raw materials are inefficient and unsustainable. Despite this, the third generation biodiesel raw materials obtained from algae appeared to be one of the

most promising alternative lipid energy sources due to their high growth speed and productivity and with their high photosynthetic efficiency. In addition to their rapid production, they can be grown more easily, and more oil can be obtained from them for biodiesel production than a number of plant types (14). Soladiesel BDR company was able to use 100% biodiesel produced from algae with standard diesel engines without making any changes in the machine. Also, this biodiesel is completely appropriate for ASTM D 6751 (ASTM D6751 (ASTM=American Society for Testing and Materials) specifications for Fatty Acid Methyl Ester based fuel (FAME), which meets ASTM D 975; and it is considered that it has significant superiority to diesel fuel due to total hydrocarbon (THC) volume, very low carbon monoxide and particle substance and ultra low sulphur content. Soladiesel BDR also stated that this biodiesel has better cold

flow properties than any kind of biodiesel available in trade (15).

With algal oil use as raw material in biodiesel production, not only biodiesel unit price will be able to be pulled down to the levels to be able to compete with petroleum based diesel fuel but also it will make it possible for the countries to diversify their energy sources; and to be able to save the country from dependence on foreign sources in energy. In the studies carried out, it is stated that like vegetable and animal oils and fats, biodiesel fuel obtained from renewable energy sources can be used as alternative to petroleum diesel and thus, that it may decrease petroleum dependency , and that it can be taken into consideration as a promising alternative fuel to reduce pollution stemming from exhaust emissions and petroleum dependency (16).
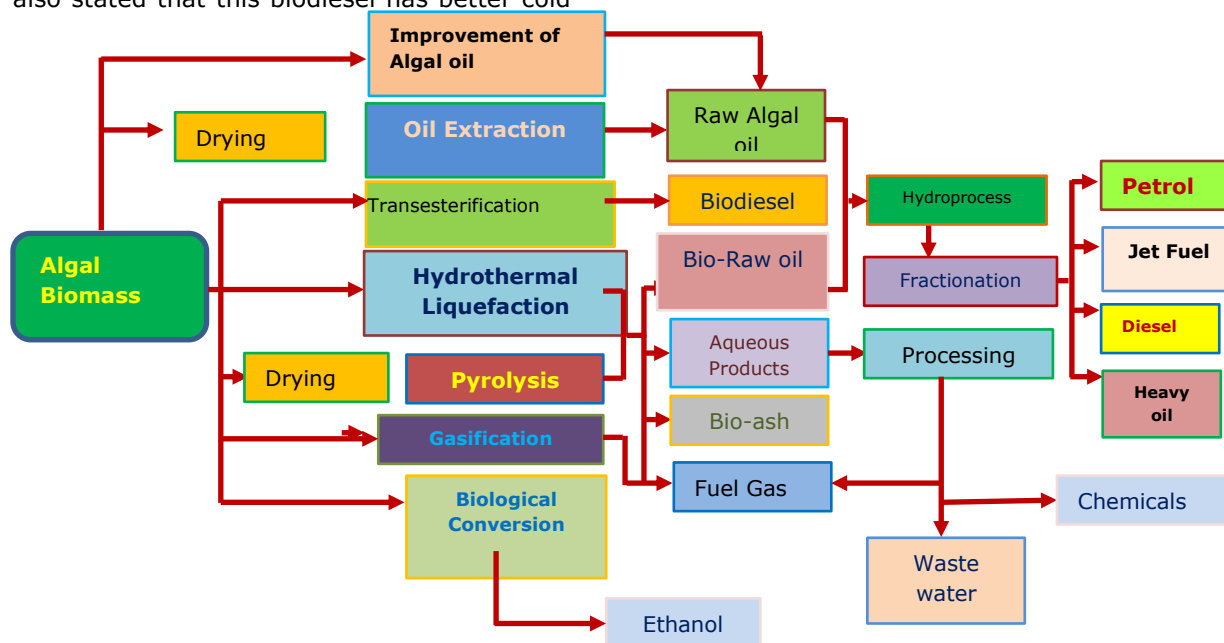
Figure 1: Production processes of bio fuels obtained from algae biomass (11).

Renewable aviation fuel/Biojet fuel

Algae-based fuels are not only limited to automobile and truck fuel in countries in general. While increasing jet fuel costs affect many airway companies economically, this has made an incentive for many companies and researchers to produce biojet fuel out of algae. For instance, it was expressed that member companies of International Aviation Transportation Association (IATA), which provides research, development and widespread use of these products, could be supported until 2017 so that they can use 10% alternative bio jet fuels. Biojet fuel is increasingly produced from raw materials such as algae, and used in flight tests. Continental Airlines flew between Houston and Chicago by using 40% algae-based biojet fuel and the US

Navy carried out a flight by utilizing 50% algal bio-jet fuel in a helicopter (17). Solazyme Company, California gave the USA Navy 1500 gallon 100% algae-based jet fuel for test and certification. The USA Navy previously explained its target that it would operate at least 50% of its fleet by means of clean, renewable fuel until 2020. Solazym produced the world's first 100% algae based jet fuel via officially patented fermentation process by cooperating with UOP Company of Honeywell in renewable jet fuel process technology (18). The fact that petroleum sources are rapidly running out, and that the aviation sector is developing every other day, and as a result, there is an increase in petroleum based aviation fuel, and fluctuations in crude oil prices, and increase in greenhouse gas

emissions and the need for energy security all promote the development of an alternative jet fuel. Biojet fuel should be technically and economically possible, eco-friendly, greener than jet fuel, locally producible, and should have a lower price than low gallon fuel for per BTU. Bio-jet fuel can be produced by blending petroleum based jet fuel with algae oil biodiesel (19).

Bio-jet fuel can be obtained from sustainable sources such as vegetable oils, sweets and animal fats and even waste biomasses; and it can be used in jet engines available now without making any changes in them. Renewable aviation fuels are different from conventional fuels because this fuel is not of a petroleum origin; it however has the same structure. One of the most important advantages of bio-jet fuels is that they provide a low emissive option for fuel in commercial and military planes. Other advantage of these fuels is that they have similar chemical properties with commercial jet fuels. As a result, these fuels are completely compatible with present engines and distribution systems, so there is no need to make any changes with these parts. Also, these fuels meet the same performance criteria with conventional fuels (12).

Biogasoline/Green gasoline

Bio gasoline is a kind of fuel which is produced from biomass of algae and contains C_6-C_{12} carbon atoms like commercial gasoline and can be used in internal combustion engines. During the use of this fuel, no changes are applied to the engine because this fuel also has the same chemical properties with commercial gasoline. As a result, bio-gasoline can be used in any kind of gasoline operating engine and at any blend (10). In the literature, there are studies in which premium gasoline is obtained from algae and vegetable oils via catalytic conversion, and accompanied with selector zeolite catalyst (20).

Biobutanol

Biobutanol can be produced from algae and diatoms utilizing a solar energy bio refinery. This fuel has 10% less energy density compared to commercial gasoline, while it can be produced more than ethanol or methanol. In addition to this, biobutanol can be used in gasoline powered engines without applying any changes. In numerous test studies, it was determined that biobutanol has similar consumption amount with gasoline; and that when compared to gasoline, biobutanol provides better performance; and that it has a higher corrosion resistance compared to E85 (8). In recent times, biobutanol obtained from algae biomass, due to its high capacity of starch content and polymeric carbohydrate

accumulating ability, has been thought as fermentable raw material convenient for biobutanol production (21). Biobutanol produced out of algal biomass is a biofuel possessing similar properties with gasoline (22).

Bioethanol

Most of the studies carried out in recent years have been about fermentation of algae and bioethanol production. Algal biomasses supply protein and carbohydrate in the form of glucose, starch and other polysaccharides, and this protein and carbohydrate may be used as carbon sources for fermentation of bacteria, yeast and fungus. For example *Chlorella vulgaris* is accepted as a potential raw material for bioethanol production since it has high starch accumulation. *Chlorococum sp.* have been used as a fermentable substance for bioethanol production under different fermentation conditions. Although there seems to be limited number of studies about fermentation of algae, it has been known that there are a lot of advantages of bioethanol production from algae by means of fermentation. Fermentation process has lower energy consumption due to the fact that it has a simpler system compared to biodiesel production. In addition, CO_2, a side product obtained in fermentation process, can be recycled as carbon source for algae. Thus, greenhouse gas emissions will be reduced and the effect of global warming will decrease (12).

Algae, third generation raw material for biofuels, are alternative to first and second generation raw materials because of its productivity and because they can be easily grown and they have appropriate harvest time. Algae, due to their high lipid contents, cellulosic structure and high amount of carbohydrate content, are considered to be quite an important source for bioethanol production (23). Some kinds of algae have high carbohydrate content in terms of starch and cellulose; besides, they are excellent sources for bioethanol production. The use of algae biomass rich in carbohydrate for bioethanol production is advantageous because algae grow faster and they fix CO_2 at higher rates than land plants (24).

Methane

Methane, one of the basic components of natural gas, can be produced from algae via methods such as gasification, pyrolysis, and anaerobic decomposition. Methane is obtained under high temperature and pressure via gasification and pyrolysis methods. Anaerobic decomposition, also known as the decomposition process of organic substances in airless environment, is a method, in which

after the solid particles are disposed to algae, the fatty acids are converted by utilizing acidic bacteria; and in which algae are separated into simple components with addition of methanogenic bacteria into the environment for the spread of a gas mixture. It has been proved with a number of successful studies that algae biomass can be converted into biogas as a result of anaerobic decomposition. Therefore, it is recommended to grow algae so that general energy balance and electric production can be bettered by means of energy regain from waste biomass via methane anaerobic decomposition (12).

Advantages of Utilizing Algal Oil as Energy Source

The oil obtained from algae can be directly used in diesel engines like other vegetable oils and can be converted into biofuel after refined.

Since algae are fed with more CO_2 and organic substances, it has been observed that the oil they produce has increased 40% in laboratory environment. Especially, algal oil utilized in biodiesel production can be used as an organic origin and environmentally friendly fuel. While algae produce oil in their structure, they utilize sunlight and CO_2 more effectively compared to oil plants; and their division potential and growth rate are quite high. Some kinds of algae contain up to 60% oil of their total weight and when the optimum conditions are provided, they can produce approximately 55,000-60,000 liters of oil annually per hectare. For all these reasons, it is possible to produce algae in small areas in large amounts and with low costs when compared to oil-based plants whose plantation is carried out in large areas. The advantages of the use of algal oil as energy source are given below (Figure 2).
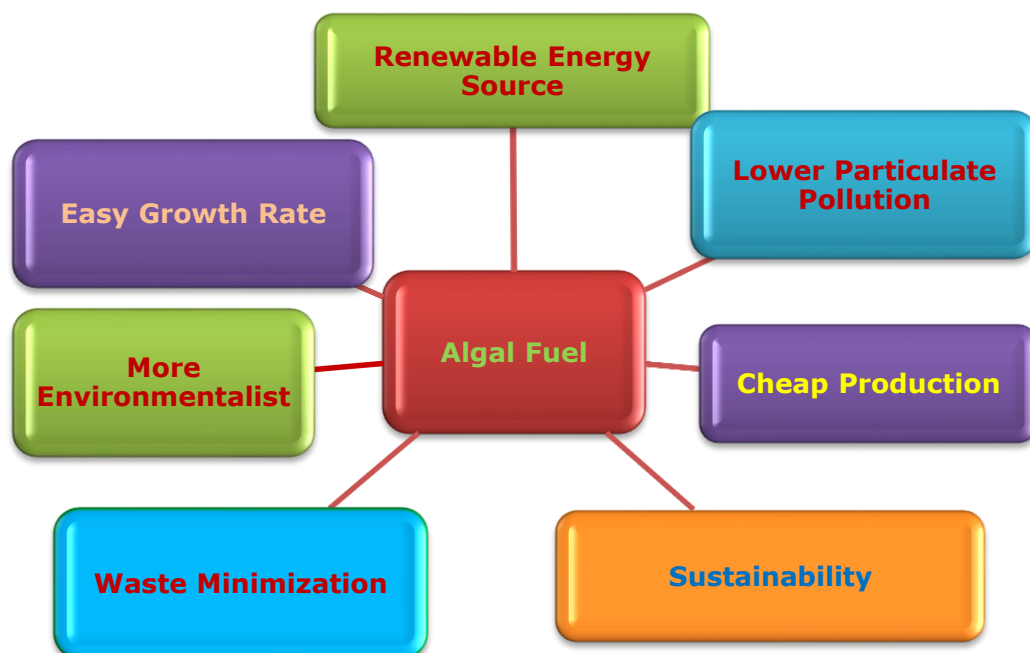
Figure 2. Advantages of algal fuel (25).

- The fact that CO_2 in industrial exhaust gases is attached to algae with bio-attachment, and the algae, which are grown and thus their oil is converted into biodiesel, decrease the effect of greenhouse gases in the atmosphere (26).
- Since they are able to be grown photosynthetically, they do not need any carbon source, and they use up carbon dioxide as energy source which is the product of previous consumptions, so, they provide carbon dioxide neutralization (27).
- The lipids, which algae accumulate, are generally in the form of triacylglycerol (>80%), they contain fatty acids rich in

C_{16}-C_{18} carbon atoms, the ratio of which is clearly seen in oil-acid distribution of algae oil we use. Although the lipid content of algal cells changes in average between 1% and 70%, when optimum conditions are provided, algae can accumulate 90% lipid.
- When compared with agricultural products and other aqueous plants, algae are known to have very fast growth rate.
- When compared to the other agricultural raw materials used for biodiesel production, smaller areas are needed for their growth. Consequently, it is stated that thanks to use of algae as raw material in biodiesel production, arable areas reserved

for growing raw materials for biodiesel production will decrease.

- It is expressed that biodiesel produced from algae either contains very little or no sulfur, and that though CO, hydrocarbon and SO_x emissions are little, NO_x emission is more in some engine types [8].
- It is known that some algae types have very high lipid content and that in optimum conditions, these photosynthetic microorganisms can produce 100 times more lipid than plant system grown in the same field.
- In the studies carried out, some scientists have found algae as matchless energy alternative, and at the same time, they

emphasized their contribution to gas emission volumes [28].

- The algae grow two fold in a day by utilizing very little water and only day light. Even, some algae complete this growth within only a few hours. Therefore, as biofuel raw materials, algae are among the most popular choices.
- Algae are great CO_2 absorbents.
- They have the properties to be grown everywhere since they do not have region selection.

Oil content, oil efficiency, field of use and biodiesel efficiencies of algal oil and different vegetable oils are given in Table 2 [29].

Table 2. Comparison of algae oil and other vegetable origin oils (30).

Raw Materials of oils	Oil Content (%)	Oil Efficiency * (L oil/ha.year)	Field of use ** (m^2 /year.L Biodiesel)	Biodiesel Efficiency *** (L Biodiesel/ha.year)
Algal (with low oil cont.)	30	58,700	0.2	61,091
Algal (With medium oil cont.)	50	97,800	0.1	101,782
Algal (With high oil cont.)	70	136,900	0.1	142,475
Corn	44	172	56	179
Hemp	33	363	26	378
Soya	18	636	15	661
Jatropha	28	741	13	772
Camelina	42	915	10	952
Canola	41	974	10	1,014
Sun flower	40	1,070	9	1,113
Castor	48	1,307	8	1,360
Palm	36	5,366	2	5,585

* : L oil / ha.year: Amount of oil in litres per hectare per year
** : m^2 /year.L Biodiesel: The amount of biodiesel obtained from m^2 per year
*** : L Biodiesel / ha.year: Amount of biodiesel per liter per year

Table 2 demonstrates that biodiesel efficiencies of algae are a lot higher than the other bio-oil raw materials especially in terms of annual oil efficiencies when low, medium and high content algal types are compared to other agricultural origin oil raw materials. In addition, when areas used for growing raw materials are examined, it can be easily seen that there is no need to use great amount of areas for algae production.

CONCLUSION

While about 9% of total renewable energy consumed in global scale is met from energy sources which are called conventional biomass and which are used for cooking and heating purposes, 10.3% of it is obtained from modern renewable energy sources. Within the context of alternative energy policies, agriculture based biomass energy, which is environment friendly and provides sustainable energy production and environment management and has properties targeting development, has found a vast application area throughout the world. However, increasing biofuel production,

which countries have, at agricultural and technological levels has brought along a lot of important debates as well. In this case, scientists have started to mention that algal biomasses, defined as third generation, could be alternative energy source and that they have many advantages. Due to increasing petroleum prices in recent years, algae have started to be seen as promising energy source as a result of researches on biomass energy. The studies, through which biofuels such as biodiesel, renewable aviation fuel/bio-jet fuel, biogasoline/green gasoline, biobutanol, bioethanol and methane are obtained out of algal biomass, have been widely developed. The fact that the agricultural areas are not utilized during algae growth, and that they reproduce very rapidly even in small areas, and that there is no need for fertile lands for their growth, and that some algae types contain more oil than field crops, and that their growing process is easier, and they are not affected by changing seasons and climatic conditions, and that they can be produced in vast amounts in a very short time make them advantageous.

REFERENCES

1. C. Escobar J, S. Lora E, J. Venturini O, E. Yanez E, F. Castillo E, Almazan O. Biofuels: Environment, technology and food security, Renewable and Sustainable Energy Reviews. 2009; 13:1275–87.

2. I. Jahirul M, G. Rasul M, Ahmed Chowdhury A, Ashwath N. Biofuels Production through Biomass Pyrolysis A Technological Review, Energies. 2012;5: 4952-5001.

3. Gegg P, Wells V. UK Macro-Algae Biofuels: A Strategic Management Review and Future Research Agenda, Journal of Marine Science and Engineering. 2017;5(3):324.

4. (anonymous). Algae products: applications and industrial uses. [Internet]. [cited 2018 May 22]. Available from: https://study.com/academy/lesson/algae-products-applications-industrial-uses.

5. Konur O. The scientometric evaluation of the research on the algae and bio-energy. Applied Energy. 2011;88(10):3532–40.

6. Hu Q. Sommerfeld M, Jarvis E, Ghirardi M, Posewitz M, Seibert M, Darzins A. Microalgae triacylglycerols as feedstocks for biofuelproduction: perspectives and advances, The Plant Journal. 2008;54:621–39.

7. Singh J, Gu S. Commercialization potential of microalgae for biofuels production, Renewable and Sustainable Energy Reviews. 2010;14:2596–610.

8. Mata T.M, Martins A A, Caetano NS. Microalgae for biodiesel production and other applications: A review, Renewable and Sustainable Energy Reviews. 2010;1:217–32.

9. Elmoraghy M. Production of bio-jet fuel from microalgae, Master's Theses and Capstones, University of New Hampshire Scholars' Repository. 2013.

10. Wen Z. Microalgae as a Feedstock for Biofuel Production, Virginia Cooperative Extention, Publication.2009;442-886.

11. Kröger M, Müller-Langer F. Review on possible algal-biofuel production processes, Journal Biofuels. 2012;3(3):333-49.

12. Brennan L, Owende P. Biofuels from microalgae—A review of technologies for production, processing, and extractions of biofuels and co-products, Renewable and Sustainable Energy Reviews. 2010;14(2):557-77.

13. Çanakçı M, Van Gerpen J. Biodiesel production from oils and fats with high free fatty acids, T. ASABE.2001;44:1429-36.

14. Ahmad A.L., Mat Yasin N.H., Derek C.J.C., Lim J.K. Microalgae as a sustainable energy source for biodiesel production: A review, Renewable and Sustainable Energy Reviews. 2011;15:584–593.

15. (anonymous). http://solazymeindustrials.com/solutions/fuel/#main-content. [Internet]. [cited 2018 April 13].

16. Yaşar F. Biodiesel production from algae oil and its use in a diesel engine as alternative fuel [Ph.D

Thesis].[Batman]:Batman University; 2016.

17.   Marie-Odile P. Fortier, Griffin W Roberts, Susan M. Stagg-Williams, Belinda S.M. Sturm. Life cycle assessment of bio-jet fuel from hydrothermal liquefaction of microalgae, Applied Energy.2014;122:73–82.

18.   (anonymous). https://www.renewableenergyworld.com/articles, Solazyme Delivers Algae Jet Fuel to US   Navy. [Internet].[cited 2018 April 13].

19.   Archambault S, Downes C.M.S, Voorhies W.V, Erickson C.A, Lammers P. Nannochloropsis   sp. algae for use as biofuel: Analyzing a translog production function using   data from   multiple sites in the southwestern United States, Algae Research. 2014;6:124-31.

20.   Milne T.A, Evans R.J, Nagle N. Catalytic conversion of microalgae and vegetable oils   to   premium Gasoline, with shape-selective zeolites, Biomass.1990;21:219-32.

21.   Figueroa-Torres, G. M, Theodoropoulos C, Pittman, J. From Microalgae Starch to   Biobutanol Production – a Combined Experimental and Computational Study. 17. AICHE   Annual Meeting:Proceedings : Sustainable Engineering Forum : Advances in Algae Biorefineries. 2017.

22.   Yeong T.K, Jiao K, Zeng X, Lin L, Pan S, Danquah M.K. Microalgae for biobutanol   production – Technology evaluation and value proposition, Algae Research. 2018;31:367-76.

23.   Özçimen D, İnan B. An Overview of Bioethanol Production From Algae, INTECH Open Science. 2015.

24.   Ho S.H, Huang S.W, Chen C.Y, Hasunuma T, Kondo A, Chang J.S. Bioethanol   production   using carbohydrate-rich microalgae biomass as feedstock, Bioresource Technology.2013;135:191–8.

25.   Paul Abishek M, Patel J, Prem Rajan A. Algae Oil: A Sustainable Renewable Fuel of Future,   Hindawi Publishing Corporation Biotechnology Research International. 2014;8.

26.   Wang B. Li. Y Wu N Lan CQ. CO_2 bio-mitigation using microalgae, Applied Microbiology and Biotechnology. 2008;79(5):707–18.

27.   Lorenz R.T, Cysewski G.R. Commercial potential for Haematococcus microalgae as a   natural source of astaxanthin, Trendes in Biotechonology.2000;18:160-7.

28.   RajvanshiS., Sharma M.P. Microalgae: A potential source of biodiesel, Journal of Sustainable Bioenergy Systems. 2012;2:49-59.

29.   Hill J Nelson E. Tilman D, Polasky S, Tiffany D. Environmental, economic, and energetic   costs and benefits of biodiesel and ethanol biofuels. Proceedings of the National Academy of Sciences, USA. 2006;103:11206–10.

30.   Rajvanshi S, Sharma M.P., Microalgae: A potential source of biodiesel, Journal of Sustainable Bioenergy Systems, 2012;2:49-59.

Investigation of Mineral Components and Antioxidant Properties of a Healthy Red Fruit: Cornelian Cherry (*Cornus mas* L.)

Merve Goksin Karaaslan[1*] ✉ iD , **Nagihan M. Karaaslan**[2] iD , **Burhan Ates**[1] iD

[1*]Inonu University, Faculty of Art and Science, Department of Chemistry, 44000, Malatya.
[2]Munzur University, Faculty of Engineering, Department of Chemical Engineering, 62000, Tunceli.

Abstract: The mineral components of the foodstuff consumed by an individual are important in the growth and development of a human being. In recent years red fruits, because of their potential beneficial health effects, are getting attention of both consumers and manufacturers. One of the red fruits, Cornelian cherry (*Cornus mas* L.), was investigated in terms of both mineral components and antioxidant properties. The mineral components include calcium (Ca), iron (Fe), potassium (K), magnesium (Mg), and zinc (Zn) in this fruit were determined using flame atomic absorption spectrometry (FAAS). The antioxidant activity tests were applied to the extracts obtained using different solvents to examine the antioxidant properties of this fruit. Statistical analysis indicated that while the best results were obtained from acetone extracts, the lowest results were obtained from water extracts for all antioxidant activity tests (p<0.05). The best average values for DPPH and ABTS radical scavenging capacity, reducing power, total phenolic content and total flavonoid content in acetone extracts were found to be 1053.72±38.12 mg TEAC/100 g FW and 2907.34±152.05 mg TEAC/100 g FW, 5894.99±251.05 mg TEAC/100 g FW, 2979.25±69.40 mg GAE/100 g FW and 255.75±14.92 mg QE/100 g FW, respectively.

INTRODUCTION

Cornelian cherry, with a sour taste, generally grows in Asia and Europe (1). This fruit which is less common in comparison with other fruits grows in the temperate regions of Turkey. *A Cornus mas L.,* belonging into the family of *Cornacea,* is one of the few species consumed by people (2). In Turkey, this fruit can be eaten directly (dried or raw) or after treatment with some processes as jam, marmelade, pestil (a dried form of marmalade), paste, and sherbet (3).

Fruits that are antioxidant sources have many health benefits since they lower the risk of heart disease, cancer, and protect the body against free radicals (4, 5). Antioxidants help diminish oxidative damage to cells that can cause several serious illnesses. As mentioned in literature, one of the red fruits (Cornelian cherry) contains high amount of ascorbic acid, anthocyanin, phenolic compound, and antioxidant activity unlike many other fruits. Anthocyanin compounds which are abundant in this fruit have powerful antioxidant properties (6, 7) and they have anti-inflammatory effects (3). Phenolic compounds and especially flavonoids have an important role in the human diet and are known to be an important component in many medicinal plants (8). Cornelian cherry

fruit has been used for the treatment of gastrointestinal disorders, diarrhea, and a number of diseases (9).

When the literature is examined thoroughly, the effect of solvent type on antioxidant activity has been disregarded in research regarding this fruit and in addition, few studies were reported dealing with its the mineral components. For this reason, the mineral components and antioxidant properties of cornelian cherry were examined in this study. The mineral components of cornelian cherry were determined by using FAAS. The antioxidant properties in different extracts (acetone, acetonitrile, ethanol, methanol and water) of this fruit were examined by using DPPH and ABTS radical scavenging capacity, reducing power, total phenolic content, and total flavonoid content tests.

MATERIAL AND METHOD

Apparatus
To analyze Ca, Fe, K, Mg, and Zn elements, a Perkin Elmer Analyst 800 FAAS (Perkin Elmer, Inc., Shelton, CT, USA) was used. The measurements were carried out by using a single slot-burner head, air-acetylene flame and a lamp. The operation conditions for FAAS: 2 L min^{-1} flow of acetylene, 17.0 L min^{-1} flow of air were utilized for all element measurements. The slit width for Ca, K, Mg, Zn was set to 0.7 nm and the slit width for Fe was adjusted to 0.2 nm. The wavelength (nm) for Ca, Fe, K, Mg, and Zn elements were set to 422.7; 248.3; 766.5; 285.2; and 213.9, respectively.

A microwave oven (Berghof, Germany) was used to dissolve the samples and standard reference materials. Before use, all glassware and reaction vessels were cleaned with 10% HNO_3 solution, then rinsed with tap water and deionized water. All antioxidant test measurements were conducted with a Shimadzu 1601 UV-Vis spectrophotometer (Tokyo, Japan).

Reagents and standards
All chemicals and solvents used were of analytically pure grade and purchased from Merck and Sigma-Aldrich. Ultrapure water (Milli-Q, Millipore 18.2 µΩ cm^{-1} resistivity) was utilized in the preparation of all solutions in this study. Standard solutions were prepared with different concentrations for the calibration graphics that are used in the determination of mineral components and applied for antioxidant activity tests.

The preparation of cornelian cherry samples
Cornelian cherries (*Cornus mas* L.) were obtained from the local markets on the season in Malatya, Turkey. The samples were cleaned with tap water and ultrapure water, respectively, and then were homogenized with a domestic blender.

Analytical procedure for mineral components
Three identical fresh samples each weighing 1.0 grams were placed in Teflon vessels. 5 mL of HNO_3/1 mL H_2O_2 was added to the samples and dissolved in the microwave applying three steps; Step 1: 10 min to reach 150 °C at 80 W, Step 2: 10 min to reach 160 °C at 80 W, Step 3: 20 min to reach 190 °C at 80 W. After cooling to room temperature, the clear solutions were diluted to 30 mL with distilled water and analyzed by FAAS. NIST-1547 peach leaves standard reference material was used to determine the accuracy of the method. All procedures applied to dissolve the samples were also applied to the standard reference material. The element concentrations were calculated in terms of mg per kg of fresh weight (mg kg^{-1} FW).

Analytical procedure for antioxidant activity tests
Three identical fresh samples of about 5 grams of cornelian cherries were prepared for each solvent, they were extracted with solvents acidified to contain 0.1% hydrochloric acid solutions for antioxidant activity tests. 10 mL volumes of acetone, acetonitrile, ethanol, methanol, and water were added to the samples and they were extracted at room temperature for 1 h. The obtained extracts were centrifuged (4000 rpm, 10 min) and then filtered. The antioxidant activity tests such as 1,1-diphenyl-2-picrylhydrazyl (DPPH) and 2,2'-azino-bis (3-ethylbenzothiazoline-6-sulfonic acid) (ABTS) radical scavenging capacity, reducing power, total phenolic content, and total flavonoid content were applied to each clear supernatant. These tests were applied to sample extracts by slightly modifying the methods described in the literature. The experimental results were expressed in terms of mg per 100 g of fresh weight (mg/100 g FW).

DPPH radical scavenging capacity
The DPPH radical scavenging capacity test was carried out using the method applied by Brand-Williams *et al*. (1995) (10). The extracts were brought to a volume of 2.5 mL with DPPH solution and incubated at room temperature for 30 min. After this incubation step, solutions' absorbance was determined at 517 nm. Trolox was used as the standard and the results were expressed as Trolox equivalent (mg TEAC/100 g) using the regression equation of the standard curve for Trolox (*y=0.123x+3.4889; R^2=0.997*).

ABTS radical scavenging capacity
The ABTS•+ radical scavenging capacity test was applied to the sample extracts using the method reported by Re *et al.* (1999) (11). The extracts were brought to a volume of 2.5 mL with ABTS•+ stock solution and incubated for 30 min at room temperature, then solutions' absorbance was measured at 734 nm. Trolox was used as the standard and the results were calculated from the

regression equation of ($y=0.1481x+4.0016$; $R^2=0.9958$) and expressed in terms of Trolox equivalent (mg TEAC/100 g).

Reducing power
The reducing power test was performed using the method reported by Oyaizu (1988) (12). The extracts were mixed with 0.2 M of phosphate buffer (pH 6.6) and 1% potassium ferricyanide solution. These mixtures were incubated in a water bath (50 °C, 20 min). After incubation, 10% of TCA was added and centrifuged (6000 rpm, 10 min). Ultra-pure water and 0.1% iron (III) chloride were added to the supernatant. After 5 min incubation, colored solutions' absorbance was determined at 700 nm. Trolox was used as the standard and the regression equation ($y=0.0003x+0.0264$; $R^2=0.9947$) was used to evaluate the results and they were expressed in terms of Trolox equivalent (mg TEAC/100 g).

Total phenolic content
Total phenolic content of the extracts was determined using the Singleton and Rossi (1965) method (13). Folin-Ciocalteu reactant and 2% sodium carbonate solution were added to the extracts. The mixtures' absorbance was measured at 755 nm after incubation (25 ºC, 30 min). Gallic acid was used as the standard and results were calculated from the regression equation of $y=0.0022x+0.0366$; $R^2=0.9926$ and expressed as gallic acid equivalent (mg GAE/100 g).

Total flavonoid content
Total flavonoid content of the extracts was determined using the method described by Zhishen *et al*. (1999) (14). 5% sodium nitrite solution, 10% aluminum chloride, 1 M sodium hydroxide were added to the extracts. The absorbances of the mixtures were detected at 510 nm after incubation (25 ºC, 15 min). The amount of total flavonoid content was calculated through regression equation ($y=0.001x+0.0498$;

$R^2=0.9988$) and stated as quercetin equivalent (mg QE/100 g).

Statistical analysis
The one-way analysis of variance (ANOVA) and Tukey's multiple comparison tests were used to determinate the significance between the groups for antioxidant activity tests. Differences were considered statistically significant when p<0.05.

RESULTS AND DISCUSSION

The essential elements from dietary sources take an important place in the human diet and essential elements such as Ca, Fe, K, Mg, and Zn play a substantial role in metabolic mechanisms and these essential elements are abundant in fruits and vegetables (15). A few studies about the mineral components of Cornelian cherry (*Cornus mas* L.) have been reported in the literature. In this study, mineral components of this fruit were stated in terms of mg/kg; 425.92±42.14 for Ca, 2.78±0.26 for Fe, 2090.82±233.27 for K, 104.23±9.37 for Mg, and 1.34±0.14 for Zn, respectively. The accuracy of these results was tested with NIST-1547 peach leaves standard reference material. The measured results were shown to be accurate since the results agreed by in 96% for Ca, 92% for Fe, 106% for K, 93% for Mg, and 94% for Zn.

The interval values of an adult's dietary reference intakes (DRIs) of related elements per day (16) are presented in Table 1. The reason why the values are given with a range is that the amounts of elements to be taken for males and females are different. All lower and upper limit values cover the amount of elements that must be taken for both an adult male and female per day. Moreover, this table also shows the percentage of the dietary reference intake values (DRI%) taken for the body by assessing the results of our study in case an adult consumes 1 kg of Cornelian cherries per day.

Table 1. The interval values of an adult's DRIs and the percentage of an adult's DRI calculated by consuming 1 kg of cornelian cherries.

Element	Dietary Reference Intakes (DRIs) for adults	DRI%
Ca	1000-1300 mg/d	32.8-42.6
Fe	8-18 mg/d	15.4-34.75
K	4.5-4.7 g/d	44.5-46.4
Mg	240-420 mg/d	24.8-43.3
Zn	8-11 mg/d	12.2-16.8

Krosniack *et al*. (2010) investigated mineral contents of plum, pear, apple, and Cornelian cherry juices. They measured Ca, Fe, K, and Zn content in the juice of the fruit in this study as 323.4±93.6 mg/L, 0.483±0.252 mg/L, 1639±270 mg/L, and 0.454±0.037 mg/L, respectively. When they compared macro-

micro elements of Cornelian cherry with other fruit juices, it was found that it is rich in terms of these elements. Therefore, since it is an important source of essential elements, it was suggested to be consumed by individuals who are particularly tolerant to dairy products (17). They were reported that the percentages of

Recommended Daily Allowance (RDA) of Ca, Fe, K and Zn in 1 L fruit juice was determined as 32.3%, 2.8%, 46.8% and 3.2%, respectively. When the results of the present study which is expressed in Table 1 were compared with the results Krosniack *et al.*, Ca and K values were found compatible, Fe and Zn values were ascertained as higher in daily intake of minerals. As a result, it is advisable to consume the fruit itself rather than the fruit juice if possible. Cetkovska *et al.* (2015) investigated basic nutritional properties of cornelian cherry cultivars. When the mineral composition of this fruit's nine cultivars was examined, the concentration intervals for the elements of this study were determined as 517±84-1164±142 mg/kg for Ca, 0.46±0.09-1.83±0.25 mg/kg for Fe, 4225±394-9729±122 mg/kg for K, 72±9-430±37 mg/kg for Mg, 0.48±0.13-4.42±0.24 mg/kg for Zn. It was determined that the element composition changes depending on the cultivars of this fruit (18). When the present data was compared to the Cetkovska *et al.* (2015) study, though the Ca and K concentrations were lower, Fe concentration were higher than the specified interval they identified. As for Mg and Zn concentration, it was found in the stated interval cited by Cetkovska *et al.* (2015) study. These differences in the results in general may be caused by such factors as the cultivars, climate, temperature, soil type, and fruit maturity.

Since the antioxidant property of phenolic compounds are vital for the development of the human body, interest in vegetables and fruits containing these compounds is increasing day by day (19). It has been reported in the literature that the content of antioxidant in red fruits is high (20). The extraction process is important in the qualitative and quantitative analysis of phenolic compounds in various products such as fruits, vegetables, plants and flowers. Conventional solvent extraction techniques are generally used in the identification of antioxidant property of red fruits (20). In the current study, this technique was followed as usually proposed in the literature. When the studies in the literature were examined especially related with extraction parameters, it was determined that the experimental results were changed depending on solvent type (21). Therefore, solvent type was regarded as a significant parameter in the extraction process. The antioxidant properties of cornelian cherry were determined by antioxidant activity tests using acetone, acetonitrile, ethanol, methanol, and water extracts. When the statistical table were examined (Table 2), the lowest results were obtained in water extracts while the highest results were obtained in acetone extract in all antioxidant activity tests (p<0.05). The average values obtained with acetone extract for DPPH and ABTS radical scavenging capacity, reducing power, total phenolic content and total flavonoid content were 1053.72±38.12 mg TEAC/100 g FW and 2907.34±152.05 mg TEAC/100 g FW, 5894.99±251.05 mg TEAC/100 g FW, 2979.25±69.40 mg GAE/100 g FW and 255.75±14.92 mg QE/100 g FW, respectively. The average values obtained with water extracts were 508.12±5.11 mg TEAC/100 g FW for DPPH and 506.08±10.36 mg TEAC/100 g FW for ABTS radical scavenging capacity, 920.65±68.03 mg TEAC/100 g FW for reducing power, 439.85±34.57 mg GAE/100 g FW for total phenolic content and 28.57±0.91 mg QE/100 g FW for total flavonoid content. DPPH and ABTS radical scavenging capacity, total phenolic content test results in order from highest to lowest for extractive solvents are as follows: acetone, methanol, ethanol, acetonitrile, water, respectively. The results for reducing power test were in decreasing order for extractive solvents are as follows; acetone, ethanol, methanol, acetonitrile, water. As for total flavonoid content, the result in decreasing order also for the extracts from acetone, acetonitrile, methanol, ethanol, and water.

Table 2. Antioxidant activity test results according to solvent type.

Solvent	DPPH (mg TEAC/100 g FW)	ABTS (mg TEAC/100 g FW)	Reducing power (mg TEAC/100 g FW)	Total phenolic (mg GAE/100 g FW)	Total flavonoid (mg QE/100 g FW)
Acetone	1053.72±38.12[d]	2907.34±152.05[e]	5894.99±251.05[d]	2979.25±69.40[d]	255.75±14.92[d]
Acetonitrile	724.49±29.18[b]	808.35±11.16[b]	1207.73±74.23[a]	721.86±28.72[b]	126.20±0.70[c]
Ethanol	922.66±21.64[c]	1567.68±53.27[c]	3531.91±172.71[c]	2006.33±31.94[c]	76.01±2.61[b]
Methanol	933.48±22.61[c]	1735.63±91.30[d]	2734.56±246.30[b]	2110.29±84.00[c]	80.54±4.71[b]
Water	508.12±5.11[a]	506.08±10.36[a]	920.65±68.03[a]	439.85±34.57[a]	28.57±0.91[a]

Different letters in a column denote significant differences (p<0.05)
Results are average values ± standard deviation, n=3

Moldovan *et al.* (2016) investigated antioxidant properties of cornelian cherry fruit. They extracted samples with the acetone, and ABTS assay values of this fruit were found as

677.88±19.25 µmol Trolox equivalents/100 g fresh weight (22). In the current study, ABTS assay of Cornelian cherry fruit was tested with different extracts and the best result was obtained with acetone extract (2907.34±152.05 mg TEAC/100 g FW). In another study, antioxidant property of cornelian cherry which is grown in Turkey was investigated by using methanol as solvent. Tural and Koca found the total phenolic content to be in the interval of 2.81-5.79 mg/g and the average value was 4.37 mg/g (1). In our study, the average total phenolic content (2110.29±84.00 mg GAE/100 g FW) in the experiment with methanolic extract was found to be significantly higher than those reported by Tural and Koca (2008). These all data demonstrated that the results in our study are consistent with the related literature. The variability of the results between these studies can be attributed to the extraction solvent, as well as the fruit-grown soil, vegetation, climatic conditions and fruit maturity. Hamid *et al.* (2011) examined antioxidant capacity and phytochemical properties of six cornelian cherry genotypes. Their findings for total phenolic content and total flavonoid content were in the intervals of 1097.19-2695.75 mg GAE/100 g and 321.27-669 mg catechin/100 g, respectively (5). In the present study, total phenolic content for different extracts were found in the range 439.85±34.57 to 2979.25±69.40 mg GAE/100 g FW and total flavonoid content were found to range from 28.57±0.91 to 255.75±14.92 mg QE/100 g FW. It was observed that the results obtained from different genotypes of the same fruit change and as for our study, the results of the same fruit changed when using different extraction methods. Contrary to total phenolic content, when the total flavonoid content was compared, the average content of total flavonoid of the current study was found to be lower (5). In the study of Pyrkosz-Biardzka *et al.* (2014), antioxidant properties of methanolic crude extracts of *Berberis vulgaris* L., *Cornus mas* L. and *Mahonia aquifolium Nutt* were examined. They found total phenolic content to be 339.36±4.59 mg GAE/100 g fresh mass and total flavonoid content as 63.86±3.04 mg RE (rutin equivalent)/100 g fresh mass for *Cornus mas* L. (23). When the related data were compared, quite high findings were obtained in the current study conducted with similar extracts. Gunduz *et al.* (2013) analyzed Cornelian cherry fruits at different stages of ripeness and reported that antioxidant activity of cornelian cherry fruits changes when its maturity level increases. In addition, they specified that the total phenolic content and antioxidant capacity results were observed to decrease as maturity increased for this fruit (2).

The findings of the study demonstrated that the mineral components and antioxidant activity of the Cornelian cherry were consistent with the studies presented in literature. As already reported in the literature slight differences can be attributed to several reasons; climatic factors, soil type, geographical and environmental conditions, degree of fruit ripeness, manipulation during fruit processing, and selection of analytical methods (18). Moreover, the differences in results for antioxidant property of this fruit can be caused by the solvent type. When the results of this study were evaluated according to the dielectric constant that is considered an indicator of the polarity, it was observed that the acetone solvent having the lowest dielectric constant value has the highest antioxidant activity data in all antioxidant tests. Because acetone, unlike other solvents, is capable of dissolving components of low to medium polar character. In addition, it was determined that water has a high dielectric constant value, which in turn has the lowest antioxidant activity data in all antioxidant tests. The results suggest that the choice of the solvent used in the antioxidant activity tests is important and should have the appropriate polarity to dissolve the desired compound.

CONCLUSIONS

In this study, the mineral components and antioxidant properties of Cornelian cherry (*Cornus mas* L.) were examined. For this purpose, mineral components including Ca, Fe, K, Mg and Zn in this fruit were investigated by using FAAS. The data obtained shown that Cornelian cherry contain several essential elements and can be considered as a significant dietary mineral supplement. As for antioxidant properties, DPPH and ABTS radical scavenging capacity, reducing power, total phenolic content and total flavonoid content were examined in different extracts of this fruit. It was determined that experimental data changed depending on the solvent type. According to these results, the best results were obtained from acetone extracts while the lowest results were obtained from water extracts for all antioxidant capacity tests. Therefore, it should necessary to investigate the solvent type as one of the important extraction parameters when conducting similar studies. It was determined that this fruit might be used as a source of health in terms of mineral components and antioxidant properties.

CONFLICT OF INTEREST

The author declares no conflict of interest.

REFERENCES

1. Tural S, Koca I, Physico-chemical and antioxidant properties of cornelian cherry fruits (*Cornus mas* L.) grown in Turkey. Scientia Horticulturae. 2008;116(4):362-6.

2. Gunduz K, Saracoglu O, Özgen M, Serce S, Antioxidant, physical and chemical characteristics of cornelian cherry fruits (*Cornus mas* L.) at different stages of ripeness. Acta Scientiarum Polonorum Hortorum Cultus. 2013;12(4):59-66.

3. Celik S, Bakırcı I, Şat IG, Physicochemical and organoleptic properties of yogurt with cornelian cherry paste. International Journal of Food Properties. 2006;9(3):401-8.

4. Shui G, Leong LP, Residue from star fruit as valuable source for functional food ingredients and antioxidant nutraceuticals. Food Chemistry. 2006;97(2):277-84.

5. Hamid H, Yousef H, Jafar H, Mohammad A, Antioxidant capacity and phytochemical properties of cornelian cherry (*Cornus mas* L.) genotypes in Iran. Scientia Horticulturae. 2011;129(3):459-63.

6. Prior RL, Absorption and metabolism of anthocyanins: potential health effects. In: phytochemicals: mechanisms of action. Boca Raton, Fla., CRC Press, Inc, 2003.

7. Zafra-Stone S, Yasmin T, Bagchi M, Chatterjee A, Vinson JA, Bagchi D, Berry anthocyanins as novel antioxidants in human health and disease prevention. Molecular Nutrition & Food Research. 2007;51(6):675-83.

8. Cooper-Driver GA, Contribution of Jeffrey Harborne and co-workers to the study of anthocyanins. Phytochemistry. 2001;56(3):229-36.

9. Dinda B, Kyriakopoulos AM, Dinda S, Zoumpourlis V, Thomaidis NS, Velegraki A, Markopoulos C, Dinda M, *Cornus mas* L. (cornelian cherry), an important European and Asian traditional food and medicine: Ethnomedicine, phytochemistry and pharmacology for its commercial utilization in drug industry. Journal of Ethnopharmacology. 2016; 193:670-90.

10. Brand-Williams W, Cuvelier ME, Berset C, Use of a free radical method to evaluate antioxidant activity. Food Science and Technology-Lebensmittel-Wissenschaft & Technolgie. 1995;28(1):25-30.

11. Re R, Pellegrini N, Proteggente A, Pannala A, Yang M, Rice-Evans C, Antioxidant activity applying an improved ABTS radical cation decolorization assay. Free Radical Biology and Medicine. 1999;26 (9-10):1231-7.

12. Oyaizu M, Antioxidative activities of browning products of glucosamine actionated by organic solvent and thin layer chromatography. Nippon Shokuhin Kogyo Gakkaishi. 1988;35:771-5.

13. Singleton VL, Rossi JA, Colorimetry of total phenolics with phosphomolybdic–phosphotungstic acid reagents. American Journal of Enology and Viticulture. 1965;16:144-58.

14. Zhishen J, Mengcheng T, Jianming W, The determination of flavonoid content in mulberry and their scavenging effects on superoxide radicals. Food Chemistry. 1999;64(4):555-9.

156. Stacewicz-Sapuntzakis M, Bowen PE, Hussain EA, Damayanti-Wood BI, Farnsworth NR, Chemical composition and potential health effects of prunes: a functional food? Critical Reviews in Food Science and Nutrition. 2001;41(4):251-86.

16. Dietary Reference Intakes: The Essential Guide to Nutrient Requirements, The National Academies Press, Washington, D.C, http://www.nap.edu/catalog/11537.html.

17. Krosniak M, Gastoł M, Szałkowski M, Zagrodzki P, Derwisz M, Cornelian cherry (*Cornus mas* L.) juices as a source of minerals in human diet. Journal of Toxicology and Environmental Health, Part A. 2010;73(17-18):1155-8.

18. Cetkovská J, Diviš P, Vespalcová M, Pořízka J, Řezníček V, Basic nutritional properties of cornelian cherry (*Cornus mas* L.) cultivars grown in the Czech Republic. Acta Alimentaria. 2015;44(3):357-364.

19. Shahidi F, Ambigaipalan P, Phenolics and polyphenolics in foods, beverages and spices: antioxidant activity and health effects-a review. Journal of Functional Foods. 2015;18:820-897.

20. Hidalgo G-I, Almajano MP, Red Fruits: Extraction of antioxidants, phenolic content, and radical scavenging determination: a review. Antioxidants. 2017;6(1):1-27.

21. Boulekbache-Makhlouf L, Medouni L, Medouni-Adrar S, Arkoub L, Madani K, Effect of solvents extraction on phenolic content and antioxidant activity of the byproduct of

eggplant. Industrial crops and products. 2013;49:668-74.

22. Moldovan B, Filip A, Clichici S, Suharoschi R, Bolfa P, David L, Antioxidant activity of cornelian cherry (*Cornus mas* L.) fruits extract and the in vivo evaluation of its anti-inflammatory effects. Journal of Functional Foods, 2016;26:77-87.

23. Pyrkosz-Biardzka K, Kucharska AZ, Sokół-Łętowska A, Strugała P, Gabrielska Janina, A comprehensive study on antioxidant properties of crude extracts from fruits of *Berberis vulgaris* L., *Cornus mas* L. and *Mahonia aquifolium* Nutt. Polish Journal of Food and Nutrition Sciences. 2014;64(2):91-9.

In situ Crosslinkable Thiol-ene Hydrogels Based on PEGylated Chitosan and β-Cyclodextrin

Mehmet Arslan* ✉ iD, **Tolga Yirmibesoglu** ✉, **Mithat Celebi** ✉

[1]University of Yalova, Faculty of Engineering, Department of Polymer Engineering, 77200, Yalova, Turkey.

Abstract: Novel β-Cyclodextrin incorporated injectable hydrogels employing PEGylated chitosan as bio-based hydrophilic matrix have been fabricated via thiol-ene reaction. As thiol bearing polymer counterpart of hydrogel precursors, native chitosan was firstly modified with polyethylene glycol groups to increase its water solubility and bioinertness and then decorated with thiol groups to facilitate thiol-ene crosslinking with acryloyl-modified β-cyclodextrin. A series of hydrogels with varying amounts of acryloyl β-CD and PEGylated chitosan feed were synthesized with high efficiency under mild aqueous conditions. The resulting hydrogels were characterized by equilibrium swelling, structural morphology and rheology. These materials were investigated as controlled drug release platforms by employing a poorly water soluble anti-inflammatory drug diclofenac as model compound. Benefiting from the inclusion complex formation of the drug with β-CD groups in gel interior, prolonged release profiles were maintained. The total drug absorption and release of hydrogels were shown to be dependent on the amount of β-CD in gel matrix. These hydrogels combined efficient crosslinking and β-CD incorporation into clinically important chitosan scaffold and might have potential applications as injectable drug reservoirs such as in regenerative tissue engineering.

INTRODUCTION

Injectable hydrogel formulations that possess *in situ* formation of crosslinking process at target contour have been of interest, especially in regenerative medicine, tissue engineering, and drug delivery (1–8). Contrary to the conventional pre-formed hydrogels or scaffolds that require proper surgical implantation to the defect site, *in situ* gel forming systems procure to reach the formulation into deep tissues with maximum invasiveness by overcoming the high risk of infections, pain, and scarring (9,10). Pre-gelation preparation of gel formulation allows straightforward inclusion of several bioagents such as, growth factors (11), drugs (12), and genes (13), into the precursor solution which are primarily responsible for supporting, healing, or rejuvenating the damaged tissues. Injectable hydrogels can take complex shapes in applied region and bind to surrounding tissues during gelation which allows advanced cell/tissue encapsulation (14).

Chitosan is a biopolymer in polysaccharide structure obtained from chitin by partial deacetylation. The molecular structure of chitosan is composed of glucosamine and N-acetyl glucosamine units in which in body, glucosamine is converted into glycosaminoglycans which are parts of extracellular matrix and cartilage tissue (15). Due to unique characteristics, such as bioavailability, biodegradability and biocompatibility, chitosan derivatives have found numerous applications in various fields of biomedicine (16). Hydrogels, especially injectable hydrogel formulations employ chitosan-based polymer precursors as building blocks that construct matrix structure of the network while imparting eximious attributes. (17, 18–20), However, low aqueous solubility of

native chitosan is often a drawback in applications and entails proper modification of the polymer structure by conjugating various small molecules or polymers (21,22).

The virtual utilization of hydrogels in drug delivery demands efficient drug loading and sustained drug release. Though covalent incorporation of drug molecules into hydrogels possess several advantages (23), a much sought and operationally simple strategy involves the physical entrapment of drug molecules into the matrix. However, several limitations are often encountered during drug loading and release, primarily due to the chemical dissimilarity of drug molecules and gel structure. Hydrophobic or poorly water-soluble drug molecules usually have low interactions with hydrophilic matrix causing weak drug loading efficiencies during formulation. On the other part, controlled or sustained release in aquatic medium is hardly maintained with hydrophilic drugs. A general strategy to overcome these limitations is the incorporation of hydrophobic pockets into the gel network to maintain increased drug-carrier interactions. In this regard, hydrogels including cyclodextrins (CDs) in gelous matrix have been investigated as promising drug delivery platforms (24–29). The unique molecular structures of CDs enable inclusion complexation of hydrophobic molecules into molecular cavities present on CD structure, thus enabling increased drug loading and prolonged release.

The addition of thiols to alkenes to form a thioether bond is referred to as thiol-ene reaction and constitutes an important reaction in polymer chemistry. Highly efficient nature of thiol-ene reactions have been exemplified in design and synthesis of diverse macromolecular platforms and polymeric material functionalization (30–37). The addition reaction of thiols over electron deficient alkene groups is a special type of thiol-ene reaction known as the nucleophilic thiol-ene reaction and is a highly valuable tool in click chemistry toolbox for fabrication and functionalization of hydrogels (26,27,38). Due to the presence or straightforward installation of thiol groups on many biomolecules or biopolymers, synthesis and modification of thiol-ene biomaterials offer ease formulation and implementation in various applications.

In this study, design, fabrication and applications of hydrogels based on PEGylated chitosan and β-cyclodextrin was reported (Figure 1). Hydrogels were synthesized using nucleophilic thiol-ene reactions between thiol-modified PEGylated chitosan and acryloyl modified β-cyclodextrin. The methodology encompasses novel O-hydrophilic modification and N-thiolation of native chitosan which provided the fabrication of hydrogels without the need of any inorganic or metal catalyst or thermal and photo-activation. The simplicity and rapid gelation kinetics suggest that this

approach can be utilized to obtain injectable hydrogels. These materials uniquely combine three biomedically-relevant polymers i.e. chitosan, polyethylene glycol and cyclodextrin in fabrication of functional soft materials and can endow potential applications in various areas of biomedical sciences such as controlled drug release.
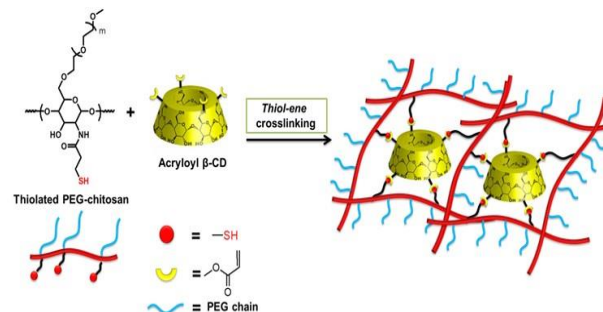
Figure 1: General representation of hydrogel formation via thiol-ene reaction of thiolated o-PEGylated chitosan and acryloyl-modified β-CD.

EXPERIMENTAL SECTION

Materials and characterization
Medium molecular weight chitosan (75-85% acetylation degree), β-cyclodextrin, poly(ethylene glycol) monomethyl ether (average Mn: 2000), phthalic anhydride, hydrazine hydrate, 3-mercaptopropionic acid, acryloyl chloride, 5,5'-dithiobis(2-nitrobenzoic acid) and diclofenac sodium salt were obtained from Aldrich Chemical Co. All solvents and inorganic materials were purchased from Merck Co. Syntheses of acryloyl-modified β-cyclodextrin (β-CD-Ac, average degree of acetylation ~5.4 per molecule) (39) and N-phthaloylated chitosan (40) were conducted according to reported procedures. p-Toluenesulfonate activation of poly(ethylene glycol) methyl ether (41) and N-hydroxysuccinimide (NHS) activation of 3-mercaptopropionic acid (42) was performed based on literature protocols. Characterization of materials was performed using ^{1}H NMR spectroscopy (Varian 400 MHz) and attenuated total reflectance-Fourier transform infrared spectroscopy (Nicolet 380). UV studies were conducted with a Varian Cary 50 Scan UV/Vis spectrophotometer. The hydrogel surface morphologies were analyzed by using an ESEM-FEG/EDAX Philips XL-30 (Philips, Eindhoven, The Netherlands) instrument with 10 kV accelerating voltage. The dynamic frequency scan analyses were performed using an Anton Paar MCR 302 rheometer with a 0.5% strain between 0.05-100 rad/s (at 25 °C). A parallel plate of 8 mm diameter was set up and the plate gap was adjusted to 2.0 mm.

Methods
Synthesis of N-phthaloylated, O-PEGylated chitosan: N-phthaloylated chitosan (1.0 g, 3.2 mmol repeating units) was charged in a two-

necked round bottom flask with magnetic stir bar and dissolved in dimethylformamide (DMF, 20 mL) by ultrasonication. To this mixture, p-toluene sulfonate-activated poly(ethylene glycol) methyl ether (8.2 g, 3.84 mmol) in 10 mL DMF and K_2CO_3 (0.53 g, 3.84 mmol) was added. The reaction mixture was stirred under nitrogen atmosphere at 80 °C for 24 h. After the reaction, the purification of the resulting polymer was conducted by dialysis against water using a dialysis membrane (MWCO 10K). The purified polymer was collected by evaporating the solvent and drying at 50 °C, overnight (Yield: 77%. FT-IR (v_{max}/cm^{-1}): 3600-3300 (broad O-H), 2882 (C-H stretching), 1771 (imide C=O), 1707 (imide C=O), 1647 (C=O acetyl), 1170-1015 (C-O stretching)).

Hydrazinolysis of N-phthaloylated, O-PEGylated chitosan: 5.4 g N-phthaloylated o-PEGylated chitosan and hydrazine hydrate (30 mL) were dissolved in distilled water (60 mL). The mixture was heated at 90 °C for 16 h. After the reaction, purification of the polymer was carried out by dialysis against water (MWCO 10K). The resulting polymer o-PEGylated chitosan was collected by removing solvent and drying the sample at 50 °C, overnight. (Yield: 86%. FT-IR (v_{max}/cm^{-1}): 3600-3300 (broad O-H), 2882 (C-H stretching), 1655 (C=O acetyl), 1170-1010 (C-O stretching)).

Thiolation of o-PEGylated chitosan: To the stirring solution of o-PEGylated chitosan (1.0 g in 10 mL DMF) was added 5 mL DMF solution of NHS-activated 3-mercaptopropionic acid (1.0 g, 5.0 mmol). The reaction was continued under argon atmosphere at 80 °C for 16 h. After the reaction, the mixture was dialyzed against water (MWCO 10K), evaporated and dried at 50 °C. (Yield: 94%. FT-IR (v_{max}/cm^{-1}): 3600-3300 (broad O-H), 2882 (C-H stretching), 1672 (C=O acetyl), 1655 (C=O acetyl), 1170-1010 (C-O stretching)).

Determination of sulfhydryl content: Total sulfhydryl content of thiolated o-PEGylated chitosan was determined using Ellman's method (43). Briefly, 4.0 mg of 5,5'-dithiobis(2-nitrobenzoic acid) was dissolved in 1 mL of reaction buffer (0.1 M sodium phosphate, pH 8.0 containing 1 mM EDTA) and to this solution, 5.0 mg of thiolated o-PEGylated chitosan in 1 mL reaction buffer was added. The resulting mixture was incubated at 37 °C for 2 h. The total sulfhydryl group content in the sample was obtained by measuring the maximum absorbance at 412 nm and using the molar extinction coefficient of 2-nitro-5-thiobenzoate (TNB^{2-}) ion (14,150 $M^{-1}cm^{-1}$) (44).

Representative hydrogel formation: Thiolated o-PEGylated chitosan (100 mg) was placed in a vial and dissolved in distilled water (200 µL). Desired amount of β-CD-Ac and catalytic amount of triethylamine (0.1 eq. of -SH) were dissolved

in distilled water in another vial (200 µL) and then added to polymer solution. The gel solution was briefly sonicated to assist homogenous gelation. In approximately 10 min, there was no flow of sample and the gelation was continued for 6 h to ensure complete available crosslinking. Thereafter, unreacted species were removed by washing the gel sample with distilled water several times. The dried hydrogels were obtained by freeze-drying of water-swollen samples. Gel conversions: 66-87% (as obtained by proportioning the obtained mass of hydrogels after purification steps to amount of starting materials).

Equilibrium swelling ratios (ESRs): ESRs were determined by sampling 20 mg of hydrogel in distilled water and then following the increase in mass of the sample as a function of time until swollen hydrogels showed a constant weight. The percentage of swelling was determined using equation 1:

$$ESR (\%) = (W_{wet} - W_{dry}) / W_{dry} \times 100$$

(Eq. 1)

The swelling studies were conducted in triplicate and average data was used for obtaining swelling curves.

Drug loading and release studies: A solution absorption method was employed to load diclofenac-Na into dry hydrogel samples. Hydrogel samples in disk shapes ($\sim$ 50 mg) were soaked in 10 mL 0.5 wt.% soaking solution at 37 °C and the solutions were incubated for 4 days, protected from light. The total amount of drug loading was calculated by subtracting the concentration in the soaking solution from the initial drug amount which was determined at 276 nm using a UV-Vis spectrophotometer.

For diclofenac-Na release, the drug-loaded hydrogels were rinsed with distilled water and then immersed in 3 mL distilled water medium at 37 °C incubation temperature. At pre-determined time intervals, 1.5 mL of release medium was collected and refreshed with same volume of fresh distilled water. The drug concentration in collected media was measured spectrophotometrically at 276 nm and the release profiles were expressed in terms of cumulative release.

RESULTS AND DISCUSSION

Synthesis and characterization of polymers
In order to obtain thiol modified chitosan-based hydrophilic polymer, a series of synthesis and post-polymerization modification steps were carried out (Figure 2). In the first step, native chitosan was phthaloylated to protect the free amine groups which were later utilized in conjugation of thiol-bearing molecule. In the next step, installation of PEG groups onto the chitosan hydroxyl functionalities was carried out

by following a 'grafting onto' approach. PEGylation is a common practice in modification of chitosan derivatives in order to increase their water solubility, as well as biocompatibility (22). Although, the common approaches of chitosan modification rely on the involvement of amino groups in chemical tailoring (22). In our study, PEG grafting was carried through hydroxyl functionalities in order to keep amine groups intact for later utilization. A nucleophilic substitution-based grafting of activated monomethoxy PEG polymer has resulted in the attachment of hydrophilic side chains onto chitosan backbone. Following the PEG grafting, protected phthaloyl groups were removed by hydrazinolysis to unveil the amino groups in their reactive form. In the last step, amino groups were conjugated with NHS-activated 3-mercaptopropionic acid to accomplish the installation of thiol-ene reactive mercapto groups onto side chains of PEGylated chitosan.
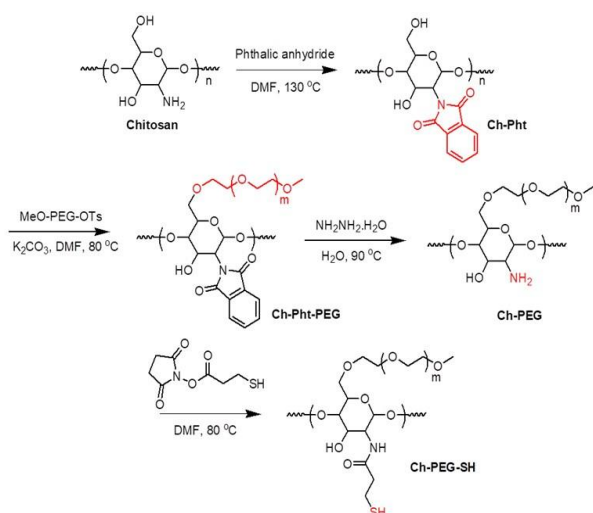
Figure 2. General reaction scheme for the synthesis of thiolated o-pegylated chitosan derivative (Ch-PEG-SH).

The synthetic steps of polymer synthesis were followed by FT-IR (Figure 3) and ^{1}H NMR (Figure 4) spectroscopic techniques to confirm the transformations. In the PEG attachment onto phthaloylated chitosan (Ch-Pht), FT-IR studies confirmed the successful grafting as evidenced by the appearance or enhancement of characteristics bands at (v_{max}/cm^{-1}) 2882 (C-H stretching), 1069 and 959 (C-O stretchings). The ^{1}H NMR analysis of resulting phthaloylated and PEGylated chitosan (Ch-Pht-PEG) revealed characteristics proton signals of chitosan pyranose groups and phthaloyl moieties, as well as signals of PEG repeating units and methoxy (-OCH$_3$) end groups. The degree of PEGylation, as determined by the integration of D-glucopyranose signal at 4.5 ppm with PEG methoxy signal at 3.4 ppm, was found as 43% (mole PEG/mole D-glucosamine). After the removal of phthaloyl groups via hydrazinolysis, FT-IR analysis revealed the disappearance of imide absorption bands at (v_{max}/cm^{-1}) 1771 and 1707. This transformation was also verified by the disappearance of phthaloyl aromatic signals at 7.3-8.0 ppm. The final step involves the reaction of free amino groups of chitosan polymer with 3-mercaptopropionic acid, pre-activated with NHS groups to give Ch-PEG-SH. Formation of a new amide band at 1672 cm^{-1} of FT-IR spectrum and aliphatic protons signals of mercaptopropionamide units in ^{1}H NMR spectrum establish the successful conjugation. In order to quantify the total number of reactive thiols groups at final polymer, a free sulfhydryl assay was accounted. According to the Ellman's analysis performed by employing 5,5'-dithiobis(2-nitrobenzoic acid), 8.4 10^{-4} mmol/g thiol content was determined.
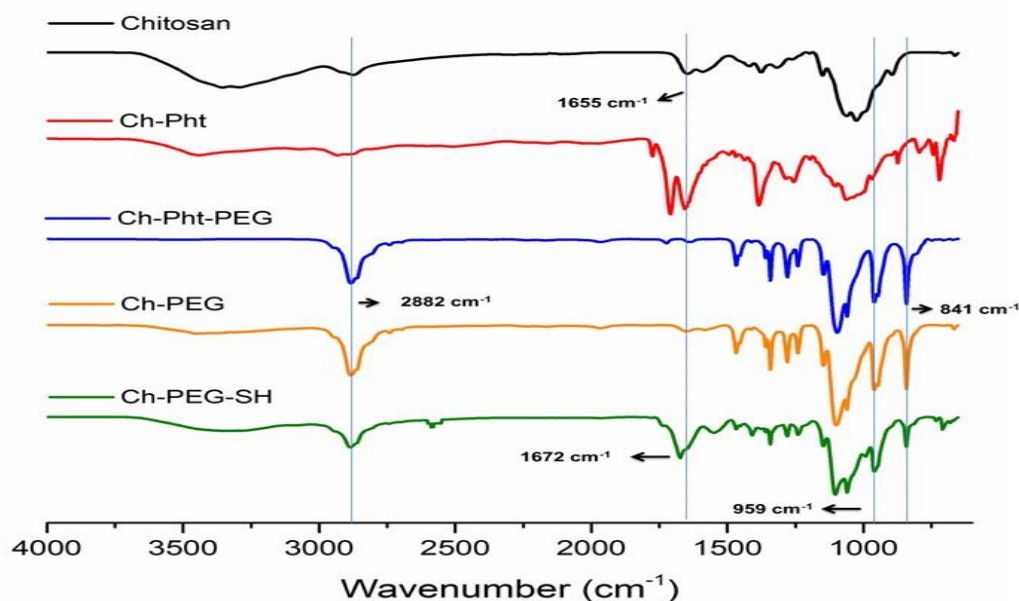
Figure 3. FT-IR structural analyses of polymers after o-PEGylation, hydrazinolysis, and thiolation steps.
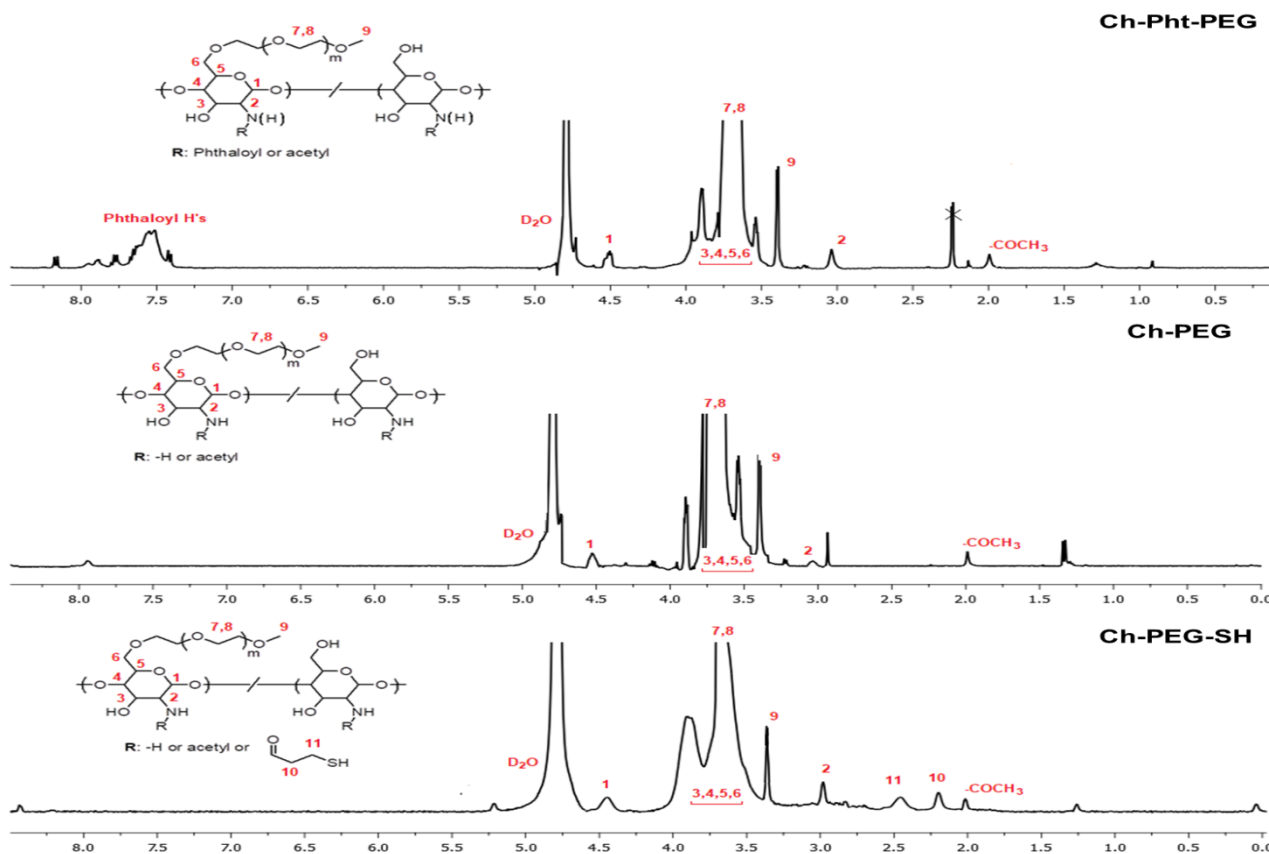
Figure 4. ^{1}H NMR structural analyses of polymers after o-PEGylation, hydrazinolysis and thiolation steps.

Synthesis and characterization of hydrogels

Hydrogels were prepared via thiol-ene reactions of thiol functionalized PEGylated chitosan polymer (Ch-PEG-SH) with acryloyl-modified β-cyclodextrin crosslinker (β-CD-Ac) (Figure 1). Through multiple additions of thiols onto acryloyl groups, fast crosslinking network formation was established in approximately ten minutes and no flow of sample was observed. To ensure complete crosslinking process, gelation was continued for 6 h. Gel formation is promoted by using a catalytic amount of trimethylamine (Et$_3$N) as a non-nucleophilic organobase. In order to compare the effect of CD-based crosslinker ratio on physical and morphological properties of resulting gels, a library of hydrogels were prepared by using various Ch-PEG-SH/β-CD-Ac feeds (Table 1, hydrogels CCH-(1-4)). The properties of obtained hydrogels were summarized in Table 1.

Table 1. Properties of hydrogels with varying Ch-PEG-SH / β-CD-Ac ratio.

Entry	Hydrogel	-SH : acrylate	Gel Conv. (%)	ESR (×100%)	Drug Load (mg/g dry gel)
1	CCH-1	0.5 : 0.5	87	9.2 (± 1.4)	88 (± 16)
2	CCH-2	0.6 : 0.4	76	13.3 (± 1.1)	74 (± 12)
3	CCH-3	0.7 : 0.3	71	15.6 (± 2.8)	66 (± 7)
4	CCH-4	0.8 : 0.2	66	19.5 (± 2.3)	61 (± 9)

Hydrogels were obtained with moderately good gel conversions via thiol-ene addition reactions of complementary functional precursors. As expected, higher gel conversions were obtained in case of using higher amount of β-CD-Ac crosslinker. The gels are clear transparent samples in their wet state appearance. The microstructure analyses based on scanning electron microscopy (SEM) revealed continuous non-porous structures (Figure 5). A very slight increase in porosity was accounted in case of employing lower crosslinker feed.
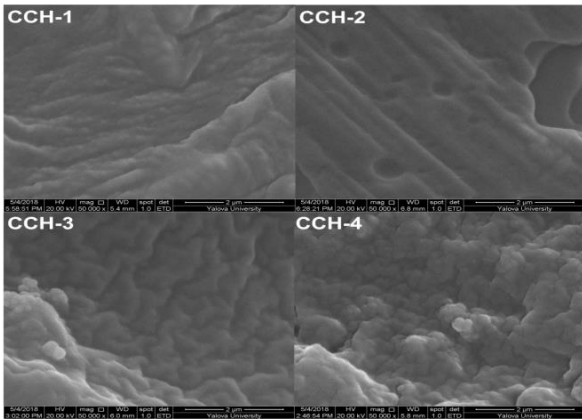
Figure 5. Representative SEM images of freeze-dried hydrogels (Scale bars: 2 μm).

Figure 6. Equilibrium swelling profiles of hydrogels in water.

Hydrogels were investigated in terms of swelling behaviors by recording the water uptake in pre-determined time intervals until a constant weight is attained. Hydrogels exhibited pronounced swelling degrees (~ 2000-1000 % with respect to initial gel amount) due to the presence of hydrophilic groups on polymer backbone and cyclodextrin crosslinker (Figure 6). Equilibrium swellings were attained in a relatively short period of time in pH-neutral hydration conditions. Although, the microstructures of obtained hydrogels possess non-porous morphology, it can be argued that the presence of hydrophilic PEG side chains have contributed to a relatively high degree of network hydration compared to the reported chitosan/cyclodextrin-based hydrogels (45-46). As expected, the swelling properties of hydrogels exhibit dependency on the feed of hydrophilic polymer and crosslinker ratios. Relatively higher swelling degrees were obtained by decreasing crosslinker ratio which can be attributed to the increase in free gel volumes of network.

The visco-elastic gel properties of water-swollen hydrogels were examined via dynamic frequency scan analysis. The measurements revealed that the storage and loss moduli of networks show relatively low oscillation frequency dependency indicating the homogenous network formation (Figure 7).(47) The storage modulus (G') and loss modulus (G") values were ranging from 10^2 to 10^5 Pa and for the all samples tested, the storage moduli were found to be over ten times higher than those of loss moduli, indicating covalently crosslinked elastic network structure. (48) Higher modulus values were obtained for hydrogels prepared by using higher amount of β-CD-based crosslinker which could be attributed to the increased network structure. Moreover, in high oscillation frequencies, the damping factor (defined as G"/G) decreases with decreasing crosslinker amount. This indicates that the elastic properties of the hydrogels show a relative increase by lowering the crosslinking density which might yield more conformational freedom to side chain PEG units. (49)
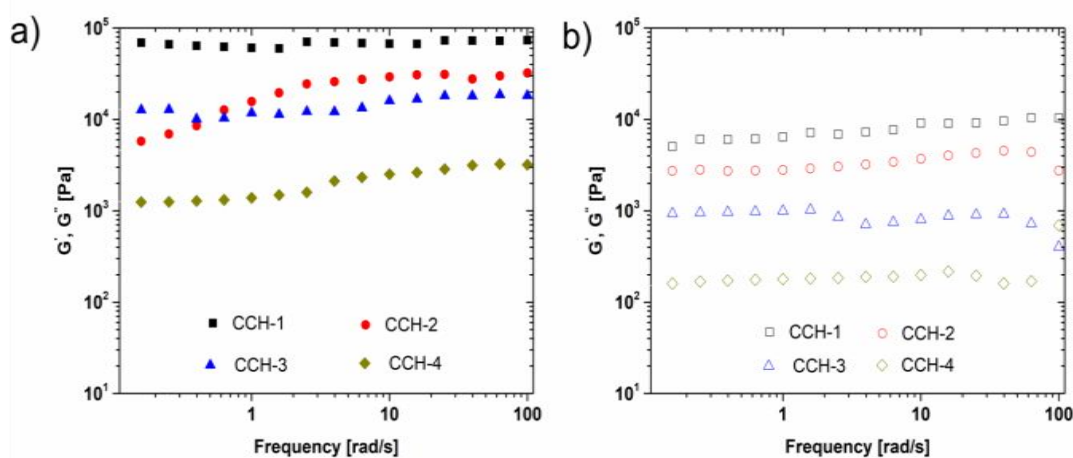
Figure 7. Dynamic frequency scan analysis of hydrogels: a) Storage and b) loss moduli of hydrogels.

Drug loading and release studies

The drug loading and release characteristics of hydrogels were examined using a model drug with low water solubility, diclofenac-Na, employed as a non-steroidal anti-inflammatory medication for treatment of several complaints and diseases. The drug was loaded to the hydrogel samples prepared as disks using solution absorption method. Pre-water swollen hydrogel disks were immersed in 0.5 wt.% soaking solution and the drug loading was monitored by UV-spectrophotometry until equilibrium was reached. The total drug amounts absorbed by the hydrogels, determined from the initial and final concentrations of soaking solutions were shown in Table 1. The loaded drug amounts were found to be affected by the β-CD-based crosslinker ratio. Highest drug loading was achieved with hydrogel CCH-1, containing the highest β-cyclodextrin ratio. In hydrogels, drugs are mainly diffused in aqueous phase or adsorbed to the polymeric backbones (50). In cyclodextrin-containing hydrogels, the ability of inclusion complexation between cyclodextrin and hydrophobic molecules provide another mean of drug loading. Since diclofenac-Na is able to form inclusion complexation with β-cyclodextrin (51), increased β-cyclodextrin ratio as going from CCH-4 to CCH-1 makes a notable contribution to drug loading.

The drug-loaded hydrogels were gently washed with distilled water before adding to the release medium. With regular time intervals, 5 mL release medium was replaced with a fresh solution and collected release solution was analyzed via UV spectrophotometer to monitor drug release. The release behavior of diclofenac-Na from hydrogels is shown in Figure 8. Initially, a burst release of the drug was observed for all hydrogels. This accelerated release is common in hydrogel based release systems and mainly attributed to the fast removal of free drug in aqueous phase and adsorbed drug on backbone of the hydrogel (52). The amount of burst release was dependent on the β-CD content in hydrogels as lowest burst release and highest sustained release was observed with hydrogel CCH-1 containing highest β-CD content. The slower release of hydrogels with higher β-CD content can be ascribed to the formation of inclusion complex of the drug with β-CD. As the relation between β-CD amounts that hydrogels bear and the drug loading capacities and sustained release profiles suggest, β-CD incorporation to hydrogel network maintains increased drug-carrier interactions while improving the versatility of fabricated biomaterials. Combining the efficient and easy fabrication with convenient attributes of hydrogel precursors, the demonstrated approach might find applications in design and synthesis of several hydrogel-based drug delivery systems.
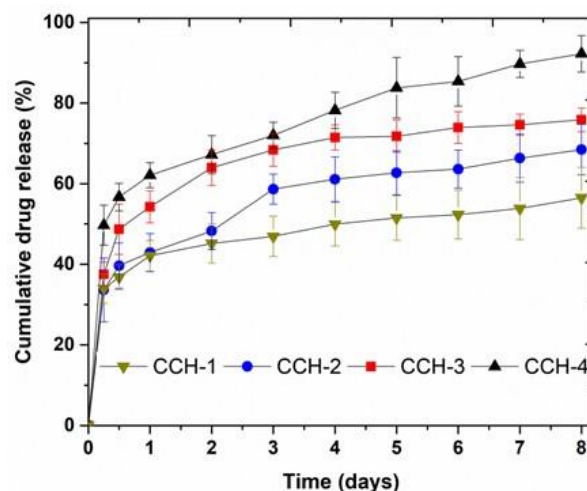
Figure 8. Cumulative release of diclofenac-Na from hydrogels.

CONCLUSION

Novel hydrogels employing PEG-modified chitosan as hydrophilic matrix and acrylated β-CD as crosslinker were synthesized using thiol-ene addition reaction. The method demonstrates the facile and efficient crosslinking process between complementary thiol and acrylate functional precursors which can be used as *in situ* injectable gel forming systems. It was shown that physical properties can be tuned by changing feed ratio between the hydrophilic polymer and crosslinker. A model drug was loaded to fabricated hydrogels and controlled release of the drug was monitored. Lower initial burst releases and more prolonged release profiles were obtained in case of increasing β-CD content in the hydrogels. The hydrogel synthesis methodology depicted here is believed to find potential application in design of macro and micro-scale controlled drug release systems especially in injectable formulations.

ACKNOWLEDGEMENTS

REFERENCES

1. Yang JA, Yeom J, Hwang BW, Hoffman AS, Hahn SK. In situ-forming injectable hydrogels for regenerative medicine. Progress in Polymer Science. 2014; 39(12): 1973-86.

2. Drury JL, Mooney DJ. Hydrogels for tissue engineering: scaffold design variables and applications. Biomaterials. 2003; 24(24): 4337-51.

3. Hunt JA, Chen R, Van Veen T, Bryan N. Hydrogels for tissue engineering and regenerative medicine. Journal of Materials Chemistry B. 2014; 2: 5319-38.

4. Vermonden T, Censi R, Hennink WE. Hydrogels for protein delivery. Chemical Reviews. 2012; 112 (5): 2853–88.

5. Yu F, Cao X, Li Y, Zeng L, Yuanab B, Chen X. An injectable hyaluronic acid/PEG hydrogel for cartilage tissue engineering formed by integrating enzymatic crosslinking and Diels–Alder "click chemistry". Polymer Chemistry. 2014; 5: 1082-90.

6. Takahashi A, Suzuki Y, Suhara T, Omichi K, Shimizu A, Hasegawa K, Kokudo N, Ohta S, Ito T. In situ cross-linkable hydrogel of hyaluronan produced via copper-free click chemistry. Biomacromolecules. 2013; 14(10): 3581-8.

7. Ahadian S, Sadeghian RB, Salehi S, Ostrovidov S, Bae H, Ramalingam M, Khademhosseini A. Bioconjugated hydrogels for tissue engineering and regenerative medicine. Bioconjugate Chemistry. 2015; 26(10): 1984-01.

8. Sivashanmugam A, Arun Kumar R, Vishnu Priya M, Nair S V., Jayakumar R. An overview of injectable polymeric hydrogels for tissue engineering. European Polymer Journal. 2015; 72: 543-65.

9. Yan S, Wang T, Feng L, Zhu J, Zhang K, Chen X, Cui L, Yin J. Injectable in situ self-cross-linking hydrogels based on poly(l-glutamic acid) and alginate for cartilage tissue engineering. Biomacromolecules. 2014; 15(12): 4495-08.

10. Xiao ZS, Ahmad S, Liu Y, Prestwich GD. Synthesis and evaluation of injectable, in situ crosslinkable synthetic extracellular matrices for tissue engineering. Journal of Biomedical Materials Research Part A. 2006; 79(4): 902-12.

11. Cai S, Liu Y, Zheng Shu X, Prestwich GD. Injectable glycosaminoglycan hydrogels for controlled release of human basic fibroblast growth factor. Biomaterials. 2005; 26(30): 6054-67.

12. Tiller JC. Increasing the local concentration of drugs by hydrogel formation. Angewandte Chemie-International Edition. 2003; 42(27): 3072-75.

13. Paul A, Hasan A, Kindi H Al, Gaharwar AK, Rao VTS, Nikkhah M, Shin SR, Krafft D, Dokmeci MR, Shum-Tim D, Khademhosseini A. Injectable graphene oxide/hydrogel-based angiogenic gene delivery system for vasculogenesis and cardiac repair. ACS Nano. 2014; 8(8): 8050-62.

14. Seliktar D. Designing cell-compatible hydrogels for biomedical applications. Science. 2012; 336(6085): 1124-8.

15. Dash M, Chiellini F, Ottenbrite RM, Chiellini E. Chitosan- A versatile semi-synthetic polymer in biomedical applications. Progress in Polymer Science. 2011; 36(8): 981-14.

16. Rinaudo M. Chitin and chitosan: Properties and applications. Progress in Polymer Science. 2006; 31(7): 603-32.

17. Bhattarai N, Gunn J, Zhang M. Chitosan-based hydrogels for controlled, localized drug delivery. Advanced Drug Delivery Reviews. 2010; 62(1): 83-99.

18. Ta HT, Dass CR, Dunstan DE. Injectable chitosan hydrogels for localised cancer therapy. Journal of Controlled Release. 2008;126(3): 205-16.

19. Bhattarai N, Ramay HR, Gunn J, Matsen FA, Zhang M. PEG-grafted chitosan as an injectable thermosensitive hydrogel for sustained protein release. Journal of Controlled Release. 2005; 103(3): 609-24.

20. Jin R, Moreira Teixeira LS, Dijkstra PJ, Karperien M, van Blitterswijk CA, Zhong ZY, Feijen J. Injectable chitosan-based hydrogels for cartilage tissue engineering. Biomaterials. 2009; 30(13): 2544-51.

21. Sashiwa H, Aiba SI. Chemically modified chitin and chitosan as biomaterials. Progress in Polymer Science. 2004; 29(9): 887-08.

22. Casettari L, Vllasaliu D, Castagnino E, Stolnik S, Howdle S, Illum L. PEGylated chitosan derivatives: Synthesis, characterizations and pharmaceutical applications. Progress in Polymer Science. 2012; 37(5): 659-85.

23. Aydin D, Arslan M, Sanyal A, Sanyal R. Hooked on cryogels: A carbamate linker based depot for slow drug release. Bioconjugate Chemistry. 2017; 28(5): 1443-51.

24. Van De Manakker F, Vermonden T, Van Nostrum CF, Hennink WE. Cyclodextrin-based polymeric materials: Synthesis, properties, and pharmaceutical/biomedical applications. Biomacromolecules. 2009; 10(12): 3157-75.

25. Li J, Loh XJ. Cyclodextrin-based supramolecular architectures: Syntheses, structures, and applications for drug and gene delivery. Advanced Drug Delivery Reviews. 2008; 60(9): 1000-17.

26. Arslan M, Gevrek TN, Sanyal A, Sanyal R. Cyclodextrin mediated polymer coupling via thiol-maleimide conjugation: Facile access to

functionalizable hydrogels. RSC Advances. 2014; 4: 57834-41.

27. Arslan M, Aydin D, Degirmenci A, Sanyal A, Sanyal R. Embedding well-defined responsive hydrogels with nanocontainers: Tunable materials from telechelic polymers and cyclodextrins. ACS Omega. 2017; 2(10): 6658-67.

28. Arslan M, Gevrek TN, Sanyal R, Sanyal A. Fabrication of poly(ethylene glycol)-based cyclodextrin containing hydrogels via thiol-ene click reaction. European Polymer Journal. 2015; 62: 426-34.

29. Arslan M, Sanyal R, Sanyal A. Cyclodextrin-containing hydrogel networks. In: Mishra M, editor. Encyclopedia of Biomedical Polymers and Polymeric Biomaterials. Taylor and Francis: New York; 2015. p. 2243-58. Available from: https://www.taylorfrancis.com/books/e/9781466 501799/chapters/10.1081%2FE-EBPP-120050543

30. Gevrek, TN, Arslan, M, Sanyal, A. Design and synthesis of maleimide group containing polymeric materials via the Diels-Alder/Retro Diels-Alder strategy. In: Theato P and Klok H, editors. Functional Polymers by Post-Polymerization Modification. Wiley-VCH Verlag GmbH & Co.; 2013. p. 123-55. Available from: https://onlinelibrary.wiley.com/doi/abs/10.1002/ 9783527655427.ch5

31. Arslan, M, Gevrek, TN, Sanyal, A. Maleimide containing thiol-reactive polymers: Synthesis and functionalization. In. Shunmugam R, editor. Functional Polymers. Apple Academic Press: New York; 2017. Ch. 7. Available from: https://www.taylorfrancis.com/books/e/9781771 882972/chapters/10.1201%2F9781315366524-17

32. Arslan M, Tasdelen MA. Polymer nanocomposites via click chemistry reactions. Polymers. 2017; 9(10): 499.

33. Arslan M, Gok O, Sanyal R, Sanyal A. Clickable poly(ethylene glycol)-based copolymers using azide-alkyne click cycloaddition-mediated step-growth polymerization. Macromolecular Chemistry and Physics. 2014; 215(22): 2237-47.

34. Oz Y, Arslan M, Gevrek TN, Sanyal R, Sanyal A. Modular fabrication of polymer brush coated magnetic nanoparticles: Engineering the interface for targeted cellular imaging. ACS Applied Materials ans Interfaces. 2016; 8(30): 19813-26.

35. Arslan M, Gevrek TN, Lyskawa J, Szunerits S, Boukherroub R, Sanyal R, Woisel P, Sanyal A. Bioinspired anchorable thiol-reactive polymers: Synthesis and applications toward surface functionalization of magnetic nanoparticles. Macromolecules. 2014; 47(15): 5124-34.

36. Yilmaz II, Arslan M, Sanyal A. Design and synthesis of novel "orthogonally" functionalizable maleimide-based styrenic copolymers. Macromolecular Rapid Communications. 2012; 33(9): 856-62.

37. Hoyle CE, Bowman CN. Thiol-ene click chemistry. Angewandte Chemie-International Edition. 2010; 49(9): 1540-73.

38. Kharkar PM, Rehmann MS, Skeens KM, Maverakis E, Kloxin AM. Thiol-ene click hydrogels for therapeutic delivery. ACS Biomaterials Science and Engineering. 2016; 2(2): 165-79.

39. Wang FP, Li, GF, Zhou QQ, Yang CX, Wang QZ. Removal of metal ions from aqueous solution with cyclodextrin-based hydrogels. 2016; 6(5): 394-02.

40. Nishimura SI, Kohgo O, Kurita K, Kuzuhara H. Chemospecific manipulations of a rigid polysaccharide: Syntheses of novel chitosan derivatives with excellent solubility in common organic solvents by regioselective chemical modifications. Macromolecules. 1991; 24(17): 4745-48.

41. Bentzen EL, Tomlinson ID, Mason J, Gresch P, Warnement MR, Wright D, Sanders-Bush E, Blakely R, Rosenthal SJ. Surface modification to reduce nonspecific binding of quantum dots in live cell assays. Bioconjugate Chemistry. 2005; 16(6): 1488-94.

42. Sharpe JC, Mitchell JS, Lin L, Sedoglavich N, Blaikie RJ. Gold nanohole array substrates as immunobiosensors. Analiytcal Chemistry. 2008; 80(6): 2244–49.

43. Ellman GL. Tissue sulfhydryl groups. Archives of Biochemistry and Biophysics. 1959; 82(1): 70-77.

44. Riddles PW, Blakeley RL, Zerner B. Reassessment of Ellman's reagent. Methods in Enzymology. 1983; 91: 49-60.

45. Kono H, Teshirogi T. Cyclodextrin-grafted chitosan hydrogels for controlled drug delivery. Int. J. Biol. Macromol. 72, 299-308 (2015).

46. Dong ZQ, Cao Y, Yuan QJ, Wang YF, Li JH, Li BJ, Zhang S. Redox- and glucose-induced shape-memory polymers. Macromol. Rapid Commun. 34, 867–872 (2013).

47. Siemoneit U, Schmitt C, Alvarez-Lorenzo C, Luzardo A, Otero-Espinar F, Concheiro A, Blanco-Méndez J. Acrylic/cyclodextrin hydrogels with enhanced drug loading and sustained

release capability. International Journal of Pharmaceutics. 2006; 312(1-2): 66-74.

48. Li R, Zhang X, Zhang Q, Liu H, Rong J, Tu M, Zeng R, Zhao J. b-cyclodextrin-conjugated hyaluronan hydrogel as a potential drug sustained delivery carrier for wound healing. Inc. J. Appl. Polym. Sci. 133, 43072 (2016).

49. Jin R, Moreira Teixeira LS, Dijkstra PJ, Karperien M, van Blitterswijk CA, Zhong ZY, vd. Injectable chitosan-based hydrogels for cartilage tissue engineering. Biomaterials. May 2009;30(13):2544-51.

50. Andrade-Vivero P, Fernandez-Gabriel E, Alvarez-Lorenzo C, Concheiro A. Improving the loading and release of NSAIDs from pHEMA hydrogels by copolymerization with functionalized monomers. Journal of Pharmaceutical Sciences. 2007; 96(4): 802-13.

51. Das S, Subuddhi U. Studies on the complexation of diclofenac sodium with β-cyclodextrin: Influence of method of preparation. Journal of Molecular Structure. 2015; 1099: 482-89.

52. Xu J, Li X, Sun F. Cyclodextrin-containing hydrogels for contact lenses as a platform for drug incorporation and release. Acta Biomaterialia. 2010; 6(2): 486-93.

In silico Molecular Docking and Pharmacokinetic Study of Selected Phytochemicals With Estrogen and Progesterone Receptors as Anticancer Agent for Breast Cancer

Sagir Yusuf Ismail[1]* ✉ iD **Adamu Uzairu[2]** ✉ **Balarabe Sagagi[1]** ✉ **Muhd Sabiu Suleiman[3]** ✉

[1]Department of Chemistry, Kano University of Science and Technology Wudil, Kano State, Nigeria.
[2]Department of Chemistry, Ahmadu Bello University Zaria, Kaduna State, Nigeria.
[4]Department of Agriculture, Bayero University Kano, Kano State, Nigeria.

Abstract: Molecular docking and pharmacokinetic study were performed on 20 selected phytochemicals with estrogen and progesterone receptors and it was found that all the phytochemicals has strong binding energy and high number of interactions when docked with estrogen and progesterone receptors, Gabridin has the highest binding energy of -10.3 kcal/mol and 12 numbers of various interactions when docked with estrogen receptor, while Quercetin has the highest binding energy of -9.6 kcal/mol and about 14 numbers of various interactions when docked with progesterone receptor. Pharmacokinetic study carried out revealed that all the leading compounds (Gabridin and Quercetin) are in agreement with Lipinski rule of five without violating any of the conditions of bioavailability, this has shown that they will be readily bioavailable. With the high binding affinity of these compounds and good pharmacokinetic parameters, most of the phytochemicals used in this study can be used in designing a highly effective and readily bioavailable anti breast cancer drug.

INTRODUCTION

Plants and their remedies have been used as herbal sources and other traditional beliefs to treat different kind of diseases among which cancer it belongs to, such plants and remedies include phytochemicals, bitter lemons, shikonin and others (1).

The word phytochemical is derived from Greek word "phyto" meaning plant, which constitutes the non-nutrient present in the plant diet (2). It has been used in the treatment and protection of chronic diseases

such as cancers, hypertension, heart disease, and other diseases (2). A phytochemical is one of the compounds with history of anticancer activity and it has been used in the treatment of cancer due to its availability, and of less toxic and safe nature (3).

There is strong evidence suggesting that taking food and beverages that are rich in phytochemicals will help in preventing many diseases, but there is need of more research on specific phytochemicals and their contribution in prevention of many form of diseases (4).

Presently, cancer is one of the main cause of death as a result of diseases in the world and without more advances and screening in developing more drugs for the treatment of this ailment, its suggested to continue to be the leading cause of death due to diseases in the coming years (5). Breast cancer is the most fast growing cancer in women, apart from lung cancer, breast cancer cause more death of women than all the other type of cancers (6). The survival rate of the breast cancer has increased due to advances in screening and treatment, In United States (US), there are about 3.1 million survivors of breast cancer. 1 in every 37 or 3% of women are at the risk of dying from breast cancer (6). Awareness of the sign and symptoms and more advances in screening of drugs for the treatment of breast cancer are important ways of reducing the risk associated with the disease (6).

Presence of fluid through the nipple, change in the thickness of breast skin, formation of lumps, and enlargement are some of the sign and symptoms of breast cancer (7), when the disease advances there may be swollen lymph nodes, feeling pain especially in the bone and decrease in the breathing rate (8). Chemotherapy is commonly used in order to inhibit and stop the growth of the cancerous cells and the main advantage of chemotherapy is its ability to stop the growth of cancer cells that has spread to other places unlike surgery and radiation therapies that treat cancer cells that are limited within specified area (5).

This study aims at establishing the binding affinity, interactions, binding distances, and the important amino acid residues that participated in the binding between the selected phytochemicals with both estrogen and progesterone receptors as well as the pharmacokinetic parameters (bioavailability) of these phytochemicals. The study also aims at establishing weather these phytochemicals can be used in designing a therapeutic lead molecule for the treatment of breast cancer targeting not only estrogen but progesterone receptors. Both estrogen and progesterone receptors interact with breast cells (cancerous and normal), but most of the common drugs for the treatment of breast cancer are design and developed to target estrogen receptor only.

MATERIALS AND METHODS

Tools and Materials Used
The three-dimensional structure of both estrogen and progesterone receptor was obtained from the protein data bank (PDB ID

2IOK AND Ie3K) respectively, while the structure of all the selected phytochemicals in this study were retrieved from pubchem compound database and from literature (reference number 9). The tools used in this study include HP beatsaudio computer system (intel corei5, 12 GB RAM, windows 8.1 operating system), pubchem data base, protein data bank, chemdraw 3D pro 12.01v, spartan 14v1.1.4, pyrex, autodock tools in autodock 4.3 program, vina wizard, and discovery studio.

Methodology
Protein Preparation: The crystal structure of both estrogen and progesterone receptors was retrieved from protein data bank PDB ID (2I0K and Ie3K) respectively, the complexes bound to the receptor was removed using discovery studio, and the non-essential water molecule was removed and polar hydrogen was added and the already prepared receptor was saved in PDB format.

Ligand Preparation: Twenty phytochemicals were selected from pubchem and from literature (Reference no. 9) based on history of their interaction with estrogen and progesterone that is phytoestrogen and phytoprogesterone, their 3D structure was drawn using chemdraw 3D pro12.01v and their energy was optimized using spartan 14v1.1.4 and the optimized molecule was saved in PDB format.

Molecular Docking Simulation
Two goals involved in docking study are to determine the most likely binding mode of the lead compound and to measure its binding affinity for the target protein (10). Estimation of ligand protein affinity is one of the major and important step in drug discovery, only the potential molecules that demonstrate desirable binding affinity for the target receptor are taken up for further analysis. The molecules that strongly bind to the receptor will inhibit its function and thus can act as a drug (10). All the twenty phytochemicals are docked using pyrex software by selecting autodock as the docking engine to find the reasonable binding geometry and discover the protein ligand connections.

Interaction Studies
To study the mode of binding, docked conformation with minimum binding energy was selected, discovery studio was used to visualize and study the interaction between the different ligands and the receptor and all the various amino acid residues that participated in binding with the various distances.

RESULT AND DISCUSSION

Molecular docking studies was performed with autodock tools, all the twenty selected phytochemicals were docked with estrogen receptor PDB ID (2IOK) and progesterone receptor PDB ID (Ie3K), and it was found that all the phytochemicals have higher binding affinity to the receptors. The highest negative binding energy was selected and interaction study was performed using discovery studio, various amino acid interactions and the distance was ascertained.

After docking of the selected phytochemicals with estrogen receptor, it was found that of all the twenty phytochemicals, Gabridin has the highest binding energy of -10.3 kcal/mol and 12 numbers of various interactions, followed by Genestein and 4-methoxycoumesterol with binding energy of -9.8 kcal/mol and -9.7 kcal/mol and also 10 and 13 numbers of various interactions respectively, while Crocetin with -6.8kcal/mol has the least binding energy. From the result of interaction between the phytochemicals and estrogen receptor, Gabridin with highest binding energy and good number of interactions can be a lead compound in designing a therapeutic lead molecule for the treatment of breast cancer targeting estrogen receptor, while the amino acids Leu346, Ala350, Phe404, Leu387, Leu384, Leu525, and Glu353 are the most important residue for potential drug targeting estrogen receptor.

From the result of interaction between the phytochemicals and progesterone receptor, it was found that Quercetin has the highest binding energy of -9.6 kcal/mol and 14 numbers of various interactions, followed by 4-methoxycoumesterol and Diosgenin with -9.2 kcal/mol each and 10 and 11 numbers of various interactions respectively, while Indole-3-carbinol with -6.2 kcal/mol has the least binding energy. Quercetin with highest binding energy and good number of interactions can be a lead compound in designing a therapeutic lead molecule for the

treatment of breast cancer targeting progesterone receptor, while the amino acids Arg766, Trp732, Pro696, Phe788, Glu695, Ile699, and Lys822 are the most important residues for the potential drug targeting progesterone receptor.

While only 5 of the 20 selected phytochemicals has additional type of interactions apart from hydrogen and hydrophobic when docked with estrogen receptor, 15 out of the 20 phytochemicals has additional type of interactions apart from hydrogen and hydrophobic interactions when docked with progesterone receptor. This shows that majority of the phytochemicals has additional type of interactions when docked with progesterone receptors.

Developing a potent drug of breast cancer targeting progesterone receptor will lead to a breakthrough in the treatment of breast cancer, even though both estrogen and progesterone receptors interact with breast cancer cells, most of the common drugs for the treatment of breast cancer are developed to target estrogen receptor only. About 80% of breast cancer cells are estrogen receptor-positive, out of this 80%, 65% are also progesterone receptor-positive, while 13% of the total breast cancer cells are estrogen receptor-positive and progesterone receptor-negative and about 2% are estrogen receptor-negative and progesterone receptor positive (11).

There is strong evidence suggesting that progesterone receptor plays an important role in the growth of breast cancer and that they might be potentially used in improving the success of endocrine treatment (12).

This study may be the subject of experimental validation and clinical trials to establish these phytochemicals as more potent drug for the treatment of breast cancer.

RESEARCH ARTICLE

Table 2: Docking result of the selected phytochemicals with estrogen receptor.

Compounds	Hydrogen bond	Hydrophobic interactions	Other interactions	Binding energy	Total number of interactions
1)4-methoxy coumesterol	OH-Glu353(2.33), O-Gly521(3.35)	C-Leu387(3.80) C-Phe404(5.10) C- Phe404(5.49) C-Leu387(4.95) C-Ala350(5.33) C-Ala350(4.86) C-Leu391(5.23) C-Leu346(4.83) C-Leu384(5.01) C-Leu525(5.43) C-Ile424(5.30)	None	-9.7	13
2)Apigenin	OH-Glu353(2.57) OH-Arg394(1.35) OH-Thr347(1.96)	C-Leu346(3.98) C-Leu387(4.92) C-Leu346(4.43) C-Phe404(5.01) C-Ala350(5.07) C-Leu525(4.92) C-Ala350(5.35) C-Leu391(5.02) C-Ala350(5.25)	None	-9.1	13
3)Biochanin	OH-Arg394(3.98)	C-Phe404(5.55) C-Leu387(4.90) C-Met388(5.29) C-Phe404(5.27) C-Leu391(5.09) C-Leu387(4.20) C-Ala350(5.04) C-Ile424(4.80) C-Ile525(5.48)	None	-9.1	10
4) Coumesterol	O-Arg394(2.44) OH-Glu353(2.33)	C-Phe404(4.94) C-Phe404(5.42) C-Leu391(4.98) C-Leu387(5.50) C-Ala350(5.37) C-Ala350(5.16) C-Leu346(4.71) C-Leu346(4.80) C-Leu346(5.11) C-Leu525(4.68) C-Leu384(5.47) C-Leu387(4.34)	None	-9.6	14

5) Crocetin	OH-Glu1353(2.10) O-Arg1394(2.72) OH-Glu1423(2.00) O-Gly1420(3.46) O-His1524(3.74)	C-Leu1525(4.34) C-Leu1384(4.79) C-Leu1525(4.60)	None	-8.1	8
6) Curcumin	OH-Leu387(2.71)	C-Leu387(3.87) C-Leu391(5.34) C-Leu525(5.13) C-Phe404(5.01) C-Ala350(4.71) C-Trp383(4.39)	None	-7.3	7
7) Daidzein	O-His524(3.64) OH-Gly525(4.39)	C-Leu387(3.92) C-Leu387(5.33) C-Phe404(5.70) C-Phe404(5.05) C-Leu384(5.40) C-Leu384(5.42) C-Ala350(5.12) C-Leu391(5.09) C-Leu525(5.39) C-Met388(5.12) C-Ile424(4.73)	None	-9.0	13
8)Diosgenin	None	C-Ile1326(4.42) C-Ile1326(5.26) C-Ile1326(4.70) C-Ile1326(4.41) C-Arg1394(5.02) C-Arg1394(3.87) C-Arg1394(4.35) C-Pro1406(5.03) C-Pro1324(4.18) C-Leu1403(5.30) C-Trp1393(5.42)	None	-9.6	11
9)Formononetin	O-Arg1394(2.37) OH-Leu1387(2.78)	C-Phe1404(5.00) C-Leu1384(5.41) C-Leu1391(4.83) C-Leu1387(4.44) C-Met1388(4.96) C-Met1421(5.22) C-Ile1424(4.42)	None	-8.9	9
10)Gabridin	None	C-Phe1404(5.00) C-Ile1424(5.27) C-Ile1424(4.57) C-Ile1424(3.81) C-Leu1391(4.51) C-Leu1387(4.42) C-Leu1384(5.16) C-Leu1384(5.15) C-Leu1525(4.99) C-Met1421(3.78) C-Met1421(4.12) C-His1524(5.08)	None	-10.3	12
11)Genestein	O-Glu353(1.65)	C-Leu525(5.48) C-Leu387(5.31) C-Leu387(4.21) C-Leu391(5.09) C-Ile425(4.78) C-Ala350(5.05) C-Phe404(5.67) C-Phe404(4.90) C-Met388(5.28)	None	-9.8	10

12)Hesperetin	OH-Met1437(2.98) O-His476(2.88) O-His476(2.12) OH-Lys472(1.38)	C-Met1437(3.88) C-Met1437(3.94) C-Lys472(3.11) C-Leu469(5.02)	C-Met1437(3.41)	-7.8	9
13)Indole-3-cabinol	O-Arg1394(2.56) NH-Phe1404(2.69) NH-Leu1327(2.62) H-Leu1327(3.04) H-Leu1327(2.51)	C-Ile1326(3.84) C-Ile1326(5.48) C-Pro1406(5.25)	C-Arg1394(3.63) C-Arg1394(3.99)	-6.2	10
14)Kaempferol	O-Leu1327(2.33) OH-Pro1325(2.96)	C-Ile1326(3.76) C-Ile1326(4.80) C-Arg1394(4.31) C-Pro1324(3.84)	C-Arg1394(3.38) C-Glu1353(3.31)	-8.5	8
15)Lignan	None	C-Phe404(4.88) C-Leu346(4.80) C-Leu346(4.95) C-Leu346(5.19) C-Leu387(5.05) C-Leu525(4.60) C-Ala350(4.77) C-Met343(5.90)	None	-7.3	8
16)Luteolin	O-His524(3.48)	C-Phe404(4.86) C-Leu384(5.46) C-Met388(5.45) C-Leu384(5.45) C-Leu346(5.25) C-Leu387(4.69) C-Leu525(5.21) C-Ala350(4.50) C-Ile424(4.77)	None	-8.9	10
17)Lycopene	O-Phe461(2.60) O-Lys472(1.88) O-Ser463(1.71) OH-Thr460(2.21) O-Phe461(2.69)	C-Leu462(4.43) C-Ala1430(4.99) C-Leu462(5.29)	None	-7.1	8
18)Naringenin	OH-Met528(2.97)	C-Thr347(4.77) C-Leu525(3.86) C-Ala350(4.31) C-Leu525(5.29)	C-Met528(5.87) C-Met343(5.19)	-7.9	7
19)Quercetin	O-Leu1327(2.32) OH-Glu1353(2.12) O-Leu1327(2.19) OH-Glu1353(2.22)	C-Ile1326(3.80) C-Arg1394(4.79) C-Arg1394(4.23) C-Pro1324(3.86)	C-Arg1394(3.37) C-Glu1353(2.26)	-8.7	10

20) Resveratrol	OH-Glu1353(2.61) OH-Leu1346(1.84)	C-Phe1404(5.06) C-Ile1424(5.42) C-Leu1387(5.26) C-Met1388(5.46) C-Leu1346(5.37) C-Ala1350(4.62) C-Phe1404(4.70) C-Leu1384(5.28) C-Ile1424(4.85) C-Met1388(5.41)	None	-8.8	12

Table 2 above shows the various interactions (hydrogen, hydrophobic, and other interactions), binding energies and the total number of interactions of the studied phytochemicals when docked with estrogen receptor. It can be seen that while Gabridin has the highest binding energy of -10.3 kcal/mol and 12 numbers of various interactions, 4-methoxycoumesterol with binding energy of -9.7 kcal/mol and 13 number of interactions has the highest number of interactions. It can also be seen that five of the selected phytochemicals (Hesperatin, Indole-3-carbinol, Kaempferol, Naringenin and Quercetin) has additional type of interaction in addition to hydrogen and hydrophobic interactions.

Table 3. Docking result for selected phytochemicals with Progesterone receptor.

Compounds	Hydrogen bond	Hydrophobic interactions	Other interactions	Binding energy	Total number of interactions
1)4-methoxy coumesterol	OH-Gln(2.25)	C-Phe778(4.70) C-Phe778(5.21) C-Leu763(5.43) C-Leu718(4.38) C-Leu718(4.93) C-Met759(5.32 C-Leu718(4.93) C-Leu715(5.28)	C-Met759(4.24)	-9.2	10
2)Apigenin	OH-Leu758(2.69) O-Gln725(2.87)	C-Arg766(5.27) C-Pro696(4.86) C-Arg766(4.38)	C-Arg766(3.49) C-Arg766(4.46) C-Glu695(3.69)	-7.8	8
3)Biochanin	OH-Leu718(2.65) OH-Gln725(2.79) OH-Met759(2.54)	C-Phe778(4.92) C-Phe778(5.25) C-Leu763(5.48) C-Met759(4.89) C-Cys891(4.71)	C-Met759(4.09) C-Met756(5.45) C-Leu763(3.91)	-8.9	11
4)Coumesterol	O-Ile699(2.25) O-Gln725(3.48) O-Arg766(3.95)	C-Arg766(5.05) C-Gln725(5.21)	C-Arg766(3.31)	-9.0	6
5)Crocetin	O-Leu876(3.80)	C-Leu799(3.80)	None	-6.6	2
6) Curcumin	OH-Asn879(2.03) OH-Lys875(2.52) OH-Lys875(2.41)	C-Thr829(3.96) C-Val925(5.20) C-Ile920(4.98)	None	-7.5	8

	O-His931(3.33) O-Ser757(3.39)				
7) Daidzein	O-Gly762(3.31)	C-Pro696(5.07) C-Arg766(4.57)	C-Arg766(4.22) C-Glu695(3.44) C-Glu695(4.07)	-7.5	6
8)Diosgenin	None	C-Pro696(5.04) C-Pro696(3.90) C-Pro696(4.47) C-Val698(5.16) C-Met692(4.75) C-His776(4.95) C-Trp765(4.74) C-Lys769(4.56) C-Arg766(4.45) C-Arg766(4.71) C-Arg766(4.51)	None	-9.2	11
9)Formononetin	O-Gly762(3.36) O-Gln725(4.05)	C-Pro696(4.59) C-Arg766(5.12)	C-Glu695(3.35) C-lu695(4.14) C-Gln725(3.2	-7.9	7
10)Gabridin	O-His770(3.67)	C-Val729(4.69) C-Val729(4.85) C-Val698(4.93) C-Lys822(5.48) C-Pro696(4.90) C-Pro696(4.70) C-Leu758(4.51) C-Arg766(4.6	C-Glu695(3.49) C-Arg766(3.58)	-8.9	11
11)Genestein	OH-Met759(2.53) OH-Gln725(2.71) OH-Arg766(2.17)	C-Phe778(4.89) C-Phe778(5.24) C-Leu718(5.04) C-Met759(5.04	C-Cys891(5.14) C-Met759(4.08)	-8.8	9
12)Hesperatin	OH-Glu695(2.18) NH-Gln815(2.92)	C-Pro696(4.75)	C-Arg766(3.99)	-7.0	4
13)Indole-3-carbinol	NH-Gln725(2.61) OH-Leu763(3.10) OH-Leu758(3.27)	C-Ile699(5.19) C-Pro696(4.80)	None	-6.8	5
14)Kaempferol	OH-Glu695(1.91)	C-Trp732(5.80) C-Val698(5.46) C-Ile699(5.12) C-Leu758(5.37) C-Lys822(6.82) C-Ile699(3.20) C-Ile699(4.30)	C-Arg766(3.59) C-Arg766(4.01) C-Lys822(3.37)	-9.0	11
15)Lignan	OH-Lys822(2.38) OH-Arg766(2.31)	C-Ile699(4.46) C-Pro696(4.96) C-Phe818(5.55) C-Val729(3.30)	None	-7.8	6
16)Luteolin	OH-Gln725(2.22) OH-Ser728(3.37) OH-Gly762(3.18) OH-Gly762(1.67)	C-Arg766(3.51) C-Pro696(4.89) C-Pro696(4.34)	C-Arg766(3.59) C-Arg766(4.44) C-Glu695(3.66)	-8.2	10

17)Lycopene	OH-Gly762(3.20)	C-Pro696(4.64)	C-Glu695(4.10) C-Glu695(4.50)	-7.9	4
18)Naringenin	OH-Arg766(2.91) OH-Pro696(2.08) NH-Val698(3.46)	C-Pro696(4.42)	C-Glu695(4.29)	-8.2	5
19)Quercetin	OH-Phe778(2.66) OH-Glu695(1.95) O-Ile699(3.33)	C-Trp732(6.99) C-Pro696(5.44) C-Arg766(5.24) C-Val698(5.28) C-Ile699(5.09) C-Trp732(5.75) C-Lys822(5.21)	C-Arg766(3.94) C-Arg695(4.12) Arg695(4.37) C-Arg766(3.62)	-9.6	14
20)Resveratrol	OH-Phe778(3.08) OH-Glu695(2.17)	C-Leu758(5.32) C-Val729(5.37) C-Pro696(5.40) C-Pro696(5.16) C-Ile699(5.10) C-Trp732(5.56) C-Trp732(5.32) C-Lys822(5.09)	C-Arg766(4.29) C-Arg766(3.68) C-Lys822(3.93)	-9.1	13

Table 3 above shows the various interactions (hydrogen, hydrophobic, and other interactions), binding energies and the total number of interactions of the studied phytochemicals when docked with progesterone receptor. It can be seen that Quercetin with binding energy of -9.6 kcal/mol and 14 numbers of various interaction has highest of both binding energy and number of interactions. It can also be seen that only 5 of the 20 selected phytochemicals (Crocetin, Curcumin, Diosgenin, Indole-3-carbinol and Lignan) has only hydrogen and hydrophobic interactions while all the remaining 15 has other type of interactions in addition to hydrogen and hydrophobic intrecations.

Pharmacokinetic Study
The process of screening, design and development of a drug is a very huge and peculiar task that needs high investment in research. This is not only limited to the cost which may engulf hundreds of millions to billions of dollars but also a long period of time between 10 to 25 years in order for a drug to reach its final (clinical) phase (13). Apart from cost and time, it also need a lot of multidisciplinary human resource. In order to avoid waste of time and resources, modern technique that utilize cost and reduce the time and manpower needed during the development of drug are mostly employed recently this include QSAR, docking and pharmacokinetic studies (14).

Some of the drugs failed at the last stage of clinical trials after spending huge amount of money and time, in order to avoid this, pharmacokinetic study is mostly carried out at the initial stage of development in order to select promising compounds that will not fail at the last stage of the development. Absorption, distribution, metabolism and excretion are the four steps of pharmacokinetic phase of drug development (ADME), with inclusion of toxicological study more recently it is abbreviated as (ADMET) study (15, 16).

There is strong correlation between some chemical descriptors and the ADMET properties, such as oral absorption that depends on low molecular weight, PSA which is the determinant of fractional absorption, the penetration of the lipid membrane by passive diffusion requires the breaking down of hydrogen bond as such needs low number of hydrogen bond and the excretion of the residue of these compounds from the body depends on low molecular weight and log P(17)

Lipinski's Rule of five: This is the most important concept in drug discovery at the preclinical stage in the last decade (18). The rule was proposed by Chris Lipinski and his teammates in 1997 as a result of their attempt to have an insight as to what properties of molecules will reduce or hinder the absorption and permeability of molecules. This rule stated that if a compound violate 2 or more of the following conditions, the compound will be poorly absorbed or it will be impermeable:
Molecular weight < 500
Number of hydrogen bond donors ≤ 5
Number of hydrogen bond acceptors ≤ 10
Calculated Log p ≤ 5
Polar surface area (PSA) <140 $Å^2$

With the use of specific softwares, these criteria can be used in removing outlier compound very easily at initial stage of drug development. Some classes of drugs that act as substrate for intestinal transporters and intravenously administered drugs are exception to Lipinski's rule of five because they do not undergo absorption (19).

In this study, these parameters was calculated using ADMET descriptors in Discovery Studio 3.5 and the descriptors from Spartan software during the optimization process as shown in Tables 4 and 5.

Table 4. Compliance of selected phytochemicals docked with estrogen receptor to Lipinki's rule of five.

Phytochemicals	Molecular weight <500	H-bond donors ≤5	H-bond acceptors ≤10	LogP ≤5	PSA <140	Number of Lipinski's rule violation
4-methoxycoumesterol	282.25	2	2	-3.03	55.35	0
Apigenin	270.24	3	3	-2.83	72.94	0
Biochanin	284.27	1	1	-1.92	59.86	0
Coumesterol	282.25	2	2	-3.03	55.35	0
Crocetin	328.41	5	5	3.78	66.52	0
Curcumin	368.39	1	1	-1.26	76.29	0
Daidzein	254.24	2	2	-0.95	58.85	0
Diosgenin	414.63	0	0	5.17	32.99	1
Formononetin	268.27	2	2	-0.84	46.13	0
Gabridin	324.38	0	0	-1.26	49.53	0
Genestein	284.27	1	1	-1.92	59.86	0
Hesperatin	302.28	4	4	-3.12	79.08	0
Indole-3-carbinol	147.18	5	3	-0.74	32.36	0
Kaempferol	286.24	2	2	-3.46	88.14	0
Lignan	302.37	0	0	0.01	76.98	0
Luteolin	286.24	1	1	-3.46	90.62	0
Lycopene	536.89	5	5	11.11	15.02	2
Naringenin	272.26	1	1	-2.15	74.62	0
Quercetin	302.24	4	4	-4.54	105.68	0
Resveratrol	228.25	3	2	-0.62	58.94	0

Source: Lipinski CA (Reference no. 19).

From Table 4 shown above, it can be seen that the pharmacokinetic study of the selected phytochemicals when docked with estrogen receptor readily complied with Lipinski's rule of five or does not violate any of the rule of bioavailability with exception of Diosgenin which violates one rule having logP > 5.0 and Lycopene that violates two rules of molecular weight > 500 and logP > 5. Violation of only one rule will not hinder the bioavailability of the compound such as Diosgenin which can be readily bioavailable while Lycopene with violation of two rules, its bioavailability cannot be confirmed according to the rule.

Table 5. Compliance of selected phytochemicals docked with progesterone receptor to Lipinski's rule of five.

Phytochemicals	Molecular weight <500	H-bond donors ≤5	H-bond acceptors ≤10	LogP ≤5	PSA <140	Number of lipinski's rule violation
4-methoxycoumesterol	282.25	1	1	-3.03	55.35	0
Apigenin	270.24	2	2	-2.83	72.94	0
Biochanin	284.27	4	4	-1.92	59.86	0
Coumesterol	282.25	3	2	-3.03	55.35	0
Crocetin	328.41	1	1	3.78	66.52	0
Curcumin	368.39	5	5	-1.26	76.29	0
Daidzein	254.24	1	1	-0.95	58.85	0
Diosgenin	414.63	0	0	5.17	32.99	1
Formononetin	268.27	3	3	-0.84	46.13	0
Gabridin	324.38	1	1	-1.26	49.53	0
Genestein	284.27	3	3	-1.92	59.86	0
Hesperatin	302.28	2	2	-3.12	79.08	0
Indole-3-carbinol	147.18	1	1	-0.74	32.36	0
Kaempferol	286.24	1	1	-3.46	88.14	0
Lignan	302.37	2	2	0.01	76.98	0
Luteolin	286.24	4	4	-3.46	90.62	0
Lycopene	536.89	1	1	11.11	15.02	2
Naringenin	272.26	3	3	-2.15	74.62	0

Quercetin	302.24	3	2	-4.54	105.68	0
Resveratrol	228.25	2	2	-0.62	58.94	0

Source: Lipinski CA (Reference no. 19).

Also from Table 5 shown above, it can be seen that the pharmacokinetic study of the selected phytochemicals when docked with progesterone receptor readily complied with Lipinski's rule of five as it does not violate any of the rule of bioavailability with exception of Diosgenin which violate one rule having logP > 5.0 and Lycopene that violate two rules of molecular weight > 500 and logP > 5. Violation of only one rule will not hinder the bioavailability of the compound as such Diosgenin can be readily bioavailable while Lycopene with violation of two rules, its bioavailability cannot be confirmed from the Lipinski's rule.
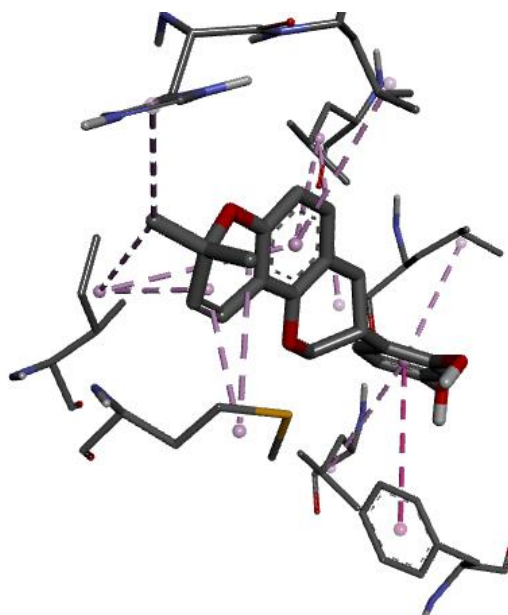

Figure 1. 3D ligand-receptor interaction between Gabridin and Estrogen receptor.
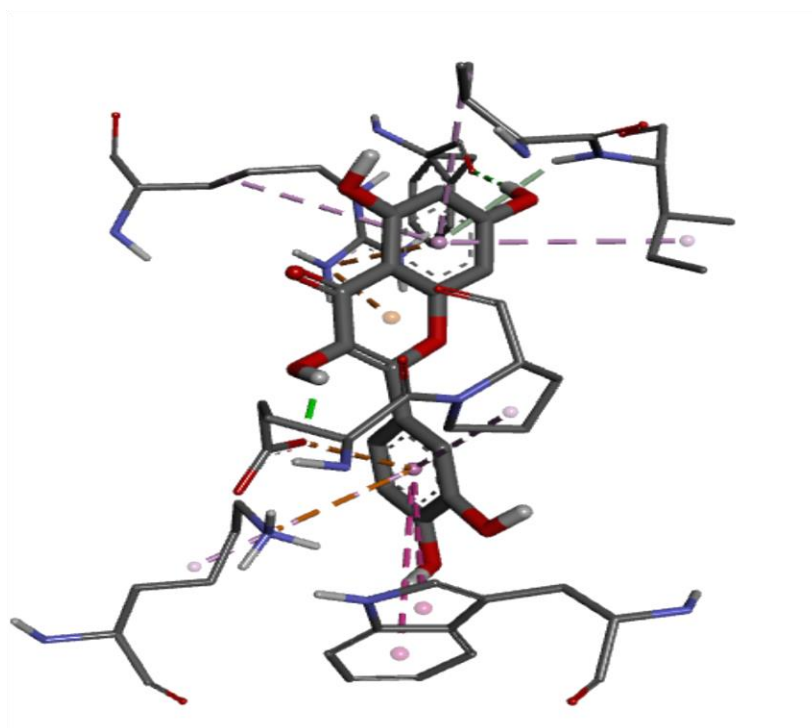

Figure 2. 3D Ligand-Receptor interaction between Quercetin and Progesterone receptor.
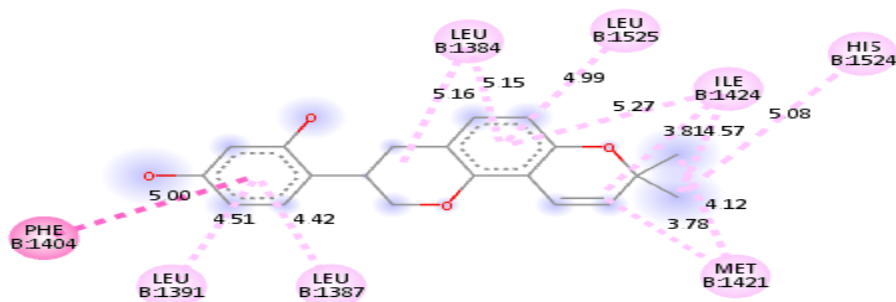
Figure 3. 2D Structure showing interaction between Gabridin and Estrogen receptor.
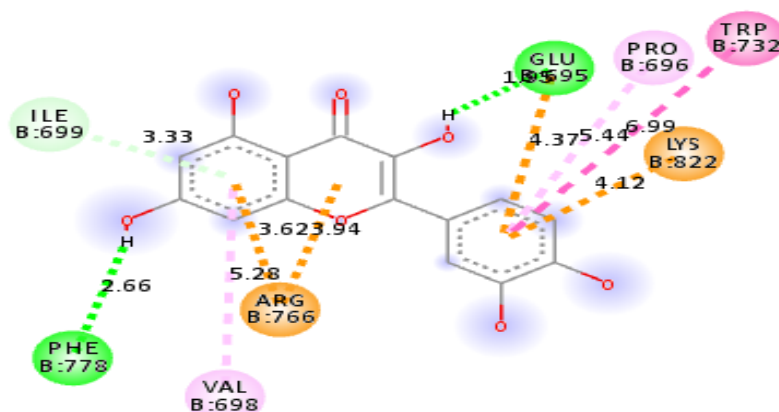

Figure 4. 2D Structure showing interaction between Quercetin and Progesterone receptor.

CONCLUSION

Breast cells, both carcinogenic and normal, have receptors for binding with both estrogen and progesterone to stimulate growth response, in the present study both estrogen and progesterone receptors was docked with selected phytochemicals, Gabridin with a binding energy of about -10.3 kcal/mol and 12 numbers of various interactions can be used as a potential lead compound for the design of novel drug for the treatment of breast cancer targeting estrogen receptor. Most of the drugs for the treatment of breast cancer are developed to target estrogen receptor only, in this study it was found that Quercetin with a binding energy of about -9.6 kcal/mol and about 14 numbers of various interactions when docked with progesterone receptor can be used as a potential lead compound for the design of a novel drug candidate for the treatment of breast cancer targeting progesterone receptor.

ACKNOWLEDGMENT

REFERENCES

1. Ogundele AV, Otun KO, Ajiboye A, Olanipekun BE, Ibrahim RB. Anti-Diabetic Efficacy and Phytochemical Screening of Methanolic Leaf Extract of Pawpaw (Carica papaya) Grown in North Central Nigeria. Journal of the Turkish Chemical Society, Section A: Chemistry. 2017;4(1):99–114.

2. Arendt EK, Zannini E. Cereal grains for the food and beverage industries. Elsevier; 2013.

3. Pratheeshkumar P, Son Y-O, Korangath P, Manu KA, Siveen KS. Phytochemicals in cancer prevention and therapy. BioMed research international. 2015;2015.

4. Webb D. Phytochemicals' Role in Good Health [Internet]. Today's Dietitian. 2013 [cited 2018 Dec 4]. Available from: https://www.todaysdietitian.com/newarchive s/090313p70.shtml

5. Arthur DE. Toxicity modelling of some active compounds against k562 cancer cell line using genetic algorithm-multiple linear regressions. Journal of the Turkish Chemical

Society, Section A: Chemistry. 2017;4(1):355–374.

6. Nordqvist C. Breast cancer: Symptoms, causes, and treatment [Internet]. What you need to know about breast cancer. [cited 2018 Dec 4]. Available from: https://www.medicalnewstoday.com/articles/37136.php

7. Anonymous. Breast Cancer Treatment (PDB (R)). National Cancer Institute; 2014.

8. Anonymous. Breast Disorders, Breast cancer. Merck; 2014.

9. Ferdous S, Mirza MU, Saeed U. Docking studies reveal phytochemicals as the long searched anticancer drugs for breast cancer. International Journal of Computer Applications. 2013;67(25):1–5.

10. Toepak E, Tambunan U. In silico design of fragment-based drug targeting host processing α-glucosidase i for dengue fever. In: IOP Conference Series: Materials Science and Engineering. IOP Publishing; 2017. p. 012017.

11. Lumachi F, Santeufemia DA, Basso SM. Current medical treatment of estrogen receptor-positive breast cancer. World journal of biological chemistry. 2015;6(3):231.

12. Giulianelli S, Molinolo A, Lanari C. Targeting progesterone receptors in breast cancer. In: Vitamins & Hormones. Elsevier; 2013. p. 161–184.

13. Davis AM, Riley RJ. Predictive ADMET studies, the challenges and the opportunities. Current opinion in chemical biology. 2004;8(4):378–386.

14. Tang Y, Zhu W, Chen K, Jiang H. New technologies in computer-aided drug design: toward target identification and new chemical entity discovery. Drug discovery today: technologies. 2006;3(3):307–313.

15. Kadam R, Roy N. Recent trends in drug-likeness prediction: A comprehensive review of In silico methods. Indian Journal of Pharmaceutical Sciences. 2007;69(5):609.

16. Geldenhuys WJ, Gaasch KE, Watson M, Allen DD, Van der Schyf CJ. Optimizing the use of open-source software applications in drug discovery. Drug Discovery Today. 2006;11(3–4):127–132.

17. Lipinski CA, Lombardo F, Dominy BW, Feeney PJ. Experimental and computational approaches to estimate solubility and permeability in drug discovery and development settings. Advanced drug delivery reviews. 1997;23(1–3):3–25.

18. Abad-Zapatero C. Analysis of the Content of SAR Databases. In: Ligand Efficiency Indices for Drug Discovery [Internet]. Elsevier; 2013 [cited 2018 Dec 4]. p. 67–79. Available from: https://linkinghub.elsevier.com/retrieve/pii/B9780124046351000050

19. Lipinski CA. Lead-and drug-like compounds: the rule-of-five revolution. Drug Discovery Today: Technologies. 2004;1(4):337–341.

RESEARCH ARTICLE

MODIFICATION OF NOVEL ISOXAZOLINES OF FULVENE DERIVATIVES WITH 1,3-DIPOLAR CYCLOADDITION REACTION

Omer T. Gunkara ✉ iD

Department of Chemistry, Faculty of Science and Arts, Yildiz Technical University, Davutpasa Campus, Istanbul, Turkey.

Abstract: In this work, 1,3-Dipolar cycloaddition reactions were studied to synthesize fulvene derivatives containing isoxazoline groups in good yields. 1,3-Dipolar cycloaddition reactions are among the most useful strategies for the preparation of organic compounds. All newly synthesized fulvene compounds were structurally characterized by FTIR, 1H, 13C NMR and GC/MS analyses.

INTRODUCTION

The 1,3-dipolar cycloaddition reaction is among the most outstanding method in organic chemistry field (1-3). It involves several dipoles and alkenes to prepare heterocycles in one step (4). The common application of 1,3-dipolar reactions in organic synthesis was first established by the systematic investigations by Huisgen (5). At the same time, the new notion of conservation of orbital symmetry, investigated by Woodward and Hoffmann, appeared in the literature (6, 7). Woodward and Hoffmann's paper was a cornerstone for the understanding of the mechanism of decided 1,3-dipolar cycloaddition chemistry. On the basis of the concept their work have further contributed to our comprehension and ability to foresee the reactivity and regioselectivity of 1,3-dipolar cycloaddition reactions (8-10).

Since their discovery in 1900, fulvenes and their analogues have collected considerable attention from scientists and industry because of their unusual features in the fields of organic chemistry, medicinal chemistry, and materials science (11-20). Fulvenes have found common use as building blocks in the preparation of natural products such as hinesol, capnellene, silphinene, hirsutene and viburtinal. They are traditionally prepared by the condensation reaction of cyclopentadienes with aldehyde or ketones, a preparation procedure which is typically limited by the availability of the cyclopentadienes, obtained from multistep reactions in which regio-selectivity and substituted group tolerance are often main difficulties.

Cycloadditions of fulvenes (e.g., [4+3], [2+2], [4+2], [2+4], [6+4], [6+2], [6+3] (21-23)) provide multiple and powerful procedures to

multifarious heterocyclic systems and natural products.

In our times, cancer has increasingly become the first reason of death over the world and seriously affecting the health of humans for a long time. All efforts have been made to find some drugs against cancer cell in the last decade as a result of research in molecular biology leading to the development of anticancer drugs capable of targeting the cancer cells with minimum side effects. Natural products have noticeably promoted to the development of a great number of potent anticancer agents.

Nearly 50% of all anticancer drugs verified internationally are either natural products or natural product analogues and were prepared on the basis of the knowledge acquired from small or macromolecules existing in nature (24).

In the last decade, several azole analogues have attracted huge attention in the field of anticancer drug investigation (25, 26). Among them, isoxazoline derivatives are an important class of five membered heterocyclic rings that exhibited promising biological activities. The common chemical formula of isoxazoline ring is shown in Figure 1.
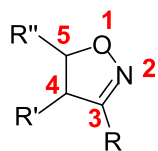
Figure 1: Chemical structure of isoxazoline.

There is too many biologically active isoxazoline derivative examples in the literature. For example, 3,5-diaryl-isoxazoline-attached 2,3-dihydroquinazolinone hybrid (27) 1 and

arylisoxazoline containing anthranilic diamide derivatives 2 (28), (Figure 2) are natural products which have got anticancer agent potential.
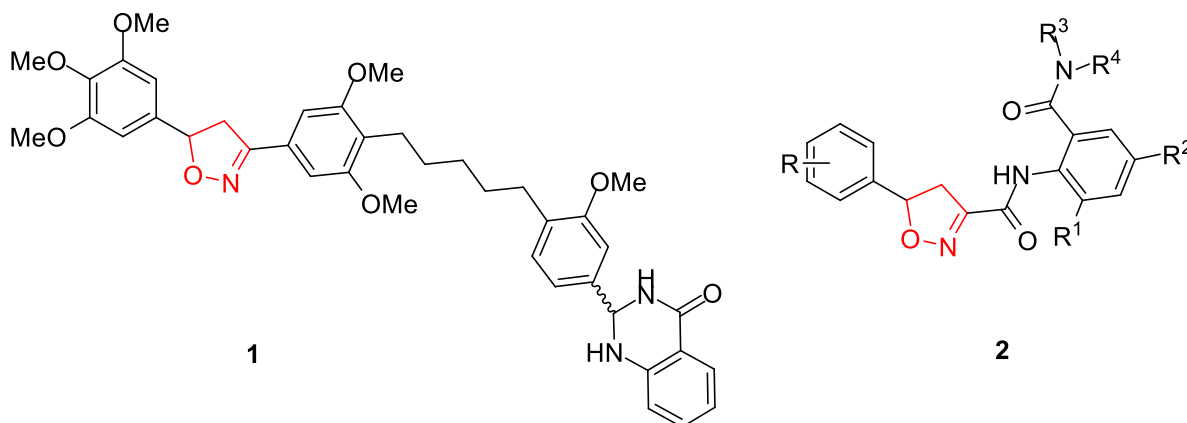
Figure 2: Chemical structures of 2,3-dihydroquinazolinone hybrid 1 and anthranilic diamide derivatives 2.

And also the other example of isoxazoline derivative is (+)-subereamolline A 3. It shows inhibition to the migration and invasion of

metastatic human breast cancer cells at the minimum dosage level (29) (Figure 3).

3

Figure 3: Chemical structures of (+)-subereamolline A.

Dibenzo[b,f]azepine-tethered isoxazoline analogues 4 (30) that show anticancer activity with an improved pharmacokinetics profile (Figure 4).

4

Figure 4: Chemical structures of dibenzo[b,f]azepinetethered isoxazoline analogues.

Because of these reasons, the preparation of isoxazoline heterocycles continues to attract the considerable attention of synthetic organic and medicinal scientists. Viewing the importance of natural products as well as isoxazoline containing pharmacop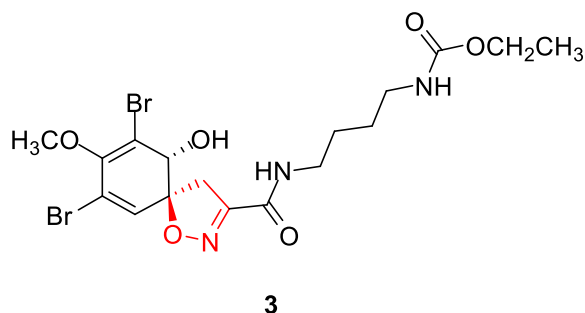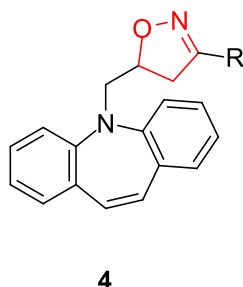hore in the field of cancer research, I am focused on synthesis fulvene derivatives which have got isoxazoline heterocycles showing anticancer activity.

EXPERIMENTAL

Materials and Methods
All reactants and reagents were commercially available and used without further purification. Thin-layer chromatography (TLC) on silica gel GF 254 was used to control reaction progress. A Gallenkamp digital thermometer was used to determine melting points of all solid compounds. IR spectra were recorded on a Perkin Elmer FT-IR spectrometer. ^{1}H and ^{13}C NMR spectra were obtained with a Bruker Avance III-500 MHz NMR system. Chemical shifts were reported in parts per million (ppm) with respect to internal standard TMS. Peak multiplicities are designated by the following abbreviations: s, singlet; d, doublet; dd, double doublet; t, triplet; dt, double triplet; m, multiplet; br, broad. Mass spectral studies were performed on an Agilent 6890N/5973 GC/IMSD system.

Synthesis and Characterization
Procedure for the synthesis of (Cyclopenta-2,4-dienylidenemethylene)dibenzene 1(31): NaOMe (540 mg, 10 mmol), ethanol (10 mL), and benzophenone (1.86 g, 10 mmol) were added to a reaction flask. Cyclopentadiene (1.6 mL, 20 mmol) was added to the reaction flask, giving a red solution. After stirring for 7 days, the orange crude solid was filtered and rinsed with 5 mL of ethanol. The crude product was refluxed in 10 mL of methanol for 1 h. After cooling to the room temperature, the solid was filtered, rinsed with 7,5 mL of methanol, and dried in under reduced pressure for 24 h to give the product as an range solid 136.18 g (86.2%). MS (GC-MS): $C_{18}H_{14}$, m/z 230.3 (M$^+$).

Procedure for the synthesis of 2-(cyclopenta-2,4-dien-1-ylidenemethyl)-1,4-dimethoxybenzene 2 (32): 0.330 g (5 mmol) of freshly distilled cyclopentadiene was dissolved 5 mL of methanol, then 0.213 g (3 mmol) of pyrrolidine was added to the reaction mixture. Then, 0.332 g of (2 mmol) 2,5-dimethoxybenzaldehyde was added slowly to the reaction flask. The solution was stirred under nitrogen atmosphere at room temperature for 6 h. 0.18 g of glacial acetic acid was added to the reaction mixture. The mixture was diluted with 20 mL of diethyl ether, the layers were separated, and the organic layer was washed

with water (2 x 15 mL). The organic phase was dried over Na_2SO_4, filtered and concentrated. The red oil was obtained after purification with column chromatography on silica gel. Yield: %78. ^{1}H NMR (500 MHz, $CDCl_3$): δ = 3.81 (s, $3OCH_3$), 3.83 (s, $3OCH_3$), 6.38-6.35 (m, 1=CH), 6.54-6.51 (m, 1=CH), 6.66-6.65 (t, J=3.19, 2=CH), 6.93-6.82 (m, 2CH), 7.18-7.14 (d, J= 2.87, 1CH), 7.53 (s, 1CH) ppm. MS (GC-MS): $C_{14}H_{14}O_2$ m/z 214 (M$^+$).

General procedure for the synthesis of oxime derivatives 3-5: Oxime derivatives were prepared with an aldehyde, hydroxylamine hydrochloride, and sodium carbonate in ethyl alcohol at room temperature with the known procedure (50-51). A solution of hydroxylamine hydrochloride (0.417 g, 6 mmol) in water (0.5 mL) and a solution of Na_2CO_3 in water (1.5 mL) were added drop wise to the solution of an aldehyde (2 mmol) in EtOH (1.5 mL), respectively. Resulting solid was filtered and purified by recrystallization from alcohol. Oxime derivatives (3-5) were obtained in almost quantitative yields.

4-Chlorobenzaldehyde oxime 3 (33): White solid, yield 100%, m.p. 92-94ºC, Rf: 0.52 (1:2 ethyl acetate/n-hexane), FT-IR (ATR) 3301 (OH), 1589 (C=N), 1496 (C-N), 971 (C-H), 694 (C-Cl) cm^{-1}, GC-MS (EI), m/z (%): 155 (M$^+$·, 99), 139 (100), 136 (82), 111 (73), 75 (70).

4-Bromobenzaldehyde oxime 4 (33): Yellow solid, yield 100%, m.p. 106-108ºC Rf: 0.45 (1:2 ethyl acetate/n-hexane), FT-IR (ATR) 3310 (OH), 1590 (C=N), 1470 (C-N), 960 (C-H), cm^{-1}, GC-MS (EI), m/z (%): 200 (M$^+$·, 70), 185 (30), 92 (40), 155 (70), 74 (100).

2,4-Dimethoxybenzaldehyde oxime 5 (34): White solid, Yield 94%, m.p. 103-105ºC, FT-IR (KBr pellet) 2944, 1610, 1504, 1466, 1414, 1270, 1206, 1112, 1026, 922, 832 cm^{-1}, ^{1}H NMR ($CDCl_3$, 500 MHz) δ 7.73 (1H, s, CH=N-OH), 7.0 (1H, d, J = 8.5 Hz, Ar-H), 6.03 (1H, s Ar-H), 6.06 (1H, d, J = 8.5 Hz, Ar-H), 3.6 (6H, s, 2xOCH3) ppm, calcd for [$C_9H_{11}NO_3$] C 59.66 H 6.11 N 7.70%, found C 60.01 H 6.19%.

General procedure for the synthesis of compound 6-9: The (cyclopenta-2,4-dienylidenemethylene)dibenzene 1 (0.203 g, 1 mmol) and compound 3-4 (p-chlorobenzaldehyde oxime or p-bromobenzaldehyde oxime, respectively) (1 mmol) were dissolved in CH_2Cl_2 (8 mL). A solution of NaOCl (1.2 mL) was added slowly to the reaction mixture at 0 °C. The reaction

mixture was stirred at 0 °C overnight. The progress of the reaction was monitored using TLC. After completion of the reaction, the mixture was extracted with CH_2Cl_2 (3x10 mL). The organic phase was dried over $MgSO_4$, filtered, and concentrated under reduced pressure. The crude product was purified by column chromatography.

3-(4-Chlorophenyl)-6-(diphenylmethylene)-6,6a-dihydro-3aH-cyclopenta[d]isoxazole 6: White solid, Yield 52%, m.p. 204-207 ºC, FT-IR (ATR) 3055 (Aromatic CH), 2952 (Aliphatic CH), 1595 (Aromatic C=C), 1179 (C-O), 1090 (C-N), 828, 827, 700, 677. ^{1}H NMR ($CDCl_3$, 500 MHz) δ 7.64 (d, J= 6.8 Hz, 2H, Ar-H), 7.42 (d, J= 6.8 Hz, 2H, Ar-H), 7.34 (d, J= 8.8 Hz, 2H, Ar-H), 7.23-7.31 (m, 6H, Ar-H), 7.15 (d, J= 8.8 Hz, 2H, Ar-H), 6.37 (dd, J= 5.8; 1.9 Hz, 1H, =CH), 6.00 (dd, J= 5.8; 1.9 Hz, 1H =CH), 5.33 (d, J= 7.8 Hz, 1H, CH), 4.62 (dt, J= 7.8; 4.8 Hz, 1H, CH) ppm. ^{13}C NMR ($CDCl_3$, 125 MHz) δ 155.7 (Cq), 141.9 (Cq), 141.5 (Cq), 140.8 (2xCq), 136.3 (2xCq), 134.5 (2xCAr), 131.3 (2xCAr), 130.3 (2xCAr), 130.2 (CAr), 129.4 (CAr), 128.3 (CAr), 128.20 (2xCAr), 128.18 (CAr), 128.11 (2xCAr), 128.07 (CAr), 127.8 (CAr), 86.2 (O-CH), 58.9 (C-CH) ppm. MS (GC-MS): $C_{25}H_{18}ClNO$, m/z 383 (M$^+$).

3-(4-Chlorophenyl)-4-(diphenylmethylene)-4,6a-dihydro-3aH-cyclopenta[d]isoxazole 7: White solid, Yield 24%, m.p. 160-162ºC, FT-IR (ATR) 3071 and 3021 (Aromatic CH), 2938 and 2850 (Aliphatic CH), 1583 (Aromatic C=C), 1488, 1442, 1287 (C-O), 1087 (C-N), 828, 830, 698, 680. ^{1}H NMR ($CDCl_3$, 500 MHz) 7.15-7.23 (m, 6H, Ar-H), 6.87-6.93 (m, 6H, Ar-H), 6.70 (d, J= 8.8 Hz, 2H, Ar-H), 6.49 (d, J= 5.8 Hz, 1H, =CH), 6.05 (dd, J= 5.8; 1.9 Hz, 1H, =CH), 5.84 (dd, J= 7.8; 1.9 Hz, 1H CH), 5.31 (d, J= 7.8 Hz, 1H, CH) ppm. ^{13}C NMR ($CDCl_3$, 125 MHz) δ 157.0 (Cq), 141.2 (Cq), 140.8 (Cq), 140.7 (Cq), 137.9 (Cq), 137.5 (2xCq), 135.4 (2xCAr), 133.8 (2xCAr), 133.5 (2xCAr), 129.1 (2xCAr), 128.8 (CAr), 127.8 (2xCAr), 127.4 (CAr), 127.3 (CAr), 127.1 (CAr), 126.9 (CAr), 126.5 (CAr), 87.1 (O-CH), 52.8 (C-CH) ppm. MS (GC-MS): $C_{25}H_{18}ClNO$, m/z 383 (M$^+$).

3-(4-Bromophenyl)-6-(diphenylmethylene)-6,6a-dihydro-3aH-cyclopenta[d]isoxazole 8: White solid, Yield 53%, m.p. 124-128ºC, FT-IR (ATR) 3050 and 3021 (Aromatic CH), 2962 (Aliphatic CH), 1595 (Aromatic C=C), 1158 (C-O), 1088 (C-N), 830, 825, 700, 675. ^{1}H NMR ($CDCl_3$, 500 MHz) δ 7.62 (d, J= 6.9 Hz, 2H, Ar-H), 7.45 (d, J= 6.9 Hz, 2H, Ar-H), 7.32 (d, J= 8.8 Hz, 2H, Ar-H), 7.20-7.27 (m, 6H, Ar-H),

7.12 (d, J= 8.8 Hz, 2H, Ar-H), 6.35 (dd, J= 5.9; 2.0 Hz, 1H, =CH), 6.00 (dd, J= 5.9; 2.0 Hz, 1H =CH), 5.30 (d, J= 7.9 Hz, 1H, CH), 4.58 (dt, J= 7.9; 4.7 Hz, 1H, CH) ppm. ^{13}C NMR (CDCl$_3$, 125 MHz) δ 156.7 (Cq), 141.8 (Cq), 140.7 (2xCq), 139.9 (Cq), 136.1 (2xCq), 134.0 (2xCAr), 131.5 (2xCAr), 130.3 (CAr), 130.2 (2xCAr), 130.0 (CAr), 128.7 (CAr), 128.3 (CAr), 128.2 (CAr), 128.1 (2xCAr), 128.0 (CAr), 127.5 (2xCAr), 86.0 (O-CH), 57.7 (C-CH) ppm. MS (GC-MS): C$_{25}$H$_{18}$BrNO, m/z 427 (M$^+$).

3-(4-Bromophenyl)-4-(diphenylmethylene)-4,6a-dihydro-3aH-cyclopenta[d]isoxazole 9: White solid, Yield 18%, m.p. 190-192ºC, FT-IR (ATR) 3051 and 3021 (Aromatic CH), 2940 and 2848 (Aliphatic CH), 1580 (Aromatic C=C), 1480, 1440, 1285 (C-O), 1076 (C-N), 832, 830, 705, 695. ^{1}H NMR (CDCl$_3$, 500 MHz) 7.21-7.29 (m, 6H, Ar-H), 6.90-6.96 (m, 6H, Ar-H), 6.75 (d, J= 8.9 Hz, 2H, Ar-H), 6.42 (d, J= 5.8 Hz, 1H, =CH), 6.10 (dd, J= 5.8; 1.7 Hz, 1H, =CH), 5.80 (dd, J= 8.1; 1.7 Hz, 1H CH), 5.28 (d, J= 8.1 Hz, 1H, CH) ppm. ^{13}C NMR (CDCl$_3$, 125 MHz) δ 157.0 (Cq), 141.2 (2xCq), 140.8 (Cq), 137.9 (Cq), 137.5 (Cq), 136.0 (Cq), 135.4 (2xCAr), 133.8 (2xCAr), 133.5 (2xCAr), 129.1 (CAr), 128.8 (2xCAr), 127.8 (2xCAr), 127.4 (CAr), 127.3 (CAr), 127.1 (CAr), 126.9 (CAr), 126.5 (CAr), 87.1 (O-CH), 52.8 (C-CH) ppm. MS (GC-MS): C$_{25}$H$_{18}$BrNO, m/z 427 (M$^+$).

Procedure for the synthesis of compound 10: The 2-(cyclopenta-2,4-dien-1-ylidenemethyl)-1,4-dimethoxybenzene 2 (0.214 g, 1 mmol) and 2,4-dimethoxybenzaldehyde oxime (0.181 g, 1 mmol) was dissolved in CH$_2$Cl$_2$ (1 mL). A solution of NaOCl (1.2 mL) was added slowly to the reaction flask at 0 °C. The reaction mixture was stirred at 0 °C overnight. The progress of the reaction was monitored using TLC. After completion of the reaction, the mixture was extracted with CH$_2$Cl$_2$ (3x10 mL). The organic phase was dried over Na$_2$SO$_4$, filtered, and concentrated. The crude product purified by column chromatography.

(E)-6-(2,5-Dimethoxybenzylidene)-3-(2,5-dimethoxyphenyl)-6,6a-dihydro-3aH-cyclopenta[d]isoxazole 10: White solid, Yield 25%, m.p. 174-176ºC, FT-IR (ATR) 3071 and 3021 (Aromatic CH), 2927 (Aliphatic CH), 1493, 1316, 1287 (C-O), 1087 (C-N), 873 cm^{-1}. ^{1}H NMR (CDCl$_3$, 500 MHz) 7.32 (d, J= 8.9 Hz, 1H, Ar-H), 6.80-6.95 (m, 5H, Ar-H), 6.60 (s, 1H, =CH), 6.10 (dd, J= 5.8; 1.7 Hz, 1H, =CH), 5.65 (dd, J= 5.8; 1.7 Hz, 1H, =CH), 5.20 (d, J= 8.1 Hz, 1H, CH), 4.62 (m, 1H, CH) 3.40 (s, 6H, OCH$_3$), 3.38 (s, 6H, OCH$_3$) ppm. ^{13}C NMR (CDCl$_3$, 125 MHz) δ 153.0 (Cq), 152.6 (Cq), 152.4 (Cq), 151.8 (Cq), 151.5 (Cq), 151.3, 140.1, 131.2, 124.6, 118.2 (CAr), 117.6 (CAr), 115.9 (Cq), 115.4 (CAr), 115.2 (CAr), 114.5 (CAr), 114.3 (CAr), 111.5 (CAr), 68.3 (O-CH), 56.2 (OCH$_3$), 55.8 (2xOCH$_3$), 55.7 (OCH$_3$), 42.9 (C-CH) ppm. MS (GC-MS): C$_{23}$H$_{23}$NO$_5$, m/z 393 (M$^+$)

RESULT AND DISCUSSION

The present paper shows my work employing the reaction of various oxime derivatives that are reacted with fulvene derivatives in the presence of NaOCl.

My first key intermediate was the (cyclopenta-2,4-dienylidenemethylene)dibenzene 1 which was easily prepared from benzophenone and cyclopentadiene (36). It was recrystallized from hot ethanol and characterized by recording its spectral data. My other key intermediate was the 2-(cyclopenta-2,4-dien-1-ylidenemethyl)-1,4-dimethoxybenzene 2 which was easily obtained with a known procedure (32) (Scheme 1). It was purified with column chromatography.
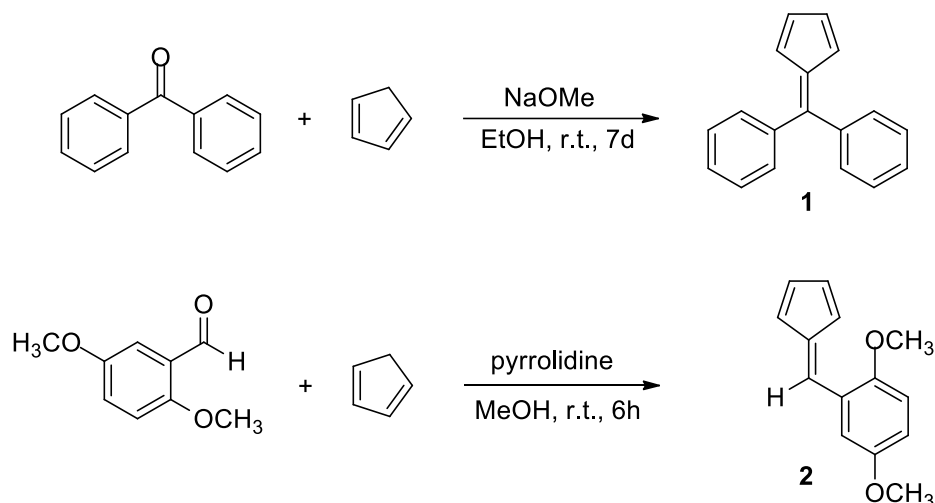
Scheme 1: Synthesis of fulvene derivatives 1-2

My goal is to prepare new fulvene derivatives with isoxazoline group. Because of this synthetic strategy, I firstly synthesized oxime derivatives 3-5 with known procedure (33, 34) (Scheme 2). Usually, oxime derivatives can be prepared by the reaction of aromatic aldehyde with hydroxyl amine hydrochloride in the presence of a base like sodium carbonate. They were obtained in almost quantitative yields with Na_2CO_3.
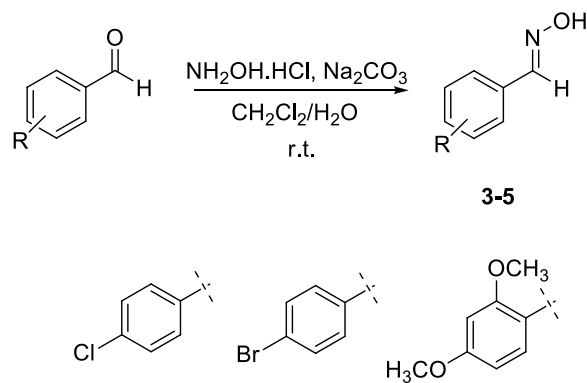
Scheme 2: Synthesis of oxime derivatives 3-5.

Compound 1 and p-chlorobenzaldehyde oxime 3 were stirred at 0 °C in dichloromethane. Adding NaOCl to the reaction mixture afforded compound 6 and compound 7 (Scheme 3) which were identified on the basis of their spectral analyses. In fact, increasing the reaction temperature from 20 °C in dichloromethane up to 40 °C results in a significant lowering of the yields. Both NMR spectra of compound 6 and 7 consistent with assigned structures.

The ^1H NMR spectrum of compound 6 revealed signals at 7.64, 7.42, 7.34, 7.23 and 7.15 ppm due to the presence of fourteen aromatic protons. The analysis of the ^{13}C NMR spectrum revealed that the signal of the alifatic carbons appeared at δ 58.9 ppm.
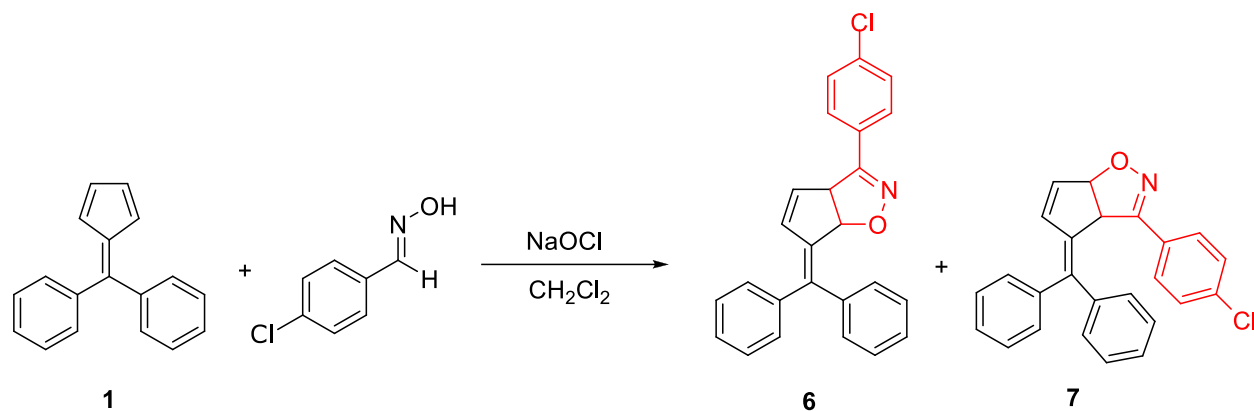
Scheme 3: Syntheses of compounds 6-7.

The ^{1}H and ^{13}C NMR spectrum of compound 7 showed the similar results and confirmed the structure of compound 7. The ^{1}H and ^{13}C NMR spectrum of compound 6 and 7 proved the the occurrence of 1,3-dipolar cycloaddition.

Compound 7's yield was lower than that of compound 6 yield because of the steric hindrance.
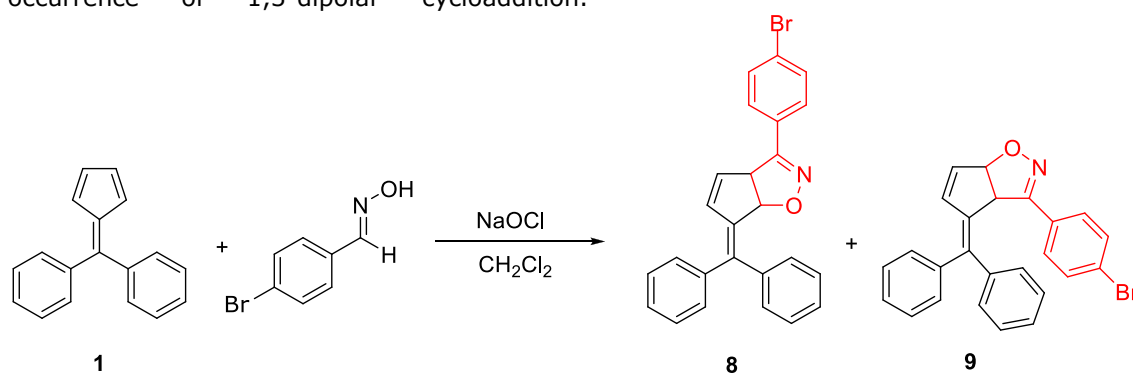
Scheme 4: Synthesis of compound 8-9.

The ^{1}H and ^{13}C NMR spectral data were also similar to those of compound 8, apart from an additional CH at 5.30 and 4.58, an extra aromatic doublet signals at 7.62 and 7.45, and a lack of a cyclopentadiene two =CH protons. The ^{13}C NMR spectrum was also similar to that

of compound 8, except two upfield signals of a CH carbons at 57.7.

Indeed, there was no inconsistency between the proposed structure 9 and the spectral data. Compound 9's yield was lower than compound 8's yield because of the steric hindrance.

Scheme 5: Synthesis of compound 10.

Finally, we could obtain the desired compound 10 by the reaction of compound 2 with oxime derivative 5 in dichloromethane in the presence of a small amount of NaOCl. The spectral features of the fulvene analog 10 agree with the structure of the pro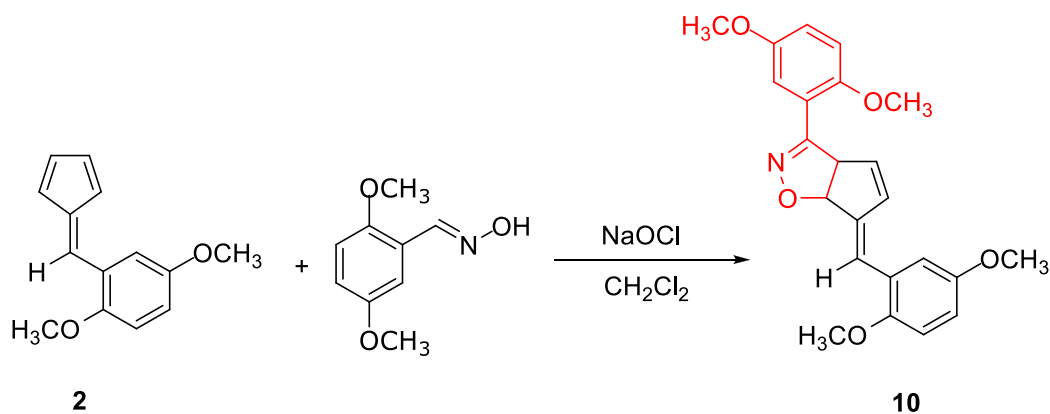duct as summarized in the Experimental Section. As was expected, no significant change was observed at the oxime aromatic ring signals. The ^{1}H NMR spectrum of compound 10 revealed 2 single signals at 3.40 and 3.38 ppm due to the presence of four methoxy groups. And also the ^{13}C NMR spectrum of compound 10 revealed signals at 56.2, 55.8 and 55.7 due to the methoxy group. Single crystals of the products could not be obtained from any organic solvents, thus no definite structures can be described.

CONCLUSION

In conclusion, I designed and synthesized new fulvene derivatives containing isoxazoline ring as possible anti-cancer agents. I characterized all of the new molecules with ^{1}H NMR, ^{13}C NMR, FTIR and GC-MS spectral data. Compound 9 yield was lower than compound 8 yield because of the steric hindrance. Compound 6 and 7 obtained together with the 52% and 24%, respectively.

Further work toward exploring anticancer activity of all newly synthesized compounds with MTT essay will be forthcoming.

ACKNOWLEDGEMENTS

REFERENCES

1. Gothelf KV, Jorgensen KA. Asymmetric 1,3-Dipolar Cycloaddition Reactions. Chem Rev. 1998;98(2):863-910.

2. Pandey G, Banerjee P, Gadre SR. Construction of enantiopure pyrrolidine ring system via asymmetric [3+2]-cycloaddition of azomethine ylides. Chem Rev. 2006;106(11):4484-517.

3. Stanley LM, Sibi MP. Enantioselective copper-catalyzed 1,3-dipolar cycloadditions. Chem Rev. 2008;108(8):2887-902.

4. Adrio J, Carretero JC. Novel dipolarophiles and dipoles in the metal-catalyzed enantioselective 1,3-dipolar cycloaddition of azomethine ylides. Chem Commun (Camb). 2011;47(24):6784-94.

5. Huisgen R, Mloston G, Polborn K. 1,3-Dipolar Activity in Cycloadditions of an Aliphatic Sulfine(,)(1). J Org Chem. 1996;61(19):6570-4.

6. Woodward RB. Recent advances in the chemistry of natural products. Science. 1966;153(3735):487-93.

7. Hoffmann R, Woodward RB. Orbital symmetry control of chemical reactions. Science. 1970;167(3919):825-31.

8. Furukawa M, Sugita M, Kojima Y. Reaction of epoxides. V. 1,3-Dipolar cycloaddition reactions of epoxides with carbon-nitrogen double bond compounds. Chem Pharm Bull (Tokyo). 1974;22(7):1468-76.

9. Kano T, Hashimoto T, Maruoka K. Asymmetric 1,3-dipolar cycloaddition reaction of nitrones and acrolein with a bis-titanium catalyst as chiral Lewis acid. J Am Chem Soc. 2005;127(34):11926-7.

10. Siadati SA, Mahboobifar A, Nasiri R. A theoretical study on the reaction pathways and the mechanism of 1,3- dipolar cycloaddition of vinyl acetylene and methyl azide. Comb Chem High Throughput Screen. 2014;17(8):703-8.

11. Beckhaus R, Lutzen A, Haase D, Saak W, Stroot J, Becke S, et al. A Novel Route to Fulvene Complexes of Titanium-Diastereoselective Complexation of Pentafulvenes to Cyclopentadienyltitanium Fragments. Angew Chem Int Ed Engl. 2001;40(11):2056-8.

12. Bryan CS, Lautens M. A tandem catalytic approach to methyleneindenes: mechanistic insights into gem-dibromoolefin reactivity. Org Lett. 2010;12(12):2754-7.

13. Ye S, Yang X, Wu J. Rapid access to 1-methyleneindenes via palladium-catalyzed tandem reactions of 1-(2,2-dibromovinyl)-2-alkynylbenzenes with arylboronic acids. Chem Commun (Camb). 2010;46(17):2950-2.

14. Ye S, Gao K, Zhou H, Yang X, Wu J. Synthesis of 1-methyleneindenes via palladium-catalyzed tandem reactions. Chem Commun (Camb). 2009(36):5406-8.

15. Abdur Rahman SM, Sonoda M, Ono M, Miki K, Tobe Y. Novel synthesis of bridged phenylthienylethenes and dithienylethenes via

Pd-catalyzed double-cyclization reactions of diarylhexadienynes. Org Lett. 2006;8(6):1197-200.

16. Schmittel M, Vavilala C. Kinetic isotope effects in the thermal C2-C6 cyclization of enyne-allenes: experimental evidence supports a stepwise mechanism. J Org Chem. 2005;70(12):4865-8.

17. Kovalenko SV, Peabody S, Manoharan M, Clark RJ, Alabugin IV. 5-Exo-dig radical cyclization of enediynes: the first synthesis of tin-substituted benzofulvenes. Org Lett. 2004;6(14):2457-60.

18. Bekele T, Christian CF, Lipton MA, Singleton DA. "Concerted" transition state, stepwise mechanism. Dynamics effects in C2-C6 enyne allene cyclizations. J Am Chem Soc. 2005;127(25):9216-23.

19. Clegg NJ, Paruthiyil S, Leitman DC, Scanlan TS. Differential response of estrogen receptor subtypes to 1,3-diarylindene and 2,3-diarylindene ligands. J Med Chem. 2005;48(19):5989-6003.

20. Krief A, Laval AM. Coupling of Organic Halides with Carbonyl Compounds Promoted by SmI(2), the Kagan Reagent. Chem Rev. 1999;99(3):745-78.

21. Hong BC, Shr YJ, Wu JL, Gupta AK, Lin KJ. Novel [6 + 2] cycloaddition of fulvenes with alkenes: a facile synthesis of the anislactone and hirsutane framework. Org Lett. 2002;4(13):2249-52.

22. Barluenga J, Martinez S, Suarez-Sobrino AL, Tomas M. New reaction pathways for Fischer carbene complexes: [6 + 3] cycloaddition of chromium alkenyl carbene complexes with fulvenes. J Am Chem Soc. 2001;123(44):11113-4.

23. Coskun N, Ma J, Azimi S, Gartner C, Erden I. 1,2-Dihydropentalenes from fulvenes by [6 + 2] cycloadditions with 1-isopropenylpyrrolidine. Org Lett. 2011;13(22):5952-5.

24. Cassady JM, Baird WM, Chang CJ. Natural-Products as a Source of Potential Cancer Chemotherapeutic and Chemopreventive Agents. J Nat Prod. 1990;53(1):23-41.

25. Vijesh AM, Isloor AM, Shetty P, Sundershan S, Fun HK. New pyrazole derivatives containing 1,2,4-triazoles and benzoxazoles as potent antimicrobial and analgesic agents. Eur J Med Chem. 2013;62:410-5.

26. Soares MIL, Brito AF, Laranjo M, Paixao JA, Botelho MF, Melo TMVDPE. Chiral 6,7-bis(hydroxymethyl)-1H,3H-pyrrolo[1,2-c]thiazoles with anti-breast cancer properties. Eur J Med Chem. 2013;60:254-62.

27. Kamal A, Bharathi EV, Reddy JS, Ramaiah MJ, Dastagiri D, Reddy MK, et al. Synthesis and biological evaluation of 3,5-diaryl isoxazoline/isoxazole linked 2,3-dihydroquinazolinone hybrids as anticancer agents. Eur J Med Chem. 2011;46(2):691-703.

28. Shi L, Hu R, Wei Y, Liang Y, Yang Z, Ke S. Anthranilic acid-based diamides derivatives incorporating aryl-isoxazoline pharmacophore as potential anticancer agents: design, synthesis and biological evaluation. Eur J Med Chem. 2012;54:549-56.

29. Shaala LA, Youssef DT, Sulaiman M, Behery FA, Foudah AI, Sayed KA. Subereamolline A as a potent breast cancer migration, invasion and proliferation inhibitor and bioactive dibrominated alkaloids from the Red Sea sponge Pseudoceratina arabica. Mar Drugs. 2012;10(11):2492-508.

30. Sadashiva MP, Basappa, NanjundaSwamy S, Li F, Manu KA, Sengottuvelan M, et al. Anti-cancer activity of novel dibenzo[b,f]azepine tethered isoxazoline derivatives. BMC Chem Biol. 2012;12:5.

31. Miller SA, Bercaw JE. Mechanism of isotactic polypropylene formation with C-1-symmetric metallocene catalysts. Organometallics. 2006;25(15):3576-92.

32. Ocal N, Bagdatli E, Arslan M. Diels-Alder reactions of new methoxysubstituted-6-arylfulvenes. Turk J Chem. 2005;29(1):7-16.

33. Puerto Galvis CE, Kouznetsov VV. An unexpected formation of the novel 7-oxa-2-azabicyclo[2.2.1]hept-5-ene skeleton during the reaction of furfurylamine with maleimides and their bioprospection using a zebrafish embryo model. Org Biomol Chem. 2013;11(3):407-11.

34. Alam MI, Alam MA, Alam O, Nargotra A, Taneja SC, Koul S. Molecular modeling and snake venom phospholipase A(2) inhibition by phenolic compounds: Structure-activity relationship. Eur J Med Chem. 2016;114:209-19.

RESEARCH ARTICLE

Lipid and essential oil constituents of *Cota hamzaoglui* Özbek & Vural (Asteraceae)

Gülmira Özek* ✉ iD **, Mehmet Ufuk Özbek²** ✉ **, Münevver Arslan³** ✉

¹Anadolu University, Faculty of Pharmacy, Department of Pharmacognosy, 26470, Eskişehir, Turkey
² Gazi University, Faculty of Science, Department of Biology, 06500, Teknikokullar, Ankara, Turkey.
³ Research Institute for Forest Soil and Ecology, p.b. 61, 26160, Eskişehir, Turkey

Abstract: In the present work, lipids and essential oil constituents of endemic *Cota hamzaoglui* Özbek & Vural were investigated with GC-FID/MS techniques. The fatty acids fraction was isolated with liquid-liquid extraction from the herb with Folch method and then methylated with BF_3 reagent. Linolenic, linoleic, oleic, and hexadecanoic acids were found to be the main fatty acids. The unsaturated fatty acids (66.0%) prevailed upon saturated (33.6%) ones. The essential oil was characterized with high percentage of the fatty acids (34.7%), alkanes (14.0%) and aliphatic aldehydes (8.3%). The present study is the first report on chemical composition of *Cota hamzaoglui Özbek & Vural* lipids and essential oil.

INTRODUCTION

The Asteraceae family contains the largest number of described species, approximately 25,000 distributed in over 2,200 genera (1-3). The plants of Asteraceae family have been found to be the most commonly used families in the traditional medical treatments in Turkey. Ethnomedicinal aspects of potency of Asteraceae plants have recently been reported by Altundag *et al.* (4). Importance of the essential oils of the Anthemideae plants has been discussed in recently reported paper by Silva (5). Many genera have been approved for applying in treatment of a number of diseases, *Tanacetum* (6), *Silybum* (7), *Matricaria* (8), *Achillea* (9), *Artemisia* (10) and *Anthemis* (11). The genus *Cota* J. Gay is represented by 63 taxa which are mainly distributed in Europe (excluding northern Europe), North Africa, Caucasia and Central Asia. In Turkey, the genus consists of 22 taxa,

nine of which are endemic (1, 2). Earlier, *Cota* was recorded as a section in the genus *Anthemis* L. in Flora of Turkey (12). Recently, the *Anthemis* section *Cota* has been accepted as a generic name, *Cota* (13, 14). The genus *Cota* morphologically resembles *Anthemis*, however differs by achenes (2). Representatives of the genus *Cota* have economic importance because of their uses for various purposes such as obtaining drug, food and dye (15).

Today there is increasing demand for cheap, safe, and scientifically approved botanicals from domestic sources. However, there are still species have not been investigated for phytochemical and biological potentials. The plants of the genus *Cota* are among less-investigated species. In literature, there is information that the flowers of the genus *Cota* were used as antiseptic and healing herbs. The main components are natural flavonoids and

essential oils (Table 1), which are widely used as antiinflammatory, antibacterial, antispasmodic, and sedative agents (16). To the best of our knowledge, there is no previous information about chemical composition and biological activity of *C. hamzaoglui*.

Table 1. Chemical composition of the essential oils of *Cota* species (literature survey)

Cota species	Plant part	Compound, (%)	Ref.
C. altissima (L.) J. Gay (syn. *Anthemis altissima* L.)	AP	α-Pinene (4.0), benzaldehyde (27.1), Δ^2 -carene (4.2), linalool (4.6), β-caryophyllene (7.6)	(17)
C. altissima (L.) J. Gay (syn. *Anthemis altissima* L.)	Fl	Decanoic acid (6.1), β-caryophyllene (25.3), α-humulene (5.2), germacrene D (6.9), spathulenol (5.4), caryophyllene oxide (6.5)	(18)
	L	Carvacrol (3.5), β-caryophyllene (17.2), spathulenol (17.4), caryophyllene oxide (9.6)	(18)
	St	*trans*-β-Farnesene (2.6), pentadecanoic acid (3.1), palmitic acid (39.6), linoleic acid (36.2)	(18)
Cota palestina Kotschy (syn. *A. melanolepis* Boiss.; *Anthemis palestina* (Reut. Ex. Kotschy) Boiss.)	AP	Benzaldehyde (0.3-13.8), *p*-cymene (4.2-11.2), chrysanthenol (3.3-4.4), benzyl alcohol (0-26.9), 2-phenyl-1-ethanol 33.6), *trans*-verbenol (3.6-10.0), caryophyllene oxide (1.5-5.7)	(17)
Cota triumfetti (L.) J. Gay (syn. *Anthemis triumfetti* (L.) DC; *A. talyshensis* A. Fedor.)	AP	α-Eudesmol (18.2), borneol (13.3), hexadecanoic acid (9.5), γ-eudesmol (8.6%), elemol (7.6)	(19)
Cota tinctoria (L.) J. Gay (syn. *A. tinctoria* L.)	Fl	1,8-Cineole (7.9), β-pinene (7.3), decanoic acid (5.4), α-pinene (4.4)	(20)
Cota triumfetti (L.) J. Gay (syn. *A. triumfetti* (L.) DC.)	AP	β-Pinene (16.9), camphor (15.0), α-pinene (14.4), 1,8-cineole (5.8)	(21)

AP: aerial parts; Fl: flowers; L: leaves; St: steams; syn: synonymous

Recently, a new species *Cota hamzaoglui* Özbek & Vural in Anthemideae tribe has been described in Turkey. Information given on the new species includes comments on the species' affinity to *Cota oxylepis* Boiss. and *C. fulvida* (Grierson) Holub (2). Several aspects on chemical and pharmacological potent of the genus *Anthemis* have recently been reported by Siasar-Karbasky *et al.* (22). A previous phytochemical studies on *Anthemis* species resulted with polyphenols (23, 24), mono- and sesquiterpenes, fatty acids (25). Biological activity investigations of *Anthemis* species encompasses antibacterial (26), antioxidant (27), cytotoxic (28), antiproliferative (29), antidiabetic (30), antiinflammatory (31) and lipoxygenase inhibition (32) potentials.

In scope of the present work, we attempted to investigate chemical composition of the essential oil as well as fatty acid compositions of *C. hamzaoglui.* We have extracted the fatty acids with Folch method (33) for subsequent analysis of their composition after methylation with boron trifluoride reagent (BF₃). So, the present work is the first comprehensive investigation of the lipids and essential oil constituents from aerial parts of *C. hamzaoglui.*

MATERIALS AND METHODS

Chemicals
Boron trifluoride reagent (BF₃), hydrochloric acid, *n*-hexane (Sigma-Aldrich, Germany), calcium chloride, anhydrous sodium sulfate (Fluka, Germany), diethyl ether (JT Baker, Holland), chloroform (Sigma-Aldrich, France), methanol (Sigma-Aldrich, Poland) were of analytical grade. A C₈–C₄₀ *n*-alkane standard solution was purchased from Fluka (Buchs, Switzerland).

Instrumentation
Agilent 5975 GC-MSD system (Agilent, USA; SEM Ltd., Istanbul, Turkey) was equipped with the HP-Innowax FSC column (60 m × 0.25 mm id with 0.25 μm film thickness, Agilent, USA). The GC-FID analysis was carried out with capillary GC using an Agilent 6890N GC system (SEM Ltd., Istanbul, Turkey).

Plant Material
The aerial parts of C*. hamzaoglui* were collected on Bursa: Uludağ, above hotels, between cable cars, and near an old tungsten mine, 2050-2100 m, 31.07.2009, U. Özbek 2812 & M. Vural, and dried under the shade. Botanical identification was performed by Dr. M. U. Özbek. The voucher specimen is keep in the Herbarium of Gazi University, under herbarium code GAZI.

Hydrodistillation of Essential Oil

The flowers and the herb of *C. hamzaoglui* were subjected to hydrodistillation (3 h) to yield essential oils in Clevenger-type apparatus according to European Pharmacopeia (34). The oil was dried over anhydrous sodium sulfate and stored in sealed vial in refrigerator (4 °C), until GC-FID and GC/MS analyses. The oil was dissolved in *n*-hexane (10 %, v/v) to conduct chromatographic determination of its composition.

Isolation of Fatty Acids and Derivatization

The ground plant material was subjected to maceration with chloroform: methanol (2:1) at room temperature for 24 h. The extract was filtered and the residue material was macerated twice (for 30 min) more with new portions of the solvent. All filtrates were combined and half of the solvent was evaporated under vacuum in a rotary evaporator. Then, half amount of chloroform was added into the extract. The obtained extract was washed (three times) with $CaCl_2$ solution (0.4%) in a separatory funnel. At the end of the procedure, the chloroform extract was filtered through anhydrous sodium sulfate to remove moisture, and then chloroform was removed under vacuum. The dried extract was subjected to saponification. To do this, the crude extract was boiled in $KOH-H_2O-MeOH$ (1:1:8) solution for 2 hours in a refluxing system. After the saponification process, 1-2 mL of *n*-hexane was added to remove non-saponified compounds. The fatty acids were extracted with diethyl ether after acidification of the extract with HCl (15% solution) (33). The methylation of the free fatty acids was performed using BF_3 reagent (35). The fatty acids methyl esters were subjected to analysis with GC/MS and GC-FID techniques.

Gas-Chromatography - Mass Spectrometry (GC/MS)

The GC/MS analysis was carried out with an Agilent 5975 GC-MSD system (Agilent, USA; SEM Ltd., Istanbul, Turkey). HP-Innowax FSC column (60 m × 0.25 mm, 0.25 □m film thickness, Agilent, USA) was used with a helium carrier gas at 0.8 mL/min. GC oven temperature was kept at 60 °C for 10 min and programmed to 220 °C at a rate of 4 °C/min, kept constant for 10 min at 220 °C, and then programmed to increase at a rate of 1 °C/min to 240 °C. The oils were analyzed with a split

ratio of 40:1. The injector temperature was 250 °C. Mass spectra were taken at 70 eV and the mass range was from m/z 35 to 450.

Gas Chromatography – Flame Ionization Detection (GC-FID)

The GC-FID analysis was carried out with capillary GC using an Agilent 6890N GC system (SEM Ltd., Istanbul, Turkey). Flame ionization detector (FID) temperature was set at 300 °C in order to obtain the same elution order with GC/MS. Simultaneous injection was performed using the same column and appropriate operational conditions.

Identification and Quantification of Compounds

Identification of the volatile constituents was based on the following: (i) comparison of GC/MS Relative Retention Indices (RRI) of the compounds on polar column determined relative to the retention times of a series of *n*-alkanes (C_8-C_{40}), with those of authentic compounds or literature data; (ii) computer matching with commercial mass spectral libraries: MassFinder software 4.0, Adams Library, Wiley GC/MS Library (Wiley, New York, NY, USA) and Nist Library, and comparison of the recorded spectra with literature data. Confirmation was also achieved using the in-house Başer Library of Essential Oil Constituents database, obtained from chromatographic runs of pure compounds performed with the same equipment and conditions (Table 2).

RESULTS AND DISCUSSION

In literature it could be found highlighting promising phytochemical properties and biological activities of diverse *Anthemis* species. However, there is no information about phytochemistry of endemic species *C. hamzaoglui Özbek & Vural*. The main goal of the present work was to evaluate chemical composition of *C. hamzaoglui Özbek & Vural* lipids and volatile metabolites.

Essential oil composition

In the present work, the essential oil of *C. hamzaoglui Özbek & Vural* has been hydrodistilled from aerial parts and chemical profile is investigated for the first time. The hydrodistillation of the flower and herb of *C. hamzaoglui* resulted with yellowish essential oil (0.04 % yield) with specific odor. Gas-chromatographic profile of *C. hamzaoglui Özbek & Vural* oil is presented on Figure 1.
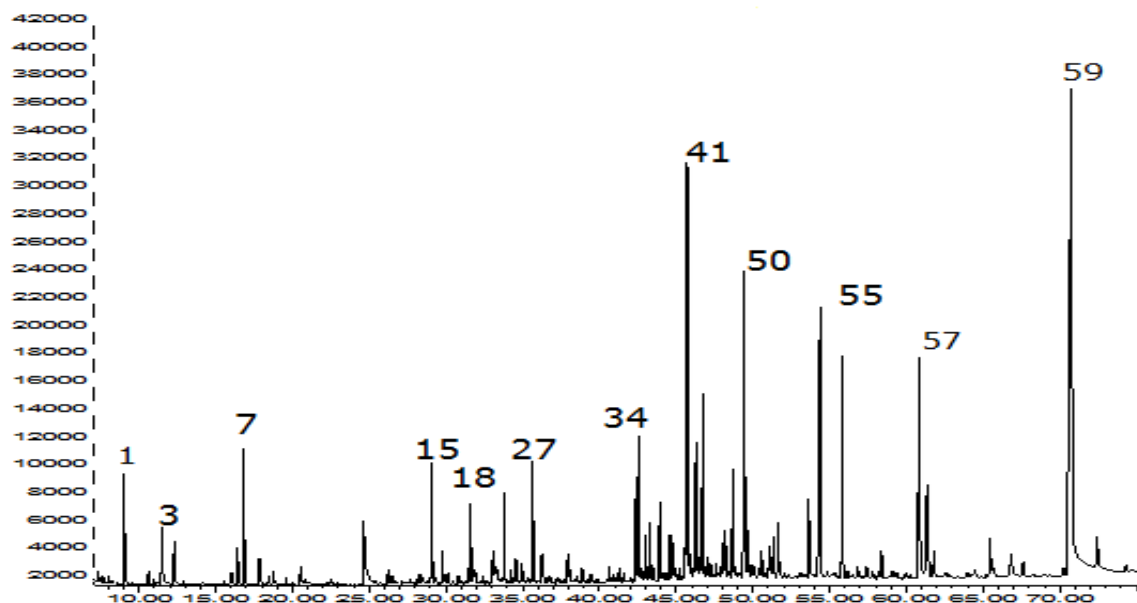
Figure 1. Gas-chromatographic profile of the essential oil of *C. hamzaoglui Özbek & Vural*. Numeration of the peaks is depicted according to list of the detected compounds in Table 2.

The list of detected compounds with their relative retention indices, relative percentages and method of identification is given in Table 2 in order of their elution on the HP-Innowax FSC column.

Table 2. Chemical composition of *C. hamzaoglui Özbek & Vural* essential oil.

No	RRI[a]	RRI[b]	Compound	%[c]	Identification method
1	1032	1032(36)	α-Pinene	1.5	d,e,f
2	1076	1076 (36)	Camphene	0.2	d,e,f
3	1093	1091 (36)	Hexanal	1.1	d,e,f
4	1118	1118(36)	β-Pinene	0.7	d,e,f
5	1194	1194 (36)	Heptanal	0.4	d,e,f
6	1203	1203 (37)	Limonene	0.7	d,e,f
7	1213	1211 (38)	1,8-Cineole	1.2	d,e,f
8	1244	1236 (39)	Amyl furan	0.5	d,e,f
9	1255	1255(36)	γ-Terpinene	t	d,e,f
10	1266	1267 (36)	(*E*)-β-Ocimene	0.3	d,e,f
11	1280	1280 (36)	*p*-Cymene	t	d,e,f
12	1282	1287 (36)	Octanal	0.3	d,e,f
13	1400	1400 (36)	Nonanal	2.0	d,e,f
14	1438	1438 (36)	Dimethyl tetradecane	t	e,f
15	1532	1532 (40)	Camphor	2.0	d,e,f
16	1548	1531 (41)	(*E*)-2-Nonenal	t	d,e,f
17	1611	1611 (36)	Terpinen-4-ol	0.6	d,e,f
18	1612	1612(36)	β-Caryophyllene	1.3	d,e,f
19	1655	1655 (36)	(*E*)-2-Decenal	0.4	d,e,f
20	1661	1661 (36)	Alloaromadendrene	0.3	e,f
21	1671	1680 (36)	Benzeneacetaldehyde	0.4	e,f
22	1687	1689(36)	α-Humulene	1.4	d,e,f
23	1706	1706(36)	α-Terpineol	0.3	d,e,f
24	1708	1709 (42)	Ledene	0.3	d,e,f
25	1719	1719 (36)	Borneol	0.3	d,e,f
26	1726	1726 (36)	Germacrene D	0.6	d,e,f
27	1755	1757 (36)	Bicyclogermacrene	1.7	d,e,f
28	1764	1762 (36)	(*E*)-2-Undecenal	0.5	d,e,f
29	1773	1774(36)	δ-Cadinene	0.4	d,e,f
30	1776	1776(36)	γ-Cadinene	0.4	d,e,f

No	RRI[a]	RRI[b]	Compound	%[c]	Identification method
31	1827	1827 (36)	(*E,E*)-2,4-Decadienal	0.3	d,e,f
32	1838	1838 (36)	(*E*)-β-Damascenone	t	e,f
33	1868	1868 (36)	(*E*)-Geranyl acetone	t	d,e,f
34	2008	2008 (36)	Caryophyllene oxide	2.1	d,e,f
35	2026	2024 (36)	Humulene epoxide II	1.3	e,f
36	2041	2041 (36)	Pentadecanal	1.1	d,e,f
37	2084	2089 (36)	Octanoic acid	0.2	d,e,f
38	2098	2098 (36)	Globulol	0.7	d,e,f
39	2104	2104 (36)	Viridiflorol	0.5	d,e,f
40	2131	2131 (43)	Hexahydrofarnesyl acetone	2.0	d,e,f
41	2144	2133 (44)	Spathulenol	5.4	d,e,f
42	2155	-	Hexadecanal	1.0	d,e,f
43	2187	2185 (40)	T-Cadinol	2.5	d,e,f
44	2192	-	Nonanoic acid	2.1	d,e,f
45	2206	-	Alismol (= 6,10(14)Guaiadien-4-β-ol)	0.4	e,f
46	2247	2247 (45)	*trans*-α-Bergamotol	0.4	d,e,f
47	2255	2255(42)	α-Cadinol	0.7	d,e,f
48	2259	-	Heptadecanal	0.5	d,e,f
49	2298	2296 (36)	Decanoic acid	1.3	d,e,f
50	2300	2300 (42)	Tricosane	5.8	d,e,f
51	2316	-	Caryophylla-2(12),6(13)-dien-5α-ol	0.7	d,e,f
52	2338	2347 (42)	Octadecanal	0.7	d,e,f
53	2392	-	Caryophylla-2(12),6-dien-5β-ol	1.0	d,e,f
54	2400	2400 (42)	Tetracosane	1.0	d,e,f
55	2500	2500 (42)	Pentacosane	7.2	d,e,f
56	2503	2503 (36)	Dodecanoic acid	1.4	d,e,f
57	2670	2670 (36)	Tetradecanoic acid	5.8	d,e,f
58	2822	2822 (36)	Pentadecanoic acid	0.9	d,e,f
59	2931	2931 (42)	Hexadecanoic acid	26.6	d,e,f
			Total	**93.4**	

[a] **RRI**: Relative Retention Indices calculated against *n*-alkanes (C_9-C_{40}) on HP-Innowax column; [b] RRI values obtained on polar column and reported in literature; [c] **%** calculated from FID data; [d] Identification based on retention index of genuine compounds on the HP-Innowax column; [e] Identification on the basis of computer matching of the mass spectra from Başer Library; [f] Tentative identified on the basis of computer matching of the mass spectra from Adams, MassFinder, Wiley and NIST libraries; *t* : Trace (< 0.1 %).

Gas-chromatographic analysis of the oil resulted with 59 compounds (total) which belong to diverse phytochemical groups, namely, fatty acids, mono- and sesquiterpene hydrocarbons and their oxygenated forms, aliphatic aldehydes and alkanes. Distribution of the main compounds groups detected in *C. hamzaoglui Özbek & Vural* oils is presented on Figure 2.
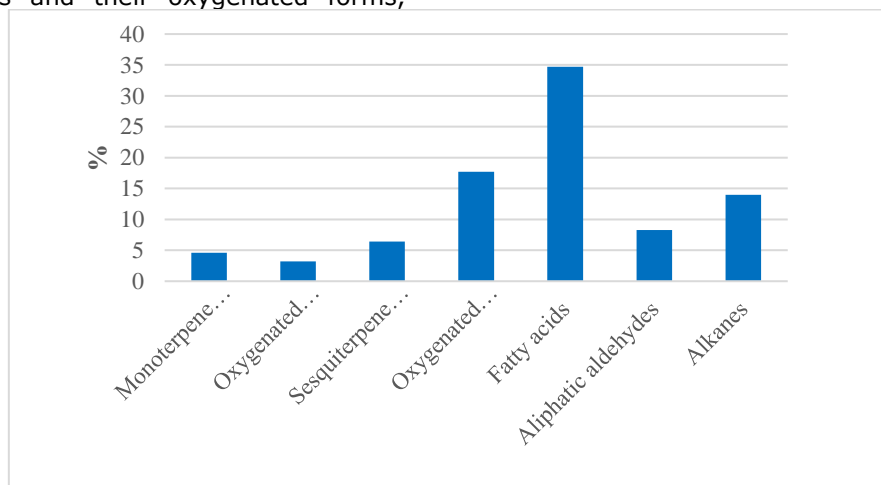

Figure 2. Distribution of the main compound groups detected in the essential oil of *C. hamzaoglui Özbek & Vural.*

In general, the essential oil was characterized with high abundance of the fatty acids (34.7%). Hexadecanoic acid (26.6%) was found as predominant fatty acid in the essential oil. It is noteworthy to mark that the oxygenated sesquiterpenes (17.7%) with spathulenol (5.4%) and caryophyllene oxide (2.1%) as the major constituents were the second important group (after fatty acids) that made contribution into volatile profile of *Cota hamzaoglui Özbek & Vural*. Camphor (2.0%) and 1,8-cineole (1.2%) were the major representatives of this compound class. The next noteworthy of mention compound's group was found to be the alkanes (14.0 %) with pentacosane (7.2%) and tricosane (5.8%) as the main representatives. Aliphatic aldehydes (8.3%) were comprised mostly by nonanal (2.0%), hexanal (1.1%), pentadecanal (1.1%) and hexadecanal (1.0%). □-Caryophyllene (1.3%), □-humulene (1.4%) and bicyclogermacrene (1.7%) comprised the sesquiterpene hydrocarbons (6.4 %) group.

It was interesting to compare the chemical profile of *Cota hamzaoglui Özbek & Vural* essential oil with those reported earlier for different Cota and *Anthemis* species. Actually, there are several reports in the literature dealing with the essential oils of diverse *Cota* or *Anthemis* species. We have recently reported about essential oil of *C. fulvida* (Grierson) Holub (46), that was characterized with hexadecanoic acid (25.6%), camphor (6.1%), caryophyllene oxide (5.3%), 1,8-cineole (4.9%) and humulene epoxide (3.9%). The fatty acids and especially hexadecanoic acid have earlier been observed to be the major constituents in previously studied essential oils obtained from aerial parts of *A. dipsacea* Bornm. (13.5%), *A. pseudocotula* Boiss. (9.5%) (47), *A. altissima* L. (39.6%) (48), *A. ruthenica* M. Bieb. (9.9%) and *A. arvensis* L. (21.2%) (49). Camphor was reported as main volatile constituent in *A.*

cretica subsp. *leucanthemoides* (Boiss.) Grierson (19.4%) (50), *A. tenuisecta* Ball. (17.5%) (51), *A. triumfetti* (L.) DC. (15.0%) (52), *A. hyalina* DC. (11.6%) (53) and *A. pseudocotula* Boiss. (9.4%) (54). 1,8-Cineole was mentioned as a major constituent in the oils of *A. pseudocotula* (39.4%) (54), *A. xylopoda* O. Schwarz (16.7%) (55), *A. widemanniana* (8.9%) (56) and *A. segetalis* Ten (6.1%) (57). Observation of the main constituents detected in different Anthemis species, it can be concluded that the oil of *Cota hamzaoglui Özbek & Vural* was found to be similar to many *Anthemis* species.

Fatty acids composition
The literature search revealed limited information about fatty acids profile of *Anthemis* or *Cota* species. In the present work, the lipid constituents of *C. hamzaoglui Özbek & Vural* isolated with liquid-liquid extraction technique from aerial part were chromatographically separated with GC-FID/MS after methylation process. To best of our knowledge, the present work is the first report about *C. hamzaoglui Özbek & Vural* lipid constituents. Gas-chromatographic analysis of *C. hamzaoglui Özbek & Vural* fatty acid methyl esters resulted with 15 compounds representing 99.6% of the plant lipids. All detected lipid constituents were classified as total saturated (SFA), unsaturated (UFA), monounsaturated (MUFA) and polyunsaturated (PUFA) fatty acids. Palmitic acid (22.2 %) was found to be the main representative of SFAs, followed by stearic acid (6.3%). Other six saturated fatty acids, C10:0, C12:0, C14:0, C15:0, C20:0 and C22:0 were found in lower percentages (0.2-1.5%). MUFA group was presented by oleic acid (20.9 %). Linoleic (26.9 %) and linolenic (13.2 %) acids from PUFA fraction were found in high amount. Table 3 summarizes the fatty acid content of *C. hamzaoglui Özbek & Vural*.

Table 3. Fatty acid composition of *Cota hamzaoglui*

No	Carbon number: double bonds number	Compound	%
1	C10:0	Methyl decanoate (=*Methyl caproate*)	1.5
2	C12:0	Methyl dodecanoate (=*Methyl laurate*)	0.2
3	C14:0	Methyl tetradecanoate (=*Methyl myristate*)	0.9
4	C15:0	Methyl pentadecanoate	0.2
5	C16:0	Methyl hexadecanoate (=*Methyl palmitate*)	22.2
6	C16:1 D-7 *cis*	(*Z*)-7-Methyl hexadecenoate	0.1
7	C16:1 D-9 *cis*	(*Z*)-9-Methylhexadecenoate (= *Methyl palmitoleate*)	0.2
8	C18:0	Methyl octadecanoate (=*Methyl stearate*)	6.3

9	C18:1 D-9 cis	(Z)-9-Methyl octadecenoate (=Methyl oleate)	20.9
10	C18:1 D-7 cis	(Z)-7-Methyl octadecenoate	2.1
11	C18:2 D-9,12 cis	(Z,Z)-9,12-Methyl octadecadienoate (=Methyl linoleate)	26.9
12	C18:1 D-9 cis	Ethyl linoleate	2.6
13	C18:3 D-9,12,15 cis	Methyl linolenate	13.2
14	C20:0	Methyl eicosanoate (=Methyl arachidate)	1.2
15	C22:0	Methyl docosanoate (=Methyl behenate)	1.1
		Σsaturated	33.6
		Σunsaturated	66.0

It was interesting to compare the fatty acids composition with other *Anthemis* or *Cota* species. The scarce reports about fatty acid's profile of *Anthemis* or *Cota* species revealed that hexadecanoic (16:0) (28.8%), (*E,E*)-9,12-octadecadienoic (18:2) (8.6%), (*Z,Z*)-9,12-octadecadienoic (13.2%), 9,12,15-octadecatrienioc (18:3) (16.3%), octadecanoic (18:0) (7.0%) were detected in *A. triumfetti* (L.) DC. [syn.: *Cota triumfetti* (L.) Gay] (58). Butyric acid (C4:0), arachidic acid (C20:0) and palmitoleic acid (C16:1) were found to be the major fatty acids in *A. wiedemanniana* Fisch. & Mey. (59). SFA constituents appeared in higher percentages than MUFA and PUFAs. SFAs were determined as 63.17%, UFAs as 20.89% and PuFAs as 15.95%. Approximately similar amounts (36% and 39%) of palmitic and linoleic acids constituted the main compounds of the stem oil of *A. altissima* L. grown in Iran. In Turkey, *A. dipsacea* Bornm., *A. pseudoculata* Boiss., *A. pectinata* Boiss.& Reute var. *pectinata* oils have been characterized with high percentage of the fatty acids with hexadecanoic acid as main representative of this compounds class (60). *A. arvensis* growing in Serbia showed a high content of palmitic (21.2%) and linoleic (6.5%) acids (61). *A. tinctoria* seed oil contained saturated (2.0%), 18:1 (18.0%), 18:2 (73.0%), 18:2 conjugated (2.0%), 18:3 (0.4%) (62) fatty acids.

CONCLUSION

We herein disclose the first report on chemical composition of the volatile and lipids profiles of endemic species *C. hamzaoglui Özbek & Vural.* This species can be considered as a source of valuable metabolites; the oil is rich with diverse fatty acids, mono- and sesquiterpenes.

ACKNOWLEDGMENTS

REFERENCES

1. Özbek M, Vural M. Distribution and Ecology of Endemic Species of Cota (Asteraceae) in Turkey. BioSystematics Berlin. 2011:21-7.

2. Özbek MU, Vural M, Daskin R. A New Species of the Genus Cota (Asteraceae) from Uludag, Turkey. Turk. J. Bot. 2011;35(4):331-6.

3. Funk VA, Robinson HE. Daisies and Sunflowers: Family Asteraceae. In: Krupnick GA, Kress WJ, editors. Plant Conservation: A Natural History Approach. Chicago and London: University of Chicago Press; 2005. p. 115-24.

4. Altundag E, Ozturk M. Ethnomedicinal Studies on the Plant Resources of East Anatolia, Turkey. Proc. Soc. Behav. Sci. 2011;19:756-77.

5. Silva JAT. Mining the Essential Oils of the Anthemideae. Afr. J. Biotechnol. . 2004;3(12):706-20.

6. Pareek A, Suthar M, Rathore GS, Bansal V. Feverfew (Tanacetum Parthenium L.): A Systematic Review. Pharm. Rev. 2011;5(9):103.

7. Kumar T, Larokar Y, Iyer SK, Kumar A, Tripathi DK. Phytochemistry and Pharmacological Activities of Silybum Marianum: A Review. Int. J. Pharm. Phytopharm. Res. 2017;1(3):124-33.

8. Gupta V, Mittal P, Bansal P, Khokra SL, Kaushik D. Pharmacological Potential of Matricaria Recutita-a Review. Int. J. Pharm. Sci. Drug Res. 2010;2(1):12-6.

9. Applequist WL, Moerman DE. Yarrow (Achillea Millefolium L.): A Neglected Panacea? A Review of Ethnobotany, Bioactivity, and

Biomedical Research. Econ. Bot. 2011;65(2):209.

10. Obolskiy D, Pischel I, Feistel B, Glotov N, Heinrich M. Artemisia Dracunculus L.(Tarragon): A Critical Review of Its Traditional Use, Chemical Composition, Pharmacology, and Safety. J. Agric. Food Chem. 2011;59(21):11367-84.

11. Al-Snafi AE. Medical Importance of Anthemis Nobilis (Chamaemelum Nobile)- a Review. As. J. Pharm. Sci. Technol. 2016 6(2):89-95.

12. Grierson AJ, Yavin Z. Anthemis L. In: Davis PH, editor. Flora of Turkey and the East Aegean Islands. 5. Edinburgh: Edinburgh University Press; 1975. p. 174–221.

13. Greuter W, Oberprieler CH, Vogt R. The Euro+Med Treatment of Anthemideae (Compositae) - Generic Concepts and Required New Names. Willdenowia. 2003;33:40-1.

14. Lo Presti RM, Oppolzer S, Oberprieler CH. A Molecular Phylogeny and a Revised Classification of the Mediterranean Genus Anthemis S.L. (Compositae, Anthemideae) Based on Three Molecular Markers and Micromorphological Characters. Taxon. 2010;59:1441-56.

15. Öztürk M, Uysal I, Gucel S, Altundag E, Dogan Y, Baslar S. Medicinal Uses of Natural Dye-Yielding Plants in Turkey. Res. J. Text. Apparel. 2013;17(2):69-80.

16. Reddish GF. Methods of Testing Antiseptics. J. Lab. Clin. Med. 1929;14(7):649-58.

17. Saroglou V, Dorizas N, Kypriotakis Z, Skaltsa HD. Analysis of the Essential Oil Composition of Eight Anthemis Species from Greece. J. Chrom. A. 2006;1104(1-2):313-22.

18. Javidnia K, Miri R, Kamalinejad M, Sarkarzadeh H, Jamalian A. Chemical Composition of the Essential Oils of Anthemis Altissima L. Grown in Iran. Flav. Fragr. J. 2004;19(3):213-6.

19. Aghajani Z, Masoudi S, Rustaiyan A. Volatile Oils of Anthemis Talyshensis A. Fedor. And Sclerorhachis Platyrachis (Boiss.) Podlech Ex Rech. F. From Iran. J. Essent. Oil Res. 2005;17(4):355-7.

20. Hollá M, Svajdlenka E, Vaverková S, Zibrunová B, Tekel J, Havránek E. Composition of the Oil from the Flowerheads of Anthemis

Tinctoria L. Cultivated in Slovak Republic. J. Essent. Oil Res. 2000;12(6):714-6.

21. Pavlović M, Kovačević N, Tzakou O, Couladis M. Essential Oil Composition of Anthemis Triumfetti (L.) Dc. Flav. Fragr. J. 2006;21(2):297-9.

22. Siasar-Karbasky M, Tehranipour M, Nejad-Shahrokhabadi K. Neuroprotective Effect of N-Butanol, Ethylacetate, Aqueous and Hydro-Alcoholic Fractions of Anthemis Nobilis Extracts through Ngf Gene Expression after Sciatic Nerve Injury in Rats. J. Gorgan Univ. Med. Sci. 2017;18(4):49-54.

23. Shokoohinia Y, Sajjadi S-E, Jassbi AR, Moradi H, Ghassemi N, Schneider B. Sesquiterpenes and Flavonoids of Anthemis Odontostephana Var. Odontostephana. Chem. Nat. Comp. 2015;51(3):491-4.

24. Eser F, Sahin Yaglioglu A, Dolarslan M, Aktas E, Onal A. Dyeing, Fastness, and Cytotoxic Properties, and Phenolic Constituents of Anthemis Tinctoria Var. Tinctoria (Asteraceae). J. Text. Inst. 2017;108(9):1489-95.

25. Maggio A, Riccobono L, Spadaro V, Scialabba A, Bruno M, Senatore F. Chemical Composition of the Essential Oils of Three Endemic Species of Anthemis Sect. Hiorthia (Dc.) R. Fern. Growing Wild in Sicily and Chemotaxonomic Volatile Markers of the Genus Anthemis L.: An Update. Chem. Biodivers. 2014;11(4):652-72.

26. Toplan GG, Tuysuz M, Mat A, Sariyar G. Antibacterial Activity of Anthemis Tricolor Boiss. From Cyprus. Planta Med. Int. Open. 2017;4(S 01):Tu-PO-149.

27. Stojkovic N, Stojkovic M, Marinkovic M, Chopra G, Kostic D, Zarubica A. Polyphenol Content and Antioxidant Activity of Anthemis Cretica L. (Asteraceae). Oxid. Commun. 2014;37(1):237-46.

28. Jassbi AR, Firuzi O, Miri R, Salhei S, Zare S, Zare M, et al. Cytotoxic Activity and Chemical Constituents of Anthemis Mirheydari. Pharm. Biol. 2016;54(10):2044-9.

29. Bardaweel SK, Tawaha KA, Hudaib MM. Antioxidant, Antimicrobial and Antiproliferative Activities of Anthemis Palestina Essential Oil. BMC Compl. Altern. Med. 2014;14(1):297-305.

30. Afifi FU, Kasabri V. Pharmacological and Phytochemical Appraisal of Selected Medicinal Plants from Jordan with Claimed Antidiabetic Activities. Sci. Pharm. 2013;81(4):889-932.

31. Özkaynak S, Kolatan HE, Yilmaz O, Kivcak B. Anti-Inflammatory Activity of Anthemis Aciphylla Var. Aciphylla Boiss. Turk. J. Biol. 2011;35(6):757-62.

32. Wei A, Shibamoto T. Antioxidant/Lipoxygenase Inhibitory Activities and Chemical Compositions of Selected Essential Oils. J. Agric. Food Chem. 2010;58(12):7218-25.

33. Folch J, Lees M, Stanley GHS. A Simple Method for the Isolation and Purification of Total Lipides from Animal Tissues. J. Biol. Chem. 1957;226:497-509.

34. EDQM, Europe Co. Determination of Essential Oils in Herbal Drugs, 2.8.12. 9th ed. Strasbourg: European Directorate for the Quality of Medicines and Healthcare; 2017. 285-6 p.

35. Morrison WR, Smith LM. Preparation of Fatty Acid Methyl Esters and Dimethylacetals from Lipids with Boron Fluoride–Methanol. J. Lipid Res. 1964;5(4):600-8.

36. Babushok V, Linstrom P, Zenkevich I. Retention Indices for Frequently Reported Compounds of Plant Essential Oils. Journal of Physical and Chemical Reference Data. 2011;40(4):043101-47.

37. Noorizadeh H, Farmany A, Noorizadeh M. Application of Ga-Pls and Ga-Kpls Calculations for the Prediction of the Retention Indices of Essential Oils. Química Nova. 2011;34(8):1398-404.

38. Orav A. Identification of Terpenes by Gas Chromatography-Mass Spectrometry: CRC Press.; 2001.

39. Wu S, Xu T, Huang D. Chemical Compositions of the Volatile Extracts from Seeds of Dendranthema Nankingense and Borago Officinalis. J. Food Drug Anal. 2015;23(2):253-9.

40. Maggio A, Rosselli S, Bruno M, Spadaro V, Raimondo FM, Senatore F. Chemical Composition of Essential Oil from Italian Populations of Artemisia Alba Turra (Asteraceae). Molecules. 2012;17(9):10232-41.

41. Careri M, Mangia A. Gas Chromatography-Mass Spectrometry Analysis Oi Flavors and Fragrances. In: Niessen WMA, editor. Current Practice of Gas Chromatography-Mass Spectrometry. New York: CRC Press; 2001. p. 528.

42. Noorizadeh H, Farmany A. Exploration of Linear and Nonlinear Modeling Techniques to Predict of Retention Index of Essential Oils. J. Chinese Chem. Soc. 2010;57(6):1268-77.

43. Küçükbay FZ, Kuyumcu E, Bilenler T, Yıldız B. Chemical Composition and Antimicrobial Activity of Essential Oil of Achillea Cretica L.(Asteraceae) from Turkey. Nat. Prod. Res. 2012;26(18):1668-75.

44. Palá-Paúl J, Brophy J, Goldsack R, Fontaniella B. Analysis of the Volatile Components of Lavandula Canariensis (L.) Mill., a Canary Islands Endemic Species, Growing in Australia. Biochem. Syst. Ecol. 2004;32(1):55-62.

45. Mancini E, Martino LD, Marandino A, Scognamiglio MR, Feo VD. Chemical Composition and Possible in Vitro Phytotoxic Activity of Helichrsyum Italicum (Roth) Don Ssp. Italicum. Molecules. 2011;16(9):7725-35.

46. Özek G, Özbek MU, Yur S, Göger F, Arslan M, Özek T. Assessment of Endemic Cota Fulvida (Asteraceae) for Phytochemical Composition and Inhibitory Activities against Oxidation, a-Amylase, Lipoxygenase, Xanthine Oxidase and Tyrosinase Enzymes. Rec. Nat. Prod. 2018;http://doi.org/10.25135/rnp.109.18.09.875 (in press).

47. Kurtulmus A, Fafal T, Mert T, Saglam H, Kivcak B, Ozturk T, et al. Chemical Composition and Antimicrobial Activity of the Essential Oils of Three Anthemis Species from Turkey. Chem. Nat. Comp. 2009;45(6):900-4.

48. Javidnia K, Miri R, Kamalinejad M, Sarkarzadeh H, Jamalian A. Chemical Composition of the Essential Oils of Anthemis Altissima L. Grown in Iran. Flavour Fragr. J. 2004;19(3):213-6.

49. Vujisić L, Vučković I, Tešević V, Đoković D, Ristić M, Janaćković P, et al. Comparative Examination of the Essential Oils of Anthemis Ruthenica and A. Arvensis Wild-Growing in Serbia. Flavour Fragr. J. 2006;21(3):458-61.

50. Başer KHC, Özek T, Demirci F, Boydağ İ. The Essential Oil of Antltemis Cretica L. Subsp. Leucanthemoides (Boiss.) Grierson. ACTA Pharm. Sci. 2002;44(3):189-94.

51. Hanbali EF, Mellouki F, Akssira M, MA B. Composition and Antimicrobial Activity of Essential Oil of Anthemis Tenuisecta Ball. J. Essent. Oil Beariing Plants. 2007;10(6):499-503.

52. Pavlović M, Kovačević N, Tzakou O, Couladis M. Essential Oil Composition of Anthemis Triumfetti (L.) Dc. Flavour Fragr. J. 2006;21(2):297-9.

53. Sajjadi SE, Mehregan I. Volatile Constituents of Flowers and Leaves of Anthemis Hyalina. Chem. Nat. Comp. 2006;42(5):531-3.

54. Kilic O, Kocak A, Bagci E. Composition of the Volatile Oils of Two Anthemis L. Taxa from Turkey. Z. Naturforschung C. 2011;66(11-12):535-40.

55. Uzel A, Guvensen A, Cetin E. Chemical Composition and Antimicrobial Activity of the Essential Oils of Anthemis Xylopoda O. Schwarz from Turkey. J. Ethnopharm. 2004;95(2):151-4.

56. Kivcak B, Mert T, Saglam H, Ozturk T, Kurkcuoglu M, Baser K. Chemical Composition and Antimicrobial Activity of the Essential Oil of Anthemis Wiedemanniana from Turkey. Chem. Nat. Comp. 2007;43(1):47-51.

57. Radulović NS, Blagojević PD, Zlatković BK, Palić RM. Chemotaxonomically Important Volatiles of the Genus Anthemis L.–a Detailed Gc and Gc/Ms Analyses of Anthemis Segetalis Ten. From Montenegro. J. Chin. Chem. Soc. 2009;56(3):642-52.

58. Pavlovic M, Kovacevic N, Tzakou O, Couladis M. Components of Cyclohexane Extract of Anthemis Triumfetti. Chem. Nat. Comp. . 2007;43(5):512-4.

59. Gönenç TM, Akkol EK, Süntar I, Erdoğan TF, Kıvçak B. Fatty Acid Composition and Preclinical Resarches on Anthemis Wiedemanniana Fisch. & Mey.: Discovery of a New Anti-Inflammatory Agent. Pharmacognosy Magazine. 2014;10(37):53-60.

60. Kurtulmus A, Fafal T, Mert T, Saglam H, Kivcak B, Ozturk T, et al. Chemical Composition and Antimicrobial Activity of the Essential Oils of Three Anthemis Species from Turkey. Chem. Nat. Comp. 2009;45(6):900-4.

61. Vujisic L, Vuckovic I, Tesevic V, Dokovic D, Ristic MS, Janackovic P, et al. Comparative Examination of the Essential Oils of Anthemis Ruthenica and A. Arvensis Wild-Growing in Serbia. Flav. Fragr. J. 2006;21(3):458-61.

62. Azimova SS, Glushenkova AI. Anthemis Tinctoria L.(Cota Tinctoria (L.) J. Gay) Var. Kelwayi. In: Azimova SS, Glushenkova AI, editors. Lipids, Lipophilic Components and Essential Oils from Plant Sources. New York: Springer Science + Business media; 2012. p. 52-.

Concentrations of Environmental Radioactivity in Sediment Cores from Kulakcayiri Lake

Erol KAM[1]* ✉ iD **, Zeki U. YUMUN**[2] ✉ iD **, Gulderen ACIKGOZ**[1] ✉ iD **, Kubra BAYRAK**[1] ✉ iD
1: Yildiz Technical University, Faculty of Sciences, Physics Dep., Istanbul, Turkey.

2: Namik Kemal University, Corlu Engineering Faculty, Environ. Engineering Dep., Tekirdag, Turkey.

Abstract: This paper is about measurements of environmental radioactivity in samples taken from a lake bed and from different depths. The study is based on gamma spectrometric analysis of some radioisotopes encountered in sediment samples. For this purpose, sediments that have accumulated for thousands of years were used. Three core samples were taken from Kulakcayiri lake by drilling and taken from heights of 5-5.5 m, 10-10.5 m and 15-15.5 m at the same point and then moved to the laboratory. The analyses of the samples were carried out in the laboratory with the semiconductor HPGe detector. According to the results, the K-40 concentrations of the samples were 325 ± 18 Bq/kg, 353 ± 19 Bq/kg and 367 ± 19 Bq/kg, while their Th-232 concentrations were 38 ± 6 Bq/kg, 43 ± 6 Bq/kg and 42 ± 6 Bq/kg, respectively. Their concentrations of Ra-226 were calculated as 29 ± 5 Bq/kg, 26 ± 5 Bq/kg and 26 ± 5 Bq/kg, while the Cs-137 concentrations of the three samples were calculated as ≤MDA (Minimum Detectable Activity) and existed at very low concentrations. The average activities of K-40, Th-232, Ra-226 and Cs-137 were found to be about 348 ± 186 Bq/kg, 41 ± 6.3 Bq/kg, 27 ± 5.1 Bq/kg and ≤MDA, respectively. The results were compared with those of similar studies. These findings and assessments are expected to be an example for future studies and to be of reference quality.

Cite this: Kam E, Yumun ZU., Acıkgoz G, Bayrak K. Concentrations of Environmental Radioactivity in Sediment Cores from Kulakcayiri Lake. JOTCSA. 2018; 5(3): 1371-1374.

INTRODUCTION

The radioactivity levels of the Earth are influenced by natural and artificial pathways. Unstable elements in the earth emit radioactive rays, which increase natural radioactivity levels. The best example of natural radioactivity is uranium decay. Artificial radioactivity occurs when stable isotopes in nature become unstable as a result of exposure to radiation. Radioactive substances emit alpha (α), beta (β) and gamma (γ) rays (1).

Natural radioactivity on Earth originates from cosmic rays, gamma rays from the Earth, radon gases in the air and in drinking water and radionuclides present in food and beverages. There is no way to reduce natural background radiation. However, the accumulated concentration of radon gas in houses can be easily reduced by ventilation (2).

There are many factors that increase the levels of radioactivity on Earth, especially nuclear power-plant accidents. Atmospheric, aquatic, and underground nuclear weapon tests, as well as nuclear reactor explosions, are activities that initiate radioactive pollution (3). Considering their possible effects on human health, it is important to investigate radioactivity in populated regions. Water, soil, food and sediments have been investigated under radioactive pollution studies.

Our study investigated the natural radioactivity levels in sediments of Kulakcayiri lake using a gamma spectrometer. Considering its proximity to the 3rd airport that will be built in Istanbul, the region around the lake is expected to become highly active in the coming years. It will be difficult to conduct a radioactivity study in this region in the future because it will become more intensely developed. For these reasons, it is expected that our work will provide a basis for future work, as well as an example for future generations.

STUDY AREA

The study area is Kulakcayiri lake, which is located in the Arnavutkoy district in Istanbul and covers approximately 500 hectares (4). Kulakcayiri lake, which is considered to be one of the great lakes of the Marmara region in the past, is a shallow lake; it used to be possible to picnic and fish along its borders, but it is now dried up. The 3rd Airport Project plans to occupy the current site of the Lake. The location map of the study area is shown in Figure 1.

Figure 1. Location Map of Study Area (5).

MATERIAL AND METHODS

Sample collection
A core was taken from a suitable spot in Kulakcayiri Lake. Sample were collected from the core at depths of approximately 5, 10 and 15 m. The co-ordinates of the samples were recorded, and the samples were named and moved to the laboratory. The coordinates of the sediment samples are shown in Figure 1.

Table 1. Locations of the samples (5)

	SAMPLE NO	X (East)	Y(North)
Kulakcayiri Lake	BH-1	645459.77	4572767.77
	BH-2	645529.00	4572399.00
	BH-3	645511.81	4572001.24

Sample preparation for radioactivity measurements
The sediment samples were taken from the study area and brought to the laboratory. They were dried for approximately 1 week at room temperature to solidify their muddy consistency. The sediments were dried in an oven for approximately 2 days at 50 °C to remove as much moisture as possible. The dried sediment samples were separately ground without mixing with each other. The samples were milled until powdered and transferred to 170 mL Marinelli beakers with standard geometry. The samples were then left to stand in the Marinelli beakers for approximately 40 days at room temperature to form radon-disintegration products and to reach equilibrium. At the end of this entire procedure, the samples were prepared for counting.

Measurement Methodology

The gamma-spectrometric analyses were performed with a high-purity, germanium-doped HPGe detector (Canberra GX5020). The instrument was calibrated prior to analysis in accordance with the geometry of the Marinelli beakers that held the samples. After calibrating, each sample was counted for approximately 1-1.5 days, and their concentrations were calculated in terms of Bq/kg (6).

RESULTS AND DISCUSSION

The gamma-spectrometry results of the core samples from Kulakcayiri lake provide information about the radioactivity levels of this region for the literature. The analysis results are shown in Table 2. According to Table 2, the concentrations of K-40 were calculated as 325 ± 18 Bq/kg, 353 ± 18 Bq/kg and 367 ± 19 Bq/kg, with an average value of 348 Bq/kg. Their Th-232 concentrations were calculated as 38 ± 6.2 Bq/kg, 43 ± 6.6 Bq/kg and 42 ± 6.5 Bq/kg, with an average value of approximately 41 Bq/kg. In addition, the measured Ra-226 activity values were 29 ± 5.4 Bq/kg, 26 ± 5.1 Bq/kg and 26 ± 5.1 Bq/kg, with an average value of approximately 27 Bq/kg. The activity of Cs-137 is below the minimum detectable activity (MDA) value for all sediment samples.

Table 2. Activity concentrations of K-40, Th-232, Ra-226 and Cs-137 in sediment samples (Bq/kg)

Sample Location	Activity (Bq/kg)			
	K-40	Th-232	Ra-226	Cs-137
BH-1	325±18	38±6.2	29±5.4	≤MDA
BH-2	353±18	43±6.6	26±5.1	≤MDA
BH-3	367±19	42±6.5	26±5.1	≤MDA

The analysis results showed that the activity of K-40 was significantly higher than those of the other radionuclides (Figure 2).
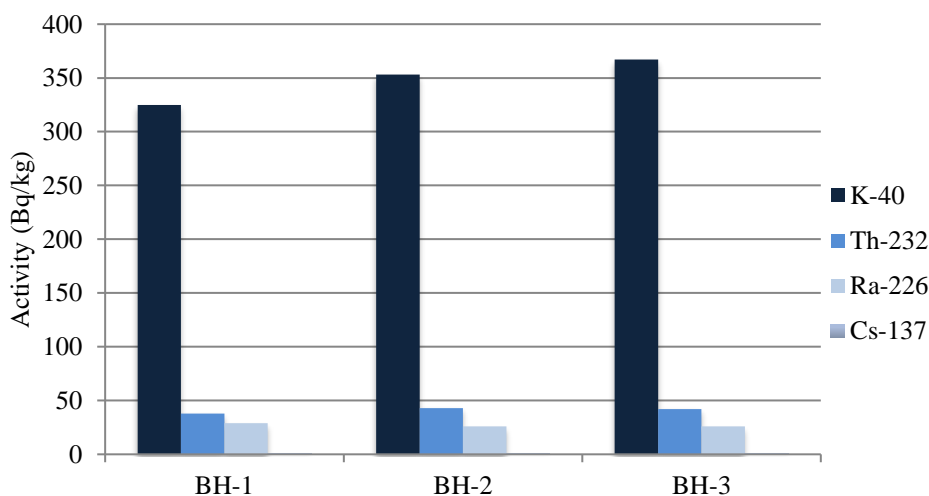

Figure 2. Distribution of Activity Concentrations.

CONCLUSION

This study was carried out in order to determine the natural radioactivity levels of the natural Kulakcayiri lake. This study started with the extraction of 3 sediment samples by sounding. Gamma spectrometric analyses were then performed using the HPGe detector, and the activities of the various radionuclides were calculated. The results of this study were compared with similar studies in other countries (Table 3).

Table 3. Comparison of Radioactivity Concentrations of Kulakcayiri Lake Sediments with Other Works.

Sample Stations	Activity (Bq/kg)				
	K-40	Th-232	Ra-226	Cs-137	References
Ionian Sea, Albania*	266-675	13-40	14-27	3-38	(7)
Hunza, Gilgit and Indus Rivers,** Pakistan	173-825	12-172	174-825	-	(8)
Miami Bay,*** Malaysia	314-495	37-5622	24-2641	-	(9)
Niger Delta, Nigeria ****	96-530	12-40	13-46	-	(10)
Algeria *****	56-607	7-32	-	2-9	(11)

*(Tsabarisa et al., 2007), ** (Shuaibu et al., 2017), ***(Qureshi et al., 2014), ****(Agbalagba et.all, 2011), ***** (Noureddıne et al., 2003)

In this study, we examined the radioactivity levels of the lake. The results of the study showed that the activity of the fission product Cs-137 fell below the MDA value, while the concentration of K-40 was found to be higher than those of the other radionuclides.

REFERENCES

1. Anonymous. Öğrenci Köşesi [Internet]. Bölüm 3 - Radyasyon "Radyasyon ve Biz." [cited 2018 Dec 15]. Available from: http://www.taek.gov.tr/ogrenci/sf3.html

2. Anonymous. Radiation, human and environment. International Atomic Energy Agency; 2009. pp. 1–81.

3. Anonymous. Radioactive particles in the environment: Sources, particle characterization and analytical techniques. Vienna: International Atomic Energy Agency; 2011. pp. 1–77.

4. Anonymous. Google Maps Coordinate [Internet]. Google, Inc.; [cited 2018 Dec 14]. Available from: https://www.google.com.tr/maps/dir/41.294 2296,28.7400292/41.3145205,28.7520213/ @41.3110729,28.7320163,14z/data=!4m2!4 m1!3e2

5. Kam E, Yümün ZÜ, Önce M, Acikgoz G. Gamma Dose Rate Values In The Kulakçayiri Natural Lake And The Vicinity (Arnavutköy, İstanbul). Journal of Engineering Technology and Applied Sciences. 2016;1(1):29–33.

6. Kurt D, Yümün Z, Barut I, Kam E. Distribution of Gamma Radiation Levels in Core Sediment Samples in Gulf of Izmir: Eastern Aegean Sea, Turkey. World Academy of Science, Engineering and Technology, International Journal of Environmental, Chemical, Ecological, Geological and Geophysical Engineering. 2016;10(3):392–6.

7. Tsabaris C, Eleftheriou G, Kapsimalis V, Anagnostou C, Vlastou R, Durmishi C, et al. Radioactivity levels of recent sediments in the Butrint Lagoon and the adjacent coast of Albania. Applied Radiation and Isotopes. 2007;65(4):445–53.

8. Qureshi AA, Tariq S, Din KU, Manzoor S, Calligaris C, Waheed A. Evaluation of excessive lifetime cancer risk due to natural radioactivity in the rivers sediments of Northern Pakistan. Journal of Radiation Research and Applied Sciences. 2014;7(4):438–47.

9. Shuaibu HK, Khandaker MU, Alrefae T, Bradley D. Assessment of natural radioactivity and gamma-ray dose in monazite rich black Sand Beach of Penang Island, Malaysia. Marine pollution bulletin. 2017;119(1):423–8.

10. Agbalagba E, Onoja R. Evaluation of natural radioactivity in soil, sediment and water samples of Niger Delta (Biseni) flood plain lakes, Nigeria. Journal of Environmental Radioactivity. 2011;102(7):667–71.

11. Noureddine A, Benkrid M, Hammadi A, Boudjenoun R, Menacer M, Khaber A, et al. Radioactivity distribution in surface and core sediment of the central part of the Algerian Coast: An estimation of the recent sedimentation rate. Mediterranean Marine Science. 2003;4(2):53–8.

RESEARCH ARTICLE

Synthesis of a Novel Benzimidazole Moiety-Appended Schiff Base Derivative: Fluorescence and Chemosensor Study

Pinar Sen[a,b]* ✉, **S. Zeki Yildiz[a]** ✉, **Necmi Dege[c]** ✉, **Göknur Yasa Atmaca[d]** ✉, **Ali Erdogmus[d]** ✉, **Mustafa Dege[e]** ✉

[a]Sakarya University, Faculty of Arts and Sciences, Department of Chemistry, 54187, Sakarya,Turkey
[b]Centre for Nanotechnology Innovation, Department of Chemistry, Rhodes University, Grahamstown, 6140, South Africa
[c]Ondokuz Mayıs University, Faculty of Arts and Sciences, Department of Physics, 55139 Samsun, Turkey
[d]Department of Chemistry, Yildiz Technical University, 34210 Esenler, Istanbul, Turkey
[e]Spraying Systems Company, Kaya Aldoğan sok. No: 3/3 34394 Zincirlikuyu Şişli-İstanbul, Turkey

Abstract: In this study, we synthesized a novel benzimidazole-based Schiff base; (E)-4,4'-methylenebis(2-((E)-(((1H-benzo[d]imidazol-2-yl)methyl)imino)methyl)phenol) (**3**) was synthesized by the condensation of 5,5'-methylenebis(2-hydroxybenzaldehyde) (**1**) and (1H-benzo[d]imidazol-2-yl)methanamine.HCl salt (**2**). This Schiff base derivative was reported for the first time and fully characterized by common spectroscopic techniques. Absorption and fluorescence spectroscopy were recorded to determine the sensing ability of **3** towards metal ions. Selectivity to Zn^{2+} ion among studied other cations was detected. The crystal structure of **2**, $C_8H_{13}Cl_2N_3O$, has been determined by single crystal X-ray diffraction method. The crystal structure of the title compound, $C_8H_{11}N_3^{2+} \cdot 2(Cl^-) \cdot H_2O$, consists of an organic 1H-benzoimidazol-3-ium ($C_8H_{11}N_3^{2+}$) cation, an inorganic $2(Cl^-)$ anion and one water (H_2O) molecule. In the cation of studied compound, $C_8H_{11}N_3^{2+}$, the benzimidazole ring is almost planar with a maximum deviation of -0.012 (3) Å. The molecule crystallized in the monoclinic structure and the space group $P2_1/c$. The crystalline stacking structure is stabilized by intramolecular N–H···Cl, N–H···O, the intermolecular N–H···Cl hydrogen bond interactions connection the molecules into a two dimensional network and between anions and the water molecules. π-π interaction between benzimidazole rings [centroid–centroid lengths = 3.4642 (2) Å, 3.5309 (2) Å and 3.5527 (2) Å] may further stabilize the structure.

INTRODUCTION

Benzimidazole derivatives have aroused interest in recent years. Researches on this heterocyclic compounds have been carried on increasingly (1). Benzimidazole derivatives are widely used due to their biological activities such as anticancer, antiulcers, antifungals, anti-inflammatory agents, antimycobacterials, and antioxidants (2-7). In addition to their biological importance, these ligands are strongly coordinating agents forming complexes with metal ions (8,9).

The benzimidazole derivatives are also important chromophores among organic fluorescent compounds containing aromatic

heterocyclic (10). Essentially the benzimidazole skeleton could be modified in order to enhance their physico-chemical properties.

Besides benzimidazoles, Schiff bases which have great interest due to possess the imine (C=N) group, have potential applications in analytical chemistry and in medicine to cure some diseases as anti-inflammatory, anticancer, antifungal agents (11,12). Schiff base derivatives are also effective molecules used for the optical detection of metal ions due to the presence of the imine group (13).

The design and synthesis of fluorescent sensors which are sensitive to metal ions is a one of the essential research area in chemistry (14). One of the reasons is more advantageous to traditional methods. It is a method that determines easy and inexpensive detection.

A good number of fluorescent receptors have been explored since they have high sensitivity for metal ion (15). Among these, the samples containing benzimidazole unit and Schiff base combination are limited (16, 17).

Development of fluorescent chemosensors capable of selectively determining Zn^{2+} ion has also been an dynamic subject among the studied metal ions recently (18). The Zn^{2+} is a crucial mineral that has an effect on the biological processes in the human body (19). The sensitivity of the sensors is measured by spectroscopically determining changes in their physical properties when encountered with the analyte.

Thus, we report herein the compound **1**, displaying a combination of benzimidazole moiety and bis-aldehyde to form Schiff base derivative that can act as a chemosensor.

We describe the synthesis and characterization of the synthesized benzimidazole-based Schiff base derivative and selectivity towards some cations was studied. The chemosensor behaviors to metal ions (Zn^{+2}, Cd^{+2}, Pb^{2+}, Hg^{+2}, Ba^{2+} and Sb^3) were also studied by absorption and fluorescence spectroscopy.

EXPERIMENTAL

Chemicals and instruments
The following chemicals were obtained from Sigma-Aldrich; 2-hydroxybenzaldehyde, 1,3,5-trioxane, 1,2-phenylenediamine, glycine, hydrochloric acid (HCl), acetic acid (AcOH), sulfuric acid (H_2SO_4), acetonitrile, n-hexane, ethylacetate, dimethylformamide

(DMF), chloroform ($CHCl_3$), methanol (MeOH), ethanol (EtOH), diethyl ether, and K_2CO_3. All solvents were stored over molecular sieves (4 Å) after they were dried and purified as described by Perrin and Armarego (20). Oxygen- free inert atmosphere was supplied by argon through dual-bank vacuum-gas manifold system. Deionized water was generated from MILLIPORE ultra-pure water supply system. Thin-Layer chromatography (TLC) was performed using silica gel 60-HF254 as an adsorbent. Column chromatography was performed with silica gel (Merck grade 60). Electronic spectra were recorded on a Hitachi U-2900 spectrophotometer with quartz cell of 1 cm. Fluorescence spectra were recorded from Hitachi F-2710 spectrofluorometer. Infrared spectra were acquired on a Perkin Elmer Spectrum two FT-IR spectrometer equipped with Perkin Elmer UATR-TWO diamond ATR and corrected by applying the ATR-correction function of Perkin Elmer Spectrum software. ^{1}H and ^{13}C NMR spectra were recorded a Varian Mercury Plus 300 MHz spectrometer. For MALDI-TOF spectra, the experiments were carried out using a Bruker microTOF (Germany) in Gebze Technical University. 2-aminomethylbenzimidazole dihydrochloride (ambmz·2HCl) and 5,5'-methylenebis(2-hydroxybenzaldehyde) were prepared as described previously (21,22).

Synthesis

(E)-4,4'-methylenebis(2-((E)-(((1H-benzo[d]imidazol-2-yl)methyl)imino)methyl) phenol) (3)
An aqueous solution of ambmz·2HCl (0.78 g, 4.29 mmol in 10 mL) was neutralized by adding aqueous K_2CO_3 solution (0.712 g, 5.2 mmol). A methanolic solution of 5,5'-methylenebis(2-hydroxybenzaldehyde) (0.5 g, 1.95 mmol in 20 mL) was added drop-wise to the above solution with stirring in 1 h. During this period, yellow precipitation slowly formed. The precipitation was then filtered, washed thoroughly with water followed by ethanol/water mixture (1/1) and dried in vacuum. The desired pure compound (**3**) was obtained as a yellow powder in sufficient purity. Yield: 84% (0, 87 g). FT-IR (UATR-TWO^{TM}) ν max/cm^{-1}: 3470 (OH), 3366 (NH), 3055-2647 (C-H (Ar) and intermolecular H bonding), 2979-2836 (Aliph., C-H), 1613 (C=N), 1569 (C=C), 1485-1358 (C-C), 1271 (Asym., Ar-O), 1208 (C-N), 1154 (Sym., Ar-O), 789, 748. UV–Vis (DMF): λmax (nm) (log ε) 262 (3.56), 294 (3.87), 324 (4.13). ^{1}H-NMR ($CHCl_3$) δ (ppm) : 12.65 (s, 2H), 10.92 (s, 2H), 8.47 (s, 1H), 8.37 (s, 1H), 7.36-7.30 (m, 4H), 7.25-7.20 (m, 2H), 7.17-7.08 (m, 2H), 7.02 (s, 2H), 6.97-6.86 (m, 4H), 5.06 (d, 4H), 3.92 (d, 2H). ^{13}C-NMR ($CHCl_3$) δ (ppm) :

160.50 (C=N), 159.53 (C12), 137.89 (C4), 133.65 (C3), 132.22 (C10), 131.20 (C9), 122.80 (C8), 120.70 (C7), 118.73 (C1), 118.25 (C11), 117.29 (C2), 57.55 (C5), 29.88 (C13). MS (MALDI-TOF): m/z 517.882 $[M+1]^+$.

X-Ray Crystal Structure Determination

A suitable single crystal with dimensions 0.55 × 0.44 × 0.24 mm was chosen for the crystallographic study and then carefully mounted on goniometer of a STOE IPDS II diffractometer. Data collection of the title compound, $C_8H_{13}Cl_2N_3O$, was performed with STOE IPDS II single crystal X-ray diffractometer using graphite monochromated Mo Kα radiation (λ = 0.71073 Å) at room temperature (296 K). Details of the data collection conditions and parameters of refinement process are given in Table 1. Cell parameters were obtained by using X-AREA (23) and data reduction was achieved with X-RED32 (23) software. The maximum peaks and deepest hole observed in the final Δρ map were 0.77 and −0.39 e Å $^{-3}$, respectively. The scattering factors were taken from SHELXL-97 (24). The molecular graphics were done using ORTEP-3 for Windows (25). All non-hydrogen

atoms were refined anisotropically. H atoms were positioned geometrically, with N-H = 0.86 Å (for NH and NH_3) and C-H = 0.93 Å for aromatic H, respectively, and constrained to ride on their parent atoms, with Uiso(H) = 1.2Ueq(C,N). The coordinates of the H atoms of the water molecule were determined from a difference Fourier map and refined isotropically subject to a restraint of O–H = 0.82 Å. The general-purpose crystallographic tool PLATON (26) was used for the structure analysis. WinGX (27) was used to prepare the data for publication. Details of the data collection conditions and the parameters of refinement process are given in Table 1.

CCDC 1474738 contains supplementary crystallographic data (excluding structure factors) for the compound reported in this article. These data can be obtained free of charge via http://www.ccdc.cam.ac.uk/deposit [or from the Cambridge Crystallographic Data Center (CCDC), 12 Union Road, Cambridge CB2 1EZ, UK; fax: +44(0)1223 336033; e-mail: deposit@ccdc.cam.ac.uk].

Table 1. Crystallographic data and refinement parameters for the compound, $C_8H_{13}Cl_2N_3O$

Crystal data

Chemical moiety formula	$C_8H_{11}N_3{}^{2+} \cdot 2(Cl^{1-}) \cdot H_2O$
Chemical sum formula	$C_8H_{13}Cl_2N_3O$
M_r	238.11
Crystal system, space group	Monoclinic, $P2_1/c$
Temperature (K)	296
a, b, c (Å)	6.9580 (3), 12.1395 (6), 25.1958 (11)
β (°)	90.402 (4)
V (Å³)	2128.15 (17)
Z	8
Radiation type	Mo Kα
μ (mm^{-1})	0.58
Crystal size (mm)	0.55 × 0.44 × 0.24

Data collection

Diffractometer	STOE IPDS 2
Absorption correction	Integration X-RED32 (Stoe & Cie, 2002)
T_{min}, T_{max}	0.730, 0.897
No. of measured, independent and observed [$I > 2\sigma(I)$] reflections	13266, 4405, 2254
R_{int}	0.123
(sin θ/λ)$_{max}$ (Å^{-1})	0.628
Refinement	
$R[F^2 > 2\sigma(F^2)]$, $wR(F^2)$, S	0.067, 0.164, 0.84
H-atom treatment	H atoms treated by a mixture of independent and constrained refinement
$\Delta\rho_{max}$, $\Delta\rho_{min}$ (e Å^{-3})	0.77, −0.39

RESULT AND DISCUSSION

Synthesis and spectroscopic characterization
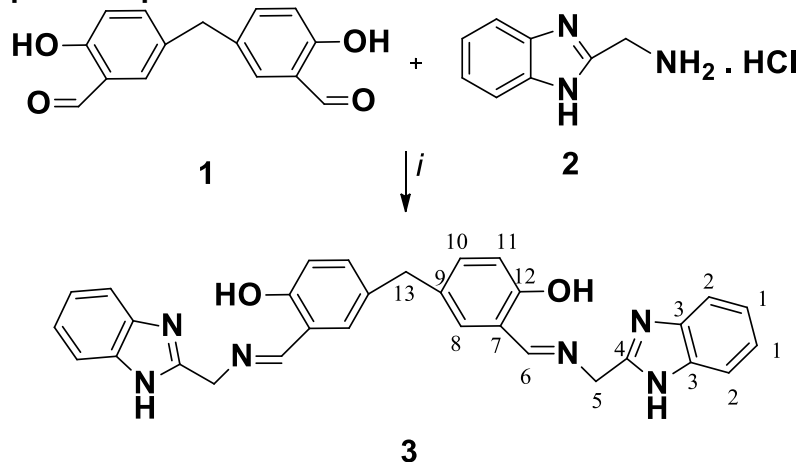
Scheme 1. Synthesis of target compound: (i) K_2CO_3, water, methanol.

As a first step, 5,5'-methylenebis(2-hydroxybenzaldehyde) (**1**) was obtained with the reaction of salicylaldehyde and 1,3,5-trioxane in the presence of a mixture of conc. H_2SO_4 and AcOH in good yield according to the reported literature (21). The reaction of the other precursor (**2**) was conducted in 5.5 M HCl with the condensation reaction of glycine and 1,2-phenylenediamine (22).

The new bis-Schiff-base ligand (**3**) was synthesized by Schiff-base condensation as stated in Scheme 1. 5,5'-methylenebis(2-hydroxybenzaldehyde) (**1**) reacted with 2-aminomethylbenzimidazole dihydrochloride (ambmz·2HCl) in methanol/water in the presence of K_2CO_3 for neutralization to afford the product **3.** The expected chemical structure was proved by spectroscopic methods such as FT-IR, ^{1}H-NMR, ^{13}C-NMR and MS analysis. The analysis results confirmed the expected structure.

When the FT-IR spectrum is evaluated comparatively, the carbonyl vibration at 1655 cm^{-1} and the C–H vibrations of aldehyde group at 2857 cm^{-1} and 2743 cm^{-1} arising from **1** were disappeared after the conversion completed to give **3**. Formation of benzimidazole-based Schiff base was also supported by the appearance of imine band at 1613 cm^{-1} and –NH stretching at 3366 cm^{-1} that the condensation reaction occurred to give **3**.

The electronic absorption spectra of **1** and **3** in DMF are shown in Figure 1. 5,5'-methylenebis(2-hydroxybenzaldehyde) (**1**) presented two absorptions at 266 and 332 nm in DMF in the UV-Vis spectrum. The UV-Vis spectrum of **3** showed three absorption maxima at 262, 294 and 324 nm. The observed broad maximum at 345 nm could be attributed to the n-п* transition of the azomethine group while the bands at 262 and 294 nm refer to the п- п* transitions in the UV-Vis spectrum of **3** (28).
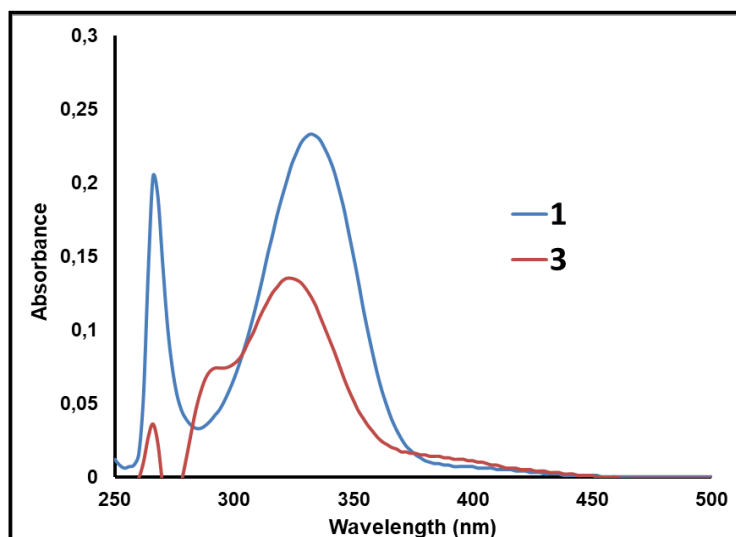
Figure 1. UV-Vis spectra of **1** and **3** in DMF. (Concentration 1×10^{-5} mol.L^{-1})

The ^{1}H-NMR data provided sufficient information for characterization of the target structure (**3**). When compared the ^{1}H-NMR spectra of compound **1** and **3**, the disappearances of HC=O proton signal of 5,5'-methylenebis(2-hydroxybenzaldehyde) (**1**) and the appearance of new peaks in aromatic region at 8.47 ppm and 8.37 ppm belongs to the imine protons and the -NH peak at 10.92 ppm shows that the imine condensation reaction has occurred. The other characteristic peak was observed at 5.06 ppm related to methylene group of the benzimidazole unit (in supporting information).

In the ^{13}C-NMR spectrum of **3** the presence of the peaks at 160.50 ppm and 159.53 ppm are attributed to the carbon atoms of the imine are the obvious differences from **1**. For the ^{13}C-NMR spectrum of **3,** the carbon atom arising from methylene group of benzimidazole was observed at 57.55 ppm (in supporting information).

The mass spectrum of **3** confirmed the expected structure with the result obtained from MALDI-TOF Mass spectrometer. The mass spectrum of **3** gave the molecular ion peaks at m/z: 517.882 $[M+1]^+$ clearly illustrating the formation of final compound.

Description of the crystal structures
The ORTEP diagram of the crystal structure, 2-(ammoniomethyl)-1H-benzoimidazol-3-ium chloride hydrate, $C_8H_{13}Cl_2N_3O$ with thermal ellipsoids drawn at a 40% probability is shown in Figure 2.

The experimental geometric parameters and hydrogen bonding given in Tables 1 and 2, respectively. The molecular structure of the title compound is illustrated in Fig. 1. The asymmetric unit of '$C_8H_{13}Cl_2N_3O$' contains one (O–H···Cl), two (N–H···O) and five (N–H···Cl) intramolecular hydrogen bonds (Figure 2).

Table 2. Hydrogen bond properties (Å, º) for $C_8H_{13}Cl_2N_3O$.

D—H···A	D—H	H···A	D···A	D—H···A
N3—H3B···Cl4[i]	0.87 (2)	2.46 (3)	3.282 (5)	156 (4)
N3—H3A···Cl1[ii]	0.87 (2)	2.27 (2)	3.130 (5)	170 (5)
N3—H3C···Cl3	0.87 (2)	2.33 (4)	3.111 (5)	149 (5)
N6—H6A···Cl4	0.87 (2)	2.24 (2)	3.113 (5)	176 (5)
N6—H6C···Cl1[iii]	0.88 (2)	2.41 (2)	3.265 (4)	165 (4)
N6—H6B···Cl2	0.86 (2)	2.32 (3)	3.111 (5)	152 (5)
O1—H1A···Cl2	0.84 (2)	2.29 (2)	3.131 (4)	171 (6)
O2—H2A···Cl3	0.84 (2)	2.36 (3)	3.157 (4)	160 (6)
N2—H2C···Cl1	0.85 (2)	2.28 (2)	3.101 (4)	161 (4)
N1—H1C···O1	0.85 (2)	1.94 (3)	2.755 (5)	161 (6)
N4—H4A···O2	0.86 (2)	1.90 (2)	2.753 (5)	171 (5)
N5—H5A···Cl4[iv]	0.84 (2)	2.30 (2)	3.141 (4)	173 (4)

Symmetry codes: (i) $x+1, y, z$; (ii) $-x+2, y-1/2, -z+3/2$; (iii) $-x+1, y-1/2, -z+3/2$;
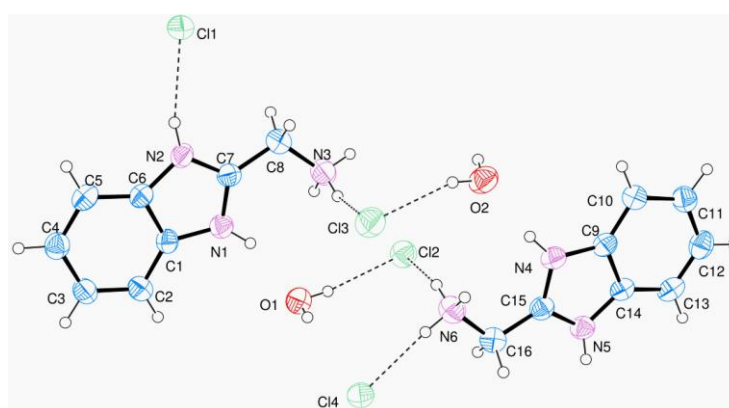(iv) $-x,-y+1, -z+1$.

Figure 2. ORTEP plot of the $C_8H_{13}Cl_2N_3O$. View of the title compound, with displacement ellipsoids for non-H atoms drawn at the 40% probability level. The intramolecular hydrogen bond for asymmetric unit is shown as a dashed line.

The r.m.s. departure of the molecule's benzimidazolium rings are 0.0071 Å for N1/C1/C2/C3/C4/C5/C6/N2/C7 (ring1), 0.0108 Å for N4/C9/C10/C11/C12/C13/C14/N5/C15 (ring2). The dihedral angle between benzimidazolium rings (ring1/ring2) is 1.156 (0.128) Å. These benzimidazolium rings are almost planar. The maximum deviation of the ring1 ring2 from planarity is -0.014 (3) Å for atom C7, 0.016 (1) Å for atom, respectively. The aromatic C–C distances for ring1 and ring 2 range from 1.3754(1) Å to 1.4145(1) Å and

from 1.3626(1) Å to 1.4040(1) Å, respectively. Geometric structure of all benzimidazolium rings is the same; particularly, the C7—N1 bond length is identical to the C15—N4 length [mean =1.332 (5) Å], while the C7—N2, C15—N5 lengths are also not significantly different [mean =1.337 (2) Å]. These values are consistent with the C7—N1 and C15—N4 bonds possessing more double-bond character than the C7—N2 and C15—N5 bonds (Table 3). This obtained bonds length is in a good accordance with previously reported values by Zheng *et al.* (29), Cui (30) and *Li et al.* (31).

Table 3. Selected bond lengths (Å) and angles (°) for $C_8H_{13}Cl_2N_3O$

Bond lengths (Å)			
N2—C7	1.334 (5)	N3—C8	1.447 (6)
N5—C15	1.340 (5)	N6—C16	1.446 (6)
N1—C7	1.332 (5)	C15—C16	1.482 (6)
N4—C15	1.332 (5)		
Bond angles (º)			
N1—C7—C8	128.2 (4)	N5—C15—C16	123.4 (4)
N2—C7—C8	122.8 (3)	N6—C16—C15	113.5 (4)
N4—C15—C16	127.0 (4)	N3—C8—C7	112.7 (4)
Torsion angles (º)			
C1—N1—C7—C8	−175.7 (4)	N4—C15—C16—N6	5.3 (7)

| C6—N2—C7—C8 | 175.9 (4) | N5—C15—C16—N6 | −178.2 (4) |
| C9—N4—C15—C16 | 175.6 (4) | N1—C7—C8—N3 | −6.1 (7) |
| C14—N5—C15—C16 | −176.1 (4) | N2—C7—C8—N3 | 176.6 (4) |

The crystal stacking of studied composite is stabilized by intramolecular hydrogen bonds, [(O−H···Cl), (N−H···O), (N−H···Cl)], intermolecular hydrogen bonds, (N−H···Cl) and intermolecular π-π stacking interactions between C1-C6 phenyl rings and C1/N1/C7/N2/C6 imidazole rings (Table 2, Figure 2 and Figure 3).

Two O atoms and six N atoms of the compound include hydrogen bonds, as shown in Table 2. The 1H-benzoimidazole cation adopts a planar conformation with an rms deviation of 0.0108 Å for the fitted atoms. The cation and anion in the asymmetric unit are linked by N6—H6B···Cl2, N1—H1C···O1 and O1—H1A···Cl2 hydrogen bonds. Among two cationic ethanaminium groups (NH_3^+) and two Cl^- anions of compound are assembled into a dimer via these hydrogen bonds. The crystal stacking is further stabilized by intermolecular π···π packing interactions {between [the C1-C6 (ring 3)/C9-C14 (ring 4) phenyl rings (symmetry code: x, y, z) of neighboring anions with centroid-to-centroid distances, 3.3462 (2) Å], [the N1/C1/C6/N2/C7 (ring 5) imidazolium/ring 4 (symmetry code: 1+x, y, z) of neighboring cations with centroid-to-centroid distances, 3.5309 (2) Å] and [the N4/C9/C14/N5/C15 (ring 6) imidazolium/ring 3 (symmetry code: 1+x, y, z) of neighbouring cations with centroid-to-centroid distances, 3.5527 (2) Å]}, respectively.
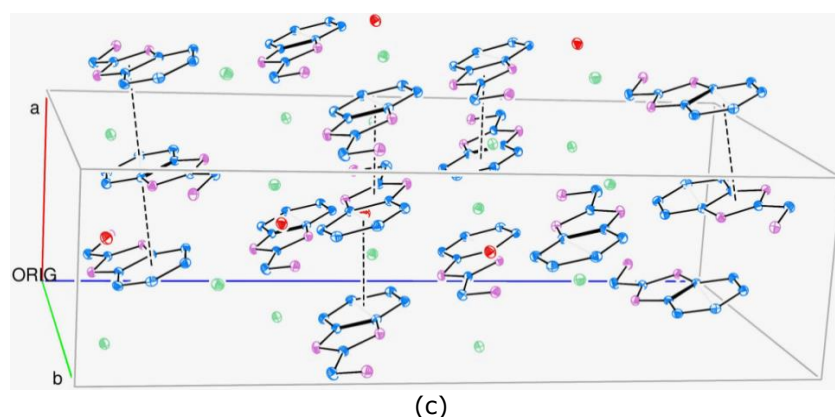

(a)

(b)

(c)
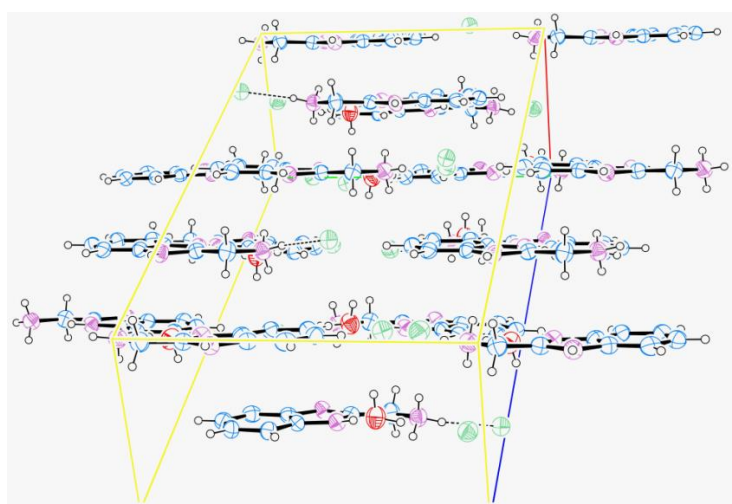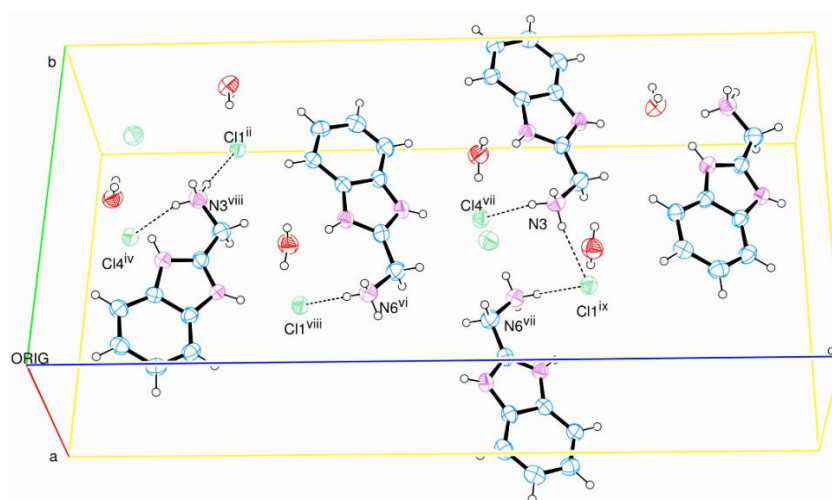
Figure 3. (a) Crystal-packing diagram of the title compound, $C_8H_{13}Cl_2N_3O$. (b) A view showing the hydrogen-bonded chains throughout the c axis. **(c)** A view showing the п-п stacking interaction chains throughout the a axis. п-п interactions with dashed lines are shown.

Spectroscopic studies of 3 toward Zn²⁺

The affinity of the chemosensor **3** toward different metal ions (Zn^{2+}, Cd^{2+}, Pb^{2+}, Hg^{2+}, Ba^{2+} and Sb^{3+}) was monitored using UV−visible and fluorescence spectroscopy. All the spectral measurements were carried out in DMF solutions ($C=1.0 \times 10^{-5}$ M) of **3**. The binding affinity experiments were performed by maintaining the ligand concentration and changing the molar ratio of the added metal ion at room temperature.

The spectra were obtained at 25 °C in a 3 mL volume cuvette by adding increasing amounts of metal ion solutions. The metal ions studied were Zn^{2+}, Cd^{2+}, Pb^{2+} , Hg^{2+} as their acetate salts, Ba^{2+} and Sb^{3+} as their nitrate and chloride salts, respectively.

The ligand **3** did not form complexes with Cd^{2+}, Pb^{2+}, Hg^{2+}, Ba^{2+}, and Sb^{3+} ions. However, when the prepared solution of ligand (**3**) is treated with a solution containing Zn^{2+} ion, the absorption spectrum of ligand **3** illustrated selectivity towards to the Zn^{2+} ion as represented in Figure 4. In case of adding Zn^{2+} solution to the Schiff base derivative (**3**), a decrease was observed in the band at 324 nm while an increment was observed at 262 and 374 nm absorbance. Besides, the observed band at 324 nm which is associated with the free ligand (**3**) shifted to 374 nm after mixing with the solution of the Zn^{2+} and this shifting is indicative for the coordination of Zn^{2+} to the **3** upon complexation (32).
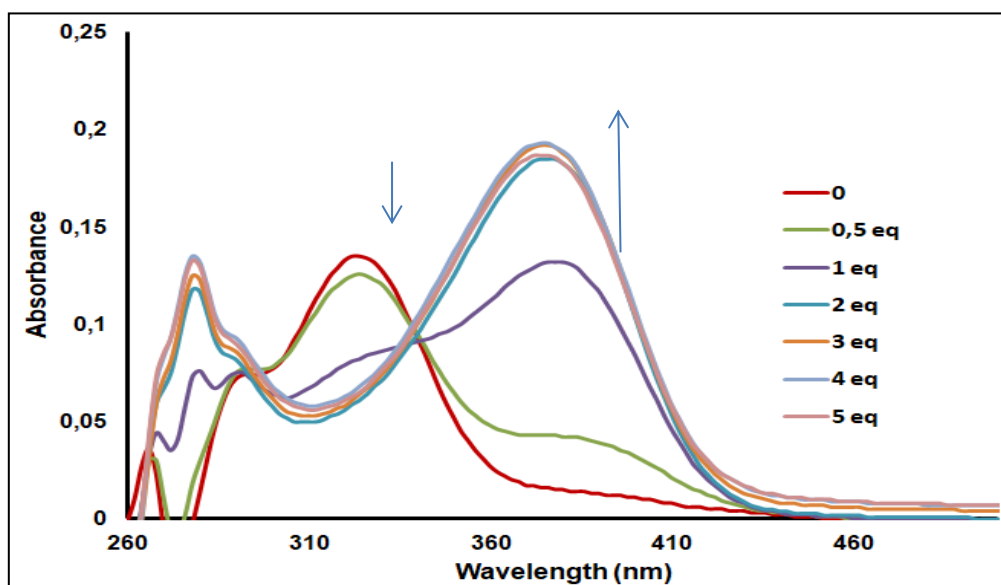

Figure 4. UV-Vis spectra of **3** (1×10^{-5} mol L⁻¹) with different amount of Zn^{2+}.

Investigations of fluorescent behavior of **3** for the various metal ions are as shown in Figure

5. Significant changes in fluorescent emission intensity were not observed in low upon

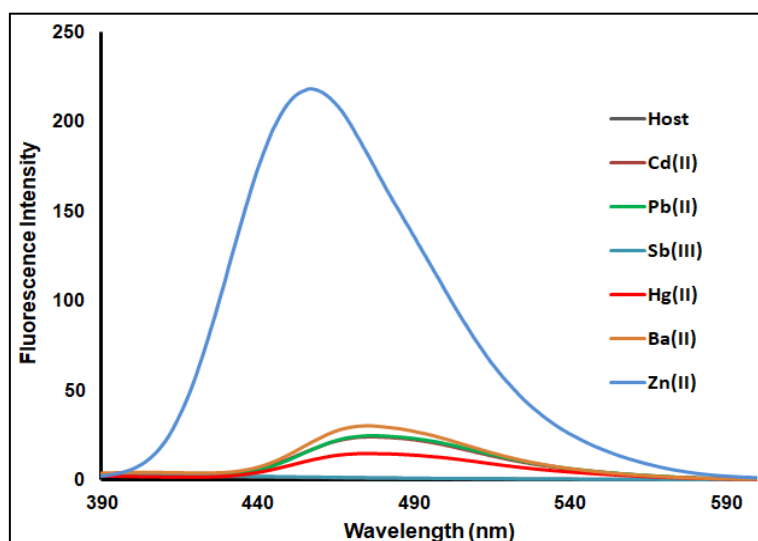addition of the cations (Cd^{2+}, Pb^{2+}, Hg^{2+}, Ba^{2+} and Sb^{3+}) except for Zn^{2+}.

Figure 5. Emission spectra of **3** (1×10^{-5} M) in the presence of Zn^{2+}, Pb^{2+}, Hg^{2+}, Cd^{2+}, Ba^{2+}, Sb^{3+}) (12×10^{-8} M) in DMF at 25°C (λ_{exc} = 378 nm).

After Schiff base (**3**) was treated with different concentrations of Zn^{2+}, the observed fluorescence emission at about 450 nm were plotted by exciting from two different wavelengths as 324 nm (Figure 6) and 378 nm (Figure 7).

Compound **3** alone exhibits weak fluorescence emission at about 383 nm when it was excited at 324 nm in DMF. After titration with Zn^{2+}, the emission intensity was dramatically increased and showed red shift to 450 nm (Figure 6).

When the fluorescence titration experiments were performed by exciting at about 378 nm which is the absorption wavelength of the formed complex, a significant enhancement at fluorescence emission intensity was observed (Figure 7). The increment of the fluorescent emission could be explained with the occurrence of a rigid metal complex system after binding of Zn^{2+} ion (18). It is clear that these significant spectral changes indicate the high selectivity of **3** for the Zn^{2+} (Figure 6-7).
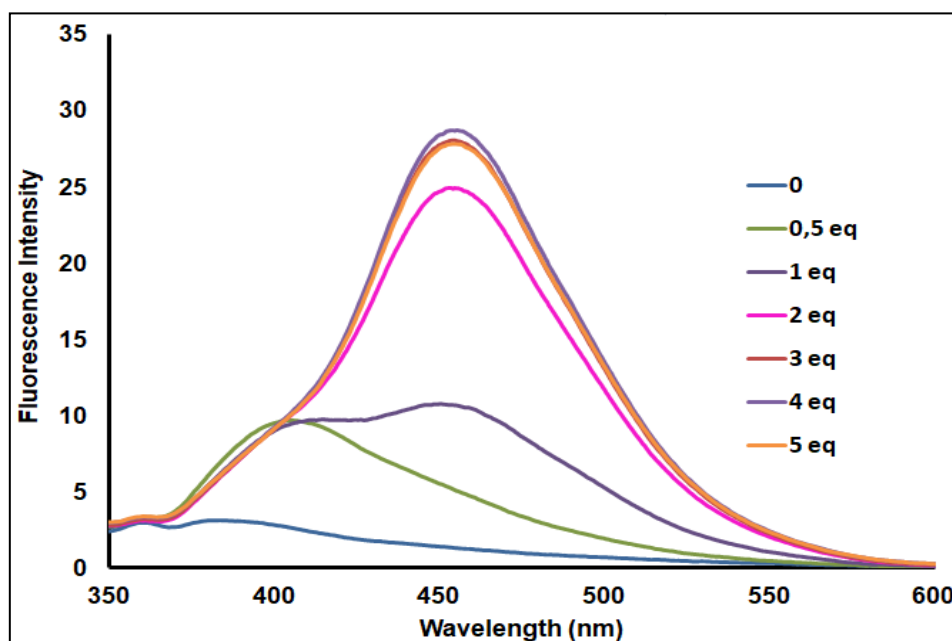

Figure 6. Emission spectra of **3** (1×10^{-5} M) in the presence of increasing amounts of Zn^{2+} in DMF at 25 °C (λ_{exc} = 324 nm).

In addition to spectral changes, the color of the ligand solution turned to fluorescent blue as a response to Zn^{2+} metal ions which is clear under visible light. The addition of other metal ions did not make a significant change in the fluorescence emission and in the color of the ligand solution. The observed bright blue reflection was provided only at **3** + Zn^{2+} composition under UV-light. The image obtained at the beginning and end of the measurement is as shown in the graph as embedded in Figure 7.
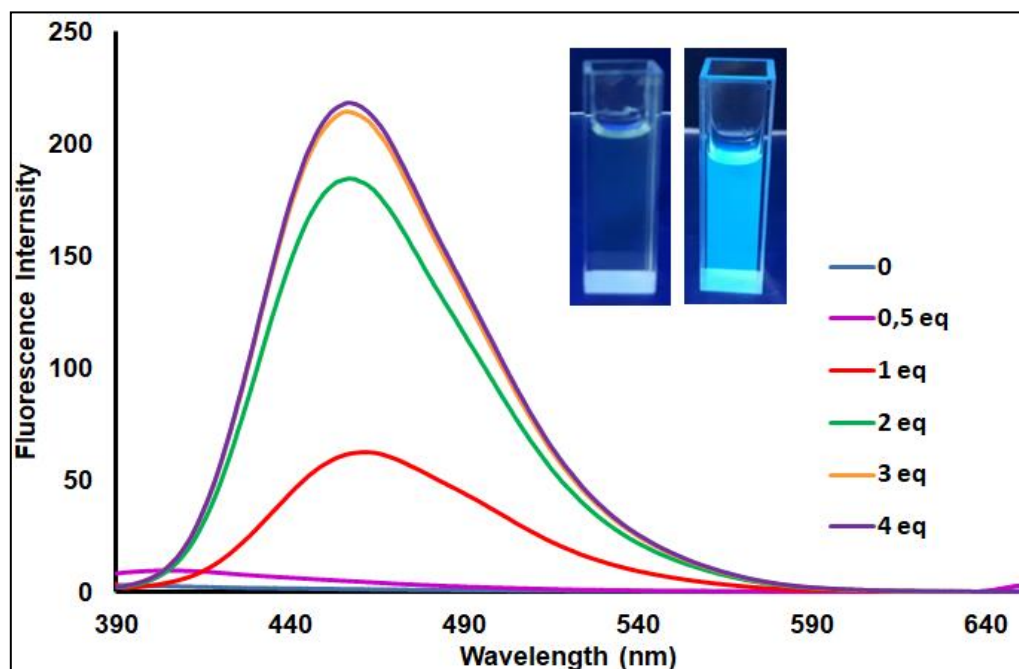

Figure 7. Emission spectra of **3** (1×10^{-5} M) in the presence of increasing amounts of Zn^{2+} in DMF at 25°C (λ_{exc} = 378 nm).

Fluorescence Spectra and Fluorescence quantum yields

The quantum yields of fluorescence were obtained using the following equation 1 (33),

$$\Phi_F = \Phi_F(Std) \frac{F \cdot A_{Std} \cdot n^2}{F_{Std} \cdot A \cdot n_{Std}^2}$$

(Eq. 1)

F and F_{Std} symbolize the areas under the emission curves of the sample and the standard, respectively (34). A and A_{Std} are the absorbances at the excitation wavelengths of the samples and standard, respectively. n^2 and n_{Std}^2 are the refractive indices of solvents which used in experiment for the samples and standard, respectively. ($\eta_{chloroform}$:1.445, η_{DMSO}:1.480, η_{DMF} :1.430)

The fluorescence emission spectra of newly synthesized compound **3** were studied in DMSO and DMF and $CHCl_3$ at 1×10^{-5} M at the room temperature and the spectra were given in (Figure 8). The peaks of fluorescence emission were observed at: 326 nm in $CHCl_3$, 329 nm in DMF and 330 nm in DMSO for **3**. The quantum yield values of fluorescene (Φ_F) were found 0.001 in $CHCl_3$, 0.05 in DMF and 0.175 in DMSO for **3**, respectively. Comparing these results, the highest value obtained in DMSO and the yields in all solvents are lower than the quantum yield of standard naphthalene (0.23) in cyclohexane.
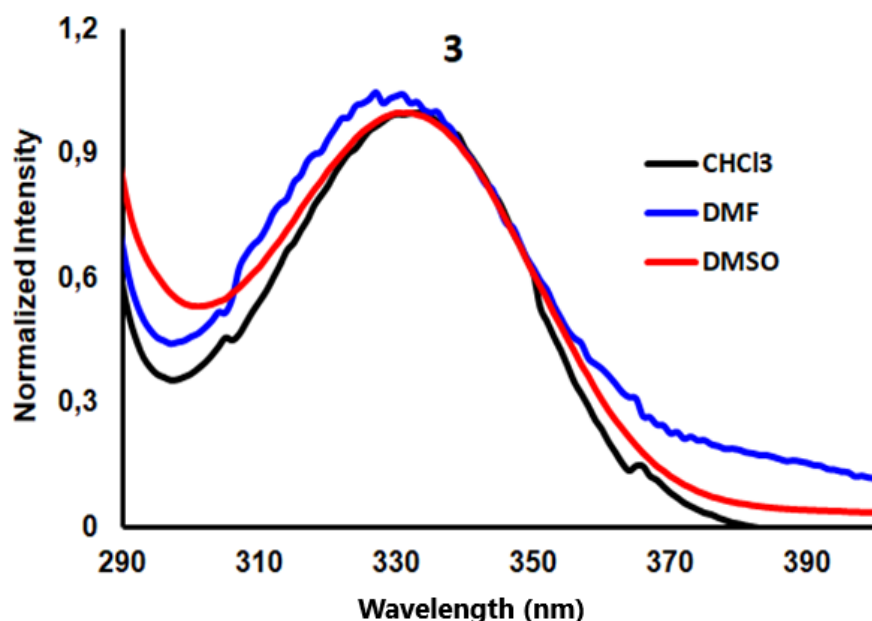
Sen P et al. JOTCSA. 2018; 5(3): 1375-1386.

RESEARCH ARTICLE

Figure 8. Normalized Emission spectra of **3** in CHCl$_3$, DMF and DMSO.

CONCLUSION

In this study, a new Schiff base derivative **3** was reported for the first time. The characterization of compound (**3**) was confirmed with the spectroscopic methods. We wanted to define a new type of molecule formed by the combination of two functional compounds which are benzimidazole unit and Schiff base, with a small number in the literature. In addition to the introduction of a new molecule to the literature, we examined the sensor behavior of this new molecule. The most possible binding mode of the complex of **3** coordinated with different cations was studied based on the absorption spectra and fluorimetric titration experiments. The newly synthesized benzimidazole based-Schiff base derivative showed highly selectivity toward Zn^{2+} ions among the metal ions examined in DMF. Absorption and fluorimetric titration experiments exhibited that the newly synthesized compound (**3**) could be utilized as chemosensors for detection of Zn^{2+} ion**.**

ACKNOWLEDGMENTS

REFERENCES

1. Preston PN. Chemistry of Heterocyclic Compounds: Benzimidazoles and Cogeneric Tricyclic Compounds. John Wiley&Sons, Inc, New York; 2008

2. El Rashedy AA, Aboul-Enein HY. Benzimidazole derivatives as potential anticancer agents**.** Mini-Rev. Med. Chem. 2013;13:399-407.

3. El-masry AH, Fahmy HH, Abdelwahed SH. Synthesis and Antimicrobial Activity of Some New Benzimidazole Derivatives. Molecules. 2000;5:1429-38.

4. Gaba M, Singh S, Mohan C. Benzimidazole: An emerging scaffold for analgesic and anti-inflammatory agents. Eur. J. Med. Chem. 2014;76:494-505.

5. Patil A, Ganguly S, Surana S. A systematic Review of benzimidazole Derivatives as an Antiulcer Agent. Rasayan J Chem. 2008;1:447-60.

6. Kus C, Kilcgil AG, Eke BC, Iscan M. Synthesis and antioxidant properties of some novel benzimidazole derivatives on lipid peroxidation in the rat liver. Arch Pharm. Res. 2004;27:156-63.

7. Kathiravan MK, Salake AB, Chothe AS, Dudhe PB, Wat RP. The biology and chemistry of antifungal agents: A review. Bioorg Med. Chem. 2012;20:5678–98.

8. Cetinkaya B, Özdemir I, Bruneau C, Dixneuf PH. Benzimidazole, Benzothiazole and Benzoxazole Ruthenium(II) Complexes; Catalytic Synthesis of 2,3-Dimethylfuran. Eur J Inorg. Chem. 2000;2000:29-32.

9. Tong Y, Zheng S, Chen X. Structures, Photoluminescence and Theoretical Studies of Two Zn^{II} Complexes with Substituted 2-(2-

Hydroxyphenyl)benzimidazoles. Eur J Inorg Chem. 2005;2005:3734–41.

10. Verdasco G, Martin MA, Castillo B, Lopez-Alvarado P, Menendez JC. Solvent effects on the fluorescent emission of some new benzimidazole derivatives. Anal Chim Acta. 1995;303:73-8.

11. Arulmurugan S, Kavitha HP, Venkatraman BR. Biological Activities of Schiff Bae and Its Complexes: A Review. Rasayan J Chem. 2010;3: 385-410.

12. Przybylski P, Huczynski A, Pyta K, Brzezinski B, Bartl F. Biological Properties of Schiff Bases and Azo Derivatives of Phenols. Curr Org. Chem. 2009;13:124-48.

13. Wang L, Qin W, Liu W. A sensitive Schiff-base fluorescent indicator for the detection of Zn^{2+}. Inorg Chem Commun**.** 2010;13:1122–25.

14. Silva AP, Gunaratne HQN, Gunnlaugsson T, Huxley AJM, McCoy CP, Rademacher JT, Rice TE, Signaling Recognition Events with Fluorescent Sensors and Switches. Chem Rev. 1997;97:1515–66.

15. Carter KP, Young AM, Palmer AE. Fluorescent Sensors for Measuring Metal Ions in Living Systems Chem Rev. 2014;114: 4564−4601.

16. Singh N, Jang DO. Benzimidazole-Based Tripodal Receptor: Highly Selective Fluorescent Chemosensor for Iodide in Aqueous Solution. Org Lett. 2007;9:1991-4.

17. Lee DY, Singh N, Jang DO. A benzimidazole-based single molecular multianalyte fluorescent probe for the simultaneous analysis of Cu^{2+} and Fe^{3+}. Tetrahedron Lett. 2010;51:1103–6.

18. Lin H, Cheng P, Wanb C, Wu A, A turn-on and reversible fluorescence sensor for zinc ion. Analyst. 2012;137: 4415-7.

19. Auld DS. Zinc coordination sphere in biochemical zinc sites. BioMetals. 2001;14:271.

20. Perrin DD, Armarego WLF, Perrin DR. Purification of Laboratory Chemicals. Pergamon Press, New York:2013.
21. Lin CH, Feng YR, Dai KH, Chang HC, Juang TY. Synthesis of a benzoxazine with precisely two phenolic OH linkages and the properties of its high-performance copolymers. J Polym Sci Part A: Polym Chem. 2013;51:2686-94.

22. Alasmary FAS, Snelling AM, Zain ME, Alafeefy AM, Awaad AS, Karodia N. Molecules. 2015;20:15206-23.

23. STOE & Cie, X-AREA (Version 1.18) and X-RED32 (Version 1.04), STOE & Cie, Darmstadt, Germany;2002.
24. Sheldrick GM. A short history of SHELX. Acta Crystallogr., Sect. A: Found. Crystallogr. 2008;64:112-122.

25. Farrugia LJ. ORTEP-3 for Windows- a version of ORTEP-III with a Graphical User Interface (GUI). J Appl Crystallogr. 1997;30:565.

26. Spek AL. Structure validation in chemical crystallography. Acta Crystallogr. 2009;D65:148-55.

27. Farrugia LJ. WinGX and ORTEP for Windows: an update. J Appl Crystallogr. 1999;32:837-838.

28. Özçelik S, Gül A. Boronic ester of a phthalocyanine precursor with a salicylaldimino moiety. J Organomet. Chem. 2012;699:87-91.

29. Zheng S, Cai Y, Zhanga X, Sua C. 2,2'-(Iminodimethylene)bis(1H-benzimidazolium)(1+) chloride. Acta Cryst. 2005;E61:642-4.

30. Cui Y. 2,2′,2″-(Nitrilotrimethylene)tris(1Hbenzimidazol-3-ium) trinitrate. Acta Cryst. 2011;E67:625-6.

31. Li G, Yang F, Yao C. 2-Amino-1H-benzoimidazol-3-ium 4,4,4- trifluoro-1,3-dioxo-1-phenylbutan-2-ide. Acta Cryst. 2008;E64:2460.

32. Jana A, Sukul PK, Mandal SK, Konar S, Ray S, Das K, et al. A novel 2,6-diformyl-4-methylphenol based chemosensor for Zn(II) ions by ratiometric displacement of Cd(II) ions and its application for cell imaging on human melanoma cancer cells. Analyst, 2014;139:495–504.

33. Sen P, Atmaca GY, Erdogmus A, Dege N, Genc H, Atalay Y, Yildiz SZ. The Synthesis, Characterization, Crystal Structure and Photophysical Properties of a New Meso-BODIPY Substituted Phthalonitrile. J Fluoresc. 2015;25:1225-34.

34. Brouwer AM. Standards for photoluminescence quantum yield measurements in solution (IUPAC Technical Report). Pure Appl Chem. *2011;*83:2213-28.

QSAR studies on some C₁₄-urea tetrandrine compounds as potent anti-cancer agents against Leukemia cell line (K562)

Mustapha Abdullahi[a]* ✉ ⓘD **, Gideon Adamu Shallangwa**[a] ✉ **, Muhammad Tukur Ibrahim**[a] ✉ **, Abdullahi Umar Bello** ✉ **, David Ebuka Arthur**[a] ✉ **, Adamu Uzairu**[a] ✉ **, and Paul Mamza**[a] ✉

[a]Faculty of Physical Sciences, Chemistry Department, Ahmadu Bello University (ABU) Zaria, Kaduna State, Nigeria

Abstract: This research applied Quantitative Structure Activity Relationship (QSAR) technique in developing a Multiple-Linear Regression (MLR) model using Genetic Functional Approximation (GFA) method in selecting optimum molecular descriptors from the structures of 24 C₁₄-urea tetrandrine compounds. Firstly, the compounds were optimized at the Density Functional Theory (DFT) level using Becke's three-parameter Lee-Yang-Parr hybrid functional (B3LYP) with the 6-31G* basis set in the Spartan 14 Version 1.1.4 software. The descriptors of the compounds were computed using Padel-software, and data set was divided into training and test set. A model was built from the training set with internal validation parameter R^2_{train} as 0.9104. The external validation of the model was done using the test set compounds with validation parameter R^2_{test} as 0.6443 that passed the criteria for acceptability of a QSAR model globally. The coefficient of determination (cR^2_p) parameter was calculated as 0.8192 which is greater than 0.5, this affirms that the generated model is robust. Furthermore, AST4p, GATS8v, and MLFER are descriptors in the model with the positive mean effect of 0.0899, 0.9098 and 0.0002 respectively. This study depicts a route in designing and synthesizing new C₁₄-urea tetrandrine compounds with better inhibitory potentials.

Keywords: QSAR; Mean Effect; Validation; Descriptors; Model; Y-randomization

***Corresponding author. E-mail:** mustychem19@gmail.com.

INTRODUCTION

Leukemia is one of the most fatal cancer type that affects tissue for blood formation in the bone marrow, lymphatic system, and spleen in the body (1). The K562 leukemic cell lines were the first human immortalized myelogenous leukemia cell line to be understood which was obtained from a 53-year-old female chronic myelogenous leukemia patient in blast crisis (2). The cells are non-adherent, rounded, positive for the BCR/ABL fusion gene, and bear some proteomic similarity to indistinguishable erythrocytes (2). In culture, they show much less clattering than many other suspension lines, perhaps due to the down-regulation of surface adhesion molecules by BCR/ABL. However, additional study lament that BCR/ABL

over-expression may actually increase cell adherence to cell culture plastic (3). The problem with K562 cells is that it undergoes excess of Aurora kinases which plays a role in the improvement of spindles, the partition of chromosomes, and cytokinesis (4). These functions are important in cells so as to split, redevelop tissues, and assume a support part in their homeostatic abilities. However, the excess of Aurora kinases takes uncontrolled cell division in to account and bringing about the tumor (4). Tetrandrines are compounds of dibenzyltetrahydroisoquinoline, derived from Chinese medicinal plant called *Stephania tetrandra* and it is reported to have anti-tumor activities, proliferation chemotherapeutic drugs and converses multidrug resistance (MDR) of tumor cell (5).

In recent decades, there was a significant number of studies that proved the success of the Quantitative Structure-Activity Relationship (QSAR) approach for prediction of various properties, such as solubility, lipophilicity, toxicity, mutagenicity, activities (6). By definition, a QSAR model is a mathematical linear equation involving molecular descriptors used in predicting the biological activity of a compound which is ought to be very useful in

designing the new compound with better activity. Therefore, the main aim of this research was to develop a QSAR model of some C_{14}-urea tetrandrine compounds which can be used to predict the biological activities of compounds against the leukemia K562 cell line using Genetic Function Approximation–Multi-Linear Regression (GFA-MLR) method.

MATERIALS AND METHODS

Data Set collection
A data set of twenty-four (24) C_{14}-urea tetrandrine compounds as potent anti-cancer agents for this study were sourced from the literature (7). The biological activities of the compounds against leukemia K562 cell line were measured in IC_{50} (μM) which is the concentration of compound required to reduce 50% of the cell viability. This is further transformed to logarithm scale (Eq. 1) so as to have linearity or normality in the concentration values. The 2D structures of the compounds were drawn using ChemDraw software version 12.0.2 as shown in "Fig 1", then aligned with their respective IC_{50} values as shown in Table 1.

$$pIC_{50} = -\log(IC_{50} \times 10^{-6})$$ (Eq. 1)
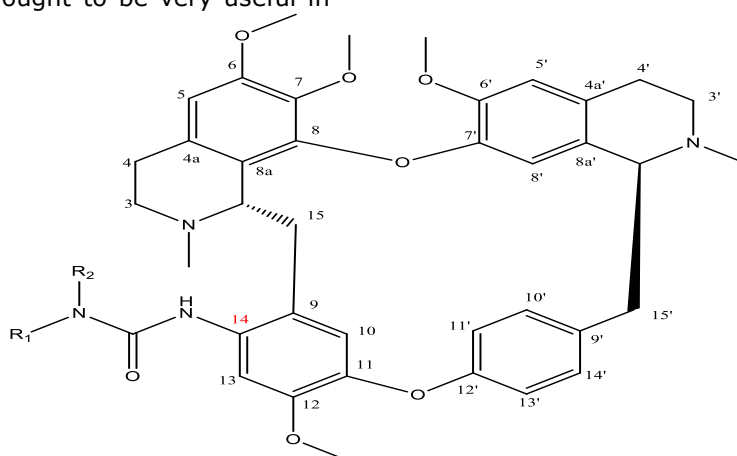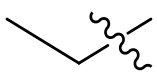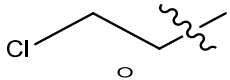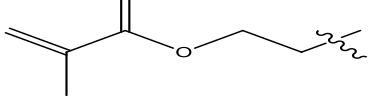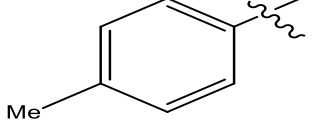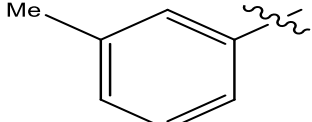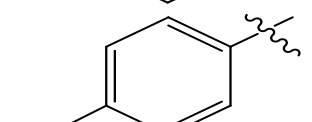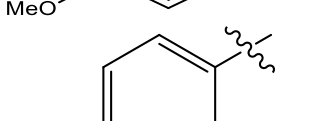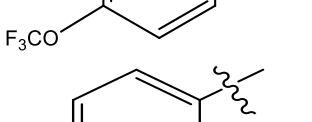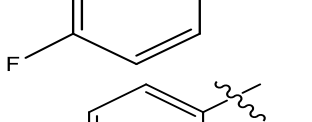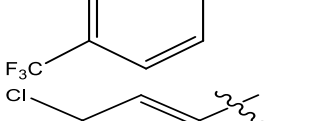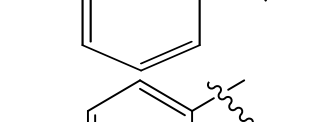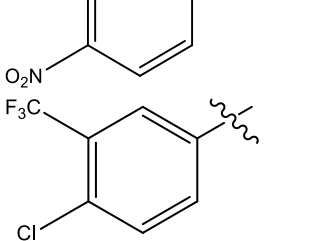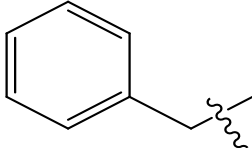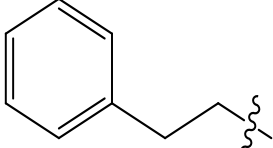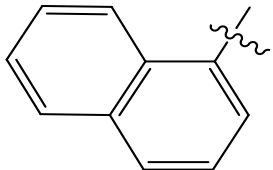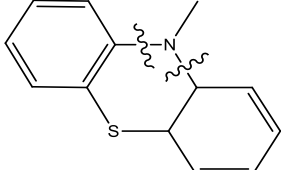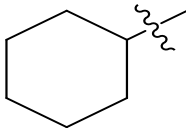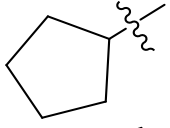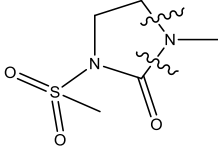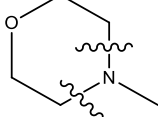
Figure 1: Main C_{14}-urea tetrandrine structure.

Table 1: Substitution pattern of C_{14}-urea tetrandrine compounds and their inhibitory concentrations (IC_{50}) against leukemia K562 cell line.

S/No.	R₁	R₂	IC₅₀ (μM)	pIC₅₀
1		H	5.09	5.2932
2		H	6.88	5.1624
3		H	4.89	5.3106

No.	Structure	R	Value 1	Value 2
4	-Me	Methyl	9.21	5.0357
5		Methyl	3.20	5.4948
6		H	6.24	5.2048
7		H	8.01	5.0963
8		H	2.89	5.5391
9		H	2.15	5.6675
10		H	3.22	5.4921
11		H	1.25	5.9030
12		H	1.81	5.7423
13		H	1.74	5.7594
14		H	2.02	5.6946
15		H	1.84	5.7351
16		H	2.05	5.6882

17		H	4.59	5.3381
18		H	4.94	5.3062
19		H	1.97	5.7055
20		-	2.49	5.6038
21		H	5.56	5.2549
22		H	6.42	5.1924
23		-	3.06	5.5142
24		-	4.33	5.3635

Equilibrium Geometry

The equilibrium geometries of all the compounds were obtained by engaging Spartan 14 version software at the density functional theory (DFT) level using Becke's three-parameter Lee-Yang-Parr hybrid functional (B3LYP) with the 6-31G* basis set (8, 9). The geometry optimization is an atomic arrangement process which gives the most stable state of the starting molecular structure.

Molecular descriptor calculation

The optimized twenty-four (24) molecules were subjected to PaDEL-Descriptor software V2.20 to calculate a total of 1875 molecular descriptors including electronic, spatial, structural, thermodynamic, and topological descriptor (10). The data generated from the PADEL- software in MS Excel (.csv) format were observed to contain redundant data, zero columns or non-informative descriptors.

Data pretreatment and Division

The data was subjected to a pretreatment process using Data Pretreatment software downloaded from Drug Theoretical and Cheminformatics Laboratory so as to curate the results (11). Consequently, the pretreated data were divided into training and test sets using Data Division software also gotten from Drug

Theoretical and Cheminformatics Laboratory (DTC Lab) using Kennard and Stone's algorithm method (12).

Model Building and Validation
The training set was used in developing the model from Material studio software version 8 by engaging the Genetic Function Approximation (GFA) method in which the dependent variable is the inhibitory concentration (IC_{50}) and the independent variables are the molecular descriptors. The model generated was evaluated using Friedman formula (Eq. 2) which determines the finest fitness score defined as; (13).

$$LOF = \frac{SEE}{\left(1 - \frac{m + s \times d}{T}\right)^2}$$ (Eq. 2)

m is the number of the terms in the model, **s** is a user-defined smoothing parameter, **d** is the total number of descriptors in the model and **T** is the number of data in the training set (14).

$$SEE = \sqrt{\frac{(Y_{exp} - Y_{pred})^2}{N - P - 1}}$$ (Eq. 3)

Where **SEE** is the Standard Error of Estimation or Sum of Squares of Errors **(SSE)**. It gives an idea about the quality of a model, low SEE value signifies better model and vice versa. It was defined by the expression (Eq. 3);

Internal Validation
The established QSAR model was validated so as to check the predictive capability and reliability of the models. The internal validation of the models was examined using the leave-one-out (LOO) cross-validation method. The cross-validation regression coefficient, R^2 (Q^2_{cv}) were also calculated using Eq. 4:

$$R^2 = 1 - \left[\frac{\Sigma(y_{exp} - y_{pred})^2}{\Sigma(y_{exp} - \overline{y}_{training})^2}\right]$$ (Eq. 4)

Where
$\overline{y}_{training}$ is the mean of experimental activities, y_{exp} is the experimental activities, and y_{pred} is the predicted activity in the training set respectively (15).

External Validation
The R^2 value are directly proportional to the number of descriptors. However, the R^2 values is not consistent for evaluating the strength of the model. Thus, R^2 is adjusted with the mandate to refurbish and stabilize the model. The adjusted R^2 is defined as like in Eq. 5:

$$R^2_{adj} = \frac{R^2 - p(n-1)}{n - p + 1}$$ (Eq. 5)

Where **p** is the number of descriptors in the model, **n** is the number of compounds that made up the training set (15).
The model developed was further subjected to external validation in order to measure its prediction competency using the test set and the coefficient of determination(R^2_{test}) value is given in Equation 6;

$$R^2_{test} = 1 - \frac{\Sigma(Ypred_{test} - Y_{exp_{test}})^2}{\Sigma(Ypred_{test} - \overline{Y}_{training})^2}$$ (Eq. 6)

Where; $Ypred_{test}$ and $Y_{exp_{test}}$ are the predicted and experimental activity test set respectively. $\overline{Y}_{training}$ is mean values of experimental activity of the training set (15).

Y-Randomization
In order to have confidence in the model built, Y-Randomization test was executed on the training set descriptors matrix (16). This is done by randomly shuffling the inhibitory concentrations (dependent variable) while keeping the descriptors (independent variables) constant resulting in the generation of random MLR models. The new QSAR models are anticipated to have significantly low R^2 and Q^2 values for 10 trials, which certify that the models are robust and cR^2_p is also calculated which should be more than 0.5 defined as:

$$cR^2_p = R \times [R^2 - (R_r)^2]^{1/2}$$ (Eq. 7)

Where cR^2_p is coefficient of determination, R is the coefficient of regression and R_r is average 'R' of random models.

Statistical analysis of the descriptors
Mean Effect
The mean effect values of each descriptor were used to evaluate their relative significances in the model and it is defined as:

$$Mean\ Effect = \frac{\beta_j \sum_i^n D_j}{\sum_j^m(\beta_j \sum_i^n D_j)}$$ (Eq. 8)

Where β_j is the coefficient of the descriptor j in that model, Dj is the value of each descriptor in the data matrix for each molecule in the training set and m is the number of the descriptor that appears in the model and n is the number of molecules in the training set (17).

Varian Inflation Factor (VIF)
The Variance Inflation Factor is a measure of the multi-collinearity among the descriptors, usually expressed as:

$$VIF = \frac{1}{(1-R^2)}$$ (Eq. 9)

Where R^2 is the correlation coefficient of the multiple regression between the variables within the model. If VIF equals to 1, no inter-correlation exists for each variable, if VIF falls into the range of 1–5, the related model is acceptable; and if VIF is larger than 10, the related model is unstable and unacceptable (18).

Applicability Domain
A QSAR model applicability domain is usually tasked to explore the area where the compound predictions can be dependably useful. As such, chemical compounds that fall outside the applicability domain cannot make a very good prediction (19, 20). Consequently, the prediction that is interpolated in the chemical space is acceptable while extrapolated predictions in the chemical space are rejected as well. The leverage method was engaged in evaluating the applicability domain of the established QSAR model and it is defined as the leverage values for the *ith* compound (Eq. 10) (21):

$$hi = X_i(X^T X)^{-1} X_i^T$$ (Eq. 10)

Where; X_i is training compounds matrix of I, X is the n × k descriptor matrix of the training set compound and X^T is the transpose matrix of X used in developing the model. The warning leverage (h^*) is the borderline of normal values for X outliers and is defined as follows (Eq. 11):

$$h^* = 3\frac{(r+1)}{n}$$ (Eq. 11)

Where n is the number of training compounds and r is the number of descriptors in the model.

The leverages of the test compounds with $hi < h^*$ are measured to be consistently predicted by the model. A plot of standardized residuals versus leverage values (Williams plot) is utilized to interpret the relevance area of the model in terms of chemical space. The area of unfailing predictions for the external test compounds, defined as compounds whose leverage values are within the threshold and standardized residuals is not greater than 2σ (2 standard deviation units). Therefore, the test compound ($hi < h^*$) are accepted as Y outlier. Similarly, the test set compounds having ($hi > h^*$) are variably projected by the model since they are extrapolated (21)

RESULT AND DISCUSSION

Descriptor Calculations
The QSAR studies were performed to generate a model that relates the structure activity relationship of twenty-four C_{14}-urea tetrandrine compounds as a potential anticancer agent against leukemia (K562) cell lines. Initially, the 32 quantum chemical descriptors for all the drawn compounds were obtained from Spartan 14 software via optimization process. These were pooled with the 1875 molecular descriptor calculated by PaDEL-Descriptor software V2.20 to give 1907.

Data Pretreatment and Division
The descriptors result in MS Excel (.csv) were subjected to data pretreatment which removed non-informative constant data and a pair of variables with a correlation coefficient greater than 0.7 using the Data Pretreatment software. The data set results from the pretreatment process was divided by using Kennard-Stone algorithm method where 16 compounds (70% of the total compounds) are considered as training set and 8 compounds (30% of the total compounds) are the test set. The division was successfully done using the Dataset Division GUI 1.2 software.

Model Building and Validation
In building the QSAR model, three (3) descriptors were used to build the model by the Genetic Function Approximation (GFA) of Material studio software and the model generated is illustrated below:

$$\text{pIC50} = -0.064954009 * \textbf{ATSC4p} + 6.794973156 \\ * \textbf{GATS8v} - 0.626117779 \\ * \textbf{MLFER\_A} \\ - 2.008205026$$
(Eq. 12)

The validation parameters of the model were presented in Table 2 which clearly shows that the model passed the criteria of acceptability. In addition, the coefficients of regression (R-squares) are 0.9104 and 0.6443 for both the training and test set compounds respectively. This is an indication of a good relationship between the predicted and experimental activities. The Centered Broto-Moreau autocorrelation-lag 4 per weighted by

polarizabilities (**ATSC4p**) descriptor is an autocorrelation of a topological structure defined as the most recognized spatial autocorrelation on a molecular graph which is given as;

$$ATS_k = \frac{1}{2}\sum_{i=1}^{A}\sum_{j=1}^{A} w_i \cdot w_j \delta(d_{ij};k) = \frac{1}{2} \cdot (w^T \cdot {}^K B \cdot w)$$

(Eq. 13)

where **w** is any atomic property, **A** is the number of atoms, **k** is the interval, and δ_{ij} is the topological distance between **ith** and **jth** atoms; $\delta(d_{ij}; k)$ is a Kronecker delta function which is equivalent to1 if $d_{ij}=k$, but if d_{ij} is not equal k, the function is said to be zero. ${}^k B$ is the kth order corresponding to the geodesic matrix, whose elements are equal to 1 only for vertices v_i and

v_j at topological distance k, and zero otherwise; w is the dimensional vector of atomic properties (22).

The Geary autocorrelation-interval 8 per weighted by the Vander Waals volumes (**GATS8v**) is a 2D autocorrelation descriptor, which is obtained from molecular graphs by summing the products of atom weights of the terminal atoms of all the paths of the considered path length (the lag 8) (22). Whereas, the **MLFER_A** descriptor is a linear free energy relation (LFERs) descriptor whose coefficient measures the acidity of hydrogen bond due to the interaction of basic solutes with acidic phase (22). The positive mean effect of these three (3) descriptors in this study inferred that there will be a positive influence on the inhibitory concentrations when each descriptor value increases in the same direction.

Table 2: Validation parameters of the model.

Validation Parameters	Model	QSAR Validation Standard
Friedman LOF	0.0280	-
R-squared (Training set)	0.9104	≥ 0.6
Adjusted R-squared	0.8880	-
Cross validated R-squared	0.8172	≥ 0.5
Significant Regression	Yes	-
Significance-of-regression F-value	40.6445	-
Critical SOR F-value (95%)	3.6506	-
Replicate points	0	-
Computed experimental error	0	-
Lack-of-fit points	12	-
Min expt. error for non-significant LOF (95%)	0.0601	-
R-square (test set)	0.6443	≥ 0.6

Univariate analysis were conducted on the inhibitory concentration values of the two set (i.e. training set and test set) as presented in Table 3. These clearly show that the training set range values are within the test set range values. Furthermore, the mean activities and standard deviation of both the training set were almost alike when compared to the test set value. This inferred that test set compounds

activities were interpolative within the activities of the training set.

The experimental, predicted inhibitory concentration (pIC_{50}) and the residual values generated from the compounds were shown in Table 4. The residual value is defined as the differences between experimental and predicted activity, and lower residual values signify that the model has a high predictive ability.

Table 3: Univariate analysis for the inhibitory concentrations (IC_{50}).

	All	Training Set	Test Set
Number of sample points	24	16	8
Range	0.8673	0.7065	0.7106
Maximum	5.9030	5.7423	5.9030
Minimum	5.0357	5.0357	5.1924
Mean	5.4624	5.4179	5.5513
Median	5.4934	5.4027	5.5798
Variance	0.0567	0.0532	0.0517
Standard deviation	0.2432	0.2383	0.2432
Mean absolute deviation	0.2106	0.2099	0.2048
Skewness	-0.0291	-0.024	-0.0499
Kurtosis	-1.3179	-1.557	-1.6534

Table 4: Experimental, predicted and residual values of tetrandrine derivatives

Training Set				Test Set			
Compound	Experimental	Predicted	Residual	Compound	Experimental	Predicted	Residual
1	5.2932	5.2300	0.0632	9	5.6675	5.7165	-0.0489
2	5.1624	5.1855	-0.0235	10	5.4921	5.7516	-0.2594
3	5.3106	5.2425	0.0680	11	5.9030	5.9345	-0.0314
4	5.0354	5.1089	-0.0732	13	5.7594	5.6038	0.1555
5	5.4945	5.4227	0.0720	14	5.6946	5.5557	0.1388
6	5.2048	5.2385	-0.0337	17	5.3381	5.2026	0.1355
7	5.0963	5.1650	-0.0687	22	5.1924	5.2129	-0.0205
8	5.5391	5.6657	-0.1266	24	5.3635	5.5647	-0.2012
12	5.7423	5.6612	0.0811	-			
15	5.7358	5.7416	-0.0064	-			
16	5.6882	5.7723	-0.0840	-			
18	5.3062	5.2613	0.0448	-			
19	5.7055	5.6388	0.0666	-			
20	5.6038	5.4989	0.1048	-			
21	5.2549	5.2974	-0.0425	-			
23	5.5142	5.5562	-0.0419	-			

Statistical Analysis of the Descriptors

In order to assess the relationships between each descriptor used in the model, the values of the three (3) descriptors were extracted from the training set, then subjected to Pearson's correlation analysis and the results were described in Table 5. These show that there is no significant inter-correlation between the descriptors used in the model because the correlation coefficients between all pairs are less than 0.5. The Variance Inflation Factor (VIF) values for all the three (3) descriptors are not greater than 2 which signifies that the descriptors are and the model is said to be stably acceptable.

Table 5: Pearson's correlation analysis for descriptor used in the QSAR model.

	ATSC4p	GATS8v	MLFER_A	VIF
ATSC4p	1			1.2954
GATS8v	0.3439	1		1.2183
MLFER_A	0.4354	0.3719	1	1.3255

VIF is the variance inflation factor

The results in Table 6 illustrate some statistical parameters of descriptors in the developed model. From results, the absolute t-statistics values for each descriptor are greater than 2, this also inferred that the selected descriptors were good (23). The p-values of all descriptors in the model are less than 0.05 which means that there is a relationship between the descriptors and the inhibitory concentration of the compounds

Table 6: Statistical parameters.

	Coefficients	Standard Error	t Stat	P-value	Mean Effect
ATSC4p	-0.0649	0.0086	-7.5382	6.87E-06	0.0899
GATS8v	6.7949	1.2599	5.3931	0.000162	0.9098
MLFER_A	-0.6261	0.1293	-4.8403	0.000405	0.0002

The output of Y-Randomization test was presented in Table 7. The cR^2_p value was calculated as 0.8192 which is greater than 0.5, this affirms that the generated model is robust.

A Plot of standardized residual against experimental activity in "Fig 3" illustrated a random scattering around the baseline of data at the standardized residual equal to zero. Hence, there was no systematic error in the model built.

Table 7: Y-randomization test

Model	R	R^2	Q^2
Original	0.9541	0.9104	0.8172
Random 1	0.4285	0.1836	-0.2395
Random 2	0.5090	0.2591	-0.1873
Random 3	0.3475	0.1208	-1.0654
Random 4	0.2729	0.0744	-0.5785
Random 5	0.3166	0.1002	-0.8467
Random 6	0.3393	0.1151	-0.5946
Random 7	0.5352	0.2865	-0.0898
Random 8	0.4387	0.1924	-0.7466
Random 9	0.2490	0.0620	-0.5746
Random 10	0.7233	0.5232	0.2392
Random models parameters			
Average R :	0.4160		
Average R^2 :	0.1917		
Average Q^2 :	-0.4684		
cRp^2 :	0.8192		
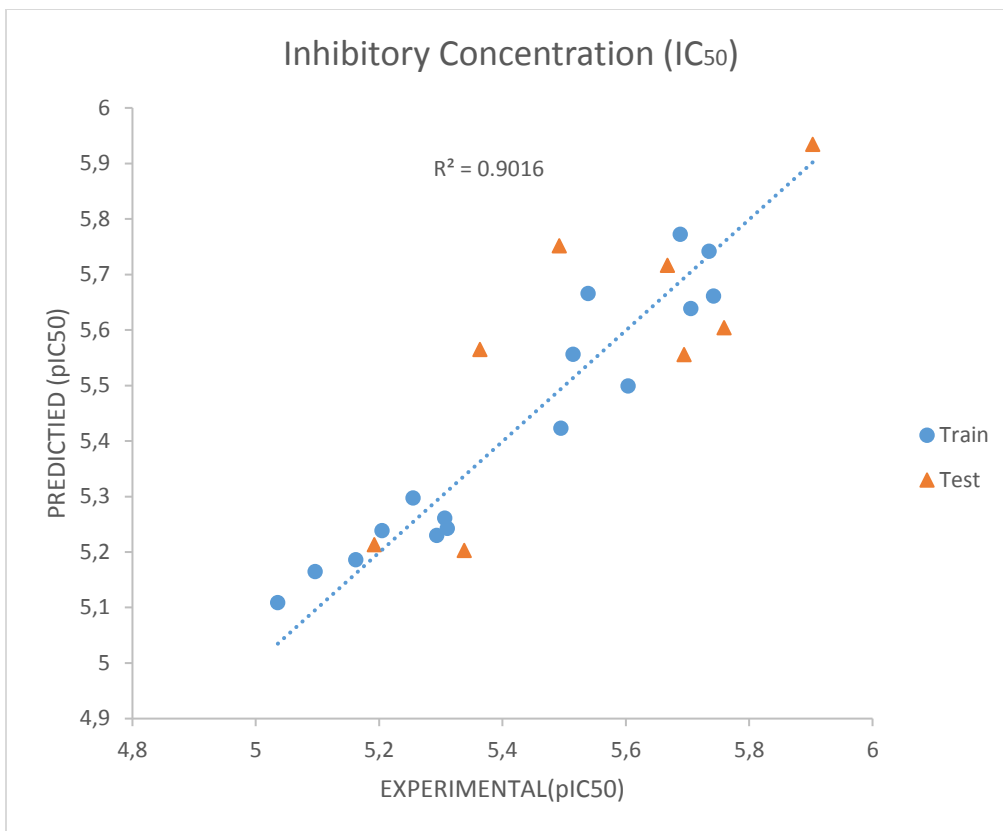
Figure 2: Plot of predicted against experimental activities (pIC$_{50}$).
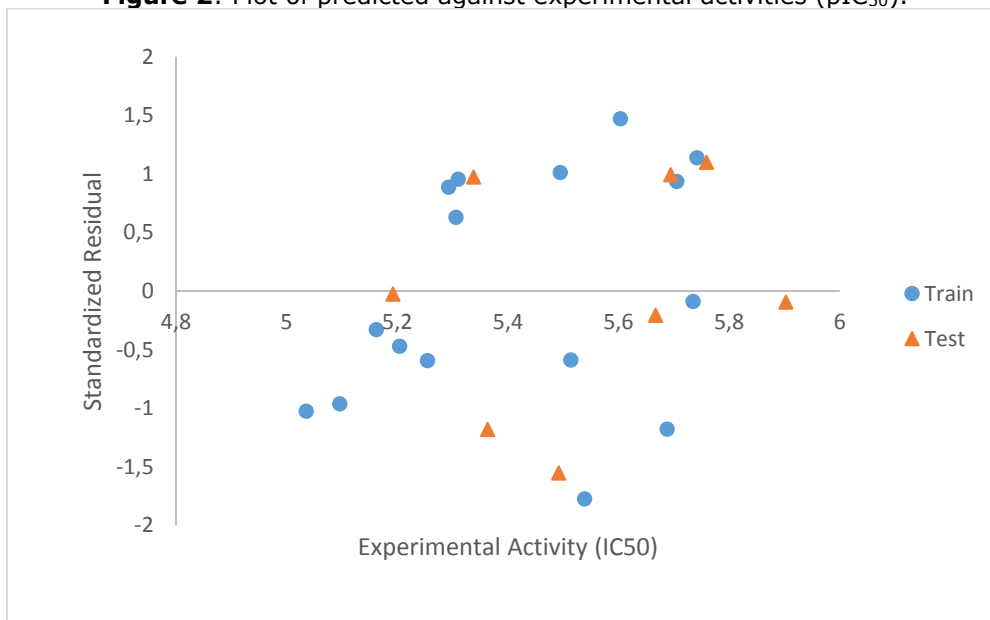
Figure 3: Plot of standardized residual against experimental activity (pIC$_{50}$).

A scatter plot for standardized residuals against the leverages termed as Williams Plot was presented in "Fig 4" so as to detect the presence of outliers and influencing compounds in the models. Our results revealed that all the compounds are within the square area ±2 of standardized deviation unit which means there is no outlier. However, the calculated warning leverage (h*) is 0.75. The plot also revealed that two (2) test set compounds (i.e.,

compound 17 and 22) are considered to be the influencing compounds because their leverages are more than the warning leverage. The reason may be attributed to the differences in the

substitution pattern of the chemical structure in the data set.
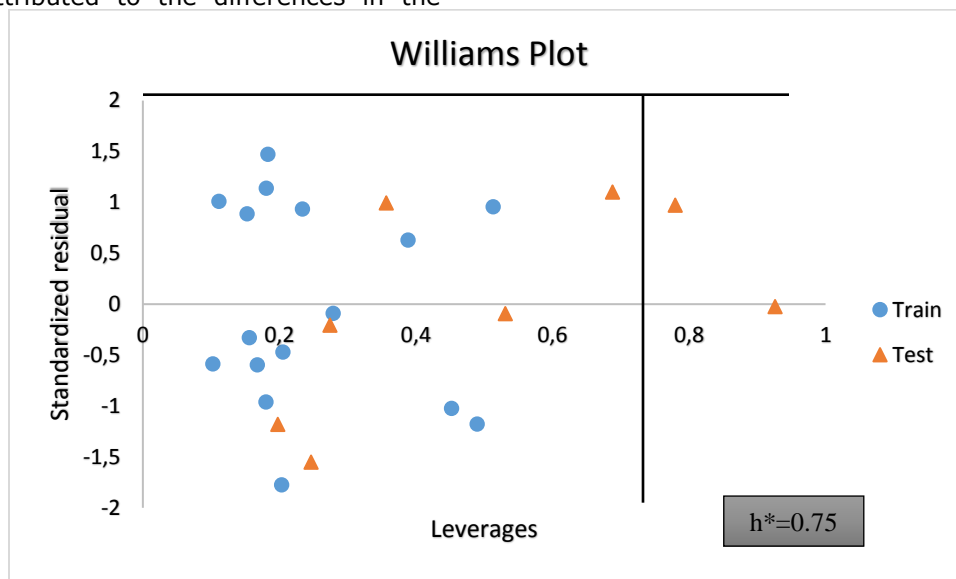
Figure 4: The williams plot (Standardized residuals vs the leverage values)

CONCLUSION

In conclusion, this research has successfully achieved its aim of constructing a QSAR model for the tetrandrine compounds which predicts the inhibitory concentration against leukemia K562 cell line using Genetic functional algorithm method. Our research findings revealed the molecular descriptors AST4p, GATS8v and MLFER with a mean effect of 0.0899, 0.9098 and 0.0002 respectively, were found to positively influence the inhibitory concentrations. This knowledge could be of vital importance in designing and synthesizing new C_{14}-urea tetrandrine compound with excellent inhibitory potentials.

REFERENCES

1. Lookward W. Leukemia (AML, CML, ALL and CLL). www.RN.ORG; ©RN.ORG®, S.A., RN.ORG®, LL; 2015. ISBN: 678-693-1-32.

2. Lozzio CB, Lozzio BB. Human Chronic Myelogenous Leukemia Cell-Line with Positive Philadelphia Chromosome. National Institute of Health. 1975; 45(1): 321–340.

3. Karimiani EG, Marriage F, Merritt AJ, Burthem J, Byers RJ, Day PJ. Single-cell analysis of K562 cells: an imatinib-resistant subpopulation is adherent and has upregulated expression of

BCR-ABL mRNA and protein. Experimental Hematology. 2014; 42(3): 183-191

4. Fan Y, Lu H, An L, Wang C, Zhou Z, Feng F, Zhao Q. Effect of active fraction of Eriocaulon sieboldianum on human leukemia K562 cells via proliferation inhibition, cell cycle arrest and apoptosis induction. Environmental Toxicology and Pharmacology. 2016; 4(3):13-20.

5. Liu T, Liu X, Li WH. Tetrandrine, a Chinese Plant-Derived Alkaloid, Is a Potential Candidate for Cancer Chemotherapy, On Co-Target. 2016; 2(7):480100–480115.

6. Perkins R, Fang H, Tong W, Welsh WJ. Quantitative Structure-Activity Relationship Methods: Perspectives on Drug Discovery and Toxicology. 2003; 22(1): 1666–1679.

7. Lan J, Huang L, Lou H, Chen C, Liu T, Hu S, Yao Y, Song J, Luo J, Liu Y, Xia B, Xia L, Zeng X, Ben-David Y, Pan W. Design and Synthesis of Novel Tetrandrine Derivatives as Potential Anti-Tumor Agents against Human Hepatocellular Carcinoma. European Journal of Medicinal Chemistry. 2017 Sep; 3-4.

8. Becke AD. Becke's three-parameter hybrid method using the LYP correlation functional. Journal of Chemical Physics. 1993; 98: 5648–5652.

9. Lee C, Yang W, Parr RG. Development of the Colle-Salvetti correlation-energy formula into a functional of the electron density. Physical Review B. 1988; 37:785

10. Alisi IO, Uzairu A, Abechi SE, Idris SO. Quantitative Structure activity relationship analysis of coumarins as free radical scavengers by genetic function algorithm. Iranian Chemical Society. 2018 Mar; 2(6):208–222

11. Ambure P, Rahul BA, Agnieszka G, Tomasz P, Kunal R. "NanoBRIDGES" Software: Open Access Tools to Perform QSAR and Nano-QSAR Modeling. Chemical Intelligent Laboratory Systems. 2015; 147: 1–13.

12. Kennard RW, Stone LA. Computer Aided Design of Experiments. Technometrics. 1969 Feb; 11(1):137–48.

13. Friedman JH, Multivariate Adaptive Regression Splines. The Annals of Statistics. 1991: 1–67.

14. Khaled KF, Abdel-Shafi NS. Quantitative structure and activity relationship modeling study of corrosion inhibitors: Genetic function approximation and molecular dynamics simulation methods. International Journal of Electrochemical Science. 2011; 6:4077-4094

15. Brand V, Orr KA, Comprehensive R archive network (CRAN):http://CRAN.Rproject.org. retrieved; 2015

16. Tropsha A. Best Practices for QSAR Model Development, Validation, and Exploitation. Molecular Informatics. 2010 Jul 6; 29(6–7):476–88.

17. Minovski N, Župerl Š, Drgan V, Novič M. Assessment of applicability domain for multivariate counter-propagation artificial neural network predictive models by minimum Euclidean distance space analysis: a case study. Analytica Chimica Acta. 2013; 759:28–42.

18. Myers RH. Classical and modern regression application. 2nd edition. Duxbury Press. CA. 1990

19. Eriksson L, Jaworska J, Worth AP, Cronin MTD, McDowell RM, Gramatica P. Methods for reliability and uncertainty assessment and for applicability evaluations of classification- and regression-baes QSARs. Environmental Health Perspectives 2003; 111:1361-1375

20. Nandi S, Monesi A, Drgan V, Merzel F, Novič M. Quantitative structure-activation barrier relationship modeling for Diels-Alder ligations utilizing quantum chemical structural descriptors. Chemistry Central Journal. 2013; 7:1-13.

21. Gramatica P, Giani E., Papa E., Statistical external validation and consensus modeling: A QSPR case study for KOC prediction. Journal of Molecular Graphics and Modelling. 2007; 25:755-66.

22. Todeschini R, Consonni V. Molecular descriptors for chemo-informatics. Weinheim: Wiley- VCH; 2009. (Methods and principles in medicinal chemistry). ISBN: 9783527318520

23. Adeniji SE, Sani U, Uzairu A, QSAR Modeling and Molecular Docking Analysis of Some Active Compounds against Mycobacterium Tuberculosis Receptor (Mtb CYP121). Journal of Pathogens Hindawi. 2018; 24-64.

Inhibition of DNase I Enzyme with Nickel(II) Triphenylphosphine Complexes Incorporating Tridentate Schiff Base Ligands in Vitro

Şükriye GÜVELİ *[1] ✉ 🆔

[1]Department of Chemistry, Engineering Faculty, Istanbul University-Cerrahpaşa, 34320, Avcilar, Istanbul, Turkey

Abstract: The nickel(II) complexes containing with ONS chelating 3-methoxy-salicylaldehyde-N^4-R thiosemicarbazones (R:-H_2,-propyl) and triphenylphosphine coligands have been synthesized. The structures of Ni(II)-centered metal complexes were approved by means of analytical and spectroscopic data. The solid-state structure of complex **2** bearing PPh3 as co-ligand was clarified by single crystal X-ray crystallography, which revealed square planar geometry around Ni(II) ion. The potential of these complexes to inhibit the DNase I enzyme, which uses DNA as a substrate, was investigated *in vitro*. The results revealed that the compounds inhibited the DNase enzyme directly and/or indirectly (by masking of DNA molecules) at ≥0.1 µg/mL concentrations *in vitro*.

INTRODUCTION

The reaction of thiosemicarbazide and an aldehyde or ketone results in thiosemicarbazone compounds. Thiosemicarbazones are an important class of chelating ligands which contain nitrogen and sulfur donor atoms and have extensive applications in various fields such as medicine, industry, analytical and organic processing (1-4). Mixed-thiosemicarbazones complexes bearing seconder ligand play essential roles in biological processes like activation of enzymes by metals (5-6). Particularly thiosemicarbazone-based nickel(II) complexes have shown significant antiviral (7), antibacterial (8) and anticancer activities (9). Investigations on interactions of DNA and thiosemicarbazone molecules have attracted significant attention over the last years (10). The square planar Ni(II)-thiosemicarbazone complexes were reported to have DNA interaction and topoisomerase II inhibition activity (11-13).

Deoxyribonuclease I, was the first enzyme to be recognized as specific for DNA, binds to the small groove of DNA and is often used as an enzymatic tool to study the interaction of DNA and proteins (14,15). DNases play a significant role in alimentary canal digestion and in pathogenesis of diverse diseases and apoptosis, while DNase inhibitors could modify or control those activities. Determining molecules that are able to cleaving/binding DNA has drawn great attention because of their important use in nanotechnology, therapeutic and biotechnology applications (16, 17).

Binding affinity in CT-DNA and protein and cytotoxicity activity against cancer cell lines HeLa, A549 and HepG2 of Ni(II) complexes consisting of 4-methoxysalicylaldehyde-N^4-R-thiosemicarbazone (R: H, Me, Et, Ph) and PPh_3 were investigated by Prabhakaran et al. The results showed that the complexes have important binding ability and cytotoxicity activity in contrast of their ligands. The binding affinity towards DNA and protein is decreased in order of $C_2H_5 > CH_3 > H > C_6H_5$ unlike in order of cytotoxic activity (11). Another paper of Prabhakaran is on DNA topoisomerase II inhibition activity of

nickel(II) complexes consisted of salicylaldehyde-N^4-R (R: Me, Ph)/2-hydroxynaphthaldehyde-N^4-R (R: Me)-thiosemicarbazone and PPh$_3$. The activity is decreased in order of [Ni(Nap-Me-tsc)(PPh$_3$)]>[Ni(Sal-Ph-tsc)(PPh$_3$)]>[Ni(Sal-Me-tsc)(PPh$_3$)].

In our previous study, two nickel complexes incorporating tridentate Schiff bases derived from

3-methoxy salicylaldehyde with triphenylphosphine were synthesized and characterized by various spectroscopic data (7). In this paper, the complexes **1,2** (Figure 1.) were firstly investigated for DNase I enzyme inhibition and the crystal structure of the complex **2** was performed by single-crystal diffraction.
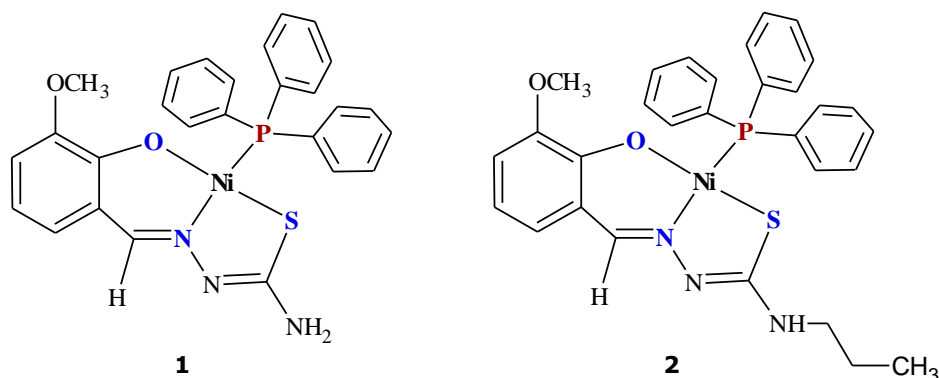
Figure 1. The chemical diagrams of complexes (**1, 2**).

EXPERIMENTAL SECTION

Synthesis

The nickel complexes were prepared by the literature method as follows (7, 12). Reactions of the solution of thiosemicarbazone ligands (1 mmol) in dichloromethane (10 mL) with the solution of dichlorobistriphenylphosphine nickel(II) (1 mmol) in 10 mL absolute ethanol in

equivalent amounts were resulted by giving the tetra-coordinated Ni(II) complexes (Figure 1). The structure of Ni(II) complexes were characterized by means of analytical and spectroscopic data (7). The complex **2**, was in the form of fine crystals, soluble in alcohols and chlorinated hydrocarbons. Recrystallization of complex **2** was resulted in the composition of [Ni(L)(PPh$_3$)].

Figure 2. Crystal structure of the complex **2**.

X-ray crystallography

The data of intensity of the complex was recorded on a Bruker D8 VENTURE diffractometer equipped with PHOTON100 detector at 304 K temperature using graphite- monochromated Mo Ka radiation (k = 0.71073 Å) by applying the multi-scan method. SHELXS program of the SHELXTL-1997 (18) software is used to solve of the structure which is refined by full-matrix least-squares methods with SHELXL-2014/7 (19, 20). Absorption corrections were performed using

SADABS (21). The intensity data were integrated by SAINT software package using a wide-frame algorithm (22). All H atoms were placed in calculated positions and treated using a riding model, fixing the bond lengths at 0.82, 0.93, 0.97, 0.97 and 0.96 Å for NH, aromatic CH, methine, methylene, methyl atoms, respectively. The details of the data collection and structure solution are collected in Table 1.

Deoxyribonuclease I (DNase I) inhibition activity

DNase I enzyme (Sigma-D4227), isolated from bovine pancreas, was used to determine the effects of complexes on DNase enzyme activity *in vitro*. The DNase enzyme was dissolved in a buffer containing 10 mM Tris (pH:7.5), 10 mM $CaCl_2$, and 50% (v/v) glycerin with ~10U/µl and stored at -20 °C. The pHKP-Luc plasmid, purified by the plasmid DNA isolation kit from *Escherichia coli* DH5α cells, was used as the DNA molecule. Plasmid DNA was obtained from K.Turan (23). The reaction was carried out in 15 µL of DNase I buffer (10 mM tris, 2.5 mM $MgCl_2$, 0.5 mM $CaCl_2$, pH 7.5) containing 2 m units of DNase, 1 µg of plasmid DNA and 0.1, 0.01 or 0.001 µg of complex by allowing to stand for 20 minutes at 37 °C. At the end of the period, DNase I enzyme was inactivated by heating the reaction mixtures at 75 °C for 10 min. To clarify the enzymatic digestion of plasmid DNAs, the reaction mixtures were analysed with agarose gel electrophoresis. For this purpose, the samples were mixed with x 6 concentrated gel loading buffer at the 1:5 ratio and applied to 1% agarose gel. Electrophoresis was completed in 25 minutes under a constant voltage of 100 V in TAE buffer. DNA was visualized with a UV transilluminator and photographed.

DNase I inhibition studies

The potential inhibition activity of the complexes on DNase I was investigated by gel electrophoresis (Figure 4). It is observed that almost entire DNase I activity were inhibited by the complexes at the concentration of 0.1 µg/mL. In the case of the diluted complex concentration of 0.01 and 0.001 µg/mL. It is revealed that the activity of the enzyme decreased. It is suggested that the inhibition efficiency of the complexes on DNase I enzyme protects the DNA structure. The observed inhibition activities against DNase I could be associated with the coordinatively unsaturated square planar geometry of the metal

RESULTS AND DISCUSSION

Crystal structure studies

The reaction of $[Ni(PPh_3)_2Cl_2]$ and the thiosemicarbazones in the same ratio gave yields, the diamagnetic Ni(II)-complexes 1, 2 containing PPh_3 co-ligand. The complexes were coordinated to Ni(II) by giving two protons from thiosemicarbazone via phenolic –OH and thiol group. In to approve the definite structure of the complex **2**, crystallographic analysis has been carried out. ORTEP-3 (19) drawing of the complex is illustrated in Figure 2. whilst the bond angles/lengths are presented in Table 2. Complex **2** includes the dibasic form of the ligand which acts as tridentate ligand by the nitrogen, sulfur and oxygen atoms resulting in the formation of six and five-membered chelate ring with O–Ni–N and S–Ni–N bite angles of 95(3)° and 86.6(2)°, respectively. The triphenylphosphine group forms the fourth coordination of Ni(II). The C–S bond-distance is 1.745(9) Å, revealing that thiolate form of thiosemicarbazone bound to metal. The P(1)–Ni–N(3) and S(1)–Ni–O(1) bond-angles deviate remarkably from 180° which shows that is significant distortion in NiSNOP core around nickel atom. Packing diagram of the complex **2** is shown in Figure 3. According to the figure, no hydrogen-bonds or important intermolecular-interactions in the structure were observed.

center which causes binding the DNA to the available vacant sites. Another possibility is that the complexes can directly and/or indirectly inhibit the DNase I enzyme. Regarding, Prabhakaran et al. has investigated DNA topoisomerase II inhibition activity of nickel(II)-PPh_3 complexes containing the thiosemicarbazones coordinated in ONS fashion. This study showed increase in the electron deficiency on metal centre and the formation of coordinative unsaturated square planar geometry was attributed to the binding of topoisomerase enzyme to the metal centre (13).

Table 1 Crystal data and structure refinement parameters for complex **2**.

Parameter	2
CCDC depository	1873557
Color/shape	Brown / Rod
Chemical formula	$C_{30}H_{30}N_3NiO_2PS$
Formula weight	586.31
Temperature (K)	304
Wavelength (Å)	0.71073 (Mo Ka)
Crystal system	Monoclinic
Space group	$P\,21$
Unit cell parameters	
a, b, c (Å)	11.546(4), 8.050(2), 15.287(6)
a, β, γ (°)	90, 97.490 (11), 90
Volume (Å^3)	1408.7(9)
Z	2
D_{calc} (g/cm^3)	1.382
μ (mm^{-1})	0.852
Absorption correction	Multi-scan
T_{min}, T_{max}	0.931, 0.983
F_{000}	612
Crystal size (mm^3)	0.020 × 0.070 × 0.200
Diffractometer	Bruker D8 VENTURE
Measurement method	multi scan
Index ranges	-13 ≤ h ≤ 13, -8≤ k ≤ 9, -18 ≤ l ≤ 18
θ range for data collection (°)	2.37 to 25.00
Reflections collected	10369
Independent reflections	4699
Observed reflections	2684
R_{int}	0.0658
Refinement method	Full-matrix least-squares on F^2
Data/restraints/parameters	4699/398/349
Goodness-of-fit on F^2	1.033
Final R indices [$I > 2\sigma(I)$]	$R_1 = 0.0542$, $wR_2 = 0.1050$
R indices (all data)	$R_1 = 0.0956$, $wR_2 = 0.1186$
$\Delta\rho_{max}$, $\Delta\rho_{min}$ (e/Å^3)	0.777, -0.440

Table 2 Important geometric parameters for complexes **2**.

Bond lengths (Å)		Bond angles (°)	
Ni1—P1	2.216(2)	P1—Ni1—S1	90.28(9)
Ni1—S1	2.137(2)	P1—Ni1—O1	88.32(17)
Ni1—O1	1.865(5)	P1—Ni1—N3	171.0(2)
Ni1—N3	1.882(6)	S1—Ni1—O1	178.08(19)
S1—C4	1.745(9)	S1—Ni1—N3	86.6(2)
O1—C9	1.313(9)	O1—Ni1—N3	95.0(3)
N2—N3	1.402(9)	S1—C4—N1	117.9(7)
N1—C3	1.473(14)	S1—C4—N2	123.6(7)
N1—C4	1.345(12)	N1—N2—C9	113.1(2)
N2—C4	1.286(11)	N2—C9—N3	119.8(3)
N3—C5	1.305(10)	N2—N3—C5	113.8(7)
		N3—C5—C6	127.5(8)
		C4—N3—C3	118.9(10)
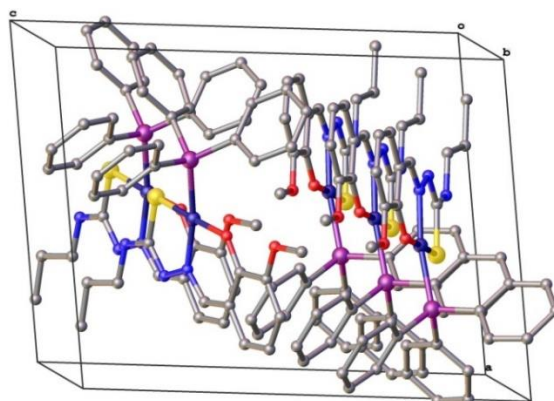
Figure 3. Molecular packing of the complex **2**.
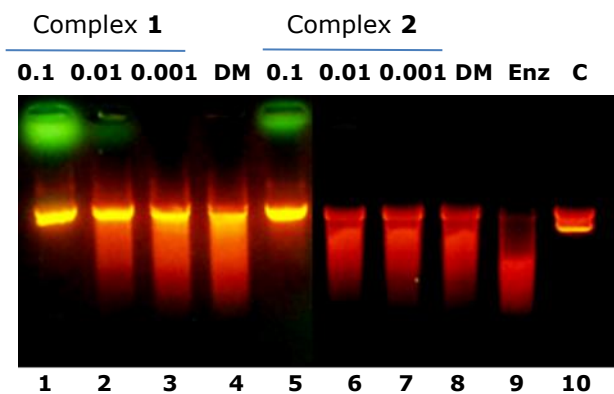
Figure 4. The diagram of the agarose gel electrophoresis shows the inhibition of DNase I enzyme by Ni(II) complexes **1, 2**: lanes 1-3 (for complex **1**): 0.1 µg/mL; 0.01 µg/mL; 0.001 µg/mL, respectively; lane 4 (DM): DNase I enzyme with DMSO control; lanes 5-7 (for complex **2**): 0.1 µg/mL; 0.01 µg/mL; 0.001 µg/mL, respectively; lane 8 (DM): DNase I enzyme with DMSO control; lane 9 (Enz): plasmid DNA incubated with DNase I; lane 10 (C): pHKP-Luc plasmid DNA alone.

CONCLUSION

The nickel-PPh$_3$ complex **2** of 3-methoxy-salicylaldehyde-N^4-propyl-thiosemicarbazone was identified by X-ray crystallographic techniques, which confirmed the dibasic forms (L^{2-}) of propyl-substituted in the nickel centered chelates. The thiosemicarbazone complexes containing N4-long chain alkyl substituent are few in literatures. The synthesized compounds have a slightly distorted square planar geometry involving the thiosemicarbazone, coordinated via ONS mode. The DNase I enzyme inhibition of Ni(II)-thiosemicarbazone complexes, which uses DNA as a substrate, was observed in electrophoresis *in vitro*. studies for the first time.

The asset of electron withdrawing groups in the coordinated thiosemicarbazones causes the increment in the electron lack on the metal. Thus, it is thought that the coordinative unsaturated square-planar geometry maybe in charge of the binding of DNA to nickel(II).

ACKNOWLEDGMENTS

REFERENCES

1. Lobana TS, Kumari P, Hundal G, Butcher RJ. Metal derivatives of N1-substituted thiosemicarbazones with divalent metal ions (Ni, Cu): Synthesis and structures. Polyhedron. 2010;29(3):1130-36.

2. Padhye S, Kauffman GB. Transition Metal Complexes of Semicarbazones and Thiosemicarbazones. Coord. Chem. Rev.1985;63:127-60.

3. Jiang ZG, Lebowitz MS, Ghanbari HA. Neuroprotective activity of 3 aminopyridine-2-carboxaldehydethiosemicarbazone (PAN-811), a cancer therapeutic agent. CNS Drug Rev. 2006;12(1):77-90.

4. Güveli S, Kılıç-Cıkla I, Ülküseven B, Yavuz M, Bal-Demirci T. 5-Methyl-2-hydroxy-acetophenone-S-methyl-thiosemicarbazone and its nickel-PPh₃ complex. Synthesis, characterization, and DFT calculations. J. Mol. Struct. 2018;1173:366-74.

5. Ekennia AC, Onwudiwe DC, Ume C, Ebenso EE. Mixed ligand complexes of N-Methyl-N-phenyl dithiocarbamate: Synthesis, characterisation, antifungal activity, and solvent extraction studies of the ligand. Bioinorgan. Chem. Appl. 2015;2015:1-10.

6. Güveli Ş, Bal-Demirci T, Ülküseven B, Özdemir N. Supramolecular nickel complex based on thiosemicarbazone. Synthesis, transfer hydrogenation and unexpected thermal behavior. Polyhedron. 2016;110: 188-96.

7. Güveli S, Turan K, Ülküseven B. Nickel(II)-PPh₃ complexes with ONS and ONN chelating thiosemicarbazones: synthesis and inhibition potential on influenza A viruses. Turk. J. Chem. 2018;42;371-84.

8. Pahontu E, Fala V, Gulea A, Poirier D, Tapcov V, Rosu T. Synthesis and characterization of some new Cu(II), Ni(II) and Zn(II) complexes with salicylidene thiosemicarbazones: antibacterial, antifungal and in vitro antileukemia activity. Molecules. 2013;18(8):8812-36.

9. Belicchi Ferrari M, Bisceglie F, Pelosi G, Sassi M, Tarasconi P, Cornia M, Capacchi S, Albertini R, Pinelli S. Synthesis, characterization and X-ray structures of new antiproliferative and proapoptotic natural aldehyde thiosemicarbazones and their nickel(II) and copper(II) complexes. J. Inorg. Biochem. 2002;90(3-4):113-26.

10. Bal Demirci T, Congur G, Erdem A, Erdem-Kuruca S, Ozdemir N, Akgun-Dar K, et al. Iron(III) and nickel(II) complexes as potential anticancer agents: synthesis, physicochemical and structural properties, cytotoxic activity and DNA interactions. New J. Chem. 2015;39(7):5643-53.

11. Umadevi C, Kalaivani P, Puschmann H, Murugan S, Mohana PS, Prabhakaran R. Substitutional impact on biological activity of new water soluble Ni(II) complexes: Preparation, spectral characterization, X-ray crystallography, DNA/protein binding, antibacterial activity and in vitro cytotoxicity. Journal of Photochemistry & Photobiology, B: Biology. 2017;167:45–57.

12. Kalaivani P, Saranya S, Poornima P, Prabhakaran R, Dallemer F, Vijaya Padma V, Natarajan K. Biological evaluation of new nickel(II) metallates: Synthesis, DNA/protein binding and mitochondrial mediated apoptosis in human lung cancer cells (A549) via ROS hypergeneration and depletion of cellular antioxidant pool. Eur. J. Med. Chem. 2014;82:584-599.

13. Prabhakaran R, Sivasamy R, Angayarkanni J, Huang R, Kalaivani P, Karvembu R, Dallemer F, Natarajan K. Topoisomerase II inhibition activity of new square planar Ni(II) complexes containing N-substituted thiosemicarbazones: Synthesis, spectroscopy, X-ray crystallography and electrochemical characterization. Inorg. Chim. Acta. 2011;374(1):647-653.

14. Nadano D, Yasuda T, and Kishi K. Measurement of Deoxyribonuclease I Activity in Human Tissues and Body Fluids by a Single Radial Enzyme-Diffusion Method. Clin. Chem. 1993;39(3):448-52.

15. Lazarides E, Lindberg U. Actin is the naturally occurring inhibitor of deoxyribonuclease I. Proc. Natl. Acad. Sci. U.S.A. 1974;71(6):4742-46.

16. Baranovskii AG, Buneva VN, Nevinsky GA. Human deoxyribonucleases. Biochem. Mosc. 2004;69(6):587-601.

17. Kolarevic A, Yancheva D, Kocic G, Smelcerovic A. Deoxyribonuclease inhibitors.

European Journal of Medicinal Chemistry. 2014;88:101-11.

18. Sheldrick G. SHELXS-97, Program for Crystal Structure Solution, Univ. Göttingen, Germany. 1997.

19. Sheldrick GM SHELXL2014/1 Programs for the Solution and Refinement of Crystal Structures. University of Göttingen. 2014.

20. Sheldrick GM. A short history of SHELX. Acta

Crystallographica Section A Foundations of Crystallography. 2008;64(1):112–22.

21. Sheldrick GM. University of Göttingen, Germany. 1996.

22. Saint P. Bruker AXS Inc., Madison, Wisconsin, USA. 2012.

23. Çağlayan E, Turan K. The effects of DNA methyl transferases on antiaging klotho gene expression. Turk. J. Biol. 2016;40(4):797-806.

RESEARCH ARTICLE

Biochemical Confirmation of Anti-Inflammatory Activity of Oxicam-Based Pharmaceutical Compositions

Syrova Ganna Olegivna ✉ iD **, Tishakova Tetyana Stanislavivna*** ✉ iD **, Levashova Olga Leonidivna** ✉ iD **, Savelieva Olena Valeryivna** ✉ iD

*Kharkiv National Medical University, Medical and Bioorganic Chemistry Department, 61022, Kharkiv, Ukraine.

Abstract: Biochemical confirmation of anti-inflammatory activity of oxicam-based pharmaceutical compositions was performed by the determination of the level of one of the main markers of inflammation-C-reactive protein. Biochemical studies were carried out on laboratory animals (white WAG rats) to study the anti-inflammatory effects of meloxicam, piroxicam, caffeine, and pharmaceutical compositions consisting of meloxicam and caffeine, piroxicam and caffeine compared to the reference drug - sodium diclofenac. The content of CRP in serum of rats was determined using the CRP latex test kit. It was shown that the composition of meloxicam and caffeine reduced the content of CRP by 16 times compared with formalin-induced edema, and by 2 times in comparison with the reference drug diclofenac sodium, which is statistically significantly different from the control.

INTRODUCTION

Modern medicine has a wide arsenal of anti-inflammatory drugs (AID), because an inflammatory process is a leading pathogenetic link of many diseases, including rheumatic diseases and musculoskeletal system diseases, which constitute about 80% of the pathology in any medical practice. However, along with pharmacological action and sufficient degree of clinical efficacy, most of them cause a number of undesirable side effects (1, 2).

The search of highly effective pharmacological compositions with minimal side effects is a relevant issue. One of these areas is the creation of pharmacological compositions based on nonsteroidal anti-inflammatory drugs (NSAIDs).

Considering the fact that both cyclooxygenase isoenzymes participate in the pathogenic mechanisms of the pain syndrome (acute pain syndrome) development, application of nonselective drugs with a balanced inhibitory activity with regard to cyclooxygenase 1 (COX-1) and cyclooxygenase 2 (COX-2) is the most viable. Piroxicam suppresses the production of prostaglandins in the area of inflammation and inhibits the production of "physiological" prostaglandins. It reduces the formation of rheumatoid factor - a protein of the acute phase of inflammation, which belongs to the group IgM; increases the ratio of Th/Ts, therefore, it is able to suppress autoimmune reactions in the area of the inflammatory organ or tissue (5-7).

Selective inhibitors include meloxicam, which differs from other drugs in terms of its high efficacy and safety. Administration of meloxicam decreases the synthesis of prostaglandins and the degree of formation of oxygen-free radicals. Meloxicam readily penetrates into the synovial fluid, which indicates that the active substance contributes to the elimination of the infectious process in the joint tissues. It is 20-fold COX-2 selective as compared to COX-1, meloxicam positively affects the metabolism of cartilage tissue and is characterized by chondroprotective properties (3, 4).

In the proposed pharmaceutical composition, we introduced an adjuvant of NSAIDs and nonnarcotic analgesic (NNA) - caffeine (8, 9-11). Furthermore, the enhancement of the analgesic effect of NNA is associated with the central cholinergic analgesic effect of caffeine (12), with the structural similarity of adenosine and caffeine molecules that contributes to the neurochemical mechanism of its action in blocking specific P1-purine receptors in the brain (13).

C-reactive protein analysis (CRP) is a non-specific indicator of inflammation. The amount of protein significantly increases in the presence of inflammatory process of any etiology, including tumoral and necrotic processes. That is why CRP is considered as a non-specific inflammatory marker. CRP enhances the mobility of leukocytes. By binding to T-lymphocytes, it affects their functional activity initiating precipitation, agglutination, phagocytosis, and complement fixation. CRP level in the blood elevates in 4 hours after onset of inflammation and disappears during the convalescence. In the presence of calcium, CRP binds ligands in polysaccharides of microorganisms and causes their elimination. The level of CRP in the serum shows the intensity of the inflammatory process. Control of CRP is an important for monitoring different inflammatory diseases (14, 15).

Our quantum chemical investigations have shown that the chosen reference drug - diclofenac is the mildest reagent in comparison with piroxicam and meloxicam. The absolute hardness of diclofenac is 2.8746, and for piroxicam and meloxicam, 4.0569 and 4.1189 respectively (16). It is also known that meloxicam is a selective COX-2 inhibitor and diclofenac with piroxicam are nonselective COX-1 and COX-2 inhibitors.

MATERIALS AND METHODS

Biochemical studies were carried out on laboratory animals (white WAG rats) in order to study the anti-inflammatory effects of meloxicam, piroxicam, caffeine, and pharmaceutical compositions consisting of meloxicam and caffeine, piroxicam and caffeine compared to the reference drug - sodium diclofenac.

The anti-inflammatory action of the above mentioned substances was studied by the experimental model of formalin-induced paw edema.

The rats were divided into 8 groups of 6 animals each. Animals of the 1st intact group intragastrically received single dose of 3% starch mucus (2 mL per 200 g of rat's weight). Animals of the 2nd group received 3% starch mucus and the formalin induced edema was modeled by sub-planar administration of 2% formalin solution into hind paw of rat. Animals from experimental groups 3-8 were intragastrically administered studied compositions in the form of a suspension of 3% starch mucus. Animals of the 3rd group - piroxicam in the dose of 1.3 mg per 1 kg of bodily weight, 4th -meloxicam in a dose of 0.6 mg per 1 kg of bodily weight, 5th - caffeine (0.6 mg per 1 kg of rat's weight), 6th group received composition of piroxicam (1.3 mg per 1 kg of rat's weight) with caffeine (0.6 mg per 1 kg of rat's weight), 7th group - composition of meloxicam (0.6 mg per 1 kg of rat's weight) with caffeine (0.6 mg per 1 kg of rat's weight), 8th group – reference medicinal product (8 mg of sodium diclofenac per 1 kg of rat's weight). Maximum development of formalin induced edema is observed 4 hours after its modeling. 3% starch mucus, drugs and their pharmaceutical compositions were administered 1 hour before, taking into account their pharmacokinetic and pharmacodynamic characteristics. Animals of all groups were decapitated under etheric anesthesia (17). Blood collection was carried out in rats of all groups. After the blood collection of blood samples of all groups of animals had been subjected to centrifugation at 1500 rpm/min for 15 minutes. The whole plasma was collected and subjected to CRP analysis using standard latex test.

The content of CRP in serum of rats was determined using the CRP latex test kit (State registration number 1248/2002, Kharkiv, Ukraine). The method is based on the detection of acute phase protein in the serum – CRP, which enters agglutination reaction with anti-CRP antibodies, adsorbed on neutral latex particles. Agglutination of latex particles is considered a positive reaction, indicating the presence of C-reactive protein at a significant and detectable level. Specimens which do not contain human CRP will not cause agglutination.

RESULTS AND DISCUSSION

The level of CRP in serum of intact rats was 6±0.004 mg/L. This indicator increased significantly and reached value 96±0.001 mg/L under the condition of formalin induced edema, which exceeds the norm by 16 times.

The biochemical study of the anti-inflammatory activity of piroxicam, meloxicam, caffeine and their composition on the content of the inflammation marker CRP showed that the investigated drugs had an effect on the CRP content in rat's serum and significantly lowered it regarding the formalin induced edema (**Table 1**).

Decrease in CRP level in the serum of rats 2 times as compared with formalin edema was observed after mono-administration of non-selective COX-1 inhibitor (piroxicam), but the obtained data statistically significant differ from the reference product diclofenac sodium: the effect of piroxicam is 4 times less than the reference medicinal product for the content of CRP in the serum of rats.

Mono-administration of the selective COX-2 inhibitor – meloxicam showed a significant decrease of the CRP content in the blood serum of rats under condition of formalin edema. The content of CRP decreased by 8 times and did not statistically significant differ from the diclofenac sodium. Thus, the selective COX-2 inhibitor (meloxicam) more

effectively affects the CRP content of serum in rats under conditions of formalin edema than the non-selective COX-1 inhibitor (piroxicam).

The mono-administration of analgesic adjuvant caffeine also reduced the CRP content of rat's serum (24±0.001 mg/L) by 4 times as compared to formalin edema, but it is 2 times less than diclofenac sodium influenced the content of CRP in serum blood in rats.

Composition of piroxicam with adjuvant caffeine reduced the content of the CRP in blood serum of rats by 4 times compared with formalin-induced edema but the obtained data did not reach the reference medicinal product (sodium diclofenac). The pharmaceutical composition of piroxicam with caffeine had 2 times less effect on the content of CRP in the serum of blood in rats then reference drug. Therefore, caffeine potentiates the anti-inflammatory effect of piroxicam in this composition.

The composition of meloxicam and caffeine proved to be the most effective and worked better than all the investigated drugs, including the reference drug. This composition reduced the content of CRP by 16 times compared with formalin-induced edema, and by 2 times in comparison with the diclofenac sodium, which is statistically significantly different from the control, *i.e.* caffeine increases and potentiates anti-inflammatory action of meloxicam.

Table 1: Anti-inflammatory action of piroxicam, meloxicam, caffeine, and their pharmaceutical compositions on the CRP level in blood serum of rats under conditions of formalin-induced edema (n = 6).

№	Groups of rats	CRP, mg/L
1	Control	6 ± 0.004
2	Formalin-induced edema	96 ± 0.001^{1}
3	Piroxicam	$48 \pm 0.003^{1/2/4/5/6/7/8}$
4	Meloxicam	$12 \pm 0.005^{1/2/3/5/6/7}$
5	Caffeine	$24 \pm 0.001^{1/2/3/4/7/8}$
6	Piroxicam + caffeine	$24 \pm 0.002^{1/2/3/4/7/8}$
7	Meloxicam + caffeine	$6 \pm 0.001^{3/3/4/5/6/8}$
8	Sodium diclofenac	$12 \pm 0.001^{1/2/3/5/6/8}$

Note 1. (mean ± error in mean)[1] - the difference is significant as compared to the control group, P <0.05;

Note 2. (mean ± error in mean)[2] - the difference is significant as compared to formalin-induced edema, P <0.05;

Note 3. (mean ± error in mean)[3] - the difference is significant as compared to the mono-administration of piroxicam, P <0.05;

Note 4. (mean ± error in mean)[4] - difference is significant as compared to mono-administration of meloxicam, P <0.05;

Note 5. (mean ± error in mean)[5] - the difference is significant as compared to the mono-administration of caffeine, P <0,05;

Note 6. (mean ± error in mean)[6] - the difference is significant as compared to the administration of the piroxicam and caffeine composition, P <0.05;

Note 7. (mean ± error in mean)[7] - the difference is significant as compared to the introduction of meloxicam and caffeine, P <0.05;

Note 8. (mean ± error in mean)[8] - the difference is significant as compared to the mono-administration of diclofenac sodium, P <0.05.

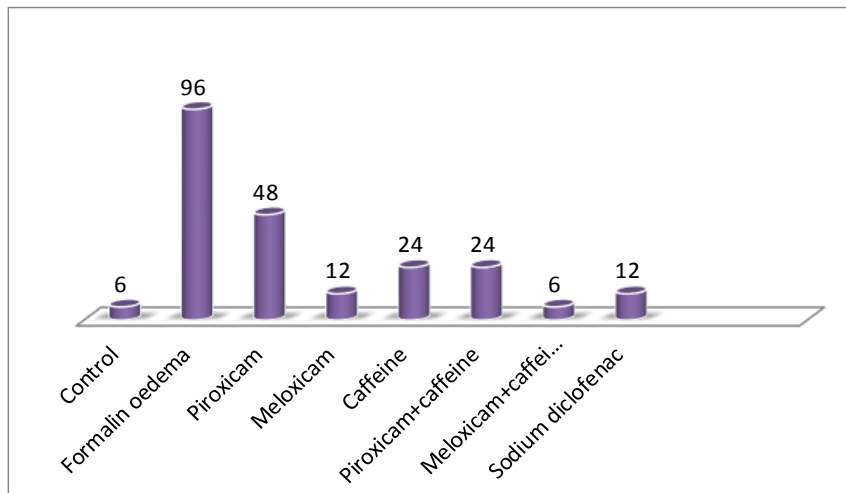Above mentioned results can be represented graphically that helps with visualization of data (Fig. 1):

Figure 1. Content of the CRP in blood serum of rats (in mg/L).

CONCLUSION

The results of biochemical studies of anti-inflammatory activity indicate that piroxicam, meloxicam, caffeine and their compositions show the pronounced anti-inflammatory effect against formalin-induced edema. The leader in biochemical studies is a two-component composition of meloxicam and caffeine, which reduces the level of the inflammation marker CRP to the level of control group and acts better than reference drug – sodium diclofenac.

ACKNOWLEDGMENTS

REFERENCES

1. Isakov VA. Gastropathy associated with the use of non-steroidal anti-inflammatory drugs pathogenesis, treatment, prevention. Clinical Pharmacology & Therapeutics . 2005; 14(2): 34—8. [in Russian]

2. Nasonov EL, Nasonova VA. The pharmacotherapy of pain: rheumatologist's glance. Consilium medicum. 2000; 2(12):509-14. [in Russian]

3. Scherbenkov IM. Problems of perioperative anaesthesis. Consilium

Medicum. 2011; 8: 78-81. [in Russian]

4. Nasonov EL, Zvetkova ES, Balabanova RM. New aspects of anti-inflammatory therapy of rheumatic diseases: theoretical background and clinical application of meloxicam. Clinical medicine. 2006; 4: 4-8. [in Russian]

5. Nakonechna SA, Honcharenko MM, Aleksieieva TM. Experimental study of antipyretic effect of paracetamol composition with caffeine. Experimental and clinical medicine. 2015; 1(66): 47-9. [in Ukrainian]

6. Dix P, Prosser DP, Streete P. A pharmacokinetic study of piroxicam in children. Anaesthesia. 2004; 59:984-7.

7. Abdallah FI, Dawaba HM, Mansour A *et al*. Evaluation of the anti-inflammatory and analgesic effects of piroxicamloaded microemulsion in topical formulations. International Journal of Pharmacy and Pharmaceutical Sciences. 2011; 3(2):66-70.

8. Boiko Ye. P., Lymanska G.O., Petunin P.O., Bachinskyi R.O. Study of the effect of caffeine composition with ibuprofen on the central component of nociceptive response in rats. Contemporary theoretical and practical aspects of clinical medicine: materials of the international conference of students and young

scientists devoted to the 155th anniversary of V.V. Podvysotsky's birth. Odesa. 2012; 116. [in Ukrainian]

9. Syrova GO, Zvyagintseva TV, Chekman IS *et al*. Quantum-pharmacological substantiation of potentiating anticoagulant properties of caffeine. Pharm. Journal. 2008; 6:85-91. [in Ukrainian]

10. Syrova GO, Zvyagintseva TV. Study of potentiating anticoagulant properties of caffeine in an experiment. Congress of the World Federation of Ukrainian Medical Associations: book of abstracts. Ivano-Frankivsk. 2008; 454. [in Ukrainian]

11. Boiko I, Syrova G, Ermolenko T. Experimental conformation of the caffeine's potentiation of the analgetic properties. 3th International Scientific interdisciplinary Congress of medical students and young doctors. Kharkiv. 2010; 14. [in Russian]

12. Ghelardini C, Galeotti N, Bartolini A. Caffeine induces central cholinergic analgesia. Naunyn Schmiedebergs Arch Pharmacol. 1997; 356(5):590-5.

13. Karelov AE, Zaychik AM, Lebedinskiy KM. Purine analgesia: From Theory to Practical Implementation. Proceedings of the III Congress of pharmacologists of Russia, St. Petersburg. 2007; 7(1): 1718 [in Russian].

14. Mazon SB, Monte AS, Almeida EA, Guariento ME. Determining the C-Reactive Protein Level in Patients With Different Clinical Forms of Chagas Disease. Rev Esp Cardiol. 2010; 63(9):1096−9.

15. Pepys MB, Hirschfield GM. C-reactive protein: a critical update. J Clin Invest. 2003; 111(12):1805–12.

16. Syrova GO, Levashova OL, Tishakova TS, Kozub SN, Chalenko NN. Investigation of quantum-chemical properties of indomethacin. The scientific heritage. 2017; 16(16):11-16.

17. Preclinical studies of drugs. Methodological recommendations edited by O.V. Stefanova. Kyiv, 2001; 527. [in Ukrainian]

RESEARCH ARTICLE

Li⁺ doped chitosan-based solid polymer electrolyte incorporated with PEDOT:PSS for electrochromic device

Esin EREN[1,2]* ✉ iD

[1] University of Suleyman Demirel, Innovative Technologies Application and Research Center, 32260, Isparta, Turkey.
[2] University of Suleyman Demirel, Faculty of Arts and Science, Department of Chemistry, 32260 Isparta, Turkey.

Abstract: In this study, solid polymer electrolyte-based on chitosan was prepared with addition of PEDOT:PSS, lithium trifluoromethane sulfonate, propylene carbonate by solvent casting technique. The chitosan-based polymer electrolytes without PEDOT:PSS, with PEDOT:PSS were characterized using electrochemical impedance spectroscopy. The ionic conductivity value was calculated as 4.2×10^{-4} S/cm for the chitosan-based electrolyte including PEDOT:PSS. The SPE having good ionic conductivity was used to fabricate electrochromic device with glass/ITO/WO₃|PEDOT:PSS-Ch-LiTRIF-PC|ITO/glass whose performance was evaluated via cyclic voltammetry, transmittance, and repeating chronoamperometry. The optical contrast of ECD was attained as 22% at 800 nm, resulting in a coloration efficiency of 67 cm²/C. The ECD displays fast response time for coloration (t_c), which is 0.29 s. Upon reversal of potential bleaching (t_b) forms within 3 s. The findings demonstrated that this SPE electrolyte has promising candidate for use in optoelectronic applications.

INTRODUCTION

SPEs have gained great interest due to their potential applications like sensors, photovoltaic cells, electrochromic devices, and smart electronics (1). An ECD acts as a thin film battery that alters optical features after application of an electric input (2, 3). In general, a conventional ECD includes five electroactive layers, an ion conducting electrolyte sandwiched via an electrochromic (EC) layer and ion-storage layer that are individually deposited on transparent conductive substrates (4). Ion conducting electrolyte supplies the ionic conduction layer between the electrochromic layer and the ion-storage layer (5). Nowadays, these devices are of great attention to technological and commercial applications, explaining why diverse SPEs have been suggested for this aim (6). WO₃ is a very encouraging cathodic electrochromic compound,

which has superior electrochromic characteristics such as optical contrast and stability. Thus, it is one of widely used as an electrochromic material (2, 7).

Biodegradable polymers such as polyethylene oxide and chitosan are commonly used, and further scientific research using SPE system are in progress (8). SPEs supply the advantages of compactness and reliability without the leakage of liquid components (8). Chitosan (Ch) is a type of cationic amino-polysaccharide that is acquired from the alkaline deacetylation of chitin (8). Its chemical structure consists of reactive amino and hydroxyl groups which feature own lone pair electrons that are appropriate to produce solid polymer electrolytes (9, 10). Due to the existence of polar functional groups along its chain, chitosan can also solvate inorganic salts and show the features adherent to polymer electrolytes (11,

12). The presence of lone pair electrons allows the chelation of a proton donor supplied by a salt (13, 14). However, chitosan-based films can display low ionic conductivity. At low pH, the primary amines get protonated to have positive charges and leave the hydroxyl groups free that produces chitosan a water-soluble cationic polyelectrolyte. This may promote ionic conduction (15, 16). One way to obtain enhanced ionic conductivity is to add plasticizers in polymer electrolytes which can be preferred due to the creation of free volume. Furthermore, ionic conductivity can be ascribed to the amorphous phase. Dissolution of salts (such lithium salts) in the polymer matrix is one of the several used approaches to acquire amorphous phase (1). Alves *et al.* fabricated ECD with $WO_3/Chitosan_{33.32}Ce(CF_3SO_3)_3/CeO_2–TiO_2$ configuration which displayed an alteration from transparent to blue color with 5% of percent transmittance change at 633 nm (17). Two years later, new SPEs of chitosan complexed with $Sm(CF_3SO_3)_3$ including glycerol were prepared for solid state electrochromic devices. The changes of transmittance of ECD with WO_3 electrochromic layer are measured as 4.1%, 4.6% at 550 nm, 633 nm, respectively (6). Herein, this study demonstrated that ECD including the biohybrid electrolyte system with PEDOT:PSS exhibited improved electrochromic characteristics, especially enhanced optical contrast, when compared to those of ECD composed of chitosan-based electrolyte systems (6, 17).

PEDOT:PSS is one of the most used electronically conducting polymers due to its robust mechanical properties, good film forming ability, and high electrical conductivity (18, 19). Zhang *et al.* prepared a novel kind of biocompatible micelles including PEDOT:PSS and chitosan for electrochemical biosensor (19). Due to the good electrostatic interaction between chitosan and PEDOT:PSS, PEDOT:PSS can be used to prepare chitosan-based SPEs (19).

The main propose of this paper is to provide a significant contribution on the chitosan-based solid polymer electrolyte with the addition of PEDOT:PSS in terms of electrochromic applications. The chitosan-based SPE consisting of acetic acid, LiTRIF and PEDOT:PSS was plasticized with PC. For this purpose, a biohybrid electrolyte-based ECD with glass/ITO/WO₃|PEDOT:PSS-Ch-LiTRIF-PC|ITO/glass was fabricated and analyzed using electrochemical, transmittance measurements. To the best of my knowledge, the WO_3-based ECD consisting of the chitosan-based electrolyte system with the addition of PEDOT:PSS has hitherto been unexplored for electrochromic applications.
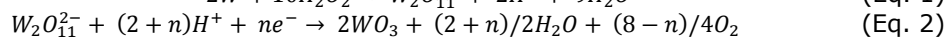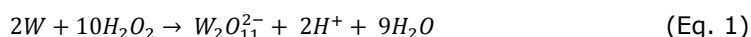
EXPERIMENTAL

Materials
W nanopowder was supplied by SkySpring Nanomaterials. Chitosan with medium molecular weight (1.10×10^6 g/mol (DD:75–85)), PEDOT:PSS were purchased from Sigma-Aldrich. LiTRIF from Sigma-Aldrich, PC from Sigma-Aldrich, DMSO from Sigma-Aldrich, and acetic acid from Merck were used as received. ITO-coated glass sheets were purchased from Plazmatek A.Ş. Company/Turkey and were cleaned with ethanol and deionized water prior to use.

Preparation of the WO₃ Film
The WO_3 sol was prepared by dissolving W powder into 30% H_2O_2 and adding ethanol and water. The electrodeposition was performed using a three-electrode electrochemical system with a platinum wire as the counter electrode, Ag/AgCl as the reference electrode and ITO coated glass as the working electrode at room temperature. Deposition was carried out by applying a constant voltage (-0.45 V) for 15 min. Then, the prepared thin film was rinsed with distilled water and dried in air.

The mechanism of the electrodeposition of WO_3 can be explained via the two-stage reaction processes (20):

$$2W + 10H_2O_2 \rightarrow W_2O_{11}^{2-} + 2H^+ + 9H_2O \qquad \text{(Eq. 1)}$$
$$W_2O_{11}^{2-} + (2+n)H^+ + ne^- \rightarrow 2WO_3 + (2+n)/2H_2O + (8-n)/4O_2 \qquad \text{(Eq. 2)}$$

Preparation of the SPE
The solution casting method was used for the preparation of chitosan-based SPE. 0.2 g of chitosan powder was dissolved in 10 mL of 2% acetic acid solution. The mixture was stirred continuously for one day to complete dissolution. Then, 1.2 g of LiTRIF and 4 g of PC as plasticizer were added into this solution under stirring at room temperature. The resulting solution was stirred for one day until homogeneous dispersion. PEDOT:PSS solution was doped with 5 wt% DMSO. The resulting PEDOT:PSS solution was then added 2.5 w% with respect to the weight of all other components. Continuous stirring for two days was conducted to ensure complete dissolution.

Construction of the ECD
The prepared viscous electrolyte was poured on ITO-coated glass sheets and dried at room temperature to form transparent SPE. The actual pixel electrode dimension was described as 1.3 cm² using double-sided adhesive foam band. The ECD was fabricated by sandwiching of SPE including chitosan and PEDOT:PSS between working (WO_3) and counter (ITO coated glass) electrodes. The schematic illustration of the electrochromic structure device is shown in Figure 1.
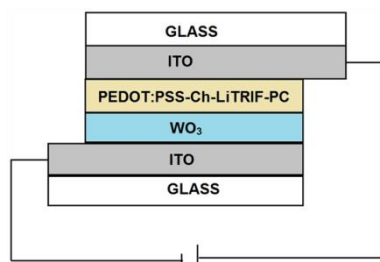
Figure 1. Schematic illustration of the electrochromic structure device

Characterization

Electrochemical properties were evaluated using a Gamry PCl4/300 model potentiostat/galvanostat. Electrochromic studies were performed using a standard three-electrode system, electrochromic film as working electrode, a Pt wire as counter electrode and a Ag/AgCl with 3 M KCl as reference electrode were used. Optical transmittance of solid-state ECD was attained using a computer-controlled setup of HR4000 (Ocean Optics, Dunedin, FL, USA) in the wavelength range of 400-900 nm. The surface morphology and composition analysis of the WO_3 film were performed using a SEM-EDS with the brand FEI Quanta FEG 250. EIS measurements were performed in the frequency range of 0.1 Hz-10 kHz by use of an AC voltage amplitude (10 mV), and CHI760E electrochemical workstation.

RESULTS AND DISCUSSION

SEM result of the WO_3 films

Figure 2 displays the SEM image of the electrodeposition of WO_3 thin film. SEM observation has shown a nano-grain formation with the close-packed structure. The WO_3 film is uniform and dense. The chemical composition of the electrodeposited WO_3 thin film was evaluated using EDS spectrum (Figure 3). The elemental composition of the WO_3 film with its at% and wt% are shown as the inset. The table demonstrates the existence of W and O. The element W is from WO_3, Sn and In are from ITO substrate, and O is from both WO_3 and ITO substrate. The absence of any other peaks except ITO substrate due to W and O confirms the deposition of WO_3 film without any elemental impurities.
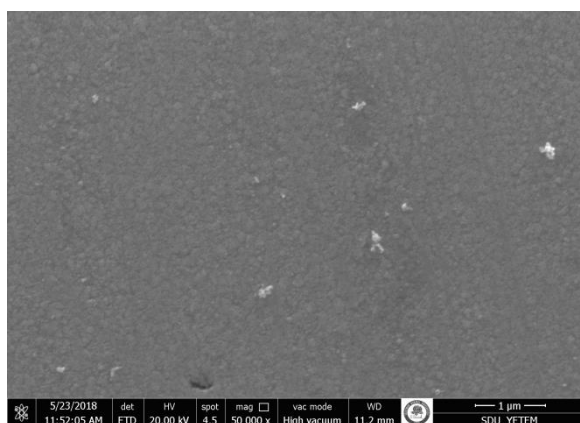
Figure 2. SEM images of WO_3 film onto ITO coated glass at 50000X magnification.

Element	Weight (%)	Atomic (%)
Tungsten (W)	36.55	4.77
Oxygen (O)	63.45	95.23
Total	100	100
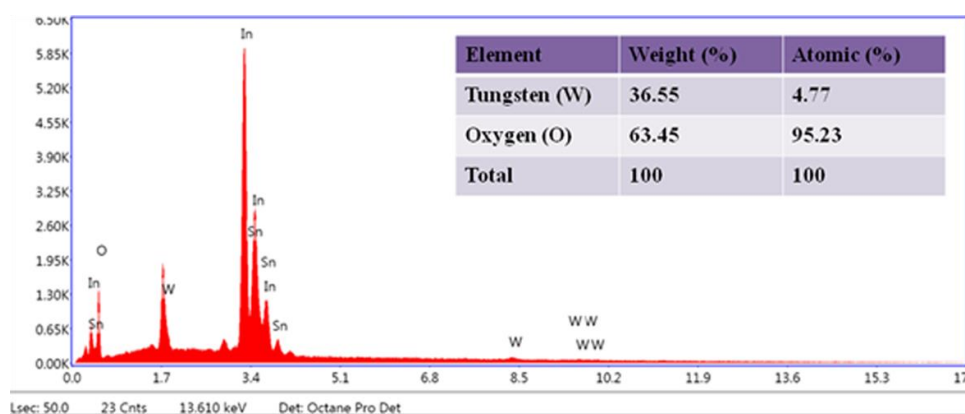
Figure 3. EDS spectrum of WO_3 film onto ITO coated glass.

Ionic Conductivity Result of SPE

The electrolyte plays a significant role in the ECD, and is used to conduct ions between the electrochromic layer and the ion-storage layer (21). One of the main criteria for applications in various electrochemical devices is to attain high ionic conductivity of electrolytes (22). Most of the electrochromic devices need to have >10^{-4} Scm^{-1} of ionic conductivity to allow effective performance (23). Ionic conductivities of the prepared solid polymer electrolyte with PEDOT:PSS and without PEDOT:PSS were measured via electrochemical impedance spectroscopy (EIS). EIS was operated with 'ITO

coated glass/electrolyte/ITO coated glass' structure at a constant potential of +0.1 V in the frequency range of 0.1 Hz-10 kHz at room temperature. In this work, the low potential (0.1 V) was used because 0.1 V potential allows to prevent from additional effect of electrode polarization on occurrence of complicated ion layers on the electrode surface (24). Figure 4 shows the Nyquist plot of chitosan-based solid polymer electrolytes with PEDOT:PSS, without PEDOT:PSS. The ionic conductivity (σ) was calculated using equation 3 (25, 26):

$$\sigma = \frac{L}{R_b * A} \qquad \text{(Eq. 3)}$$

where σ is the ionic conductivity, L is the distance between the two electrodes, R_b is the bulk resistance of the SPE, and A is the area of the sample (1 cm^2). R_b (bulk resistance) value of the solid electrolyte can be obtained from the intercept with the Z'-axis (27-30). The ionic

conductivities of the chitosan-based electrolyte without PEDOT:PSS and with PEDOT:PSS solution were calculated as 3.40 x 10^{-4}, 4.2 x 10^{-4} S/cm, respectively. The decrease of R_b leads to the enhanced ionic conductivity after introduction of PEDOT:PSS in chitosan-based electrolyte, as seen in Figure 4. Ionic conductivity plays one of significant roles for availability of the mobility of ions during the electrochromic switching procedure. Enhancement in ionic conductivity can lead to rapid switching time (31). Similar results were acquired for electrolytes based on other polysaccharides (32, 33). For example, Andrade *et al.* prepared plasticized pectin-based gel electrolytes with 68 wt.% of glycerol that showed an ionic conductivity of 4.7 x 10^{-4} S/cm (32). Alves *et al*. prepared a type of erbium triflate doped chitosan electrolytes using solvent casting method. The highest ionic conductivity values were calculated as 2.06 x 10^{-5} and 5.91 x 10^{-4} Scm^{-1} at 30 °C, 90 °C, for electrolytes including higher amount of glycerol, respectively (1).
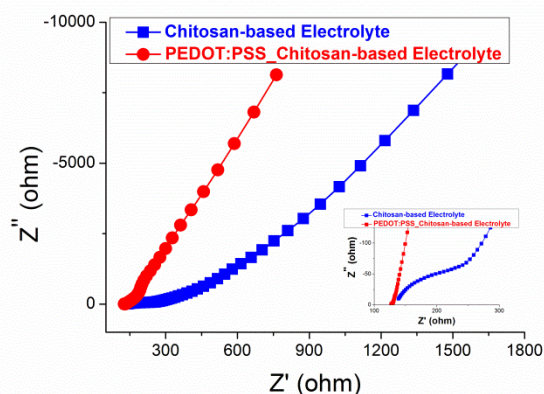

Figure 4. Nyquist diagrams corresponding to chitosan-based electrolyte with PEDOT:PSS and without PEDOT:PSS.

Performance of the ECDs
Figure 5 displays *in situ* transmittance responses at 800 nm of ECD with potential being switched between +3 V and -3 V for 30 s per step. Electrochromic switching of ECD was evaluated by probing the transmittance modulations under a square-wave potential step. The response time was controlled by stepping the potential repeatedly between coloration and bleaching states. The transmittance change was analyzed as a function of time at a certain wavelength. For WO$_3$-based ECD, the voltage was stepwise switched between +3 V and -3 V at 800 nm via applying a square-wave potential step of 30 s with 3 cycles. The coloration and bleaching times are described as the time required for a 90 % change in the whole transmittance modulation at 800 nm (34). The optical contrast (ΔT) for this ECD was found as 22% with the switching time of 0.29 s for coloring step and 3 s for bleaching step. Rocha *et al.* prepared an ECD with configuration ITO/NiO/LiClO$_4$-PC-PMMA/WO$_3$/ITO that had optical contrast values ranging from 8% to 28% (35). As reported by Ling *et al.*, the hybrid electrochromic films consisting of WO$_3$

nanoparticles, PEDOT: PSS and PEI showed the optical contrast of 20% at the wavelength of around 633 nm (36). Aiming to figure out the reversibility of WO$_3$-based ECD with chitosan electrolyte incorporating PEDOT:PSS, the ECD was subjected to CA cycling by application of different electric potentials (-3 V , +3 V) with a time step of 30 s for 3 cycles (Figure 5b). The decrease in current density as a function of time is due to the enhanced chemical potential of the injected cations (Li$^+$) as intercalation steps (18, 37). As seen from Figure 5, there is no significant change of transmittance percent or current density during repetitive cycle, indicating superior stability and reversibility of ECD. The ECD displays response time for coloration (t$_c$) is 0.29 s. Upon reversal of potential rapid bleaching (t$_b$) forms within 3 s. As published by Chang-Jian *et al.*, WO$_3$/PEDOT:PSS-based ECD incorporated with TEMPO and LiClO$_4$ reveals a response time of 1.1 s (38). ECD was prepared using PProDOTMe$_2$ as the working electrode, Li-Ti-NiO as the counter electrode. The ECD with polyvinyl butyral and polyethylene glycol-based hybrid QSPEs attain a fast response between colored and bleached state

$(t_c=1.2$ s, $t_b=2.6)$ (4). Liu *et al*. incorporated carbon nanotubes and chitosan into WO_3 films, resulting in the optical modulation of 13.5%, rapid coloration $(t_c=1.9$ s) and bleaching times $(t_b=1.0$ s) (34). In this study, the obtained optical contrast and response times for ECD were comparable with literature (4,34,38). The calculated switching times of ECD were faster than 4 s, which contributes for requirements of electrochemical devices (0.1-10s) (39).
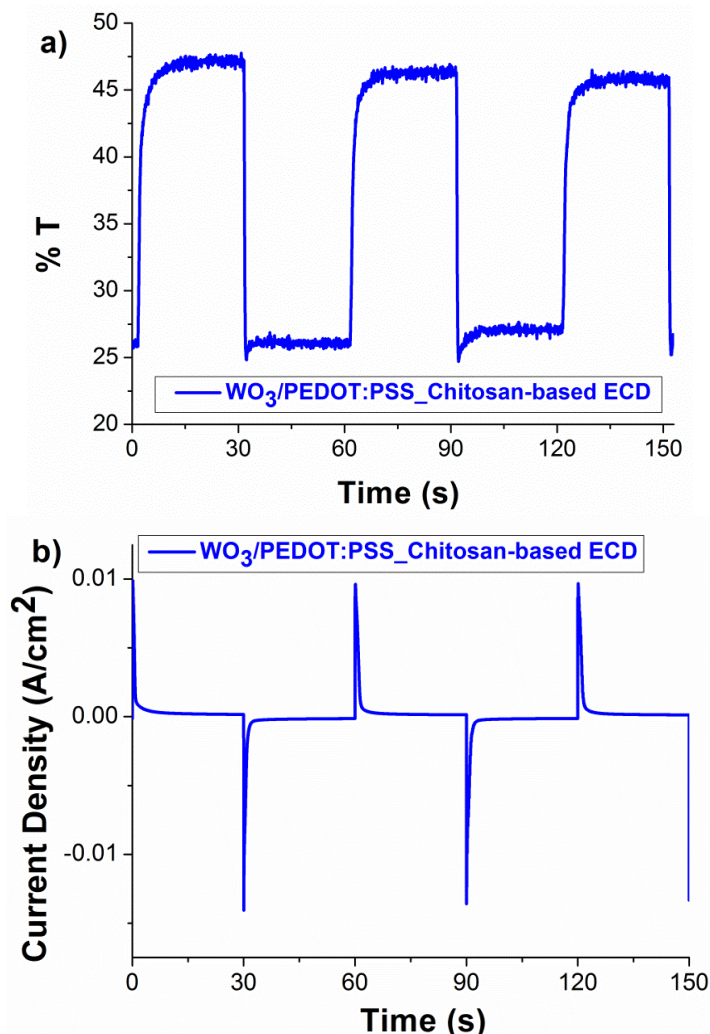
Figure 5. a) Transmittance and b) current density change of electrochromic devices based on WO_3/PEDOT:PSS_Chitosan for applied potentials of ±3 V (monitored at 800 nm).

The colored and bleached states of ECD are displayed in Figure 6. Upon the applied voltage of -3 V, Li^+ ions insert into the PEDOT:PSS layer with the charge balancing counter flow of electrons through the external circuit to compensate for the negative charges of the SO_3^- groups on the PSS polyanion which leads to reduction of PEDOT:PSS layer. The Li^+ ions permeate down to the WO_3 layer with the counter electrons which causes the reduction from W^{6+} ions to W^{5+} ions. The above mentioned processes induces to an alternation in the electron density in the ECD changing the color from light blue to dark blue color. On the other hand, when the applied potential is increased to the positive potential (+3 V), the deintercalations of the Li^+ ions and electrons take place, and the bleached state occurred as a result of the oxidation procedure (40). The electrochemical behavior of WO_3 and PEDOT:PSS accompanies the following electrochemical reaction (2, 41, 42):

$$WO_3 + xLi^+ + xe^- \leftrightarrow Li_xWO_3$$

(colorless, oxidized)   (deep blue, reduced)   (Eq. 4)

$$PEDOT^+PSS^- + Li^+ + e^- \leftrightarrow PEDOT^0 + PSS^-Li^+$$

(light blue, oxidized)   (dark blue, reduced)   (Eq. 5)
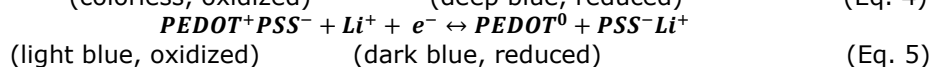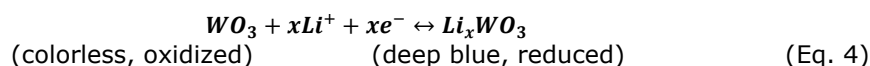
Figure 6. Photographs of the electrochromic device (ECD) based on WO₃/PEDOT:PSS_Chitosan in the two extreme states (a) in its bleached state at + 3 V (b) in its colored state at - 3 V.

Typical cyclic voltammograms of this ECD, recorded during the 1st, 10th, and 20th cycles at 50 mVs⁻¹, are shown in Figure 7. According to the CV scan results in Figure 7, the application of an increasingly negative voltage to the ECD in the dark blue color state brings about an enhanced cathodic current due to the reduction of WO_3, and it is accompanied via a simultaneous alteration to bleached state (43). A large anodic peak has its
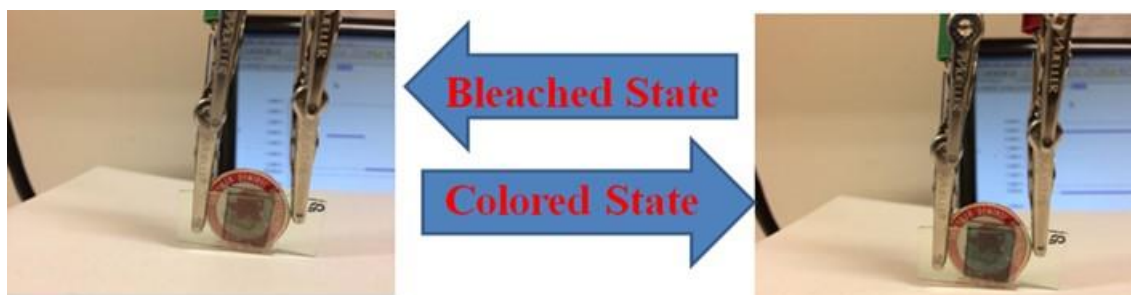
maximum centered at 0.79 V. Moreover, the broad voltammetric wave was seen during both anodic and cathodic processes. It can belong to overlapping of WO_3 and PEDOT:PSS redox peaks (33). After the 20th cycle, cyclic voltammetric studies also showed a nice electrochemically reversible behavior with a little loss of current density, however.
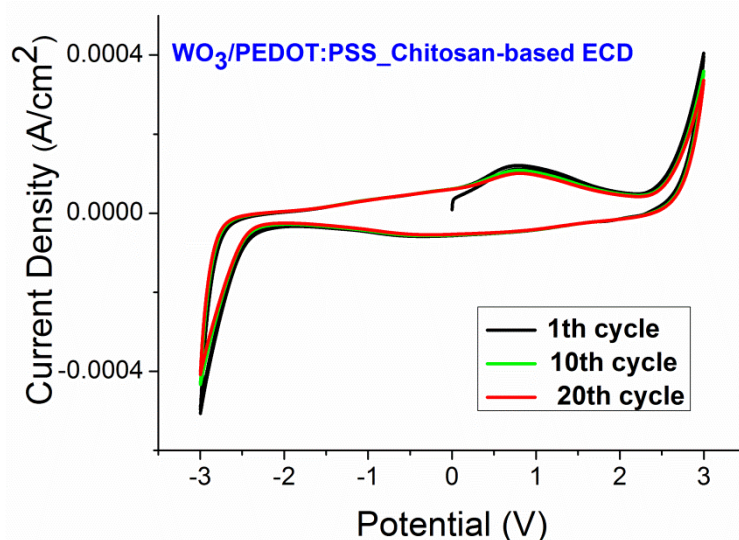
Figure 7. Cyclic voltammograms of electrochromic device (ECD) based on WO₃/PEDOT:PSS_Chitosan during 20 cycles.

CVs were carried out for ECDs with linear potential sweep between -3.0 V and +3.0 V at various scan rates ranging from 25 to 200 mV/s⁻¹ (Figure 8a). The area of CVs possesses a direct associated with the amount of charge involved in the intercalation process. The electrochemical characteristics shift to higher value with the

increase of the scan rate (Figure 8b). The perfect linear relationship indicated that the redox process of the electroactive film is controlled by the ion from the electrolyte to the electrode surface and redox processes were reversible in all cases even at elevated scan rates (2, 44).
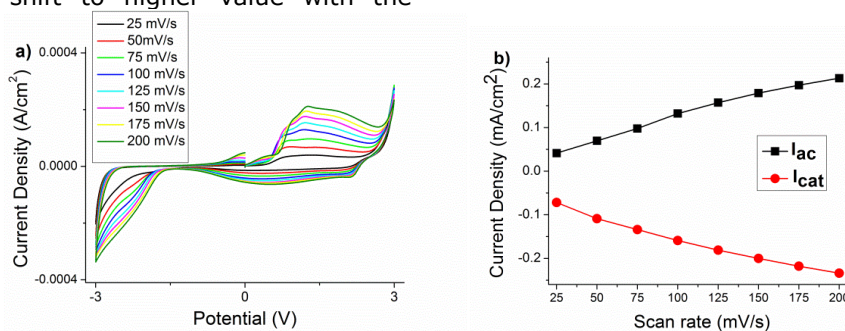
Figure 8. CVs of the ECD at different scan rates (a) plot of cathodic/anodic current density versus scan rate where I_{ac} and I_{cat} denote the anodic and cathodic peak current density, respectively (b).

Chronocoulometric (CC) measurement was performed for WO$_3$/PEDOT:PSS_Chitosan- based ECD at ±3 V for a step of 30 s to evaluate the alternation in their charge density of Li$^+$ during the intercalation and deintercalation process as a function of time (Figure 9). The percent electrochromic reversibility of ECD was calculated using Equation 6 (2, 45):

$$Reversibility\ (\%) = \frac{Q_{di}}{Q_i} \times 100 \qquad \text{(Eq. 6)}$$

where Q$_i$ and Q$_{di}$ are the amount of charge intercalated and deintercalated in the electrode, respectively. The reversibility was calculated as 82.19% for WO$_3$/PEDOT:PSS_Chitosan-based ECD.
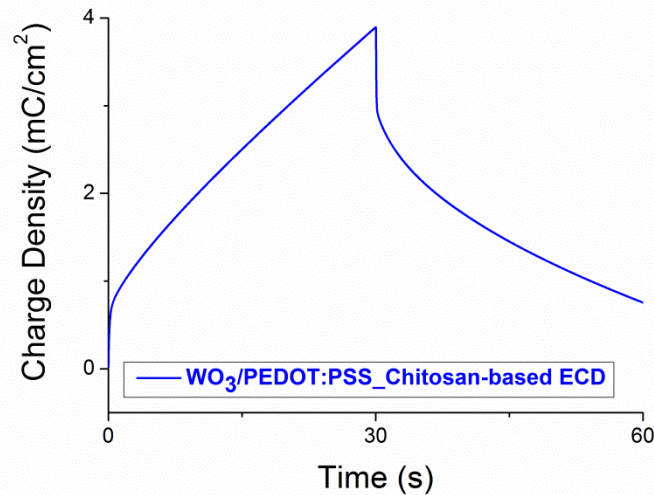
Figure 9. Chronocoulometric study for WO$_3$/PEDOT:PSS_Chitosan- based ECD.

Coloration efficiency (CE) is a critical factor to evaluate the power consumption of an ECD since it signifies the alteration in optical density at the monitoring wavelength per inserted (extracted) charge (46). In general, the CE value can be calculated using the following equations (2, 44).

$$\Delta OD = log(\frac{T_b}{T_c}) \qquad \text{(Eq. 7)}$$

$$CE = \frac{\Delta OD}{Q_d} \qquad \text{(Eq. 8)}$$

where T$_b$ and T$_c$ represent the transmittances of the ECD in the bleached and colored states at a specific wavelength, respectively. ΔOD is the change in optical density, which is proportional to the amount of formed color centers. Q$_d$ is the charge density inserted (extracted). CE was calculated as 67 cm^2/C. Bathe *et al.* investigated the electrochromic features of fibrous reticulated WO$_3$ films fabricated from ammonium tungstate precursor using a pulsed spray. The electrochromic optical contrast and coloration efficiency were found to be ~12%, 34 cm^2/C, respectively (47). The electrochromic device with the configuration ITO/WO$_3$-PEDOT/ACN:PC:PMMA:LiClO$_4$ gel electrolyte/ ITO has a CE of 41.61 cm^2/C (48). In another study, the coloration efficiency of WO$_3$-based ECD with Li$^+$ and Er^{3+} doped poly(ε-caprolactone)/siloxane biohybrid electrolytes was calculated as 10.8 cm^2/C (49). In this study, the calculated CE value of ECD is better than those several reported earlier (47-49). Electrochromic performance comparison of this work and several reported works based on electrochromic applications are presented in Table 1. In this study, the ECD obviously shows a higher value in optical contrast when compared to chitosan-based ECDs (6,17). Moreover, the response times is still faster than those in previous reports which utilized WO$_3$ as electrochromic material (36, 50). As a result, the electrochromic performance is higher than the several published articles based on electrochromic applications (6,17,36, 50, 51).

Table 1. Electrochromic performance comparison of this work and several published work on electrochromic applications

Sample	Electrolyte	Δ%T	t_c (s)	t_b (s)	CE (cm²/C)	References
WO₃	Chitosan/LiTRIF/ PEDOT:PSS	22	0.29	3	67	This work
WO₃	**PMMA/LiClO₄**	**20.17**	**21.4**	**18.5**	**76.82**	**50**
PEDOT:PSS	PEO:LiClO₄	28	10	1	377	51
WO₃/ PEDOT:PSS/PEI	**LiClO₄**	**20**	**8**	**-**	**117.7**	**36**
WO₃/CeO₂-TiO₂	Chitosan-Ce(CF₃SO₃)₃	5	-	-	-	17
WO₃/CeO₂-TiO₂	**Chitosan/ Samarium (III) triflate**	**4.6**	**-**	**-**	**-**	**6**
Prussian blue (PB)	Chitosan/ Samarium (III) triflate	9.2	-	-	-	6

CONCLUSION

This study elucidates on the fabrication of ionically conducting systems based on Ch as the base polymer matrix, PEDOT:PSS as conductive polymer, LiTRIF as guest salt, and PC as the plasticizer. The fabricated electrolyte including PEDOT:PSS showed an ionic conductivity value of 4.2 x 10⁻⁴ S/cm. ECD in ITO/WO₃|PEDOT:PSS-Ch-PC|ITO was assembled. The performance of the electrochromic device was analyzed via CV, transmittance, and CA measurements. The as-fabricated ECD displays reversible color changes from colorless to blue meaning the transformation from oxidized state to reduced state upon switching electrical potential. The ECD shows a transmittance modulation of 22% at 800 nm with fast response times of 0.29 s for coloring and 3 s for bleaching and coloration efficiency of 67 cm²/C. It is highly probable that this configuration of SPE can be helpful to investigate applications in smart windows and other electrochromic devices.

LIST OF ABBREVIATIONS

CA: Chronoamperometry
CE: Coloration efficiency
CC: Chronocoulometry
Ch: Chitosan
CV: Cyclic voltammetry / cyclic voltammogram
ECD: Electrochromic device
EIS: Electrochemical impedance spectroscopy
LiTRIF: Lithium trifluoromethane sulfonate
PC: Propylene carbonate
PEDOT:PSS: poly(3,4-ethylenedioxythiophene): polystyrene sulfonate
PEI: Polyethyleneimine
QSPE: Quasi-solid polymeric electrolyte
SEM-EDS: Scanning electron microscopy-energy dispersive X-ray spectroscopy
SPE: Solid polymer electrolyte

REFERENCES

1. Alves R, Sentanin F, Sabadini RC, Pawlicka A, Silva MM. Green polymer electrolytes of chitosan doped with erbium triflate. Journal of Non-Crystalline Solids. 2018;482:183–191.

2. Eren E, Karaca GY, Koc U, Oksuz L, Oksuz AU. Electrochromic characteristics of radio frequency plasma sputtered WO₃ thin films onto flexible polyethylene terephthalate substrates. Thin Solid Films. 2017; 634: 40–50.

3. Alves R, Sentanin F, Sabadini RC, Pawlicka A, Silva MM. Solid polymer electrolytes based on chitosan and Dy(CF₃SO₃)₃ for electrochromic devices. Solid State Ionics. 2017; 310:112–120.

4. Wang W, Guan S, Li M, Zheng J, Xu C. A novel hybrid quasi-solid polymer electrolyte based on porous PVB and modified PEG for electrochromic application. Organic Electronics.2018; 56:268–275.

5. Thakur VK, Ding G, Ma J, Lee PS, Lu X. Hybrid materials and polymer electrolytes for electrochromic device applications. Adv. Mater. 2012;*24*:4071–4096.

6. Alves R, Sentanin F, Sabadini RC, Fernandes M, Zea Bermudez Vd, Pawlicka A, Silva MM. Samarium (III) triflate-doped chitosan electrolyte for solid state electrochromic devices. Electrochimica Acta. 2018; 267: 51-62.

7. Ataalla M, Afify AS, Hassan M, Abdallah M, Milanova M, Aboul-Enein HYA, Mohamed A. Tungsten-based glasses for photochromic, electrochromic, gas sensors, and related applications: A review. Journal of Non-Crystalline Solids. 2018; 491: 43–54.

8. Patel GB, Singh NL, Singh F. Modification of chitosan-based biodegradable polymer by irradiation with MeV ions for electrolyte

applications. Materials Science & Engineering B. 2017;225: 150–159.

9. Eren E, Aslan E, Oksuz AU. The Effect of Anionic Surfactant on the Properties of Polythiophene/Chitosan Composites. Polymer Engineering and Science. 2014; 54(11):2632-2640.

10. Aziz SB, Abidin ZHZ, Arof AK. Influence of silver ion reduction on electrical modulus parameters of solid polymer electrolyte based on chitosan silver triflate electrolyte membrane. eXPRESS Polymer Letters. 2010; 4(5):300–310.

11. Arof AK, Osman Z, Morni NM, Kamarulzaman N, Ibrahim Z A, Muhamad M R, Chitosan-based electrolyte for secondary lithium cells. Journal of Materials Science. 2001; 36 : 791– 793.

12. Leones R, Reis PM, Sabadini RC, Ravaro LP, Silva IDA, Camargo ASS de, Donosco JP, Magon CJ, Esperança JMSS, Pawlicka A, Silva MM. A luminescent europium ionic liquid to improve the performance of chitosan polymer electrolytes. Electrochimica Acta. 2017; 240 : 474–485.

13. Alves R, Sabadini RC, Silva DA, Donoso JP, Magon CJ, Pawlicka A, Silva MM, Binary Ce(III) and Li(I) triflate salt composition for solid polymer electrolytes. Ionics. 2018; 24:2321–2334.

14. Majid SR, Arof AK, Electrical behavior of proton-conducting chitosan-phosphoric acid-based electrolytes. Physica B. 2007; 390: 209–215.

15. Cifarelli A, Parisini A, Berzina T, Iannotta S, Organic memristive element with Chitosan as solid polyelectrolyte. Microelectronic Engineering. 2018; 193: 65–70.

16. Chávez E L, Oviedo-Roa R, Contreras-Pérez G, Martínez-Magadán JM, Castillo-Alvarado FL, Theoretical studies of ionic conductivity of crosslinked chitosan membranes.International Journal of hydrogen energy. 2010; 3 5: 12141-12146.

17. Alves R, Sentanin F, Sabadini RC, Pawlicka A, Silva MM. Influence of cerium triflate and glycerol on electrochemical performance of chitosan electrolytes for electrochromic devices. Electrochimica Acta. 2016; 217: 108–116.

18. Eren E, Karaca GY, Alver C, Oksuz AU. Fast electrochromic response for RF-magnetron sputtered electrospun V_2O_5 mat. European Polymer Journal. 2016; 84: 345–354.

19. Zhang R, Xu X, Fan X, Yang R, Wu T, Zhang C. Application of conducting micelles self-assembled from commercial poly(3,4-ethylenedioxythiophene):poly(styrene sulfonate) and chitosan for electrochemical biosensor.

Colloid and Polymer Science. 2018; 296:495–502.

20. Poongodi S, Kumar PS, Mangalaraj D, Ponpandian N, Meena P, Masuda Y, Lee C. Electrodeposition of WO_3 nanostructured thin films for electrochromic and H_2S gas sensor applications. Journal of Alloys and Compounds. 2017; 719:71-81.

21. Tang Q, Li H, Yue Y, Zhang Q, Wang H, Li Y, Chen P, 1-Ethyl-3-methylimidazolium tetrafluoroborate-doped high ionic conductivity gel electrolytes with reduced anodic reaction potentials for electrochromic devices. Materials and Design. 2017; 118: 279–285.

22. Deka J R, Saikia D, Lou G-W, Lin C-H, Fang J, Yang Y-C, Kao H-M, Design, synthesis and characterization of polysiloxane and polyetherdiamine based comb-shaped hybrid solid polymer electrolytes for applications in electrochemical devices. Materials and Design. 2017; 118: 279–285.

23. Puguan J M C, Boton L B, Kim H, Triazole-based ionene exhibiting tunable structure and ionic conductivity obtained via cycloaddition reaction: A new polyelectrolyte for electrochromic devices. Solar Energy Materials and Solar Cells. 2018; 18: 210–218.

24. Ramanavicius A, Genys P, Ramanaviciene A, Electrochemical Impedance Spectroscopy Based Evaluation of 1,10-Phenanthroline-5,6-dione and Glucose Oxidase Modified Graphite Electrode. Electrochimica Acta. 2014; 146: 659–665.

25. Wang J-Y, Wang M-C, Jan D-J. Synthesis of poly(methyl methacrylate)-succinonitrile composite polymer electrolyte and its application for flexible electrochromic devices. Solar Energy Materials & Solar Cells.2017; 160: 476–483.

26. Virbukas D, Sriubas M, Laukaitis G. Structural and electrical study of samarium doped cerium oxide thin films prepared by e-beam evaporation. Solid State Ionics. 2015; 271: 98–102.

27. Leones R, Sabadini R C, Esperança J M S S, Pawlicka A, Silva MM, Effect of storage time on the ionic conductivity of chitosan-solid polymer electrolytes incorporating cyano-based ionic liquids. Electrochimica Acta. 2017;232:22–29.

28. Ge Q., Zhou L., Lian Y.-M., Zhang X., Chen R., Yang W., Metal-phosphide-doped $Li_7P_3S_{11}$ glass-ceramic electrolyte with high ionic conductivity for all-solid-state lithium-sulfur batteries. Electrochemistry Communications. 2018; 97: 100–104.

29. Kim H., Kim Y.-II, Partial nitridation of Li_4SiO_4 and ionic conductivity of $Li_{4.1}SiO_{3.9}N_{0.1}$. Ceramics International. 2018; 44 : 9058–9062.

30. Liu H-M, Saikia D, Wu C-G, Fang J, Kao H-M, Solid polymer electrolytes based on coupling of polyetheramine and organosilane for applications in electrochromic devices. Solid State Ionics . 2017; 303:144–153.

31. Zhu Y, Otley M T, Alamer F A, Kumar A, Zhang X, Mamangun D M D, Li M, Arden B G, Sotzing G A, Electrochromic properties as a function of electrolyte on the performance of electrochromic devices consisting of a single-layer polymer. Organic Electronics. 2014; 15 : 1378–1386.

32. Andrade JR, Raphael E, Pawlicka A. Plasticized pectin-based gel electrolytes. Electrochimica Acta. 2009; 54: 6479–6483.

33. Ledwon P, Andrade JR, Lapkowski M, Pawlicka A. Hydroxypropyl cellulose-based gel electrolyte for electrochromic devices. Electrochimica Acta. 2015; 159:227-233.

34. Liu S, Wang W. Improved electrochromic performances of WO_3-based thin films via addition of CNTs. J Sol-Gel Sci Technol. 2016; 80:480–486.

35. Rocha MD, He Y, Diao X, Rougier A. Influence of cycling temperature on the electrochromic properties of WO3/NiO devices built with various thicknesses. Solar Energy Materials and Solar Cells. 2018; 177: 57–65.

36. Ling H, Liu L, Lee PS, Mandler D, Lu X. Layer-by-Layer Assembly of PEDOT:PSS and WO3 Nanoparticles: Enhanced Electrochromic Coloration Efficiency and Mechanism Studies by Scanning Electrochemical Microscopy. Electrochimica Acta. 2015; 174:57–65.

37. Kadam LD, Patil PS. Studies on electrochromic properties of nickel oxide thin films prepared by spray pyrolysis technique. Solar Energy Materials & Solar Cells. 2001; 69:361-369.

38. Chang-Jian C-W, Cho E-C, Yen S-C, Ho B-C, Lee K-C, Huang J-H, Hsiao Y-S. Facile preparation of WO_3/PEDOT:PSS composite for inkjet printed electrochromic window and its performance for heat shielding. Dyes and Pigments. 2018; 148:465-473.

39. Zhang S, Sun G, He Y, Fu R, Gu Y, Chen S. Preparation, Characterization, and Electrochromic Properties of Nanocellulose-Based Polyaniline Nanocomposite Films. ACS Appl. Mater. Interfaces 2017, 9, 16426−16434.

40. Kalagi S S, Dalavi D S, Mali S S, Inamdar A I, Patil R S, Patil P S, Study of Novel WO_3-PEDOT:PSS Bilayered Thin Film for Electrochromic Applications. Nanoscience and Nanotechnology Letters. 2012;4:1146-1154.

41. Patil DS, Pawar SA, Hwang J, Kim JH, Patil PS, Shşn JC. Silver incorporated PEDOT: PSS for

enhanced electrochemical performance. Journal of Industrial and Engineering Chemistry. 2016;42: 113–120.

42. Kawahara J, Ersman PA, Engquist I, Berggren M. Improving the color switch contrast in PEDOT:PSS-based electrochromic displays. Organic Electronics. 2012; 13 :469–474.

43. Assis LMN, Leones R, Kanicki J, Pawlicka A, Silva MM. Prussian blue for electrochromic devices. Journal of Electroanalytical Chemistry. 2016. 777:33–39.

44. Eren E, Alver C, Karaca GY, Uygun E, Oksuz AU. Enhanced electrochromic performance of WO_3 hybrids using polymer plasma hybridization process. Synthetic Metals. 2018; 235: 115–124.

45. Firat YE, Peksoz A, Efficiency enhancement of electrochromic performance in NiO thin film via Cu doping for energy-saving potential. Electrochimica Acta. 2019; 295:645-654.

46. Chen X, Yang M, Qu Q, Zhao Q, Zou W. A regiosymmetric blue-to-transmissive electrochromic polymer based on 3,4-ethylenedioxythiophene with bromomethyl pendant groups. Journal of Electroanalytical Chemistry. 2018; 820 : 60–66.

47. Bathe RB, Patil PS. Electrochromic characteristics of fibrous reticulated WO_3 thin films prepared by pulsed spray pyrolysis technique. Solar Energy Materials & Solar Cells. 2007; 91: 1097–1101.

48. Kiristi M, Bozduman F, Oksuz AU, Oksuz L, Hala A. Solid State Electrochromic Devices of Plasma Modified WO3 Hybrids. Ind. Eng. Chem. Res. 2014; 53: 15917−15922.

49. Fernandes M, Freitas VT, Pereira S, Fortunato E, Ferreira RAS, Carlos LD, Rego R, Bermudez VdZ. Green Li^+-and Er^{3+}-doped poly(ε-caprolactone)/siloxanebiohybrid electrolytes for smart electrochromic windows. Solar Energy Materials & Solar Cells 2014; 123: 203–210.

50. Dulgerbaki C, Oksuz AU. Fabricating polypyrrole/tungsten oxide hybrid based electrochromic devices using different ionic liquids. Polym. Adv. Technol. 2016;27: 73–81.

51. Santos GH, Gavim AAX, Silva RF, Rodrigues PC, Kamikawachi RC, Deus JFd, Macedo AG. Roll-to-roll processed PEDOT:PSS thin films: application in flexible electrochromic devices. J Mater Sci: Mater Electron.2016; 27(10) 11072-11079.

Investigation of Organic Solvents' Effects on Kenaf (Hibiscus cannabinus L.) Biomass Conversion in Subcritical Water

Bahar Meryemoğlu[1]* ✉ iD **, Arif Hasanoğlu[1]** ✉ iD **, Mehtap Kurtuluş[1]** ✉ iD **,
Sibel Irmak[2]** ✉ iD

[1] Department of Chemistry, Çukurova University, 01330, Adana, Turkey
[2] Department of Biological Systems Engineering, University of Nebraska-Lincoln, Lincoln, NE 68583, USA

Abstract: Kenaf biomass was hydrolyzed under subcritical water conditions in the presence of various organic solvents. The solvents tested were tetrahydrofuran (THF), acetone, xylene (mixed isomers) and methanol. The organic compounds released into hydrolysates, total organic contents, water-soluble total phenols, and the molecular weight distributions of the polysaccharides in the hydrolysates, solid residues leftover after hydrolysis and gaseous products formed during the solubilization process were determined. The results showed that organic solvents significantly enhanced the dissolution of kenaf biomass (methanol < (omp)xylene ≤ acetone ~ tetrahydrofuran). The hydrolysis percentage was found to be between 75-82% depending on the type of the solvent. Hydrolysis yield and total organic carbons released into hydrolysates highly differed when the solubilization process was performed under carbon dioxide pressure and this effect considerably varied based on the type of solvent used in hydrolysis process. The main gas product formed during hydrolysis process was carbon dioxide with ~80% composition. Morphological measurements of the solid biomass residues left after hydrolysis showed substantial degradations with increasing number of pores on the biomass surfaces.

INTRODUCTION

The need for energy has been increasing continuously as a result of the rapid increase of the world's population. There is growing interest worldwide in the utilization of renewable sources for fuels, materials, and chemicals due to the depletion of fossil resources and environmentally non-friendly nature of the synthetic products. Lignocellulosic biomass can substitute for fossil resources in the production of a wide range of value-added products such as biofuels, bioproducts, and chemicals. Lignocellulosic biomass materials are abundant, cheap, and renewable resources and their non-edible alternatives are particularly important since they do not compete with the food related raw materials in conversion into useful products (1).

The complex and rigid structures of lignocellulosic biomass require an effective pretreatment before breaking down into soluble components with the processes of hydrolysis. The methods of pretreatment can be physical, physicochemical, chemical, or biological (2). Extent of lignin and hemicellulose removals, reduction in cellulose crystallinity, and increasing the porosity of the biomass structure depend on the pretreatment method applied (1). Subcritical water is a liquid under pressure and in the temperature range of 100-374 °C. This liquid usually is used in the extraction of plants. The optimal conditions are determined by changing the pressure and temperatures to obtain the maximum efficiency of the material to be extracted. Significant changes occur in the physical and chemical properties of the water, especially in the dielectric constant (ε) under high pressure and

temperature. The extraction efficiency was equivalent to the supercritical fluid or solvent extraction yield even without reaching the critical temperature point. The extraction with subcritical water began as an alternative to supercritical fluid extraction and solvent extraction. There are many advantages to using subcritical water. Some of these are environmental friendly, inexpensive, easy to find, non-toxic, and produces no organic waste at all. Subcritical water hydrolysis is an alternative pretreatment method to break down lignocellulosic biomass by operating process temperature and pressure conditions. This method is totally environmentally friendly and uses water in as reaction medium. The maximum solubilization yields of biomass materials with this method were found to be 70-75% at 250 °C (3,4). Organic solvents play an important role in enhancing yields of the process in many applications. Several studies for biomass conversion were performed with this method using various organic solvents in the reaction medium (5-11). For this purpose, the present study was designed to solubilize lignocellulosic biomass in subcritical water by addition of non-polar (omp-xylene), aprotic polar (tetrahydrofuran, acetone) and polar protic (methanol) solvents into reaction medium. Thus, the partial solubility of lignin will be improved in this study.

EXPERIMENTAL SECTION

Hydrolysis of Kenaf biomass
Kenaf biomass (Hibiscus cannabinus L.) was hydrolyzed under subcritical water condition. The amount of 10 g of kenaf and 350 mL of water were placed into a 500 mL stainless steel high pressure reactor (Parr Model 4575 HP/HT, Parr Instrument Co., Moline, IL, USA). Then, the reactor was heated until 250 °C and pressurized with/without CO_2 using ISCO 260D pump (Isco Inc., Lincoln, Nebraska, USA) to 27.58 MPa for 2 h. After 2 h, the reactor was cooled up at room temperature within the reactor. The experiments with organic solvents were performed by addition of 3% of THF, acetone, xylene or methanol into reactor. After experiment, kenaf hydrolysate and solid residue were collected for analysis. The solid residue were dried at 100 °C in order to determine the percentage of hydrolysis. The experiments were performed in duplicate.

Analysis
The solid residues leftover after hydrolysis were characterized by FTIR using ATR (Perkin Elmer Spectrum RX-I FTIR System) and SEM analysis (ZEISS SUPRA 55). The hydrolysates were analyzed by TOC (total organic carbon analyzer), UV-VIS, GC-MS, and HPLC. Total organic carbon content was determined using Tekmar Dohrmann Apollo 9000 instrument.

The compositions of volatile organic compounds in the hydrolysates were determined by a Thermo Finnigan Trace Gas Chromatograph and Mass Spectrometer (GC-MS) using Thermo TR-5 MS capillary column (60 m x 0.25 mm ID x 0.25 mm film thickness). For this analysis, 50 mL of kenaf hydrolysate was extracted with diethyl ether and dried through a Na_2SO_4 column. Diethylether was removed by using a rotary evaporator. The oven temperature of the GC-MS system was as follows: holding at 40 ºC for 5 min; increasing the temperature from 40 ºC to 280 ºC with 2.5 ºC/min heating rate and holding at this temperature for 10 min. Inlet temperature was 240 ºC. The 70 eV and 240 ºC were set as ionization voltage and ion source temperature, respectively. The 1 µL of sample was injected in splitless mode. Solvent delay was 6 min. The NIST 2002 mass spectral library was used in identification.

The molecular weight distributions of the polysaccharides in the hydrolysates were determined by gel permeation chromatography (GPC) using 4400, 9900, 21,400, 43,500, 124,000, 196,000, 277,000 and 401,000 Da dextran standards. The hydrolysates were filtered through 0.22 µm syringe filter before analysis. GPC analysis was performed by an LC-6AD Shimadzu high performance liquid chromatograph equipped with SIL-10AF Shimadzu auto injector (Shimadzu, Kyoto, Japan) and Shimadzu RID-10A refractive index detector (RID).

Total water-soluble phenolics contents of the hydrolysates were determined by Folin–Ciocalteu assay (12). Absorbance at 765 nm was recorded using a spectrophotometer (Thermo Scientific Genesys 10S UV/Vis).

RESULTS AND DISCUSSION

Hydrolysis yields of kenaf biomass under different water-organic solvents mixture
Kenaf samples were subjected to omp-xylene (non-polar), THF (aprotic polar), acetone (aprotic polar) and methanol (polar protic) solvents under subcritical water condition under pressure of carbon dioxide. It is known that polar aprotic solvents are good solvents for lignin solubilization.

Some experiments were performed to examine the effect of the amount of solvent on the percentage hydrolysis and product distribution using THF. The 1%, 3% and 5% of THF were used. The percentage hydrolysis was increased with increasing THF amount from 1% (75,1±4,4) to 3% (82,5±3,6). When the %5 of THF was used, it was seen that the percentage hydrolysis was decreased (78,8±2,7). Similarly, the phenolics concentrations of hydrolysates were also affected by the amount of THF. According to results, the phenolics concentrations of hydrolysates increased in following order 2021,9 <2832,1 <3213,1 ppm for %1, %5 and %3 of THF respectively. It was decided that %3 organic solvent was more suitable because of the highest

percentage hydrolysis and phenolic contents, less gas formation in the hydrolysis process, more polysaccharide.

The percentage hydrolysis and total organic carbon (TOC) values obtained after these treatments were presented in Figure 1. As given in Figure 1, the percentage hydrolysis increased in the following order; methanol < omp-xylene ≤ acetone ~ tetrahydrofuran. The hydrolysis with non-polar and aprotic polar solvents was observed to be better compared to one performed with a polar protic solvent. Previous studies about solubility of lignin in the mixtures of water-organic solvents showed that our results are in harmony (13-16). The organic solvents are known to affect reaction rate, reaction mechanism, and yield and product distributions in many reaction systems. The changes in dipole moment and the hydrogen bonds between solvent and solute (biomass) can significantly change dissolution process, thermodynamic state of the reactants, activation energy of the products, and compositions of the reaction

mixture (17). It was observed that yield of hydrolysis and TOC released highly differed when the solubilization process was performed under carbon dioxide pressure and this effect considerably varied as based on the type of solvent used in hydrolysis process (Figure 1). The maximum TOC released was observed when THF solvent was used in solubilization media.

During hydrolysis process, gasification reactions can also take place. It is preferable to be gasification less but dissolution more. To determine solvent effect correctly, amount of gas formed during hydrolysis must be determined along with hydrolysis percentage and total organic carbon contents of the hydrolysates. The amount of gas mixtures formed during hydrolysis were determined by GC using TCD detector and presented in Table 1. The amount of the gas was 745 mL when acetone was used in hydrolysis in the absence of carbon dioxide pressure. The gas amounts in other solvents were ranged between 525 and 630 mL.
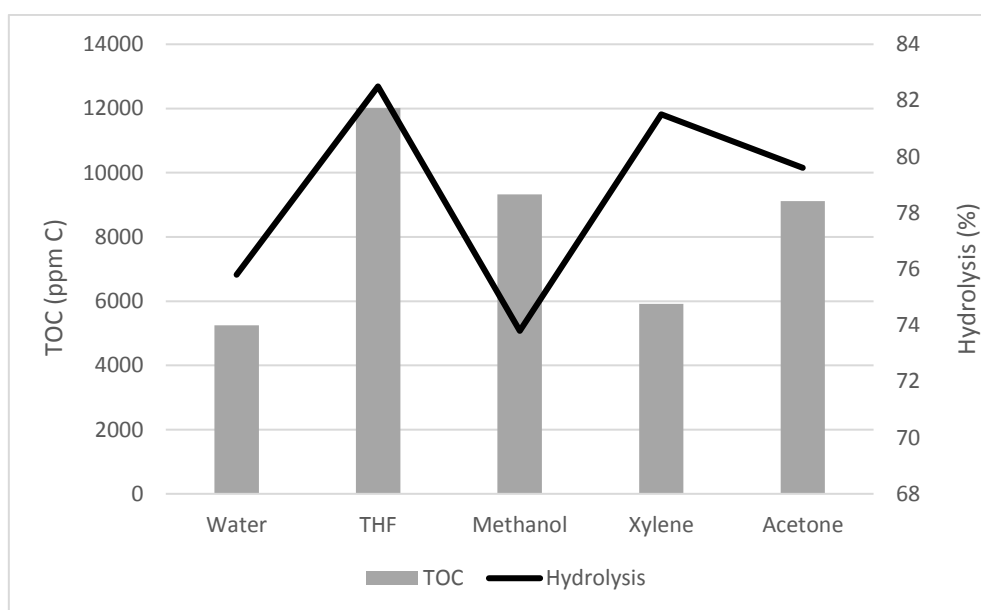
Figure 1. The percentage hydrolysis and TOC yield of kenaf biomass with different water-organic solvent mixture.

The main product in the gas mixtures was found to be carbon dioxide (78-83%) that followed by carbon monoxide (14-19%) (Table 1). Hydrogen

composition was between 2.1-2.8% in all hydrolysis experiments. The gas mixtures contained trace amount of methane (0.2%).

Table 1. The gas composition of kenaf biomass with different water-organic solvent mixture (CO_2 pressure was not applied).

Solvents	Gas Volume (mL)	Gas composition (%)			
		H_2	CH_4	CO_2	CO
Water	630±30	2.3±0.8	0.2±0.1	78.5±1.1	19.0±1.1
Water+ 3 % THF	525±35	2.5±0.1	0.2±0.0	80.6±0.5	16.7±0.8
Water+ 3 % Methanol	650±30	2.8±0.2	0.3±0.1	80.9±0.4	16.0±0.6
Water+ 3 % Acetone	745±15	2.7±0.3	0.3±0.1	82.7±1.2	14.3±0.4
Water+ 3 % Omp-Xylene	670±20	2.1±0.3	0.2±0.1	81.0±2.1	16.7±0.9

Based on these results, we can conclude that THF is the best organic solvent for hydrolysis process resulting the highest hydrolysis percentage (82.5%) and TOC (> 10,500 ppm) values by producing the least gas volume (525 mL).

Products

The products in the hydrolysates were characterized by GC-MS, UV-Vis and GPC analytical techniques. Table 2 shows the compounds formed after hydrolysis of kenaf biomass in different water-organic solvent mixtures. Carbon dioxide was used as a pressurizing gas in the hydrolysis process. Differences in the viscosity, the dielectric constant, polarity of the solvents (18,19) affected the solubilization of biomass.

In many studies, lignocellulosic material was treated with organic solvents and as a result of this treatment, most of lignin was removed (20-22). And also, higher hemicellulose conversion was obtained with use of organic solvent such as dimethylformamide (DMF) in the processes (23).

Although these studies were conducted, the comparison of organic solvents on kenaf subcritical water hydrolysis has not been reported yet. The use of organic solvents in hydrolysis partially hydrolyzes the lignin bonds and lignin-carbohydrate bonds, and solid residues leftover after hydrolysis mainly consists of cellulose and hemicellulose. In this study, the organic solvent removes the lignin from the lignocellulosic material but most of the hemicellulose sugars are also dissolved in this process. Because of that the compounds were mainly phenolics which were released from lignin fraction of biomass. Water-soluble phenolic composition of the hydrolysates varies depending on the solvent used in experiments (Table 3). The phenolics concentrations were highest in water-xylene mixture. The total phenolics in this solvent mixture were found to be 3601.1 mg/L. On the other hand, water-THF mixture yielded the lowest phenolics in the hydrolysis (Table 3). From our work, it was found that the use of organic solvents in hydrolysis process provided enhancing the product distribution as well as hydrolysis yield.

Table 2. GC-MS analysis of kenaf hydrolysates in different water- organic solvent mixtures

Retention time (min)	Compound Name	MS fragments used in identification (m/z)
15.69	Furfural	96 (M$^+$), 95, 68, 67, 51
18.7	Corylon (2-hydroxy-3-methyl-2-cyclopenten-1-one)	112 (M$^+$), 97, 83, 41, 27
22.3	2-methoxyphenol	124 (M$^+$), 109, 95,81, 53
28.06	3-methyl-1,2-cyclopentadione	112 (M$^+$), 97, 83, 69, 55
31.23	4-methyl phenol	110, 108 (M$^+$), 107,79, 53
36.8	2-6-dimethoxyphenol (Syringol)	154 (M$^+$), 139, 96, 65, 51
40.27	Hydroxymethylfurfural	126, 97(M$^+$), 81, 69, 53
47.21	2-methoxy- 3-methyl hydroxy quinone	154 (M$^+$), 139, 93, 68,65
49.81	Vanillin	152, 151 (M$^+$), 123, 109, 81
51.5	4-hydroxy-3,5-dimethoxybenzaldehyde (syringyl aldehyde)	182 (M$^+$), 181, 111, 93, 65
56.25	7-acetyl-2,3,4,5,6,7-hexahydrobenzofuran-4-one	180, 138, 137 (M$^+$), 122, 94
67.0	1,2-diphenyl propan-2-one	210, 192 (M$^+$), 168,167,123
79.59	2 2'-methylenebis 6-(1 1-dimethylethyl)-4-methyl-phenol	340, 284, 177 (M$^+$), 161, 149

Table 3. Water-soluble phenolic contents and polysaccharide distrubution of kenaf hydrolysates

Solvents	Phenolic content (mg/L)	Polysaccharides Mp, Da
Water	1431.1	6975; 25
Water+ 3 % THF	3213.1	6075; 3332
Water+ 3 % Methanol	3415.3	68477; 22390; 24
Water+ 3 % Acetone	3562.8	58519;19705; 25
Water+ 3 % omp-Xylene	3601.1	70496; 23116; 23

The results showed that organic solvents affect the hydrolysis and molecular mass distribution of the polysaccharides in the hydrolysates. Kenaf biomass had three fractions of polysaccharides after hydrolysis (Table 3). These fractions are also associated with phenolic fragments in the biomass. Type of the organic solvent used in hydrolysis process was the main factor on the

differences of polysaccharides distributions (Table 3).

Characterization of kenaf samples after hydrolysis

Chemical changes that occured in the structure of kenaf biomass were determined by taking FTIR spectra of the samples before and after

hydrolysis. Kenaf biomass spectra before and after treatments were given in Figure 2. The 3340-3350 cm^{-1} in the original kenaf infrared spectrum was assigned to O-H vibrations. This band belongs to hydroxyl groups located together by hydrogen bonds between the repeating units in the cellulose matrix. The band between 2890-2920 cm^{-1} belongs to the C-H stretching. The 1742 cm^{-1} band is due to stretching of the carbonyl group in the hemicellulose structures (24). The functional group C = O was observed at 1600-1650 cm^{-1}. This band takes place in the lower region of 1700 cm^{-1} because of water absorption in the structure (25,26).
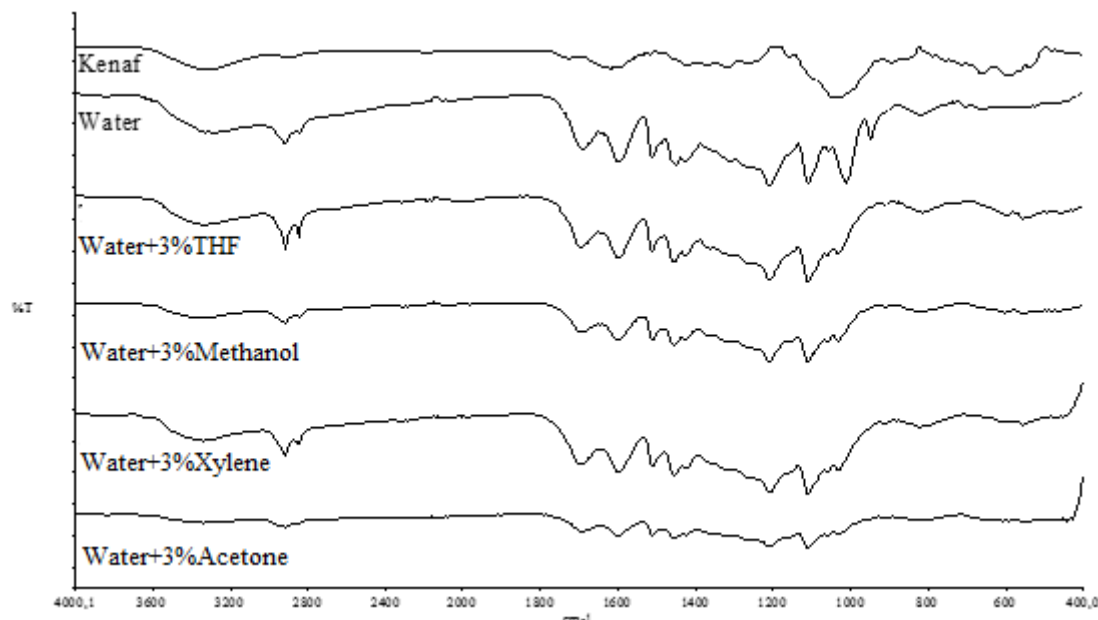

Figure 2. FTIR spectra of kenaf after hydrolysis with different water- organic solvent mixtures.

The weak bands seen around 1500-1514 cm^{-1} belong to lignin (25,26). The C-H vibrations in the cellulose at 1429 cm^{-1} and C-O-C antisymmetric vibration in glycosidic band at 1161 cm^{-1} were observed. The 1370 cm^{-1} is assigned to stretching of C-H peaks in cellulose (26). The band at 1160-1000 cm^{-1} is due to the C-O vibrations. The bands that belong to typical xylan hemicellulose structures were observed between 1175 and 1000 cm^{-1} (25,26). The weak band around 1109 cm^{-1} indicates stress of glucose ring in cellulose and the presence of a band at 890 cm^{-1} in original kenaf attributed to β-glycosidic bonds in the cellulose structure (27,28).

The band at 1742 cm^{-1} in the original kenaf sample disappeared after hydrolysis since acetyl, uronic, and ferulic ester bonds in hemicellulose fraction were completely broken (Figure 2). The cleavages of ester bonds caused releases of phenolic compounds (27, 26). The guaiacyl aromatic C-O band stretchings in lignin structure could be seen at 1510 cm^{-1} (29). These bands became prominent in the non-hydrolyzed kenaf treated with any solvents. The 1460 cm^{-1} and 1320 cm^{-1} show absorption bands of syringyl ring in lignin structure (29-30). The morphological changes in kenaf samples after hydrolysis were also examined by taking SEM images (Figure 3). The original kenaf structure was straight and it consisted of thin fibrils. The SEM image of non-hydrolyzed kenaf indicated that dense and compact outer surface were reduced by treatments. The formations of a number of pores having a few micrometer diameters were observed after hydrolysis process with solvents (Figure 3). Substantial degradation with increasing number of pores in the rigid structure of kenaf increased after hydrolysis with omp-xylene, acetone and methanol. THF hydrolysis resulted in more degradation in the kenaf structure. The cell wall structure was completely fragmented after hydrolysis in xylene. Some droplets which are known to be lignin based fragments released after lignin degradation were observed as a result of hydrolysis of the lignocellulosic material (33-35).
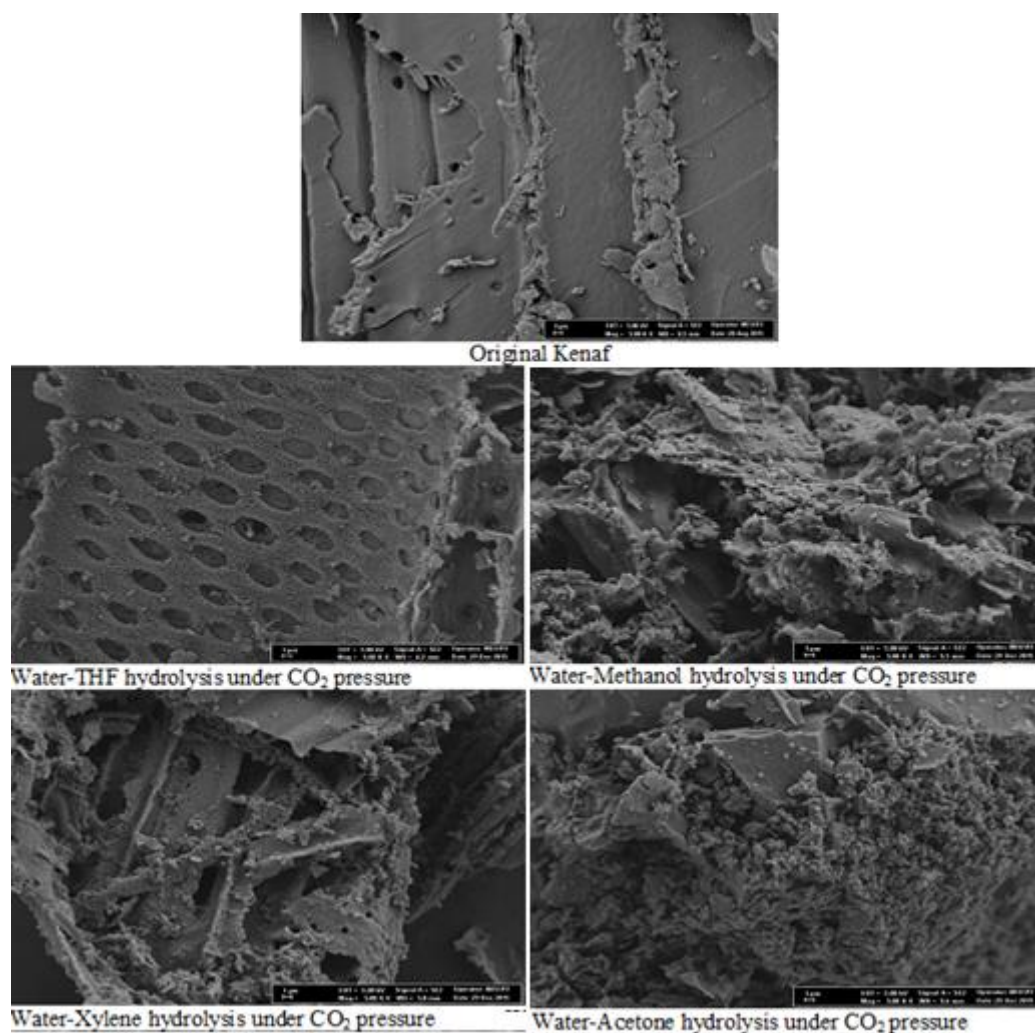
Figure 3. SEM images of kenaf samples after hydrolysis in different water- organic solvent mixture.

CONCLUSION

Use of organic solvents in the subcritical water hydrolysis process increased the dissolution of kenaf biomass. However, product distribution in the hydrolysates did not considerably change. Non-polar (omp-xylene) and aprotic polar (THF, acetone) solvents enhanced the hydrolysis more than polar protic (methanol) solvent. The hydrolysis process with organic solvents generated soluble polysaccharides which could be utilized for production of various value-added products including biofuels and bioproducts by thermochemical and biochemical conversion processes.

ACKNOWLEDGMENTS

REFERENCES

1. Hasyierah Noor MS, Zulkali MMD, Syahidah Ku KI. Ferulic acid from lignocellulosic biomass: Review. Malaysian Universities Conferences on Engineering and Techonology March 8-10, 2008, Putra Brasmana, Perlis, Malaysia.

2. Saha BC. Hemicellulose bioconversion. J Ind Microbiol Biotechnol. 2003; 30:279 - 91.

3. Meryemoglu B, Hesenov A, Irmak S, Atanur OM and Erbatur O. Aqueous-phase reforming of biomass using various types of supported precious metal and raney-nickel catalysts for hydrogen production. Int.J. Hydrogen Energy 2010;35:12580-7.

4. Meryemoglu B, Hasanoglu A, Kaya B, Irmak S, Erbatur O. Hydrogen production from aqueous-phase reforming of sorghum biomass: An application of the response surface methodology. Renew Energ. 2014;(62):535-41.

5. Shuai L, Yang Q, Zhu JY, Lu FC, Weimer PJ, Ralph J, Pan XJ. Comparative study of SPORL and dilute-acid pretreatments of spruce for cellulosic ethanol production. Bioresour. Technol. 2010;(101):3106–14.

6. Xin D, Yang Z, Liu F, Xu X, Zhang J. Comparison of aqueous ammonia and dilute acid

pretreatment of bamboo fractions: structure properties and enzymatic hydrolysis. Bioresour. Technol. 2015;(175):529–36.

7. Li C, Knierim B, Manisseri C, Arora R, Scheller HV, Auer M, Vogel KP, Simmons BA, Singh S. Comparison of dilute acid and ionic liquid pretreatment of switchgrass: Biomass recalcitrance, delignification and enzymatic saccharification. Bioresour. Technol. 2010;101:4900 – 6.

8. Kootstra AMJ, Beeftink HH, Scott EL, Sanders JPM. Comparison of dilute mineral and organic acid pretreatment for enzymatic hydrolysis of wheat straw. Biochem. Eng. J. 2009;46:126–31.

9. Hsu TC, Guo GL, Chen WH, Hwang WS. Effect of dilute acid pretreatment of rice straw on structural properties and enzymatic hydrolysis. Bioresour. Technol. 2010;101:4907–13.

10. Yan L, Zhang L, Yang B. Enhancement of total sugar and lignin yields through dissolution of poplar wood by hot water and dilute acid flowthrough pretreatment. Biotechnol. Biofuels. 2014;7:76.

11. Akpinar O, Levent O, Sabanci S, Uysal RS, Sapci B. Optimization and comparison of dilute acid pretreatment of selected agricultural residues for recovery of xylose. Bio Resources 2011;6:4103–16.

12. Caboni E, Tonelli MG, Lauri P, Iacovacci P, Kevers C, Damiano C, Gaspar T. Biochemical aspects of almond microcuttings related to in vitro rooting ability. Biologia Plant. 1997; 39: 91-7.

13. Ni Y, and Hu Q. Alcell Lignin Solubility in Ethanol-Water Mixtures. Journal of Applied Polymer Science. 1995;57:1441-6.

14. Wang Q, Chen K, Li J, Yang G, Liu S, Xu J. The solubility of lignin from bagasse in a 1,4-butanediol/water system. BioResources.2011;6;3034-43.

15. Boeriu CG, Fiţigău FI, Gosselink RJA, Frissen AE, Stoutjesdijk J, Peter F. Fractionation of five technical lignins by selective extraction in green solvents and characterisation of isolated fractions. Ind Crops Prod. 2014;62:481–90.

16. Ye Y, Liu Y, and Chang J. Application of solubility parameter theory to organosolv extraction of lignin from enzymatically hydrolyzed cornstalks. BioRes. 2014;9:3417-27.

17. Reichardt C, Welton T. Solvents and Solvent Effects in Organic Chemistry, Wiley-VCH, Weinheim, 2006.

18. Maurel P. Relevance of Dielectric Constant and Solvent Hydrophobicity to the Organic Solvent Effect in Enzymology J. Biol. Chem. 1978;253:1677–83.

19. Mariella RP, Raube RR, Budde J, Moore CE. The effect of the dielectric constant of the solvent on the ultraviolet absorption spectra of some non-aromatic ketones J. Org. Chem. 1954; 19: 678–82.

20. Sun RC, Sun XF, Ma XH. Effect of ultrasound on the structural and physicochemical properties of organosolv soluble hemicelluloses from wheat straw. Ultrasonics Sonochemistry. 2002; 9: 95-101.

21. Sun RC, Tomkınson J. Separation and Characterization of Cellulose from Wheat Straw. Separation Science and Technology. 2004;39: 391-411.

22. Buranov AU, Mazza G. Extraction and characterization of hemicelluloses from flax shives by different methods. Carbohydrate Polymers. 2010;79: 17–25.

23. Corredor DY. Pretreatment and enzymatic hydrolysis of lignocellulosic biomass. PhD dissertation. Department of Biological and Agricultural Engineering, Kansas State University, Manhattan, Kansas, 2008.

24. Espinoza-Acosta JL, Torres-Chávez PI, Carvajal-Millán E, Ramírez-Wong B, Bello-Pérez LA, Montaño-Leyva B. Ionic liquids and organic solvents for recovering lignin from lignocellulosic biomass. BioResources. 2014; 9:3660– 87.

25. Araque E, Parra C, Freer J, Contreras D, Rodríguez J, Mendonça R, Baeza J. Evaluation of organosolv pretreatment for the conversion of Pinus radiata D. Don to ethanol. Enzyme Microb. Technol. 2008; 43:214–9.

26. Ghozatloo A, Mohammadi-Rovshandeh J, Hashemi S. Optimization of pulp properties by dimethyl formamide pulping of rice straw. Cellul. Chem. Technol. 2006;40:659–67.

27. Zhao X, Cheng K, Liu D. Organosolv pretreatment of lignocellulosic biomass for enzymatic hydrolysis. Appl. Microbiol. Biotechnol. 2009;82:815–27.

28. Sun R, Lawther JM, Banks WB. Fractional and structural characterization of wheat straw hemicelluloses. Carbohydrrate Polymers. 1999;49:415-23.

29. Sene CFB, Mccan MC, Wilson RH and Grinter R. Fourier-transform Raman and Fourier-transform infrared spectroscopy. An investigation of five higher plant cell walls and their components. Plant Physiology. 1994;106:1623-31.

30. Pandey KK. A study of chemical structure

of soft- and hardwood and wood polymers by FTIR spectroscopy. J. Appl Polym Sci. 1999;71:1969–75.

31. Faix O. Fourier Transform Infrared Spectroscopy, In: Methods in Lignin Chemistry, T.E. Timell (Ed.), Springer-Verlag, Germany, 1992.

32. Sun RC, Tomkınson J. Separation and Characterization of Cellulose from Wheat Straw. Separation Science and Technology 2004;39:391-411.

33. Micic M, Benitez I, Ruano M, Mavers M, Jeremic M, Radotic K, Moy V, Leblanc RM. Probing

the lignin nanomechanical properties and lignin-lignin interactions using the atomic force microscopy. Chemical Physics Letters. 2001;347:41-5.

34. Donohoe BS, Decker SR, Tucker MP, Himmel ME, Vinzant TB. Visualizing Lignin Coalescence and Migration Through Maize Cell Walls Following Thermochemical Pretreatment. Biotechnology and Bioengineering. 2008;101:913-25.

35. Selig MJ, Viamajala S, Decker SR, Tucker MP, Himmel MP, Vinzant TB. Deposition of Lignin Droplets Produced During Dilute Acid Pretreatment of Maize Stems Retards Enzymatic Hydrolysis of Cellulose, Biotechnology Progress. 2007;23:1333-9.

RESEARCH ARTICLE

Determination of 5-hydroxymethylfurfural (5-HMF) in Expired Pharmaceutical Syrups by Using HPLC-DAD Method

Songül Ünüvar*

University of Inonu, Faculty of Pharmacy, Department of Pharmaceutical Toxicology, 44280, Malatya, Turkey.

Abstract: The Maillard reaction product 5-hydroxymethylfurfural (5-HMF) is formed under acidic conditions by the dehydration of sugars in carbohydrate-based food and pharmaceutical products during heating and storage. As pharmaceutical syrup formulations contain sugar and are stored under room temperature, they provide favorable conditions for the formation of 5-HMF. The long-term storage of syrup bottles after their cap has been opened and the unintentional use of expired syrups can lead to the formation of undesirable products such as 5-HMF in medications. Although legal limits have been established for 5-HMF content in pharmaceutical preparations, these levels may exceed those limits in hot climates or under inappropriate storage conditions. The present study detects and measures 5-HMF levels in expired pharmaceutical syrups through the HPLC-DAD (High Performance Liquid Chromatography with Diode Array Detection) method, and investigates the effects on 5-HMF levels of the 72-hour storage of syrups at temperatures of 40 °C. The 5-HMF level in syrups stored at room temperature varied between 1.34 µg/mL to 15.63 µg/mL, while in syrups stored at higher temperatures, the levels ranged from 2.24 µg/mL to 18.24 µg/mL. This indicated that 5-HMF content in syrups stored at 40 °C was higher than those measured in syrups stored at room temperature, although the increase was not found to be statistically significant (p>0.05). In addition to measuring the amount of 5-HMF in pharmaceutical syrups, this study also examined the changes in the levels of this dehydration product in syrup formulations under hot climates and according to storage conditions.

INTRODUCTION

The compound 5-HMF consists of a furan ring along with aldehyde and alcohol functional groups. Its chemical formula is 5-(hydroxymethyl)-2-furancarboxaldehyde ($C_6H_6O_3$) (1), and it is used in the synthesis of certain organic compounds (2) and novolac resins (3). It is also used as an intermediate substance in the synthesis of some crown ethers (4), and in the production processes of some polymers, surfactants, solvents, pharmaceutics and plant protection agents (5). It is one of the most significant products of non-enzymatic Maillard

reaction (6). Upon heating food that contains sugar or carbohydrates, it forms as a result of hexose reduction reaction in the presence of amino-acids or proteins (7).

The presence of 5-HMF has been reported in several foods, including honey, grain products, biscuits, cereals, UHT milk, tomato products, instant coffee, dried fruits, bread, pasta, citrus juices, beer, syrup, jams, canned peach, dried grape, alcohol, apple juice, milk and cereal-based infant formula. The presence of 5-HMF in foods reflects a breakdown or change of substances containing sugar, which is why 5-HMF levels in

food are generally analyzed for quality control purposes (8-12). Food processing conditions, such as temperature, time and water activity, affect 5-HMF content in foods. The daily uptake of 5-HMF in foods may occasionally reach 150 mg/day (13) and it may be present in foods at varying levels (10,14). Very high levels of 5-HMF can be found in such foods as dried fruits or caramelized products (> 1 g/kg) (7). In addition to caramelized foods, 5-HMF has also been identified in caramel-colored pharmaceutical syrups (15). Although the concentrations reported in pharmaceutical syrups are very low, there are concerns about the potential interactions between 5-HMF and functional amino groups of pharmaceutics (11).

The formation of 5-HMF occurs as a result of the acid-catalyzed dehydration process of fructose, sucrose and, to a lesser extent, glucose. As a result, it may, in addition to food, also be found in heat-sterilized parenteral nutritional solutions containing glucose/fructose (16). The quantitative analysis of 5-HMF in clinical research and therapeutics is of great importance as in foods (17). Various methods have been defined for the measurement of 5-HMF levels, including colorimetric, spectroscopic, chromatographic, polarographic and two spectrophotometric methods; White's method and Winkler's method (6,18,19). HPLC method and spectrophotometric methods were recently tested by the International Honey Commission (IHC) (20). The first used before the spectrophotometric methods were optical and chemical methods (17). The basis of the White's method is based on the measurement of UV absorbance of clarified aqueous honey solutions with and without bisulfite. In the other spectrophotometric Winkler method, the UV absorbance of honey solutions with barbituric acid and p-toluidine is measured. Although these two methods are fast, their sensitivity and specificity are not sufficient. In addition, the use of carcinogen p-toluidine in the Winkler's method is a disadvantage. The disadvantage of the HPLC method is that it is more expensive, but it provides advantages in terms of both labor and time (20,21). In the HPLC method is according to Jeuring and Kuppers: firstly honey is dissolved in water. 5-HMF is determined on a reversed phase HPLC column with water and methanol as isocratic mobile phase after millipore filtration (21). Borate is used as supporting electrolyte in electrochemical method. The basis of the method is a single and sharp reduction signal against the silver or silver chloride (22). Yuan *et al.* have used the ion exchange liquid chromatography with photodiode array detection technique (23). Another method used in 5-HMF analysis is the automated flow injection method which provides a detection range of 5-40 ppm (24). Caffeine is used as an internal standard in micellar electrokinetic capillary chromatography, which is used in 5-HMF analysis. This technique allows rapid quantification of the sample, especially in honey

without prior pretreatment (25). The real time coupled with time of flight mass spectrometry is another method used in 5-HMF analysis (26). Based on the information from the literature review, we conclude that the differences between the methods cause very low levels of changes in the 5-HMF results. On the other hand, the use of incorrect or inadequate procedures in the 5-HMF determination leads to inaccurate results. We preferred the HPLC-DAD method among these listed methods. Because this method is a rapid, sensitive and automated method that separates 5-HMF from other related compounds in syrup samples and prevent interference in the determination. To our knowledge this is the first study to measure 5-HMF amount in pharmaceutical syrups by using HPLC-DAD method. Apart from syrups, several other pharmaceutical preparations, including tablets, capsules, micropellets, pills, ampules, mouthwashes, pomades and creams, tend to be stored at room temperature, which is defined as 25 °C degrees or lower (15–25 °C). However, in Turkey, ambient temperatures may exceed 40 °C during the summer. It is known that 5-HMF levels increase in foods and pharmaceutical preparations stored at high temperatures and for long durations after production.

The present study investigates the effects of post-expiration temperatures on 5-HMF levels in pharmaceutical syrup formulations exposed to high temperatures after their expiration date.

MATERIALS AND METHODS

Chemicals
The 5-Hydroxymethyl-2-furfural (5-HMF) was obtained from Dr. Ehrenstorfer GmbH (Germany). Methanol was analytical grade and was obtained from Merck (Darmstadt, Germany). Ultrapure water was used in all experiments (Milli-Q system, Millipore, Bedford, MA).

Preparation of stock and standard solutions
On the day of the experiment, 10 mg of high purity (>98%) 5-HMF standard was weighed using an analytic scale and completed to 100 mL with ultrapure water in a 100 mL volumetric flask. This provided 100 ppm of stock standard solution. From this stock standard, 1, 2, 5, 10 and 50 mL solutions were transferred to 100 mL volumetric flasks and the volumes were completed to the mark line using ultrapure water, which provided 1, 2, 5, 10 and 50 ppm standard solutions.

Preparation of samples
The study was carried out using 10 different pharmaceutical syrup samples obtained from the pharmacy. The syrups were kept at room temperature (25±2 °C) for 72 hours. Separate 30 g samples were taken from each syrup and stored for 72 hours in an incubator set to 40±2 °C (Thermo Scientific Heratherm). Then, 10 grams of the samples were taken from the syrups kept at both temperatures and dissolved in 25 mL of

ultrapure water, quantitatively transferred to a 50 mL volumetric flask and completed to 50 mL with ultrapure water. The flasks were placed in a shaker for 15 minutes to ensure complete dissolution of the syrup. Before injection into the HPLC column, the solutions were sampled into syringes and passed through a 0.45 µm filter (SIMPLEPURE) and then transferred to 2 mL amber vials. The 5-HMF samples were kept protected from light and air throughout the study.

Instruments

Chromatography analyses were carried out with an Agilent 1100 HPLC device, which comprises a degasser (G1379A), quaternary pump (G1311A), autosampler (G1313A) and diode array detector (DAD) model G1315. Separations were carried out in an ACE C18 column, 250 x 4.6 mm x 5 µm particle sized. The mobile phase used was methanol: water (90: 10, v/v); the prepared mobile phase was placed into the HPLC device and passed through the column at a flow rate of 1 mL/min to condition the column. The samples transferred to the vials were injected into the HPLC system. Flow rate: 1 mL/min. Injection time: 20 min. The temperature of the column compartment was 25 °C and injection volume was

20 µL. Monitoring of the analytes was carried out using a DAD detector at 284 nm wavelength (27).

The determined limit of detection (LOD, S/N=3) and limit of quantification (LOQ, S/N=10) values for 5-HMF substances were 0.011 µg/mL and 0.036 µg/mL, respectively. The linearity of the method used was tested in the concentration range of 1-50 mg/L by means of an 5-HMF standard (GmbH, Germany).

Statistical analysis

The statistical analysis of the data was carried out using the SPSS Version 11.5 statistical package software (SPSS Inc., Chicago, IL, USA) and was expressed as mean±SD. A Mann-Whitney U-test was used for the comparison of the two independent groups and a Pearson correlation test was used in the evaluation of the correlations. P values <0.05 were considered statistically significant.

RESULTS AND DISCUSSION

The analyzed syrups contained raspberry, orange, grape and mixed-fruit sweeteners, and all of the samples had reached their expiration date (Table 1).

Table 1: Flavor and sweetener contents of the expired pharmaceutical syrups.

Sample name	Expiration date (month)	Sweetener	Flavor
S1	2	Sucrose	-
S2	4	Sucrose	Mixed-fruits
S3	15	Glycerin	Mixed-fruits
S4	11	Glycerin	Orange
S5	12	Sucralose	Mixed-fruits
S6	5	Sucrose	Raspberry
S7	6	Sodium saccharine	Mixed-fruits
S8	4	Sucrose	Orange
S9	15	Sodium saccharine	Raspberry
S10	1	Sucrose	Grape

Figure 1 shows the calibration curve of standard solutions, and the chromatograms of standard solutions of 5-HMF and a syrup sample injected with 5-HMF content. The calibration curve was drawn using peak areas of increasing concentrations of standard solutions (1, 2, 5, 10, and 50 µg/mL) (Figure 1A). Calibration curve of increasing concentrations of 5-HMF standards was drawn by evaluating five replicates of each.

Retention time was estimated as minute 10.038 for the chromatogram of the 10 µg/mL standard solution (Figure 1B). In the syrup sample, the

peak level for 5-HMF was attained at minute 10.493 (Figure 1C). 5-HMF was not detected in not expired syrup sample of S7 (Figure 1D).Three replicates of syrup samples were analyzed. The mean 5-HMF level in the syrup samples stored at room temperature was 7.50 µg/mL, while the mean 5-HMF level in the incubated syrup samples was 8.88 µg/mL. A total of four samples were studied from each syrup sample to keep two of them in room temperature and the other two in incubation. Table 2 shows the 5-HMF levels of syrups stored at different temperatures for 72 hours.

Table 2: 5-HMF concentrations in syrups stored at different temperatures (µg/mL).

Sample name	25±2 ºC	40±2 ºC
S1	4.94±0.11	6.54±0.80
S2	6.98±0.14	9.10±0.18
S3	n.d.	n.d.
S4	n.d.	n.d.
S5	1.34±0.31	4.85±1.24
S6	2.87±0.03	2.24±0.20
S7	15.63±0.92	18.24±2.08
S8	10.84±1.37	11.56±1.22
S9	13.21±0.20	13.92±1.33
S10	4.20±0.42	4.59±0.41

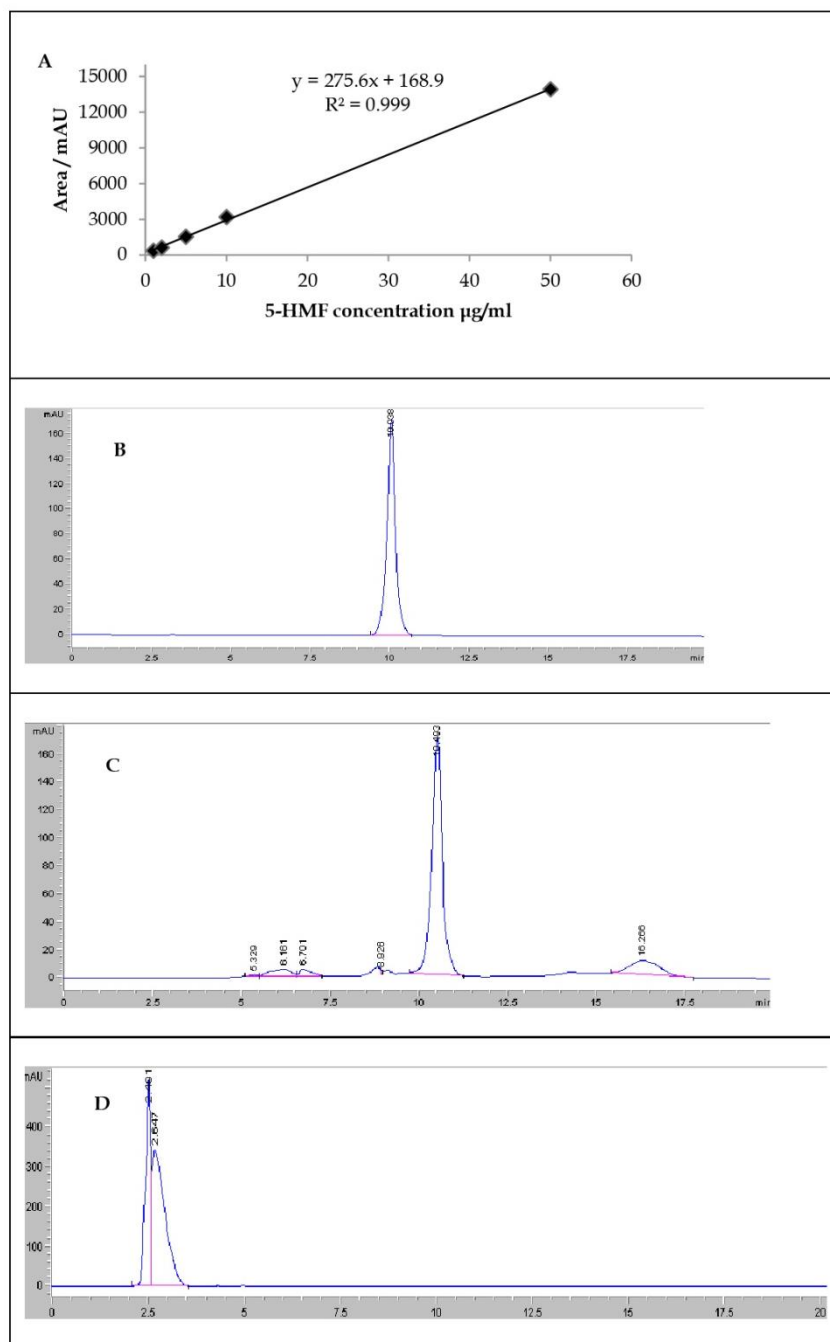n.d: not detected. Results are presented as mean ± SD.

Figure 1. A) Calibration curve of standard solutions of 5-HMF. **B)** Chromatogram of injected standard 5-HMF **C)** Chromatogram of 5-HMF in a expired syrup sample.**D)**HPLC result of not expired pharmaceutical syrup sample.

Although heat treatment increased 5-HMF content in all samples except one, the increases were not statistically significant (p: 0.638).

The relationship between time after expiration and 5-HMF content was evaluated for syrups with different expiration dates (Figure 2). Although a positive correlation was found, the relationship between the variables was weak (r: 0.227) and insignificant (p: 0.588).
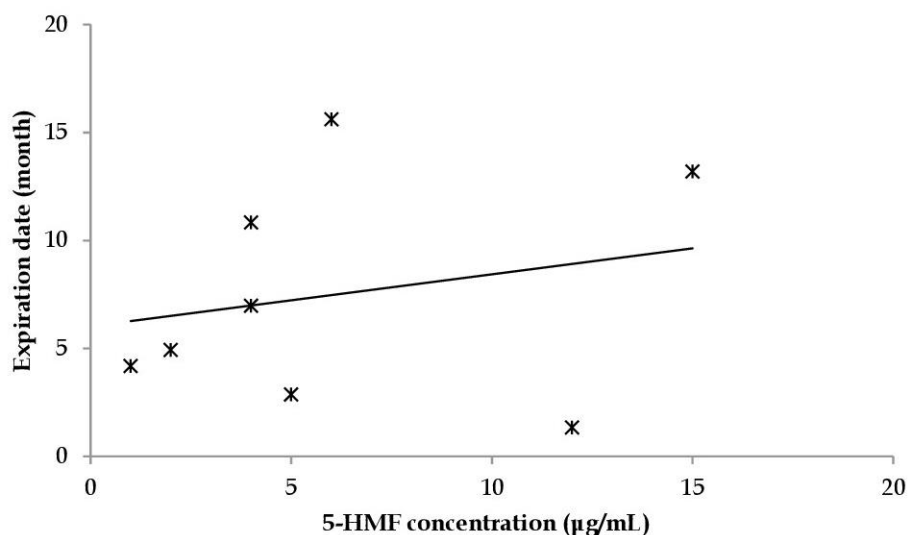
Figure 2. Correlation between time after expiration and 5-HMF content.

Human exposure to 5-HMF essentially occurs through the consumption of processed foods and beverages, the use of pharmaceutical preparations and the inhalation of tobacco smoke. It may also occur occasionally through occupational exposure as a result of the inhalation of the vapor of solutions including 5-HMF, and dermal contact with these compounds in facilities producing or using 5-HMF-derived polymers or chemicals (11).

5-HMF is metabolically activated through the sulfonation of the allylic hydroxyl functional groups by sulfotransferases (SULT1A1), and its bioactivation results in the formation of 5-sulfoxymethylfurfural (SMF) (28,29). It shows no effect in standard genotoxicity tests, but its mutagenic and carcinogenic activities depend on the reactive by product SMF (30). In cell culture studies, it has been reported to have weak genotoxic effects on the HepG2 cell lines (31), and it can also cause DNA damage in cells, irrespective of SULT1A1 activity. However, DNA damage caused by 5-HMF has only been observed in high concentrations. For instance, a significant level of 5-HMF-induced DNA damage was reported after exposure to 5-HMF at a concentration of 100 mM for three hours (28). Both 5-HMF and SMF were found to be weak intestinal carcinogens in mice (32). In addition, high concentrations of 5-HMF have been shown to have irritant effects on the upper respiratory airways, eyes, skin and mucosal membranes. Based on findings obtained from experimental animals, 5-HMF was suggested to have tumorigenic and colon cancer-stimulating effects (6), and some researchers have reported that 5-HMF can act as a neurotoxin, and that its accumulation in the body and interactions with proteins may result in muscle and visceral lesions (33). Taking all this into account, it has become a substance of interest for researchers, and the presence of 5-HMF in foods has raised toxicological concerns (29).

Later studies have suggested that this is not the case, and the carcinogenic activity of 5-HMF has been rejected through direct or indirect investigations (34). Apart from the absence of established genotoxic, mutagenic or carcinogenic activities, some studies in recent years have reported that 5-HMF may even have some favorable effects, for example, as a potential new antioxidant in the fight against cancer (35). It is also shown to have beneficial physiological effects, such as reducing oxidative stress resulting from high glucose levels (36), neuroprotective effects (37), anti-hypoxic effects (38), anti-allergenic effects (39) and anti-inflammatory activity (40).

While several countries have established limits for 5-HMF content in food products, it is important to consider countries with hot climate conditions when defining such limits for 5-HMF content. The 5-HMF limit in honey has been defined as 40 ppm, whereas a level of 80 ppm was considered the standard for countries with hot climates (41). In Turkey, the upper limits for honey, fruit juice and molasses products have been defined as 40 mg/kg, 20 mg/kg, and 75 mg/kg, respectively (42).

While 5-HMF is formed spontaneously, it is generally produced during autoclaving. If pharmaceutical fluids contain glucose, the heat applied during sterilization may cause breakdown and the formation of 5-HMF, and it has been detected in dialysis solutions containing 1 to 60 percent glucose (pH 1-8) that were heat-sterilized at 121 °C (43). The concentrations detected in sterile glucose solutions, intravenous solutions and glucose solutions vary between 1–90 mg/L, 3–56 mg/L and 1–4 mg/L, respectively. 5-HMF concentrations have also been positively correlated with high acidity (pH<4), high sterilization temperatures (>110 °C) and long sterilization times (30 min) (11).

Another study investigated preparations of intravenous injection solutions containing 10 percent fructose, which had a pH lower than 3.5–4.0 and were sterilized at temperatures between 110 and 130 °C. Concentrations of 5-HMF in a newly prepared 50 percent dextrose solution were found to be 0.10 µg/mL, while this level increased to 0.72 µg/mL 24 hours after preparation, and following four years of storage at 70 °F (21.1 °C), 5-HMF levels increased to 5.8 µg/mL (44).

Fruits contain varying amounts of 5-HMF due to different sugar and organic acid contents (citric, malic, and ascorbic acids, etc.). Both the highest and the lowest 5-HMF levels were found in syrup samples with mixed fruit as flavor agent. Also the second lowest and the second highest levels were found in grape flavored syrups. On the other hand, 5-HMF was not detected in syrup samples containing glycerin as a sweetener. 5-HMF is produced as a result of dehydration of fructose, glucose, and other reducing sugars and in the early stages of the Maillard reaction. Therefore, 5-HMF formation is not expected in the syrup samples containing glycerin. The reason for using two syrup samples containing glycerin in this study is to contribute to this situation. The results show that there is no effect of flavors on 5-HMF levels.

A positive correlation has been noted in the evaluation of 5-HMF level and expiration date, although this cannot be directly associated with the expiration date, as syrup samples contain different types and amounts of sweeteners. There is also the same situation in food products not only in pharmaceutical formulations. The formation of 5-HMF increases in parallel with the storage time of foods.

High temperatures induce the formation of 5-HMF. Aside for in one sample, the 5-HMF content in syrups kept at 40±2 °C was found to be higher than those kept at room temperature. But this increase was not statistically significant (p>0.05). There may be a significant increase in the longer incubation time at higher temperatures. However, our aim was to show that the level could be increased even in short-term small temperature increases.

The highest levels were found in two samples that sodium saccharin used as a sweetener. 5-HMF commonly occurs by the dehydration of monosaccharides and disaccharides. A study investigated the effects of different temperatures and pH values on 5-HMF formation while preparing simple syrups, and based on the findings, the authors concluded that pH and storage temperature had significant effects on 5-HMF formation. Accordingly, the best way to avoid 5-HMF formation is to prepare the syrup under high pH conditions while maintaining low storage temperatures, although there have been no studies to date concerning the effects of pH and temperature on 5-HMF formation in syrups (16).

The presence of 5-HMF and similar compounds in some parenteral preparations containing dextrose, solutions prepared for peritoneal dialysis and also some excipients used in pharmaceutical sector is a marker of quality for pharmaceutical products. Based on European Pharmacopeia, the level of dextrose in solutions used for peritoneal dialysis should not exceed 10 µg 5-HMF and 25 mg dextrose if they contain no bicarbonate, and 20 µg 5-HMF and 25 mg dextrose if they contain bicarbonate (45). While 5-HMF limits are set by the relevant regulations, factors such as technological processes, the sugar content of medical products, and the storage conditions of foods and pharmaceutical products should be considered.

CONCLUSION

The storage conditions of medications are generally defined according to mild climatic conditions and low sunlight. If extremely hot climatic conditions are not taken into account, the stability of medications may become a source of significant problems in countries with high temperature and sunlight levels. None of the syrup samples we analyzed were contain 5-HMF above the legal limits set for foods. Although 5-HMF content was not found to be high in the syrups analyzed in the present study, there may still be interactions with the amino groups in pharmaceutical formulations, and changes might be seen in the activity of such drug products. Accordingly, even insignificant amounts of 5-HMF and similar by products in medical formulations and foods should not be ignored. 5-HMF levels can exceed legal limit in several food items. The only food for which a legal limit on 5-HMF concentrations has been set is honey. 5-HMF may exceed tolerable daily intake as a result of taking from different sources such as foods and medicine. Therefore monitoring of 5-HMF contents in foods and medical products used by sensitive populations, especially children seems to be necessary. Syrups containing sweeteners were used in our study. This type of syrups are mostly used by children. Other 5-HMF sources include sugar-containing foods such as honey, jam, fruit juices, which children consume frequently. A low concentration of 5-HMF does not mean that it does not cause toxicity. Because it can accumulate during both nutrition and medical treatment.

REFERENCES

1. National Center for Biotechnology Information. PubChem Compound Database; CID=237332, https://pubchem.ncbi.nlm.nih.gov/compound/237332 (accessed July 3, 2018).

2. Zakrzewska ME, Bogel-Lukasik E. Bogel-Lukasik R. Ionic Liquid-Mediated Formation of 5-hydroxymethylfurfural - a Promising Biomass-

Derived Building Block. Chem Rev. 2011;111(2):397-417.

3. Brode GL, Mark HF, Othmer DF, Overberger CG, Seaborg GT, Grayson M. In Encyclopedia of Chemical Technology, Kirk RE, Othmer DF, Eds. Wiley, New York, 1982;17:411-3.

4. Larousse C, Rigal L, Gaset A. Synthesis of 5,5'-oxydimethyl bis (2-furfural) by Thermal Dehydratation of 5-hydroxymethyl Furfural in the Presence of Dimethylsulfoxide. J Chem Technol Biotechnol. 1992;53(1):111-6.

5. Kunz M. Hydroxymethylfurfural, a Possible Basic Chemical Industrial Intermediates. In Inulin and Inulin-Containing Crops, Fuchs A, Ed. Elsevier Science Publishers, Amsterdam, The Netherlands, 1993;3:149-60.

6. Morales FJ. Hydroxymethylfurfural (HMF) and related compounds. Process-Induced Food Toxicants: Occurence, Formation, Mitigation and Health Risks, (eds: Stadler, R H, Lineback DR), A john Wiley & Sons Inc Publications, 2009.

7. Ruiz-Matute AI, Weiss M, Sammataro D, Finely J, Sanz ML. Carbohydrate Composition of High-Fructose Corn Syrups (HFCS) Used for Bee Feeding: Effect on Honey Composition. J Agric Food Chem. 2010;58(12):7317-22.

8. Arribas-Lorenzo G, Morales FJ. Estimation of Dietary Intake of 5-hydroxymethylfurfural and Related Substances From Coffee to Spanish Population.Food Chem Toxicol. 2010;48(2):644-9.

9. Husøy T, Haugen M, Murkovic M, Jöbstl D, Stølen LH, Bjellaas T, Rønningborg C, Glatt H, Alexander J. Dietary Exposure to 5-hydroxymethylfurfural From Norwegian Food and Correlations with Urine Metabolites of Short-term Exposure. Food Chem Toxicol. 2008;46(12):3697-3702.

10. Rufían-Henares JA, de la Cueva SP. Assessment of Hydroxymethylfurfural Intake in the Spanish Diet. Food Addit Contam Part A Chem Anal Control Expo Risk Assess. 2008;25(11):1306-12.

11. NTP, Testing Status of Agents at NTP. 5-(Hydroxymethyl)-2-furfural. Nomination Background. Washington, DC: National Toxicology Program, Dept Health Human Serv. https://ntp.niehs.nih.gov/testing/noms/search/summary/nm-n95002.html (accessed May 18, 2018).

12. Gökmen V, Senyuva HZ. Improved Method for the Determination of Hydroxymethylfurfural in Baby Foods Using Liquid Chromatography-mass Spectrometry. J Agric Food Chem. 2006;54(8):2845-9.

13. Delgado-Andrade C, Seiquer I, Navarro MP, Morales FJ. Maillard Reaction Indicators in Diets Usually Consumed by Adolescent Population. Mol Nutr Food Res. 2007;51(3):341-51.

14. Abraham K, Gürtler R, Berg K, Heinemeyer G, Lampen A, Appel KE. Toxicology and Risk Assessment of 5-Hydroxymethylfurfural in Food. Mol Nutr Food Res. 2011;55(5):67-78.

15. Hewala II, Blaih SM,nZoweil AM, Onsi SM. Detection and Determination of Interfering 5-hydroxymethylfurfural in the Analysis of Caramel-coloured Pharmaceutical Syrups. J Clin Pharm Ther. 1993;18(1):49-53.

16. Ghaderi F, Shadbad MRS, Hoseinzadehm. Effect of pH and Storage Temperature on 5-(hydroxymethyl) Furfural (5HMF) Formation in USP Syrup Preparation. Pharm Sci. 2015;21(1):1-5.

17. Shapla UM, Solayman M, Alam N, Khalil MI, Gan SH. 5-Hydroxymethylfurfural (HMF) Levels in Honey and Other Food Products: Effects on Bees and Human Health. Chem Cent J. 2018;12(1):35.

18. Zappalà M, Fallico B, Arena E, Verzera A. Methods for the Determination of HMF in Honey: a Comparison. Food Control. 2005;16(3):273-7.

19. Sivakesava S, Irudayaraj J. A Rapid Spectroscopic Technique for Determining Honey Adulteration with Corn Syrup Direct Electrochemical Determination of Hydroxymethylfurfural (HMF) and its Application to Honey Samples. J Food Sci. 2001;66(6):787-92.

20. IHC, The International Honey Commission. Bogdanov S. 1999; 1–54. http://www.ihc-platform.net/ihcmethods2009.pdf (accessed October 18, 2018).

21. Wootton M, Ryall L. A Comparison of Codex Alimentarius Commission and HPLC Methods for 5-hydroxymethyl-2-furaldehyde Determination in Honey. J Apic Res. 1985;24(2):120124.

22. Reyes-Salas EO, Manzanilla-Cano JA, Barceló-Quintal MH, Juárez-Mendoza D, Reyes-Salas M. Direct Electrochemical Determination of Hydroxymethylfurfural (HMF) and its Application to Honey Samples. Anal Lett. 2006;39(1):161-171.

23. Yuan JP, Chen F. Separation and Identification of Furanic Compounds in Fruit Juices and Drinks by High-performance Liquid Chromatography Photodiode Array Detection. J Agric Food Chem. 1998;46:1286-91.

24.   De la Iglesia F, Lázaro F, Puchades R, Maquieira A. Automatic Determination of 5-hydroxymethylfurfural (5-HMF) by a Flow Injection Method. Food Chem. 1997;60(2):245-50.

25.   Rizelio VM, Gonzaga LV, Borges GdSC, Micke GA, Fett R, Costa ACO. Development of a Fast MECK Method for Determination of 5-HMF in Honey Samples. Food Chem. 2012;133:1640-5.

26.   Rajchl A, Drgová L, Grégrová A, Čížková H, Ševčík R, Voldřich M. Rapid Determination of 5-hydroxymethylfurfural by DART Ionization with Time-of-flight Mass Spectrometry. Anal Bioanal Chem. 2013;405:4737-45.

27.   Jeurings J, Kuppers F. High Performance Liquid Chromatography of Furfural and Hydroxymethylfurfural in Spirits and Honey. J Assoc Off Anal Chem. 1980;63(6):1215-8.

28.   Durling LJ, Busk L, Hellman BE. Evaluation of the DNA Damaging Effect of the Heat-induced Food Toxicant 5-hydroxymethylfurfural (HMF) in Various Cell Lines with Different Activities of Sulfotransferases. Food Chem Toxicol. 2009;47(4):880-4.

29.   Murkovic M, Pichler N. Analysis of 5-hydroxymethylfurfual in Coffee, Dried Fruits and Urine. Mol Nutr Food Res. 2006;50(9):842-6.

30.   Bakhiya N, Monien B, Frank H, Seidel A, Glatt H. Renal Organic Anion Transporters OAT1 and OAT3 Mediate the Cellular Accumulation of 5 Sulfooxymethylfurfural, a Reactive, Nephrotoxic Metabolite of the Maillard Product 5-hydroxymethylfurfural. Biochem Pharmacol. 2009;78(4):414-9.

31.   Severin I, Dumont C, Jondeau-Cabaton A, Graillot V, Chagnon MC. Genotoxic Activities of the Food Contaminant 5-hydroxymethylfurfural Using Different in Vitro Bioassays. Toxicol Lett. 2010;192(2):189-94.

32.   Svendsen C, Husoy T, Glatt H, Paulsen JE, Alexander J. 5-Hydroxymethylfurfural and 5-Sulfooxymethylfurfural Increase Adenoma and Flat ACF Number in the Intestine of Min/+ Mice. Anticancer Res. 2009;29(6):1921-6.

33.   Li Y, Lu X. Investigation on the Origin of 5-HMF in Shengmaiyin Decoction by RP-HPLC Method. J Zhejiang Univ Sci B. 2005;6(10):1015-21.

34.   Michail K, Matzi V, Maier A, Herwig R, Greilberger J, Juan H, Kunert O, Wintersteiger R. Hydroxymethylfurfural: an Enemy or a Friendly Xenobiotic? A Bioanalytical Approach. Anal Bioanal Chem. 2007;387(8):2801-14.

35.   Zhao L, Chen J, Su J, Li L, Hu S, Li B, Zhang X, Xu Z, Chen T. In vitro Antioxidant and Antiproliferative Activities of 5-hydroxymethylfurfural. J Agric Food Chem. 2013;61(44):10604-11.

36.   Cao G, Cai H, Cai B, Tu S. Effect of 5-hydroxymethylfurfural Derived from Processed Cornus Officinalis on the Prevention of High Glucose-induced Oxidative Stres in Human Umbilical Vein Endothelial Cells and Its Mechanism. Food Chem. 2013;140(1-2):273-9.

37.   Liu A, Zhao X, Li H, Liu Z, Liu B, Mao X Guo L, Bi K, Jia Y. 5-Hydroxymethylfurfural, an Antioxidant Agent from Alpinia Oxyphylla Miq. İmproves Cognitive Impairment in Aβ 1−42 Mouse Model of Alzheimer's Disease. Int Immunopharmacol. 2014;23(2):719-25.

38.   Li MM, Wu LY, Zhao T, Xiong L, Huang X, Liu ZH Fan XL, Xiao CR, Gao Y, Ma YB, Chen JJ, Zhu LL, Fan M. The Protective Role of 5-HMF Against Hypoxic Injury. Cell Stress Chaperones 2011;16(3):267-73.

39.   Yamada P, Nemoto M, Shigemori H, Yokota S, Isoda H. Isolationof 5-(hydroxymethyl) Furfural from Lycium Chinense and its Inhibitory Effect on the Chemical Mediator Release by Basophilic Cells. Planta Med. 2011;77(5):434-40.

40.   Alizadeh M, Khodaei H, Mesgari Abbasi M, Saleh-Ghadimi S. Assessing the Effect of 5-hydroxymethylfurfural on Selected Components of Immune Responses in Mice Immunised with Ovalbumin. J Sci Food Agric. 2017;97(12):3979-84.

41.   JECFA, Joint of FAO/WHO Food Standards Ppogramme Codex Committee on Sugars Seventh Session London, United Kingdom, 9-11 February 2000. www.fao.org/input/download/standards/310/cxs_012e.pdf (accessed January 11, 2018).

42.   TFC. Turkish Food Codex, Meyve Suyu ve Benzeri Ürünler Tebliği, Tebliğ No: 2014/34. http://www.resmigazete.gov.tr/eskiler/2014/08/20140806-17.htm. (accessed January 18, 2018).

43.   Kjellstrand P, Martinson E, Wieslander A, Kjellstrand K, Jeppsson E, Svensson E, Järkelid L, Linden T, Olsson LF. Degradation in Peritoneal Dialysis Fluids may be Avoided by Using Low pH and High Glucose Concentration. Perit Dial Int. 2001;21(4):338-44.

44.   Ulbricht RJ, Northup SJ, Thomas JA. A Review of 5-hydroxymethylfurfural (HMF) in Parenteral Solutions. Fundam Appl Toxicol. 1984;4(5):843-53.

45.   European Council Directive 2001/110/EC of 20.12.2001. European Pharmacopoeia 8.0,

Council of Europe. European Directorate for the Quality of Medicines and Health Care. https://www.fsai.ie/uploadedFiles/Consol_Dir2001_110.pdf. (accessed April 7, 2018).